NORTHWESTERN UNIVERSITY

Control of Electronic Spin in the Design of Transition Metal-Based Bioresponsive Magnetic Resonance Imaging Probes and Metal-Organic Magnets

A DISSERTATION

SUBMITTED TO THE GRADUATE SCHOOL
IN PARTIAL FULFILLMENT OF THE REQUIREMENTS

for the degree

DOCTOR OF PHILOSOPHY

Field of Chemistry

By

Agnes Eva Thorarinsdottir

EVANSTON, ILLINOIS

December 2019

Abstract

Control of Electronic Spin in the Design of Transition Metal-Based Bioresponsive Magnetic Resonance Imaging Probes and Metal-Organic Magnets

Agnes Eva Thorarinsdottir

Molecules and materials featuring unpaired electrons are fundamental elements of modern energy, device, and imaging technologies. The high sensitivity of electronic spins to their surroundings renders these compounds further attractive as environmental sensors. In order to successfully realize these applications, the electronic spins must be precisely controlled. One promising strategy toward generating compounds with improved performances and emerging properties involves spin control using the chemical design of coordination compounds. Transition metal-based compounds are especially well suited to this end owing to their exceptional synthetic tunability, high environmental responsiveness, and ease of manipulating their spin state and electronic structure. Nevertheless, the employment of molecule-based transition metal compounds in practical settings is scarce and further investigations are necessary to develop design principles that allow for the rational synthesis of such compounds that meet society's expectations.

In this dissertation, I report efforts to manipulating the electronic structure and spin state of series of transition metal complexes to design responsive magnetic resonance imaging (MRI) probes and to elucidate design principles for molecule-based magnets with high operating temperatures. I have focused on compounds featuring Fe^{II} and Co^{II} metal centers due to their favorable magnetic and nuclear magnetic resonance (NMR) properties. Chapter 1 describes the need for new bioresponsive MRI probes and metal-organic magnets and outlines our synthetic strategies to these ends. Chapter 2 details the first example of a spin-crossover Fe^{II} complex for sensing temperature using ^{19}F NMR chemical shift and illustrates that a temperature-dependent

change in electronic spin state can significantly improve the sensitivity of ^{19}F MR thermometers. Chapter 3 describes a novel proof-of-principle study for the ratiometric quantitation of pH using Co^{II}_2 paramagnetic chemical exchange saturation transfer (PARACEST) probes. Building on the strategy developed in Chapter 3, Chapters 4 and 5 are complementary in describing our thorough investigation of how ligand modifications can enhance the performance of this family of Co^{II}_2 PARACEST pH probes. These studies lead to the discovery of a probe that exhibits one of the highest pH sensitivity yet reported for a ratiometric MRI probe in the physiological pH range. Chapter 6 illustrates that changes in the magnetic anisotropy at Co^{II} can be employed to distinguish between Ca^{2+} and Na^{+} ions in solution, providing the first example of a ratiometric quantitation of Ca^{2+} concentration using PARACEST. Finally, Chapter 7 examines the effects of bridging ligand substituents on magnetic exchange coupling in two series of benzoquinoid-bridged Fe^{II}_2 complexes and Chapter 8 provides a thorough survey of structurally characterized metal-organic framework magnets. Together, these results demonstrate that the high chemical and magnetic tunability of transition metals enables the realization of compounds with unprecedented properties.

Acknowledgments

I would certainly not be where I am today without the support of many great people. I am going to try my best to acknowledge them below.

First of all, I would like to thank my advisor, Prof. Dave Harris, for his excellent mentorship and continuous support throughout my time at Northwestern, and for sharing his scientific curiosity and passion for science. Dave developed me into the scientist that I am today, and I am very grateful that he paid attention to my application and accepted me into his group even though I was so shy at that time that I could barely communicate what I liked about his research! Dave taught me to carry out every single experiment with rigor, to thoroughly analyze every aspect of the data, and to be my own biggest criticizer. But not only did Dave advance my scientific thinking and laboratory skills, he also helped me a lot improve my science communication skills in both written and spoken language. Specifically, he taught me the importance of telling a story when giving a presentation or writing a paper. Before I started graduate school, I did not realize how extremely important it is to be able to communicate effectively, but I certainly do now, and I am very grateful for all his constructive feedback. Furthermore, I greatly appreciate the trust Dave put in me early on and the opportunities he provided that have led to my professional development, including improving my laboratory management, mentoring, and teaching skills. The broad experience that I gained in the Harris group will be very valuable for my future career. I also want to thank Dave for connecting me with a wide range of people within the inorganic chemistry community, including big leaders in the field. I am sure that these connections will be highly beneficial for my future career as well.

Second, I want to thank Prof. Danna Freedman, who I was very fortunate to have as my second advisor. Danna was extremely supportive of me throughout my entire graduate school career and

very approachable whenever I needed a piece of advice. I greatly appreciate Danna's mentorship and all the scientific and non-scientific advice she gave me over the past couple of years that have helped me to grow both as an independent researcher and as a person. Danna has been a great inspiration to me and she has taught me many important things regarding running a research group and interacting with colleagues and administrative parties, which will be a valuable knowledge for my future career. I hope that I will one day follow in her successful footsteps!

Next, I would like to thank Prof. Tom Meade and Prof. Tom O'Halloran for their guidance and continuous support over the years, in particular throughout my qualifying exam and research proposal. I greatly appreciate their interest in my work and constructive feedback, and that I could always come to them to get some advice on any problems that I had. They taught me the importance of thinking every single experiment and research idea fully through, and to always keep the big picture in mind. I would further like to thank Tom Meade for allowing me to use his laboratory space and equipment. This greatly advanced my research and his group members were like a second family for me. I would also like to thank Tom O'Halloran for allowing me to audit his graduate class and teaching me how to write a NIH proposal and how the organization functions. This was a valuable learning experience that will surely be of great help in my future career.

I owe big thanks to all my colleagues and friends in the Harris and Freedman groups: Dr. Alison Altman, Jeremy Amdur, Dr. Samantha Clarke, Benjamin Coleman, Kelsey Collins, Dr. Scott Coste, Dr. Jordan DeGayner, Dr. Kang Du, Dr. Majed Fataftah, Dr. Audrey Gallagher, Dr. Alexandra Gaudette, Dr. Michael Graham, Dr. Carol Hua, Dr. Ryan Klein, Daniel Laorenza, Dr. Jung Yoon Lee, Liang Li, Dr. Luke Liu, Nina Pappas, Tyler Pearson, Steph Petry, Dr. Lei Sun, Alexandra Tamerius, Scott Tatro, Dr. Stephen von Kugelgen, Dr. James Walsh, Ella Wang, Dr.

Mikey Wojnar, Raymond Yu, Dr. Joe Zadrozny, and Dr. David Zee. This team of wonderful people and hard-working scientists provided a stimulating and supportive research environment, which enabled me to grow both as a scientist and as a person and enjoy every single minute of it (at least 99%!). Specifically, I owe immense thanks to Dr. Kang Du for teaching me everything that I know about CEST. If it were not for him, I would not have mastered my qualifying exam. Kang also taught me so many tricks in the lab relevant to synthesis, experimental setup, and instrumentation. I wished that I had a tiny bit of his creativity! I thank him for being an awesome lab mate and an even better friend. I want to thank Ben, Ella, and Luke for introducing me to MOF chemistry and teaching me how to use the PXRD, Raman, and SQUID instruments, as well as preparing SQUID samples. I also want to give Dr. David Zee special thanks for teaching me so many things related to Mössbauer spectroscopy and electrochemistry, and for introducing me to all kinds of uncommon laboratory tools! On top of that, David is a great friend that I can always trust on whenever I need some advice on scientific as well as non-scientific things. I want to thank Tyler for solving all my computer-related issues and Raymond for all the evening conversations, which ranged from teaching me baseball rules to deep discussions on research ideas. Many thanks to Dr. James Walsh for teaching me so many important things, including how to manage a website, make nice-looking figures in Adobe Illustrator and Photoshop, prepare SQUID samples restricted in an eicosane matrix, and fit magnetic data. I really hope that I will be as successful postdoctoral researcher as he was! I also want to thank the superb undergraduate students, Scott and Nina, that I was fortunate to get an opportunity to train and work with. I really enjoyed working with them and greatly appreciate all their help with my science. I hope that I trained them well!

I would like to express my gratitude to past and present Meade group members for treating me as one of them and for not being bothered when I was running around their lab and using their

equipment. I want to thank Dr. Laura Lilley and Dr. Ruby Krueger for training me on the HPLC and lyophilizer, and for giving me advice on organic syntheses. I further want to thank Casey Adams, Dr. Liz Bajema, Chris Brue, Dr. Mike Caldwell, Andrew Johnson, Megan Kaster, Hao Li, Shaunna McLeod, Kaleigh Roberts, and Meghan Ward for helping me with my research over the past couple of years.

During my tenure at Northwestern, I was fortunate to work with a lot of fantastic people through my involvement with two student organizations – the chemistry graduate student honorary society PLU and the student-led safety organization RSSI. I would like to thank all my peers that I served with in these organizations, as well as the staff and faculty that helped us making our events successful. I would also like to thank the Research Safety staff, especially Dr. Michael Blayney, Iwona Spath, and Gwen Sullivan, for their support and assistance with everything related to RSSI, as well as my personal research. Special thanks to Di Wang for getting me involved in RSSI and being a great friend. I know that I can always turn to her when I have problems, not only safety-related issues!

My research would not have been nearly as successful without the help from excellent staff at the core research facilities at Northwestern and external collaborators. Specifically, I would like to thank Dr. Yongbo Zhang for all the help with running CEST and other non-traditional NMR experiments, as well as the troubleshooting after the “lovely” Bruker instruments arrived. I also owe thanks to other staff at IMSERC: Arsen Gaisin, Dr. Christos Malliakas, Saman Shafaie, Charlotte Stern, and Dr. Yuyang Wu, for being always willing to assist me with experiments and data analysis. Furthermore, I would like to thank Dr. Keith MacRenaris and Rebecca Sponenburg at QBIC for help with ICP measurements, Dr. Chad Haney and Dr. Alex Waters at CAMI for help with MRI experiments, and Dr. Fraser Aird, Dr. Irawati Kandela, and Iwona Stepien at DTC for

help with animal studies. Lastly, I would like to thank my collaborator Dr. James H. P. Collins at the National High Magnetic Field Laboratory in Gainesville, Florida, for assistance with phantom imaging studies and for training me in acquiring MRI data.

I am very fortunate to have a big supportive family and I would never have made it to the United States without their support. My parents have been extremely supportive throughout my entire education. For instance, they helped me move between towns in Iceland and brought a lot of my stuff to Evanston, and I am extremely thankful for that. Furthermore, I thank them for keeping me posted on what was happening in Iceland through our weekly video calls. I did appreciate our conversations, even though the most frequent questions and comments from them were: “did you do anything fun this week?” or “when are you going to take a day off?” or “you need to sleep more!” Nevertheless, they knew and understood that I was living my dream and therefore did everything they could to support me. I cannot thank them enough! I owe my two favorite brothers, Steinar and Auðunn, many thanks for always keeping me on my toes and giving me opportunities to take on a teacher or parenting role. I hope that they have finally realized that they are better off following my advice! I would also like to thank my grandparents and other relatives for always believing in me and supporting me, even though they have a limited understanding on what I do on a daily basis. Specifically, I want to express my deepest gratitude to my grandfather, Páll Hlöðvesson, who got me passionate about science and taught me the value in mentoring and teaching others. I am thankful for all the afternoons and evenings that we spent together solving math and physics problems. I thank him for supporting me in whatever I did and for always being the first one to call me to ask for my grades. I further thank him for providing me with various tutoring opportunities and driving me all around Akureyri to attend sport practices (so I had more time to do my homework!). I deeply wished that we would have had more time

together.

I am very grateful to my awesome friends, Heiðrún, Kolbrún, Harpa, and Steinar, who I have known since my childhood and high school years in Akureyri. They have made my life so much more enjoyable despite the long distance. I greatly appreciate their friendship and I am sorry for not giving myself more time to keep in touch with them. I hope that I can make it up to them someday!

Finally, I would like to thank my family in Libertyville for their company and assistance since I moved to Evanston. It was a happy surprise when I found out about Patrick, Amy, the boys, and the dogs, and they have been extremely helpful to me. I thank them especially for assisting me with finding an apartment, buying furniture, and moving. I also thank them for introducing me to traditional American Thanksgiving and birthday parties, and for all the sailing trips, dog walks, and dinners. I feel like I have known them forever and I cannot thank them enough for everything they have done for me. I will certainly miss them when I move to the East Coast!

List of Abbreviations

2D	two-dimensional
3D	three-dimensional
ac	alternating current
AFM	antiferromagnetic
anal	analytical
ATR	attenuated total reflectance
BET	Brunauer–Emmett–Teller
C	Celcius
ca	circa
CAFM	canted antiferromagnetic
calcd	calculated
CEST	chemical exchange saturation transfer
cm	centimeter(s)
CT	coefficient of temperature
d	day(s)
dc	direct current
ESI-MS	electrospray ionization mass spectrometry
FC	field-cooled
FiM	ferrimagnetic
FM	ferromagnetic
FTIR	Fourier-transform infrared spectroscopy
FWHM	full width at half maximum

h	hour(s)
HPLC	high-performance liquid chromatography
HS	high-spin
Hz	hertz
ICP-OES	inductively coupled plasma optical emission spectroscopy
IR	infrared
IUPAC	International Union of Pure and Applied Chemistry
K	kelvin
kHz	kilohertz
LIESST	light-induced excited spin state trapping
LMCT	ligand-to-metal charge transfer
LS	low-spin
M	molar
max	maximum
MCD	magnetic circular dichroism
mer	meridional
MHz	megahertz
min	minute(s)
MLCT	metal-to-ligand charge transfer
mm	millimeter(s)
mM	millimolar
MOF	metal-organic framework
MR	magnetic resonance

MRI	magnetic resonance imaging
MRS	magnetic resonance spectroscopy
mV	millivolt(s)
m/*z*	mass-to-charge ratio
NHE	normal hydrogen electrode
NIR	near infrared
nm	nanometer(s)
NMR	nuclear magnetic resonance
p	*para*
PARACEST	paramagnetic chemical exchange saturation transfer
ppm	parts per million
PRF	proton resonance frequency
PXRD	powder X-ray diffraction
rac	racemate
ref	reference
s	second(s)
SCE	saturated calomel electrode
SCM	single-chain magnet
SCXRD	single-crystal X-ray diffraction
SQUID	superconducting quantum interference device
UV	ultraviolet
v/v	volume/volume
Vis	visible

vs	versus
VT	variable-temperature
w/v	weight/volume
w/w	weight/weight
ZFC	zero-field-cooled
μM	micromolar
μT	microtesla
B_1	saturation power
$(BH)_{max}$	maximum energy density
D	axial zero-field splitting parameter
$E_{1/2}$	half-wave potential
ΔE_Q	quadrupole splitting
g	electron spin g-factor
H_c	coercive field
ΔH	enthalpy change
J	coupling constant
K_d	dissociation constant
k_{ex}	proton exchange rate constant
M_r	remanent magnetization
M_s	saturation magnetization
M_z	on-resonance magnetization
M_0	off-resonance magnetization
S	electronic spin state

ΔS	entropy change
T_1	spin–lattice relaxation time
T_2	spin–spin relaxation time
$T_{1/2}$	spin-crossover temperature
T_b	magnetic bifurcation temperature
T_B	magnetic blocking temperature
T_c	critical magnetic ordering temperature
T_C	Curie temperature
T_{comp}	magnetic compensation temperature
T_N	Néel temperature
U_{eff}	effective energy barrier
χ_M	molar dc magnetic susceptibility
χ_M'	molar ac in-phase magnetic susceptibility
χ_M''	molar ac out-of-phase magnetic susceptibility
δ	chemical shift/isomer shift
Δ_τ	relaxation barrier
ε	molar absorptivity
Σ	octahedral distortion parameter
γ_{HS}	high-spin molar fraction
Γ_L	line width of the left line of a quadrupole doublet
Γ_R	line width of the right line of a quadrupole doublet
λ	wavelength
τ	relaxation time

τ_0	pre-exponential factor
θ	Weiss constant/temperature
Me	methyl
Et	ethyl
Pr	propyl
^{i}Pr	*iso*-propyl
Bu	butyl
^{t}Bu	*tert*-butyl
Pe	pentyl
Hx	hexyl
Hp	heptyl
Ph	phenyl
Bz	benzyl
AcOH	acetic acid
TFA	trifluoroacetic acid
DMA	*N*,*N*-dimethylacetamide
DMF	*N*,*N*-dimethylformamide
DEF	*N*,*N*-diethylformamide
DMSO	dimethylsulfoxide
MeOH	methanol
EtOH	ethanol
PrOH	propanol
CyOH	cyclohexanol

MeBuOH	3-methyl-1-butanol
TFE	trifluoroethanol
MeCN	acetonitrile
$MeNO_2$	nitromethane
Et_2O	diethyl ether
THF	tetrahydrofuran
PhMe	toluene
4-ClPhMe	4-chlorotoluene
PhBr	bromobenzene
PhCl	chlorobenzene
PhI	iodobenzene
PhCN	cyanobenzene
$PhNO_2$	nitrobenzene
FBS	fetal bovine serum
HEPES	4-(2-hydroxyethyl)-1-piperazineethanesulfonic acid
PBS	phosphate-buffered saline
ox^{2-}	oxalate
Me_2pma^{2-}	*N*-2,6-dimethylphenyloxamate
Et_2pma^{2-}	*N*-2,6-diethylphenyloxamate
$opba^{4-}$	*N*,*N*′-1,2-phenylenebis(oxamate)
$mpba^{4-}$	*N*,*N*′-1,3-phenylenebis(oxamate)
Me_3mpba^{4-}	2,4,6-trimethyl-*N*,*N*′-1,3-phenylenebis(oxamate)
mdp^{4-}	methylenediphosphonate

edp^{4-}	ethylenediphosphonate
$hedp^{4-}$	(1-hydroxyethylidene)diphosphonate
$1,4\text{-}xdp^{4-}$	1,4-xylenediphosphonate
cmp^{3-}	carboxymethylphosphonate
cep^{3-}	2-carboxyethylphosphonate
$2\text{-}pmb^{3-}$	2-(phosphonomethyl)benzoate
$Hpmab^{2-}$	4-((phosphonatomethylammonio)methyl)benzoate
mal^{2-}	malonate
$succ^{2-}$	succinate
$2,2\text{-}dmsucc^{2-}$	2,2-dimethylsuccinate
meso-$2,3\text{-}dmsucc^{2-}$	*meso*-2,3-dimethylsuccinate
glu^{2-}	glutarate
$adip^{2-}$	adipate
pim^{2-}	pimelate
$seba^{2-}$	sebacate
$O\text{-}lac^{2-}$	2-oxidopropanoate
$hypa^{2-}$	2-hydroxy-2-phenylacetate
ma^{2-}	malate
$O\text{-}ma^{3-}$	2-oxidosuccinate
$tart^{2-}$	tartrate
cit^{3-}	citrate
$O\text{-}cit^{4-}$	2-oxidopropane-1,2,3-tricarboxylate
asp^{2-}	aspartate

thiosal^{2-}	thiosalicylate
ca^{2-}	camphoric acid dianion
squ^{2-}	squarate
cbut^{4-}	1,2,3,4-cyclobutanetetracarboxylate
trans-1,2-chdc^{2-}	*trans*-1,2-cyclohexanedicarboxylate
cis-1,4-chdc^{2-}	*cis*-1,4-cyclohexanedicarboxylate
trans-1,4-chdc^{2-}	*trans*-1,4-cyclohexanedicarboxylate
cis,*cis*-1,3,5-chtc^{3-}	*cis*,*cis*-1,3,5-cyclohexanetricarboxylate
chhc^{6-}	*trans*,*trans*,*trans*,*trans*,*trans*-1,2,3,4,5,6-cyclohexanehexacarboxylate
1,3-bdc^{2-}	1,3-benzenedicarboxylate
1,4-bdc^{2-}	1,4-benzenedicarboxylate
bpdc^{2-}	4,4′-biphenyldicarboxylate
bpybc	1,1′-bis(4-carboxybenzyl)-4,4′-bipyridinium
2,5-dobdc^{4-}	2,5-dioxido-1,4-benzenedicarboxylate
1,3,5-btc^{3-}	1,3,5-benzenetricarboxylate
1,2,4,5-btec^{4-}	1,2,4,5-benzenetetracarboxylate
bptc^{4-}	3,3′,5,5′-biphenyltetracarboxylate
tptc^{4-}	(1,1′:4′,1″-terphenyl)-2′,3,3″,5′-tetracarboxylate
bpc^{5-}	benzenepentacarboxylate
hfipbb^{2-}	hexafluoroisopropylidenebis(benzoate)
pyz	pyrazine
pzdo	pyrazine-1,4-dioxide
pym	pyrimidine

H-pymo^{-}	2-pyrimidinolate
F-pymo^{-}	5-fluoro-2-pyrimidinolate
Cl-pymo^{-}	5-chloro-2-pyrimidinolate
Br-pymo^{-}	5-bromo-2-pyrimidinolate
I-pymo^{-}	5-iodo-2-pyrimidinolate
4,4′-bpy	4,4′-bipyridine
bpp	1,3-bis(4-pyridyl)propane
1,4-dimb	1,4-di-(1-imidazolylmethyl)benzene
bpea	1,2-bis(4-pyridyl)ethane
iqno	isoquinoline-*N*-oxide
hypH	hypoxanthine
trz^{-}	1,2,4-triazolate
tz^{-}	tetrazolate
im^{-}	imidazolate
2-Meim^{-}	2-methylimidazolate
4-abim^{-}	4-azabenzimidazolate
bta^{2-}	bis(5-tetrazolyl)amine
5-ptz^{-}	5-(pyrimidin-2-yl)tetrazolate
tzmb	*N*-(tetrazolmethyl)-4,4′-bipyridinium
3-pyc^{-}	3-pyridinecarboxylate
4-pyc^{-}	4-pyridinecarboxylate
2-pyco^{2-}	3-oxido-2-pyridinecarboxylate
2,4-pydc^{2-}	pyridine-2,4-dicarboxylate

3,4-$pydc^{2-}$	pyridine-3,4-dicarboxylate
$pybz^{-}$	4-(4-pyridyl)benzoate
$pymca^{-}$	2-pyrimidinecarboxylate
4-$imac^{-}$	4-imidazoleacetate
$btca^{2-}$	benzotriazolate-5-carboxylate
$trzdc^{3-}$	1,2,3-triazolate-4,5-dicarboxylate
$tdac^{2-}$	2,1,3-thiadiazole-4,5-dicarboxylate
5-tzc^{2-}	tetrazolate-5-carboxylate
$TEOA^{3-}$	triethanolamine trianion
gly^{2-}	glycerolate
en	ethylenediamine
1,3-dahp	1,3-diamino-2-hydroxypropane
1,3-dap	1,3-diaminopropane
1,3-pdiol	1,3-propanediol
phz	phenazine
ppz	piperazine
py	pyridine
H_2bdt	5,5′-(1,4-phenylene)bis(1*H*-tetrazole)
$dhbq^{2-}/H_2An^{2-}$	2,5-dioxidobenzoquinone
Cl_2An^{2-}	chloranilate
Br_2An^{2-}	bromanilate
I_2An^{2-}	iodoanilate
$ClCNAn^{2-}$	chlorocyanoanilate

4-MePyNO$^{+\bullet}$	2-(4-*N*-methylpyridinium)-4,4,5,5-tetramethylimidazoline-1-oxyl-3-oxide radical
4-EtPyNO$^{+\bullet}$	2-(4-*N*-ethylpyridinium)-4,4,5,5-tetramethylimidazoline-1-oxyl-3-oxide radical
4-PrPyNO$^{+\bullet}$	2-(4-*N*-propylpyridinium)-4,4,5,5-tetramethylimidazoline-1-oxyl-3-oxide radical
TOAPB	1,3,5-tris(*p*-(*N*-*tert*-butyl-*N*-oxyamino)phenyl)benzene triradical
BAPN	bis(3-*tert*-butyl-5-(*N*-oxy-*tert*-butylamino)phenyl) nitroxide triradical
BPNN	*p*-butoxyphenyl nitronyl nitroxide radical
NITIm$^{-\bullet}$	2-(2-imidazol-1-ide)-4,4,5,5-tetramethylimidazoline-1-oxyl-3-oxide radical
PTMTC$^{3-\bullet}$	polychlorinated triphenylmethyl tricarboxylate radical
TCNE	tetracyanoethylene
TCNQ/TCNQH$_4$	7,7,8,8-tetracyano-*p*-quinodimethane
TCNQF$_2$	2,5-fluoro-7,7,8,8-tetracyano-*p*-quinodimethane
TCNQCl$_2$	2,5-chloro-7,7,8,8-tetracyano-*p*-quinodimethane
TCNQBr$_2$	2,5-bromo-7,7,8,8-tetracyano-*p*-quinodimethane
TCNQMe$_2$	2,5-dimethyl-7,7,8,8-tetracyano-*p*-quinodimethane
TCNQ(OMe)$_2$	2,5-dimethoxy-7,7,8,8-tetracyano-*p*-quinodimethane
TCNQF$_4$	2,3,5,6-tetrafluoro-7,7,8,8-tetracyano-*p*-quinodimethane
BTDA-TCNQ	bis(1,2,5-thiadiazolo)tetracyano-*p*-quinodimethane
hfac$^-$	1,1,1,5,5,5-hexafluoroacetylacetonate
TFA$^-$	trifluoroacetate
1,2-Fbz$^-$	1,2-difluorobenzoate
1,3-Fbz$^-$	1,3-difluorobenzoate

1,4-Fbz^-	1,4-difluorobenzoate
1,2-$Clbz^-$	1,2-dichlorobenzoate
2,3,5-$Clbz^-$	2,3,5-trichlorobenzoate
Cp^-	cyclopentadienyl anion
Cp^{*-}	pentamethylcyclopentadienyl anion
$salen^{2-}$	*N*,*N*′-ethylenebis(salicylideneiminate)
TPP^{2-}	*meso*-tetraphenylporphyrinato
$TFPP^{2-}$	*meso*-tetrakis(4-fluorophenyl)porphyrinato
$TClPP^{2-}$	*meso*-tetrakis(4-chlorophenyl)porphyrinato
$TBrPP^{2-}$	*meso*-tetrakis(4-bromophenyl)porphyrinato
$TIPP^{2-}$	*meso*-tetrakis(4-iodophenyl)porphyrinato
QCl_4	tetrachloro-1,4-benzoquinone
2,2′-bpy	2,2′-bipyridine
ppy^-	2-phenylpyridine anion
bppy	2,6-(bispyrazol-3-yl)pyridine
pyimH	2-(1*H*-imidazol-2-yl)pyridine
$pmha^-$	*N*-(2-pyridylmethylene)-2-oxyaniline
im_2-trien	bis(*N*-(imidazol-4-yl)methylidene-3-aminoethyl)ethylenediamine
Me_3TPyA	tris(6-methyl-2-pyridylmethyl)amine
tacn	1,4,7-triazacyclononane
tren(6-Mepy)$_3$	tris(3-aza-4-(6-methyl-2-pyridyl)but-3-enyl)amine
tren-im_3	tris((2-((1*H*-imidazol-4-yl)methylidene)amino)ethyl)amine
$H_2(acac_2$-trien)	4,15-dimethyl-5,8,11,14-tetraazaoctadeca-2,4,14,16-tetraene-2,17-diol

H_2(sal$_2$-trien)	*N*,*N*′-disalicylidenetriethylenetetramine
H_2(3-Cl-sal$_2$-trien)	6,6'-(2,5,8,11-tetraazadodeca-1,11-diene-1,12-diyl)bis(2-chlorophenol)
H_2(3-Br-sal$_2$-trien)	6,6'-(2,5,8,11-tetraazadodeca-1,11-diene-1,12-diyl)bis(2-bromophenol)
H_2(3-OMe-sal$_2$-trien)	6,6'-(2,5,8,11-tetraazadodeca-1,11-diene-1,12-diyl)bis(2-methoxyphenol)
H_2(4-OH-sal$_2$-trien)	4,4′-(2,5,8,11-tetraazadodeca-1,11-diene-1,12-diyl)bis(benzene-1,3-diol)
H_2(4-Br-sal$_2$-trien)	6,6'-(2,5,8,11-tetraazadodeca-1,11-diene-1,12-diyl)bis(3-bromophenol)
H_2(5-Cl-sal$_2$-trien)	2,2′-(2,5,8,11-tetraazadodeca-1,11-diene-1,12-diyl)bis(4-chlorophenol)
H_2(5-Br-sal$_2$-trien)	2,2′-(2,5,8,11-tetraazadodeca-1,11-diene-1,12-diyl)bis(4-bromophenol)
H_2(5-NO_2-sal$_2$-trien)	2,2′-(2,5,8,11-tetraazadodeca-1,11-diene-1,12-diyl)bis(4-nitrophenol)
H_2(5-OMe-sal$_2$-trien)	2,2′-(2,5,8,11-tetraazadodeca-1,11-diene-1,12-diyl)bis(4-methoxyphenol)
H_2(sal$_2$-epe)	2,2′-(2,5,9,12-tetraazatrideca-1,12-diene-1,13-diyl)diphenol
dams$^+$	4-(2-(4-dimethylaminophenyl)ethenyl)-1-methylpyridinium
PNP$^+$	bis(triphenylphosphine)iminium
MV^{2+}	methylviologen dication
tag$^+$	triaminoguanidinium
BEDT-TTF	bis(ethylenedithio)tetrafulvalene

This thesis is dedicated to:

My grandfather, Páll Hlöðvesson

&

My parents, Katrín and Þórarinn

Table of Contents

Abstract 3

Acknowledgments 5

List of Abbreviations 11

List of Schemes 36

List of Figures 37

List of Tables 60

Chapter 1: Introduction 64

1.1 Electronic Spin Manipulation 65

1.2 Magnetic Resonance Imaging 66

1.3 Chemical Shift-Based Probes 67

1.4 Paramagnetic Chemical Exchange Saturation Transfer Probes 69

1.5 Summary of MRI Part of Thesis 73

1.6 Molecule-Based Magnets 73

1.7 The Metal–Radical Approach 74

1.8 Semiquinoid-Based Bridging Ligands 75

1.9 Dinuclear Complexes as Model Systems 77

Chapter 2: Spin-Crossover and High-Spin Iron(II) Complexes as Chemical Shift ^{19}F Magnetic Resonance Thermometers 79

2.1 Introduction 80

2.2 Experimental Section 82

2.3 Results and Discussion 89

2.3.1 Syntheses and Structures 89

2.3.2 UV-Vis Spectroscopy 94

2.3.3 Magnetic Properties 97

2.3.4 VT NMR Spectroscopy 98

2.4 Conclusions 104

2.5 Supporting Information 104

2.5.1 Supplementary Experimental Details 104

2.5.2 Supplementary Scheme 112

2.5.3 Supplementary Figures 113

2.5.4 Supplementary Tables 154

Chapter 3: Ratiometric pH Imaging with a Co^{II}_2 MRI Probe via CEST Effects of Opposing pH Dependences 163

3.1 Introduction 164

3.2 Experimental Section 165

3.3 Results and Discussion 177

3.3.1 Syntheses and Structures 177

3.3.2 UV-Vis Spectroscopy 180

3.3.3 Solution Magnetic Properties 181

3.3.4 NMR Spectroscopy 181

3.3.5 CEST Properties 183

3.3.6 Ratiometric CEST Analysis 186

3.3.7 Temperature Effects 187

3.3.8 Complex Stability and Biocompatibility Studies 189

3.3.9 NMR Studies of pH-Induced Structural Changes 190

3.3.10 MR Phantom Imaging 192

3.4 Conclusions 194

3.5 Supporting Information 194

3.5.1 Supplementary Experimental Details 194

3.5.2 Supplementary Schemes 200

3.5.3 Supplementary Figures 202

3.5.4 Supplementary Tables 272

Chapter 4: Electronic Effects of Ligand Substitution in a Family of Co^{II}_2 PARACEST pH Probes 279

4.1 Introduction 280

4.2 Experimental Section 282

4.3 Results and Discussion 292

4.3.1 Design and Syntheses 292

4.3.2 Crystal Structures 294

4.3.3 UV-Vis Spectroscopy 296

4.3.4 Solution Magnetic Properties 297

4.3.5 ^{19}F NMR Spectroscopy 298

4.3.6 ^{1}H NMR Spectroscopy 299

4.3.7 CEST Properties 301

4.3.8 pK_a Determination by ^{1}H NMR Spectroscopy 303

4.3.9 Exchange Rate Analysis 304

4.3.10 Ratiometric CEST Properties 305

4.3.11 Concentration Effects 307

4.3.12 Stability Studies 308

4.4 Conclusions 309

4.5 Supporting Information 310

4.5.1 Supplementary Experimental Details 310

4.5.2 Supplementary Schemes 318

4.5.3 Supplementary Figures 320

4.5.4 Supplementary Tables 413

Chapter 5: Dramatic Enhancement in pH Sensitivity and Signal Intensity Through Ligand Modification of a Dicobalt PARACEST Probe 421

5.1 Introduction 422

5.2 Experimental Section 423

5.3 Results and Discussion 430

5.3.1 Design and Synthesis 430

5.3.2 UV-Vis Spectroscopy 431

5.3.3 Solution Magnetic Properties 432

5.3.4 NMR Spectroscopy 432

5.3.5 CEST Properties 433

5.3.6 Ratiometric CEST Analysis 434

5.3.7 pK_a Determination by ^{1}H NMR Spectroscopy 436

5.3.8 Stability Studies 436

5.4 Conclusions 437

5.5 Supporting Information 437

5.5.1 Supplementary Experimental Details 437

5.5.2 Supplementary Figures 439

5.5.3 Supplementary Tables 472

Chapter 6: Selective Binding and Quantitation of Calcium with a Cobalt-Based Magnetic Resonance Probe 476

6.1 Introduction 477

6.2 Experimental Section 479

6.3 Results and Discussion 489

6.3.1 Syntheses and Structures 489

6.3.2 Solid-State Magnetic Properties 491

6.3.3 Solution ^{1}H NMR Properties 492

6.3.4 Assessment of Cation Binding Affinities by ^{1}H NMR 493

6.3.5 CEST Properties 495

6.3.6 Quantitation of Ca^{2+} Concentration in Aqueous Solutions 496

6.3.7 Stability Studies 500

6.4 Conclusions 501

6.5 Supporting Information 502

6.5.1 Supplementary Experimental Details 502

6.5.2 Supplementary Scheme 507

6.5.3 Supplementary Figures 508

6.5.4 Supplementary Tables 537

Chapter 7: Minimal Impact of Ligand Substitution on Magnetic Coupling in a Series of Semiquinoid Radical-Bridged Fe_2 Single-Molecule Magnets 540

7.1 Introduction 541

7.2 Experimental Section 544

7.3 Results and Discussion 561

7.3.1 Syntheses, Structures, and Electrochemistry 561

7.3.2 Mössbauer Spectroscopy 568

7.3.3 UV-Vis-NIR Spectroscopy 570

7.3.4 Static Magnetic Properties 572

7.3.5 Dynamic Magnetic Properties 577

7.4 Conclusions 579

7.5 Supporting Information 580

7.5.1 Supplementary Experimental Details 580

7.5.2 Supplementary Scheme 584

7.5.3 Supplementary Figures 585

7.5.4 Supplementary Tables 673

Chapter 8: Metal-Organic Framework Magnets 682

8.1 Introduction 683

8.1.1 Classes of Magnetic Order 685

8.1.2 Experimental Characterization of Magnetic Order 687

8.1.3 Scope and Structure of the Review 690

8.2 Toward Structurally-Characterized MOF Magnets 692

8.3 MOF Magnets with Diamagnetic Bridging Ligands 698

8.3.1 Introduction 698

8.3.2 Phosphonate-Containing Compounds 700

8.3.3 Oxalate-Containing Compounds 703

8.3.3.1 Introduction 703

8.3.3.2 2D Frameworks 704

8.3.3.3 3D Frameworks 713

8.3.4 Oxamate-Containing Compounds 721

8.3.4.1 Introduction 721

8.3.4.2 2D Frameworks 722

8.3.4.3 3D Frameworks 724

8.3.5 Carboxylate-Containing Compounds 728

8.3.5.1 Introduction 728

8.3.5.2 Malonate Compounds 729

8.3.5.3 Succinate Compounds 730

8.3.5.4 Glutarate Compounds 734

8.3.5.5 Adipate, Pimelate, and Sebacate Compounds 735

8.3.5.6 Carboxylates with Additional Functional Groups 737

8.3.5.7 Cyclic Multi-Carboxylate Compounds 742

8.3.5.8 Cyclohexanecarboxylate Compounds 745

8.3.5.9 Benzenecarboxylate Compounds 749

8.3.6 Compounds Containing N-Heterocyclic Ligands 762

8.3.6.1 Introduction 762

8.3.6.2 2D Frameworks 763

8.3.6.3 Pyrimidinolate 3D Frameworks 765

8.3.6.4 Imidazolate 3D Frameworks 768

8.3.6.5 Tri- and Tetrazolate 3D Frameworks 770

8.3.7 Compounds Containing Mixed O- and N-Donor Ligands..... 771

8.3.7.1 Introduction 771

8.3.7.2 Pyridinecarboxylate Compounds 772

8.3.7.3 Pyrimidinecarboxylate Compounds 774

8.3.7.4 Azole- and Azolatecarboxylate Compounds..... 775

8.3.8 Compounds Containing Diamagnetic Benzoquinoid Ligands..... 778

8.3.8.1 Introduction 778

8.3.8.2 Benzoquinoid Compounds 779

8.4 MOF Magnets with Radical Bridging Ligands..... 787

8.4.1 Introduction..... 787

8.4.2 Nitroxide Radical-Bridged Compounds 788

8.4.3 Triphenylmethyl Radical-Bridged Compounds..... 792

8.4.4 Organonitrile Radical-Bridged Compounds 794

8.4.4.1 TCNE Radical-Bridged Compounds..... 794

8.4.4.2 TCNQ Radical-Bridged Compounds 799

8.4.5 Semiquinoid Radical-Bridged Compounds 805

8.4.6 A Pyrazine Radical-Bridged Compound 810

8.5 Conclusions and Outlook 812

8.6 Supporting Information 814

8.6.1 Supplementary Tables 814

References 844

References for Chapter 1 845

References for Chapter 2 861

References for Chapter 3 869

References for Chapter 4 876

References for Chapter 5 883

References for Chapter 6 888

References for Chapter 7 894

References for Chapter 8 908

List of Schemes

Scheme 1.1 Redox series of deprotonated benzoquinoid ligands..... 76

Scheme 2.1 Synthesis of ligands L_x (x = 1–3) 112

Scheme 3.1 Syntheses of organic precursors and ligand HL..... 200

Scheme 3.2 Syntheses of organic precursors and ligand HL′..... 201

Scheme 4.1 Syntheses of organic precursors..... 318

Scheme 4.2 Synthesis of ligands H(^{X}L′) (X = NO_2, F, Me) 319

Scheme 6.1 Syntheses of H_2L and **1**..... 507

Scheme 7.1 Redox series of deprotonated benzoquinoid ligands with substituents R..... 543

Scheme 7.2 Syntheses of ligands..... 584

List of Figures

Figure 1.1 Schematic illustration of chemical shift-based MRI, using a temperature-responsive probe as an example. 67

Figure 1.2 Schematic illustration of a thermally-induced spin-crossover phenomenon in octahedral Fe^{II} complexes, highlighting the concomitant variations in NMR chemical shift..... 68

Figure 1.3 Schematic illustration of how MRI contrast is generated through the PARACEST technique and depiction of a CEST spectrum with key parameters highlighted 70

Figure 1.4 Schematic illustration of the CEST properties of an ideal PARACEST probe for the ratiometric quantitation of pH. 72

Figure 1.5 Schematic illustration of different magnetic exchange coupling mechanisms in metal-organic magnetic materials 74

Figure 2.1 Molecular structures of ligands L_x (x = 1–3)..... 90

Figure 2.2 Crystals structures of $[Fe(L_1)]^{2+}$, $[Fe(L_2)]^{2+}$, $[Zn(L_1)]^{2+}$, and $[Zn(L_2)]^{2+}$, as observed in **1a**·0.5MeCN, **2a**, **1b**, and **2b**, respectively..... 92

Figure 2.3 UV-Vis spectra of **1a**, **2a**, and **3a** in MeCN at selected temperatures 95

Figure 2.4 VT dc magnetic susceptibility data for **1a** and **2a** in H_2O 97

Figure 2.5 Plot of the temperature dependence of the ^{19}F NMR chemical shift for **1a**, **1b**, **2a**, and **2b** in H_2O 100

Figure 2.6 VT ^{19}F NMR spectra of **1a** and **2a** in FBS..... 103

Figure 2.7 Crystal structure of $[Fe(L_3)]^{2+}$ at 100 K 113

Figure 2.8 VT UV-Vis spectra of **1a** in MeCN 114

Figure 2.9 VT UV-Vis spectra of **2a** in MeCN 115

Figure 2.10 VT UV-Vis spectra of **3a** in MeCN 116

Figure 2.11 VT UV-Vis spectra of **1b** in MeCN..... 117

Figure 2.12 VT UV-Vis spectra of **2b** in MeCN..... 118

Figure 2.13 UV-Vis spectra of **1a**, **2a**, and **3a** in MeCN at −35 °C 119

Figure 2.14 UV-Vis spectra of **1a**, **2a**, and **3a** in MeCN at 65 °C 120

Figure 2.15 UV-Vis spectra of **1a** in H_2O 121

Figure 2.16 UV-Vis spectra of **2a** in H_2O 122

Figure 2.17 UV-Vis spectra of **3a** in H_2O 123

Figure 2.18 UV-Vis spectra of **1b** in H_2O 124

Figure 2.19 UV-Vis spectra of **2b** in H_2O 125

Figure 2.20 Plot of high-spin molar fraction of **1a** vs *T* in H_2O 126

Figure 2.21 Thermodynamic data for the spin transition of **1a** in H_2O 127

Figure 2.22 Dc magnetic susceptibility of **1a** vs *T* in H_2O and MeCN 128

Figure 2.23 High-spin molar fraction of **1a** vs *T* in H_2O and MeCN 129

Figure 2.24 VT ^{1}H NMR spectra of **1b** in MeCN-d_3 130

Figure 2.25 VT ^{1}H NMR spectra of **2b** in MeCN-d_3 131

Figure 2.26 VT ^{1}H NMR spectra of **3a** in MeCN-d_3 132

Figure 2.27 VT ^{1}H NMR spectra of **2a** in MeCN-d_3 133

Figure 2.28 VT ^{1}H NMR spectra of **1a** in MeCN-d_3 134

Figure 2.29 VT ^{1}H NMR spectra of **1a** in D_2O 135

Figure 2.30 Plot of the temperature dependence of ^{19}F NMR chemical shift of TFE in H_2O ... 136

Figure 2.31 VT ^{19}F NMR spectra of **1b** in 2.1 mM TFE(aq) 137

Figure 2.32 VT ^{19}F NMR spectra of **2b** in 2.1 mM TFE(aq) 138

Figure 2.33 VT ^{19}F NMR spectra of **2a** in 2.1 mM TFE(aq) 139

Figure 2.34 VT ^{19}F NMR spectra of **2a** in 2.1 mM TFE(aq) referenced to **2b** 140

Figure 2.35 VT ^{19}F NMR spectra of **1a** in 2.1 mM TFE(aq) 141

Figure 2.36 VT ^{19}F NMR spectra of **1a** in 2.1 mM TFE(aq) referenced to **1b** 142

Figure 2.37 Plot of ^{19}F NMR chemical shift separation vs *T* for **1a** in 2.1 mM TFE(aq) 143

Figure 2.38 VT ^{19}F NMR spectra of a H_2O solution of TFE and NaF 144

Figure 2.39 VT ^{19}F NMR spectra of **1a** in FBS 145

Figure 2.40 VT ^{19}F NMR spectra of **2a** in FBS 146

Figure 2.41 ^{19}F NMR spectra of **1a** in FBS at 25 °C at different times 147

Figure 2.42 ^{19}F NMR spectra of **2a** in FBS at 25 °C at different times 148

Figure 2.43 VT ^{19}F NMR spectra of **1a** in MeCN-d_3 149

Figure 2.44 VT ^{19}F NMR spectra of **2a** in MeCN-d_3 150

Figure 2.45 VT ^{19}F NMR spectra of **1b** in MeCN-d_3 151

Figure 2.46 VT ^{19}F NMR spectra of **2b** in MeCN-d_3 152

Figure 2.47 Plot of ^{19}F NMR chemical shift separation vs *T* for **1a** in MeCN-d_3 153

Figure 3.1 Molecular structures of the anionic Co^{II}_2 complexes in **1**, **2**, and **3** 167

Figure 3.2 Crystal structures of $[LCo_2(\text{etidronate})]^-$ and $[LCo_2(\text{CMDP})]^-$, as observed in **1′** and **2′**, respectively 178

Figure 3.3 Variable-pH CEST spectra for 12.8 mM buffer solutions of **1** at 37 °C 183

Figure 3.4 Plot of ratios of CEST peak intensities vs pH for buffer solutions of **1** and **2**, and a semilog form of the plot for **1** 186

Figure 3.5 Plot of the pH dependence of the ^{1}H NMR chemical shift of the etidronate CH_3 group for **1** and a depiction of the pH-dependent protonation state of etidronate 191

Figure 3.6 CEST images of phantoms containing buffer solutions of **1** at multiple pH values in the range 6.40–7.88 193

Figure 3.7 FT-IR spectra of **1**–**3** 202

Figure 3.8 Variable-pH UV-Vis spectra of **1** in buffer 203

Figure 3.9 Variable-pH UV-Vis spectra of **2** in buffer..... 204

Figure 3.10 Variable-pH UV-Vis spectra of **3** in buffer..... 205

Figure 3.11 UV-Vis spectra of **1**–**3** in pH 7.4 buffer..... 206

Figure 3.12 Diffuse reflectance UV-Vis spectrum of **1′**..... 207

Figure 3.13 Diffuse reflectance UV-Vis spectrum of **2′**..... 208

Figure 3.14 Variable-pH dc magnetic susceptibility data for **1** in buffer at 37 °C..... 209

Figure 3.15 Variable-pH dc magnetic susceptibility data for **2** in buffer at 37 °C..... 210

Figure 3.16 Variable-pH dc magnetic susceptibility data for **3** in buffer at 37 °C..... 211

Figure 3.17 ^{1}H NMR spectra of **1** in pH 7.18 buffer and neutral D_2O at 37 °C..... 212

Figure 3.18 Variable-pH ^{1}H NMR spectra of **1** in buffer at 37 °C..... 213

Figure 3.19 ^{1}H NMR spectra of **2** in pH 7.18 buffer and neutral D_2O at 37 °C..... 214

Figure 3.20 ^{1}H NMR spectra of **1** and **2** in pH 7.18 buffer at 37 °C..... 215

Figure 3.21 Variable-pH ^{1}H NMR spectra of **2** in buffer at 37 °C..... 216

Figure 3.22 ^{1}H NMR spectra of **1**–**3** in buffer at 37 °C..... 217

Figure 3.23 ^{1}H NMR spectra of **3** in pH 8.08 buffer and slightly basic D_2O at 37 °C..... 218

Figure 3.24 Variable-pH ^{1}H NMR spectra of **3** in buffer at 37 °C..... 219

Figure 3.25 pH dependences of CEST effects for 12.8 mM of **1** in buffer at 37 °C..... 220

Figure 3.26 Variable-pH CEST spectra for **2** in buffer at 37 °C..... 221

Figure 3.27 pH dependences of CEST effects for **2** in buffer at 37 °C..... 222

Figure 3.28 Variable-pH CEST spectra for **3** in buffer at 37 °C..... 223

Figure 3.29 pH dependences of CEST effects for **3** in buffer at 37 °C..... 224

Figure 3.30 Omega plots of the CEST effect at 68–69 ppm for **2** in buffer at 37 °C..... 225

Figure 3.31 Omega plots of the CEST effect at 102 ppm for **2** in buffer at 37 °C..... 226

Figure 3.32 pH dependences of proton exchange rate constants for **2** in buffer at 37 °C 227

Figure 3.33 Omega plots of the CEST effect at 94–103 ppm for **3** in buffer at 37 °C..... 228

Figure 3.34 pH dependence of the proton exchange rate constant for **3** in buffer at 37 °C 229

Figure 3.35 Omega plots of the CEST effect at 64–66 ppm for **1** in buffer at 37 °C..... 230

Figure 3.36 Omega plots of the CEST effect at 101–106 ppm for **1** in buffer at 37 °C..... 231

Figure 3.37 pH dependences of proton exchange rate constants for **1** in buffer at 37 °C 232

Figure 3.38 Variable-pH CEST spectra for 6.4 mM of **1** in buffer at 37 °C 233

Figure 3.39 Variable-pH CEST spectra for 8.5 mM of **1** in buffer at 37 °C 234

Figure 3.40 pH dependences of CEST effects for 6.4 mM of **1** in buffer at 37 °C 235

Figure 3.41 pH dependences of CEST effects for 8.5 mM of **1** in buffer at 37 °C 236

Figure 3.42 pH dependence of the CEST effect at 64 ppm for various concentrations of **1**..... 237

Figure 3.43 pH dependence of the CEST effect at 104 ppm for various concentrations of **1**... 238

Figure 3.44 pH dependence of $CEST_{104\ ppm}/CEST_{64\ ppm}$ for 6.4 mM of **1** in buffer at 37 °C.... 239

Figure 3.45 pH dependence of $CEST_{104\ ppm}/CEST_{64\ ppm}$ for 8.5 mM of **1** in buffer at 37 °C.... 240

Figure 3.46 pH dependence of $CEST_{104\ ppm}/CEST_{64\ ppm}$ for various concentrations of **1** 241

Figure 3.47 pH calibration curves for various concentrations of **1** 242

Figure 3.48 Variable-pH ^{1}H NMR spectra of **1** in buffer at 35 °C..... 243

Figure 3.49 Variable-pH CEST spectra for **1** in buffer at 35 °C 244

Figure 3.50 Variable-pH ^{1}H NMR spectra of **1** in buffer at 39 °C..... 245

Figure 3.51 Variable-pH CEST spectra for **1** in buffer at 39 °C 246

Figure 3.52 ^{1}H NMR spectra of **1** in pH 7.38 buffer at various temperatures..... 247

Figure 3.53 pH dependences of CEST effects for **1** in buffer at 35 °C 248

Figure 3.54 pH dependences of CEST effects for **1** in buffer at 39 °C 249

Figure 3.55 pH dependence of the CEST effect at 64 ppm for **1** at various temperatures 250

Figure 3.56 pH dependence of the CEST effect at 104 ppm for **1** at various temperatures 251

Figure 3.57 pH dependence of $CEST_{104\ ppm}/CEST_{64\ ppm}$ for **1** in buffer at 35 °C 252

Figure 3.58 pH dependence of $CEST_{104\ ppm}/CEST_{64\ ppm}$ for **1** in buffer at 39 °C 253

Figure 3.59 pH dependence of $CEST_{104\ ppm}/CEST_{64\ ppm}$ for **1** at various temperatures 254

Figure 3.60 pH calibration curves for **1** at various temperatures 255

Figure 3.61 Modified pH calibration curves for **1** at various temperatures 256

Figure 3.62 Cyclic voltammogram of **1** in pH 7.4 buffer 257

Figure 3.63 ^{1}H NMR spectra of **1** in pH 7.3 buffer with/without presence of anions at 37 °C. 258

Figure 3.64 ^{1}H NMR spectra of **1** in pH 7.3 buffer with/without presence of Ca^{2+} at 37 °C.... 259

Figure 3.65 Variable-pH ^{1}H NMR spectra of **1** in FBS at 37 °C 260

Figure 3.66 Variable-pH CEST spectra for **1** in FBS at 37 °C 261

Figure 3.67 pH dependences of CEST effects for **1** in FBS at 37 °C 262

Figure 3.68 pH dependence of $CEST_{104\ ppm}/CEST_{64\ ppm}$ for **1** in FBS at 37 °C 263

Figure 3.69 pH calibration curves for **1** in FBS and buffer at 37 °C 264

Figure 3.70 Cell viability data for **1** 265

Figure 3.71 pH dependences of ^{1}H NMR chemical shifts of carboxamide protons for **1** 266

Figure 3.72 pH dependence of the ^{1}H NMR chemical shift of CH_3 from etidronate for **3** 267

Figure 3.73 pH dependences of ^{1}H NMR chemical shifts of carboxamide protons for **2** 268

Figure 3.74 pH dependence of the ^{1}H NMR chemical shift of CH from $CMDP^{4-}$ for **2** 269

Figure 3.75 MR image of phantom samples of **1** highlighting the regions used for analysis ... 270

Figure 3.76 pH calibration curve from phantom imaging of **1** in buffer at 37 °C 271

Figure 4.1 Molecular structures of the anionic Co^{II}_2 complexes in **1** and **2-X**

(X = NO_2, F, Me) 284

Figure 4.2 Crystal structures of [(^{X}L′)Co_2(etidronate)]$^{-}$, as observed in **2′-X** (X = NO_2, F, Me) 294

Figure 4.3 Selected parts of ^{1}H NMR spectra and full ^{19}F NMR spectra for buffer solutions of **2-X** (X = NO_2, F, Me) at 37 °C 299

Figure 4.4 Variable-pH CEST spectra for buffer solutions of **2-X** (X = NO_2, F, Me) at 37 °C 302

Figure 4.5 Depiction of the mechanism for pH-induced changes in NMR frequencies of etidronate resonances for **2-X** (X = NO_2, F, Me) 303

Figure 4.6 Plots of ratios of OH and NH CEST peak intensities vs pH for buffer solutions of **2-X** (X = NO_2, F, Me) and semilog forms of the plots 306

Figure 4.7 FT-IR spectra of H(^{X}L′) (X = NO_2, F, Me) 320

Figure 4.8 FT-IR spectra of **2-X** (X = NO_2, F, Me) 321

Figure 4.9 Variable-pH UV-Vis spectra of **2-NO_2** in buffer 322

Figure 4.10 Variable-pH UV-Vis spectra of **2-F** in buffer 323

Figure 4.11 Variable-pH UV-Vis spectra of **2-Me** in buffer 324

Figure 4.12 UV-Vis spectra of **2-X** (X = NO_2, F, Me) in buffer 325

Figure 4.13 UV-Vis spectra of H(^{X}L′) (X = NO_2, F, Me) in MeOH 326

Figure 4.14 Diffuse reflectance UV-Vis spectrum of **2′-NO_2** 327

Figure 4.15 Diffuse reflectance UV-Vis spectrum of **2′-F** 328

Figure 4.16 Diffuse reflectance UV-Vis spectrum of **2′-Me** 329

Figure 4.17 Variable-pH dc magnetic susceptibility data for **2-NO_2** in buffer at 37 °C 330

Figure 4.18 Variable-pH dc magnetic susceptibility data for **2-F** in buffer at 37 °C 331

Figure 4.19 Variable-pH dc magnetic susceptibility data for **2-Me** in buffer at 37 °C 332

Figure 4.20 Variable-pH ^{19}F NMR spectra of **2-NO_2** in buffer 333

Figure 4.21 Variable-pH ^{19}F NMR spectra of **2-F** in buffer 334

Figure 4.22 Variable-pH ^{19}F NMR spectra of **2-Me** in buffer 335

Figure 4.23 ^{1}H NMR spectra of **2-NO$_2$** in pH 6.48 buffer and slightly acidic D_2O 336

Figure 4.24 Variable-pH ^{1}H NMR spectra of **2-NO$_2$** in buffer 337

Figure 4.25 ^{1}H NMR spectra of **2-F** in pH 7.19 buffer and neutral D_2O 338

Figure 4.26 Variable-pH ^{1}H NMR spectra of **2-F** in buffer 339

Figure 4.27 ^{1}H NMR spectra of **2-Me** in pH 6.48 buffer and slightly acidic D_2O 340

Figure 4.28 Variable-pH ^{1}H NMR spectra of **2-Me** in buffer 341

Figure 4.29 ^{1}H NMR spectra of **2-X** (X = NO_2, F, Me) in pH 7.4 buffer 342

Figure 4.30 pH dependences of CEST effects for 8 mM of **2-NO$_2$** in buffer 343

Figure 4.31 pH dependence of max. OH CEST effect for 8 mM of **2-NO$_2$** in buffer 344

Figure 4.32 pH dependences of CEST effects for 9 mM of **2-F** in buffer 345

Figure 4.33 pH dependence of max. OH CEST effect for 9 mM of **2-F** in buffer 346

Figure 4.34 pH dependences of CEST effects for 8 mM of **2-Me** in buffer 347

Figure 4.35 pH dependence of max. OH CEST effect for 8 mM of **2-Me** in buffer 348

Figure 4.36 pH dependences of OH CEST effects for 8–9 mM of **2-X** (X = NO_2, F, Me) 349

Figure 4.37 pH dependences of NH CEST effects for 8–9 mM of **2-X** (X = NO_2, F, Me) 350

Figure 4.38 pH dependences of max. OH CEST effects for 8–9 mM of **2-X** (X = NO_2, F, Me) 351

Figure 4.39 pH dependence of the ^{1}H NMR chemical shift of etidronate Me group for **2-NO$_2$** 352

Figure 4.40 pH dependence of the ^{1}H NMR chemical shift of etidronate Me group for **2-F** ... 353

Figure 4.41 pH dependence of the ^{1}H NMR chemical shift of etidronate Me group for **2-Me** 354

Figure 4.42 Omega plots of the CEST effect at 112–117 ppm for **2-NO$_2$** in buffer 355

Figure 4.43 Omega plots of the CEST effect at 91–92 ppm for **2-NO$_2$** in buffer 356

Figure 4.44 Omega plots of the CEST effect at 88–89 ppm for **2-NO$_2$** in buffer 357

Figure 4.45 Omega plots of the CEST effect at 43–45 ppm for **2-NO$_2$** in buffer 358

Figure 4.46 pH dependences of proton exchange rate constants for **2-NO$_2$** in buffer 359

Figure 4.47 Omega plots of the CEST effect at 90–97 ppm for **2-F** in buffer 360

Figure 4.48 Omega plots of the CEST effect at 81 ppm for **2-F** in buffer 361

Figure 4.49 Omega plots of the CEST effect at 78–79 ppm for **2-F** in buffer 362

Figure 4.50 Omega plots of the CEST effect at 48–51 ppm for **2-F** in buffer 363

Figure 4.51 pH dependences of proton exchange rate constants for **2-F** in buffer 364

Figure 4.52 Omega plots of the CEST effect at 85–92 ppm for **2-Me** in buffer 365

Figure 4.53 Omega plots of the CEST effect at 79 ppm for **2-Me** in buffer 366

Figure 4.54 Omega plots of the CEST effect at 76–77 ppm for **2-Me** in buffer 367

Figure 4.55 Omega plots of the CEST effect at 51–53 ppm for **2-Me** in buffer 368

Figure 4.56 pH dependences of proton exchange rate constants for **2-Me** in buffer 369

Figure 4.57 pH dependences of k_{ex} for OH protons for **2-X** (X = NO_2, F, Me)..... 370

Figure 4.58 pH dependences of k_{ex} for NH protons 1 for **2-X** (X = NO_2, F, Me)..... 371

Figure 4.59 pH dependences of k_{ex} for NH protons 2 for **2-X** (X = NO_2, F, Me)..... 372

Figure 4.60 pH dependences of k_{ex} for NH protons 3 for **2-X** (X = NO_2, F, Me)..... 373

Figure 4.61 pH dependences of $CEST_{OH}/CEST_{NH}$ for 8–9 mM of **2-X** (X = NO_2, F, Me)..... 374

Figure 4.62 pH calibration curves for 8–9 mM of **2-X** (X = NO_2, F, Me) 375

Figure 4.63 Variable-pH CEST spectra for 4 mM of **2-NO$_2$** in buffer 376

Figure 4.64 Variable-pH CEST spectra for 4 mM of **2-F** in buffer 377

Figure 4.65 Variable-pH CEST spectra for 4 mM of **2-Me** in buffer 378

Figure 4.66 pH dependences of CEST effects for 4 mM of **2-NO$_2$** in buffer 379

Figure 4.67 pH dependence of the CEST effect at 115 ppm for various concentrations of **2-NO$_2$** 380

Figure 4.68 pH dependence of the CEST effect at 88 ppm for various concentrations of **2-NO$_2$** 381

Figure 4.69 pH dependence of the CEST effect at 44 ppm for various concentrations of **2-NO$_2$** 382

Figure 4.70 pH dependence of max. OH CEST effect for 4 mM of **2-NO$_2$** in buffer 383

Figure 4.71 pH dependence of max. OH CEST effect for various concentrations of **2-NO$_2$** ... 384

Figure 4.72 pH dependences of CEST effects for 4 mM of **2-F** in buffer 385

Figure 4.73 pH dependence of the CEST effect at 93 ppm for various concentrations of **2-F** . 386

Figure 4.74 pH dependence of the CEST effect at 79 ppm for various concentrations of **2-F** . 387

Figure 4.75 pH dependence of the CEST effect at 49 ppm for various concentrations of **2-F** . 388

Figure 4.76 pH dependence of max. OH CEST effect for 4 mM of **2-F** in buffer..... 389

Figure 4.77 pH dependence of max. OH CEST effect for various concentrations of **2-F** 390

Figure 4.78 pH dependences of CEST effects for 4 mM of **2-Me** in buffer 391

Figure 4.79 pH dependence of the CEST effect at 88 ppm for various concentrations of **2-Me** 392

Figure 4.80 pH dependence of the CEST effect at 76 ppm for various concentrations of **2-Me** 393

Figure 4.81 pH dependence of the CEST effect at 51 ppm for various concentrations of **2-Me** 394

Figure 4.82 pH dependence of max. OH CEST effect for 4 mM of **2-Me** in buffer..... 395

Figure 4.83 pH dependence of max. OH CEST effect for various concentrations of **2-Me** 396

Figure 4.84 pH dependences of OH CEST effects for 4 mM of **2-X** (X = NO_2, F, Me)..... 397

Figure 4.85 pH dependences of NH CEST effects for 4 mM of **2-X** (X = NO_2, F, Me)..... 398

Figure 4.86 pH dependences of max. OH CEST effects for 4 mM of **2-X** (X = NO_2, F, Me).. 399

Figure 4.87 pH dependence of $CEST_{115\ ppm}/CEST_{88\ ppm}$ for 4 mM of **2-NO_2** in buffer..... 400

Figure 4.88 pH dependence of $CEST_{115\ ppm}/CEST_{88\ ppm}$ for various concentrations of **2-NO_2**. 401

Figure 4.89 pH calibration curves for various concentrations of **2-NO_2**..... 402

Figure 4.90 pH dependence of $CEST_{93\ ppm}/CEST_{79\ ppm}$ for 4 mM of **2-F** in buffer..... 403

Figure 4.91 pH dependence of $CEST_{93\ ppm}/CEST_{79\ ppm}$ for various concentrations of **2-F** 404

Figure 4.92 pH calibration curves for various concentrations of **2-F** 405

Figure 4.93 pH dependence of $CEST_{88\ ppm}/CEST_{76\ ppm}$ for 4 mM of **2-Me** in buffer..... 406

Figure 4.94 pH dependence of $CEST_{88\ ppm}/CEST_{76\ ppm}$ for various concentrations of **2-Me**.... 407

Figure 4.95 pH calibration curves for various concentrations of **2-Me** 408

Figure 4.96 pH dependences of $CEST_{OH}/CEST_{NH}$ for 4 mM of **2-X** (X = NO_2, F, Me)..... 409

Figure 4.97 pH calibration curves for 4 mM of **2-X** (X = NO_2, F, Me) 410

Figure 4.98 pH calibration curves in the pH range 6.2–7.6 for various concentrations of **2-F**. 411

Figure 4.99 Cyclic voltammograms of **2-X** (X = NO_2, F, Me) in pH 7.3 buffer..... 412

Figure 5.1 Molecular structures of the Co^{II}_2 PARACEST pH probes $[LCo_2(etidronate)]^-$, $[(^XL')Co_2(etidronate)]^-$, and $LCo_2(HL')$, as observed in **1**, **2-X** (X = NO_2, F, Me), and **3**, respectively 431

Figure 5.2 Variable-pH CEST spectra for buffer solutions of **3** at 37 °C and a plot of CEST peak intensities at 48 and 67 ppm vs pH 433

Figure 5.3 Plot of ratios of CEST peak intensities at 48 and 67 ppm vs pH..... 435

Figure 5.4 FT-IR spectrum of **3**..... 439

Figure 5.5 Diffuse reflectance UV-Vis spectrum of **3**..... 440

Figure 5.6 Variable-pH UV-Vis spectra of **3** in buffer..... 441

Figure 5.7 Variable-pH dc magnetic susceptibility data for **3** in buffer at 37 °C..... 442

Figure 5.8 ^{1}H NMR spectra of **3** in pH 7.02 buffer and neutral D_2O at 37 °C..... 443

Figure 5.9 ^{1}H NMR spectra of **3** and **1** in buffer at 37 °C..... 444

Figure 5.10 Variable-pH ^{1}H NMR spectra of **3** in buffer at 37 °C..... 445

Figure 5.11 Omega plots of the CEST effect at 67 ppm for **3** in buffer at 37 °C..... 446

Figure 5.12 Omega plots of the CEST effect at 48 ppm for **3** in buffer at 37 °C..... 447

Figure 5.13 pH dependences of proton exchange rate constants for **3** in buffer at 37 °C..... 448

Figure 5.14 Variable-pH CEST spectra for 5 mM of **3** in buffer at 37 °C..... 449

Figure 5.15 pH dependences of CEST effects for 5 mM of **3** in buffer at 37 °C..... 450

Figure 5.16 pH calibration curve for 5 mM of **3** in buffer at 37 °C..... 451

Figure 5.17 pH dependence of the CEST effect at 48 ppm for various concentrations of **3**..... 452

Figure 5.18 pH dependence of the CEST effect at 67 ppm for various concentrations of **3**..... 453

Figure 5.19 pH calibration curves for various concentrations of **3**..... 454

Figure 5.20 Scheme highlighting the ionization process in solution for Co^{II}_2 complex in **3**..... 455

Figure 5.21 pH dependences of ^{1}H NMR chemical shifts of bisphosphonate CH_2 protons for **3**..... 456

Figure 5.22 Cyclic voltammogram of **3** in pH 7.4 buffer..... 457

Figure 5.23 ^{1}H NMR spectra of **3** in pH 7.4 buffer with/without presence of phosphates at 37 °C..... 458

Figure 5.24 Variable-pH ^{1}H NMR spectra of **3** in FBS at 37 °C..... 459

Figure 5.25 Variable-pH CEST spectra for **3** in FBS at 37 °C..... 460

Figure 5.26 pH dependences of CEST effects for **3** in FBS at 37 °C..... 461

Figure 5.27 pH calibration curve for **3** in FBS at 37 °C 462

Figure 5.28 Variable-pH ^{1}H NMR spectra of **3** in gelatin gels at 37 °C 463

Figure 5.29 Variable-pH CEST spectra for **3** in gelatin gels at 37 °C 464

Figure 5.30 pH dependences of CEST effects for **3** in gelatin gels at 37 °C 465

Figure 5.31 pH calibration curve for **3** in gelatin gels at 37 °C 466

Figure 5.32 pH dependence of the CEST effect at 48 ppm for **3** in various media 467

Figure 5.33 pH dependence of the CEST effect at 67 ppm for **3** in various media 468

Figure 5.34 pH calibration curves for **3** in various media 469

Figure 5.35 Omega plots of the CEST effects for **3** in pH 7.46 FBS at 37 °C 470

Figure 5.36 Omega plots of the CEST effects for **3** in pH 7.22 gelatin gel at 37 °C 471

Figure 6.1 Synthesis and molecular structure of LCo 481

Figure 6.2 Crystal structures of LCo, $[LCoNa(H_2O)]^+$, and $[LCoCa(NO_3)(MeOH)]^+$, as observed in **1′**, **2′**, and **3′**, respectively, and low-temperature magnetization data for **1**–**3** at selected dc fields 490

Figure 6.3 Plot of the change in ^{1}H NMR chemical shift upon addition of $NaNO_3$ to a solution of **1** in D_2O and a plot of changes in ^{1}H NMR signal intensities upon addition of $Ca(NO_3)_2$ to a solution of **1** in D_2O containing KNO_3 493

Figure 6.4 CEST spectra for a buffer solution of **1** at 37 °C without and with the presence of Na^+ and Ca^{2+} 495

Figure 6.5 Variable-$[Ca^{2+}]$ CEST spectra for 2.0 mM solution of **1** in buffer at 37 °C and a plot of ratios of CEST peak intensities at 80 and 69 ppm vs $[Ca^{2+}]$ 497

Figure 6.6 ^{1}H NMR spectra of **1** in H_2O in the absence and presence of Na^+ and Ca^{2+} 508

Figure 6.7 ^{1}H NMR spectra of **1** in D_2O in the absence and presence of Na^+ and Ca^{2+} 509

Figure 6.8 Variable-$[Na^+]$ ^{1}H NMR spectra of peak at ca. 123 ppm for **1** in D_2O 510

Figure 6.9 Variable-$[Mg^{2+}]$ ^{1}H NMR spectra of peak at ca. 202 ppm for **1** in D_2O 511

Figure 6.10 Variable-[Mg^{2+}] ^{1}H NMR spectra of peak at ca. 123 ppm for **1** in D_2O..... 512

Figure 6.11 Change in ^{1}H NMR chemical shift at ca. 202 ppm vs [Na^+] for **1** in D_2O..... 513

Figure 6.12 Change in ^{1}H NMR chemical shift at ca. 123 ppm vs [Na^+] for **1** in D_2O..... 514

Figure 6.13 Change in ^{1}H NMR chemical shift at ca. 202 ppm vs [Mg^{2+}] for **1** in D_2O 515

Figure 6.14 Change in ^{1}H NMR chemical shift at ca. 123 ppm vs [Mg^{2+}] for **1** in D_2O 516

Figure 6.15 Variable-[K^+] ^{1}H NMR spectra of peak at ca. 212 ppm for **1** in D_2O..... 517

Figure 6.16 Variable-[K^+] ^{1}H NMR spectra of peak at ca. 133 ppm for **1** in D_2O..... 518

Figure 6.17 Change in ^{1}H NMR chemical shift at ca. 212 ppm vs [K^+] for **1** in D_2O 519

Figure 6.18 Change in ^{1}H NMR chemical shift at ca. 133 ppm vs [K^+] for **1** in D_2O 520

Figure 6.19 Mole fraction of [LCoCa]$^{2+}$ vs [Ca^{2+}] monitored by $I_{245\ ppm}/I_{207\ ppm}$ in D_2O..... 521

Figure 6.20 Change in ^{1}H NMR chemical shift at ca. 123 ppm vs [Na^+] for **1** at pH 7.3 522

Figure 6.21 Change in ^{1}H NMR chemical shift at ca. 123 ppm vs [Na^+] for **1** at pH 7.4 523

Figure 6.22 Change in ^{1}H NMR chemical shift at ca. 123 ppm vs [Na^+] for **1** at pH 7.5 524

Figure 6.23 UV-Vis spectra for **1** in the absence and presence of Na^+ and Ca^{2+} 525

Figure 6.24 Omega plots for **1** in the absence and presence of Na^+ and Ca^{2+}..... 526

Figure 6.25 Variable-[Ca^{2+}] CEST spectra for 2.8 mM of **1**..... 527

Figure 6.26 Variable-[Ca^{2+}] CEST spectra for 5.6 mM of **1**..... 528

Figure 6.27 Variable-[Ca^{2+}] CEST spectra for 11 mM of **1**..... 529

Figure 6.28 Variable-[Ca^{2+}] CEST spectra for 2.8 mM of **1** in the presence of cations 530

Figure 6.29 $CEST_{80\ ppm}/CEST_{69\ ppm}$ vs [Ca^{2+}] for 2.8 mM of **1** in the presence of cations 531

Figure 6.30 Exponential fit to $CEST_{80\ ppm}/CEST_{69\ ppm}$ vs [Ca^{2+}] data for **1** 532

Figure 6.31 Alternative exponential fit to $CEST_{80\ ppm}/CEST_{69\ ppm}$ vs [Ca^{2+}] data for **1**..... 533

Figure 6.32 Cyclic voltammogram of **1** in the absence of physiological cations..... 534

Figure 6.33 Cyclic voltammogram of **1** in the presence of physiological cations 535

Figure 6.34 UV-Vis spectra for **1** oxidized in air 536

Figure 7.1 Synthesis of compounds $[(Me_3TPyA)_2Fe_2(^RL)]^{n+}$ (R = OMe, Cl, NO_2, SMe_2), as observed in **1-OMe** (*n* = 2), **1-Cl** (*n* = 2), **1-NO_2** (*n* = 2), and **1-SMe_2** (*n* = 4) 561

Figure 7.2 Crystal structures of $[(Me_3TPyA)_2Fe_2(^RL)]^{4+/2+}$ and $[(Me_3TPyA)_2Fe_2(^RL)]^{3+/1+}$, as observed in **1-R**·solvent and **2-R**·solvent (R = OMe, Cl, NO_2, SMe_2), respectively 564

Figure 7.3 Cyclic voltammograms for MeCN solutions of **1-R** (R = OMe, Cl, NO_2, SMe_2) . 565

Figure 7.4 Zero-field ^{57}Fe Mössbauer spectra for polycrystalline samples of **1-R** and **2-R** (R = OMe, Cl, NO_2, SMe_2) at 80 K..... 568

Figure 7.5 UV-Vis spectra for MeCN solutions of **1-R** and **2-R** (R = OMe, Cl, NO_2, SMe_2) 570

Figure 7.6 VT dc magnetic susceptibility data for **1-R** (R = OMe, Cl, NO_2, SMe_2)..... 572

Figure 7.7 VT dc magnetic susceptibility data for **2-R** (R = OMe, Cl, NO_2, SMe_2)..... 575

Figure 7.8 Variable-frequency out-of-phase ac susceptibility data and Arrhenius plot of relaxation time for **2-OMe** 577

Figure 7.9 FT-IR spectra for **1-R** (R = OMe, Cl, NO_2, SMe_2) 585

Figure 7.10 FT-IR spectra for **2-R** (R = OMe, Cl, NO_2, SMe_2) 586

Figure 7.11 FT-IR spectra for **1-OMe** and **2-OMe** 587

Figure 7.12 FT-IR spectra for **1-Cl** and **2-Cl** 588

Figure 7.13 FT-IR spectra for **1-NO_2** and **2-NO_2** 589

Figure 7.14 FT-IR spectra for **1-SMe_2** and **2-SMe_2** 590

Figure 7.15 Plot of $E_{1/2}$ for the ligand-based redox process $^RL^{x-/(x+1)-\bullet}$ (*x* = 2: R = OMe, Cl, NO_2; *x* = 0: R = SMe_2) against the Hammett substituent constant σ_p for **1-R** (R = OMe, Cl, NO_2, SMe_2) 591

Figure 7.16 Plot of $E_{1/2}$ for the metal-based redox process $Fe^{II}Fe^{II}/Fe^{II}Fe^{III}$ against the Hammett substituent constant σ_p for **1-R** (R = OMe, Cl, NO_2, SMe_2)..... 592

Figure 7.17 ^{1}H NMR spectrum for **1-OMe** in MeCN-d_3 593

Figure 7.18 ^{1}H NMR spectrum for **1-Cl** in MeCN-d_3 594

Figure 7.19 ^{1}H NMR spectrum for **1-NO$_2$** in MeCN-d_3 595

Figure 7.20 ^{1}H NMR spectrum for **1-SMe$_2$** in MeCN-d_3 596

Figure 7.21 ^{1}H NMR spectra for **1-R** (R = OMe, Cl, NO$_2$, SMe$_2$) in MeCN-d_3 597

Figure 7.22 ^{1}H NMR spectrum for **2-OMe** in MeCN-d_3 598

Figure 7.23 ^{1}H NMR spectra for **1-OMe** and **2-OMe** in MeCN-d_3 599

Figure 7.24 ^{1}H NMR spectrum for **2-Cl** in MeCN-d_3 600

Figure 7.25 ^{1}H NMR spectra for **1-Cl** and **2-Cl** in MeCN-d_3 601

Figure 7.26 ^{1}H NMR spectrum for **2-NO$_2$** in MeCN-d_3 602

Figure 7.27 ^{1}H NMR spectra for **1-NO$_2$** and **2-NO$_2$** in MeCN-d_3 603

Figure 7.28 ^{1}H NMR spectrum for **2-SMe$_2$** in MeCN-d_3 604

Figure 7.29 ^{1}H NMR spectra for **1-SMe$_2$** and **2-SMe$_2$** in MeCN-d_3 605

Figure 7.30 ^{1}H NMR spectra for **2-R** (R = OMe, Cl, NO$_2$, SMe$_2$) in MeCN-d_3 606

Figure 7.31 UV-Vis spectrum for Me$_3$TPyA in MeCN 607

Figure 7.32 UV-Vis-NIR spectrum for H$_2$(^{OMe}L) in MeCN 608

Figure 7.33 UV-Vis-NIR spectrum for H$_2$(^{Cl}L) in MeCN. 609

Figure 7.34 UV-Vis-NIR spectrum for Na$_2$(^{NO2}L) in MeCN. 610

Figure 7.35 UV-Vis-NIR spectrum for (^{SMe2}L)·2.0AcOH in MeCN. 611

Figure 7.36 UV-Vis-NIR spectra for **1-R** (R = OMe, Cl, NO$_2$, SMe$_2$) in the 350–1150 nm range 612

Figure 7.37 UV-Vis-NIR spectra for **2-R** (R = OMe, Cl, NO$_2$, SMe$_2$) in the 450–1150 nm range 613

Figure 7.38 UV-Vis NIR spectra for **1-OMe** and **2-OMe** 614

Figure 7.39 UV-Vis NIR spectra for **1-Cl** and **2-Cl** 615

Figure 7.40 UV-Vis NIR spectra for **1-NO_2** and **2-NO_2** 616

Figure 7.41 UV-Vis NIR spectra for **1-SMe_2** and **2-SMe_2** 617

Figure 7.42 Diffuse reflectance UV-Vis spectrum for **1-OMe** 618

Figure 7.43 Diffuse reflectance UV-Vis spectrum for **1-Cl** 619

Figure 7.44 Diffuse reflectance UV-Vis spectrum for **1-NO_2** 620

Figure 7.45 Diffuse reflectance UV-Vis spectrum for **1-SMe_2** 621

Figure 7.46 Diffuse reflectance UV-Vis spectrum for **2-OMe** 622

Figure 7.47 Diffuse reflectance UV-Vis spectrum for **2-Cl** 623

Figure 7.48 Diffuse reflectance UV-Vis spectrum for **2-NO_2** 624

Figure 7.49 Diffuse reflectance UV-Vis spectrum for **2-SMe_2** 625

Figure 7.50 Variable-field magnetization data for **1-OMe** collected at 100 K 626

Figure 7.51 Variable-field magnetization data for **1-Cl** collected at 100 K 627

Figure 7.52 Variable-field magnetization data for **1-NO_2** collected at 100 K 628

Figure 7.53 Variable-field magnetization data for **1-SMe_2** collected at 100 K 629

Figure 7.54 Variable-field magnetization data for **2-OMe** collected at 100 K 630

Figure 7.55 Variable-field magnetization data for **2-Cl** collected at 100 K 631

Figure 7.56 Variable-field magnetization data for **2-NO_2** collected at 100 K 632

Figure 7.57 Variable-field magnetization data for **2-SMe_2** collected at 100 K 633

Figure 7.58 Low-temperature magnetization data for **1-OMe** at 1–7 T dc fields 634

Figure 7.59 Low-temperature magnetization data for **1-Cl** at 1–7 T dc fields 635

Figure 7.60 Low-temperature magnetization data for **1-NO_2** at 1–7 T dc fields 636

Figure 7.61 Low-temperature magnetization data for **1-SMe$_2$** at 1–7 T dc fields..... 637

Figure 7.62 Low-temperature magnetization data for **2-OMe** at 1–7 T dc fields..... 638

Figure 7.63 Low-temperature magnetization data for **2-Cl** at 1–7 T dc fields..... 639

Figure 7.64 Low-temperature magnetization data for **2-NO$_2$** at 1–7 T dc fields 640

Figure 7.65 Low-temperature magnetization data for **2-SMe$_2$** at 1–7 T dc fields..... 641

Figure 7.66 Plot of in-phase ac magnetic susceptibility against frequency for **1-OMe**. 642

Figure 7.67 Plot of out-of-phase ac magnetic susceptibility against frequency for **1-OMe**. 643

Figure 7.68 Plot of in-phase ac magnetic susceptibility against frequency for **1-Cl**..... 644

Figure 7.69 Plot of out-of-phase ac magnetic susceptibility against frequency for **1-Cl**..... 645

Figure 7.70 Plot of in-phase ac magnetic susceptibility against frequency for **1-NO$_2$** 646

Figure 7.71 Plot of out-of-phase ac magnetic susceptibility against frequency for **1-NO$_2$**..... 647

Figure 7.72 Plot of in-phase ac magnetic susceptibility against frequency for **1-SMe$_2$**. 648

Figure 7.73 Plot of out-of-phase ac magnetic susceptibility against frequency for **1-SMe$_2$**..... 649

Figure 7.74 Plot of in-phase ac magnetic susceptibility against frequency for **2-OMe**. 650

Figure 7.75 Plot of in-phase ac magnetic susceptibility against temperature for **2-OMe**..... 651

Figure 7.76 Plot of out-of-phase ac magnetic susceptibility against temperature for **2-OMe** .. 652

Figure 7.77 Plot of in-phase ac magnetic susceptibility against frequency for **2-Cl**..... 653

Figure 7.78 Plot of in-phase ac magnetic susceptibility against temperature for **2-Cl**. 654

Figure 7.79 Plot of out-of-phase ac magnetic susceptibility against frequency for **2-Cl**. 655

Figure 7.80 Plot of out-of-phase ac magnetic susceptibility against temperature for **2-Cl**..... 656

Figure 7.81 Plot of in-phase ac magnetic susceptibility against frequency for **2-NO$_2$**. 657

Figure 7.82 Plot of in-phase ac magnetic susceptibility against temperature for **2-NO$_2$**. 658

Figure 7.83 Plot of out-of-phase ac magnetic susceptibility against frequency for **2-NO$_2$**..... 659

Figure 7.84 Plot of out-of-phase ac magnetic susceptibility against temperature for **2-NO$_2$** ... 660

Figure 7.85 Plot of in-phase ac magnetic susceptibility against frequency for **2-SMe$_2$**. 661

Figure 7.86 Plot of in-phase ac magnetic susceptibility against temperature for **2-SMe$_2$**. 662

Figure 7.87 Plot of out-of-phase ac magnetic susceptibility against frequency for **2-SMe$_2$**..... 663

Figure 7.88 Plot of out-of-phase ac magnetic susceptibility against temperature for **2-SMe$_2$**.. 664

Figure 7.89 Cole–Cole plots for **2-OMe** 665

Figure 7.90 Cole–Cole plots for **2-Cl** 666

Figure 7.91 Arrhenius plot of relaxation time for **2-Cl** 667

Figure 7.92 Cole–Cole plots for **2-NO$_2$** 668

Figure 7.93 Arrhenius plot of relaxation time for **2-NO$_2$** 669

Figure 7.94 Cole–Cole plots for **2-SMe$_2$** 670

Figure 7.95 Arrhenius plot of relaxation time for **2-SMe$_2$** 671

Figure 7.96 Plot of U_{eff} against the Hammett substituent constant σ_p for **2-R** (R = OMe, Cl, NO_2, SMe_2). 672

Figure 8.1 Schematic depiction of spin interactions for different classes of magnets 686

Figure 8.2 Plot of dc magnetic susceptibility vs temperature for different magnetic behavior. 687

Figure 8.3 Overview of magnetometry-based experimental methods employed to determine the magnetic ordering temperature of a material 688

Figure 8.4 Schematic illustration of a magnetic hysteresis curve for permanent magnets, along with key parameters 689

Figure 8.5 Summary of metal-binding modes for carboxylato ligands bearing one carboxylate group 697

Figure 8.6 Examples of short bridging pathways between two metal centers provided by N-heterocyclic ligands 699

Figure 8.7 Multitopic phosphonato ligands discussed in the review..... 700

Figure 8.8 Oxamato ligands discussed in the review 700

Figure 8.9 Multitopic carboxylato ligands discussed in the review 702

Figure 8.10 N-heterocyclic ligands discussed in the review 703

Figure 8.11 Ligands bearing both carboxylate groups and N-heterocycles discussed in the review, along with other ligands discussed..... 704

Figure 8.12 Crystal structure of $Co^{II}_2(OH)$(2-pmb) and variable-field dc magnetization data collected at selected temperatures..... 705

Figure 8.13 Synthesis and chirality of mixed-valence $(A)[M^{II}M^{III}(ox)_3]$ 2D frameworks of honeycomb topology..... 706

Figure 8.14 Crystal structure of the anionic 2D lattice for compounds $[K(18\text{-crown-}6)]_3[M^{II}_3(H_2O)_4(M^{III}(ox)_3)_3]$ (M^{II} = Mn^{II}, Fe^{II}, Co^{II}, Ni^{II}, Cu^{II}; M^{III} = Cr^{III}, Fe^{III}) .. 707

Figure 8.15 Crystal structure of $[Co^{II}(H_2O)_2]_3[Cr^{III}(ox)_3]_2\cdot 2(18\text{-crown-}6)$..... 709

Figure 8.16 Proton conductivity vs relative humidity profiles at 25 °C for $(R_3(CH_2COOH)N)[M^{II}M^{III}(ox)_3]\cdot xH_2O$ (R = Et, Bu; M^{II} = Mn^{II}, Fe^{II}; M^{III} = Cr^{III}, Fe^{III}; x = 0, 2) 710

Figure 8.17 Crystal structures of $[Fe^{III}(sal_2\text{-trien})][Mn^{II}Cr^{III}(ox)_3]\cdot CH_2Br_2$ and $[Fe^{III}(sal_2\text{-trien})]_2[Mn^{II}_2(ox)_3]\cdot 4H_2O\cdot$DMF..... 713

Figure 8.18 Synthesis, crystal structure, and chirality of mixed-valence $[Z^{II}(2,2'\text{-bpy})_3][M^{II}M^{III}(ox)_3](ClO_4)$ (Z^{II} = Fe^{II}, Co^{II}, Ni^{II}, Ru^{II}; M^{II} = Mn^{II}, Fe^{II}, Co^{II}, Ni^{II}, Cu^{II}; M^{III} = Cr^{III}, Fe^{III}) 3D frameworks of (10,3) net topology 714

Figure 8.19 Schematic depiction of the orientation of the crystallographic C_3 axes for adjacent metal centers in chiral 2D and 3D metal oxalate frameworks 715

Figure 8.20 Crystal structure of $[Mn^{III}(salen)(H_2O)]_2[Mn^{II}Cr^{III}(ox)_3]_2\cdot$MeOH·2MeCN and variable-field dc magnetization data for $[Mn^{III}(salen)(H_2O)]_2[Mn^{II}Cr^{III}(ox)_3]_2$ ·MeOH·2MeCN, $[Mn^{III}(salen)(H_2O)]_2[Zn^{II}Cr^{III}(ox)_3]_2\cdot$MeOH·2MeCN, and $[In^{III}(sal_2\text{-trien})][Mn^{II}Cr^{III}(ox)_3]\cdot 0.25H_2O\cdot 0.25$MeOH·0.25MeCN collected at 0.43 K..... 718

Figure 8.21 Crystal structure of $[Fe^{III}_2O(ox)_2Cl_2]^{2-}$, as observed in $(A)_2[Fe^{III}_2O(ox)_2Cl_2]\cdot 2H_2O$

(A^+ = $(NH_4)^+$, $(MeNH_3)^+$, $(Me_2NH_2)^+$, $(EtNH_3)^+$, $(H_3O)^+$) 719

Figure 8.22 Variable-field dc magnetization data for $(EtNH_3)[Fe^{III}_2(OH)(ox)_2Cl_2]\cdot 2H_2O$ and $(H_3O)(EtNH_3)[Fe^{III}_2O(ox)_2Cl_2]\cdot H_2O$, collected at 2.0 K 720

Figure 8.23 Crystal structure and spin topology of $[Cu^{II}_2(mpba)_2]^{4-}$ 721

Figure 8.24 Crystal structure and magnetic data for $Co^{II}_2Cu^{II}_2(mpba)_2(H_2O)_6\cdot 6H_2O$ 722

Figure 8.25 Crystal structure of $[Mn^{II}_4(Cu^{II}_2(Me_3mpba)_2(H_2O)_{3.33})_3]^{4-}$, as observed in $[Na(H_2O)_{3.25}]_4[Mn^{II}_4(Cu^{II}_2(Me_3mpba)_2(H_2O)_{3.33})_3]\cdot 37H_2O$, and VT out-of-phase ac magnetic susceptibility data with different guest molecules..... 726

Figure 8.26 Crystal structure of Mn^{II}(succ)..... 731

Figure 8.27 Crystal structures of Mn^{II}(*meso*-2,3-dmsucc) and Mn^{II}(*meso*-2,3-dmsucc)$(H_2O)\cdot H_2O$ 733

Figure 8.28 Crystal structure of the corrugated twenty-membered ring in $Ni^{II}_{20}(glu)_{20}(H_2O)_8\cdot 40H_2O$ and crystal structure of Co^{II}(glu) 735

Figure 8.29 Crystal structure of $Co^{II}_4(OH)_2(seba)_3$ and VT ac magnetization data 736

Figure 8.30 Crystal structure of $Co^{II}_2(hypa)_2(4,4'\text{-bpy})\cdot 1.5H_2O$ 738

Figure 8.31 Crystal structure of Co^{II}_2(O-ma)(4-pyc)$\cdot 2H_2O$ 741

Figure 8.32 Crystal structures of $Mn^{II}_2(OH)_2(squ)$ and $Co^{II}_3(OH)_2(squ)_2\cdot 3H_2O$ 744

Figure 8.33 Crystal structure of $Co^{II}_2(cbut)(H_2O)_3$ 746

Figure 8.34 Crystal structure of $Ni^{II}_3(OH)_2$(*cis*-1,4-chdc)$_2(H_2O)_4\cdot 2H_2O$..... 747

Figure 8.35 Crystal structures of V^{III}(OH)(1,4-bdc)$\cdot$0.75(1.4-H_2bdc) (MIL-47as) and V^{IV}(O)(1,4-bdc) (MIL-47) 750

Figure 8.36 Crystal structure of Cu^{II}_2(1,3,-bdc)$_2(py)_2$ 754

Figure 8.37 Crystal structure, spin topology, and VT dc magnetic susceptibility data for $Co^{II}_5(OH)_2$(1,2,4,5-btec)$_2$(bpp) 758

Figure 8.38 Crystal structures of Co^{II}_3(OH)(bpc)$(H_2O)_3$ and Co^{II}(thiosal)..... 760

Figure 8.39 Representation of the spin polarization mechanism between two paramagnetic metal

centers through pyrazine, pyrazine-1,4-dioxide, and pyrimidine linkers..... 764

Figure 8.40 Crystal structures of $Co^{II}(F\text{-}pymo)_2\cdot 2.5H_2O$ and $Cu^{II}(F\text{-}pymo)_2\cdot 1.25H_2O$, and VT dc magnetic susceptibility data for $Cu^{II}(F\text{-}pymo)_2\cdot 1.25H_2O$ and its anhydrous analogue with/without presence of CO_2 766

Figure 8.41 Crystal structures of $Fe^{II}_3(im)_6(imH)_2$ and $Fe^{II}(2\text{-}Meim)_2\cdot 0.13(Cp_2Fe^{II})$..... 769

Figure 8.42 Crystal structure of $Cu^{II}(trz)(N_3)$..... 770

Figure 8.43 Crystal structure of $Co^{II}_3(\textit{rac}\text{-}O\text{-}lac)_2(pybz)_2\cdot 3DMF$..... 773

Figure 8.44 Comparison of bis-bidentate ligands with N_4, N_2O_2, NO_3, and O_4 donor sets 775

Figure 8.45 Crystal structure of $[Fe^{II}_2(pymca)_3](OH)\cdot H_2O$..... 776

Figure 8.46 Crystal structure of $Co^{II}_3(OH)_2(btca)_2\cdot 3.7H_2O$ and VT ac magnetic susceptibility data 777

Figure 8.47 Redox series of deprotonated benzoquinoid ligands with donor atoms E and substituents R 779

Figure 8.48 VT ac magnetic susceptibility data for $(Bu_4N)[Mn^{II}Cr^{III}(R_2An)_3]$ (R = Cl, Br, I, H) and a plot of magnetic ordering temperature and Weiss temperature vs Pauling electronegativity of the R substituents 780

Figure 8.49 Crystal structures of $(Et_2NH_2)[Mn^{II}Cr^{III}(Br_2An)_3]$ and $(Et^{\textit{i}}Pr_2NH)[Mn^{II}Cr^{III}(Br_2An)_3]\cdot 0.5CHCl_3\cdot H_2O$..... 784

Figure 8.50 VT electrical resistivity data for $[(H_3O)(H_2O)(phz)_3][Fe^{II}Fe^{III}(R_2An)_3]\cdot 12H_2O$ (R = Cl, Br) along different orientations and Arrhenius plots of the data..... 785

Figure 8.51 Organic radical linkers discussed in the review..... 788

Figure 8.52 Crystal structure of $(4\text{-}MePyNO)_2Mn^{II}_2(Cu^{II}(opba))_3(DMSO)_2\cdot 2H_2O$..... 790

Figure 8.53 Crystal structure of $Cu^{II}_3(PTMTC)_2(py)_6(EtOH)_2(H_2O)\cdot 10EtOH\cdot 6H_2O$ 793

Figure 8.54 Crystal structure and magnetic data for $Mn^{II}(TCNE^{-\bullet})_{1.5}(I_3)_{0.5}\cdot 0.5THF$ 797

Figure 8.55 Crystal structure of $Mn^{II}(TCNE^{-\bullet})I(H_2O)$ 798

Figure 8.56 Crystal structure of $(Ru_2(TFA)_4)_2(TCNQF_4)\cdot 3(\textit{p}\text{-xylene})$ and VT dc magnetic

susceptibility data 800

Figure 8.57 Crystal structure of $(Ru_2(1,3\text{-}Fbz)_4)_2(BTDA\text{-}TCNQ)\cdot 1.6(4\text{-}ClPhMe)\cdot 3.4CH_2Cl_2$ 804

Figure 8.58 VT FC dc magnetization data for $(Me_2NH_2)_2[Fe_2(Cl_2An)_3]\cdot 2H_2O\cdot 6DMF$ and $(Me_2NH_2)_2[Fe_2(Cl_2An)_3]$, and variable-field dc magnetization data at selected temperatures 806

Figure 8.59 Plot comparing the magnetic ordering temperature and room-temperature electrical conductivity values for structurally-characterized metal-organic solids 807

Figure 8.60 Plot of current density vs electrical field strength for $(Me_4N)_2[Mn^{II}_2(Cl_2An^{2-})_3]\cdot 3.2Et_2O$ and $Na_3(Me_4N)_2[Mn^{II}_2(Cl_2An^{3-\bullet})_3]\cdot 3.9THF$, collected at 295 K 808

Figure 8.61 Crystal structure of $(Bu_4N)_2[Fe^{III}_2(dhbq^{3-\bullet})_2(dhbq^{2-})]$ and VT electrical conductivity data for $(Bu_4N)_2[Fe^{III}_2(dhbq^{3-\bullet})_2(dhbq^{2-})]$ and $Na_{0.9}(Bu_4N)_{1.8}[Fe^{III}_2(dhbq^{3-\bullet})_{2.7}(dhbq^{2-})_{0.3}]$ 809

List of Tables

Table 2.1 Selected mean interatomic distances and angles for **1a**·0.5MeCN, **1b**, **2a**, **2b**, and **3a** at 100 K 93

Table 2.2 Summary of ^{19}F NMR properties for **1a** and **2a** in MeCN-d_3, H_2O, and FBS 101

Table 2.3 Crystallographic data for **1a**·0.5MeCN and **1b** at 100 K 154

Table 2.4 Crystallographic data for **2a** and **2b** at 100 K 155

Table 2.5 Crystallographic data for **3a** at 100 K 156

Table 2.6 ^{19}F NMR chemical shifts of the internal standards TFE and NaF in H_2O 157

Table 2.7 Summary of ^{19}F NMR properties for **1a**, **1b**, **2a**, and **2b** in 2.1 mM TFE(aq) 158

Table 2.8 ^{19}F NMR chemical shifts of **1a** and **2a** in 2.1 mM TFE(aq) referenced to **1b** and **2b** 159

Table 2.9 Summary of ^{19}F NMR properties for **1a** and **2a** in FBS 160

Table 2.10 ^{19}F NMR chemical shifts of **1a** and **2a** in FBS referenced to **1b** and **2b** 161

Table 2.11 Summary of ^{19}F NMR properties for **1a**, **1b**, **2a**, and **2b** in MeCN-d_3 162

Table 3.1 Selected mean interatomic distances and angles for **1′** and **2′** at 100 K 179

Table 3.2 Crystallographic data for **1′** and **2′** at 100 K 272

Table 3.3 Summary of solution dc magnetic susceptibility data for **1**–**3** 273

Table 3.4 CEST frequencies used for Omega plots of **2** 274

Table 3.5 CEST frequencies used for Omega plots of **3** 275

Table 3.6 CEST frequencies used for Omega plots of **1** 276

Table 3.7 T_1 relaxation times of H_2O for various concentrations of **1** in buffer at 37 °C 277

Table 3.8 pH from phantom imaging of **1** in buffer at 37 °C vs pH electrode 278

Table 4.1 Selected mean interatomic distances and angles for **1′** and **2′-X** (X = NO_2, F, Me) at 100 K 295

Table 4.2 Crystallographic data for **2′-X** (X = NO_2, F, Me) at 100 K 413

Table 4.3 Summary of solution dc magnetic susceptibility data for **2-X** (X = NO_2, F, Me) . 414

Table 4.4 CEST frequencies used for Omega plots of **2-NO_2** 415

Table 4.5 CEST frequencies used for Omega plots of **2-F** 416

Table 4.6 CEST frequencies used for Omega plots of **2-Me** 417

Table 4.7 CEST frequencies for max. OH CEST effect for 4 mM of **2-NO_2** 418

Table 4.8 CEST frequencies for max. OH CEST effect for 4 mM of **2-F** 419

Table 4.9 CEST frequencies for max. OH CEST effect for 4 mM of **2-Me** 420

Table 5.1 Summary of solution dc magnetic susceptibility data for **3** 472

Table 5.2 Proton exchange rate constants for **3** in buffer and FBS at 37 °C 473

Table 5.3 Proton exchange rate constants for **3** in buffer and gelatin gel at 37 °C 474

Table 5.4 T_1 relaxation times of H_2O in buffer and FBS at 37 °C 475

Table 6.1 Selected mean interatomic distances and octahedral distortion parameter for **1′**–**3′** and axial zero-field splitting parameter for **1**–**3** 491

Table 6.2 Dissociation constants for cation-bound complexes of **1** in D_2O at 37 °C 494

Table 6.3 Crystallographic data for **1′**–**3′** at 100 K 537

Table 6.4 Summary of K_d values for $[LCoM]^{+/2+}$ ($M^{+/2+}$ = Na^+, Mg^{2+}, K^+) in D_2O 538

Table 6.5 Summary of K_d values for $[LCoNa]^+$ in D_2O and buffers 539

Table 7.1 Selected mean interatomic distances and octahedral distortion parameter for **1-R**·solvent and **2-R**·solvent (R = OMe, Cl, NO_2, SMe_2) 562

Table 7.2 Summary of Mössbauer parameters for **1-R**·solvent and **2-R**·solvent (R = OMe, Cl, NO_2, SMe_2) at 80 K 569

Table 7.3 Summary of magnetic parameters for **1-R**·solvent and **2-R**·solvent (R = OMe, Cl, NO_2, SMe_2) 573

Table 7.4 Crystallographic data for **1-OMe**·4.0MeCN and **2-OMe**·2.0MeCN 673

Table 7.5 Crystallographic data for **1-Cl**·0.7H_2O and **2-Cl**·0.5Et_2O 674

Table 7.6 Crystallographic data for **1-NO_2**·4.0MeCN and **2-NO_2**..... 675

Table 7.7 Crystallographic data for **1-SMe**·4.0MeCN and **2-SMe_2**·0.9MeCN·0.5Et_2O..... 676

Table 7.8 Determination of *D* from magnetic data for **1-SMe_2** 677

Table 7.9 Determination of *D* from magnetic data for **2-OMe**..... 678

Table 7.10 Determination of *D* from magnetic data for **2-Cl** 679

Table 7.11 Determination of *D* from magnetic data for **2-NO_2** 680

Table 7.12 Determination of *D* from magnetic data for **2-SMe_2** 681

Table 8.1 Magnetic data for 2D metal-organic framework magnets with diamagnetic bridging ligands 815

Table 8.2 Magnetic data for 3D metal-organic framework magnets with diamagnetic bridging ligands 820

Table 8.3 Magnetic data for 2D oxalate frameworks of formula (A)[$Fe^{II}Fe^{III}(ox)_3$] 827

Table 8.4 Magnetic data for 2D oxalate frameworks of formula (A)[$Mn^{II}Fe^{III}(ox)_3$]..... 828

Table 8.5 Magnetic data for 2D oxalate frameworks of formula [K(18-crown-6)]$_3$[$M^{II}{}_3(H_2O)_4(M^{III}(ox)_3)_3$] 829

Table 8.6 Magnetic data for 2D oxalate frameworks of formula [$M^{II}(H_2O)_2$]$_3$[$M^{III}(ox)_3$]$_2$ ·2(18-crown-6) 830

Table 8.7 Magnetic data for 2D oxalate frameworks of formula [$Cp^*{}_2Fe^{III}$][$M^{II}M^{III}(ox)_3$]... 831

Table 8.8 Magnetic data for 2D oxalate frameworks of formula [$Cp^*{}_2Co^{III}$][$M^{II}M^{III}(ox)_3$] .. 832

Table 8.9 Magnetic data for 2D oxalate frameworks of formula ($R_3(CH_2COOH)N$)[$M^{II}M^{III}(ox)_3$]·*x*H_2O 833

Table 8.10 Magnetic data for 2D oxalate frameworks with intercalated spin-crossover Fe^{III} complexes or diamagnetic In^{III} analogues..... 834

Table 8.11 Magnetic data for other 2D oxalate frameworks..... 835

Table 8.12 Magnetic data for 3D oxalate frameworks of formula $[(Z^{II+n})(2,2'\text{-bpy})_3][M^{II}_2(ox)_3](ClO_4)_n$..... 836

Table 8.13 Magnetic data for 3D oxalate frameworks of formula $[Z^{I+n}][M^{II}Cr^{III}(ox)_3](ClO_4)_n$ 837

Table 8.14 Magnetic data for 3D oxalate frameworks of formula $[Z^{II}(2,2'\text{-bpy})_3][M^{II}Fe^{III}(ox)_3](ClO_4)$ 838

Table 8.15 Magnetic data for 3D oxalate frameworks of formula $[Ir^{III}(ppy)_2(2,2'\text{-bpy})][M^{II}M^{III}(ox)_3]\cdot 0.5H_2O$ 839

Table 8.16 Magnetic data for 3D oxalate frameworks with intercalated spin-crossover Fe^{II}/Fe^{III} complexes or diamagnetic In^{III} analogues..... 840

Table 8.17 Magnetic data for 3D oxalate frameworks of formula $(A)_2[Fe^{III}_2O(ox)_2Cl_2]\cdot xH_2O$ (x = 1, 2, 4) 841

Table 8.18 Magnetic data for 2D metal-organic framework magnets with radical bridging ligands 842

Table 8.19 Magnetic data for 3D metal-organic framework magnets with radical bridging ligands 843

Chapter 1: Introduction

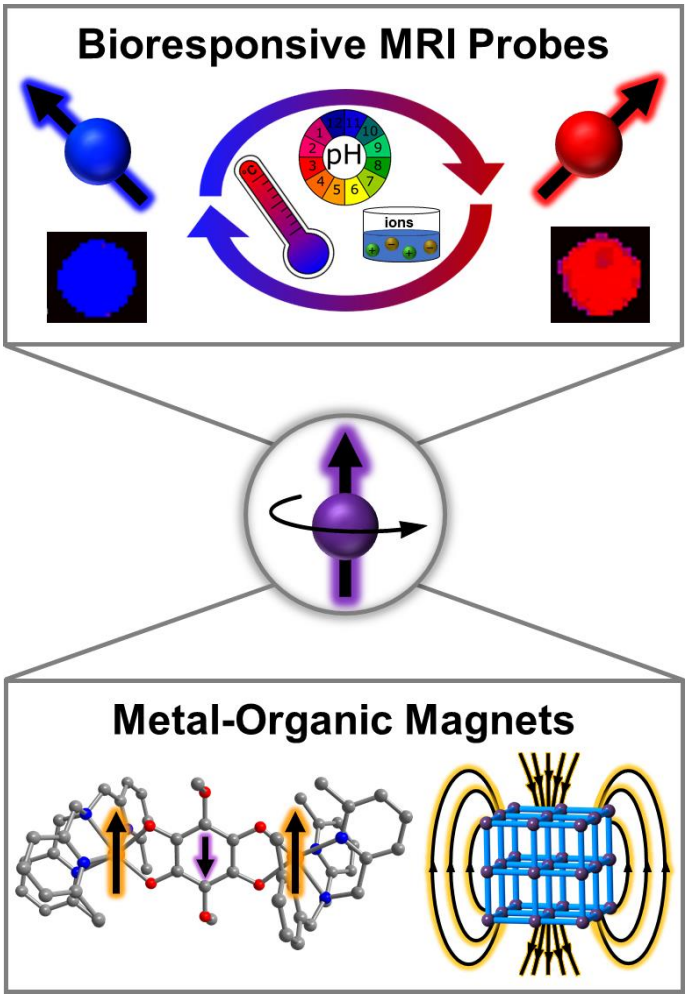

1.1 Electronic Spin Manipulation

Molecules and materials with unpaired electrons are of tremendous importance in biology as well as everyday life. For instance, dioxygen (O_2), which constitutes 21% of the air that we breathe, features two unpaired electrons, giving rise to a triplet $S = 1$ electronic ground state. Furthermore, metalloproteins of various structures and functions have active sites with transition metal ions or clusters that adopt a wide range of oxidation states and spin states.[1] In addition to these paramagnetic species, compounds that show permanent magnetic behavior owing to strong long-range interactions between electronic spins are critical to the function of a myriad of electronic devices. Furthermore, permanent magnets have revolutionized the field of data storage and processing and greatly impacted renewable energy technologies.[2]

The high sensitivity of electronic spins to their surroundings and the ability to manipulate electronic spin states in a number of ways has been employed extensively in the fields of catalysis,[3] molecule-based magnetism,[2c,e,f,4] and quantum information science[2b,d,g,5–7] to generate compounds with unique properties. Specifically, paramagnetic transition metal complexes have recently been demonstrated to be promising candidates for electronic spin-based quantum bits,[7a–l,n,p] the smallest unit of a quantum information system, and as sensors for detecting various analytes and environmental factors.[8] Here, the exceptional synthetic tunability and well-defined structures of transition metal complexes enable careful control of the local chemical environment to furnish compounds with targeted structures and properties. Furthermore, because small structural variations may lead to drastic changes in chemical and/or physical properties, this class of compounds comprise an ideal platform to develop design principles for numerous applications, ranging from magnetic resonance imaging contrast agents to quantum sensors.

The electronic structure and spin state of transition metal complexes can be modulated through a suite of external stimuli such as light, temperature, pH, pressure, electric field, microwave radiation, and the presence of different ions and analytes.[7a–l,n,p,8–10] Such highly tunable properties have engendered novel magnetic materials, some of which show fascinating multifunctional behavior.[7i,8a,c,f,i,9] My thesis work demonstrates how chemical control of electronic spins in transition metal complexes can be employed to generate novel magnetic resonance imaging (MRI) probes that are sensitive to changes in temperature, pH, and cation concentrations (Chapters 2–6), and may be utilized in developing design principles for strongly coupled molecule-based magnets that operate at high temperatures (Chapters 7 and 8).

1.2 Magnetic Resonance Imaging

Since its development in the 1970s, magnetic resonance imaging (MRI) has emerged as one of the most powerful diagnostic method in clinical medicine.[11] This non-invasive imaging technique employs non-ionizing radiofrequency radiation with unlimited tissue penetration depth to generate images with high spatiotemporal resolution.[12] Traditional MRI techniques exploit the properties of endogenous H_2O molecules to generate contrast. Specifically, changes in the spin–lattice relaxation time (T_1), spin–spin relaxation time (T_2), and proton density are commonly used to provide different image intensities for distinct types of tissues.[12c] Nevertheless, the administration of exogenous MRI contrast agents is often needed to enhance signal intensity and thus provide more reliable assessments. Most MRI contrast agents used in clinics are based on Gd^{III} chelates,[13] owing largely to the optimal electronic properties of Gd^{III} centers, including a well-isolated $S = {}^7/_2$ electronic ground state and a long room-temperature electronic relaxation time (ca. 10^{-9} s).[12a,b,14]

As such, Gd^{III} complexes are highly efficient in reducing T_1 of protons on H_2O molecules, affording both stronger signals and more rapid acquisitions.

Variations in the tissue microenvironment are prominent features of a number of pathologies including cancer, ischemia, and inflammation.[15] Because these changes may be subtle at an early stage, the use of highly responsive contrast agents is required to accurately detect physiological abnormalities. Despite the success of Gd^{III}-based contrast agents over the past few decades, lanthanide-based probes suffer from low environmental responsiveness due to the predominantly ionic nature of lanthanide–ligand bonds. Such limitation hampers their employment in imaging changes in biomarkers such as temperature, pH, and ion concentrations in vivo. Accordingly, the development of transition metal-based MRI probes, which feature more covalent metal–ligand bonds and high sensitivity to their local chemical environment, with the ability to quantitate physiological biomarkers has garnered significant recent interest.[16] Such probes are of high value for improving the understanding, early detection, and treatment of many diseases and disorders.

1.3 Chemical Shift-Based Probes

One class of bioresponsive MRI contrast agents are those based on nuclear magnetic resonance (NMR) chemical shift. Here, the chemical shift (δ) of NMR-active nuclei (typically ^1H) on endogenous molecules or exogenous contrast

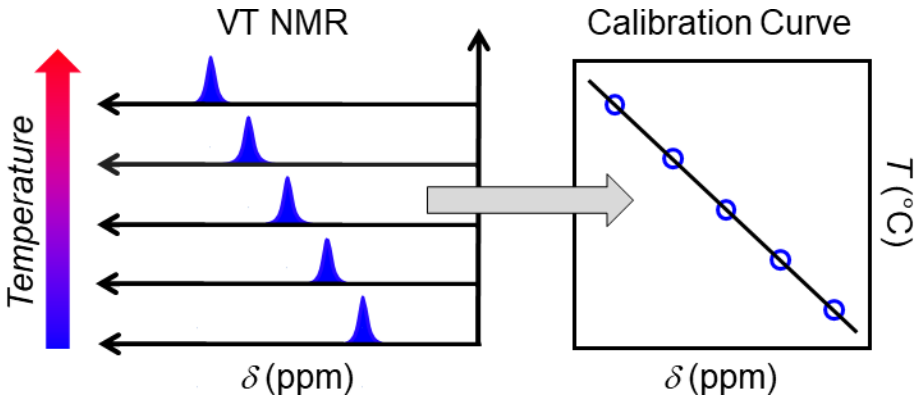

Figure 1.1 Schematic illustration of chemical shift-based MRI, using a temperature-responsive probe as an example.

agents changes as a function of external stimuli and a calibration curve may be generated and employed to quantify parameters under unknown conditions (see Figure 1.1). In contrast to NMR signal intensity, the NMR chemical shift is independent of the concentration of the probe. Such concentration-independent detection of biomarkers is critical, as an unequal biodistribution of the probe or the biomarker is not easily accounted for in vivo and may lead to false assessments. Indeed, chemical shift-based methods are commonly utilized for mapping temperature in vivo. Specifically, in discriminating normal from abnormal tissue and to ensure that thermal treatments are localized and do not damage healthy tissue.[12c,17]

While methods based on the proton resonance frequency of H_2O are most widely used, they suffer from a low temperature sensitivity of ca. −0.01 ppm per °C.[12c,18] Paramagnetic lanthanide- and high-spin transition metal-based probes featuring Tm^{III}, Tb^{III}, Dy^{III}, Yb^{III} and Fe^{II}, Co^{II} metal centers, respectively, have been developed and shown to exhibit temperature sensitivities up to 1.8 ppm per °C.[19] Despite the 180-fold enhancement in sensitivity over diamagnetic H_2O molecules, the temperature dependence of the chemical shift for these compounds is limited to the inherent Curie temperature dependence of chemical shift for paramagnetic compounds.[14]

An alternative approach that we have envisioned may provide highly temperature-responsive chemical shift probes centers on employing molecules that change its electronic spin state (*S*) as a function of temperature, as both contact and dipolar paramagnetic chemical shift scale as

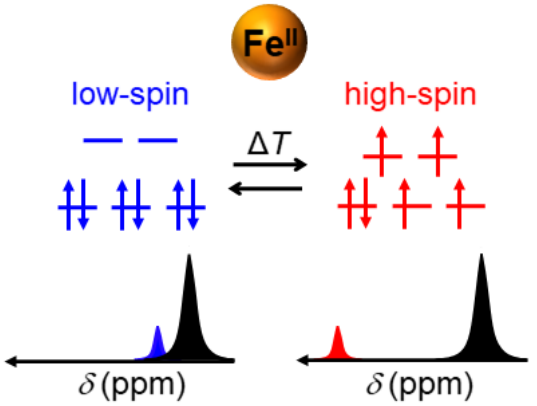

Figure 1.2 Schematic illustration of a thermally-induced spin-crossover phenomenon in octahedral Fe^{II} complexes (top), highlighting the concomitant variations in NMR chemical shift (bottom). The black peaks correspond to a diamagnetic reference compound.

$S(S+1)$.[14] One class of molecules that fulfills this criterion is spin-crossover Fe^{II} complexes that undergo a thermally-induced electronic spin transition from a low-spin $S = 0$ ground state to a high-spin $S = 2$ excited states (see Figure 1.2).[8a,9] A study that combines this strategy with using ^{19}F NMR chemical shift for temperature detection is detailed in Chapter 2. ^{19}F MRI probes are largely underexplored for temperature sensing applications but provide important benefits over conventional ^{1}H MR chemical shift-based probes. Most importantly, the absence of endogenous fluorine signal in soft tissue and wide chemical shift window afford simple NMR spectra with non-overlapping resonances.[20] Chapter 2 highlights the promise of spin-crossover Fe^{II} complexes for monitoring temperature changes in physiological environments through ^{19}F NMR chemical shift. However, collective efforts of inorganic chemists and physicists are still required to maximize sensitivity and realize practical applications with these and related ^{19}F-based MRI probes.

1.4 Paramagnetic Chemical Exchange Saturation Transfer Probes

Another class of MRI contrast agents that are well suited for detecting changes in biomarkers are those that function through the paramagnetic chemical exchange saturation transfer (PARACEST) effect. Here, exchange of labile protons on a paramagnetic molecule with those of bulk H_2O molecules is exploited to generate contrast.[21] The labile protons deliver saturation to H_2O through chemical exchange upon presaturation with radiofrequency radiation, resulting in a reduction of the H_2O signal intensity (see Figure 1.3, top). Accordingly, PARACEST contrast can be turned on and off at will, as the exchange interaction is only present upon selective irradiation at the resonance frequency of the labile protons on the probe. Importantly, the presaturation frequency-selective contrast enables simultaneous detection of multiple non-overlapping CEST peaks, which is ideal for the design of bioresponsive probes (see below).

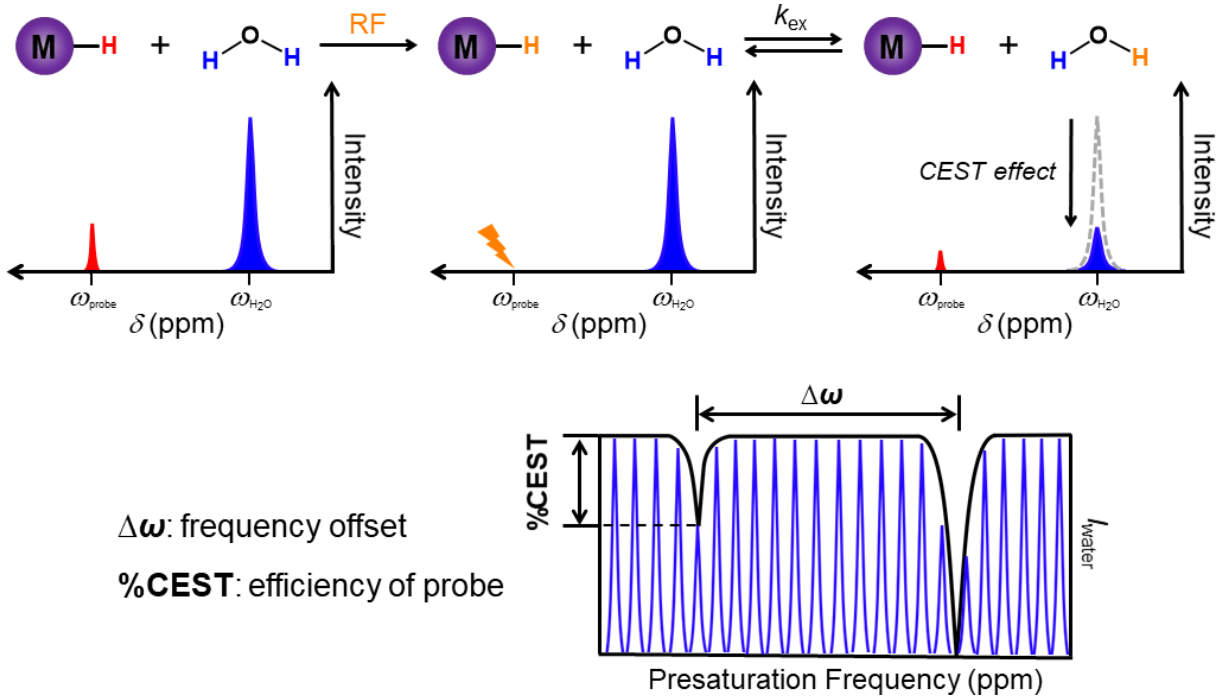

Figure 1.3 Top: Schematic illustration of how MRI contrast is generated through the PARACEST technique. Bottom: Depiction of a CEST spectrum with key parameters highlighted. RF denotes radiofrequency.

By convention, CEST spectra (i.e. Z-spectra) are plotted as the normalized integration of the H_2O signal against applied presaturation frequency (see Figure 1.3, bottom). Compared to traditional ^1H NMR spectra, CEST spectra display fewer peaks, as only those corresponding to labile protons from the PARACEST probes are observed in addition to the bulk H_2O signal, which is typically set to 0 ppm.

The efficiency of PARACEST probes is largely determined by two factors: (1) the intensity of the CEST signal (i.e. %CEST effect), and (2) the chemical shift difference between the protons on the probe and bulk H_2O (i.e. frequency offset). The latter provides an upper limit for the value of the proton exchange rate constant (k_{ex}). Within this slow-to-intermediate regime, faster exchange generally leads to stronger CEST signals, as it allows for a greater number of exchange interactions. However, less efficient saturation transfer is observed when k_{ex} is very large, resulting

in spectral broadening. One advantage of PARACEST probes over their diamagnetic analogues is the large chemical shift of their labile protons, thus avoiding interference from exchangeable protons from endogenous biomolecules.[22]

The first reported PARACEST probe was a Eu^{III} chelate featuring a coordinating H_2O molecule responsible for the CEST effect.[22a] Since this seminal work in 2001, the field of PARACEST MRI probes has been expanded to other lanthanide and transition metal complexes featuring various organic functional groups with labile protons, including amide, amine, and hydroxyl protons, along with those on N-heterocyclic ligands.[16a–c,e–k,m–p,23] These probes have been reported to detect a number of biomarkers, such as redox-environment,[16g,o] temperature,[16j,k] Zn^{2+} ions,[24] and pH.[16h,m,23,25] Of these biomarkers, PARACEST probes are especially well suited for monitoring changes in pH, due to the inherent pH sensitivity of the exchange rates of their labile protons.[22,23] Furthermore, thanks to the frequency selectivity of the PARACEST technique, multiple CEST peaks can be addressed simultaneously, allowing for the facile design of ratiometric probes. Such ratiometric approach should provide a concentration-independent measure of biomarkers and thus overcomes the intrinsic concentration dependence of the CEST signal intensity. Indeed a handful of probes have been shown to map extracellular pH in biological environments.[23c,25c,e–g,26] Nevertheless, the development of a single probe that features: (1) highly shifted CEST peaks, (2) high pH responsiveness in the physiological pH range, and (3) displays good stability in physiological environments is challenging.

Toward this end, we proposed that the utilization of a PARACEST probe featuring two distinct CEST-active groups located on distinct ligand scaffolds, whose labile protons show opposing pH-dependent changes in proton exchange rates, is an attractive strategy. The ratio of the intensities for the two distinct CEST peaks for such probe should exhibit pronounced pH sensitivity (see

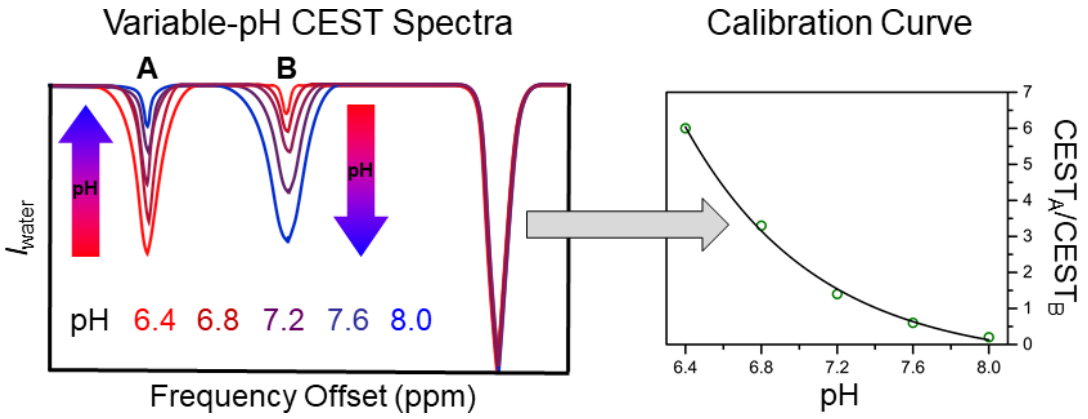

Figure 1.4 Schematic illustration of the CEST properties of an ideal PARACEST probe for the ratiometric quantitation of pH. A and B denote CEST peaks originating from two distinct functional groups on the PARACEST probe.

Figure 1.4). Chapter 3 details this novel approach toward sensing pH and demonstrates the potential of dinuclear Co^{II} complexes for the ratiometric quantitation of pH in physiological environments. Chapters 4 and 5 build on the proof-of-principle study presented in Chapter 3. Specifically, Chapter 4 focuses on the effects that ligand modifications may have on the pH-sensing performance of Co^{II}_2 PARACEST probes. In particular, how electronic effects of remote ligand substitution allow for fine-tuning of pH sensitivity and detection range. Similarly, Chapter 5 details the results of incorporating different CEST-active functional groups onto the ancillary bisphosphonate ligand in this family of Co^{II}_2 PARACEST pH probes. Notably, this work provided one of the most sensitive ratiometric MRI probe for pH sensing applications reported so far.

In addition to manipulating the distinct pH dependences of proton exchange rates for different CEST-active functional groups, other methods such as changes in local electronic environment at the metal center may also be employed for imaging biomarkers through PARACEST.[16g,j,m] Specifically, changes in magnetic anisotropy at the metal center may lead to drastic changes in the chemical shift of ligand protons. Chapter 6 details a strategy for designing such probe based on a mononuclear Co^{II} complex for detecting the concentration of Ca^{2+} ions under physiologically

relevant conditions. By utilizing the ratio of the CEST signal intensities from Ca^{2+}- and Na^{+}-bound probes, a concentration-independent measure of the concentration of Ca^{2+} ions was realized. Such studies are of immediate interest, as the concentration of Ca^{2+} in blood serum is a vital biomarker for bone-related diseases.[27]

1.5 Summary of MRI Part of Thesis

To summarize this part of my thesis, although chemical shift and PARACEST MRI probes are limited to only a handful of transition metal centers, most commonly high-spin Fe^{II}, Co^{II}, and Ni^{II} centers, that possess a short electronic relaxation time ($< 10^{-11}$ s) and thus afford sharp NMR peaks,[14] the extensive library of organic ligands and high chemical tunability of these paramagnetic complexes have enabled the creation of highly sensitive bioresponsive MRI probes. The work presented in Chapters 2–6 demonstrates the power and endless potential of synthetic inorganic chemistry.

1.6 Molecule-Based Magnets

Magnetic materials have had a profound impact on energy-related technologies, memory storage media, and innumerable electronic devices.[2,28] Nevertheless, the ever-increasing demands of modern society and call for renewable energy sources necessitates the development of new magnetic materials with improved properties and unprecedented functions. Toward this end, molecule-based magnets have been the subject of immense interest in the past few decades as potential alternatives to traditional solid-state inorganic magnets due to their exceptional chemical programmability and tunability.[4,29] Specifically, these features enable the rational design of molecules-based magnets with targeted structures and properties. Furthermore, the low density of these compounds and ease of functionalization renders them attractive candidates as lightweight

permanent magnets,[2a,e,f,4,29–32] building blocks in spintronic devices,[2b–e,h] and magnetic conductors.[30,32,33]

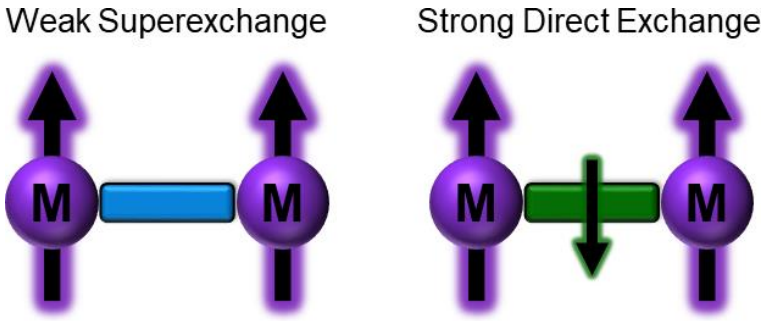

Figure 1.5 Schematic illustration of different magnetic exchange coupling mechanisms in metal-organic magnetic materials. Left: Weak indirect superexchange mechanism through a diamagnetic bridging ligand. Right: Strong direct exchange mechanism through a radical bridging ligand.

Indeed, a vast number of metal-organic materials have demonstrated fascinating single-molecule magnet[29f,34] or 1D single-chain magnet behaviors.[35] However, extending this methodology to the creation of 2D and 3D metal-organic magnets represents a formidable challenge. To illustrate, strong magnetic exchange coupling between spin centers is required to achieve permanent magnetic materials,[4,36] whereas magnetic communications through long multiatom organic bridging ligands are typically weak, as the coupling takes place via an indirect superexchange mechanism (see Figure 1.5, left).[4a] This contrasts with the direct superexchange mechanism through single-atom oxo bridges[37] and direct metal–metal bonding[38] found in conventional solid-state inorganic magnets. The latter two interactions mediate much stronger interactions between metal centers due to the greater overlap between magnetic orbitals over shorter distances.[29d,39] As such, the synthesis of metal-organic framework magnets that operate at high temperatures is a challenging task (see Chapter 8).

1.7 The Metal–Radical Approach

In contrast to the employment of diamagnetic organic bridging ligands, an alternative strategy to the generation of metal-organic framework magnets centers on the use of radical-based ligands.[29f,40] Here, the radical bridging ligand engenders strong direct magnetic exchange coupling

between spin centers owing to the direct overlap of metal- and radical-based magnetic orbitals (see Figure 1.5, right). This approach has been successfully implemented for systems featuring nitroxide,[29f,35a,c,h,40a,41] organonitrile,[30,31,33a,42] perchlorotriphenylmethyl,[43] triplet carbene,[44] and pyrazine[33b] radical ligands. Indeed, this class of compounds provides a handful of structurally-characterized framework magnets with ordering temperatures exceeding 100 K.[30b,d,31b–d] The current record holders are 2D and 3D Mn^{II} frameworks bridged by tetracyanoethylene radical ligands.[31c,d] These compounds exhibit permanent magnetic behavior below 171 K. Notably, amorphous compounds of similar compositions have been found to exhibit long-range magnetism above room temperature,[45] demonstrating the high potential of the metal–radical approach in realizing molecule-based magnets suitable for practical applications.

Another advantage of using radical bridging ligands in the construction of magnetic networks is their inherent redox activity. Such redox-active ligands are amenable to promoting electrical conductivity and thus facilitate the formation of multifunctional materials with simultaneous long-range magnetic order and high electrical conductivity,[30,32,34] which is an exceedingly rare but highly desired phenomenon among coordination solids.

1.8 Semiquinoid-Based Bridging Ligands

Despite the notable success of the radical-bridged systems mentioned in the previous section, the low charges and monodentate binding mode of each of the coordinating functional group of these ligands limit the strength of metal–radical interactions. Ligands with high negative charges and ability to engender the chelate effect should provide much stronger magnetic exchange interactions between cationic metal centers and radicals.

Toward this end, the family of benzoquinoid ligands offers an ideal platform for the construction of radical-bridged molecule-based magnets with strong magnetic coupling.[32,33c,35j,46] Specifically, these ligands possess three readily accessible negative oxidation states – the dianionic diamagnetic benzoquinoid state, the trianionic semiquinoid radical state, and the tetraanionic fully aromatic hydroquinoid state. All these forms of benzoquinoid ligands bind to metal centers in a bis-bidentate fashion. Such multidentate and rigid binding furnishes compounds with well-defined structures and high kinetic and thermal stability, even for the semiquinoid radical form.[32,33c] The facile redox chemistry and tight metal binding of benzoquinoid ligands have provided 2D frameworks with coexisting high magnetic ordering temperatures (up to 105 K) and high room-temperature electrical conductivity.[32a,b] Such high values for both properties are nearly unprecedented in a metal-organic material. An attractive switchability of magnetic order and conductivity has also been achieved by modulating the ligand oxidation state.[33c]

Furthermore, benzoquinoid ligands are prone to a high degree of chemical functionalization,[47] allowing for the rational design of magnets with targeted structures and properties. In particular, the donor atoms can be varied from oxygen atoms to nitrogen, sulfur, and phosphorus donors that feature more diffuse orbitals and thus should afford stronger coupling between spin centers (see Scheme 1.1, E). Indeed,

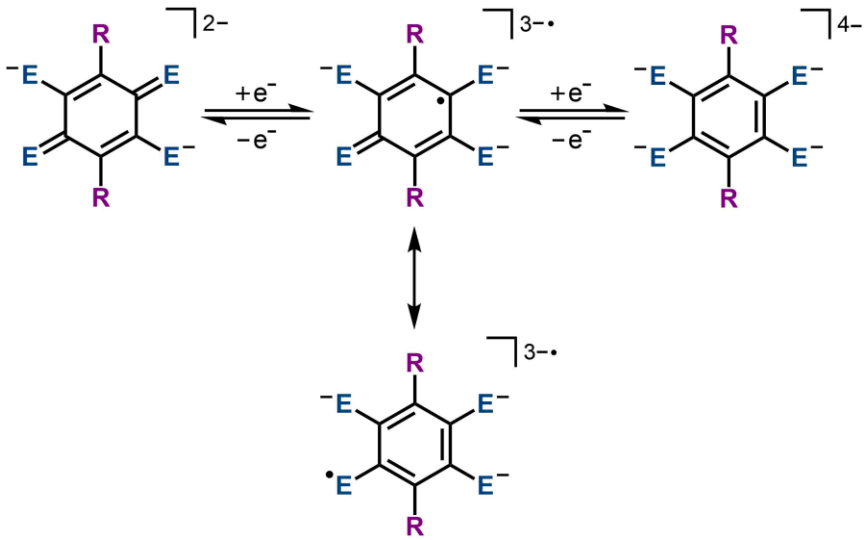

Scheme 1.1 Redox series of deprotonated benzoquinoid ligands with donor atoms E and substituents R.

dinuclear semiquinoid radical-bridged complexes featuring nitrogen- and sulfur-based donors have been shown to exhibit exceptionally strong magnetic coupling.[46c,d,f] Introduction of these types of benzoquinoid ligands into extended solids is an active area of research among inorganic chemists, but the field is currently dominated by compounds featuring more synthetically tractable tetraoxolene (all oxygen donors) ligand derivatives.

In addition to changing the donor atoms, various functional groups with different steric and electronic properties can be introduced to the two open positions on the benzoquinoid ring to further tune the magnetism in these systems (see Scheme 1.1, R). Nevertheless, there is a dearth of studies that probe the effects of bridging ligand substituents on magnetic properties for benzoquinoid compounds. To the best of our knowledge, such studies are currently limited to systems featuring diamagnetic benzoquinoid bridging ligands.[48] Accordingly, there is a significant interest in understanding how and to what extent changing the substituents on semiquinoid radical ligands influences the exchange coupling in magnetic materials. Such investigations may provide important design principles for metal-organic magnets with improved performances.

1.9 Dinuclear Complexes as Model Systems

As a first step toward addressing this lack of knowledge, we have turned to dinuclear complexes as model systems due to their structural simplicity and well-understood magnetic behaviors. Specifically, the magnetic exchange coupling constant *J* can be readily quantified and compared across a series of compounds featuring different bridging ligand derivatives. Furthermore, dinuclear complexes with strong coupling between spin centers may exhibit single-molecule magnet behavior,[29f,46c,d] and thus provide additional magnetic parameters to explore as a function of ligand identity. Chapter 7 details the synthesis, characterization, and magnetic

properties of two series of isostructural dinuclear Fe^{II} complexes, one featuring diamagnetic benzoquinoid bridging ligands and the other bearing semiquinoid radical bridging ligands. The radical-bridged derivatives do behave as single-molecule magnets. Within both series of compounds, the electronic properties of the bridging ligand substituents are varied to enable a systematic investigation of the effects of ring substituents on magnetic interactions in quinoid-based systems. This chapter highlights that the effects of ligand substitution on magnetic coupling strength in benzoquinoid compounds are highly dependent on the redox state of the bridging ligand.

Chapter 2: Spin-Crossover and High-Spin Iron(II) Complexes as Chemical Shift ^{19}F Magnetic Resonance Thermometers

Reprinted with permission from:

Thorarinsdottir, A. E.; Gaudette, A. I.; Harris, T. D. *Chemical Science* **2017**, *8*, 2448–2456.

This work was performed in collaboration with the co-authors listed above.

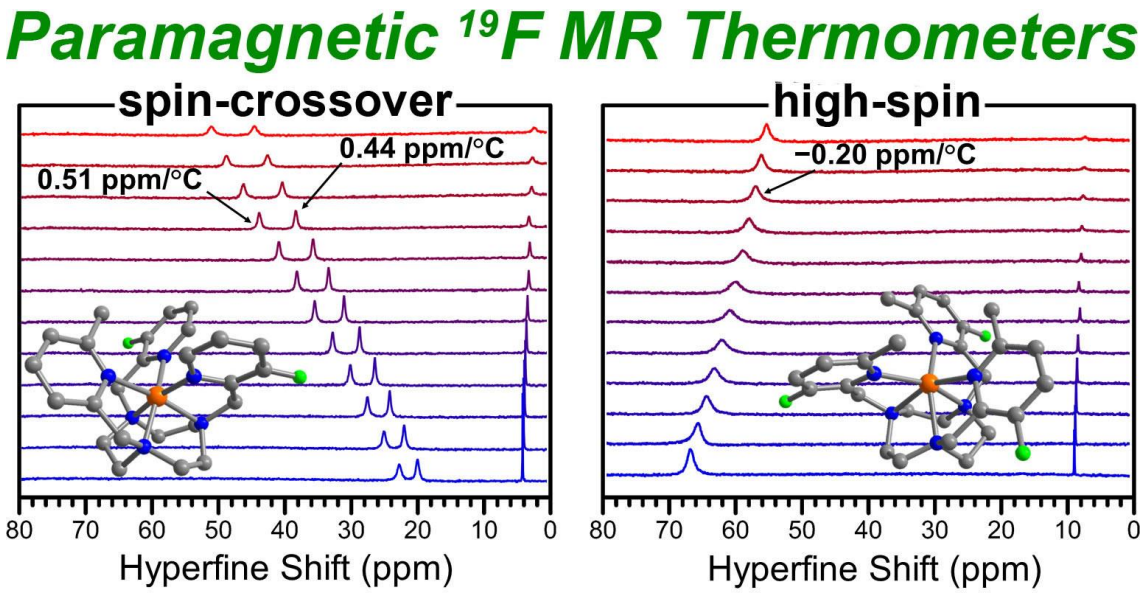

2.1 Introduction

The non-invasive measurement of temperature in vivo represents a growing area of research, largely due to its utility in medical applications such as low-temperature hyperthermia,[1,2] high-temperature thermal ablation,[1,2] and the treatment of heart arrhythmias.[3] Here, thermometry may be used to discriminate normal from abnormal tissue, and also to ensure that thermal treatments are localized to prevent damage to healthy tissue.[1,2,4] Magnetic resonance spectroscopy (MRS) and imaging (MRI) are particularly well suited toward this end, owing to their use of non-ionizing radiation and ability to deeply penetrate tissue.[1,5] Indeed, a number of temperature-sensitive MR parameters of water, including T_1 and T_2 relaxation times, proton resonance frequency (PRF), diffusion coefficient, and proton density, can be used to monitor tissue temperature.[1,4,6] Currently, methods based on water PRF shift are the most widely used for imaging temperature in clinical studies due to their high-resolution and independence on tissue type.[7] However, these techniques suffer from a low temperature sensitivity of ca. –0.01 ppm per °C, and their ability to accurately determine absolute temperature is limited.[1,7,8]

In order to overcome sensitivity limitations, paramagnetic lanthanide[9] and transition metal complexes[10] that function as MRS probes have been developed for thermometry. These complexes feature paramagnetically shifted proton resonances, thus minimizing the interference from background signal in biological tissue. In particular, proton resonances of Tm^{3+}, Tb^{3+}, Dy^{3+} and Yb^{3+} complexes have been shown to exhibit temperature sensitivities of up to 1.8 ppm per °C,[9q] and have been employed for temperature mapping in vitro and in vivo.[9] Additionally, transition metal MRS probes have been shown to exhibit similar sensitivity[10] and may alleviate toxicity concerns associated with lanthanides.[11]

While paramagnetic MRS probes offer significant improvements in sensitivity over PRF thermometry, they are nevertheless limited to the inherent Curie temperature dependence of chemical shift in paramagnetic compounds.[12] Alternatively, one can employ a strategy of tuning a physical parameter that itself depends on temperature and governs chemical shift. Since both contact (through-bond) and dipolar (through-space) hyperfine shift scale as $S(S + 1)$, where S represents the electronic spin state, variation of S as a function of temperature can result in dramatic changes in chemical shift.[12] As such, an ideal temperature-responsive chemical shift probe might feature a value of S that changes with temperature. Spin-crossover Fe^{II} complexes that undergo a thermally-induced electronic spin transition from a low-spin, $S = 0$ ground state to a high-spin, $S = 2$ excited state satisfy just such a criterion. Moreover, the ligand field in spin-crossover complexes can be chemically modulated to precisely tune the crossover temperature ($T_{1/2}$), defined as the temperature at which the low-spin and high-spin states are equally populated,[13] to near 37 °C. Indeed, the utility of spin-crossover in MR thermometry has been demonstrated through T_2^* modulation in Fe^{II}-based nanoparticles[14] and through paramagnetic chemical exchange saturation transfer (PARACEST) in molecular Fe^{II} complexes.[15]

While the vast majority of MRS thermometry probes exploit changes in the chemical shift of ^1H NMR resonances, the employment of ^{19}F MR offers several key advantages. First, the ^{19}F nucleus features a 100% natural abundance, a nuclear spin of $I = {}^1/_2$, and a gyromagnetic ratio and sensitivity close to that of ^1H.[16] Moreover, the near absence of endogenous fluorine signals in the body, the large spectral window of ^{19}F resonances, and the remarkable sensitivity of ^{19}F chemical shift to the local environment, give rise to NMR spectra with minimal peak overlap.[17] Indeed, it has been demonstrated that ^{19}F chemical shifts of transition metal porphyrin complexes are highly

sensitive to their solution electronic structure, in particular to oxidation state and spin state.[18] In addition, lanthanide-based ^{19}F chemical shift probes for monitoring pH have been reported.[19] However, despite the potential of *S* as a tunable parameter to increase the temperature sensitivity of ^{19}F MR chemical shift, to our knowledge no paramagnetic ^{19}F MR thermometers have been reported. In fact, diamagnetic perfluorocarbons represent the only examples of ^{19}F MR thermometry, but the application of these compounds is limited by the small temperature dependence of their ^{19}F chemical shifts that affords a maximum sensitivity of only 0.012 ppm per °C.[20]

Given the advantages of ^{19}F over ^{1}H MR, in conjunction with the temperature sensitivity of ^{1}H MR chemical shifts of our previously reported spin-crossover Fe^{II} PARACEST probes[15] and the high-spin Fe^{II} ^{1}H MR shift probes reported by Morrow and coworkers,[10] we sought to develop fluorine-substituted spin-crossover and high-spin Fe^{II} complexes for chemical shift ^{19}F MR thermometry. Herein, we report a series of complexes that feature new symmetrically and asymmetrically-substituted 1,4,7-triazacyclononane (tacn) derivatives with fluorinated 2-picolyl donors. The potential utility of spin-crossover and high-spin Fe^{II} complexes as chemical shift ^{19}F MR thermometers is demonstrated through detailed analysis of their temperature-dependent spectroscopic and magnetic properties. Furthermore, these compounds exhibit excellent stability in a physiological environment, as revealed by VT ^{19}F NMR spectra recorded in fetal bovine serum (FBS). To our knowledge, this work provides the first examples of paramagnetic chemical shift ^{19}F MR thermometers.

2.2 Experimental Section

General Considerations. Unless otherwise specified, the manipulations described below were

carried out at ambient atmosphere and temperature. Air- and water-free manipulations were performed under a dinitrogen atmosphere in a Vacuum Atmospheres Nexus II glovebox or using a standard Schlenk line. Glassware was oven-dried at 150 °C for at least 4 h and allowed to cool in an evacuated antechamber prior to use in the glovebox. Acetonitrile (MeCN), dichloromethane (CH_2Cl_2), diethyl ether (Et_2O) and methanol (MeOH) were dried using a commercial solvent purification system from Pure Process Technology and stored over 3 or 4 Å molecular sieves prior to use. Water was obtained from a purification system from EMD Millipore. Elemental analysis was conducted by Midwest Microlab Inc. Deuterated solvents were purchased from Cambridge Isotope Laboratories and stored over 3 or 4 Å molecular sieves prior to use. The compounds Ts_3-dient (*N,N′,N″*-tri(*p*-toluenesulfonyl)diethylenetriamine) and Ts_2-glycol (1,2-di(*p*-toluenesulfonyloxy)ethane) were synthesized following literature procedures.[21] All other chemicals and solvents were purchased from commercial vendors and used without further purification. Experimental details on the syntheses of ligands and organic precursors are provided in Section 2.5.1.

*Synthesis of [Fe(L_1)](BF_4)$_2$·0.5MeCN (**1a**·0.5MeCN).* Under an inert atmosphere of dinitrogen, a pale pink suspension of $Fe(BF_4)_2·6H_2O$ (44.7 mg, 0.130 mmol) in MeCN (1.5 mL) was added dropwise to a stirring orange solution of L_1 (62.9 mg, 0.140 mmol) in MeCN (2.5 mL). During the addition, a color change to dark orange, then red, and finally to dark olive green was observed. The solution was stirred at ambient temperature for 1.5 h and then filtered. Vapor diffusion of Et_2O into the resulting dark olive green solution afforded dark red block-shaped crystals of **1a**·0.5MeCN (0.036 g, 39%) suitable for single-crystal X-ray diffraction analysis. The compound was placed under vacuum at ambient temperature for 24 h to give desolvated **1a**. Anal. Calcd. for

$C_{25}H_{30}B_2F_{10}FeN_6$: C, 44.03; H, 4.43; N, 12.32%. Found: C, 43.90; H, 4.60; N, 12.39%. UV-Vis absorption spectra (59 μM; H_2O, 25 °C): 263 nm (ε = 12400 M^{-1} cm^{-1}), 436 nm (ε = 5400 M^{-1} cm^{-1}); (55 μM; MeCN, 25 °C): 264 nm (ε = 10700 M^{-1} cm^{-1}), 424 nm (ε = 2800 M^{-1} cm^{-1}). ESI-MS (*m*/*z*): calcd. for $C_{25}H_{30}F_2FeN_6$ ($[M]^{2+}$) 254.09, found: 253.96.

*Synthesis of [Zn(L₁)](BF₄)₂ (**1b**)*. Under an inert atmosphere of dinitrogen, a colorless solution of $Zn(BF_4)_2 \cdot 5.3H_2O$ (11.8 mg, 0.035 mmol) in MeCN (1.5 mL) was added dropwise to a stirring dark orange solution of L_1 (16.7 mg, 0.037 mmol) in MeCN (2.5 mL). No distinct color change was observed during the addition of the metal salt, and the light orange solution was stirred at ambient temperature for 3 h and then filtered. Removal of the solvent under reduced pressure afforded a red-brown oily residue which was dissolved in a MeOH/MeCN 3:1 mixture (0.8 mL). Vapor diffusion of Et_2O into this dark red solution afforded a mixture of a polycrystalline colorless solid and a light orange solid that was washed with Et_2O. Colorless plate-shaped crystals of **1b** (0.011 g, 45%) suitable for single-crystal X-ray diffraction analysis were grown from a concentrated dark orange solution of the polycrystalline solid (10 mg/mL) in MeOH/MeCN (2:1). Anal. Calcd. for $C_{25}H_{30}B_2F_{10}N_6Zn$: C, 43.42; H, 4.37; N, 12.15%. Found: C, 43.67; H, 4.52; N, 12.13%. UV-Vis absorption spectra (72 μM; H_2O, 25 °C): 268 nm (ε = 11200 M^{-1} cm^{-1}); (8.8 × 10^{-6} M; MeCN, 25 °C): 268 nm (ε = 30500 M^{-1} cm^{-1}). ESI-MS (*m*/*z*): Calcd. for $C_{25}H_{30}F_2N_6Zn$ ($[M]^{2+}$) 258.09, found: 257.98.

*Synthesis of [Fe(L₂)](BF₄)₂ (**2a**)*. Under an inert atmosphere of dinitrogen, a pale pink suspension of $Fe(BF_4)_2 \cdot 6H_2O$ (41.3 mg, 0.120 mmol) in MeCN (1.5 mL) was added dropwise to a stirring light orange solution of L_2 (64.1 mg, 0.130 mmol) in MeCN (3.5 mL). The resulting dark orange solution was stirred at ambient temperature for 3 h and then filtered. The dark orange filtrate

was concentrated under reduced pressure to give a dark yellow solid. Vapor diffusion of Et_2O into a concentrated dark orange solution (10 mg/mL) of this solid in MeOH/MeCN (1:1) gave light yellow plate-shaped crystals of **2a** (0.042 g, 48%) suitable for single-crystal X-ray diffraction analysis. Anal. Calcd. for $C_{27}H_{36.2}B_2F_{11}FeN_6O_{1.6}$ (**2a**·$1.6H_2O$): C, 42.84; H, 4.82; N, 11.10%. Found: C, 43.00; H, 4.76; N, 11.00%. UV-Vis absorption spectra (69 μM; H_2O, 25 °C): 276 nm (ε = 18800 M^{-1} cm^{-1}), 369 nm (ε = 1600 M^{-1} cm^{-1}); (55 μM; MeCN, 25 °C): 273 nm (ε = 11100 M^{-1} cm^{-1}), 371 nm (ε = 800 M^{-1} cm^{-1}). ESI-MS (*m*/*z*): Calcd. for $C_{27}H_{33}F_3FeN_6$ $([M]^{2+})$ 277.10, found: 276.99.

*Synthesis of [Zn(L₂)](BF₄)₂ (**2b**)*. Under an inert atmosphere of dinitrogen, a colorless solution of $Zn(BF_4)_2$·$5.3H_2O$ (20 mg, 0.059 mmol) in MeCN (1.5 mL) was added dropwise to a stirring light orange solution of L_2 (31 mg, 0.062 mmol) in MeCN (2.5 mL). The resulting light orange solution was stirred at ambient temperature for 3 h, then filtered and concentrated under vacuum to give a light brown oily solid. Colorless block-shaped crystals of **2b** (0.022 g, 51 %) suitable for single-crystal X-ray diffraction analysis were grown from a concentrated light orange solution of the solid (15 mg/mL) in MeOH/MeCN (1:1). Anal. Calcd. for $C_{27}H_{34.4}B_2F_{11}N_6O_{0.7}Zn$ (**2b**·$0.7H_2O$): C, 43.22; H, 4.62; N, 11.20%. Found: C, 43.26; H, 4.76; N, 11.20%. UV-Vis absorption spectra (30 μM; H_2O, 25 °C): 278 nm (ε = 13400 M^{-1} cm^{-1}); (25 μM; MeCN, 25 °C): 278 nm (ε = 35700 M^{-1} cm^{-1}). ESI-MS (*m*/*z*): Calcd. for $C_{27}H_{33}F_3N_6Zn$ $([M]^{2+})$ 281.10, found: 280.97.

*Synthesis of [Fe(L₃)](BF₄)₂ (**3a**)*. Under an inert atmosphere of dinitrogen, a pale pink suspension of $Fe(BF_4)_2$·$6H_2O$ (42.6 mg, 0.126 mmol) in MeCN (1 mL) was added dropwise to a stirring yellow-orange solution of L_3 (63.4 mg, 0.139 mmol) in MeCN (2 mL) to give a dark red

solution. This solution was stirred at ambient temperature for 1.5 h and then filtered. Removal of the solvent under reduced pressure yielded a red oily residue. Vapor diffusion of Et_2O into a concentrated dark red solution (10 mg/mL) of this compound in MeOH/MeCN (1:1) gave dark red hexagonal prism-shaped crystals of **3a** (0.046 g, 53%) suitable for single-crystal X-ray diffraction analysis. Anal. Calcd. for $C_{24}H_{27}B_2F_{11}FeN_6$: C, 42.02; H, 3.97; N, 12.25%. Found: C, 41.52; H, 4.13; N, 12.39%. UV-Vis absorption spectra (51 μM; H_2O, 25 °C): 260 nm (ε = 13900 M^{-1} cm^{-1}), 437 nm (ε = 7900 M^{-1} cm^{-1}); (40 μM; MeCN, 25 °C): 261 nm (ε = 17700 M^{-1} cm^{-1}), 436 nm (ε = 10600 M^{-1} cm^{-1}). ESI-MS (*m*/*z*): Calcd. for $C_{24}H_{27}F_3FeN_6$ ($[M]^{2+}$) 256.08, found: 255.95.

X-ray Structure Determination. Single crystals of **1a**·0.5MeCN, **1b**, **2a**, **2b**, and **3a** were directly coated with Paratone-N oil, mounted on a MicroMounts rod and frozen under a stream of dinitrogen during data collection. The crystallographic data were collected at 100 K on a Bruker Kappa Apex II diffractometer equipped with an APEX-II detector and MoKα sealed tube source. Raw data were integrated and corrected for Lorentz and polarization effects with *SAINT* v8.34A.[22] Absorption corrections were applied using the program SADABS.[23] Space group assignments were determined by examining systematic absences, E-statistics, and successive refinement of the structures. Structures were solved using direct methods in SHELXT and refined by SHELXL[24] operated within the OLEX2 interface.[25] All hydrogen atoms were placed at calculated positions using suitable riding models and refined using isotropic displacement parameters derived from their parent atoms. Thermal parameters for all non-hydrogen atoms were refined anisotropically. Crystallographic data for these compounds at 100 K and the details of data collection are listed in Tables 2.3–2.5. Significant disorder of $(BF_4)^-$ counterions was modelled in the crystal structures of **1a**·0.5MeCN and **3a**. However, only partial modelling of the disorder was achieved for

1a·0.5MeCN, where the disordered $(BF_4)^-$ ions accounted for the highest peaks in the difference Fourier map. Disordered lattice solvent molecules were present in the void space in the structures of compounds **2a** and **2b**, these species could not be identified and modelled properly. Therefore, they were treated as a diffuse contribution to the overall scattering without specific atom positions using the solvent masking procedure implemented in OLEX2. One of the two molecules in the asymmetric unit in the crystal structure of **1b** was severely disordered and had to be refined using restraints on all atoms. Positional disorder on the 2-picolyl groups was modelled with partial occupancies, where the sum of the occupancies of fluorine atoms was set equal to two, and the sum of methyl substituents was set equal to one.

^{1}H and ^{19}F NMR Experiments. ^{1}H and ^{19}F NMR spectra of ligands L_x (x = 1–3) and ligand precursors were collected at 25 °C on either an Agilent DD2 500 MHz (11.7 T) system, at 500 and 470 MHz frequencies respectively, or on an automated Agilent DD MR 400 MHz (9.40 T) system equipped with Agilent 7600 96-sample autosampler, at 400 and 376 MHz frequencies respectively. VT ^{1}H and ^{19}F NMR spectra of compounds **1a**, **1b**, **2a**, **2b** and **3a**, were collected on an Agilent DD2 500 MHz (11.7 T) system at 500 and 470 MHz frequencies respectively. A temperature calibration curve for the NMR spectrometer was used to convert the set temperatures on the thermostat to the actual temperatures of the measurements. NMR spectra of samples in 2.1 mM aqueous solutions of trifluoroethanol (TFE), and in 2.1 mM fetal bovine serum (FBS) solutions of NaF, were acquired using gradient autoshimming on the water proton resonance. Chemical shift values (δ) are reported in ppm and referenced to residual proton signals from the deuterated solvents for all ^{1}H NMR spectra (7.26 ppm for $CDCl_3$, 4.79 ppm for D_2O/H_2O, and 1.94 ppm for MeCN-d_3). ^{19}F NMR chemical shift values for spectra recorded in $CDCl_3$ and MeCN-d_3 solvents

were referenced to trichlorofluoromethane ($CFCl_3$) at 0 ppm. For spectra of compounds **1a**, **1b**, **2a**, **2b**, and **3a** in MeCN-d_3, the ^{19}F NMR chemical shift of the $(BF_4)^-$ counterions was set to −151.44 ppm at all temperatures to make the comparison between compounds consistent. TFE was used as an internal standard for VT ^{19}F NMR measurements of compounds **1a**, **1b**, **2a**, **2b**, and **3a**, in aqueous solutions. The temperature dependence of the ^{19}F NMR chemical shift of TFE in a 2.1 mM water solution was determined relative to $CFCl_3$, and the resulting chemical shift values were used as reference points for the ^{19}F NMR chemical shifts of compounds **1a**, **1b**, **2a**, **2b**, and **3a**, at each measured temperature (4–61 °C). VT ^{19}F NMR spectra of compounds **1a** and **2a** in FBS were collected under the same conditions as ^{19}F NMR spectra of these compounds in aqueous TFE solutions, except NaF (2.1 mM) was used as an internal standard because of potential reactivity of TFE with serum albumin. The ^{19}F NMR chemical shift of NaF at each recorded temperature was determined with respect to TFE in a separate experiment, conducted in an aqueous solution containing 1.1 mM TFE and 5.2 mM NaF. All coupling constants (*J*) were measured in hertz (Hz). The MestReNova 10.0 NMR data processing software was used to analyze and process all recorded NMR spectra.

Solution Magnetic Measurements. The solution magnetic moments of compounds **1a** and **2a** were determined using the Evans method[26] by collecting VT ^1H NMR spectra using a Varian Inova 400 MHz (9.40 T) spectrometer. For aqueous solution measurements, the compounds **1a** and **2a** were dissolved in a 2.1 mM solution of TFE in H_2O and dimethyl sulfoxide (DMSO) was added as a reference (2% (v/v) of DMSO). The resulting solution was placed in a NMR tube containing a sealed capillary with a solution of H_2O and DMSO (2% (v/v) of DMSO). For measurements in MeCN, compound **1a** was dissolved in a mixture of MeCN-d_3 and CH_2Cl_2 (2% (v/v) of CH_2Cl_2),

and the resulting solution was placed in a NMR tube containing a sealed capillary with a solution of MeCN-d_3 and CH_2Cl_2 (2% (v/v) of CH_2Cl_2). The average of three measurements afforded the resulting data. All data were corrected for diamagnetic contributions from the core diamagnetism of each sample (estimated using Pascal's constants).[27] The molar fraction of spin-crossover compound **1a** in high-spin state as a function of temperature was estimated by Equation 2.1:

$$\gamma_{HS} = (\chi_M T_{obs} - \chi_M T_{LS})/(\chi_M T_{HS} - \chi_M T_{LS}) \approx \chi_M T_{obs}/\chi_M T_{HS} \quad (2.1)$$

$\chi_M T$ for the fully populated $S = 0$ (low-spin) ground state ($\chi_M T_{LS}$) was approximated to be equal to 0 $cm^3\,K\,mol^{-1}$. An average value of $\chi_M T$ for the high-spin compound **2a** (3.63 $cm^3\,K\,mol^{-1}$) in an aqueous solution, over the temperature range studied (278–333 K) was used as the fully populated $S = 2$ (high-spin) excited state limit ($\chi_M T_{HS}$). The thermodynamic parameters, ΔH and ΔS, associated with the spin transition in solution, as measured by the Evans method, were obtained using the regular solution model:[28]

$$R \times \ln(\gamma_{HS}/(1 - \gamma_{HS})) = -\Delta H/T + \Delta S \quad (2.2)$$

UV-Vis Absorption Spectroscopy. UV-Vis experiments were carried out on an Agilent Cary 5000 UV-Vis-NIR spectrometer. UV-Vis spectra were collected in the 200–800 nm range in MeCN and H_2O solvents using 9–75 μM solutions of compounds **1a**, **1b**, **2a**, **2b** and **3a**.

Electrospray Ionization Mass Spectrometry (ESI-MS) Measurements. ESI-MS spectra were recorded on a LC-MS Bruker Amazon SL quadrupole ion trap instrument, equipped with a Compass Software 1.3 SR2. All measurements were carried out in a CH_2Cl_2/MeOH (4:1) carrier solvent using positive ionization mode.

2.3 Results and Discussion

2.3.1 Syntheses and Structures

With the goal to prepare air- and water-stable complexes, tacn-based ligands bearing three pendent pyridyl groups offer an ideal platform, as these hexadentate scaffolds have been shown to afford highly-stable Fe^{II} complexes.[10,29] In addition, the ligand field can be readily tuned to obtain spin-crossover complexes within a physiologically relevant temperature range by chemical modulation of the electronic and steric properties of the pyridyl donors.[29e,30] Toward this end, we sought to synthesize related ligands that support Fe^{II} complexes in selected spin states through controlled introduction of methyl groups into the 6-position of the pyridyl groups, which serves to weaken the ligand field by virtue of steric crowding at the Fe^{II} center. In addition, in order to enable utilization of these compounds in ^{19}F MRS thermometry, we installed fluorine substituents onto the 3-positions of the pyridyl groups.

The preparation of ligands L_x (x = 1–3; see Figure 2.1) was carried out through a five-step synthesis involving stepwise addition of 2-picolyl derivatives to the tacn backbone via reductive amination of the corresponding 2-pyridinecarboxaldehydes with tacn precursors (see Section 2.5.1 and Scheme 2.1). Through judicious selection of the aldehyde reagent in each step, this synthetic route enabled the preparation of both symmetric and asymmetric tri-functionalized tacn-based ligands, appended with one or two types of 2-picolyl donors. Metalation of the ligands with Fe^{II} and Zn^{II} was effected through reaction of equimolar amounts of L_x and the corresponding divalent metal ion in

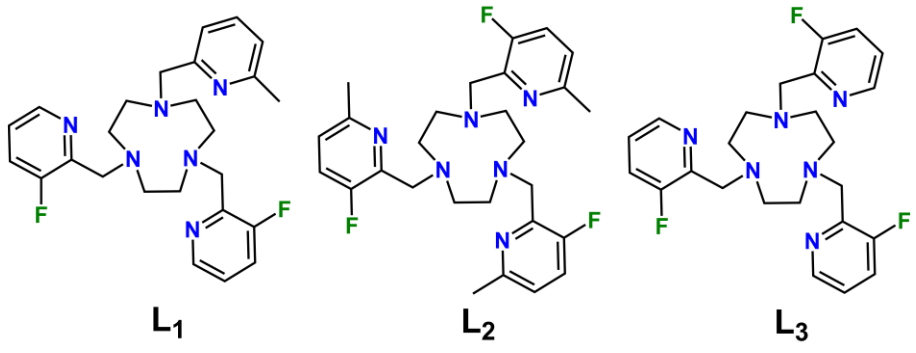

Figure 2.1 Molecular structures of ligands L_x (x = 1–3).

MeCN. Subsequent diffusion of Et_2O into a concentrated MeCN or MeOH/MeCN solution afforded crystalline $[Fe(L_1)](BF_4)_2 \cdot 0.5MeCN$ (**1a**·0.5MeCN), $[Zn(L_1)](BF_4)_2$ (**1b**), $[Fe(L_2)](BF_4)_2$ (**2a**), $[Zn(L_2)](BF_4)_2$ (**2b**), and $[Fe(L_3)](BF_4)_2$ (**3a**).

Single-crystal X-ray diffraction analysis for **1a**·0.5MeCN, **1b**, **2a**, **2b**, and **3a**, was carried out at 100 K (see Tables 2.3–2.5). Compound **1a**·0.5MeCN crystallized in the triclinic space group $P\bar{1}$, and features two $[Fe(L_1)]^{2+}$ cations in the asymmetric unit. Compound **1b** crystallized in the monoclinic space group *Pc*, with the asymmetric unit comprised of two $[Zn(L_1)]^{2+}$ cations. In contrast to the metal complexes of asymmetric L_1, compounds **2a** and **2b** are isostructural and crystallized in the cubic space group $F\bar{4}3c$, with one third of the $[M(L_2)]^{2+}$ (M = Fe, Zn) cation in the asymmetric unit. In these two structures, the M^{II} metal center resides on a site of crystallographic three-fold symmetry. Finally, the asymmetric unit of the crystal structure of **3a**, which crystallized in the trigonal space group *P*3, features one-third of three unique $[Fe(L_3)]^{2+}$ cations, with the remainder of each complex related through a crystallographic three-fold axis (see Figure 2.7).

In the cationic complex of each compound, the M^{II} center resides in a distorted octahedral coordination environment, comprised of three facially bound tertiary amine nitrogen atoms from the tacn backbone and three picolyl nitrogen atoms (see Figure 2.2). Examination of bond distances associated with the Fe^{II} cations reveals the spin state of these complexes in the solid-state at 100 K (see Table 2.1). The mean Fe–N bond distances for **1a**·0.5MeCN and **3a** fall in the ranges 1.974(2)–2.088(2) and 1.969(3)–1.999(3) Å, respectively, indicative of low-spin Fe^{II}.[15,30,31] In **1a**·0.5MeCN, the $Fe–N_{Me\text{-}pyr}$ bond lengths of 2.085(2) and 2.090(2) Å are significantly longer than

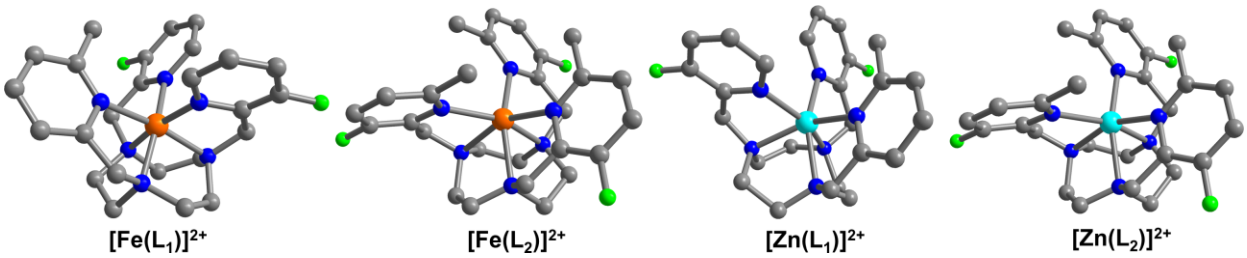

Figure 2.2 Left–Right: Crystal structures of $[Fe(L_x)]^{2+}$ (x = 1, 2), as observed in **1a**·0.5MeCN and **2a**, and $[Zn(L_x)]^{2+}$ (x = 1, 2), as observed in **1b** and **2b**. Turquoise, orange, green, blue, and gray spheres represent Zn, Fe, F, N and C atoms, respectively; H atoms are omitted for clarity.

the Fe–$N_{F\text{-}pyr}$ bond distances of 1.970(2)–1.978(2) Å, due to the steric effects imposed by the methyl substituent on one of the picolyl groups.[30] In contrast, the average Fe–$N_{MeF\text{-}pyr}$ and Fe–N_{tacn} bond distances for **2a** of 2.224(2) and 2.230(2) Å, respectively, are substantially longer and are characteristic of high-spin Fe^{II}.[30,31a–c,32] Finally, the mean Zn–N bond distances of 2.196(3) and 2.212(2) Å for **1b** and **2b**, respectively, are consistent with reported distances for Zn^{II} ions in similar coordination environments.[33]

The presence of fluoro and methyl substituents on the 2-picolyl pendent groups of ligands $L_{1–3}$ leads to a distortion from octahedral coordination at the metal centers. This deviation from perfect octahedral geometry can be quantified through the octahedral distortion parameter Σ, defined as the sum of the absolute deviations of the 12 *cis*-oriented N–M–N angles from 90°.[34] Analysis of the Fe^{II} centers in **1a**·0.5MeCN, **2a**, and **3a** gives values of Σ = 72.4(3), 134.8(3), and 59.9(4)°, respectively. The much larger value for **2a** than for **1a**·0.5MeCN and **3a** reflects the significant steric crowding in **2a** and further corroborates the high-spin and low-spin assignments of these complexes.[35] The larger distortion of the $[Fe(L_1)]^{2+}$ cation in **1a**·0.5MeCN relative to $[Fe(L_3)]^{2+}$ in **3a** is attributed to presence of one vs zero picolyl methyl substituents, respectively. The coordination environment of the Fe^{II} complex in **2a** and its isostructural Zn^{II} analogue in **2b**

Table 2.1 Selected mean interatomic distances (Å) and angles (°) for **1a**·0.5MeCN, **1b**, **2a**, **2b** and **3a** at 100 K.

	1a·0.5MeCN	**1b**[e]	**2a**	**2b**	**3a**
M–N_{tacn}	2.009(2)	2.206(3)	2.230(2)	2.217(2)	1.999(3)
M–$N_{Me\text{-}pyr}$[a]	2.088(2)	2.225(4)	—	—	—
M–$N_{F\text{-}pyr}$[b]	1.974(2)	2.167(4)	—	—	1.969(3)
M–$N_{MeF\text{-}pyr}$[c]	—	—	2.224(2)	2.207(2)	—
N_{tacn}–M–N_{tacn}	85.07(6)	79.1(2)	78.40(8)	79.39(7)	86.3(2)
cis N_{tacn}–M–$N_{Me\text{-}pyr}$	90.38(6)	97.4(2)	—	—	—
cis N_{tacn}–M–$N_{F\text{-}pyr}$	89.08(6)	93.2(2)	—	—	90.0(1)
cis N_{tacn}–M–$N_{MeF\text{-}pyr}$	—	—	87.05(8)	87.34(7)	—
$N_{Me\text{-}pyr}$–M–$N_{F\text{-}pyr}$	96.79(7)	97.7(2)	—	—	—
$N_{F\text{-}pyr}$–M–$N_{F\text{-}pyr}$	94.59(6)	94.9(2)	—	—	94.07(9)
$N_{MeF\text{-}pyr}$–M–$N_{MeF\text{-}pyr}$	—	—	105.27(7)	104.21(6)	—
trans N_{tacn}–M–$N_{Me\text{-}pyr}$	166.76(7)	148.9(2)	—	—	—
trans N_{tacn}–M–$N_{F\text{-}pyr}$	168.02(7)	150.9(2)	—	—	169.7(1)
trans N_{tacn}–M–$N_{MeF\text{-}pyr}$	—	—	156.40(8)	157.85(7)	—
Σ[d]	72.4(3)	159.7(5)	134.8(3)	127.7(2)	59.9(4)
M···F	5.102(2)	5.260(3)	5.277(2)	5.258(2)	5.094(2)

[a] $N_{Me\text{-}pyr}$ corresponds to a N atom on a 6-methyl-2-picolyl group. [b] $N_{F\text{-}pyr}$ corresponds to a N atom on a 3-fluoro-2-picolyl group. [c] $N_{MeF\text{-}pyr}$ corresponds to a N atom on a 3-fluoro-6-methyl-2-picolyl group. [d] Octahedral distortion parameter (Σ) = sum of the absolute deviations from 90° of the 12 *cis* angles in the [MN_6] coordination sphere. [e] Data obtained from Zn1 due to severe crystallographic disorder associated with Zn2.

are similar, where **2b** is slightly less distorted than **2a**, evident from a smaller Σ value of 127.7(2)°. In contrast, the difference between the structures of **1a**·0.5MeCN and **1b** is substantial. Upon moving from Fe to Zn, the mean N_{tacn}–M–N_{tacn} angle decreases by 7.1%, from 85.07(6) to 79.1(2)°, and the mean *trans* N_{tacn}–M–N_{pyr} angles decrease by 10.7 ($N_{Me\text{-}pyr}$) and 10.2% ($N_{F\text{-}pyr}$), respectively. Finally, a more than 2-fold increase in Σ is observed for **1b** relative to **1a**·0.5MeCN. These differences reflect a much greater degree of distortion at the Zn^{II} center in **1b** than at the Fe^{II} center in **1a**·0.5MeCN, which likely stems from increased coordination flexibility at the d^{10} Zn^{II} ion due to lack of ligand field stabilization, and the larger six-coordinate ionic radius of Zn^{II} (0.88 Å) compared to low-spin Fe^{II} (0.75 Å).[35a]

Compounds **1a**·0.5MeCN, **1b**, **2a**, **2b**, and **3a** feature intramolecular M···F distances in the range 5.094(2)–5.277(2) Å. The shortest M···F distances are observed between the 3-fluoro-2-picolyl pendent groups and the Fe^{II} centers in compounds **1a**·0.5MeCN and **3a**, with slightly longer M···F distances of 5.26–5.28 Å in compounds **1b**, **2a**, and **2b**. The longer Zn···F distance in **1b**, compared to the corresponding Fe···F distance in **1a**·0.5MeCN, can be attributed to the longer Zn–N bond distances relative to Fe. In the case of compounds **2a** and **2b**, the presence of bulky 3-fluoro-6-methyl-2-picolyl groups increases the M···F distances relative to **1a**·0.5MeCN and **3a**. Importantly, the M···F distances of **1a** and **2a** are within the optimal range of 4.5–7.5 Å to balance the benefits of paramagnetic hyperfine shift with the decrease in sensitivity due to spectral broadening,[19d,e] which demonstrates the potential of these complexes as candidates for ^{19}F chemical shift MR probes.

2.3.2 UV-Vis Spectroscopy

To probe the solution electronic structures of the cationic complexes in **1a**, **1b**, **2a**, **2b**, and **3a**, UV-Vis absorption spectra were collected for crystalline samples in MeCN solution. The spectrum of **1a** obtained at 25 °C exhibits an intense band at 264 nm (ε = 10700 M^{-1} cm^{-1}), in addition to a weaker broad band at 424 nm (ε = 2800 M^{-1} cm^{-1}) with a high-energy shoulder (see Figures 2.3 and 2.8). Based on literature precedent of Fe^{II} complexes in similar ligand environments, we assign these absorption bands as ligand-centered π–π^* and metal–ligand charge transfer (MLCT) transitions, respectively.[30,36] The UV-Vis spectrum of **2a** at 25 °C is dominated by the intense π–π^* band (λ_{max} = 273 nm, ε_{max} = 11100 M^{-1} cm^{-1}), and an additional broad feature of low intensity between 320 and 460 nm (λ_{max} = 375 nm) corresponds to a MLCT transition (see Figures 2.3, bottom, and 2.9). The weak intensity and the small temperature dependence between −35 and 65

°C for the latter band (ε_{max} = 1000 vs 700 M^{-1} cm^{-1}, respectively) are characteristic of high-spin Fe^{II}.[36c,37] Compound **3a** is also relatively insensitive to temperature changes and at 25 °C displays a similar ligand-centered π–π* transition at 261 nm, but with a more intense MLCT band at 436 nm (ε_{max} = 10600 M^{-1} cm^{-1}), and as such is indicative of low-spin Fe^{II} (see Figures 2.3, bottom, and 2.10).[30,38] The VT UV-Vis spectra of the Zn^{II} compounds **1b** and **2b** in MeCN each exhibit a single intense band with λ_{max} = 268 and 278 nm, respectively (see Figures 2.11 and 2.12), consistent with ligand-centered π–π* transitions.[39]

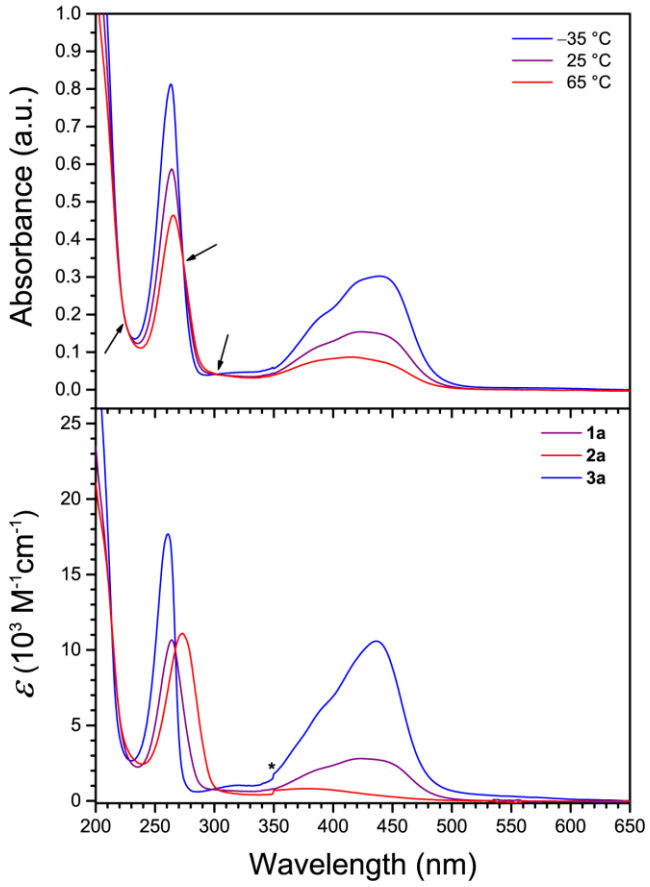

Figure 2.3 Top: UV-Vis spectra of **1a** in MeCN at selected temperatures (see inset). Arrows denote isosbestic points. Bottom: UV-Vis spectra of **1a**, **2a**, and **3a** in MeCN at 25 °C. The asterisk denotes an instrumental artifact.

The absorption spectra of **1a** demonstrate remarkable temperature dependence between −35 and 65 °C (see Figure 2.3, top). While the position of the π–π* band is relatively invariant to temperature, ε_{max} decreases significantly from 14800 to 8400 M^{-1} cm^{-1} upon warming, as has been observed for related pyridyl complexes.[40] At −35 °C, the MLCT band exhibits a λ_{max} value of 439 nm (ε_{max} = 5500 M^{-1} cm^{-1}) with a shoulder at ca. 385 nm. Upon warming, the MLCT bands broaden and decrease in intensity, resulting in a single peak with λ_{max} = 385 nm (ε_{max} = 1600 M^{-1} cm^{-1}) at 65 °C that corresponds

to ca. 3.5-fold reduction in intensity from the −35 °C spectrum. This temperature dependence of the spectra is indicative of a thermally-induced spin state transition.[30,41] Indeed, approximating a metal complex of O_h symmetry, the intensity of the MLCT band is directly correlated to the number of electrons in t_{2g} orbitals.[40c,d] As such, moving from low-spin Fe^{II} (t_{2g}^6) to high-spin Fe^{II} ($t_{2g}^4e_g^2$) with increasing temperature results in a weaker absorption. Moreover, the presence of three isosbestic points at 222, 273, and 302 nm suggests an equilibrium between two spin states for the Fe^{II} centers in **1a**.

The temperature-dependent spin state of Fe^{II} in **1a** in MeCN can be further examined by comparing the UV-Vis spectra of **1a** with the corresponding spectra of the high-spin compound **2a** and the low-spin compound **3a** (see Figure 2.3, bottom). At lower temperature, the spectrum of **1a** strongly resembles that of **3a** (see Figure 2.13), whereas at higher temperature the broad spectrum resembles that of **2a** (see Figure 2.14). These temperature-dependent spectral changes demonstrate the thermally-induced spin-crossover of **1a** in MeCN solution from primary population of a low-spin state at −35 °C to a high-spin state at 65 °C.

With an eye toward employing these complexes in MR thermometry, UV-Vis spectra were collected for aqueous solutions of compounds **1a**, **1b**, **2a**, **2b**, and **3a** at ambient temperature. All compounds show similar characteristics in H_2O as in MeCN, giving comparable values of λ_{max} and ε_{max} (see Figures 2.15–2.19). Nevertheless, the spectrum of **1a** in H_2O reveals some key differences from the spectrum obtained in MeCN at 25 °C. The absorption maximum of the MLCT band is shifted to a longer wavelength in H_2O (λ_{max} = 436 nm), and the intensity of this band compared to the intensity of the analogous band for **3a** in the same solvent is considerably greater in H_2O than in MeCN (H_2O: $\varepsilon_{max,\mathbf{3a}}/\varepsilon_{max,\mathbf{1a}}$ = 1.5; MeCN: $\varepsilon_{max,\mathbf{3a}}/\varepsilon_{max,\mathbf{1a}}$ = 3.8). These observations indicate that

moving from MeCN to H_2O serves to stabilize the low-spin state of $[Fe(L_1)]^{2+}$, leading to a higher $T_{1/2}$. Similar trends have been reported for other spin-crossover Fe^{II} complexes and stem from the donor strength of the two solvents.[42] Importantly, **1a** exhibits remarkable water and air stability, as the absorption spectra of this compound in deoxygenated water and after four weeks in oxygenated water are identical (see Figure 2.15).

2.3.3 Magnetic Properties

To probe the magnetic properties of compounds **1a** and **2a**, VT magnetic susceptibility data were collected in the temperature range 5–60 °C for aqueous solutions in a 9.4 T NMR spectrometer using the Evans method (see Figure 2.4).[26] For **2a**, $\chi_M T$ is constant over this temperature range, with an average value of $\chi_M T$ = 3.63 cm^3 K mol^{-1} that corresponds to a high-spin, S = 2 Fe^{II} ion with g = 2.20. In stark contrast, for **1a**, $\chi_M T$ increases nearly linearly with increasing temperature, from a minimum value of 0.93 cm^3 K mol^{-1} at 5 °C to a maximum value of 1.99 cm^3 K mol^{-1} at 60 °C, indicative of thermally-induced spin-crossover. Note that the high-spin excited state contributes considerably to the overall magnetic moment of **1a** at 5 °C, as the observed value of $\chi_M T$ = 0.93 cm^3 K mol^{-1} is significantly higher than the theoretical value of 0 cm^3 K mol^{-1} for a solely populated S = 0 ground state. Analogously, a mixture of low-spin and high-spin Fe^{II} centers is present at 60 °C, as

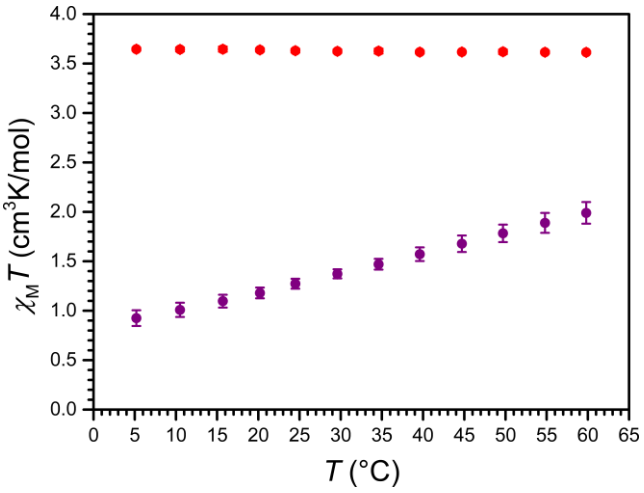

Figure 2.4 VT dc magnetic susceptibility data for aqueous solutions of **1a** (purple) and **2a** (red), obtained in a 9.4 T NMR spectrometer using the Evans method. Error bars represent standard deviations of the measurements.

evident from the significant deviation of $\chi_M T$ = 1.99 cm^3 K mol^{-1} from the average value of the high-spin analogue **2a**. Considering a value of $\chi_M T$ = 0 cm^3 K mol^{-1} for a solely populated S = 0 low-spin state and $\chi_M T$ = 3.63 cm^3 K mol^{-1} for a solely populated S = 2 high-spin state with g = 2.20, the high-spin molar fraction of Fe^{II} centers in **1a** was calculated as a function of temperature (see Figure 2.20). A linear fit to the data gives $T_{1/2}$ = 325(1) K or 52(1) °C. Moreover, the data were simulated using the regular solution model[28,43] to estimate thermodynamic parameters of ΔH = 18.0(3) kJ mol^{-1} and ΔS = 55.5(9) J K^{-1} mol^{-1}, which are similar in magnitude to related mononuclear spin-crossover Fe^{II} complexes (see Figure 2.21).[15,28,36c,44]

To test our hypothesis that the low-spin state of $[Fe(L_1)]^{2+}$ in **1a** is stabilized in H_2O relative to MeCN, VT dc magnetic susceptibility data were collected for a MeCN solution of **1a**, using the same procedure as described above (see Figure 2.22). As observed in aqueous solution, $\chi_M T$ increases nearly linearly with increasing temperature, from 0.62 cm^3 K mol^{-1} at −42 °C to 2.71 cm^3 K mol^{-1} at 60 °C. Furthermore, a linear fit to the data affords $T_{1/2}$ = 17(1) °C, which is 35 °C lower than observed in H_2O, and demonstrates the different donor strengths of H_2O and MeCN (see Figure 2.23).

2.3.4 VT NMR Spectroscopy

To further investigate the solution properties of compounds **1a**, **1b**, **2a**, **2b**, and **3a**, VT ^{1}H NMR spectra were collected in MeCN-d_3 at selected temperatures. The ^{1}H NMR spectra of compounds **1b**, **2b**, and **3a** resemble those of their respective ligands and show minimal changes in the temperature range 25–56 °C, confirming diamagnetic electronic structures (see Figures 2.24–2.26). In contrast, the ^{1}H NMR spectra of **2a** display nine paramagnetically shifted resonances, consistent with time-averaged C_3 symmetry in MeCN solution (see Figure 2.27). At

−1 °C, these resonances span −18 to 225 ppm, typical for high-spin Fe^{II} complexes.[10,12,29b,d,e,g,h,36c] As the temperature is increased to 56 °C, the peaks shift linearly toward the diamagnetic region. This Curie behavior ($\delta \propto T^{-1}$) is characteristic of high-spin complexes and confirms that **2a** remains $S = 2$ over the entire temperature range. In contrast, the ^{1}H NMR resonances of **1a** show anti-Curie behavior, shifting away from the diamagnetic region with increasing temperature (see Figure 2.28). Specifically, at −38 °C, the proton resonances are dispersed between −2 and 13 ppm, barely beyond the diamagnetic region, suggesting primary population of an $S = 0$ ground state. Increasing the temperature to 56 °C results in an expansion of the chemical shift range to −25–150 ppm, indicative of thermal population of the high-spin excited state. An analogous trend is observed in the VT ^{1}H NMR spectra of **1a** in D_2O, though the resonances are broader and less shifted than in MeCN-d_3 at analogous temperatures, giving a chemical shift range from −17 to 107 ppm at 56 °C (see Figure 2.29). These observations are consistent with the higher $T_{1/2}$ in H_2O relative to MeCN, as evident from solution magnetic measurements and UV-Vis data.

In order to determine the effect of spin state on ^{19}F resonances, and to assess these compounds as candidates for ^{19}F MRS thermometry, we collected VT ^{19}F NMR spectra for aqueous solutions of **1a** and **2a** from 4 to 61 °C, using trifluoroethanol (TFE) as an internal standard (see Section 2.2, Figure 2.30, and Table 2.6). To better understand how the temperature dependence of ^{19}F NMR chemical shifts is affected by the electronic spin state, and to quantify the hyperfine shifts of the paramagnetic Fe^{II} compounds **1a** and **2a**, their corresponding Zn^{II} analogues, **1b** and **2b**, were employed as diamagnetic references (see Table 2.2).[18c] Importantly, the chemical shifts of the fluorine resonances of Zn^{II} compounds **1b** and **2b** are effectively invariant to temperature changes (see Figures 2.5, 2.31, and 2.32).

At 4 °C, the ^{19}F NMR spectrum of the high-spin compound **2a** displays a single resonance at −59.4 ppm vs $CFCl_3$ that is shifted +67.3 ppm from its diamagnetic Zn^{II} analogue **2b**. As the temperature is raised to 61 °C, the chemical shift of the paramagnetic signal shifts upfield to −71.4 ppm, closer to the ^{19}F resonance of its diamagnetic analogue, as expected for Curie behavior (see Figures 2.33 and 2.34, and Tables 2.7 and 2.8). The observation of a single signal for **2a** further supports the C_3 symmetry of the $[Fe(L_2)]^{2+}$ cation in solution, as suggested by ^{1}H NMR spectroscopy. Analysis of the temperature dependence of the ^{19}F NMR chemical shift reveals a linear temperature dependence over 4–61 °C following the equation $\delta_{ppm} = -0.21 \times T - 58.8$, affording a temperature coefficient[45] of CT = −0.21(1) ppm per °C (see Figure 2.5 and Table 2.2). Since linewidth has a significant effect on the precision of MRS probes, the value |CT|/FWHM (FWHM = full width at half maximum) is also a useful measure of probe sensitivity. At 40 °C, the fluorine resonance of **2a** exhibits a FWHM of 868 Hz, giving a |CT|/FWHM = 0.11 per °C.

The ^{19}F NMR spectrum of **1a** obtained at 4 °C exhibits two resonances of equal intensity at −99.3 and −102.1 ppm vs $CFCl_3$ (see Figure 2.35 and Table 2.7), suggesting that the two 3-fluoro-2-picolyl arms of L_1 are inequivalent on the NMR timescale. These peaks are shifted +23.1 and +20.3 ppm from the diamagnetic Zn^{II} analogue **1b** (see Figure 2.36 and Table 2.8), which exhibits two overlapping resonances

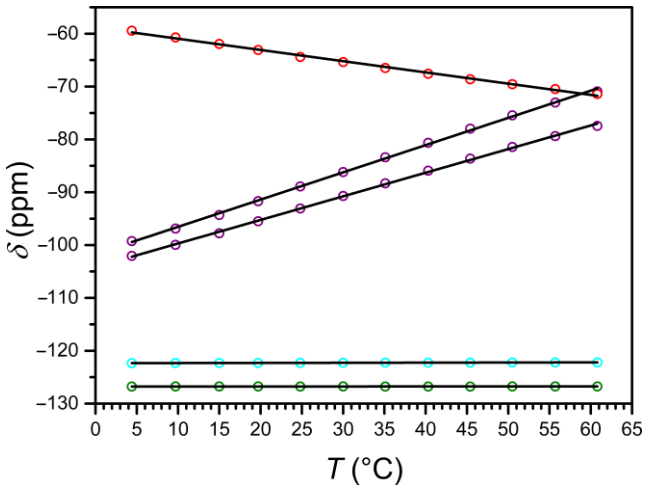

Figure 2.5 Plot of the temperature dependence of the ^{19}F NMR chemical shift for **1a** (purple), **1b** (cyan), **2a** (red), and **2b** (green) in H_2O. Chemical shift values are corrected with TFE internal standard and referenced to $CFCl_3$. Solid black lines represent linear fits to the data.

Table 2.2 Summary of ^{19}F NMR properties for compounds **1a** and **2a** in MeCN-d_3, H_2O, and FBS solutions.

	MeCN-d_3		H_2O		FBS	
	1a	**2a**	**1a**	**2a**	**1a**	**2a**
δ (ppm)[a]	59.4 / 52.6	55.9	41.6 / 36.3	59.2	40.7 / 35.5	59.0
$\Delta\delta$ (ppm)	+40.9[b] / +36.2[b]	−13.6[b]	+28.3[c] / +24.6[c]	−12.0[c]	+28.8[c] / +25.1[c]	−11.7[c]
CT (ppm °C^{-1})	+0.67(2)[b] / +0.59(2)[b]	−0.24(2)[b]	+0.52(1)[c] / +0.45(1)[c]	−0.21(1)[c]	+0.52(1)[c] / +0.45(1)[c]	−0.21(1)[c]
FWHM (Hz)[d]	287 / 270	105	282 / 243	868	251 / 241	872
|CT|/FWHM (°C^{-1})	1.10 / 1.03	1.07	0.87 / 0.87	0.11	0.97 / 0.88	0.11

[a]Referenced to corresponding Zn^{II} analogues at 40 °C. [b]Obtained from the temperature range −22–40 °C. [c]Obtained from the temperature range 4–61 °C. [d]Obtained from data at 40 °C.

centered at −122.3 ppm (see Figure 2.31). Increasing the temperature to 61 °C results in a downfield shift of the resonances of **1a** to +51.3 and +44.8 ppm from **1b**, consistent with the anti-Curie behavior observed in the corresponding ^{1}H NMR spectra. The ^{19}F chemical shift of both resonances for **1a** vary linearly between 4 and 61 °C following the equations $\delta_{ppm} = 0.52 \times T - 101.7$ and $\delta_{ppm} = 0.45 \times T - 104.2$, providing temperature sensitivities of CT = +0.52(1) and +0.45(1) ppm per °C, respectively (see Figure 2.5 and Table 2.2). Fluorine resonances with the narrowest linewidths are obtained at 20 °C, but the peaks broaden significantly above 55 °C (FWHM > 500 Hz). At 40 °C, the fluorine resonances each shows a value of |CT|/FWHM = 0.87 per °C.

The two ^{19}F NMR resonances of **1a** exhibit 2.5- and 2.1-fold higher CT values than that of the high-spin **2a**. Furthermore, the narrower linewidths of the resonances of **1a** afford an 8-fold higher |CT|/FWHM value than **2a** at 40 °C. Remarkably, the two ^{19}F resonances of **1a** represent 43- and 38-fold enhancement of temperature sensitivity compared to diamagnetic perfluorocarbons that have been employed for in vivo thermometry.[20] Despite the much narrower peak widths of the

diamagnetic fluorine resonances relative to those of **1a**, the |CT|/FWHM value of **1a** at 40 °C is 2.9-fold higher owing to the strong temperature dependence of the chemical shift of its two resonances. These observations demonstrate that the use of spin-crossover complexes may provide an excellent strategy for improving the sensitivity of ^{19}F MR thermometers.

Furthermore, the separation between the two fluorine resonances of **1a** varies strongly with temperature, from 2.81 ppm at 4 °C to 6.52 ppm at 61 °C, following the linear relationship $\Delta\delta_{ppm} = 0.069 \times T + 2.47$ (see Figure 2.37). This peak separation provides an internal method of correcting errors in the ^{19}F chemical shift that arise from complicating physiological effects, such as motion, magnetic susceptibility changes, and varying oxygen tension.[20] Overall, three temperature-dependent parameters of compound **1a** can be followed for MR thermometry, namely the ^{19}F NMR chemical shifts of two inequivalent fluorine substituents, and the chemical shift difference between these signals.

To evaluate the efficacy of **1a** and **2a** in a physiological environment, ^{19}F NMR spectra were collected from 4 to 61 °C on 13.4 and 15.0 mM solutions of **1a** and **2a**, respectively, in fetal bovine serum (FBS), using NaF as an internal standard (see Figure 2.38). The ^{19}F NMR spectra in FBS are essentially identical to those recorded in H_2O and provide the same CT values (see Figures 2.39 and 2.40, and Tables 2.9 and 2.10). Plots of the temperature dependence of fluorine chemical shifts of compounds **1a** and **2a** in FBS are depicted in Figure 2.6, where the chemical shifts of the Fe^{II} complexes have been referenced to the corresponding shifts of Zn^{II} analogues **1b** and **2b** in H_2O (see Table 2.10). The linewidths for the resonance of **2a** are similar in FBS and H_2O, while **1a** exhibits slightly narrower peaks in the high-temperature region (>30 °C) in FBS compared to those in H_2O, resulting in higher |CT|/FWHM values in FBS. Furthermore, both complexes remain

intact while incubated with FBS for over 24 h, as evidenced by identical ^{19}F NMR spectra recorded at 25 °C initially and after 24 h (see Figures 2.41 and 2.42). Taken together, these results demonstrate the stability of compounds **1a** and **2a** in a physiological environment and indicate that temperature measurements with +0.52(1) and −0.21(1) ppm per °C sensitivity, respectively, can be achieved with these probes through chemical shift ^{19}F MR thermometry. Moreover, the excellent stability and favorable ^{19}F MR properties of **1a** under physiological conditions suggest that this compound is a viable candidate for in vivo studies.

A comparison of the ^{19}F NMR properties of compounds **1a** and **2a** in MeCN-d_3 (see Figures 2.43–2.47), H_2O and FBS is summarized in Table 2.2. The hyperfine shift of the spin-crossover compound **1a** is significantly affected by the solvent, in contrast to high-spin **2a** (see Tables 2.7 and 2.11). Along these lines, the resonances of **1a** display a 1.3-fold higher temperature sensitivity in MeCN-d_3 than in H_2O, which is consistent with a lower $T_{1/2}$ in MeCN-d_3. These observations reflect the pronounced effects of spin state on ^{19}F NMR chemical

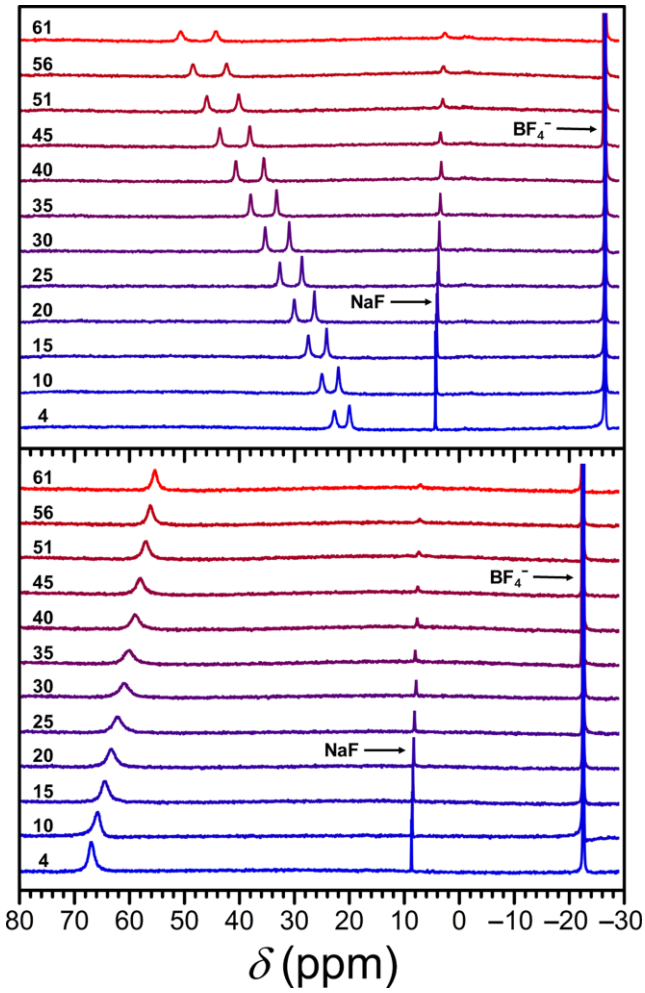

Figure 2.6 VT ^{19}F NMR spectra of **1a** (top) and **2a** (bottom) in FBS, using a NaF internal standard. The chemical shifts of the Fe^{II} compounds **1a** and **2a** are referenced to their corresponding Zn^{II} analogues **1b** and **2b**, set to 0 ppm. Black numbers correspond to temperature in °C.

shift, as has been previously reported for transition metal porphyrin complexes.[18] Nevertheless, the results presented here provide a rare examination of spin state effects on ^{19}F NMR spectra across a series of metal complexes.

2.4 Conclusions

The foregoing results demonstrate the potential utility of paramagnetic Fe^{II} complexes as chemical shift ^{19}F MR thermometers. Most importantly, we show that the sensitivity of ^{19}F MR thermometers can be improved by employing a temperature-dependent change in spin state, as illustrated in a series of Fe^{II} complexes. To our knowledge, these complexes represent the first examples of paramagnetic ^{19}F MR chemical shift agents proposed for thermometry applications. Future efforts will focus on in vitro and in vivo MRS thermometry experiments on these compounds and the synthesis of spin-crossover complexes with higher sensitivity by exploiting the chemical tunability of the tacn-based ligand scaffold.

2.5 Supporting Information

2.5.1 Supplementary Experimental Details

Synthesis of N,N′,N″-tritosyl-1,4,7-triazacyclononane (Ts$_3$-tacn). This compound was synthesized following a modified literature procedure.[46] Ts$_3$-dient (14.2 g, 25.2 mmol) and cesium carbonate (17.2 g, 52.8 mmol) were stirred vigorously in *N*,*N*-dimethylformamide (DMF; 135 mL) at 25 °C for 1 h. To this white suspension, a solution of Ts$_2$-glycol (9.30 g, 25.2 mmol) in DMF (60 mL) was added dropwise. The resulting pale yellow mixture was stirred at ambient temperature for 12 h. After that time the color of the reaction mixture had turned orange. The mixture was filtered and the red-orange filtrate added slowly to deionized water (800 mL) to give the product

as a white precipitate. The solid was collected by vacuum filtration and suspended in DMF/H_2O 1:1 mixture (90 mL) and stirred for 3 h to wash. The resulting white solid was collected by vacuum filtration, washed thoroughly with deionized water and dried under vacuum for 6 h. The crude product was recrystallized from CH_2Cl_2/ethanol to give the title compound as colorless needles (12.9 g, 87 %). ^{1}H NMR (400 MHz, $CDCl_3$, 25 °C): δ 7.70 (d, J = 6.6 Hz, 6H), 7.33 (d, J = 6.8 Hz, 6H), 3.42 (s, 12 H), 2.43 (s, 9 H).

Synthesis of N-monotosyl-1,4,7-triazacyclononane (H_2Ts-tacn). This compound was synthesized following a modified literature procedure.[46] Ts_3-tacn (3.51 g, 5.91 mmol) and phenol (4.56 g, 47.3 mmol) were introduced into a 250 mL round bottom flask connected to a reflux condenser. To this, a solution of 33 % HBr in acetic acid (36 mL) was slowly added. The orange-colored reaction mixture was carefully heated to 90 °C under a dinitrogen atmosphere and stirred for 16 h. During that time a white precipitate of H_2Ts-tacn·2HBr was formed. The orange suspension was cooled to ambient temperature and then filtered through a fritted glass funnel. The white precipitate was washed with glacial acetic acid (10 mL), dissolved in deionized water (50 mL) and basified with 1 M aqueous NaOH solution (50 mL) to give a clear solution. This solution was extracted with $CHCl_3$ (3 × 50 mL) and the colorless extracts were combined, dried over $MgSO_4$(s) and filtered. The product was collected as a white powder after evaporating the chloroform solvent to dryness (1.11 g, 66 %). ^{1}H NMR (400 MHz, $CDCl_3$, 25 °C): δ 7.63 (d, J = 7.9 Hz, 2H), 7.25 (d, J = 8.0 Hz, 2H), 3.13 (br s, 4 H), 3.02 (br s, 4 H), 2.83 (s, 4H), 2.36 (s, 3 H), 1.91 (s, 2H).

Synthesis of 3-fluoro-2-formyl-6-methylpyridine. This compound was synthesized following a modified literature procedure.[47] Under a dinitrogen atmosphere, 2-bromo-3-fluoro-6-

methylpyridine (3.73 g, 19.6 mmol) was dissolved in dry toluene (30 mL) and that colorless solution was added dropwise to a stirred solution of *n*-butyllithium (1.6 M in hexanes, 12.3 mL, 19.6 mmol) in dry toluene (30 mL) at −78 °C. The resulting red-orange solution was stirred at −78 °C for 1 h and then anhydrous DMF (4.30 g, 58.9 mmol) was slowly added to give a bright red solution. That solution was stirred at −78 °C for additional 2 h, then warmed to ambient temperature and quenched with water (50 mL). The bright yellow aqueous layer was extracted with ethylacetate (EtOAc; 2 × 200 mL), the combined organic layer was washed with saturated aqueous NaCl solution (100 mL), dried over $MgSO_4$(s) and filtered. Removing the solvent under reduced pressure afforded a red oil which was dissolved in a minimum amount of EtOAc (15 mL) and eluted through a plug of diatomaceous earth. The red-colored solution was concentrated in vacuo and further dried under vacuum for 12 h to afford the product as a red crystalline solid (2.23 g, 80 %). ^{1}H NMR (400 MHz, $CDCl_3$, 25 °C): δ 10.21 (s, 1H), 7.48 (dd, J = 7.5, 7.2 Hz, 1H), 7.41 (dd, J = 6.9, 3.0 Hz, 1H), 2.66 (s, 3H). ^{19}F NMR (376 MHz, $CDCl_3$, 25 °C): δ −129.75 (dd, J = 9.7, 3.9 Hz).

General procedure for the synthesis of N,N′-di(2-picolyl)-N″-monotosyl-1,4,7-triazacyclononane. A 50 mL Schlenk flask was charged with 1.0 equivalent of H_2Ts-tacn and a magnetic stir bar. To this, dry CH_2Cl_2 (20 mL) was added to solubilize the ligand precursor completely to give a light yellow solution. Under a dinitrogen atmosphere, 2.5 equivalents of a 2-pyridinecarboxaldehyde derivative was added as a solid in a single portion. After stirring the mixture at ambient temperature for 1 h, 5.0 equivalents of sodium triacetoxyborohydride was added and the resulting suspension was heated to 40 °C and refluxed under a dinitrogen atmosphere for 1–3 h. The reaction was monitored by ESI-MS in CH_2Cl_2 solvent. When no remaining starting

material was observed, the reaction mixture was cooled to ambient temperature and evaporated to dryness under reduced pressure. The crude residue was partitioned between 2 M aqueous NaOH solution (20 mL) and $CHCl_3$ (40 mL), and the organic phase was collected, dried over $MgSO_4$(s), filtered and concentrated in vacuo. The obtained oil was washed with 6 M aqueous NaOH solution (15 mL) by stirring for 1–2 h at ambient temperature, and then extracted into $CHCl_3$ (25 mL). The organic phase was dried over $MgSO_4$(s) and filtered, and the $CHCl_3$ solvent was removed under reduced pressure to afford the product as an oil or an oily solid which was used in a subsequent step after drying under vacuum for 6 h.

Synthesis of N,N′-di(3-fluoro-2-picolyl)-N″-monotosyl-1,4,7-triazacyclononane. According to the general procedure, *N,N′*-di(3-fluoro-2-picolyl)-*N″*-monotosyl-1,4,7-triazacyclononane was prepared as a pale yellow oil in near quantitative yield from H_2Ts-tacn (0.361 g, 1.28 mmol), 3-fluoro-2-formylpyridine (0.399 g, 3.19 mmol) and sodium triacetoxyborohydride (1.36 g, 6.40 mmol). ESI-MS (*m*/*z*): Calcd. for $C_{25}H_{30}F_2N_5O_2S$ $(M+H)^+$ 502.21, found 502.18. ^{1}H NMR (400 MHz, $CDCl_3$, 25 °C): δ 8.33 (dd, J = 3.7, 1.1 Hz, 2H), 7.63 (d, J = 6.6 Hz, 2H), 7.33 (ddd, J = 7.2, 7.2, 1.1 Hz, 2H), 7.26 (d, J = 6.2 Hz, 2H), 7.24–7.27 (m, 2 H), 7.17–7.20 (m, 2H), 3.88 (d, J = 1.8 Hz, 4H), 3.21–3.24 (m, 4H), 3.07–3.10 (m, 4H), 2.76 (s, 4H), 2.40 (s, 3H). ^{19}F NMR (376 MHz, $CDCl_3$, 25 °C): δ −123.83 (m).

Synthesis of N,N′-di(3-fluoro-6-methyl-2-picolyl)-N″-monotosyl-1,4,7-triazacyclononane. According to the general procedure, *N,N′*-di(3-fluoro-6-methyl-2-picolyl)-*N″*-monotosyl-1,4,7-triazacyclononane was prepared as a red-brown oil in near quantitative yield from H_2Ts-tacn (0.459 g, 1.64 mmol), 3-fluoro-2-formyl-6-methylpyridine (0.570 g, 4.10 mmol) and sodium triacetoxyborohydride (1.74 g, 8.20 mmol). ESI-MS (*m*/*z*): Calcd. for $C_{27}H_{34}F_2N_5O_2S$ $(M+H)^+$

530.24, found 530.21. ^{1}H NMR (400 MHz, $CDCl_3$, 25 °C): δ 7.64 (d, J = 8.2 Hz, 2H), 7.26 (dd, J = 7.8 Hz, 2H), 7.20 (dd, J = 8.4, 8.4 Hz, 2H), 7.00 (dd, J = 8.4, 3.7 Hz, 2H), 3.82 (d, J = 2.2 Hz, 4H), 3.23–3.27 (m, 4H), 3.05–3.08 (m, 4H), 2.72 (s, 4H), 2.48 (s, 6H), 2.40 (s, 3H). ^{19}F NMR (376 MHz, $CDCl_3$, 25 °C): δ −129.85 (d, J = 9.4 Hz).

General procedure for the synthesis of N,N′-di(2-picolyl)-1,4,7-triazacyclononane. The monotosylated ligand precursor and a magnetic stir bar were introduced into a 25 mL round bottom flask. To this, concentrated sulfuric acid solution (10 mL) was slowly added and the resulting orange mixture was purged under vacuum for 1 h. Afterwards, the reaction flask was connected to a reflux condenser and the homogeneous light orange solution was heated to 120 °C under a dinitrogen atmosphere and left stirring at that temperature for 16 h. The resulting black reaction mixture was allowed to reach ambient temperature and then added to stirring cold ethanol (60 mL). Addition of Et_2O (300 mL) resulted in the formation of a white suspension, which was filtered to give a gray oily solid. This compound was dissolved in 2 M aqueous NaOH solution (50 mL), yielding a faint brown-colored solution. The aqueous layer was extracted with $CHCl_3$ (3 × 100 mL) and the pale-yellow extracts were combined, dried over $MgSO_4$(s), filtered and concentrated under reduced pressure to afford the product as an oil. The collected oil was dried under vacuum for 6 h before proceeding to the next step.

Synthesis of N,N′-di(3-fluoro-2-picolyl)-1,4,7-triazacyclononane. According to the general procedure, *N,N′*-di(3-fluoro-2-picolyl)-1,4,7-triazacyclononane was prepared as a yellow-orange oil (0.328 g) from *N,N′*-di(3-fluoro-2-picolyl)-*N″*-monotosyl-1,4,7-triazacyclononane. ESI-MS (*m*/*z*): Calcd. for $C_{18}H_{24}F_2N_5$ $(M+H)^+$ 348.20, found 348.18. ^{1}H NMR (400 MHz, $CDCl_3$, 25 °C): δ 8.35 (ddd, J = 5.0, 1.1 Hz, 2H), 7.36 (dd, J = 7.4, 7.4 Hz, 2H), 7.19–7.24 (m, 2 H), 3.91 (d, J =

1.6 Hz, 4H), 2.76–2.80 (m, 4H), 2.76 (s, 4H), 2.57–2.61 (m, 4H). ^{19}F NMR (376 MHz, $CDCl_3$, 25 °C): δ −123.93.

Synthesis of N,N′-di(3-fluoro-6-methyl-2-picolyl)-1,4,7-triazacyclononane. According to the general procedure, *N,N′*-di(3-fluoro-6-methyl-2-picolyl)-1,4,7-triazacyclononane was prepared as a red-brown oil (0.318 g, 59 %) from *N,N′*-di(3-fluoro-6-methyl-2-picolyl)-*N″*-monotosyl-1,4,7-triazacyclononane (0.762 g, 1.44 mmol). ESI-MS (*m*/*z*): Calcd. for $C_{20}H_{28}F_2N_5$ $(M+H)^+$ 376.23, found 376.22. ^{1}H NMR (400 MHz, $CDCl_3$, 25 °C): δ 7.20 (dd, J = 8.9, 8.9 Hz, 2H), 7.00 (dd, J = 8.2, 3.5 Hz, 2 H), 3.84 (d, J = 2.0 Hz, 4H), 2.73–2.77 (m, 4H), 2.62 (s, 4H), 2.56–2.61 (m, 4H), 2.50 (s, 6H). ^{19}F NMR (376 MHz, $CDCl_3$, 25 °C): δ −129.93 (d, J = 9.0 Hz).

General procedure for the synthesis of N,N′,N″-tri(2-picolyl)-1,4,7-triazacyclononane. To a solution of 1.0 equivalent of a *N,N′*-di(2-picolyl)-1,4,7-triazacyclononane derivative in dry CH_2Cl_2 (15 mL), 1.2 equivalents of a 2-pyridinecarboxaldehyde derivative was added as a solid and the resulting mixture was stirred at ambient temperature under an atmosphere of dinitrogen for 1 h. After that time, 3.0 equivalents of sodium triacetoxyborohydride were added and the resulting suspension was heated to 40 °C and refluxed under dinitrogen atmosphere for 1–3 h. When the reaction was complete, as judged by ESI-MS analysis in CH_2Cl_2 solvent, the reaction mixture was allowed to reach ambient temperature and evaporated to dryness under vacuum. The crude residue was partitioned between 2 M aqueous NaOH solution (20 mL) and $CHCl_3$ (40 mL), and the organic phase was collected, dried over $MgSO_4$(s) and filtered. Removal of the $CHCl_3$ solvent under reduced pressure afforded the product as an oil, which was stirred in 8 M aqueous NaOH solution (15 mL) for 1–2 h at ambient temperature to wash. The aqueous emulsion was then extracted with $CHCl_3$ (25 mL) and the organic phase was collected, dried over $MgSO_4$(s), filtered and

concentrated. Drying under vacuum for 6 h afforded the ligands as oils or oily solids that were used in the metalation steps without further purification.

Synthesis of N,N′-di(3-fluoro-2-picolyl)-N″-mono(6-methyl-2-picolyl)-1,4,7-triazacyclononane (L_1). According to the general procedure, *N,N′*-di(3-fluoro-2-picolyl)-*N″*-mono(6-methyl-2-picolyl)-1,4,7-triazacyclononane was prepared as an yellow-orange oil (0.232 g, 63 %) from *N,N′*-di(3-fluoro-2-picolyl)-1,4,7-triazacyclononane (0.192 g, 0.820 mmol), 2-formyl-6-methyl-pyridine (0.257 g, 2.05 mmol) and sodium triacetoxyborohydride (0.869 g, 4.10 mmol). ESI-MS (*m*/*z*): Calcd. for $C_{25}H_{31}F_2N_6$ $(M+H)^+$ 453.26, found 453.25. ^{1}H NMR (400 MHz, $CDCl_3$, 25 °C): δ 8.34 (dd, *J* = 3.8, 1.1 Hz, 2H), 7.50 (dd, *J* = 6.1, 6.1 Hz, 1H), 7.33 (ddd, *J* = 7.1, 7.1, 1.1 Hz, 2H), 7.28 (d, *J* = 6.2 Hz, 1 H), 7.16–7.20 (m, 2H), 6.96 (d, *J* = 6.1 Hz, 1 H), 3.84 (d, *J* = 1.7 Hz, 4H), 3.73 (s, 2H), 2.91 (s, 4H), 2.86–2.89 (m, 4H), 2.72–2.76 (m, 4H), 2.50 (s, 3H). ^{19}F NMR (470 MHz, $CDCl_3$, 25 °C): δ −123.64 (d, *J* = 10.1 Hz). ^{19}F NMR (470 MHz, MeCN-d_3, 25 °C): δ −125.49 (s).

Synthesis of N,N′,N″-tri(3-fluoro-6-methyl-2-picolyl)-1,4,7-triazacyclononane (L_2). According to the general procedure, *N,N′,N″*-tri(3-fluoro-6-methyl-2-picolyl)-1,4,7-triazacyclononane was prepared as a red-brown oily solid (0.247 g, 58 %) from *N,N′*-di(3-fluoro-6-methyl-2-picolyl)-1,4,7-triazacyclononane (0.318 g, 0.850 mmol), 3-fluoro-2-formyl-6-methyl-pyridine (0.142 g, 1.02 mmol) and sodium triacetoxyborohydride (0.540 g, 2.55 mmol). ESI-MS (*m*/*z*): Calcd. for $C_{27}H_{34}F_3N_6$ $(M+H)^+$ 499.28, found 499.25. ^{1}H NMR (500 MHz, $CDCl_3$, 25 °C): δ 7.20 (dd, *J* = 8.9, 8.9 Hz, 3H), 6.99 (dd, *J* = 8.4, 3.6 Hz, 3H), 3.76 (d, *J* = 2.1 Hz, 6H), 2.82 (s, 12H), 2.49 (s, 9H). ^{19}F NMR (470 MHz, $CDCl_3$, 25 °C): δ −129.59 (d, *J* = 9.4 Hz). ^{19}F NMR (470 MHz, MeCN-d_3, 25 °C): δ −131.53 (d, *J* = 9.2 Hz).

Synthesis of N,N′,N″-tri(3-fluoro-2-picolyl)-1,4,7-triazacyclononane (L_3). According to the general procedure, *N,N′,N″*-tri(3-fluoro-2-picolyl)-1,4,7-triazacyclononane was prepared as an orange oil (0.204 g, 47 %) from *N,N′*-di(3-fluoro-2-picolyl)-1,4,7-triazacyclononane (0.328 g, 0.944 mmol), 3-fluoro-2-formylpyridine (0.142 g, 1.13 mmol) and sodium triacetoxyborohydride (0.600 g, 2.83 mmol). ESI-MS (*m*/*z*): Calcd. for $C_{24}H_{28}F_3N_6$ $(M+H)^+$ 457.23, found 457.18. ^{1}H NMR (400 MHz, $CDCl_3$, 25 °C): δ 8.34 (dd, J = 3.8, 1.1 Hz, 3H), 7.35 (ddd, J = 7.2, 7.2, 1.1 Hz, 3H), 7.17–7.23 (m, 3H), 3.82 (d, J = 1.7 Hz, 6H), 2.86 (s, 12H). ^{19}F NMR (376 MHz, $CDCl_3$, 25 °C): δ −123.70 (dd, J = 9.2, 3.4 Hz). ^{19}F NMR (470 MHz, MeCN-d_3, 25 °C): δ −125.56 (dd, J = 10.6, 1.4 Hz).

2.5.2 Supplementary Scheme

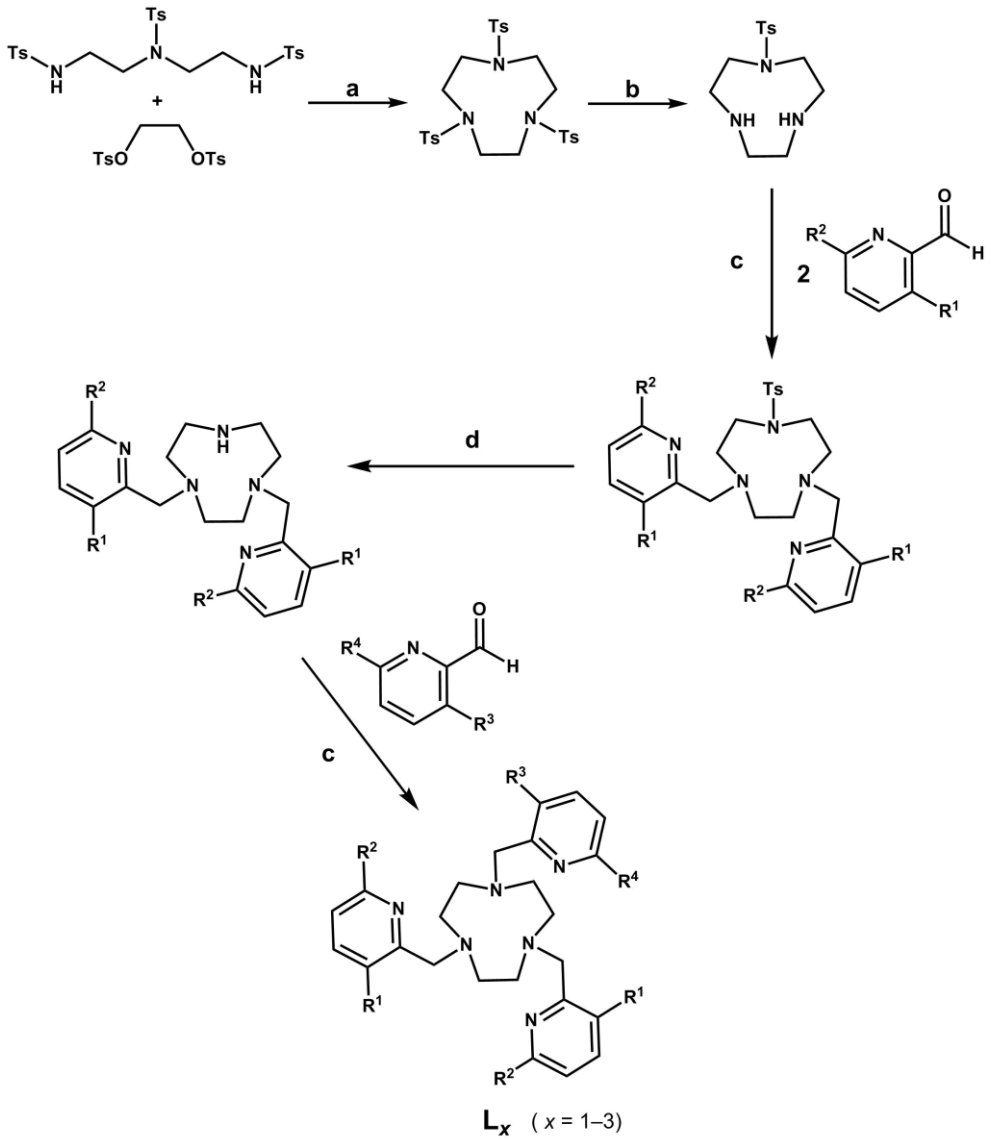

Scheme 2.1 Synthesis of ligands L_x (x = 1–3). Reagents and solvents: (a) Cs_2CO_3, DMF; (b) HBr/HOAc; (c) $Na(OAc)_3BH$, CH_2Cl_2; (d) conc. H_2SO_4.

2.5.3 Supplementary Figures

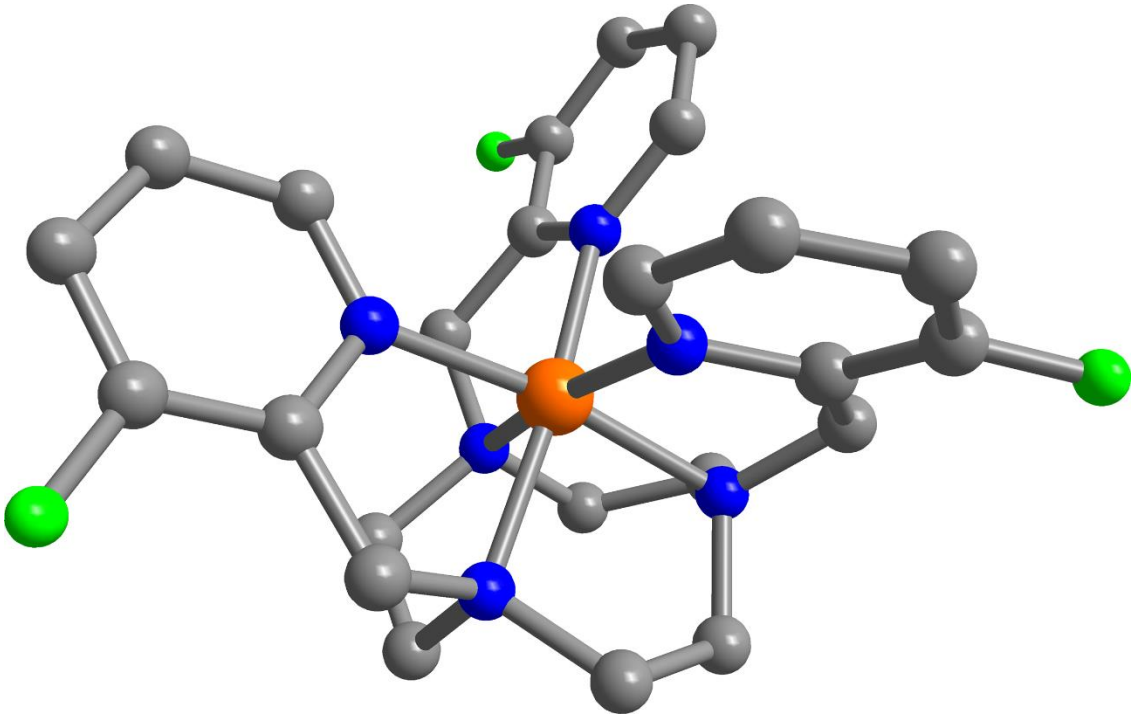

Figure 2.7 Crystal structure of $[Fe(L_3)]^{2+}$, as observed in **3a**. Orange, green, blue, and gray spheres represent Fe, F, N, and C atoms, respectively; H atoms are omitted for clarity.

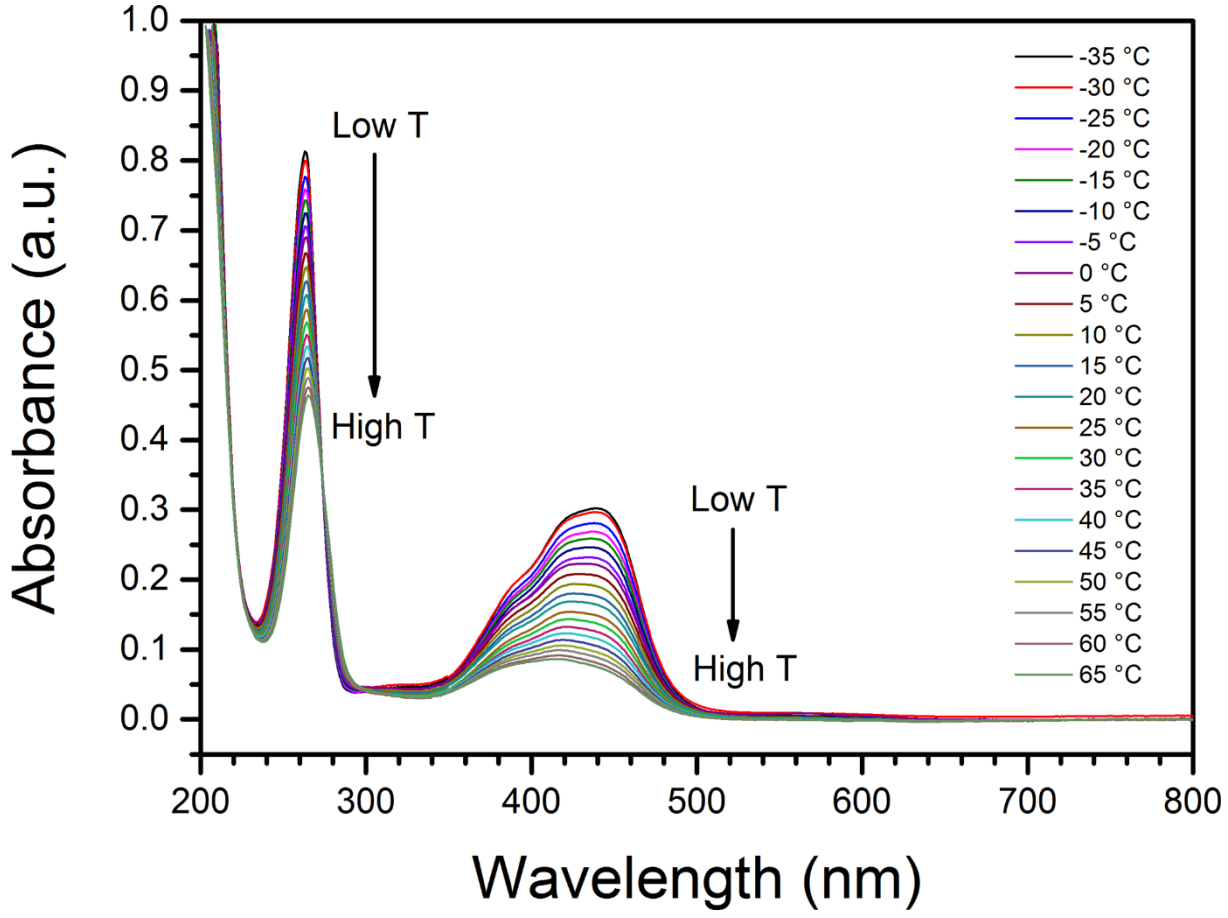

Figure 2.8 VT UV-Vis spectra of a 55 µM solution of **1a** in dry MeCN. Spectra were measured in the temperature range −35–65 °C with 5 °C increments. The temperature of each recorded spectrum is given with the color assignment in the legend.

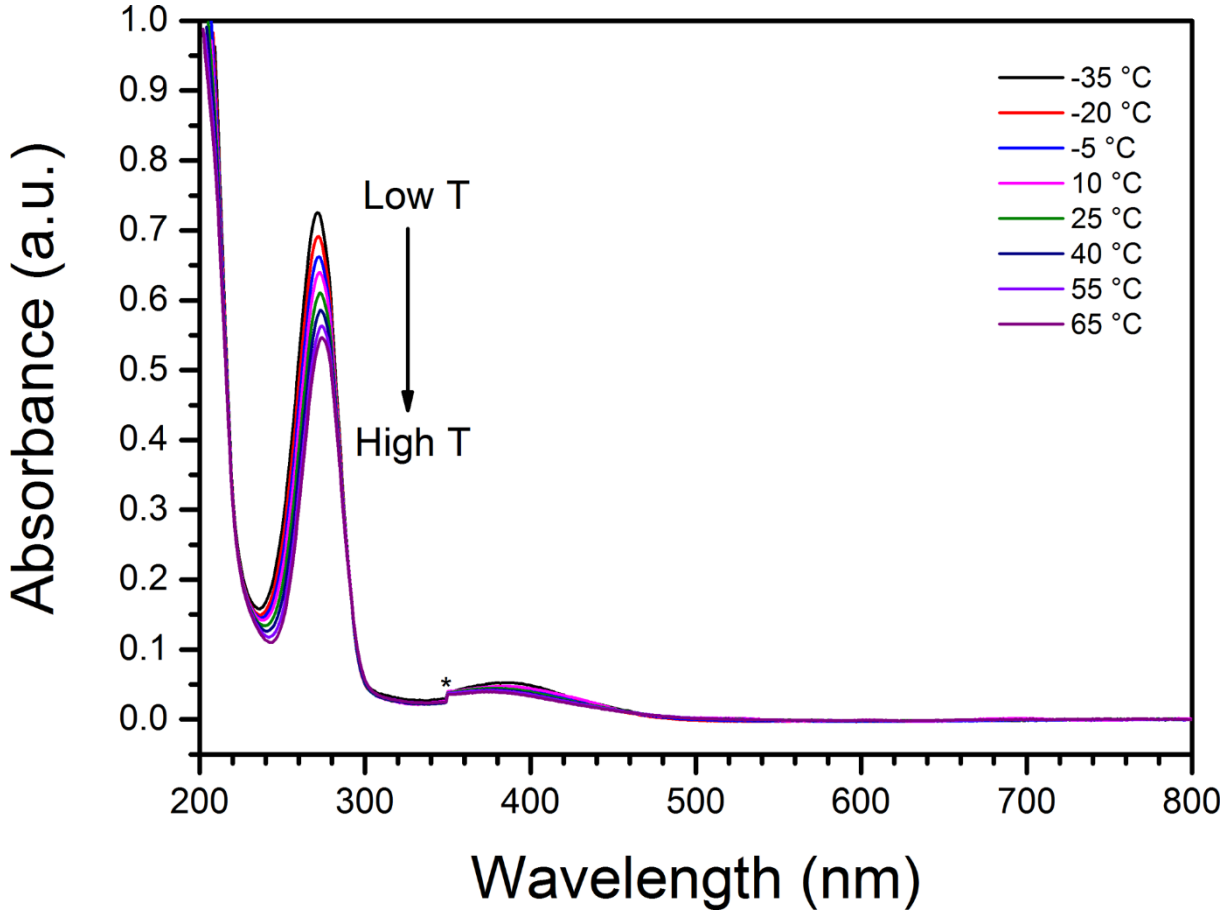

Figure 2.9 VT UV-Vis spectra of a 55 μM solution of **2a** in dry MeCN. Spectra were measured in the temperature range −35–65 °C with either 10 or 15 °C increments. The temperature of each recorded spectrum is given with the color assignment in the legend. The asterisk denotes an instrument-derived artifact.

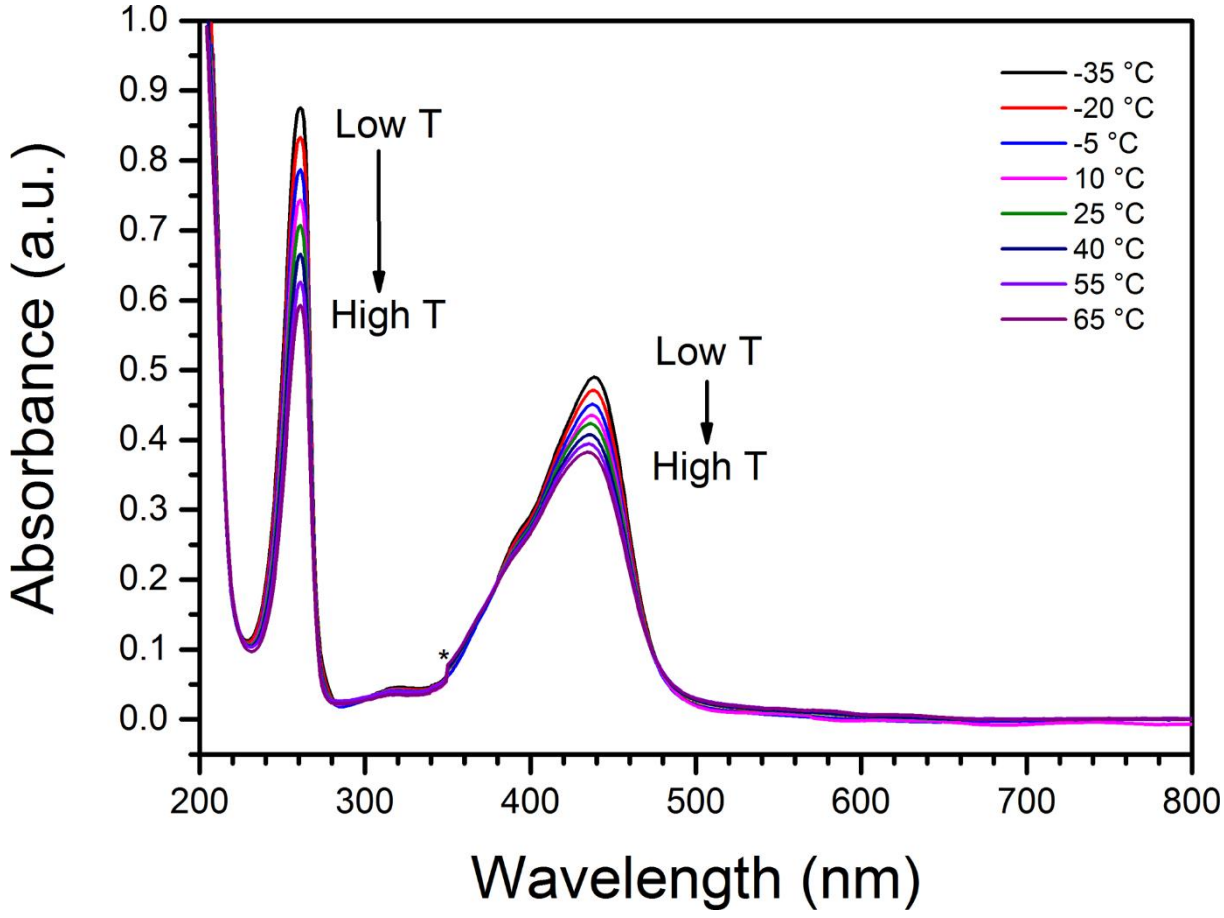

Figure 2.10 VT UV-Vis spectra of a 40 μM solution of **3a** in dry MeCN. Spectra were measured in the temperature range −35–65 °C with either 10 or 15 °C increments. The temperature of each recorded spectrum is given with the color assignment in the legend. The asterisk denotes an instrument-derived artifact.

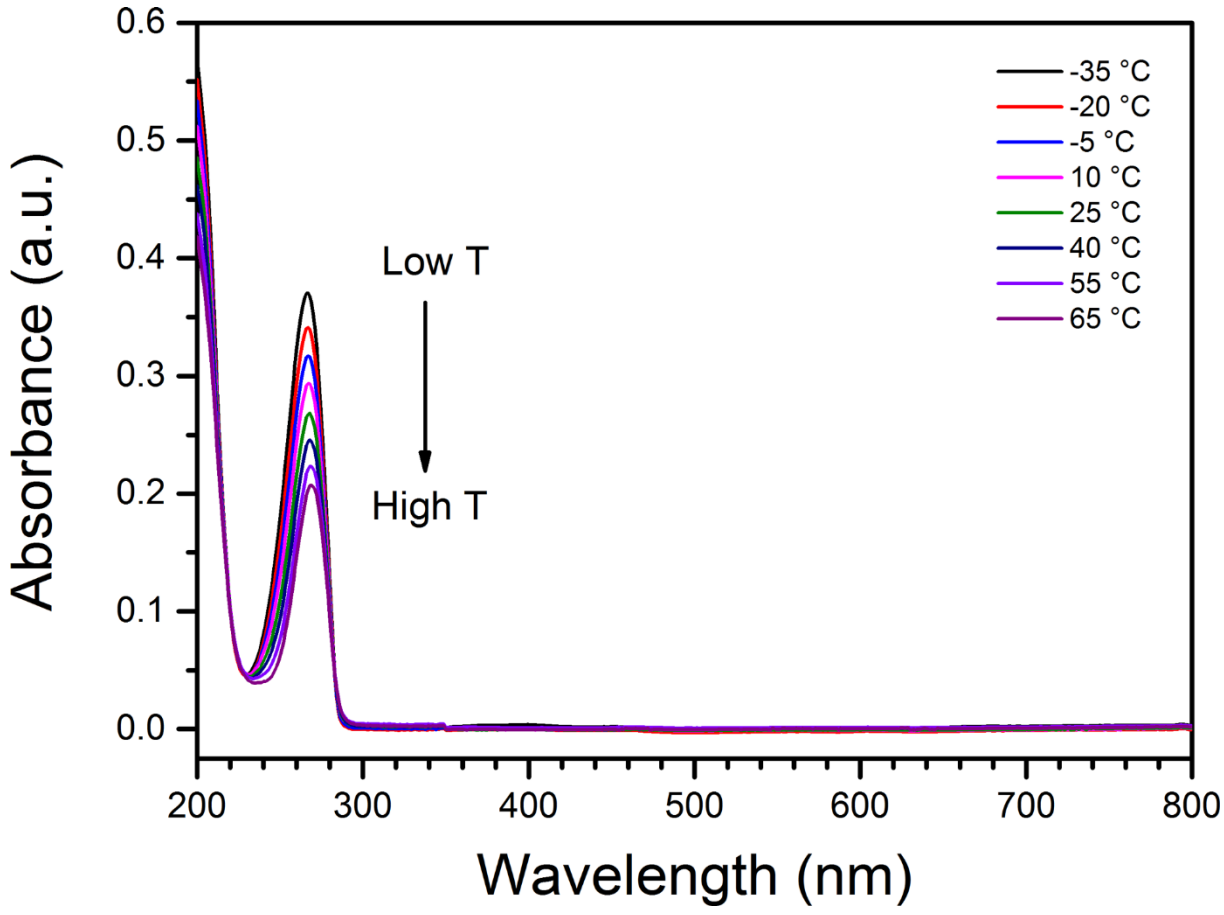

Figure 2.11 VT UV-Vis spectra of an 8.8 μM solution of **1b** in dry MeCN. Spectra were measured in the temperature range −35–65 °C with either 10 or 15 °C increments. The temperature of each recorded spectrum is given with the color assignment in the legend.

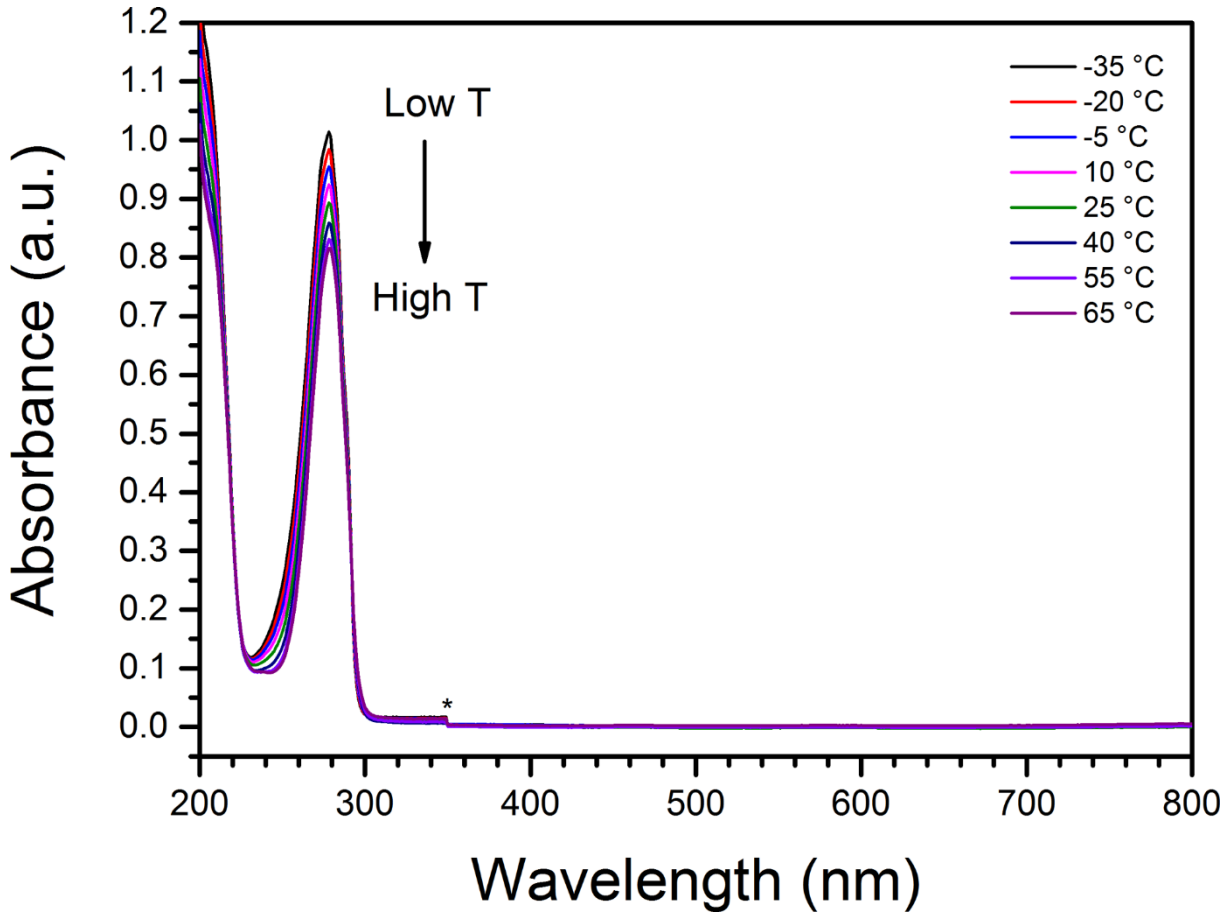

Figure 2.12 VT UV-Vis spectra of a 25 μM solution of **2b** in dry MeCN. Spectra were measured in the temperature range −35–65 °C with either 10 or 15 °C increments. The temperature of each recorded spectrum is given with the color assignment in the legend. The asterisk denotes an instrument-derived artifact.

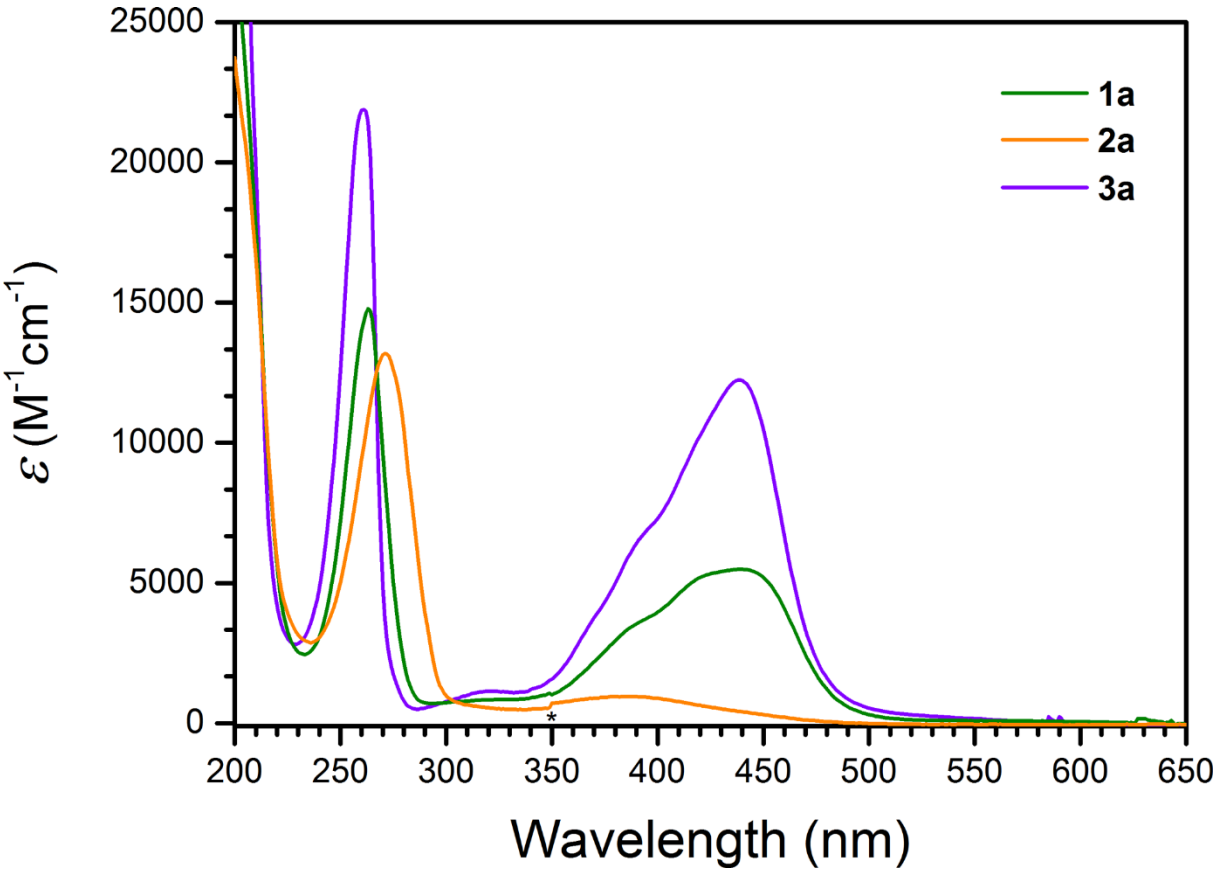

Figure 2.13 Comparison of UV-Vis spectra of compounds **1a**, **2a** and **3a** in dry MeCN at −35 °C. Note that the molar absorptivity (ε), instead of absorbance, is plotted as a function of wavelength to correct for the different concentrations of samples of **1a**, **2a** and **3a**. The asterisk denotes an instrument-derived artifact.

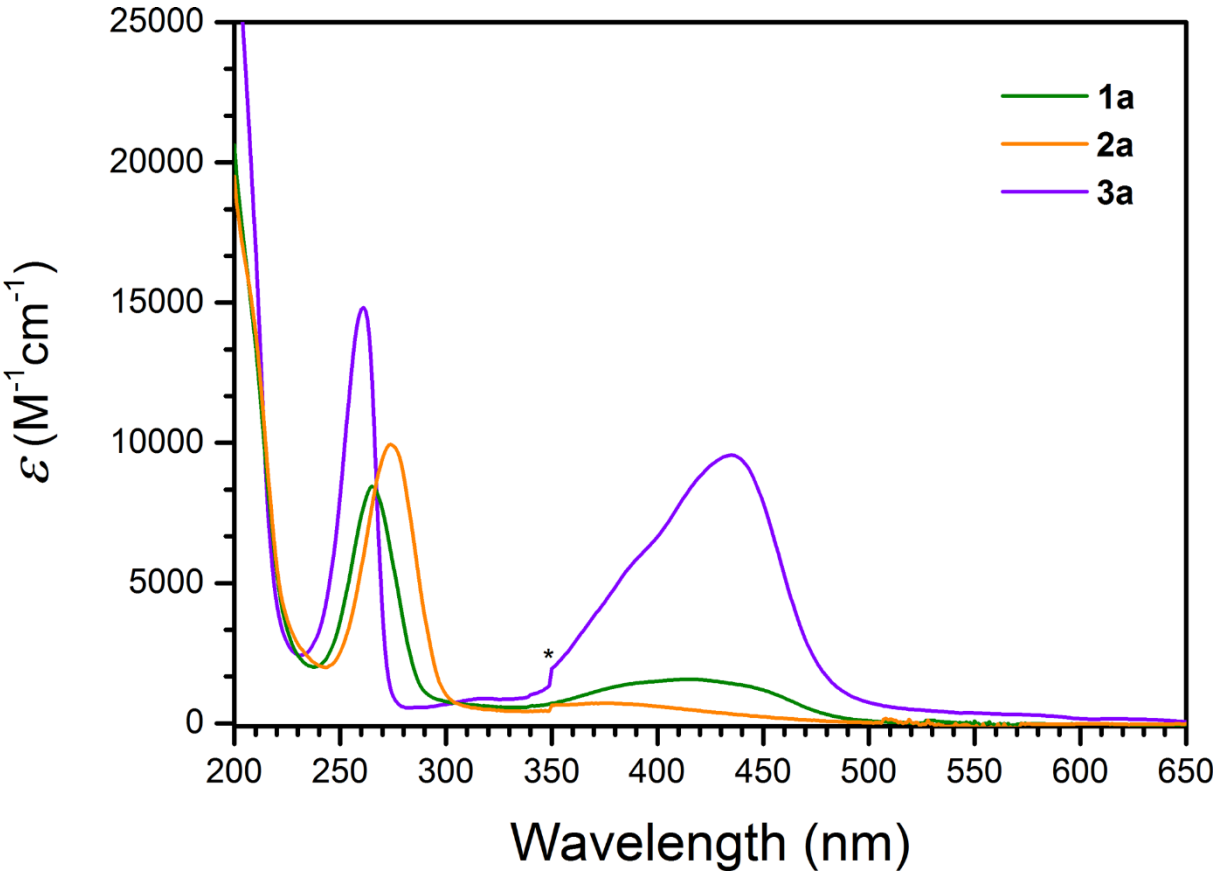

Figure 2.14 Comparison of UV-Vis spectra of compounds **1a**, **2a** and **3a** in dry MeCN at 65 °C. Note that the molar absorptivity (ε), instead of absorbance, is plotted as a function of wavelength to correct for the different concentrations of samples of **1a**, **2a** and **3a**. The asterisk denotes an instrument-derived artifact.

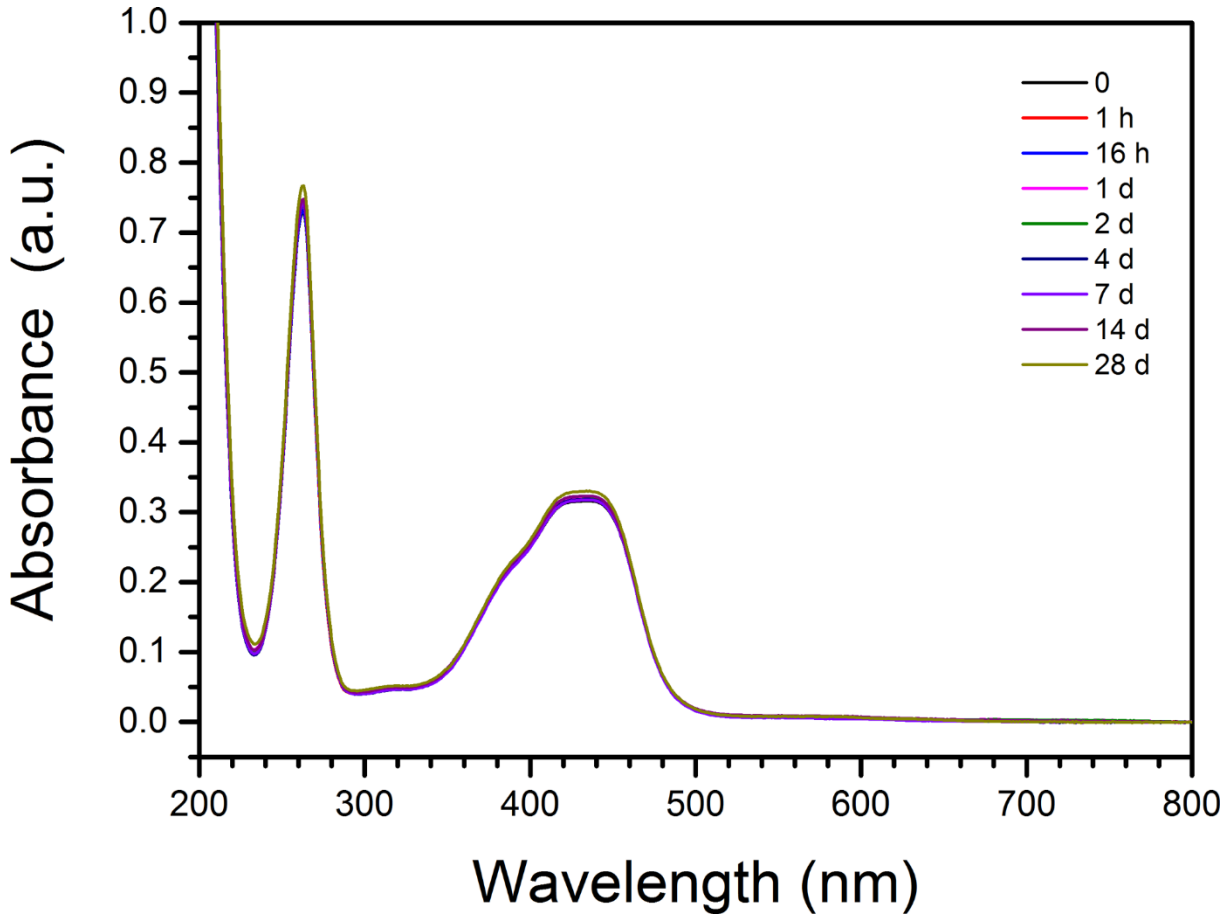

Figure 2.15 UV-Vis spectra of a 59 μM solution of **1a** in deoxygenated H_2O and under aerobic conditions, respectively, at ambient temperature. The color assignment in the legend indicates the time that the sample solution was open to air prior to the measurement was performed.

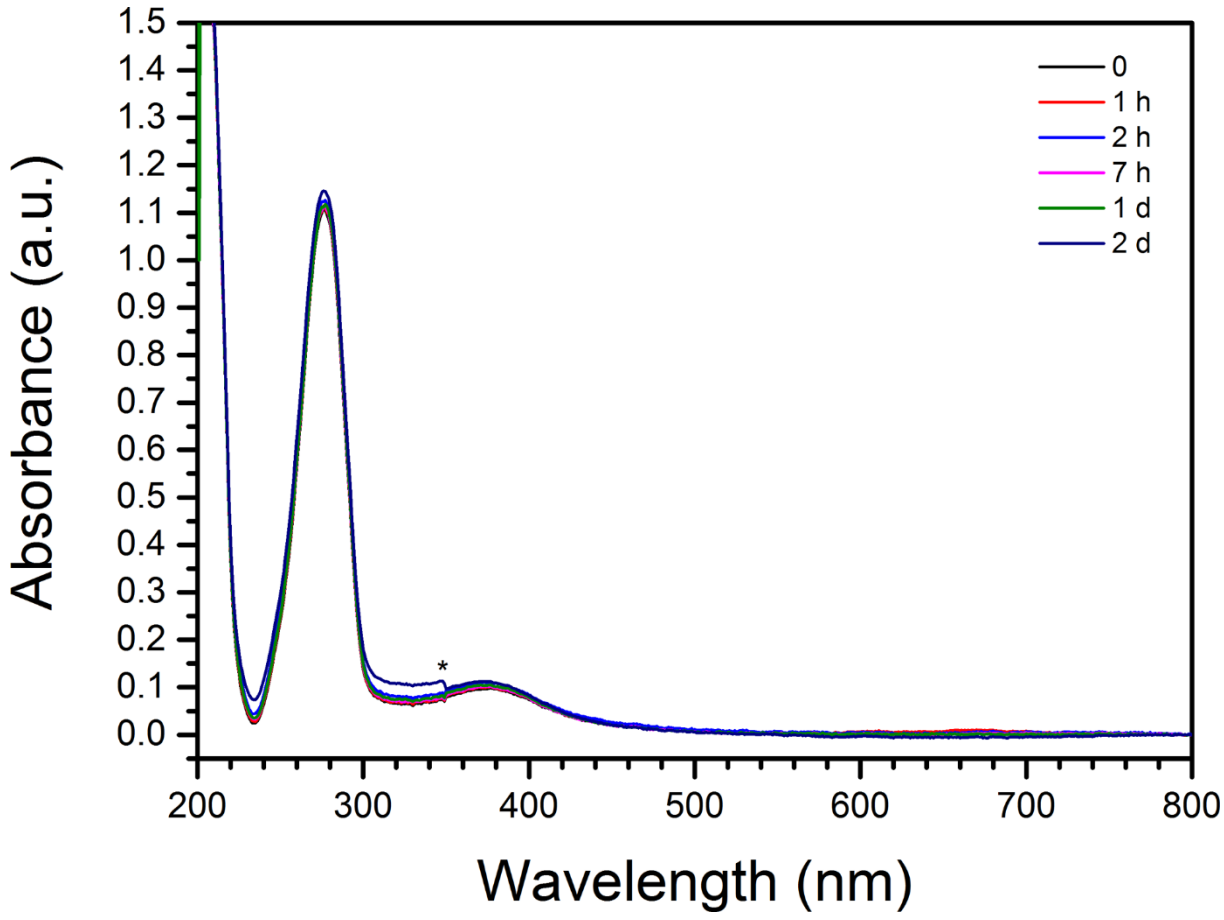

Figure 2.16 UV-Vis spectra of a 69 μM solution of **2a** in deoxygenated H_2O and under aerobic conditions, respectively, at ambient temperature. The color assignment in the legend indicates the time that the sample solution was open to air prior to the measurement was performed. The asterisk denotes an instrument-derived artifact.

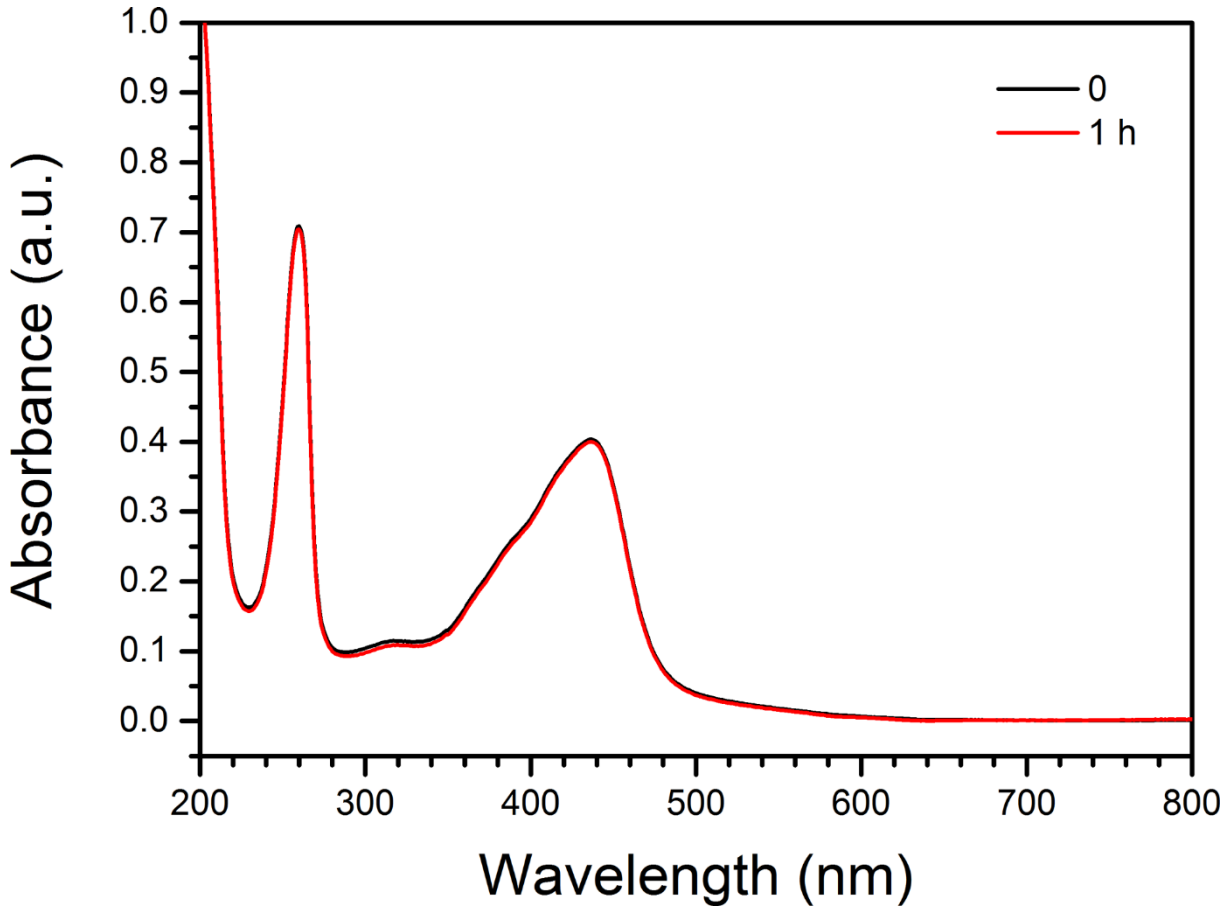

Figure 2.17 UV-Vis spectra of a 51 μM solution of **3a** in deoxygenated H_2O (black curve) and under aerobic conditions (red curve) at ambient temperature. The color assignment in the legend indicates the time that the sample solution was open to air prior to the measurement was performed.

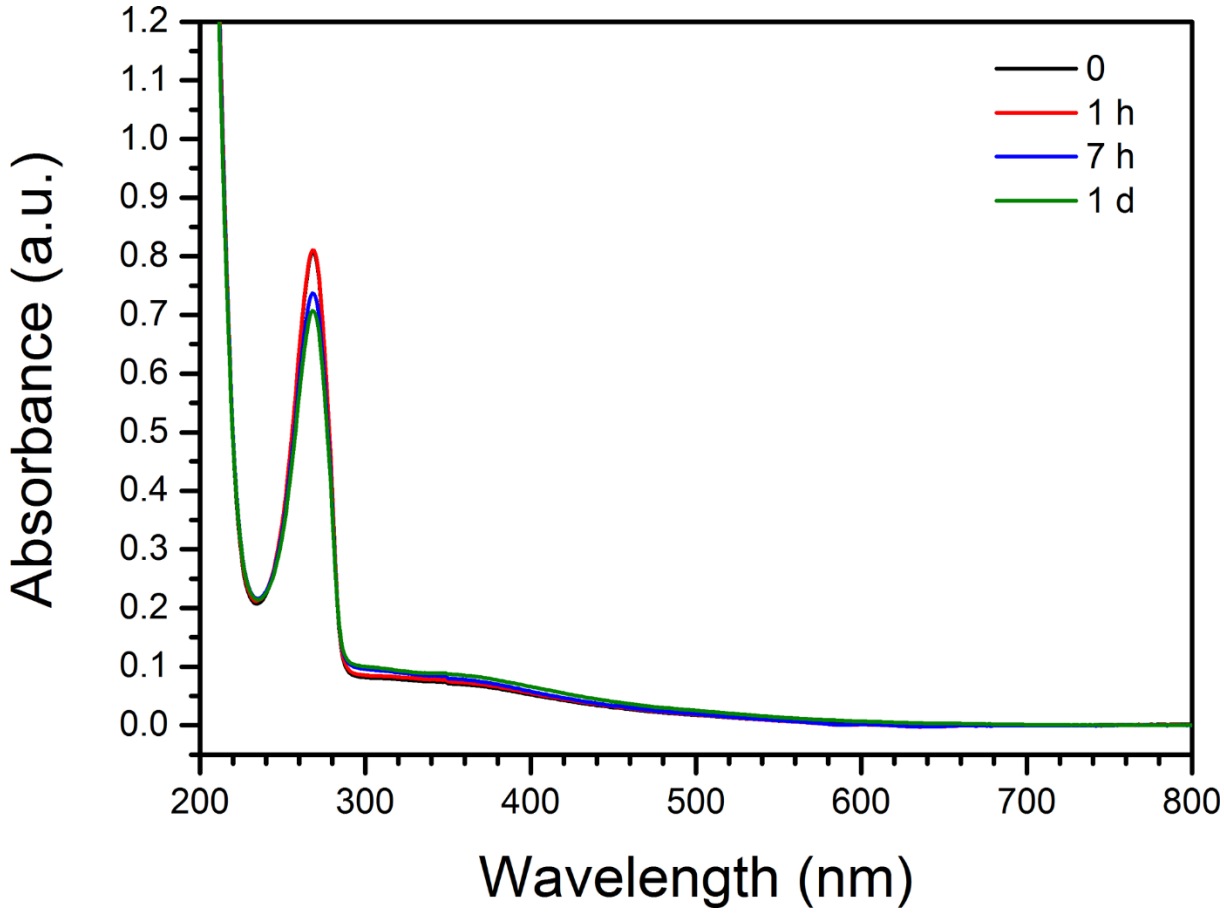

Figure 2.18 UV-Vis spectra of a 72 μM solution of **1b** in deoxygenated H_2O and under aerobic conditions, respectively, at ambient temperature. The color assignment in the legend indicates the time that the sample solution was open to air prior to the measurement was performed. Note that the slight decrease in intensity observed with time in air is attributed to a dilution of the sample solution that took place when the sample was moved back and forth between the cuvette and a sample container.

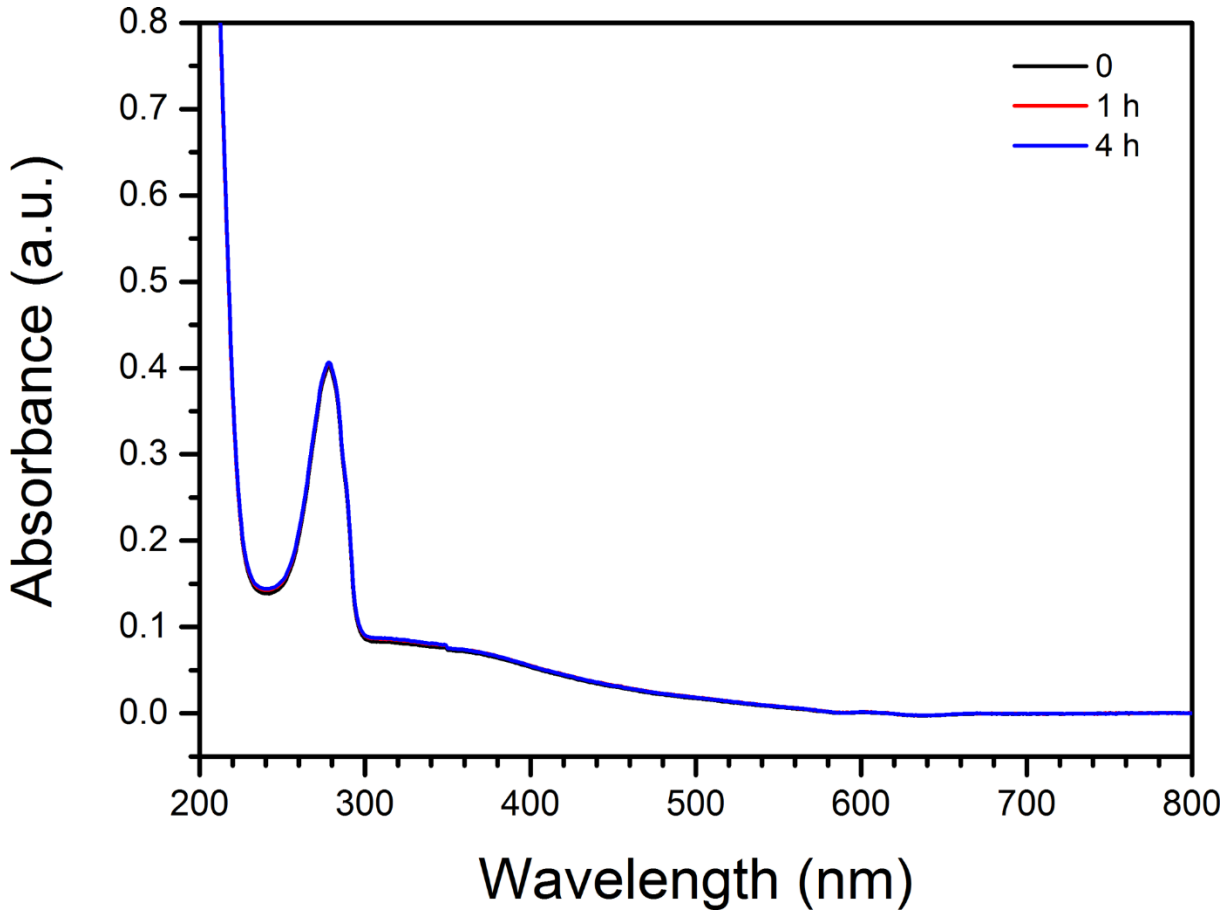

Figure 2.19 UV-Vis spectra of a 30 μM solution of **2b** in deoxygenated H_2O and under aerobic conditions, respectively, at ambient temperature. The color assignment in the legend indicates the time that the sample solution was open to air prior to the measurement was performed.

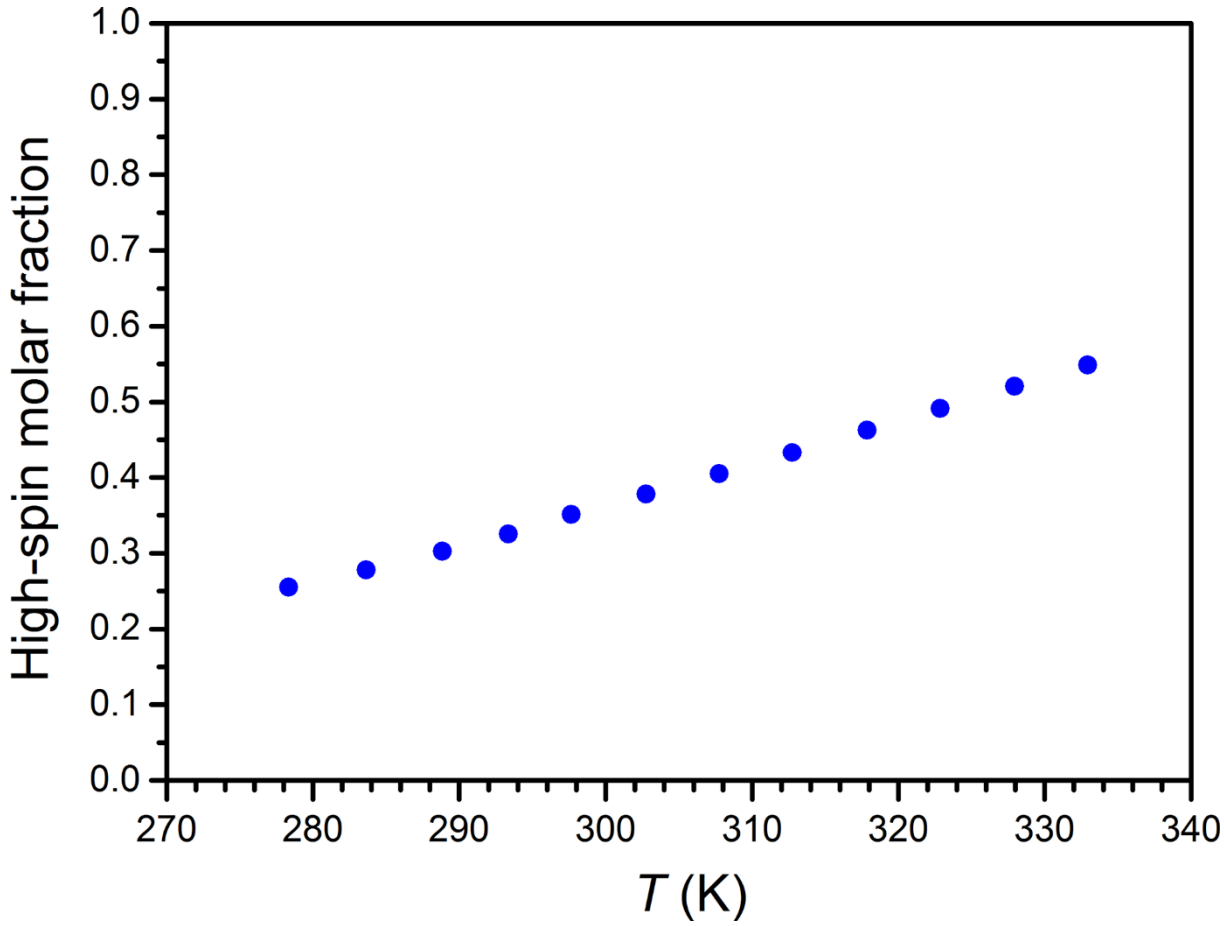

Figure 2.20 Plot of the molar fraction of **1a** in high-spin state as a function of temperature, obtained for aqueous solutions using Equation 2.1. A linear fit to the data gives a spin-crossover temperature ($T_{1/2}$) of 325(1) K.

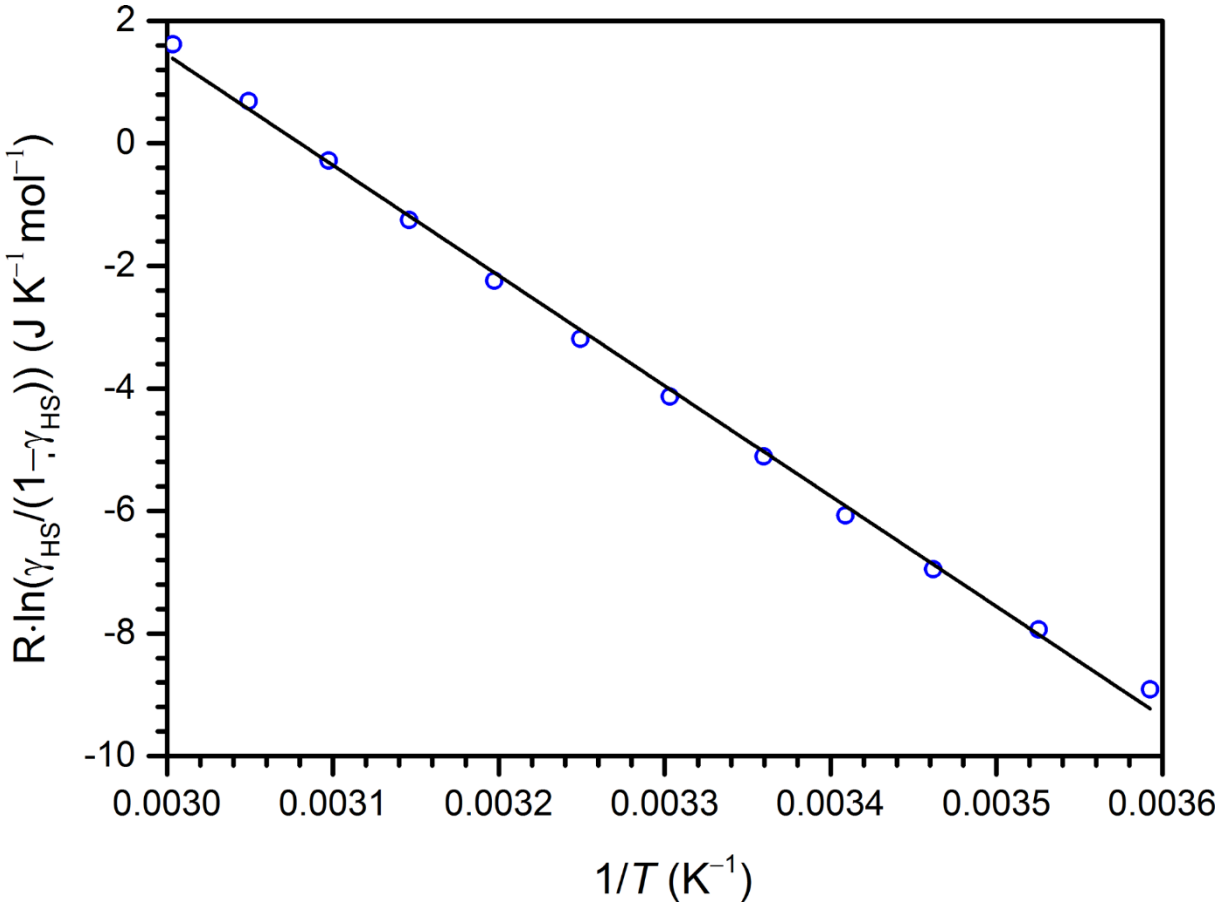

Figure 2.21 Thermodynamic data for the spin transition of **1a** in H_2O, as measured by the Evans method, obtained using the regular solution model (see Equation 2.2). The solid black line indicates a linear fit to the data (R^2 = 0.998), giving the following thermodynamic parameters: ΔH = 18.0(3) kJ mol^{-1} and ΔS = 55.5(9) J K^{-1} mol^{-1}.

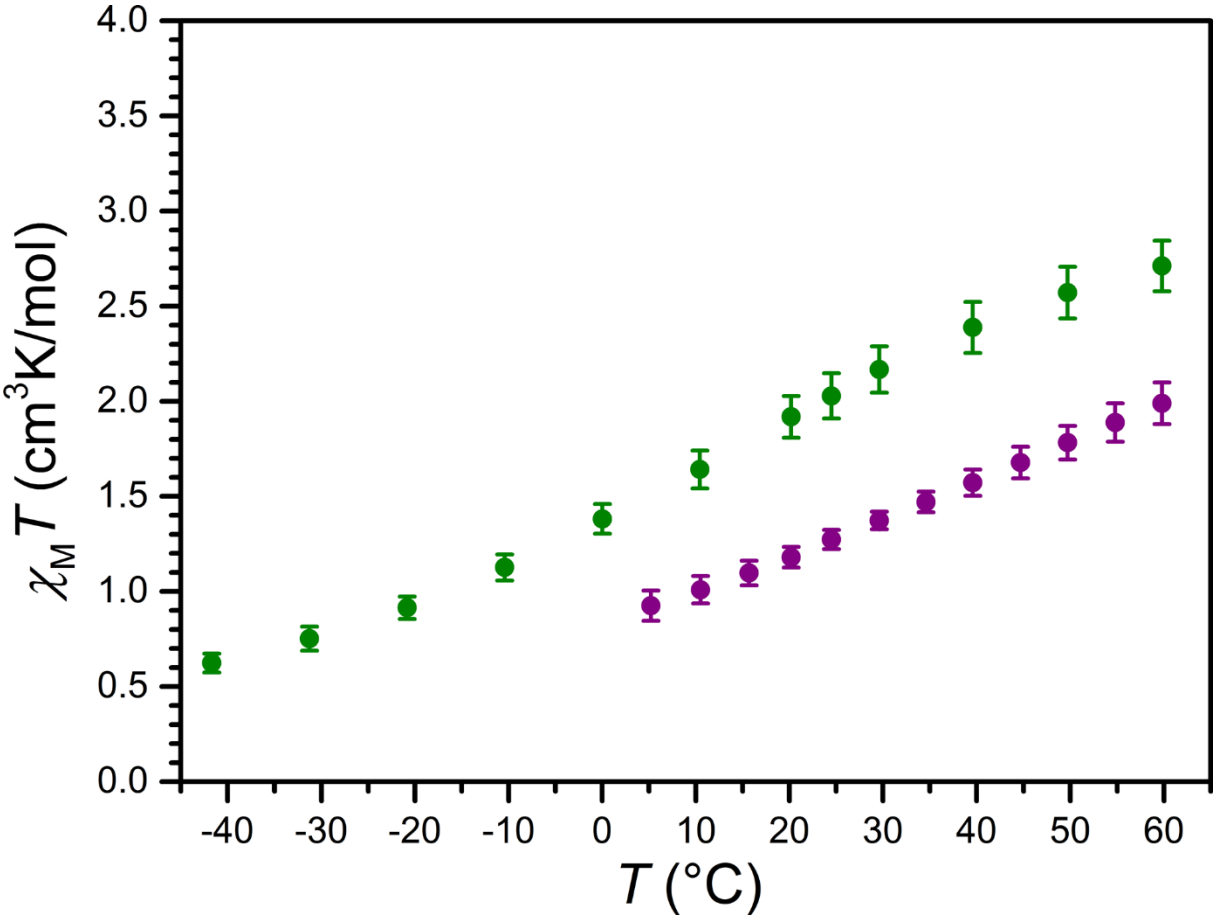

Figure 2.22 VT solution dc magnetic susceptibility data for **1a** in H_2O (purple) and MeCN (green), obtained using the Evans method. Error bars represent standard deviations of the measurements.

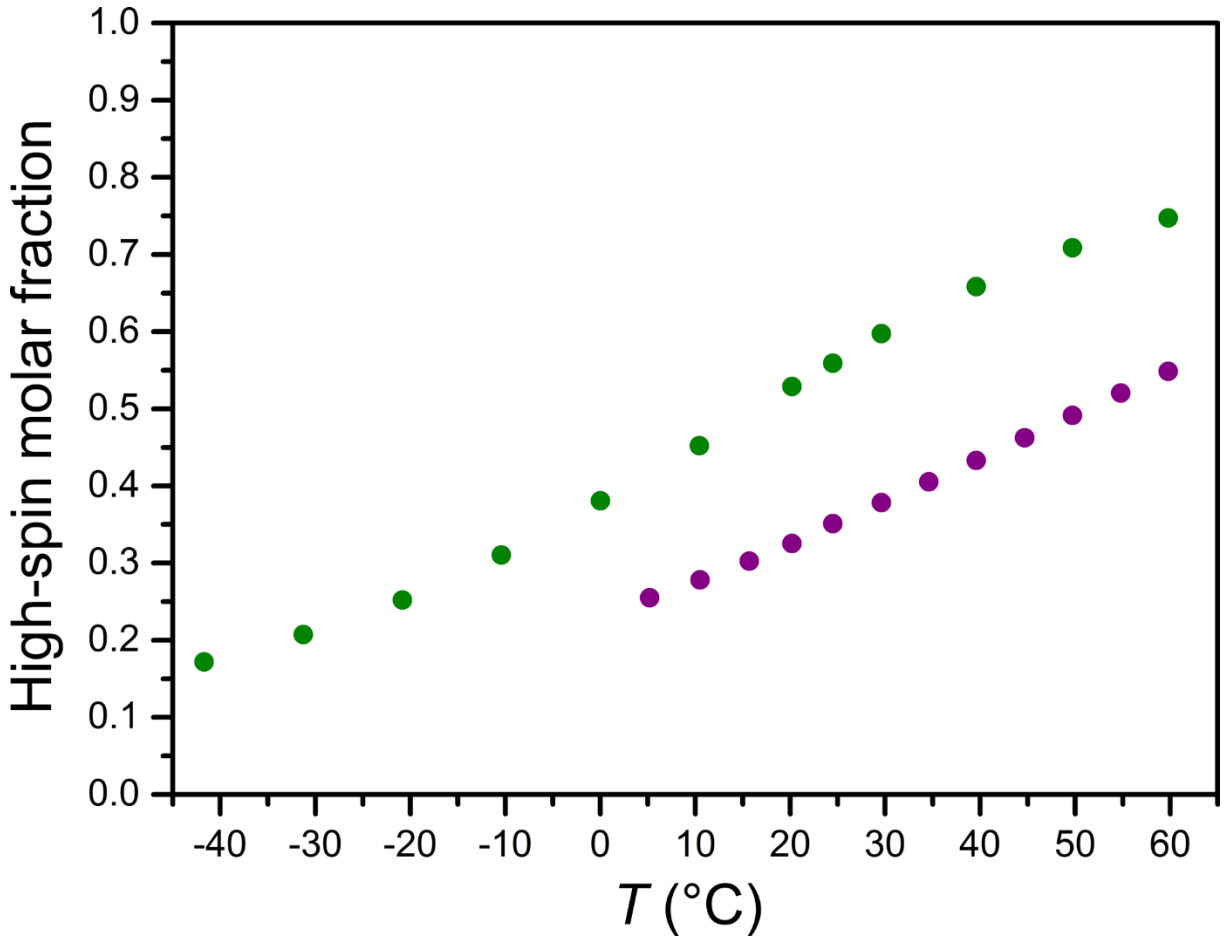

Figure 2.23 Comparison of the molar fraction of **1a** in high-spin state as a function of temperature in H_2O (purple) and MeCN (green), obtained using Equation 2.1. Linear fits to the data give spin-crossover temperatures ($T_{1/2}$) of 52(1) and 17(1) °C in H_2O and MeCN, respectively.

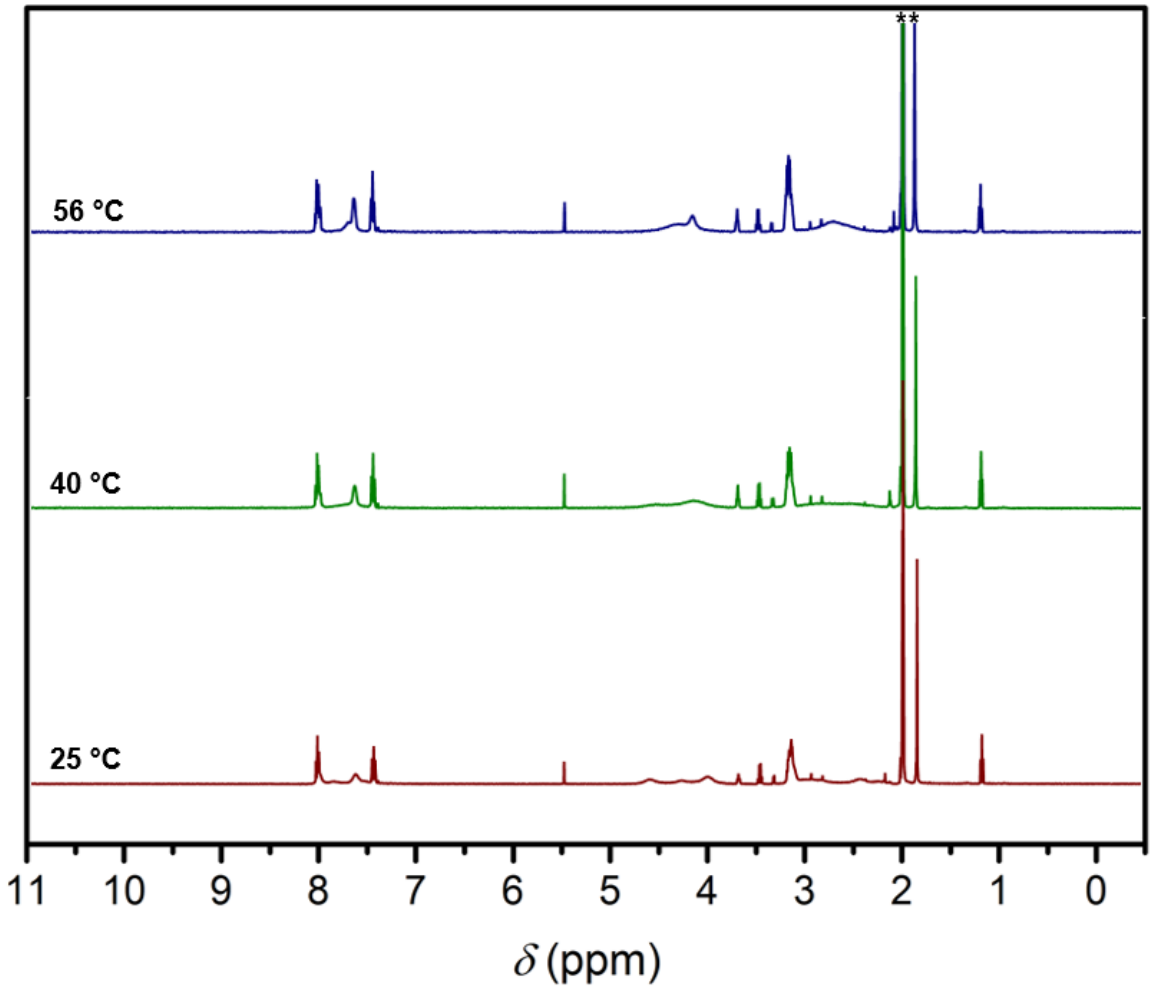

Figure 2.24 VT ^{1}H NMR spectra of **1b** in MeCN-d_3 at 25 to 56 °C. The asterisks denote residual solvent peaks.

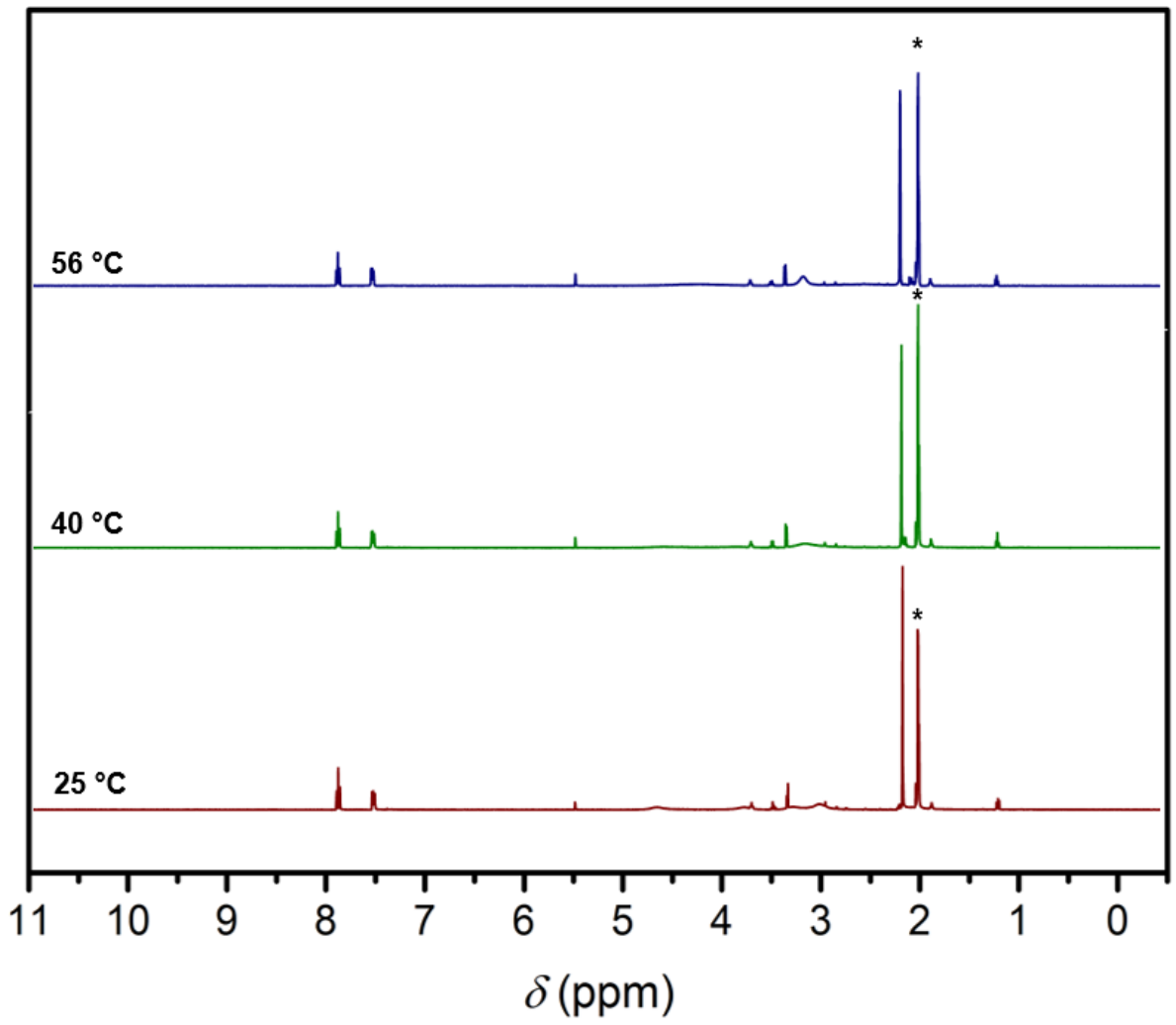

Figure 2.25 VT ^{1}H NMR spectra of **2b** in MeCN-d_3 at 25 to 56 °C. The asterisk denotes residual solvent peaks.

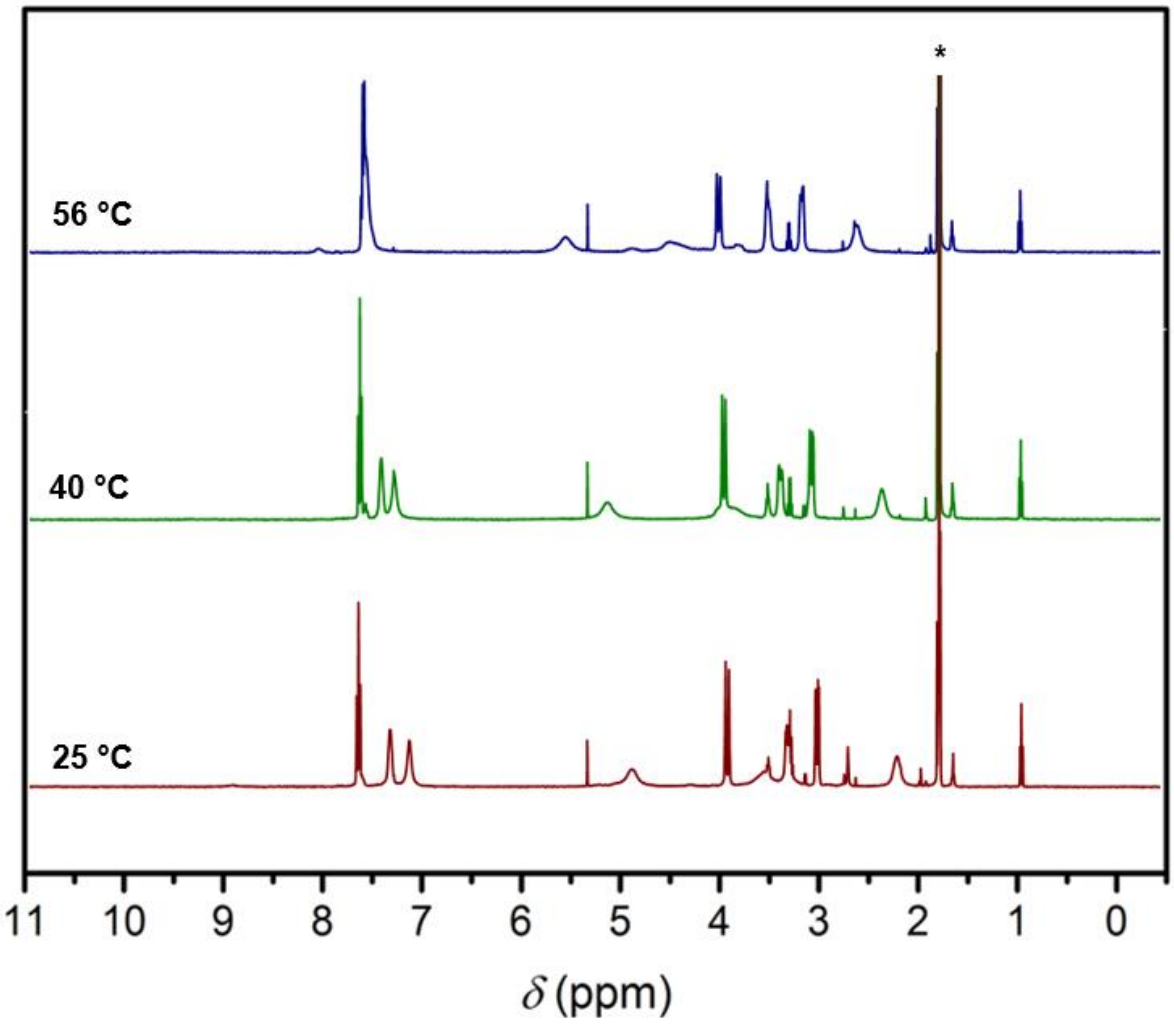

Figure 2.26 VT ^{1}H NMR spectra of **3a** in MeCN-d_3 at 25 to 56 °C. The asterisk denotes residual solvent peaks.

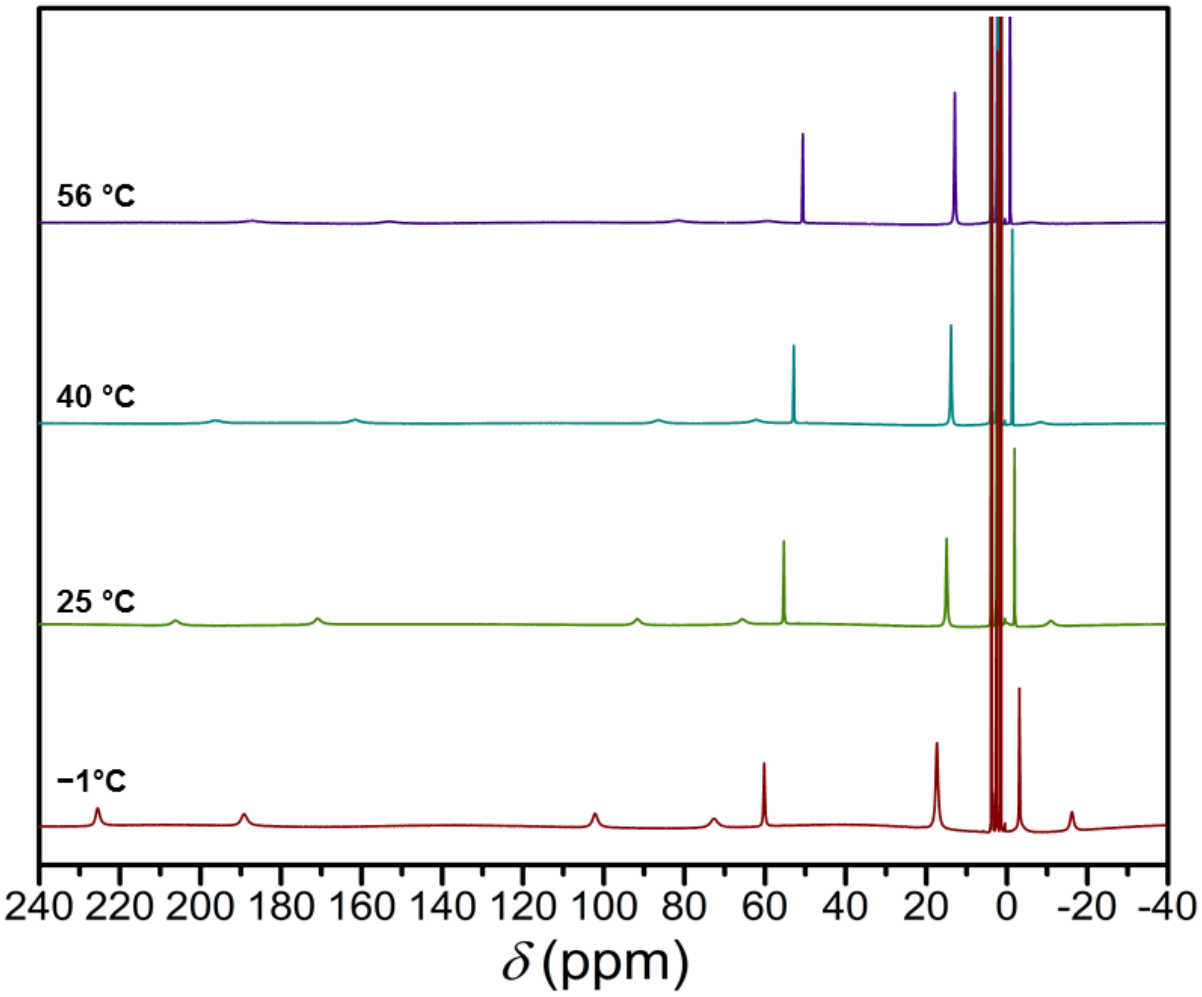

Figure 2.27 VT ^{1}H NMR spectra of **2a** in MeCN-d_3 at −1 to 56 °C.

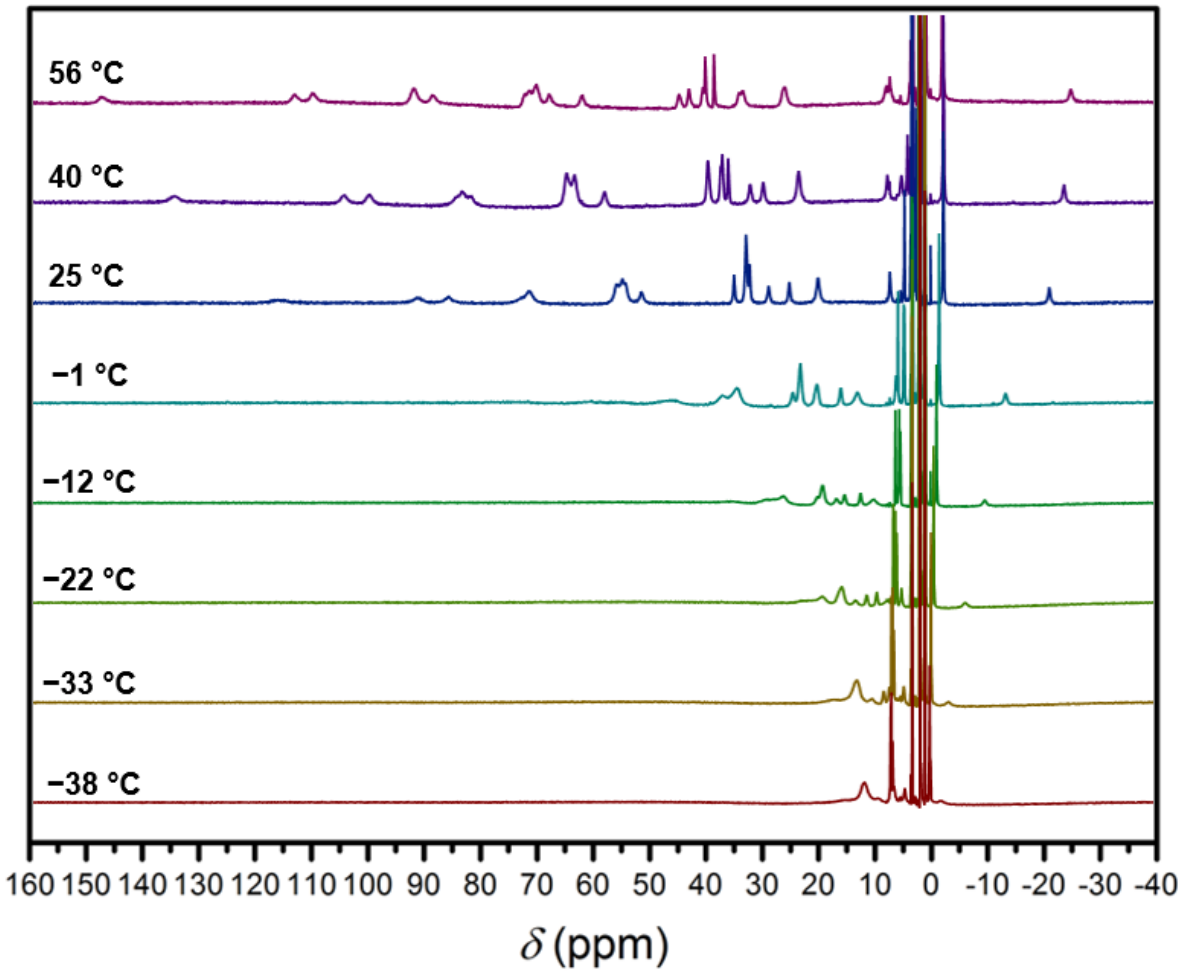

Figure 2.28 VT ^{1}H NMR spectra of **1a** in MeCN-d_3 at −38 to 56 °C.

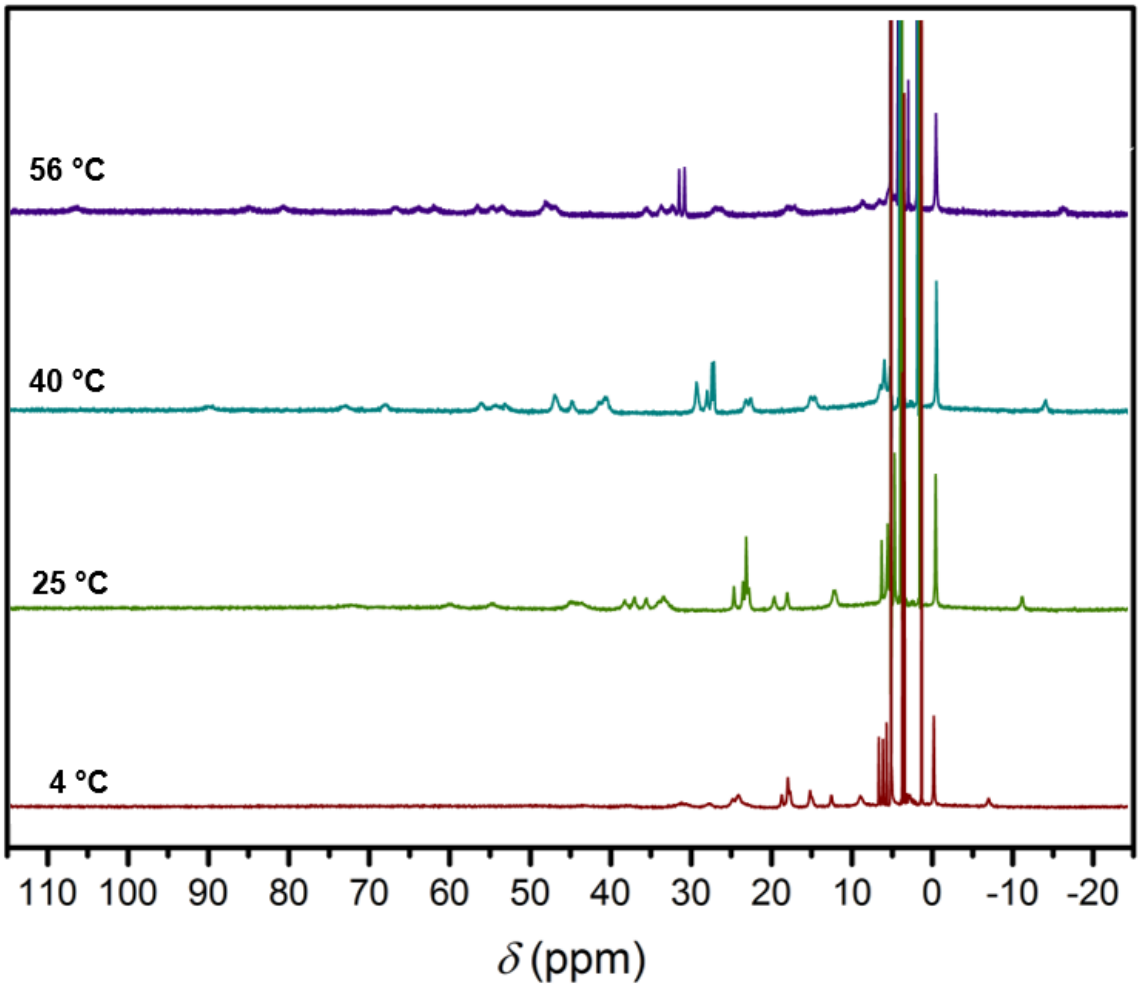

Figure 2.29 VT ^{1}H NMR spectra of **1a** in D_2O at 4 to 56 °C.

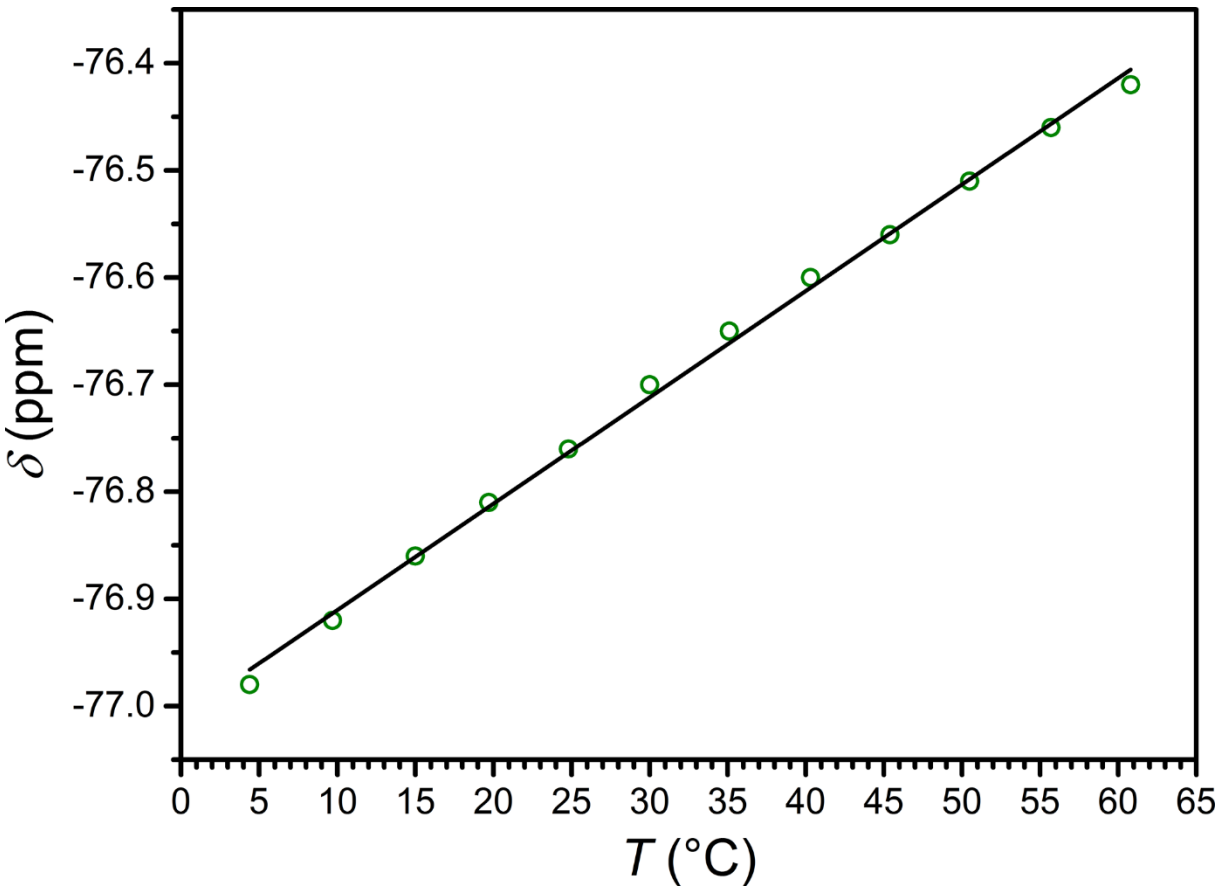

Figure 2.30 Plot of the temperature dependence of the ^{19}F NMR chemical shift for TFE in a 2.1 mM H_2O solution. The chemical shift values are referenced to $CFCl_3$. TFE was used as an internal standard for ^{19}F NMR measurements of compounds **1a**, **1b**, **2a**, **2b**, and **3a** in H_2O, where the chemical shift of TFE at each measured temperature was set to the values shown in the graph above and Table 2.6. The black solid line corresponds to a linear fit to the data with the following equation: $\delta = 0.0099 \times T - 77.010$; $R^2 = 0.998$.

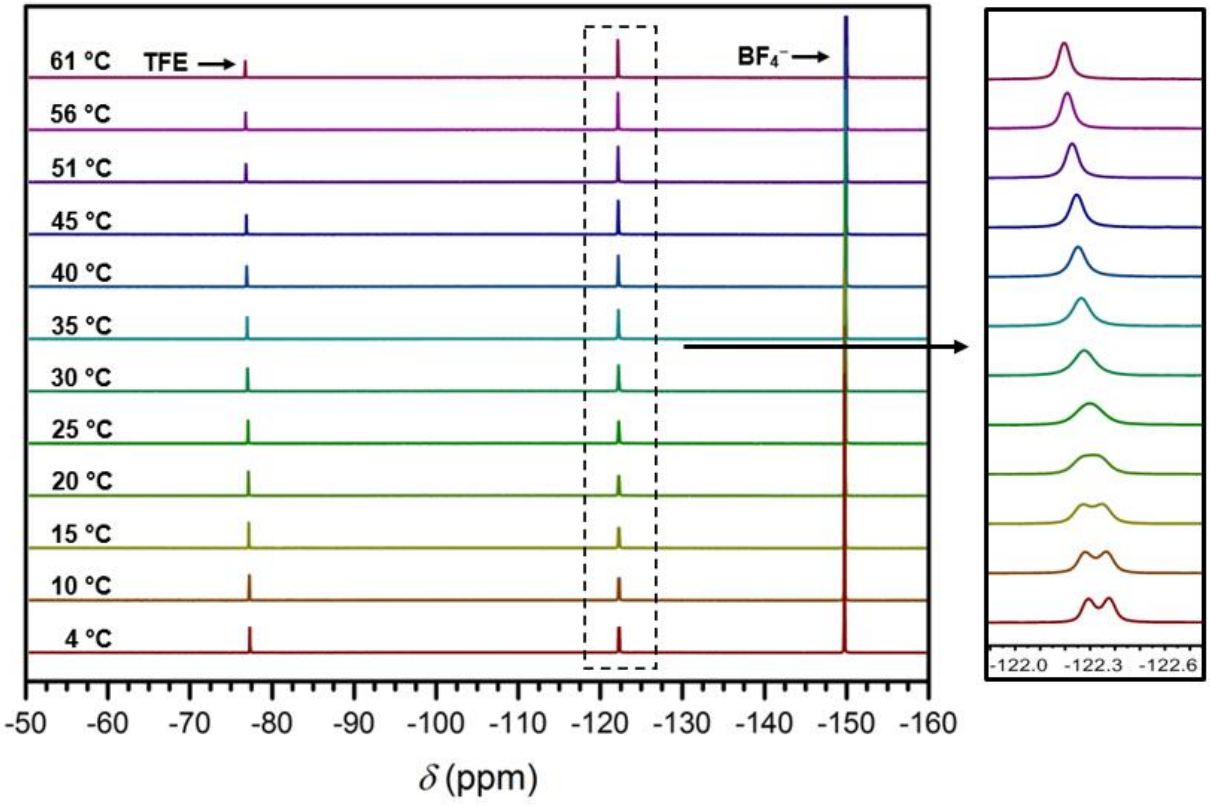

Figure 2.31 Left: VT ^{19}F NMR spectra of **1b** (7.0 mM) in a H_2O solution containing 2.1 mM TFE at 4 to 61 °C. Right: Expansion showing the ^{19}F NMR resonances of **1b**, demonstrating the two overlapping resonances observed at 4 °C and the coalescence of the two peaks upon warming.

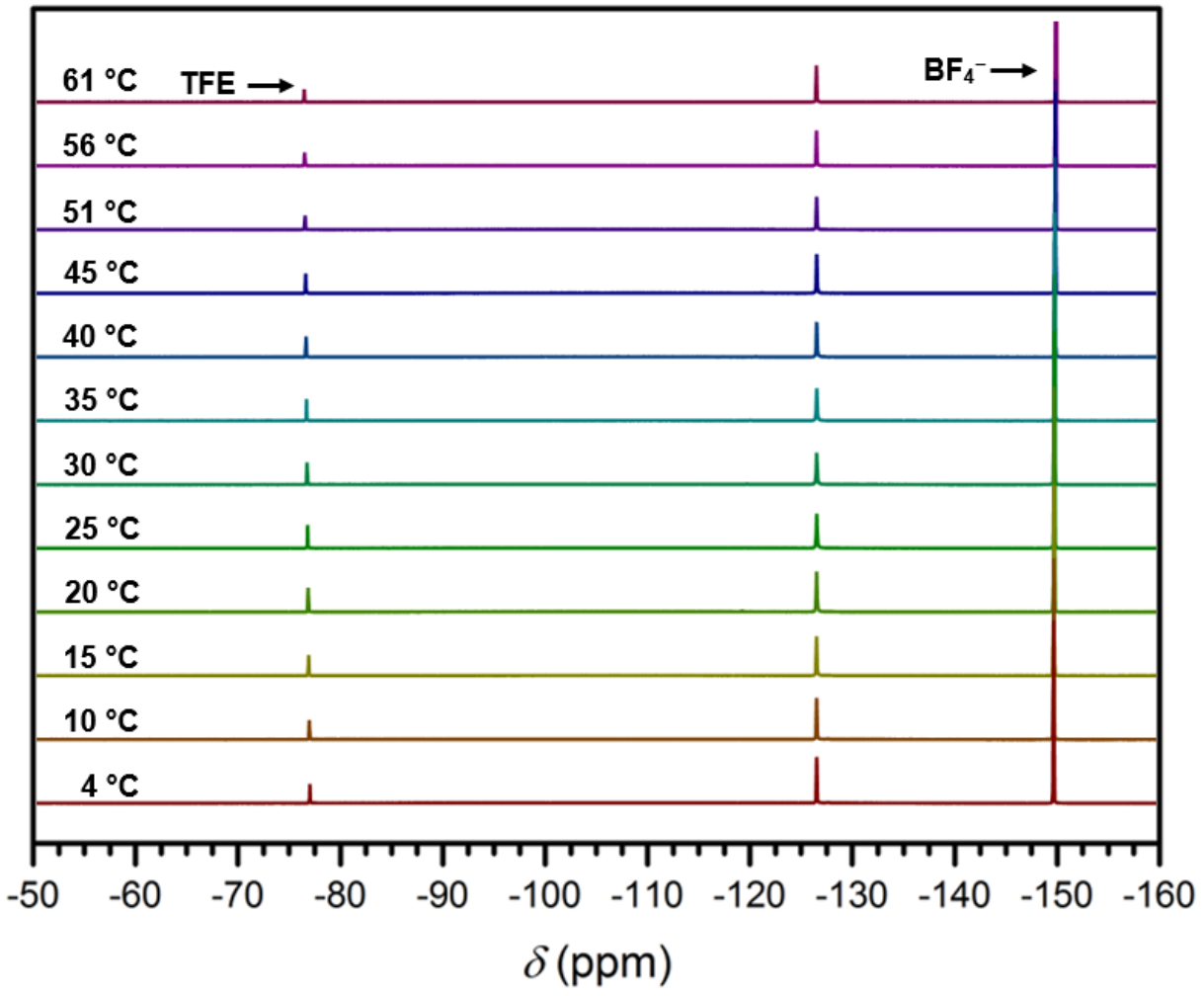

Figure 2.32 VT ^{19}F NMR spectra of **2b** (10.9 mM) in a H_2O solution containing 2.1 mM TFE at 4 to 61 °C.

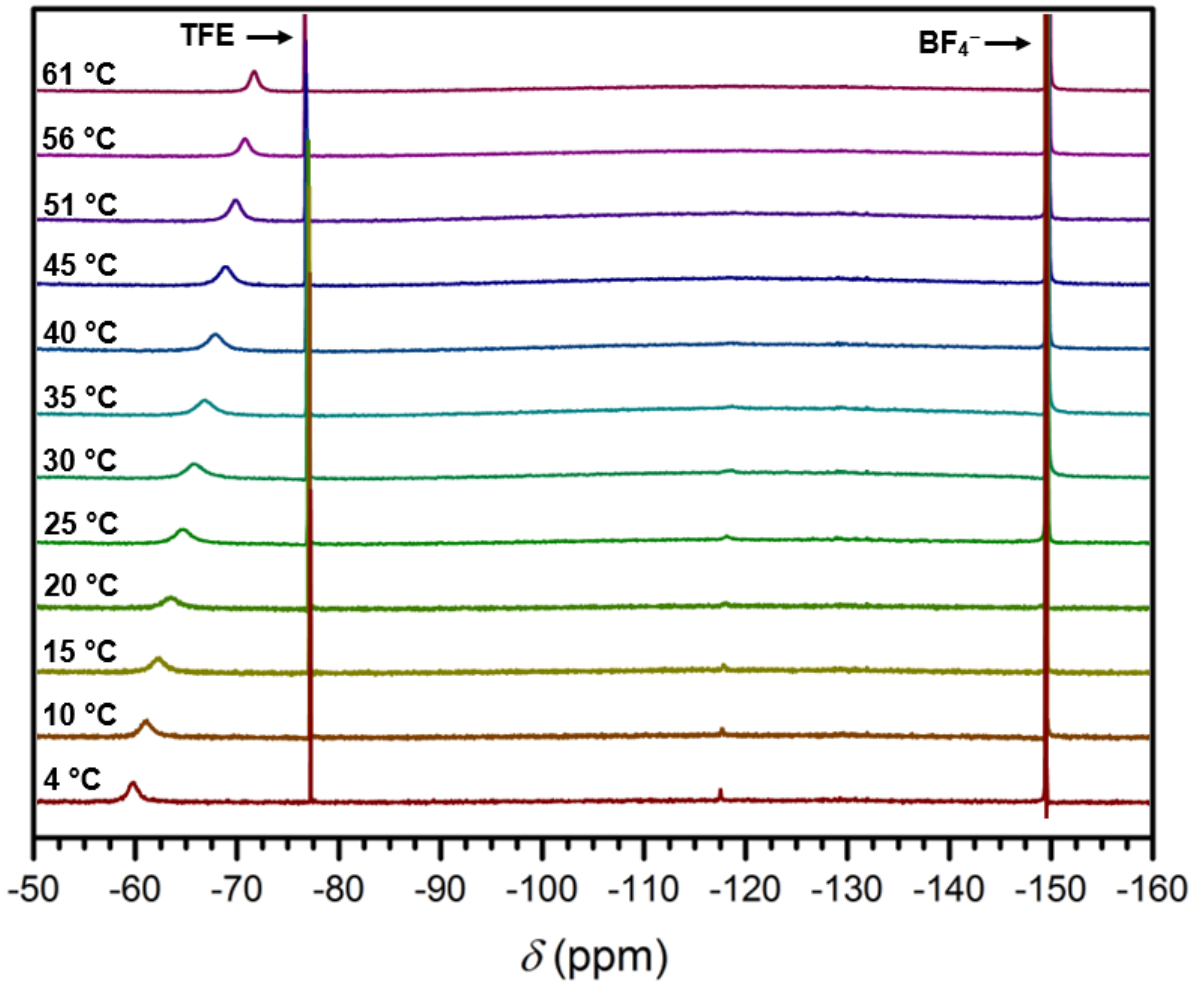

Figure 2.33 VT ^{19}F NMR spectra of **2a** (12.9 mM) in a H_2O solution containing 2.1 mM TFE at 4 to 61 °C.

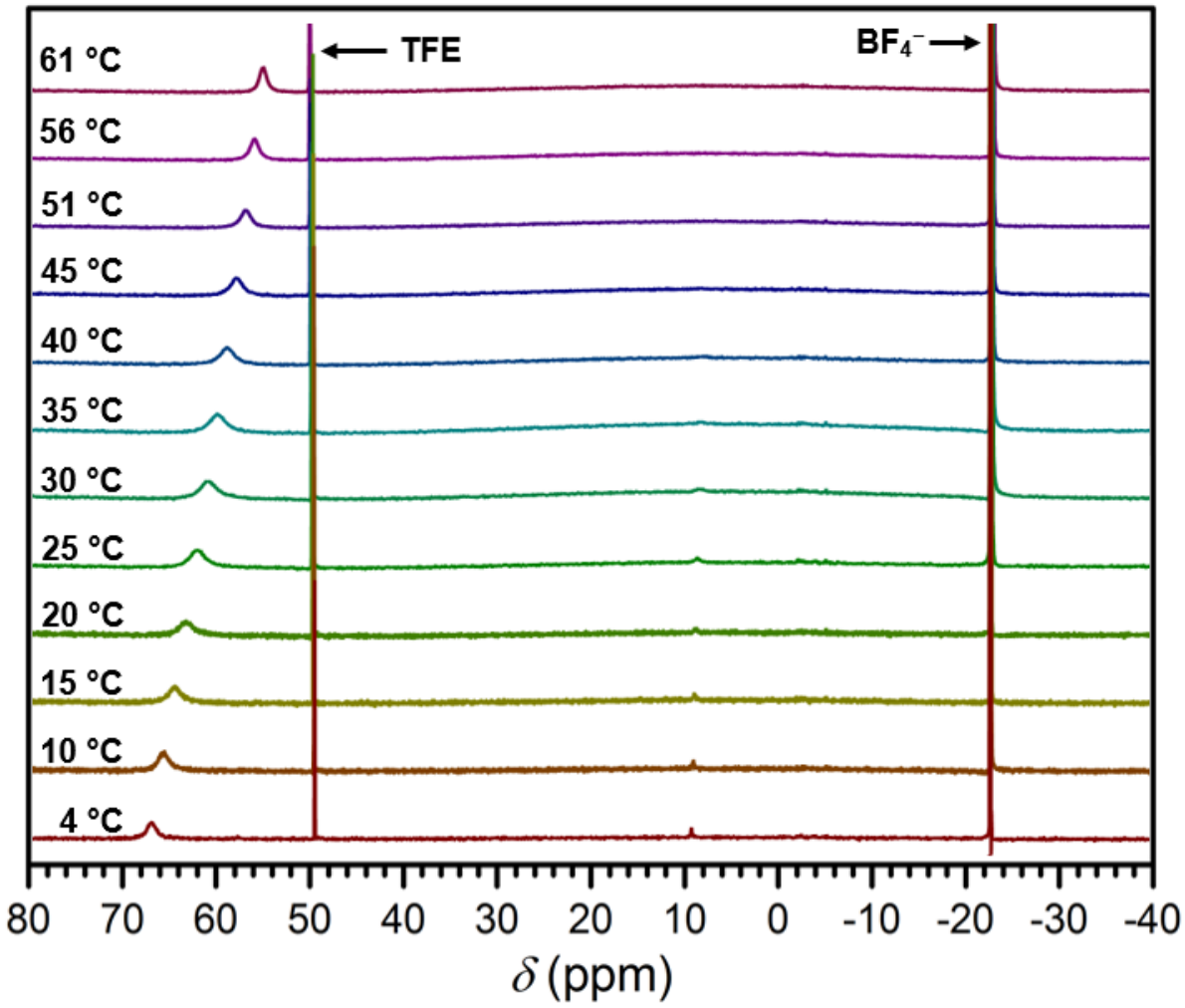

Figure 2.34 VT ^{19}F NMR spectra of **2a** (12.9 mM) in a H_2O solution containing 2.1 mM TFE at 4 to 61 °C referenced to its diamagnetic Zn^{II} analogue **2b** at 0 ppm.

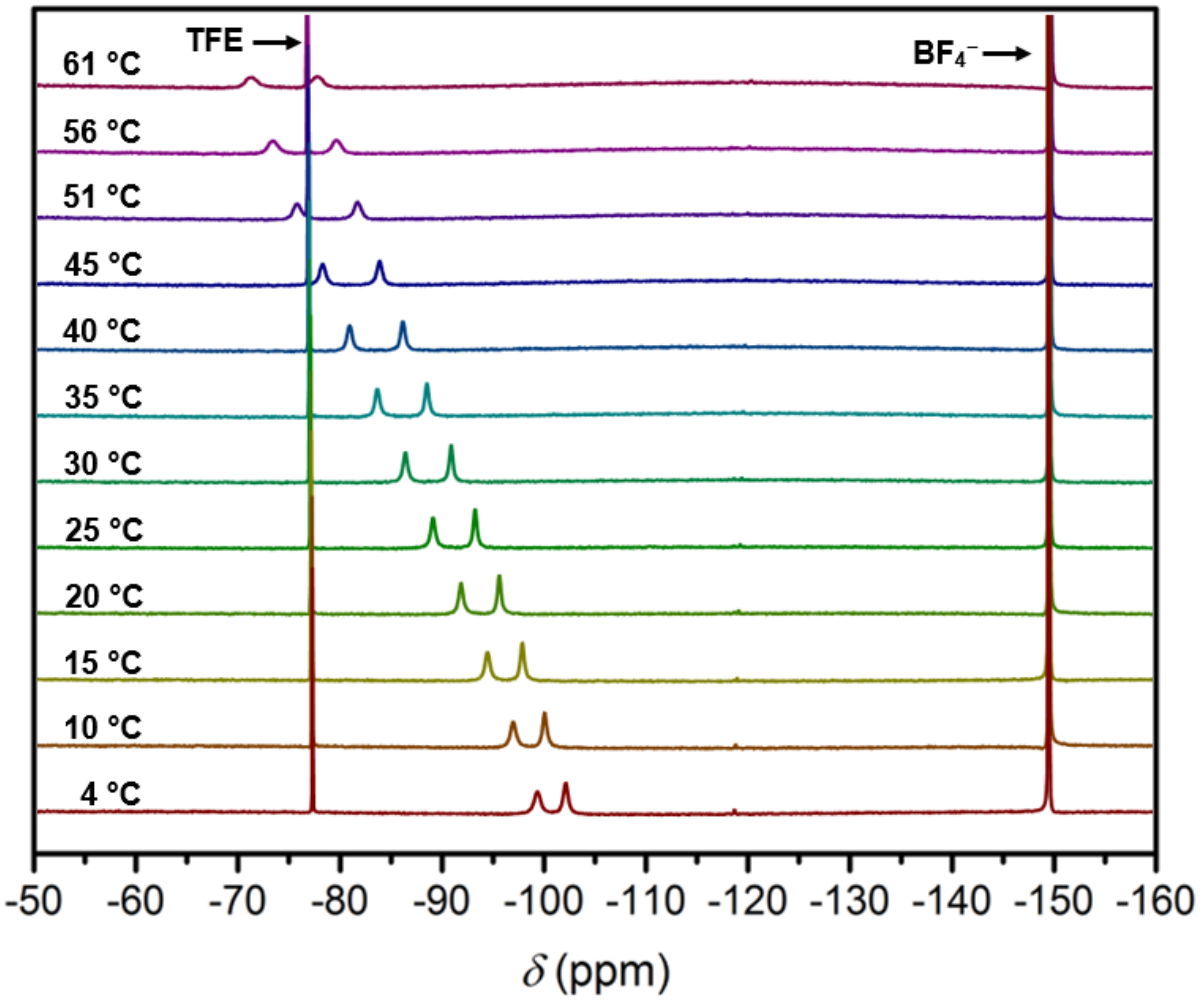

Figure 2.35 VT ^{19}F NMR spectra of **1a** (14.4 mM) in a H_2O solution containing 2.1 mM TFE at 4 to 61 °C.

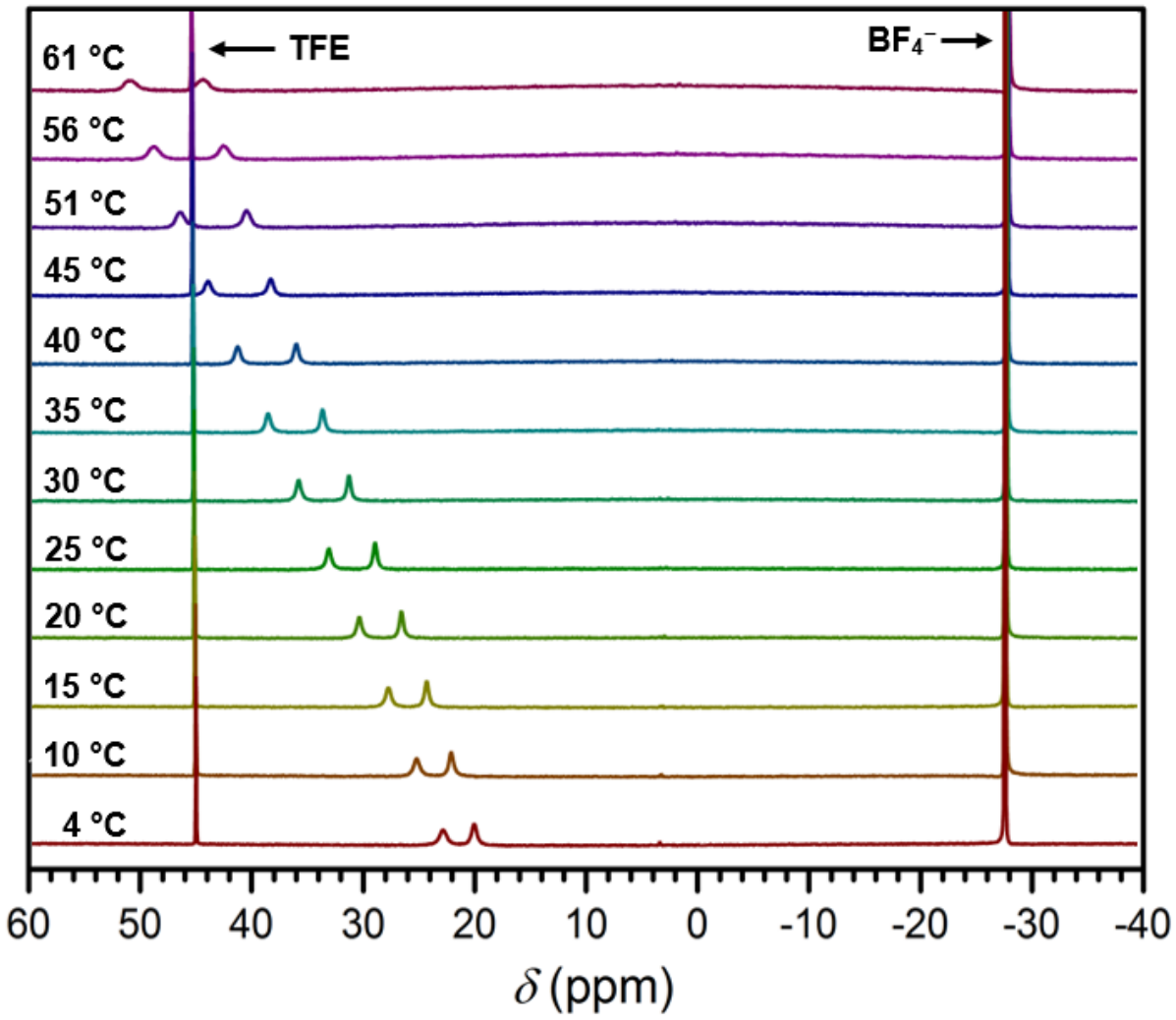

Figure 2.36 VT ^{19}F NMR spectra of **1a** (14.4 mM) in a H_2O solution containing 2.1 mM TFE at 4 to 61 °C referenced to its diamagnetic Zn^{II} analogue **1b** at 0 ppm.

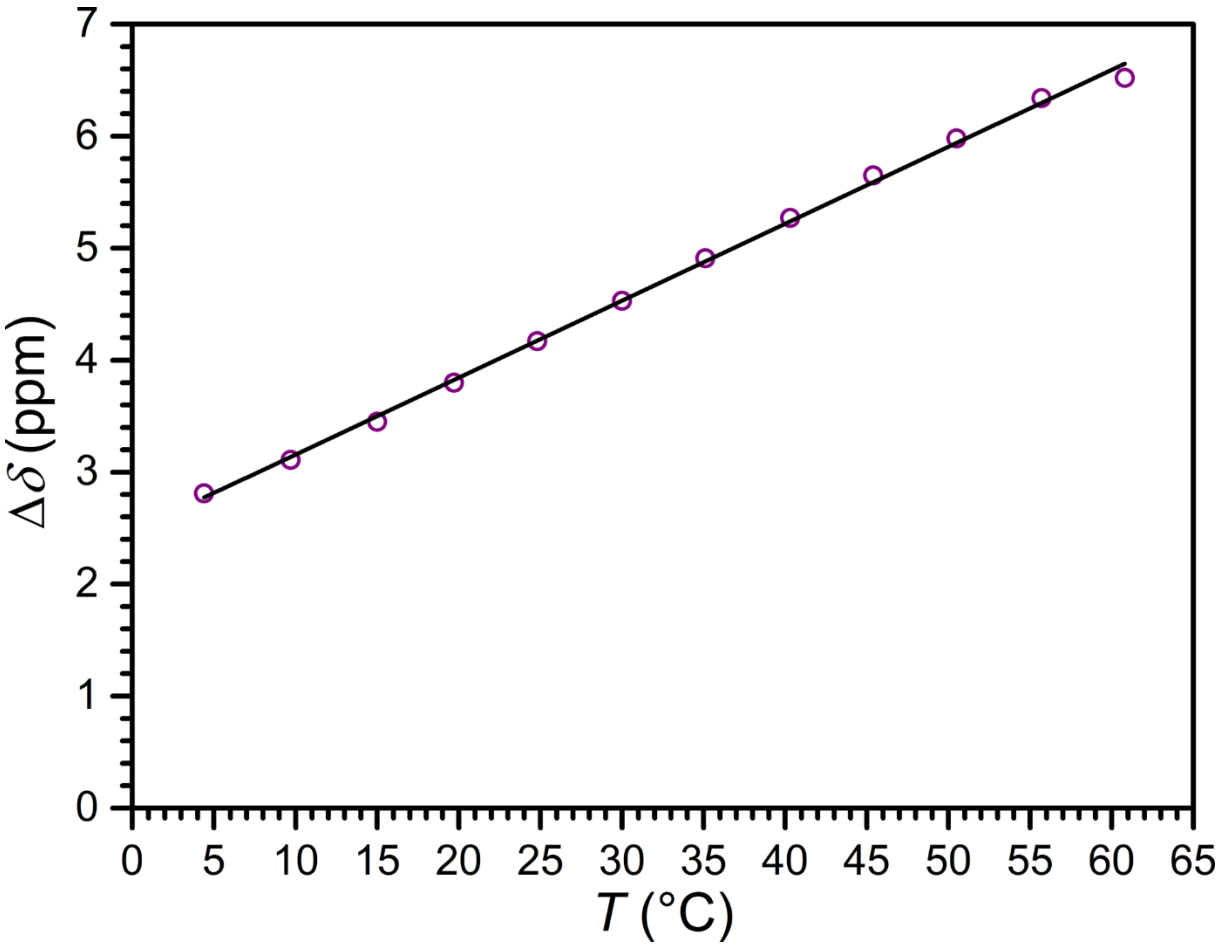

Figure 2.37 Plot of the ^{19}F NMR chemical shift separation between the two ^{19}F peaks of **1a** in a H_2O solution containing 2.1 mM TFE as a function of temperature. The black line corresponds to a linear fit to the data with the following equation: $\Delta\delta = 0.0687 \times T + 2.471$; $R^2 = 0.999$.

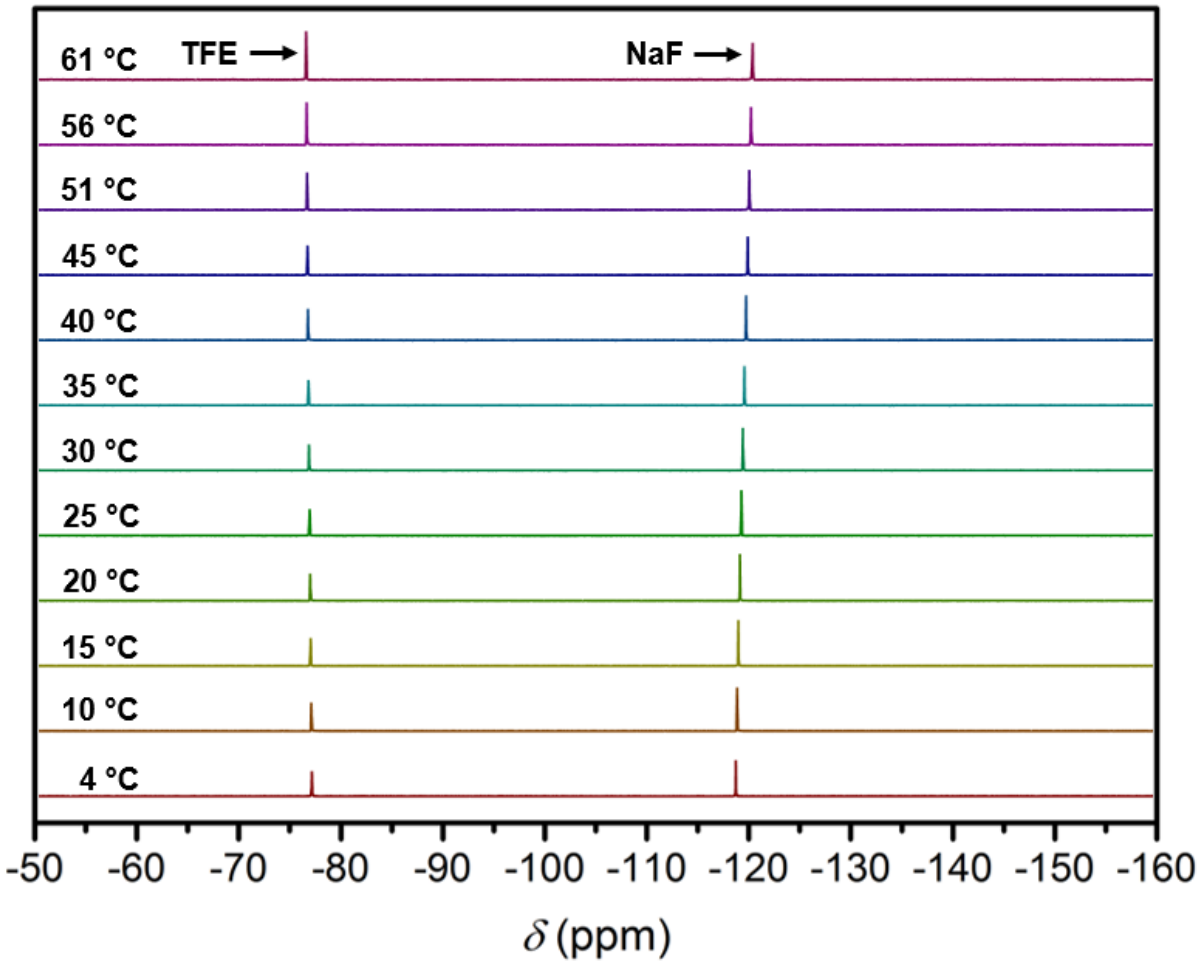

Figure 2.38 VT ^{19}F NMR spectra of a H_2O solution containing 1.1 mM TFE and 5.2 mM NaF at 4 to 61 °C. The chemical shift values are referenced to $CFCl_3$ after being adjusted to the chemical shift of TFE at each measured temperature, as illustrated in Figure 2.30 and Table 2.6.

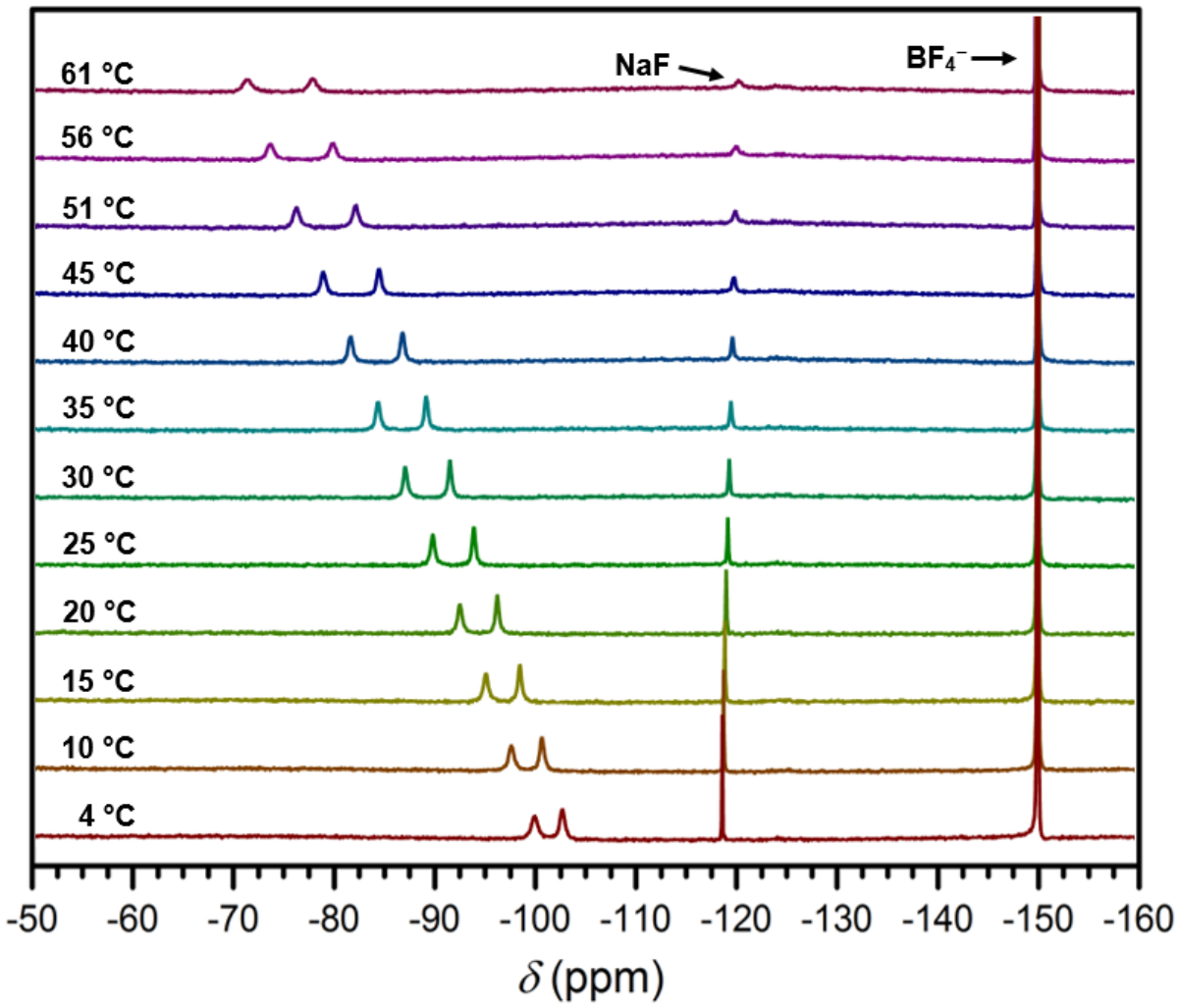

Figure 2.39 VT ^{19}F NMR spectra of **1a** (13.4 mM) in a FBS solution containing 2.1 mM NaF at 4 to 61 °C. The chemical shift of NaF was adjusted to the chemical shift of TFE at each measured temperature, as illustrated in Figure 2.30 and Table 2.6.

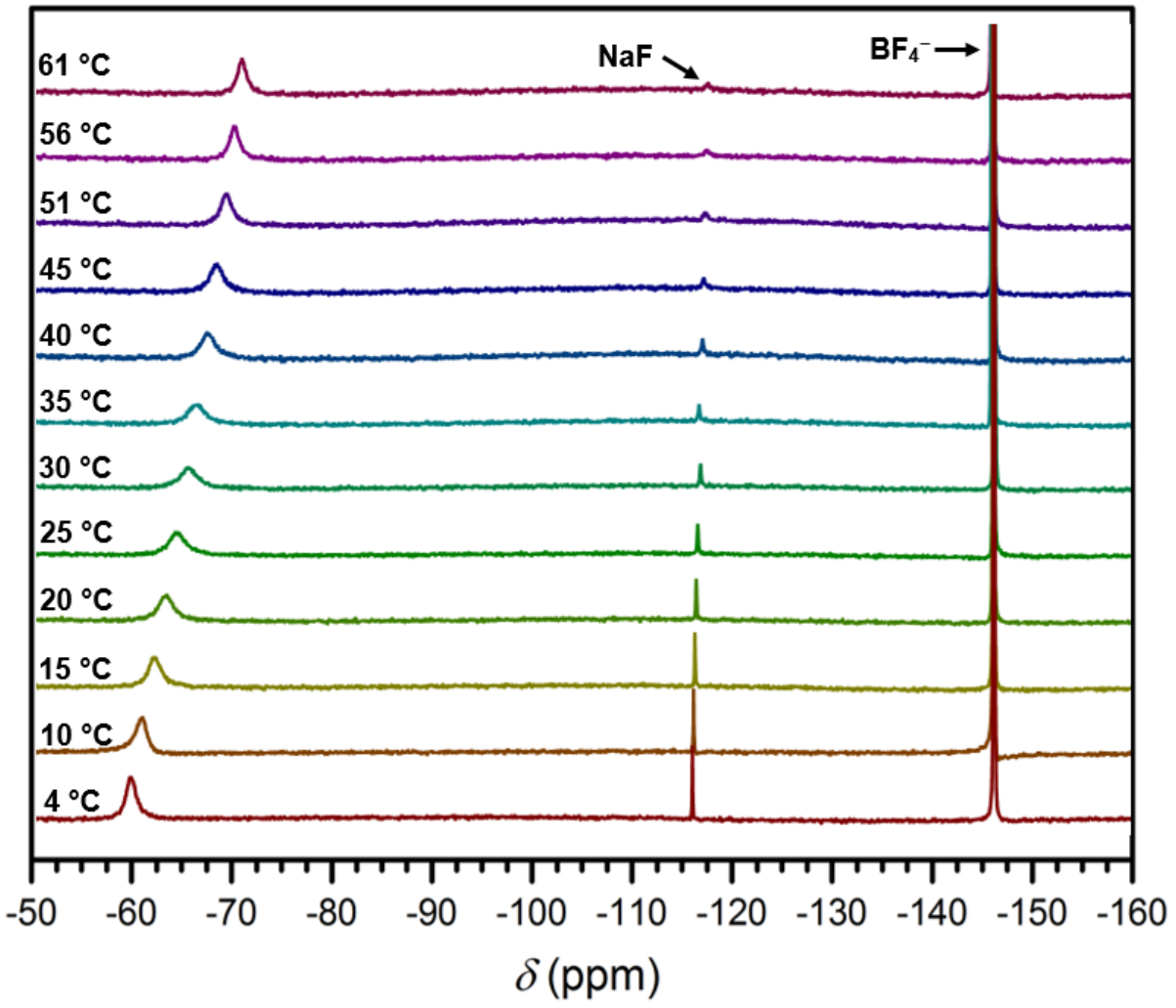

Figure 2.40 VT ^{19}F NMR spectra of **2a** (15.0 mM) in a FBS solution containing 2.1 mM NaF at 4 to 61 °C. The chemical shift of NaF was adjusted to the chemical shift of TFE at each measured temperature, as illustrated in Figure 2.30 and Table 2.6.

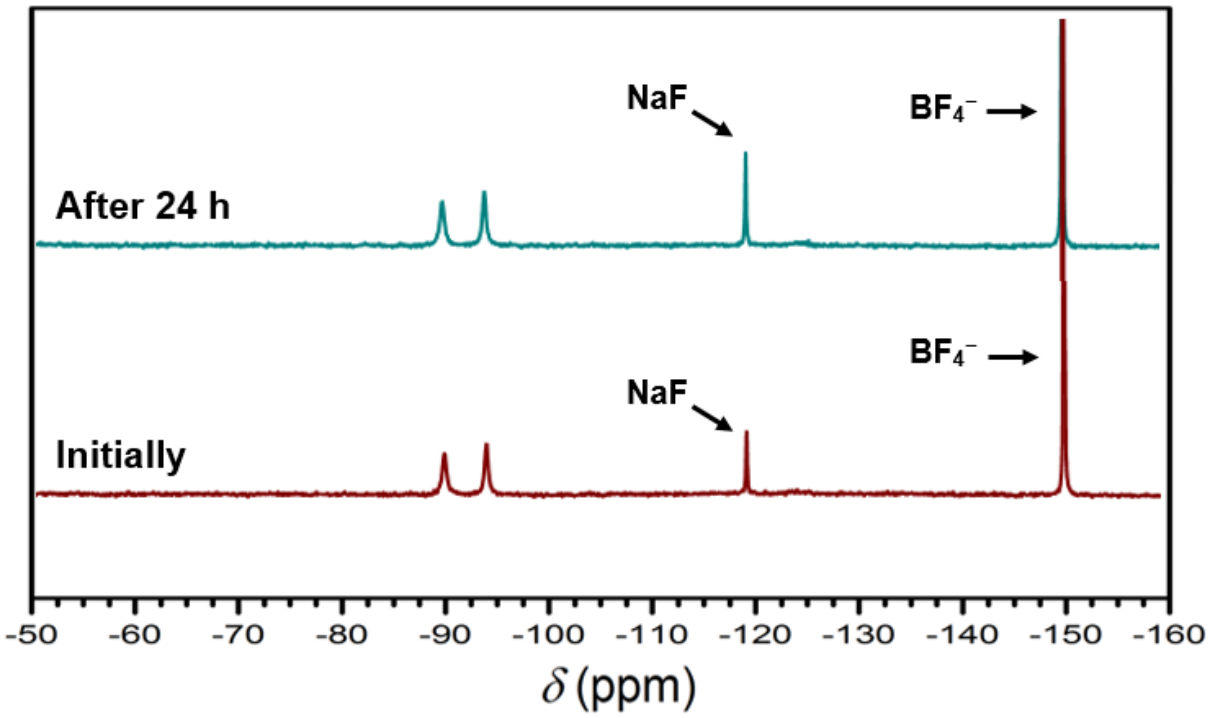

Figure 2.41 Comparison of ^{19}F NMR spectra of **1a** (13.4 mM) in a FBS solution containing 2.1 mM NaF recorded at 25 °C. The bottom spectrum corresponds to a ^{19}F NMR spectrum of a freshly prepared sample, and the top spectrum corresponds to a ^{19}F NMR spectrum of the same sample after standing open to air for 24 h at ambient temperature.

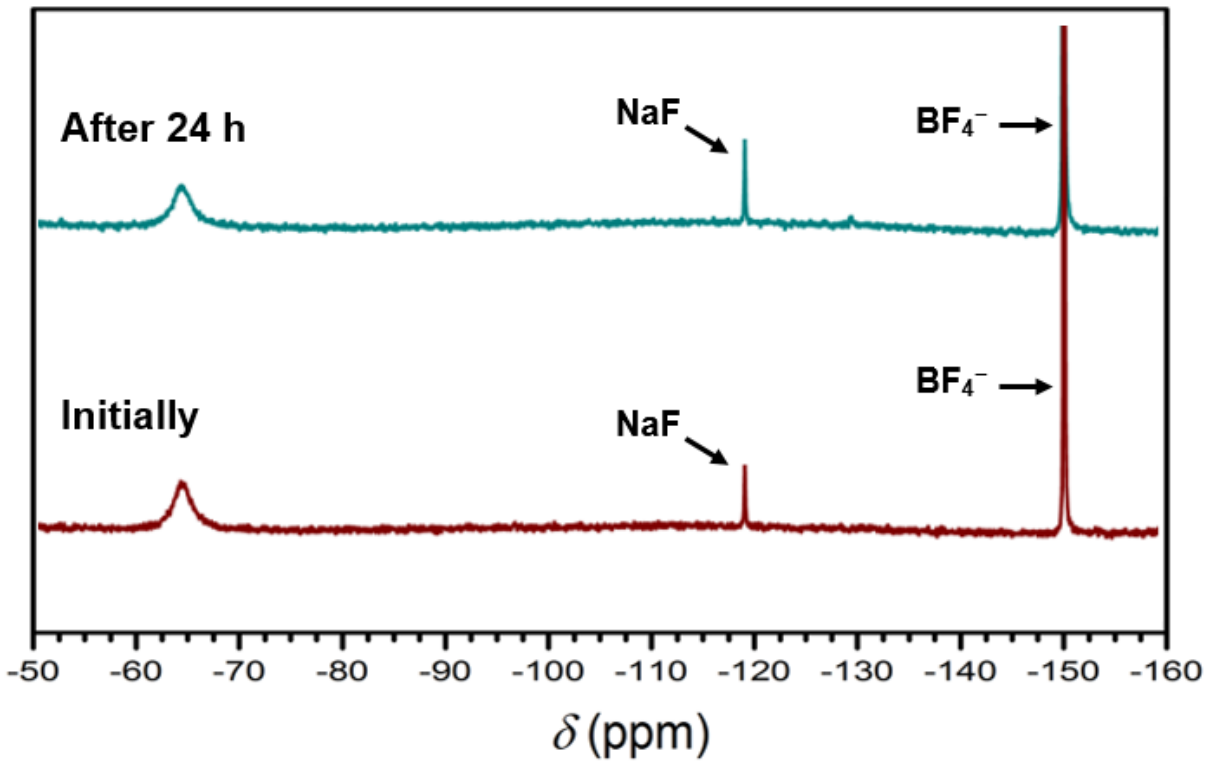

Figure 2.42 Comparison of ^{19}F NMR spectra of **2a** (15.0 mM) in a FBS solution containing 2.1 mM NaF recorded at 25 °C. The bottom spectrum corresponds to a ^{19}F NMR spectrum of a freshly prepared sample, and the top spectrum corresponds to a ^{19}F NMR spectrum of the same sample after standing open to air for 24 h at ambient temperature.

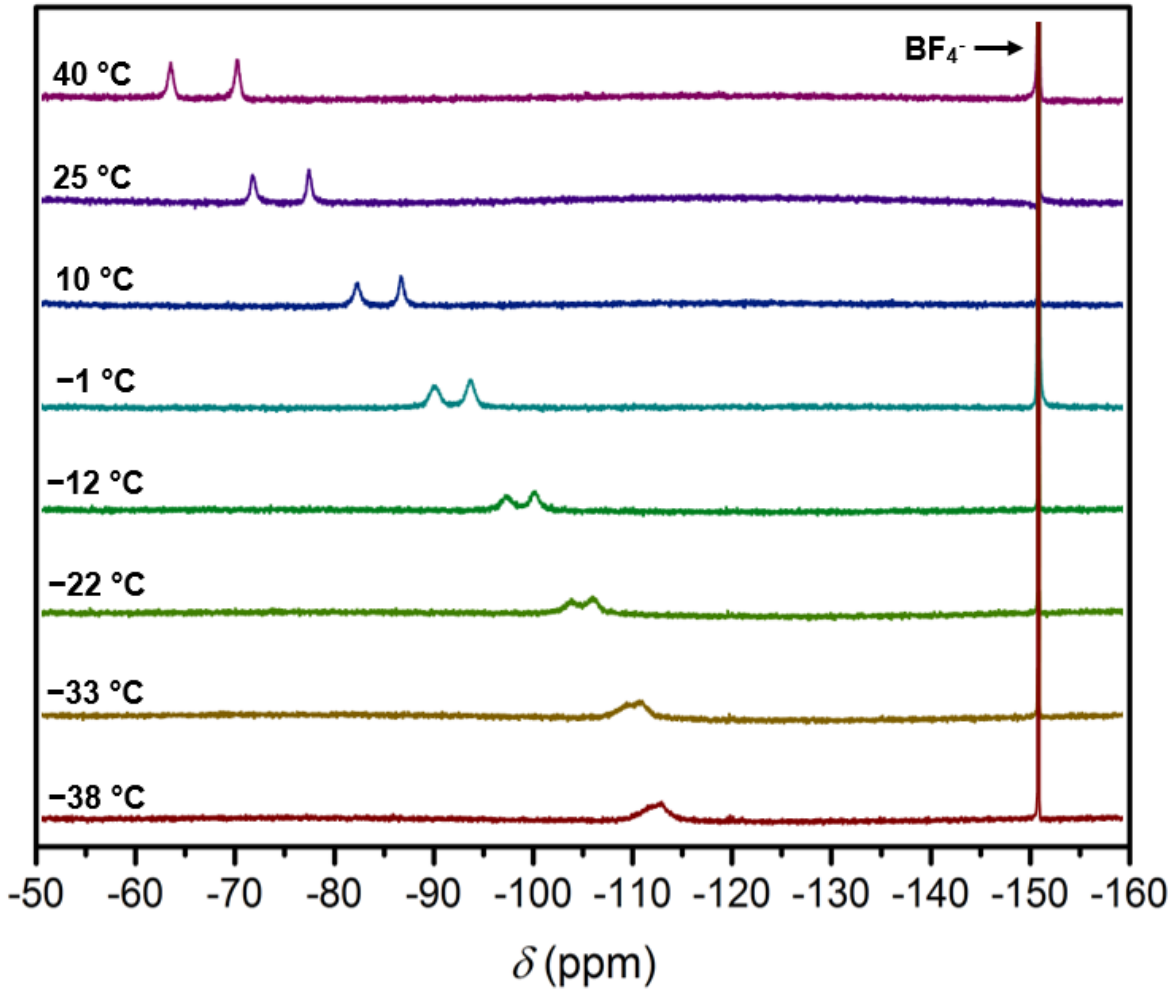

Figure 2.43 VT ^{19}F NMR spectra of **1a** in MeCN-d_3 at −38 to 40 °C.

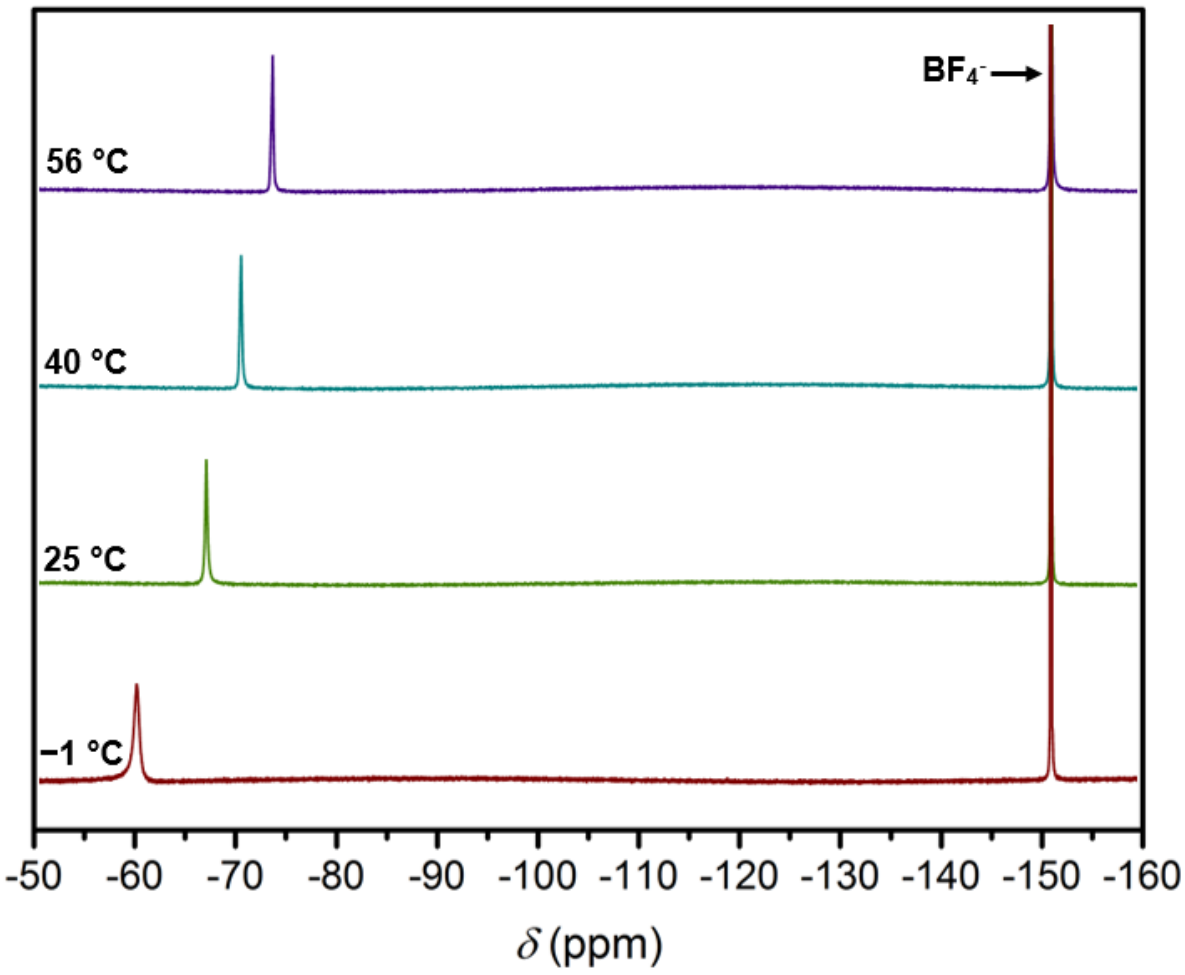

Figure 2.44 VT ^{19}F NMR spectra of **2a** in MeCN-d_3 at −1 to 56 °C.

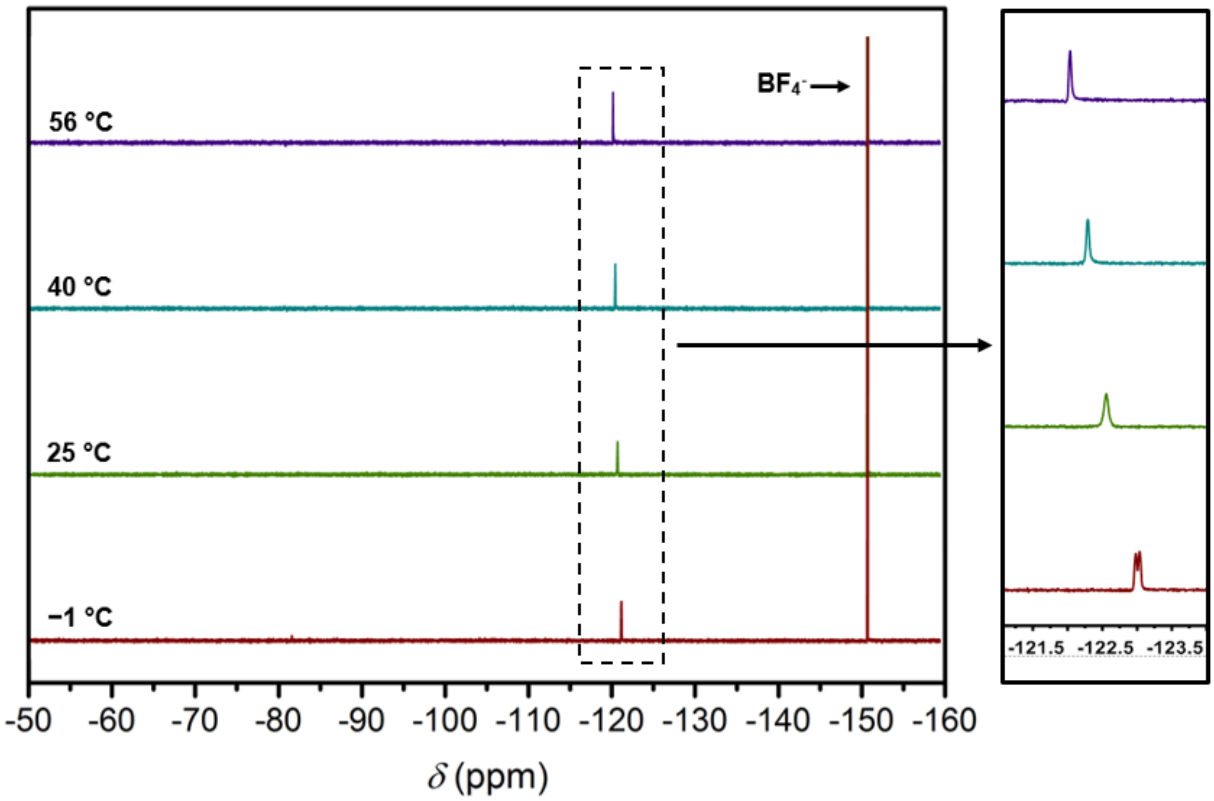

Figure 2.45 Left: VT ^{19}F NMR spectra of **1b** in MeCN-d_3 at −1 to 56 °C. Right: Expansion showing the ^{19}F NMR resonances of **1b**, demonstrating the two overlapping resonances observed at −1 °C and the coalescence of the two peaks upon warming.

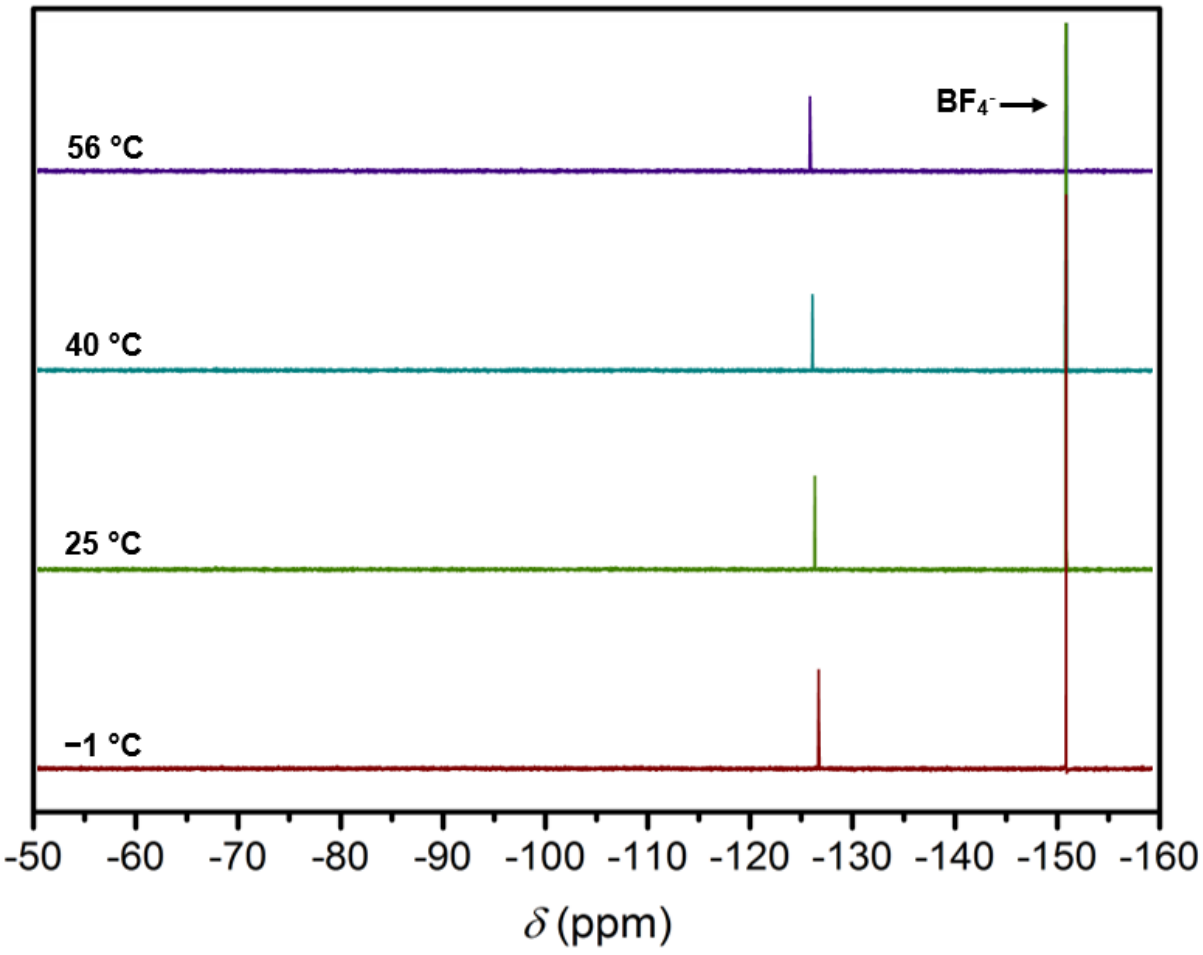

Figure 2.46 VT ^{19}F NMR spectra of **2b** in MeCN-d_3 at −1 to 56 °C.

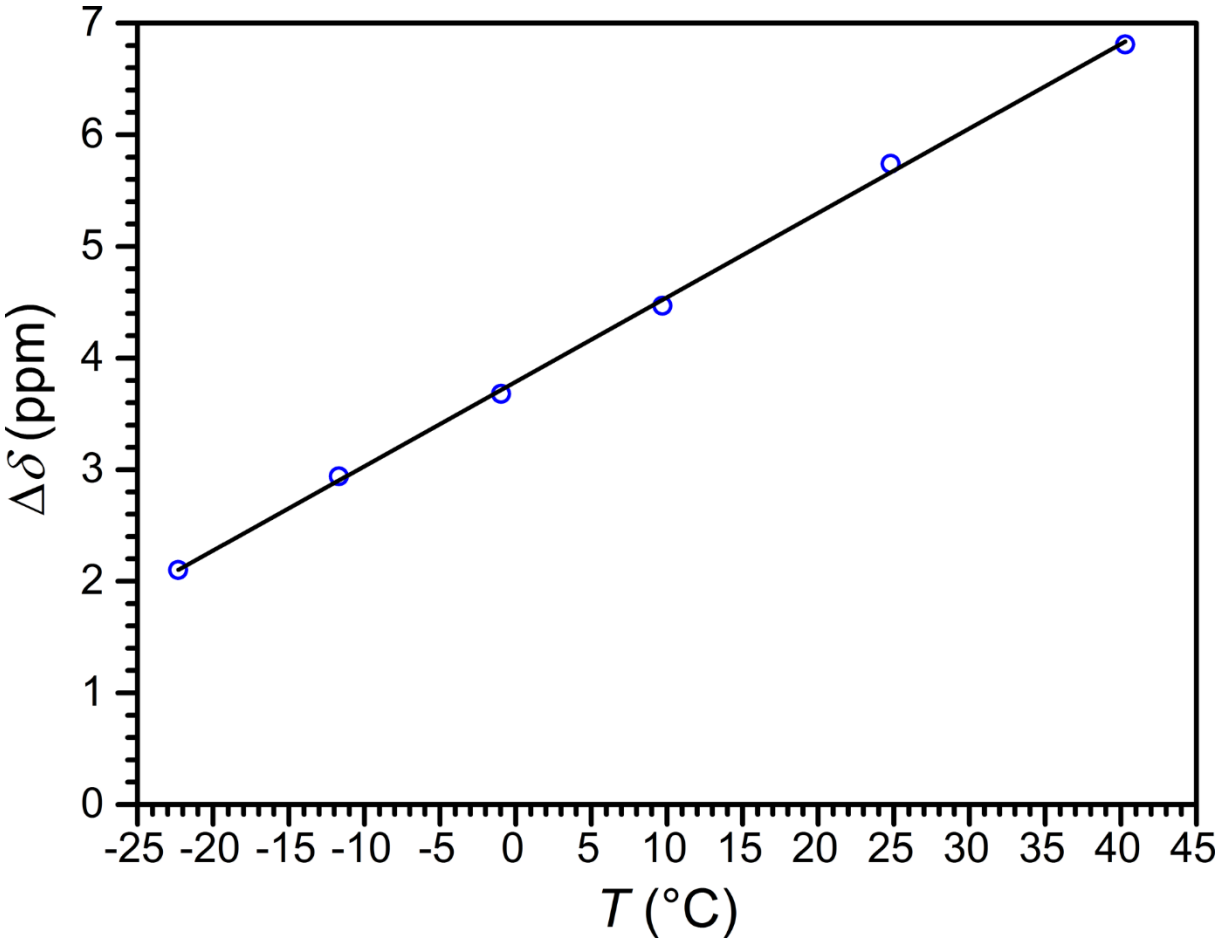

Figure 2.47 Plot of the ^{19}F NMR chemical shift separation between the two ^{19}F peaks of **1a** in MeCN-d_3 as a function of temperature. The black solid line corresponds to a linear fit to the data with the following equation: $\Delta\delta = 0.0756 \times T + 3.788$; $R^2 = 0.999$.

2.5.4 Supplementary Tables

Table 2.3 Crystallographic data for **1a**·0.5MeCN and **1b** at 100 K.

	1a·0.5MeCN	**1b**
Empirical formula	$C_{26}H_{31.5}B_2F_{10}FeN_{6.5}$	$C_{25}H_{30}B_2F_{10}N_6Zn$
Formula weight, g mol^{-1}	702.55	691.54
Crystal system	Triclinic	Monoclinic
Space group	$P\bar{1}$	*P*c
Wavelength, Å	0.71073	0.71073
Temperature, K	100	100
a, Å	11.4603(7)	13.6092(4)
b, Å	14.9231(8)	14.5112(4)
c, Å	18.6992(11)	14.1222(4)
α, °	110.254(3)	90
β, °	106.434(3)	90.875(1)
γ, °	91.133(3)	90
V, Å^3	2853.0(3)	2788.61(14)
Z	4	4
ρ_{calcd}, g cm^{-3}	1.636	1.647
μ, mm^{-1}	0.626	0.977
Reflections coll./unique	126647/16997	80246/16461
R(int)	0.0360	0.0355
R_1 $(I > 2\sigma(I))^a$	0.0448	0.0429
wR_2 $(all)^b$	0.1153	0.1088
GoF	1.059	1.025

^{a} $R_1 = \Sigma||F_0| - |F_C||/\Sigma|F_0|$, ^{b} $wR_2 = [\Sigma w(F_0^2 - F_C^2)^2/\Sigma w(F_0^2)^2]^{1/2}$.

Table 2.4 Crystallographic data for **2a** and **2b** at 100 K.

	2a	**2b**
Empirical formula	$C_{27}H_{33}B_2F_{11}FeN_6$	$C_{27}H_{33}B_2F_{11}N_6Zn$
Formula weight, g mol^{-1}	728.06	737.58
Crystal system	Cubic	Cubic
Space group	$F\bar{4}3c$	$F\bar{4}3c$
Wavelength, Å	0.71073	0.71073
Temperature, K	100	100
a, Å	29.3374(7)	29.2820(8)
b, Å	29.3374(7)	29.2820(8)
c, Å	29.3374(7)	29.2820(8)
α, °	90	90
β, °	90	90
γ, °	90	90
V, Å^3	25250.2(18)	25107(2)
Z	32	32
ρ_{calcd}, g cm^{-3}	1.532	1.561
μ, mm^{-1}	0.573	0.878
Reflections coll./unique	448528/5143	274422/4026
R(int)	0.0574	0.0396
R_1 $(I > 2\sigma(I))^a$	0.0486	0.0355
wR_2 $(all)^b$	0.1548	0.1030
GoF	1.049	1.073

^{a} $R_1 = \Sigma||F_0| - |F_C||/\Sigma|F_0|$, ^{b} $wR_2 = [\Sigma w(F_0^2 - F_C^2)^2/\Sigma w(F_0^2)^2]^{1/2}$.

Table 2.5 Crystallographic data for **3a** at 100 K.

	3a
Empirical formula	$C_{24}H_{27}B_2F_{11}FeN_6$
Formula weight, g mol^{-1}	685.98
Crystal system	Trigonal
Space group	*P*3
Wavelength, Å	0.71073
Temperature, K	100
a, Å	16.8376(5)
b, Å	16.8376(5)
c, Å	7.8829(3)
α, °	90
β, °	90
γ, °	120
V, Å^3	1935.43(14)
Z	3
ρ_{calcd}, g cm^{-3}	1.766
μ, mm^{-1}	0.694
Reflections coll./unique	115769/12595
R(int)	0.0390
R_1 *(I >2σ(I))*[a]	0.0365
wR_2 *(all)*[b]	0.0958
GoF	1.026

[a] $R_1 = \Sigma||F_0| - |F_C||/\Sigma|F_0|$, [b] $wR_2 = [\Sigma w(F_0^2 - F_C^2)^2/\Sigma w(F_0^2)^2]^{1/2}$.

Table 2.6 Chemical shifts of ^{19}F NMR resonances for the internal standards used in this study, TFE and NaF, in H_2O.[a]

T **(°C)**	**^{19}F NMR chemical shift (ppm)**	
	TFE	**NaF**
4	−76.98	−118.85
10	−76.92	−118.98
15	−76.86	−119.11
20	−76.81	−119.25
25	−76.76	−119.41
30	−76.70	−119.55
35	−76.65	−119.71
40	−76.60	−119.87
45	−76.56	−120.03
51	−76.51	−120.19
56	−76.46	−120.35
61	−76.42	−120.52

[a] Chemical shift values are referenced to $CFCl_3$.

Table 2.7 Chemical shifts and peak widths of ^{19}F NMR resonances for compounds **1a**, **1b**, **2a** and **2b**, in H_2O solutions containing 2.1 mM TFE as a function of temperature.

T **(°C)**	**1a**		**2a**	**1b**	**2b**
	^{19}F NMR chemical shift (ppm)				
4	−99.25	−102.06	−59.44	−122.33[a]	−126.77
10	−96.86	−99.97	−60.71	−122.32[a]	−126.76
15	−94.31	−97.76	−61.94	−122.32[a]	−126.76
20	−91.68	−95.48	−63.08	−122.32	−126.76
25	−88.91	−93.08	−64.39	−122.30	−126.77
30	−86.17	−90.70	−65.37	−122.28	−126.76
35	−83.39	−88.30	−66.49	−122.26	−126.77
40	−80.65	−85.92	−67.57	−122.25	−126.77
45	−77.97	−83.62	−68.61	−122.25	−126.77
51	−75.45	−81.43	−69.56	−122.23	−126.76
56	−73.02	−79.36	−70.47	−122.21	−126.75
61	−70.92	−77.44	−71.40	−122.20	−126.74
	Δ*δ* (ppm)				
	28.33	24.62	−11.96	0.13	0.03
	Temperature coefficient (CT) (ppm °C^{-1})[b]				
	0.52(1)	0.45(1)	−0.21(1)	0.002(1)	0.0002(1)
T **(°C)**	**Peak width in FWHM (Hz)**				
4	371	266	561	56	25
10	311	235	635	63	28
15	272	210	745	74	32
20	235	189	854	71	36
25	244	192	955	56	41
30	243	196	990	46	42
35	264	214	960	39	42
40	282	243	868	33	38
45	332	298	761	30	30
51	444	365	614	28	27
56	553	501	510	25	28
61	655	634	421	25	26
T **(°C)**	**|CT|/FWHM (°C^{-1})[c]**				
40	0.87	0.87	0.11	0.03	0.002

[a] Value based on the center of the two overlapping peaks. [b] CT values are given by the slopes of the linear fits to the data of δ vs T plots. [c] Calculated for FWHM (ppm) measured at 40 °C.

Table 2.8 Chemical shifts of ^{19}F NMR resonances for Fe^{II} compounds **1a** and **2a** in H_2O solutions containing 2.1 mM TFE as a function of temperature, referenced to their corresponding Zn^{II} analogues **1b** and **2b**.

T **(°C)**	**1a**		**2a**
	^{19}F NMR hyperfine shift (ppm)		
4	23.08	20.27	67.33
10	25.46	22.35	66.05
15	28.01	24.56	64.82
20	30.64	26.84	63.68
25	33.39	29.22	62.38
30	36.11	31.58	61.39
35	38.87	33.96	60.28
40	41.60	36.33	59.20
45	44.28	38.63	58.16
51	46.78	40.80	57.20
56	49.19	42.85	56.28
61	51.28	44.76	55.34

Table 2.9 Chemical shifts and peak widths of ^{19}F NMR resonances of Fe^{II} compounds **1a** and **2a**, in FBS solutions containing 2.1 mM NaF as a function of temperature.

T **(°C)**	**1a**		**2a**
	^{19}F NMR chemical shift (ppm)		
4	−100.03	−102.82	−59.72
10	−97.70	−100.77	−60.82
15	−95.16	−98.57	−62.20
20	−92.55	−96.30	−63.43
25	−89.84	−93.94	−64.43
30	−87.08	−91.56	−65.72
35	−84.35	−89.18	−66.63
40	−81.59	−86.80	−67.79
45	−78.85	−84.45	−68.74
51	−76.17	−82.10	−69.79
56	−73.56	−79.81	−70.56
61	−71.23	−77.74	−71.40
	Δδ (ppm)		
	28.80	25.08	−11.68
	Temperature coefficient (CT) (ppm °C^{-1})[b]		
	0.52(1)	0.45(1)	−0.21(1)
T **(°C)**	**Peak width in FWHM (Hz)**		
4	362	281	582
10	314	241	675
15	275	200	767
20	261	185	869
25	234	182	972
30	228	188	957
35	244	207	1055
40	251	241	872
45	272	254	760
51	342	311	691
56	394	379	588
61	515	467	510
T **(°C)**	**|CT|/FWHM (°C^{-1})**[c]		
40	0.97	0.88	0.11

[a] CT values are given by the slopes of the linear fits to the data of δ vs T plots. [b] Calculated for FWHM (ppm) measured at 40 °C.

Table 2.10 Chemical shifts of ^{19}F NMR resonances for Fe^{II} compounds **1a** and **2a** in FBS solutions containing NaF as a function of temperature, referenced to their corresponding Zn^{II} analogues **1b** and **2b**.

T **(°C)**	**1a**		**2a**
	^{19}F NMR hyperfine shift (ppm)		
4	22.30	19.51	67.05
10	24.62	21.55	65.94
15	27.16	23.75	64.56
20	29.77	26.02	63.33
25	32.46	28.36	62.34
30	35.20	30.72	61.04
35	37.91	33.08	60.14
40	40.66	35.45	58.98
45	43.40	37.80	58.03
51	46.06	40.13	56.97
56	48.65	42.40	56.19
61	50.97	44.46	55.34

Table 2.11 Chemical shifts and peak widths of ^{19}F NMR resonances for compounds **1a**, **1b**, **2a** and **2b**, in MeCN-d_3 as a function of temperature.

T **(°C)**	**1a**		**2a**	**1b**	**2b**
	^{19}F NMR chemical shift (ppm)				
−38	−112.3[a]		—	—	—
−33	−110.1[a]		—	—	—
−22	−103.80	−105.90	—	—	−103.80
−12	−97.09	−100.03	—	—	−97.09
−1	−89.78	−93.46	−60.06	−123.01[b]	−89.78
10	−81.93	−86.40	—	—	−81.93
25	−71.28	−77.02	−67.02	−122.55	−71.28
40	−62.87	−69.68	−70.48	−122.29	−62.87
56	—	—	−73.63	−122.04	—
	Δ*δ* (ppm)				
	40.93[c]	36.22[c]	−13.57[d]	0.97[d]	0.86[d]
	Temperature coefficient (CT) (ppm °C^{-1})[b]				
	0.67(2)[c]	0.59(2)[c]	−0.24(2)[d]	0.017(1)[d]	0.015(1)[d]
T **(°C)**	**Peak width in FWHM (Hz)**				
−1	624	504	293	38	10
10	381	296	N/A	N/A	N/A
25	302	246	116	32	17
40	287	270	105	21	20
56	N/A	N/A	150	18	15
T **(°C)**	**|CT|/FWHM (°C^{-1})[c]**				
40	1.10	1.03	1.07	0.38	0.35

[a] Estimated ^{19}F chemical shift because of broad and overlapping resonances, based on the center of the peak. [b] Value based on the center of the two overlapping peaks. [c] The temperature range from −22 °C to 40 °C was used for calculations. [d] The temperature range from −1 °C to 56 °C was used for calculations. [e] CT values are given by the slopes of the linear fits to the data of δ vs T plots. [f] Calculated for FWHM (ppm) measured at 40 °C.

Chapter 3: Ratiometric pH Imaging with a Co^{II}_2 MRI Probe via CEST Effects of Opposing pH Dependences

Reprinted with permission from:

Thorarinsdottir, A. E.; Du, K.; Collins, J. H. P.; Harris, T. D. *Journal of the American Chemical Society* **2017**, *139*, 15836–15847.

This work was performed in collaboration with the co-authors listed above.

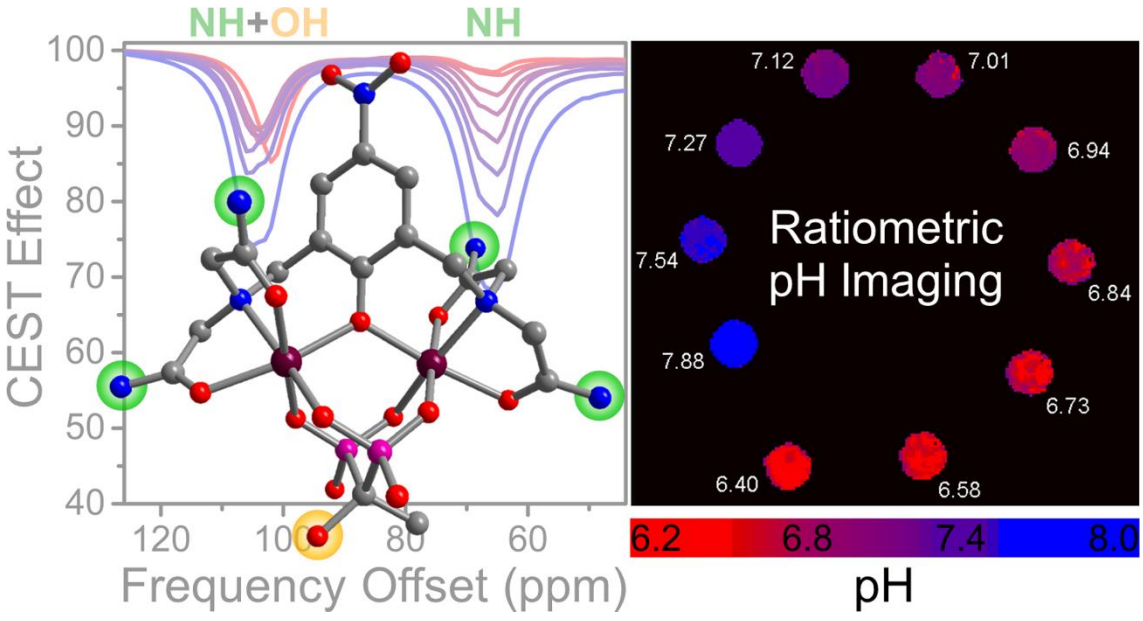

3.1 Introduction

Acidic extracellular pH features prominently in a number of pathological conditions, including cancer,[1] ischemia,[1f,2] inflammation,[1h,2c] and infection.[1h] As such, the ability to measure and spatially map tissue pH would provide valuable information regarding the role of acidosis in both the initiation and the progression of diseases.[1–3] Toward this end, magnetic resonance imaging (MRI) represents an ideal non-invasive modality for probing pH, owing to its ability to deeply penetrate tissue and generate images with high spatiotemporal resolution.[4] Indeed, a number of MR techniques have been developed to measure pH in vivo, and these methods commonly rely on the presence of pH-sensitive exogenous molecular probes. Among these probes, complexes that exhibit the paramagnetic chemical exchange saturation transfer (PARACEST) effect, where exchange of protons on a paramagnetic molecule with those of bulk H_2O upon selective irradiation is exploited to generate contrast,[5] are particularly well suited, due to large hyperfine shifts of their labile protons and the inherent pH sensitivity of their exchange rates.[6]

The intrinsic concentration dependence of the CEST effect intensity requires that the concentration of a PARACEST probe in the imaged region must be known. A number of strategies have been reported to overcome this limitation, including the development of probes with pH-dependent changes in the frequency[7] or linewidth[8] of the CEST peak or in the ratio of CEST intensities from two presaturation frequencies.[7a,c,9] Moreover, the ability of these probes to map extracellular pH in biological environments has been demonstrated.[7c,8,9c,e,g,h]

Despite these promising advances, the development of a single probe that features CEST peaks shifted outside the tissue magnetization transfer window,[10] is highly responsive in the physiological pH range, and displays good stability under physiological conditions remains elusive. Toward this

end, transition metal-based PARACEST probes[7d,9f,11] offer potential advantages over their more common lanthanide counterparts. Specifically, the chemical shifts of transition metal complexes are primarily governed by through-bond interactions rather than the dominant through-space interactions of lanthanide complexes, which renders exchangeable protons extremely sensitive to the metal coordination environment and thus amenable to the design of responsive probes.[12]

In conjunction with the employment of transition metal ions, one can envision incorporation of two distinct ligand scaffolds on a single complex, where the two ligands exhibit CEST effects with opposing pH dependences. For such a system, the ratio of the two CEST peak intensities should change dramatically as a function of pH. Along these lines, we recently reported Fe_2, Cu_2, and CuGa complexes supported by a modular dinucleating tetra(carboxamide) ligand and bisphosphonate ancillary ligands.[11l,m] Among these ancillary ligands, etidronate notably features a pendent hydroxyl group that can potentially give rise to CEST. Indeed, the presence of both base-catalyzed exchange of carboxamide protons and acid-catalyzed proton exchange of etidronate highlights the potential of these dinuclear complexes to exhibit pronounced pH sensitivity. Accordingly, we herein report a Co^{II}_2 complex that displays CEST spectra featuring highly pH-sensitive and shifted peaks, by virtue of CEST-active carboxamide and hydroxyl groups with opposing pH dependences. The complex exhibits excellent chemical stability and retains its CEST activity in fetal bovine serum, which underscores the potential suitability of this and related complexes for pH quantitation in living systems.

3.2 Experimental Section

General Considerations. Unless otherwise specified, the manipulations described below were carried out at ambient atmosphere and temperature. Air- and water-free manipulations were

performed under a dinitrogen atmosphere in a Vacuum Atmospheres Nexus II glovebox or using standard Schlenk line techniques. Glassware was oven-dried at 150 °C for at least 4 h and allowed to cool in an evacuated antechamber prior to use in the glovebox. Acetonitrile (MeCN), diethyl ether (Et_2O), *N*,*N*-diisopropylethylamine (DIPEA), and methanol (MeOH) were dried using a commercial solvent purification system from Pure Process Technology and stored over 3 or 4 Å molecular sieves prior to use. The solvent H_2O was obtained from a purification system from EMD Millipore. Deuterated solvents were purchased from Cambridge Isotope Laboratories and Sigma Aldrich. The synthesis of 2,2′-iminobis(acetamide) was carried out according to a previously reported procedure.[11l] Anhydrous hydrogen chloride gas was generated by adding concentrated hydrochloric acid to a stirring solution of concentrated sulfuric acid. The gas was passed through a bubbler filled with concentrated sulfuric acid. All other reagents and solvents were purchased from commercial vendors and used without further purification. Experimental details on the synthesis of ligands and organic precursors are provided in Section 3.5.1.

*Synthesis of Na[LCo₂(etidronate)]·0.2NaNO₃·2.7H₂O (**1**).* A pink solution of $Co(NO_3)_2 \cdot 6H_2O$ (71 mg, 0.24 mmol) in MeOH (2 mL) was added dropwise to a stirring yellow suspension of HL (52 mg, 0.12 mmol) in MeOH (3 mL) to give a dark orange solution. To this solution, a colorless solution of etidronic acid monohydrate (27 mg, 0.12 mmol) in MeOH (2 mL) was added dropwise to give a light orange solution. Subsequent addition of sodium methoxide (33 mg, 0.61 mmol) in MeOH (2 mL) resulted in the formation of a light orange slurry. After stirring at 25 °C for 3 h, the orange solid was collected by vacuum filtration, washed with MeOH (5 mL) and Et_2O (15 mL), and dried under reduced pressure for 16 h to give **1** (44 mg, 44%) as an orange solid. Anal. Calcd.

for $C_{18}H_{31.4}Co_2N_{7.2}Na_{1.2}O_{17.3}P_2$: C, 25.96; H, 3.80; N, 12.11%. Found: C, 25.96; H, 3.83; N, 12.16%. ICP-OES: Co:P = 1.02:1.00. UV-Vis absorption spectrum (64 μM; 50 mM 4-(2-hydroxyethyl)-1-piperazineethanesulfonic acid (HEPES) buffered at pH 7.4, 25 °C): 375 nm (ε = 13800 M^{-1} cm^{-1}). ESI-MS (*m*/*z*): Calcd. for $C_{18}H_{26}Co_2N_7O_{14}P_2$ ($[LCo_2(etidronate)]^-$): 743.97, found: 743.95; calcd. for $C_{18}H_{28}Co_2N_7O_{14}P_2$ ($[LCo_2(etidronate)+2H]^+$): 745.98, found 745.92. FT-IR (ATR, cm^{-1}): 3341 (m, broad); 3178 (m, broad); 2930 (w); 1665 (s); 1595 (m); 1499 (w); 1446 (m); 1307 (s); 1097 (s); 1060 (s); 911 (m); 826 (w); 799 (m); 751 (w); 706 (m); 539 (s); 470 (s). Slow diffusion of MeCN vapor into a concentrated solution of **1** in H_2O afforded dark orange plate-shaped crystals of $Na[LCo_2(etidronate)]\cdot 6.8H_2O$ (**1′**) suitable for single-crystal X-ray diffraction analysis.

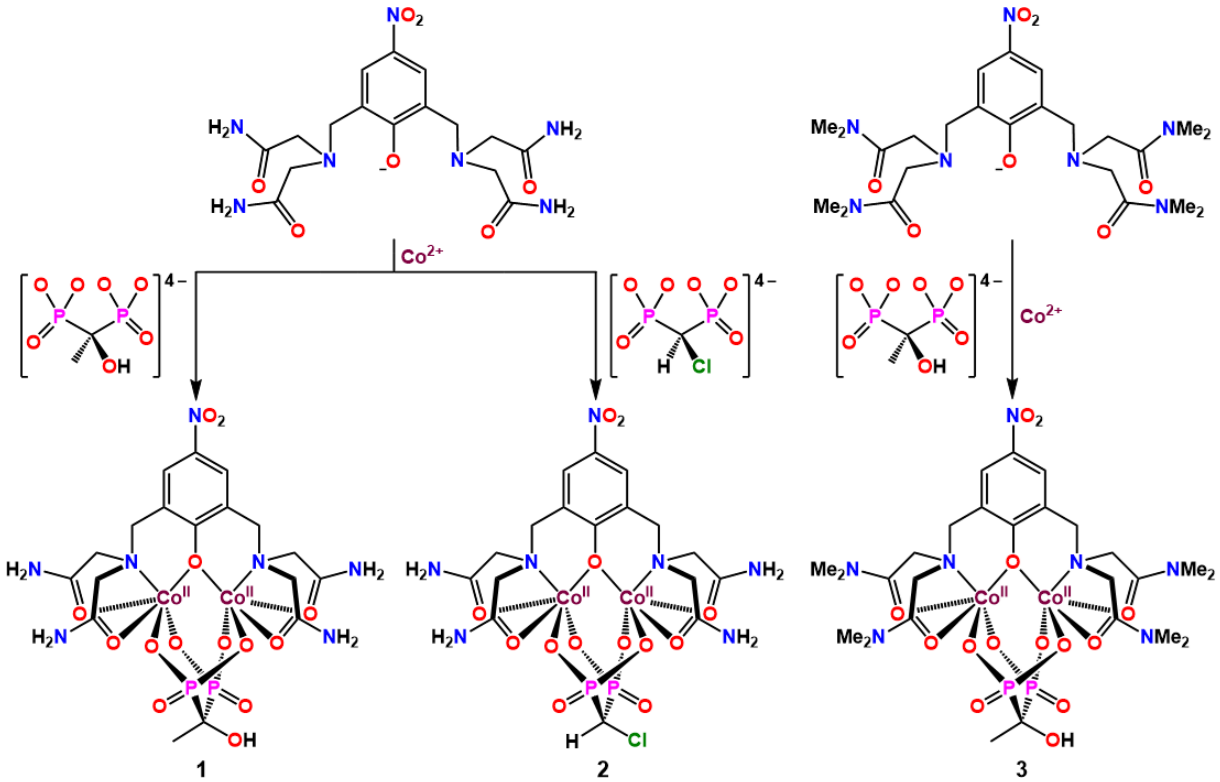

Figure 3.1 Reaction of L^-, Co^{2+}, and etidronate (left) or $CMDP^{4-}$ (center) to form $[LCo_2(etidronate)]^-$ or $[LCo_2(CMDP)]^-$, as observed in **1** and **2**, respectively. Reaction of L'^-, Co^{2+}, and etidronate to form $[L'Co_2(etidronate)]^-$, as observed in **3** (right).

*Synthesis of Na[LCo$_2$(CMDP)]·4.5H$_2$O·MeOH (**2**)*. A pink solution of Co(NO$_3$)$_2$·6H$_2$O (67 mg, 0.23 mmol) in MeOH (2 mL) was added dropwise to a stirring yellow suspension of HL (49 mg, 0.11 mmol) in MeOH (3 mL) to give a dark orange solution. A colorless solution of chloromethanediphosphonic acid (H$_4$CMDP) (27 mg, 0.13 mmol) in MeOH (2 mL) was then slowly added, resulting in a light orange solution. Subsequently, a colorless solution of Na(OMe) (31 mg, 0.58 mmol) in MeOH (2 mL) was added dropwise to give a light orange suspension. The reaction mixture was stirred at 25 °C for 2.5 h, and then the orange solid was collected by vacuum filtration, washed with MeOH (10 mL) and Et$_2$O (15 mL), and dried under reduced pressure for 19 h to give **2** (46 mg, 45%) as an orange solid. Anal. Calcd. for $C_{18}H_{36}ClCo_2N_7NaO_{18.5}P_2$: C, 24.43; H, 4.10; N, 11.08%. Found: C, 24.49; H, 3.65; N, 10.74%. ICP-OES: Co:P = 1.02:1.00. UV-Vis absorption spectrum (80 μM; 50 mM HEPES buffered at pH 7.4, 25 °C): 375 nm (ε = 14100 M^{-1} cm^{-1}). ESI-MS (*m*/*z*): Calcd. for $C_{17}H_{23}ClCo_2N_7O_{13}P_2$ ([LCo$_2$(CMDP)]$^-$): 747.92, found 747.93; calcd. for $C_{17}H_{25}ClCo_2N_7O_{13}P_2$ ([LCo$_2$(CMDP)+2H]$^+$): 749.93, found 749.89. FT-IR (ATR, cm^{-1}): 3339 (w, broad); 3173 (w, broad); 1663 (s); 1596 (m); 1500 (w); 1447 (m); 1311 (s); 1133 (s); 1097 (s); 911 (m); 878 (w); 799 (w); 752 (m); 688 (m); 662 (m); 529 (s); 475 (s). Slow diffusion of MeCN vapor into a concentrated solution of **2** in H$_2$O gave dark orange block-shaped crystals of Na[LCo$_2$(CMDP)]·8.2H$_2$O (**2′**) suitable for single-crystal X-ray diffraction analysis.

*Synthesis of Na[L'Co$_2$(etidronate)]·1.2NaNO$_3$·1.9H$_2$O (**3**)*. A pink solution of Co(NO$_3$)$_2$·6H$_2$O (54 mg, 0.19 mmol) in MeOH (2 mL) was added dropwise to a stirring yellow solution of HL′ (50 mg, 0.093 mmol) in MeOH (2 mL) to give an orange solution. After stirring at 25 °C for 5 min, a colorless solution of etidronic acid monohydrate (21 mg, 0.093 mmol) in MeOH (2 mL) was added

dropwise, followed by addition of sodium methoxide (25 mg, 0.46 mmol) in MeOH (2 mL). The resulting orange solution was stirred at 25 °C for 2 h, collected by vacuum filtration, and dried under reduced pressure. The resulting red-orange residue was stirred in MeCN (10 mL) for 15 min and a small amount of white solid was removed by vacuum filtration. The filtrate was dried under reduced pressure, and the ensuing solid was further dried for 16 h to give **3** (92 mg, 97%) as a red-orange solid. Anal. Calcd. for $C_{26}H_{45.8}Co_2N_{8.2}Na_{2.2}O_{19.5}P_2$: C, 30.74; H, 4.55; N, 11.31%. Found: C, 30.88; H, 4.40; N, 11.52%. ICP-OES: Co:P = 1.01:1.00. UV-Vis absorption spectrum (87 μM; 50 mM HEPES buffered at pH 7.4, 25 °C): 379 nm (ε = 12300 M^{-1} cm^{-1}). ESI-MS (*m*/*z*): Calcd. for $C_{26}H_{44}Co_2N_7O_{14}P_2$ ($[L'Co_2(etidronate)+2H]^+$): 858.11, found 858.11. FT-IR (ATR, cm^{-1}): 3300 (w, broad); 2930 (w); 1612 (s); 1502 (w); 1408 (w); 1297 (s); 1169 (m); 1124 (m); 1061 (s); 896 (m); 809 (w); 751 (w); 688 (w); 645 (w); 542 (s); 462 (s).

X-ray Structure Determination. Single crystals of $Na[LCo_2(etidronate)]\cdot 6.8H_2O$ (**1′**) and $Na[LCo_2(CMDP)]\cdot 8.2H_2O$ (**2′**) were directly coated with Paratone-N oil, mounted on a MicroMounts rod, and frozen under a stream of dinitrogen during data collection. The crystallographic data were collected at 100 K on a Bruker Kappa Apex II diffractometer equipped with an APEX-II detector and MoKα sealed tube source. Raw data were integrated and corrected for Lorentz and polarization effects with Bruker APEX2 version 2014.11-0.[13] Absorption corrections were applied using the program SADABS.[14] Space group assignments were determined by examining systematic absences, E-statistics, and successive refinement of the structures. Structures were solved using direct methods in SHELXT and refined by SHELXL[15] operated within the OLEX2 interface.[16] All hydrogen atoms were placed at calculated positions using suitable riding models and refined using isotropic displacement parameters derived from

their parent atoms. In the crystal structure of **2′**, the Cl atom on the $CMDP^{4-}$ ligand is positionally disordered over two positions. The occupancy of the Cl was freely refined over the two positions. Partially-occupied solvent H_2O molecules not directly bonded to the sodium ions were modeled isotropically. Thermal parameters for all other non-hydrogen atoms were refined anisotropically. Crystallographic data for these compounds at 100 K and the details of data collection are listed in Table 3.2.

NMR Spectroscopy. ^{1}H and $^{31}P\{^{1}H\}$ NMR spectra of ligands and organic precursors were collected at 25 °C at 500 and 202 MHz frequencies, respectively, on Agilent DD2 500 MHz (11.7 T) or Varian Inova 500 MHz (11.7 T) spectrometers, or on an automated Agilent DD MR 400 MHz (9.4 T) spectrometer at 400 and 162 MHz frequencies, respectively. $^{13}C\{^{1}H\}$ NMR spectra of ligands were obtained at 25 °C on a Bruker Avance III 500 MHz (11.7 T) system at 126 MHz frequency. Variable-temperature ^{1}H NMR spectra of compounds **1**–**3** were collected on Agilent DD2 500 MHz (11.7 T) and Agilent DD2 400 MHz (9.4 T) spectrometers. ^{1}H NMR spectra of samples in aqueous solutions containing 50 mM HEPES and 100 mM NaCl buffered at various pH values were acquired using D_2O in an inner capillary to lock the sample. Variable-pH ^{1}H NMR spectra of samples in fetal bovine serum (FBS) were recorded similarly. The pH of commercially available FBS (Fisher Scientific, catalog no. MT35010CV) was adjusted to the desired values by addition of minimal amounts of dilute aqueous nitric acid and sodium hydroxide solutions. Chemical shift values (δ) are reported in ppm and referenced to residual signals from the deuterated solvents (^{1}H NMR spectra: 7.26 ppm for $CDCl_3$, 4.79 ppm for D_2O, and 3.31 ppm for MeOH-d_4; $^{13}C\{^{1}H\}$ NMR spectra: 77.16 ppm for $CDCl_3$, and 49.00 ppm for MeOH-d_4). ^{13}C NMR measurements in D_2O were carried out with 5% (v/v) MeOH added as a reference (δ = 49.50 ppm).

$^{31}P\{^{1}H\}$ NMR spectra are referenced to an external standard of 85% phosphoric acid solution in D_2O (δ = 0 ppm). For measurements of **1**–**3** in D_2O or H_2O, the chemical shift of the solvent signal was set to 0 ppm to simplify comparison between ^{1}H NMR spectra and the corresponding CEST spectra (Z-spectra). All coupling constants (J) are reported in hertz (Hz). The MestReNova 10.0 NMR data processing software was used to analyze and process all recorded NMR spectra. T_1 relaxation times of H_2O were measured after detuning the Agilent DD2 400 MHz instrument to 392 MHz to account for radiation damping, and obtained by fitting H_2O signal intensities from experiments with an array of relaxation times implemented in the program vnmr.

Estimation of pK_a by ^{1}H NMR Analysis. The pH-dependent ^{1}H NMR chemical shifts of the CH_3 resonance from etidronate for compounds **1** and **3**, and the CH resonance from $CMDP^{4-}$ for **2** were used to estimate the pK_a values of compounds **1**–**3**. The change in ^{1}H NMR chemical shift for these resonances as a function of pH was fitted to a Boltzmann sigmoidal function[17] to model a single ionization event according to the following equation:

$$\delta = A_2 + (A_1 - A_2)/(1 + \exp((\mathrm{pH} - \mathrm{p}K_a)/dx)) \qquad (3.1)$$

In this equation, δ is the obtained chemical shift, A_2 is the theoretical chemical shift of the fully deprotonated species, A_1 is the theoretical chemical shift of the fully protonated species, pK_a is the inflection point of the graph, and dx is a parameter describing the steepness of the curve.

CEST Experiments. Variable-temperature CEST experiments were carried out on an Agilent DD2 400 MHz (9.4 T) spectrometer. In a typical CEST experiment, 6–15 mM samples of **1**–**3** in either an aqueous buffer solution containing 50 mM HEPES and 100 mM NaCl or FBS at desired pH values (measured with a pH electrode immediately before ^{1}H NMR and CEST data collection) were measured. Z-spectra (CEST spectra) were obtained according to the following protocol: ^{1}H

NMR spectra were acquired from −50 to 130 ppm with a step increase of 1 ppm using a presaturation pulse applied for 6 s at a power level (B_1) of 24 μT. D_2O was placed in an inner capillary within the NMR sample tube to lock the sample. The normalized integrations of the H_2O signal from the obtained spectra were plotted against frequency offset to generate a Z-spectrum. Generally, direct saturation of the H_2O signal was set to 0 ppm, but ±1 ppm shift was observed for several samples.

Exchange rate constants (k_{ex}) were calculated following a previously reported method,[18] where the *x*-intercept ($-1/k_{ex}^2$) was obtained from a plot of $M_z/(M_0 - M_z)$ (M_z and M_0 are the magnetization of the on- and off-resonance, respectively) against $1/\omega_1^2$ (ω_1 in rad s^{-1}). ^1H NMR spectra were acquired at various presaturation power levels ranging from 10 to 24 μT applied for 6 s at 37 °C. The B_1 values were calculated based on the calibrated 90° pulse on a linear amplifier. To correct for baseline variations, a linear baseline was drawn directly between the first data point (129–131 ppm) and the data point at 45 ppm frequency offset. Note that due to poor baseline for the pH 6.62 sample for **2**, a linear baseline correction was applied for each CEST peak by using the data points at 129 and 85 ppm, and at 85 and 45 ppm, respectively. Reported values of %CEST ($(1 - M_z/M_0) \times 100\%$) are the differences in $\%H_2O$ signal reduction between applied on-resonance presaturations (raw data) and the values obtained by inserting the corresponding frequencies into the linear baseline equations. To calculate k_{ex}, the CEST intensities at the frequency offsets corresponding to maximum H_2O signal reductions at 24 μT power level were monitored for each pH value. The pH calibration curves were generated by taking the base 10 logarithm of the ratios of two CEST signal intensities (reported as $M_0/M_z - 1$)[9c–e,19,20] after a baseline correction was applied.

Solution Magnetic Measurements. The solution magnetic moments of compounds **1**–**3** were determined using the Evans method,[21] by collecting variable-pH ^{1}H NMR spectra at 37 °C (310 K) on an Agilent DD2 500 MHz (11.7 T) spectrometer. In a typical experiment, the compound (3–7 mM) was dissolved in a mixture of 2% (v/v) *tert*-butanol in an aqueous solution containing 50 mM HEPES and 100 mM NaCl buffered at a specific pH value. The resulting solution was placed in an NMR tube containing a sealed capillary with the same solvent mixture but without the to-be-characterized paramagnetic compound as a reference solution. Diamagnetic corrections were carried out based on the empirical formula of each compound (as determined by elemental analysis) using Pascal's constants.[22] The paramagnetic molar susceptibility χ_M^{para} ($cm^3\ mol^{-1}$) was calculated using the following equation:[21]

$$\chi_M^{para} = (3\Delta\nu M_w)/(4\pi\nu_0 m) - \chi_M^{dia} \qquad (3.2)$$

In this equation, $\Delta\nu$ is the frequency difference (Hz) between the *tert*-butyl resonance of *tert*-butanol in the sample and reference solutions, M_w is the molecular mass of the paramagnetic compound (g mol^{-1}), ν_0 is the operating frequency of the NMR spectrometer (Hz), m is the concentration of the paramagnetic compound (g cm^{-3}), and χ_M^{dia} is the diamagnetic contribution to the molar susceptibility ($cm^3\ mol^{-1}$).

UV-Vis Absorption Spectroscopy. Solution and solid-state UV-Vis spectra were collected in the 200–800 nm range on an Agilent Cary 5000 UV-Vis-NIR spectrometer equipped with an integrating sphere for diffuse reflectance measurements. Solution spectra were collected on 64–87 μM samples of compounds **1**–**3** in aqueous buffer solutions containing 50 mM HEPES and 100 mM NaCl in the pH range used for CEST experiments. Diffuse reflectance spectra were collected on crystalline samples of **1′** and **2′**. Samples were prepared by grinding single crystals of the

compounds, followed by mixing with $BaSO_4$ powder for a 2-fold dilution.

Electrochemical Measurements. Cyclic voltammetry measurements were carried out in a standard one-compartment cell under dinitrogen using CH Instruments 760c potentiostat. The cell consisted of a glassy carbon electrode as a working electrode, a platinum wire as a counter electrode, and a saturated calomel electrode (SCE) as a reference electrode. Analytes were measured in aqueous solutions with 100 mM NaCl and 50 mM HEPES buffered at pH 7.4. All potentials were converted and referenced to the normal hydrogen electrode (NHE), using a literature conversion factor.[23]

Other Physical Measurements. Preparative reverse-phase HPLC was performed on a Waters 19 × 250 mm^2 XBridge C18 column, using a Varian Prostar 500 system equipped with a Varian 363 fluorescence detector and a Varian 335 UV-Vis detector. During HPLC experiments, H_2O was used as solvent A and MeCN as solvent B. The absorbances at 220 and 285 nm were monitored. The electrode-based pH measurements were carried out using a Thermo Scientific Orion 9110DJWP double junction pH electrode connected to a VWR sympHony B10P pH meter. The pH meter was calibrated using standardized pH buffer solutions at 4.01, 7.00, and 10.00 purchased from LaMotte Company. Elemental analysis was conducted by Midwest Microlab Inc. Infrared spectra were recorded for solid samples of **1**–**3** on a Bruker Alpha FTIR spectrometer equipped with an attenuated total reflectance (ATR) accessory. These data are provided in Figure 3.7. Electrospray ionization mass spectrometry **(**ESI-MS) measurements were performed on a LC-MS Bruker AmaZon X quadrupole ion trap instrument, equipped with a Compass software version 1.4. All measurements were carried out in MeOH carrier solvent using positive and/or negative ionization mode. Inductively coupled plasma optical emission spectroscopy (ICP-OES) was

performed on a Thermo iCAP 7600 dual view ICP-OES instrument equipped with a CETAC ASX520 240-position autosampler. Samples were dissolved in a 3% aqueous nitric acid solution and the emissions for Co and P compared to standard solutions.

Cell Viability Measurement. Melanoma B16F10 cells were purchased from American Type Culture Collection and cultured in Dulbecco's Modified Eagle's Media (Life Technologies) with 10% (v/v) FBS (Fisher Scientific), 1 mM sodium pyruvate (Sigma Aldrich), 0.1 mM non-essential amino acids (Sigma Aldrich), and 4 mM of L-glutamate. Cells were grown in a humidified incubator operating at 37 °C and 5.0% CO_2, and harvested by incubation with 0.25% TrypLE for 5 min at 37 °C in a 5.0% CO_2 incubator. Cells for the experiment were sub-cultivated twice after thawing the cell stocks. B16F10 cells were seeded at a density of 25,000 cells per well in a 24-well plate and allowed to grow for 24 h before incubation. Cells were incubated with media containing concentrations of **1** ranging from 0.2–11.3 mM (300 μL, 7 concentrations) for 24 h before viability measurements were carried out. The stock solution of **1** was filtered with a 0.2 μm sterile filter prior to incubation with the cells. Cell viability was measured using a Guava easyCyte HT flow cytometer equipped with a 96-well plate/10 tube autosampler (EMD Millipore). Each sample subjected for analysis contained 50 μL of a well-mixed cell suspension in phosphate buffered saline (PBS) and 150 μL of Guava ViaCount reagent. Samples were transferred to a 96-well plate and immediately counted using the Guava ViaCount software module. Viability was measured using the EasyFit Analysis feature. Attempts to use cells not treated with **1** as a control to estimate normal cell death remained unsuccessful. For that reason, cell viability (in %) is reported without taking normal cell death into account. Therefore, the reported viability corresponds to the lower limit of cell survival at each concentration of **1**. Note, however, that we

observed a considerable number of dead cells in the control solution not treated with **1**, even though this number could not be accurately quantified.

MRI Phantom Experiments. Samples for phantom experiments contained 17 mM of **1** in aqueous solutions with 50 mM of HEPES and 100 mM of NaCl buffered at selected pH values ranging from 6.40 to 7.88. All samples were filtered through a 0.22 μm nylon membrane, transferred to borosilicate glass capillaries (0.2 mm thickness, 1.5–1.8 mm outer diameter), and flame sealed. A bundle of 10 capillaries, each containing a solution of **1** buffered at a specific pH, was placed within an NMR tube (18 mm outer diameter) filled with an aqueous solution containing 1 mM gadodiamide (Omniscan) for T_1 matching. CEST experiments were carried out on an 89 mm vertical bore Bruker Avance III HD 750 MHz (17.6 T) MRI scanner running ParaVision 6.0.1 (Bruker Biospin, Billerica, MA, USA). Temperature was maintained at 37 °C using heated water flowing through the gradient coils. The probe and samples were allowed to equilibrate at this temperature for 1 h before acquisition. CEST images were acquired using a standard spin echo imaging sequence with presaturation pulses (74.3 μT, 570 ms total duration) consisting of a train of 1250 Gaussian pulses, each of 0.44 ms (6.2 kHz bandwidth), applied at 64 and 104 ppm frequency offsets (M_z), respectively. Other imaging acquisition parameters were as follows: field of view (FOV) = 15 × 15 mm^2; matrix = 256 × 256; repetition time (TR) = 2000 ms; echo time (TE) = 3.75 ms; flip angle = 210°; slice thickness = 2 mm; averages = 3. Reference unsaturated images were acquired at 0 ppm frequency offset (M_0) using identical parameters except the pulse amplitude was set to 0 μT. Due to a slight difference in observed chemical shift (ca. 1 ppm) between the H_2O signals in the capillaries and the surrounding solution, 0 ppm was defined as the H_2O signal in the capillary tubes. To reduce chemical shift artifacts in the images, 1.2 kHz

bandwidth excitation and refocusing pulses were used in the spin echo sequence. A sine smoothing filter was applied to the raw k-space data to remove Gibbs ringing artifacts in the images.

All images were produced in MATLAB R2016b version 9.1.0 (The MathWorks Inc., Natick, MA, USA). Custom scripts were written in MATLAB to calculate the CEST images, $CEST_{104\ ppm}/CEST_{64\ ppm}$ ratios, and to apply the pH calibration to produce pH maps of the samples. Gating images were produced to remove noise from the remainder of the images, as well as signals from the surrounding doped H_2O. These were generated from binary gating images acquired with no saturation pulses, and dedicated images suppressing signals from only the capillaries. The difference between these produces binary gating images of just the capillary tubes. An image erosion routine was used to shrink these images to the central region of the capillary tubes (75.4% of the total cross-sectional area), to remove unwanted partial volume and susceptibility effects. These central regions were used for CEST data analysis and are shown in Figure 3.6. Values of %CEST are reported as $\%CEST = (1 - M_z/M_0) \times 100\%$. Averaged intensities of the regions shown in Figure 3.6, top, were employed to calculate the $CEST_{104\ ppm}/CEST_{64\ ppm}$ ratios and the corresponding $\log_{10}(CEST_{104\ ppm}/CEST_{64\ ppm})$ values used to generate the pH calibration curve between pH 6.58 and 7.54. Note that for both the CEST intensity ratios and the pH calibration curve, the CEST signal intensities are reported as $M_0/M_z - 1$,[9c–e,19,20] in analogy to the data obtained from NMR measurements.

3.3 Results and Discussion

3.3.1 Syntheses and Structures

The nitro-substituted tetra(carboxamide) chelating ligand HL was selected as a CEST-active ligand, and its permethylated analogue HL′ was selected as a CEST-inactive counterpart. These

ligands were synthesized through S_N2 reactions between 2,2′-iminobis(acetamide) derivatives and 2,6-bis-(bromomethyl)-4-nitrophenol (see Section 3.5.1 and Schemes 3.1 and 3.2). Reaction of the ligands with two equivalents of $Co(NO_3)_2 \cdot 6H_2O$ and one equivalent of etidronic or chloromethanediphosphonic acid (H_4CMDP) in MeOH, in the presence of five equivalents of Na(OMe), afforded compounds $Na[LCo_2(etidronate)] \cdot 0.2NaNO_3 \cdot 2.7H_2O$ (**1**), $Na[LCo_2(CMDP)] \cdot 4.5H_2O \cdot MeOH$ (**2**), and $Na[L'Co_2(etidronate)] \cdot 1.2NaNO_3 \cdot 1.9H_2O$ (**3**) as orange solids (see Section 3.2 and Figure 3.1). The ancillary ligand etidronate was selected based on the potential for the hydroxyl group to exhibit the CEST effect. The related ligand $CMDP^{4-}$ was prepared to serve as an analogous ancillary ligand with no exchangeable protons, as the two bisphosphonates feature similar steric and electronic properties.

Slow diffusion of MeCN vapor into a concentrated solution of **1** and **2** in H_2O afforded plate- and block-shaped crystals of $Na[LCo_2(etidronate)] \cdot 6.8H_2O$ (**1′**) and $Na[LCo_2(CMDP)] \cdot 8.2H_2O$ (**2′**), respectively. Single-crystal X-ray diffraction analysis at 100 K revealed that **1′** and **2′** are

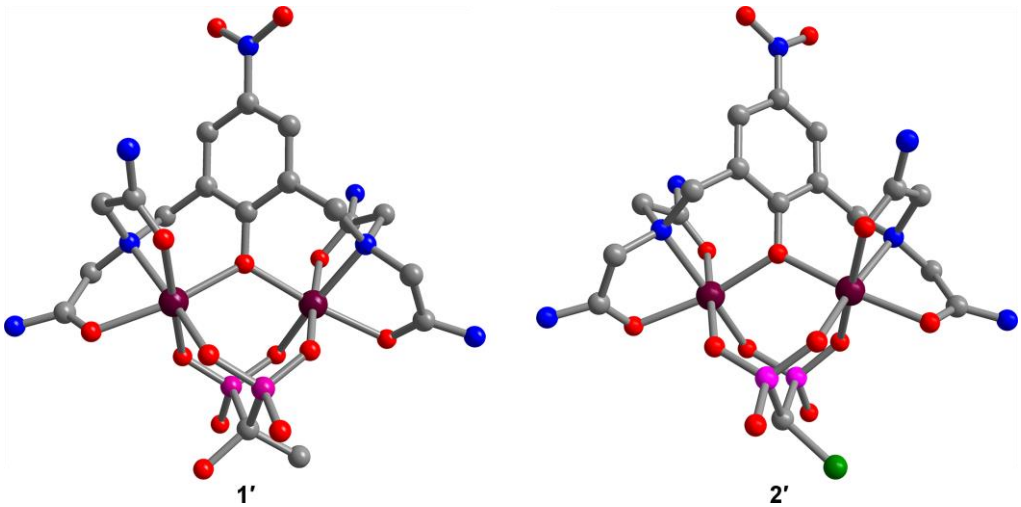

Figure 3.2 Crystal structures of the anionic complexes $[LCo_2(etidronate)]^-$ (left) and $[LCo_2(CMDP)]^-$ (right), as observed in **1′** and **2′**, respectively. Purple, green, magenta, red, blue, and gray spheres represent Co, Cl, P, O, N, and C atoms, respectively; H atoms are omitted for clarity.

Table 3.1 Selected mean interatomic distances (Å) and angles (°) for **1′** and **2′** at 100 K.

	1′	**2′**
Co–$O_{phenoxo}$	2.0920(2)	2.0913(2)
Co–O_{amide}	2.1127(1)	2.1044(1)
Co–$O_{phosphonate}$	2.0618(1)	2.0684(1)
Co–N	2.1558(2)	2.1578(2)
Co···Co	3.6740(3)	3.6780(3)
Co–$O_{phenoxo}$–Co	122.837(4)	123.136(5)
O–P–O	113.882(3)	113.993(4)
P–C–P	111.486(6)	112.901(6)
trans O–Co–E[a]	170.324(1)	170.451(1)
Σ_{sum}[b]	62.27(2)	62.83(2)
Σ_{mean}	5.19(1)	5.24(1)
ω[c]	49.120(4)	49.260(4)

[a]E denotes either a N or an O atom from the [$CoNO_5$] coordination sphere. [b]Octahedral distortion parameter (Σ) = absolute deviation from 90° of each 12 *cis* angle in [$CoNO_5$]. [c]Dihedral angle between the Co–$O_{phenoxo}$–Co plane and the plane of the phenolate ring of L^-.

isostructural and crystallize in the monoclinic space group $P2_1/n$, with one anionic Co_2 complex and one Na^+ ion constituting the asymmetric unit (see Table 3.2). In each complex, the two nearly identical Co centers reside in distorted octahedral coordination environments, each comprised of a μ-phenoxo oxygen atom, a tertiary amine nitrogen atom, and two carboxamide oxygen atoms from L^-. The remaining two coordination sites are occupied by oxygen atoms from the bridging bisphosphonate, which coordinates the metal ions in a μ^2–κ^4 binding mode (see Figure 3.2). The hexagonal plane of the aromatic ring of L^- and the trigonal plane defined by the two Co centers and the μ-phenoxo oxygen atom are twisted relative to another, with dihedral angles of 49.120(4) and 49.260(4)° for **1′** and **2′**, respectively (see Table 3.1).

The mean Co–O bond distances range from 2.0618(1) to 2.1127(1) Å in **1′**, and from 2.0684(1) to 2.1044(1) Å in **2′**. In comparison, the slightly longer mean Co–N bond lengths of 2.1558(2) and 2.1578(2) Å for **1′** and **2′**, respectively, reflect weaker coordination of the tertiary amines to the metal centers due to steric conflicts. These mean bond distances, in conjunction with the average deviations from 90° observed in the bond angles for the 12 *cis* angles in the [$CoNO_5$] coordination sphere of 5.19(1) and 5.24(1)° for **1′** and **2′**, respectively, are consistent with a high-spin Co^{II}

electronic configuration.[24,25] Furthermore, the intramolecular Co···Co distance and Co–$O_{phenoxo}$–Co angle of 3.6740(3) Å and 122.837(4)° for **1′** and 3.6780(3) Å and 123.136(5)° for **2′** are consistent with related phenoxo-bridged Co^{II}_2 complexes.[24,25] Finally, the similar O–P–O and P–C–P bond angles for the etidronate and $CMDP^{4-}$ ligands in **1′** and **2′**, respectively, verify the insignificant structural changes associated with altering the ancillary bisphosphonate. Taken together, these comparable structural metrics for **1′** and **2′** provide validation for the use of $CMDP^{4-}$ as a CEST-inactive analogue of etidronate.

3.3.2 UV-Vis Spectroscopy

To probe the electronic structure of compounds **1**–**3** in solution, UV-Vis absorption spectra were collected for samples in aqueous buffer solutions containing 50 mM HEPES and 100 mM NaCl. The spectrum for a sample of **1** buffered at pH 7.4 features a strong absorption at 375 nm (ε = 13800 M^{-1} cm^{-1}) (see Figure 3.8). Similarly, a solution of **2** shows a nearly identical absorption band at this wavelength (ε = 14100 M^{-1} cm^{-1}) under the same conditions (see Figure 3.9). Based on these observations and literature precedent for similar phenoxo-bridged Co_2 complexes,[24c,25a] we assign these absorptions to ligand–metal charge transfer (LMCT) transitions from the phenolate to Co^{II}. The close similarity of the spectrum for **3** in pH 7.4 buffer, which exhibits a single intense band at 379 nm (ε = 12300 M^{-1} cm^{-1}), further supports the assignments of these spectral features (see Figures 3.10 and 3.11). Notably, both the positions and intensities of the absorption bands are relatively unaffected by pH between 5.8 and 8.3 (see Figures 3.8–3.10). Furthermore, the diffuse reflectance spectra collected for crystalline solid-state samples of **1′** and **2′** feature peaks with maxima at 379 and 376 nm, respectively (see Figures 3.12 and 3.13). These data indicate that the structures of $[LCo_2(etidronate)]^-$ and $[LCo_2(CMDP)]^-$ determined from X-ray diffraction analysis

are preserved in aqueous HEPES solutions in the physiological pH range.

3.3.3 Solution Magnetic Properties

To assess the magnetic behavior of the three Co_2 complexes, dc magnetic susceptibility data were obtained at 37 °C for aqueous buffer solutions in the pH range 5.8–8.4 using the Evans method[21] (see Section 3.2). The resulting plots of $\chi_M T$ vs pH are shown in Figures 3.14–3.16. For all compounds, $\chi_M T$ varies insignificantly with pH, affording average values of $\chi_M T$ = 6.3(3), 6.0(2), and 6.1(2) cm^3 K mol^{-1} for **1**, **2**, and **3**, respectively (see Table 3.3). The mean magnetic moments per Co^{II} site correspond to *g* values ranging from 2.5(1) to 2.6(1), indicative of a significant contribution from orbital angular momentum to the magnetic moments of **1**–**3**. These data are in accord with the high magnetic anisotropy of octahedral, $S = {}^3/_2$ Co^{II} centers,[12a] and agree with values reported for structurally similar high-spin Co^{II}_2 complexes.[24] In sum, the magnetic properties of **1**–**3** are nearly identical in aqueous solution within the physiologically relevant pH range at 37 °C.

3.3.4 NMR Spectroscopy

To further examine and compare the solution properties of the Co_2 complexes, ^{1}H NMR spectra were collected for aqueous solutions of **1**–**3** buffered at selected pH values. All compounds gave sharp, well-resolved NMR spectra, consistent with high-spin Co^{II} ions in pseudo-octahedral geometry.[12] The spectrum for **1** at pH 7.18 features 22 paramagnetically shifted resonances that range in chemical shift from −110 to 185 ppm vs H_2O (see Figure 3.17, top). The resonances at 9.5, 13, 64, 68, 102, 104, and 105 ppm are assigned to exchangeable protons on the carboxamide groups and the etidronate hydroxyl group, as evidenced by their disappearance in the analogous spectrum recorded in neutral D_2O (see Figure 3.17, bottom). The anticipated two additional amide

resonances are most likely concealed by the broad H_2O signal. The appearance of the 22 NMR signals as 10 pairs of closely spaced peaks is consistent with the pseudo-C_2 symmetry of $[LCo_2(etidronate)]^-$ in **1**, where a slight lowering from C_2 results from the asymmetry of the etidronate ligand. The two remaining peaks correspond to the hydroxyl and methyl substituents on etidronate. Upon raising the pH from 6.18 to 8.14, the exchangeable proton resonances become significantly broader, indicative of faster proton exchange (see Figure 3.18).

In comparison, the spectrum for **2** at pH 7.18 exhibits 23 paramagnetically shifted peaks in the range −105–180 ppm vs H_2O, with exchangeable carboxamide signals at 4.7, 6.8, 9.5, 11, 68, 70, 102, and 104 ppm, verified by comparison of the spectra recorded in H_2O and D_2O (see Figure 3.19). Notably, the presence of four highly-shifted amide resonances that are well separated from the four remaining amide peaks confirms the inequivalency of the two amide NH protons due to restricted C–N bond rotation.[26] This inequivalence is a common observation for amide-appended transition metal complexes.[9f,11a–f,h,j,26a,c] The close similarity between the spectra for **1** and **2** (see Figure 3.20) suggests that these compounds are structurally similar in solution, as observed in the solid-state. The replacement of the intense peak at 66 ppm in the spectrum for **1** with a peak at 138 ppm in the spectrum for **2** indicates that these signals correspond to the CH_3 and CH resonances from the etidronate and $CMDP^{4-}$ ancillary ligands, respectively. Moreover, the linewidths of the carboxamide peaks for **2** show similar pH dependence between pH 6.62 and 8.34, as observed for **1** (see Figure 3.21).

In analogy to the ^1H NMR features of the Co_2 complexes of L^-, the resonances in the spectrum for **3** at pH 7.47 span from −110 to 190 ppm vs H_2O and display a similar spectral profile (see Figure 3.22). The intense peaks at −9.8, −7.5, −3.7, 1.6, 2.0, 22, and 26 ppm are assigned to methyl

groups on L′⁻, and the CH_3 resonance from etidronate is observed at 62 ppm. Furthermore, comparison of the spectra recorded in pH 8.08 buffer and slightly basic D_2O reveals the disappearance of the peak at 103 ppm (see Figure 3.23). This observation indicates that the etidronate hydroxyl group provides a well-resolved NMR signal under basic conditions, and further corroborates the presence of three exchangeable proton resonances for **1** in the 102–105 ppm range. Upon lowering the pH to 5.80, the hydroxyl peak for **3** undergoes significant line broadening, suggesting an increase in the proton exchange rate (see Figure 3.24). Importantly, inspection of the NMR linewidths of the carboxamide peaks for **1** and **2** and the hydroxyl resonance for **3** implies opposing pH dependences of the proton exchange rates for these two functional groups, and therefore highlights the potential utility of **1** for ratiometric pH imaging.

3.3.5 CEST Properties

In order to investigate the feasibility of employing **1** as a pH-responsive PARACEST probe, CEST spectra were collected for aqueous solutions containing 12.8 mM of **1** with 50 mM HEPES and 100 mM NaCl buffered at pH values ranging from 6.50 to 8.14 (see Figure 3.3). The spectrum at pH 6.50 exhibits two peaks, centered at 66 and 102 ppm, with 2.0 and 14% H_2O signal reduction, respectively. Note that CEST signals from the labile protons below 13 ppm are masked by direct saturation of the H_2O

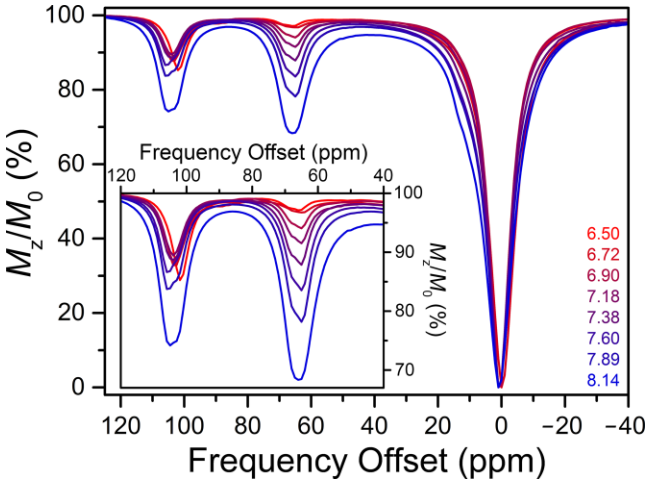

Figure 3.3 CEST spectra collected at 37 °C for 12.8 mM aqueous solutions of **1** with 50 mM HEPES and 100 mM NaCl buffered at pH 6.50–8.14 (red to blue). The legend gives the pH and corresponding color of each sample. Inset: Expanded view of the CEST peaks of interest.

solvent. As the pH is raised to 8.14, the CEST peak at 66 ppm shifts to 64–65 ppm, and the intensity increases monotonically to 27%. This increase in CEST intensity with pH is consistent with base-catalyzed proton exchange that is typical for carboxamides.[9a,f,11a,d–f,h,20]

In stark contrast, the CEST effect of the downfield-shifted peak shows a very different pH profile. First, the frequency corresponding to maximum CEST intensity is markedly affected by pH variations and shifts from 102 to 106 ppm in the pH range 6.50–8.14. Surprisingly, the CEST intensity remains relatively constant between pH 6.50 and 7.60, but then undergoes a significant increase when the pH is raised further. The dramatically different pH dependences of the two CEST features for **1** are evident from a plot of the CEST intensities at 64 and 104 ppm vs pH (see Figure 3.25). We hypothesize that the unusual CEST behavior at 104 ppm stems from contributions of overlapping carboxamide and hydroxyl resonances to the observed CEST effect, as suggested by ^{1}H NMR analysis.

To better understand the causes for the unusual CEST properties of **1**, analogous variable-pH CEST spectra were collected for aqueous solutions containing 12 mM of **2** or 13 mM of **3**. The spectra for **2** in the pH range 6.62–8.34 show two peaks at 68 and 102 ppm with CEST intensities that increase significantly when the pH is raised (see Figure 3.26), similar to that observed for the peak at ca. 64 ppm for **1**. Importantly, the nearly identical pH dependences of the two CEST effects for **2** (see Figure 3.27) supports the hypothesis that the unique CEST behavior of **1** can be attributed to the etidronate hydroxyl group. Indeed, CEST spectra for **3** obtained between pH 5.80 and 8.08 confirm the PARACEST activity of the ancillary etidronate, as a single peak that shifts from 94 to 103 ppm is observed (see Figure 3.28). The nature of this pH-induced shift in CEST frequency is discussed below. In conjunction with this frequency shift, the hydroxyl CEST signal undergoes a

significant decrease in intensity with increasing pH, after reaching a maximum intensity of 20% at pH 6.11 (see Figure 3.29). The observation of optimal CEST under slightly acidic conditions is consistent with PARACEST agents bearing alcohol donors.[11f,27] Interestingly, all previously reported PARACEST agents with CEST-active hydroxyl protons feature OH groups directly bonded to the metal center.[9b,g,11f,27,28] This further demonstrates the remarkably high CEST peak shift and intensity of the ancillary hydroxyl group in **1** and **3**.

The proton exchange rates at 37 °C were estimated by employing the Omega plot method.[18] The rate constants (k_{ex}) for the amide protons in **2** increase from 2.7(2) × 10^2 (68–69 ppm) and 3.5(3) × 10^2 (102 ppm) s^{-1} at pH 6.62 to 1.0(1) × 10^3 (68–69 ppm) and 8.0(3) × 10^2 (102 ppm) s^{-1} at pH 8.34 (see Figures 3.30–3.32 and Table 3.4). These values are consistent with rates reported for mono-[9f,11a,d–f,h,j] and dinuclear[11l,m] transition metal PARACEST agents bearing pendent carboxamides. In contrast, the hydroxyl proton exchange in **3** is fastest at pH 5.80 (k_{ex} = 1.5(1) × 10^3 s^{-1}), and then decreases sharply as the pH is raised to 7.47 (k_{ex} = 2.5(2) × 10^2 s^{-1}) (see Figures 3.33 and 3.34, and Table 3.5). The opposite pH trends for exchange rates in **2** and **3** are in accord with ^{1}H NMR and CEST data, and reflect the base- and acid-catalyzed exchange of the NH and OH protons, respectively, in these Co_2 complexes. To compare, the rate constants for the two CEST features of **1** are similar to those for **2** and **3**, with values of 2.1(3)–7.3(3) × 10^2 (64–66 ppm) and 2.8(2)–7.6(3) × 10^2 (101–106 ppm) s^{-1} in the pH range 6.18–8.14 (see Figures 3.35–3.37 and Table 3.6). Note that the pH-dependent changes of the rate constants for **1** are less obvious than those observed for **2** and **3**. Most likely, this difference results from asymmetric CEST peaks for **1** and the contribution of both NH and OH protons to the CEST effect at 101–106 ppm. Therefore, more elaborate methods are needed to accurately determine the exchange rate for each CEST effect

of **1**.

3.3.6 Ratiometric CEST Analysis

To assess the potential of compound **1** to enable ratiometric pH quantitation, the pH dependence of the ratio of CEST intensities at 104 and 64 ppm ($CEST_{104\ ppm}/CEST_{64\ ppm}$) was investigated. Remarkably, the data reveal a substantial decrease in the intensity ratio from a value of 8.35 to 0.82 in the pH range 6.50–7.60, while no significant change is observed at higher pH (see Figure 3.4).

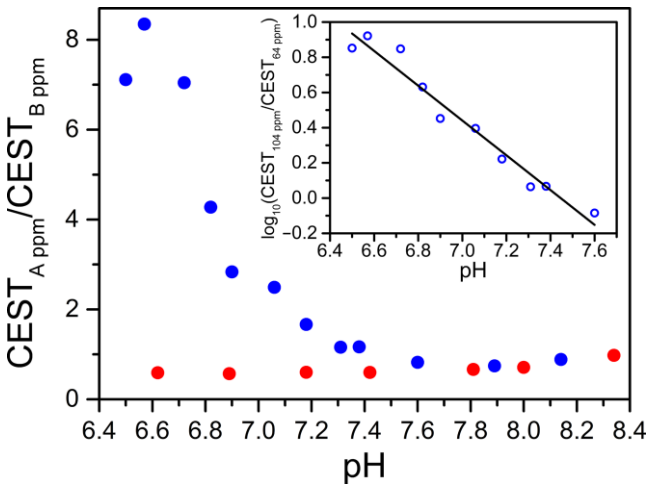

Figure 3.4 Ratios of CEST intensities ($CEST_{A\ ppm}/CEST_{B\ ppm}$) from presaturation at 104 (A) and 64 (B) ppm for 12.8 mM aqueous buffer solutions of **1** (blue), and at 102 (A) and 68 (B) ppm for 12 mM solutions of **2** (red) vs pH. Inset: Semilog form of the plot for **1**. Circles denote experimental data, and the black line corresponds to a linear fit to the data.

Moreover, the logarithm (log)[29] of this ratio was found to vary linearly with pH in this range (see Figure 3.4, inset), according to the following equation:

$$\log(CEST_{104\ ppm}/CEST_{64\ ppm}) = -0.99 \times pH + 7.4 \qquad (3.3)$$

Conversely, the analogous ratio of CEST intensities at 102 and 68 ppm ($CEST_{102\ ppm}/CEST_{68\ ppm}$) for **2** is relatively unaffected by pH changes, with values of 0.57–0.98 between pH 6.62 and 8.34 (see Figure 3.4). This comparison highlights the essential role of the etidronate hydroxyl group to enable ratiometric quantitation of pH in the physiological range with **1**, using Equation 3.3 as a calibration curve. The slope of a linear calibration curve provides a useful measure of probe sensitivity. Notably, the absolute value of 0.99(7) pH $unit^{-1}$ obtained for **1** is ca. 2–4-fold greater than those reported for related ratiometric PARACEST pH probes at 37 °C, even when compared to instances where the CEST intensity ratios are employed directly.[7a,c,9c–f]

To further evaluate the efficacy of **1** as a ratiometric pH probe, we first sought to determine whether this pH calibration curve is affected by the concentration of the probe, since a concentration-independent measure is critical for physiological applications. Toward this end, CEST spectra for aqueous buffer solutions containing 6.4 and 8.5 mM of **1** were recorded analogously to the 12.8 mM sample (see Figures 3.38 and 3.39). The CEST effects at 64 and 104 ppm did not vary significantly with different probe concentrations (see Figures 3.40–3.43). This observation suggests that the spin-lattice relaxation rate of H_2O is close to the proton exchange rates within this concentration range,[6e,f,9d,h,30] consistent with T_1 analysis (see Table 3.7). Most importantly, these experiments show that plots of $CEST_{104\ ppm}/CEST_{64\ ppm}$ vs pH are nearly identical for the three concentrations in the pH range 6.50–8.15 (see Figures 3.44–3.46). Indeed, linear fits of the corresponding $\log(CEST_{104\ ppm}/CEST_{64\ ppm})$ values as a function of pH afforded the following equations (see Figures 3.44 and 3.45, insets):

$$\text{6.4 mM: } \log(CEST_{104\ ppm}/CEST_{64\ ppm}) = -1.05 \times pH + 7.9 \qquad (3.4)$$

$$\text{8.5 mM: } \log(CEST_{104\ ppm}/CEST_{64\ ppm}) = -1.03 \times pH + 7.7 \qquad (3.5)$$

The pH calibration curves obtained for various concentrations of **1** (Equations 3.3–3.5) are summarized in Figure 3.47. For a given $\log(CEST_{104\ ppm}/CEST_{64\ ppm})$ value, the deviation in pH was found to be ca. 0.02–0.09 pH units over the pH range 6.50–7.60. This observation demonstrates the ability of **1** to quantitate solution pH in a concentration-independent manner within the error of 0.1 pH unit.

3.3.7 Temperature Effects

An important challenge facing pH-responsive MR probes is the ability to deconvolute pH responses from temperature effects of the CEST peak frequency and intensity, owing to the

temperature dependences of hyperfine shifts[12] and proton exchange rates.[9] To examine how temperature variation affects the pH calibration curve, variable-pH ^{1}H NMR and CEST spectra were collected at the additional temperatures 35 and 39 °C on 12.8 mM solutions of **1** buffered at pH 6.50–8.14. The data show very similar pH-dependent behavior as observed at 37 °C (see Figures 3.48–3.51), albeit with nearly all resonances shifted by ca. 1 ppm away and toward the H_2O signal at 35 and 39 °C, respectively (see Figure 3.52), consistent with Curie behavior of high-spin Co^{II}.[12] Upon increasing the temperature from 35 to 39 °C, a moderate increase in CEST intensities at 64 and 104 ppm was observed (see Figures 3.53–3.56). Importantly, temperature changes do not affect the $CEST_{104\ ppm}/CEST_{64\ ppm}$ values above pH 7.0. In contrast, temperature changes cause significant deviations in the pH profile of $CEST_{104\ ppm}/CEST_{64\ ppm}$ below pH 7.0 (see Figures 3.57–3.59). Here, fits of the $\log(CEST_{104\ ppm}/CEST_{64\ ppm})$ vs pH plots using data from the pH range 6.50–7.60 gave the following linear equations (see Figures 3.57 and 3.58, insets):

$$35\ °C: \log(CEST_{104\ ppm}/CEST_{64\ ppm}) = -1.19 \times pH + 8.9 \quad (3.6)$$

$$39\ °C: \log(CEST_{104\ ppm}/CEST_{64\ ppm}) = -0.79 \times pH + 5.9 \quad (3.7)$$

The significant effect of temperature variations on the pH calibration curve is primarily due to the temperature-induced shifts in CEST frequencies (see Figure 3.60). Indeed, fits of the $\log(CEST_{105\ ppm}/CEST_{65\ ppm})$ and $\log(CEST_{103\ ppm}/CEST_{63\ ppm})$ vs pH plots for the data obtained from pH 6.50–7.60 at 35 and 39 °C, respectively, provided excellent linear correlations following the equations:

$$35\ °C: \log(CEST_{105\ ppm}/CEST_{65\ ppm}) = -1.06 \times pH + 7.8 \quad (3.8)$$

$$39\ °C: \log(CEST_{103\ ppm}/CEST_{63\ ppm}) = -0.95 \times pH + 7.1 \quad (3.9)$$

The calibration curves represented by Equations 3.8 and 3.9 closely resemble that obtained at

37 °C (see Figure 3.61), demonstrating that the %CEST at 105 and 65 ppm, and at 103 and 63 ppm, should be employed for pH measurements at 35 and 39 °C, respectively. One potential route to address temperature heterogeneity in physiological environments with this Co_2 probe could involve constructing multiple pH calibration curves, one at each temperature, and then determine the surrounding temperature independently by exploiting the ^{1}H NMR chemical shift of a resonance that shifts insignificantly with pH. Such simultaneous quantitation of pH and temperature using PARACEST probes has been reported.[8,9b,g,h]

3.3.8 Complex Stability and Biocompatibility Studies

The cyclic voltammogram collected for an aqueous solution of **1** in HEPES buffer at pH 7.4 exhibits an irreversible oxidation process at ca. 560 mV vs NHE (see Figure 3.62). We assign this event to the Co^{II}_2/$Co^{II}Co^{III}$ oxidation, which verifies that **1** is inert towards reaction with oxygen in solution.[31]

In order to further assess the stability of **1** under physiological conditions, 10 mM aqueous solutions of the Co_2 complex buffered at pH 7.3 were incubated with 10 mM solutions of the ions $H_2PO_4^-$/HPO_4^{2-}, CO_3^{2-}, SO_4^{2-}, CH_3COO^-, and Ca^{2+} for 16 h at 25 °C. The ^{1}H NMR spectra of these solutions collected at 37 °C appear identical to the spectrum obtained previously at the same pH, albeit showing the additional ions (see Figures 3.63 and 3.64). Furthermore, compound **1** exhibits analogous NMR and CEST properties in fetal bovine serum (FBS) as in HEPES buffer in the pH range 6.6–7.6 (see Figures 3.65–3.68). The observation of a slightly broader H_2O resonance in FBS compared to buffer is presumably due to contributions from labile protons of proteins in the serum. Importantly, the highly-shifted CEST peaks for **1** are unaffected by this broadness near the diamagnetic region, and the pH calibration curves obtained in FBS and buffer are essentially

identical (see Figure 3.69). It is important to note that the additional feature at ca. 88 ppm in the CEST spectra does not impact the CEST analysis of **1**. The exact nature of this feature is currently unknown but likely stems from a miniscule amount of an OH-containing impurity, as it is most prominent at acidic pH and no signals are observed in this regime in the corresponding ^{1}H NMR spectra. Taken together, these results demonstrate the high stability of **1** in physiological environments and suggest its potential for in vivo studies.

To further investigate the biocompatibility of **1**, preliminary cell viability experiments were carried out using melanoma B16F10 cells as a model. The study revealed that >50% of the cells are viable after incubation with millimolar concentrations of **1** for 24 h (see Figure 3.70). Note that the %viability values are reported without taking normal cell death into account, which can be appreciable, and thus only correspond to the lower limits of cell survivals at given probe concentrations (see Section 3.2).

3.3.9 NMR Studies of pH-Induced Structural Changes

In addition to changes in CEST peak intensities with pH, variations in the frequency of CEST peaks may also be employed for ratiometric pH sensing.[7a,c] Such CEST frequency changes are typically caused by a pH-dependent interconversion between species of different protonation states.[7] Indeed, the CEST peaks for **1**–**3** show slight shifts with pH, which suggests modest structural changes in solution. To gain further insight into potential pH-induced structural changes in the Co_2 complexes, ^{1}H NMR spectra were collected for samples of **1**–**3** in aqueous buffer solutions over a broad pH range. The carboxamide peaks for **1** show moderate changes in chemical shifts between pH 2.69 and 8.87 (see Figure 3.71), while the CH_3 resonance from etidronate shifts dramatically, by 19.55 ppm, following a sigmoidal pH profile.

A fit of the CH_3 chemical shift vs pH data to Equation 3.1 gave a pK_a value of 5.01(3) (see Figure 3.5). Similarly, the etidronate CH_3 resonance for **3** shifts from 44.00 to 62.68 ppm in the pH range 1.56–8.82, and a corresponding sigmoidal fit to the data afforded a value of pK_a = 5.28(5) (see Figure 3.72). In addition, the changes in resonance frequencies of the carboxamides for **2** resemble those for **1**, albeit less pronounced (see Figure 3.73). Comparably, a fit of the chemical shift vs pH data for the CH resonance from $CMDP^{4-}$ to Equation 3.1 yielded a pK_a of 4.40(2) (see Figure 3.74). These dramatic pH-dependent chemical shift changes of the CH_3 and CH resonances from the bisphosphonates strongly suggest that the ancillary ligands become protonated at low pH. The similar trends observed for all complexes and the excellent agreement of the data to a model for a single ionization event, together with the p*K*a values of the free bisphosphonic acids,[32] are most consistent with protonation/deprotonation of one of the cobalt-coordinated P–O oxygen atoms as the source of peak shifts in this pH range (see Figure 3.5, inset). Indeed, protonated phosphonate oxygen donors have been observed in the solid-state in transition metal bisphosphonate complexes.[33]

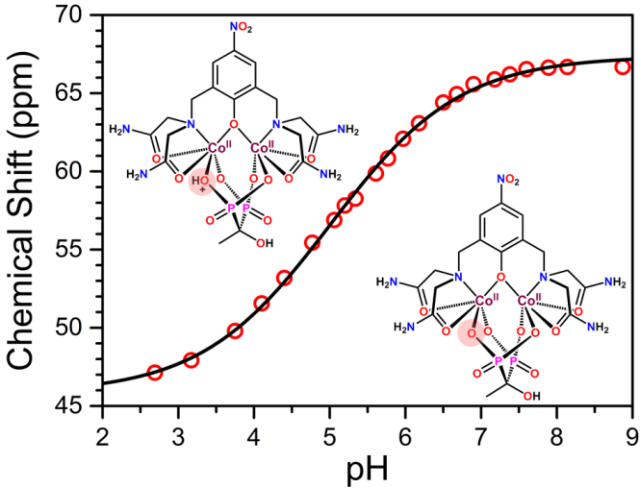

Figure 3.5 ^{1}H NMR chemical shift (frequency offset) of the CH_3 resonance from etidronate vs pH for aqueous buffer solutions of **1**. Red circles denote experimental data, and the black line corresponds to a sigmoidal fit to the data (Equation 3.1). Inset: Schematics of the anion from **1**, highlighting the protonation state of etidronate.

The observation of a considerably lower pK_a for **2** than **1** is in accord with the insignificant variation in CEST frequencies of the amide peaks for **2**, as $CMDP^{4-}$ is nearly completely

deprotonated above pH 6.5. Furthermore, the value of pK_a = 5.28(5) for **3** is in line with the observed pH dependence of the hydroxyl CEST frequency. This behavior stems from transitioning from a state with considerable contributions from both protonation states of etidronate at pH 5.8, to a state with near exclusively the fully deprotonated ligand above pH 7.1. Finally, these NMR studies establish the integrity of **1**–**3** in aqueous solutions over a wide pH range.

3.3.10 MR Phantom Imaging

To further examine the practicality of **1** for ratiometric pH imaging through PARACEST, CEST images of phantoms containing a series of 17 mM aqueous solutions of **1** buffered at selected pH values from 6.40 to 7.88 were collected on a 17.6 T MRI scanner. For each pH value, two images were acquired at 37 °C after irradiation at 64 and 104 ppm vs H_2O, respectively, using 74.3 μT presaturation pulses. Corresponding control images were collected at 0 ppm frequency offset with 0 μT power. Note that the high presaturation power was required to saturate the labile protons of **1** owing to the larger Zeeman splitting on the 17.6 T MRI scanner. The %CEST at 64 ppm increased from 1.1 to 24% upon moving from pH 6.40 to 7.88, while presaturation at 104 ppm afforded values of 5.4 to 15% within this range (see Figures 3.75 and 3.6, top). These pH-dependent trends in CEST intensity are consistent with those observed in the NMR study. Moreover, the ratio of CEST intensities at 104 and 64 ppm ($CEST_{104\ ppm}/CEST_{64\ ppm}$) decreased substantially from pH 6.58 to 7.54 (see Figures 3.76 and 3.6, bottom left), and a plot of log of the ratios between averaged phantom intensities at these frequencies ($\log(CEST_{104\ ppm}/CEST_{64\ ppm})$) vs pH gave an excellent linear fit in analogy to Equations 3.3–3.9 (see Figure 3.76, inset). Using this calibration curve and the $CEST_{104\ ppm}/CEST_{64\ ppm}$ values per pixel, a pH map was generated (see Figure 3.6, bottom right). This result highlights that the pH-dependent changes in CEST intensity ratios can be clearly

visualized by MRI. Furthermore, the pH values calculated from the calibration curve are in good agreement with those independently measured by a pH electrode (see Table 3.8). In sum, phantom imaging experiments further demonstrate the ability of **1** to ratiometrically quantitate solution pH in the physiological pH range 6.5–7.6. Future efforts will be geared toward improving the homogeneity and overall quality of CEST images through pulse sequence optimization, as well as to investigate the feasibility of pH imaging with **1** on lower field MRI scanners. Eventually, the actual potential of the Co^{II}_2 probe for ratiometric mapping of pH will be evaluated in small animal

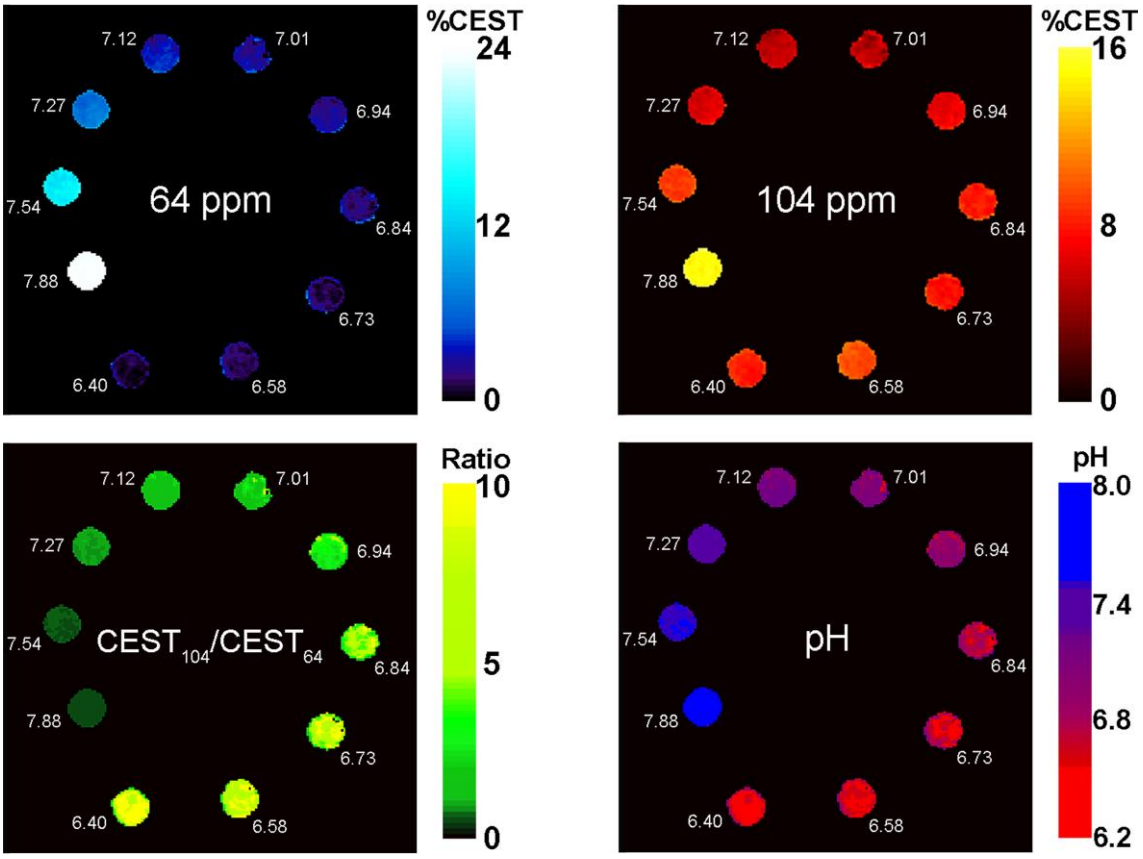

Figure 3.6 CEST images of phantoms containing 17 mM aqueous buffer solutions of **1** in the pH range 6.40–7.88, collected at 37 °C on a 17.6 T MRI scanner. Top: Images constructed from CEST effects upon presaturation at 64 ppm (left) and 104 ppm (right), respectively. Bottom: Ratiometric $CEST_{104\ ppm}/CEST_{64\ ppm}$ map obtained by taking the pixel-wise ratios of CEST signal intensities at 104 and 64 ppm (left), and a pixel-wise pH map calculated from the corresponding $\log(CEST_{104\ ppm}/CEST_{64\ ppm})$ values by using the calibration curve displayed in Figure 3.76, obtained from averaged phantom intensities at 64 and 104 ppm between pH 6.58 and 7.54 (right). White numbers next to each phantom sample denote the pH of the corresponding solution measured by a pH electrode.

imaging studies.

3.4 Conclusions

The foregoing results demonstrate the ability of Co_2 complexes to provide a concentration-independent measure of solution pH over a range relevant for detecting physiological abnormalities through ratiometric PARACEST imaging. In particular, the systematic study of **1**–**3** illustrates the opposing pH-dependent CEST properties of carboxamide NH and etidronate OH protons. The potential of Co^{II}_2 complexes as ratiometric pH probes is further highlighted by the stability of **1** in physiological environments and good agreement between pH from phantom images of **1** and those measured by an electrode. Considering the excellent tunability of the phenoxo-bridged dinuclear platform, ongoing work is focused on investigating the CEST behavior of related ancillary bisphosphonate ligands, and on incorporating other CEST-active functional groups on the dinucleating ligand scaffold, in efforts to optimize the pH-dependent CEST properties of this family of molecules for imaging pH in vivo. We anticipate that this broadly generalizable platform will aid in developing pH-responsive probes with higher sensitivity and stability, in particular those suitable for in vivo applications.

3.5 Supporting Information

3.5.1 Supplementary Experimental Details

Synthesis of 8-acetoxymethyl-6-nitro-1,3-benzodioxene. This compound was synthesized following a modified literature procedure.[34] Nitrophenol (35.0 g, 0.252 mol) was added to a stirring colorless solution of paraformaldehyde (31.8 g, 1.01 mol), glacial acetic acid (250 mL) and concentrated sulfuric acid (60 mL) at 80 °C. The resulting suspension was heated at 80 °C under

a dinitrogen atmosphere for 16 h. Deionized H_2O (1000 mL) was then added to the off-white suspension at 25 °C, and the mixture was neutralized by slow addition of solid potassium carbonate (150 g, 1.09 mol). The resulting yellow precipitate was collected by vacuum filtration, washed with cold deionized H_2O (600 mL) and dried with suction on the filter for 3 h. The crude product was recrystallized from ethanol to give the title compound as a light yellow solid (31.7 g, 50%). ^{1}H NMR (500 MHz, $CDCl_3$, 25 °C): δ 8.14 (d, $^4J_{HH}$ = 2.7 Hz, 1H), 7.90 (d, $^4J_{HH}$ = 2.6 Hz, 1H), 5.37 (s, 2H), 5.15 (s, 2H), 4.96 (s, 2H), 2.16 (s, 3H).

Synthesis of 2,6-bis(bromomethyl)-4-nitrophenol. This compound was synthesized following a modified literature procedure.[34a] A mixture of 8-acetoxymethyl-6-nitro-1,3-benzodioxene (7.00 g, 27.6 mmol) and 48% (w/w) hydrobromic acid solution in H_2O (200 mL) was stirred at reflux for 12 h. The reaction flask was connected to a potassium hydroxide base trap to neutralize the hydrogen bromide gas that evolved in the reaction. The resulting gray precipitate was collected by vacuum filtration at 25 °C, washed with deionized H_2O (600 mL) and dried with suction on the filter for 3 h. Recrystallization from $CHCl_3$ afforded the title compound as an off-white powder (3.95 g, 44%). ^{1}H NMR (500 MHz, $CDCl_3$, 25 °C): δ 8.22 (s, 2H), 6.39 (s, 1H), 4.57 (s, 4H).

Synthesis of 2,2′-(benzylazanediyl)bis(N,N′-dimethylacetamide). This compound was synthesized following a modified literature procedure.[35] Benzylamine (1.19 g, 11.1 mmol) and 2-chloro-*N*,*N*′-dimethylacetamide (2.70 g, 22.2 mmol) were stirred in dry MeCN (200 mL). Subsequently, potassium carbonate (6.14 g, 44.4 mmol) and potassium iodide (2.21 g, 13.3 mmol) were added. The resulting off-white suspension was stirred at reflux under a dinitrogen atmosphere for 18 h. The reaction mixture was then cooled to 25 °C and filtered to give a light yellow filtrate, which was concentrated under reduced pressure to give a pale yellow solid. This solid was

dissolved in $CHCl_3$ (100 mL), filtered, and the solvent removed under reduced pressure to afford the product as a light yellow oil (2.23 g, 73%). ^{1}H NMR (500 MHz, $CDCl_3$, 25 °C): δ 7.37 (d, $^3J_{HH}$ = 7.6 Hz, 2H), 7.29 (dd, $^3J_{HH}$ = 7.4, 7.5 Hz, 2H), 7.23 (t, $^3J_{HH}$ = 7.3 Hz, 1H), 3.82 (s, 2H), 3.47 (s, 4H), 2.94 (s, 6H), 2.90 (s, 6H).

Synthesis of 2,2′-(azanediyl)bis(N,N′-dimethylacetamide). This compound was synthesized following a modified literature procedure.[35] Pd/C (10 wt%, 100 mg, 0.09 mmol Pd) was carefully added to a pale yellow solution of 2,2′-(benzylazanediyl)bis(*N*,*N*′-dimethylacetamide) (2.23 g, 8.10 mmol) in dry MeOH (75 mL). The resulting dark suspension was stirred at 25 °C under 35 psi pressure of dihydrogen for 24 h. The reaction flask was then vented, and a second fraction of Pd/C (10 wt%, 100 mg, 0.09 mmol Pd) was added. The reaction was re-pressurized with 35 psi of dihydrogen and stirred for additional 16 h at 25 °C. This process was then repeated, and after stirring for additional 30 h, ESI-MS indicated that the reaction was complete. The black suspension was filtered through diatomaceous earth, and the colorless solution was concentrated under reduced pressure to give the title compound as a white solid (1.15 g, 76%). ^{1}H NMR (500 MHz, $CDCl_3$, 25 °C): δ 3.55 (s, 4H), 2.95 (broad s, 12 H).

Synthesis of N,N′-[(2-hydroxy-5-nitro-1,3-phenylene)bis(methylene)]bis[N-(carboxymethyl)-glycinamide] (HL). This compound was synthesized following a modified literature procedure[111] Under an atmosphere of dinitrogen, 2,2′-iminobis(acetamide) (2.12 g, 16.2 mmol) and *N*,*N*-diisopropylethylamine (2.09 g, 16.2 mmol) were suspended in MeCN (200 mL). The light brown suspension was heated to reflux, and to it was added dropwise with stirring a light yellow solution of 2,6-bis(bromomethyl)-4-nitrophenol (1.50 g, 4.62 mmol) in MeCN (20 mL) over the course of 1.5 h. The resulting yellow reaction mixture was stirred at reflux for 24 h and then was evaporated

to dryness. The resulting yellow-brown residue was dissolved in a 10% (v/v) aqueous MeOH solution (30 mL) and subsequently purified by C18 reverse-phase HPLC using H_2O and MeCN as eluents. The title compound came off the column at 36% MeCN composition. The collected solution was evaporated to dryness to give HL as a light yellow powder (0.207 g, 11%). ESI-MS (*m*/*z*): Calcd. for $C_{16}H_{24}N_7O_7$ $(M+H)^+$: 426.17, found 426.18. ^{1}H NMR (500 MHz, MeOH-d_4, 25 °C): δ 8.13 (s, 2H), 3.90 (s, 4H), 3.35 (s, 8H). $^{13}C\{^1H\}$ NMR (126 MHz, MeOH-d_4, 25 °C): δ 176.11 (C=O), 163.57 (Ar–OH), 140.79 (Ar–NO_2), 127.67 (Ar–H), 125.70 (Ar–CH_2), 57.90 (N–**C**H_2–CO), 55.95 (Ar–**C**H_2–N). UV-Vis absorption spectra (16 μM; MeOH, 25 °C): 404 nm (ε = 38900 M^{-1} cm^{-1}); (13 μM; 10 mM HEPES buffered at pH 7.3, 25 °C): 414 nm (ε = 13100 M^{-1} cm^{-1}). FT-IR (ATR, cm^{-1}): 3304 (w, broad); 3190 (w, broad); 1657 (s); 1594 (m); 1511 (m); 1448 (w); 1413 (w); 1326 (s); 1280 (m); 1262 (m); 1132 (w); 1099 (m); 984 (w); 745 (w); 580 (m).

Synthesis of N,N′-[(2-hydroxy-5-nitro-1,3-phenylene)bis(methylene)]bis[N-(carboxymethyl)-(N,N′-dimethylglycinamide)] (HL′). This compound was synthesized following a modified literature procedure.[11l] Under an atmosphere of dinitrogen, 2,2′-(azanediyl)bis(*N*,*N*′-dimethylacetamide) (1.14 g, 6.09 mmol) was dissolved in MeCN (200 mL) to give a pale yellow solution, and *N*,*N*-diisopropylethylamine (0.826 g, 6.39 mmol) was subsequently added. This solution was heated to reflux and while stirring, a light yellow solution of 2,6-bis(bromomethyl)-4-nitrophenol (0.988 g, 3.04 mmol) in MeCN (20 mL) was added dropwise over the course of 1 h. The resulting orange solution was stirred at reflux for 20 h, and the solvent was subsequently removed under reduced pressure to give a brown residue. The crude solid was stirred in THF (100 mL) for 12 h at 25 °C, then filtered and the orange filtrate was evaporated to dryness to give an orange oil. Purification by column chromatography (aluminum oxide basic, 10:90,

MeOH:CH_2Cl_2) yielded HL′ as a light orange solid (0.817 g, 50%). ESI-MS (*m*/*z*): Calcd. for $C_{24}H_{40}N_7O_7$ $(M+H)^+$: 538.30, found 538.21. ^{1}H NMR (500 MHz, $CDCl_3$, 25 °C): δ 8.06 (s, 2H), 3.89 (s, 4H), 3.52 (s, 8H), 2.91 (broad s, 24H). $^{13}C\{^1H\}$ NMR (126 MHz, $CDCl_3$, 25 °C): δ 170.48 (C=O), 162.49 (Ar–OH), 139.43 (Ar–NO_2), 125.78 (Ar–H), 125.06 (Ar–CH_2), 55.36 (N–**C**H_2–CO), 54.06 (Ar–**C**H_2–N), 36.71 (CH_3), 35.69 (CH_3). UV-Vis absorption spectrum (56 μM; MeOH, 25 °C): 325 nm (ε = 9500 M^{-1} cm^{-1}). FT-IR (ATR, cm^{-1}): 3449 (w, broad); 2927 (w, broad); 1632 (s); 1590 (m); 1505 (m); 1445 (w); 1398 (m); 1324 (s); 1282 (s); 1260 (s); 1121 (m); 1094 (m); 992 (w); 812 (w); 750 (w); 640 (w).

Synthesis of tetraisopropyl dichloromethanediphosphonate. This compound was synthesized following a modified literature procedure.[36] To a vigorously stirred aqueous solution of 5% (w/v) sodium hypochlorite (173 g, 116 mmol) at 0 °C, tetraisopropyl methanediphosphonate (5.00 g, 14.5 mmol) was added dropwise. The colorless solution became cloudy, and then it was warmed to 25 °C and stirred for an additional 1 h. The resulting white suspension was extracted with hexanes (4 × 50 mL), and the combined extracts were dried over magnesium sulfate, filtered, and dried under reduced pressure to give the title compound as a white solid (5.69 g, 95%). ^{1}H NMR (500 MHz, $CDCl_3$, 25 °C): δ 4.96 (m, 4H), 1.41 (d, $^3J_{HH}$ = 6.2 Hz, 24H). $^{31}P\{^1H\}$ NMR (202 MHz, $CDCl_3$, 25 °C): δ 6.70 (s).

Synthesis of tetraisopropyl chloromethanediphosphonate. This compound was synthesized following a modified literature procedure.[36] Tetraisopropyl dichloromethanediphosphonate (1.50 g, 3.63 mmol) was dissolved in ethanol (15 mL) and stirred vigorously at 0 °C. To this, a solution of sodium sulfite (1.69 g, 13.4 mmol) in deionized H_2O (50 mL) was added dropwise over the course of 5 min, resulting in the formation of a cloudy solution. The reaction mixture was stirred

for an additional 1 h at 25 °C and then extracted with $CHCl_3$ (4 × 50 mL). The combined colorless $CHCl_3$ layer was dried over magnesium sulfate, filtered, and the solvent removed under reduced pressure to give the product as a colorless oil (1.10 g, 80%). ^{1}H NMR (500 MHz, $CDCl_3$, 25 °C): δ 4.86 (m, 4H), 3.89 (t, $^{2}J_{HP}$ = 17.7 Hz, 1H), 1.38 (broad d, $^{3}J_{HH}$ = 6.5 Hz, 24H). $^{31}P\{^{1}H\}$ NMR (202 MHz, $CDCl_3$, 25 °C): δ 11.56 (s).

Synthesis of chloromethanediphosphonic acid (H_4CMDP). Tetraisopropyl chloromethanediphosphonate (1.10 g, 2.90 mmol) was dissolved in 6 M hydrochloric acid solution in deionized H_2O (25 mL) and stirred under reflux for 24 h. The pale yellow solution was evaporated to dryness, the resulting light yellow oil was dissolved in MeOH (50 mL), and the solvent removed under reduced pressure. The obtained light yellow oil was dried under reduced pressure for 48 h to afford the title compound as a pale yellow oil in near quantitative yield. ^{1}H NMR (400 MHz, D_2O, 25 °C): δ 4.01 (t, $^{2}J_{HP}$ = 16.2 Hz, 1H). $^{31}P\{^{1}H\}$ NMR (162 MHz, D_2O, 25 °C): δ 11.59 (s). $^{13}C\{^{1}H\}$ NMR (126 MHz, D_2O, 25 °C): δ 46.57 (t, $^{1}J_{CP}$ = 134.5 Hz, 1C).

3.5.2 Supplementary Schemes

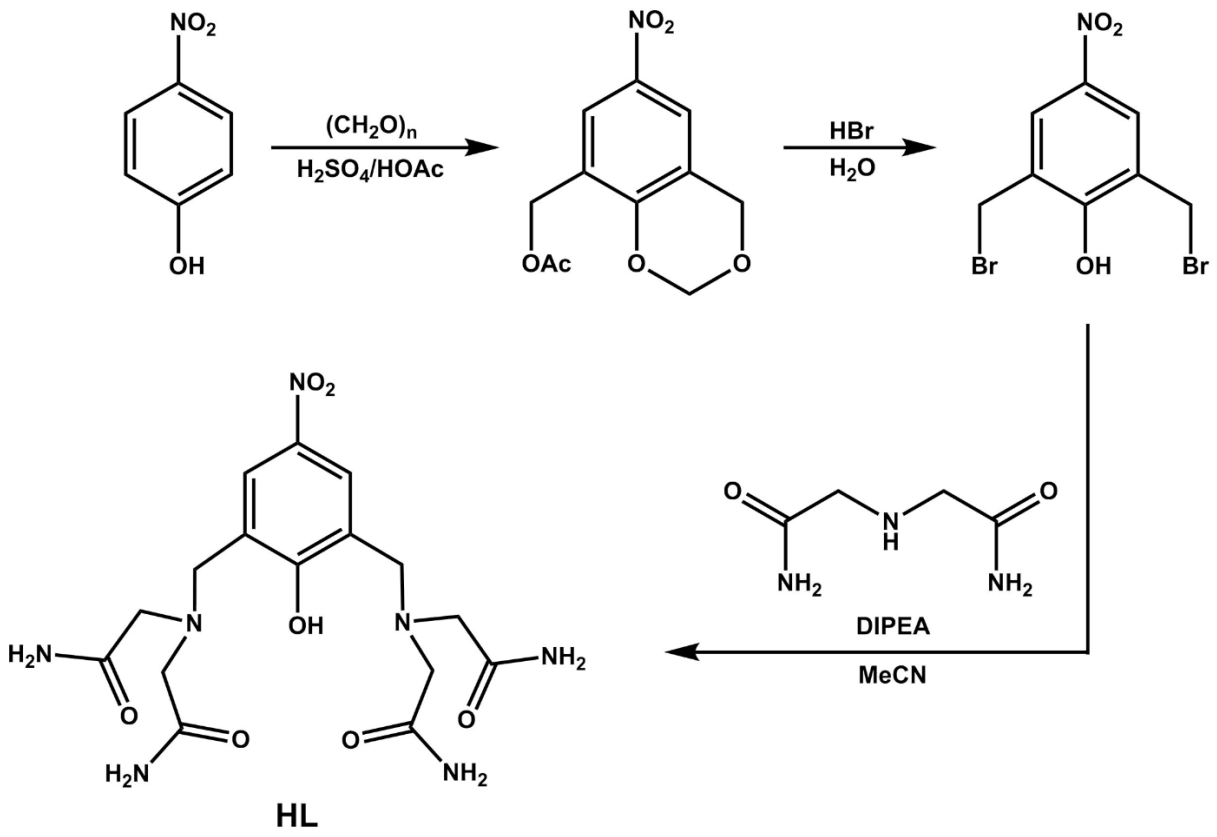

Scheme 3.1 Syntheses of organic precursors and ligand HL.

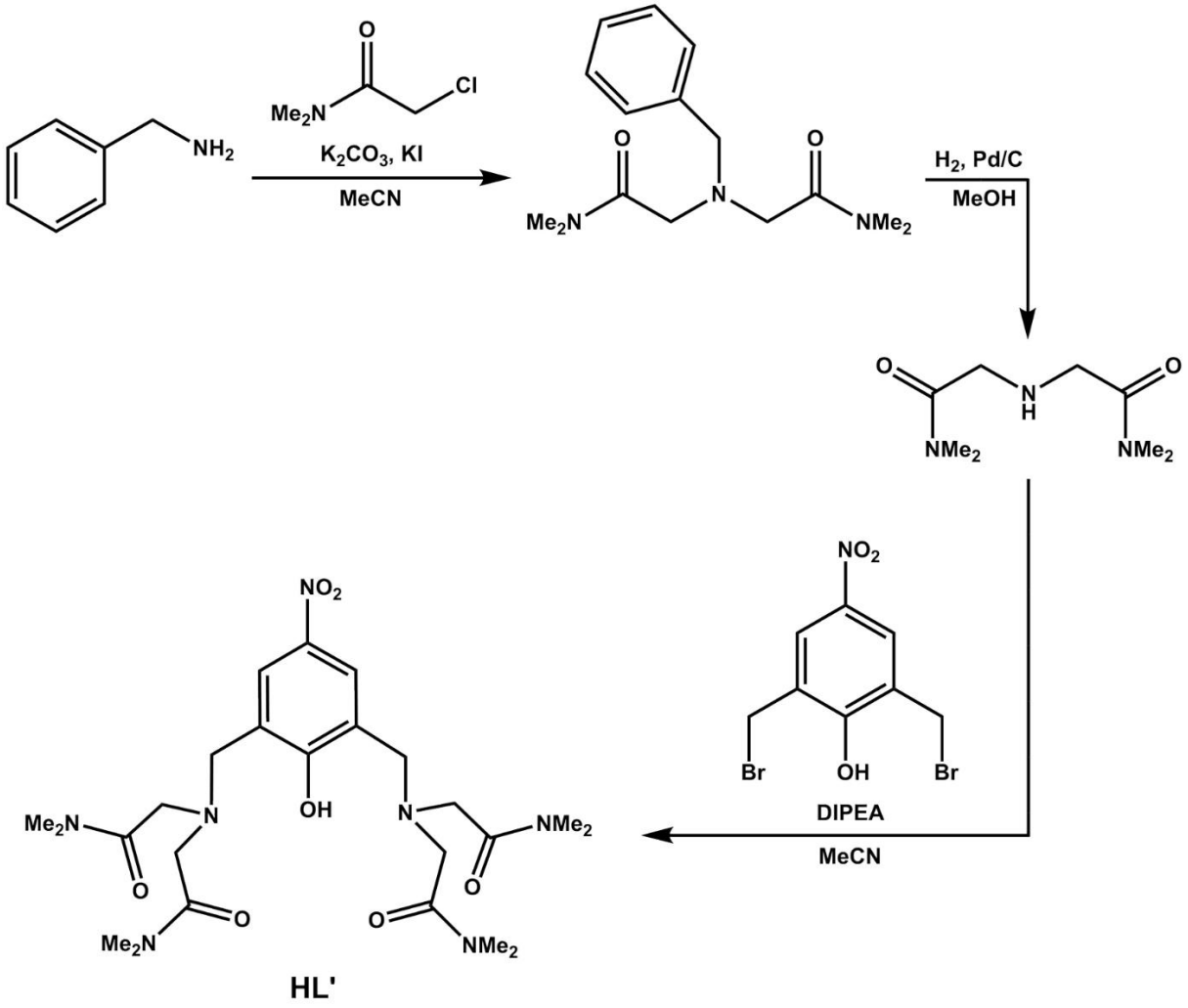

Scheme 3.2 Syntheses of organic precursors and ligand HL′.

3.5.3 Supplementary Figures

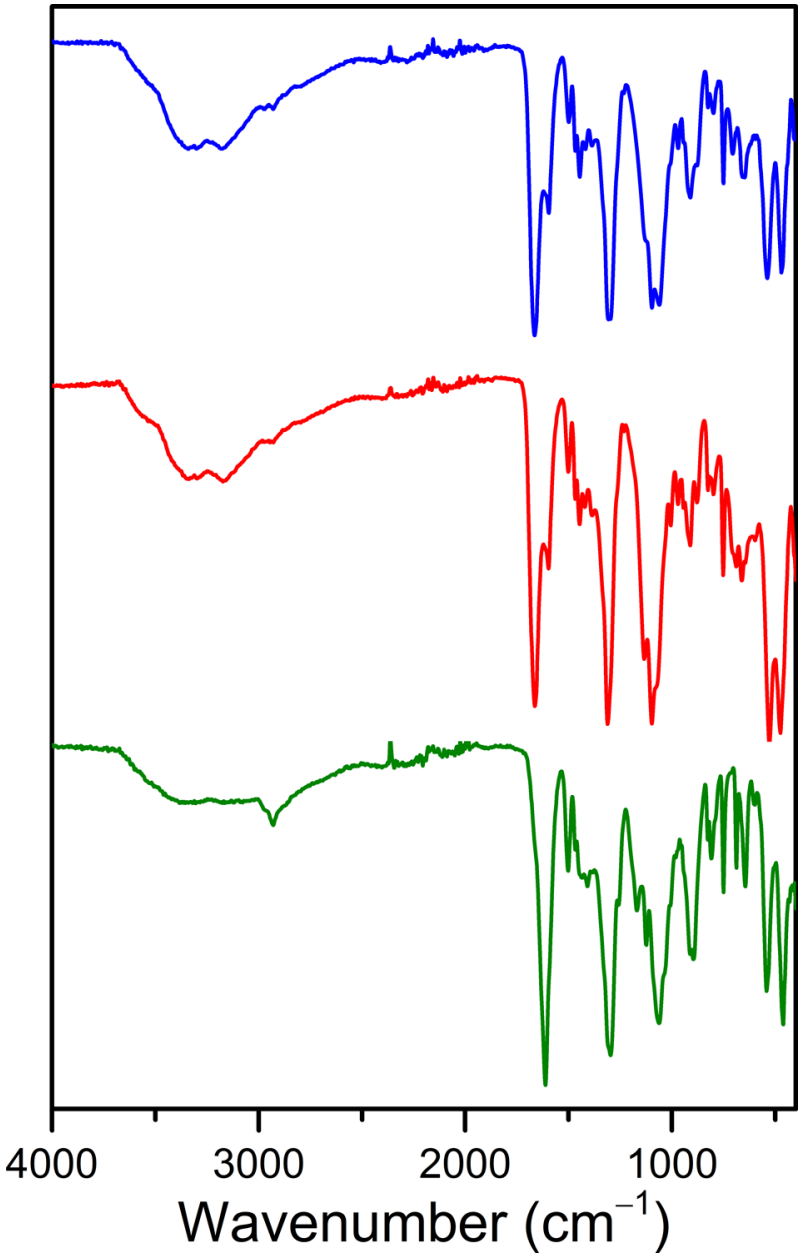

Figure 3.7 Stacked FT-IR spectra of **1** (blue), **2** (red), and **3** (green) at ambient temperature.

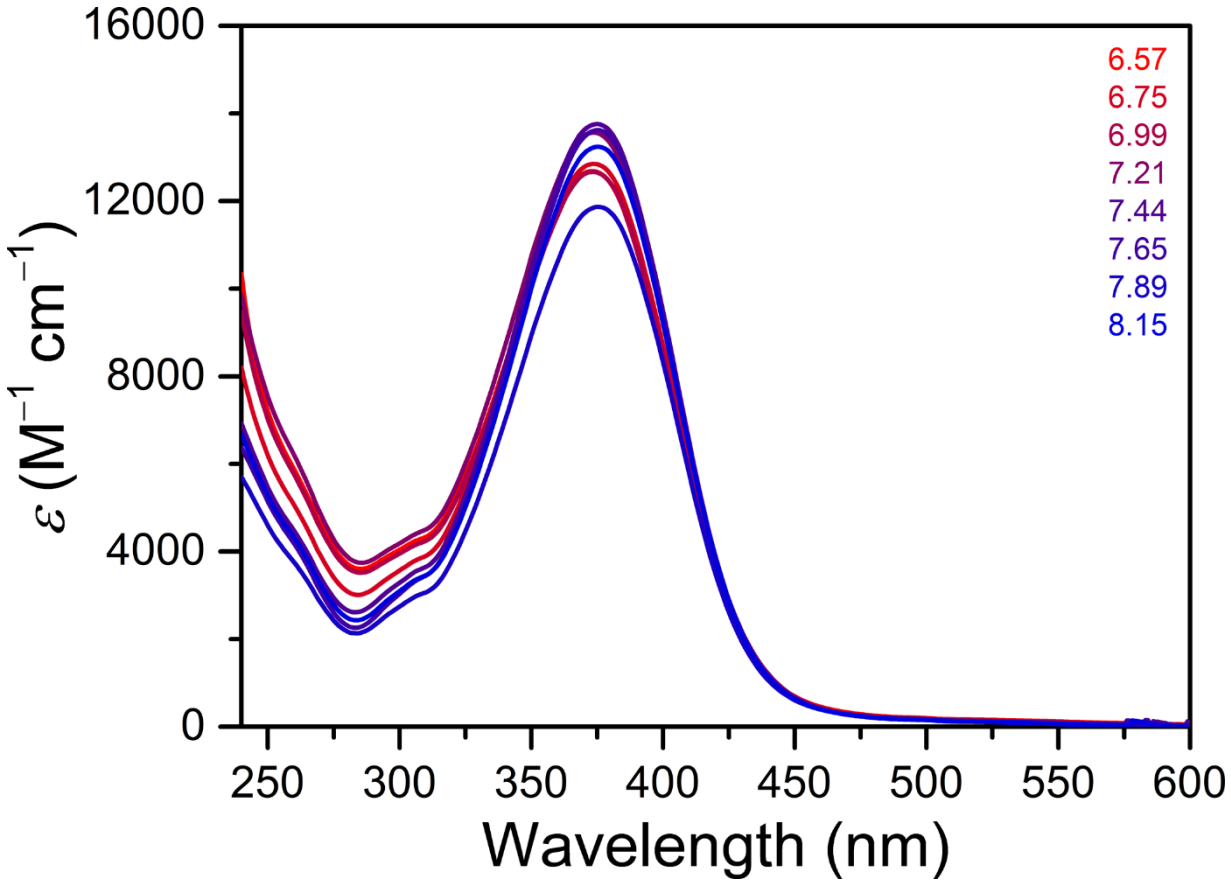

Figure 3.8 Variable-pH UV-Vis absorption spectra for 64 μM of **1** in aqueous solutions containing 50 mM HEPES and 100 mM NaCl at ambient temperature. Spectra were measured in the pH range used for CEST experiments, from pH 6.57 to 8.15. Colored numbers in the legend denote the pH of the solutions measured with a pH electrode and the corresponding color of each sample. Note that the molar absorptivity (ε) is plotted against wavelength.

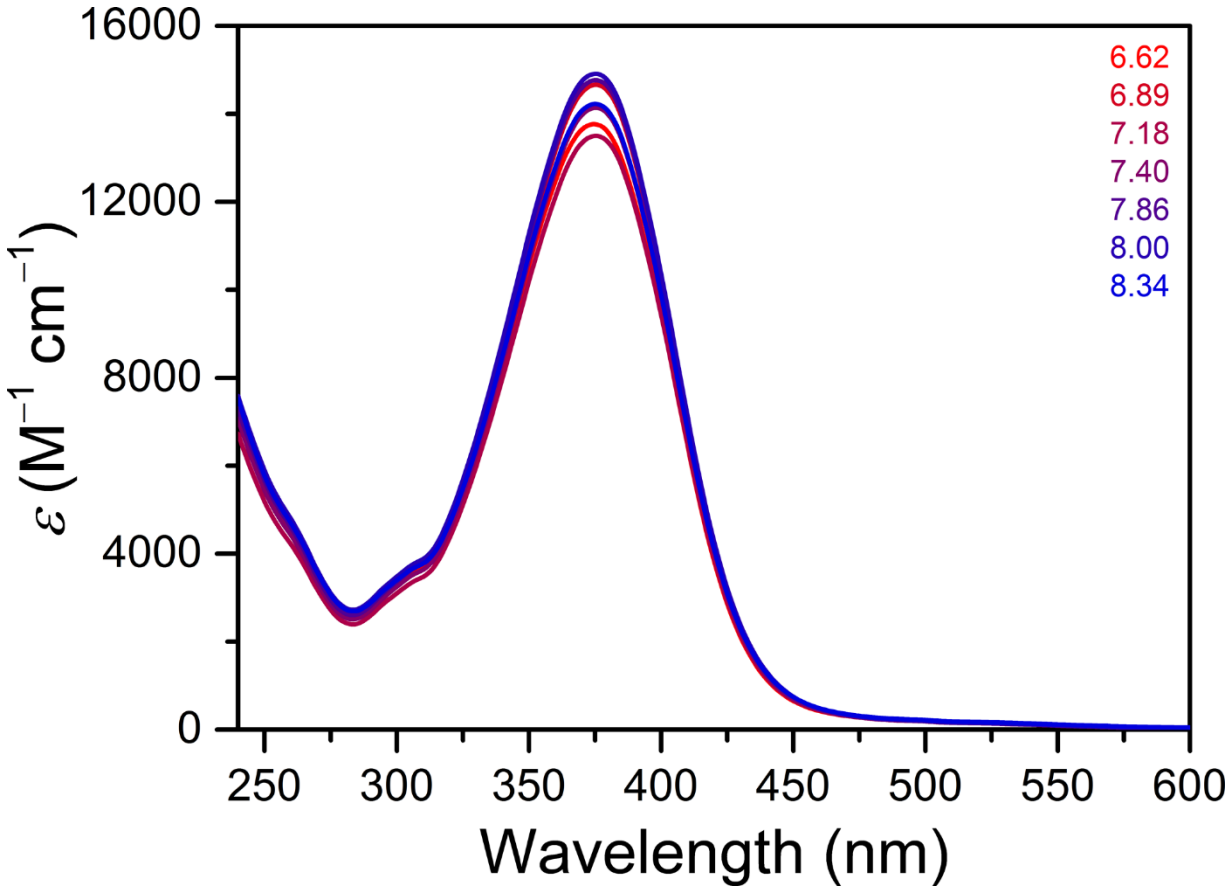

Figure 3.9 Variable-pH UV-Vis absorption spectra for 80 μM of **2** in aqueous solutions containing 50 mM HEPES and 100 mM NaCl at ambient temperature. Spectra were measured in the pH range used for CEST experiments, from pH 6.62 to 8.34. Colored numbers in the legend denote the pH of the solutions measured with a pH electrode and the corresponding color of each sample. Note that the molar absorptivity (ε) is plotted against wavelength.

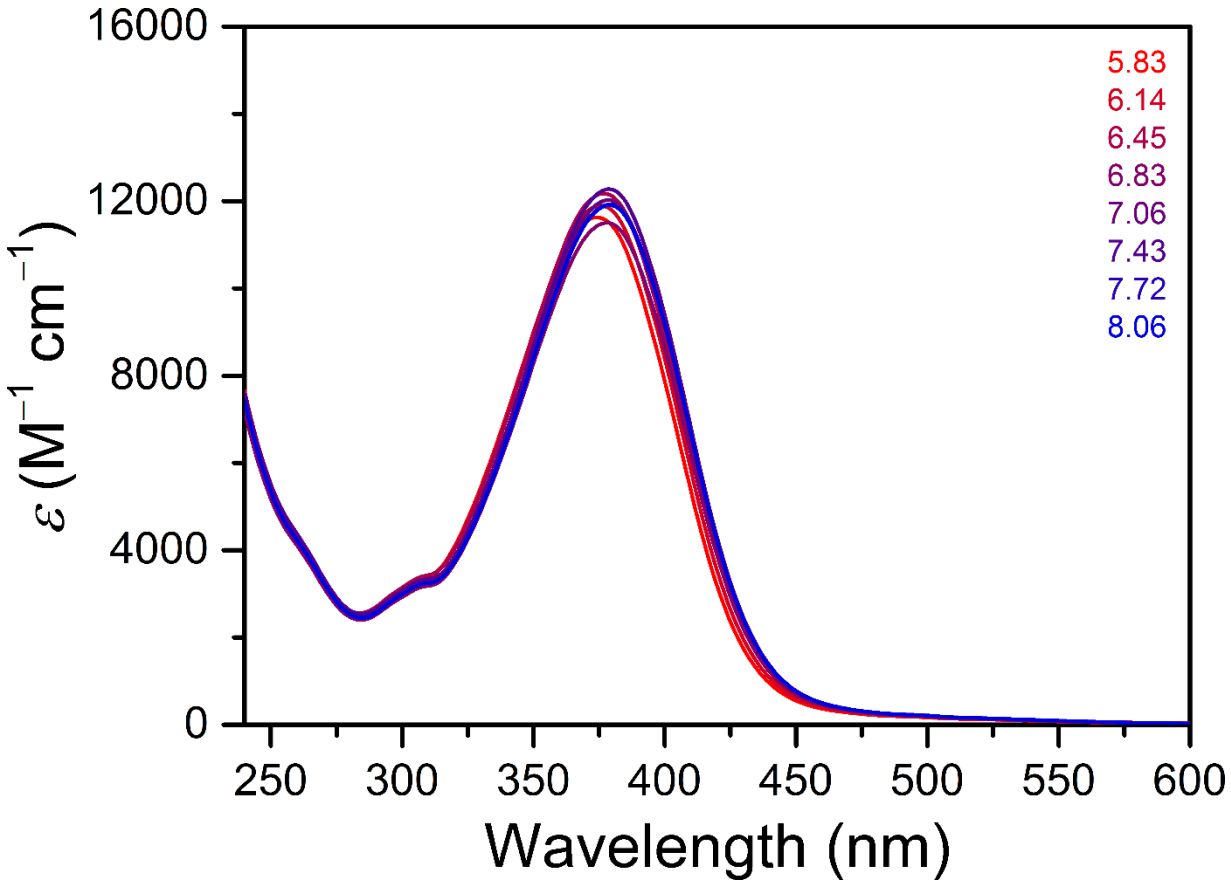

Figure 3.10 Variable-pH UV-Vis absorption spectra for 87 μM of **3** in aqueous solutions containing 50 mM HEPES and 100 mM NaCl at ambient temperature. Spectra were measured in the pH range used for CEST experiments, from pH 5.83 to 8.06. Colored numbers in the legend denote the pH of the solutions measured with a pH electrode and the corresponding color of each sample. Note that the molar absorptivity (ε) is plotted against wavelength.

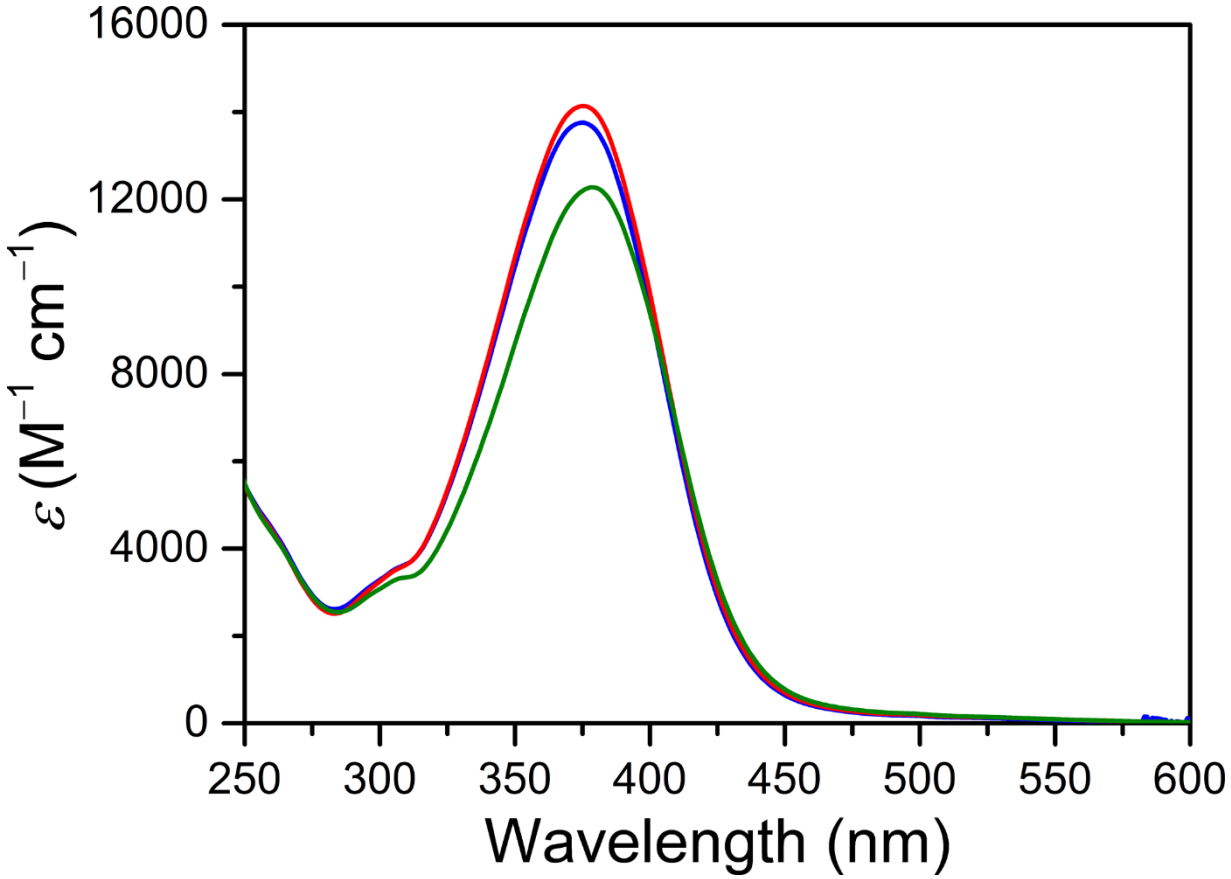

Figure 3.11 Comparison of the UV-Vis absorption spectra for **1** (blue), **2** (red), and **3** (green) in aqueous solutions containing 50 mM HEPES and 100 mM NaCl buffered at pH 7.4 at ambient temperature. Note that the molar absorptivity (ε) is plotted against wavelength.

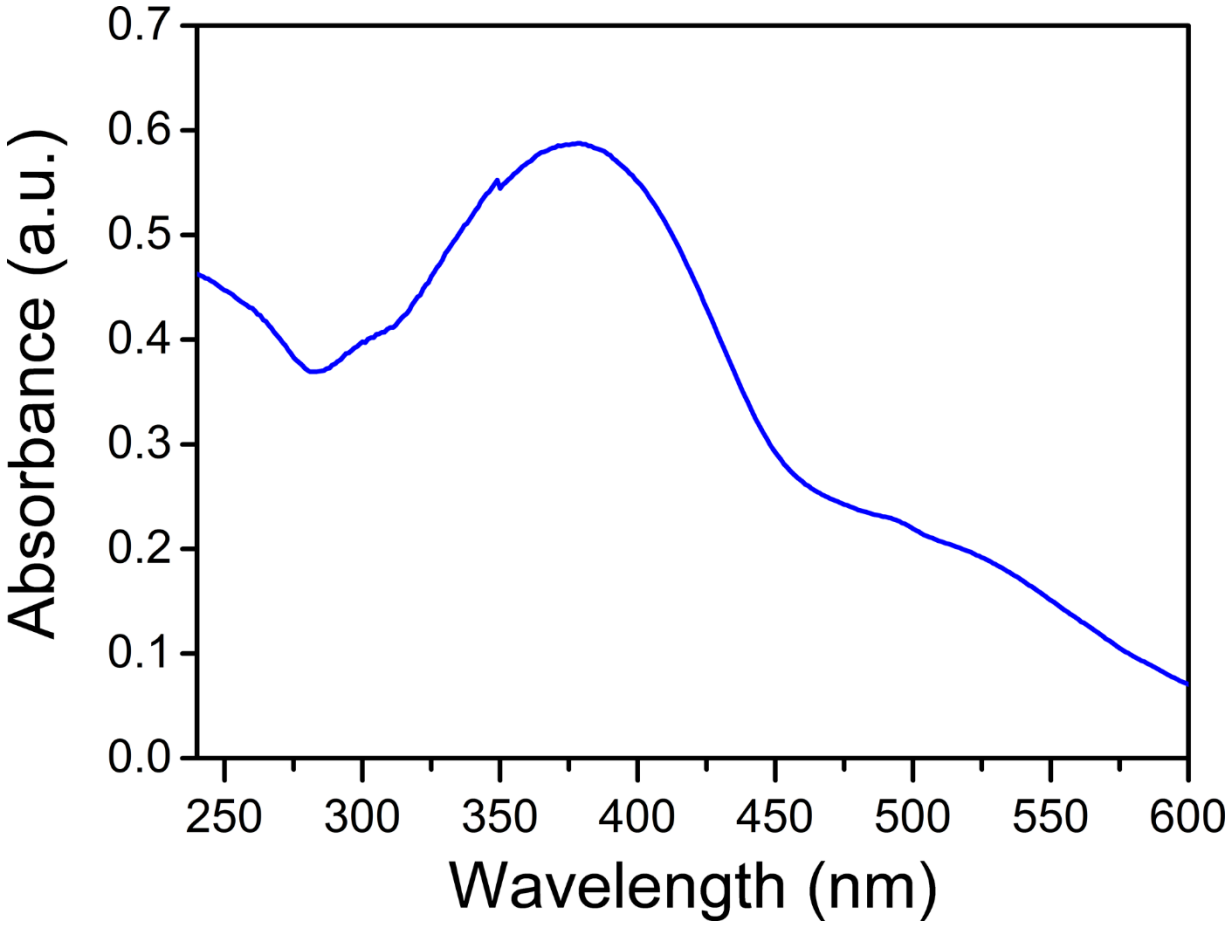

Figure 3.12 Diffuse reflectance UV-Vis spectrum of a crystalline sample for **1′** diluted with $BaSO_4$ powder at ambient temperature.

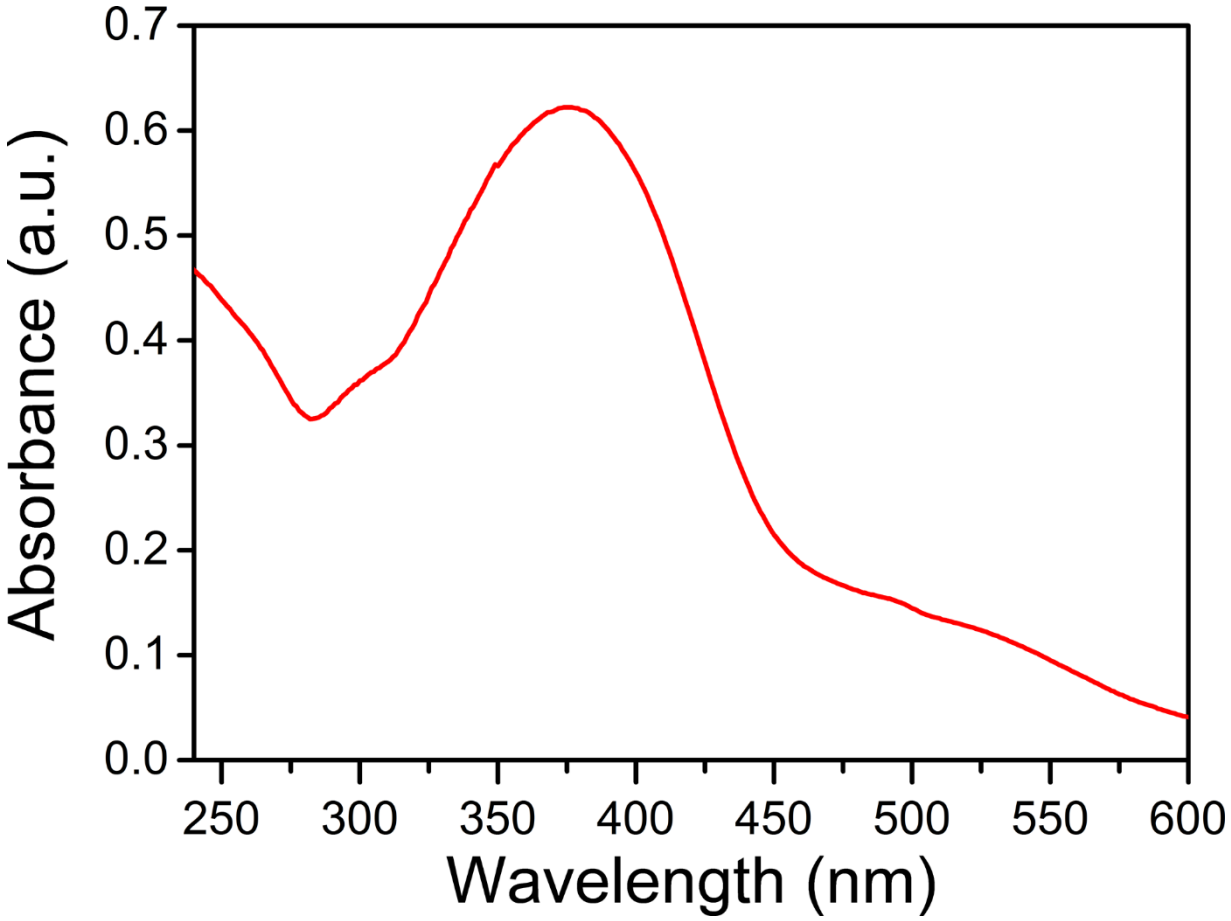

Figure 3.13 Diffuse reflectance UV-Vis spectrum for a crystalline sample of **2′** diluted with $BaSO_4$ powder at ambient temperature.

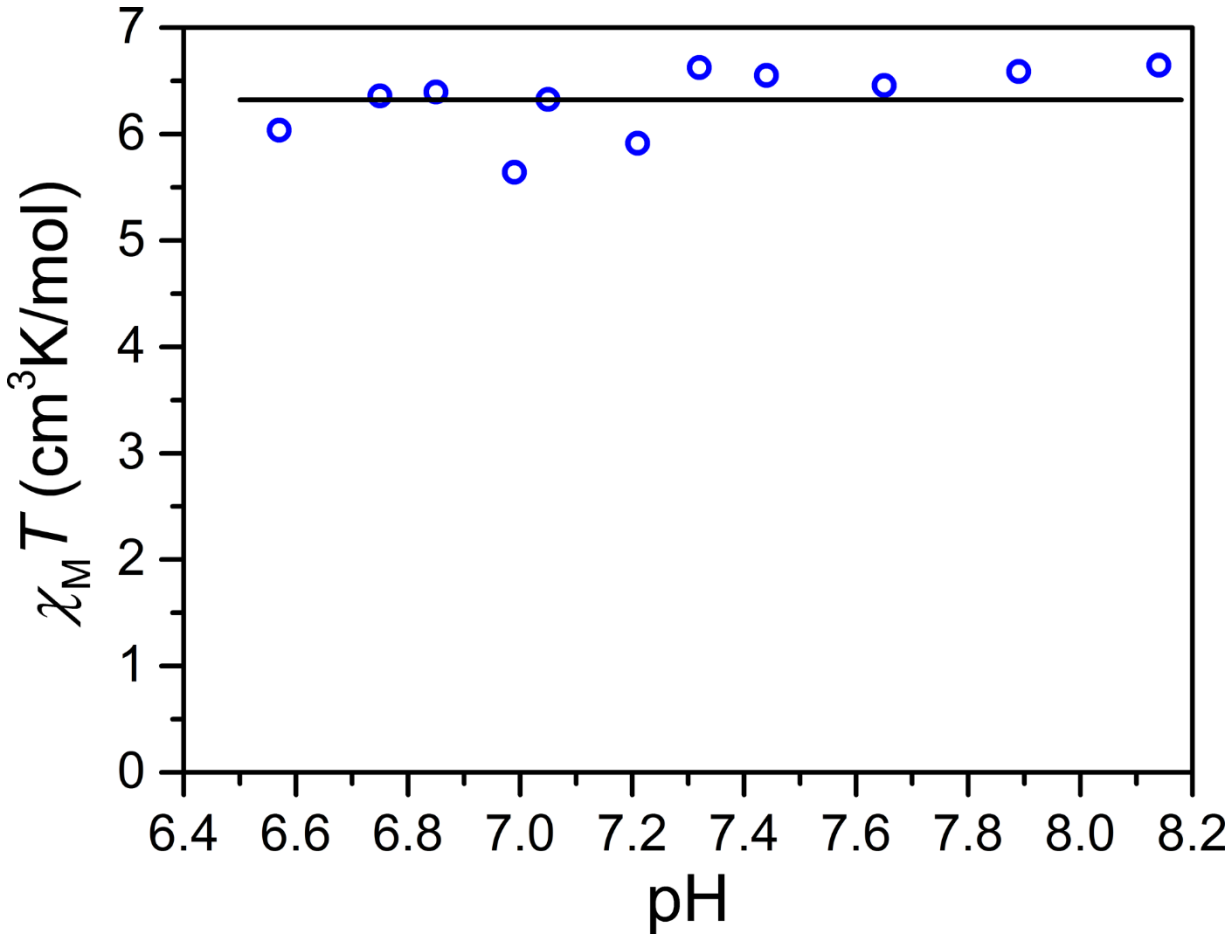

Figure 3.14 Variable-pH dc magnetic susceptibility data for **1** in aqueous solutions containing 50 mM HEPES and 100 mM NaCl at 37 °C, obtained using the Evans method[21] (see Equation 3.2). Circles represent experimental data and the solid black line denotes the average value of $\chi_M T$ = 6.3(3) cm^3 K mol^{-1} (see Table 3.3).

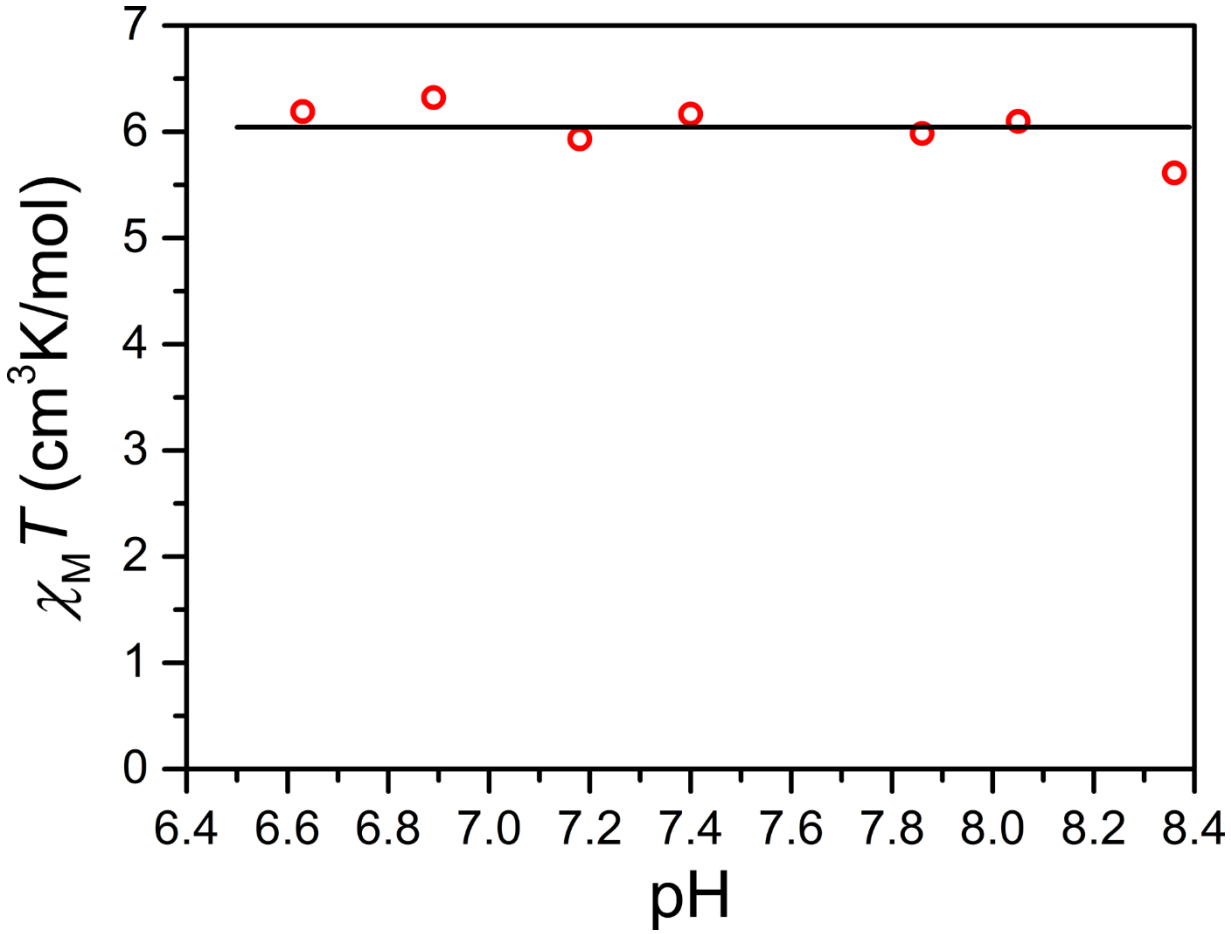

Figure 3.15 Variable-pH dc magnetic susceptibility data for **2** in aqueous solutions containing 50 mM HEPES and 100 mM NaCl at 37 °C, obtained using the Evans method[21] (see Equation 3.2). Circles represent experimental data and the solid black line denotes the average value of $\chi_M T$ = 6.0(2) cm^3 K mol^{-1} (see Table 3.3).

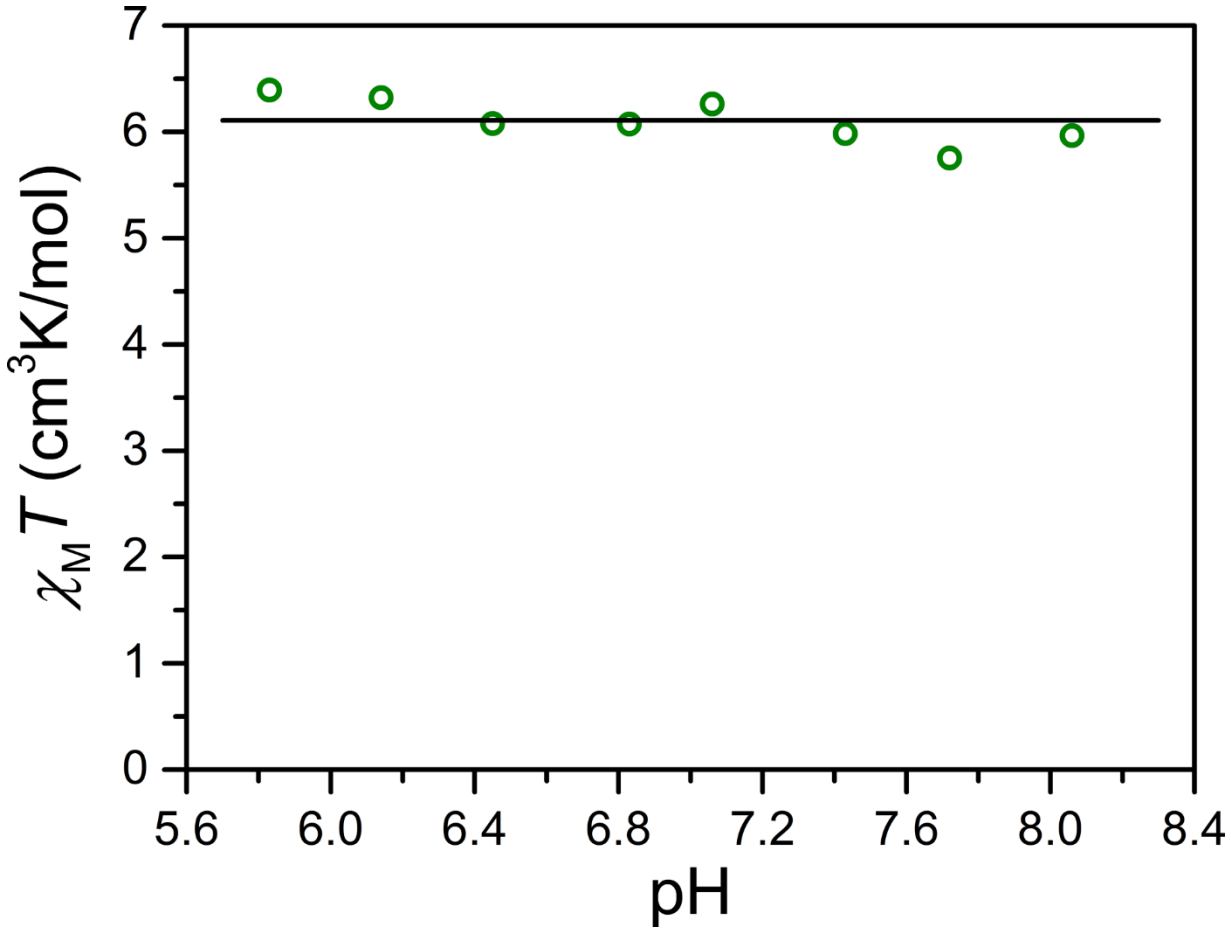

Figure 3.16 Variable-pH dc magnetic susceptibility data for **3** in aqueous solutions containing 50 mM HEPES and 100 mM NaCl at 37 °C, obtained using the Evans method[21] (see Equation 3.2). Circles represent experimental data and the solid black line denotes the average value of $\chi_M T$ = 6.1(2) cm^3 K mol^{-1} (see Table 3.3).

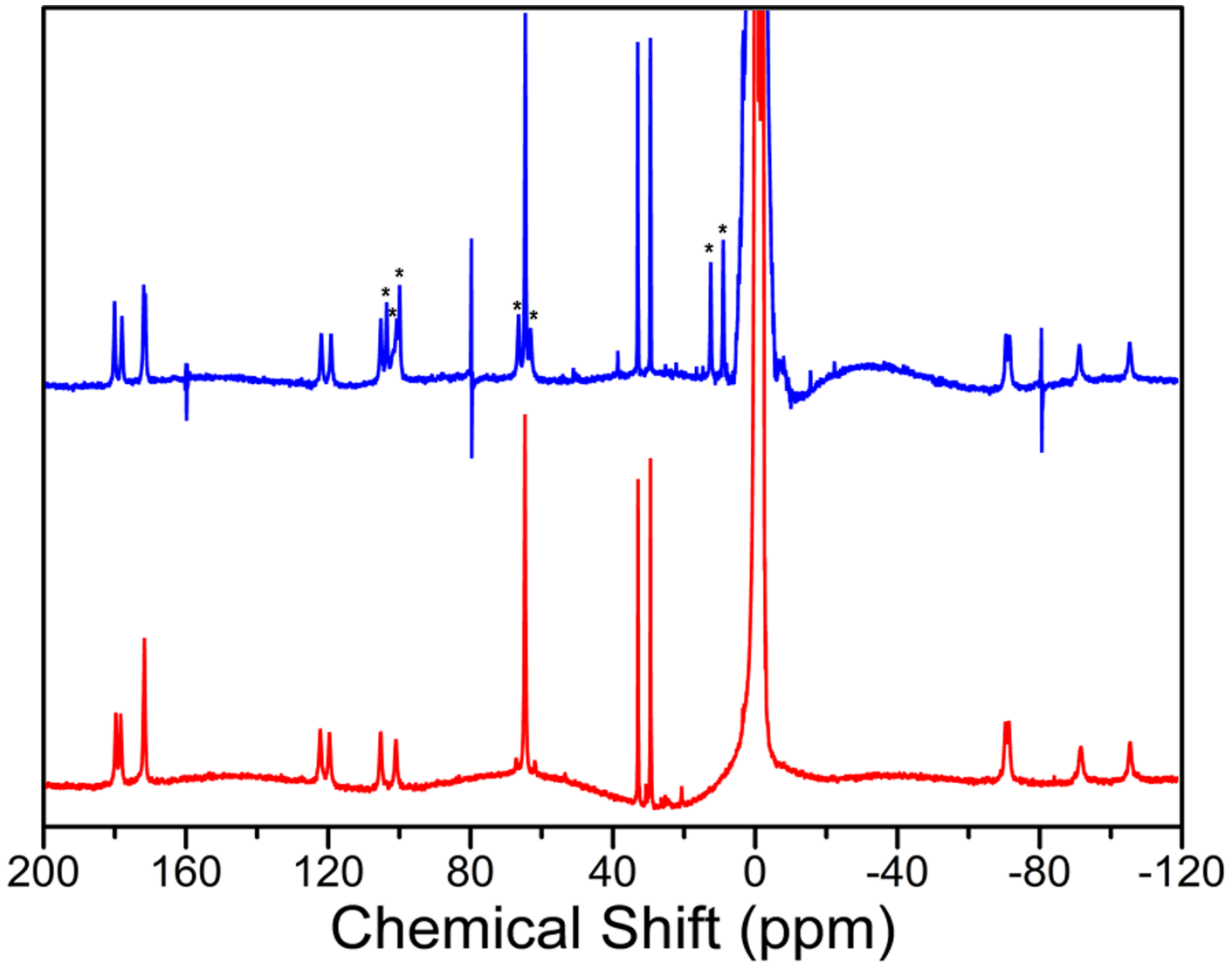

Figure 3.17 Stacked ^{1}H NMR spectra of **1** in an aqueous solution containing 50 mM HEPES and 100 mM NaCl buffered at pH 7.18 (blue) and in neutral D_2O (red) at 37 °C. The asterisks denote peaks corresponding to exchangeable carboxamide and hydroxyl protons that are not present in the spectrum recorded in D_2O. The sharp features at 160, 80, and −80 ppm in the spectrum recorded in buffer are instrument-derived artifacts.

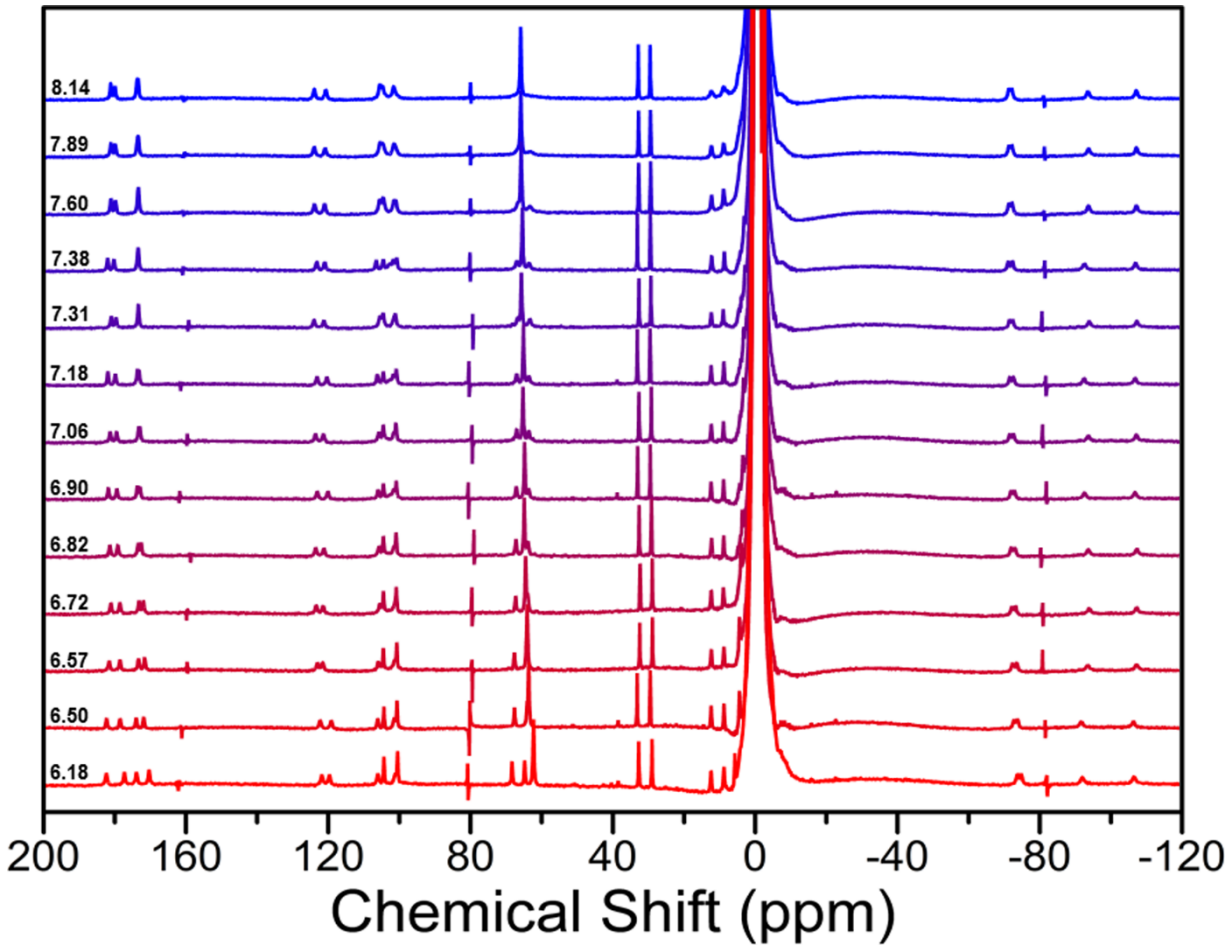

Figure 3.18 Variable-pH ^{1}H NMR spectra of 12.8 mM of **1** in aqueous solutions containing 50 mM HEPES and 100 mM NaCl buffered at various pH values at 37 °C. Black numbers on the left denote the pH of the NMR sample solutions measured with a pH electrode. The sharp features at 160, 80, and −85 ppm are instrument-derived artifacts.

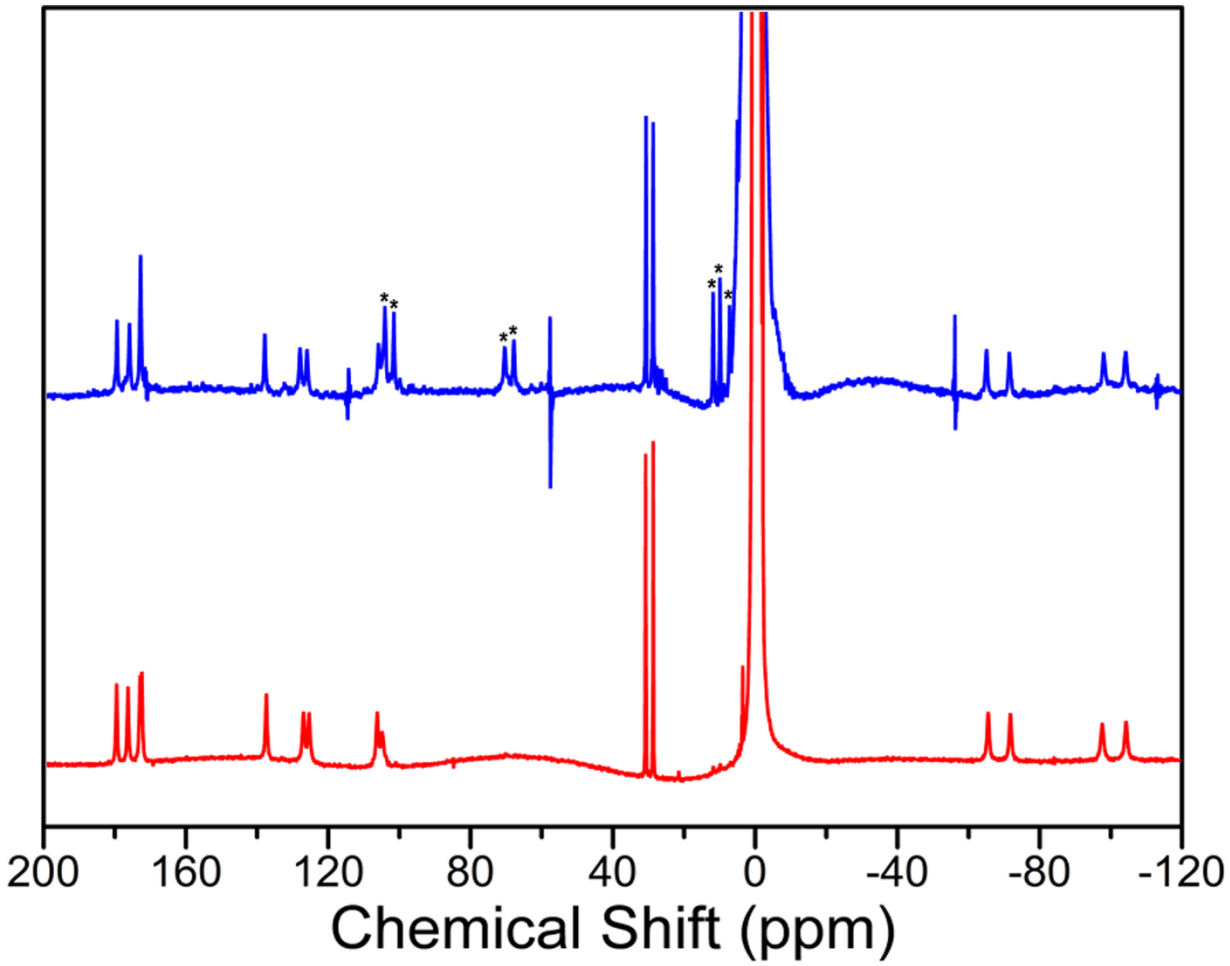

Figure 3.19 Stacked ^{1}H NMR spectra of **2** in an aqueous solution containing 50 mM HEPES and 100 mM NaCl buffered at pH 7.18 (blue) and in neutral D_2O (red) at 37 °C. The asterisks denote exchangeable carboxamide proton resonances that are not present in the spectrum recorded in D_2O. The sharp features at 114, 57, −57, and −114 ppm in the spectrum recorded in buffer are instrument-derived artifacts.

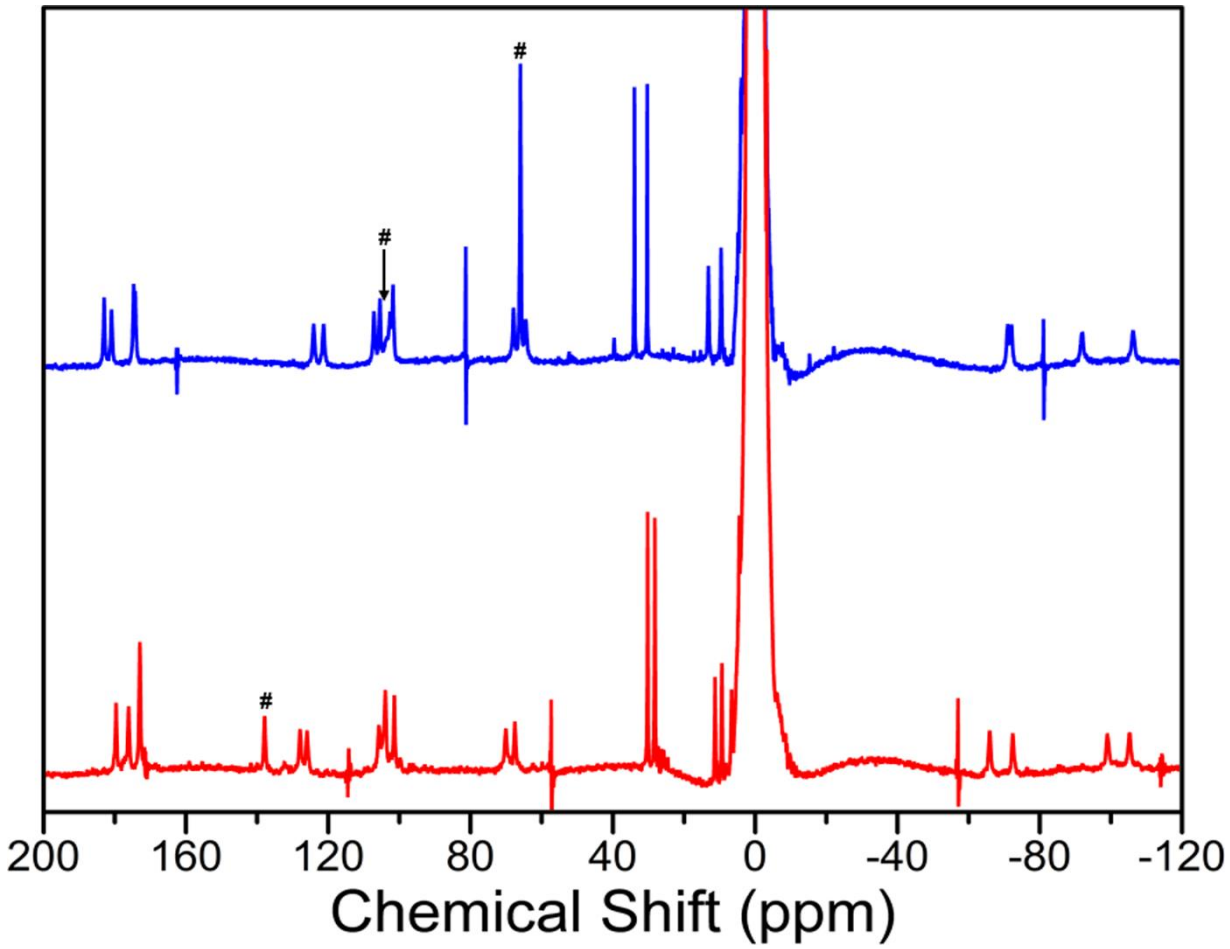

Figure 3.20 Stacked ^{1}H NMR spectra of **1** (blue) and **2** (red) in aqueous solutions containing 50 mM HEPES and 100 mM NaCl buffered at pH 7.18 at 37 °C. The number signs highlight resonances corresponding to protons on the ancillary bisphosphonates. The sharp features at 162, 81, and −81 ppm in the spectrum for **1**, and at 114, 57, −57, and −114 ppm in the spectrum for **2** are instrument-derived artifacts.

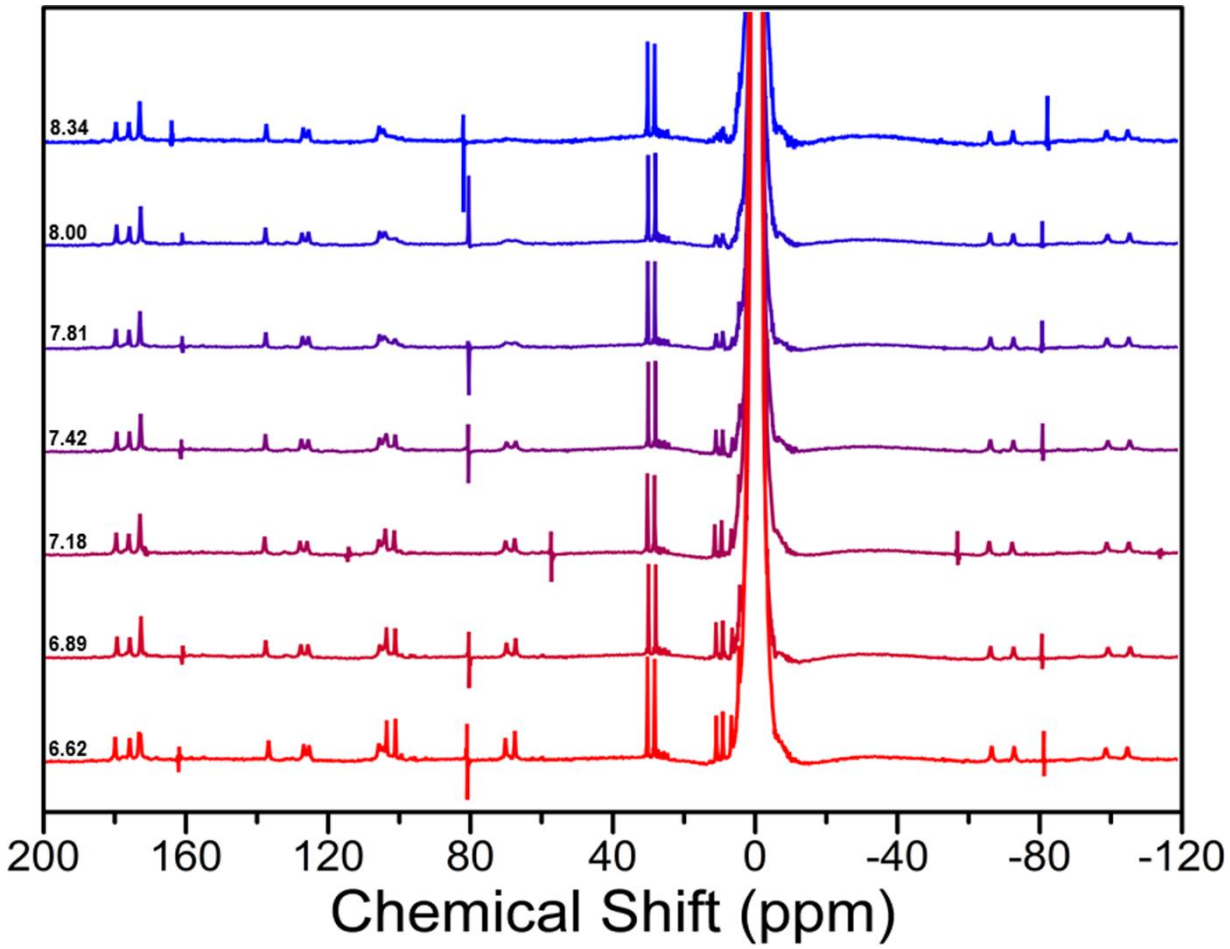

Figure 3.21 Variable-pH ^{1}H NMR spectra of 12 mM of **2** in aqueous solutions containing 50 mM HEPES and 100 mM NaCl buffered at various pH values at 37 °C. Black numbers on the left denote the pH of the NMR sample solutions measured with a pH electrode. The sharp features at 161, 81, and −81 ppm are instrument-derived artifacts. Note that these artifacts are shifted to 115, 57, and −57 ppm in the spectrum at pH 7.18.

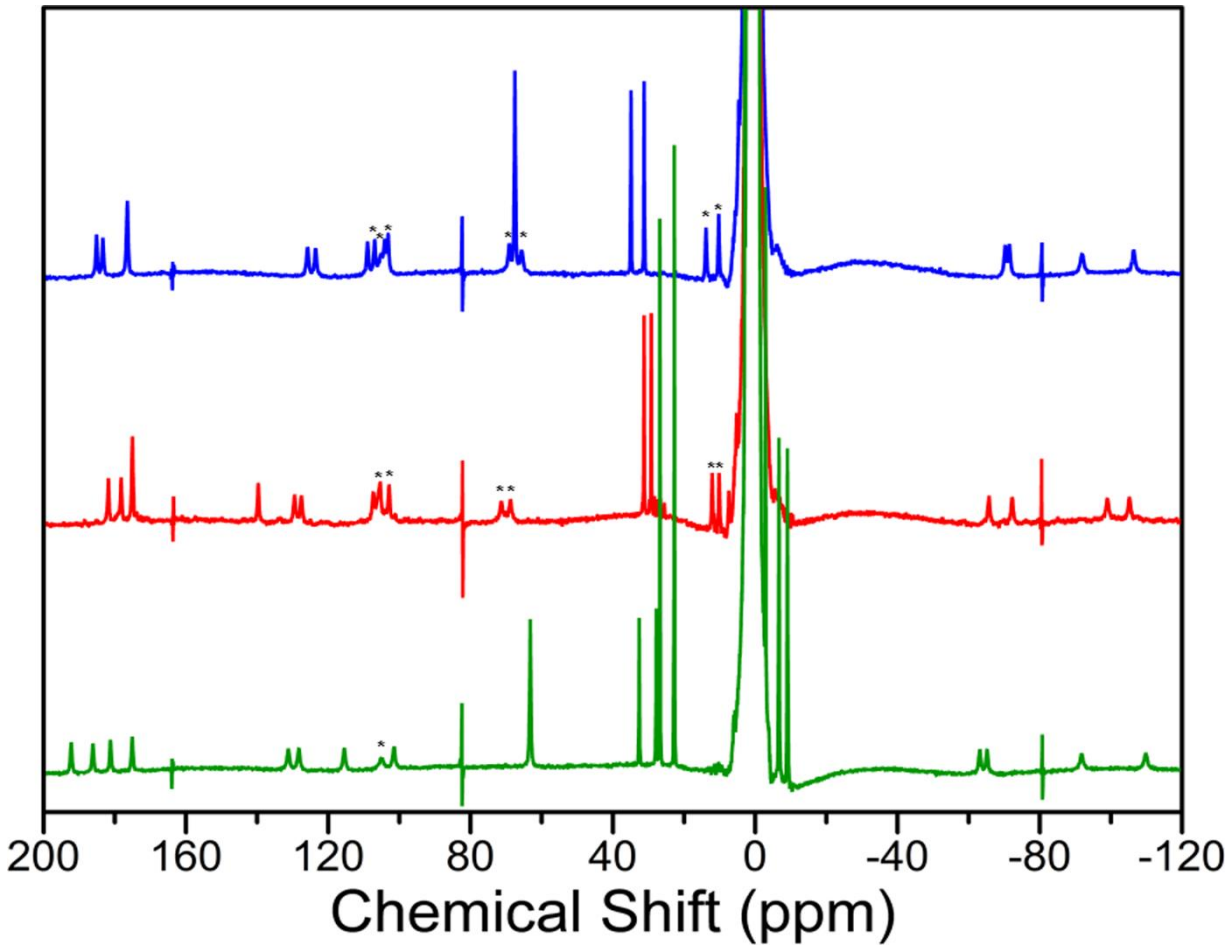

Figure 3.22 Stacked ^{1}H NMR spectra of **1** (blue), **2** (red), and **3** (green) in aqueous solutions containing 50 mM HEPES and 100 mM NaCl buffered at pH 7.38, 7.42, and 7.47, respectively, at 37 °C. The asterisks denote resonances corresponding to exchangeable protons that generate CEST peaks. The sharp features at 162, 81, and −81 ppm are instrument-derived artifacts.

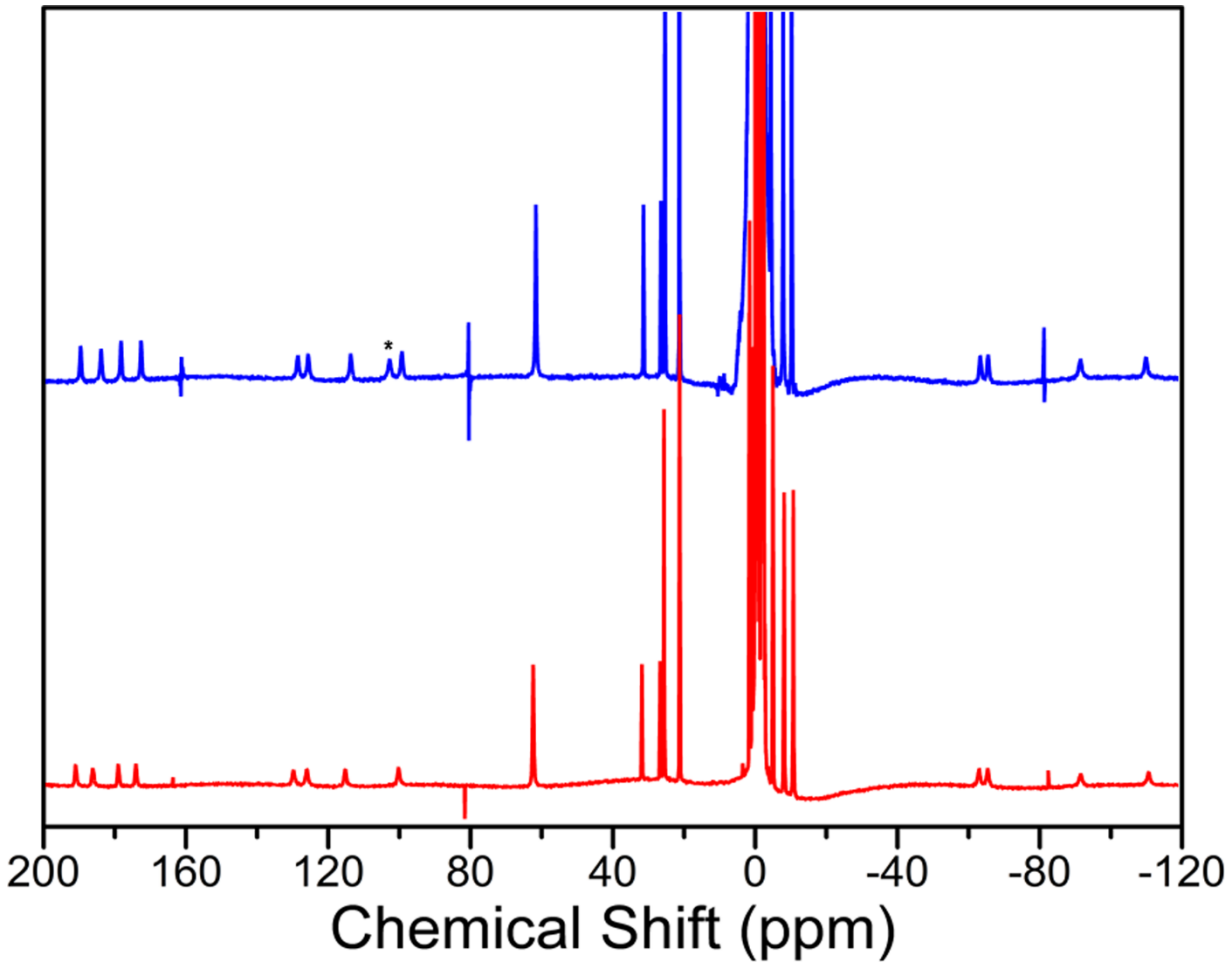

Figure 3.23 Stacked ^{1}H NMR spectra of **3** in an aqueous solution containing 50 mM HEPES and 100 mM NaCl buffered at pH 8.08 (blue) and in slightly basic D_2O (red) at 37 °C. The asterisk denotes the exchangeable hydroxyl proton resonance from etidronate that is not present in the spectrum recorded in D_2O. The sharp features at 165, 82, and −85 ppm are instrument-derived artifacts.

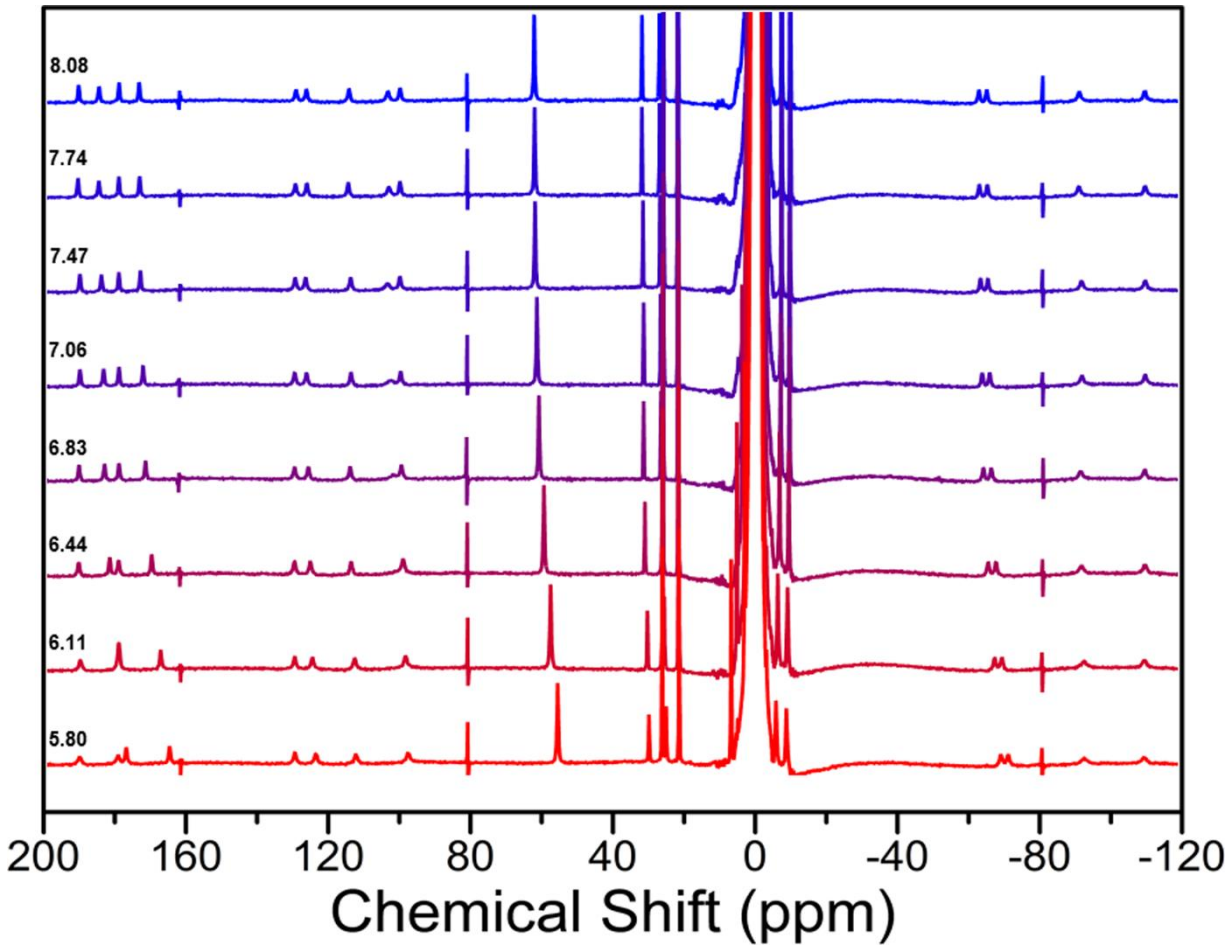

Figure 3.24 Variable-pH ^{1}H NMR spectra of 13 mM of **3** in aqueous solutions containing 50 mM HEPES and 100 mM NaCl buffered at various pH values at 37 °C. Black numbers on the left denote the pH of the NMR sample solutions measured with a pH electrode. The sharp features at 162, 81, and −81 ppm are instrument-derived artifacts.

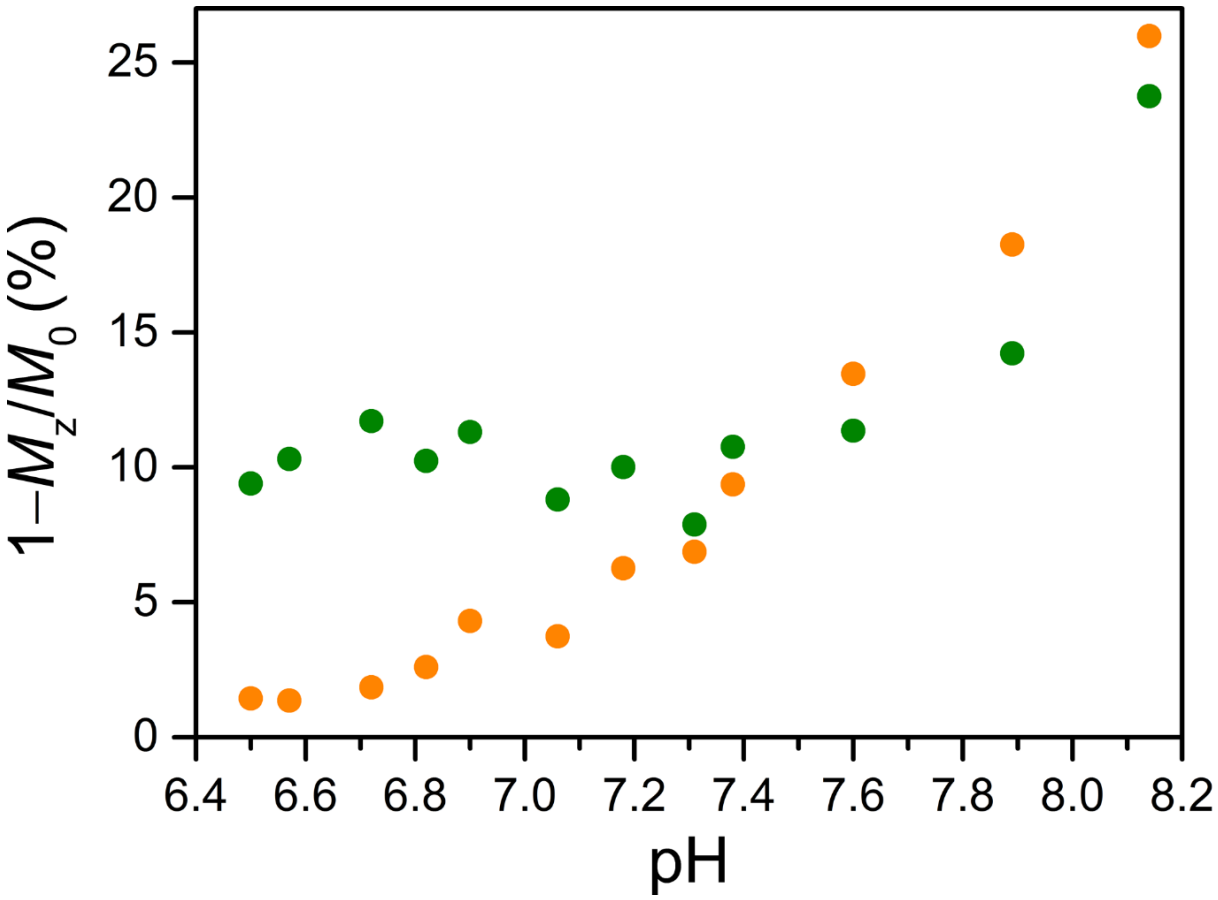

Figure 3.25 pH dependences of the CEST effects from application of presaturation at 64 ppm (yellow) and 104 ppm (green) for 12.8 mM of **1** in aqueous solutions containing 50 mM HEPES and 100 mM NaCl at 37 °C.

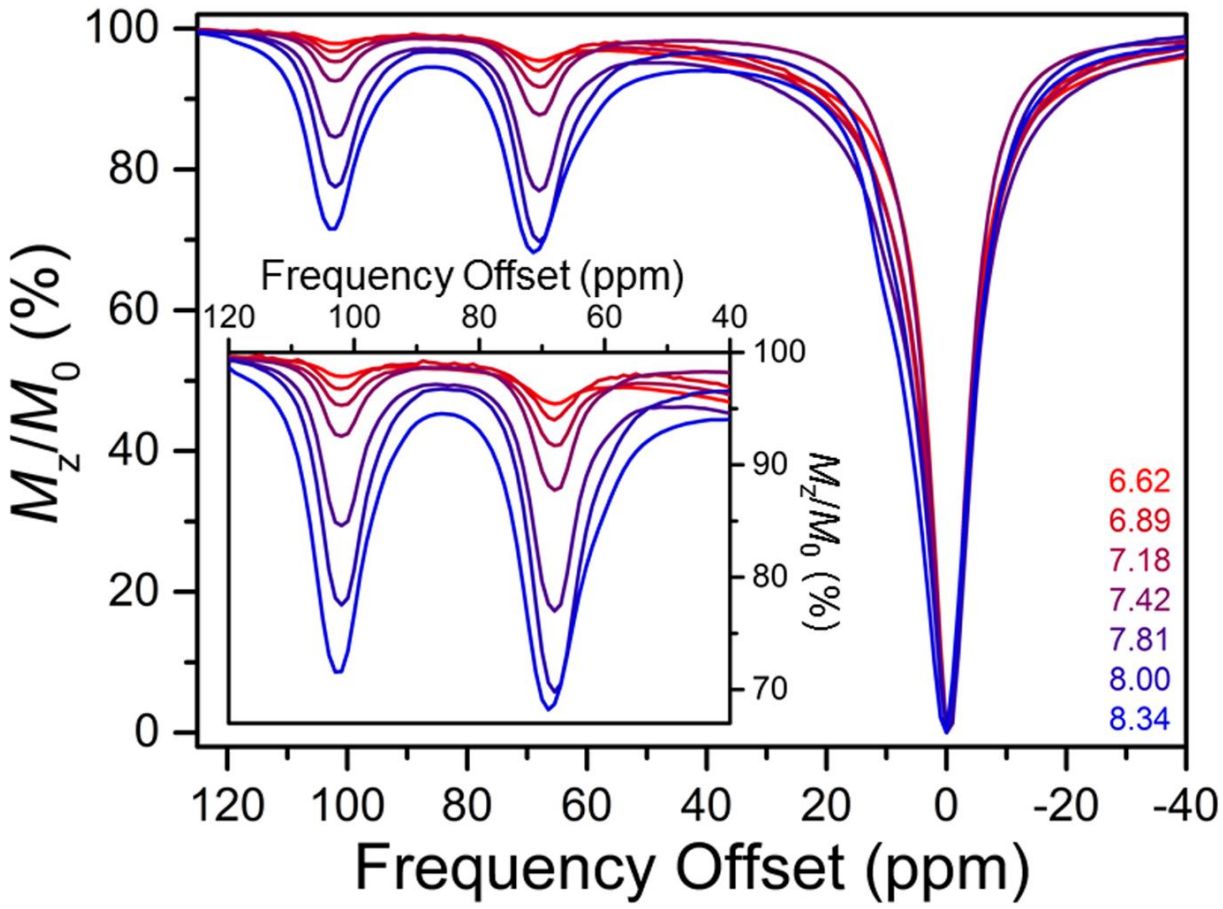

Figure 3.26 Variable-pH CEST spectra for 12 mM of **2** in aqueous solutions containing 50 mM HEPES and 100 mM NaCl buffered at pH 6.62–8.34 (red to blue) at 37 °C. Colored numbers in the legend denote the pH of the solutions measured with a pH electrode and the corresponding color of each sample. Inset: Expanded view of the CEST peaks of interest.

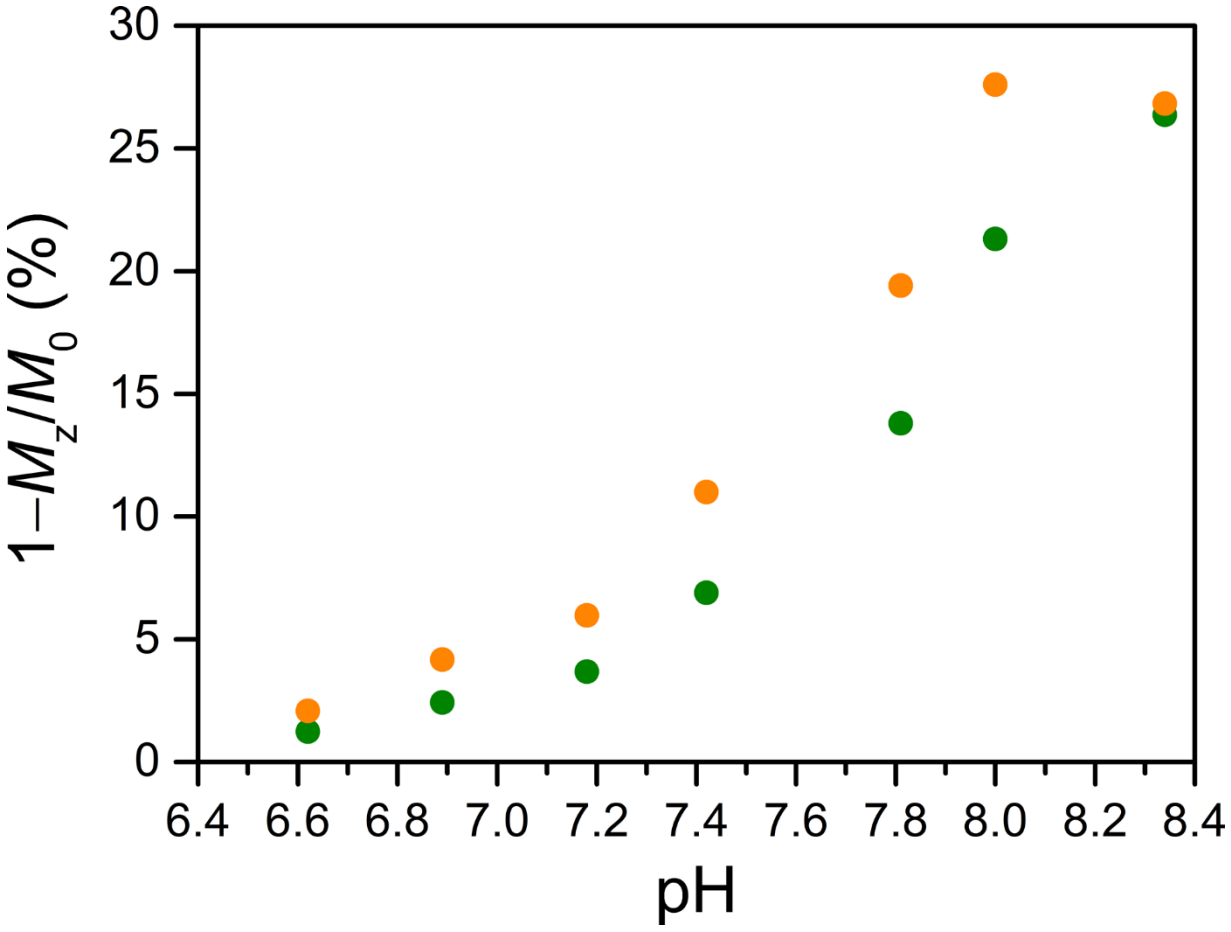

Figure 3.27 pH dependences of the CEST effects from application of presaturation at 68 ppm (yellow) and 102 ppm (green) for 12 mM of **2** in aqueous solutions containing 50 mM HEPES and 100 mM NaCl at 37 °C.

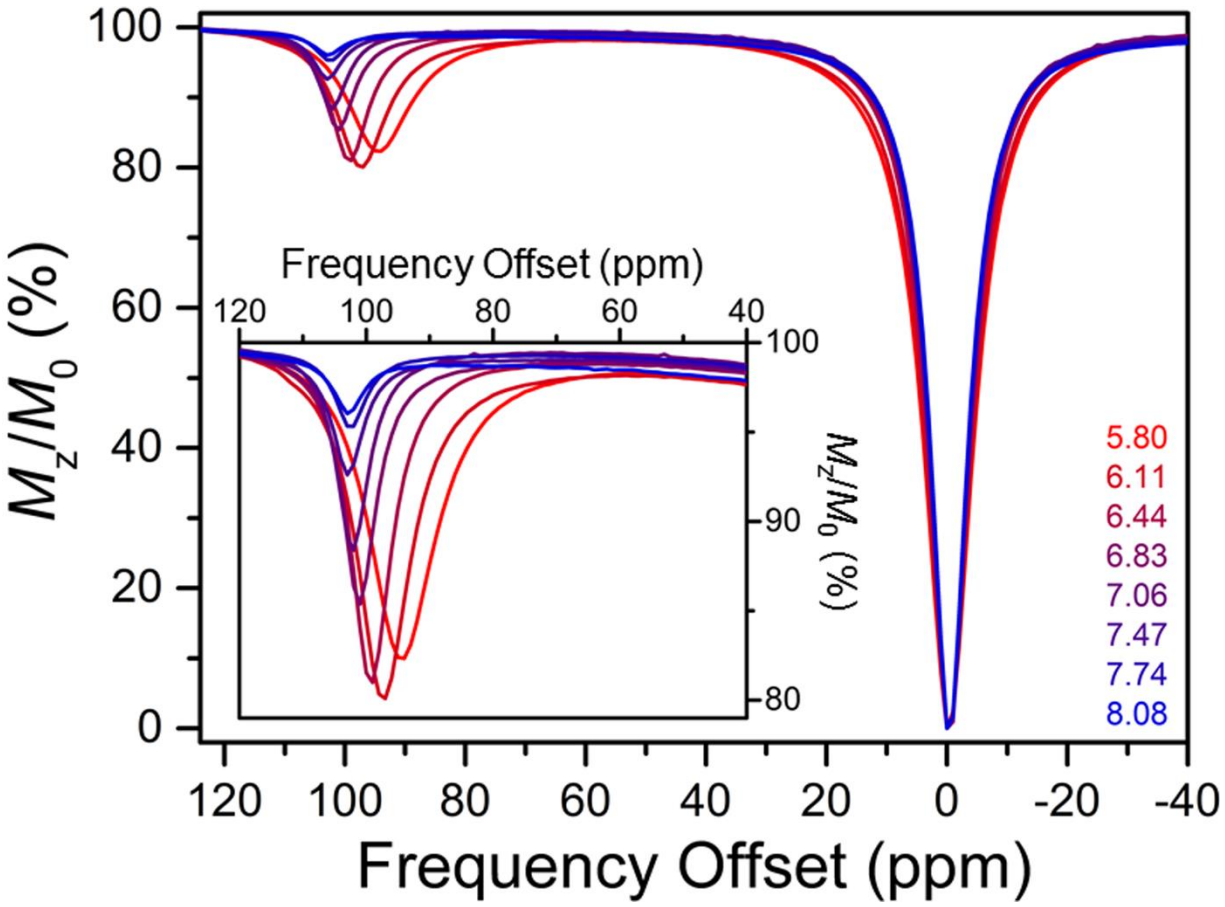

Figure 3.28 Variable-pH CEST spectra for 13 mM of **3** in aqueous solutions containing 50 mM HEPES and 100 mM NaCl buffered at pH 5.80–8.08 (red to blue) at 37 °C. Colored numbers in the legend denote the pH of the solutions measured with a pH electrode and the corresponding color of each sample. Inset: Expanded view of the CEST peaks of interest.

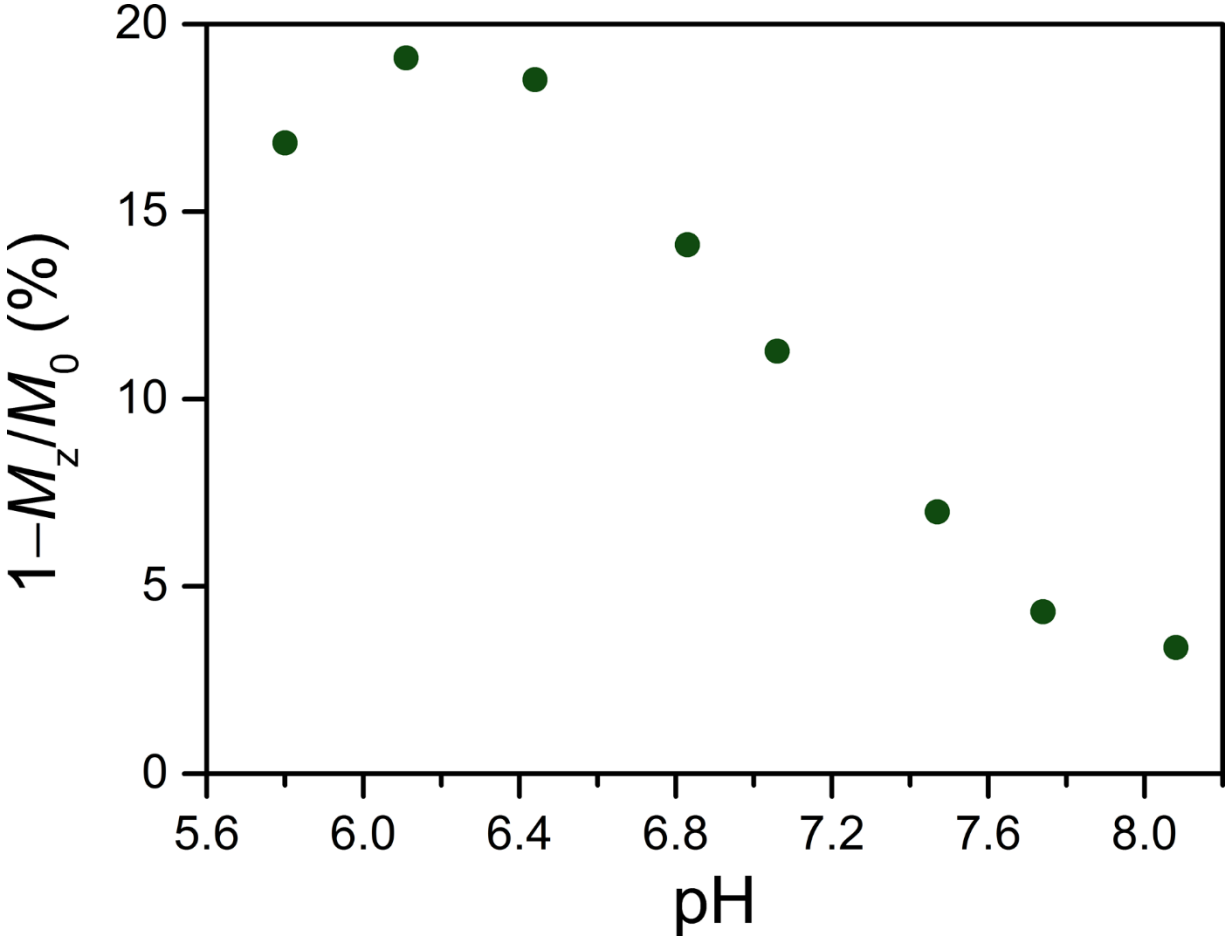

Figure 3.29 pH dependence of the CEST effect from application of presaturation at 94–103 ppm for 13 mM of **3** in aqueous solutions containing 50 mM HEPES and 100 mM NaCl at 37 °C. For each pH value, presaturation at the frequency offset corresponding to maximum reduction in the H_2O signal intensity was employed (see Table 3.5).

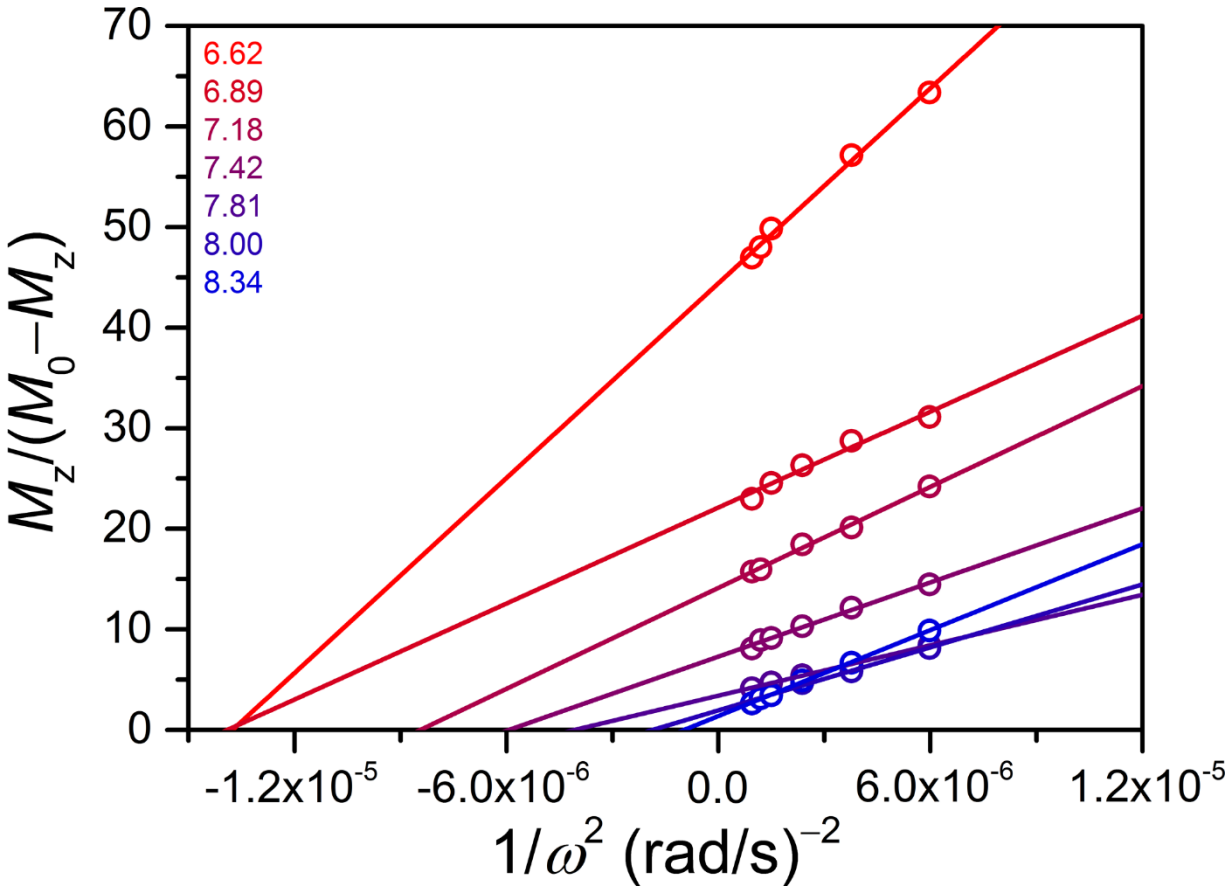

Figure 3.30 Omega plots of the CEST effect from application of presaturation at 68–69 ppm for 12 mM of **2** in aqueous solutions containing 50 mM HEPES and 100 mM NaCl buffered at pH 6.62–8.34 (red to blue) at 37 °C. Colored numbers in the legend denote the pH of the solutions measured with a pH electrode and the corresponding color of each sample. Presaturation at the frequency offset corresponding to maximum reduction in the H_2O signal intensity was monitored for each pH value (see Table 3.4). Circles represent experimental data and lines represent the linear fits.

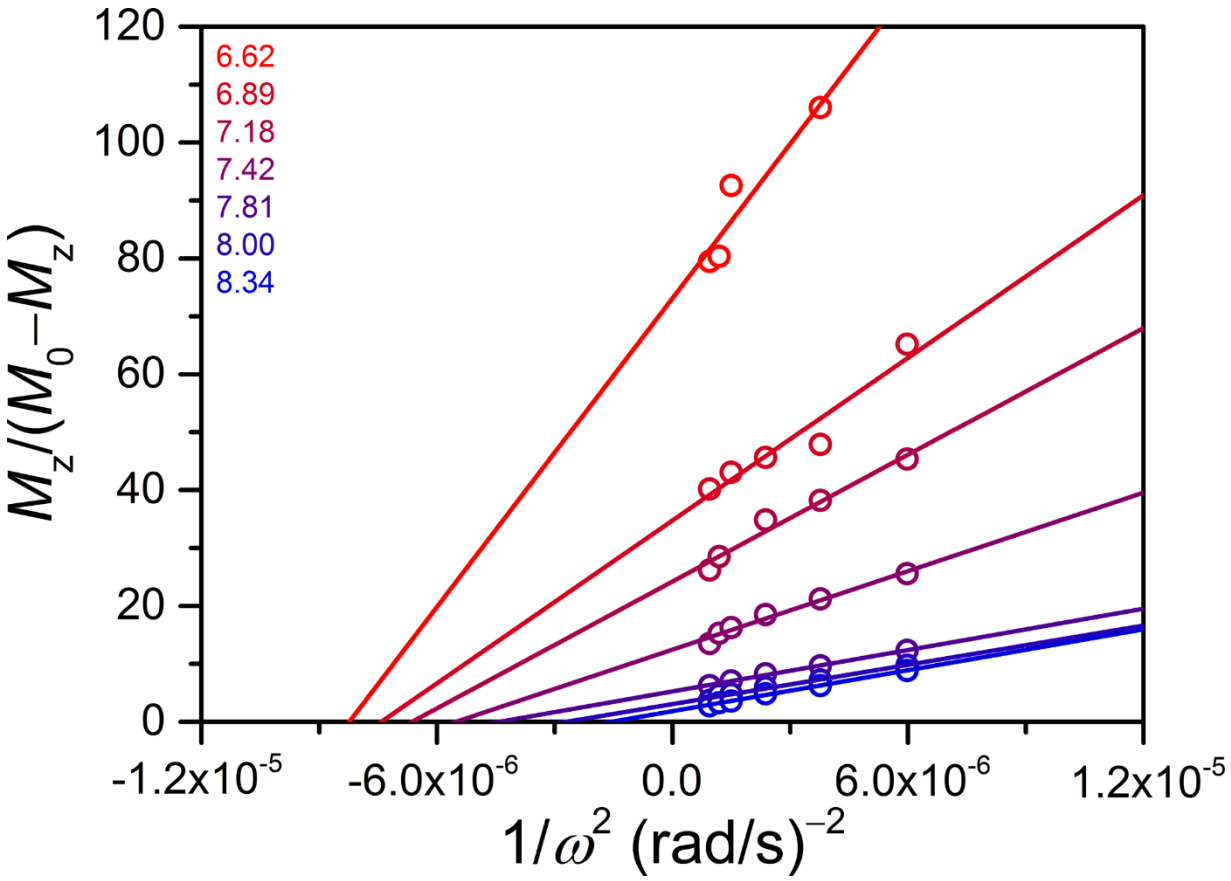

Figure 3.31 Omega plots of the CEST effect from application of presaturation at 102 ppm for 12 mM of **2** in aqueous solutions containing 50 mM HEPES and 100 mM NaCl buffered at pH 6.62–8.34 (red to blue) at 37 °C. Colored numbers in the legend denote the pH of the solutions measured with a pH electrode and the corresponding color of each sample. Circles represent experimental data and lines represent the linear fits.

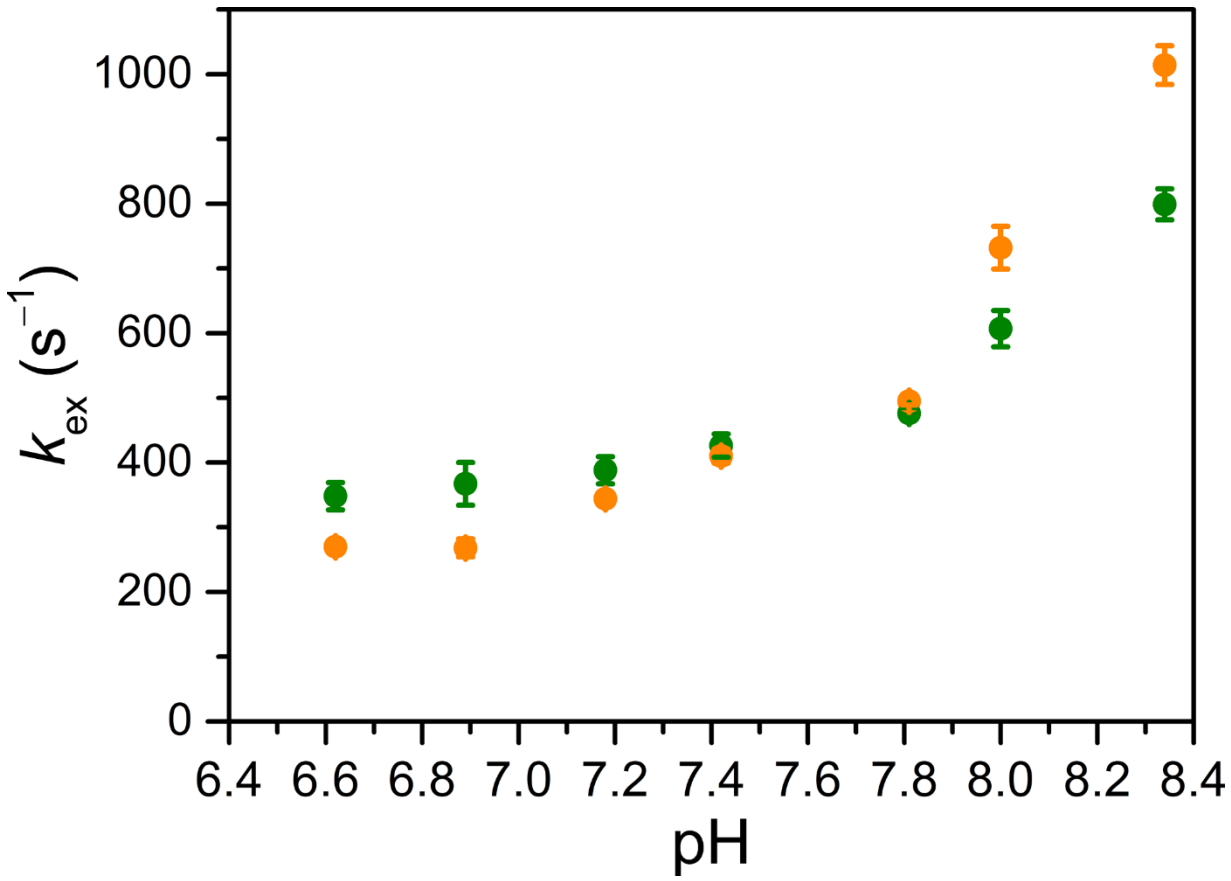

Figure 3.32 pH dependences of the proton exchange rate constants (k_{ex}) for the CEST effects at 68–69 ppm (yellow) and 102 ppm (green) for 12 mM of **2** in aqueous solutions containing 50 mM HEPES and 100 mM NaCl at 37 °C, obtained from Omega plots. Circles represent experimental data and the error bars represent standard deviations of the linear fits to the Omega plot data (see Figures 3.30 and 3.31).

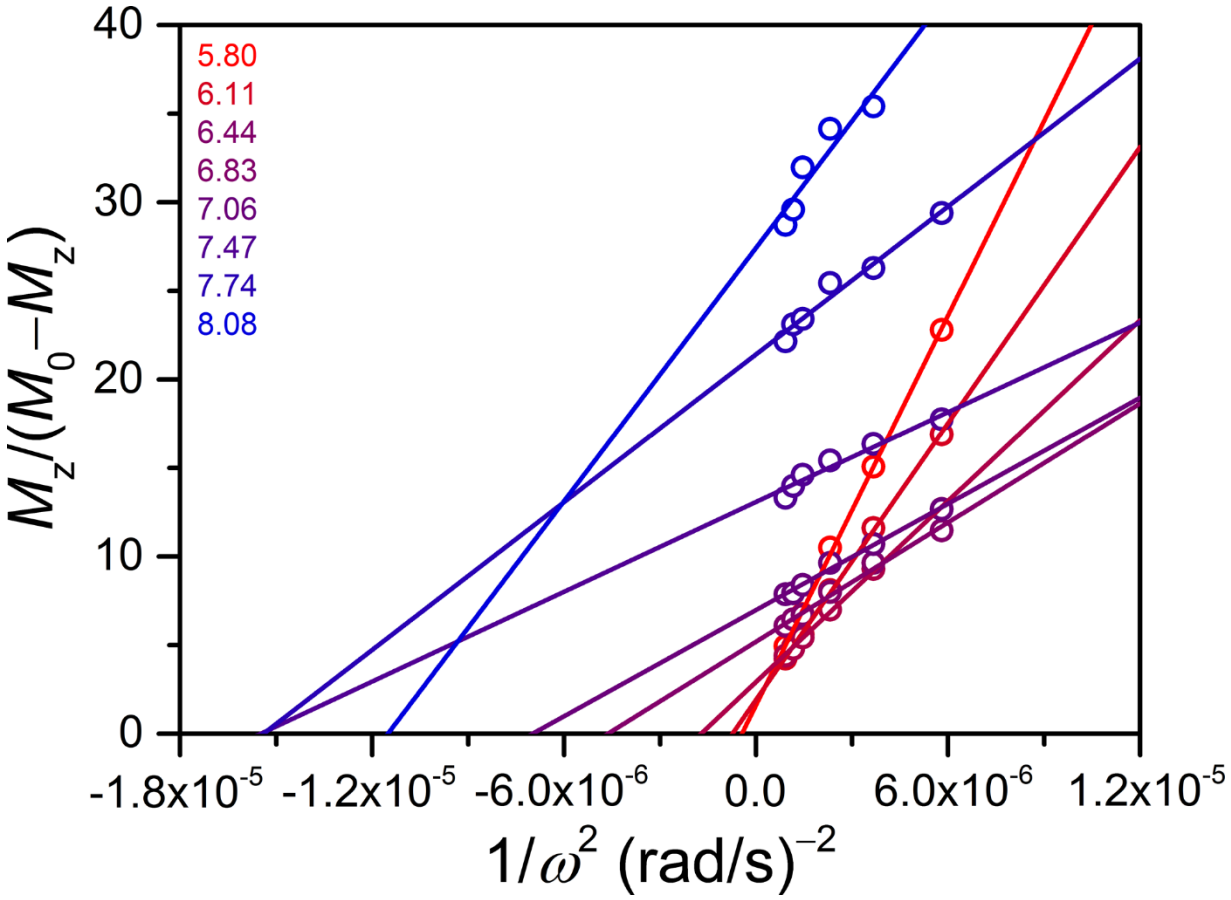

Figure 3.33 Omega plots of the CEST effect from application of presaturation at 94–103 ppm for 13 mM of **3** in aqueous solutions containing 50 mM HEPES and 100 mM NaCl buffered at pH 5.80–8.08 (red to blue) at 37 °C. Colored numbers in the legend denote the pH of the solutions measured with a pH electrode and the corresponding color of each sample. Presaturation at the frequency offset corresponding to maximum reduction in the H_2O signal intensity was monitored for each pH value (see Table 3.5). Circles represent experimental data and lines represent the linear fits.

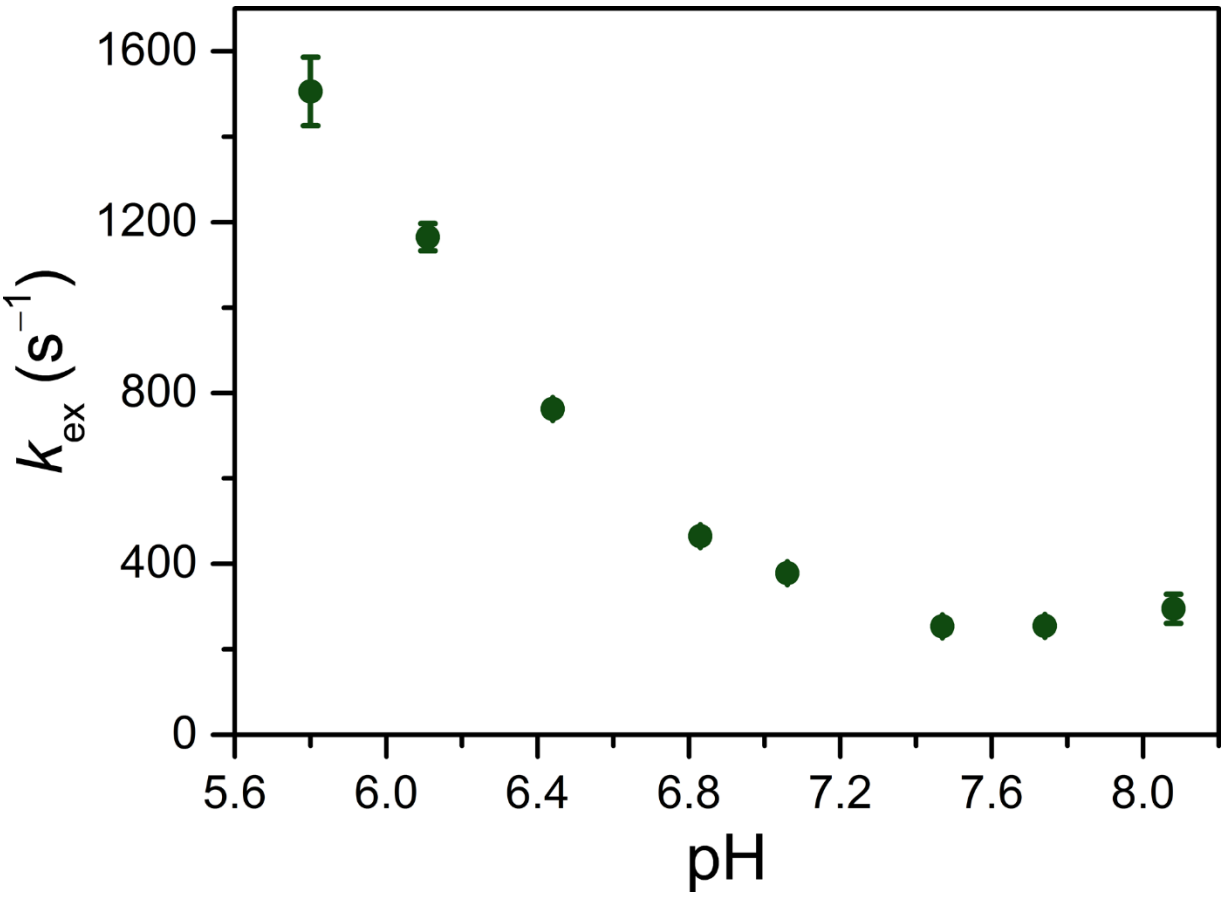

Figure 3.34 pH dependence of the proton exchange rate constant (k_{ex}) for the CEST effect at 94–103 ppm for 13 mM of **3** in aqueous solutions containing 50 mM HEPES and 100 mM NaCl at 37 °C, obtained from Omega plots. Circles represent experimental data and the error bars represent standard deviations of the linear fits to the Omega plot data (see Figure 3.33).

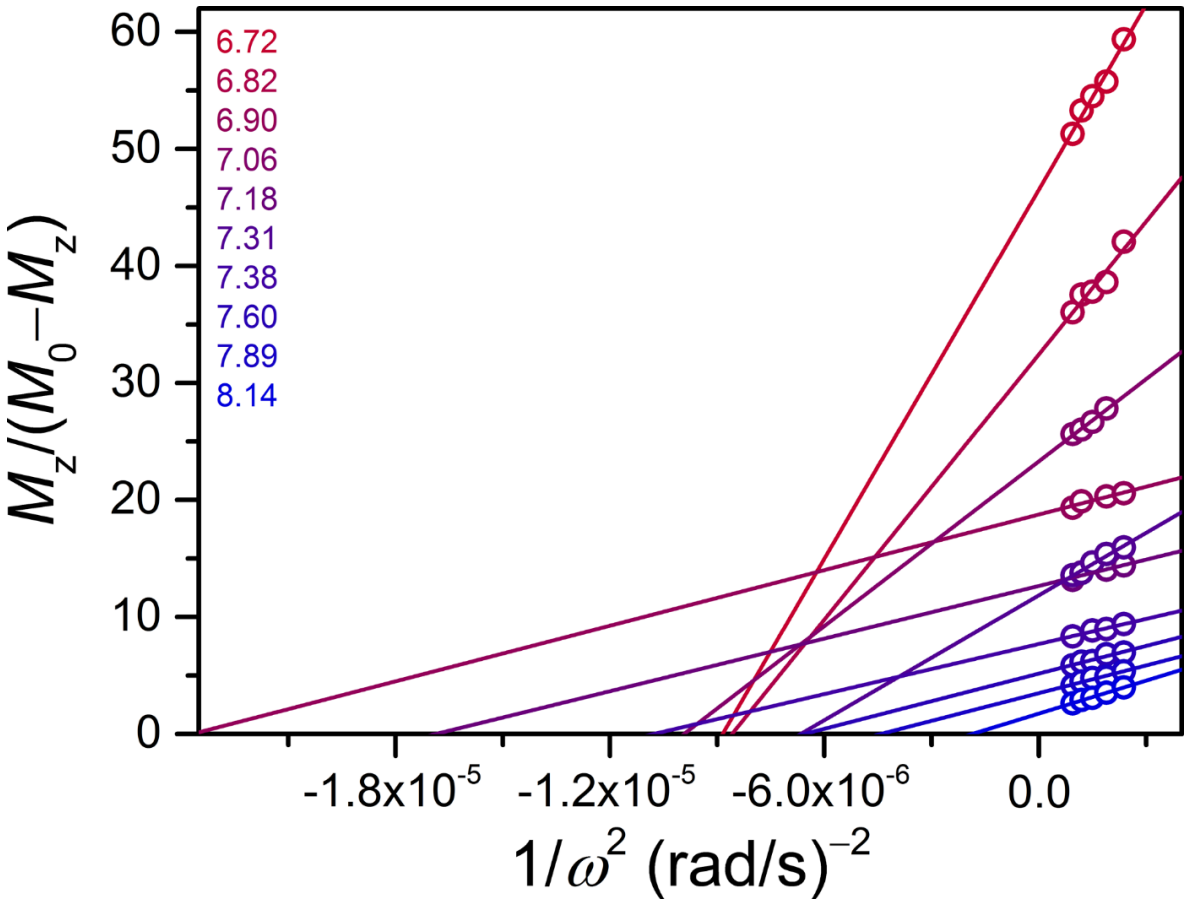

Figure 3.35 Omega plots of the CEST effect from application of presaturation at 64–66 ppm for 12.8 mM of **1** in aqueous solutions containing 50 mM HEPES and 100 mM NaCl buffered at pH 6.72–8.14 (red-purple to blue) at 37 °C. Colored numbers in the legend denote the pH of the solutions measured with a pH electrode and the corresponding color of each sample. Presaturation at the frequency offset corresponding to maximum reduction in the H_2O signal intensity was monitored for each pH value (see Table 3.6). Circles represent experimental data and lines represent the linear fits.

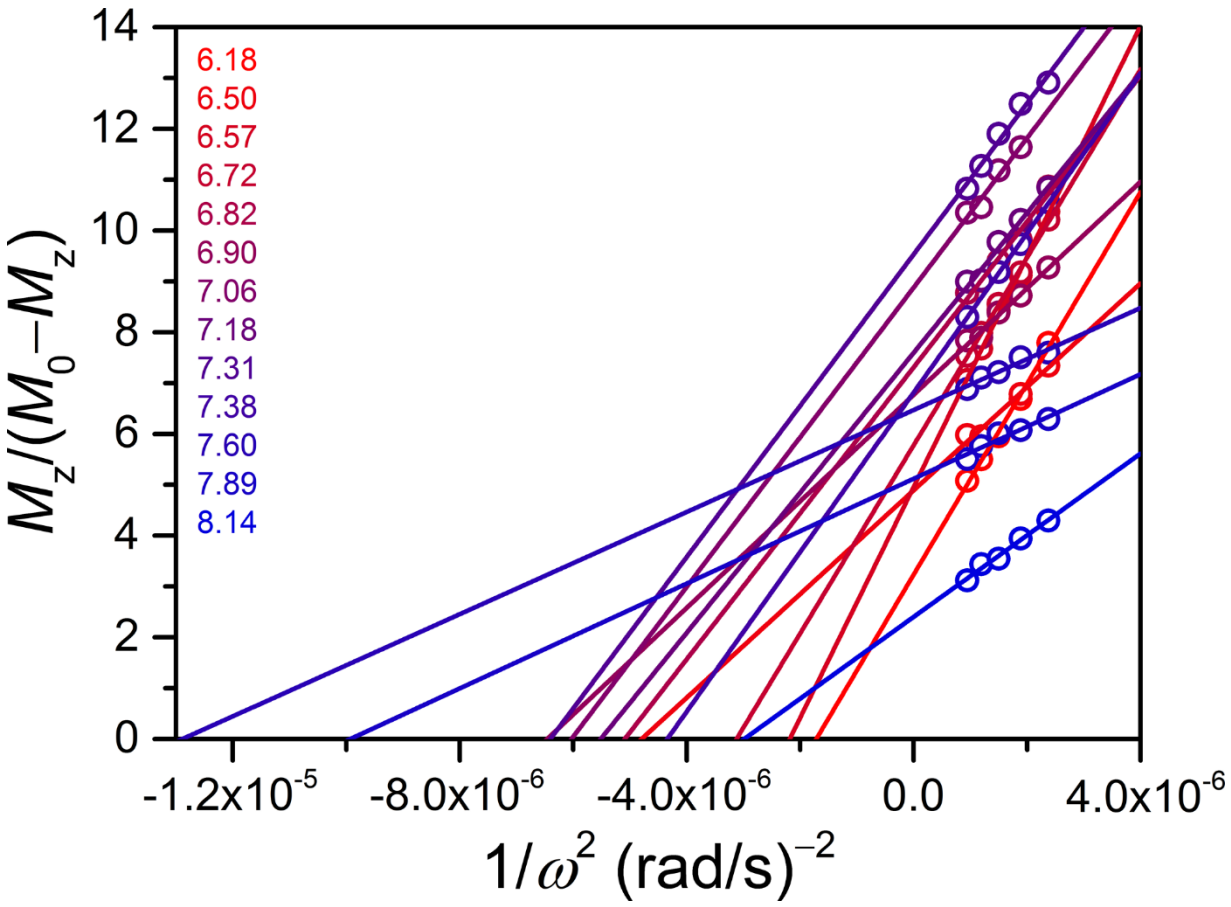

Figure 3.36 Omega plots of the CEST effect from application of presaturation at 101–106 ppm for 12.8 mM of **1** in aqueous solutions containing 50 mM HEPES and 100 mM NaCl buffered at pH 6.18–8.14 (red to blue) at 37 °C. Colored numbers in the legend denote the pH of the solutions measured with a pH electrode and the corresponding color of each sample. Presaturation at the frequency offset corresponding to maximum reduction in the H_2O signal intensity was monitored for each pH value (see Table 3.6). Circles represent experimental data and lines represent the linear fits.

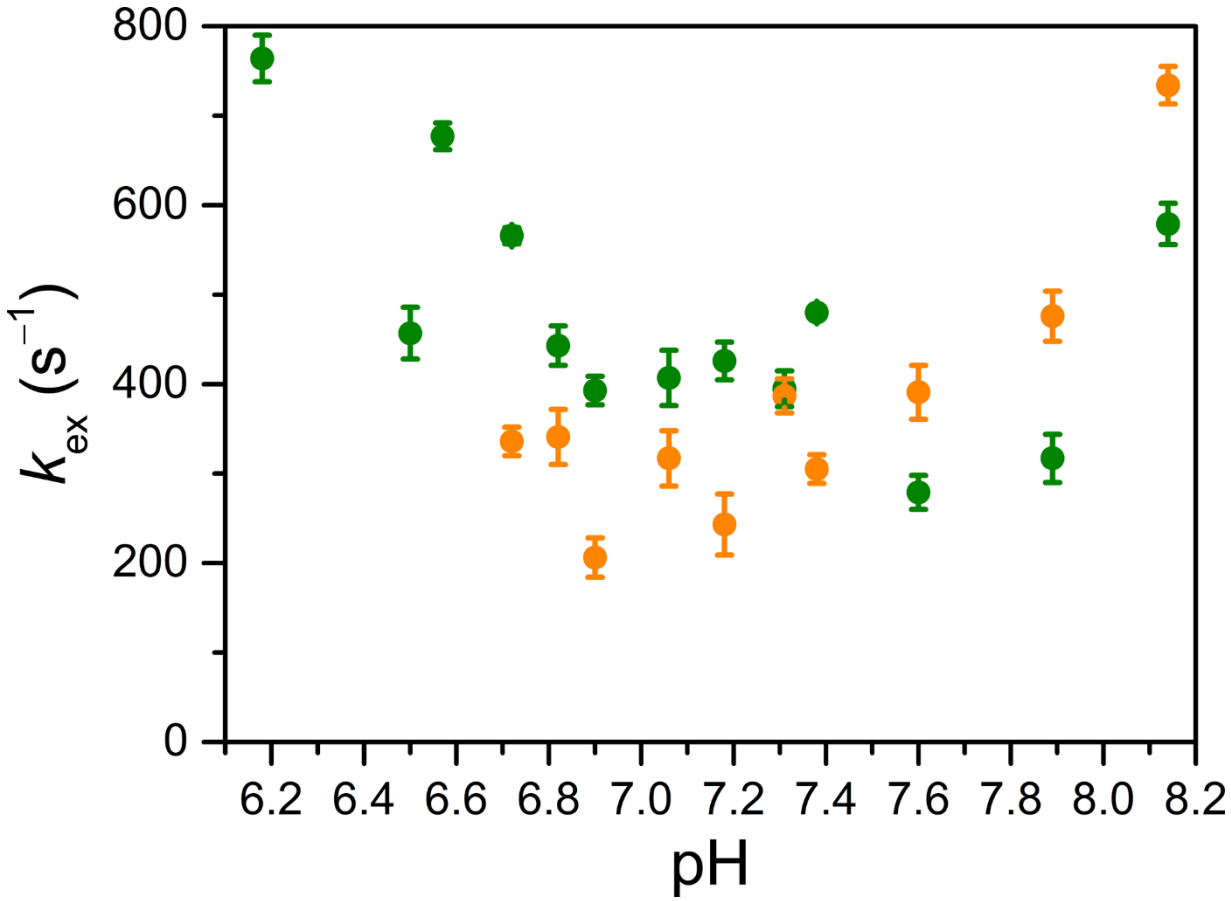

Figure 3.37 pH dependences of the proton exchange rate constants (k_{ex}) for the CEST effects at 64–66 ppm (yellow) and 101–106 ppm (green) for 12.8 mM of **1** in aqueous solutions containing 50 mM HEPES and 100 mM NaCl at 37 °C, obtained from Omega plots. Circles represent experimental data and the error bars represent standard deviations of the linear fits to the Omega plot data (see Figures 3.35 and 3.36).

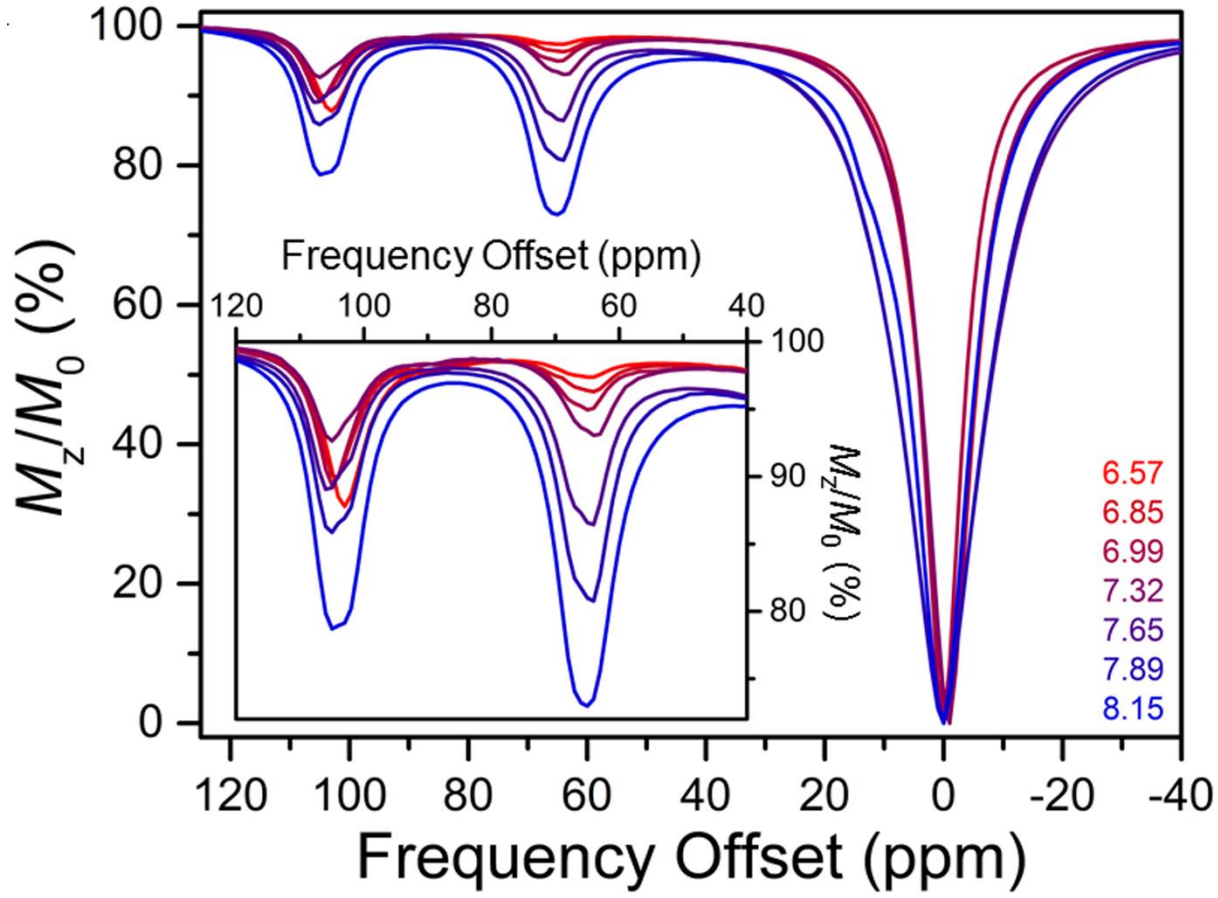

Figure 3.38 Variable-pH CEST spectra for 6.4 mM of **1** in aqueous solutions containing 50 mM HEPES and 100 mM NaCl buffered at pH 6.57–8.15 (red to blue) at 37 °C. Colored numbers in the legend denote the pH of the solutions measured with a pH electrode and the corresponding color of each sample. Inset: Expanded view of the CEST peaks of interest.

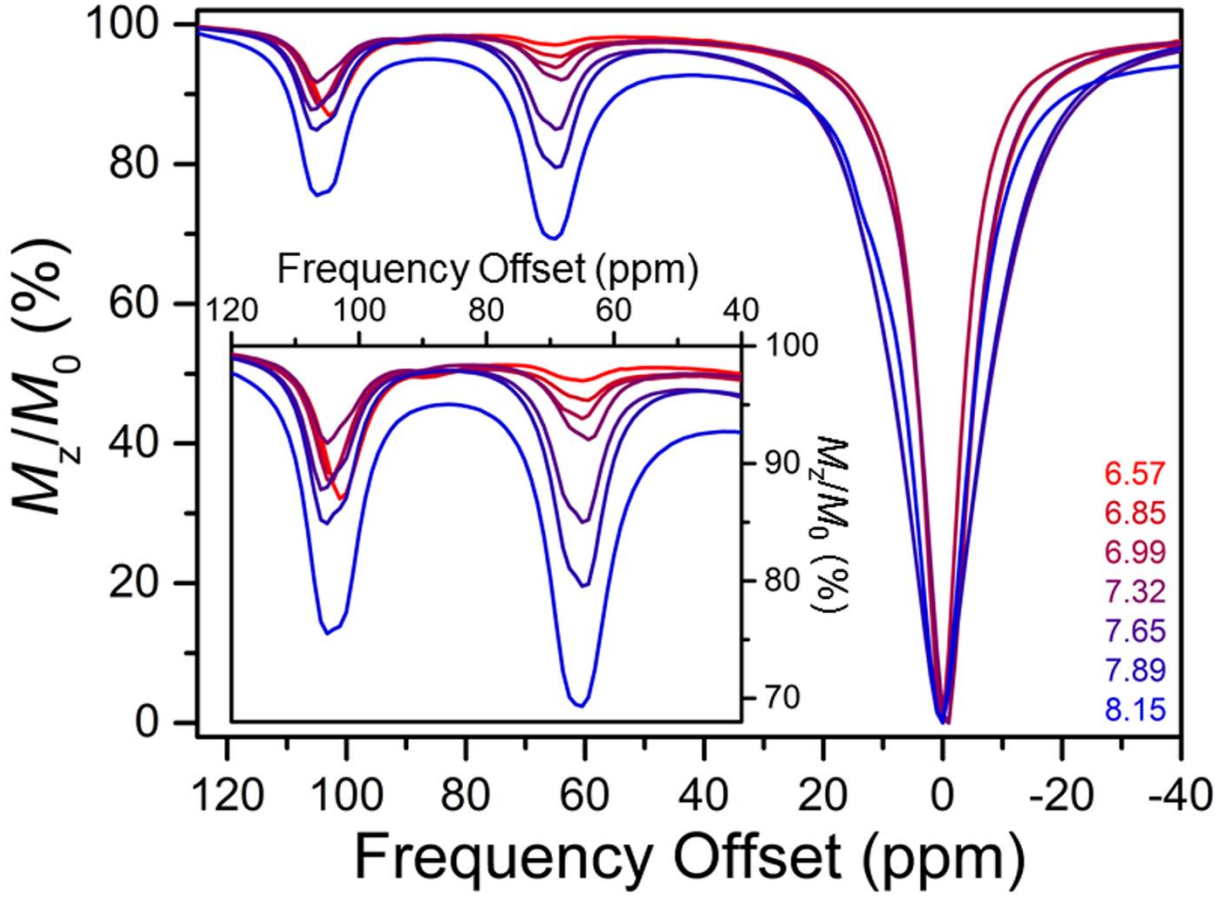

Figure 3.39 Variable-pH CEST spectra for 8.5 mM of **1** in aqueous solutions containing 50 mM HEPES and 100 mM NaCl buffered at pH 6.57–8.15 (red to blue) at 37 °C. Colored numbers in the legend denote the pH of the solutions measured with a pH electrode and the corresponding color of each sample. Inset: Expanded view of the CEST peaks of interest.

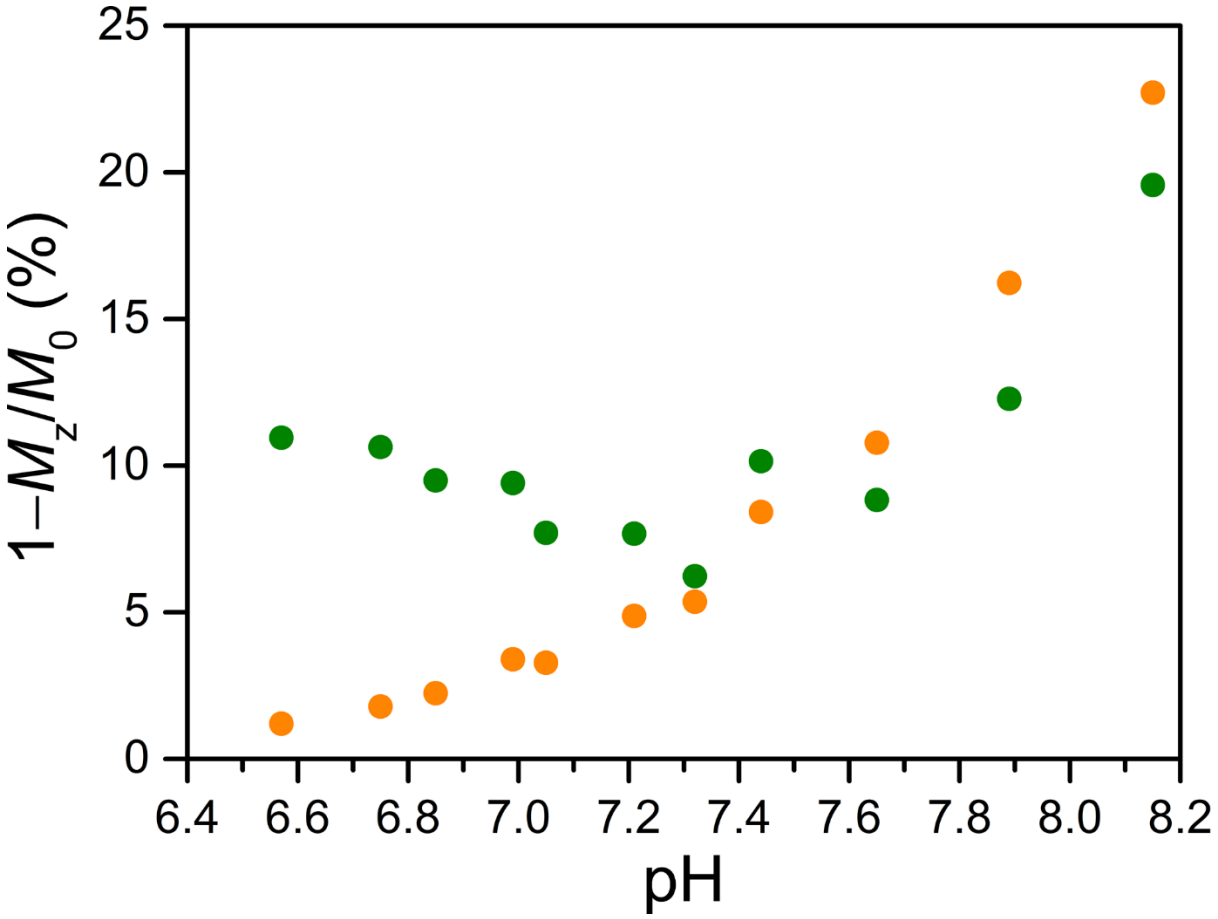

Figure 3.40 pH dependences of the CEST effects from application of presaturation at 64 ppm (yellow) and 104 ppm (green) for 6.4 mM of **1** in aqueous solutions containing 50 mM HEPES and 100 mM NaCl at 37 °C.

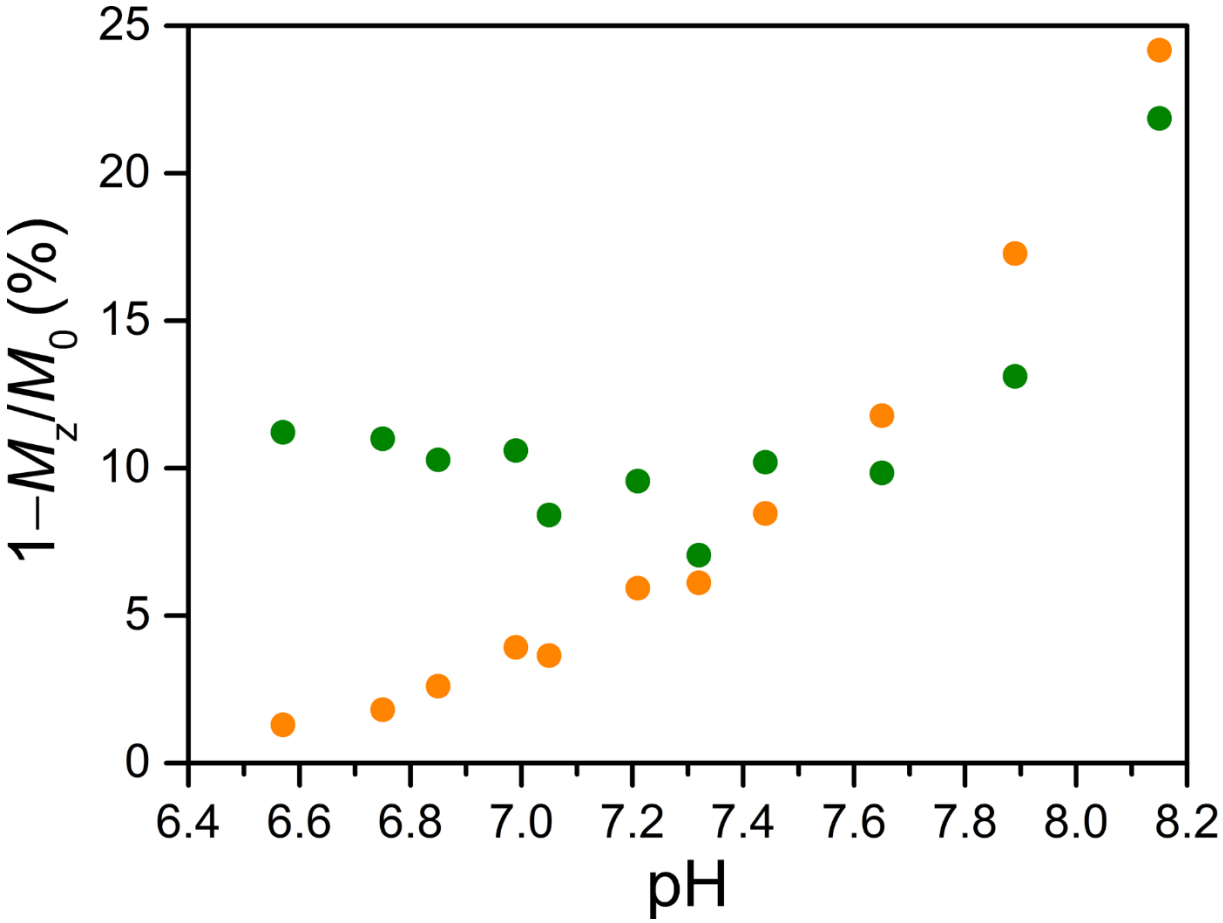

Figure 3.41 pH dependences of the CEST effects from application of presaturation at 64 ppm (yellow) and 104 ppm (green) for 8.5 mM of **1** in aqueous solutions containing 50 mM HEPES and 100 mM NaCl at 37 °C.

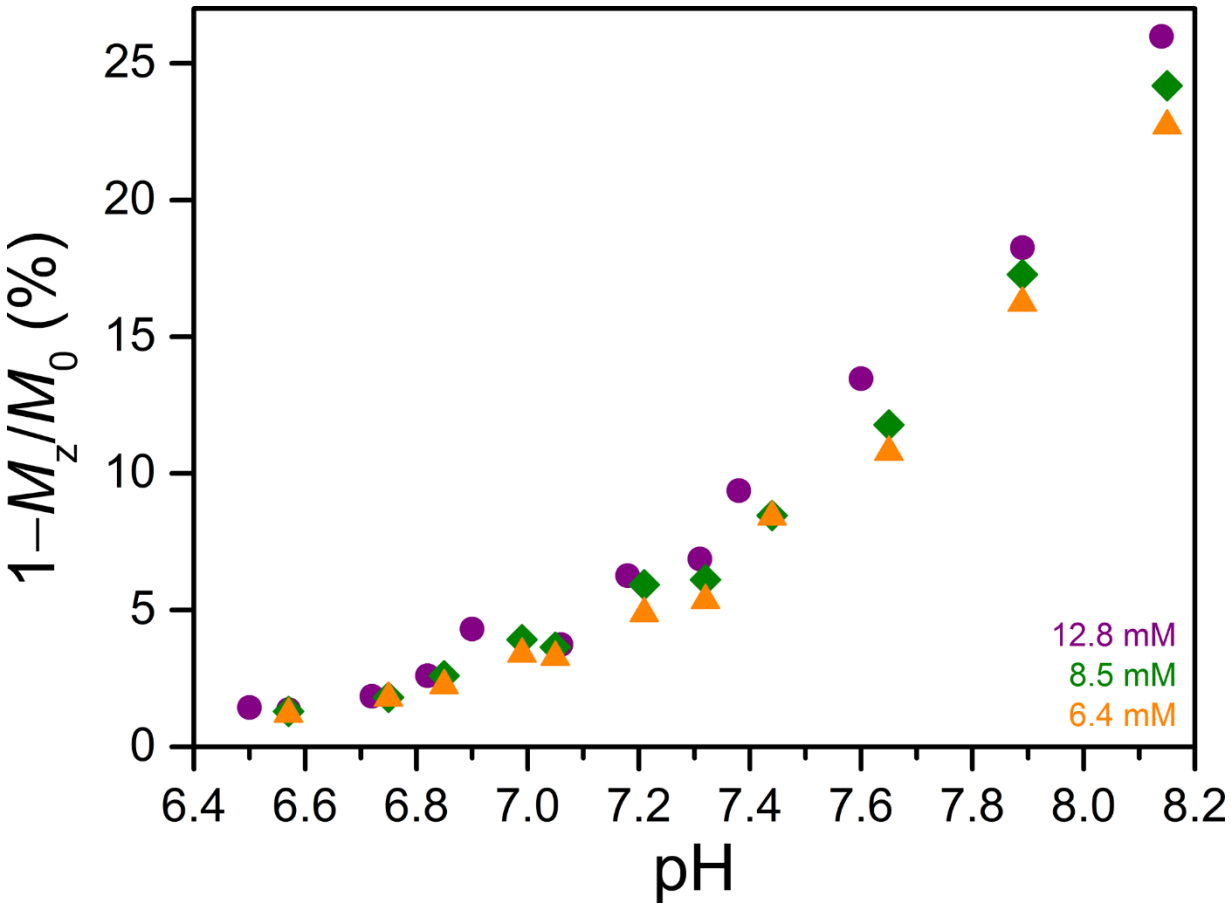

Figure 3.42 Comparison of the pH dependence of the CEST effect from application of presaturation at 64 ppm for various concentrations of **1** (see legend) in aqueous solutions containing 50 mM HEPES and 100 mM NaCl at 37 °C.

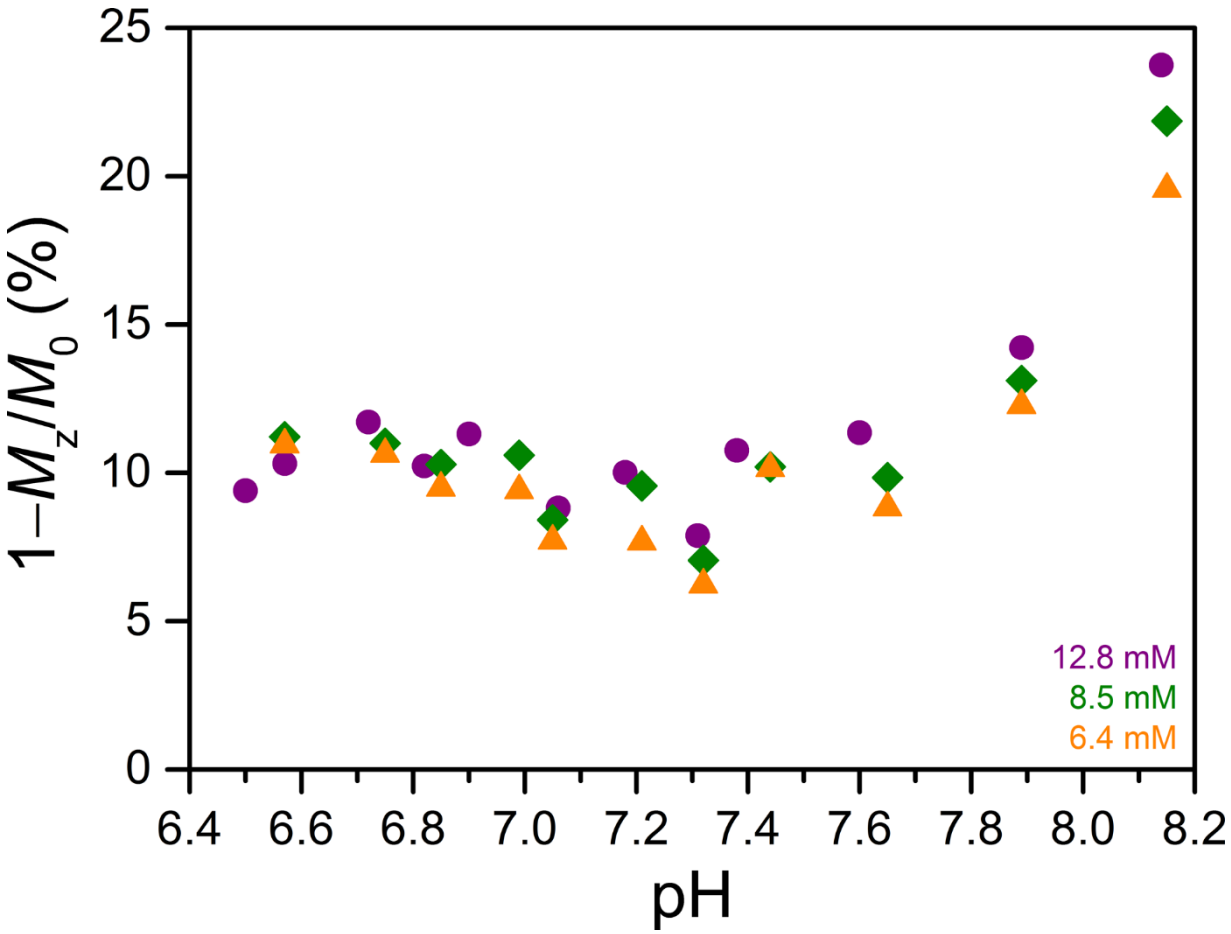

Figure 3.43 Comparison of the pH dependence of the CEST effect from application of presaturation at 104 ppm for various concentrations of **1** (see legend) in aqueous solutions containing 50 mM HEPES and 100 mM NaCl at 37 °C.

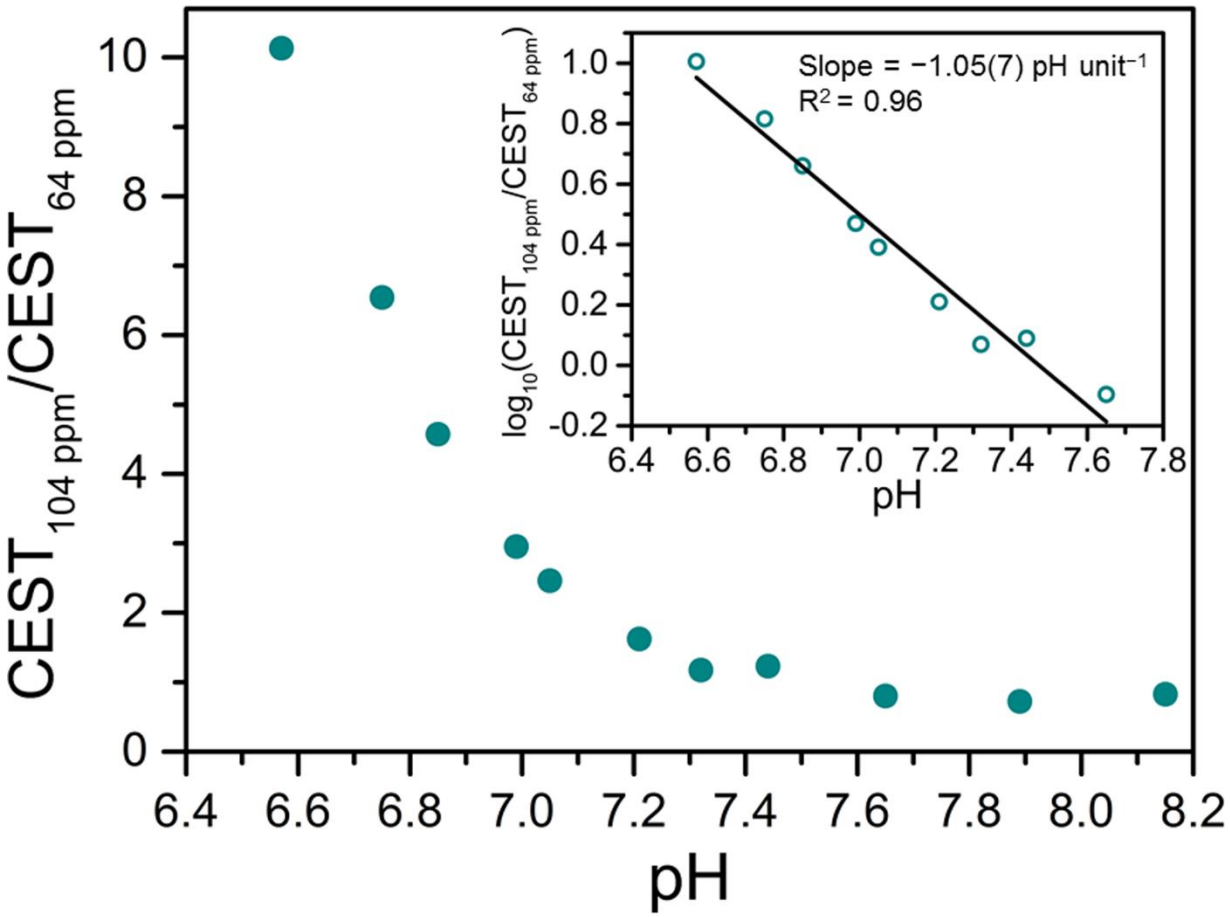

Figure 3.44 pH dependences of the ratio of CEST effects from application of presaturation at 104 and 64 ppm, and the base 10 logarithm of the ratio (inset) for 6.4 mM of **1** in aqueous solutions containing 50 mM HEPES and 100 mM NaCl at 37 °C. Dark cyan circles represent experimental data and the solid black line denotes a linear fit to the data with the following equation: $\log_{10}(CEST_{104\ ppm}/CEST_{64\ ppm}) = -1.05(7) \times pH + 7.9(5)$; $R^2 = 0.96$.

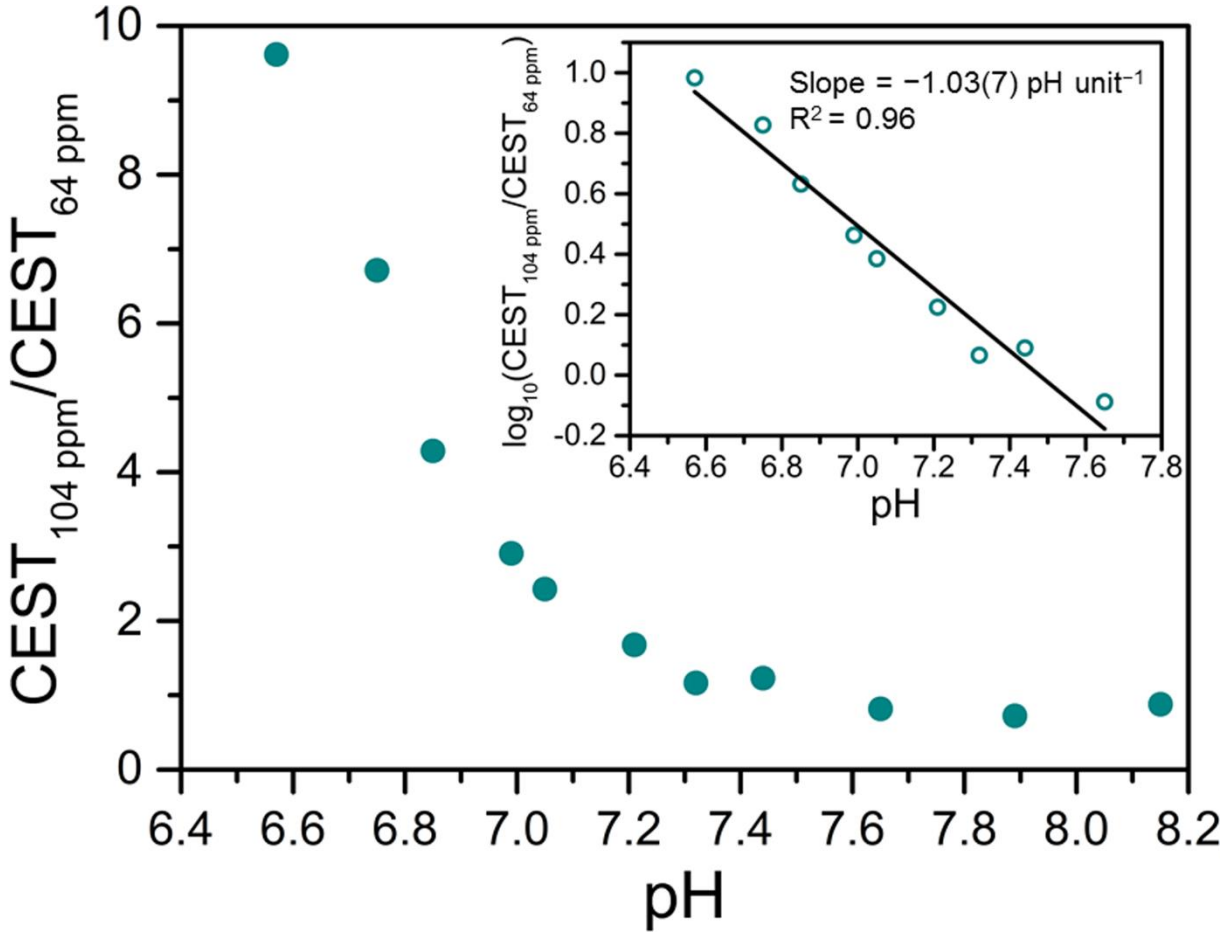

Figure 3.45 pH dependences of the ratio of CEST effects from application of presaturation at 104 and 64 ppm, and the base 10 logarithm of the ratio (inset) for 8.5 mM of **1** in aqueous solutions containing 50 mM HEPES and 100 mM NaCl at 37 °C. Dark cyan circles represent experimental data and the solid black line denotes a linear fit to the data with the following equation: $\log_{10}(CEST_{104\ ppm}/CEST_{64\ ppm}) = -1.03(7) \times pH + 7.7(5)$; $R^2 = 0.96$.

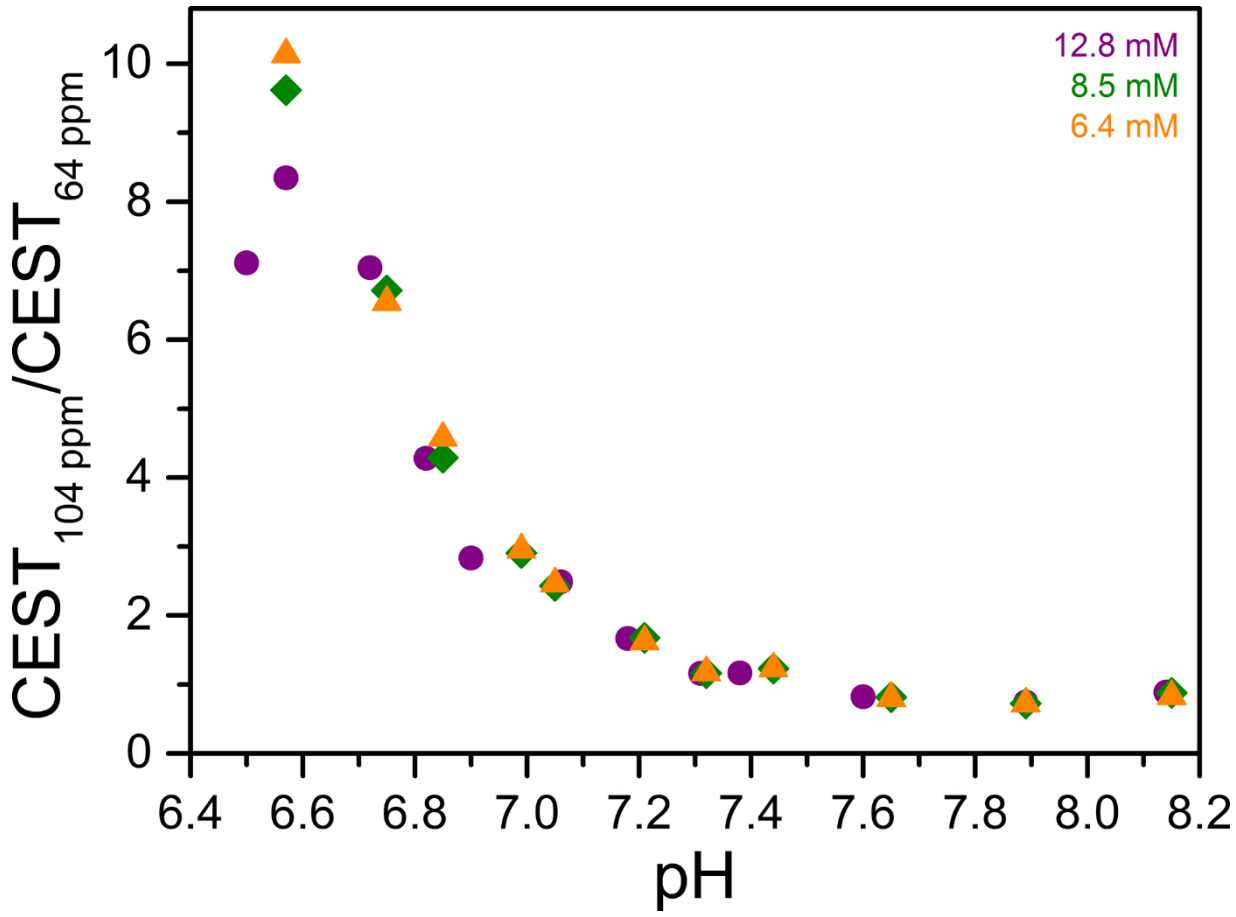

Figure 3.46 Comparison of the pH dependence of the ratio of CEST effects from application of presaturation at 104 and 64 ppm for various concentrations of **1** (see legend) in aqueous solutions containing 50 mM HEPES and 100 mM NaCl at 37 °C.

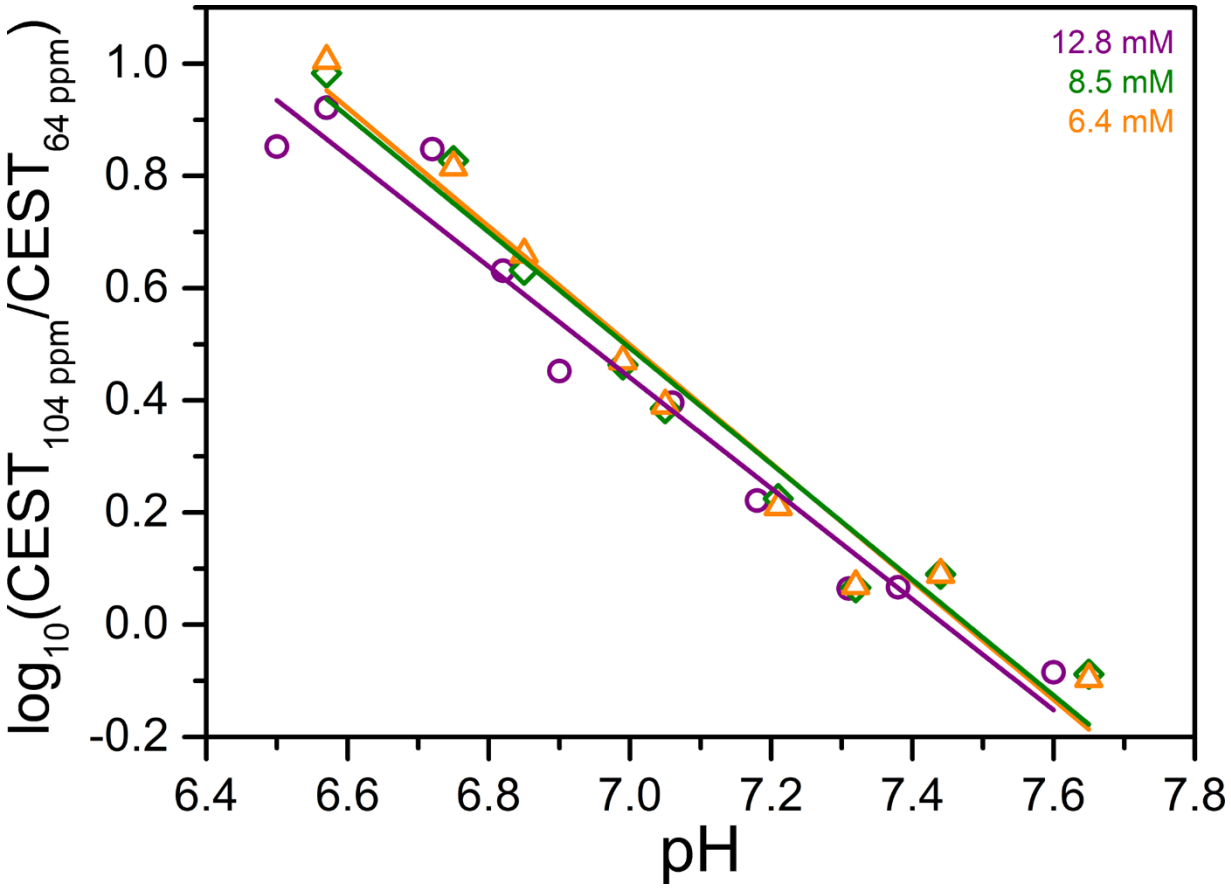

Figure 3.47 Comparison of the pH calibration curves obtained by taking the base 10 logarithm of the ratios of CEST effects from application of presaturation at 104 and 64 ppm for various concentrations of **1** (see legend) in aqueous solutions containing 50 mM HEPES and 100 mM NaCl at 37 °C. See Equations 3.3–3.5 for the equations of the linear fits to the data.

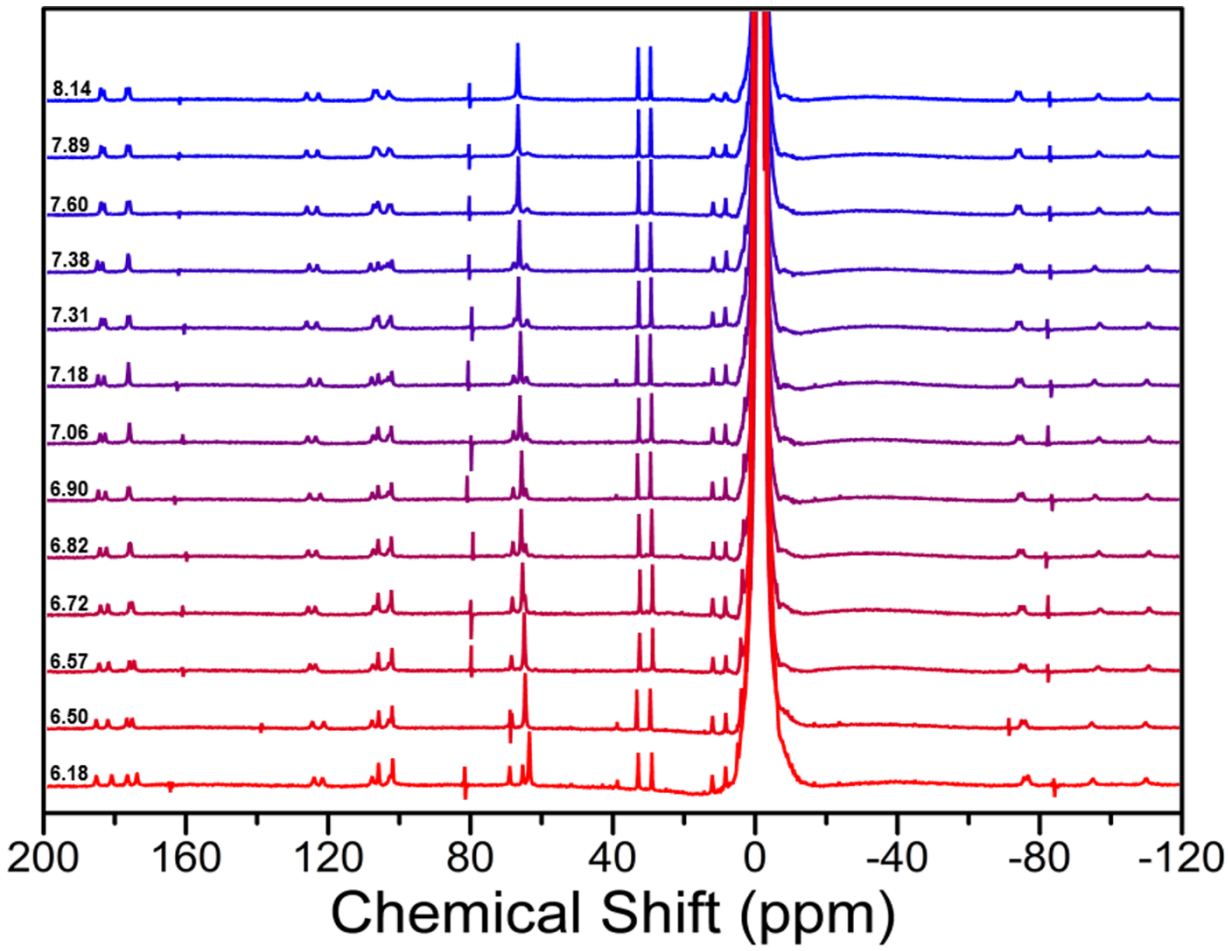

Figure 3.48 Variable-pH ^{1}H NMR spectra of 12.8 mM of **1** in aqueous solutions containing 50 mM HEPES and 100 mM NaCl buffered at various pH values at 35 °C. Black numbers on the left denote the pH of the NMR sample solutions measured with a pH electrode. The sharp features at 160–165, 80–82, and −85 ppm are instrument-derived artifacts. Note that these artifacts are shifted to 140, 70, and −70 ppm in the spectrum at pH 6.50.

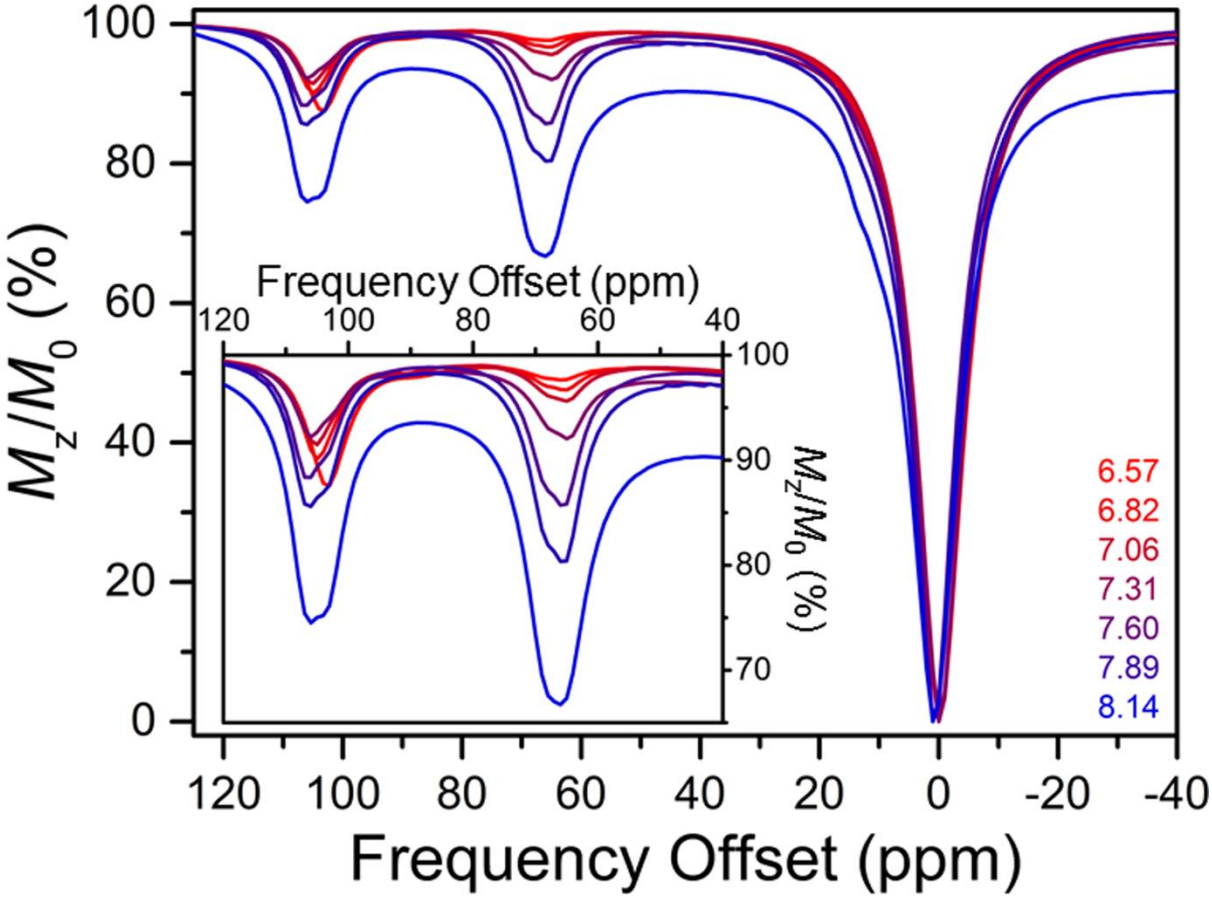

Figure 3.49 Variable-pH CEST spectra for 12.8 mM of **1** in aqueous solutions containing 50 mM HEPES and 100 mM NaCl buffered at pH 6.57–8.14 (red to blue) at 35 °C. Colored numbers in the legend denote the pH of the solutions measured with a pH electrode and the corresponding color of each sample. Inset: Expanded view of the CEST peaks of interest.

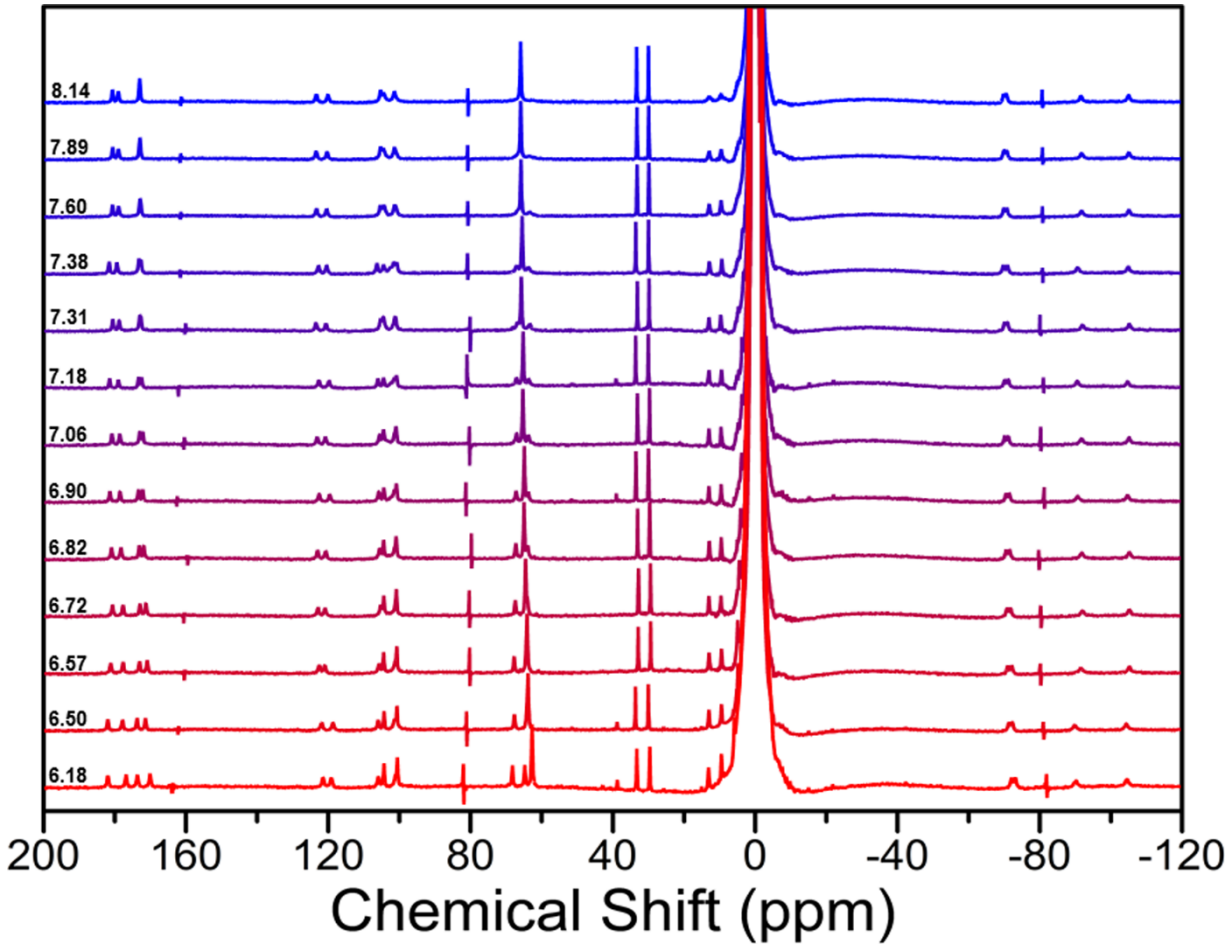

Figure 3.50 Variable-pH ^{1}H NMR spectra of 12.8 mM of **1** in aqueous solutions containing 50 mM HEPES and 100 mM NaCl buffered at various pH values at 39 °C. Black numbers on the left denote the pH of the NMR sample solutions measured with a pH electrode. The sharp features at 160–165, 80–82, and −85 ppm are instrument-derived artifacts.

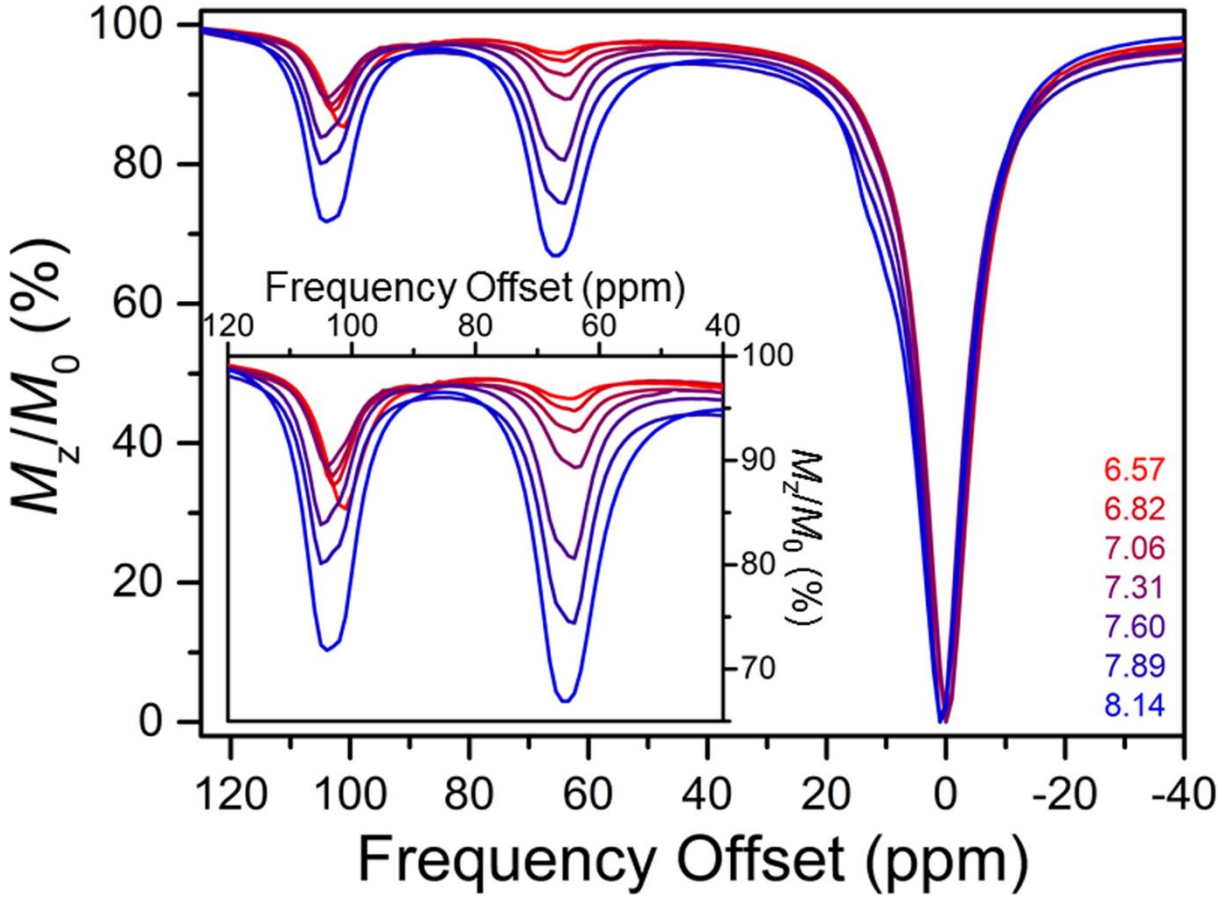

Figure 3.51 Variable-pH CEST spectra for 12.8 mM of **1** in aqueous solutions containing 50 mM HEPES and 100 mM NaCl buffered at pH 6.57–8.14 (red to blue) at 39 °C. Colored numbers in the legend denote the pH of the solutions measured with a pH electrode and the corresponding color of each sample. Inset: Expanded view of the CEST peaks of interest.

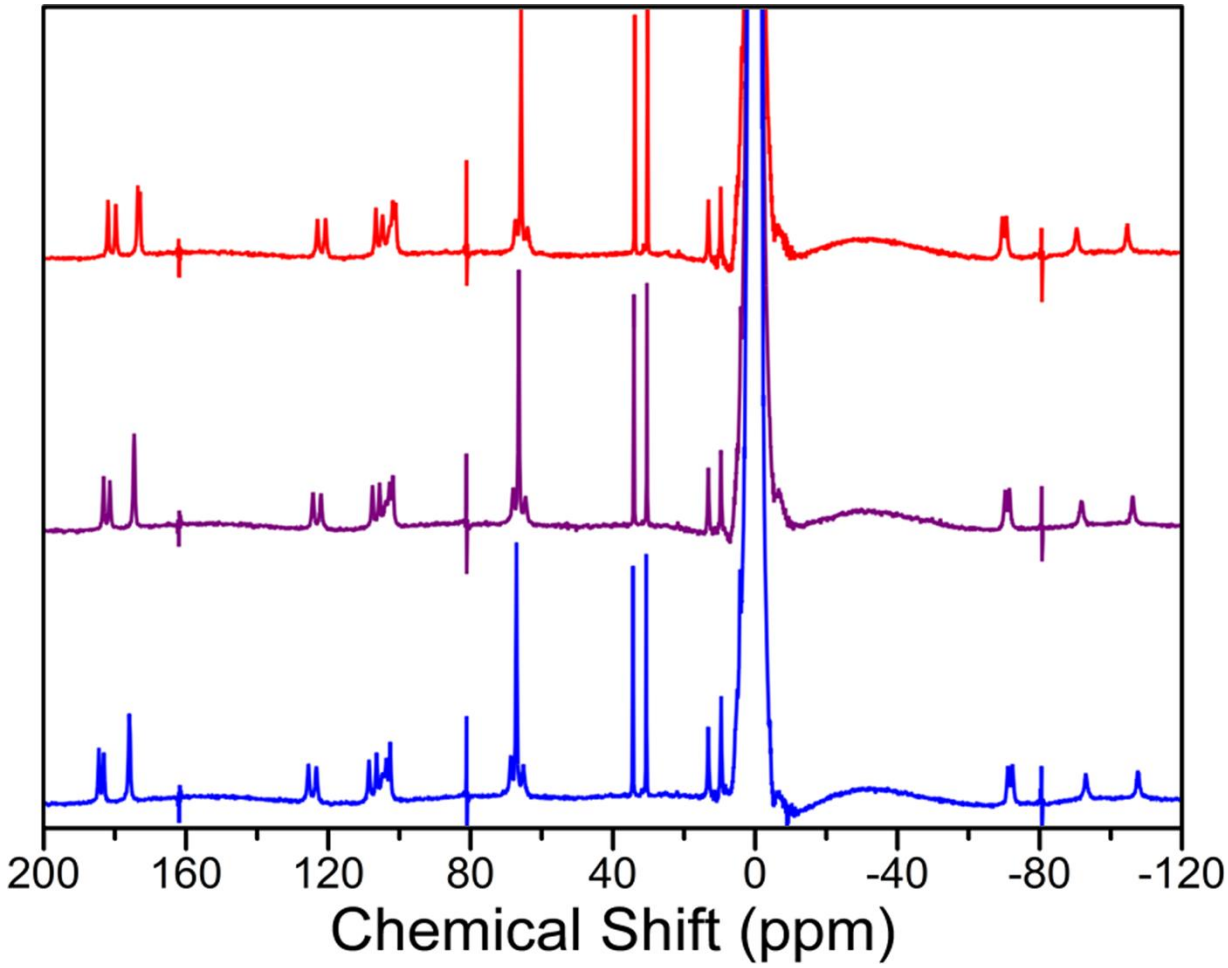

Figure 3.52 Stacked ^{1}H NMR spectra of 12.8 mM of **1** in an aqueous solution containing 50 mM HEPES and 100 mM NaCl buffered at pH 7.38 at 35 °C (blue), 37 °C (purple), and 39 °C (red). The sharp features at 165, 82, and −82 ppm are instrument-derived artifacts.

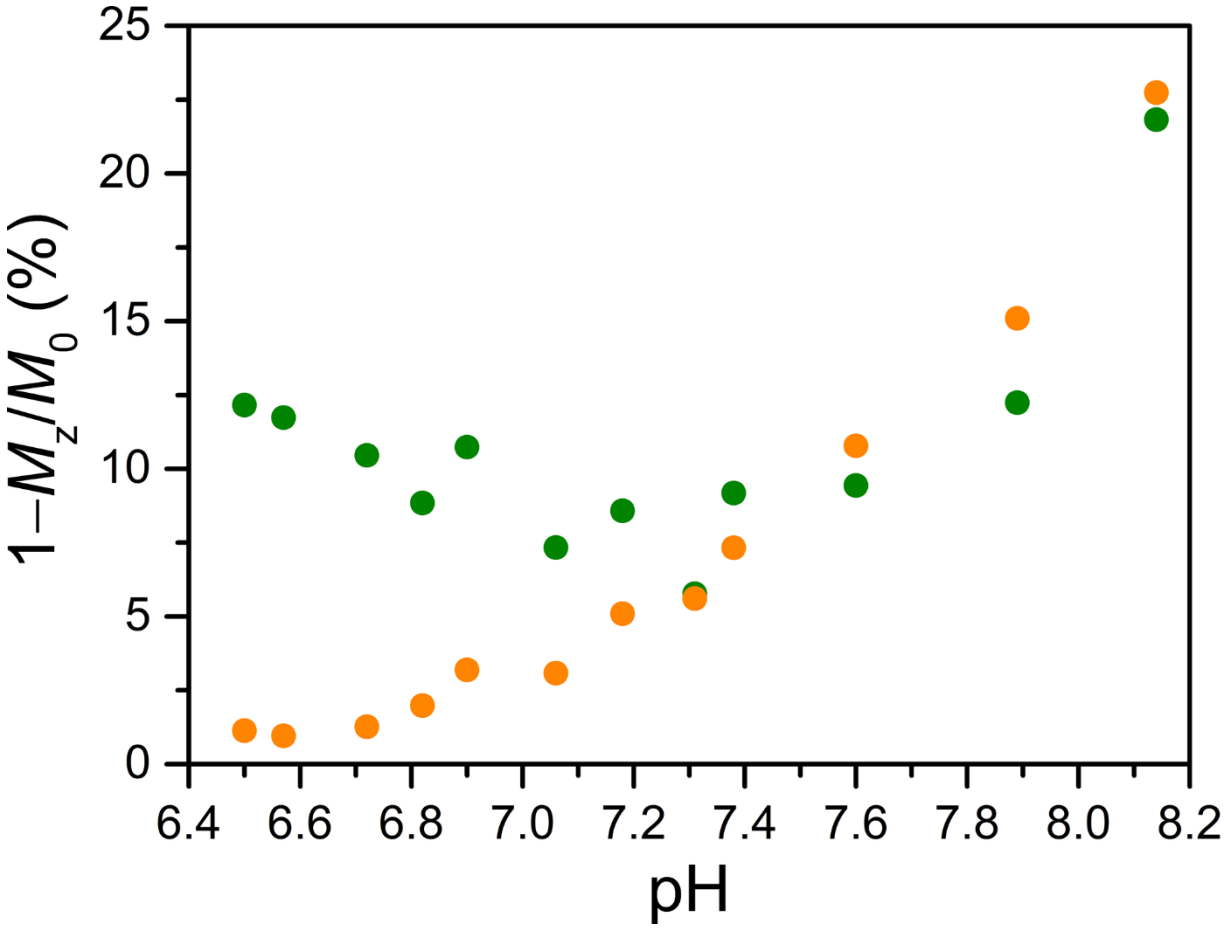

Figure 3.53 pH dependences of the CEST effects from application of presaturation at 64 ppm (yellow) and 104 ppm (green) for 12.8 mM of **1** in aqueous solutions containing 50 mM HEPES and 100 mM NaCl at 35 °C.

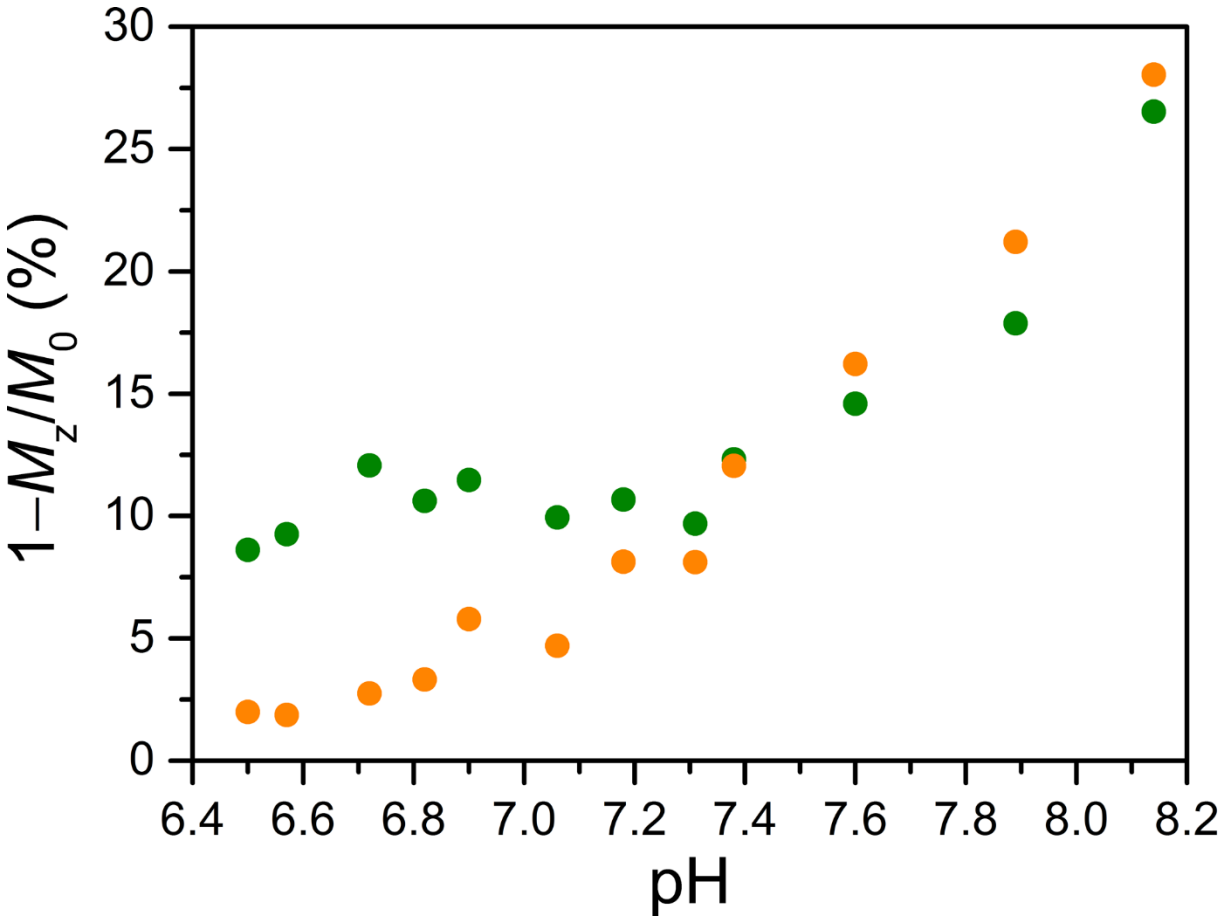

Figure 3.54 pH dependences of the CEST effects from application of presaturation at 64 ppm (yellow) and 104 ppm (green) for 12.8 mM of **1** in aqueous solutions containing 50 mM HEPES and 100 mM NaCl at 39 °C.

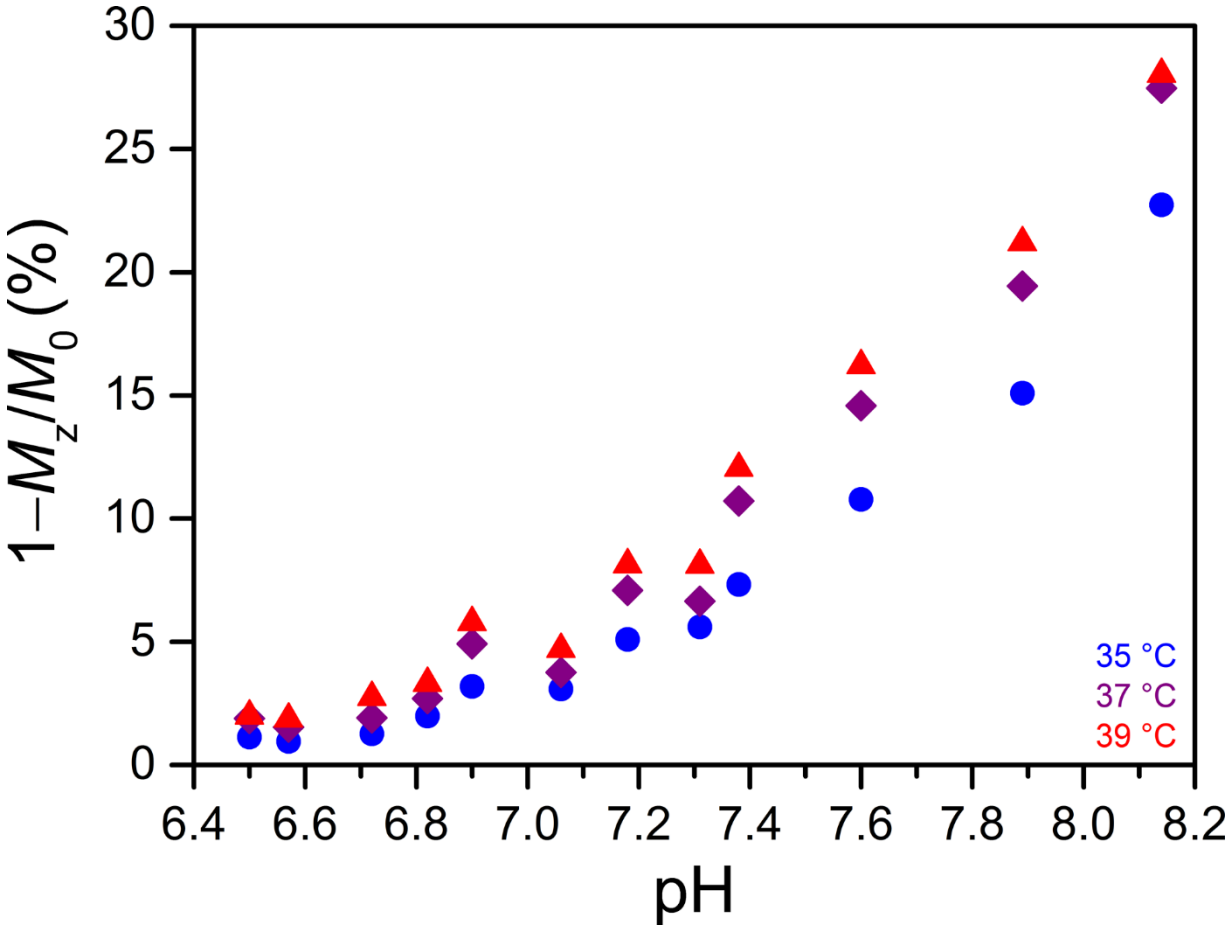

Figure 3.55 Comparison of the pH dependence of the CEST effect from application of presaturation at 64 ppm for 12.8 mM of **1** in aqueous solutions containing 50 mM HEPES and 100 mM NaCl at various temperatures (see legend).

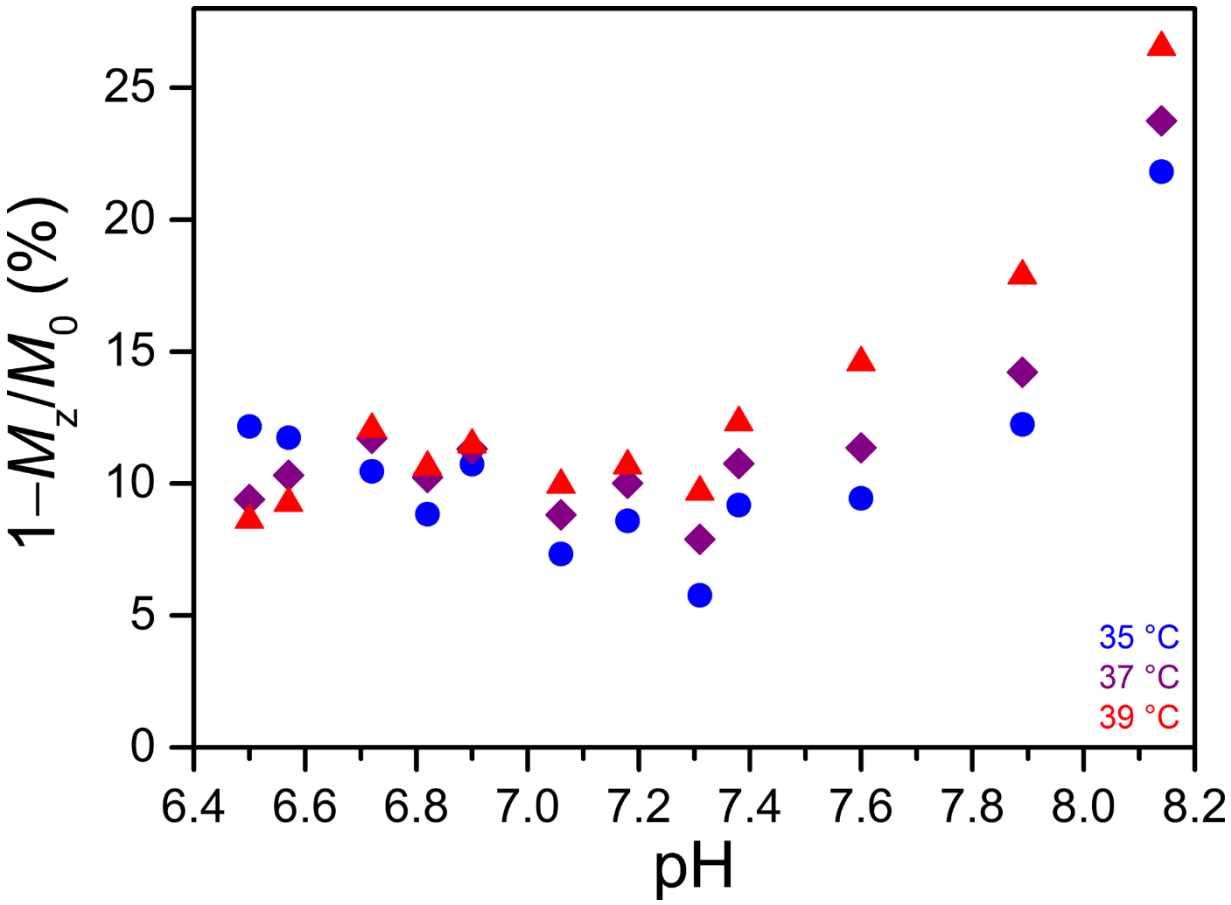

Figure 3.56 Comparison of the pH dependence of the CEST effect from application of presaturation at 104 ppm for 12.8 mM of **1** in aqueous solutions containing 50 mM HEPES and 100 mM NaCl at various temperatures (see legend).

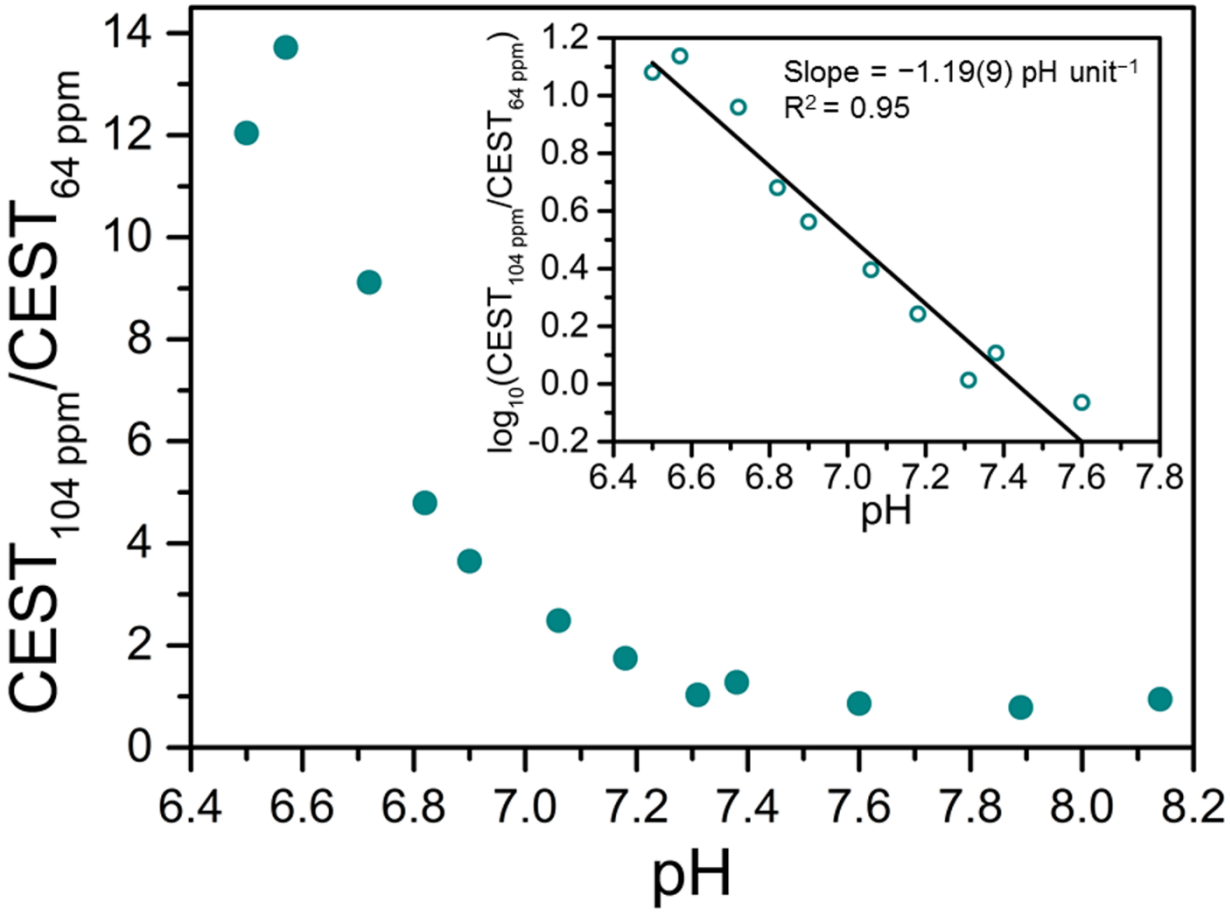

Figure 3.57 pH dependences of the ratio of CEST effects from application of presaturation at 104 and 64 ppm, and the base 10 logarithm of the ratio (inset) for 12.8 mM of **1** in aqueous solutions containing 50 mM HEPES and 100 mM NaCl at 35 °C. Dark cyan circles represent experimental data and the solid black line denotes a linear fit to the data with the following equation: $\log_{10}(CEST_{104\ ppm}/CEST_{64\ ppm}) = -1.19(9) \times pH + 8.9(6)$; $R^2 = 0.95$.

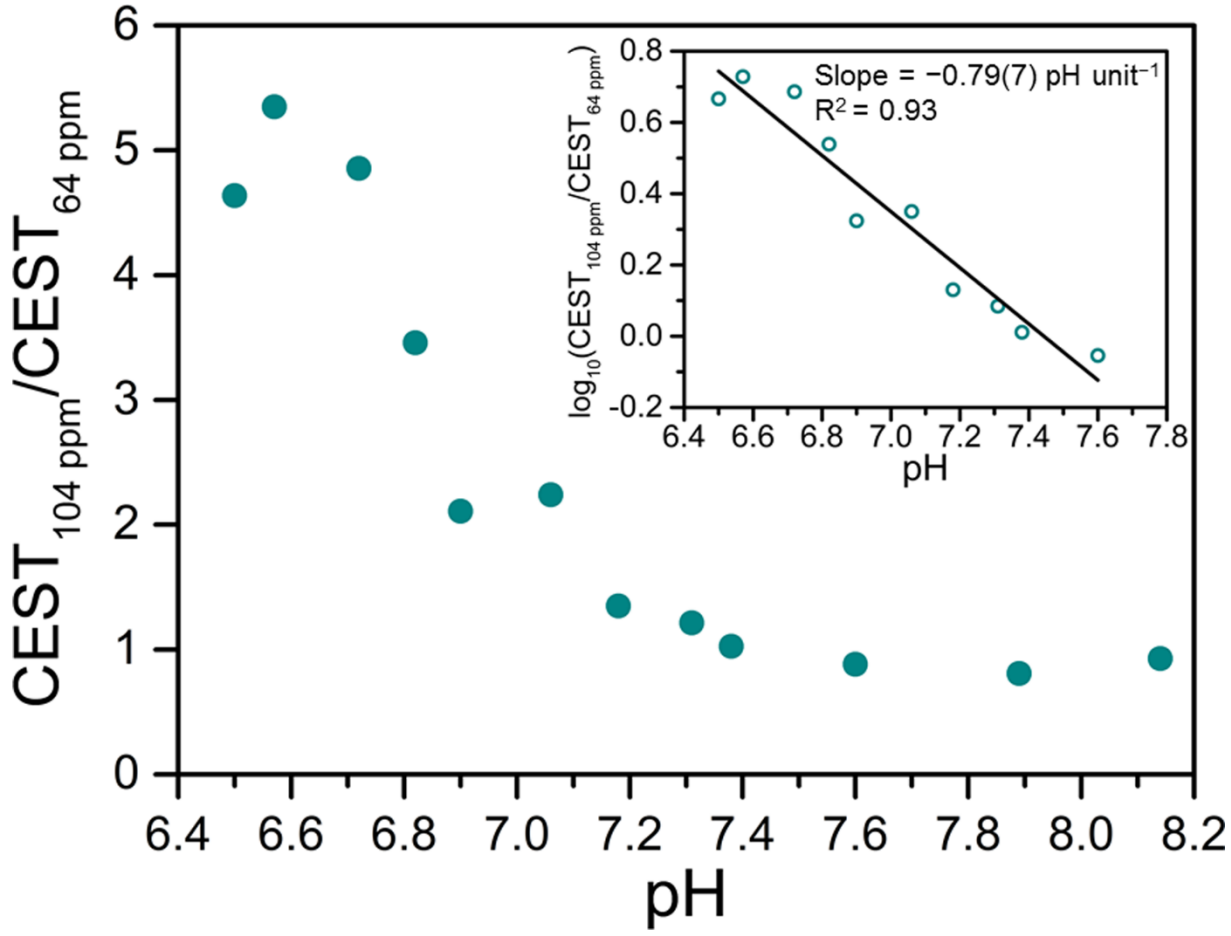

Figure 3.58 pH dependences of the ratio of CEST effects from application of presaturation at 104 and 64 ppm, and the base 10 logarithm of the ratio (inset) for 12.8 mM of **1** in aqueous solutions containing 50 mM HEPES and 100 mM NaCl at 39 °C. Dark cyan circles represent experimental data and the solid black line denotes a linear fit to the data with the following equation: $\log_{10}(CEST_{104\ ppm}/CEST_{64\ ppm}) = -0.79(7) \times pH + 5.9(5)$; $R^2 = 0.93$.

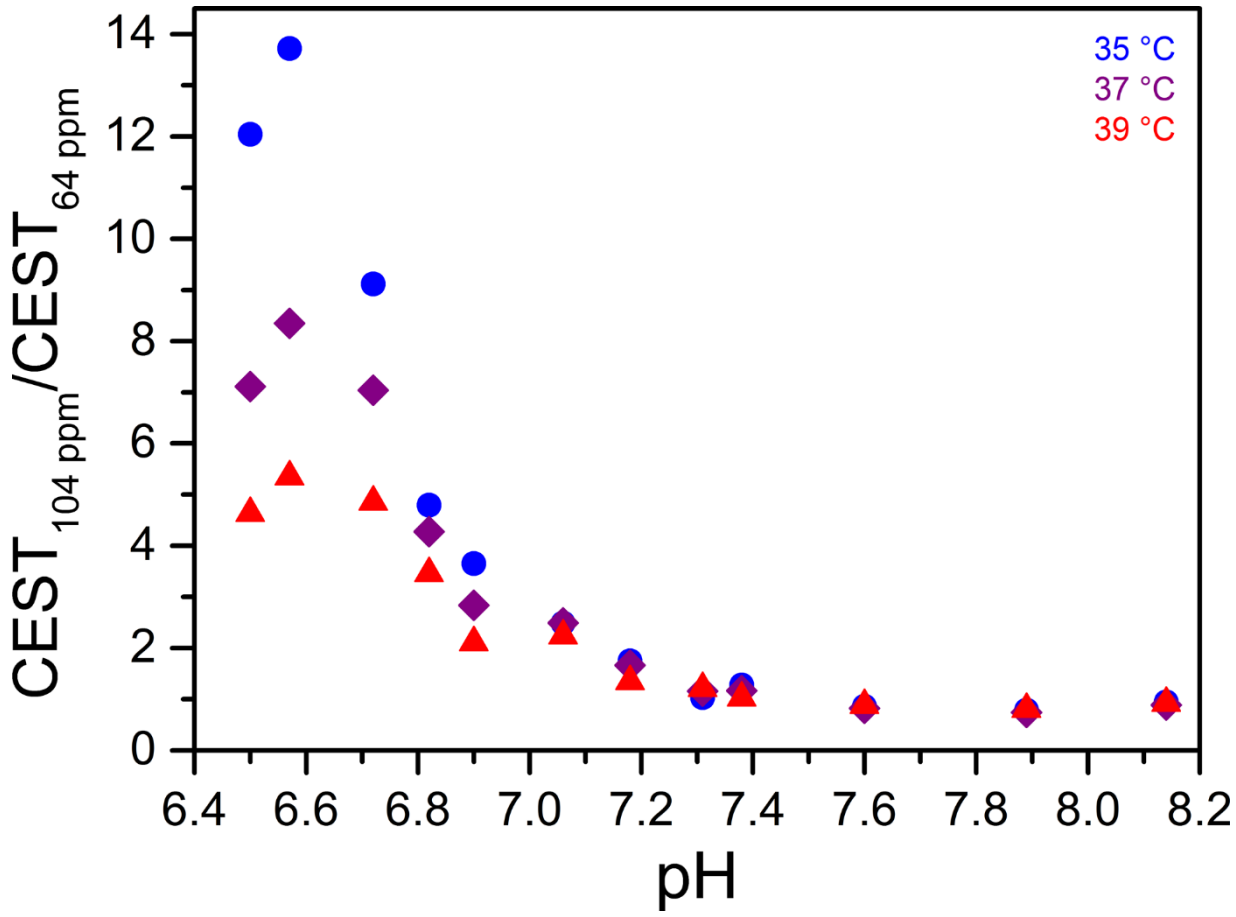

Figure 3.59 Comparison of the pH dependence of the ratio of CEST effects from application of presaturation at 104 and 64 ppm for 12.8 mM of **1** in aqueous solutions containing 50 mM HEPES and 100 mM NaCl at various temperatures (see legend).

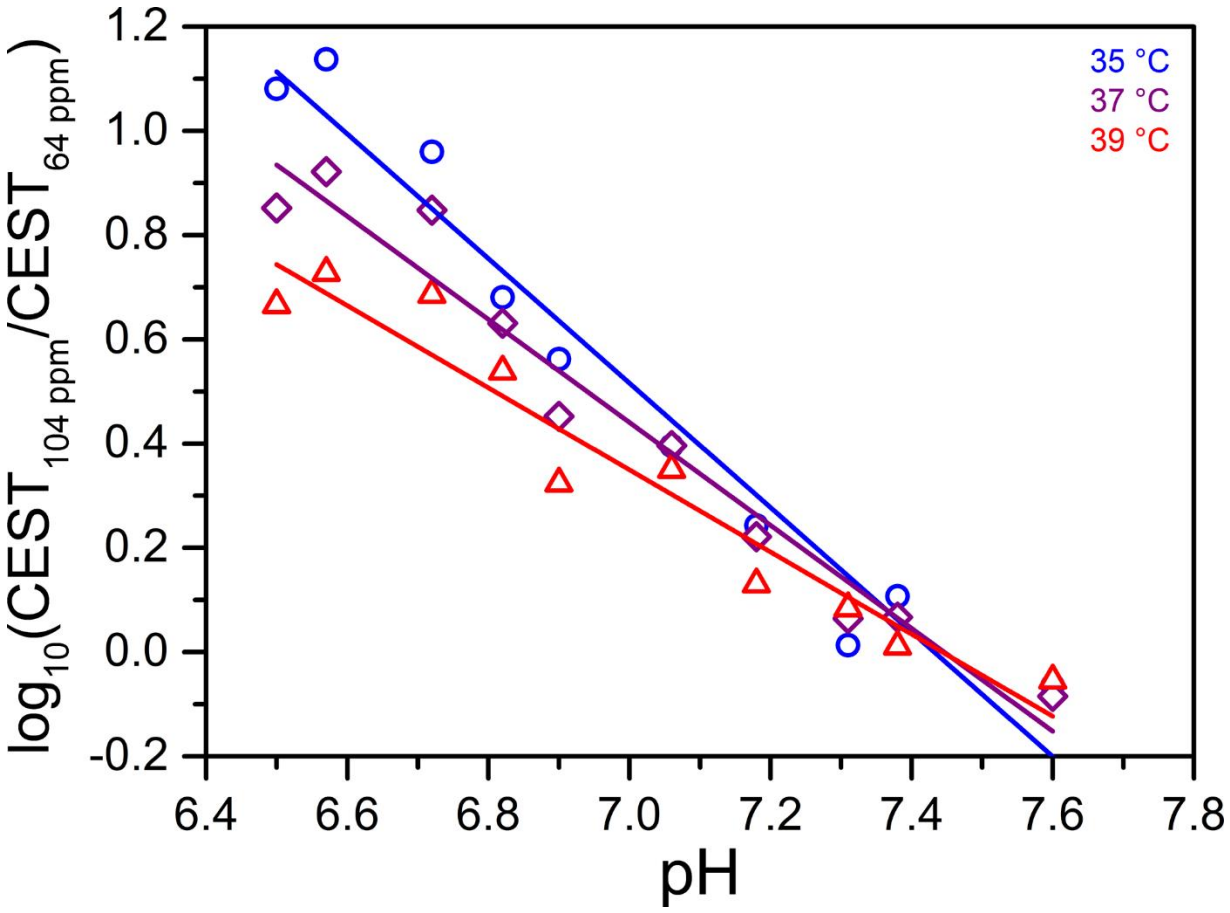

Figure 3.60 Comparison of the pH calibration curves obtained by taking the base 10 logarithm of the ratios of CEST effects from application of presaturation at 104 and 64 ppm for 12.8 mM of **1** in aqueous solutions containing 50 mM HEPES and 100 mM NaCl at various temperatures (see legend). Symbols represent experimental data and the colored lines denote linear fits to the data. See Equations 3.3, 3.8, and 3.9 for the equations of the linear fits to the data.

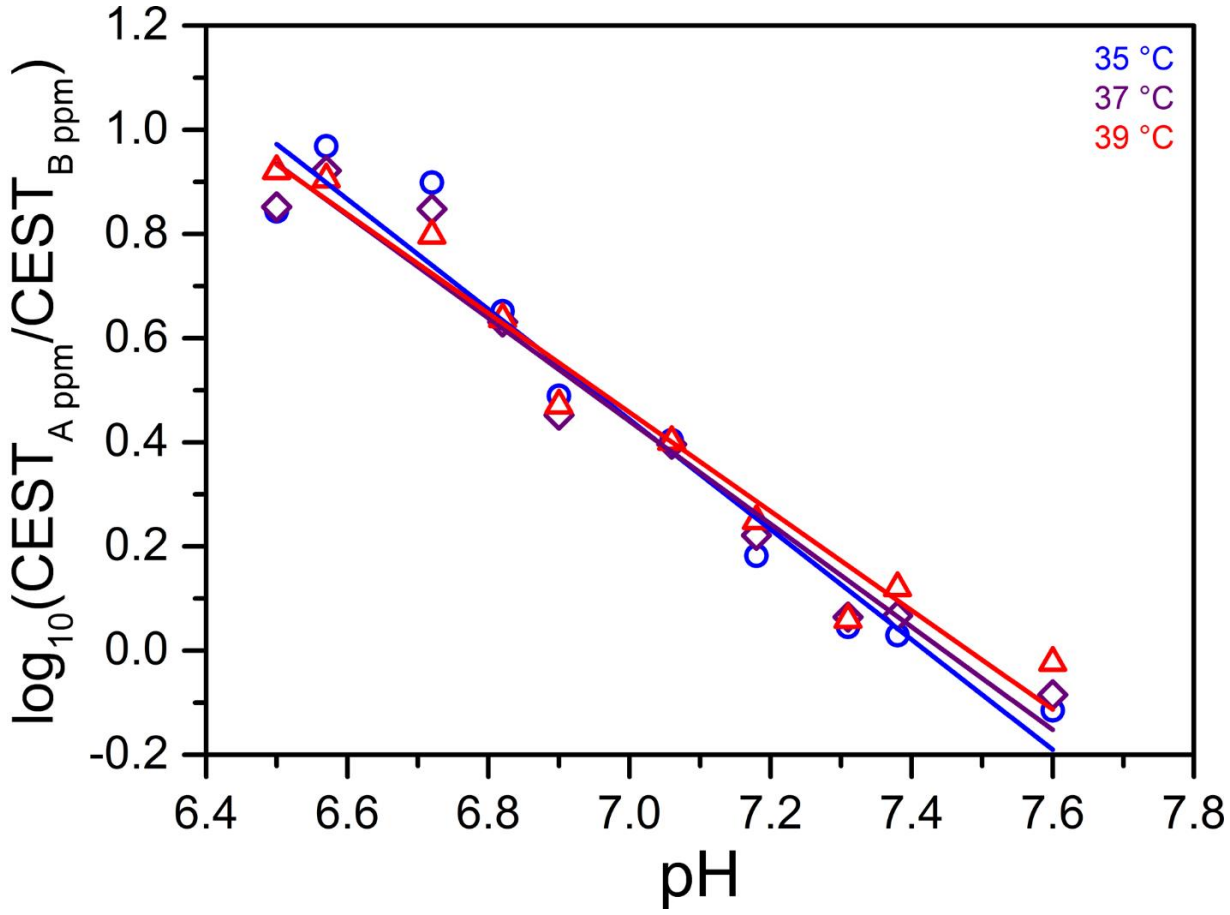

Figure 3.61 Comparison of the pH calibration curves obtained by taking the base 10 logarithm of the ratios of CEST effects from application of presaturation at 105 and 65 ppm, at 104 and 64 ppm, and at 103 and 63 ppm for 12.8 mM of **1** in aqueous solutions containing 50 mM HEPES and 100 mM NaCl at 35, 37, and 39 °C, respectively (see legend). Symbols represent experimental data and the colored lines denote linear fits to the data with the following equations: 35 °C: $\log_{10}(CEST_{105\ ppm}/CEST_{65\ ppm}) = -1.06(8) \times pH + 7.8(6)$, $R^2 = 0.95$; 37 °C: $\log_{10}(CEST_{104\ ppm}/CEST_{64\ ppm}) = -0.99(7) \times pH + 7.4(5)$, $R^2 = 0.96$; 39 °C: $\log_{10}(CEST_{103\ ppm}/CEST_{63\ ppm}) = -0.95(6) \times pH + 7.1(4)$, $R^2 = 0.97$.

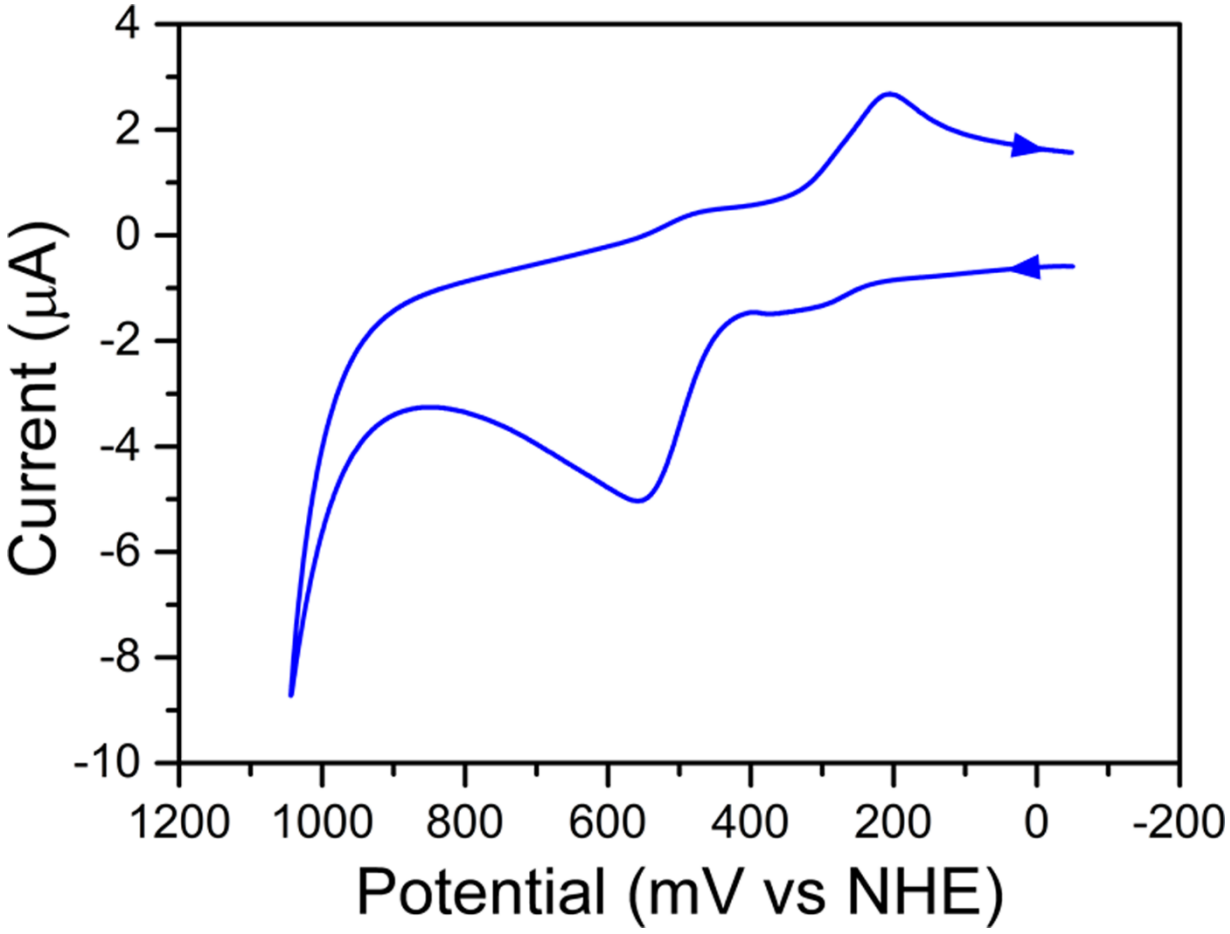

Figure 3.62 Cyclic voltammogram for 1 mM of **1** in an aqueous solution containing 50 mM HEPES and 100 mM NaCl buffered at pH 7.4. Measurements were carried out at ambient temperature using a glassy carbon electrode as a working electrode and a 100 mV s^{-1} scan rate. The blue arrows denote the scan direction. The oxidation event observed at ca. 560 mV vs NHE is assigned to an oxidation from Co^{II}_2 to $Co^{II}Co^{III}$, and the reduction event at ca. 205 mV vs NHE is assigned to the reduction from $Co^{II}Co^{III}$ to Co^{II}_2. Note that the baseline fluctuations observed near 350 and 450 mV vs NHE in the forward and backward scan, respectively, most likely correspond to a miniscule amount of impurity.

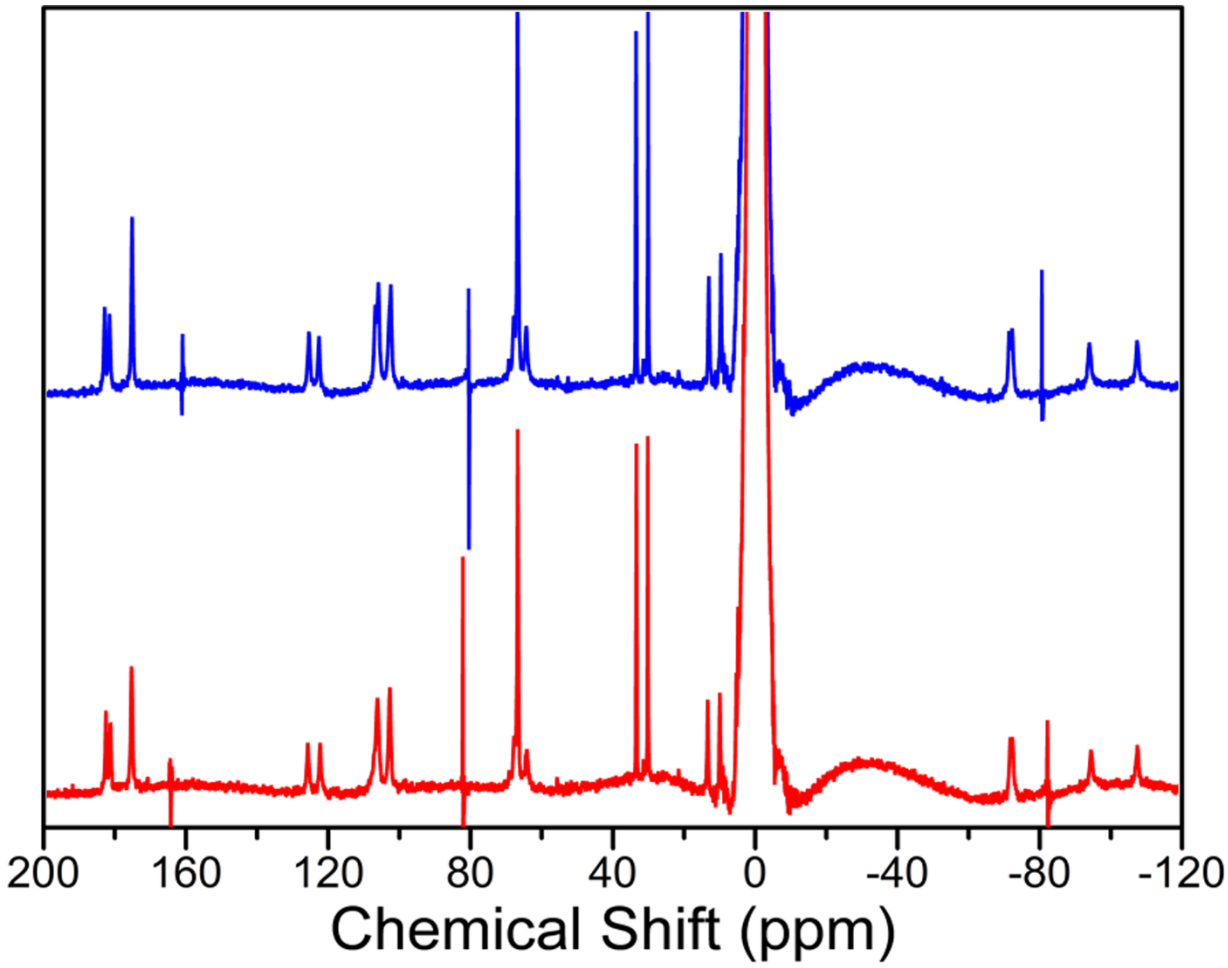

Figure 3.63 Stacked ^{1}H NMR spectra of 10 mM of **1** in aqueous solutions containing 50 mM HEPES and 100 mM NaCl buffered at pH 7.3 without (blue) and with (red) the presence of 10 mM of each NaOAc, Na_2CO_3, NaH_2PO_4, and Na_2SO_4 at 37 °C. Note that compound **1** was incubated with the solution of the anions at 25 °C for 16 h prior to the NMR experiment. The sharp features at 165, 82, and −82 ppm are instrument-derived artifacts.

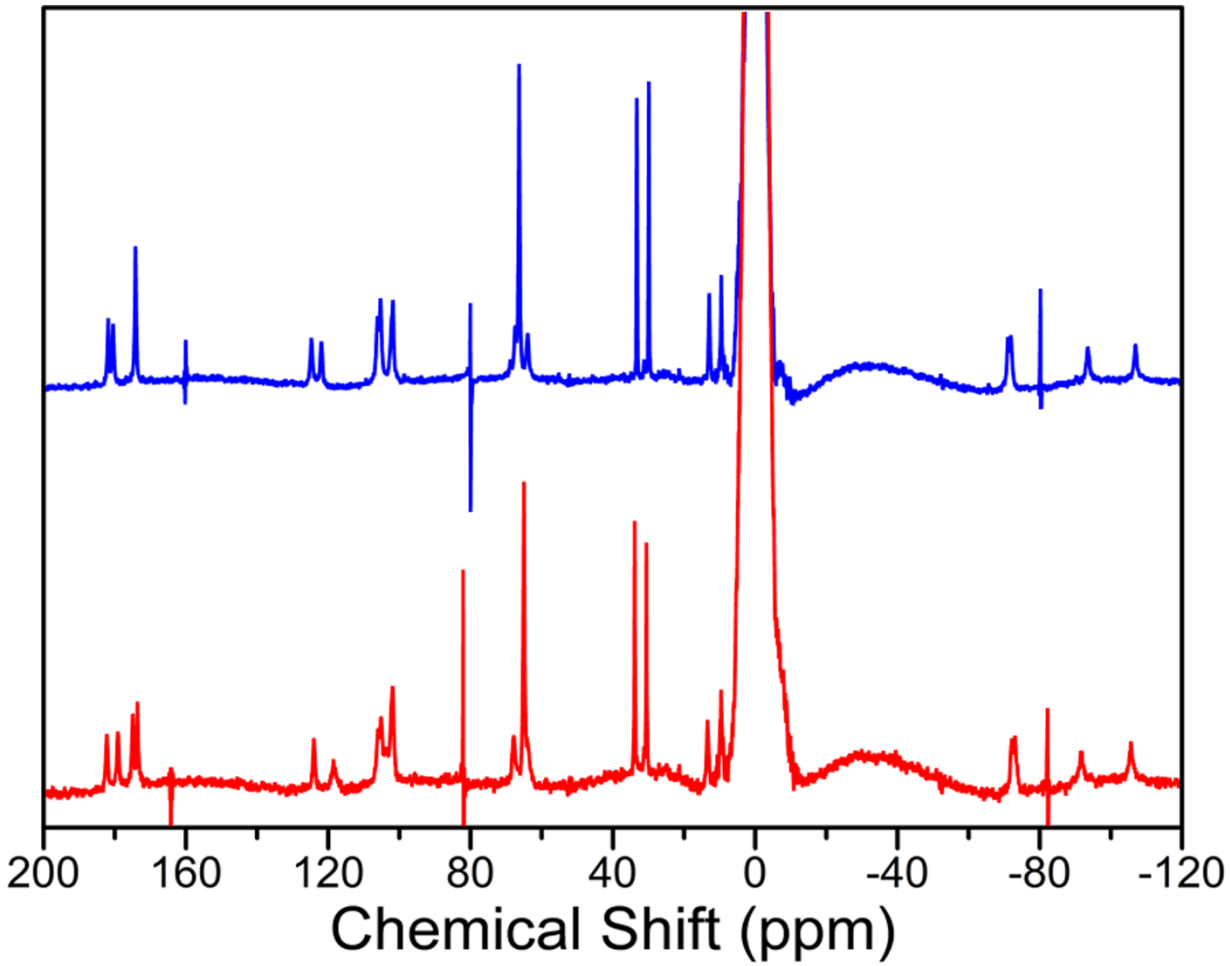

Figure 3.64 Stacked ^{1}H NMR spectra of 10 mM of **1** in aqueous solutions containing 50 mM HEPES and 100 mM NaCl buffered at pH 7.3 without (blue) and with (red) the presence of 10 mM of $Ca(NO_3)_2$ at 37 °C. Note that compound **1** was incubated with the Ca^{2+} solution at 25 °C for 16 h prior to the NMR experiment. The sharp features at 165, 82, and −82 ppm are instrument-derived artifacts.

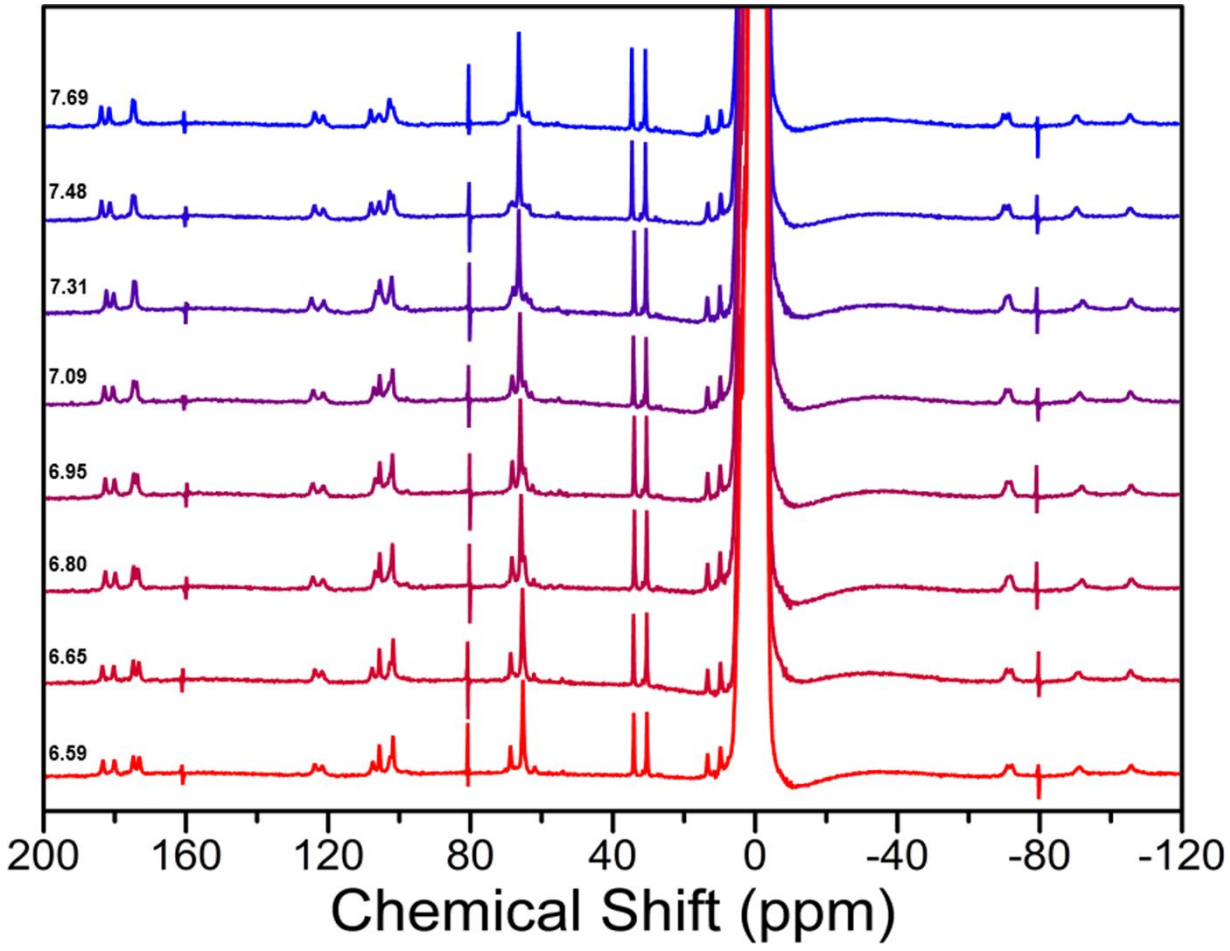

Figure 3.65 Variable-pH ^{1}H NMR spectra of 15 mM of **1** in FBS at various pH values at 37 °C. Black numbers on the left denote the pH of the NMR sample solutions measured with a pH electrode. The sharp features at 160, 80, and −80 ppm are instrument-derived artifacts.

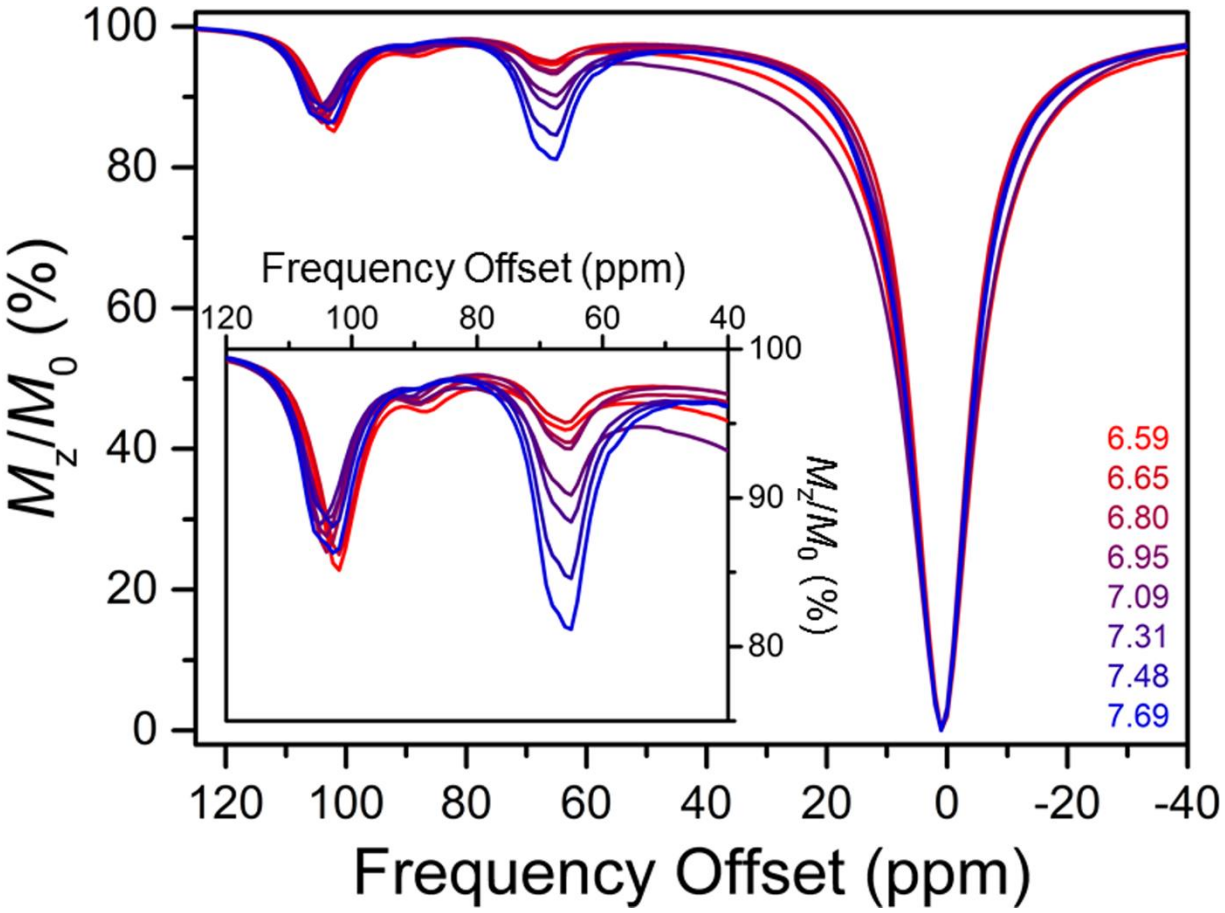

Figure 3.66 Variable-pH CEST spectra for 15 mM of **1** in FBS collected at pH 6.59–7.69 (red to blue) at 37 °C. Colored numbers in the legend denote the pH of the solutions measured with a pH electrode and the corresponding color of each sample. Note that the feature at ca. 88 ppm in the CEST spectra is not observed in the corresponding ^{1}H NMR spectra and most likely derives from a miniscule amount of an OH-containing impurity, as it is most prominent under acidic conditions. The exact nature of this feature is currently unknown but note that its presence does not interfere with the analysis of the two CEST effects from **1**.

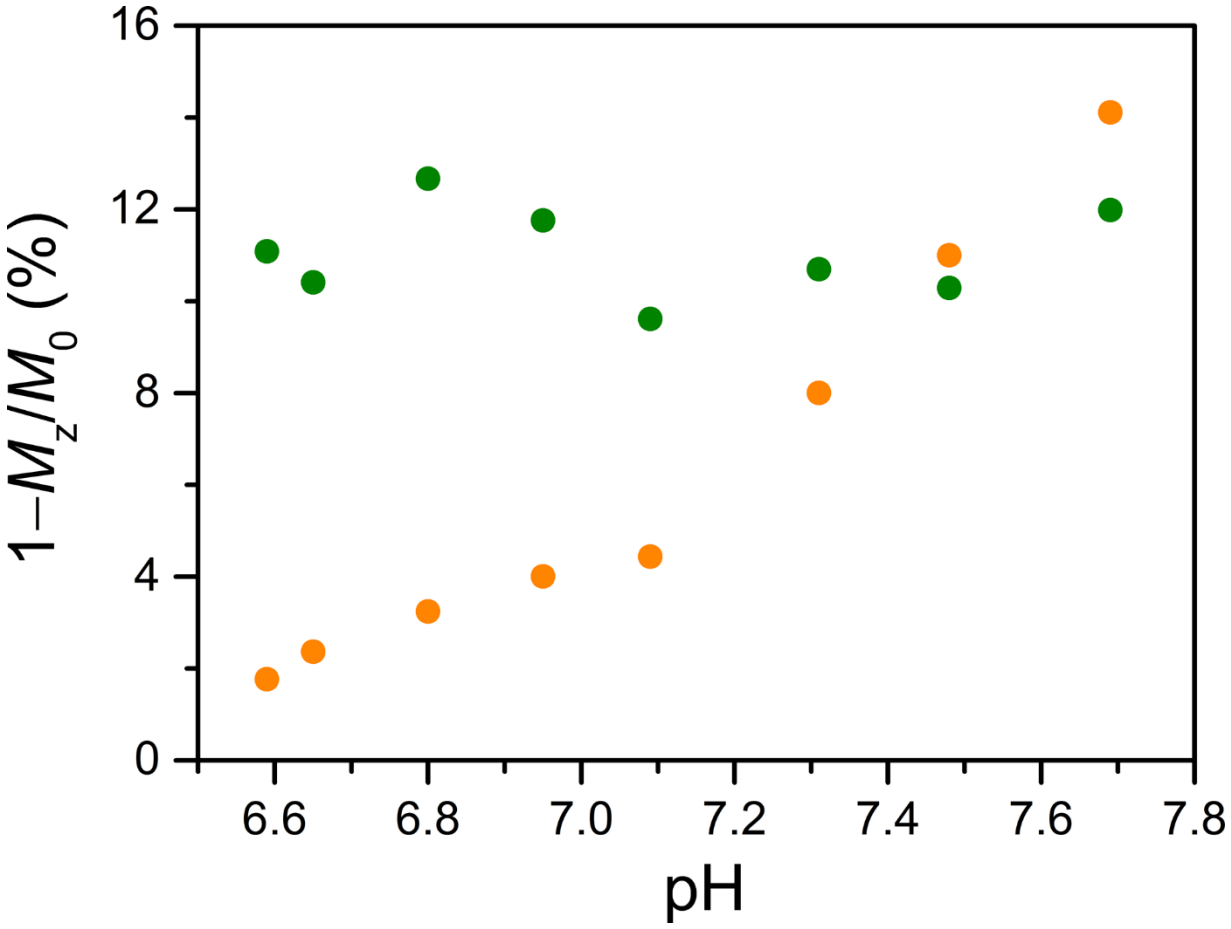

Figure 3.67 pH dependences of the CEST effects from application of presaturation at 64 ppm (yellow) and 104 ppm (green) for 15 mM of **1** in FBS at 37 °C.

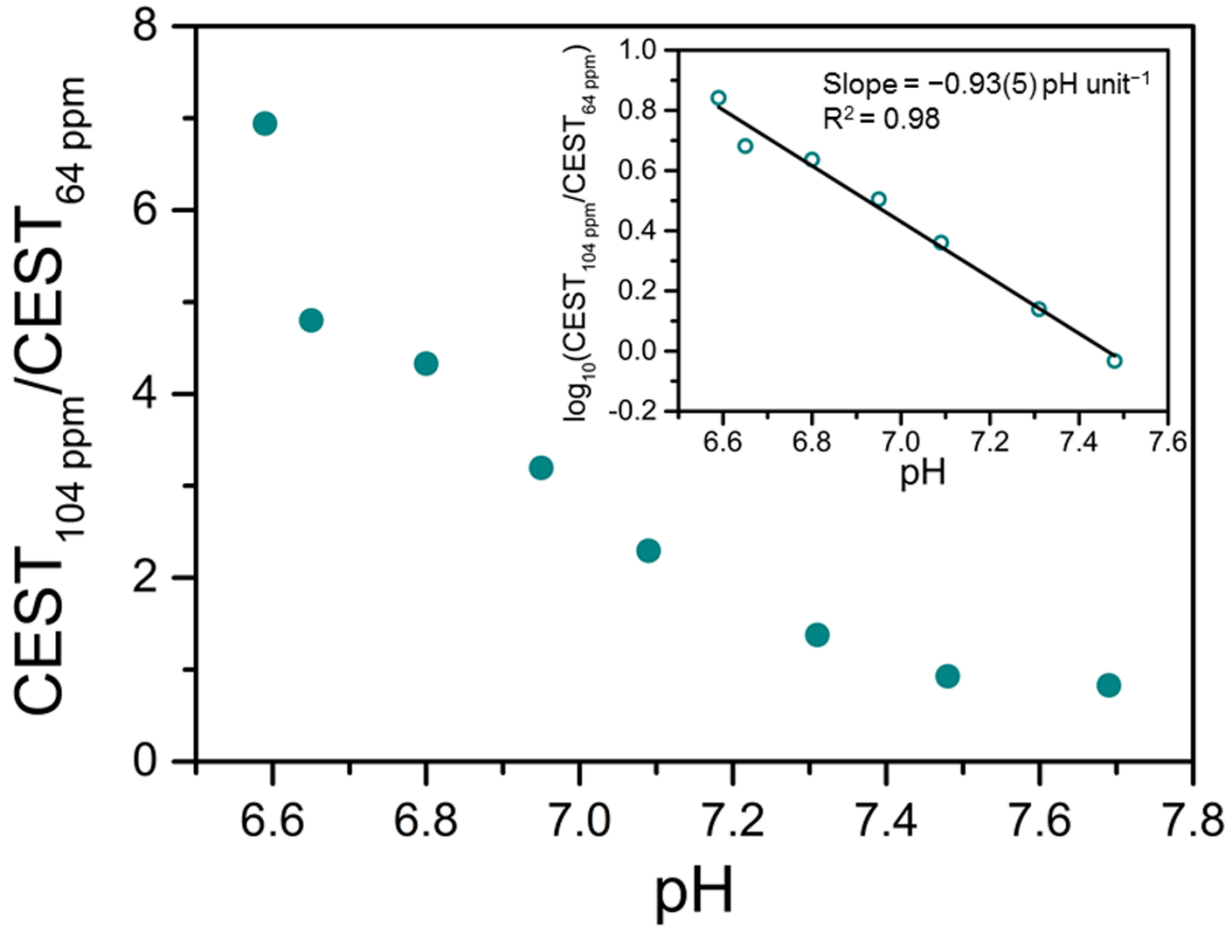

Figure 3.68 pH dependences of the ratio of CEST effects from application of presaturation at 104 and 64 ppm, and the base 10 logarithm of the ratio (inset) for 15 mM of **1** in FBS at 37 °C. Dark cyan circles represent experimental data and the solid black line denotes a linear fit to the data with the following equation: $\log_{10}(CEST_{104\ ppm}/CEST_{64\ ppm}) = -0.93(5) \times pH + 6.9(3)$; $R^2 = 0.98$.

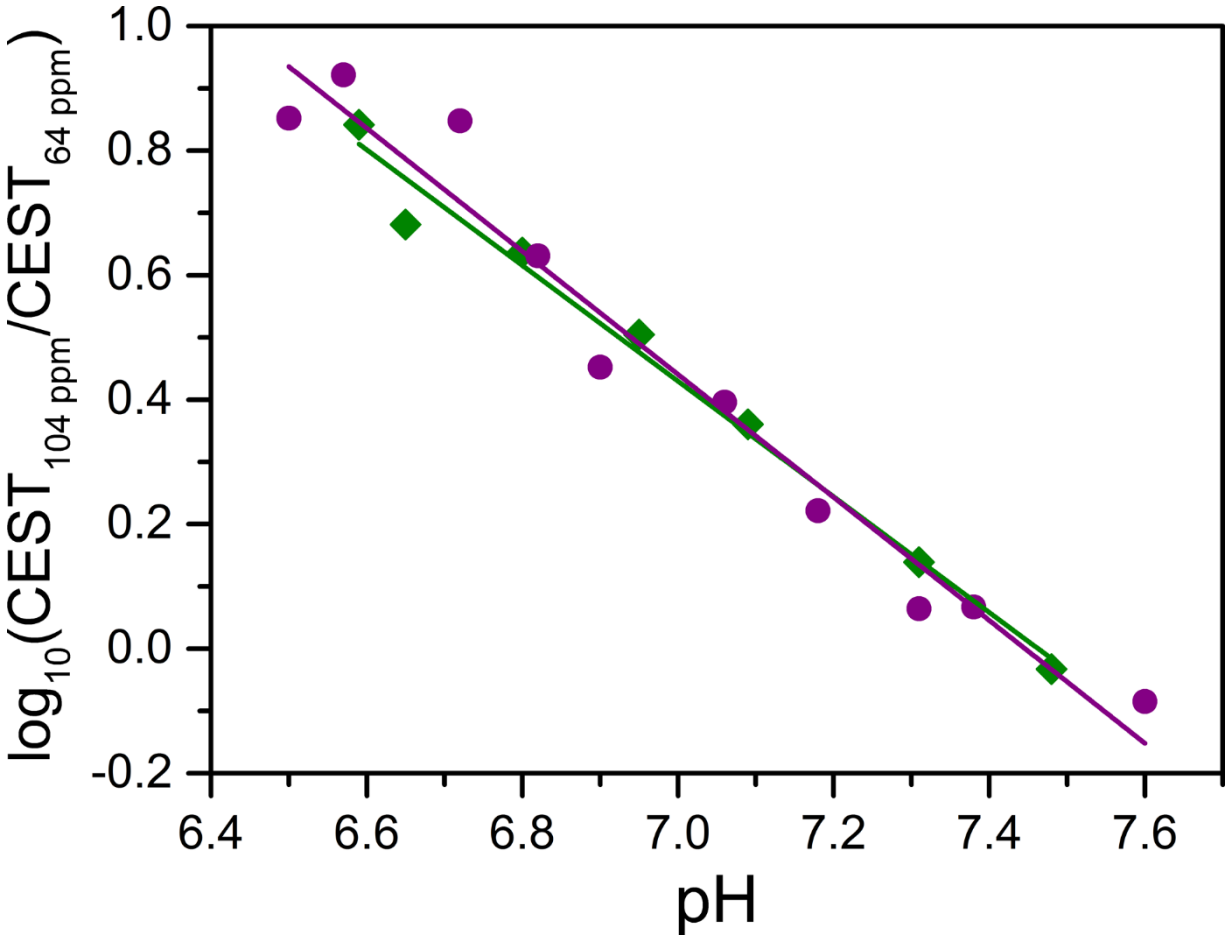

Figure 3.69 Comparison of the pH calibration curves obtained by taking the base 10 logarithm of the ratios of CEST effects from application of presaturation at 104 and 64 ppm for 12.8 mM of **1** in 50 mM HEPES buffers with 100 mM NaCl (purple), and for 15 mM of **1** in FBS (green) at 37 °C. Circles and diamonds represent experimental data and the solid lines denote linear fits to the data. See Figure 3.68 and Equation 3.3 for the equations of the linear fits to the data.

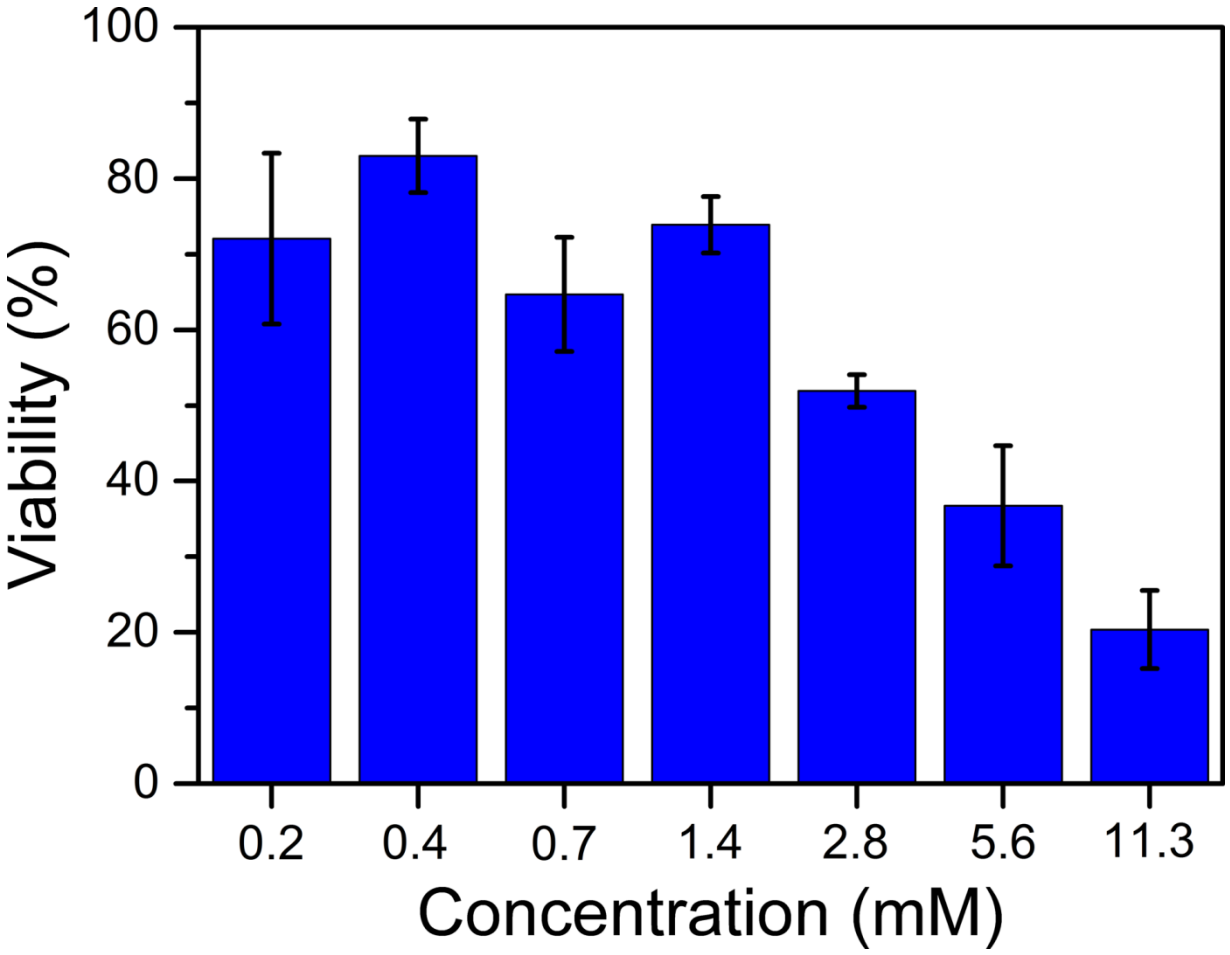

Figure 3.70 Cell survival (in %) after incubation with various concentrations of **1** for 24 h at 37 °C and 5.0% CO_2. Error bars represent standard deviations of three measurements. Note that %viability is reported without taking normal cell death into account (see Section 3.2).

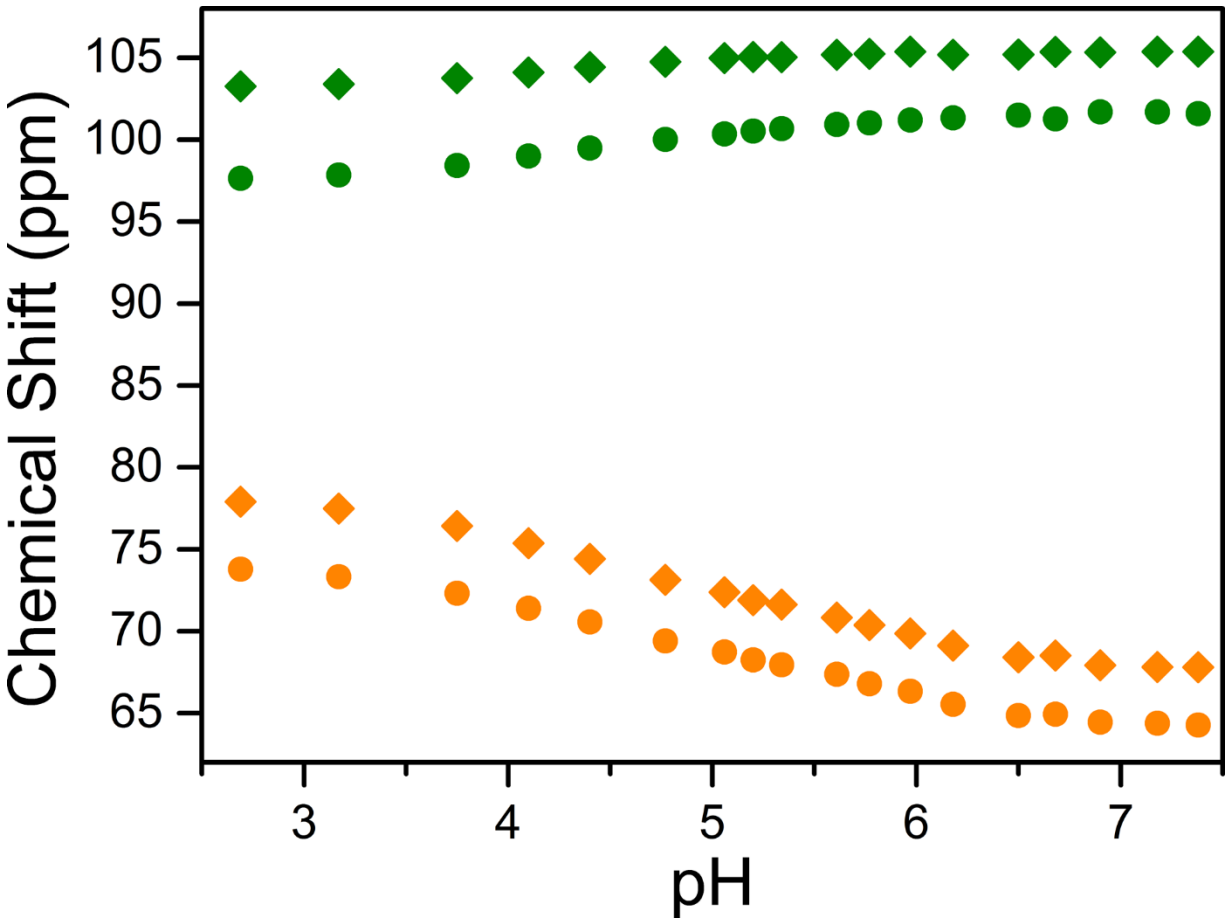

Figure 3.71 pH dependences of the ^{1}H NMR chemical shifts (reported as frequency offsets) of the four furthest downfield-shifted carboxamide resonances for **1** in aqueous solutions containing 50 mM HEPES and 100 mM NaCl at 37 °C. The yellow and green data points correspond to amide protons giving rise to CEST effects at ca. 64 and 104 ppm, respectively.

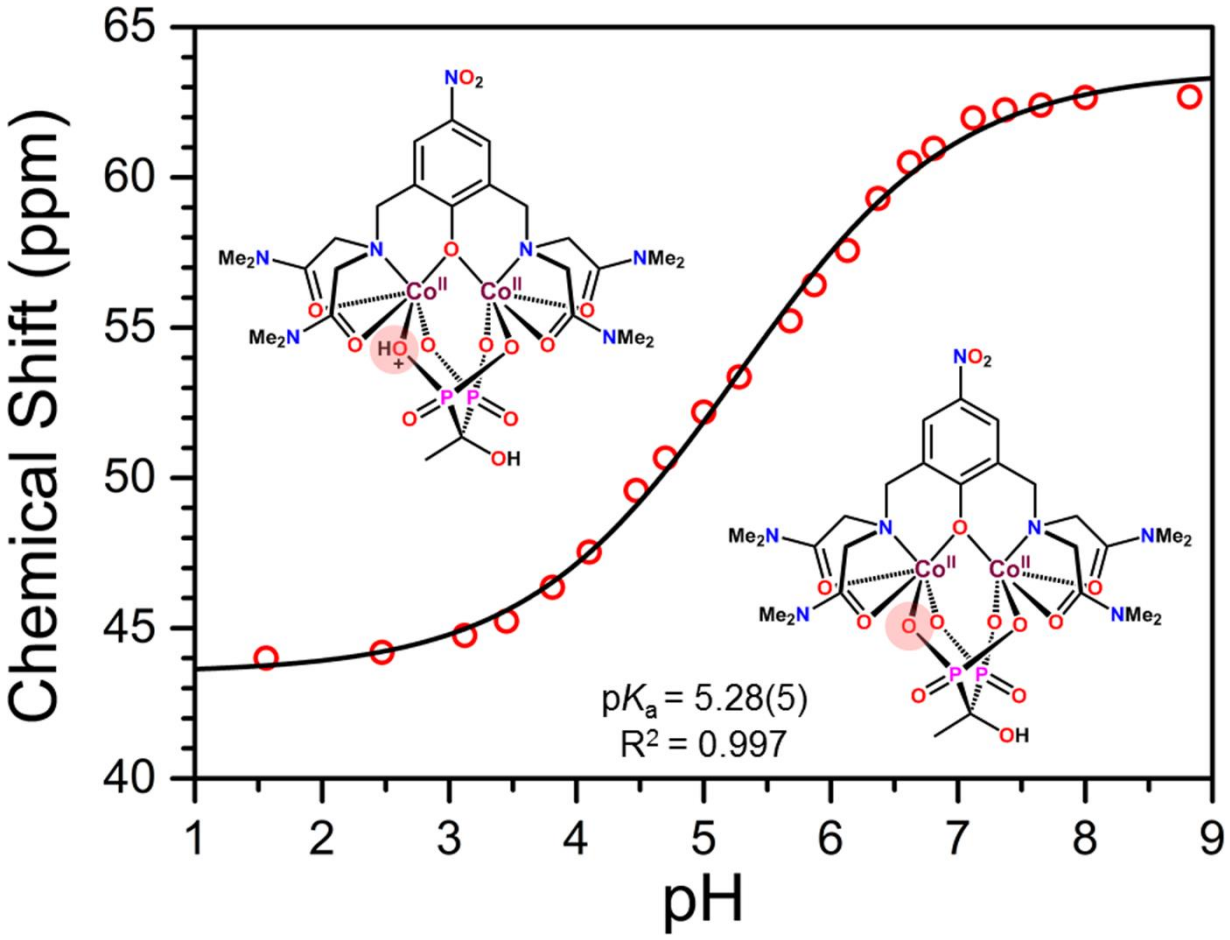

Figure 3.72 pH dependence of the ^{1}H NMR chemical shift (reported as frequency offset) of the CH_3 resonance from etidronate for **3** in aqueous solutions containing 50 mM HEPES and 100 mM NaCl at 37 °C. Red circles represent experimental data and the solid black line corresponds to a sigmoidal fit to the data (see Equation 3.1), giving pK_a = 5.28(5) with R^2 = 0.997. The ionization process taking place on the ancillary bisphosphonate is highlighted with the schematics of the complex.

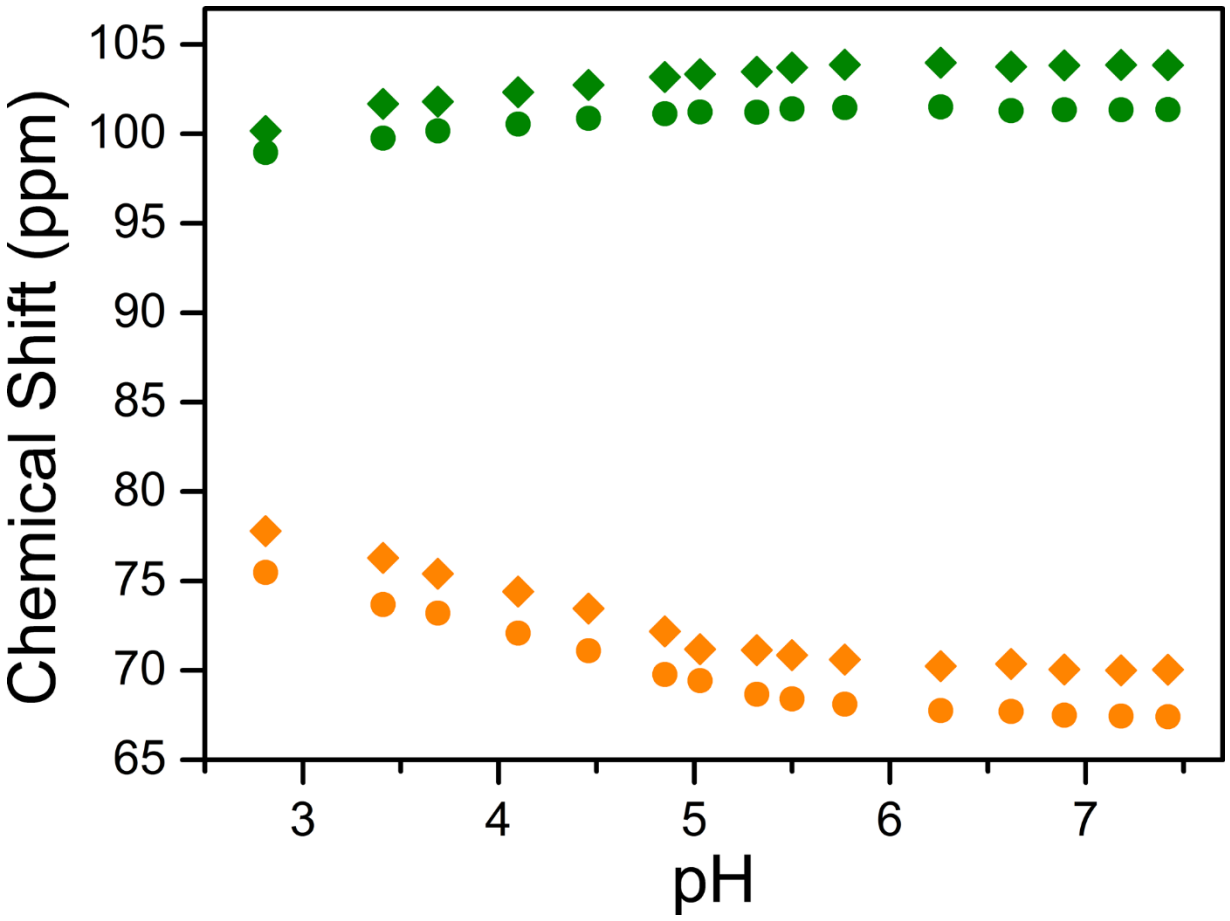

Figure 3.73 pH dependences of the ^{1}H NMR chemical shifts (reported as frequency offsets) of the four furthest downfield-shifted carboxamide resonances for **2** in aqueous solutions containing 50 mM HEPES and 100 mM NaCl at 37 °C. The yellow and green data points correspond to amide protons giving rise to CEST effects at ca. 68 and 102 ppm, respectively.

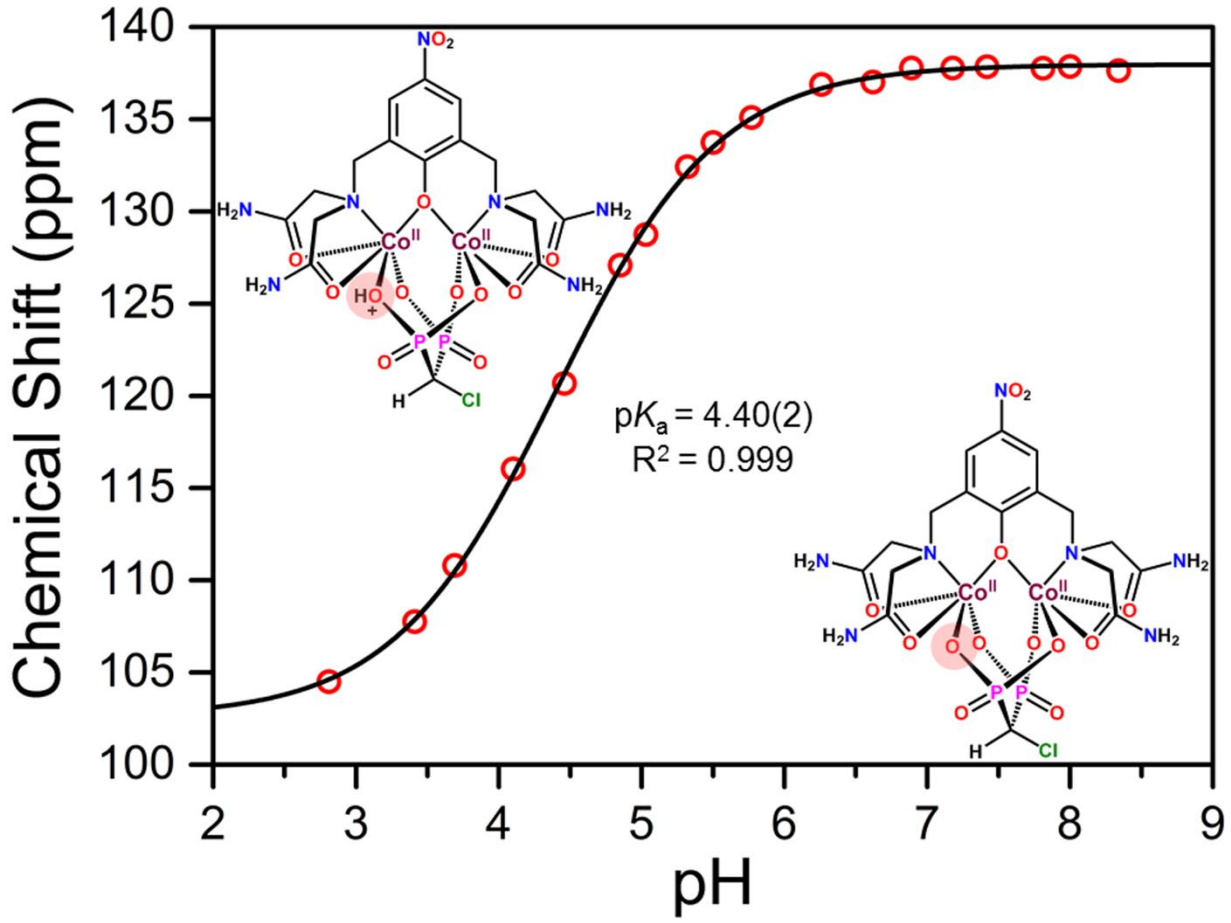

Figure 3.74 pH dependence of the ^{1}H NMR chemical shift (reported as frequency offset) of the CH resonance from $CMDP^{4-}$ for **2** in aqueous solutions containing 50 mM HEPES and 100 mM NaCl at 37 °C. Red circles represent experimental data and the solid black line corresponds to a sigmoidal fit to the data (see Equation 3.1), giving pK_a = 4.40(2) with R^2 = 0.999. The ionization process taking place on the ancillary bisphosphonate is highlighted with the schematics of the complex.

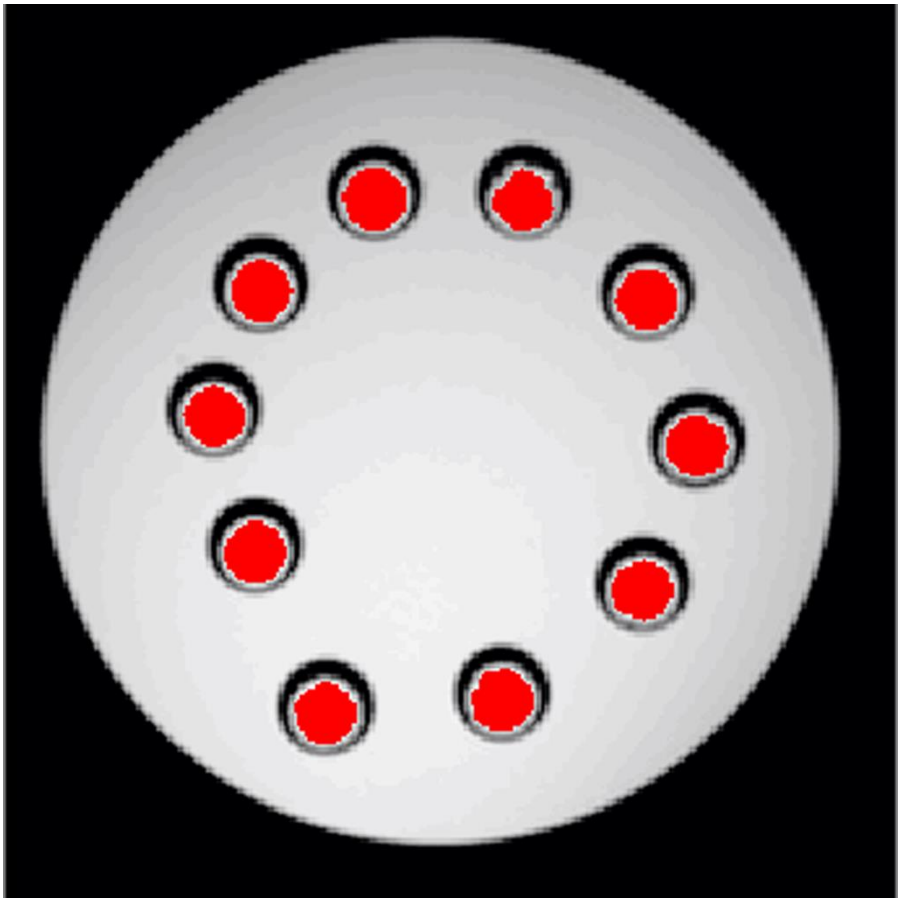

Figure 3.75 MR image of a series of capillary tubes containing 17 mM of **1** in aqueous solutions with 50 mM HEPES and 100 mM NaCl buffered at selected pH values from 6.40 to 7.88, used for phantom experiments. The red circular areas highlight the regions shown in Figure 3.6, which were used for CEST data analysis. These regions correspond to 75.4% of the total cross-sectional area of the inner capillary tubes. The remaining areas near the edges of the capillary tubes were not included in the data analysis due to partial volume and susceptibility effects observed (see Section 3.2).

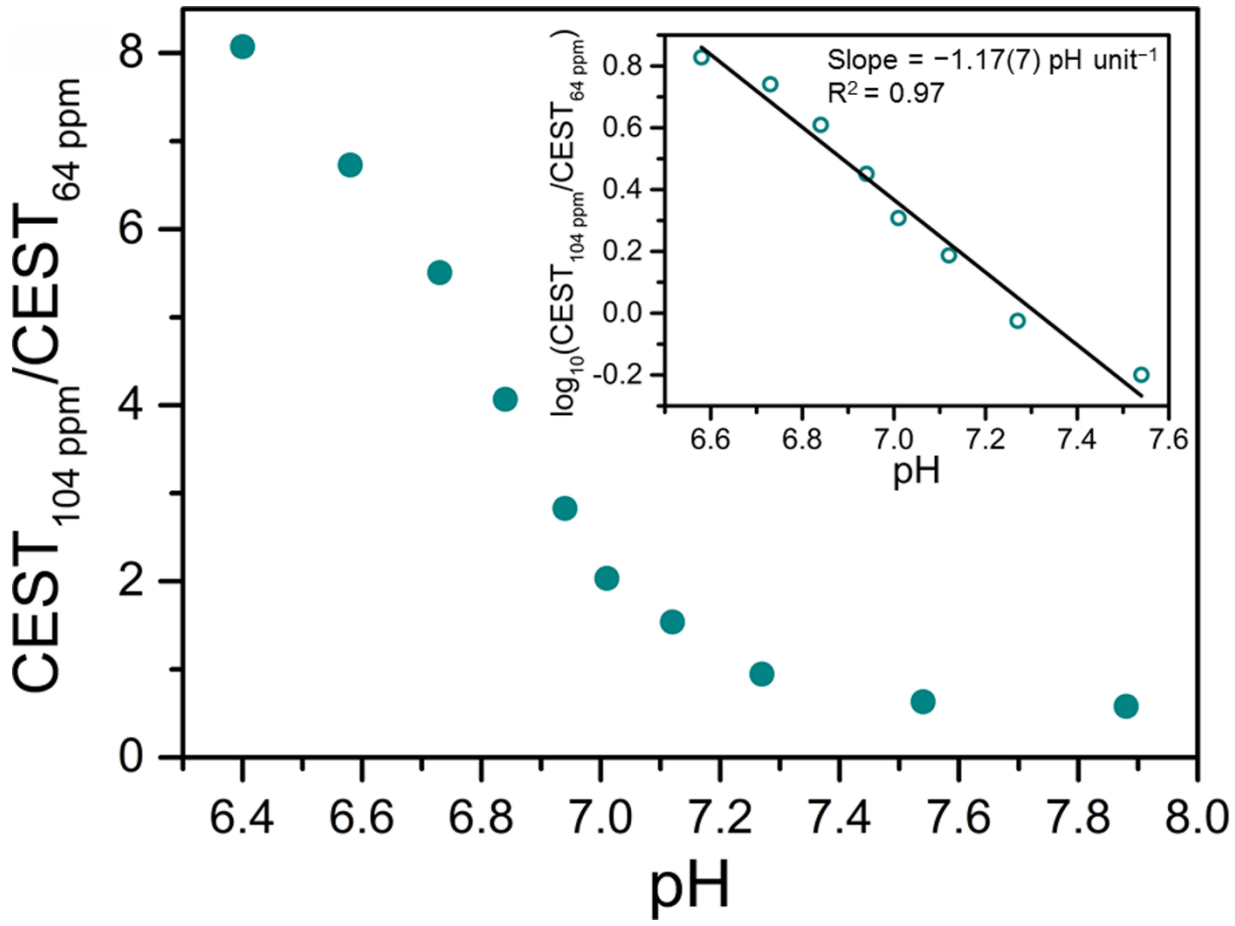

Figure 3.76 pH dependences of the ratio of CEST effects from the averaged phantom image intensities with presaturation at 104 and 64 ppm, and the base 10 logarithm of the ratio (inset) for 17 mM of **1** in aqueous solutions with 50 mM HEPES and 100 mM NaCl at 37 °C. Dark cyan circles represent experimental data and the solid black line denotes a linear fit to the data with the following equation: $\log_{10}(CEST_{104\ ppm}/CEST_{64\ ppm}) = -1.17(7) \times pH + 8.6(5)$; $R^2 = 0.97$.

3.5.4 Supplementary Tables

Table 3.2 Crystallographic data for **1′** and **2′** at 100 K.

	1′	**2′**
Empirical formula	$C_{18}H_{28}Co_2N_7NaO_{20.8}P_2$	$C_{17}H_{29}ClCo_2N_7NaO_{21.2}P_2$
Formula weight, g mol^{-1}	878.06	908.83
Crystal system	Monoclinic	Monoclinic
Space group	$P2_1/n$	$P2_1/n$
Wavelength, Å	0.71073	0.71073
Temperature, K	100	100
a, Å	9.1253(9)	9.1331(9)
b, Å	16.614(2)	16.658(2)
c, Å	23.152(2)	22.867(2)
α, °	90	90
β, °	94.827(5)	93.543(5)
γ, °	90	90
V, Å^3	3497.7(6)	3472.4(6)
Z	4	4
ρ_{calcd}, g cm^{-3}	1.667	1.738
μ, mm^{-1}	1.143	1.230
Reflections coll./unique	130306/13616	106421/10816
R(int)	0.0728	0.0352
R_1 $(I > 2\sigma(I))^a$	0.1290	0.0448
wR_2 $(all)^b$	0.3852	0.1198
GoF	1.933	1.070

^{a} $R_1 = \Sigma||F_0| - |F_C||/\Sigma|F_0|$, ^{b} $wR_2 = [\Sigma w(F_0^2 - F_C^2)^2/\Sigma w(F_0^2)^2]^{1/2}$.

Table 3.3 Summary of average solution dc magnetic susceptibility data for compounds **1**–**3** at 37 °C, obtained using the Evans method[21] (see Equation 3.2) for aqueous solutions with 50 mM HEPES and 100 mM NaCl buffered at various pH values (see Figures 3.14–3.16).

Average values	**1**	**2**	**3**
$\chi_M T$ ($cm^3\,K\,mol^{-1}$)	6.3(3)	6.0(2)	6.1(2)
$\chi_M T$ per Co^{II} ($cm^3\,K\,mol^{-1}$)	3.2(2)	3.0(1)	3.1(1)
μ_{eff} per Co^{II} (μ_B)[a]	5.0(2)	4.9(1)	5.0(1)
g per Co^{II} [b]	2.6(1)	2.5(1)	2.6(1)

[a] The relationship between μ_{eff} and $\chi_M T$ is as follows: $\mu_{eff} = (8\chi_M T)^{1/2}\mu_B$. [b] The relationship between $\chi_M T$ and g is as follows: $\chi_M T = (g^2 S(S+1))/8$. Note, here $S = {}^3/_2$.

Table 3.4 Frequency offsets corresponding to maximum CEST effects at 24 μT power level (B_1) for each pH value for 12 mM of **2** in aqueous solutions containing 50 mM HEPES and 100 mM NaCl at 37 °C, used to estimate the proton exchange rate constants (k_{ex}).

pH	Frequency Offset (ppm)[a]	
	Peak 1	Peak 2
6.62	68	102
6.89	68	102
7.18	68	102
7.42	68	102
7.81	68	102
8.00	68	102
8.34	69	102

[a] Frequency offset is the ^{1}H NMR chemical shift difference between a resonance of the compound and the H_2O solvent.

Table 3.5 Frequency offsets corresponding to the maximum CEST effect at 24 μT power level (B_1) for each pH value for 13 mM of **3** in aqueous solutions containing 50 mM HEPES and 100 mM NaCl at 37 °C, used to estimate the proton exchange rate constant (k_{ex}).

pH	Frequency Offset (ppm)[a]
5.80	94
6.11	97
6.44	99
6.83	101
7.06	102
7.47	103
7.74	103
8.08	103

[a] Frequency offset is the ^{1}H NMR chemical shift difference between a resonance of the compound and the H_2O solvent.

Table 3.6 Frequency offsets corresponding to maximum CEST effects at 24 μT power level (B_1) for each pH value for 12.8 mM of **1** in aqueous solutions containing 50 mM HEPES and 100 mM NaCl at 37 °C, used to estimate the proton exchange rate constants (k_{ex}).

pH	Frequency Offset (ppm)[a]	
	Peak 1	**Peak 2**
6.18	N/A[b]	101
6.50	N/A[b]	102
6.57	N/A[b]	102
6.72	65	104
6.82	65	104
6.90	65	104
7.06	64	104
7.18	65	104
7.31	64	105
7.38	65	104
7.60	65	106
7.89	65	106
8.14	66	105

[a] Frequency offset is the ^{1}H NMR chemical shift difference between a resonance of the compound and the H_2O solvent. [b] The exchange rate constant for the CEST effect at 64–66 ppm was not estimated at this pH value due to low intensity.

Table 3.7 T_1 relaxation times of H_2O in samples containing various concentrations of **1** in aqueous solutions with 50 mM HEPES and 100 mM NaCl buffered at different pH values at 37 °C.

pH	T_1 **(s)**		
	12.8 mM	**8.5 mM**	**6.4 mM**
6.82	0.64(1)	0.92(2)	1.20(3)
7.31	0.72(3)	1.01(3)	1.20(3)

Table 3.8 Comparison of pH values calculated from the linear pH calibration curve from CEST imaging data and those measured by a pH electrode for 17 mM of **1** in aqueous solutions with 50 mM HEPES and 100 mM NaCl at 37 °C.

Sample	pH electrode	CEST imaging
1	6.40	N/A[a]
2	6.58	6.61
3	6.73	6.68
4	6.84	6.79
5	6.94	6.93
6	7.01	7.05
7	7.12	7.15
8	7.27	7.33
9	7.54	7.48
10	7.88	N/A[a]

[a] The data obtained at this pH value falls outside the linear regime of the $\log_{10}(CEST_{104\ ppm}/CEST_{64\ ppm})$ vs pH plot and therefore was not considered for the linear fit to the data, used to derive the pH calibration curve.

Chapter 4: Electronic Effects of Ligand Substitution in a Family of Co^{II}_2 PARACEST pH Probes

Reprinted with permission from:

Thorarinsdottir, A. E.; Tatro, S. M.; Harris, T. D. *Inorganic Chemistry* **2018**, *57*, 11252–11263.

This work was performed in collaboration with the co-authors listed above.

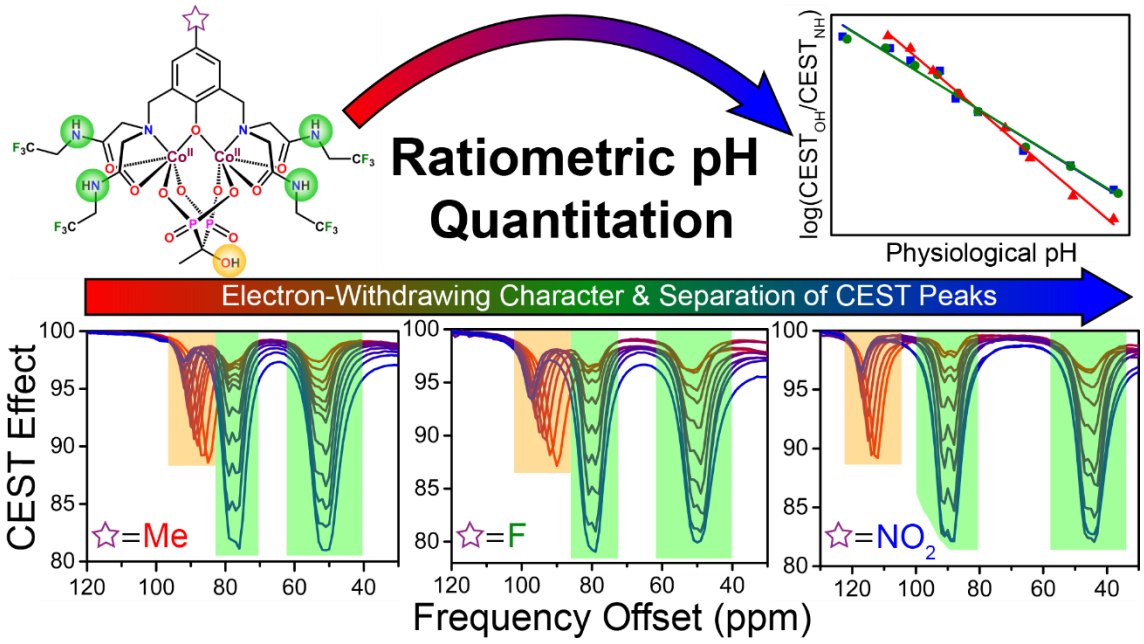

4.1 Introduction

The realization of chemical probes with the ability to accurately map small pH changes in vivo represents an important synthetic challenge, as acidic extracellular pH is a prominent feature of pathological conditions such as cancer,[1] ischemia,[1e,2] and inflammation.[1g,2c] Magnetic resonance imaging (MRI) is an ideal non-invasive imaging modality for probing pH in vivo due to its high spatiotemporal image resolution and unlimited tissue penetration depth.[3] Therefore, spatial mapping of tissue pH through MRI may aid in the early detection of pathologies and provide valuable information about the progression of diseases and the efficacy of treatments.[1,2,4]

Toward developing pH-responsive MRI contrast agents, transition metal complexes that function as paramagnetic chemical exchange saturation transfer (PARACEST)[5–8] agents are of particular interest owing to the inherent environmental responsiveness of the exchangeable protons on these compounds.[9] Here, contrast is generated through exchange of protons on a paramagnetic molecule with bulk H_2O protons upon frequency-specific irradiation, resulting in a decrease in the bulk H_2O signal.[10] Importantly, the rate of proton exchange is highly dependent on pH, as well as the pK_a of the exchangeable proton and its proximity to the transition metal ion.[6–8,11] Furthermore, these paramagnetic probes exhibit exchangeable protons with large chemical shifts,[7c,d,8] and thereby improve sensitivity by minimizing interference from biological background signals.[12] Nevertheless, the CEST signal intensity is also affected by the concentration of the probe, which significantly complicates in vivo studies.

One strategy to surmount the challenge of concentration dependence is to employ PARACEST probes featuring two distinct types of exchangeable protons that exhibit different pH-dependent changes in CEST signal intensity. The ratio of the intensities of the two CEST signals provides a

concentration-independent measure of pH.[7d,8e,13] We recently demonstrated that a Co_2 PARACEST probe supported by a dinucleating tetra(carboxamide) ligand and an ancillary etidronate ligand can be employed to ratiometrically map solution pH in a physiologically relevant range.[7d] The high pH sensitivity of 0.99(7) pH unit^{-1} for this probe is attributed to the base- and acid-catalyzed exchange of the carboxamide (NH) and hydroxyl (OH) protons on the two ligands, respectively, which results in CEST intensities that are proportional and inversely proportional to pH, respectively. However, considering that the most downfield-shifted CEST peak for this Co_2 complex is comprised of overlapping NH and OH signals, one can envision that PARACEST probes bearing two types of exchangeable protons that give rise to well-separated CEST peaks with opposing pH-dependent intensities have the potential to exhibit much higher sensitivities.

Transition metal-based PARACEST probes offer an ideal platform for the design of highly sensitive ratiometric pH probes by virtue of their high environmental responsiveness and excellent tunability through ligand design.[6–8] In particular, modest structural changes such as modification of the ligand backbone or pendent groups of azamacrocyclic ligands can lead to drastic changes in the chemical shift and intensity of CEST peaks.[8e,i,l] Nevertheless, there is a dearth of studies that probe electronic effects on the pH dependence of CEST for paramagnetic compounds. As such, there is a significant interest in understanding how electronic effects of ligand substitution influence the pH behavior of transition metal-based PARACEST probes. Combining such electronic studies with structural investigations would enhance our understanding of the factors that govern the pH dependence of the CEST effect and facilitate the design of chemical probes with optimal pH responsiveness for targeted applications.

The observation of highly pH-sensitive CEST peak intensity ratios for the previously reported Co_2 probe,[7d] in conjunction with the high modularity of the dinucleating ligand scaffold, prompted us to investigate the pH dependence of CEST properties for Co^{II}_2 complexes bearing CF_3-functionalized tetra(carboxamide) ligands. Specifically, we sought to examine how the CEST properties of these compounds are affected by the nature of the *para*-substituent on the bridging phenoxo ligand. Herein, we report a series of new Co^{II}_2 complexes as ratiometric PARACEST pH probes and demonstrate that small changes in the electronic structure of Co^{II} centers through remote ligand substitution can lead to notable differences in CEST profiles. These studies underscore that proper ligand design is a key attribute toward optimizing the performance of ratiometric PARACEST pH sensors, particularly in fine-tuning the pH sensitivity and detection range.

4.2 Experimental Section

General Considerations. Unless otherwise specified, the manipulations described below were carried out at ambient atmosphere and temperature. Air- and water-free manipulations were performed under a dinitrogen atmosphere in a Vacuum Atmospheres Nexus II glovebox or using standard Schlenk line techniques. Syntheses of metal complexes were carried out in an MBraun LABstar glovebox, operated under a humid dinitrogen atmosphere. Glassware was oven-dried at 150 °C for at least 4 h and allowed to cool in an evacuated antechamber prior to use in the gloveboxes. Acetonitrile (MeCN), diethyl ether (Et_2O), *N*,*N*-diisopropylethylamine (DIPEA), and methanol (MeOH) were dried using a commercial solvent purification system from Pure Process Technology and stored over 3 or 4 Å molecular sieves prior to use. H_2O was obtained from a purification system from EMD Millipore. Deuterated solvents were purchased from Cambridge

Isotope Laboratories. The syntheses of *N*,*N*′-[(2-hydroxy-5-nitro-1,3-phenylene)bis-(methylene)]bis[*N*-(carboxymethyl)glycineamide] (HL) and Na[LCo$_2$(etidronate)]·0.2NaNO$_3$ ·2.7H$_2$O (**1**) were carried out as reported previously.[7d] All other reagents and solvents were purchased from commercial vendors and used without further purification. Experimental details on the syntheses of ligands and organic precursors are provided in Section 4.5.1.

Synthesis of Na[(^{NO2}L′)Co$_2$(etidronate)]·1.0NaNO$_3$·1.5MeOH ***(2-NO$_2$)***. A pink solution of Co(NO$_3$)$_2$·6H$_2$O (84 mg, 0.29 mmol) in MeOH (2 mL) was added dropwise to a stirring pale yellow solution of H(^{NO2}L′) (110 mg, 0.15 mmol) in MeOH (3 mL) to give a dark orange solution. To this solution, a colorless solution of etidronic acid monohydrate (32 mg, 0.14 mmol) in MeOH (2 mL) was added dropwise, followed by addition of sodium methoxide (39 mg, 0.72 mmol) in MeOH (2 mL) to give a light orange solution. After stirring at 25 °C for 3 h, the orange solution was evaporated to dryness and the resulting orange residue was stirred in MeCN (10 mL) for 30 min. The orange solid was collected by filtration, washed with MeCN (5 mL) and Et$_2$O (5 mL), and dried under reduced pressure for 16 h. Diffusion of Et$_2$O vapor into a concentrated solution of the orange solid in MeOH (2 mL) afforded a crystalline light orange solid that was washed with Et$_2$O (2 × 3 mL) and dried under reduced pressure for 24 h to give **2-NO$_2$** (63 mg, 34%) as a light orange solid. Anal. Calcd. for C$_{27.5}$H$_{36}$Co$_2$F$_{12}$N$_8$Na$_2$O$_{18.5}$P$_2$: C, 26.89; H, 2.95; N, 9.12%. Found: C, 26.99; H, 3.01; N, 9.20%. ICP-OES: Co:P = 0.96:1.00. UV-Vis absorption spectrum (22 μM; 50 mM HEPES buffered at pH 6.94, 25 °C): 371 nm (ε = 13800 M^{-1} cm^{-1}). ESI-MS (*m*/*z*): Calcd. for C$_{26}$H$_{30}$Co$_2$F$_{12}$N$_7$O$_{14}$P$_2$ ([(^{NO2}L′)Co$_2$(etidronate)]$^-$): 1071.98, found: 1072.01; calcd. for C$_{26}$H$_{32}$Co$_2$F$_{12}$N$_7$O$_{14}$P$_2$ ([(^{NO2}L′)Co$_2$(etidronate)+2H]$^+$): 1073.99, found: 1074.01. FT-IR (ATR, cm^{-1}): 3248 (m); 3076 (m); 2969 (w); 1738 (w); 1640 (s); 1593 (m); 1507 (w); 1398 (m); 1312

(s); 1272 (m); 1156 (s); 1074 (s); 992 (w); 901 (m); 833 (m); 802 (m); 749 (m); 671 (m). Slow diffusion of Et_2O vapor into a concentrated solution of **2-NO₂** in MeOH afforded light orange plate-shaped crystals of $Na[(^{NO2}L')Co_2(etidronate)]\cdot 1.0NaNO_3$ (**2′-NO₂**) suitable for single-crystal X-ray diffraction analysis.

Synthesis of $Na[(^{F}L')Co_2(etidronate)]\cdot 2.2NaNO_3\cdot 1.0H_2O$ *(**2-F**).* A pink solution of $Co(NO_3)_2\cdot 6H_2O$ (96 mg, 0.33 mmol) in MeOH (2 mL) was added dropwise to a stirring colorless solution of $H(^{F}L')$ (120 mg, 0.17 mmol) in MeOH (3 mL) to give a dark pink solution. To this solution, a colorless solution of etidronic acid monohydrate (37 mg, 0.17 mmol) in MeOH (2 mL)

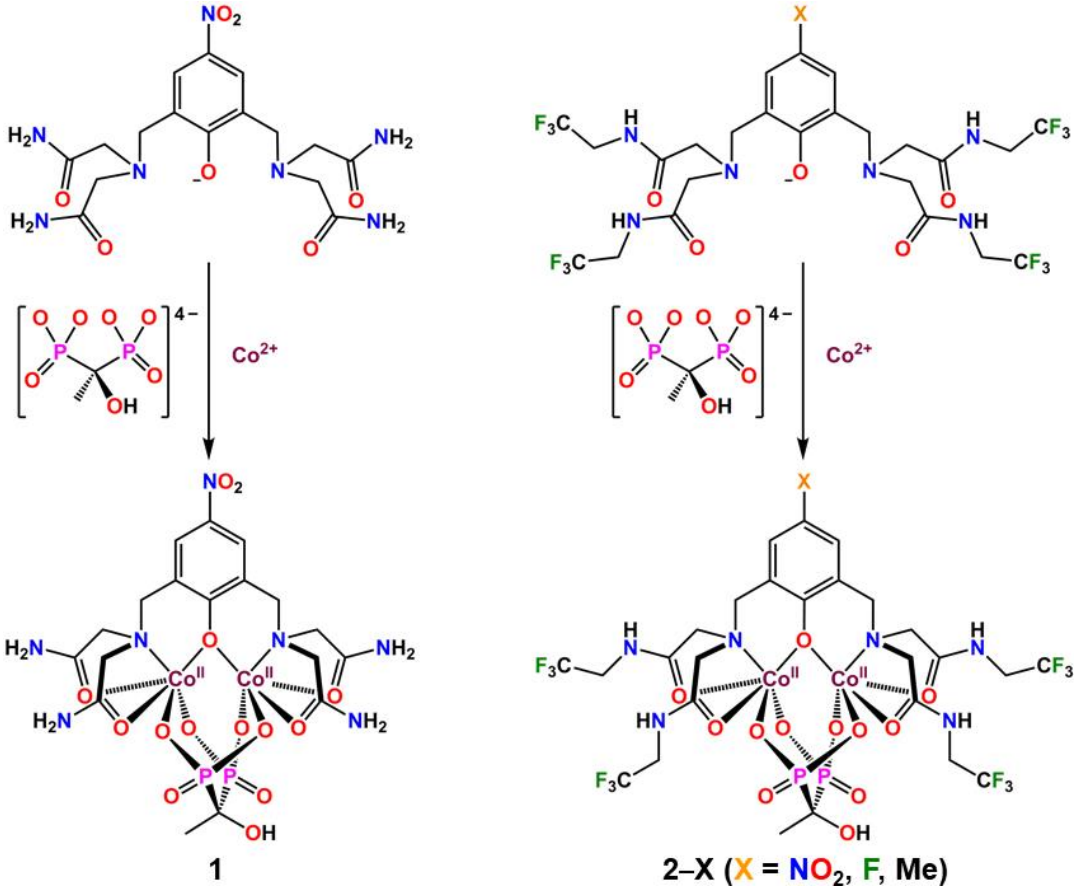

Figure 4.1 Reaction of L^-, Co^{2+}, and etidronate to form $[LCo_2(etidronate)]^-$, as observed in **1** (left). Reaction of $(^{X}L')^-$, Co^{2+}, and etidronate to form $[(^{X}L')Co_2(etidronate)]^-$, as observed in **2-X** (X = NO_2, F, Me) (right).

was added dropwise, followed by addition of sodium methoxide (45 mg, 0.83 mmol) in MeOH (2 mL) to give a pink solution. After stirring at 25 °C for 3 h, the pink solution was evaporated to dryness and the resulting pink residue was stirred in MeCN (10 mL) for 20 min. The pink solid was collected by filtration, washed with MeCN (5 mL) and Et_2O (5 mL), and dried under reduced pressure for 16 h. Diffusion of Et_2O vapor into a concentrated solution of the pink solid in MeOH (2 mL) afforded a crystalline pink solid that was washed with Et_2O (2 × 3 mL) and dried under reduced pressure for 24 h to give **2-F** (163 mg, 75%) as a dark pink solid. Anal. Calcd. for $C_{26}H_{32}Co_2F_{13}N_{8.2}Na_{3.2}O_{19.6}P_2$: C, 24.52; H, 2.53; N, 9.02%. Found: C, 24.73; H, 2.69; N, 9.25%. ICP-OES: Co:P = 1.01:1.00. UV-Vis absorption spectrum (87 μM; 50 mM HEPES buffered at pH 6.95, 25 °C): 309 nm (ε = 4400 M^{-1} cm^{-1}). ESI-MS (*m*/*z*): Calcd. for $C_{26}H_{30}Co_2F_{13}N_6O_{12}P_2$ ([(^{F}L′)Co_2(etidronate)]$^-$): 1044.99, found: 1045.08; calcd. for $C_{26}H_{32}Co_2F_{13}N_6O_{12}P_2$ ([(^{F}L′)Co_2(etidronate)+2H]$^+$): 1047.00, found: 1047.04. FT-IR (ATR, cm^{-1}): 3249 (m); 3078 (m); 2969 (w); 1738 (m); 1643 (s); 1575 (m); 1470 (m); 1431 (m); 1375 (m); 1352 (m); 1287 (w); 1258 (m); 1154 (s); 1074 (s); 991 (w); 907 (m); 890 (m); 834 (m); 799 (m); 673 (m). Slow diffusion of Et_2O vapor into a concentrated solution of **2-F** in MeOH afforded pink prism-shaped crystals of Na[(^{F}L′)Co_2(etidronate)]·1.0$NaNO_3$·1.0MeOH (**2′-F**) suitable for single-crystal X-ray diffraction analysis.

*Synthesis of Na[(^{Me}L′)Co_2(etidronate)]·4.0$NaNO_3$·3.4H_2O (**2-Me**).* A pink solution of $Co(NO_3)_2$·6H_2O (79 mg, 0.27 mmol) in MeOH (2 mL) was added dropwise to a stirring colorless solution of H(^{Me}L′) (97 mg, 0.13 mmol) in MeOH (3 mL) to give a dark pink solution. To this solution, a colorless solution of etidronic acid monohydrate (33 mg, 0.15 mmol) in MeOH (2 mL) was added dropwise, followed by addition of sodium methoxide (36 mg, 0.67 mmol) in MeOH (2

mL) to give a pink solution. After stirring at 25 °C for 3 h, the pink solution was evaporated to dryness and the resulting pink residue was stirred in MeCN (10 mL) for 20 min. The pink solid was collected by filtration, washed with MeCN (5 mL) and Et_2O (5 mL), and dried under reduced pressure for 20 h. Diffusion of Et_2O vapor into a concentrated solution of the pink solid in MeOH (2 mL) afforded a crystalline pink solid that was washed with Et_2O (2 × 3 mL) and dried under reduced pressure for 24 h to give **2-Me** (59 mg, 31%) as a pink solid. Anal. Calcd. for $C_{27}H_{39.8}Co_2F_{12}N_{10}Na_5O_{27.4}P_2$: C, 22.13; H, 2.74; N, 9.56%. Found: C, 22.03; H, 2.56; N, 9.44%. ICP-OES: Co:P = 0.92:1.00. UV-Vis absorption spectrum (42 μM; 50 mM HEPES buffered at pH 6.95, 25 °C): 307 nm (ε = 3900 M^{-1} cm^{-1}). ESI-MS (*m*/*z*): Calcd. for $C_{27}H_{33}Co_2F_{12}N_6O_{12}P_2$ ([(^{Me}L′)Co_2(etidronate)]$^-$): 1041.01, found: 1041.15; calcd. for $C_{27}H_{35}Co_2F_{12}N_6O_{12}P_2$ ([(^{Me}L′)Co_2(etidronate)+2H]$^+$): 1043.03, found: 1043.06. FT-IR (ATR, cm^{-1}): 3254 (m); 3094 (m); 2970 (w); 1739 (m); 1638 (s); 1568 (m); 1476 (w); 1428 (m); 1372 (m); 1350 (m); 1317 (m); 1254 (m); 1157 (s); 1081 (s); 1017 (w); 995 (w); 952 (w); 916 (m); 881 (m); 833 (m); 799 (m); 744 (w); 671 (m); 650 (w). Slow diffusion of Et_2O vapor into a concentrated solution of **2-Me** in MeOH afforded pink plate-shaped crystals of Na[(^{Me}L′)Co_2(etidronate)]·solvent (**2′-Me**) suitable for single-crystal X-ray diffraction analysis. Note that the term "solvent" in the formula above denotes a combination of crystallographically disordered MeOH, Et_2O, and H_2O molecules (see below).

X-ray Structure Determination. Single crystals of **2′-X** (X = NO_2, F, Me) were directly coated with Paratone-N oil, mounted on a MicroMounts rod, and frozen under a stream of dinitrogen during data collection. The crystallographic data were collected at 100 K on a Bruker Kappa Apex II diffractometer equipped with an APEX-II CCD detector and a MoKα IμS microsource with MX Optics (**2′-NO$_2$**, **2′-Me**), or on a Bruker Kappa Apex II diffractometer equipped with an APEX-II

CCD detector and a MoKα sealed tube source with a Triumph monochromator (**2′-F**). Raw data were integrated and corrected for Lorentz and polarization effects with Bruker APEX2 version 2014.11–0.[14] Absorption corrections were applied using the program SADABS.[15] Space group assignments were determined by examining systematic absences, E-statistics, and successive refinement of the structures. Structures were solved using direct methods in SHELXT and refined by SHELXL[16] operated within the OLEX2 interface.[17] All hydrogen atoms were placed at calculated positions using suitable riding models and refined using isotropic displacement parameters derived from their parent atoms. Thermal parameters for all non-hydrogen atoms were refined anisotropically.

In the crystal structure of **2′-Me**, the solvent molecules were severely disordered and could not be modeled properly. Therefore, the solvent masking procedure as implemented in OLEX2 was used. Two void volumes of 955.4 $Å^3$, each with 242 electrons, were estimated per unit cell and ascribed to a combination of MeOH, Et_2O, and H_2O solvent molecules. Due to this disorder, the nomenclature of the single crystals of **2′-Me** is noted as Na[(^{Me}L′)Co_2(etidronate)]·solvent. The Na^+ ions in all three crystal structures were disordered, resulting in large atomic displacement parameters. Specifically, in the crystal structure of **2′-Me**, the occupancy of Na^+ was freely refined over two positions using the EADP constraint, and in the crystal structure of **2′-F**, three out of four Na^+ ions in the asymmetric unit were positionally disordered over two positions and their occupancy was freely refined over the two positions. In the crystal structure of **2′-NO_2**, the CF_3 groups and $NaNO_3$ cocrystallite were severely disordered. This disorder was modeled by using a combination of the restraints SADI, DFIX, and ISOR. Crystallographic data for compounds **2′-X** (X = NO_2, F, Me) and the details of data collection are listed in Table 4.2.

NMR Spectroscopy. ^{1}H and ^{19}F NMR spectra for the ligands H(^{X}L′) (X = NO_2, F, Me) and organic precursors were collected at 25 °C at 500 and 470 MHz frequencies, respectively, on Agilent DD2 500 MHz (11.7 T) or Varian Inova 500 MHz (11.7 T) spectrometers, or on an automated Agilent DD MR 400 MHz (9.4 T) spectrometer at 400 and 376 MHz frequencies, respectively. ^{13}C{^{1}H} NMR spectra for H(^{X}L′) were collected at 126 MHz frequency using a Bruker Avance III 500 MHz (11.7 T) system equipped with a DCH CryoProbe. ^{1}H and ^{19}F NMR spectra for compounds **2-X** (X = NO_2, F, Me) in D_2O and for aqueous solution samples containing 50 mM HEPES and 100 mM NaCl buffered at various pH values were collected on an Agilent DD2 500 MHz (11.7 T) spectrometer. For samples in buffer, spectra were acquired using an inner capillary containing a solution of 3% (v/v) trifluoroacetic acid (TFA) in D_2O to lock the samples. All chemical shift values (δ) are reported in ppm and coupling constants (J) are reported in hertz (Hz). ^{1}H NMR spectra for H(^{X}L′) and organic precursors are referenced to residual proton signals from the deuterated solvents (7.26 ppm for $CDCl_3$, 4.79 ppm for D_2O, 3.31 ppm for MeOH-d_4, 2.50 ppm for DMSO-d_6, and 1.94 ppm for MeCN-d_3). ^{13}C{^{1}H} NMR spectra for H(^{X}L′) in MeCN-d_3 are referenced to the CD_3 carbon signal from the deuterated solvent (δ = 1.32 ppm). ^{19}F NMR spectra for ligands and organic precursors are referenced to an external standard of $CFCl_3$ (δ = 0 ppm). ^{19}F NMR spectra for **2-X** are referenced to an internal standard of TFA at −76.00 ppm. For measurements of **2-X** in D_2O or H_2O, the chemical shift of the solvent signal in the ^{1}H NMR spectra was set to 0 ppm to simplify comparison between ^{1}H NMR spectra and the corresponding CEST spectra (Z-spectra). The MestReNova 10.0 NMR data processing software was used to analyze and process all recorded NMR spectra.

Determination of pK_a by ^{1}H NMR Analysis. The pH-dependent ^{1}H NMR chemical shift of the

Me resonance from etidronate was used to estimate the pK_a values for compounds **2-X** (X = NO_2, F, Me). The change in ^{1}H NMR chemical shift of the Me resonance as a function of pH was fitted to a Boltzmann sigmoidal function[18] for each compound to model a single ionization event according to the following equation:

$$\delta = A_2 + (A_1 - A_2)/(1 + \exp((\mathrm{pH} - \mathrm{p}K_a)/dx)) \quad (4.1)$$

In this equation, δ is the obtained chemical shift, A_2 is the theoretical chemical shift of the fully deprotonated species, A_1 is the theoretical chemical shift of the fully protonated species, pK_a is the inflection point of the graph, and dx is a parameter describing the steepness of the curve.

CEST Experiments. All CEST experiments were carried out at 37 °C on an Agilent DD2 500 MHz (11.7 T) spectrometer. For CEST experiments, 4 mM or 8–9 mM samples of **2-X** (X = NO_2, F, Me) in aqueous buffer solutions containing 50 mM HEPES and 100 mM NaCl at desired pH values (measured with a pH electrode before ^{1}H NMR and CEST data collection) were measured. Z-spectra (CEST spectra) were obtained according to the following protocol: ^{1}H NMR spectra were acquired from −50 to 150 ppm with a step increase of 1 ppm using a presaturation pulse applied for 4 s at a power level (B_1) of 21 μT. An inner capillary containing a solution of 3% (v/v) TFA in D_2O was placed within the NMR sample tube to lock the sample. The normalized integrations of the H_2O signal from the obtained spectra were plotted against frequency offset to generate a Z-spectrum, where direct saturation of the H_2O signal was set to 0 ppm.

Exchange rate constants (k_{ex}) were calculated following a previously reported method,[19] where the x-intercept ($-1/k_{ex}^2$) was obtained from a plot of $M_z/(M_0 - M_z)$ (M_z and M_0 are the magnetization of the on- and off-resonance, respectively) against $1/\omega_1^2$ (ω_1 in rad s^{-1}). ^{1}H NMR spectra were acquired at various presaturation power levels ranging from 13 to 21 μT applied for 4 s at 37 °C.

The B_1 values were calculated based on the calibrated 90° pulse on a linear amplifier. To correct for baseline variations, a linear baseline was applied for two CEST regimes. For **2-NO$_2$**, the data points at 130 and 72 ppm, and at 72 and 30 ppm where employed for the two regimes. For **2-F**, the data points at 130 and 68 ppm, and at 68 and 37 ppm where used for the two regimes. For **2-Me**, the data points at 130 and 68 ppm, and at 68 and 37 ppm where used for the two regimes in the pH range 6.01–7.20, whereas the data points at 102 and 68 ppm, and at 68 and 37 ppm where employed in the pH range 7.38–7.80 owing to a poor baseline in the downfield region of the spectra. Reported values of %CEST [$(1 - M_z/M_0) \times 100\%$] are the differences in %H_2O signal reduction between applied on-resonance presaturations (raw data) and the values obtained by inserting the corresponding frequencies into the linear baseline equations. To calculate k_{ex}, the CEST intensities at the frequency offsets corresponding to maximum H_2O signal reductions at 21 μT power level were monitored for each pH value. The pH calibration curves were generated by taking the logarithm with base 10 ($\log_{10}$) of the ratios of two CEST signal intensities after a baseline correction was applied.

Solution Magnetic Measurements. The solution magnetic moments of compounds **2-X** (X = NO_2, F, Me) were determined using the Evans method,[20] by collecting variable-pH ^{1}H NMR spectra at 37 °C (310 K) on an Agilent DD2 500 MHz (11.7 T) spectrometer. In a typical experiment, the compound (3–5 mM) was dissolved in a mixture of 2% (v/v) *tert*-butanol in an aqueous solution containing 50 mM HEPES and 100 mM NaCl buffered at a specific pH value. The resulting solution was placed in an NMR tube containing a sealed capillary with the same solvent mixture but without the to-be-characterized paramagnetic compound as a reference solution. Diamagnetic corrections were carried out based on the empirical formula of each

compound (as determined by elemental analysis) using Pascal's constants.[21] The paramagnetic molar susceptibility χ_M^{para} ($cm^3\ mol^{-1}$) was calculated using the following equation:[20]

$$\chi_M^{para} = (3\Delta\nu M_w)/(4\pi\nu_0 m) - \chi_M^{dia} \quad (4.2)$$

In this equation, $\Delta\nu$ is the frequency difference (Hz) between the *tert*-butyl resonance of *tert*-butanol in the sample and reference solutions, M_w is the molecular mass of the paramagnetic compound (g mol^{-1}), ν_0 is the operating frequency of the NMR spectrometer (Hz), m is the concentration of the paramagnetic compound (g cm^{-3}), and χ_M^{dia} is the diamagnetic contribution to the molar susceptibility ($cm^3\ mol^{-1}$).

UV-Vis Absorption Spectroscopy. Solution and solid-state UV-Vis spectra were collected at ambient temperature in the 200–800 nm range on an Agilent Cary 5000 UV-Vis-NIR spectrophotometer equipped with an integrating sphere for diffuse reflectance measurements. Solution spectra were collected for 97–370 μM samples of ligands H(^{X}L′) (X = NO_2, F, Me) in MeOH, and for 22–87 μM samples of compounds **2-X** (X = NO_2, F, Me) in aqueous buffer solutions containing 50 mM HEPES and 100 mM NaCl at three different pH values, covering the range used for CEST experiments. Diffuse reflectance spectra were collected on crystalline samples of **2′-X** (X = NO_2, F, Me). Samples for measurements were prepared by mixing polycrystalline samples of the compounds with $BaSO_4$ powder for a 2-fold dilution to give smooth, homogeneous powders. The data were treated with a background correction of $BaSO_4$ and the spectra are reported as normalized Kubelka-Munk transformation F(R) of the raw diffuse reflectance spectra, where F(R) for each compound was normalized with the strongest absorbance set to F(R) = 1.

Electrochemical Measurements. Cyclic voltammetry measurements were carried out in a

standard one-compartment cell under a dinitrogen atmosphere using CH Instruments 760c potentiostat. The cell consisted of a platinum electrode as a working electrode, a platinum wire as a counter electrode, and a saturated calomel electrode (SCE) as a reference electrode. Analytes were measured in aqueous solutions with 100 mM NaCl and 50 mM HEPES buffered at pH 7.3. All potentials were converted and referenced to the normal hydrogen electrode (NHE), using a literature conversion factor.[22]

Other Physical Measurements. Electrode-based pH measurements were carried out using a Thermo Scientific Orion 9110DJWP double junction pH electrode connected to a VWR sympHony B10P pH meter. The pH meter was calibrated using standardized pH buffer solutions at 4.01, 7.00, and 10.00 purchased from LaMotte Company. Elemental analyses of all compounds were conducted by Midwest Microlab Inc. Infrared spectra were recorded for solid samples of ligands H(^{X}L′) (X = NO_2, F, Me) and Co_2 complexes **2-X** (X = NO_2, F, Me) on a Bruker Alpha FTIR spectrometer equipped with an attenuated total reflectance accessory (ATR). These data are provided in Figures 4.7 and 4.8. Electrospray ionization mass spectrometry **(**ESI-MS) measurements were performed on a Bruker AmaZon SL quadrupole ion trap instrument. All measurements were carried out in MeOH carrier solvent using positive and/or negative ionization mode. Inductively coupled plasma optical emission spectroscopy (ICP-OES) was performed on a Thermo iCAP 7600 dual view ICP-OES instrument equipped with a CETAC ASX520 240-position autosampler. Samples were dissolved in a 3% aqueous nitric acid solution and the emissions for Co and P compared to standard solutions.

4.3 Results and Discussion

4.3.1 Design and Syntheses

The NO_2-substituted tetra(carboxamide) dinucleating ligand HL and the corresponding Co^{II}_2 complex Na[LCo_2(etidronate)]·0.2$NaNO_3$ ·2.7H_2O (**1**) featuring ancillary etidronate ligand were prepared as previously described (see Figure 4.1, left).[7d] With the goal of achieving Co^{II}_2 complexes that exhibit more intense CEST effects for carboxamide protons in the pH range 6.0–6.5, we synthesized CF_3-functionalized analogues of HL. Here, replacement of the primary carboxamide groups (-$CONH_2$) with secondary amides bearing CF_3 substituents (-$CONHCH_2CF_3$) serves to lower the pK_a of the amide protons by virtue of the electron-withdrawing character of the CF_3 groups. Such an increase in acidity of the labile protons engenders faster proton exchange at more acidic pH values, and thus provides greater CEST peak intensities.[8a–e,h,13,23] Furthermore, to more thoroughly investigate the electronic effects of ligand substitution on the CEST properties of transition metal-based PARACEST probes, three derivatives of the CF_3-functionalized ligand H(^{X}L′) (X = NO_2, F, Me) were targeted. For this ligand series, the identity of the *para*-substituent X on the bridging phenoxo moiety is varied from a strongly electron-withdrawing NO_2 group to an electron-donating Me group. These dinucleating ligands were accessed through S_N2 reactions between 2,2′-(azanediyl)bis(*N*-(2,2,2-trifluoroethyl)acetamide) and *para*-substituted 2,6-bis(bromomethyl)phenol derivatives similarly to HL (see Section 4.5.1 and Schemes 4.1 and 4.2).

Reaction of H(^{X}L′) with two equivalents of $Co(NO_3)_2$·6H_2O, one equivalent of etidronic acid, and five equivalents of Na(OMe) in MeOH afforded Co_2 complexes analogous to that in **1**. Namely, Na[(^{NO2}L′)Co_2(etidronate)]·1.0$NaNO_3$·1.5MeOH (**2-NO_2**) was isolated as a light orange solid, Na[(^{F}L′)Co_2(etidronate)]·2.2$NaNO_3$·1.0H_2O (**2-F**) as a dark pink solid, and Na[(^{Me}L′)Co_2(etidronate)]·4.0$NaNO_3$·3.4H_2O (**2-Me**) as a pink solid (see Figure 4.1, right). Note

that all four Co_2 complexes feature the ancillary bisphosphonate etidronate. The central OH group on this ligand has been shown to give rise to highly shifted and pH-sensitive CEST peaks,[7d] rendering it suitable for incorporation into PARACEST pH sensors.

4.3.2 Crystal Structures

Single crystals of **2′-X** (X = NO_2, F, Me) suitable for X-ray diffraction analysis were obtained by slow diffusion of Et_2O vapor into a concentrated solution of **2-X** (X = NO_2, F, Me) in MeOH. Specifically, light orange plate-shaped crystals of Na[(^{NO2}L′)Co_2(etidronate)]·1.0$NaNO_3$ (**2′-NO_2**), pink prism-shaped crystals of Na[(^{F}L′)Co_2(etidronate)]·1.0$NaNO_3$·1.0MeOH (**2′-F**), and pink plate-shaped crystals of Na[(^{Me}L′)Co_2(etidronate)]·solvent (**2′-Me**) were obtained for the three compounds. Analysis at 100 K revealed that **2′-NO_2** and **2′-Me** crystallized in the orthorhombic space groups $P2_12_12_1$ and *Pccn*, respectively, whereas **2′-F** crystallized in the triclinic space group $P\bar{1}$ (see Table 4.2). The different space groups across the **2′-X** series most likely result from different cocrystallization of salts and solvent molecules in these structures.

Similar to that in Na[LCo_2(etidronate)]·6.8H_2O (**1′**), the general structure of the anionic complexes in **2′-X** consists of two nearly identical Co centers in distorted octahedral coordination

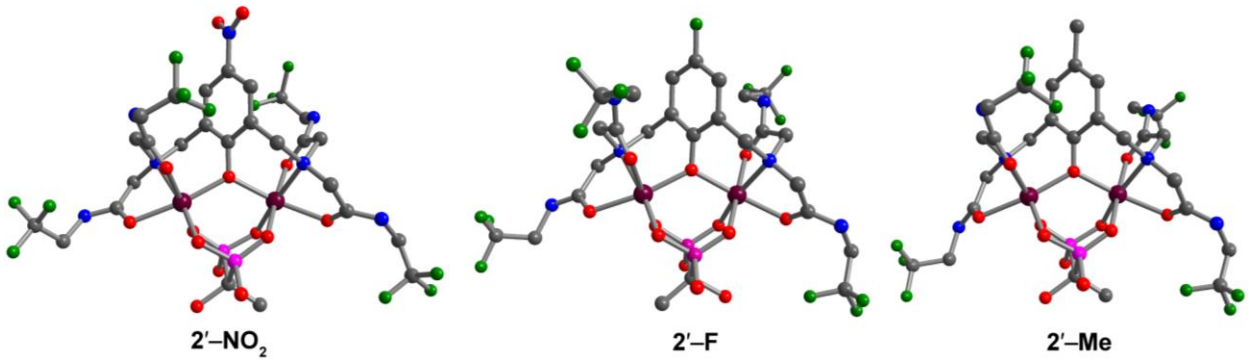

Figure 4.2 Crystal structures of the anionic complexes [(^{X}L′)Co_2(etidronate)]$^-$, as observed in **2′-X** (X = NO_2, F, Me). Purple, magenta, green, red, blue, and gray spheres represent Co, P, F, O, N, and C atoms, respectively; H atoms are omitted for clarity.

Table 4.1 Selected mean interatomic distances (Å) and angles (°) for **1′** and **2′-X** (X = NO_2, F, Me) at 100 K.

	1′ [d]	**2′-NO_2**	**2′-F**	**2′-Me**
Co–$O_{phenoxo}$	2.0920(2)	2.0655(2)	2.0373(3)	2.0240(2)
Co–O_{amide}	2.1127(1)	2.1180(1)	2.1316(2)	2.1379(1)
Co–$O_{phosphonate}$	2.0618(1)	2.0500(1)	2.0835(2)	2.0735(1)
Co–N	2.1558(2)	2.1674(1)	2.1543(2)	2.1538(2)
Co···Co	3.6740(3)	3.6664(3)	3.6265(5)	3.5806(3)
Co–$O_{phenoxo}$–Co	122.837(4)	125.133(3)	125.754(7)	124.394(3)
O–P–O	113.882(3)	117.080(3)	116.823(6)	116.531(3)
P–C–P	111.486(6)	108.147(5)	109.86(1)	109.144(2)
trans O–Co–E [a]	170.324(1)	170.153(1)	169.479(1)	169.031(1)
Σ_{sum} [b]	62.27(2)	54.09(2)	65.68(3)	60.41(2)
Σ_{mean}	5.19(1)	4.51(1)	5.47(1)	5.03(1)
ω [c]	49.120(4)	54.641(4)	53.491(4)	51.177(3)

[a] E denotes either a N or an O atom from the [$CoNO_5$] coordination sphere. [b] Octahedral distortion parameter (Σ) = absolute deviation from 90° of each 12 *cis* angle in [$CoNO_5$]. [c] Dihedral angle between the Co–$O_{phenoxo}$–Co plane and the plane of the phenolate ring of L^- or $(^XL')^-$. [d] Values obtained from reference 7d.

environments. Each coordination sphere is made up of two amide O atoms, a μ-phenoxo O atom, and a N atom from $(^XL')^-$, together with two O atoms from the μ^2–κ^4 etidronate ligand (see Figure 4.2). The mean dihedral angle between the Co–$O_{phenoxo}$–Co trigonal plane and the hexagonal plane of the phenolate ring of $(^XL')^-$ ranges from 51.177(3)° for **2′-Me** to 54.641(4)° for **2′-NO_2**. These angles are slightly larger than observed for **1′**, in accord with the bulkier amide substituents in **2′-X** (see Table 4.1).

The mean Co–O distances of 2.0655(2), 2.1180(1), and 2.0500(1) Å for the Co–$O_{phenoxo}$, Co–O_{amide}, and Co–$O_{phosphonate}$ bonds in **2′-NO_2**, respectively, are similar to those observed in **1′**. For **2′-F** and **2′-Me**, the mean Co–$O_{phenoxo}$ distance is slightly shorter, and the Co–O_{amide}, and Co–$O_{phosphonate}$ distances are slightly longer, as compared to the NO_2-substituted analogue. The decrease in Co–$O_{phenoxo}$ bond length across the **2′-X** series is consistent with higher negative charge

density on the μ-phenoxo O atom for ligands bearing electron-donating *para*-substituents than electron-withdrawing substituents.[24] The mean Co–N distance is similar for all four Co_2 complexes, ranging from 2.1538(2) Å in **2′-Me** to 2.1674(1) Å in **2′-NO₂**. In contrast, the average intramolecular Co···Co distance decreases from 3.6664(3) Å in **2′-NO₂** to 3.6265(5) Å in **2′-F** and 3.5806(3) Å in **2′-Me**. Note that this decrease in intramolecular Co···Co distance across the **2′-X** series follows the same trend as the Co–$O_{phenoxo}$ distance. This observation, in conjunction with the similar intramolecular Co···Co distance for **1′** and **2′-NO₂**, implies that the electronic properties of the bridging phenoxo ligand significantly affect the structural features of these Co_2 complexes.

The mean intramolecular Co–$O_{phenoxo}$–Co angle does not vary significantly across the **2′-X** series, but was found to be slightly larger for **2′-X** than **1′**. This difference in Co–$O_{phenoxo}$–Co angle most likely stems from the increased steric bulk of the pendent amides in $(^{X}L')^{-}$ compared to those in L^{-}. Accordingly, the O–P–O and P–C–P bond angles increase and decrease slightly, respectively, for **2′-X**, compared to the corresponding angles for **1′**. Taken together, the interatomic distances and angles for **2′-X**, in conjunction with an average octahedral distortion parameter (Σ) ranging from 4.51(1) to 5.47(1)° across the series, are consistent with two high-spin $S = {}^{3}/_{2}$ Co^{II} ions bridged by a deprotonated OH group from $H(^{X}L')$.[7d,24–27] Notably, the solid-state structures of **2′-X** are influenced by a combination of electronic and steric factors.

4.3.3 UV-Vis Spectroscopy

To probe the electronic structures of compounds **2-X** (X = NO_2, F, Me) in aqueous solution, UV–Vis absorption spectra were collected for samples in 50 mM HEPES buffers containing 100 mM NaCl. The spectrum for **2-NO₂** in pH 6.94 buffer shows an intense absorption band at 371 nm

(ε = 13800 M^{-1} cm^{-1}) (see Figure 4.9) in analogy to the spectral features of **1**.[7d] In contrast, the spectra for **2-F** and **2-Me** in pH 6.95 buffer solution exhibit weaker absorptions centered at 309 nm (ε = 4400 M^{-1} cm^{-1}) and 307 nm (ε = 3900 M^{-1} cm^{-1}), respectively (see Figures 4.10 and 4.11). We assign these absorption bands to ligand−metal charge transfer (LMCT) transitions from the bridging phenolate to Co^{II}, in accord with similar phenoxo-bridged Co_2 complexes.[25c,26] The red shift of the LMCT band and dramatic increase in molar absorptivity in moving from **2-Me** to **2-NO₂** (see Figure 4.12) are in good agreement with the influence of the *para*-substituent on the extent of π-conjugation in the phenolate ligands. Note that the same trend is observed for MeOH solutions of the ligands H(^{X}L′) (see Figure 4.13). The intensities of the absorption bands for **2-X** increase slightly when the pH is raised from 5.95 to 7.96 (see Figures 4.9–4.11), suggesting a minimal increase in ligand donor strength with increased pH.[28] Finally, the close similarities between the diffuse reflectance spectra collected for crystalline samples of **2′-X** (see Figures 4.14–4.16) and the spectra obtained for aqueous solutions of **2-X** indicate that the structures of the Co_2 complexes determined from X-ray diffraction are preserved in HEPES buffer solutions in the pH range 6.0–8.0.

4.3.4 Solution Magnetic Properties

To further probe the solution electronic structures of **2-X** (X = NO_2, F, Me) and to assess their magnetic properties, variable-pH dc magnetic susceptibility data were collected at 37 °C for aqueous buffer solutions using the Evans method[20] (see Section 4.2). The plots of $\chi_M T$ vs pH, as depicted in Figures 4.17–4.19, reveal that $\chi_M T$ varies insignificantly with pH in the pH range 5.8–8.1. Over this pH range, average values of $\chi_M T$ = 5.75(8), 5.6(1), and 5.5(1) cm^3 K mol^{-1} were obtained for **2-NO₂**, **2-F**, and **2-Me**, respectively (see Table 4.3). Assuming two magnetically non-

interacting Co^{II} centers, these values correspond to g = 2.48(2), 2.44(6), and 2.42(3) for **2-NO_2**, **2-F**, and **2-Me**, respectively. These data are consistent with values reported for structurally similar high-spin Co_2 complexes featuring octahedral, $S = {}^3/_2$ Co^{II} centers.[7d,9a,25] Taken together, the solution magnetic measurements of **2-X** corroborate the high-spin assignment of the Co^{II} ions evident from UV-Vis spectroscopy and illustrate that the magnetic properties of this family of Co_2 complexes do not change significantly in the physiological pH range.

4.3.5 ^{19}F NMR Spectroscopy

In order to further investigate and compare the solution electronic structures and properties of **2-X** (X = NO_2, F, Me), ^{19}F NMR spectra were collected for aqueous solutions buffered at selected pH values between 6.0 and 7.8. The spectrum for **2-NO_2** at pH 5.97 features two sets of two closely separated peaks positioned at −67.14 and −68.42 ppm, and at −73.13 and −74.05 ppm, respectively (see Figure 4.20). These resonances have equal integration and are assigned to the four inequivalent CF_3 groups in **2-NO_2**, in accord with the pseudo-C_2 symmetry of the complex. Upon raising the pH to 7.77, the less upfield-shifted peaks shift slightly upfield, while the frequencies of the more upfield-shifted set reveal no change. The spectra for **2-F** and **2-Me** exhibit analogous features and pH behavior as those for **2-NO_2** (see Figures 4.21 and 4.22), but significant differences in chemical shifts are observed (see Figure 4.3, right). Interestingly, the chemical shifts of the more upfield-shifted sets of peaks are nearly identical for all three compounds, while the resonance frequencies of the less upfield-shifted peaks are drastically different. These peaks shift upfield with increasing electron-withdrawing character of X. Consequently, the separation between the two sets of CF_3 peaks is largest for **2-Me** and smallest for **2-NO_2**. These experiments demonstrate that ^{19}F NMR is a useful tool for probing the electronic structures of **2-X** in solutions. Finally, note that

the additional peak at ca. −49.3 ppm in the spectra for **2-F** corresponds to the *para*-F substituent and is not significantly affected by pH in the range studied (see Figure 4.21).

4.3.6 ^{1}H NMR Spectroscopy

To probe the effects of ligand substitution on NMR properties in this family of Co_2 complexes, ^{1}H NMR spectra were collected for buffer solutions of **2-X** (X = NO_2, F, Me) in the pH range 6.0–7.8. The spectrum for **2-NO_2** at pH 6.48 exhibits paramagnetically shifted resonances with chemical shifts ranging from −105 to 185 ppm vs H_2O (see Figure 4.23, top). The sharp resonances at 32 and 35 ppm are assigned to the two protons on the phenolate ring of $(^{NO2}L')^{-}$ and the intense peak at 71 ppm corresponds to the etidronate Me group. Furthermore, the resonances at 44, 48, 88, and 92 ppm correspond to two sets of slightly inequivalent carboxamide NH protons, whereas the etidronate OH group resonates at 115 ppm. The assignment of the exchangeable proton resonances was verified by their disappearance in the spectrum recorded in D_2O (see Figure 4.23, bottom). The etidronate Me and OH peaks for **2-NO_2** are shifted downfield compared to those obtained for **1**,[7d] whereas the opposite trend is observed for the

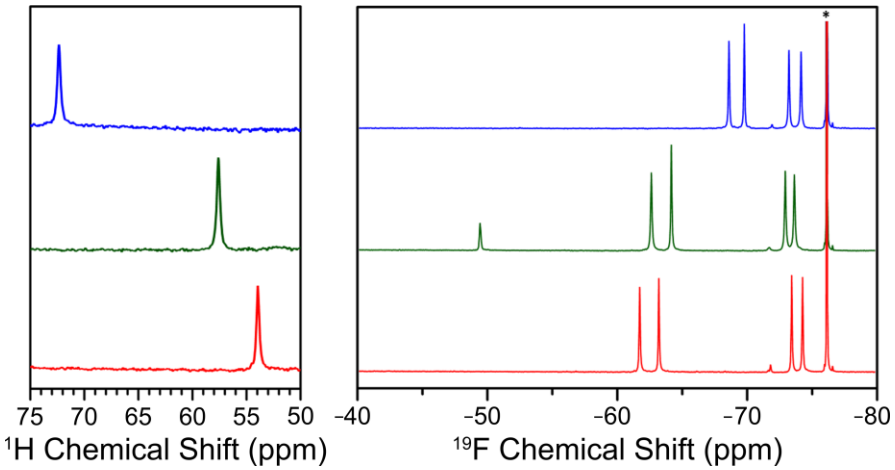

Figure 4.3 Left: Portions of ^{1}H NMR spectra for aqueous solutions of **2-NO_2** (blue), **2-F** (green), and **2-Me** (red) buffered at pH 7.38, 7.40, and 7.38, respectively, highlighting the chemical shift of the etidronate Me group. Right: ^{19}F NMR spectra for aqueous solutions of **2-NO_2** (blue), **2-F** (green), and **2-Me** (red) buffered at pH 7.38, 7.40, and 7.38, respectively. All spectra were collected for solutions in 50 mM HEPES buffers with 100 mM NaCl at 37 °C. The ^{1}H NMR chemical shifts are reported as frequency offsets with the H_2O chemical shift set to 0 ppm. The chemical shift of TFA internal standard was set to −76.00 ppm for ^{19}F NMR data, as denoted by the asterisk.

carboxamide peaks. Interestingly, the four amide proton resonances for **2-NO$_2$** are well shifted from the H_2O resonance, indicating that these protons adopt a *trans* configuration with respect to the carbonyl O atom.[29] The line widths of the NH peaks increase markedly when the pH is raised from 5.97 to 7.77, whereas the OH resonance shifts downfield by 5 ppm and becomes sharper (see Figure 4.24). These pH-dependent properties of the exchangeable proton resonances for **2-NO$_2$** are consistent with those observed for **1** and indicate base- and acid-catalyzed exchange of the NH and OH protons, respectively.[7d]

The compounds **2-F** and **2-Me** exhibit similar spectral profiles and pH dependences as does **2-NO$_2$** in the pH range 6.0–7.8, albeit with some key differences in chemical shifts and line widths (see Figures 4.25–4.29). First, the resonances for **2-F** and **2-Me** span a smaller chemical shift range than those for **2-NO$_2$**, from −75 to 175 ppm vs H_2O. Moreover, the protons on the phenolate ring of $(^{X}L')^{-}$ are shifted downfield by 7 and 9 ppm for **2-F** and **2-Me**, respectively. The opposite trend in chemical shift changes across the series is observed for the resonances from the ancillary etidronate. For solutions buffered at pH 7.4, the etidronate Me peak shifts from 54 to 73 ppm in moving from X = Me to X = NO_2 (see Figure 4.3, left). Furthermore, the OH resonance shifts from 92 to 117 ppm across the series (see Figure 4.29). The OH peak becomes sharper with increasing pH for all complexes, however, the peak for **2-F** is significantly broader than for **2-NO$_2$** and **2-Me**. This observation suggests a faster OH proton exchange for **2-F** than for the other two Co_2 complexes between pH 6.0 and 7.8. Lastly, the two most downfield-shifted NH resonances are shifted upfield by ca. 10 ppm for **2-F** and **2-Me**, as compared to those for **2-NO$_2$**, whereas the less shifted sets of NH peaks are shifted slightly downfield. Overall, the ^{1}H NMR chemical shifts of the **2-X** series are extremely sensitive to the electronic properties of the X substituent. Remarkably,

the resonance frequencies of the protons on the distant etidronate are highly affected, demonstrating that even modest changes in ligand structure can lead to drastic changes in NMR properties.

4.3.7 CEST Properties

To investigate and compare the potential of **2-X** (X = NO_2, F, Me) as pH-responsive PARACEST probes, CEST spectra were collected for 8–9 mM solutions of **2-X** in 50 mM HEPES buffers with 100 mM NaCl at pH 6.0–7.8 (see Figure 4.4). The spectrum for **2-NO_2** at pH 5.97 displays three main features, namely a peak at 112 ppm with 11% H_2O signal reduction, two overlapping peaks at 87 and 91 ppm, and a broad signal centered at 45 ppm. As the pH is raised to 7.77, the peak at 112 ppm shifts to 117 ppm and its intensity decreases to 3.0%. In stark contrast, the positions of the other CEST peaks are relatively insensitive to pH changes and the intensities of these peaks greatly increase to 15–17% (see Figure 4.4, left). These data are consistent with variable-pH ^{1}H NMR experiments, and the three CEST features correspond to the etidronate OH group and two sets of overlapping NH protons, where the further downfield-shifted set can be resolved into two peaks. Note that the OH and NH CEST peaks for **2-NO_2** are well separated from one another, in contrast to the overlapping peaks observed at ca. 104 ppm in the spectra for **1**. Furthermore, the NH CEST effects for **2-NO_2** are significant at pH 5.97, whereas they are barely detectable below pH 6.50 for **1**.[7d] Therefore, incorporation of electron-withdrawing CF_3 groups serves to (1) shift the OH peak downfield and (2) increase the NH CEST intensities at lower pH values, and as such has dramatic effects on the CEST properties of Co_2 complexes.

The CEST spectra for **2-F** and **2-Me** reveal analogous features and pH-dependent changes in signal intensities as observed for **2-NO_2** (see Figure 4.4, center and right). The NH peaks for **2-F**

are shifted relative to those for **2-NO$_2$**, to 49, 79, and 81 ppm, and the peaks for **2-Me** are further shifted to 51, 76, and 79 ppm. These data are in accord with ^{1}H NMR analysis. Notably, the separation between the OH and NH CEST peaks for **2-X** decreases substantially when X is varied from NO_2 to Me. Additionally, while the OH peak for **2-NO$_2$** shifts 5 ppm downfield between pH 6.0 and 7.8, this peak shifts downfield by 7 ppm for the other two complexes in this pH range, from 90 to 97 ppm and 85 to 92 ppm for **2-F** and **2-Me**, respectively. The higher susceptibility of the OH CEST frequencies for **2-F** and **2-Me** to pH variations than observed for **2-NO$_2$** likely arises from the higher pK_a values of one of the coordinated $O_{phosphonate}$ atom in these compounds (see below).

The pH dependences of the CEST effects for **2-X** are summarized in Figures 4.30–4.35. The CEST intensities of the OH peak in the middle of the frequency range and of one peak for each NH CEST feature were monitored for each Co_2 complex. The OH CEST effects for **2-NO$_2$**, **2-F**, and **2-Me** at 115, 93, and 88 ppm, respectively, show very similar pH dependences in the pH range 6.0–7.8 (see Figure 4.36). Likewise, the intensities of the NH CEST peaks at 88, 79, and 76 ppm for **2-NO$_2$**, **2-F**, and **2-Me**, respectively, increase analogously with increasing pH (see Figure 4.37).

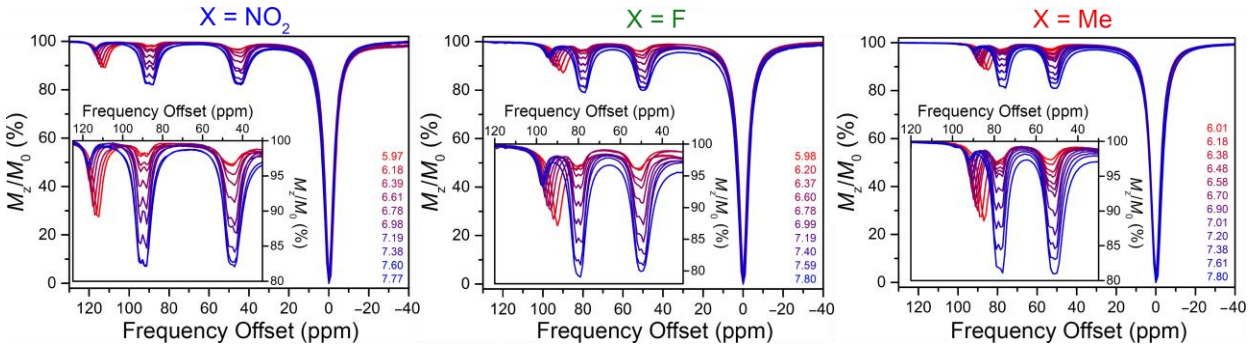

Figure 4.4 Variable-pH CEST spectra collected at 37 °C for 8 mM of **2-NO$_2$** (left), 9 mM of **2-F** (center), and 8 mM of **2-Me** (right) in aqueous solutions containing 50 mM HEPES and 100 mM NaCl buffered at pH 6.0–7.8 (red to blue). Values of pH are given in the legend. Insets: Expanded views of the CEST peaks of interest.

Furthermore, the maximum OH CEST effects for the three compounds vary similarly when the pH is raised from 6.0 to 7.4, revealing a near linear intensity decrease. However, slight discrepancies are observed above pH 7.4. While the intensity of the OH CEST peak for **2-Me** keeps decreasing, the intensities for **2-NO₂** and **2-F** reach a plateau (see Figure 4.38). In sum, the frequencies of the OH and NH CEST peaks for **2-X** are greatly affected by the nature of the *para*-substituent X, whereas the CEST intensities and their pH profiles are significantly less affected.

4.3.8 pK_a Determination by ^{1}H NMR Spectroscopy

The variations in the frequencies giving rise to maximum OH CEST effects for **2-X** (X = NO_2, F, Me) in the pH range 6.0–7.8 suggest that these Co_2 complexes undergo modest pH-induced structural changes in solution (see Figure 4.5). We previously hypothesized that these CEST peak shifts result from protonation of the ancillary bisphosphonate ligand at low pH, in particular one of the cobalt-coordinated $O_{phosphonate}$ atom.[7d] This hypothesis was supported by (1) dramatic chemical shift changes for the bisphosphonate resonances that followed sigmoidal pH profiles, (2) pK_a

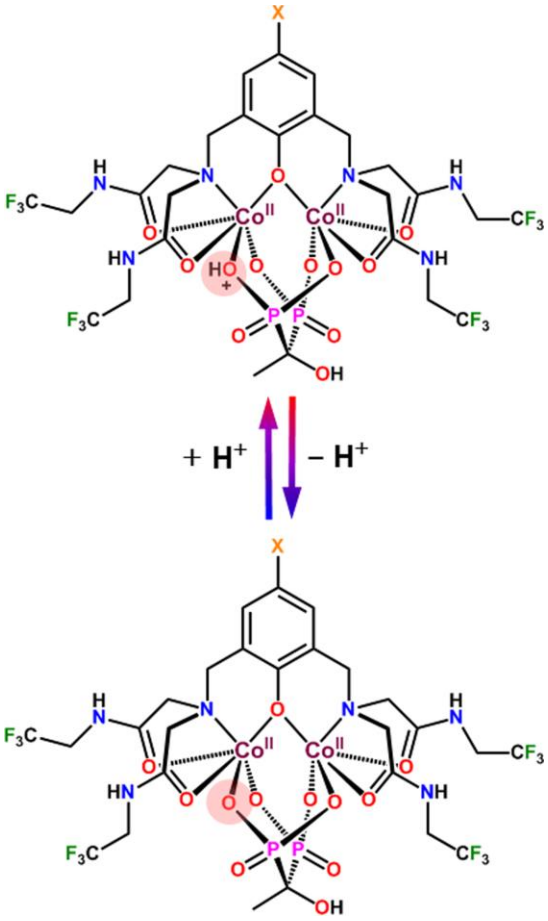

Figure 4.5 Scheme depicting the mechanism for pH-induced changes in NMR frequencies of etidronate resonances for **2-X** (X = NO_2, F, Me). The ionization process taken place on etidronate is highlighted with the light red circles.

values of the free bisphosphonic acids,[30] and (3) previous reports of protonated $O_{phosphonate}$ atoms in transition metal complexes.[31] Indeed, the chemical shifts of the etidronate Me group for **2-X** exhibit pronounced pH dependences. The Me resonance for **2-NO₂** shifts from 52.87 to 72.62 ppm vs H_2O between pH 2.30 and 7.77, and exhibits a sigmoidal pH profile. Similarly, the Me resonances for **2-F** and **2-Me** shift by 17.56 and 18.76 ppm, respectively, in the pH ranges 3.01–7.80 and 2.72–7.80, respectively. Fits of the Me chemical shifts as a function of pH to Equation 4.1 afforded pK_a = 4.76(7), 5.41(6), and 5.38(6) for **2-NO₂**, **2-F**, and **2-Me**, respectively (see Figures 4.39–4.41). The pK_a value obtained for **2-NO₂** is considerably lower than the value of 5.01(3) obtained for **1**,[7d] as expected given the electron-withdrawing nature of the CF_3 substituents. Furthermore, the pK_a for **2-NO₂** is lower than the values for **2-F** and **2-Me** by ca. 0.6. This observation agrees well with the smaller change in OH CEST frequency for **2-NO₂** in the pH range 6.0–7.8. To illustrate, the etidronate ligands in **2-F** and **2-Me** have greater contributions from both protonation states in this pH range, which renders the etidronate resonances more sensitive to small variations in pH. Finally, note that changes in the ^{1}H NMR frequency of the etidronate OH peak cannot be employed directly to estimate the pK_a values for **2-X** owing to the broadness of this peak below pH 6.0 for all compounds.

4.3.9 Exchange Rate Analysis

The proton exchange rates for **2-X** (X = NO_2, F, Me) were estimated at 37 °C using the Omega plot method[19] to gain further insight into the pH-dependent changes in NMR and CEST signal intensities. For **2-NO₂**, the rate constant (k_{ex}) for OH proton exchange decreases from 1.0(1) × 10^3 to 3.1(1) × 10^2 s^{-1} in the pH range 5.97–7.77 (see Figure 4.42 and Table 4.4). In contrast, k_{ex} for the NH protons increase from 3.3(1) × 10^2 (43–45 ppm), 2.5(4) × 10^2 (88–89 ppm), and 2.2(3) ×

10^2 (91–92 ppm) s^{-1} to 1.7(2) × 10^3 (43–45 ppm), 1.5(2) × 10^3 (88–89 ppm), and 1.6(2) × 10^3 (91–92 ppm) s^{-1} over the pH range 6.39–7.77 (see Figures 4.43–4.45 and Table 4.4). The opposite pH behavior for OH and NH proton exchange rates (see Figure 4.46) is consistent with ^{1}H NMR and CEST data and illustrates the acid- and base-catalyzed exchange of the OH and NH protons, respectively.[7d,8a–f,h,13,23,32]

The exchange rate constants for OH and NH protons in **2-F** and **2-Me** vary similarly with pH between pH 6.0 and 7.8 as those for **2-NO$_2$** (see Figures 4.47–4.56 and Tables 4.5 and 4.6). Nevertheless, close comparison of the pH dependences of k_{ex} across the **2-X** series reveals some important differences. Specifically, k_{ex} for OH proton exchange in **2-F** is slightly larger than the corresponding rate constants for the other two Co_2 complexes (see Figure 4.57). These data support the hypothesis that the broader OH resonances in the ^{1}H NMR spectra for **2-F**, compared to those for **2-NO$_2$** and **2-Me**, originate from a faster proton exchange. Furthermore, the NH proton exchange rates for **2-X** become considerably different at the basic end of the pH range investigated, where increasing electron-withdrawing character of X leads to faster exchange (see Figures 4.58–4.60). In addition, note that k_{ex} for the OH protons reveal a slight increase above pH 7.4 for all compounds (see Figure 4.57). This observation suggests that even though OH proton exchange is primarily acid-catalyzed in the pH range 6.0–7.8, catalysis by base might become important at more alkaline pH values.

4.3.10 Ratiometric CEST Properties

To assess and compare the ability of **2-X** (X = NO_2, F, Me) to quantify pH in a ratiometric manner, the pH dependences of the ratios of OH and NH CEST intensities ($CEST_{OH}/CEST_{NH}$) were investigated. In particular, the intensities of the OH peak midway between its position at pH

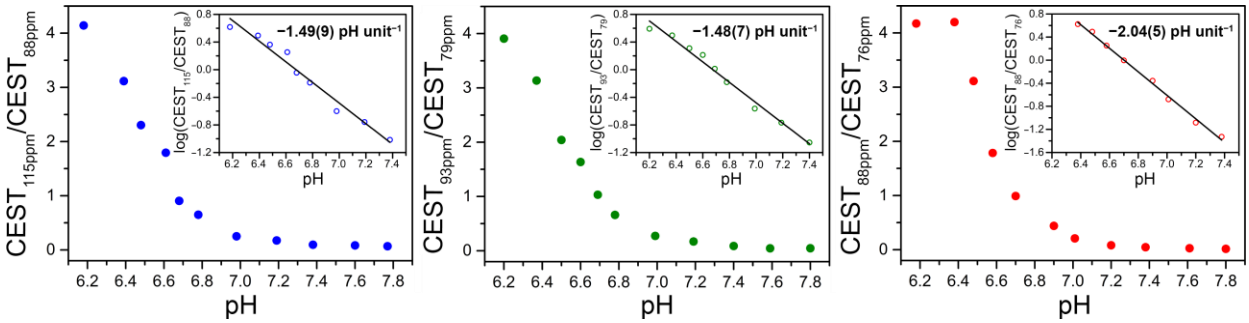

Figure 4.6 Plots of the ratios of OH and NH CEST intensities from presaturation at 115 and 88 ppm for 8 mM aqueous buffer solutions of **2-NO₂** (left), at 93 and 79 ppm for 9 mM solutions of **2-F** (center), and at 88 and 76 ppm for 8 mM solutions of **2-Me** (right) vs pH. Insets: Semilog forms of the plots. Colored circles denote experimental data and the black lines correspond to linear fits to the data. The black numbers in the insets represent the slopes of the linear fits to the data.

6.0 and pH 7.8, and the second most downfield-shifted NH peak were employed for each Co_2 complex to provide significant CEST intensities across the whole pH range. The ratios of CEST intensities at 115 and 88 ppm for **2-NO₂**, at 93 and 79 ppm for **2-F**, and at 88 and 76 ppm for **2-Me** reveal substantial and very similar pH dependences (see Figures 4.6 and 4.61). The ratiometric values decrease markedly between pH 6.2 and 7.4, whereas near no change is observed at higher pH. Importantly, linear pH calibration curves could be generated for **2-X** by plotting the logarithm[33] of the intensity ratios vs pH, in analogy to those reported for **1**.[7d] Linear fits of the $\log(CEST_{OH}/CEST_{NH})$ vs pH data for **2-X** afforded the following equations (see Figure 4.6, insets and Figure 4.62):

$$\textbf{NO}_2\text{: } \log(CEST_{115\ ppm}/CEST_{88\ ppm}) = -1.49 \times pH + 10.0 \qquad (4.3)$$

$$\textbf{F}\text{: } \log(CEST_{93\ ppm}/CEST_{79\ ppm}) = -1.48 \times pH + 9.9 \qquad (4.4)$$

$$\textbf{Me}\text{: } \log(CEST_{88\ ppm}/CEST_{76\ ppm}) = -2.04 \times pH + 13.7 \qquad (4.5)$$

Remarkably, the slope of the calibration curve for **2-NO₂** represents 1.5-fold enhancement in pH sensitivity compared to that obtained for **1**,[7d] owing to the complete separation of OH and NH CEST peaks and thus more contrasting pH-dependent intensity changes. Furthermore, the CF_3-

functionalized Co_2 complex enables detection of pH down to 6.2, compared to pH 6.5 for **1**. However, the trade-off of separating the two CEST peaks is a loss of signal intensity. Therefore, an ideal ratiometric PARACEST pH probe should demonstrate a compromise between pH sensitivity and CEST peak intensities.

Interestingly, the pH calibration curves obtained for **2-NO$_2$** and **2-F** in the pH range 6.2–7.4 are almost identical, while the curve for **2-Me** has a significantly steeper slope of −2.04(5) pH unit^{-1} (see Figure 4.62). Note, however, that the linear range of measuring pH using **2-Me** is between pH 6.4 and 7.4. The higher pH sensitivity observed for **2-Me** than **2-NO$_2$** may be attributed to the larger change in the chemical shift of the OH peak for **2-Me** in this pH range, which leads to more dramatic changes in OH CEST intensity (see Figure 4.36). Along these lines, the reason for the close similarities between the pH responsiveness of **2-NO$_2$** and **2-F**, despite the greater change in OH chemical shift for the latter, remains unclear. However, it is important to note that the slopes of the pH calibration curves for **2-X** are highly affected by the choice of OH CEST frequencies because of the variations in the frequencies giving rise to maximum OH CEST effects with pH.

4.3.11 Concentration Effects

To investigate the effects of probe concentration on the pH calibration curves, we collected variable-pH CEST spectra for 4 mM aqueous buffer solutions of **2-X** (X = NO_2, F, Me) in analogy to the 8–9 mM samples. All compounds exhibit similar pH-dependent changes in CEST frequencies and intensities for the OH and NH peaks as observed for the more concentrated samples (see Figures 4.63–4.86 and Tables 4.7–4.9). Accordingly, the plots of $CEST_{OH}/CEST_{NH}$ vs pH and the corresponding pH calibration curves for each Co_2 complex are nearly identical for

the different concentrations (see Figures 4.87–4.97). Specifically, linear fits of the log($CEST_{OH}/CEST_{NH}$) vs pH data for 4 mM of **2-X** provided the following pH calibration equations (see Figures 4.87, 4.90, 4.93, and 4.97):

$$\textbf{NO}_2\textbf{: } \log(CEST_{115\ ppm}/CEST_{88\ ppm}) = -1.51 \times pH + 10.2 \quad (4.6)$$

$$\textbf{F: } \log(CEST_{93\ ppm}/CEST_{79\ ppm}) = -1.48 \times pH + 9.9 \quad (4.7)$$

$$\textbf{Me: } \log(CEST_{88\ ppm}/CEST_{76\ ppm}) = -2.0 \times pH + 13.7 \quad (4.8)$$

These experiments reveal that the pH calibration curves for **2-X** are not significantly affected by the concentration of the Co_2 complex in this concentration range, and therefore demonstrate that these PARACEST probes provide a concentration-independent measure of pH in the pH range 6.2–7.4 for **2-NO₂** and **2-F**, and 6.4–7.4 for **2-Me**. Additionally, note that **2-F** affords a linear pH calibration curve over the pH range 6.2–7.6 (see Figure 4.98), and thus has the largest pH detection window of the three Co_2 probes.

4.3.12 Stability Studies

Finally, we sought to examine the stability of the Co_2 complexes in aqueous solutions. Cyclic voltammetry measurements were carried out for solutions of **2-X** (X = NO_2, F, Me) in HEPES buffer at pH 7.3. The cyclic voltammograms of **2-Me** and **2-F** each exhibit an irreversible oxidation process centered at ca. 1150 mV vs NHE (see Figure 4.99), which we assign to the metal-based Co^{II}/Co^{III} oxidation. As a comparison, the voltammogram of **2-NO₂** reveals a less obvious oxidation process at the onset of the potential window of the solvent (see Figure 4.99). These observations indicate that the electron-withdrawing CF_3 substituents in **2-X** serve to anodically shift the Co^{II}/Co^{III} oxidation wave by ca. 600 mV compared to that observed for **1**.[7d] Most importantly, these studies demonstrate that **2-X** are inert toward reaction with O_2 in aqueous

solutions.[34] Indeed, these Co_2 complexes are extremely robust in aqueous solutions, as evident from their identical NMR and CEST properties after weeks in HEPES buffers at pH 6.0–7.8.

4.4 Conclusions

The foregoing results demonstrate that modest variations in the electronic structure of Co^{II} centers through remote ligand substitution can lead to significant changes in the CEST properties of Co^{II}_2 complexes and can be employed for optimizing their pH sensing performance. Specifically, incorporation of CF_3-substituted amides into a ratiometric Co^{II}_2 PARACEST pH probe afforded a 1.5-fold enhancement in pH sensitivity owing to the complete separation of OH and NH CEST peaks that exhibit opposing pH-dependent intensity changes. In addition, the introduction of electron-withdrawing CF_3 groups led to a shift of the detection window to a more acidic range, from pH 6.5–7.6 to pH 6.2–7.4. Furthermore, CEST frequencies were found to be highly affected by the ligand electronic properties in a series of CF_3-functionalized Co^{II}_2 complexes **2-X** (X = NO_2, F, Me). Across the series, the OH peak shifts downfield and the separation between the two sets of NH peaks increases with increasing electron-withdrawing character of X. In contrast, the pH-dependent changes in CEST intensities were found to be significantly less affected by the identity of X.

While the CF_3-functionalized Co^{II}_2 PARACEST probes are attractive candidates for ratiometric pH quantitation due to their high pH sensitivities and stabilities in aqueous solutions, the variations in the frequencies providing maximum OH CEST intensities with pH are not ideal for intensity-based CEST probes. To address this issue, we will seek to design related probes with a compromise between pH sensitivity and CEST intensities by using the lessons learned from this study and taking advantage of the chemical tunability of the phenoxo-bridged dinuclear platform.

In particular, work is underway to modify the bisphosphonate ligand through incorporation of different substituents and CEST-active functional groups in an effort to minimize the pH dependence of CEST peak frequencies.

4.5 Supporting Information

4.5.1 Supplementary Experimental Details

Synthesis of 8-acetoxymethyl-6-nitro-1,3-benzodioxene. This compound was synthesized following a modified literature procedure.[35] Nitrophenol (35.0 g, 0.252 mol) was added to a stirring colorless solution of paraformaldehyde (31.8 g, 1.06 mol), glacial acetic acid (250 mL) and concentrated sulfuric acid (60 mL) at 80 °C. The resulting suspension was heated at 80 °C under a dinitrogen atmosphere for 16 h. Deionized H_2O (1000 mL) was then added to the off-white suspension at 25 °C, and the mixture was neutralized by slow addition of solid potassium carbonate (150 g, 1.09 mol). The resulting yellow precipitate was collected by vacuum filtration, washed with cold deionized H_2O (600 mL) and dried with suction on the filter for 3 h. The crude product was recrystallized from ethanol to give the title compound as a light yellow solid (31.7 g, 50%). ^{1}H NMR (500 MHz, $CDCl_3$, 25 °C): δ 8.14 (d, $^4J_{HH}$ = 2.7 Hz, 1H), 7.90 (d, $^4J_{HH}$ = 2.6 Hz, 1H), 5.37 (s, 2H), 5.15 (s, 2H), 4.96 (s, 2H), 2.16 (s, 3H).

Synthesis of 2,6-bis(bromomethyl)-4-nitrophenol. This compound was synthesized following a modified literature procedure.[35a] A mixture of 8-acetoxymethyl-6-nitro-1,3-benzodioxene (7.00 g, 27.6 mmol) and 48% (w/w) hydrobromic acid solution in H_2O (200 mL) was stirred at reflux for 20 h. Note that the reaction flask was connected to a potassium hydroxide base trap to neutralize the hydrogen bromide gas that evolved in the reaction. The resulting gray precipitate was collected by vacuum filtration at 25 °C, washed with deionized H_2O (600 mL) and dried with suction on the

filter for 3 h. Recrystallization from $CHCl_3$ afforded the title compound as an off-white powder (5.67 g, 64%). ^{1}H NMR (500 MHz, $CDCl_3$, 25 °C): δ 8.22 (s, 2H), 6.39 (s, 1H), 4.57 (s, 4H).

Synthesis of 2,6-bis(hydroxymethyl)-4-fluorophenol. This compound was synthesized following a modified literature procedure.[36] 4-Fluorophenol (20.0 g, 178 mmol) was dissolved in a solution of sodium hydroxide (10.0 g, 250 mmol) in deionized H_2O (60 mL), and a 37% (w/w) formaldehyde solution in H_2O (60 mL) was added dropwise with stirring. The resulting light orange solution was stirred at 25 °C for 72 h to give a dark red-orange solution. The volume of the solution was reduced to 20 mL, resulting in the formation of an orange precipitate. The orange solid was collected by vacuum filtration, dried with suction on the filter for 1 h, and then dissolved in deionized H_2O (120 mL) and filtered to give a dark orange solution. This solution was cooled to 0 °C in an ice-water bath and glacial acetic acid (20 mL) was added with vigorous stirring to give a light orange precipitate within a few min. The resulting suspension was stirred at 0 °C for additional 2 h. The orange solid was collected by vacuum filtration and dried with suction on the filter for 3 h, and further in vacuo for 14 h to give the product as a light orange solid (12.5 g, 41%). ^{1}H NMR (500 MHz, DMSO-d_6, 25 °C): δ 6.92 (d, $^3J_{HF}$ = 9.4 Hz, 2H), 4.51 (s, 4H). ^{19}F NMR (376 MHz, DMSO-d_6, 25 °C): δ −124.68 (t, $^3J_{FH}$ = 9.5 Hz).

Synthesis of 2,6-bis(bromomethyl)-4-fluorophenol. This compound was synthesized following a modified literature procedure.[36a] 2,6-Bis(hydroxymethyl)-4-fluorophenol (6.00 g, 34.9 mmol) was dissolved in 48% (w/w) hydrobromic acid solution in H_2O (30 mL) and stirred at reflux for 24 h. Note that the reaction flask was connected to a potassium hydroxide base trap to neutralize the hydrogen bromide gas that evolved in the reaction. The resulting orange precipitate was collected by vacuum filtration, washed with deionized H_2O (75 mL) and dried with suction on the

filter for 1 h. Recrystallization from $CHCl_3$ afforded the title compound as a light orange powder (5.45 g, 53%). ^{1}H NMR (400 MHz, $CDCl_3$, 25 °C): δ 7.01 (d, $^3J_{HF}$ = 8.2 Hz, 2H), 5.39 (s, 1H), 4.51 (s, 4H). ^{19}F NMR (376 MHz, $CDCl_3$, 25 °C): δ −121.58 (t, $^3J_{FH}$ = 8.2 Hz).

Synthesis of 2,6-bis(hydroxymethyl)-4-methylphenol. This compound was synthesized following a modified literature procedure.[36] 4-Methylphenol (9.70 g, 89.7 mmol) was dissolved in a solution of sodium hydroxide (4.50 g, 113 mmol) in deionized H_2O (18 mL). To a stirring solution of this, a 37% (w/w) formaldehyde solution in H_2O (18 mL) was added dropwise and the resulting light yellow solution was stirred for 20 h at 25 °C to afford a white suspension. The white solid was collected by vacuum filtration and dissolved in deionized H_2O (200 mL). The pH of this solution was adjusted to ca. 6 by addition of glacial acetic acid. Stirring for 15 min at 25 °C resulted in the formation of a white precipitate, which was collected by vacuum filtration and dried with suction on the filter for 2 h to afford the title compound as a white solid (8.70 g, 57%). ^{1}H NMR (400 MHz, DMSO-d_6, 25 °C): δ 7.89 (s, 1H), 7.30 (s, 2H), 6.92 (s, 2H), 4.82 (s, 4H), 2.28 (s, 3H).

Synthesis of 2,6-bis(bromomethyl)-4-methylphenol. This compound was synthesized following a modified literature procedure.[36] 2,6-Bis(hydroxymethyl)-4-methylphenol (8.70 g, 51.7 mmol) was dissolved in 33% (w/w) hydrobromic acid solution in acetic acid (40 mL) to give a yellow-white suspension. After stirring vigorously at 25 °C for 24 h, the mixture was diluted with deionized H_2O (40 mL) and stirred for additional 30 min. The resulting precipitate was collected by vacuum filtration, washed with deionized H_2O (50 mL) and dried with suction on the filter for 3 h to give the product as an off-white solid (9.27 g, 61%). ^{1}H NMR (400 MHz, $CDCl_3$, 25 °C): δ 7.08 (s, 2H), 6.74 (broad s, 1H), 4.54 (s, 4H), 2.26 (s, 3H).

Synthesis of 2-chloro-N-(2,2,2-trifluoroethyl)acetamide. This compound was synthesized

following a modified literature procedure.[37] 2,2,2-Trifluoroethylamine hydrochloride (10.0 g, 73.8 mmol) was dissolved in deionized H_2O (60 mL) and added to a solution of sodium hydroxide (6.08 g, 152 mmol) in deionized H_2O (50 mL). Subsequently, *tert*-butyl methyl ether (^{t}BuOMe; 85 mL) was added and the resulting mixture was stirred at 0 °C in an ice-water bath for 30 min. Chloroacetyl chloride (8.75 g, 77.5 mmol) in ^{t}BuOMe (9 mL) was then added dropwise to the stirring reaction. The mixture was stirred for an additional 1 h at 0 °C and extracted with ^{t}BuOMe (2 × 50 mL). The organic fractions were combined, dried over magnesium sulfate, filtered, and the solvent was removed under reduced pressure to afford a white solid. This solid was suspended in deionized H_2O (50 mL) and the mixture extracted with $CHCl_3$ (100 mL). The $CHCl_3$ layer was dried over magnesium sulfate, filtered, and the solvent removed under reduced pressure to afford the product as a white crystalline solid (8.13 g, 63%). ^{1}H NMR (400 MHz, $CDCl_3$, 25 °C): δ 7.01 (broad s, 1H), 4.13 (s, 2H), 4.00–3.93 (m, 2H). ^{19}F NMR (376 MHz, $CDCl_3$, 25 °C): δ −72.46 (t, $^3J_{FH}$ = 8.9 Hz).

Synthesis of 2,2'-(benzylazanediyl)bis(N-(2,2,2-trifluoroethyl)acetamide). This compound was synthesized following a modified literature procedure.[38] Benzylamine (2.42 g, 22.6 mmol) and 2-chloro-*N*-(2,2,2-trifluoroethyl)acetamide (8.13 g, 46.3 mmol) were stirred in dry MeCN (300 mL). Subsequently, potassium carbonate (12.8 g, 92.6 mmol) and potassium iodide (4.61 g, 27.8 mmol) were added. The resulting off-white suspension was stirred at reflux under a dinitrogen atmosphere for 18 h. The reaction mixture was then cooled to 25 °C and filtered to give a light yellow filtrate, which was concentrated under reduced pressure to give a pale orange solid. This solid was dissolved in $CHCl_3$ (100 mL), filtered, and the solvent removed under reduced pressure to afford the product as a fluffy off-white solid (4.12 g, 47%). ^{1}H NMR (500 MHz, $CDCl_3$, 25 °C): δ 7.37–

7.26 (m, 5H), 6.98 (broad t, 2H), 3.94–3.87 (m, 4H), 3.75 (s, 2H), 3.31 (s, 4H). ^{19}F NMR (470 MHz, $CDCl_3$, 25 °C): δ −72.56 (t, $^3J_{FH}$ = 9.0 Hz).

Synthesis of 2,2′-(azanediyl)bis(N-(2,2,2-trifluoroethyl)acetamide). This compound was synthesized following a modified literature procedure.[38] Pd/C (10 wt%, 100 mg, 0.09 mmol Pd) was carefully added to a clear solution of 2,2′-(benzylazanediyl)bis(*N*-(2,2,2-trifluoroethyl)acetamide) (3.00 g, 7.79 mmol) in dry MeOH (75 mL). The resulting dark suspension was stirred at 25 °C under 50 psi pressure of dihydrogen for 24 h. The reaction flask was then vented, and a second fraction of Pd/C (10 wt%, 100 mg, 0.09 mmol Pd) was added. The reaction was re-pressurized with 50 psi of dihydrogen and stirred for additional 24 h at 25 °C. After that time, ESI-MS indicated that the reaction was complete. The black suspension was filtered through diatomaceous earth and the colorless solution was concentrated under reduced pressure to give the title compound as a white solid (1.92 g, 83%). ^{1}H NMR (400 MHz, $CDCl_3$, 25 °C): δ 6.87 (broad t, 2H), 4.00–3.91 (m, 4H), 3.37 (s, 4H). ^{19}F NMR (376 MHz, $CDCl_3$, 25 °C): δ −72.60 (t, $^3J_{FH}$ = 9.0 Hz).

Synthesis of N,N′-[(2-hydroxy-5-nitro-1,3-phenylene)bis(methylene)]bis[N-(carboxymethyl)-(N-(2,2,2-trifluoroethyl)glycinamide)] [H(^{NO_2}*L′)]*. This compound was synthesized following a modified literature procedure.[7b,d] Under an atmosphere of dinitrogen, 2,2′-(azanediyl)bis(*N*-(2,2,2-trifluoroethyl)acetamide) (2.27 g, 7.69 mmol) was dissolved in MeCN (200 mL) to give a colorless solution, and *N*,*N*-diisopropylethylamine (DIPEA; 0.994 g, 7.69 mmol) was subsequently added. This solution was heated to reflux and while stirring, a light yellow solution of 2,6-bis(bromomethyl)-4-nitrophenol (1.00 g, 3.07 mmol) in MeCN (20 mL) was added dropwise over the course of 1.5 h. The resulting yellow solution was stirred at reflux for 24 h, and the solvent

was subsequently removed under reduced pressure to give a brown residue. The crude residue was stirred in CH_2Cl_2 (50 mL) for 20 min at 25 °C, the solvent was decanted off and the residue was subsequently stirred in Et_2O (50 mL) at 25 °C for 16 h to afford an off-white solid that was collected by vacuum filtration. Recrystallization from $CHCl_3$ afforded H(^{NO2}L′) as a pale yellow powder (0.821 g, 36%). ESI-MS (*m*/*z*): Calcd. for $C_{24}H_{28}F_{12}N_7O_7$ $(M+H)^+$: 754.19, found: 754.16. ^{1}H NMR (400 MHz, MeCN-d_3, 25 °C): δ 8.03 (s, 2H), 7.44 (broad t, 4H), 3.94–3.85 (m, 8H), 3.83 (s, 4H), 3.34 (s, 8H). ^{13}C{^{1}H} NMR (126 MHz, MeCN-d_3, 25 °C): δ 172.36 (C=O), 162.99 (Ar–OH), 140.72 (Ar–NO_2), 127.51 (Ar–H), 125.59 (q, $^1J_{CF}$ = 278.5 Hz; CF_3), 125.24 (Ar–CH_2), 57.64 (N–**C**H_2–CO), 55.50 (Ar–**C**H_2–N), 40.75 (q, $^2J_{CF}$ = 34.5 Hz; NH–**C**H_2–CF_3). ^{19}F NMR (376 MHz, MeCN-d_3, 25 °C): δ −73.14 (t, $^3J_{FH}$ = 9.5 Hz). UV-Vis absorption spectrum (97 μM; MeOH, 25 °C): 307 nm (ε = 3600 M^{-1} cm^{-1}), 405 nm (ε = 10000 M^{-1} cm^{-1}). FT-IR (ATR, cm^{-1}): 3326 (m); 3269 (m); 3082 (w); 2925 (w); 2863 (w); 1661 (m); 1596 (w); 1553 (m); 1519 (m); 1479 (w); 1434 (m); 1422 (m); 1401 (m); 1344 (m); 1295 (m); 1270 (m); 1235 (m); 1154 (s); 1104 (m); 1014 (w); 987 (w); 969 (w); 941 (w); 914 (w); 872 (w); 833 (m); 747 (w); 712 (w); 666 (m).

Synthesis of N,N′-[(5-fluoro-2-hydroxy-1,3-phenylene)bis(methylene)]bis[N-(carboxymethyl)-(N-(2,2,2-trifluoroethyl)glycinamide)] [H(^{F}L′)]. This compound was synthesized following a modified literature procedure.[7b,d] Under an atmosphere of dinitrogen, 2,2′-(azanediyl)bis(*N*-(2,2,2-trifluoroethyl)acetamide) (1.58 g, 5.35 mmol) was dissolved in MeCN (200 mL) to give a colorless solution, and DIPEA (0.692 g, 5.35 mmol) was subsequently added. This solution was heated to reflux and while stirring, a colorless solution of 2,6-bis(bromomethyl)-4-fluorophenol (0.798 g, 2.70 mmol) in MeCN (20 mL) was added dropwise over the course of 1.5 h. The resulting light yellow solution was stirred at reflux for 24 h, and the solvent was subsequently removed under

reduced pressure to give a yellow residue. This residue was stirred in Et_2O (300 mL) at 25 °C for 16 h to give a light yellow solid that was collected by vacuum filtration and dried with suction on the filter for 1 h. The obtained solid was then stirred in CH_2Cl_2 (3 × 50 mL) at 25 °C for 30 min each time to wash. The CH_2Cl_2 layer was decanting off between washes. The resulting white solid was collected by vacuum filtration and dried under suction on the filter for 3 h and further in vacuo for 16 h to give H(^{F}L′) as a white powder (0.988 g, 50%). ESI-MS (*m*/*z*): Calcd. for $C_{24}H_{28}F_{13}N_6O_5$ $(M+H)^+$: 727.19, found: 727.18. ^{1}H NMR (400 MHz, MeCN-d_3, 25 °C): δ 10.50 (broad s, 1H), 7.51 (broad t, 4H), 6.88 (d, $^3J_{HF}$ = 8.4 Hz, 2H), 3.94–3.85 (m, 8H), 3.72 (s, 4H), 3.32 (s, 8H). ^{13}C{^{1}H} NMR (126 MHz, MeCN-d_3, 25 °C): δ 172.39 (C=O), 156.30 (d, $^1J_{CF}$ = 235.8 Hz; Ar–F), 152.71 (d, $^4J_{CF}$ = 2.1 Hz; Ar–OH), 125.71 (d, $^3J_{CF}$ = 7.2 Hz; Ar–CH_2), 125.62 (q, $^1J_{CF}$ = 278.5 Hz; CF_3), 117.84 (d, $^2J_{CF}$ = 23.0 Hz; Ar–H), 57.70 (N–**C**H_2–CO), 55.86 (Ar–**C**H_2–N), 40.72 (q, $^2J_{CF}$ = 34.5 Hz; NH–**C**H_2–CF_3). ^{19}F NMR (376 MHz, MeCN-d_3, 25 °C): δ −73.16 (t, $^3J_{FH}$ = 9.5 Hz, 12F), −127.24 (t, $^3J_{FH}$ = 8.6 Hz, 1F). UV-Vis absorption spectrum (0.37 mM; MeOH, 25 °C): 287 nm (ε = 3900 M^{-1} cm^{-1}). FT-IR (ATR, cm^{-1}): 3328 (m); 3260 (m); 3082 (w); 1672 (s); 1552 (m); 1485 (m); 1446 (w); 1421 (w); 1402 (m); 1350 (w); 1296 (m); 1286 (m); 1266 (m); 1225 (m); 1154 (s); 1088 (m); 1010 (m); 993 (w); 966 (m); 891 (m); 881 (w); 858 (w); 834 (m); 774 (w); 704 (m); 665 (m); 646 (m).

Synthesis of N,N′-[(2-hydroxy-5-methyl-1,3-phenylene)bis(methylene)]bis[N-(carboxy-methyl)(N-(2,2,2-trifluoroethyl)glycinamide)] [H(^{Me}L′)]. This compound was synthesized following a modified literature procedure.[7b,d] Under an atmosphere of dinitrogen, 2,2′-(azanediyl)bis(*N*-(2,2,2-trifluoroethyl)acetamide) (2.47 g, 8.37 mmol) was dissolved in MeCN (200 mL) to give a colorless solution, and DIPEA (1.08 g, 8.36 mmol) was subsequently added.

This solution was heated to reflux and while stirring, a colorless solution of 2,6-bis(bromomethyl)-4-methylphenol (0.977 g, 3.32 mmol) in MeCN (20 mL) was added dropwise over the course of 1.5 h. The resulting pale yellow solution was stirred at reflux for 24 h, and the solvent was subsequently removed under reduced pressure to give a yellow residue. This residue was stirred in Et_2O (100 mL) at 25 °C for 16 h to give a light yellow solid that was collected by vacuum filtration and dried with suction on the filter for 1 h. The obtained solid was then stirred in CH_2Cl_2 (50 mL) for 20 min at 25 °C, the solvent was decanted off and the resulting white solid was collected by vacuum filtration. Recrystallization from $CHCl_3$ afforded H(^{Me}L′) as a white powder (0.981 g, 41%). ESI-MS (*m*/*z*): Calcd. for $C_{25}H_{31}F_{12}N_6O_5$ $(M+H)^+$: 723.22, found: 723.22. ^{1}H NMR (400 MHz, MeCN-d_3, 25 °C): δ 10.38 (broad s, 1H), 7.58 (broad t, 4H), 6.90 (s, 2H), 3.93–3.86 (m, 8H), 3.69 (s, 4H), 3.30 (s, 8H), 2.20 (s, 3H). ^{13}C{^{1}H} NMR (126 MHz, MeCN-d_3, 25 °C): δ 172.49 (C=O), 154.07 (Ar–OH), 132.57 (Ar–H), 129.25 (Ar–CH_3), 125.63 (q, $^1J_{CF}$ = 278.5 Hz; CF_3), 124.14 (Ar–CH_2), 57.70 (N–**C**H_2–CO), 56.31 (Ar–**C**H_2–N), 40.71 (q, $^2J_{CF}$ = 34.6 Hz; NH–**C**H_2–CF_3), 20.30 (CH_3). ^{19}F NMR (376 MHz, MeCN-d_3, 25 °C): δ −73.15 (t, $^3J_{FH}$ = 9.4 Hz). UV-Vis absorption spectrum (0.30 mM; MeOH, 25 °C): 287 nm (ε = 3400 M^{-1} cm^{-1}). FT-IR (ATR, cm^{-1}): 3298 (m); 3243 (m); 3088 (w); 1697 (m); 1657 (s); 1562 (m); 1486 (w); 1429 (w); 1397 (w); 1310 (m); 1273 (m); 1238 (m); 1157 (s); 1142 (s); 1090 (m); 995 (m); 975 (m); 964 (m); 875 (w); 859 (w); 832 (m); 761 (w); 670 (m).

4.5.2 Supplementary Schemes

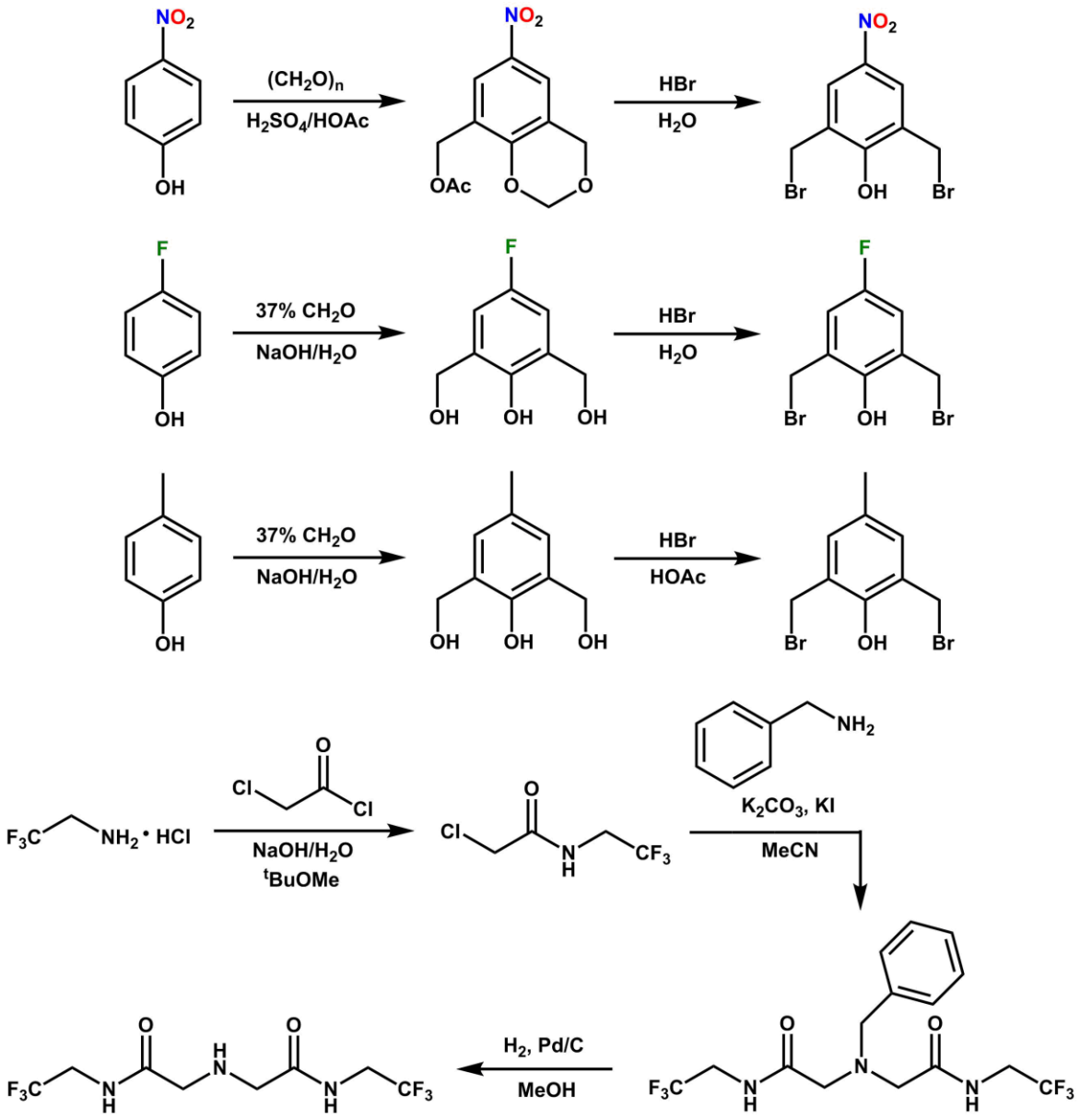

Scheme 4.1 Syntheses of organic precursors.

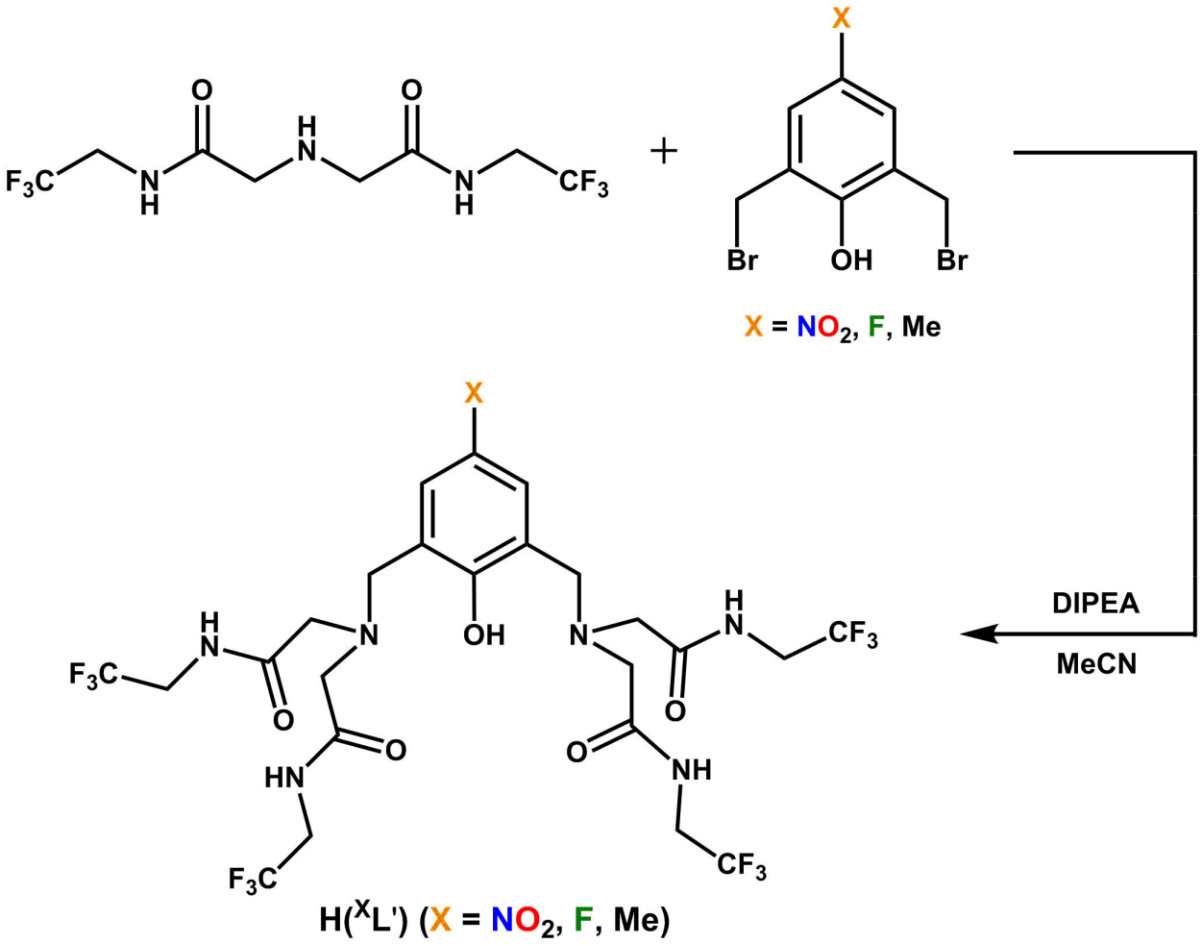

Scheme 4.2 Synthesis of ligands H(^{X}L′) (X = NO_2, F, Me).

4.5.3 Supplementary Figures

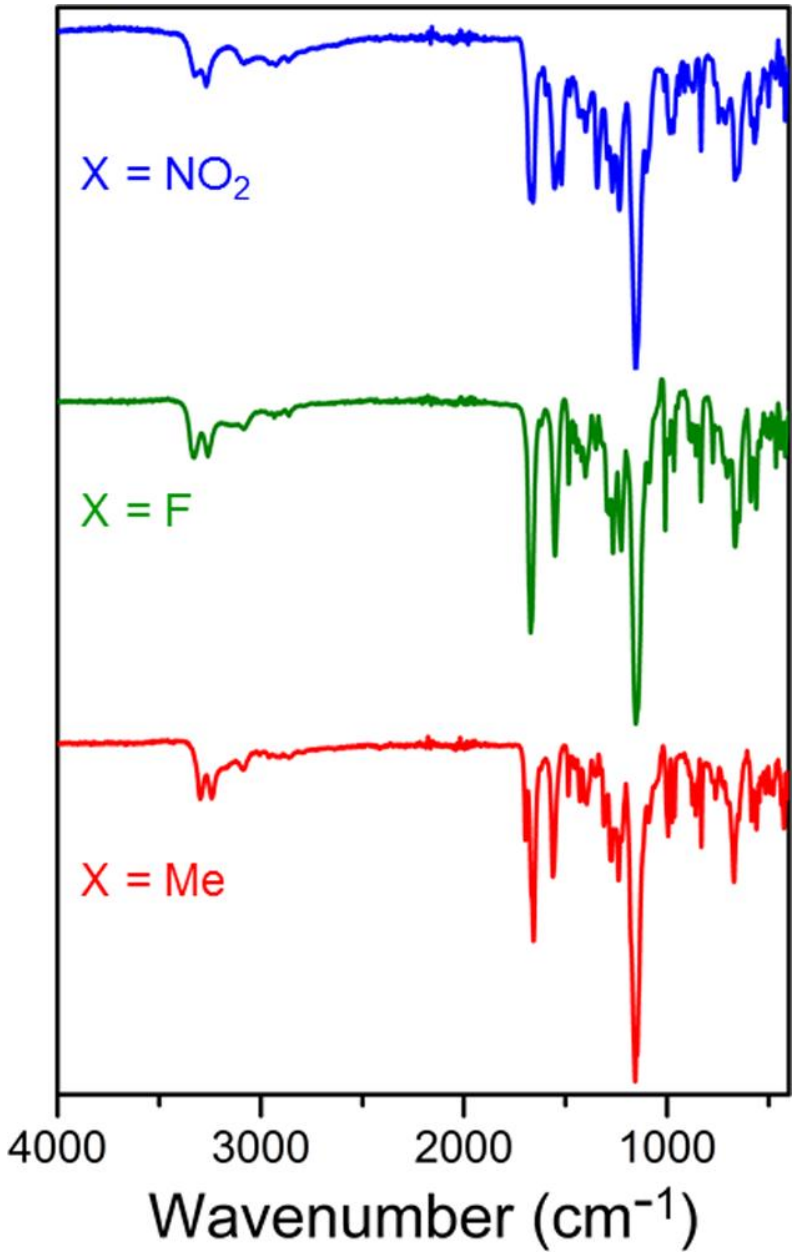

Figure 4.7 Stacked FT-IR spectra of ligands H(^{NO2}L′) (blue), H(^{F}L′) (green), and H(^{Me}L′) (red) at ambient temperature.

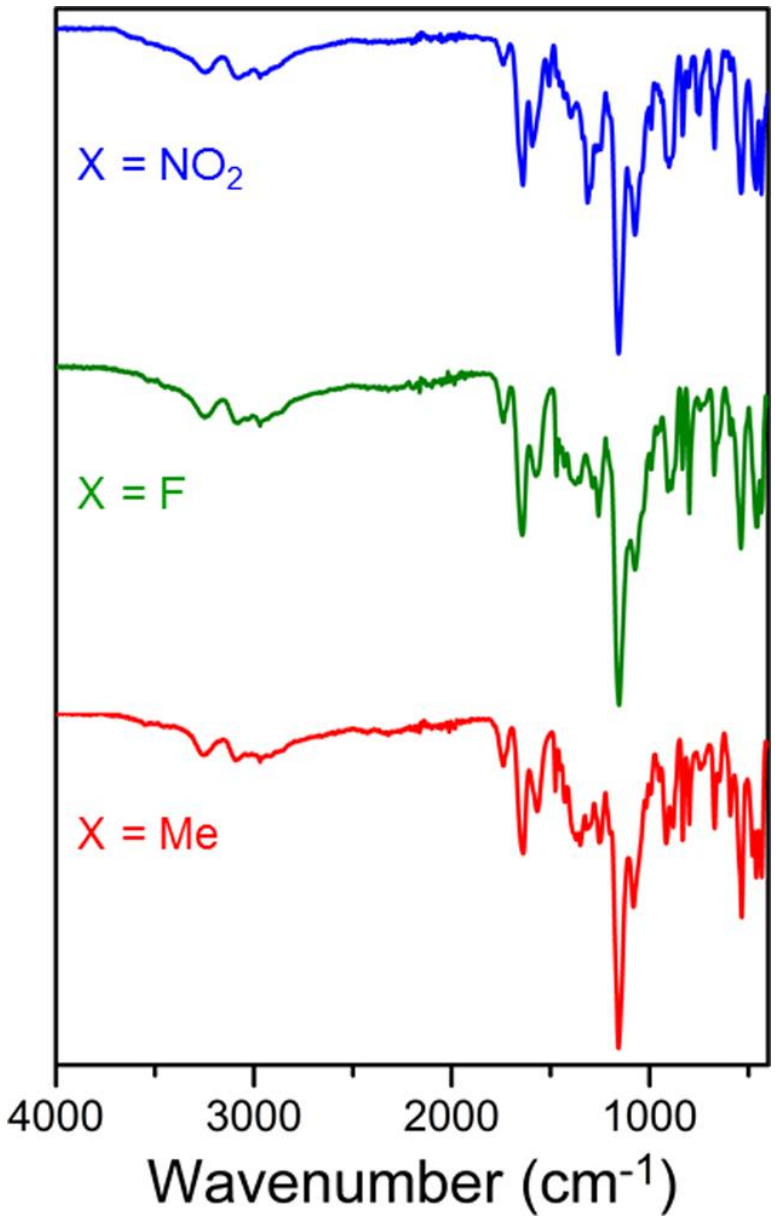

Figure 4.8 Stacked FT-IR spectra of **2-NO₂** (blue), **2-F** (green), and **2-Me** (red) at ambient temperature.

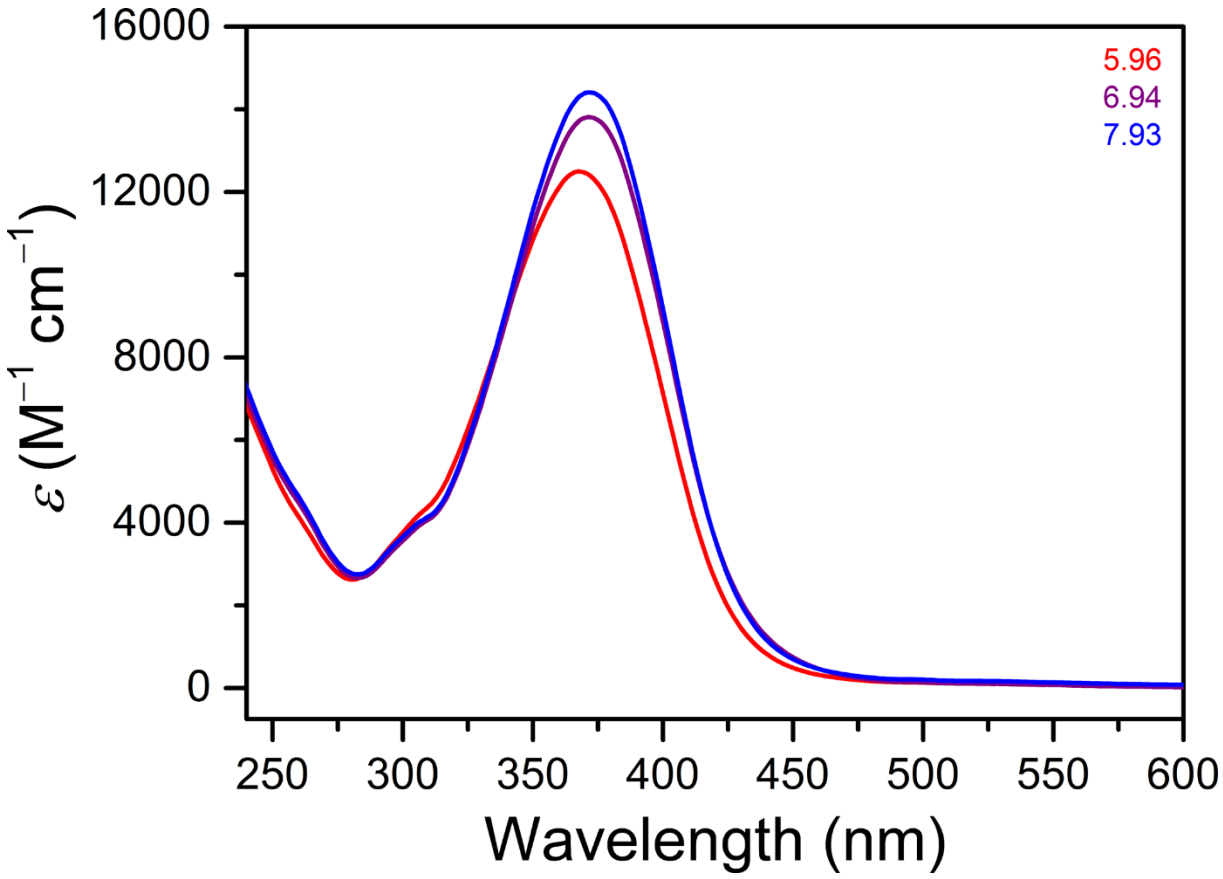

Figure 4.9 Variable-pH UV-Vis absorption spectra of 22–42 μM of **2-NO₂** in aqueous solutions containing 50 mM HEPES and 100 mM NaCl at ambient temperature. Spectra were measured in the pH range used for CEST experiments, from pH 5.96 to 7.93. Colored numbers in the legend denote the pH of the solutions measured with a pH electrode and the corresponding color of each sample. Note that the molar absorptivity (ε) is plotted against wavelength.

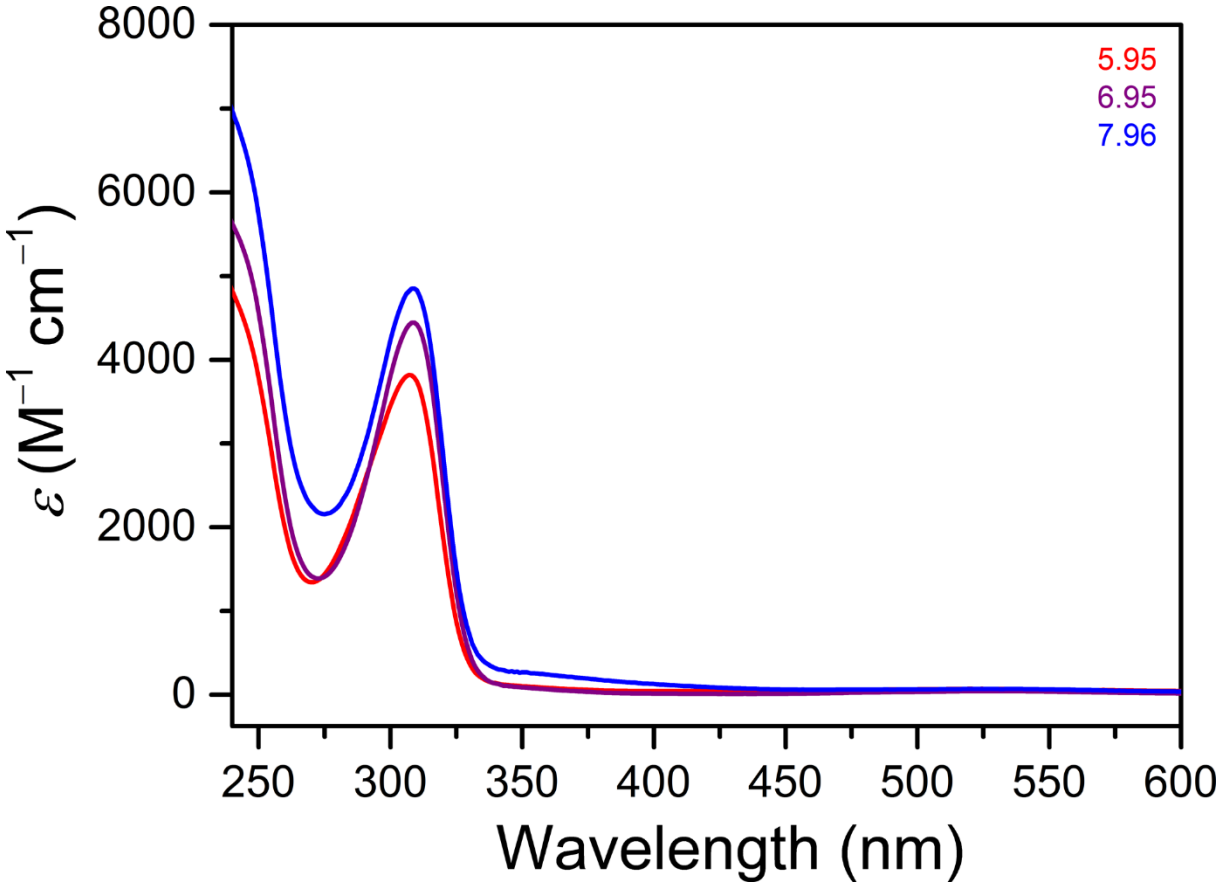

Figure 4.10 Variable-pH UV-Vis absorption spectra of 30–87 μM of **2-F** in aqueous solutions containing 50 mM HEPES and 100 mM NaCl at ambient temperature. Spectra were measured in the pH range used for CEST experiments, from pH 5.95 to 7.96. Colored numbers in the legend denote the pH of the solutions measured with a pH electrode and the corresponding color of each sample. Note that the molar absorptivity (ε) is plotted against wavelength.

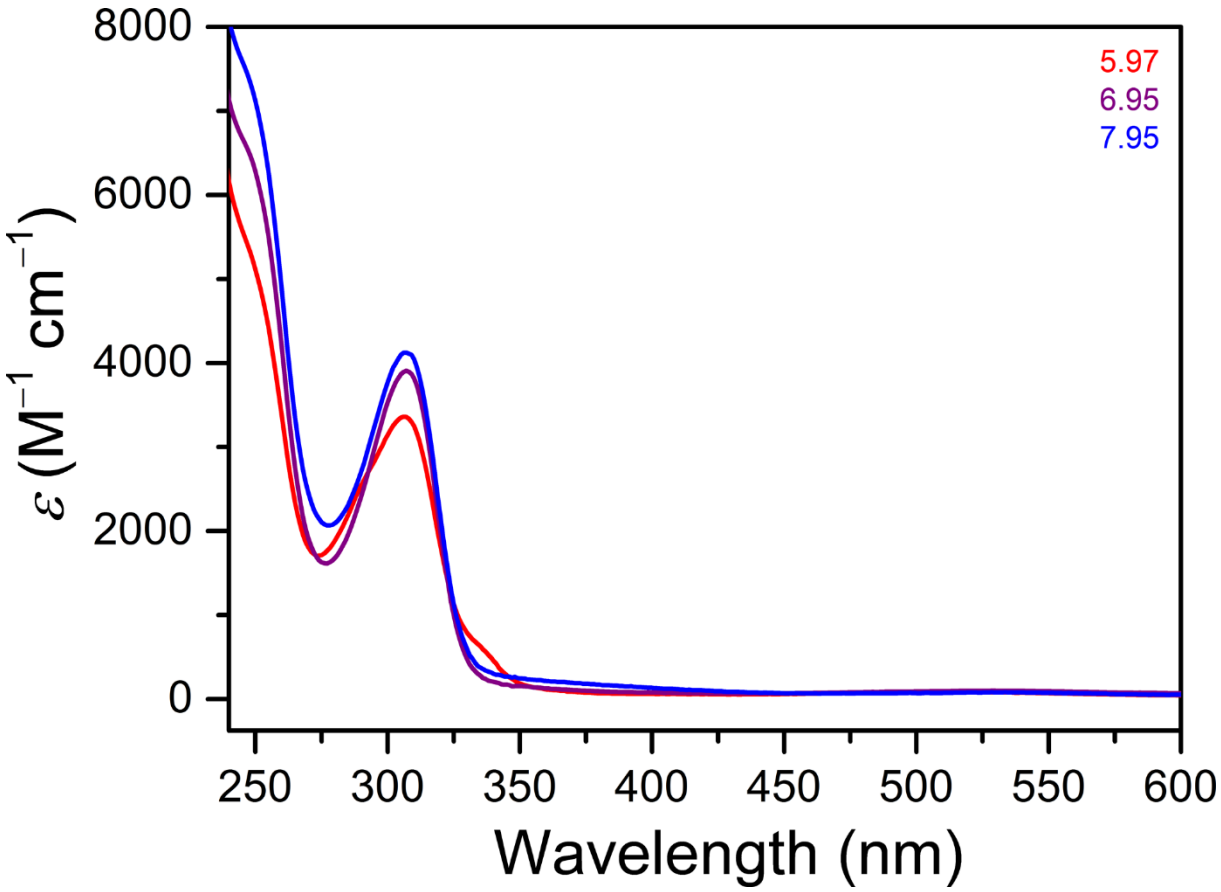

Figure 4.11 Variable-pH UV-Vis absorption spectra of 22–42 μM of **2-Me** in aqueous solutions containing 50 mM HEPES and 100 mM NaCl at ambient temperature. Spectra were measured in the pH range used for CEST experiments, from pH 5.97 to 7.95. Colored numbers in the legend denote the pH of the solutions measured with a pH electrode and the corresponding color of each sample. Note that the molar absorptivity (ε) is plotted against wavelength.

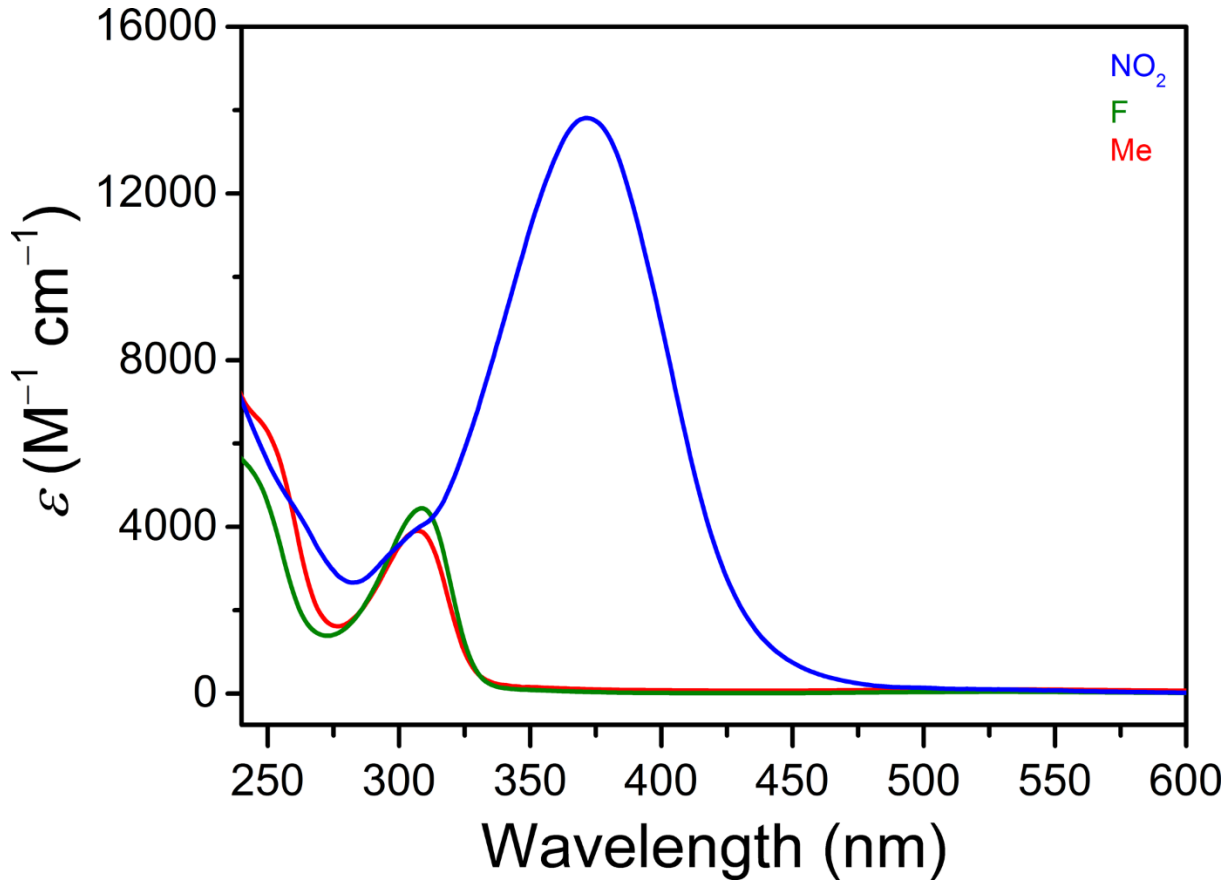

Figure 4.12 Comparison of the UV-Vis absorption spectra of **2-NO₂** (blue), **2-F** (green), and **2-Me** (red) in aqueous solutions containing 50 mM HEPES and 100 mM NaCl buffered at pH 6.94–6.95 at ambient temperature. Note that the molar absorptivity (ε) is plotted against wavelength.

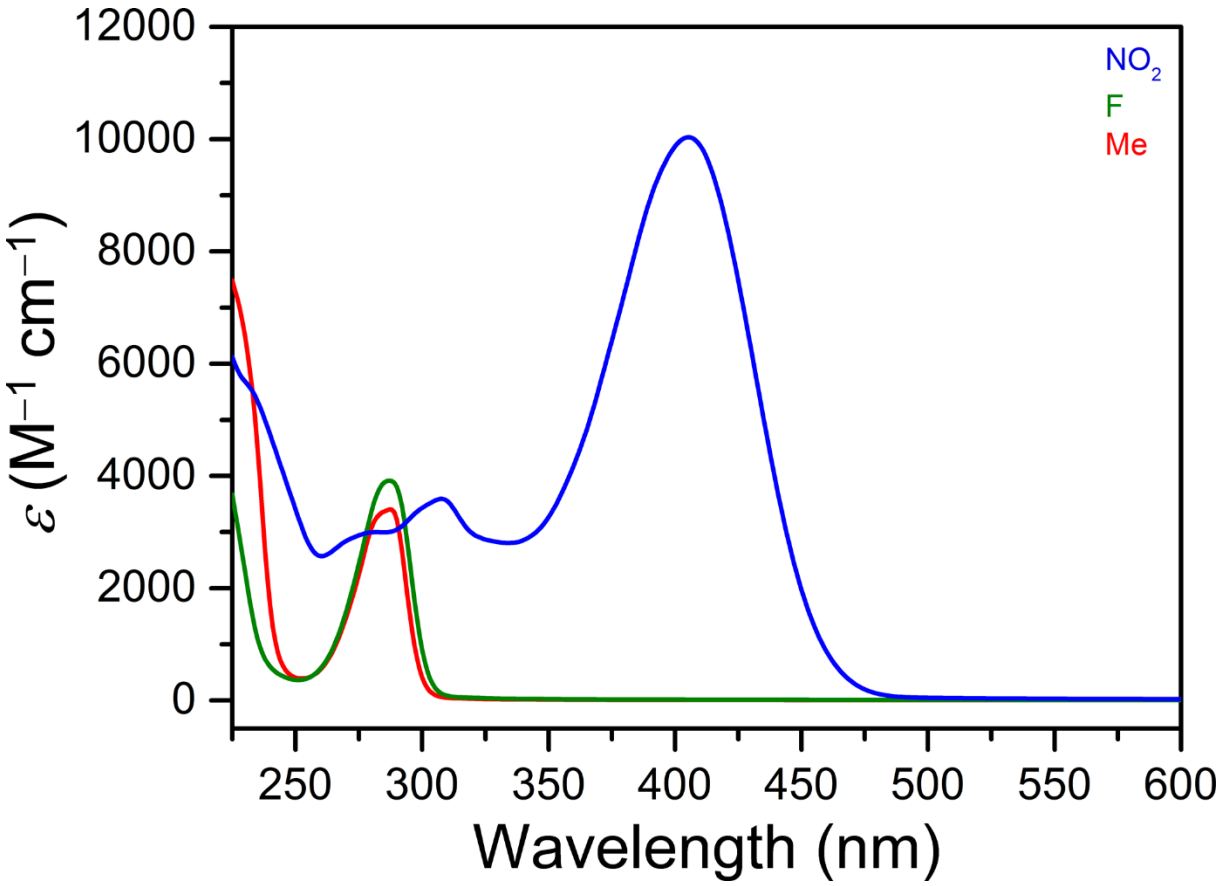

Figure 4.13 UV-Vis absorption spectra for 97–370 μM samples of ligands H(^{NO2}L′) (blue), H(^{F}L′) (green), and H(^{Me}L′) (red) in MeOH at ambient temperature. Note that the molar absorptivity (ε) is plotted against wavelength.

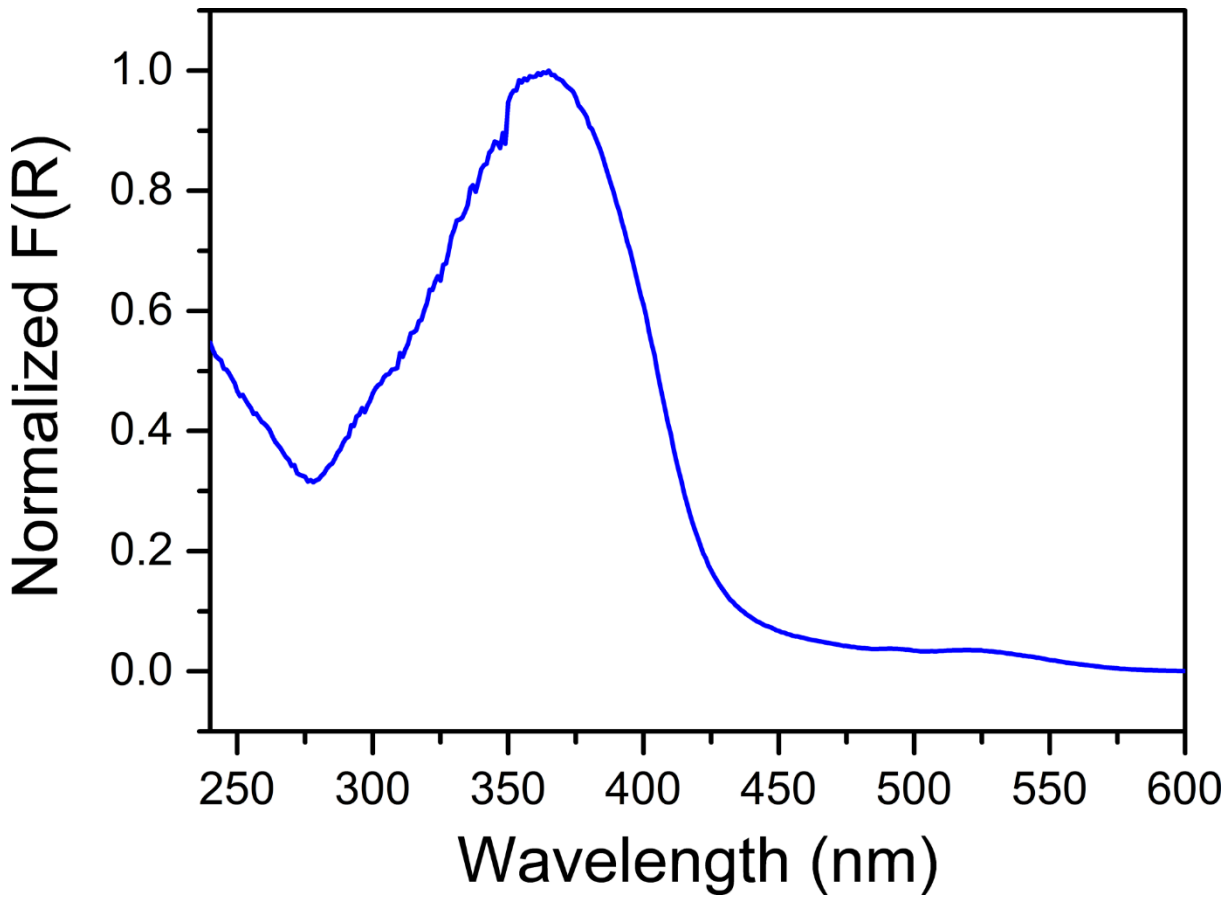

Figure 4.14 Diffuse reflectance UV-Vis spectrum of a polycrystalline sample of **2′-NO_2** diluted with $BaSO_4$ powder at ambient temperature. The spectrum is plotted as normalized Kubelka-Munk transformation F(R).

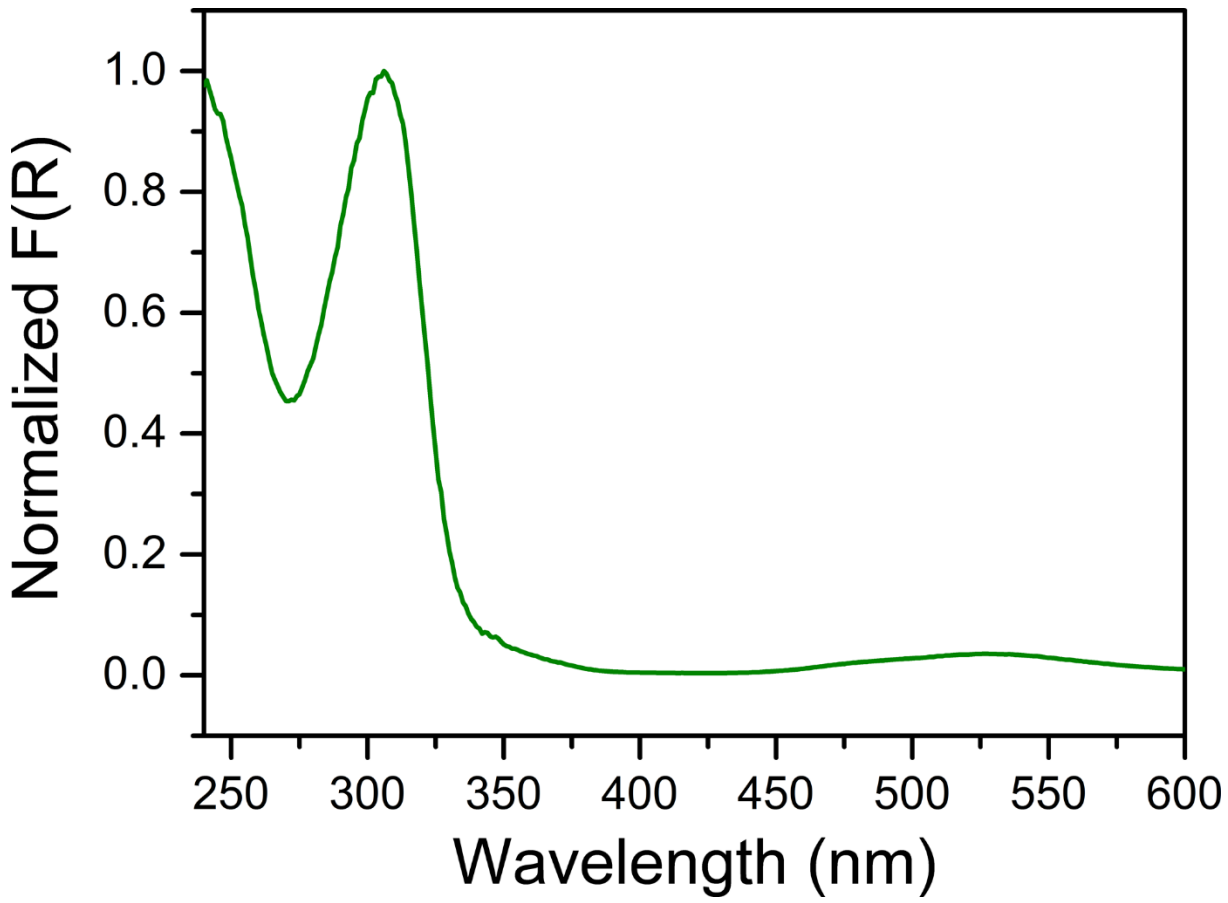

Figure 4.15 Diffuse reflectance UV-Vis spectrum of a polycrystalline sample of **2′-F** diluted with $BaSO_4$ powder at ambient temperature. The spectrum is plotted as normalized Kubelka-Munk transformation F(R).

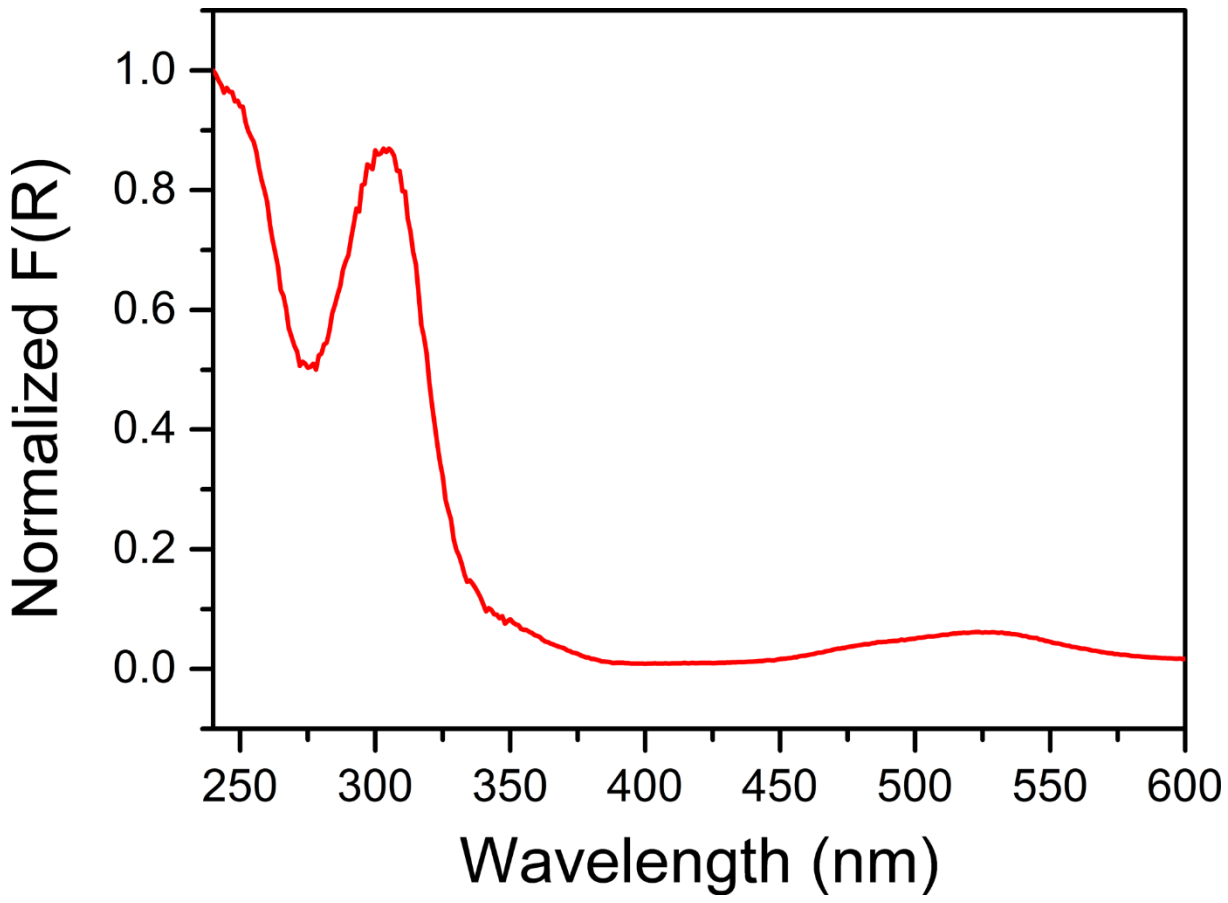

Figure 4.16 Diffuse reflectance UV-Vis spectrum of a polycrystalline sample of **2′-Me** diluted with $BaSO_4$ powder at ambient temperature. The spectrum is plotted as normalized Kubelka-Munk transformation F(R).

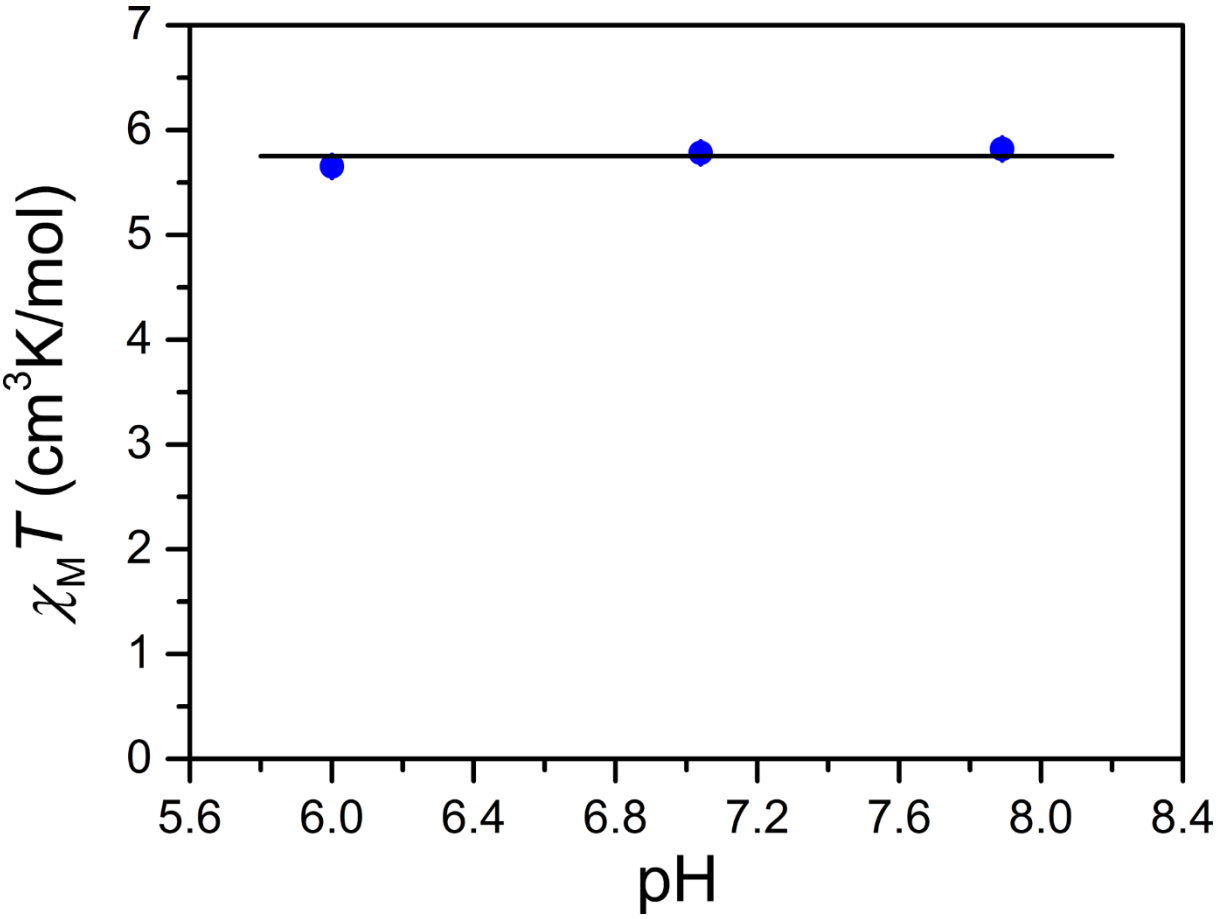

Figure 4.17 Variable-pH dc magnetic susceptibility data for **2-NO₂** in aqueous solutions containing 50 mM HEPES and 100 mM NaCl at 37 °C, obtained using the Evans method[20] (see Equation 4.2). Blue circles represent experimental data and error bars represent standard deviations of three measurements. The solid black line denotes the average value of $\chi_M T$ = 5.75(8) cm^3 K mol^{-1} (see Table 4.3).

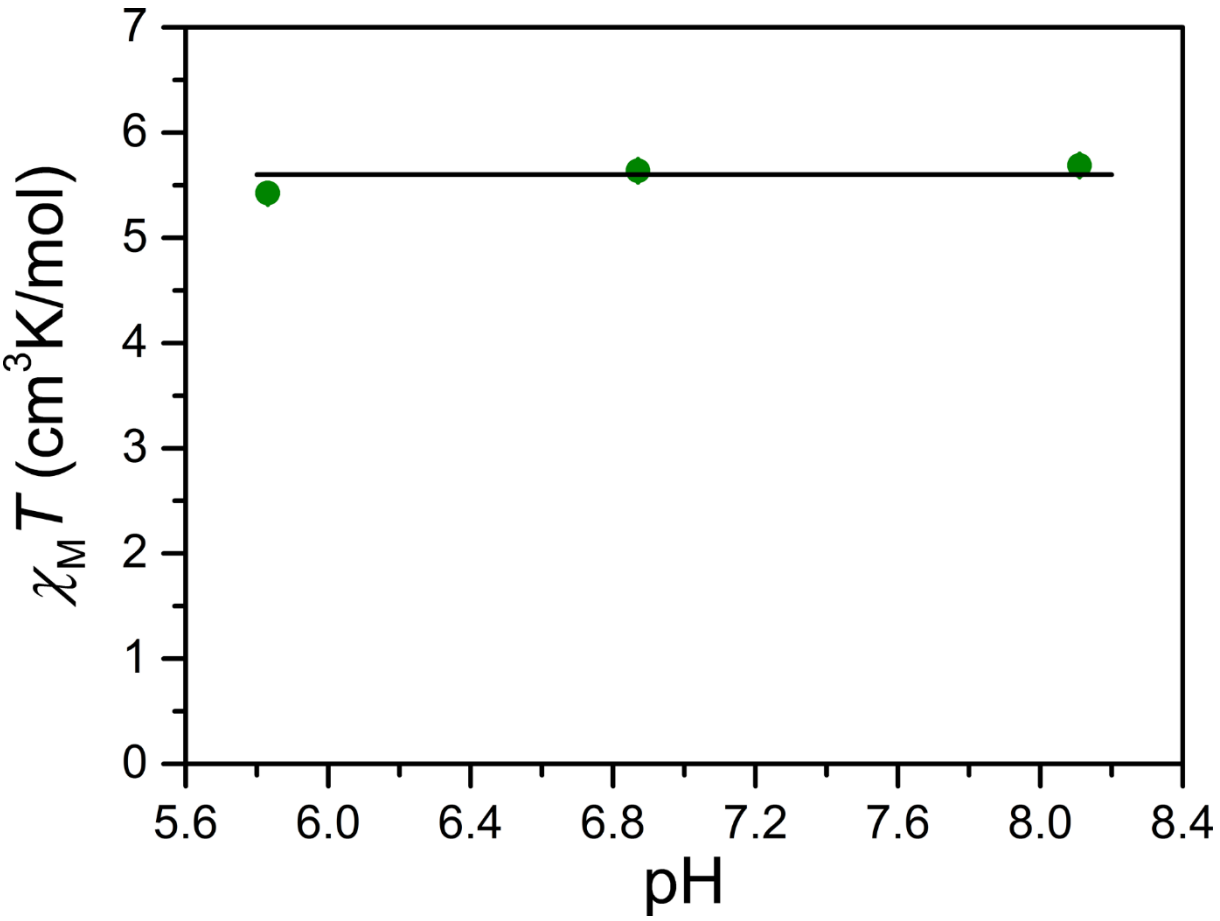

Figure 4.18 Variable-pH dc magnetic susceptibility data for **2-F** in aqueous solutions containing 50 mM HEPES and 100 mM NaCl at 37 °C, obtained using the Evans method[20] (see Equation 4.2). Green circles represent experimental data and error bars represent standard deviations of three measurements. The solid black line denotes the average value of $\chi_M T$ = 5.6(1) cm^3 K mol^{-1} (see Table 4.3).

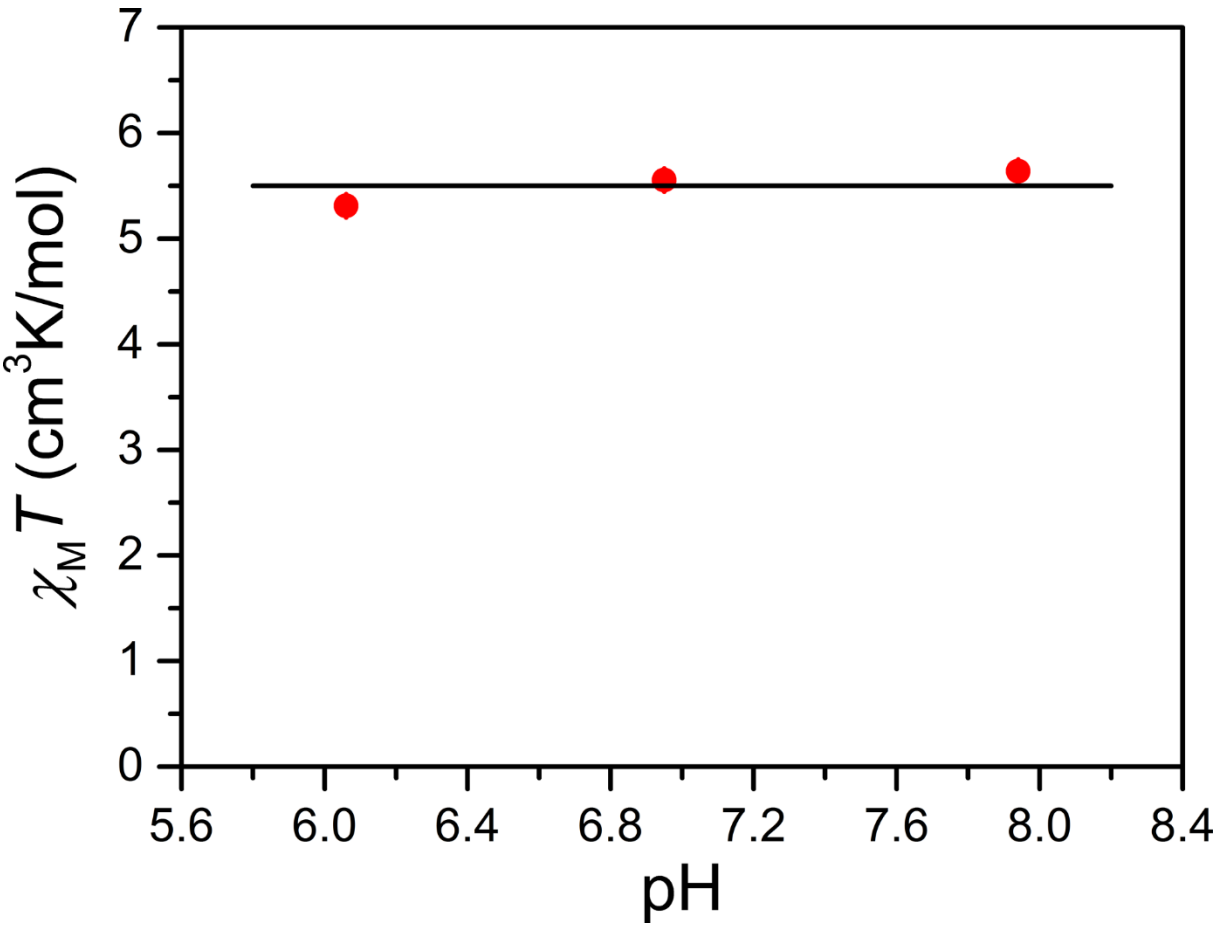

Figure 4.19 Variable-pH dc magnetic susceptibility data for **2-Me** in aqueous solutions containing 50 mM HEPES and 100 mM NaCl at 37 °C, obtained using the Evans method[20] (see Equation 4.2). Red circles represent experimental data and error bars represent standard deviations of three measurements. The solid black line denotes the average value of $\chi_M T$ = 5.5(1) cm^3 K mol^{-1} (see Table 4.3).

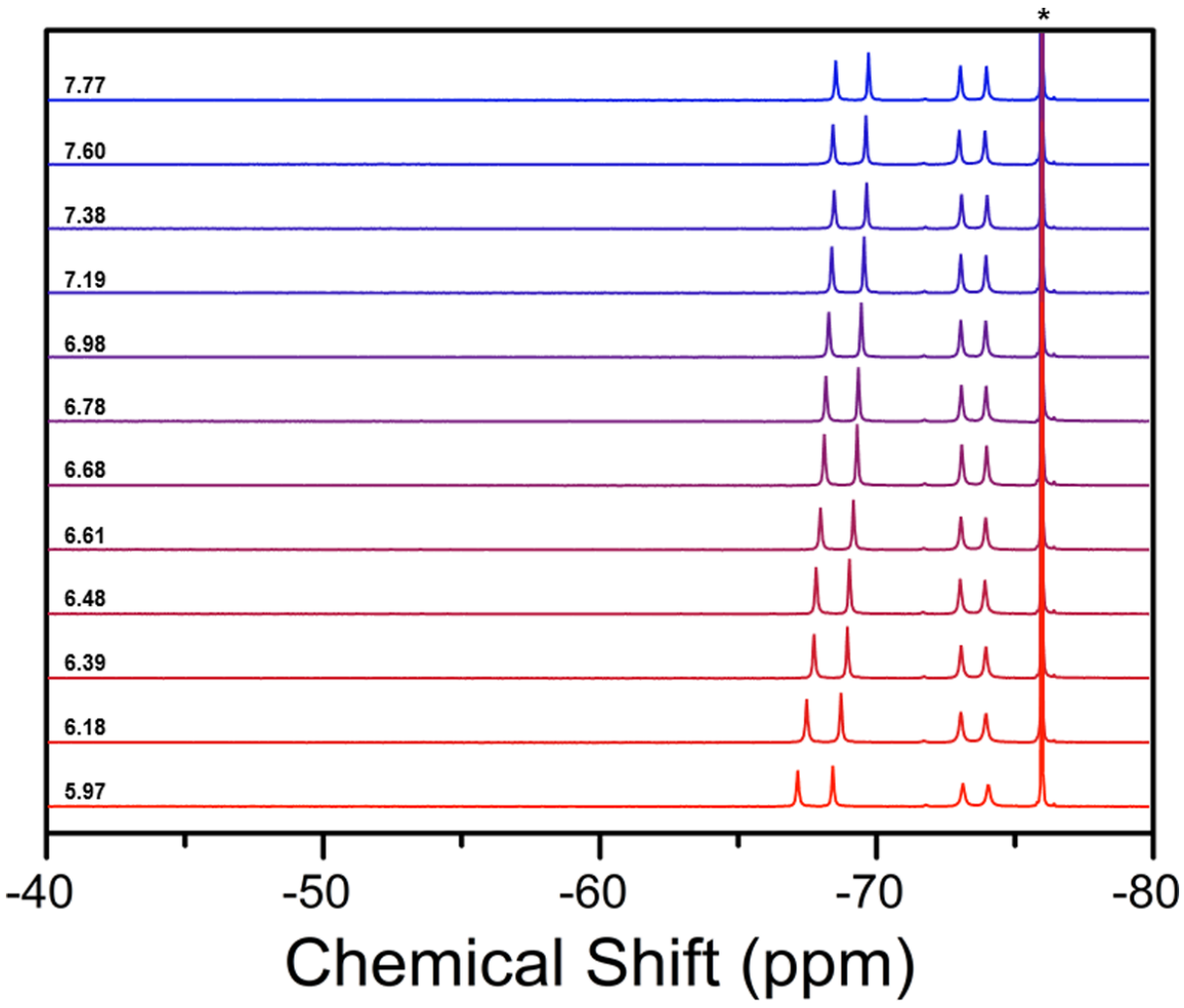

Figure 4.20 Variable-pH ^{19}F NMR spectra for 8 mM of **2-NO$_2$** in aqueous solutions containing 50 mM HEPES and 100 mM NaCl buffered at various pH values at 37 °C. Black numbers on the left denote the pH of the NMR sample solutions measured with a pH electrode. The asterisk denotes the TFA reference signal at –76.00 ppm. Note that the very small peak at ca. −71.8 ppm originates from a miniscule amount of an unreacted ligand impurity.

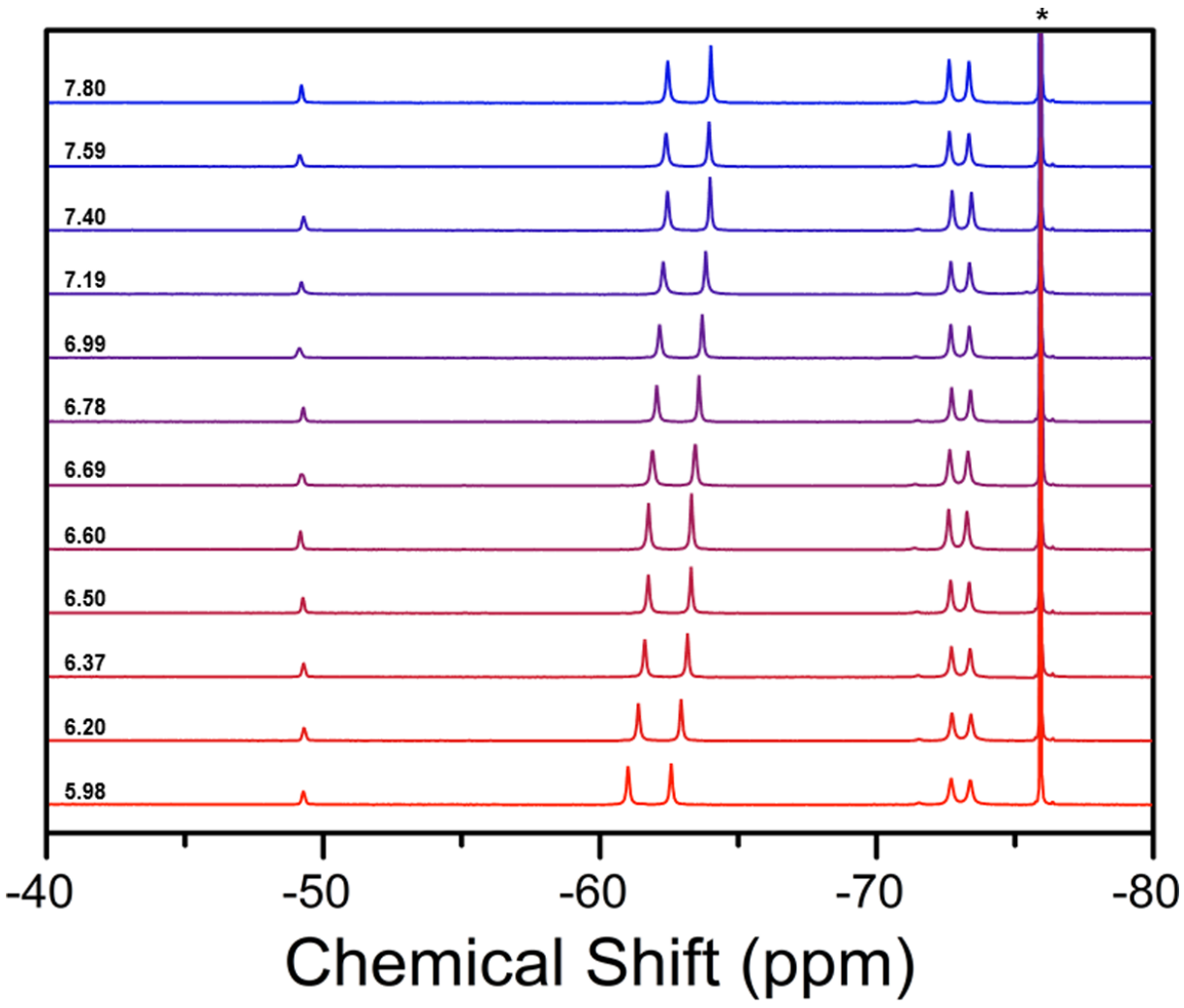

Figure 4.21 Variable-pH ^{19}F NMR spectra for 9 mM of **2-F** in aqueous solutions containing 50 mM HEPES and 100 mM NaCl buffered at various pH values at 37 °C. Black numbers on the left denote the pH of the NMR sample solutions measured with a pH electrode. The asterisk denotes the TFA reference signal at –76.00 ppm. Note that the very small peak at ca. −71.5 ppm originates from a miniscule amount of an unreacted ligand impurity.

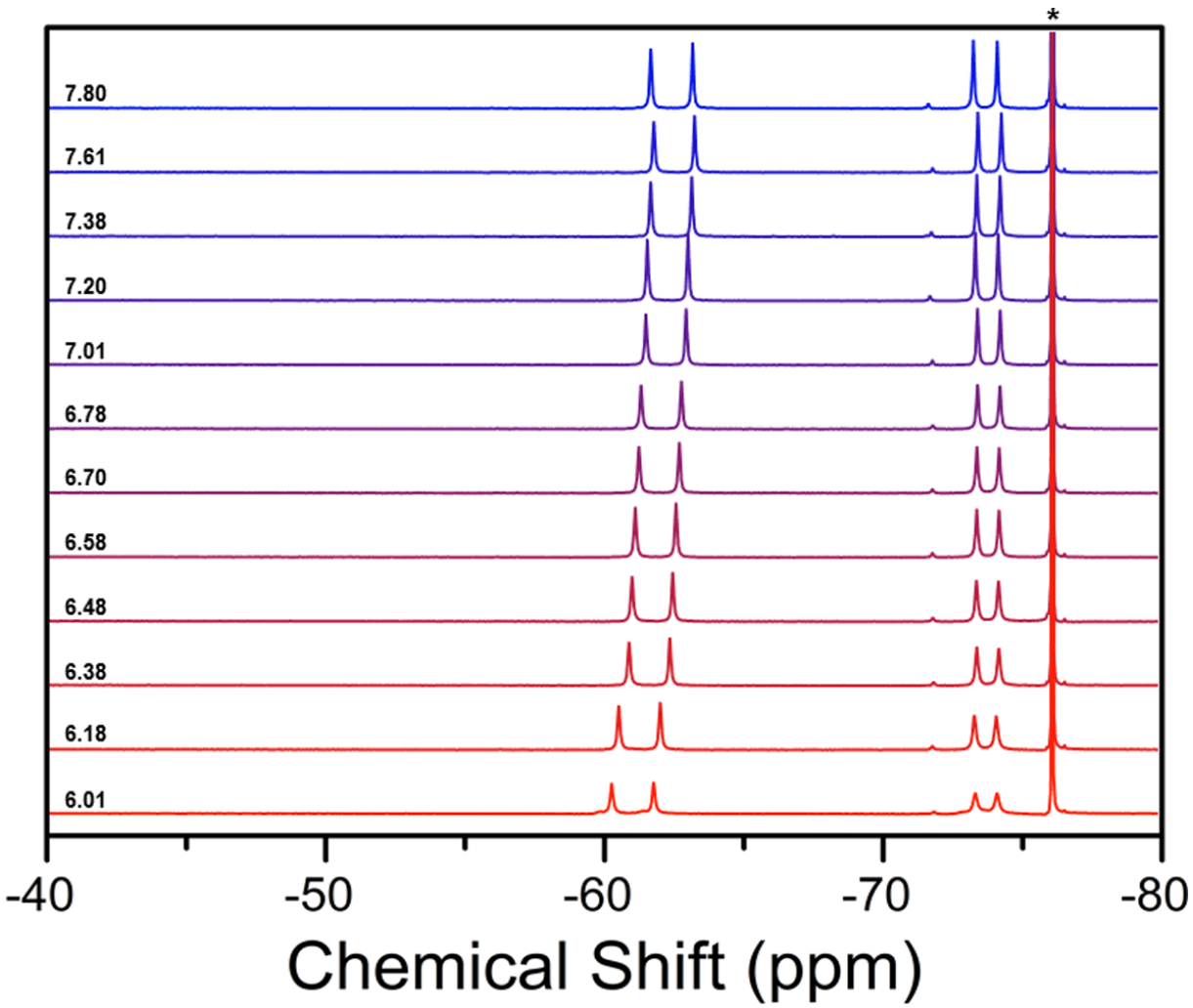

Figure 4.22 Variable-pH ^{19}F NMR spectra for 8 mM of **2-Me** in aqueous solutions containing 50 mM HEPES and 100 mM NaCl buffered at various pH values at 37 °C. Black numbers on the left denote the pH of the NMR sample solutions measured with a pH electrode. The asterisk denotes the TFA reference signal at –76.00 ppm. Note that the very small peak at ca. −71.7 ppm originates from a miniscule amount of an unreacted ligand impurity.

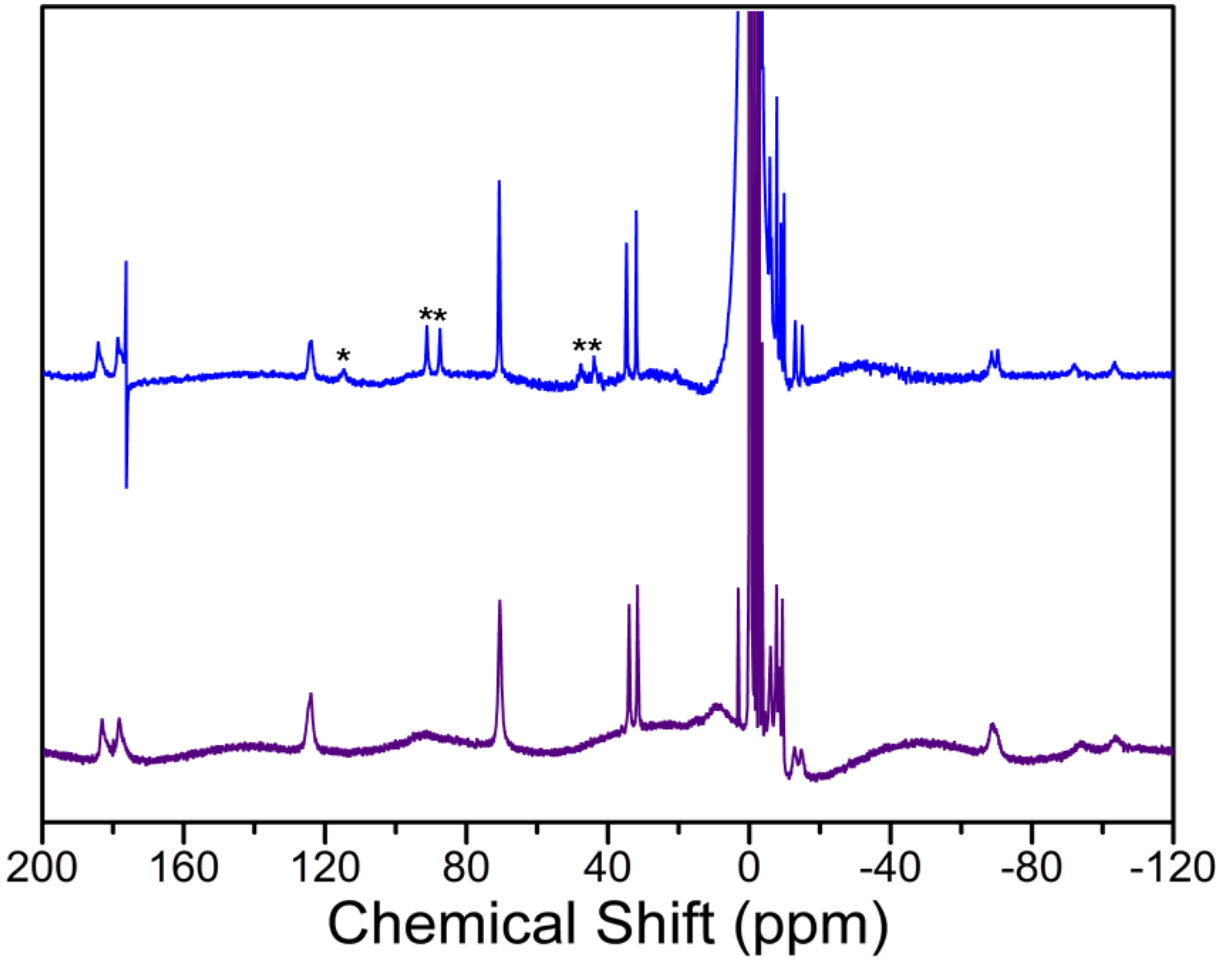

Figure 4.23 Stacked ^{1}H NMR spectra of **2-NO$_2$** in an aqueous solution containing 50 mM HEPES and 100 mM NaCl buffered at pH 6.48 (blue) and in slightly acidic D_2O (purple) at 37 °C. The asterisks denote peaks corresponding to exchangeable carboxamide and hydroxyl protons that are not present in the spectrum recorded in D_2O. The sharp feature at 177 ppm in the spectrum recorded in buffer is an instrument-derived artifact.

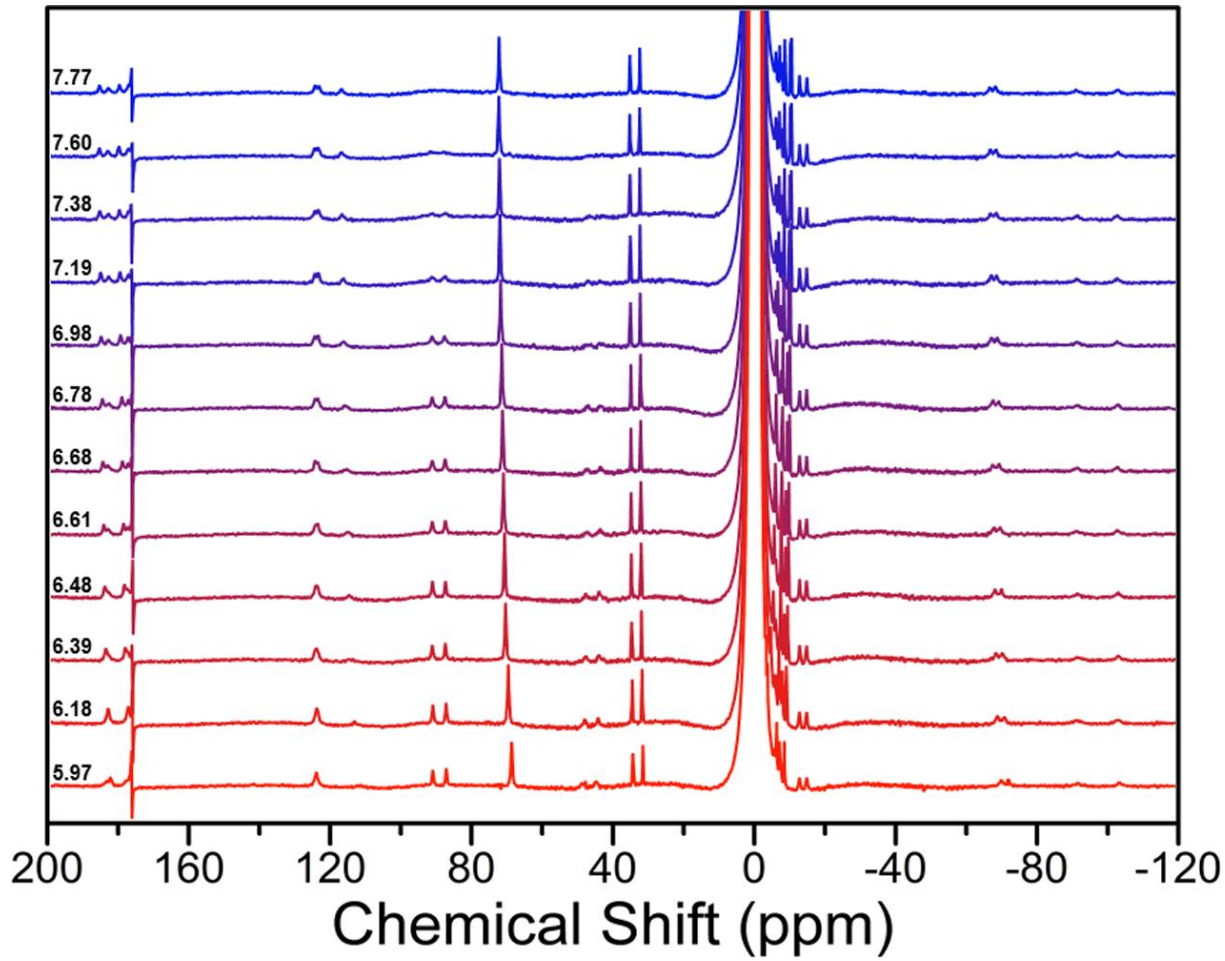

Figure 4.24 Variable-pH ^{1}H NMR spectra for 8 mM of **2-NO$_2$** in aqueous solutions containing 50 mM HEPES and 100 mM NaCl buffered at various pH values at 37 °C. Black numbers on the left denote the pH of the NMR sample solutions measured with a pH electrode. The sharp features at 177 ppm are instrument-derived artifacts.

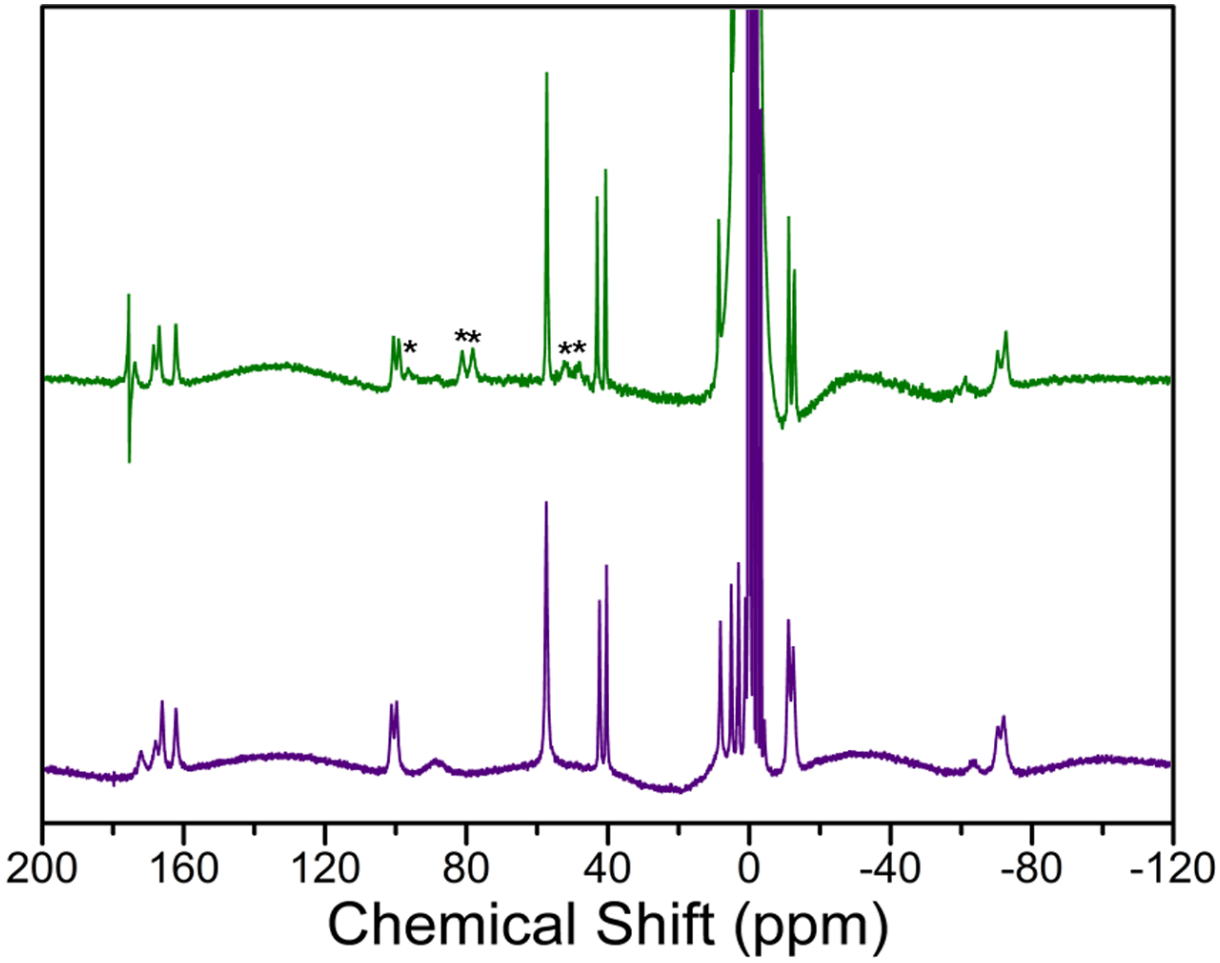

Figure 4.25 Stacked ^{1}H NMR spectra of **2-F** in an aqueous solution containing 50 mM HEPES and 100 mM NaCl buffered at pH 7.19 (green) and in neutral D_2O (purple) at 37 °C. The asterisks denote peaks corresponding to exchangeable carboxamide and hydroxyl protons that are not present in the spectrum recorded in D_2O. The sharp feature at 176 ppm in the spectrum recorded in buffer is an instrument-derived artifact.

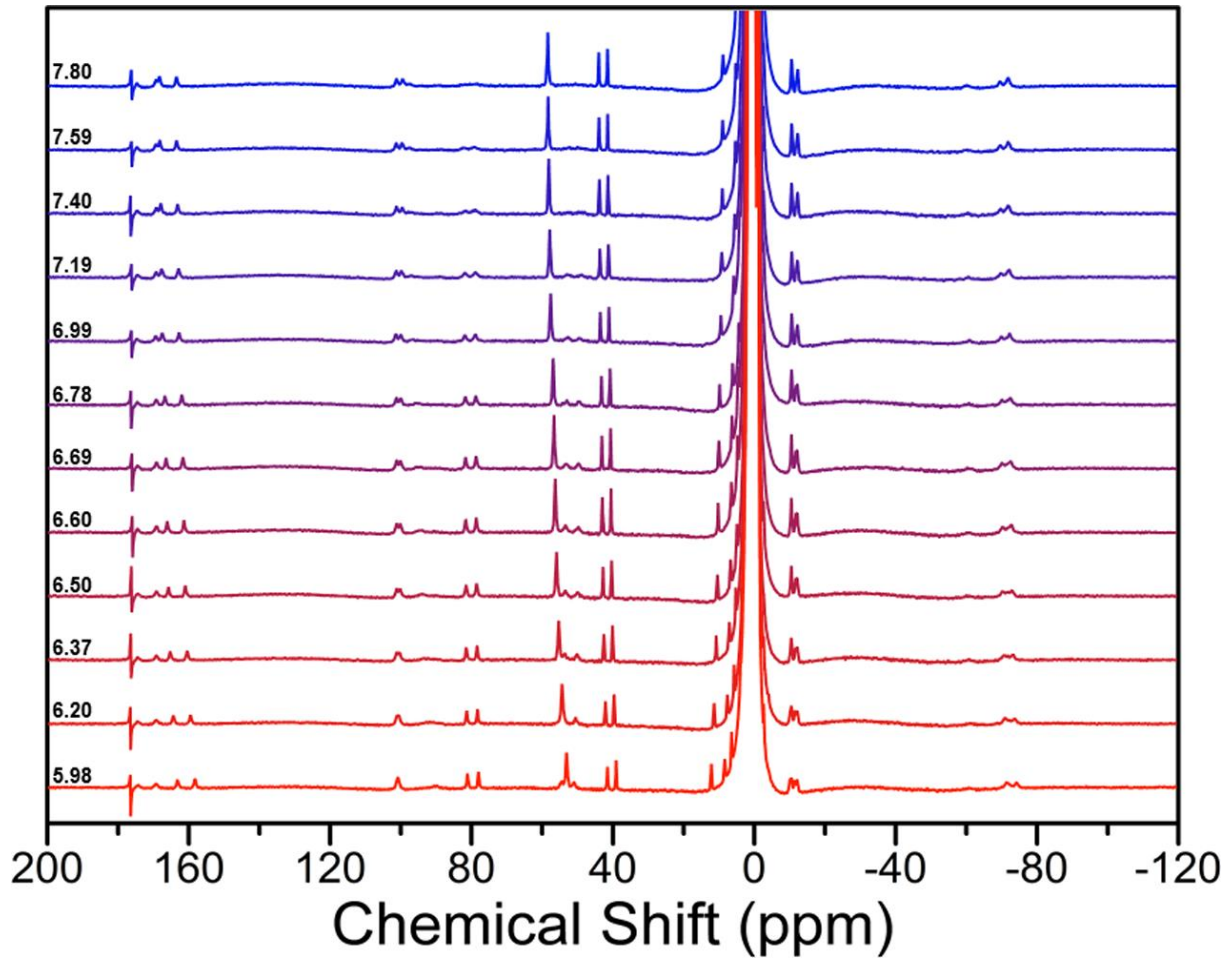

Figure 4.26 Variable-pH ^{1}H NMR spectra for 9 mM of **2-F** in aqueous solutions containing 50 mM HEPES and 100 mM NaCl buffered at various pH values at 37 °C. Black numbers on the left denote the pH of the NMR sample solutions measured with a pH electrode. The sharp features at 176 ppm are instrument-derived artifacts.

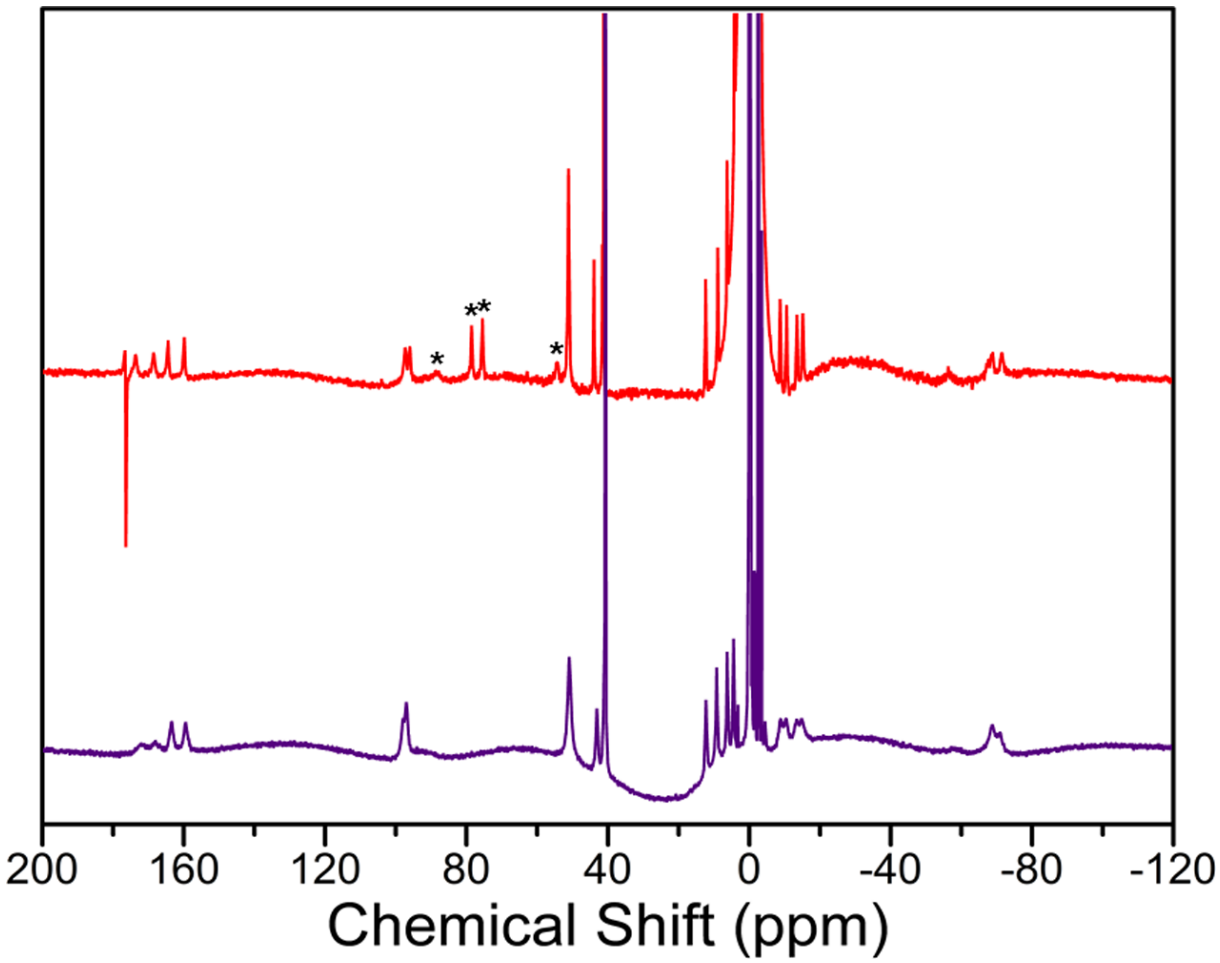

Figure 4.27 Stacked ^{1}H NMR spectra of **2-Me** in an aqueous solution containing 50 mM HEPES and 100 mM NaCl buffered at pH 6.48 (red) and in slightly acidic D_2O (purple) at 37 °C. The asterisks denote peaks corresponding to exchangeable carboxamide and hydroxyl protons that are not present in the spectrum recorded in D_2O. The sharp feature at 177 ppm in the spectrum recorded in buffer is an instrument-derived artifact.

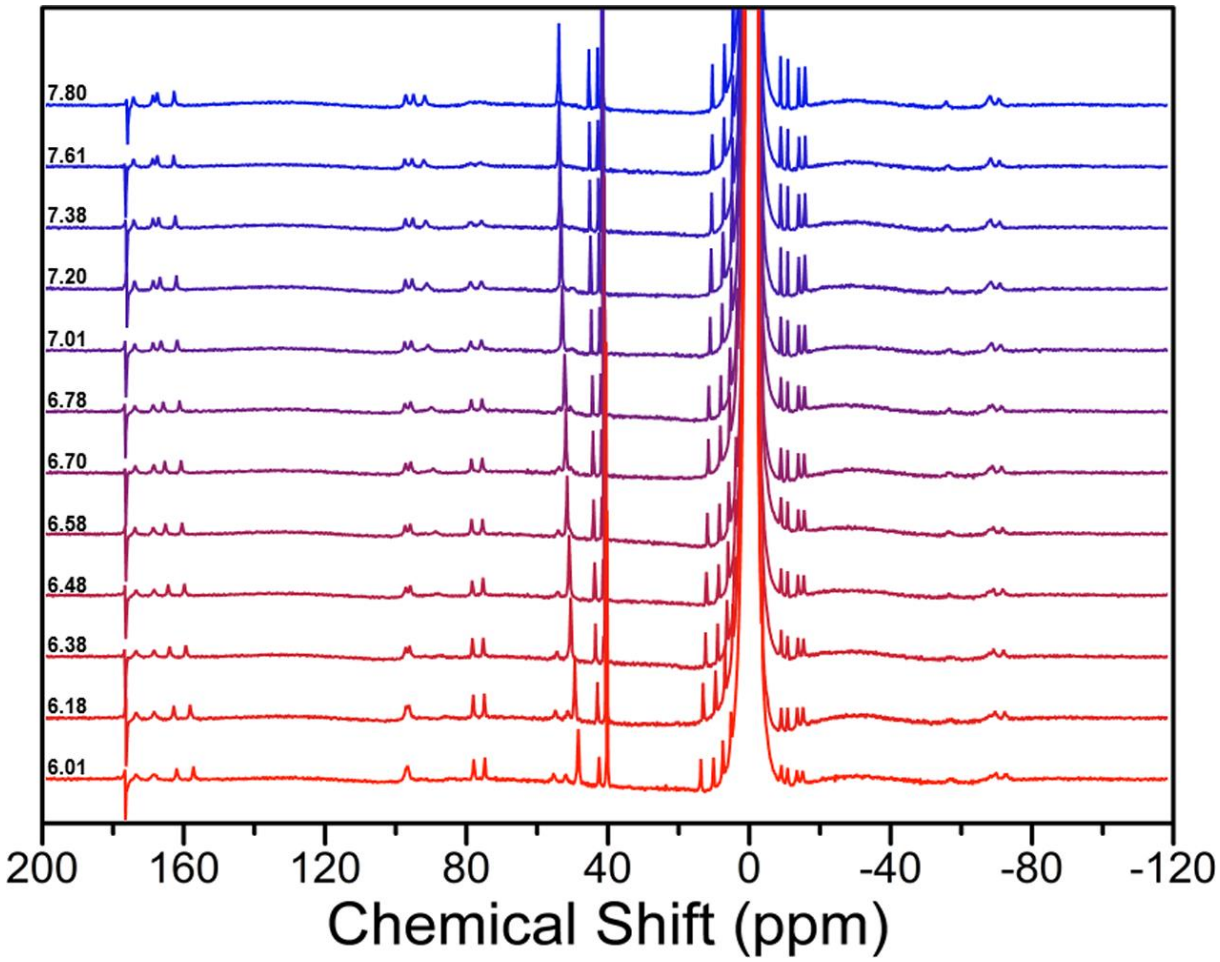

Figure 4.28 Variable-pH ^{1}H NMR spectra for 8 mM of **2-Me** in aqueous solutions containing 50 mM HEPES and 100 mM NaCl buffered at various pH values at 37 °C. Black numbers on the left denote the pH of the NMR sample solutions measured with a pH electrode. The sharp features at 177 ppm are instrument-derived artifacts.

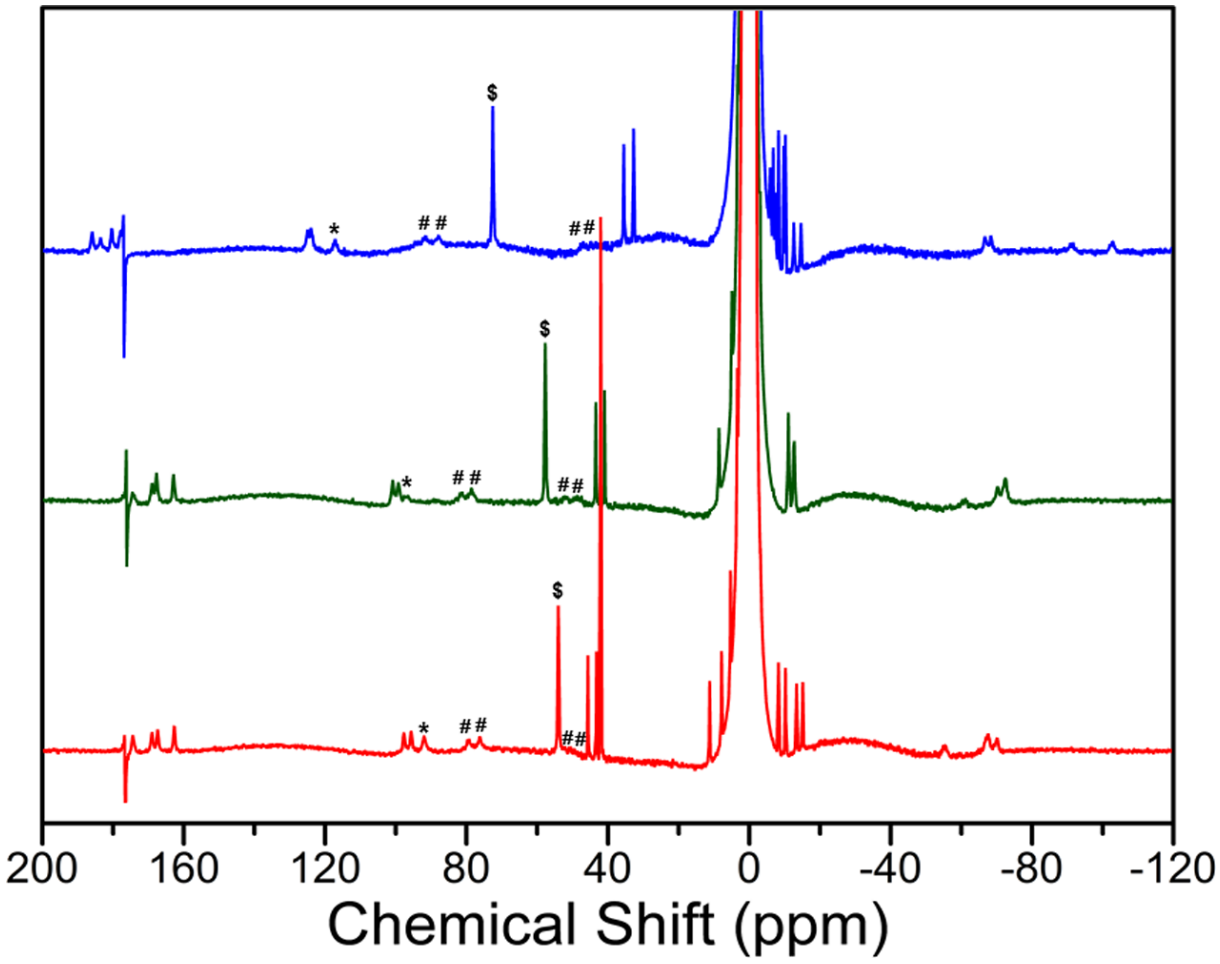

Figure 4.29 Stacked ^{1}H NMR spectra of **2-NO$_2$** (blue), **2-F** (green), and **2-Me** (red) in aqueous solutions containing 50 mM HEPES and 100 mM NaCl buffered at pH 7.38, 7.40, and 7.38, respectively, at 37 °C. The asterisks (*) denote resonances corresponding to the hydroxyl proton on etidronate. The peaks labelled with a number sign (#) correspond to carboxamide protons on the dinucleating ligand. The dollar signs ($) denote resonances corresponding to the methyl protons on etidronate. The sharp features at 177 ppm are instrument-derived artifacts.

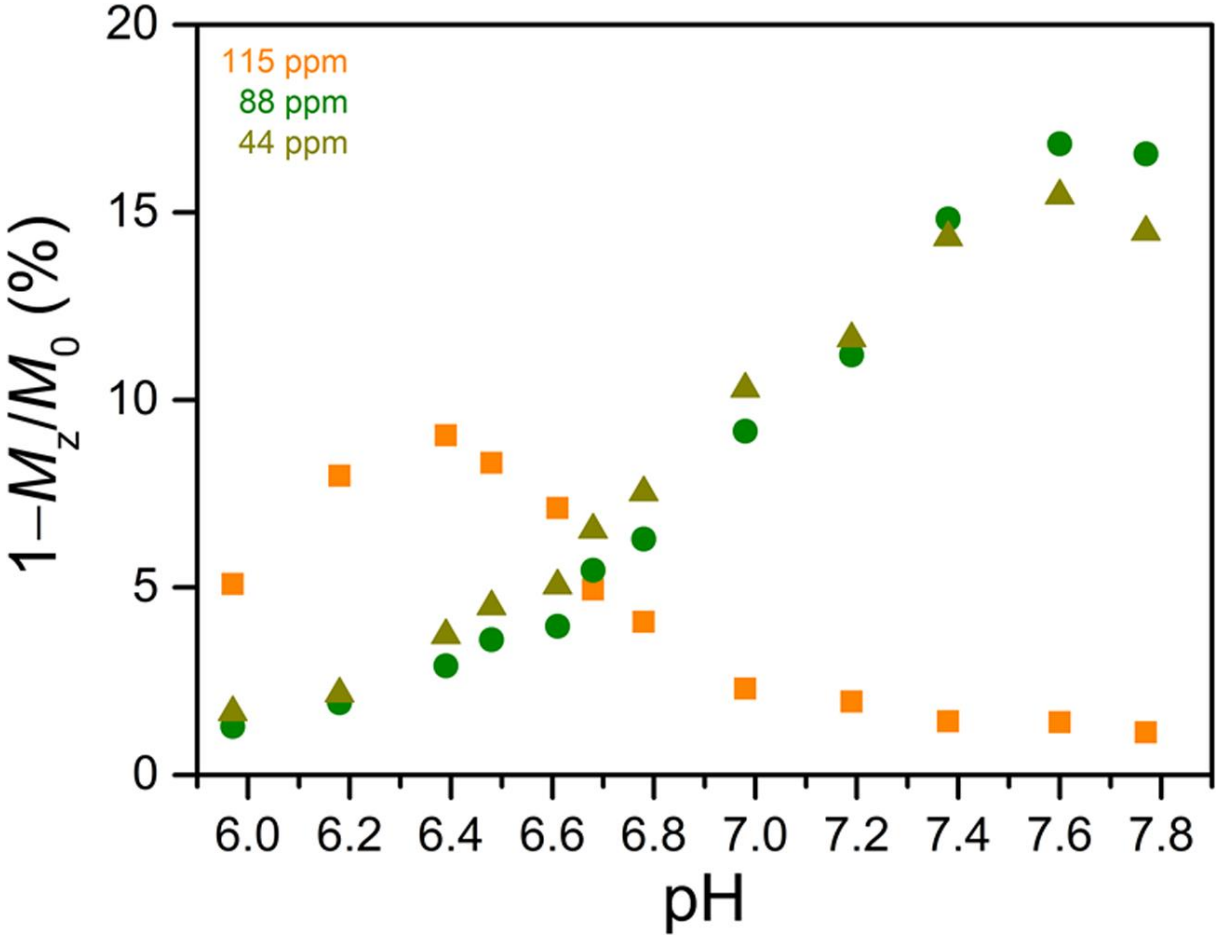

Figure 4.30 pH dependences of the CEST effects from application of presaturation at 115 ppm (yellow), 88 ppm (green), and 44 ppm (dark yellow) for 8 mM of **2-NO_2** in aqueous solutions containing 50 mM HEPES and 100 mM NaCl at 37 °C.

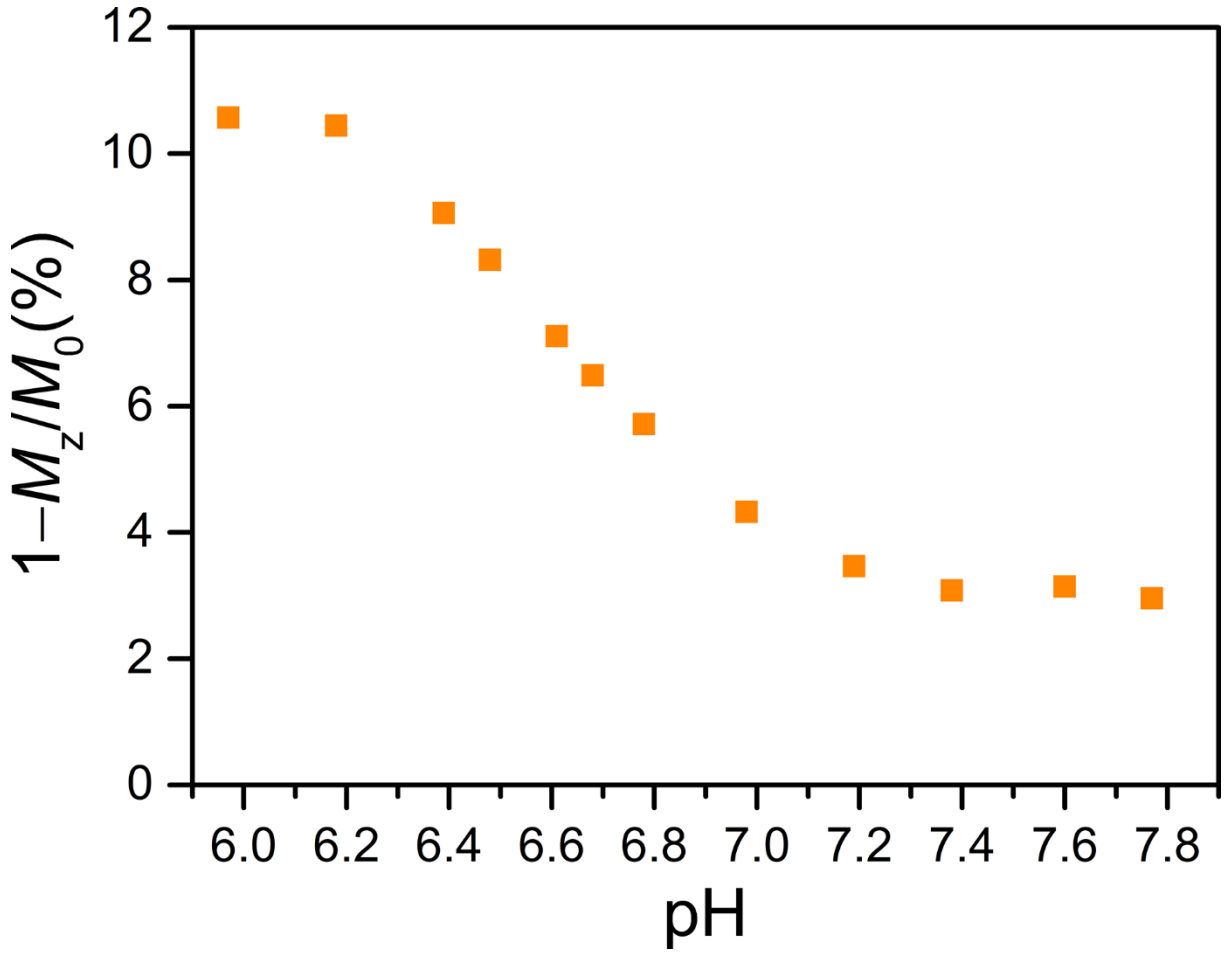

Figure 4.31 pH dependence of the CEST effect from application of presaturation at 112–117 ppm for 8 mM of **2-NO$_2$** in aqueous solutions containing 50 mM HEPES and 100 mM NaCl at 37 °C. For each pH value, presaturation at the frequency offset corresponding to maximum reduction in the H_2O signal intensity was employed (see Table 4.4).

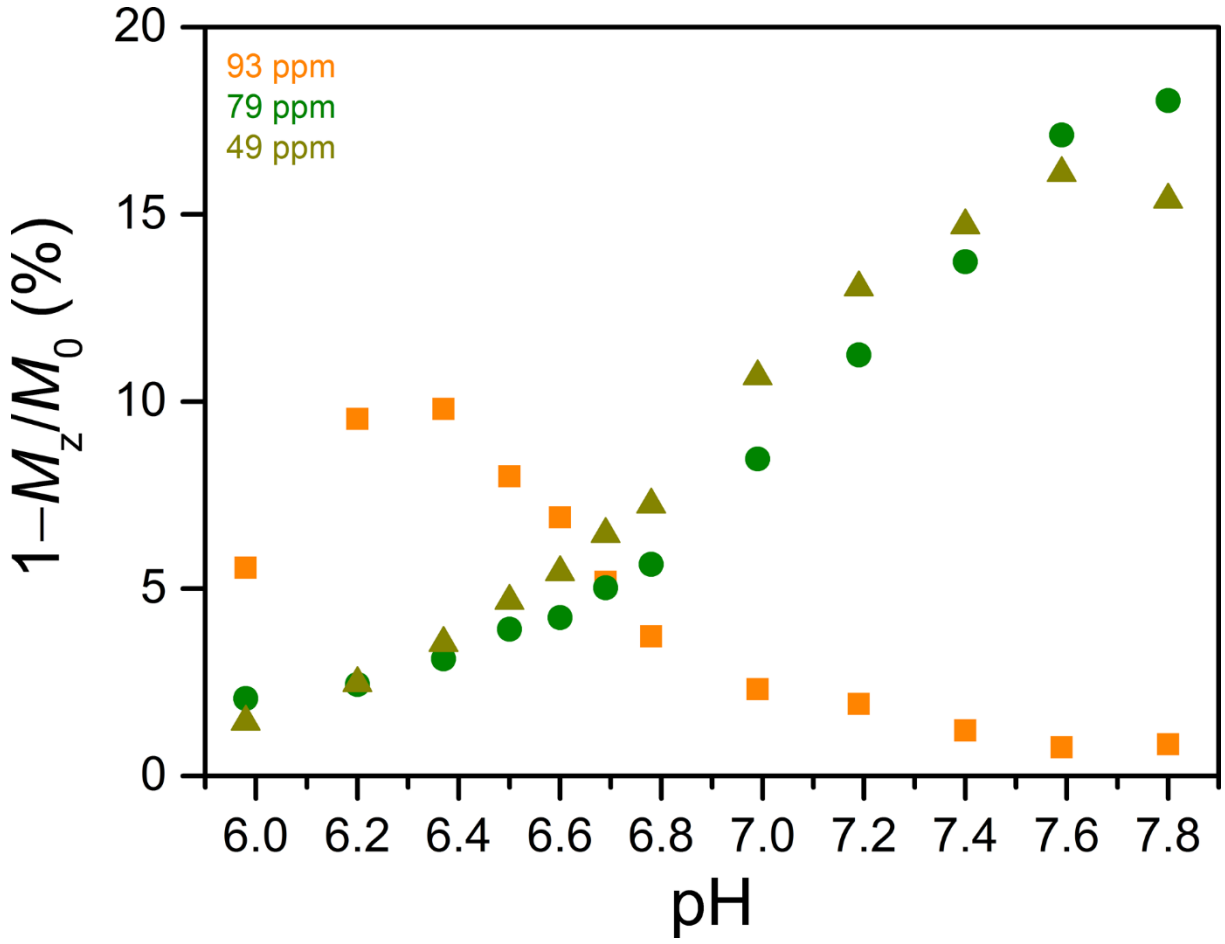

Figure 4.32 pH dependences of the CEST effects from application of presaturation at 93 ppm (yellow), 79 ppm (green), and 49 ppm (dark yellow) for 9 mM of **2-F** in aqueous solutions containing 50 mM HEPES and 100 mM NaCl at 37 °C.

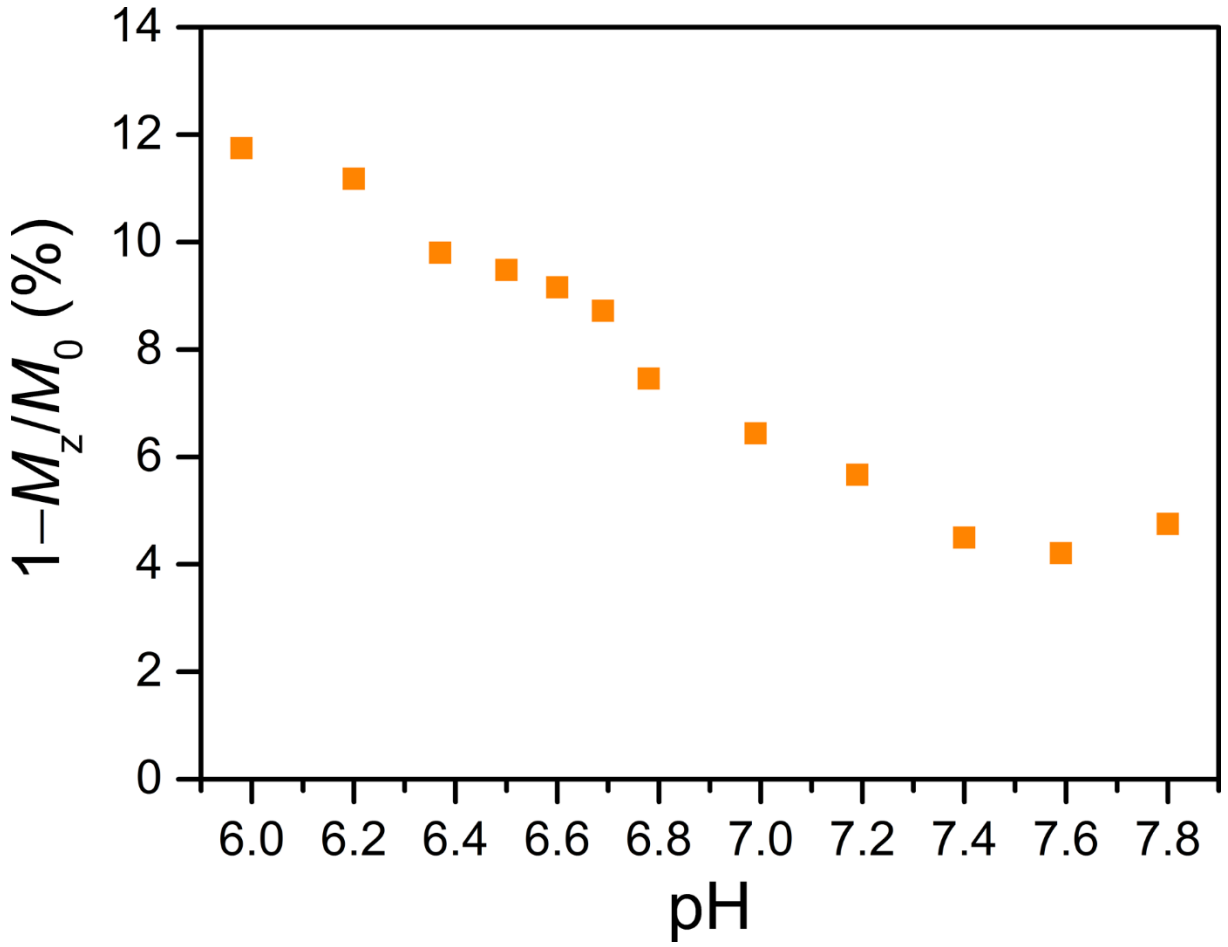

Figure 4.33 pH dependence of the CEST effect from application of presaturation at 90–97 ppm for 9 mM of **2-F** in aqueous solutions containing 50 mM HEPES and 100 mM NaCl at 37 °C. For each pH value, presaturation at the frequency offset corresponding to maximum reduction in the H_2O signal intensity was employed (see Table 4.5).

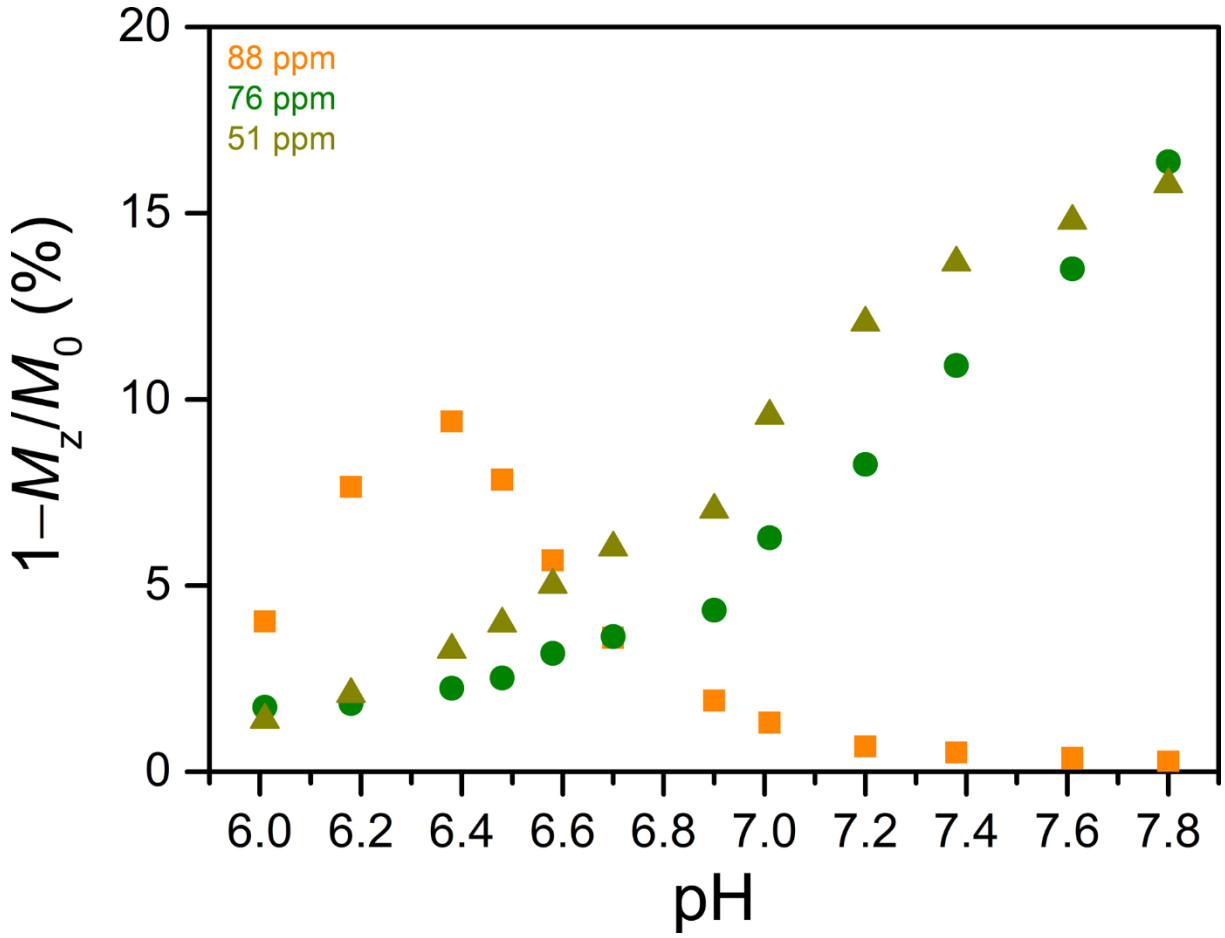

Figure 4.34 pH dependences of the CEST effects from application of presaturation at 88 ppm (yellow), 76 ppm (green), and 51 ppm (dark yellow) for 8 mM of **2-Me** in aqueous solutions containing 50 mM HEPES and 100 mM NaCl at 37 °C.

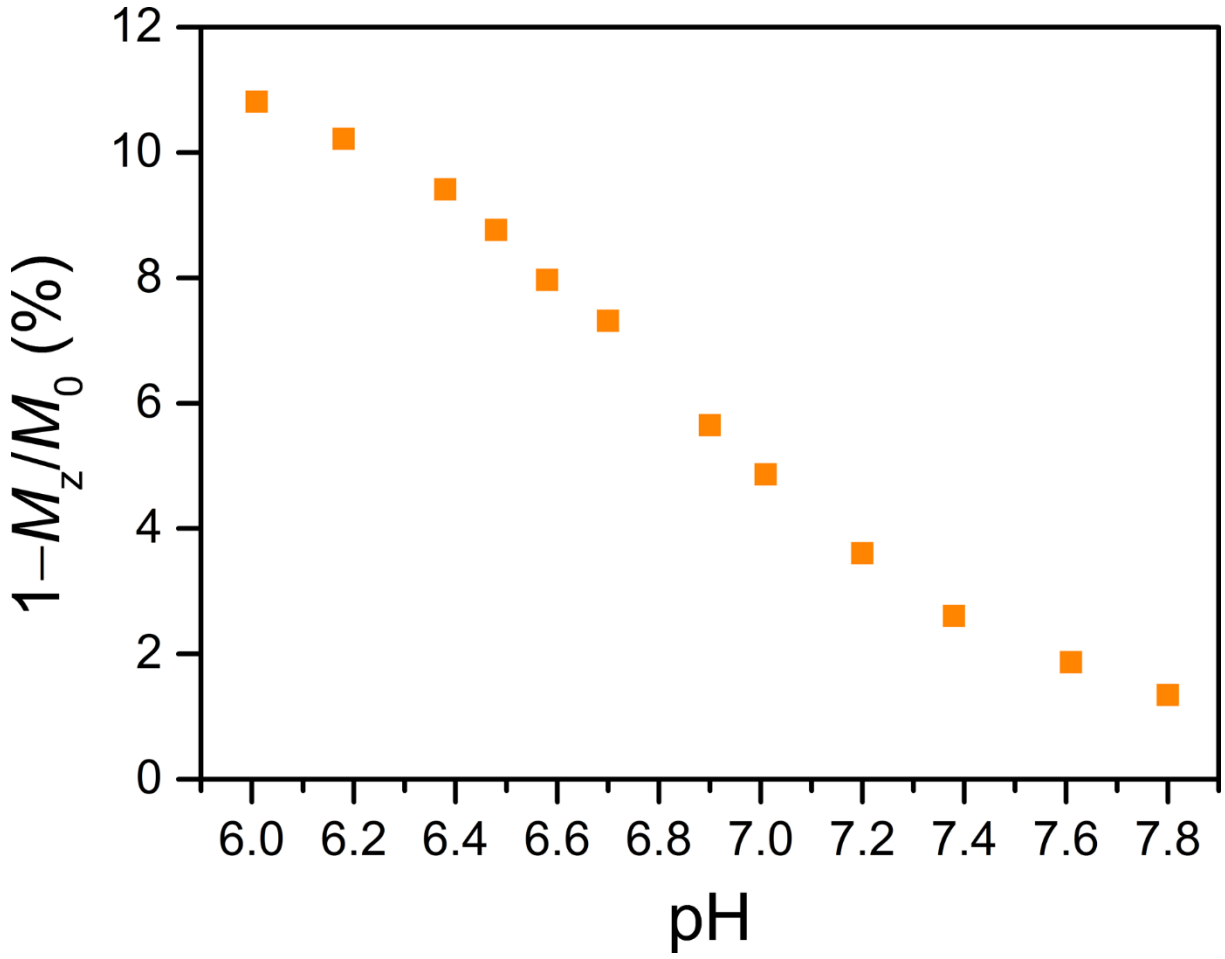

Figure 4.35 pH dependence of the CEST effect from application of presaturation at 85–92 ppm for 8 mM of **2-Me** in aqueous solutions containing 50 mM HEPES and 100 mM NaCl at 37 °C. For each pH value, presaturation at the frequency offset corresponding to maximum reduction in the H_2O signal intensity was employed (see Table 4.6).

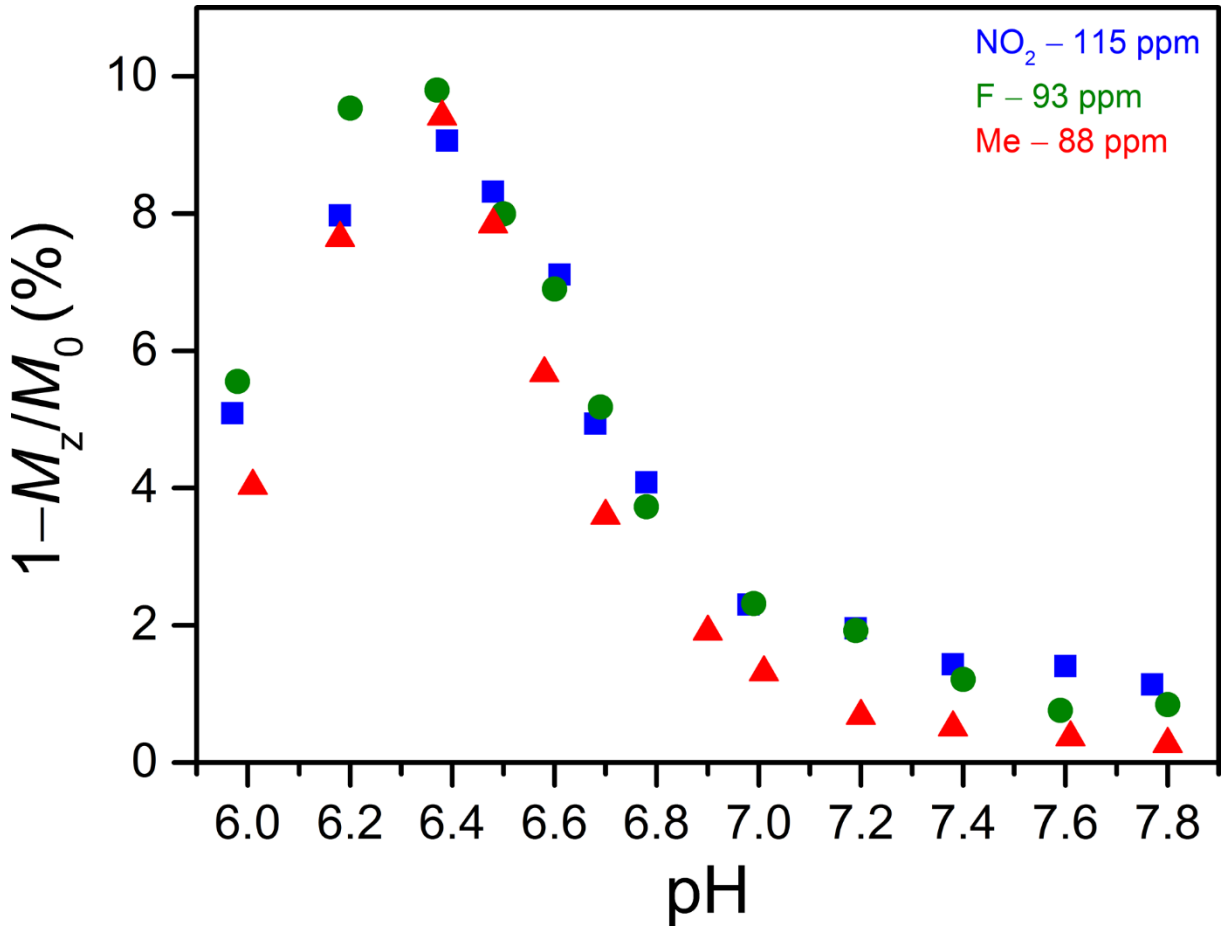

Figure 4.36 Comparison of the pH dependence of the OH CEST effect for 8 mM of **2-NO₂** (blue), 9 mM of **2-F** (green), and 8 mM of **2-Me** (red) in aqueous solutions containing 50 mM HEPES and 100 mM NaCl at 37 °C. The presaturation frequency employed for each compound is denoted in the legend.

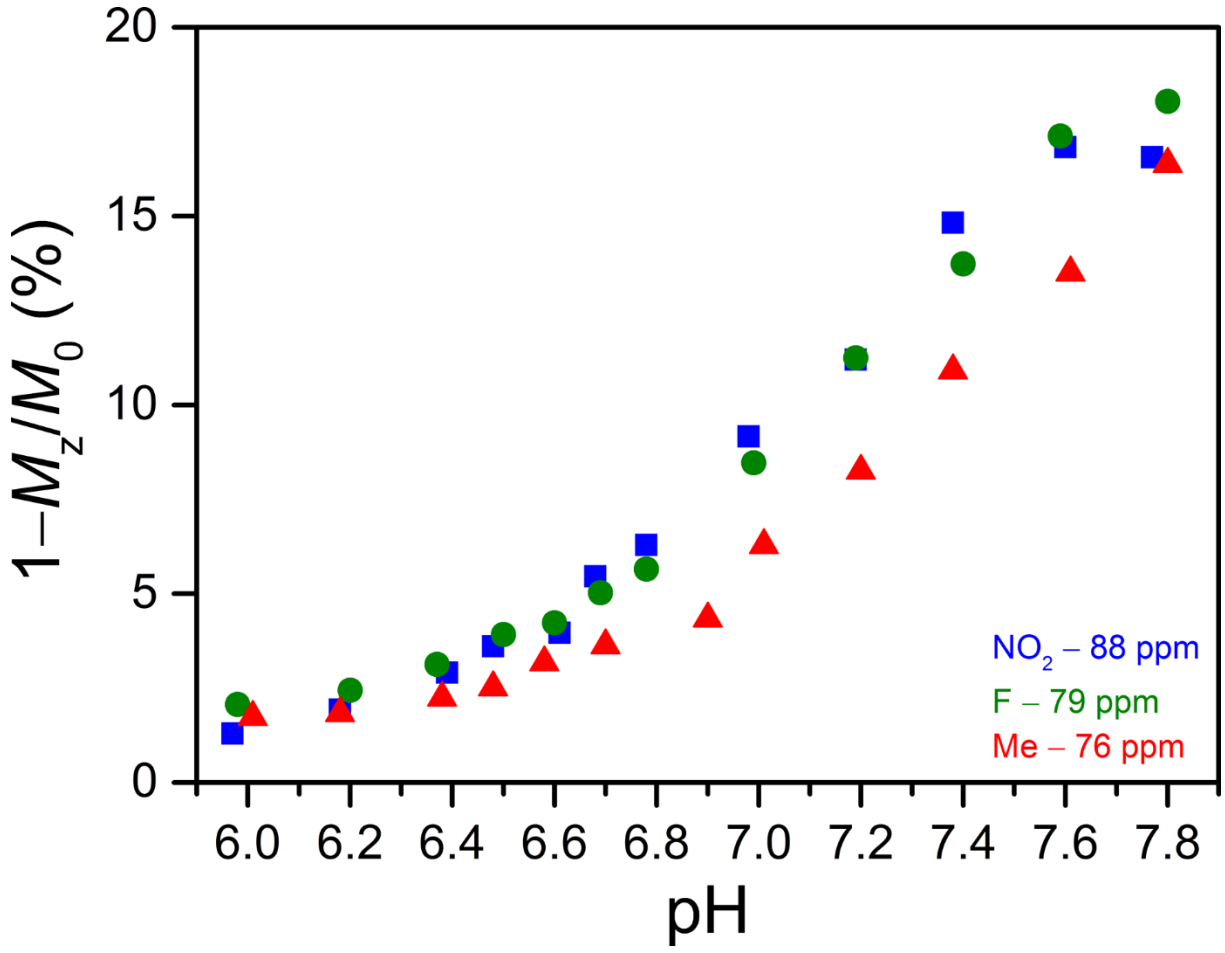

Figure 4.37 Comparison of the pH dependence of NH CEST effect for 8 mM of **2-NO₂** (blue), 9 mM of **2-F** (green), and 8 mM of **2-Me** (red) in aqueous solutions containing 50 mM HEPES and 100 mM NaCl at 37 °C. The presaturation frequency employed for each compound is denoted in the legend.

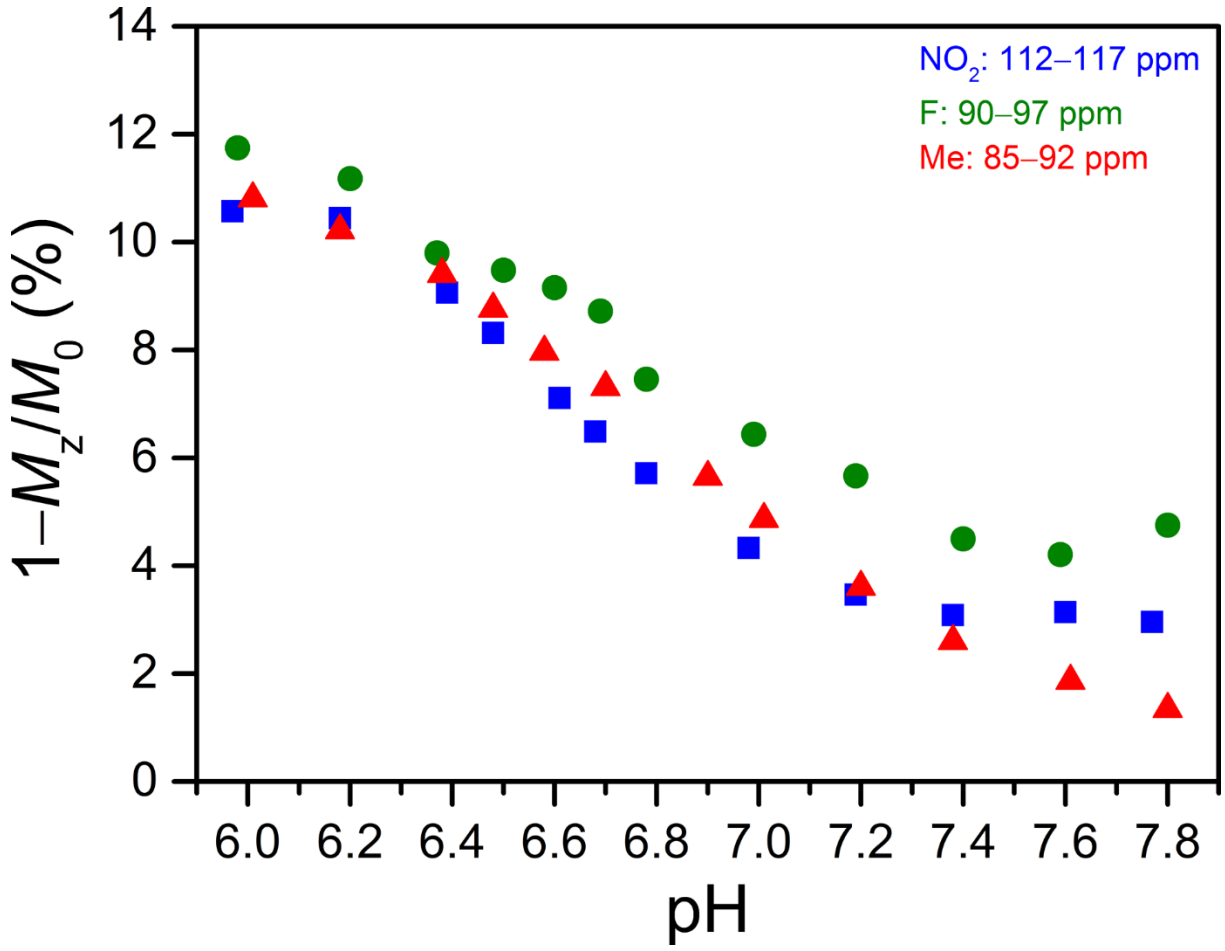

Figure 4.38 Comparison of the pH dependence of the maximum OH CEST effect for 8 mM of **2-NO$_2$** (blue), 9 mM of **2-F** (green), and 8 mM of **2-Me** (red) in aqueous solutions containing 50 mM HEPES and 100 mM NaCl at 37 °C. For each pH value, presaturation at the frequency offset corresponding to maximum reduction in the H_2O signal intensity was employed (see Tables 4.4–4.6). The range of presaturation frequencies employed for each compound is denoted in the legend.

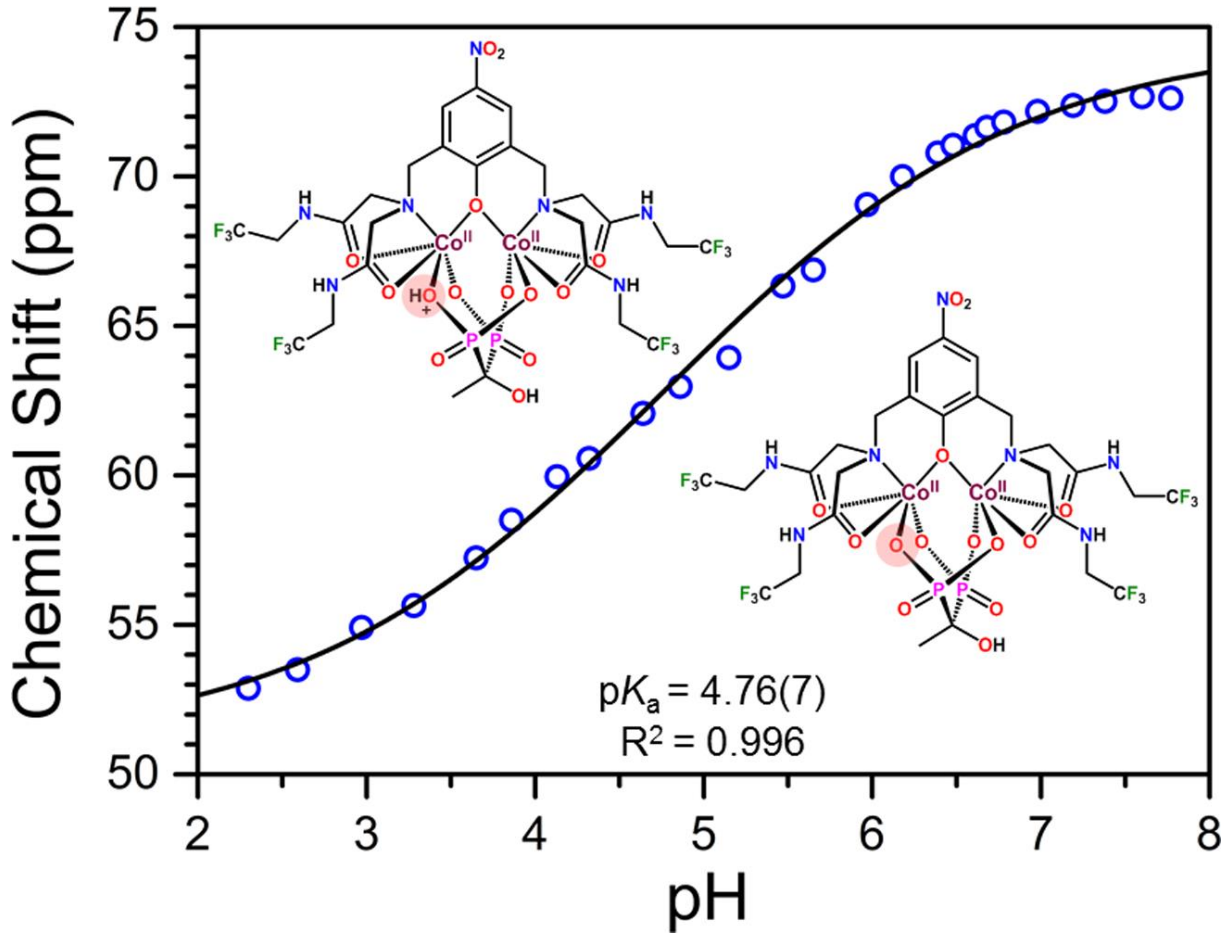

Figure 4.39 pH dependence of the ^{1}H NMR chemical shift (reported as frequency offset) of the Me resonance from etidronate for **2-NO$_2$** in aqueous solutions containing 50 mM HEPES and 100 mM NaCl at 37 °C. Blue circles represent experimental data and the solid black line corresponds to a sigmoidal fit to the data (see Equation 4.1), giving pK_a = 4.76(7) with R^2 = 0.996. The ionization process taking place on etidronate is highlighted with the schematics of the complex.

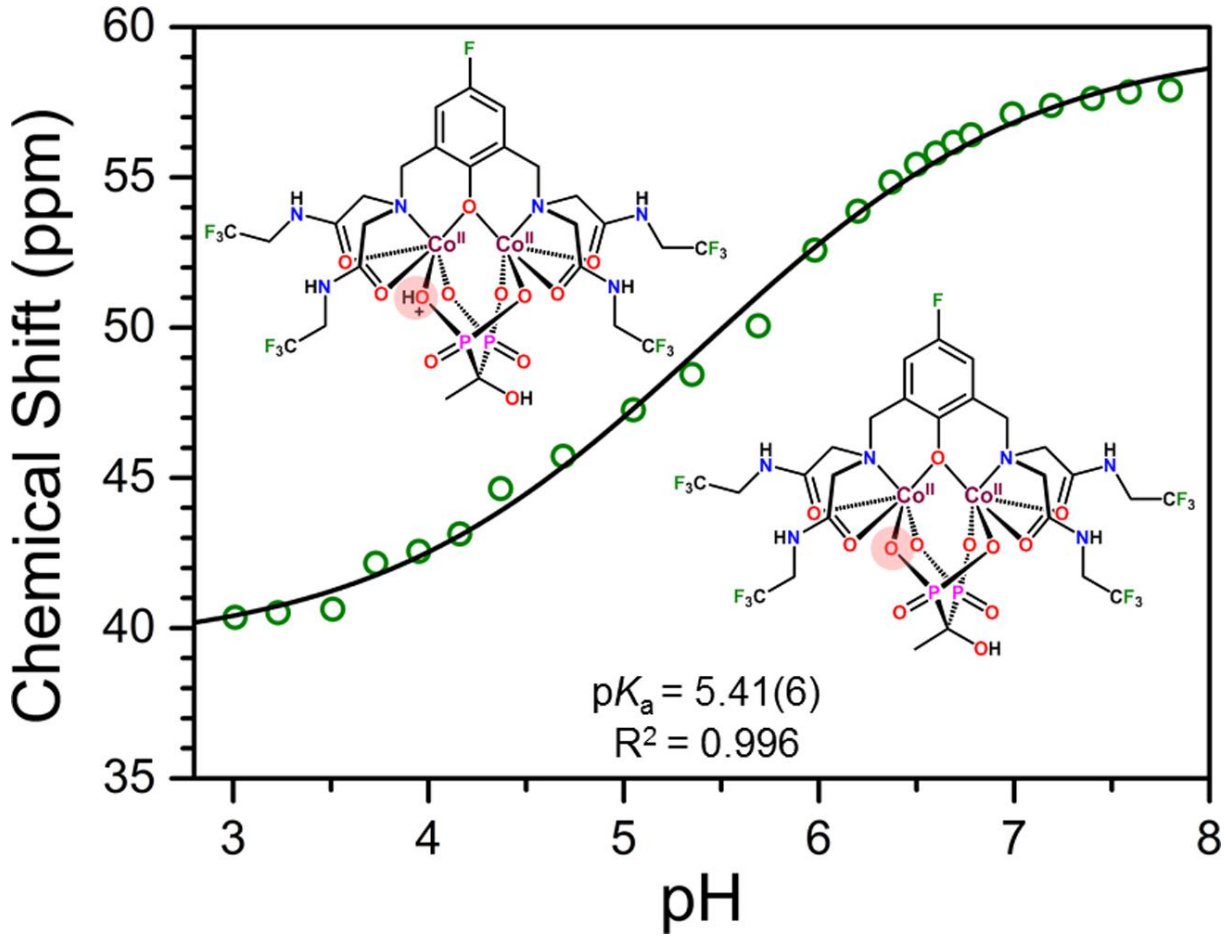

Figure 4.40 pH dependence of the ^{1}H NMR chemical shift (reported as frequency offset) of the Me resonance from etidronate for **2-F** in aqueous solutions containing 50 mM HEPES and 100 mM NaCl at 37 °C. Green circles represent experimental data and the solid black line corresponds to a sigmoidal fit to the data (see Equation 4.1), giving pK_a = 5.41(6) with R^2 = 0.996. The ionization process taking place on etidronate is highlighted with the schematics of the complex.

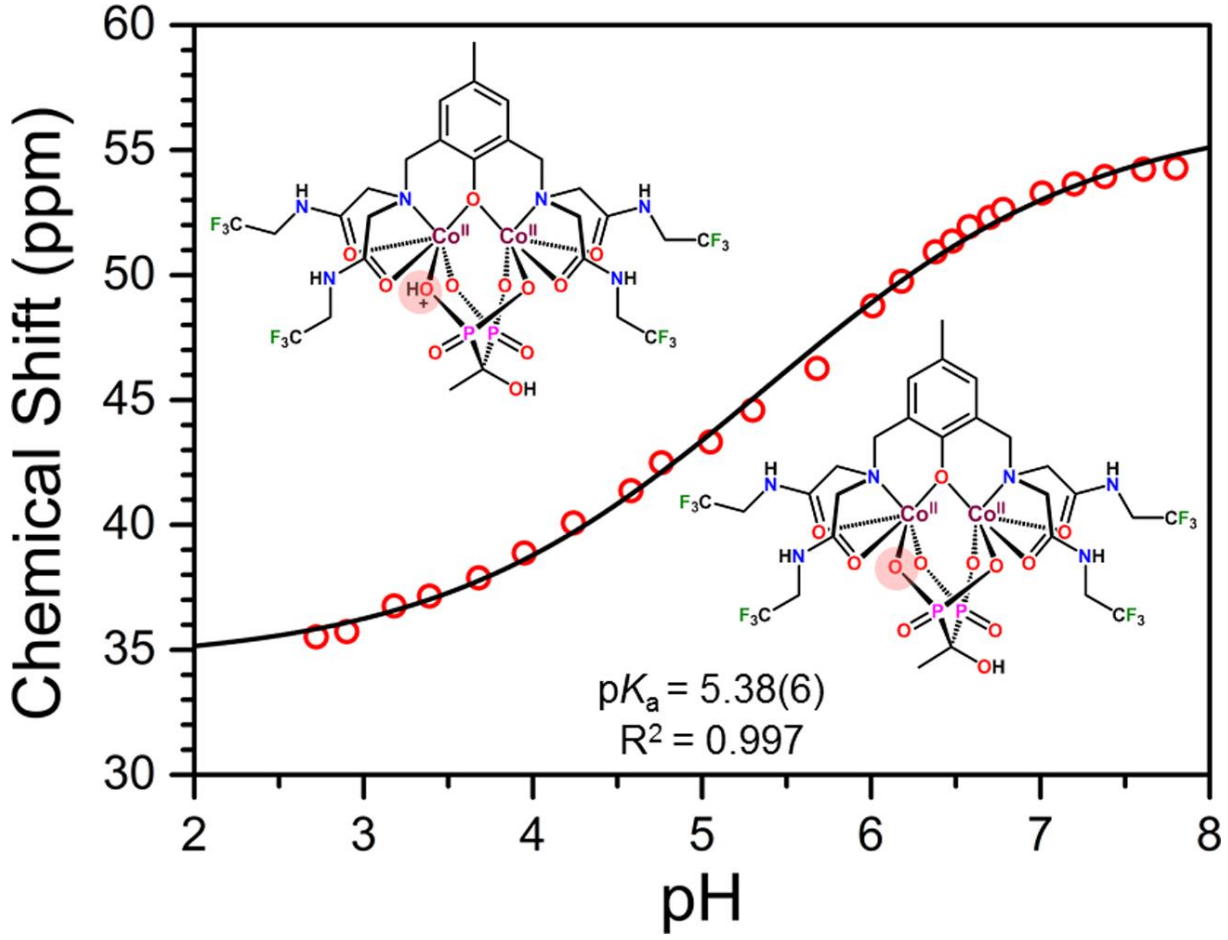

Figure 4.41 pH dependence of the ^{1}H NMR chemical shift (reported as frequency offset) of the Me resonance from etidronate for **2-Me** in aqueous solutions containing 50 mM HEPES and 100 mM NaCl at 37 °C. Red circles represent experimental data and the solid black line corresponds to a sigmoidal fit to the data (see Equation 4.1), giving pK_a = 5.38(6) with R^2 = 0.997. The ionization process taking place on etidronate is highlighted with the schematics of the complex.

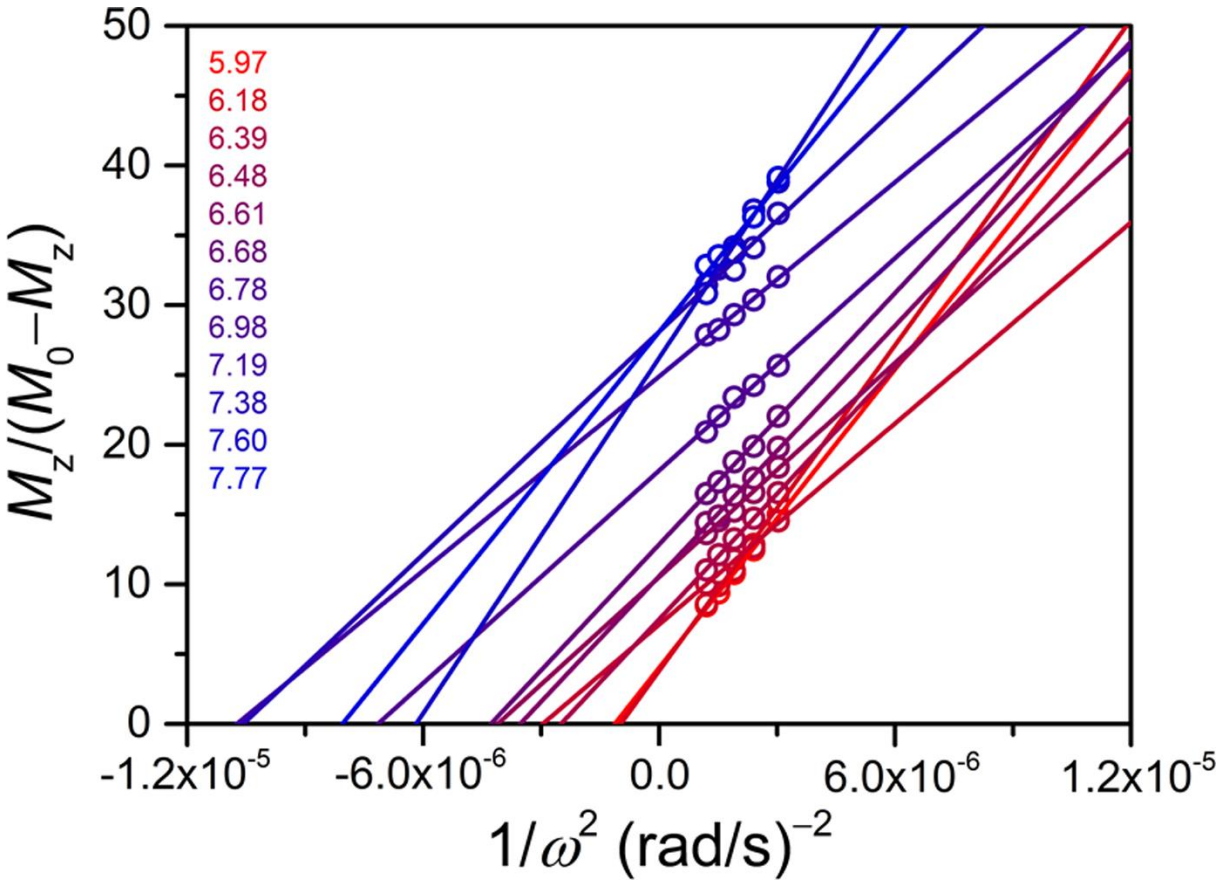

Figure 4.42 Omega plots of the CEST effect from application of presaturation at 112–117 ppm (OH peak) for 8 mM of **2-NO$_2$** in aqueous solutions containing 50 mM HEPES and 100 mM NaCl buffered at pH 5.97–7.77 (red to blue) at 37 °C. Colored numbers in the legend denote the pH of the solutions measured with a pH electrode and the corresponding color of each sample. Presaturation at the frequency offset corresponding to maximum reduction in the H_2O signal intensity was monitored for each pH value (see Table 4.4). Circles represent experimental data and lines represent the linear fits.

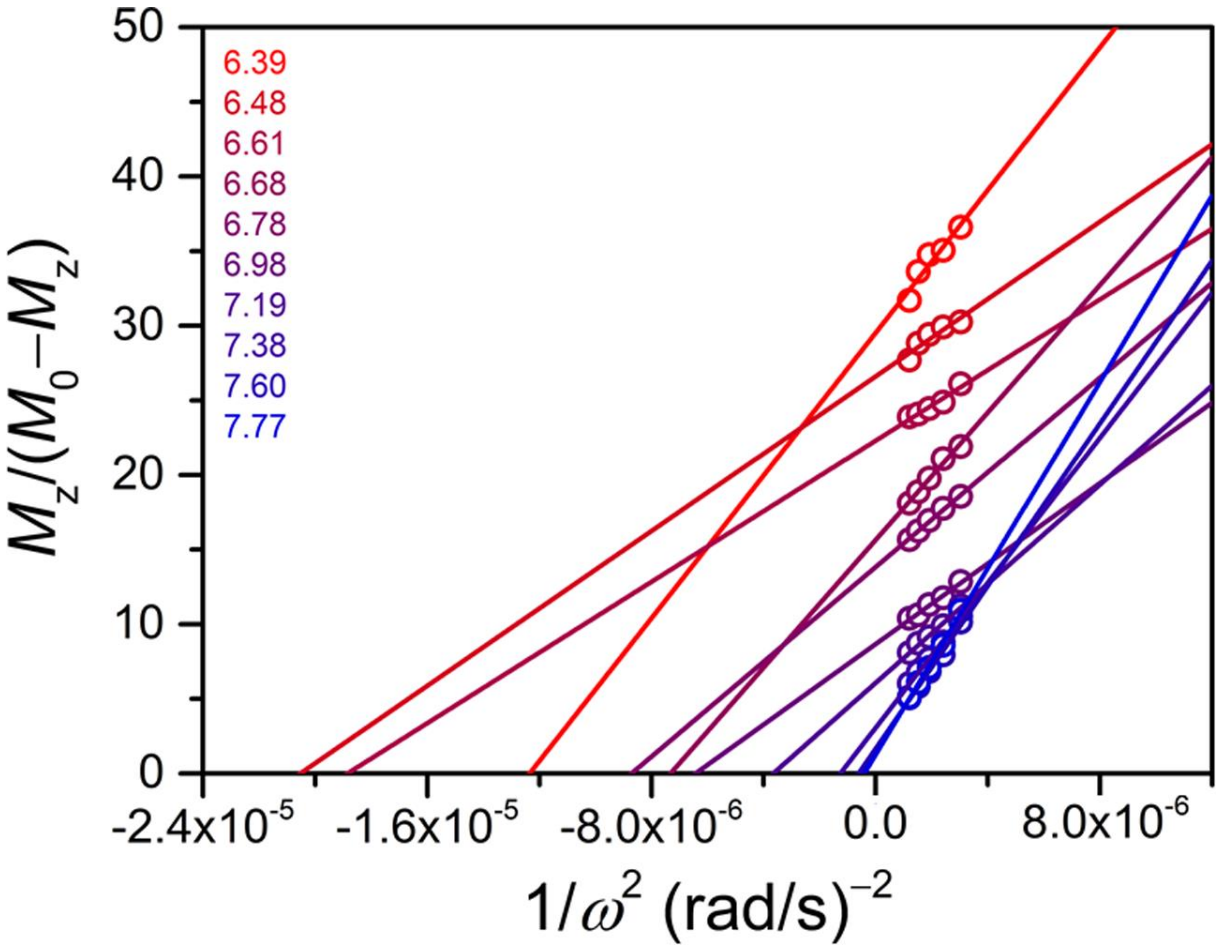

Figure 4.43 Omega plots of the CEST effect from application of presaturation at 91–92 ppm (NH peak 1) for 8 mM of **2-NO₂** in aqueous solutions containing 50 mM HEPES and 100 mM NaCl buffered at pH 6.39–7.77 (red to blue) at 37 °C. Colored numbers in the legend denote the pH of the solutions measured with a pH electrode and the corresponding color of each sample. Presaturation at the frequency offset corresponding to maximum reduction in the H_2O signal intensity was monitored for each pH value (see Table 4.4). Circles represent experimental data and lines represent the linear fits.

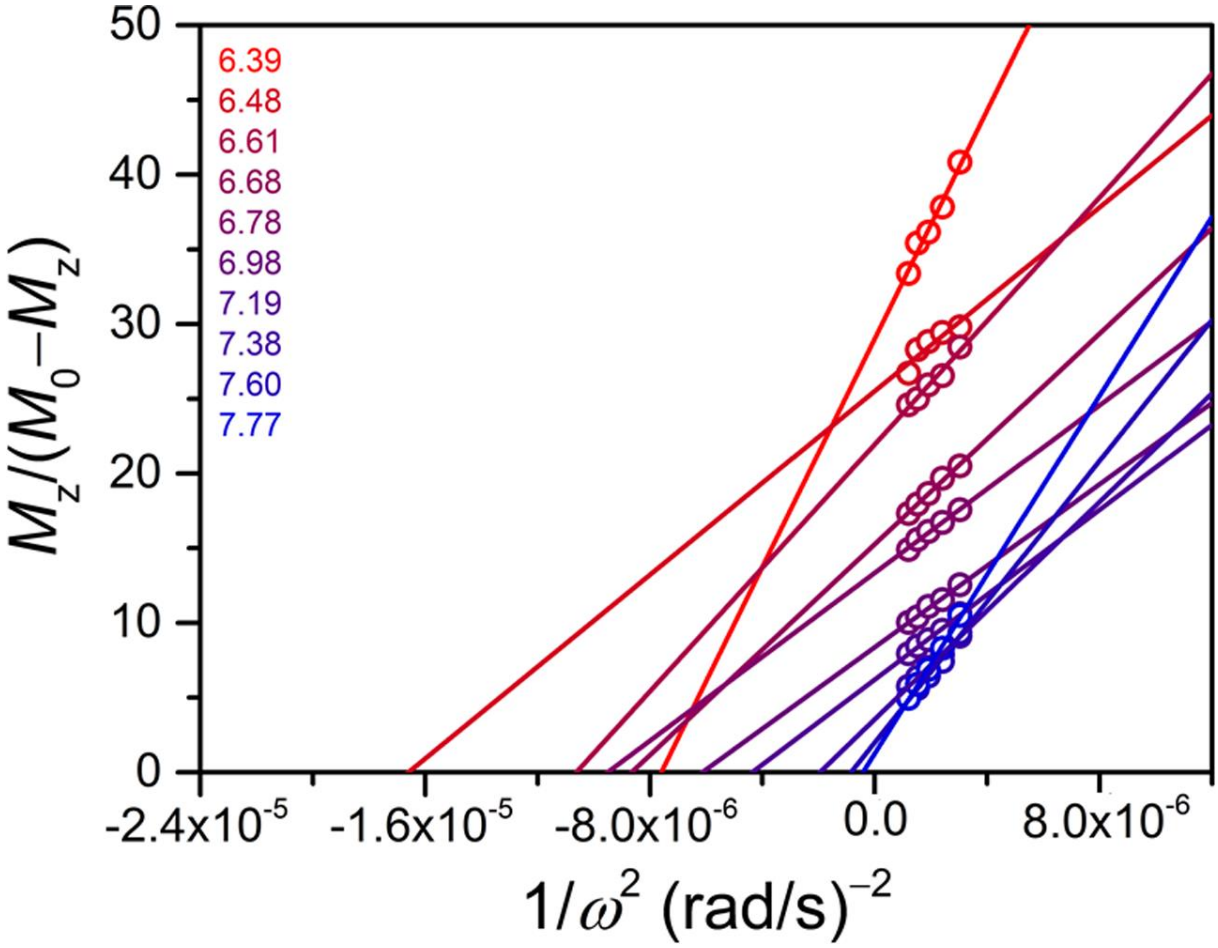

Figure 4.44 Omega plots of the CEST effect from application of presaturation at 88–89 ppm (NH peak 2) for 8 mM of **2-NO$_2$** in aqueous solutions containing 50 mM HEPES and 100 mM NaCl buffered at pH 6.39–7.77 (red to blue) at 37 °C. Colored numbers in the legend denote the pH of the solutions measured with a pH electrode and the corresponding color of each sample. Presaturation at the frequency offset corresponding to maximum reduction in the H_2O signal intensity was monitored for each pH value (see Table 4.4). Circles represent experimental data and lines represent the linear fits.

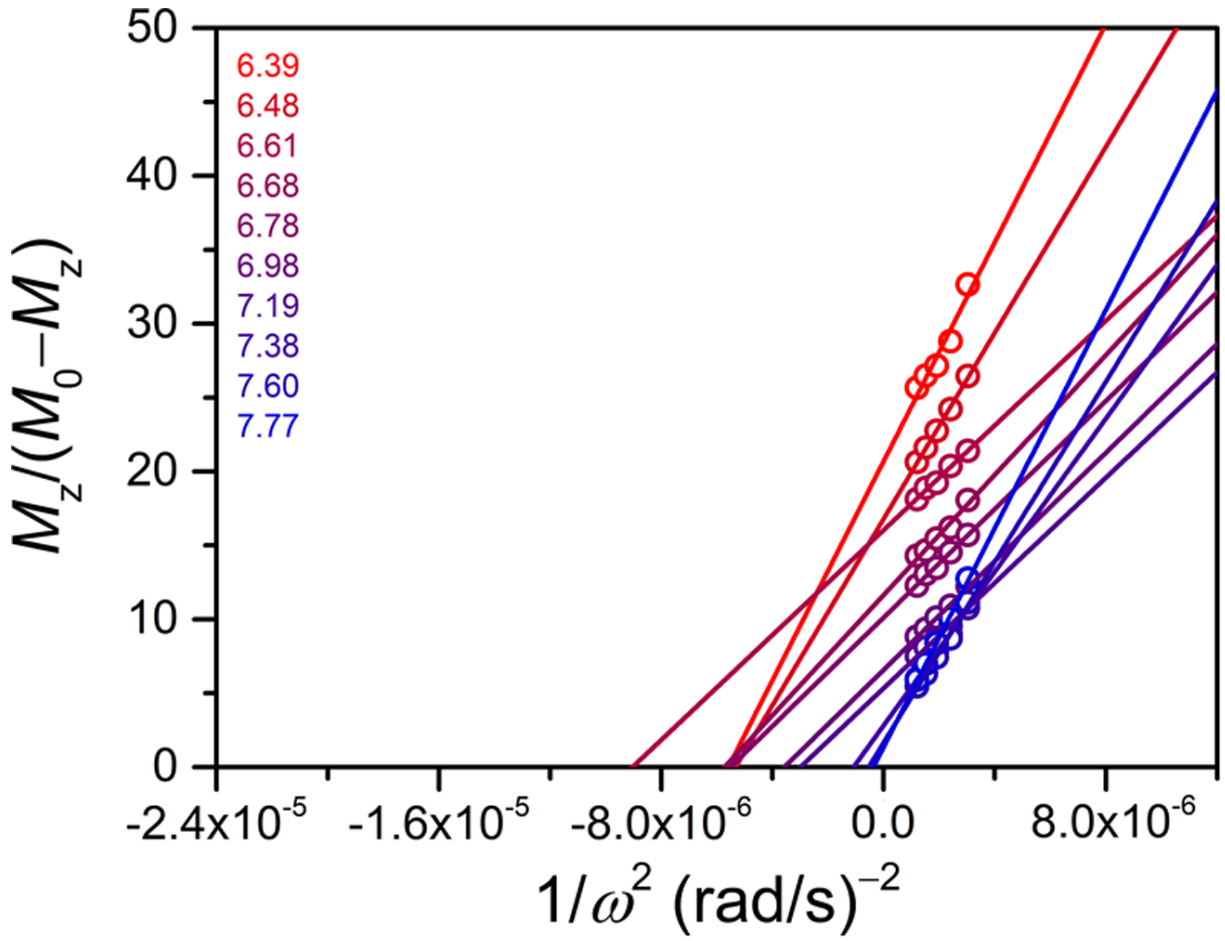

Figure 4.45 Omega plots of the CEST effect from application of presaturation at 43–45 ppm (NH peak 3) for 8 mM of **2-NO₂** in aqueous solutions containing 50 mM HEPES and 100 mM NaCl buffered at pH 6.39–7.77 (red to blue) at 37 °C. Colored numbers in the legend denote the pH of the solutions measured with a pH electrode and the corresponding color of each sample. Presaturation at the frequency offset corresponding to maximum reduction in the H_2O signal intensity was monitored for each pH value (see Table 4.4). Circles represent experimental data and lines represent the linear fits.

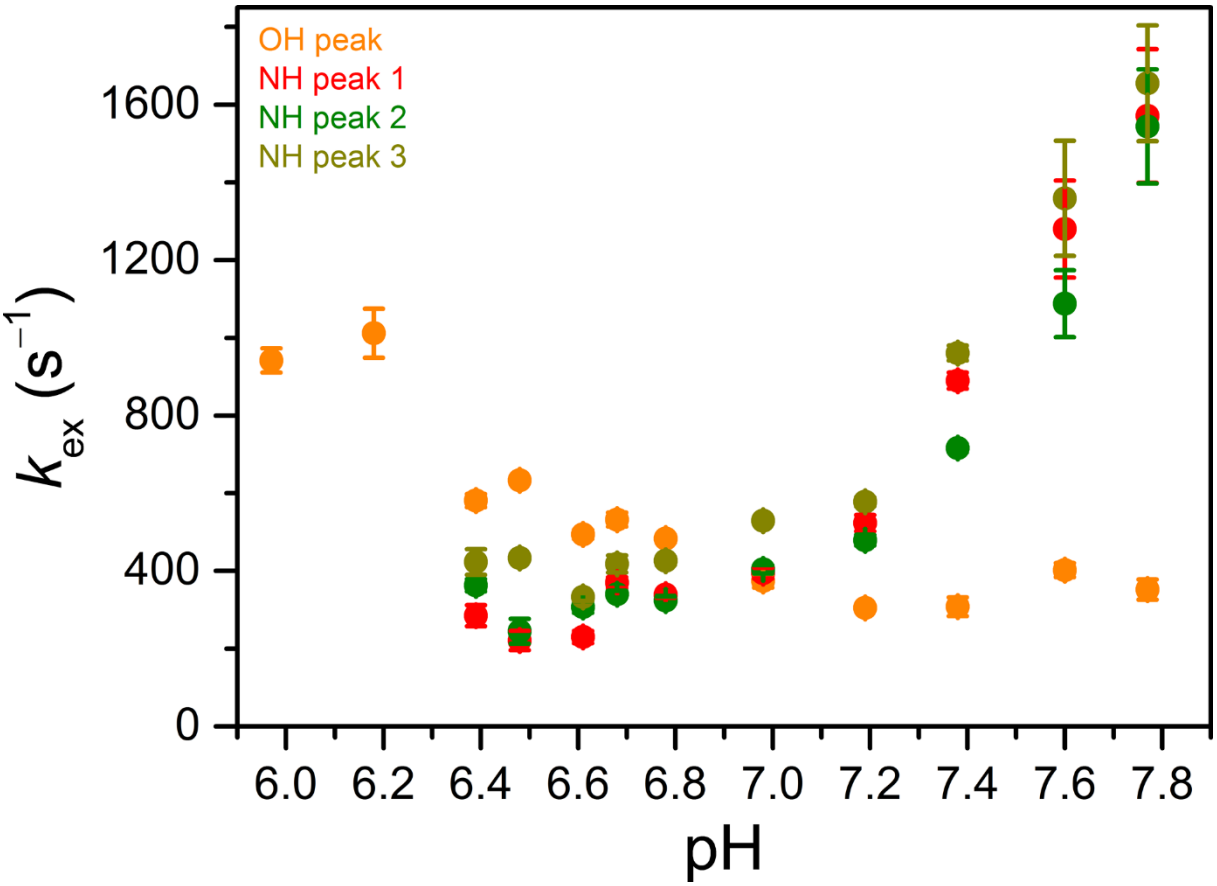

Figure 4.46 pH dependences of the proton exchange rate constants (k_{ex}) for the CEST effects at 112–117 ppm (yellow; OH peak), 91–92 ppm (red; NH peak 1), 88–89 ppm (green; NH peak 2), and 43–45 ppm (dark yellow; NH peak 3) for 8 mM of **2-NO$_2$** in aqueous solutions containing 50 mM HEPES and 100 mM NaCl at 37 °C, obtained from Omega plots. Circles represent experimental data and the error bars represent standard deviations of the linear fits to the Omega plot data (see Figures 4.42–4.45).

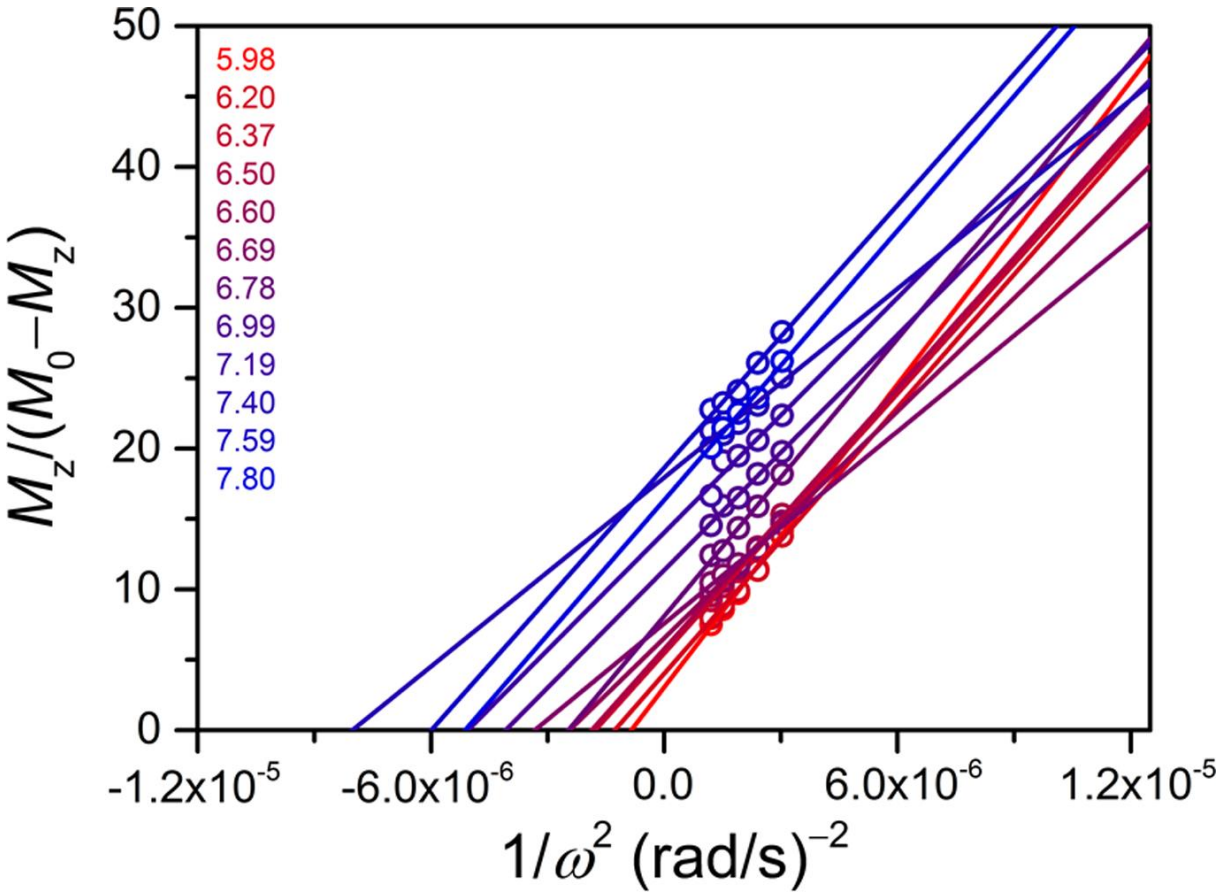

Figure 4.47 Omega plots of the CEST effect from application of presaturation at 90–97 ppm (OH peak) for 9 mM of **2-F** in aqueous solutions containing 50 mM HEPES and 100 mM NaCl buffered at pH 5.98–7.80 (red to blue) at 37 °C. Colored numbers in the legend denote the pH of the solutions measured with a pH electrode and the corresponding color of each sample. Presaturation at the frequency offset corresponding to maximum reduction in the H_2O signal intensity was monitored for each pH value (see Table 4.5). Circles represent experimental data and lines represent the linear fits.

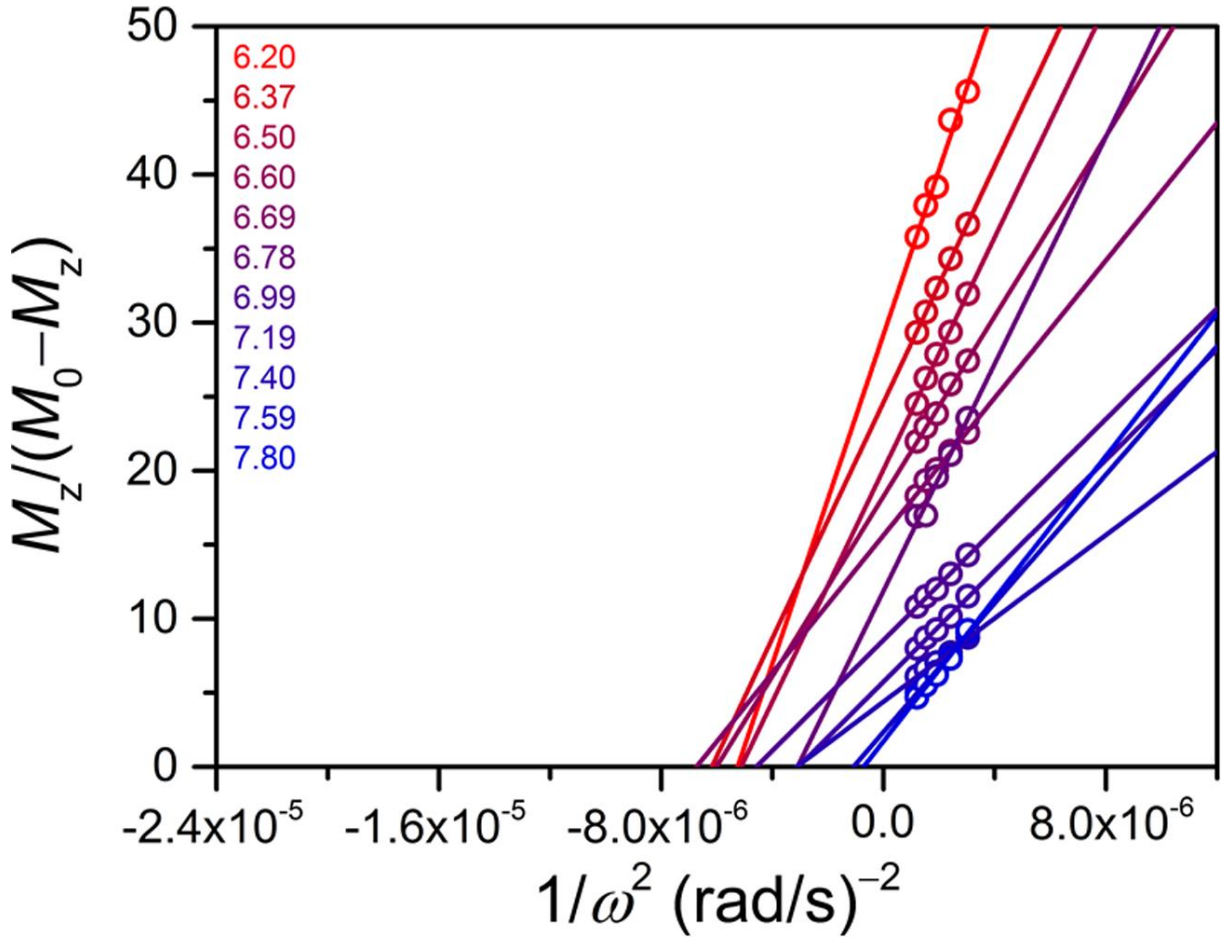

Figure 4.48 Omega plots of the CEST effect from application of presaturation at 81 ppm (NH peak 1) for 9 mM of **2-F** in aqueous solutions containing 50 mM HEPES and 100 mM NaCl buffered at pH 6.20–7.80 (red to blue) at 37 °C. Colored numbers in the legend denote the pH of the solutions measured with a pH electrode and the corresponding color of each sample. Circles represent experimental data and lines represent the linear fits.

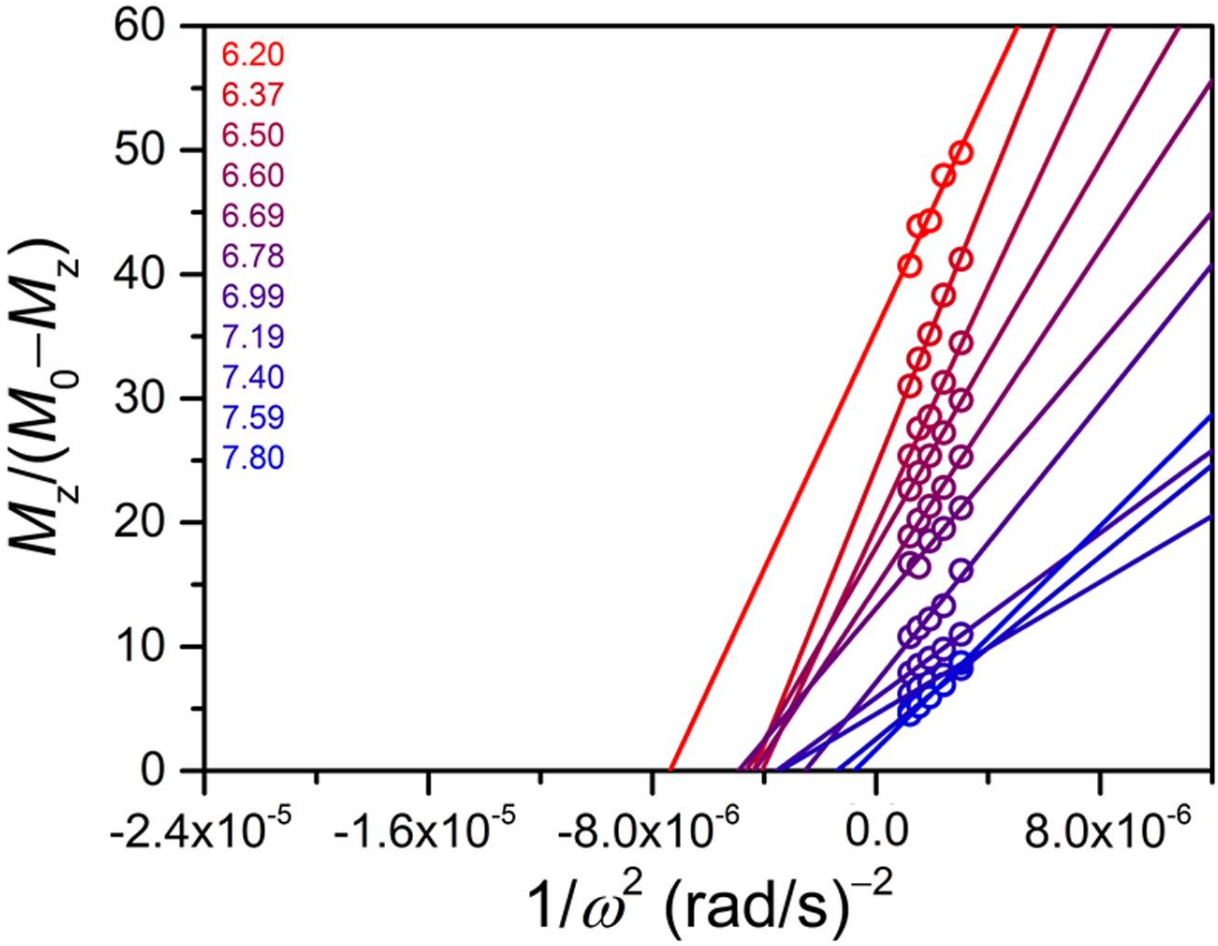

Figure 4.49 Omega plots of the CEST effect from application of presaturation at 78–79 ppm (NH peak 2) for 9 mM of **2-F** in aqueous solutions containing 50 mM HEPES and 100 mM NaCl buffered at pH 6.20–7.80 (red to blue) at 37 °C. Colored numbers in the legend denote the pH of the solutions measured with a pH electrode and the corresponding color of each sample. Presaturation at the frequency offset corresponding to maximum reduction in the H_2O signal intensity was monitored for each pH value (see Table 4.5). Circles represent experimental data and lines represent the linear fits.

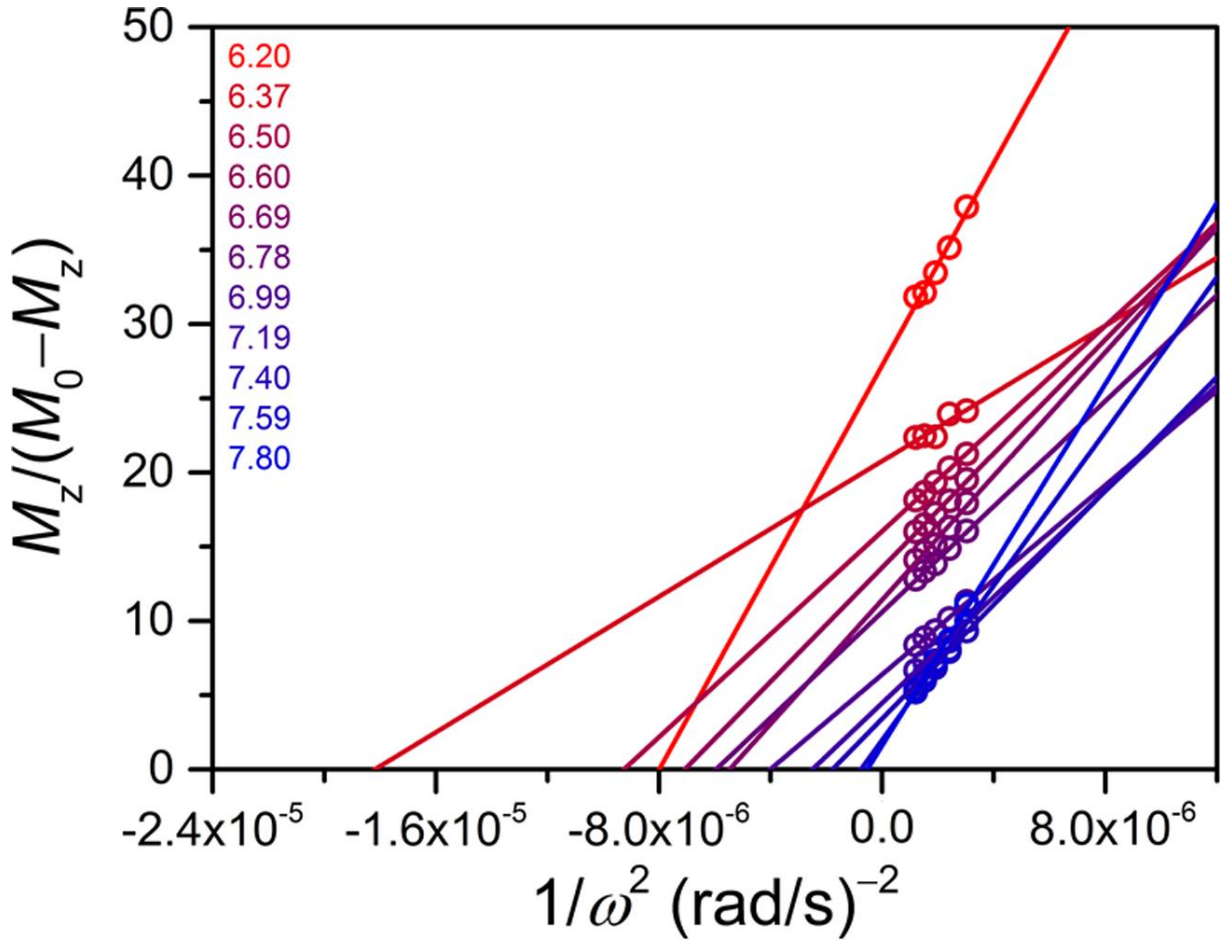

Figure 4.50 Omega plots of the CEST effect from application of presaturation at 48–51 ppm (NH peak 3) for 9 mM of **2-F** in aqueous solutions containing 50 mM HEPES and 100 mM NaCl buffered at pH 6.20–7.80 (red to blue) at 37 °C. Colored numbers in the legend denote the pH of the solutions measured with a pH electrode and the corresponding color of each sample. Presaturation at the frequency offset corresponding to maximum reduction in the H_2O signal intensity was monitored for each pH value (see Table 4.5). Circles represent experimental data and lines represent the linear fits.

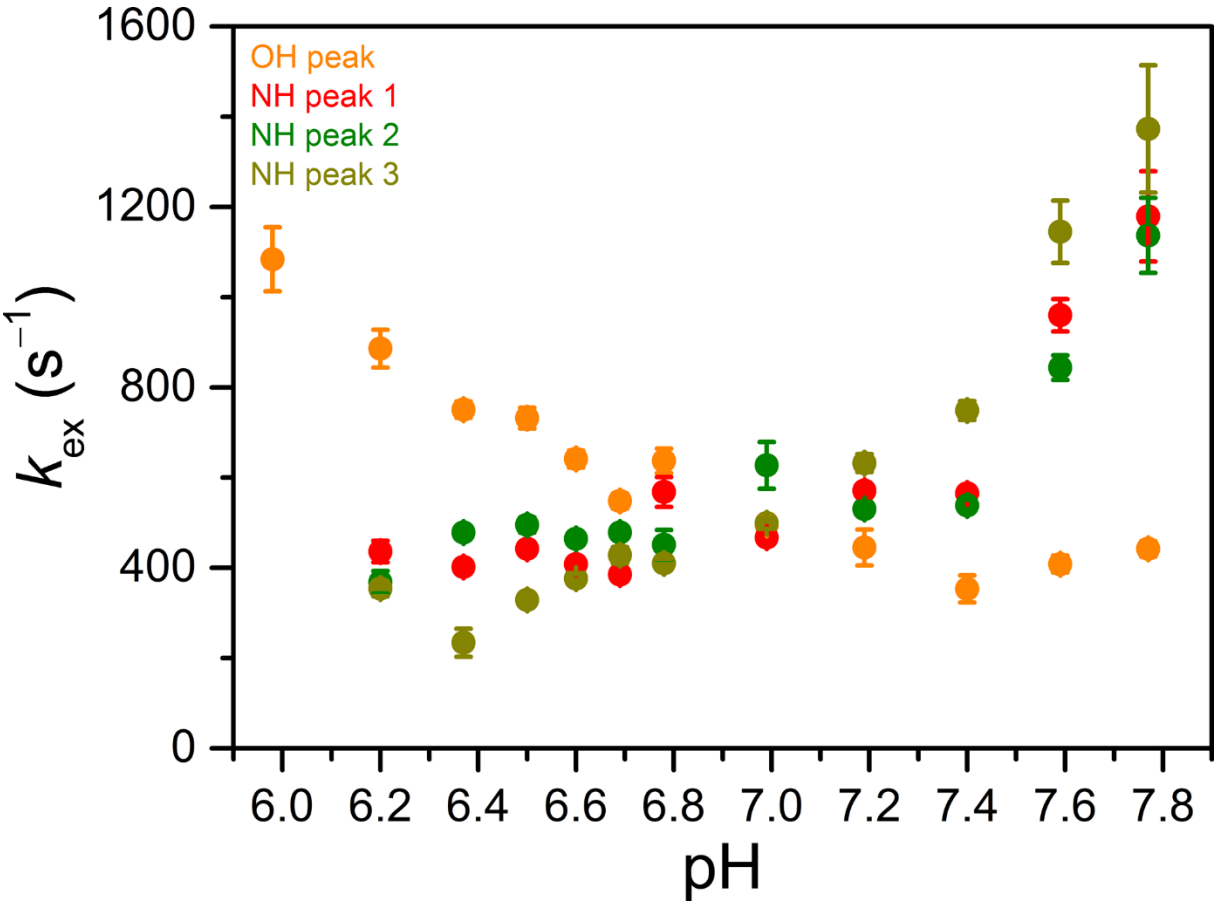

Figure 4.51 pH dependences of the proton exchange rate constants (k_{ex}) for the CEST effects at 90–97 ppm (yellow; OH peak), 81 ppm (red; NH peak 1), 78–79 ppm (green; NH peak 2), and 48–51 ppm (dark yellow; NH peak 3) for 9 mM of **2-F** in aqueous solutions containing 50 mM HEPES and 100 mM NaCl at 37 °C, obtained from Omega plots. Circles represent experimental data and the error bars represent standard deviations of the linear fits to the Omega plot data (see Figures 4.47–4.50).

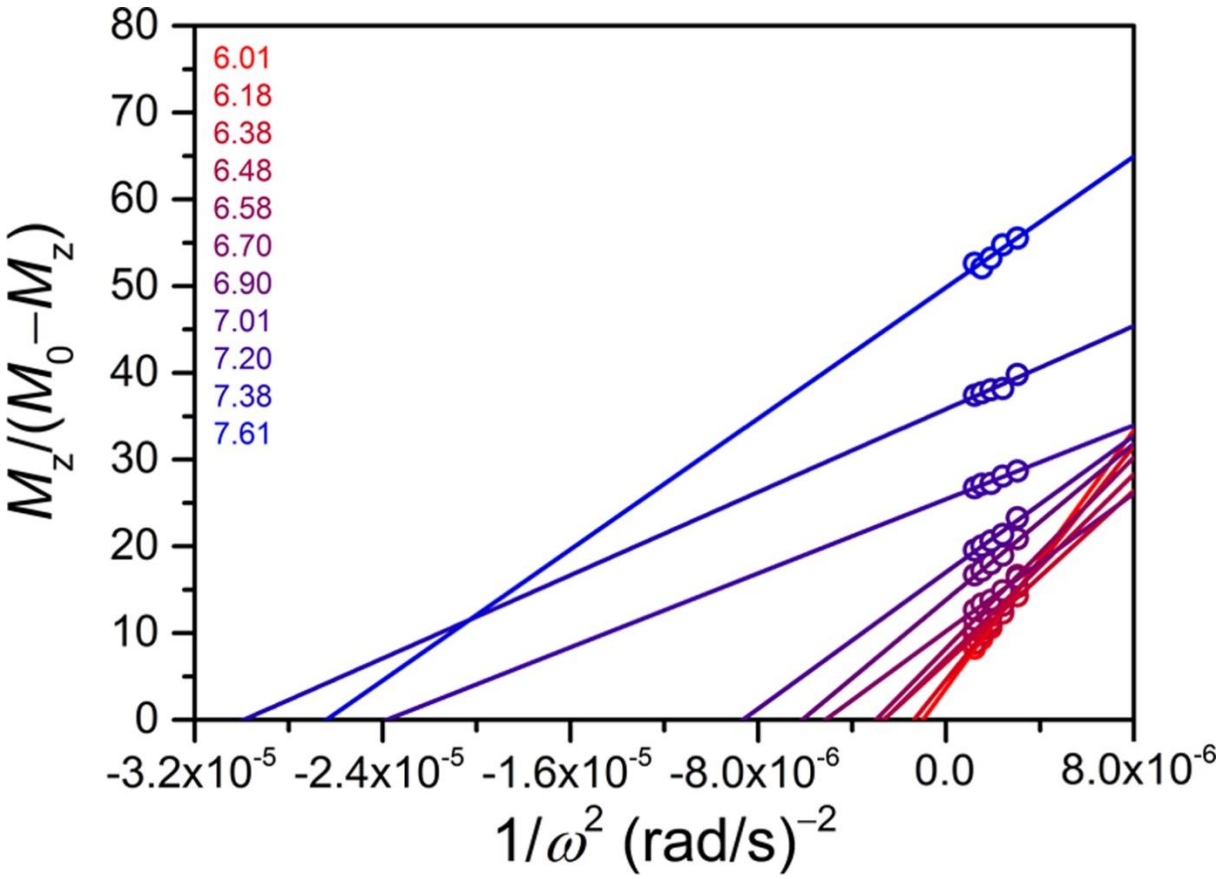

Figure 4.52 Omega plots of the CEST effect from application of presaturation at 85–92 ppm (OH peak) for 8 mM of **2-Me** in aqueous solutions containing 50 mM HEPES and 100 mM NaCl buffered at pH 6.01–7.61 (red to blue) at 37 °C. Colored numbers in the legend denote the pH of the solutions measured with a pH electrode and the corresponding color of each sample. Presaturation at the frequency offset corresponding to maximum reduction in the H_2O signal intensity was monitored for each pH value (see Table 4.6). Circles represent experimental data and lines represent the linear fits.

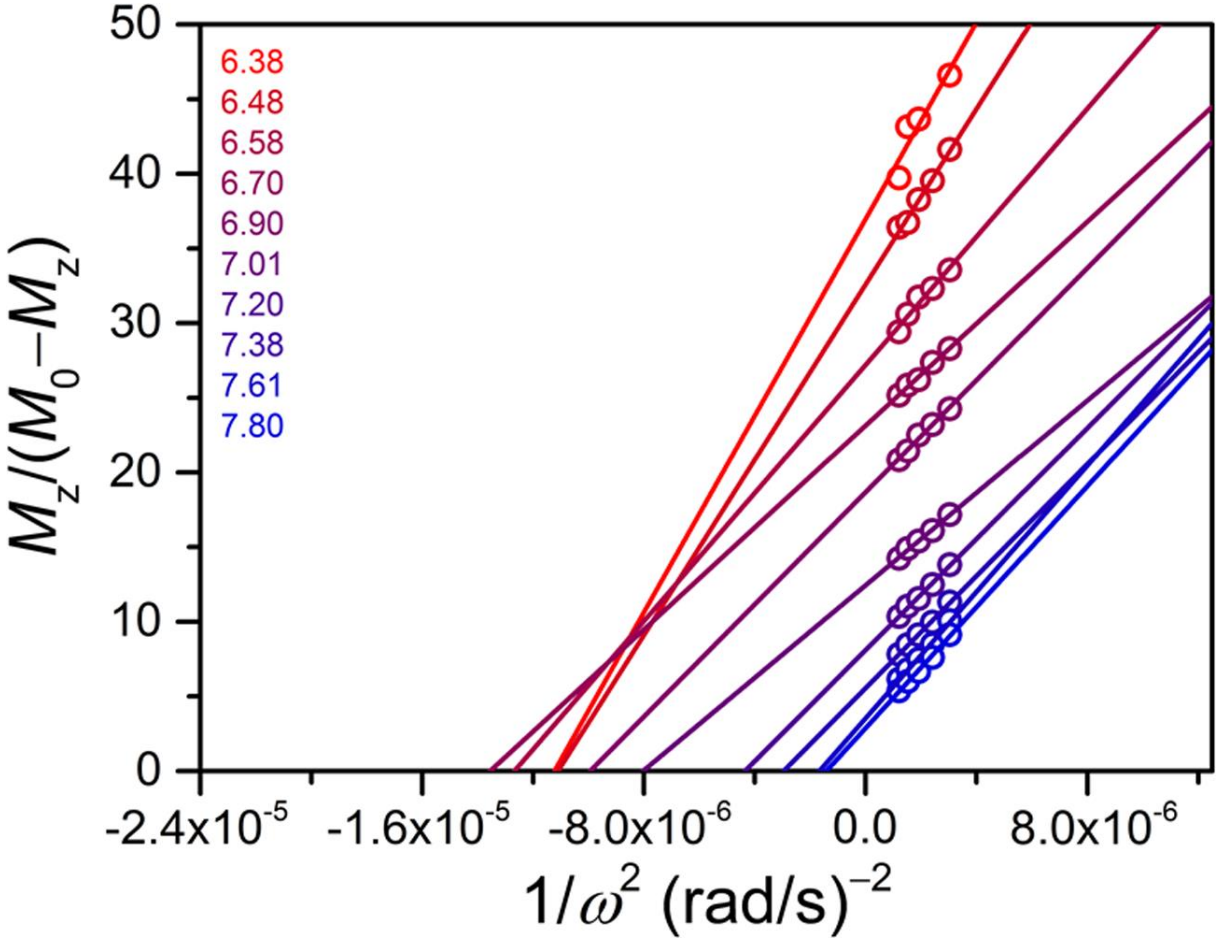

Figure 4.53 Omega plots of the CEST effect from application of presaturation at 79 ppm (NH peak 1) for 8 mM of **2-Me** in aqueous solutions containing 50 mM HEPES and 100 mM NaCl buffered at pH 6.38–7.80 (red to blue) at 37 °C. Colored numbers in the legend denote the pH of the solutions measured with a pH electrode and the corresponding color of each sample.

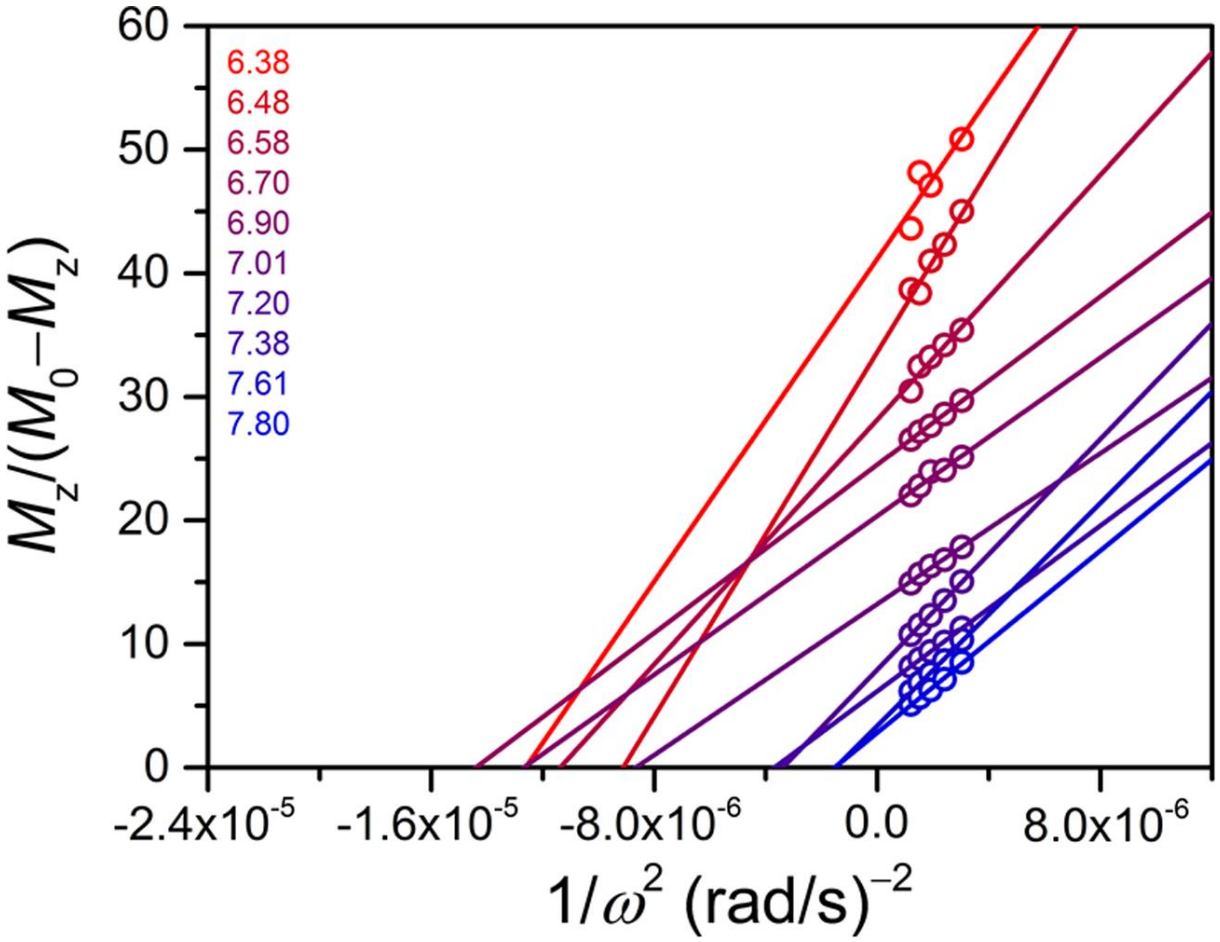

Figure 4.54 Omega plots of the CEST effect from application of presaturation at 76–77 ppm (NH peak 2) for 8 mM of **2-Me** in aqueous solutions containing 50 mM HEPES and 100 mM NaCl buffered at pH 6.38–7.80 (red to blue) at 37 °C. Colored numbers in the legend denote the pH of the solutions measured with a pH electrode and the corresponding color of each sample. Presaturation at the frequency offset corresponding to maximum reduction in the H_2O signal intensity was monitored for each pH value (see Table 4.6). Circles represent experimental data and lines represent the linear fits.

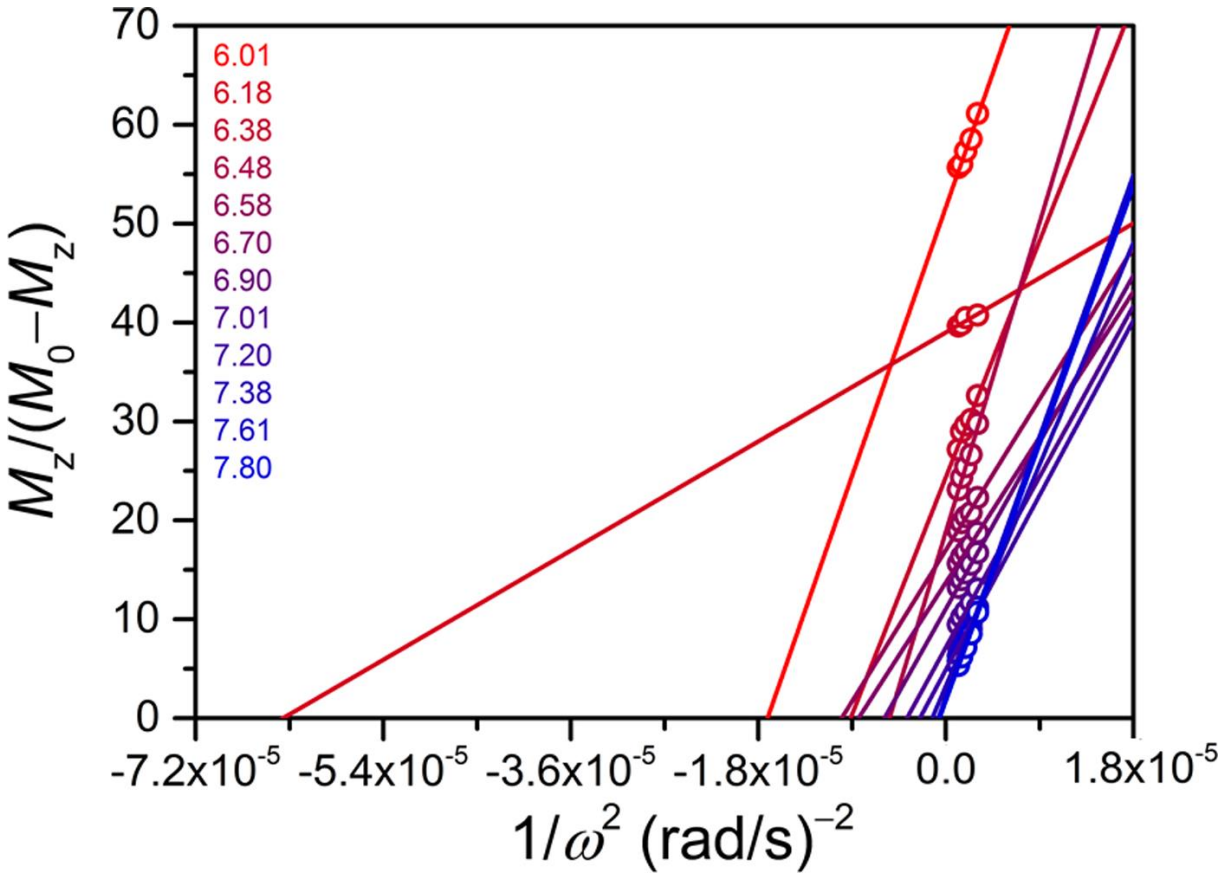

Figure 4.55 Omega plots of the CEST effect from application of presaturation at 51–53 ppm (NH peak 3) for 8 mM of **2-Me** in aqueous solutions containing 50 mM HEPES and 100 mM NaCl buffered at pH 6.01–7.80 (red to blue) at 37 °C. Colored numbers in the legend denote the pH of the solutions measured with a pH electrode and the corresponding color of each sample. Presaturation at the frequency offset corresponding to maximum reduction in the H_2O signal intensity was monitored for each pH value (see Table 4.6). Circles represent experimental data and lines represent the linear fits.

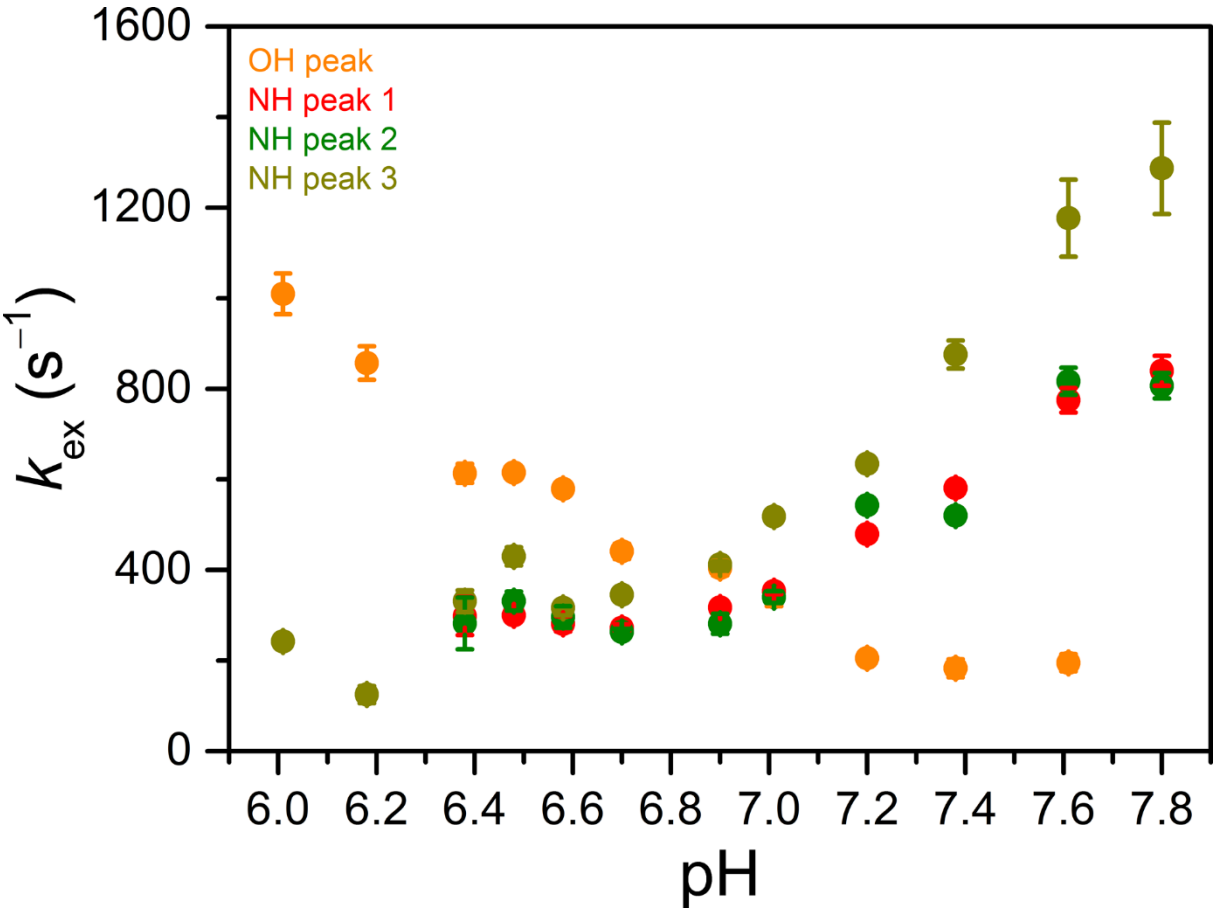

Figure 4.56 pH dependences of the proton exchange rate constants (k_{ex}) for the CEST effects at 85–92 ppm (yellow; OH peak), 79 ppm (red; NH peak 1), 76–77 ppm (green; NH peak 2), and 51–53 ppm (dark yellow; NH peak 3) for 8 mM of **2-Me** in aqueous solutions containing 50 mM HEPES and 100 mM NaCl at 37 °C, obtained from Omega plots. Circles represent experimental data and the error bars represent standard deviations of the linear fits to the Omega plot data (see Figures 4.52–4.55).

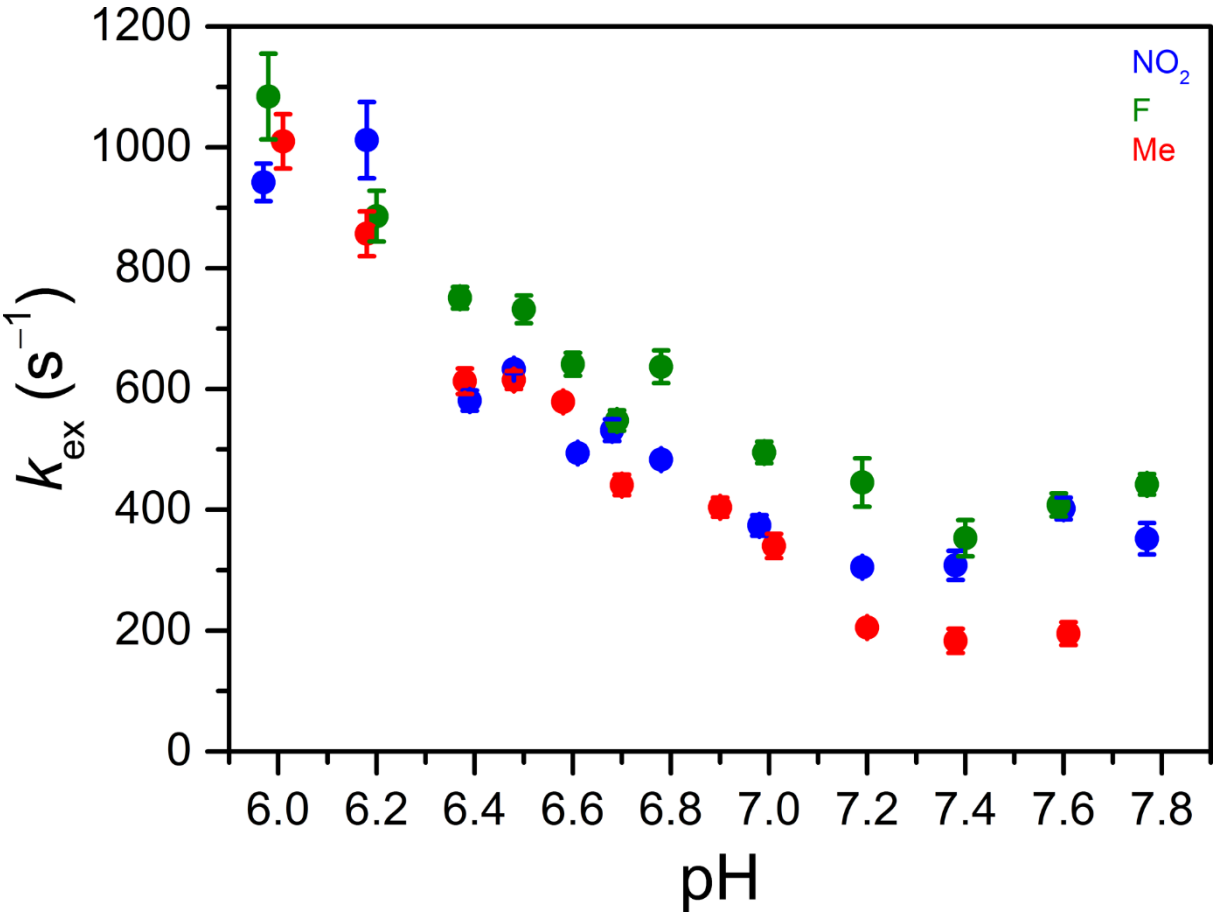

Figure 4.57 Comparison of the pH dependence of the rate constant for OH proton exchange for 8 mM of **2-NO₂** (blue; 112–117 ppm), 9 mM of **2-F** (green; 90–97 ppm), and 8 mM of **2-Me** (red; 85–92 ppm) in aqueous solutions containing 50 mM HEPES and 100 mM NaCl at 37 °C.

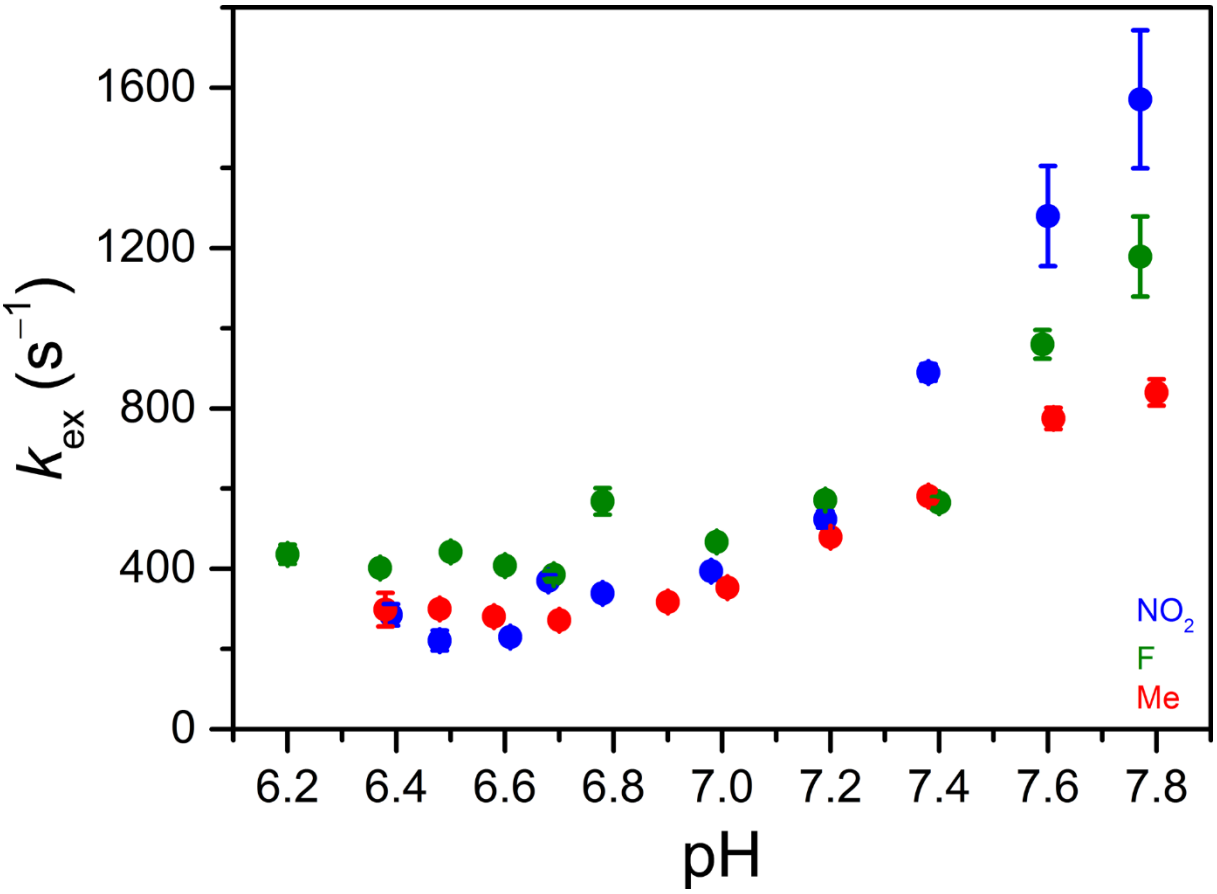

Figure 4.58 Comparison of the pH dependence of the proton exchange rate constant for NH peak 1 for 8 mM of **2-NO_2** (blue; 91–92 ppm), 9 mM of **2-F** (green; 81 ppm), and 8 mM of **2-Me** (red; 79 ppm) in aqueous solutions containing 50 mM HEPES and 100 mM NaCl at 37 °C.

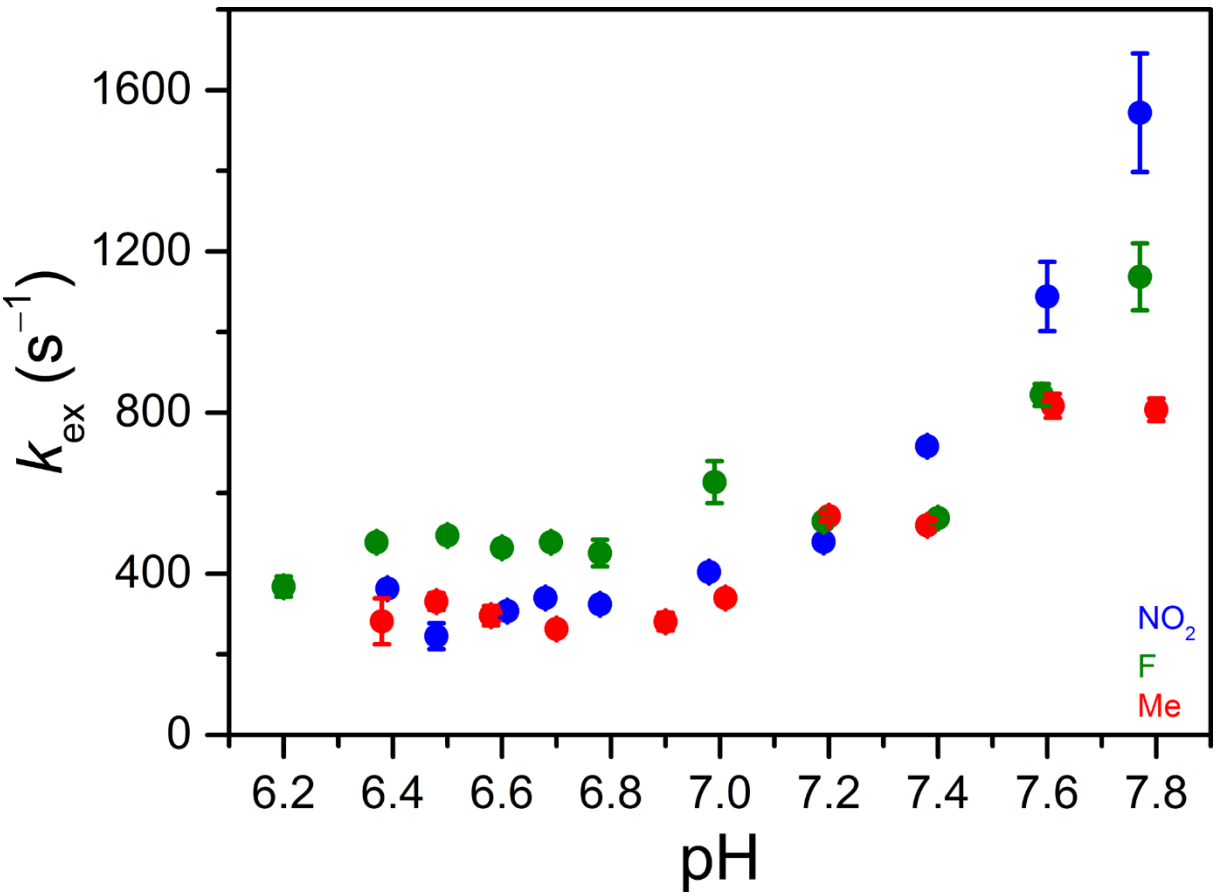

Figure 4.59 Comparison of the pH dependence of the proton exchange rate constant for NH peak 2 for 8 mM of **2-NO_2** (blue; 88–89 ppm), 9 mM of **2-F** (green; 78–79 ppm), and 8 mM of **2-Me** (red; 76–77 ppm) in aqueous solutions containing 50 mM HEPES and 100 mM NaCl at 37 °C.

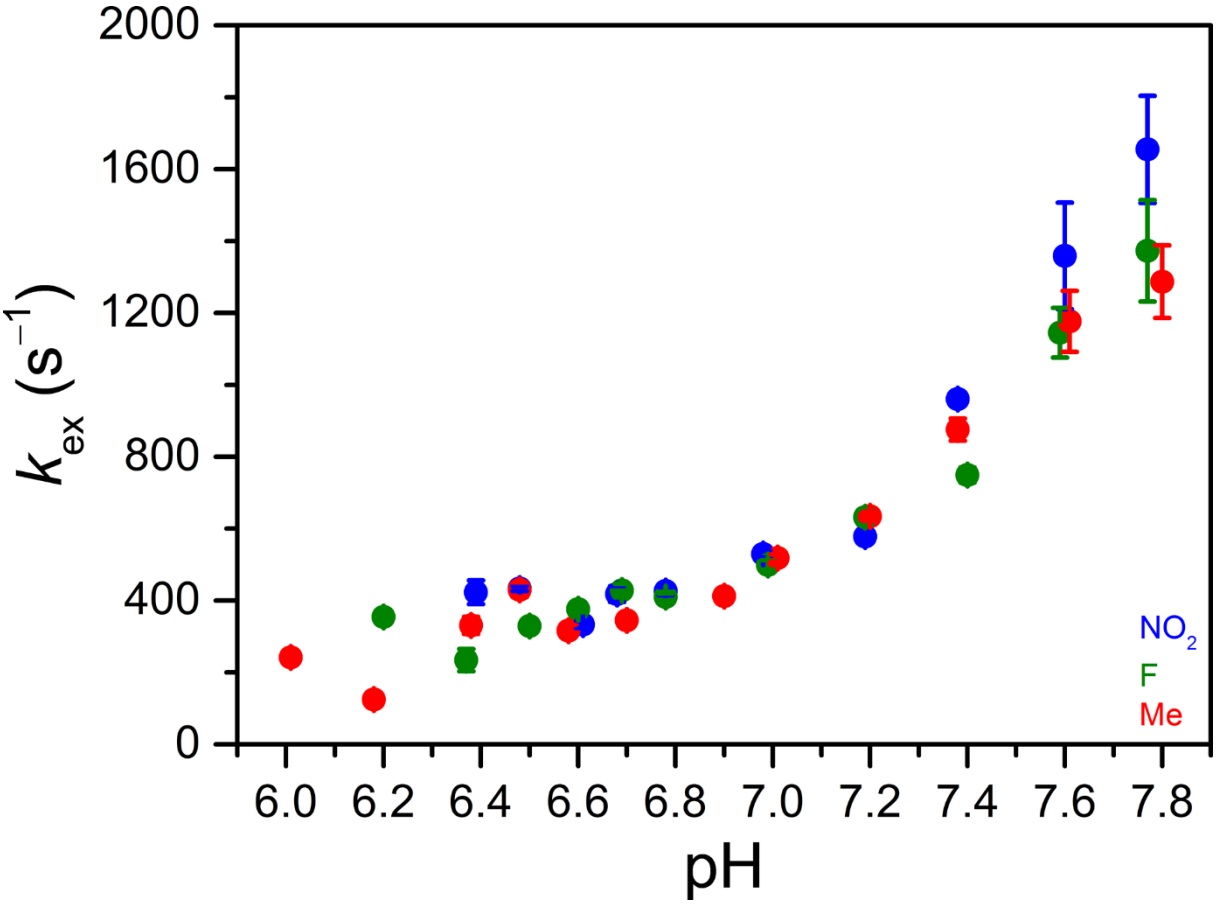

Figure 4.60 Comparison of the pH dependence of the proton exchange rate constant for NH peak 3 for 8 mM of **2-NO₂** (blue; 43–45 ppm), 9 mM of **2-F** (green; 48–51 ppm), and 8 mM of **2-Me** (red; 51–53 ppm) in aqueous solutions containing 50 mM HEPES and 100 mM NaCl at 37 °C.

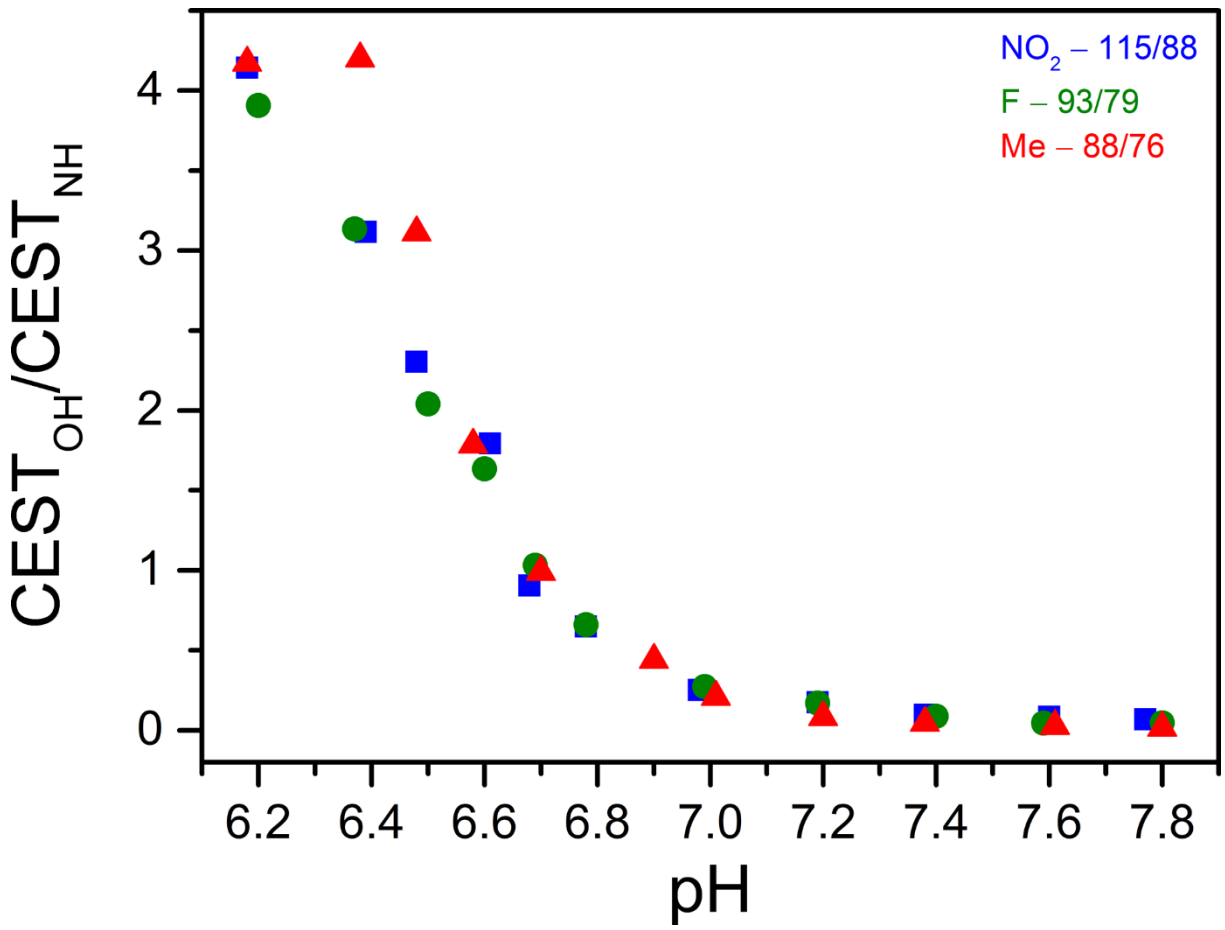

Figure 4.61 Comparison of the pH dependence of the ratio of OH and NH CEST effects for 8 mM of **2-NO_2** (blue), 9 mM of **2-F** (green), and 8 mM of **2-Me** (red) in aqueous solutions containing 50 mM HEPES and 100 mM NaCl at 37 °C. The presaturation frequencies employed for the two CEST effects for each compound are given in the legend.

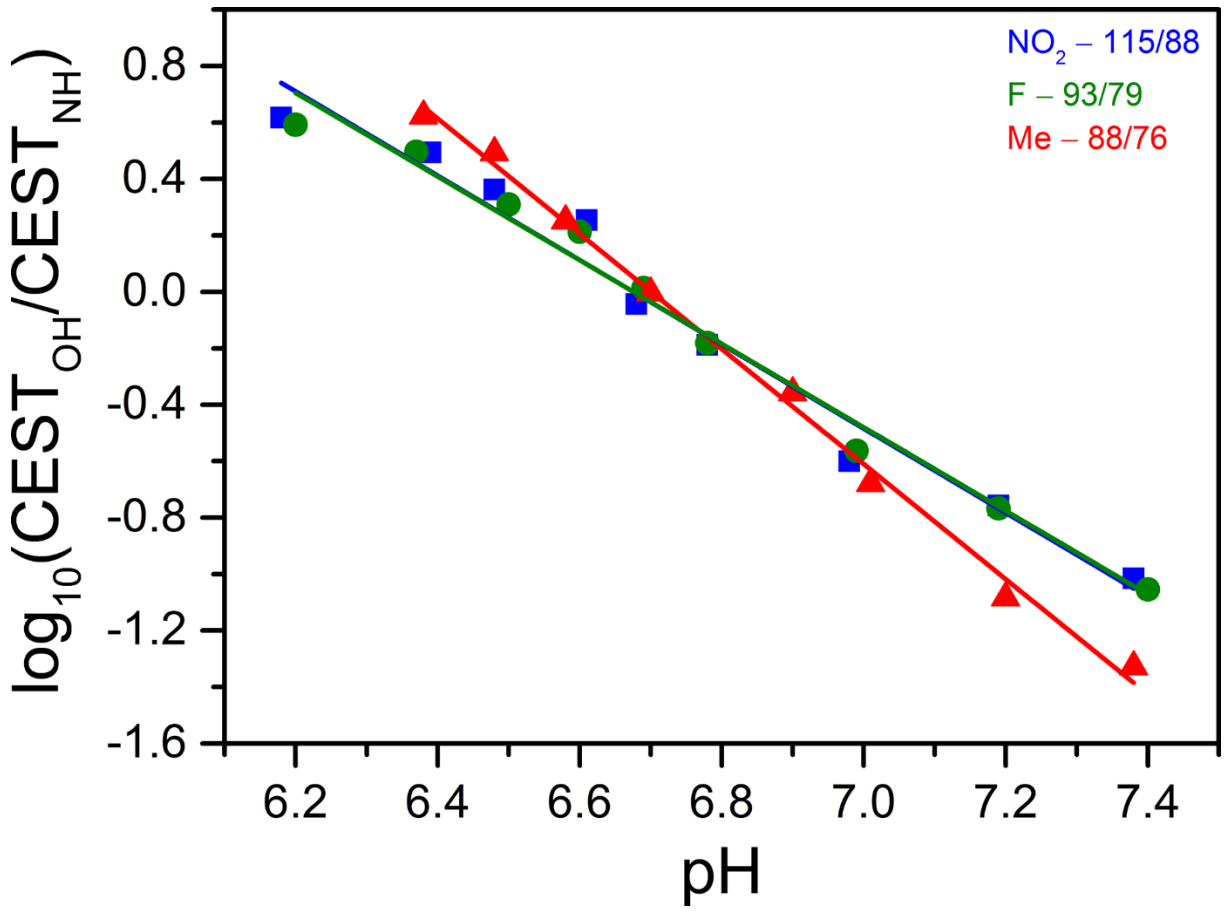

Figure 4.62 Comparison of the pH calibration curves obtained by taking the logarithm with base 10 of the ratios of OH and NH CEST effects for 8 mM of **2-NO$_2$** (blue), 9 mM of **2-F** (green), and 8 mM of **2-Me** (red) in aqueous solutions containing 50 mM HEPES and 100 mM NaCl at 37 °C. The presaturation frequencies employed for the two CEST effects for each compound are given in the legend. Solid symbols represent experimental data and the lines denote linear fits to the data with the following equations: $\log_{10}(CEST_{115\ ppm}/CEST_{88\ ppm}) = -1.49(9) \times pH + 10.0(6)$, $R^2 = 0.97$; $\log_{10}(CEST_{93\ ppm}/CEST_{79\ ppm}) = -1.48(7) \times pH + 9.9(5)$, $R^2 = 0.98$; $\log_{10}(CEST_{88\ ppm}/CEST_{76\ ppm}) = -2.04(5) \times pH + 13.7(4)$, $R^2 = 0.99$.

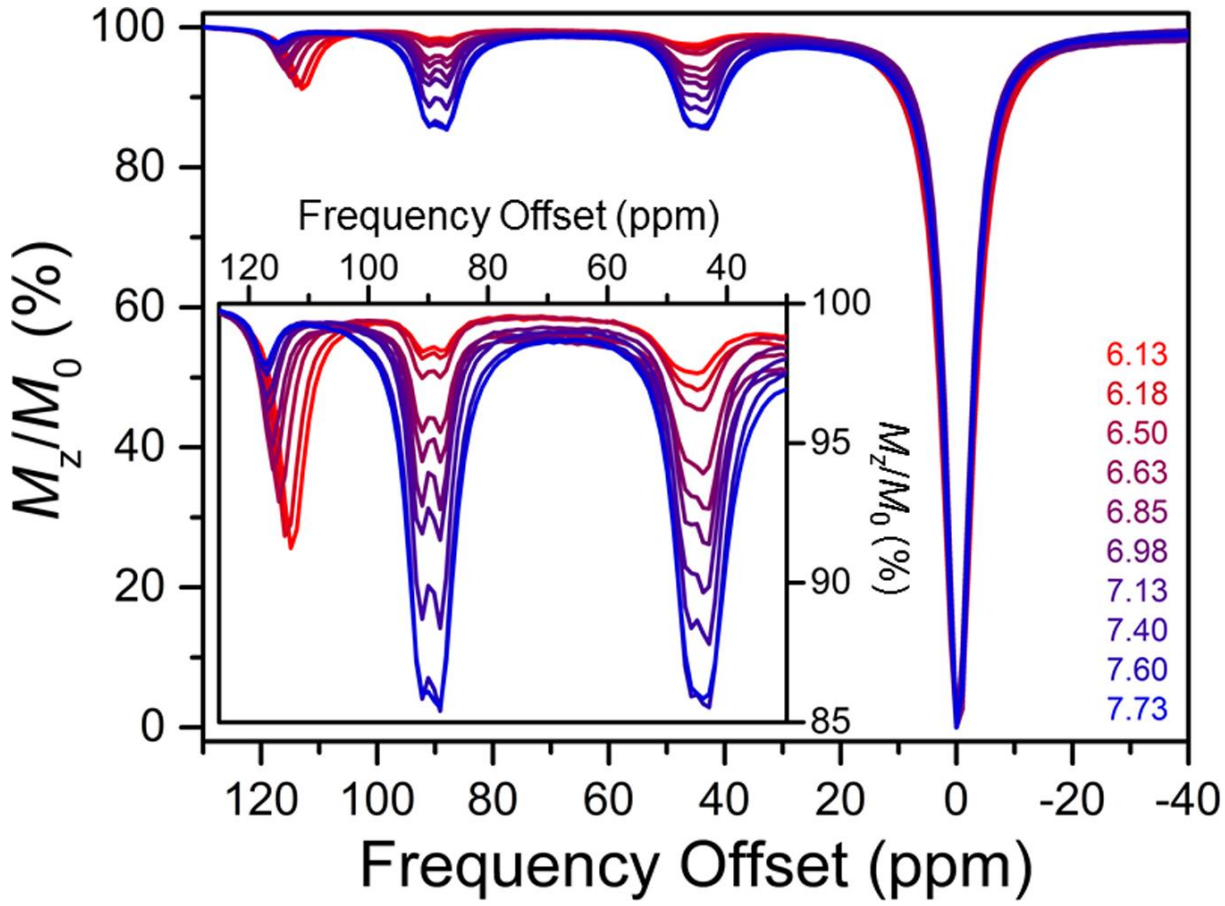

Figure 4.63 Variable-pH CEST spectra for 4 mM of **2-NO_2** in aqueous solutions containing 50 mM HEPES and 100 mM NaCl buffered at pH 6.13–7.73 (red to blue) at 37 °C. Colored numbers in the legend denote the pH of the solutions measured with a pH electrode and the corresponding color of each sample. Inset: Expanded view of the CEST peaks of interest.

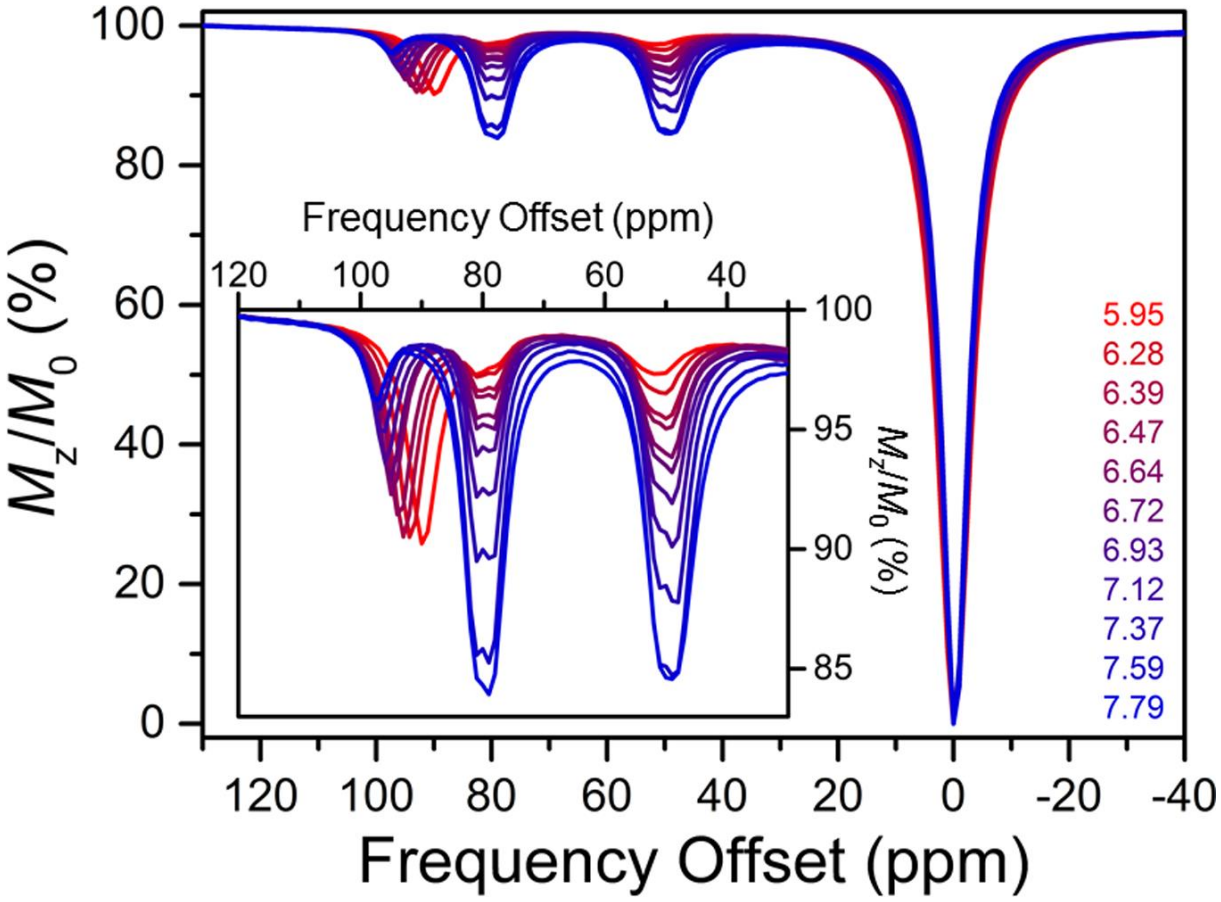

Figure 4.64 Variable-pH CEST spectra for 4 mM of **2-F** in aqueous solutions containing 50 mM HEPES and 100 mM NaCl buffered at pH 5.95–7.79 (red to blue) at 37 °C. Colored numbers in the legend denote the pH of the solutions measured with a pH electrode and the corresponding color of each sample. Inset: Expanded view of the CEST peaks of interest.

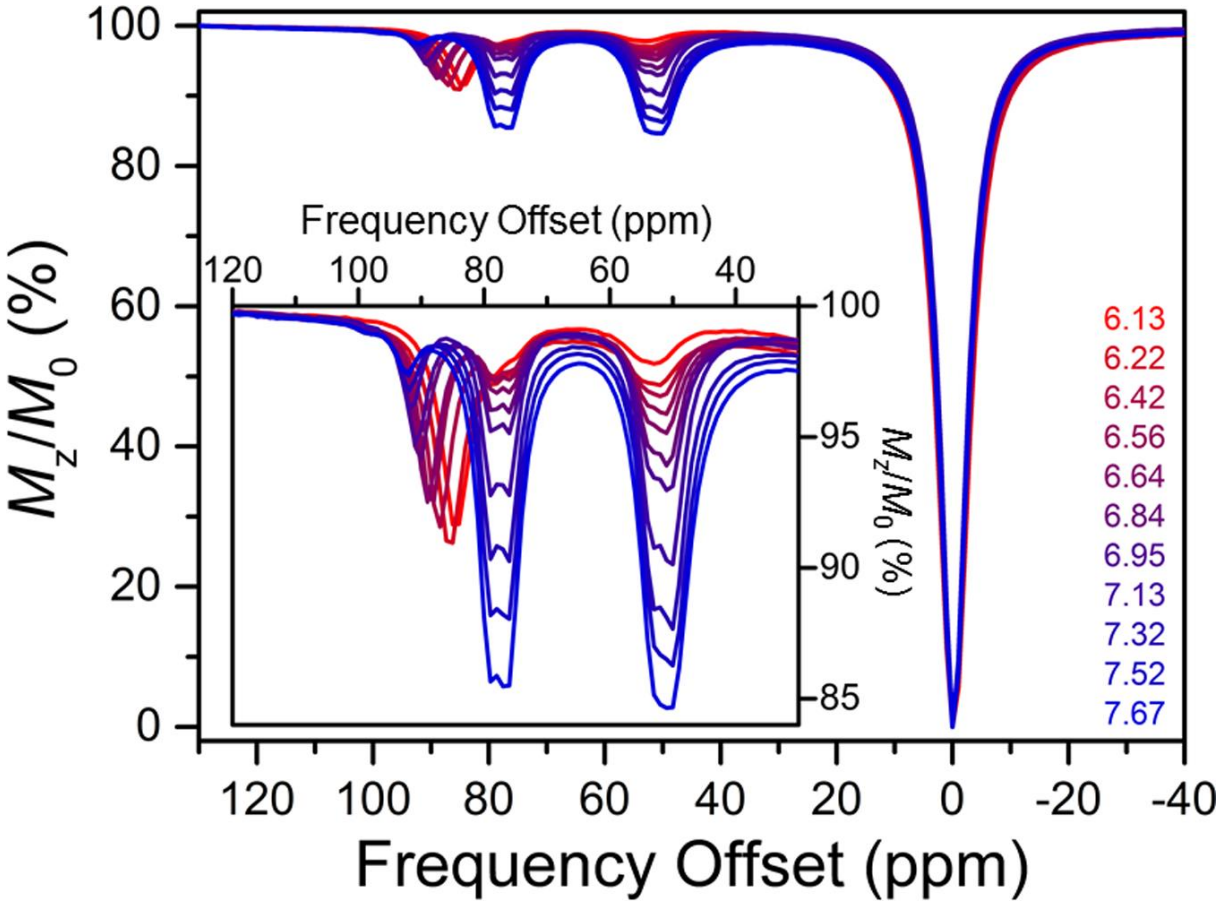

Figure 4.65 Variable-pH CEST spectra for 4 mM of **2-Me** in aqueous solutions containing 50 mM HEPES and 100 mM NaCl buffered at pH 6.13–7.67 (red to blue) at 37 °C. Colored numbers in the legend denote the pH of the solutions measured with a pH electrode and the corresponding color of each sample. Inset: Expanded view of the CEST peaks of interest.

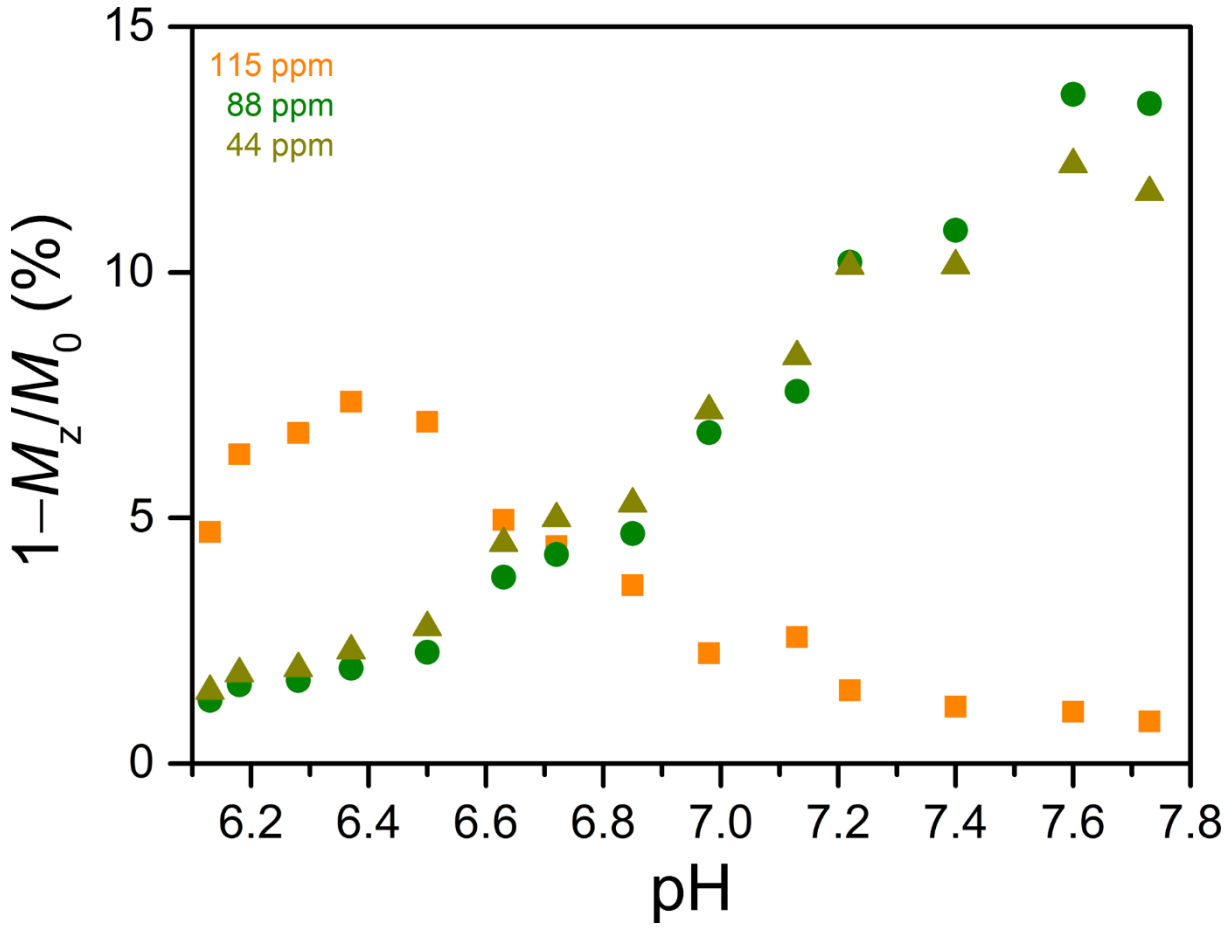

Figure 4.66 pH dependences of the CEST effects from application of presaturation at 115 ppm (yellow), 88 ppm (green), and 44 ppm (dark yellow) for 4 mM of **2-NO$_2$** in aqueous solutions containing 50 mM HEPES and 100 mM NaCl at 37 °C.

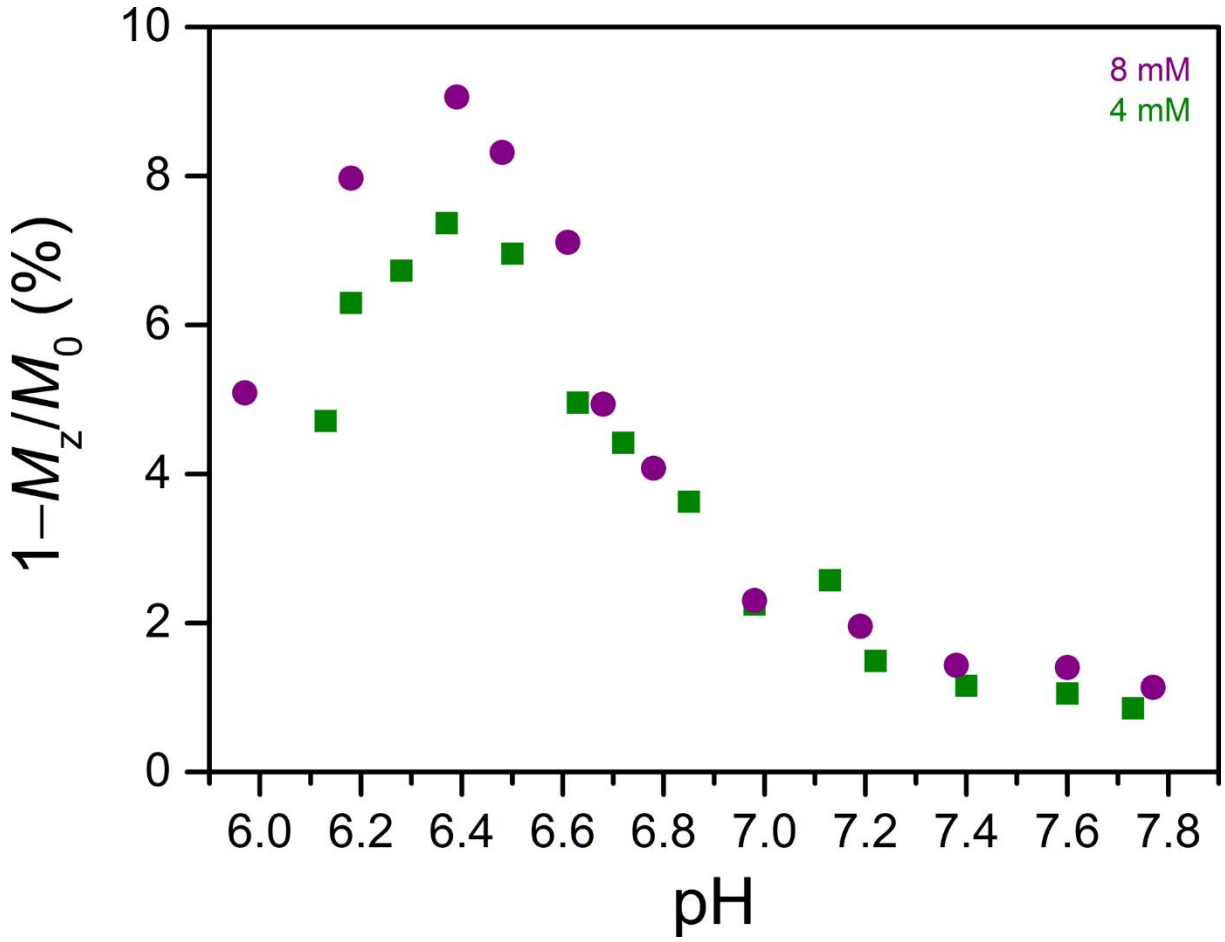

Figure 4.67 Comparison of the pH dependence of the CEST effect from application of presaturation at 115 ppm for various concentrations of **2-NO_2** (see legend) in aqueous solutions containing 50 mM HEPES and 100 mM NaCl at 37 °C.

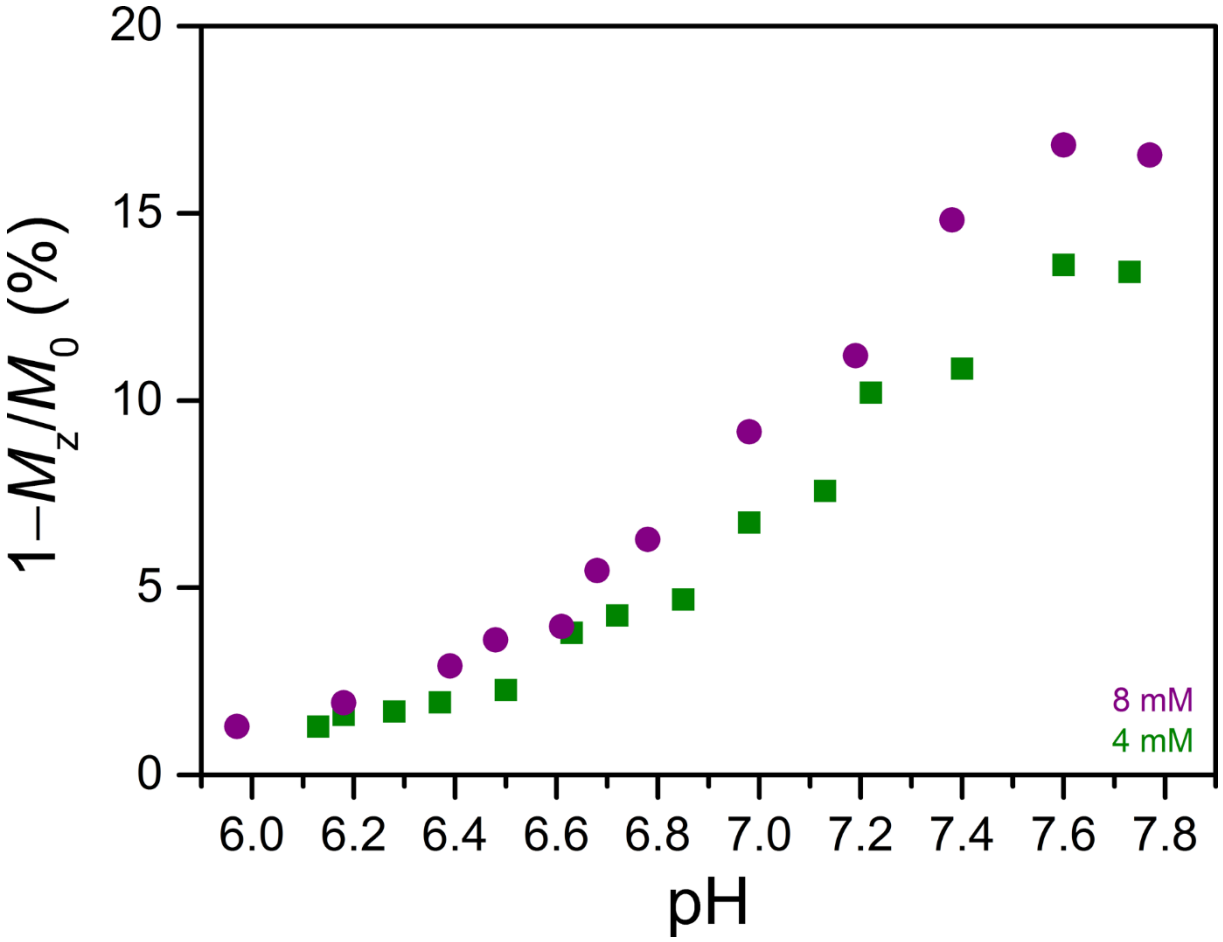

Figure 4.68 Comparison of the pH dependence of the CEST effect from application of presaturation at 88 ppm for various concentrations of **2-NO₂** (see legend) in aqueous solutions containing 50 mM HEPES and 100 mM NaCl at 37 °C.

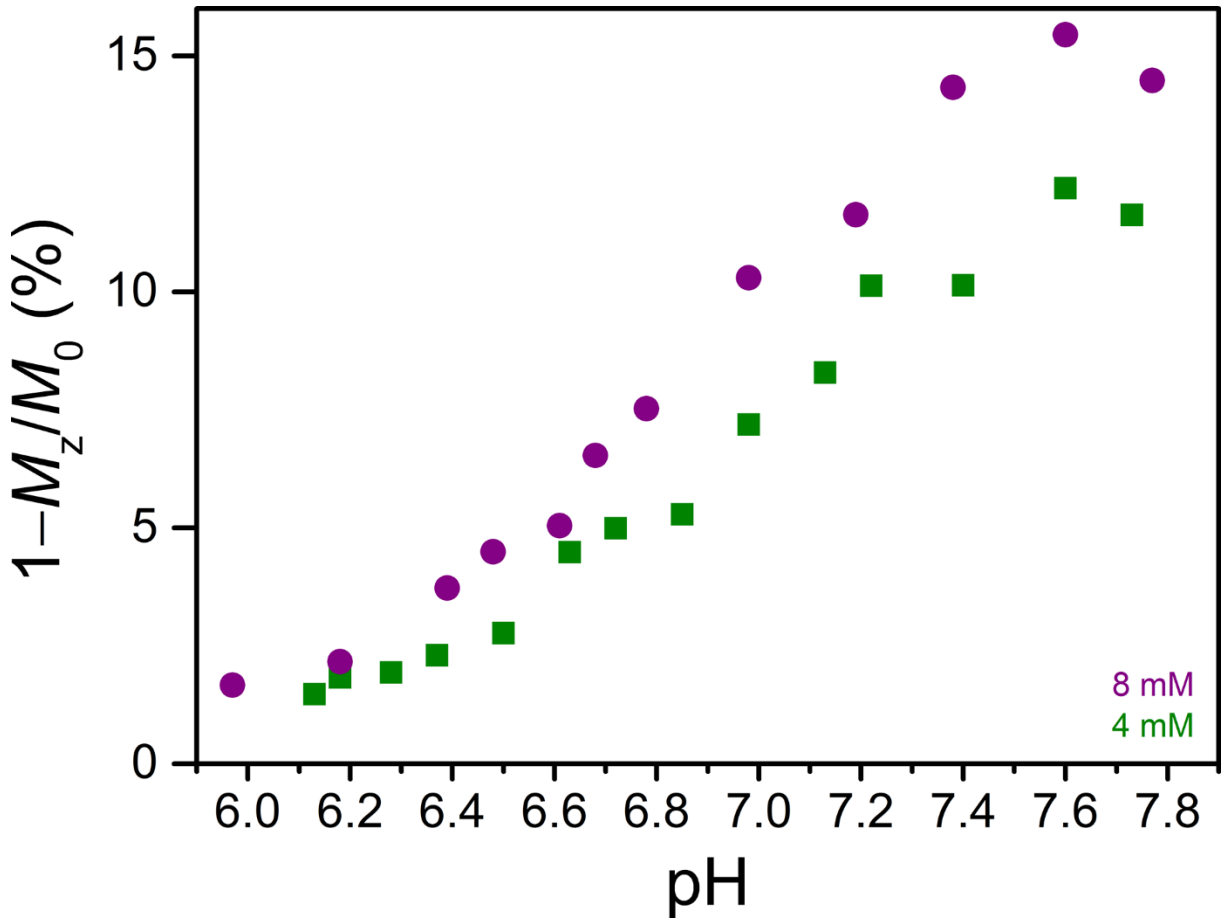

Figure 4.69 Comparison of the pH dependence of the CEST effect from application of presaturation at 44 ppm for various concentrations of **2-NO$_2$** (see legend) in aqueous solutions containing 50 mM HEPES and 100 mM NaCl at 37 °C.

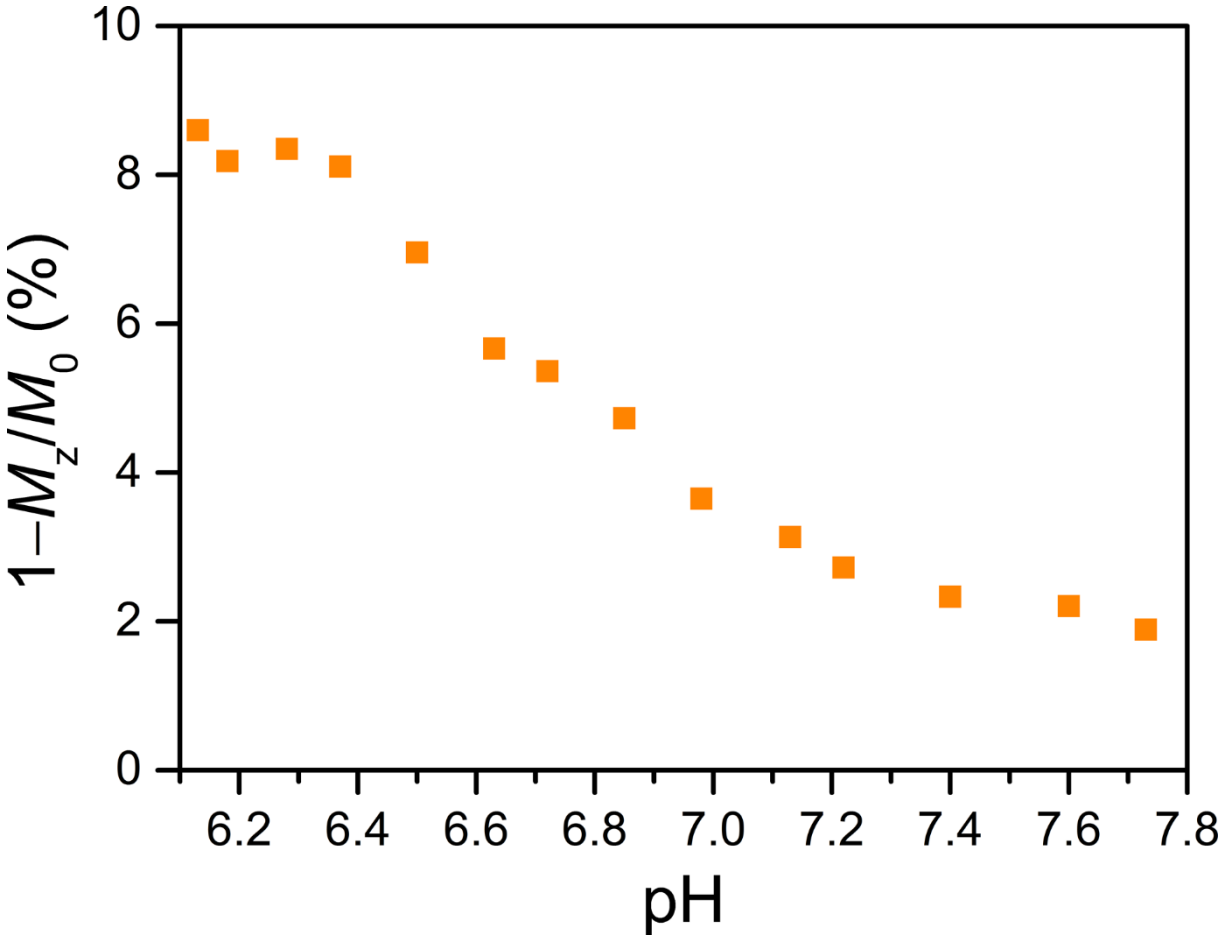

Figure 4.70 pH dependence of the CEST effect from application of presaturation at 113–117 ppm for 4 mM of **2-NO$_2$** in aqueous solutions containing 50 mM HEPES and 100 mM NaCl at 37 °C. For each pH value, presaturation at the frequency offset corresponding to maximum reduction in the H_2O signal intensity was employed (see Table 4.7).

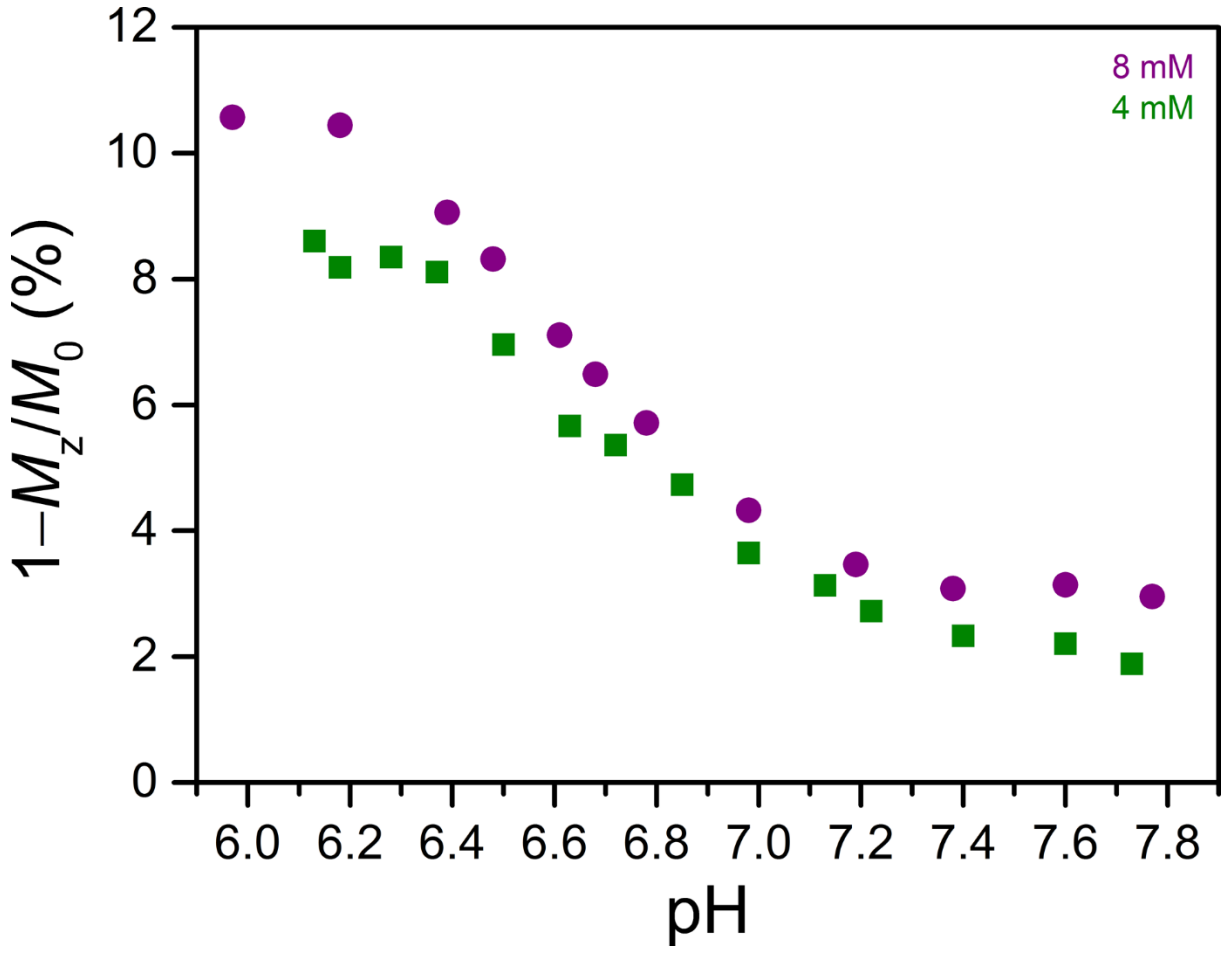

Figure 4.71 Comparison of the pH dependence of the maximum OH CEST effect for various concentrations of **2-NO_2** (see legend) in aqueous solutions containing 50 mM HEPES and 100 mM NaCl at 37 °C. For each pH value, presaturation at the frequency offset corresponding to maximum reduction in the H_2O signal intensity was employed (see Tables 4.4 and 4.7).

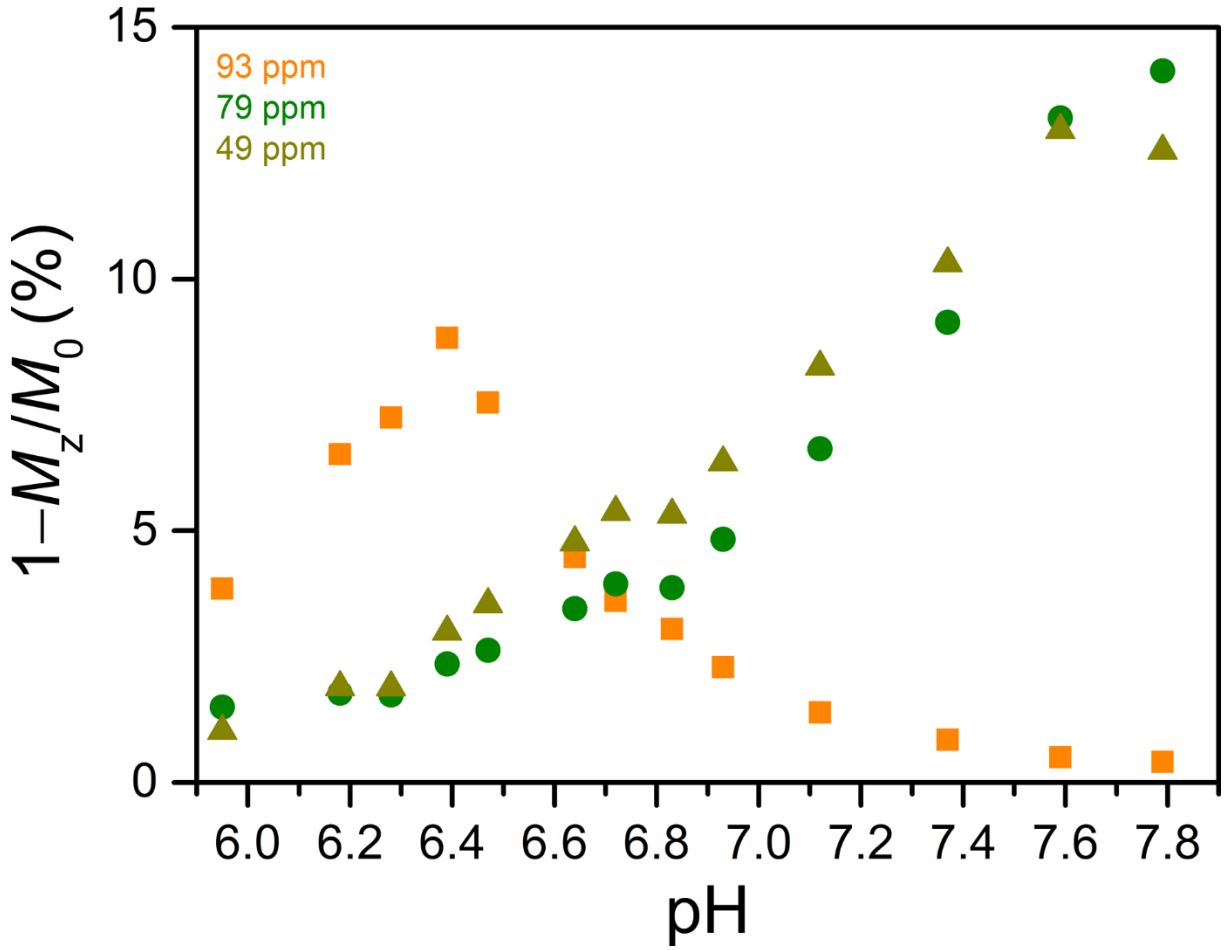

Figure 4.72 pH dependences of the CEST effects from application of presaturation at 93 ppm (yellow), 79 ppm (green), and 49 ppm (dark yellow) for 4 mM of **2-F** in aqueous solutions containing 50 mM HEPES and 100 mM NaCl at 37 °C.

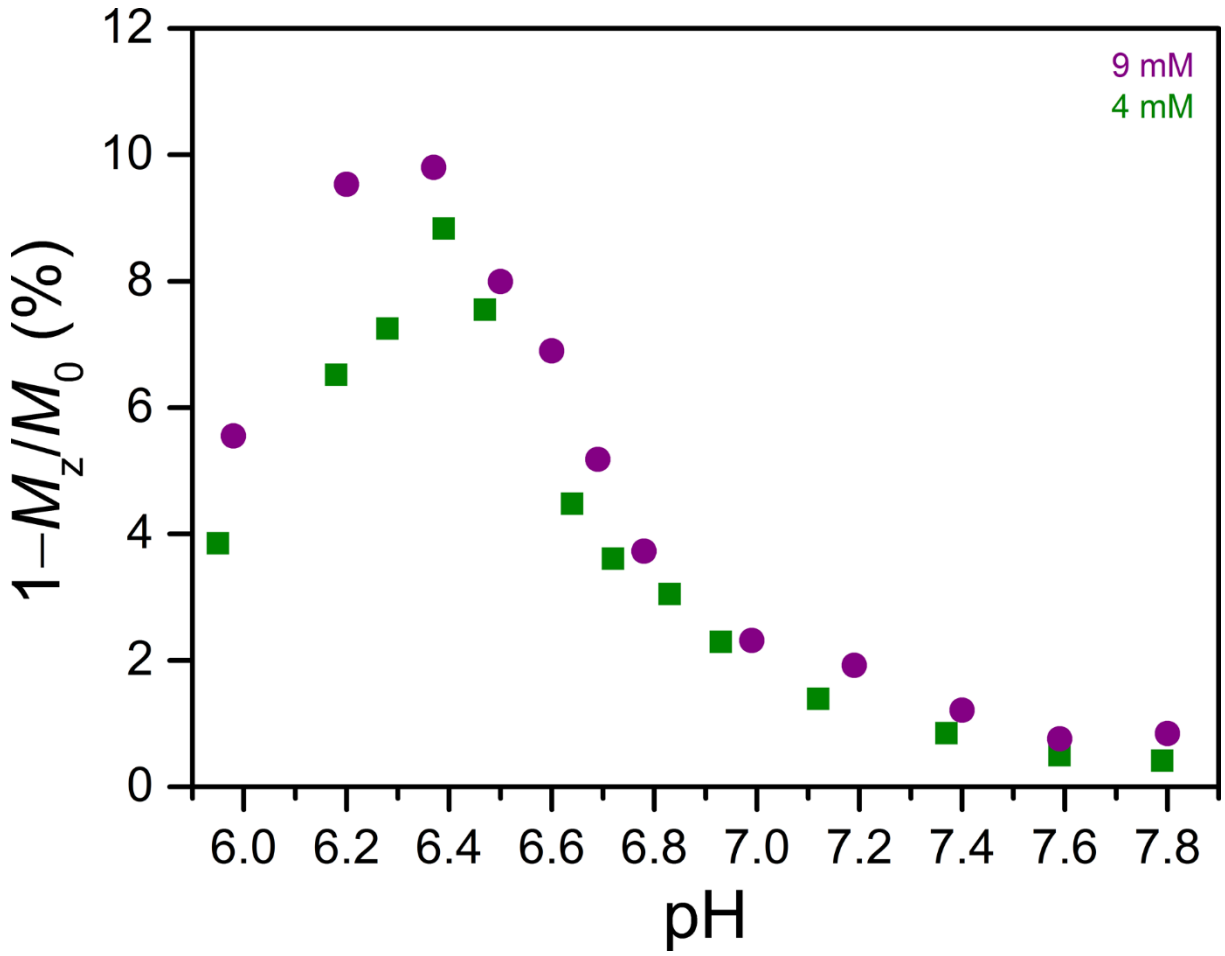

Figure 4.73 Comparison of the pH dependence of the CEST effect from application of presaturation at 93 ppm for various concentrations of **2-F** (see legend) in aqueous solutions containing 50 mM HEPES and 100 mM NaCl at 37 °C.

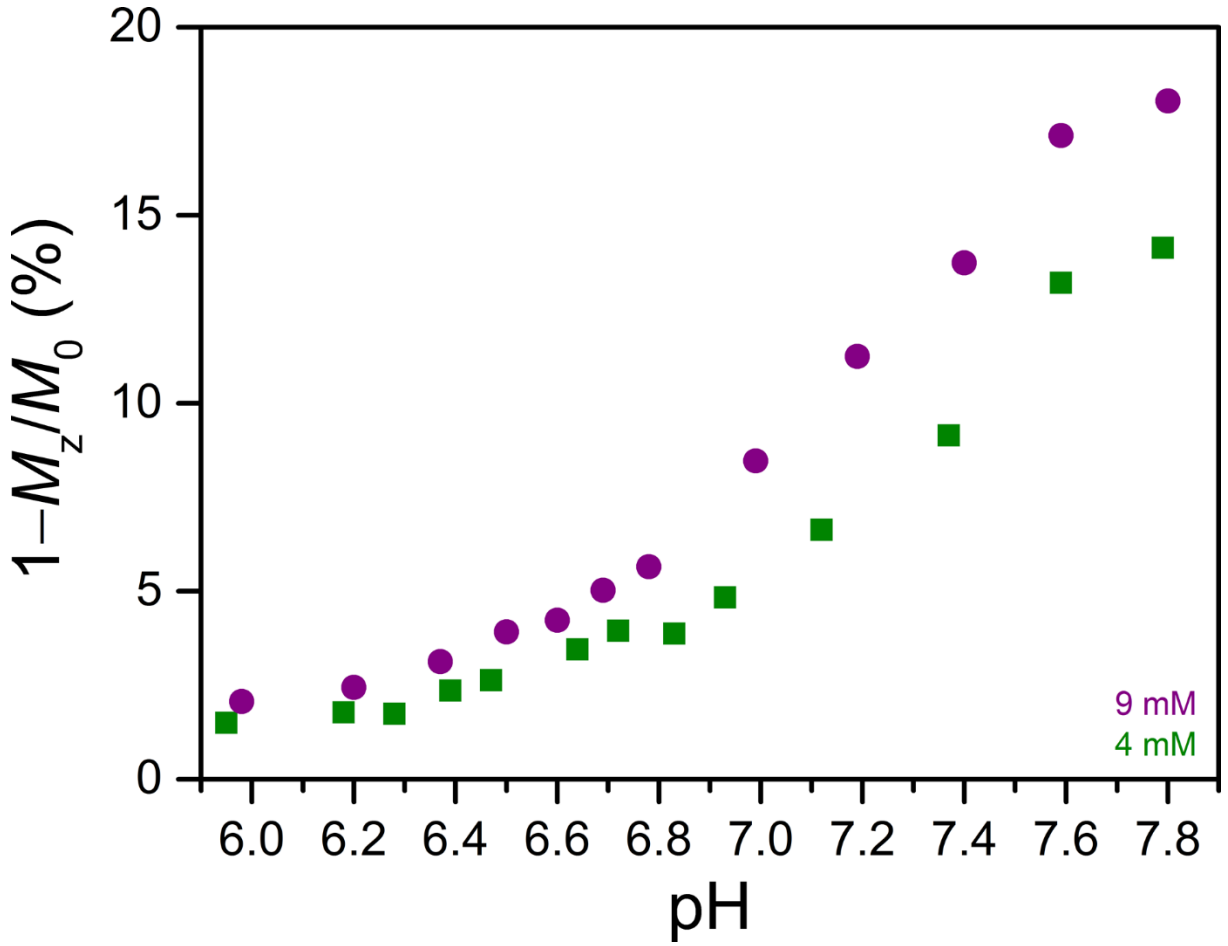

Figure 4.74 Comparison of the pH dependence of the CEST effect from application of presaturation at 79 ppm for various concentrations of **2-F** (see legend) in aqueous solutions containing 50 mM HEPES and 100 mM NaCl at 37 °C.

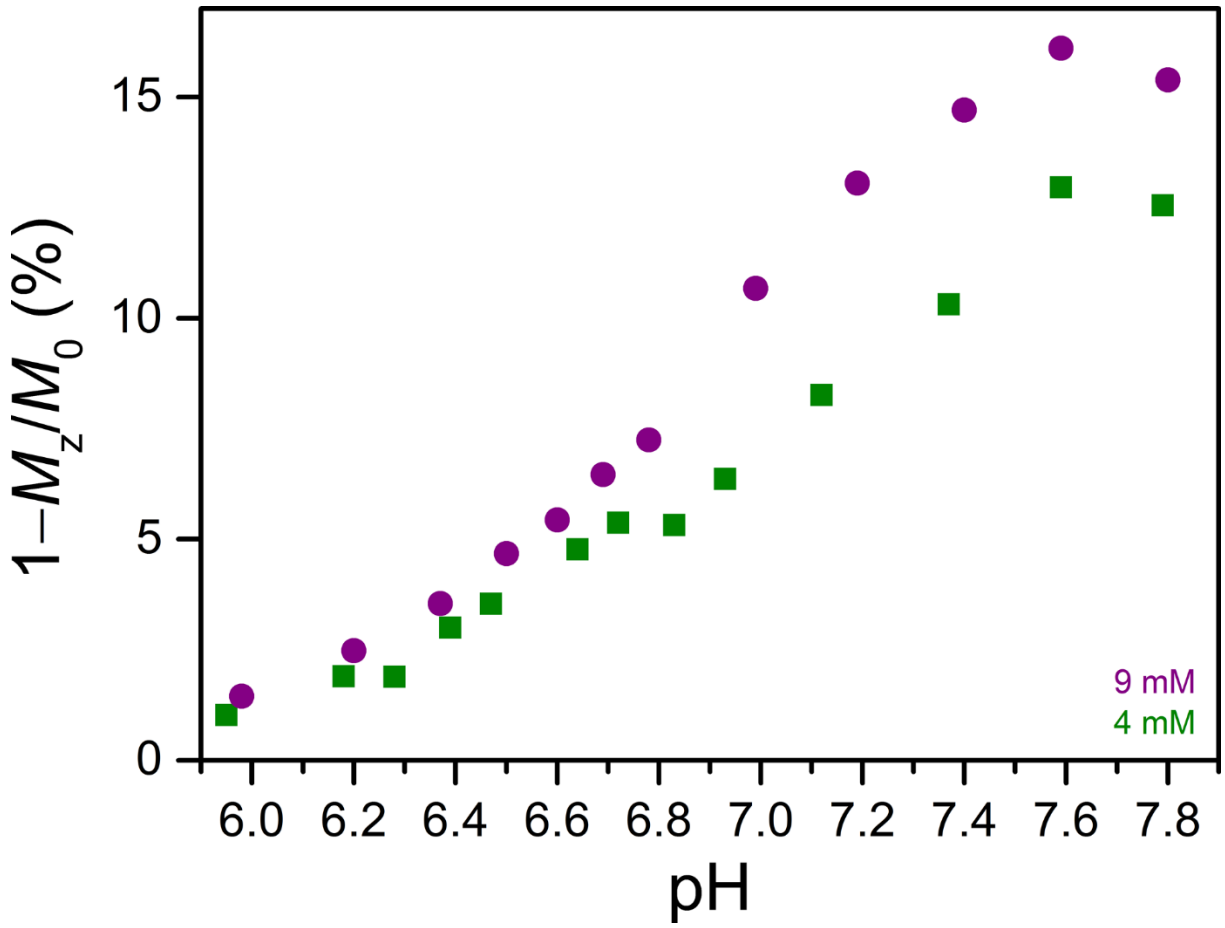

Figure 4.75 Comparison of the pH dependence of the CEST effect from application of presaturation at 49 ppm for various concentrations of **2-F** (see legend) in aqueous solutions containing 50 mM HEPES and 100 mM NaCl at 37 °C.

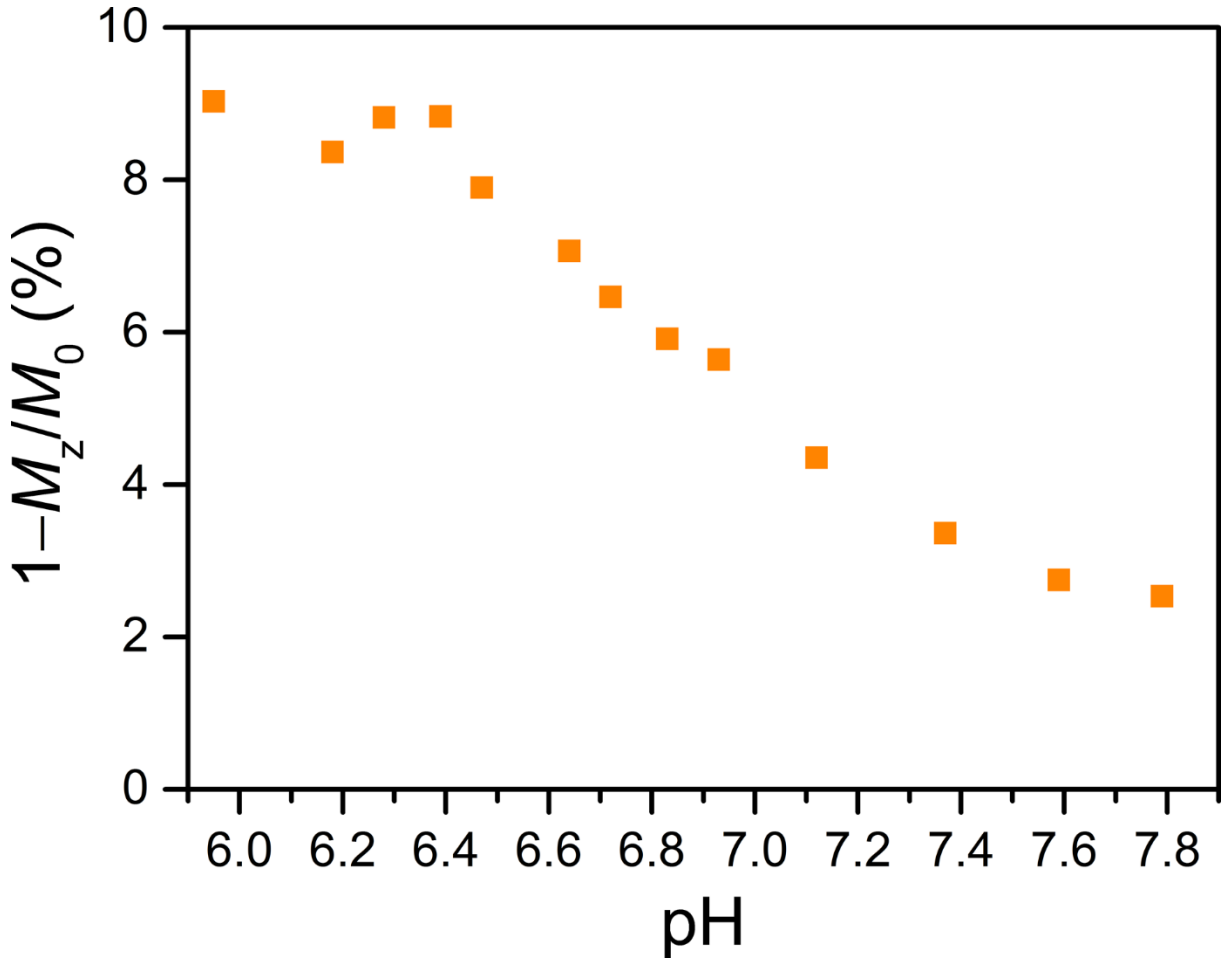

Figure 4.76 pH dependence of the CEST effect from application of presaturation at 90–97 ppm for 4 mM of **2-F** in aqueous solutions containing 50 mM HEPES and 100 mM NaCl at 37 °C. For each pH value, presaturation at the frequency offset corresponding to maximum reduction in the H_2O signal intensity was employed (see Table 4.8).

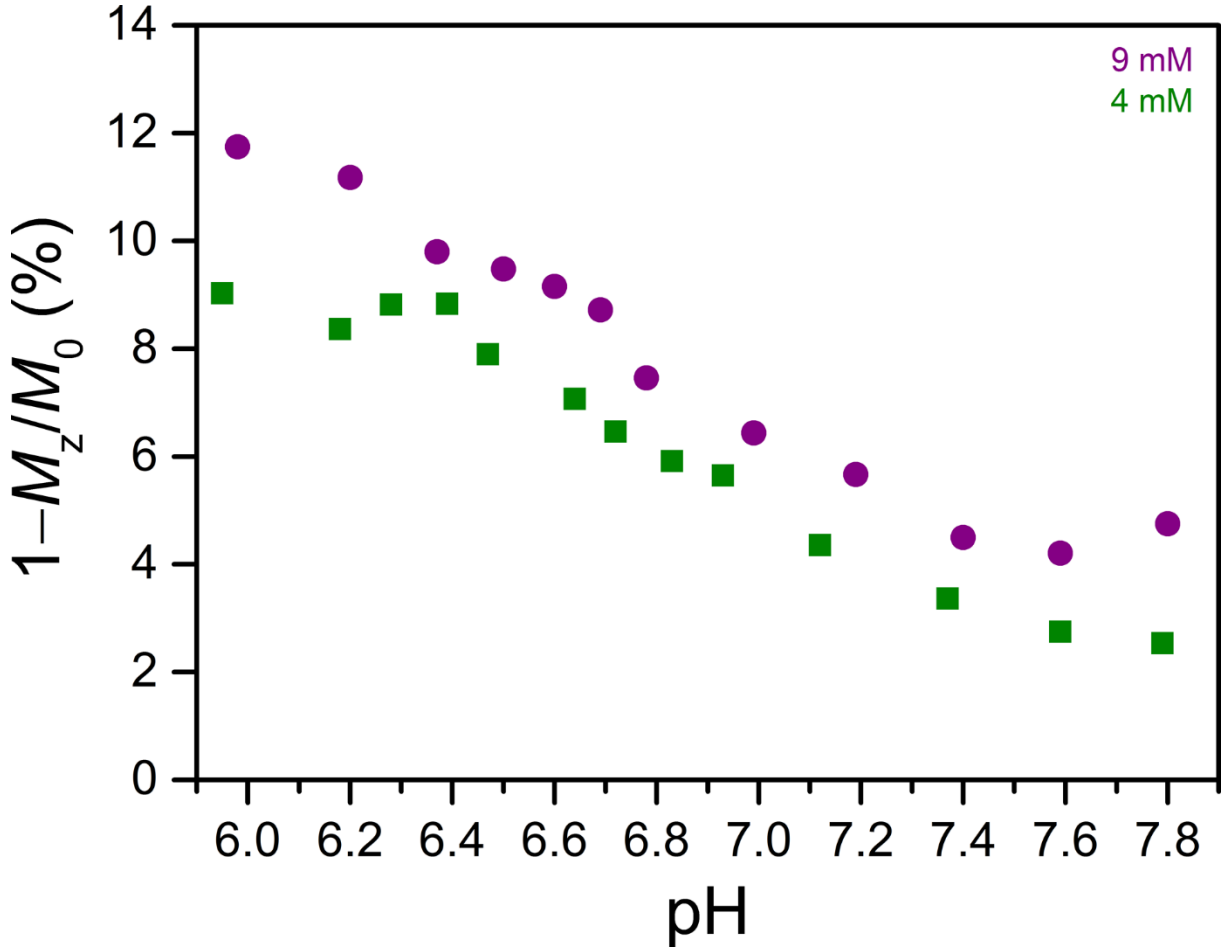

Figure 4.77 Comparison of the pH dependence of the maximum OH CEST effect for various concentrations of **2-F** (see legend) in aqueous solutions containing 50 mM HEPES and 100 mM NaCl at 37 °C. For each pH value, presaturation at the frequency offset corresponding to maximum reduction in the H_2O signal intensity was employed (see Tables 4.5 and 4.8).

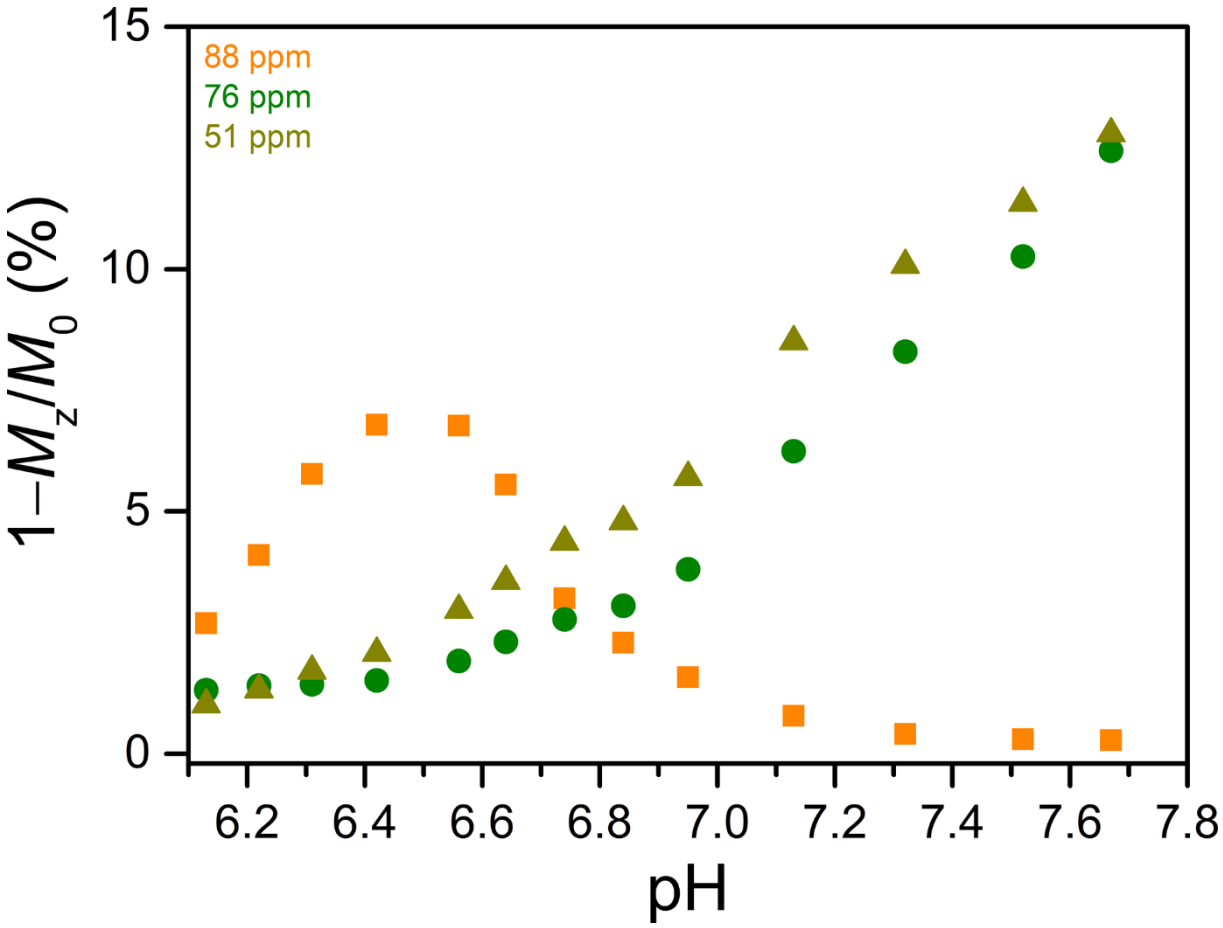

Figure 4.78 pH dependences of the CEST effects from application of presaturation at 88 ppm (yellow), 76 ppm (green), and 51 ppm (dark yellow) for 4 mM of **2-Me** in aqueous solutions containing 50 mM HEPES and 100 mM NaCl at 37 °C.

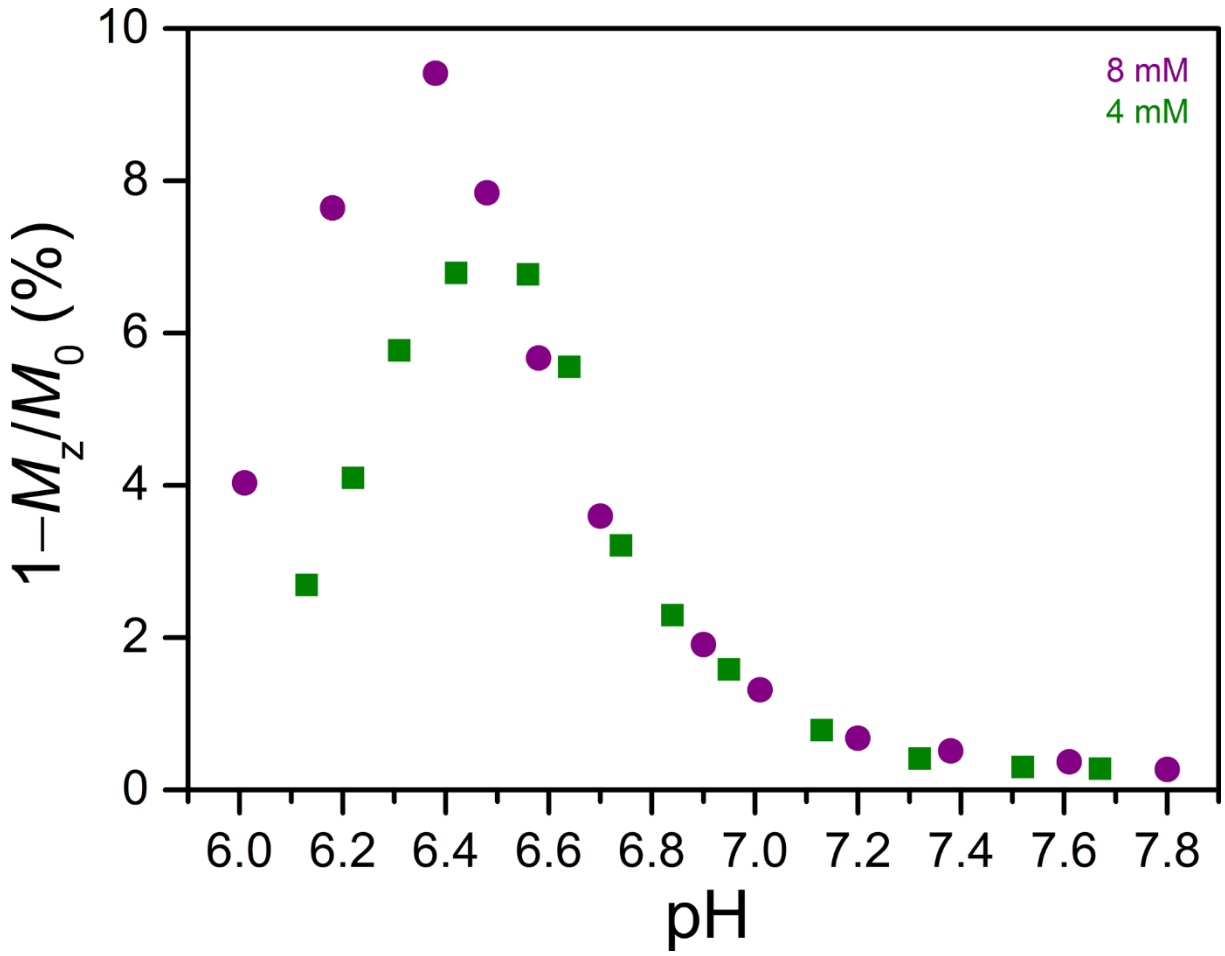

Figure 4.79 Comparison of the pH dependence of the CEST effect from application of presaturation at 88 ppm for various concentrations of **2-Me** (see legend) in aqueous solutions containing 50 mM HEPES and 100 mM NaCl at 37 °C.

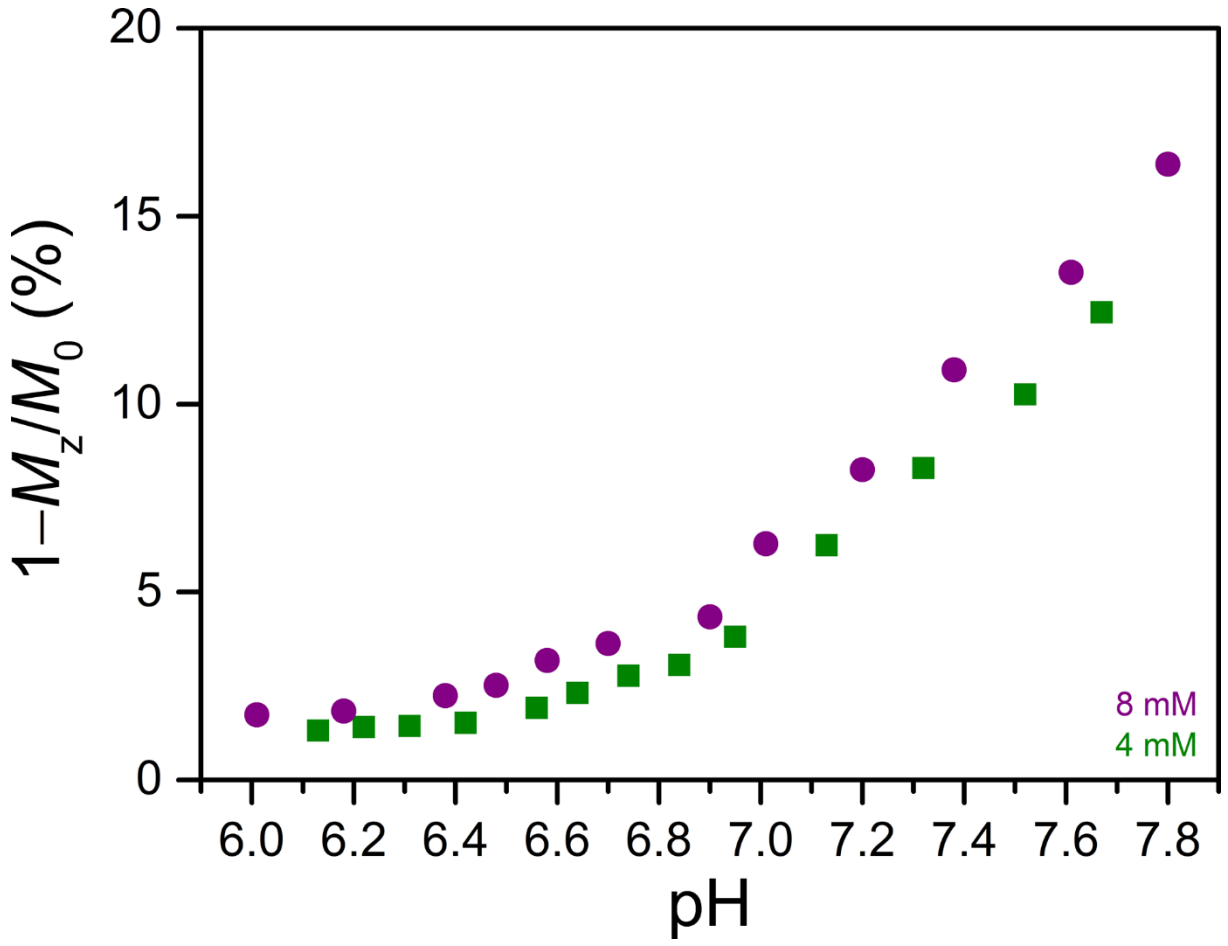

Figure 4.80 Comparison of the pH dependence of the CEST effect from application of presaturation at 76 ppm for various concentrations of **2-Me** (see legend) in aqueous solutions containing 50 mM HEPES and 100 mM NaCl at 37 °C.

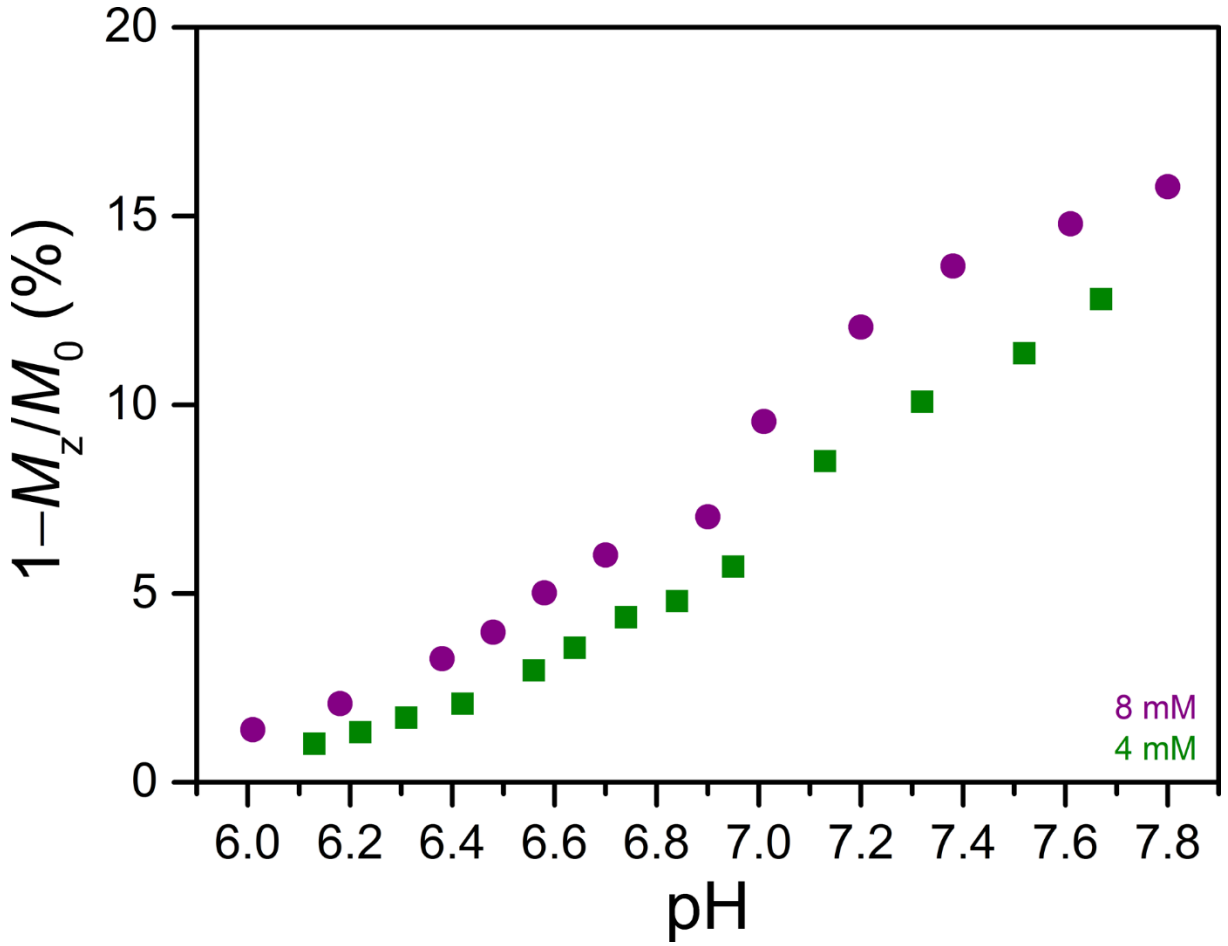

Figure 4.81 Comparison of the pH dependence of the CEST effect from application of presaturation at 51 ppm for various concentrations of **2-Me** (see legend) in aqueous solutions containing 50 mM HEPES and 100 mM NaCl at 37 °C.

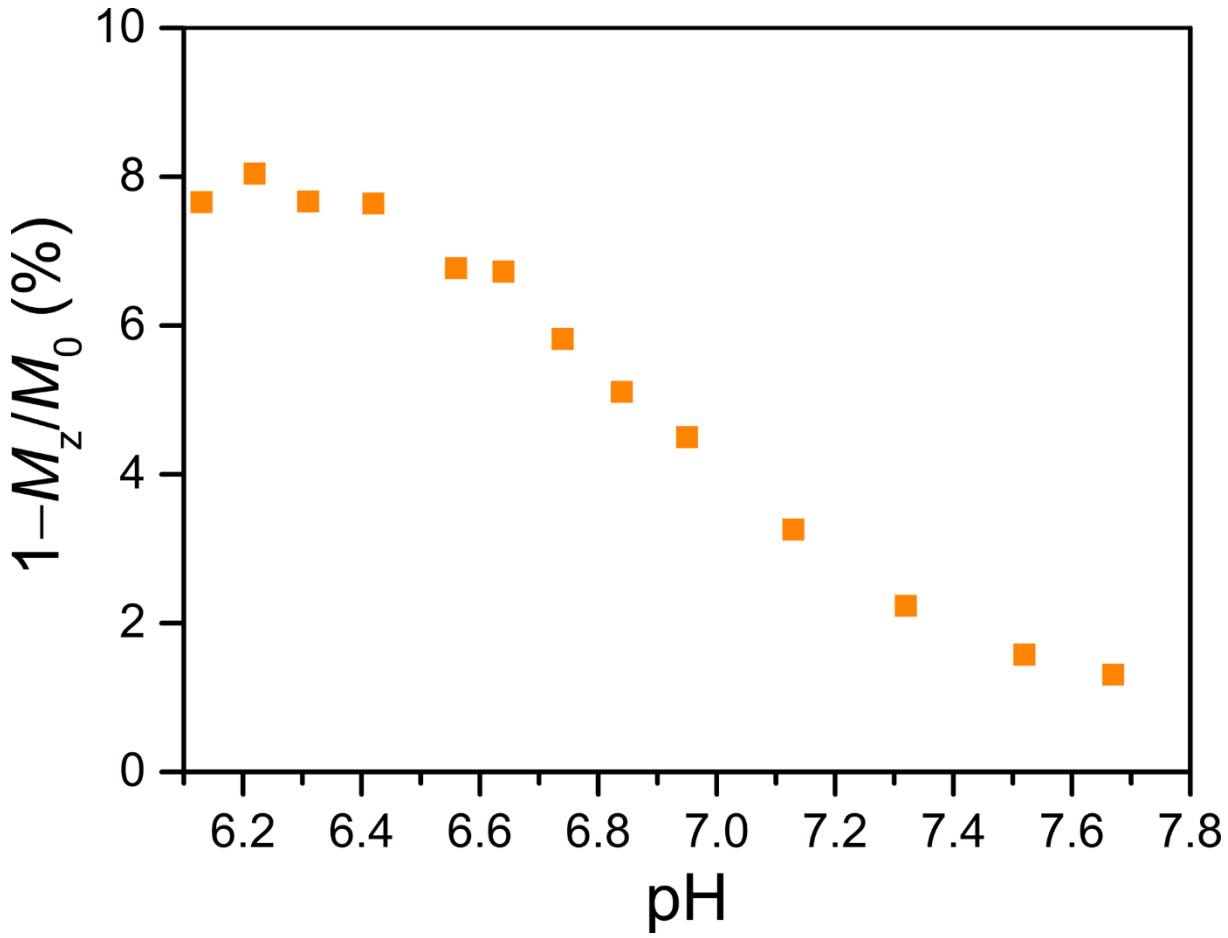

Figure 4.82 pH dependence of the CEST effect from application of presaturation at 85–92 ppm for 4 mM of **2-Me** in aqueous solutions containing 50 mM HEPES and 100 mM NaCl at 37 °C. For each pH value, presaturation at the frequency offset corresponding to maximum reduction in the H_2O signal intensity was employed (see Table 4.9).

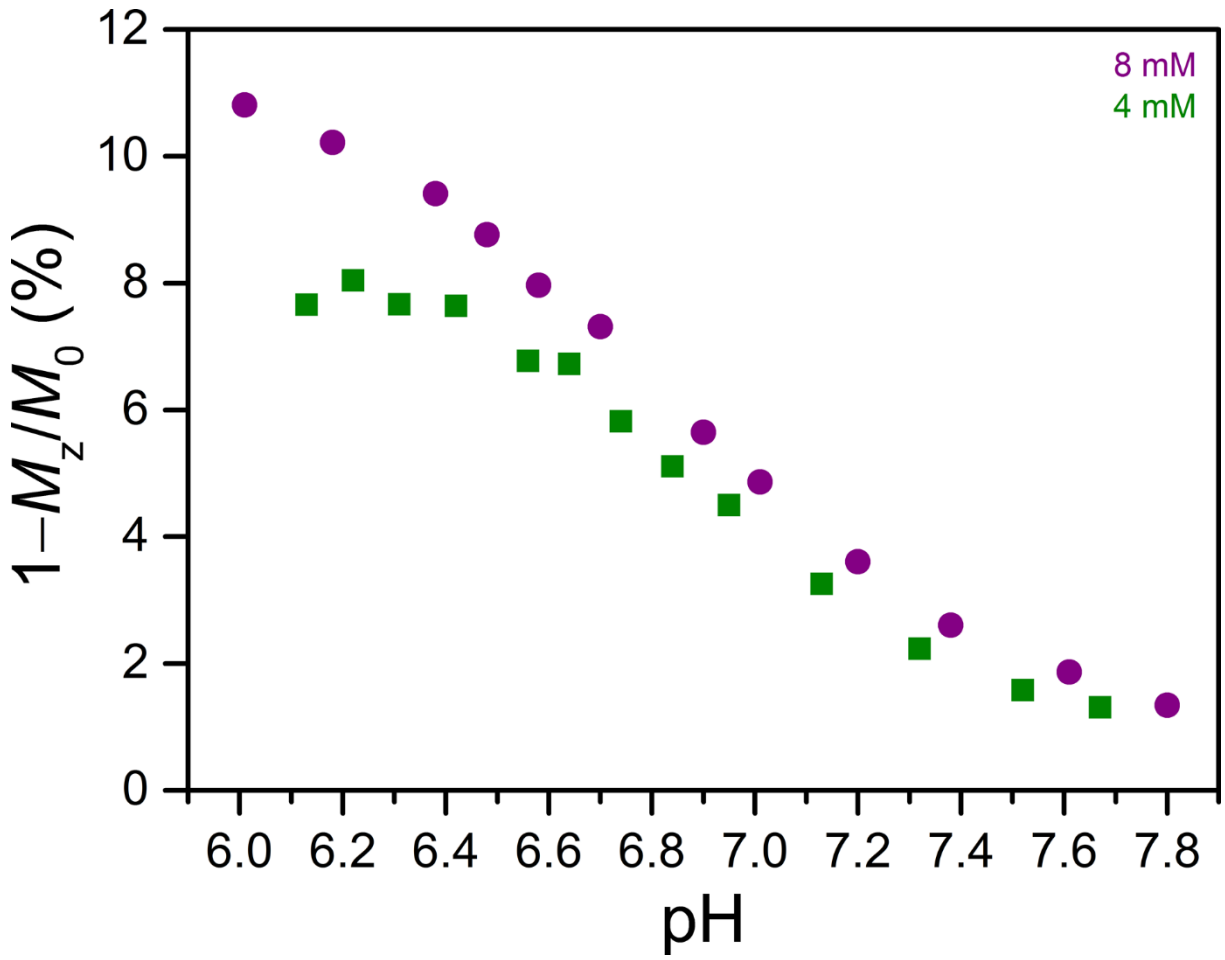

Figure 4.83 Comparison of the pH dependence of the maximum OH CEST effect for various concentrations of **2-Me** (see legend) in aqueous solutions containing 50 mM HEPES and 100 mM NaCl at 37 °C. For each pH value, presaturation at the frequency offset corresponding to maximum reduction in the H_2O signal intensity was employed (see Tables 4.6 and 4.9).

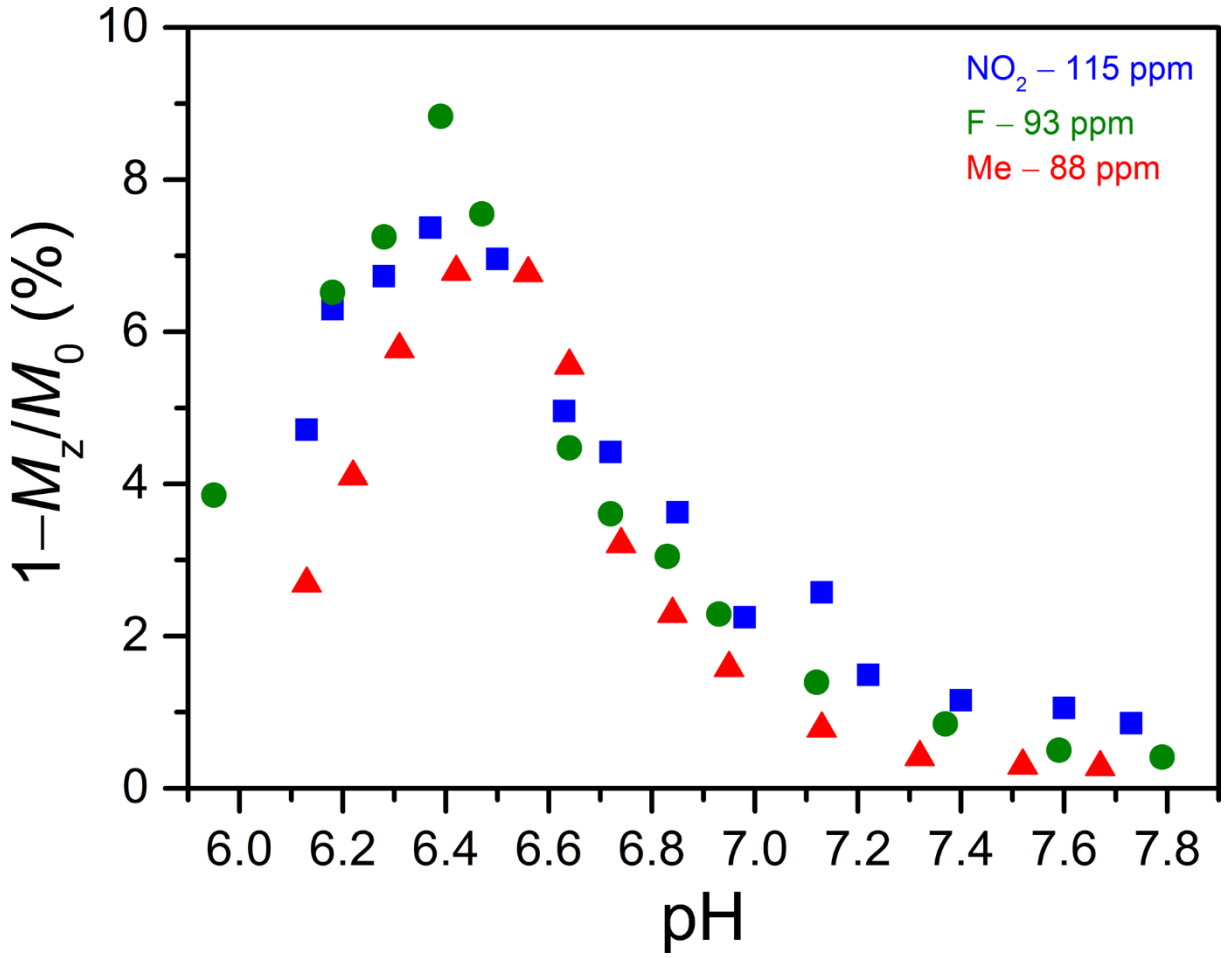

Figure 4.84 Comparison of the pH dependence of the OH CEST effect for 4 mM of **2-NO_2** (blue), **2-F** (green), and **2-Me** (red) in aqueous solutions containing 50 mM HEPES and 100 mM NaCl at 37 °C. The presaturation frequency employed for each compound is denoted in the legend.

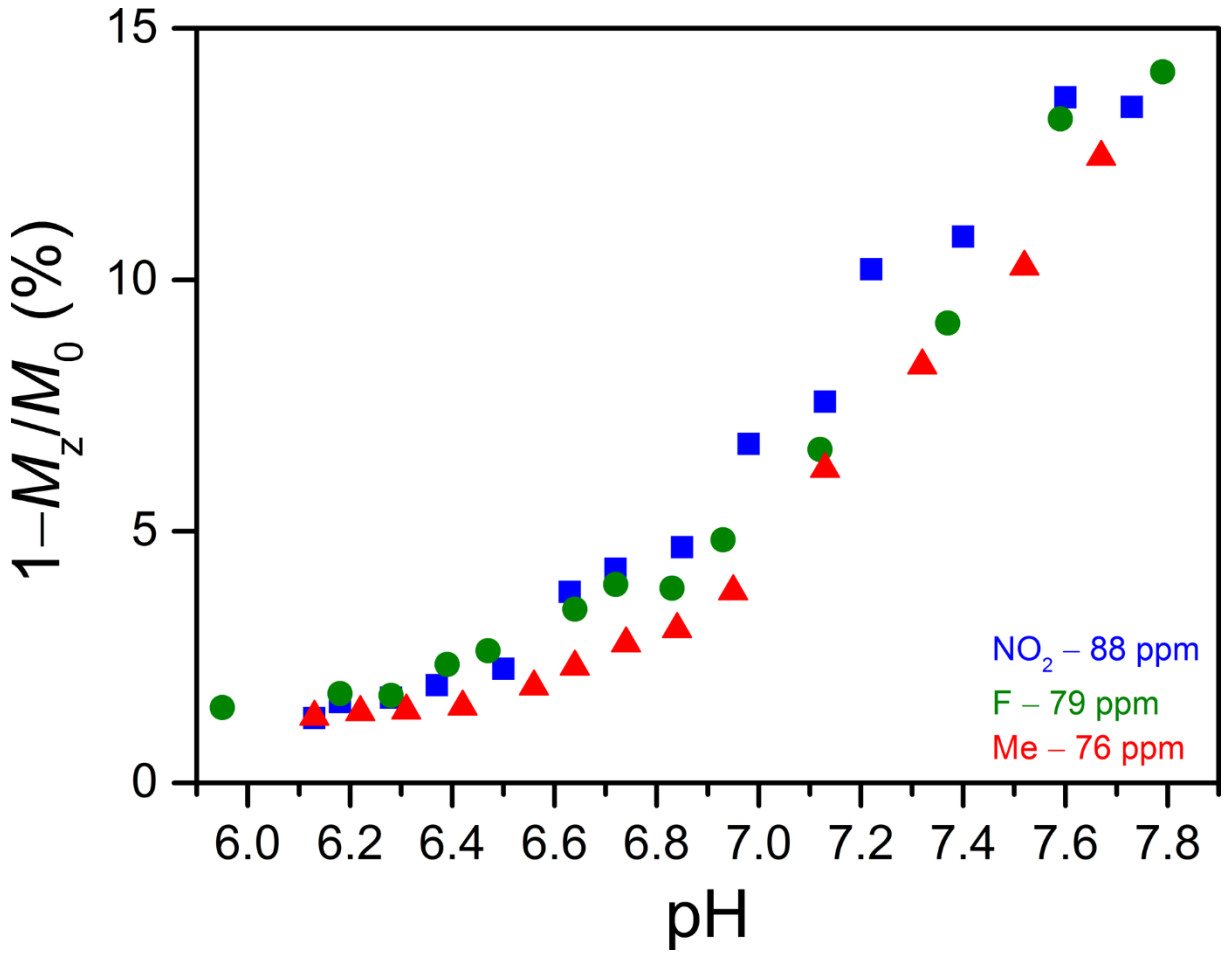

Figure 4.85 Comparison of the pH dependence of NH CEST effect for 4 mM of **2-NO₂** (blue), **2-F** (green), and **2-Me** (red) in aqueous solutions containing 50 mM HEPES and 100 mM NaCl at 37 °C. The presaturation frequency employed for each compound is denoted in the legend.

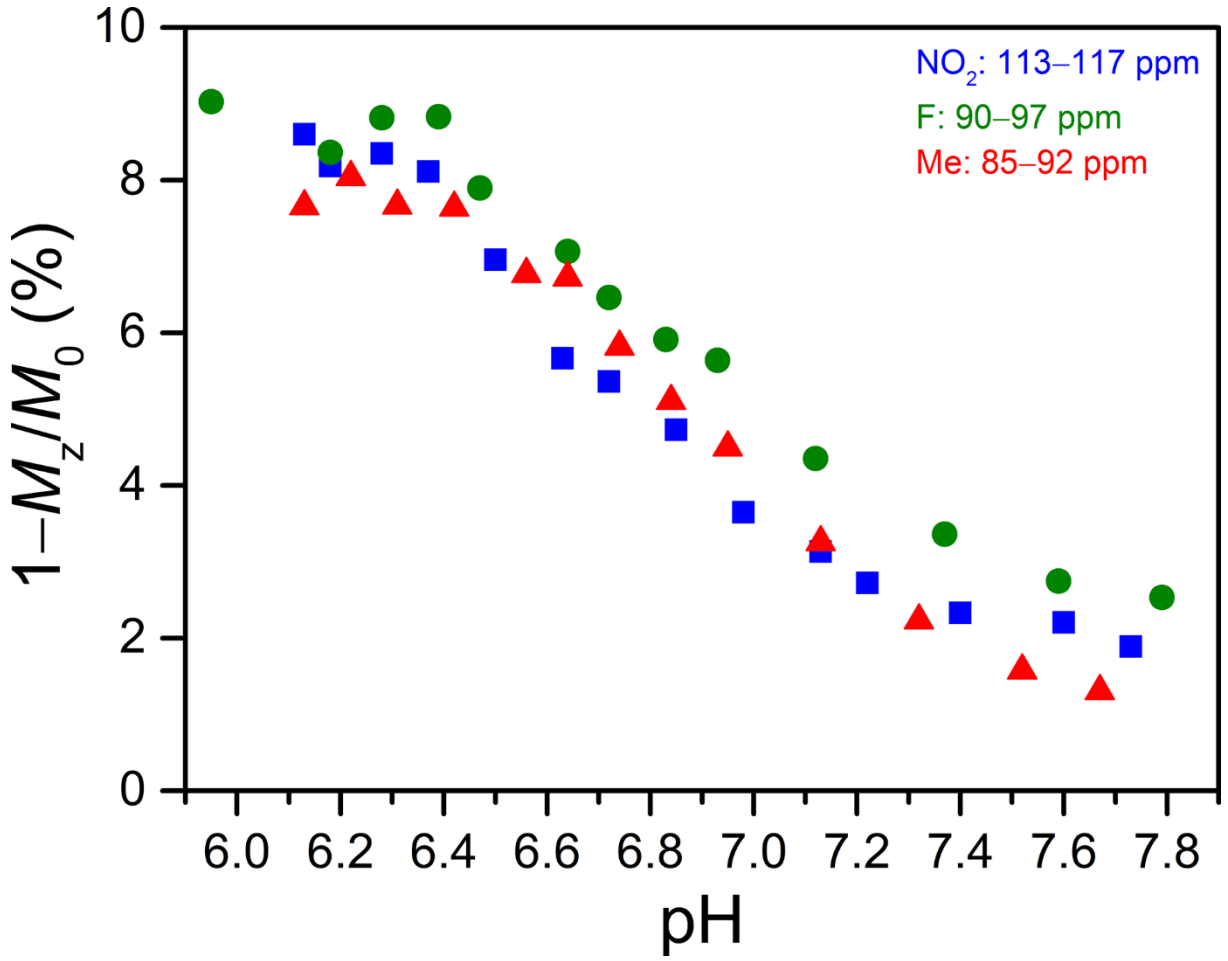

Figure 4.86 Comparison of the pH dependence of the maximum OH CEST effect for 4 mM of **2-NO_2** (blue), **2-F** (green), and **2-Me** (red) in aqueous solutions containing 50 mM HEPES and 100 mM NaCl at 37 °C. For each pH value, presaturation at the frequency offset corresponding to maximum reduction in the H_2O signal intensity was employed (see Tables 4.7–4.9). The range of presaturation frequencies employed for each compound is denoted in the legend.

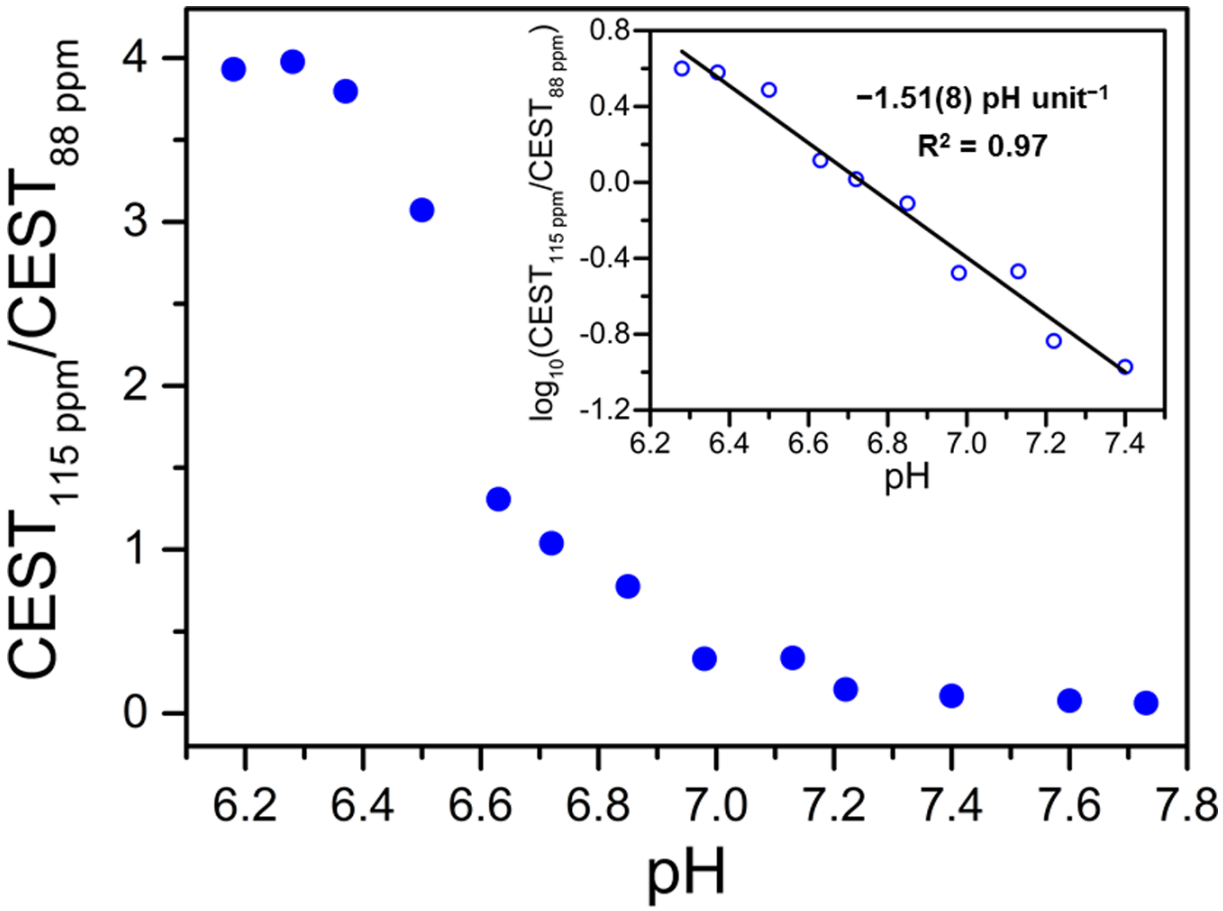

Figure 4.87 pH dependences of the ratio of CEST effects from application of presaturation at 115 and 88 ppm, and the logarithm with base 10 of the ratio (inset) for 4 mM of **2-NO₂** in aqueous solutions containing 50 mM HEPES and 100 mM NaCl at 37 °C. Blue circles represent experimental data and the solid black line denotes a linear fit to the data with the following equation: $\log_{10}(CEST_{115\ ppm}/CEST_{88\ ppm}) = -1.51(8) \times pH + 10.2(6)$; $R^2 = 0.97$.

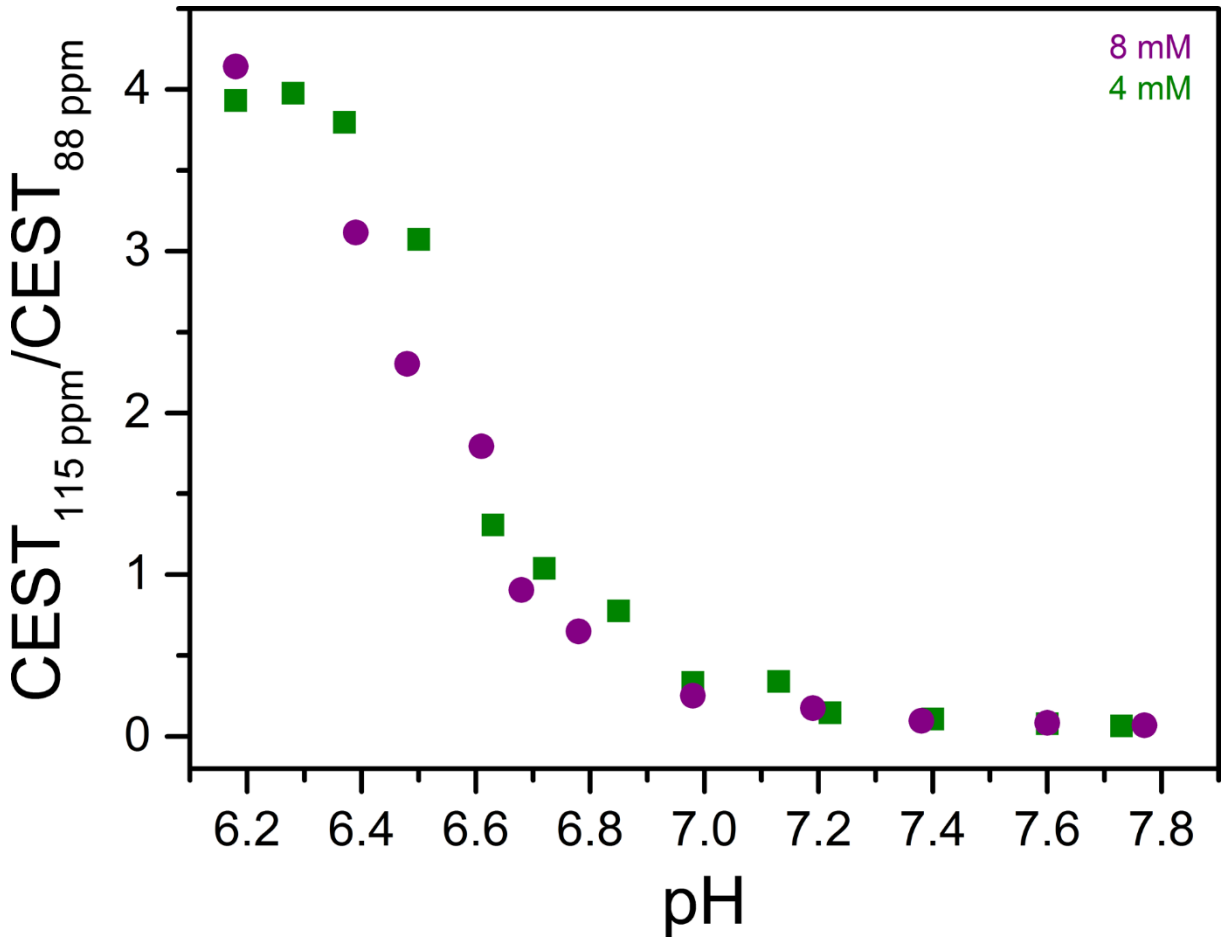

Figure 4.88 Comparison of the pH dependence of the ratio of CEST effects from application of presaturation at 115 and 88 ppm for various concentrations of **2-NO_2** (see legend) in aqueous solutions containing 50 mM HEPES and 100 mM NaCl at 37 °C.

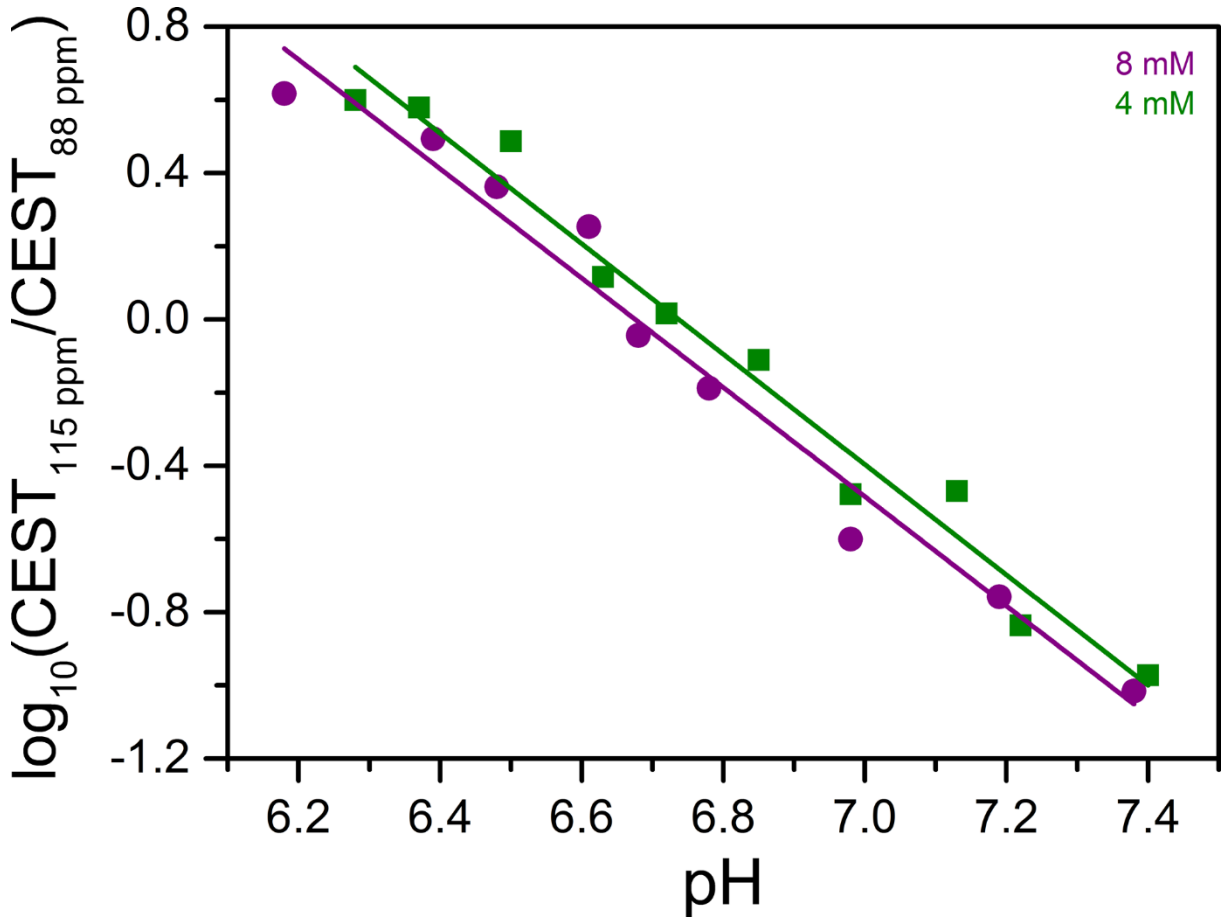

Figure 4.89 Comparison of the pH calibration curves obtained by taking the logarithm with base 10 of the ratios of CEST effects from application of presaturation at 115 and 88 ppm for various concentrations of **2-NO_2** (see legend) in aqueous solutions containing 50 mM HEPES and 100 mM NaCl at 37 °C. See Figures 4.62 and 4.87 for the equations of the linear fits to the data.

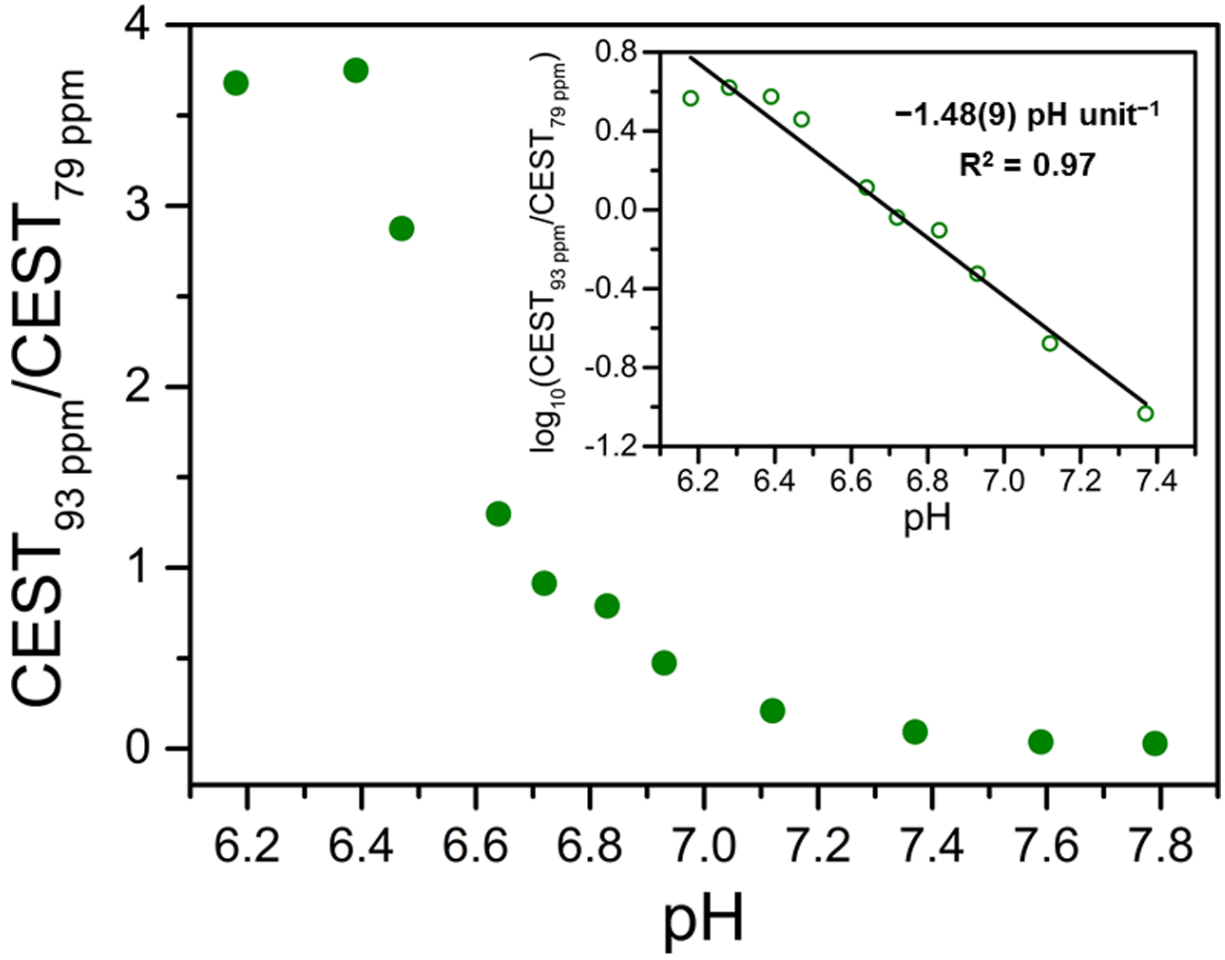

Figure 4.90 pH dependences of the ratio of CEST effects from application of presaturation at 93 and 79 ppm, and the logarithm with base 10 of the ratio (inset) for 4 mM of **2-F** in aqueous solutions containing 50 mM HEPES and 100 mM NaCl at 37 °C. Green circles represent experimental data and the solid black line denotes a linear fit to the data with the following equation: $\log_{10}(CEST_{93\ ppm}/CEST_{79\ ppm}) = -1.48(9) \times pH + 9.9(6)$; $R^2 = 0.97$.

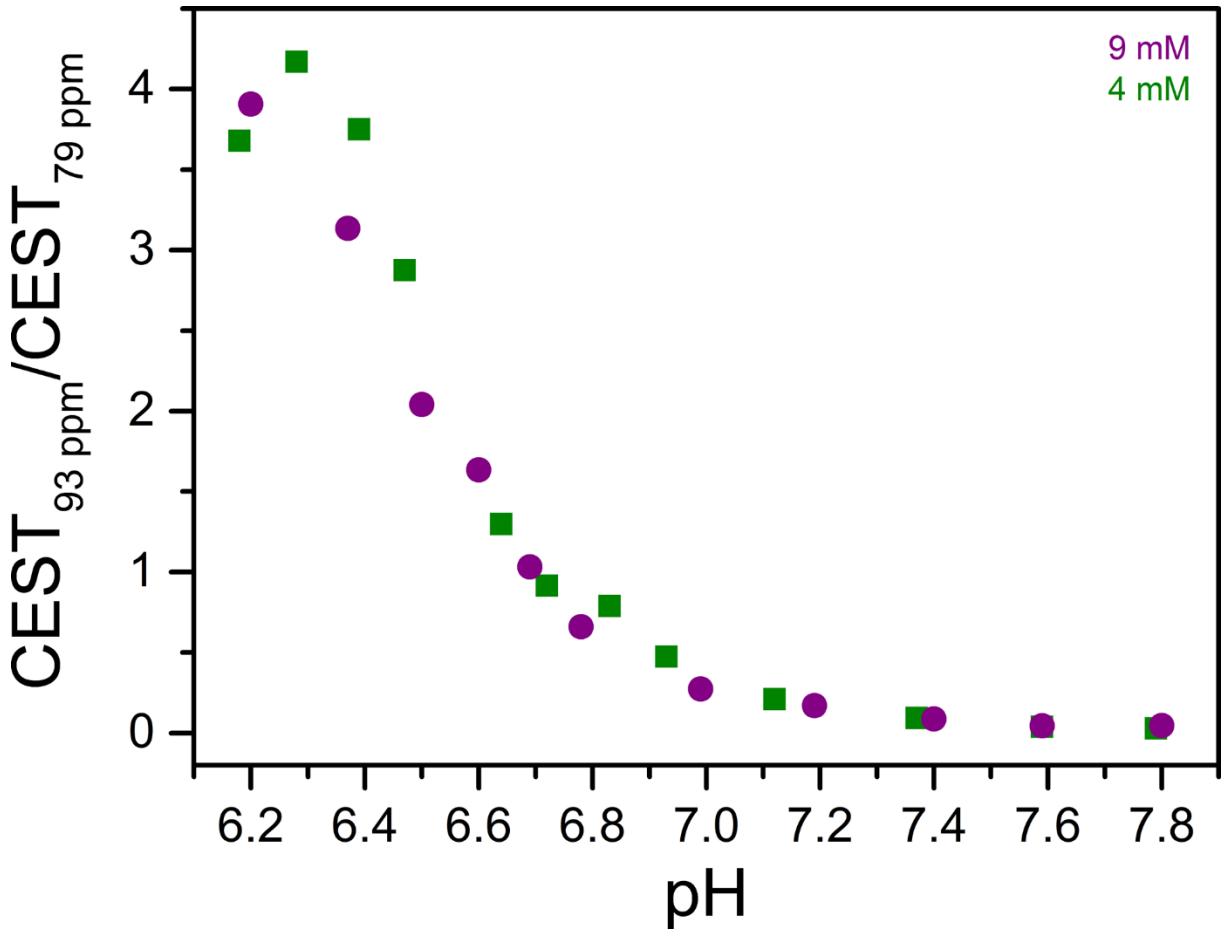

Figure 4.91 Comparison of the pH dependence of the ratio of CEST effects from application of presaturation at 93 and 79 ppm for various concentrations of **2-F** (see legend) in aqueous solutions containing 50 mM HEPES and 100 mM NaCl at 37 °C.

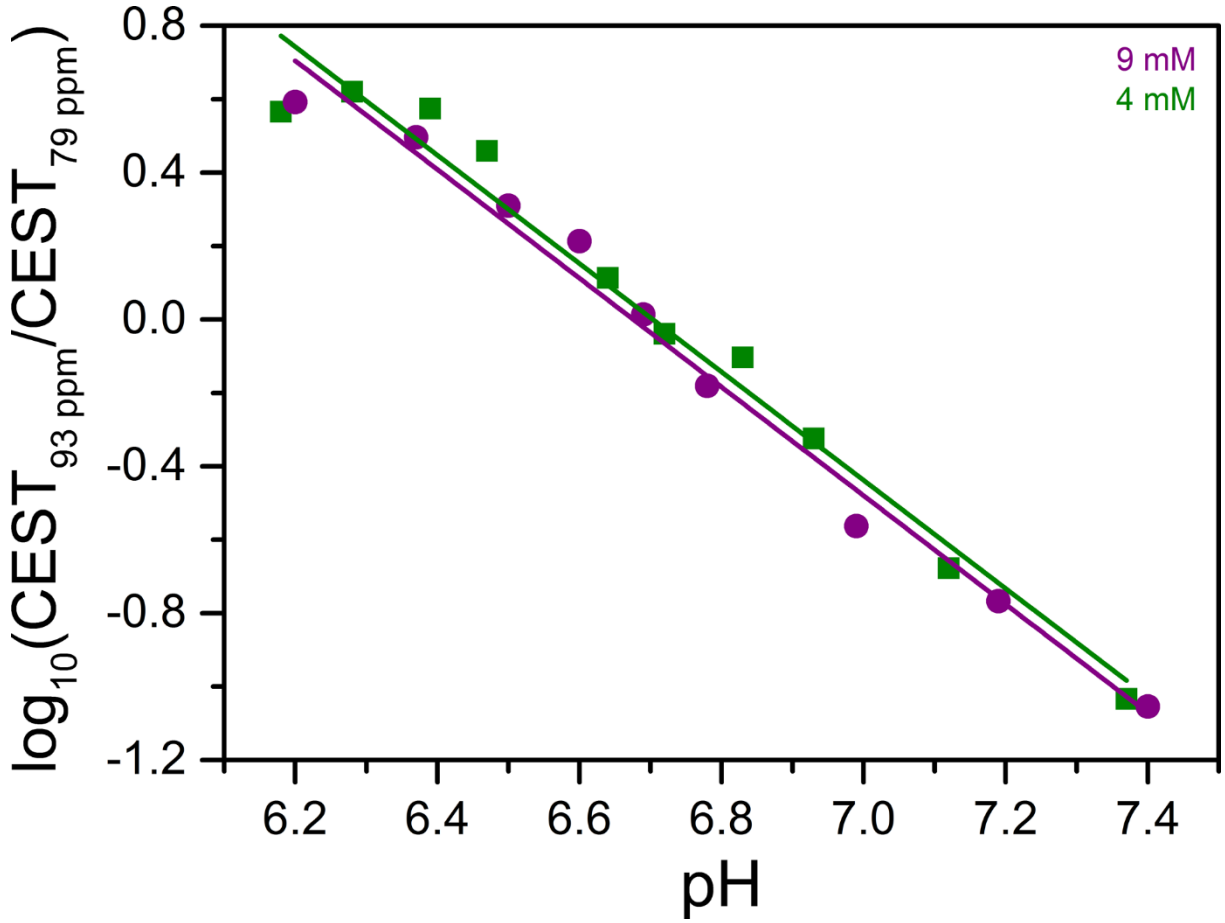

Figure 4.92 Comparison of the pH calibration curves obtained by taking the logarithm with base 10 of the ratios of CEST effects from application of presaturation at 93 and 79 ppm for various concentrations of **2-F** (see legend) in aqueous solutions containing 50 mM HEPES and 100 mM NaCl at 37 °C. See Figures 4.62 and 4.90 for the equations of the linear fits to the data.

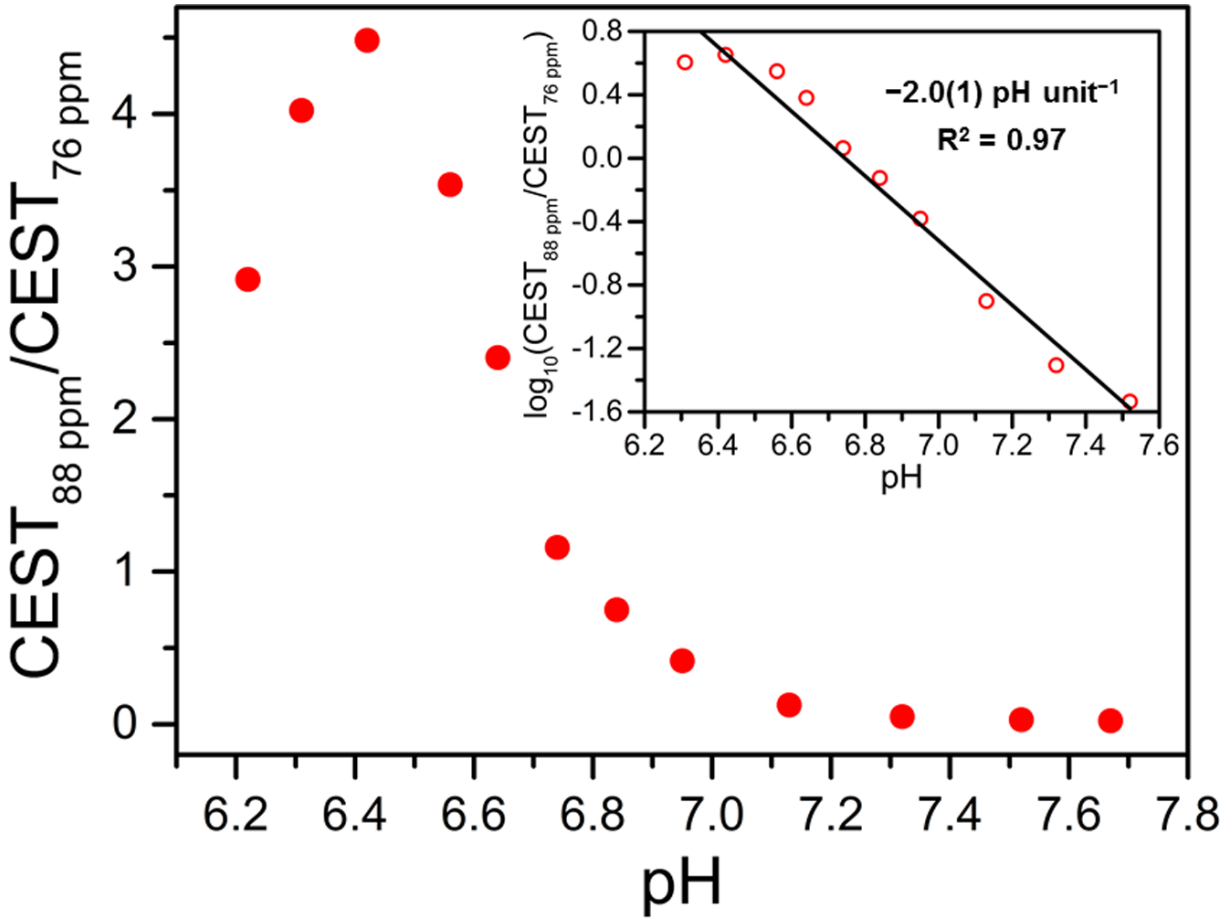

Figure 4.93 pH dependences of the ratio of CEST effects from application of presaturation at 88 and 76 ppm, and the logarithm with base 10 of the ratio (inset) for 4 mM of **2-Me** in aqueous solutions containing 50 mM HEPES and 100 mM NaCl at 37 °C. Red circles represent experimental data and the solid black line denotes a linear fit to the data with the following equation: $\log_{10}(CEST_{88\ ppm}/CEST_{76\ ppm}) = -2.0(1) \times pH + 13.7(9)$; $R^2 = 0.97$.

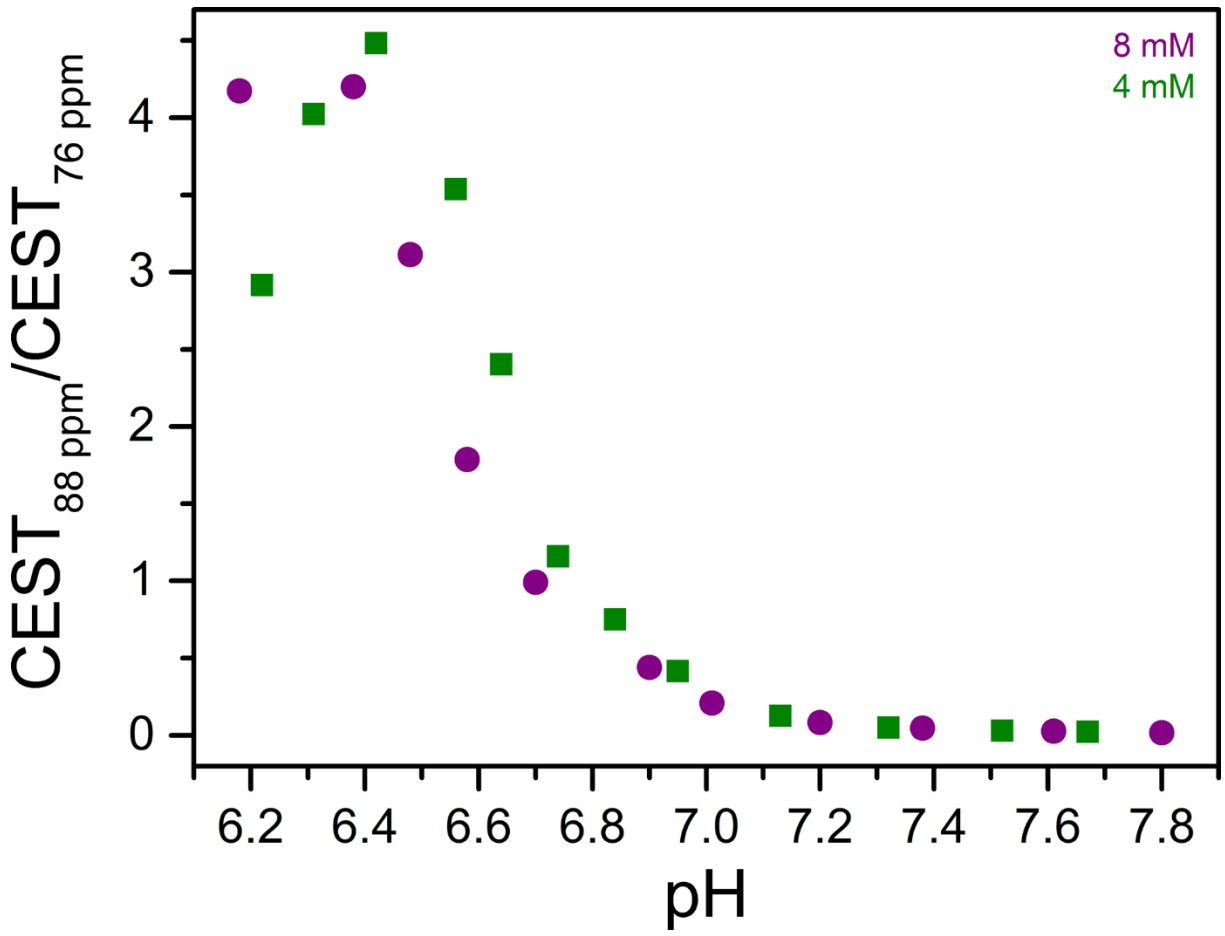

Figure 4.94 Comparison of the pH dependence of the ratio of CEST effects from application of presaturation at 88 and 76 ppm for various concentrations of **2-Me** (see legend) in aqueous solutions containing 50 mM HEPES and 100 mM NaCl at 37 °C.

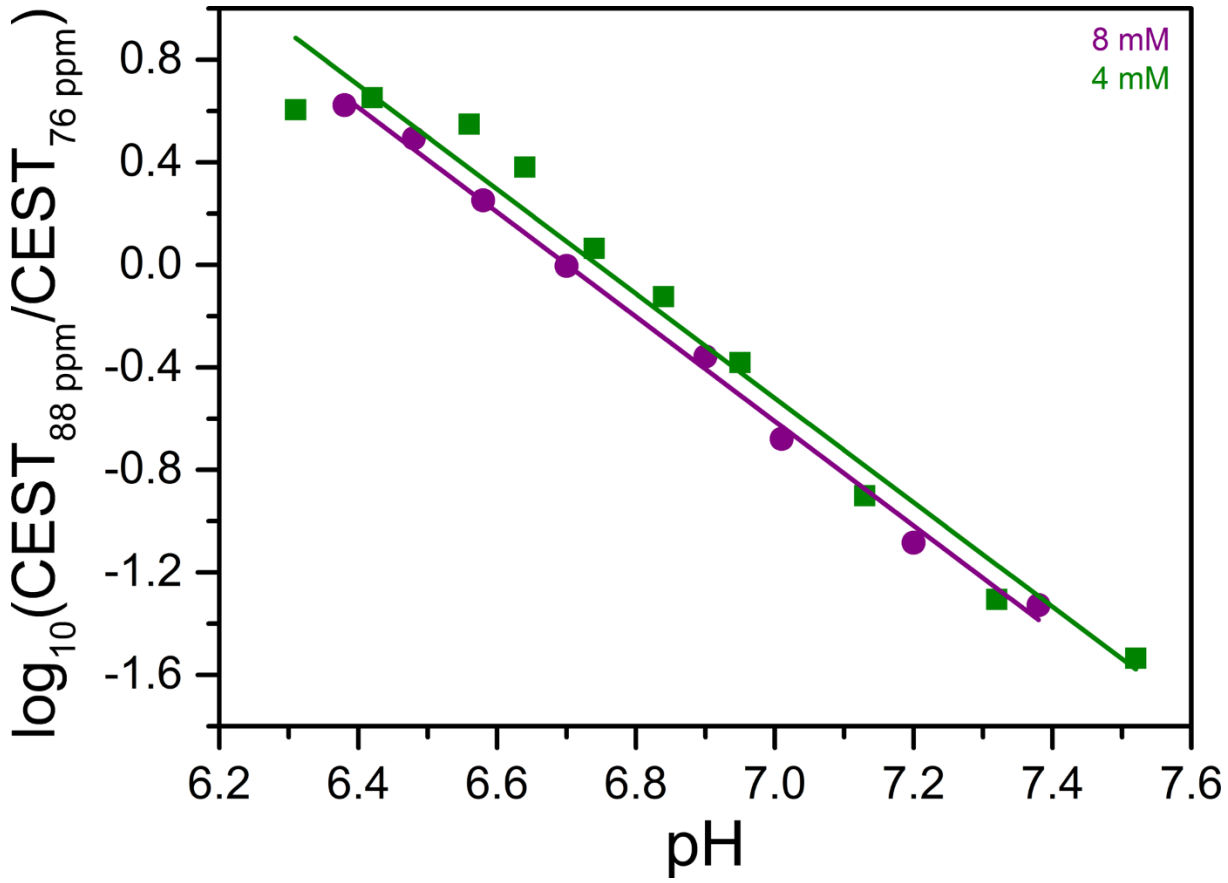

Figure 4.95 Comparison of the pH calibration curves obtained by taking the logarithm with base 10 of the ratios of CEST effects from application of presaturation at 88 and 76 ppm for various concentrations of **2-Me** (see legend) in aqueous solutions containing 50 mM HEPES and 100 mM NaCl at 37 °C. See Figures 4.62 and 4.93 for the equations of the linear fits to the data.

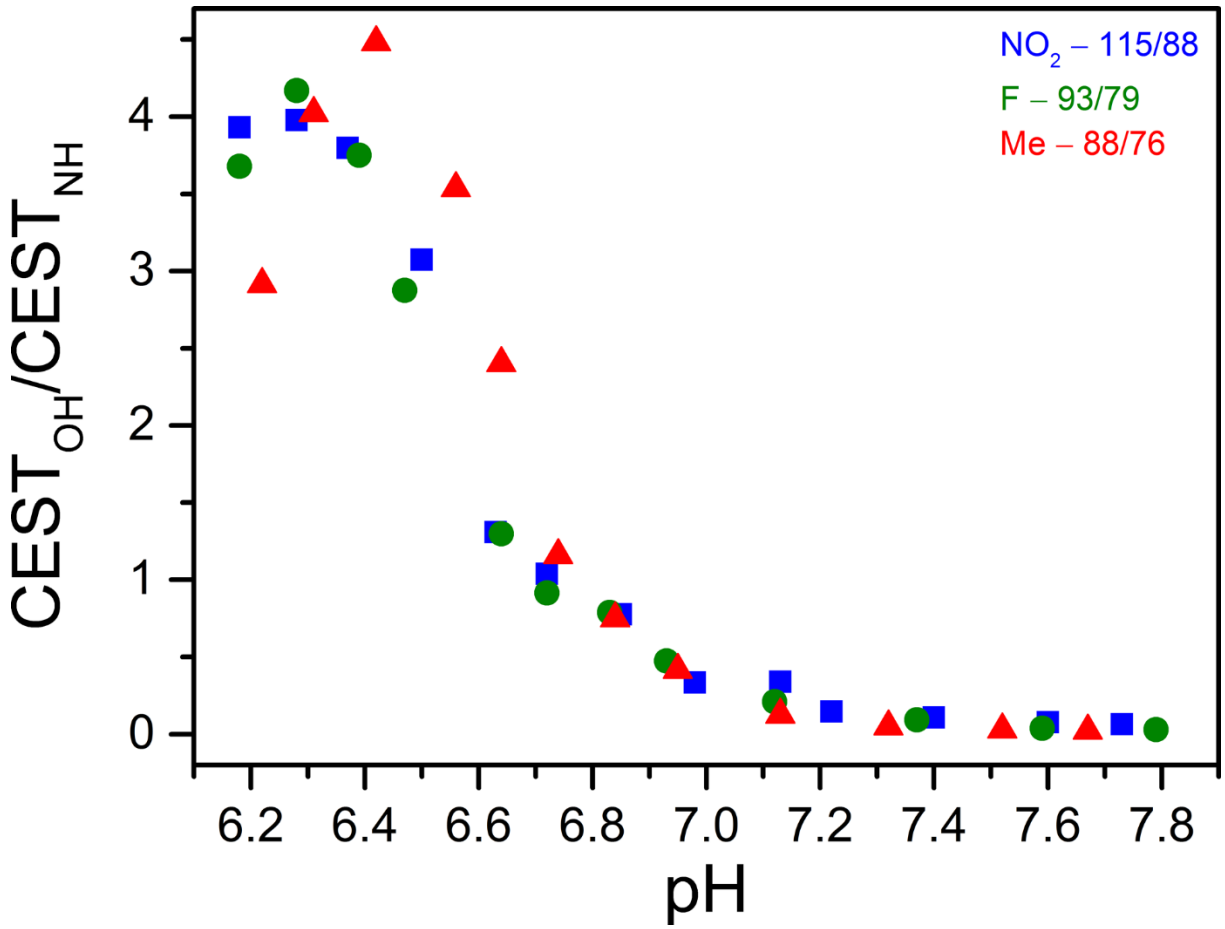

Figure 4.96 Comparison of the pH dependence of the ratio of OH and NH CEST effects for 4 mM of **2-NO_2** (blue), **2-F** (green), and **2-Me** (red) in aqueous solutions containing 50 mM HEPES and 100 mM NaCl at 37 °C. The presaturation frequencies employed for the two CEST effects for each compound are given in the legend.

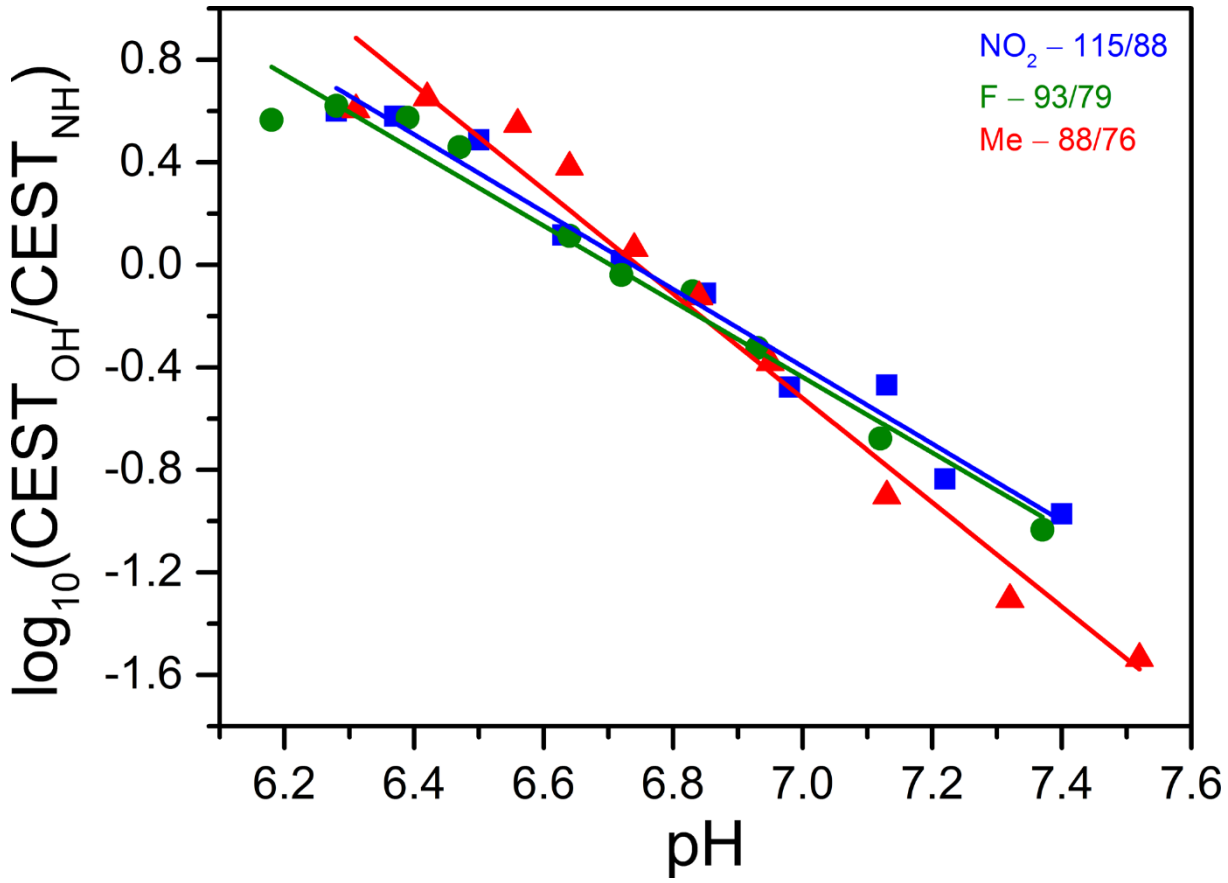

Figure 4.97 Comparison of the pH calibration curves obtained by taking the logarithm with base 10 of the ratios of OH and NH CEST effects for 4 mM of **2-NO₂** (blue), **2-F** (green), and **2-Me** (red) in aqueous solutions containing 50 mM HEPES and 100 mM NaCl at 37 °C. The presaturation frequencies employed for the two CEST effects for each compound are given in the legend. Solid symbols represent experimental data and the lines denote linear fits to the data. See Figures 4.87, 4.90, and 4.93 for the equations of the linear fits to the data.

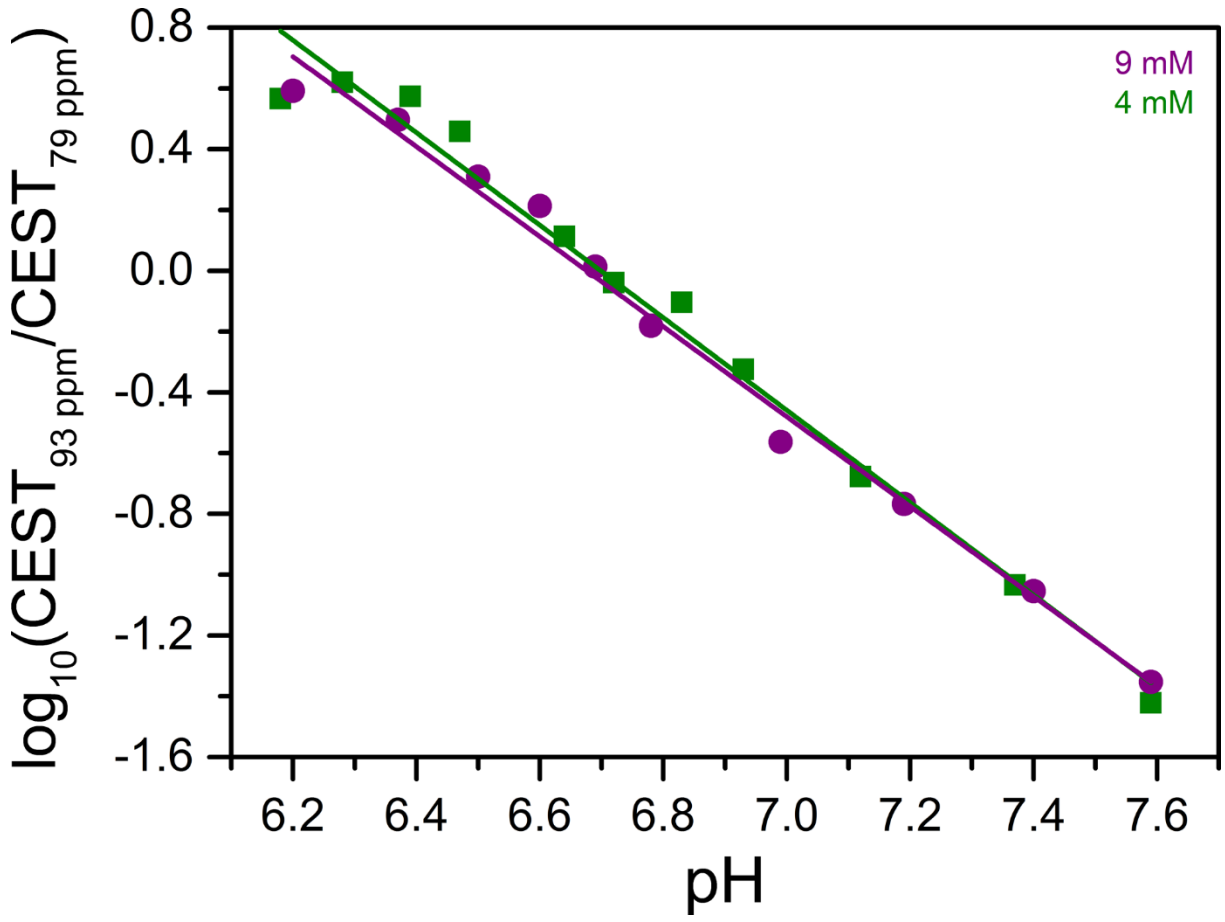

Figure 4.98 Comparison of the pH calibration curves obtained by taking the logarithm with base 10 of the ratios of CEST effects from application of presaturation at 93 and 79 ppm for various concentrations of **2-F** (see legend) in aqueous solutions containing 50 mM HEPES and 100 mM NaCl at 37 °C. These calibration curves were obtained from data in the pH range 6.2–7.6, whereas the calibration curves shown in Figure 4.92 were obtained from data in the pH range 6.2–7.4. Linear fits to the experimental data gave the following equations: (9 mM) $\log_{10}(\text{CEST}_{93\text{ ppm}}/\text{CEST}_{79\text{ ppm}}) = -1.48(5) \times \text{pH} + 9.9(4)$; $R^2 = 0.99$; (4 mM) $\log_{10}(\text{CEST}_{93\text{ ppm}}/\text{CEST}_{79\text{ ppm}}) = -1.52(7) \times \text{pH} + 10.2(5)$; $R^2 = 0.98$.

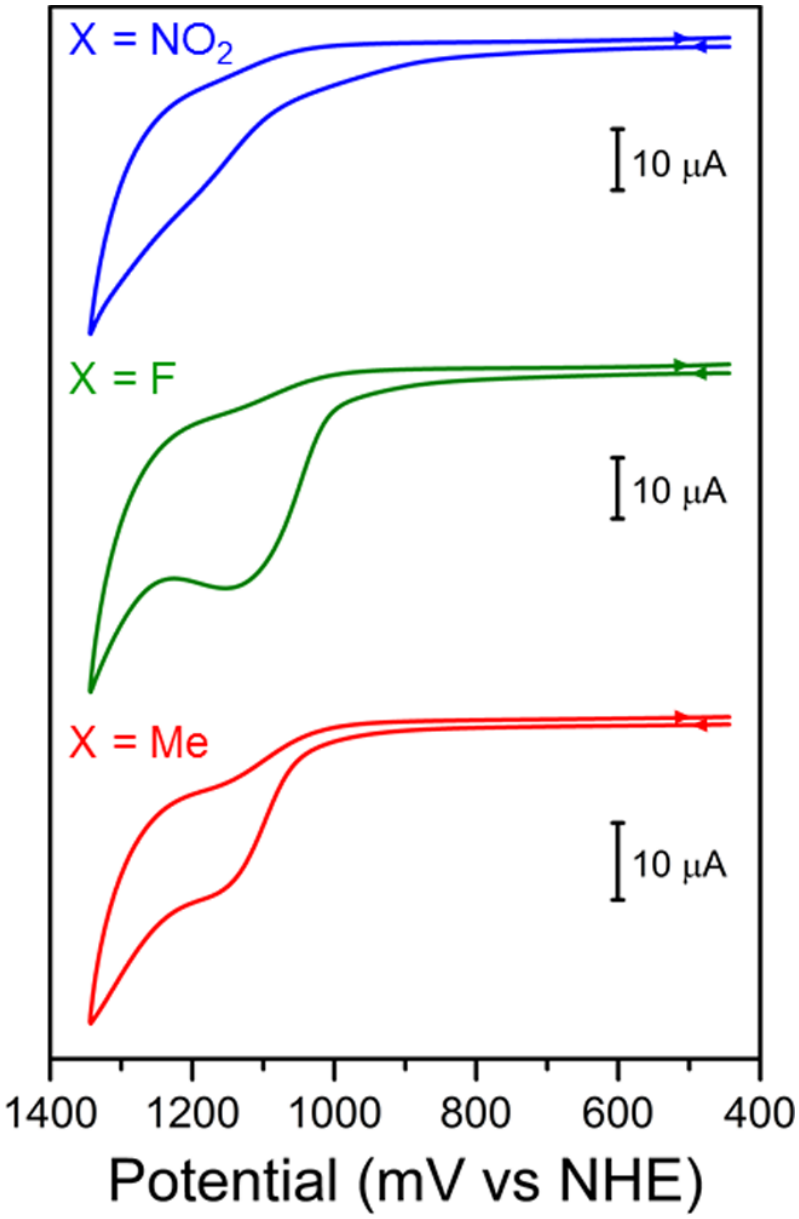

Figure 4.99 Stacked cyclic voltammograms for 1 mM of **2-NO₂** (blue), **2-F** (green), and **2-Me** (red) in aqueous solutions containing 50 mM HEPES and 100 mM NaCl buffered at pH 7.3. Measurements were carried out at ambient temperature using a platinum electrode as a working electrode and 20 mV s^{-1} scan rate. The arrows denote the scan direction and scale bars denote 10 μA current.

4.5.4 Supplementary Tables

Table 4.2 Crystallographic data for **2′-X** (X = NO_2, F, Me) at 100 K.

	2′-NO_2	**2′-F**	**2′-Me**
Empirical formula	$C_{26}H_{30}Co_2F_{12}N_8Na_2O_{17}P_2$	$C_{27}H_{34}Co_2F_{13}N_7Na_2O_{16}P_2$	$C_{27}H_{33}Co_2F_{12}N_6NaO_{12}P_2$
Formula weight, g mol^{-1}	1180.36	1185.39	1064.38
Crystal system	Orthorhombic	Triclinic	Orthorhombic
Space group	$P2_12_12_1$	$P\bar{1}$	*Pccn*
Wavelength, Å	0.71073	0.71073	0.71073
Temperature, K	100.04	100.02	99.99
a, Å	15.103(2)	16.853(4)	17.851(2)
b, Å	16.169(2)	17.200(4)	21.568(2)
c, Å	21.107(2)	17.668(4)	26.363(3)
α, °	90	85.615(6)	90
β, °	90	79.344(6)	90
γ, °	90	86.314(6)	90
V, $Å^3$	5154.3(8)	5012(2)	10150(1)
Z	4	4	8
ρ_{calcd}, g cm^{-3}	1.521	1.571	1.393
μ, mm^{-1}	0.832	0.856	0.821
Reflections coll./unique	161312/7563	218581/24964	410276/10596
R(int)	0.1293	0.0860	0.1009
R_1 $(I > 2\sigma(I))^a$	0.0970	0.0875	0.1037
wR_2 $(all)^b$	0.2872	0.2523	0.3006
GoF	1.060	1.070	1.093

[a] $R_1 = \Sigma||F_0| - |F_C||/\Sigma|F_0|$, [b] $wR_2 = [\Sigma w(F_0^2 - F_C^2)^2/\Sigma w(F_0^2)^2]^{1/2}$.

Table 4.3 Summary of the average solution dc magnetic susceptibility data for compounds **2-X** (X = NO_2, F, Me), obtained using the Evans method[20] (see Equation 4.2) for aqueous solutions with 50 mM HEPES and 100 mM NaCl buffered at various pH values (see Figures 4.15–4.17).

Average values	**2-NO_2**	**2-F**	**2-Me**
$\chi_M T$ ($cm^3\,K\,mol^{-1}$)	5.75(8)	5.6(1)	5.5(1)
$\chi_M T$ per Co^{II} ($cm^3\,K\,mol^{-1}$)	2.88(4)	2.79(6)	2.75(7)
μ_{eff} per Co^{II} (μ_B)[a]	4.79(3)	4.73(5)	4.69(6)
g per Co^{II} [b]	2.48(2)	2.44(6)	2.42(3)

[a] The relationship between μ_{eff} and $\chi_M T$ is as follows: $\mu_{eff} = (8\chi_M T)^{1/2}\mu_B$. [b] The relationship between $\chi_M T$ and g is as follows: $\chi_M T = (g^2 S(S+1))/8$. Note, here $S = {}^3/_2$.

Table 4.4 Frequency offsets corresponding to maximum CEST effects at each pH value for 8 mM of **2-NO_2** in aqueous solutions containing 50 mM HEPES and 100 mM NaCl, used to estimate the exchange rate constants (k_{ex}).

pH	Frequency Offset (ppm)[a]			
	OH peak	**NH peak 1**	**NH peak 2**	**NH peak 3**
5.97	112	N/A[b]	N/A[b]	45[c]
6.18	114	N/A[b]	N/A[b]	45[c]
6.39	115	91	88	45
6.48	115	92	88	45
6.61	115	91	88	44
6.68	116	92	88	44
6.78	116	92	88	44
6.98	117	92	88	44
7.19	117	91	88	43
7.38	117	91	88	44
7.60	117	91	88	44
7.77	117	91	89	44

[a] Frequency offset is the ^{1}H NMR chemical shift difference between the resonance of the compound and the bulk H_2O solvent. [b] The exchange rate constant for the NH CEST effect was not estimated at this pH value due to low intensity. [c] The NH CEST effect did not change when the presaturation power was varied from 13 to 21 μT, which indicates very slow proton exchange. Therefore, the exchange rate constant could not be estimated using the Omega plot method.

Table 4.5 Frequency offsets corresponding to maximum CEST effects at each pH value for 9 mM of **2-F** in aqueous solutions containing 50 mM HEPES and 100 mM NaCl, used to estimate the exchange rate constants (k_{ex}).

pH	Frequency Offset (ppm)[a]			
	OH peak	**NH peak 1**	**NH peak 2**	**NH peak 3**
5.98	90	N/A[b]	N/A[b]	51[c]
6.20	92	81	78	51
6.37	93	81	79	50
6.50	94	81	79	50
6.60	95	81	79	50
6.69	95	81	79	50
6.78	96	81	79	49
6.99	96	81	79	49
7.19	97	81	79	49
7.40	97	81	78	48
7.59	97	81	79	49
7.80	97	81	79	50

[a] Frequency offset is the ^{1}H NMR chemical shift difference between the resonance of the compound and the bulk H_2O solvent. [b] The exchange rate constant for the NH CEST effect was not estimated at this pH value due to low intensity. [c] The NH CEST effect did not change when the presaturation power was varied from 13 to 21 μT, which indicates very slow proton exchange. Therefore, the exchange rate constant could not be estimated using the Omega plot method.

Table 4.6 Frequency offsets corresponding to maximum CEST effects at each pH value for 8 mM of **2-Me** in aqueous solutions containing 50 mM HEPES and 100 mM NaCl, used to estimate the exchange rate constants (k_{ex}).

pH	Frequency Offset (ppm)[a]			
	OH peak	**NH peak 1**	**NH peak 2**	**NH peak 3**
6.01	85	N/A[b]	N/A[b]	53
6.18	87	N/A[b]	N/A[b]	52
6.38	88	79	76	52
6.48	89	79	76	52
6.58	89	79	76	51
6.70	90	79	76	51
6.90	91	79	76	51
7.01	91	79	76	51
7.20	92	79	77	51
7.38	92	79	76	51
7.61	92	79	77	51
7.80	92[c]	79	76	51

[a] Frequency offset is the ^{1}H NMR chemical shift difference between the resonance of the compound and the bulk H_2O solvent. [b] The exchange rate constant for the NH CEST effect was not estimated at this pH value due to low intensity. [c] The OH CEST effect did not change when the presaturation power was varied from 13 to 21 μT, which indicates very slow proton exchange. Therefore, the exchange rate constant could not be estimated using the Omega plot method.

Table 4.7 Frequency offsets corresponding to maximum CEST effects for the OH peak at each pH value for 4 mM of **2-NO_2** in aqueous solutions containing 50 mM HEPES and 100 mM NaCl.

pH	Frequency Offset (ppm)[a]
6.13	113
6.18	114
6.28	114
6.37	114
6.50	115
6.63	116
6.72	116
6.85	116
6.98	117
7.13	117
7.22	117
7.40	117
7.60	117
7.73	117

[a] Frequency offset is the ^{1}H NMR chemical shift difference between a resonance of the compound and the H_2O solvent.

Table 4.8 Frequency offsets corresponding to maximum CEST effects for the OH peak at each pH value for 4 mM of **2-F** in aqueous solutions containing 50 mM HEPES and 100 mM NaCl.

pH	Frequency Offset (ppm)[a]
5.95	90
6.18	92
6.28	92
6.39	93
6.47	94
6.64	95
6.72	95
6.83	95
6.93	96
7.12	96
7.37	97
7.59	97
7.73	97

[a] Frequency offset is the ^{1}H NMR chemical shift difference between a resonance of the compound and the H_2O solvent.

Table 4.9 Frequency offsets corresponding to maximum CEST effects for the OH peak at each pH value for 4 mM of **2-Me** in aqueous solutions containing 50 mM HEPES and 100 mM NaCl.

pH	Frequency Offset (ppm)[a]
6.13	85
6.22	85
6.31	87
6.42	87
6.56	88
6.64	89
6.74	90
6.84	90
6.95	91
7.13	92
7.32	92
7.52	92
7.67	92

[a] Frequency offset is the ^{1}H NMR chemical shift difference between a resonance of the compound and the H_2O solvent.

Chapter 5: Dramatic Enhancement in pH Sensitivity and Signal Intensity Through Ligand Modification of a Dicobalt PARACEST Probe

Reprinted with permission from:

Thorarinsdottir, A. E.; Harris, T. D. *Chemical Communications* **2019**, *55*, 794–797.

This work was performed in collaboration with the co-author listed above.

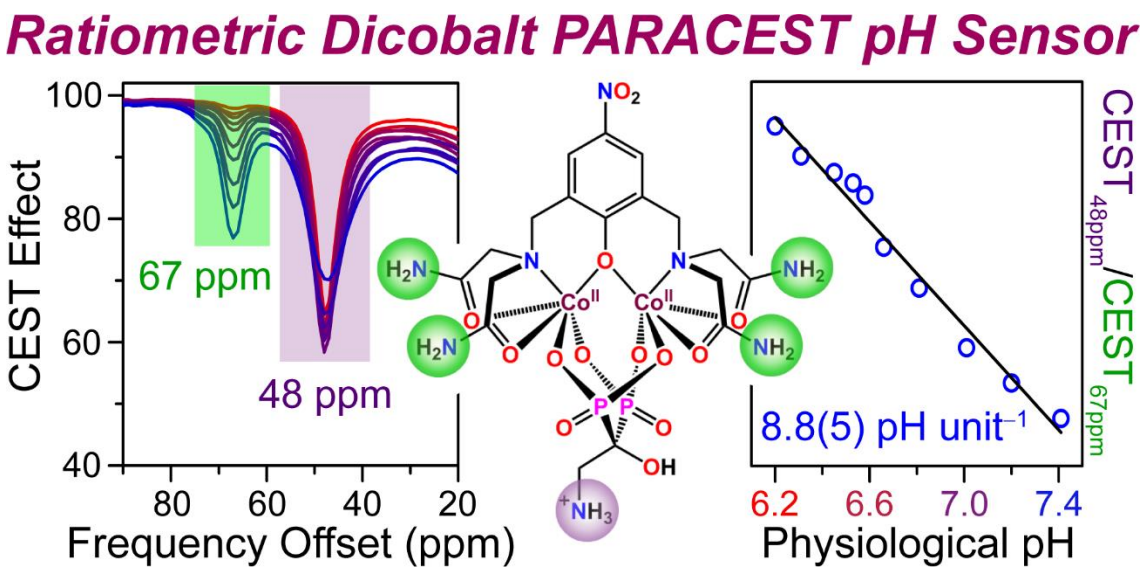

5.1 Introduction

Bioresponsive molecular magnetic resonance imaging (MRI) contrast agents are of tremendous interest for visualizing and monitoring biological processes.[1] MRI is ideally suited for molecular imaging in vivo owing to its high spatiotemporal image resolution and unlimited tissue penetration depth,[2] but bioresponsive contrast agents are needed to improve specificity and add valuable physiological information to the anatomical images.[3] These molecular probes undergo changes in MRI signals in response to variations in biomarkers such as temperature,[1a,c,4] pH,[1a,c,5] redox status,[1a,6] enzymes,[1a,c,7] metal ions,[1a,8] and metabolites,[1a,c,9] and are therefore capable of reporting on their local physiological environment. In particular, pH-responsive probes are attractive since acidic extracellular pH is a prominent feature of various diseases and disorders.[10] As such, the ability to differentiate small changes in pH through MRI is an important step toward improving the understanding, early detection, and treatment of pathologies.

In targeting pH-responsive MRI contrast agents, the employment of paramagnetic transition metal complexes that exploit the chemical exchange saturation transfer (CEST) mechanism is a promising strategy owing to their high sensitivity to environmental changes and tunability through ligand design.[11] Here, contrast is generated through proton exchange between the paramagnetic molecule and bulk H_2O upon frequency-specific irradiation.[12] The large chemical shifts of the exchangeable protons on these paramagnetic probes[4b,5f,g,6c,d,13] improve sensitivity and specificity by minimizing overlap with biological background signals.[14] Moreover, since the exchange rates of these ligand protons typically show a strong pH dependence,[5f,g,6c,13] a dramatic change in CEST signal intensity with pH can be achieved. However, due to the inherent concentration dependence of the intensity of CEST peaks, a ratiometric method is required to effectively exploit the CEST

signal intensity for pH mapping in physiological environments, where the distribution of the probe is usually unknown. Toward this end, a single PARACEST probe that features two types of exchangeable protons that display markedly different pH-dependent changes in CEST signal intensity offers an ideal platform, as the ratio of the two peak intensities should be highly sensitive to pH variations.

We recently employed this approach to demonstrate the ability of dicobalt PARACEST probes to measure solution pH in a physiologically relevant range with high sensitivities of 0.99(7)–2.04(5) pH unit^{-1}.[5f,g] These probes feature a phenoxo-centered tetra(carboxamide) ligand and an ancillary bisphosphonate ligand bearing amide and hydroxyl protons, respectively, with opposing pH-dependent CEST peak intensities (see Figure 5.1, **1** and **2-X**). Notably, the chemical shifts and intensities of the CEST signals could be tuned by chemically modifying the pendent amides and *para*-substituents on the phenoxo-centered ligand.[5g] Building on these results, we sought to increase the pH sensitivity and signal intensities of this family of ratiometric PARACEST probes by modifying the ancillary bisphosphonate ligand. Herein, we report a new dicobalt complex that features an amine-substituted bisphosphonate ligand and exhibits dramatically enhanced pH sensitivity by virtue of an intense and pH-insensitive CEST signal from the distant amine group.

5.2 Experimental Section

General Considerations. Unless otherwise specified, the manipulations described below were carried out at ambient atmosphere and temperature. Air- and water-free manipulations were performed under a dinitrogen atmosphere in a Vacuum Atmospheres Nexus II glovebox or using standard Schlenk line techniques. Glassware was oven-dried at 150 °C for at least 4 h and allowed to cool in an evacuated antechamber prior to use in the glovebox. Acetonitrile (MeCN), diethyl

ether (Et_2O), *N*,*N*-diisopropylethylamine (DIPEA), and methanol (MeOH) were dried using a commercial solvent purification system from Pure Process Technology and stored over 3 or 4 Å molecular sieves prior to use. H_2O was obtained from a purification system from EMD Millipore. Deuterated solvents were purchased from Cambridge Isotope Laboratories. The synthesis of *N*,*N*′-[(2-hydroxy-5-nitro-1,3-phenylene)bis(methylene)]bis[*N*-(carboxymethyl)glycineamide] (HL) was carried out as reported previously.[5f] All other reagents and solvents were purchased from commercial vendors and used without further purification. Experimental details on the synthesis of H_4L' are provided in Section 5.5.1.

*Synthesis of Na[LCo$_2$L′]·3.8NaNO$_3$·5.9H$_2$O (**3**)*. A pink solution of $Co(NO_3)_2·6H_2O$ (58.7 mg, 0.202 mmol) in H_2O (2 mL) was added dropwise to a stirring yellow suspension of HL (42.9 mg, 0.101 mmol) in H_2O (3 mL) to give an orange solution. To this solution, a colorless solution of H_4L' (22.3 mg, 0.101 mmol) in H_2O (2 mL) was added dropwise. The pH of this solution was adjusted to 7.5 by addition of a dilute sodium hydroxide solution in H_2O. The resulting dark orange solution was stirred at 25 °C for 2.5 h. The solvent was removed under reduced pressure and the obtained orange solid was washed by stirring in MeCN (15 mL) for 40 min. The resulting orange powder was collected by vacuum filtration, washed with Et_2O (15 mL), and dried under reduced pressure for 24 h to give **3** (101 mg, 83%). Anal. Calcd. for $C_{18}H_{38.8}Co_2N_{11.8}Na_{4.8}O_{31.3}P_2$: C, 17.84; H, 3.23; N, 13.64%. Found: C, 17.87; H, 3.15; N, 13.57%. ICP-OES: Co:P = 1.01:1.00. UV-Vis absorption spectrum (37 μM; 50 mM HEPES buffered to pH 6.98, 25 °C): 371 nm (ε = 12400 M^{-1} cm^{-1}). UV-Vis diffuse reflectance spectrum: 370 nm. ESI-MS (*m*/*z*): Calcd. for $C_{18}H_{27}Co_2N_8O_{14}P_2$ ($[LCo_2L']^-$): 758.98, found: 759.06; calcd. for $C_{18}H_{29}Co_2N_8O_{14}P_2$ ($[LCo_2L'+2H]^+$): 760.99, found: 760.99. FT-IR (ATR, cm^{-1}): 3280 (broad, m); 3172 (broad, m); 1667 (s); 1595 (m); 1497 (w);

1471 (w); 1353 (s); 1313 (s); 1095 (s); 1031 (m); 970 (m); 876 (w); 834 (w); 752 (w); 659 (m); 597 (m); 556 (m). Slow diffusion of MeCN vapor into a concentrated solution of **3** in H_2O (pH ca. 6) afforded light orange plate-shaped crystals. However, despite repeated attempts, crystals suitable for single-crystal X-ray diffraction analysis could not be obtained for **3**. Note that changing the pH of the H_2O solution of **3**, and exchanging the Na^+ ions for $(Me_4N)^+$ ions also only gave weekly diffracting crystals of the dicobalt complex.

Preparation of Fetal Bovine Serum (FBS) and Gelatin Gel Samples. Samples of **3** in FBS were prepared by dissolving solid samples of **3** in commercially available FBS (Fisher Scientific, catalog no. MT35010CV) and adjusting the pH to the desired values by addition of minimal amounts of dilute aqueous hydrochloric acid and sodium hydroxide solutions. To prepare 17% (w/v) gelatin gel samples of **3**, 8 mM solutions (0.60 mL) of **3** in 50 mM HEPES buffers containing 100 mM NaCl were added to NMR tubes containing gelatin powder (0.10 g) from bovine skin (Sigma Aldrich, catalog no. G9391). The resulting suspensions were heated by hot air and thoroughly shaken to form homogeneous, orange mixtures. The mixtures were slowly cooled to ambient temperature and further cooled to 4 °C and stored at that temperature for 2 h to form the gels. The pH values of the gelatin gel samples were recorded immediately following ^{1}H NMR and CEST data acquisition by submerging a pH electrode in the gels. The recorded pH values of the gels were 0.15–0.24 pH units lower than those of the HEPES buffer solutions used to prepare the samples. Note that an analogous decrease in pH was observed for gelatin gels prepared using HEPES buffer solutions without **3**. Further note that the concentration of **3** (as determined by inductively coupled plasma optical emission spectroscopy) did not change significantly upon formation of the gels, thus 17% (w/v) gelatin gels containing 8 mM of **3** were used for experiments.

NMR Spectroscopy. ^{1}H and ^{31}P{^{1}H} NMR spectra for ligand H_4L' were collected at 25 °C at 500 and 202 MHz frequencies, respectively, on an Agilent DD2 500 MHz (11.7 T) spectrometer. The ^{13}C{^{1}H} NMR spectrum for H_4L' was collected at 25 °C at 126 MHz frequency using a Bruker Avance III 500 MHz (11.7 T) system equipped with a DCH CryoProbe. ^{1}H NMR spectra for **3** in D_2O and for aqueous solution samples containing 50 mM HEPES and 100 mM NaCl buffered to various pH values were collected on an Agilent DD2 500 MHz (11.7 T) spectrometer at 37 °C. ^{1}H NMR spectra for **3** in solutions containing 50 mM HEPES and 100 mM NaCl buffered to pH 7.4 with/without the presence of various physiological phosphate ions, in FBS, and in 17% (w/v) gelatin gels were recorded at 37 °C on a Bruker Neo 600 MHz (14.1 T) system equipped with a QCI-F CryoProbe. For samples in HEPES buffers, FBS, and gelatin, spectra were acquired using an inner capillary containing D_2O to lock the samples. All chemical shift values (δ) are reported in ppm and coupling constants (J) are reported in hertz (Hz). The ^{1}H NMR spectrum for H_4L' is referenced to the residual proton signal from the D_2O solvent at 4.79 ppm. The ^{31}P{^{1}H} NMR spectrum for H_4L' is referenced to an external standard of 85% (v/v) phosphoric acid solution in D_2O (δ = 0 ppm). The ^{13}C{^{1}H} NMR spectrum for H_4L' in D_2O was recorded with 5% (v/v) MeOH added as an internal reference (δ = 49.50 ppm). For measurements of **3** in D_2O or other aqueous media, the chemical shift of the solvent signal in the ^{1}H NMR spectra was set to 0 ppm to simplify comparison between ^{1}H NMR spectra and the corresponding CEST spectra (Z-spectra). The MestReNova 10.0 NMR data processing software was used to analyze and process all recorded NMR spectra. T_1 relaxation times of H_2O were measured on a Varian Inova 500 MHz (11.7 T) instrument after detuning the probe to account for radiation damping and obtained by fitting the H_2O signal intensities from experiments with an array of relaxation times implemented in the

program vnmr.

Determination of pK_a by ^{1}H NMR Analysis. The pH-dependent ^{1}H NMR chemical shifts of the two methylene resonances from the ancillary bisphosphonate ligand $(H_nL')^{(4-n)-}$ (n = 1, 2) were used to estimate the pK_a value for **3**. The change in ^{1}H NMR chemical shift for each methylene resonance as a function of pH was fit to a Boltzmann sigmoidal function[15] to model a single ionization event according to the following equation:

$$\delta = A_2 + (A_1 - A_2)/(1 + \exp((\mathrm{pH} - \mathrm{p}K_a)/dx)) \quad (5.1)$$

In this equation, δ is the obtained chemical shift, A_2 is the theoretical chemical shift of the fully deprotonated species, A_1 is the theoretical chemical shift of the fully protonated species, pK_a is the inflection point of the graph, and dx is a parameter describing the steepness of the curve.

CEST Experiments. All CEST experiments were carried out at 37 °C on a Varian Inova 500 MHz (11.7 T) spectrometer. For these experiments, 5–9 mM samples of **3** in aqueous buffer solutions containing 50 mM HEPES and 100 mM NaCl or in FBS or in 17% (w/v) gelatin gels at desired pH values (measured with a pH electrode before and/or after ^{1}H NMR and CEST data collection) were measured. Z-spectra (CEST spectra) were obtained according to the following protocol: ^{1}H NMR spectra were acquired from −50 to 130 ppm with a step increase of 1 ppm using a presaturation pulse applied for 2 s at a power level (B_1) of 22 μT. An inner capillary containing D_2O was placed within the NMR sample tubes to lock the samples. The normalized integrations of the H_2O signal from the obtained spectra were plotted against frequency offset to generate a Z-spectrum, where direct saturation of the H_2O signal was set to 0 ppm. CEST intensities are reported as %CEST = $[(1 - M_z/M_0) \times 100\%]$ (M_z and M_0 are the magnetization on-resonance and off-resonance values, respectively). The ratios of the CEST signal intensities at 48 and 67 ppm

($CEST_{48\ ppm}/CEST_{67\ ppm}$) were used to construct the pH calibration curves.

Exchange rate constants (k_{ex}) were calculated following a previously reported method,[16] where the *x*-intercept ($-1/k_{ex}^2$) was obtained from a plot of $M_z/(M_0 - M_z)$ against $1/\omega_1^2$ (ω_1 in rad s^{-1}). ^1H NMR spectra were acquired at various presaturation power levels ranging from 14 to 22 μT applied for 6 s at 37 °C. The B_1 values were calculated based on the calibrated 90° pulse on a linear amplifier. To correct for baseline variations between the Z-spectra obtained using different presaturation powers, a linear baseline was applied for two CEST regimes. The data points at 75 and 60 ppm, and at 60 and 30 ppm were employed for the CEST peaks at 67 and 48 ppm, respectively.

Solution Magnetic Measurements. The solution magnetic moment of compound **3** was determined using the Evans method,[17] by collecting variable-pH ^1H NMR spectra at 37 °C (310 K) on a Bruker Avance III HD 500 MHz (11.7 T) spectrometer. In a typical experiment, the compound (2–3 mM) was dissolved in a mixture of 2% (v/v) *tert*-butanol in an aqueous solution containing 50 mM HEPES and 100 mM NaCl buffered to a specific pH value. The resulting solution was placed in an NMR tube containing a sealed capillary with the same solvent mixture but without the to-be-characterized paramagnetic compound as a reference solution. Diamagnetic corrections were carried out based on the empirical formula of the compound (as determined by elemental analysis) using Pascal's constants.[18] The paramagnetic molar susceptibility χ_M^{para} (cm^3 mol^{-1}) was calculated using the following equation:[17]

$$\chi_M^{para} = (3\Delta\nu M_w)/(4\pi\nu_0 m) - \chi_M^{dia} \quad (5.2)$$

In this equation, $\Delta\nu$ is the frequency difference (Hz) between the *tert*-butyl resonance of *tert*-butanol in the sample and reference solutions, M_w is the molecular mass of the paramagnetic

compound (g mol^{-1}), ν_0 is the operating frequency of the NMR spectrometer (Hz), *m* is the concentration of the paramagnetic compound (g cm^{-3}), and χ_M^{dia} is the diamagnetic contribution to the molar susceptibility (cm^3 mol^{-1}).

UV-Vis Absorption Spectroscopy. Solution and solid-state UV-Vis spectra were collected at ambient temperature in the 200–800 nm range on an Agilent Cary 5000 UV-Vis-NIR spectrometer equipped with an integrating sphere for diffuse reflectance measurements. Solution spectra were collected for 34–49 μM samples of **3** in aqueous buffer solutions containing 50 mM HEPES and 100 mM NaCl at three different pH values, covering the range used for CEST experiments. A diffuse reflectance spectrum was collected on a solid sample of **3**. A sample for the measurement was prepared by mixing a solid sample of **3** with $BaSO_4$ powder for a 2-fold dilution to give a smooth, homogeneous powder. The data were treated with a background correction of $BaSO_4$ and the spectrum is reported as normalized Kubelka-Munk transformation F(R) of the raw diffuse reflectance spectrum, where F(R) was normalized with the strongest absorbance set to F(R) = 1.

Electrochemical Measurements. Cyclic voltammetry measurements were carried out at ambient temperature in an MBraun LABstar glovebox, operated under a humid dinitrogen atmosphere. A standard one-compartment cell and a CH Instruments 760c potentiostat were employed for the measurements. The cell consisted of a glassy carbon electrode as a working electrode, a platinum wire as a counter electrode, and a saturated calomel electrode (SCE) as a reference electrode. A sample of **3** was measured in an aqueous solution with 100 mM NaCl and 50 mM HEPES buffered to pH 7.4. All potentials were converted and referenced to the normal hydrogen electrode (NHE), using a literature conversion factor.[19]

Other Physical Measurements. Electrode-based pH measurements were carried out using a

Thermo Scientific Orion 9110DJWP double junction pH electrode connected to a VWR sympHony B10P pH meter. The pH meter was calibrated using standardized pH buffer solutions at 4.01, 7.00, and 10.00 purchased from LaMotte Company. Elemental analysis of **3** was conducted by Midwest Microlab Inc. An infrared spectrum of a solid sample of **3** was recorded on a Bruker Alpha FTIR spectrometer equipped with an attenuated total reflectance (ATR) accessory. These data are provided in Figure 5.4. Electrospray ionization mass spectrometry **(**ESI-MS) measurements were performed on a Bruker AmaZon SL quadrupole ion trap instrument. All measurements were carried out in MeOH carrier solvent using positive and/or negative ionization mode. Inductively coupled plasma optical emission spectroscopy (ICP-OES) was performed on a Thermo iCAP 7600 dual view ICP-OES instrument equipped with a CETAC ASX520 240-position autosampler. Samples were dissolved in a 3% (v/v) nitric acid solution in H_2O and the emissions for Co and P were compared to standard solutions.

5.3 Results and Discussion

5.3.1 Design and Synthesis

In an attempt to address the modest intensity and pH-dependent frequency of the etidronate hydroxyl CEST peak for our previously reported PARACEST probes,[5f,g] we targeted the amine-substituted bisphosphonate ligand $(L')^{4-}$, with the expectation that the equivalent amine protons would give rise to a stronger CEST effect. Furthermore, the different pK_a values of amine and amide protons have been shown to result in distinct pH-dependent changes in CEST peak intensity suitable for ratiometric pH sensing, albeit only for probes that exhibit small chemical shifts and modest pH sensitivity.[20] As such, we envisioned that a dinucleating ligand platform comprised of $(L')^{4-}$ and a phenoxo-centered tetra(carboxamide) ligand known for providing highly shifted and

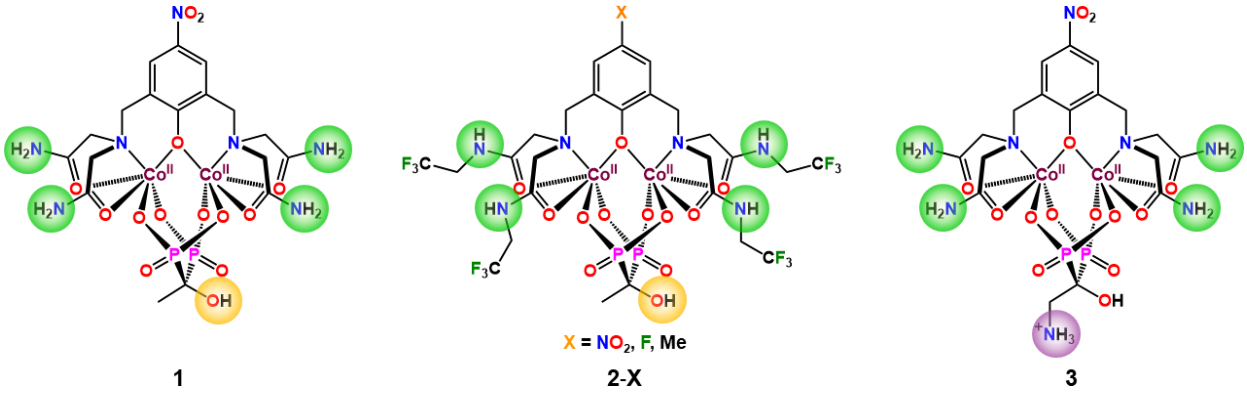

Figure 5.1 Structures of previously reported dicobalt PARACEST pH probes $[LCo_2(etidronate)]^-$ (left) and $[(^XL')Co_2(etidronate)]^-$ (center), as observed in **1** and **2-X** (X = NO_2, F, Me), respectively, and the new dicobalt complex $LCo_2(HL')$ (right), as observed in **3**, reported here. The exchangeable amide, hydroxyl, and amine protons are highlighted in green, orange, and purple, respectively.

pH-sensitive amide CEST peaks could afford dicobalt PARACEST probes better suited for ratiometric pH quantitation.

Reaction of the nitro-substituted tetra(carboxamide) ligand HL with two equivalents of $Co(NO_3)_2{\cdot}6H_2O$ in the presence of one equivalent of H_4L' in H_2O at pH 7.5 afforded $Na[LCo_2L']{\cdot}3.8NaNO_3{\cdot}5.9H_2O$ (see Figure 5.1, **3**) as an orange solid (see Section 5.2). Slow diffusion of MeCN vapor into a concentrated H_2O solution of **3** gave light orange plate-shaped crystals that were not of sufficient quality for single-crystal X-ray diffraction analysis. However, the close similarity between the diffuse reflectance UV-Vis spectra for **1′** and **3** (see Figure 5.5) suggests analogous solid-state structures.[5f]

5.3.2 UV-Vis Spectroscopy

To assess the electronic structure of **3** in aqueous solution, UV-Vis absorption spectra were collected for samples in 50 mM HEPES buffers with 100 mM NaCl. For a solution at pH 6.98, the spectrum exhibits a single strong peak at 371 nm (ε = 12400 M^{-1} cm^{-1}) (see Figure 5.6), which is consistent with the spectra for **1** and **2-NO₂**[5f,g] and can be unambiguously assigned to a ligand–

metal charge transfer (LMCT) transition from the bridging phenolate to Co^{II}.[21] Note that the position and intensity of this band are essentially identical between pH 6.1 and 8.0, indicating the presence of a single species in solution in this pH range. Based on precedent in amine-bisphosphonate molecular complexes,[22] in conjunction with a notable increase in solubility of **3** at more alkaline pH, we assign this species to the neutral dicobalt complex $LCo_2(HL')$, where the amine of the bisphosphonate ligand is protonated.

5.3.3 Solution Magnetic Properties

The oxidation state and spin state of Co in **3** was further probed by variable-pH magnetic susceptibility measurements for aqueous buffer solutions at 37 °C using the Evans method.[17] The $\chi_M T$ data do not significantly change in the pH range 6.1–8.0, affording an average value of $\chi_M T$ = 5.96(6) cm^3 K mol^{-1} (see Figure 5.7 and Table 5.1). These data are in good agreement with those obtained for **1** and **2-X**, indicative of pseudo-octahedral high-spin Co^{II} centers ($S = {}^3/_2$) with significant magnetic anisotropy.[5f,g,11a,21b,23]

5.3.4 NMR Spectroscopy

To further probe the solution structure and properties of **3**, ^{1}H NMR spectra were collected at 37 °C for aqueous solutions buffered to selected pH values. The spectrum at pH 7.02 exhibits sharp and paramagnetically shifted resonances with chemical shifts from −103 to 182 ppm vs H_2O (see Figure 5.8, top), consistent with the presence of high-spin Co^{II}.[11] Comparison to the spectrum recorded in D_2O (see Figure 5.8, bottom) and the spectrum for **1** at pH 7.06 (see Figure 5.9) reveals that the resonances at 4, 6, 11, 13, 66, 68, 103, and 106 ppm correspond to four sets of two slightly inequivalent amide protons, whereas the peaks at 48 and 101 ppm correspond to amine and hydroxyl protons on $(HL')^{3-}$, respectively. Furthermore, the two methylene protons on $(HL')^{3-}$

resonate at 69 and 74 ppm, in accord with the etidronate methyl peak at 66 ppm for **1**. Together, these observations indicate pseudo-C_2 symmetry of $LCo_2(HL')$ in **3**, as observed for the anionic complexes in **1** and **2-X**.[5f,g] Moreover, the close similarity between the ^{1}H NMR profiles for **1** and **3** corroborates our previous observations that the chemical shifts of resonances from L^- are not significantly affected by modest modifications of the bisphosphonate ligand.[5f] Importantly, the amine resonance for **3** is highly shifted and well separated from the amide peaks, suggesting the potential utility of these two functional groups for pH sensing using ratiometric PARACEST. Finally, whereas no chemical shift changes are observed upon increasing the pH from 5.99 to 7.80, the exchangeable proton resonances broaden significantly, indicating faster proton exchange (see Figure 5.10).

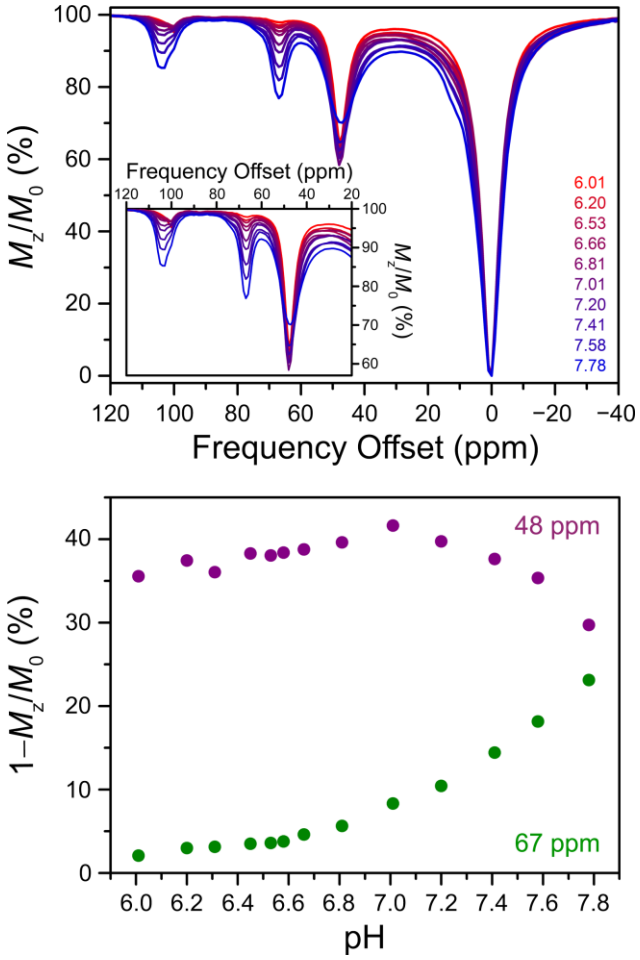

Figure 5.2 Top: Variable-pH CEST spectra collected at 11.7 T and 37 °C using a 2 s presaturation pulse and B_1 = 22 μT for 9 mM aqueous solutions of **3** with 50 mM HEPES and 100 mM NaCl buffered to pH 6.01–7.78 (see legend). Inset: Expanded view of the CEST peaks of interest. Bottom: Plot of CEST intensities from presaturation at 48 ppm (purple) and 67 ppm (green) vs pH.

5.3.5 CEST Properties

To further investigate the possibility of employing **3** as a pH-responsive PARACEST probe, variable-pH CEST spectra were collected at 37 °C for 9 mM

solutions of **3** in HEPES buffers. The spectrum at pH 6.01 exhibits three peaks at 48, 67, and 100 ppm with 36, 2.1, and 4.8% CEST intensity, respectively (see Figure 5.2, top). The CEST peaks at 48 and 67 ppm correspond to amine and two overlapping amide resonances, respectively, as evidenced by ^{1}H NMR analysis. As the pH is raised to 7.58, the intensity of the amine peak remains relatively constant, reaching a maximum value of 42% at pH 7.01. However, further increasing the pH to 7.78 leads to a significant peak broadening and concurrent intensity reduction (see Figure 5.2). In stark contrast, the CEST effect at 67 ppm increases nearly linearly in this pH range, affording a maximum value of 23% at pH 7.78 (see Figure 5.2). This increase in CEST peak intensity with pH is consistent with the base-catalyzed amide proton exchange observed for **1** and **2-X**.[5f,g] Indeed, exchange rate analysis using the Omega plot method[16] reveals that the rate constant (k_{ex}) for the amide protons at 67 ppm for **3** increases from 2.9(4) × 10^2 to 6.1(1) × 10^2 s^{-1} between pH 6.53 and 7.78 (see Figures 5.11 and 5.13). These values agree well with those previously reported for dicobalt complexes of L^-.[5f] To compare, k_{ex} for the amine protons in **3** exhibits a relatively small pH dependence below pH 7.0 but then undergoes a dramatic increase when the pH is raised further, reaching a maximum of k_{ex} = 1.5(1) × 10^3 s^{-1} at pH 7.78 (see Figures 5.12 and 5.13). These observations are consistent with NMR line width and CEST intensity analyses, indicating that k_{ex} = 800–900 s^{-1} provides optimal amine CEST effect for the dinuclear system. Finally, note that the CEST peak at 100–103 ppm stems from overlapping amide and hydroxyl resonances, as observed for **1**.[5f] Despite the high chemical shift, the broadness of this peak and pH-dependent frequency render it unsuitable for use in ratiometric pH quantitation.

5.3.6 Ratiometric CEST Analysis

The markedly different pH dependences of the amine and amide CEST intensities at 48 and 67

ppm, respectively, prompted us to assess the utility of **3** in the ratiometric quantitation of pH. Indeed, the ratio of CEST intensities at 48 and 67 ppm ($CEST_{48\ ppm}/CEST_{67\ ppm}$) exhibits a pronounced pH dependence. Upon increasing the pH from 6.20 to 7.41, $CEST_{48\ ppm}/CEST_{67\ ppm}$ shows a linear decrease and a fit to the data provided a pH calibration curve with the following equation (see Figure 5.3):

$$CEST_{48\ ppm}/CEST_{67\ ppm} = -8.8 \times pH + 67 \quad (5.3)$$

Remarkably, the pH sensitivity of 8.8(5) for **3**, as estimated by the absolute value of the slope of the linear calibration curve, is over 4-fold higher than for other dicobalt complexes in this family of PARACEST pH probes.[5f,g] In fact, to our knowledge, **3** exhibits the highest pH sensitivity in the physiological range yet reported for a ratiometric MR-based paramagnetic probe at 37 °C.[24] The dramatic increase in pH sensitivity for **3** stems from the linear relationship between $CEST_{48\ ppm}/CEST_{67\ ppm}$ and pH, rather than the logarithm of the intensity ratios, as observed for all previously reported dicobalt analogues.[5f,g] Importantly, the pH calibration curve for **3** is not significantly affected by the concentration of the complex, as the slopes obtained for 5 and 9 mM samples of **3** fall within error of one another (see Figures 5.14–5.19). This observation illustrates that the ratiometric method using **3** provides a concentration-independent measure of pH in the range 6.20–7.41, which is in line with

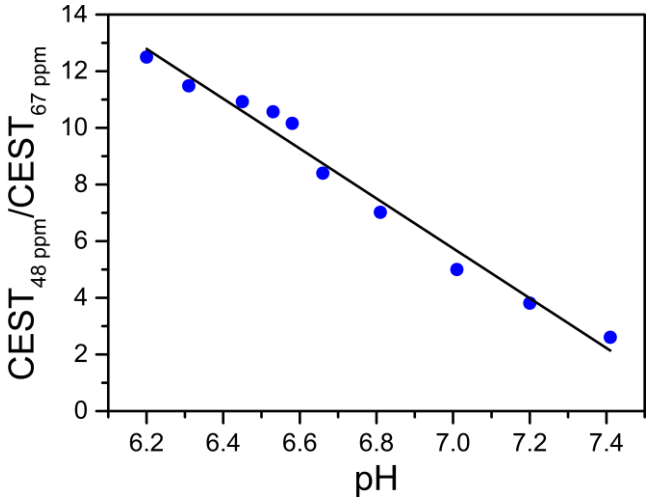

Figure 5.3 Plot of the ratios of CEST intensities from presaturation at 48 and 67 ppm for 9 mM aqueous buffer solutions of **3** vs pH. Circles denote experimental data and the line corresponds to a linear fit to the data.

previous findings for **1** and **2-X**.[5f,g] Taken together, these results show that a substantial sensitivity improvement in ratiometric pH quantitation is achieved by using an amine-functionalized dinucleating ligand platform. Furthermore, the amine group from $(HL')^{3-}$ affords a CEST peak with much higher intensity than does the etidronate hydroxyl group in **1** and **2-X**.[5f,g]

5.3.7 pK_a Determination by ^{1}H NMR Spectroscopy

The observation of no shifts in ^{1}H NMR frequencies between pH 6.0 and 7.8 for **3** contrasts with that of **1** and **2-X**,[5f,g] suggesting that the pK_a corresponding to protonation of one of the cobalt-coordinated $O_{L'}$ atoms (see Figure 5.20) is significantly lower for **3** than for **1** and **2-X**.[5f,g] Indeed, sigmoidal fits (see Section 5.2) to the chemical shift vs pH data for the two methylene resonances from the bisphosphonate ligand between pH 1.50 and 7.80 gave values of pK_a = 3.57(8) and 3.96(4) for **3** (see Figure 5.21). The slight discrepancy between the pK_a values estimated from the two protons likely arises from their different distances from the $O_{L'}$ atoms. Most importantly, both values are substantially lower than those of 5.01(3) and 4.76(7) reported for **1** and **2-NO$_2$**, respectively,[5f,g] indicating that pH-induced shifts in CEST peak frequencies in the physiological pH range can be prevented for this family of probes by decreasing the pK_a of the ionization process below 4.0. This is highly advantageous for intensity-based PARACEST probes and was accomplished for **3** through incorporation of a protonated amine group.

5.3.8 Stability Studies

Finally, the high solution stability of **3** was confirmed by cyclic voltammetry and ligand substitution studies. The absence of an oxidation process within the potential window of the solvent indicates that **3** is inert toward reaction with O_2 in aqueous solutions (see Figure 5.22).[25] Moreover, **3** remains intact in the presence of physiological phosphates, demonstrating its high

kinetic inertness (see Figure 5.23).

5.4 Conclusions

The foregoing results demonstrate the utility of a new amine-functionalized dicobalt PARACEST probe for the ratiometric quantitation of pH, and highlight the excellent tunability of the dinucleating ligand platform to enhance pH sensitivity and CEST signal intensities. Efforts are underway to investigate the stability and performance of this probe in physiological environments. Toward this end, preliminary NMR and CEST experiments for **3** in fetal bovine serum (FBS) and 17% (w/v) gelatin gels revealed similar pH-dependent trends and linear pH calibration curves as observed in HEPES buffers. Note, however, that the pH calibration equation is slightly affected by the surrounding medium owing to differences in proton exchange rates and/or T_1 relaxation times between media (see Figures 5.24–5.36 and Tables 5.2–5.4). Thus, for in vivo studies, the pH calibration curve must be constructed in a medium that closely mimics the targeted environment.

5.5 Supporting Information

5.5.1 Supplementary Experimental Details

Synthesis of (2-amino-1-hydroxyethane-1,1-diyl)bis(phosphonic acid) (H_4L'). This compound was synthesized following a modified literature procedure.[26] Under an atmosphere of dinitrogen, a colorless 1.0 M catecholborane solution in tetrahydrofuran (THF) (10.8 g, 11.3 mmol) was added to solid glycine (0.274 g, 3.65 mmol) at 25 °C. The resulting white suspension was stirred at 25 °C for 3 h to give a colorless solution. To this stirring solution, tris(trimethylsilyl) phosphite (4.47 g, 15.0 mmol) was slowly added and the resulting colorless solution was stirred at 25 °C for additional 22 h. Then MeOH (5 mL) was added to give a spongy white suspension and stirring

was continued for 1 h at 25 °C. The volatiles were removed under reduced pressure to give a white residue which was triturated with MeOH (20 mL) to afford a white solid. The solid was stirred in THF (15 mL) for 1.5 h to wash, collected by vacuum filtration, and washed with Et_2O (2 × 5 mL). Recrystallization from H_2O and drying under reduced pressure afforded the title compound as a white powder (0.172 g, 21%). ^{1}H NMR (500 MHz, D_2O, 25 °C): δ 3.48 (t, $^{3}J_{HP}$ = 11.9 Hz, 2H). $^{13}C\{^{1}H\}$ NMR (126 MHz, D_2O, 25 °C): δ 70.70 (t, $^{1}J_{CP}$ = 137.3 Hz), 42.75 (s). $^{31}P\{^{1}H\}$ NMR (202 MHz, D_2O, 25 °C): δ 14.95 (s).

5.5.2 Supplementary Figures

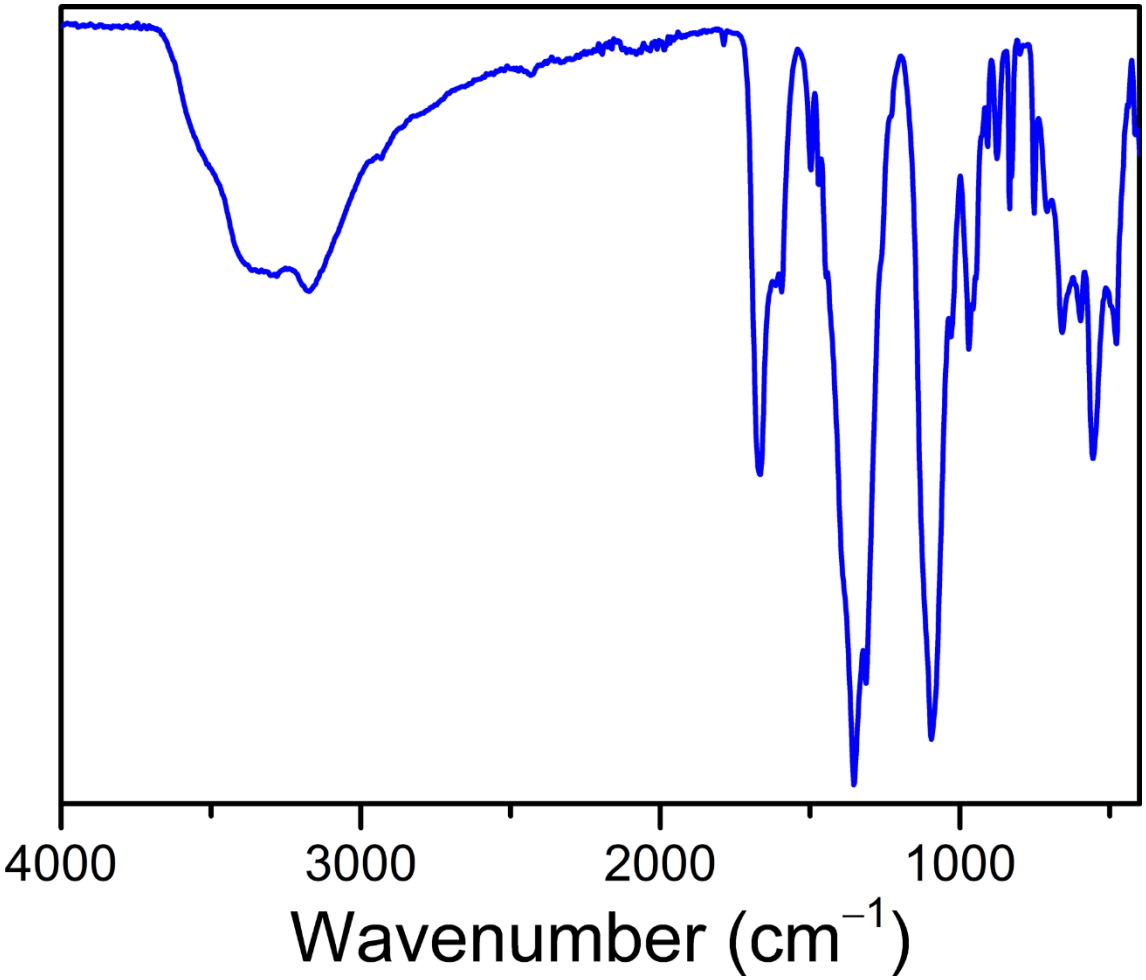

Figure 5.4 FT-IR spectrum of a solid sample of **3** at ambient temperature.

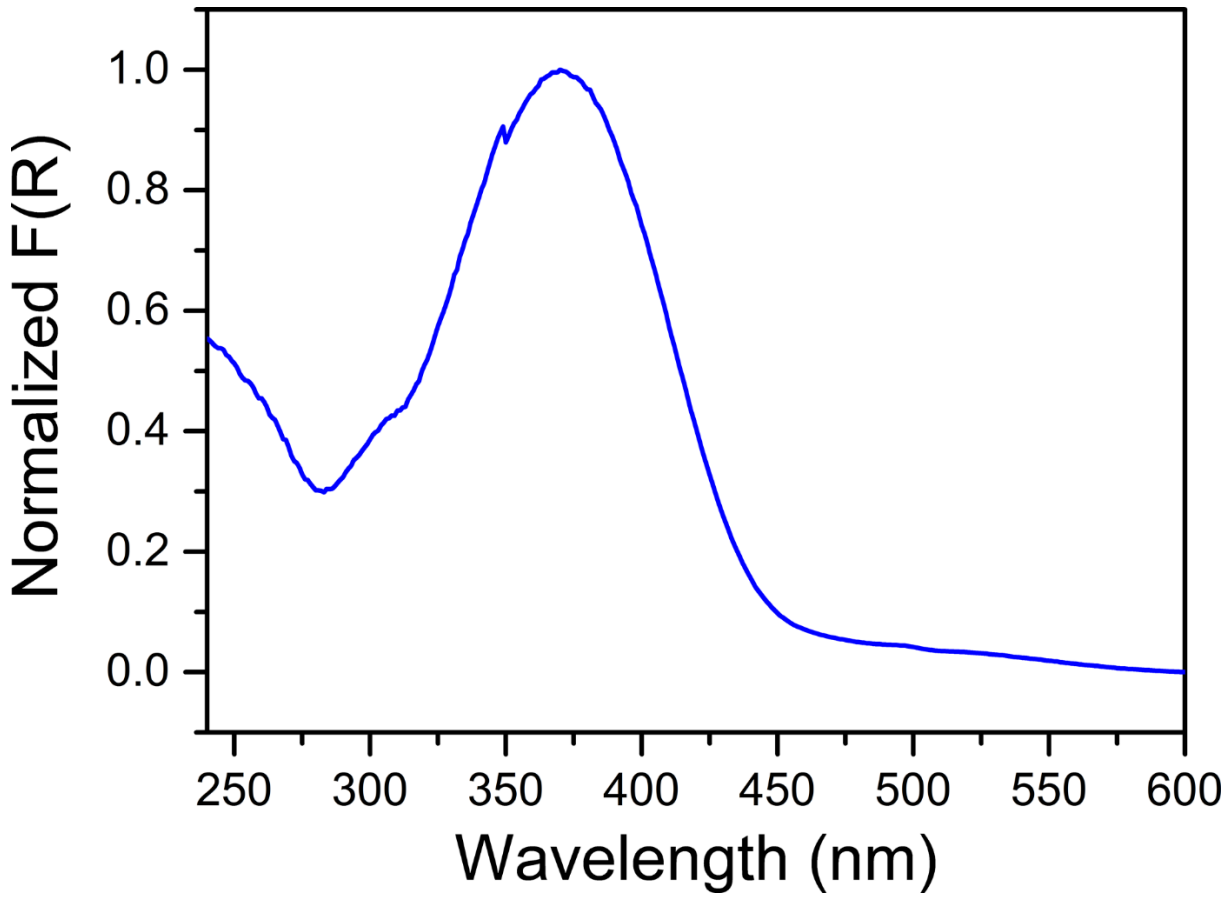

Figure 5.5 Diffuse reflectance UV-Vis spectrum of a solid sample of **3** diluted with $BaSO_4$ powder at ambient temperature. The spectrum is plotted as normalized Kubelka-Munk transformation F(R).

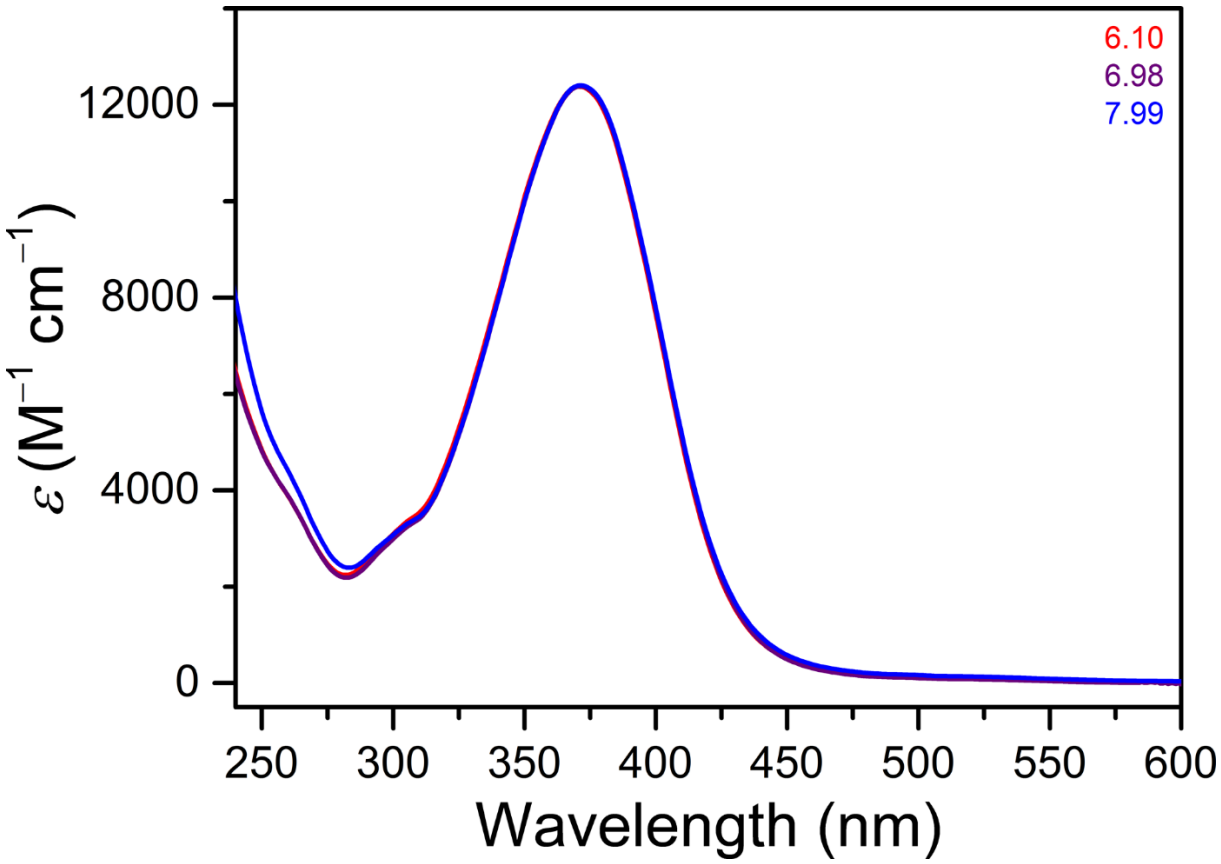

Figure 5.6 Variable-pH UV-Vis absorption spectra of 34–49 μM of **3** in aqueous solutions containing 50 mM HEPES and 100 mM NaCl at ambient temperature. Spectra were measured in the pH range used for CEST experiments, from pH 6.10 to 7.99. Colored numbers in the legend denote the pH of the solutions measured with a pH electrode and the corresponding color for each sample. Note that the molar absorptivity (ε) is plotted against wavelength.

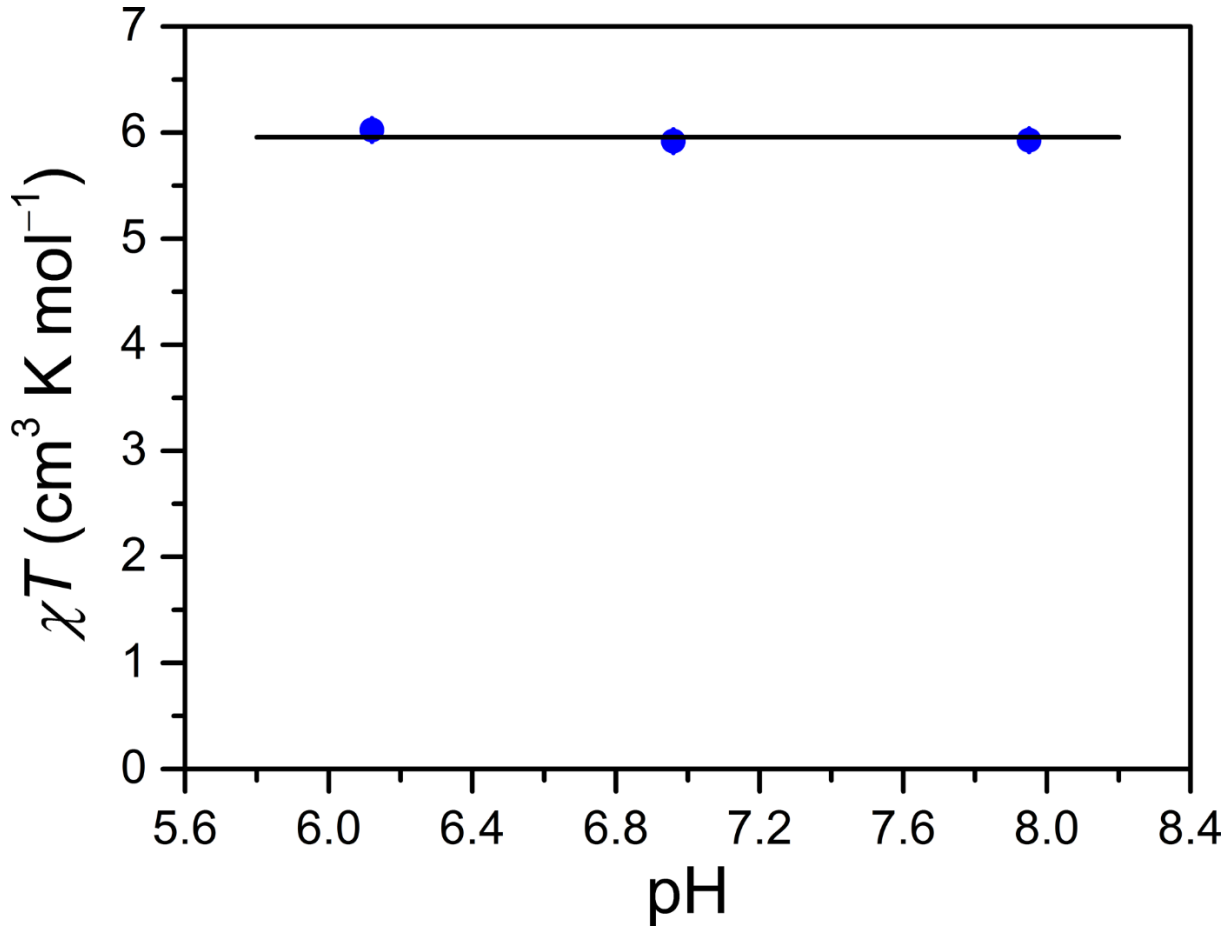

Figure 5.7 Variable-pH dc magnetic susceptibility data for **3** in aqueous solutions containing 50 mM HEPES and 100 mM NaCl, collected at 37 °C and 11.7 T using the Evans method[17] (see Equation 5.2). Blue circles represent experimental data and the solid black line denotes the average value of $\chi_M T$ = 5.96(6) cm^3 K mol^{-1} (see Table 5.1).

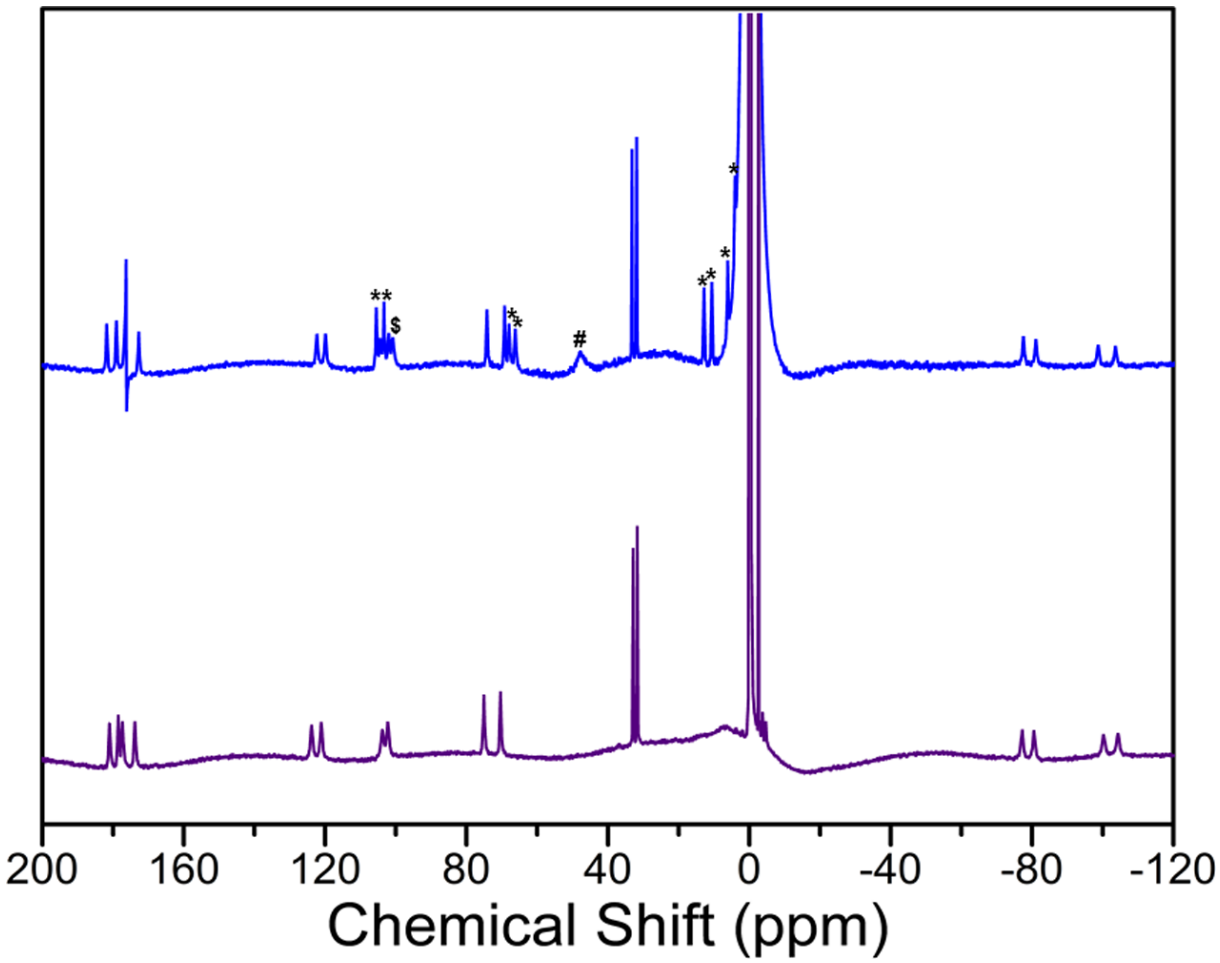

Figure 5.8 Stacked ^{1}H NMR spectra of **3** in an aqueous solution containing 50 mM HEPES and 100 mM NaCl buffered to pH 7.02 (blue) and in neutral D_2O (purple), collected at 37 °C and 11.7 T. The labelled peaks correspond to exchangeable ligand protons that are not present in the spectrum recorded in D_2O. In particular, the asterisks (*) denote peaks corresponding to amide protons from the tetra(carboxamide) ligand, and the dollar sign ($) and number sign (#) correspond to hydroxyl and amine protons, respectively, from the ancillary bisphosphonate ligand. The sharp feature at 176 ppm in the spectrum recorded in buffer is an instrument-derived artifact.

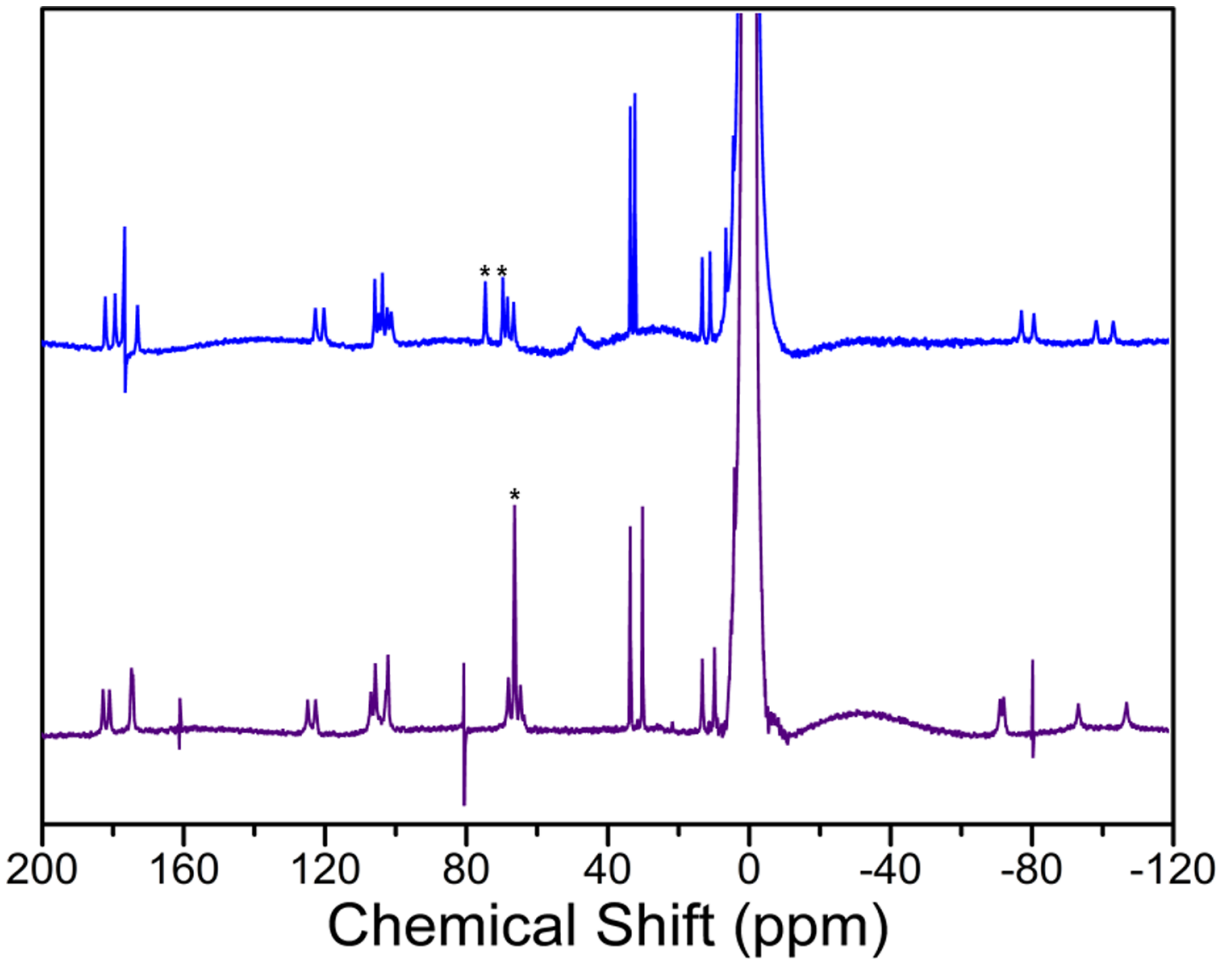

Figure 5.9 Stacked ^{1}H NMR spectra of **3** (blue) and **1** (purple) in aqueous solutions containing 50 mM HEPES and 100 mM NaCl buffered to pH 7.02 and 7.06, respectively, collected at 37 °C and 11.7 T. The asterisks denote non-exchangeable proton resonances from the ancillary bisphosphonate ligands. The sharp feature at 176 ppm in the spectrum of **3** and the features at 161, 80, and −80 ppm in the spectrum of **1** are instrument-derived artifacts.

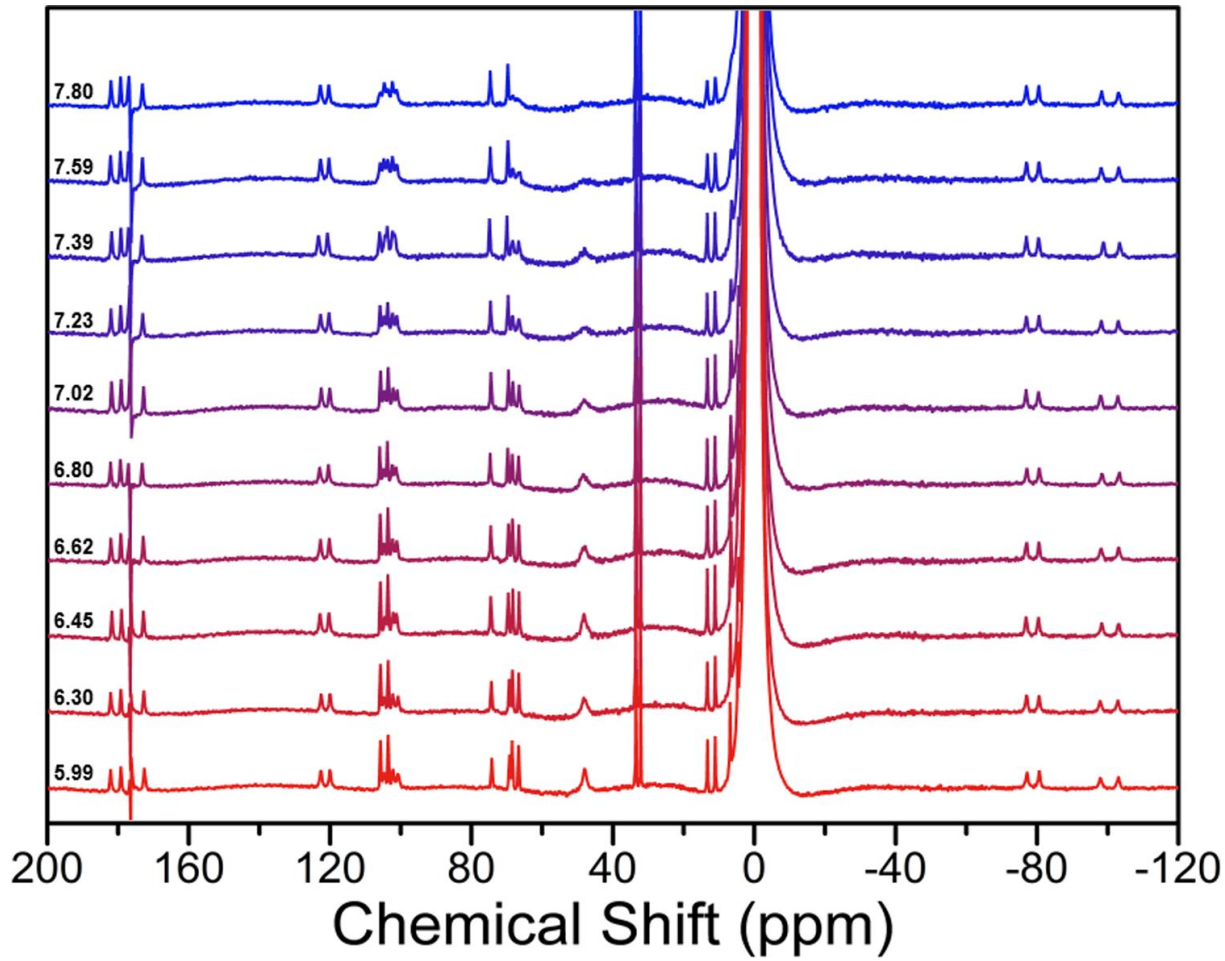

Figure 5.10 Variable-pH ^{1}H NMR spectra of 10 mM of **3** in aqueous solutions containing 50 mM HEPES and 100 mM NaCl buffered to various pH values, collected at 37 °C and 11.7 T. Black numbers on the left denote the pH of the NMR sample solutions measured with a pH electrode. The sharp feature at 176 ppm is an instrument-derived artifact.

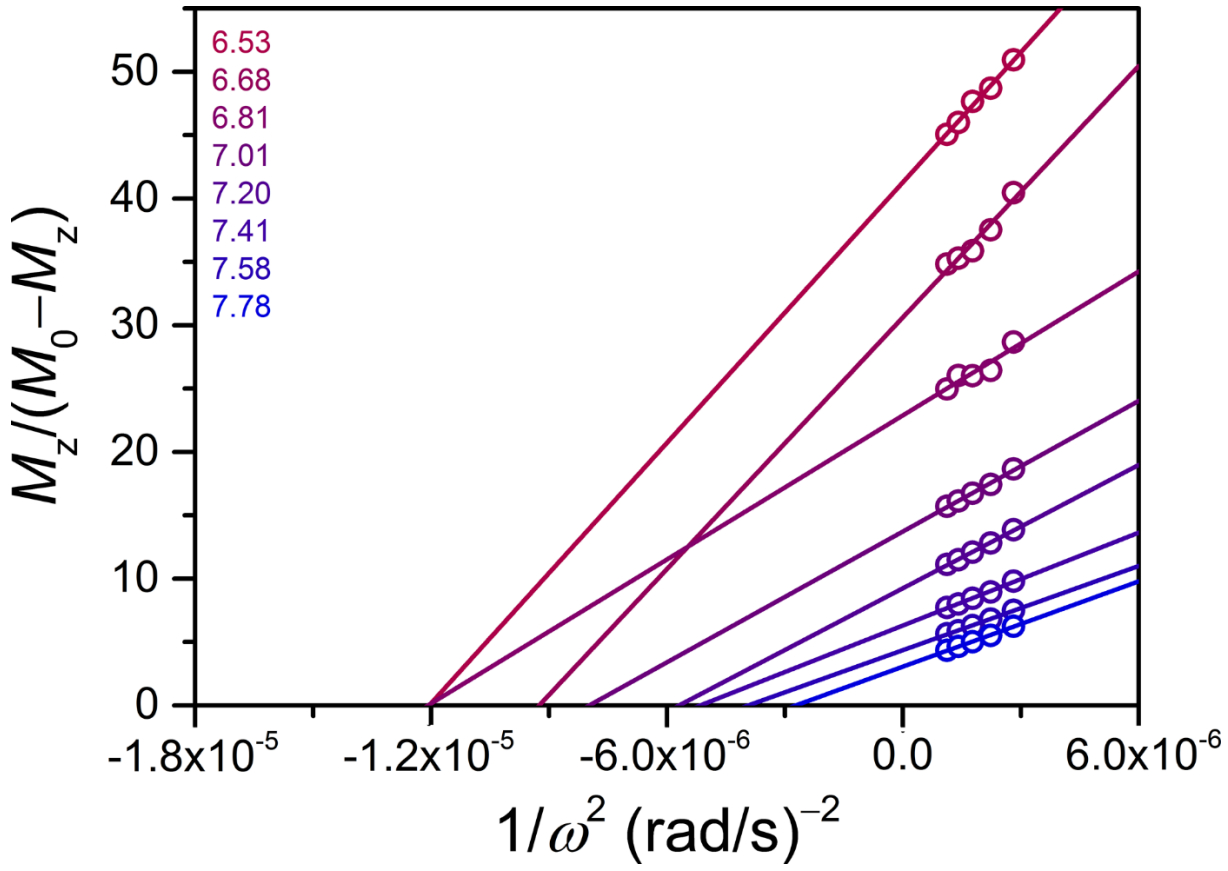

Figure 5.11 Omega plots of the CEST effect from application of 6 s presaturation at 67 ppm using B_1 = 14–22 μT for 9 mM of **3** in aqueous solutions containing 50 mM HEPES and 100 mM NaCl buffered to pH 6.53–7.78 (red-purple to blue), collected at 37 °C and 11.7 T. Colored numbers in the legend denote the pH of the solutions measured with a pH electrode and the corresponding color for each sample. Circles represent experimental data and lines represent linear fits to the data. Note that for pH values below 6.53, the amide CEST effect did not change when the presaturation power was varied from 14 to 22 μT, which indicates very slow proton exchange. Therefore, the exchange rate constant could not be estimated for those pH values using the Omega plot method.

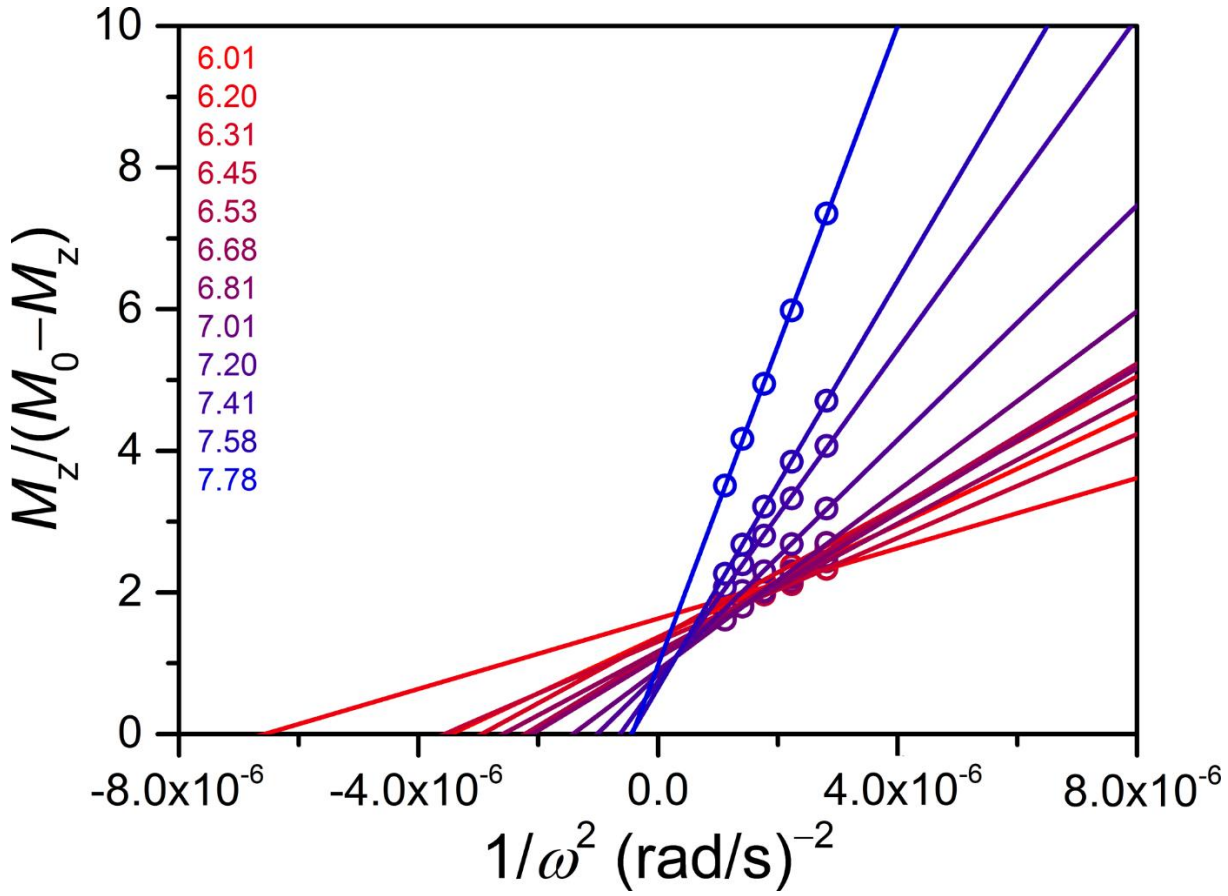

Figure 5.12 Omega plots of the CEST effect from application of 6 s presaturation at 48 ppm using B_1 = 14–22 μT for 9 mM of **3** in aqueous solutions containing 50 mM HEPES and 100 mM NaCl buffered to pH 6.01–7.78 (red to blue), collected at 37 °C and 11.7 T. Colored numbers in the legend denote the pH of the solutions measured with a pH electrode and the corresponding color for each sample. Circles represent experimental data and lines represent linear fits to the data.

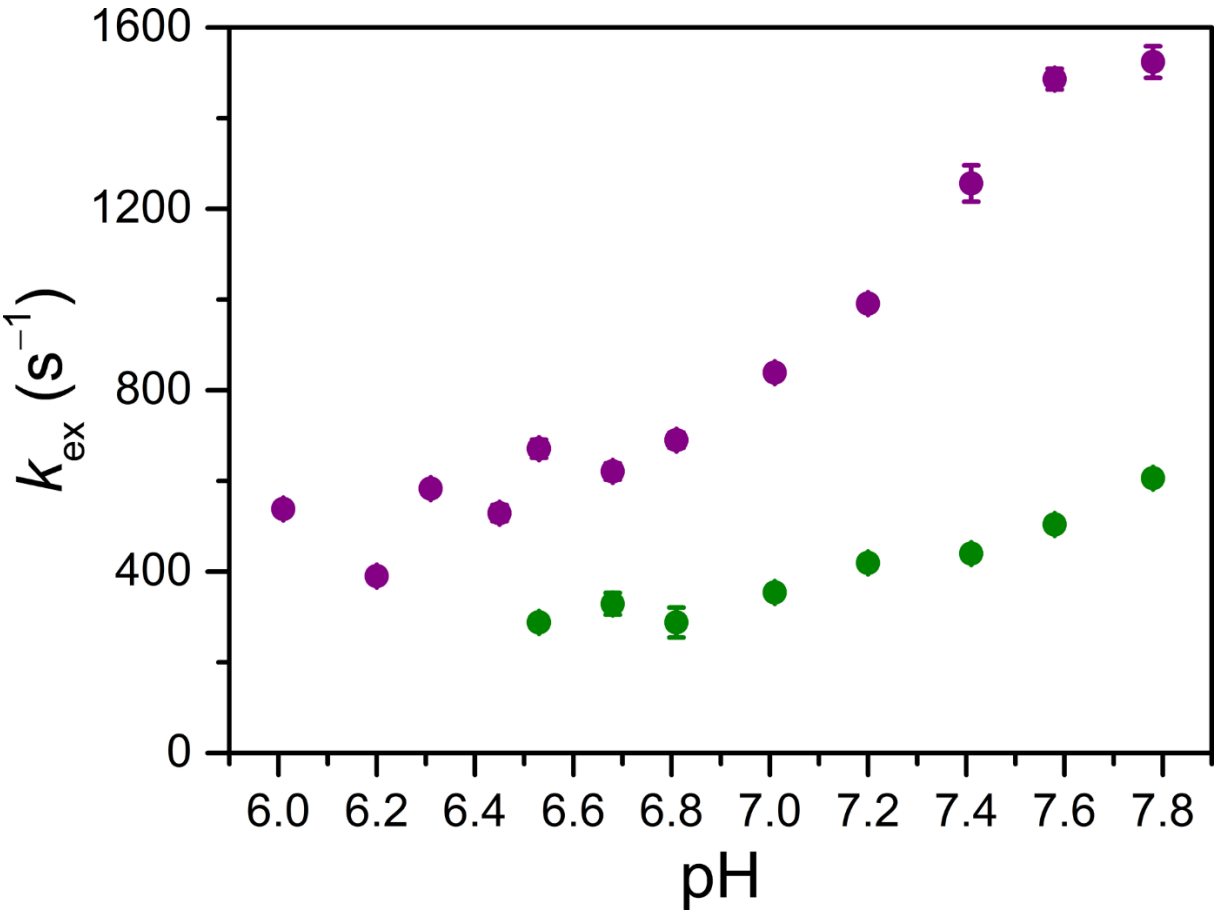

Figure 5.13 pH dependences of the proton exchange rate constants (k_{ex}) for the CEST effects at 48 ppm (purple) and 67 ppm (green) for 9 mM of **3** in aqueous solutions containing 50 mM HEPES and 100 mM NaCl at 37 °C and 11.7 T, obtained from Omega plots. Circles represent experimental data and error bars represent standard deviations of the linear fits to the Omega plot data (see Figures 5.11 and 5.12).

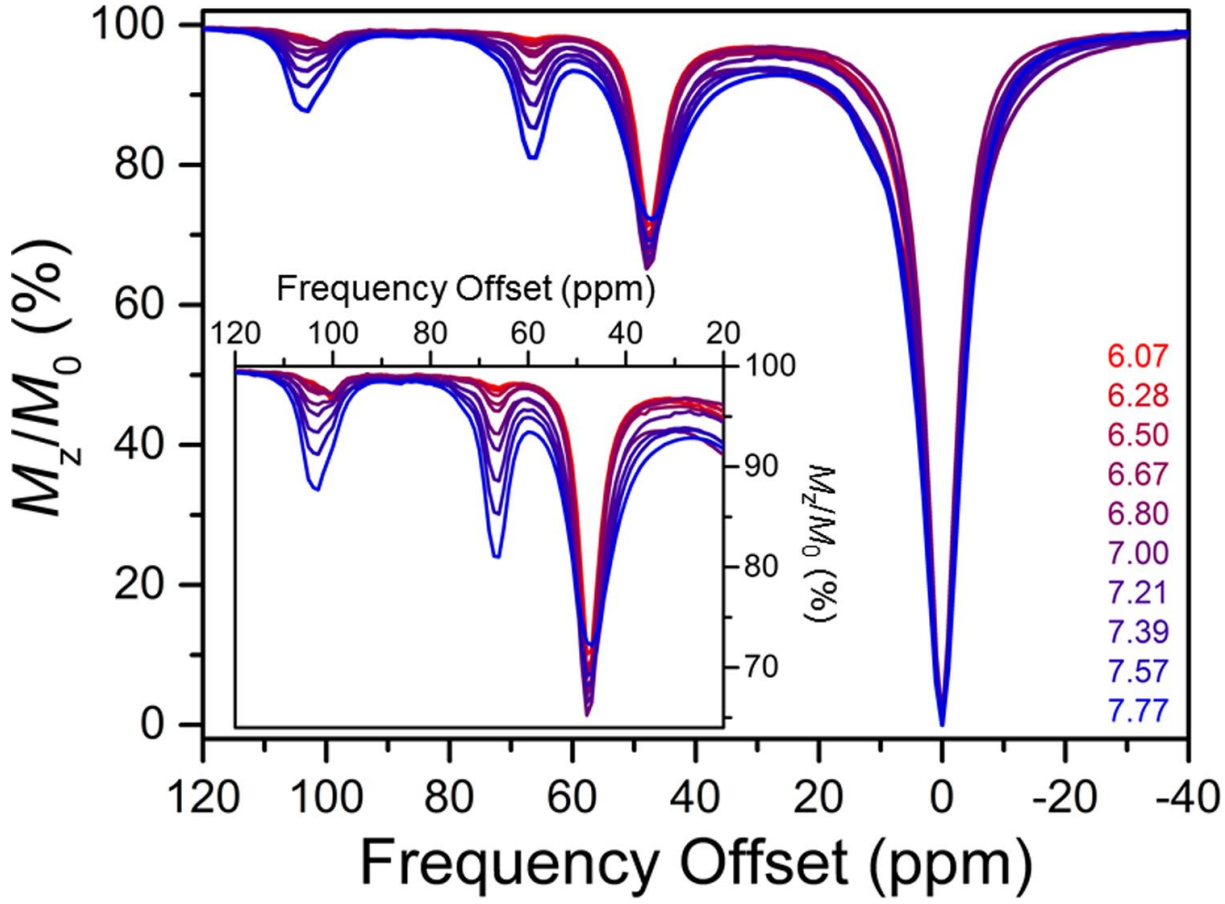

Figure 5.14 Variable-pH CEST spectra collected at 11.7 T and 37 °C using 2 s presaturation pulse and B_1 = 22 μT for 5 mM of **3** in aqueous solutions containing 50 mM HEPES and 100 mM NaCl buffered to pH 6.07–7.77 (red to blue). Colored numbers in the legend denote the pH of the solutions measured with a pH electrode and the corresponding color for each sample. Inset: Expanded view of the CEST peaks of interest.

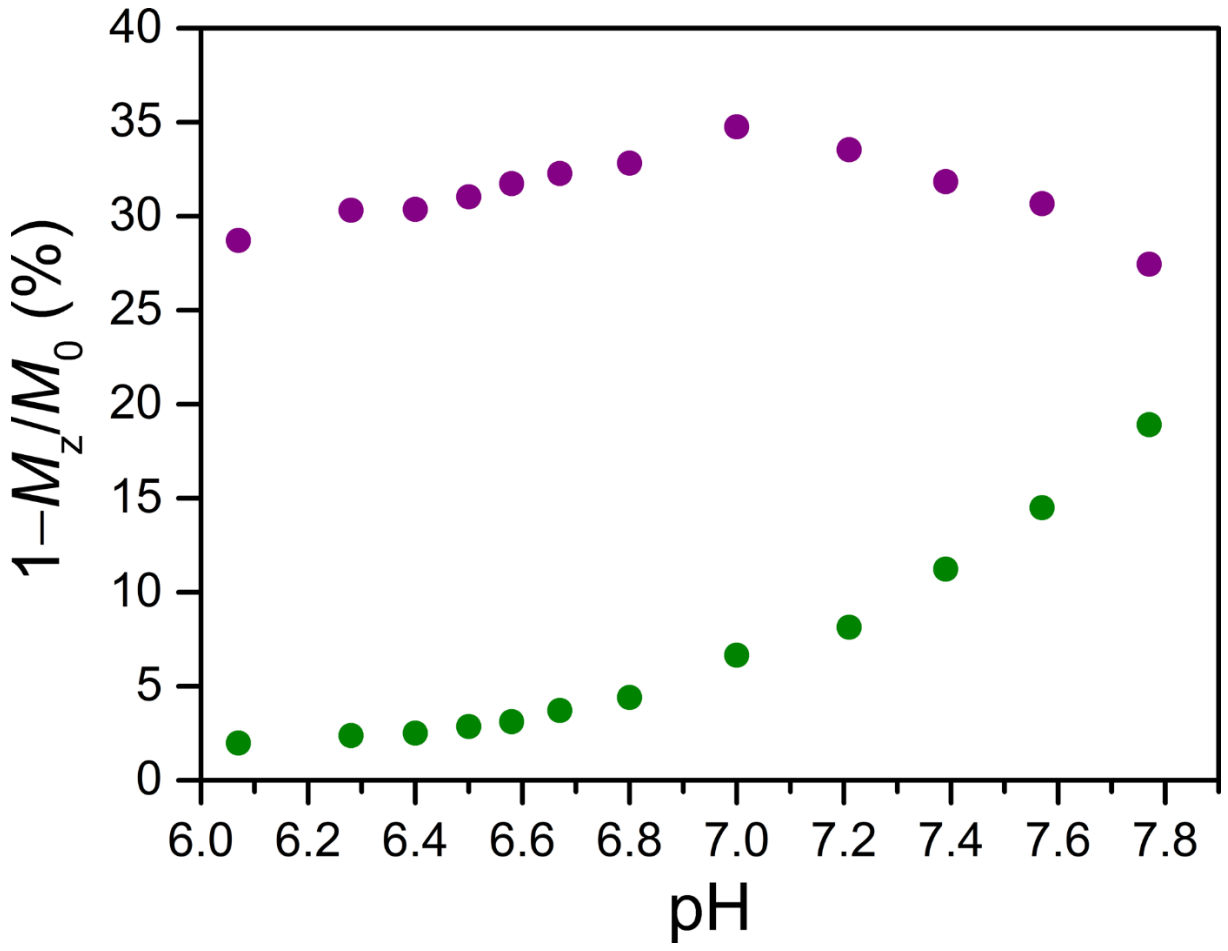

Figure 5.15 pH dependences of the CEST intensities from application of 2 s presaturation at 48 ppm (purple) and 67 ppm (green) using B_1 = 22 μT for 5 mM of **3** in aqueous solutions containing 50 mM HEPES and 100 mM NaCl, collected at 37 °C and 11.7 T.

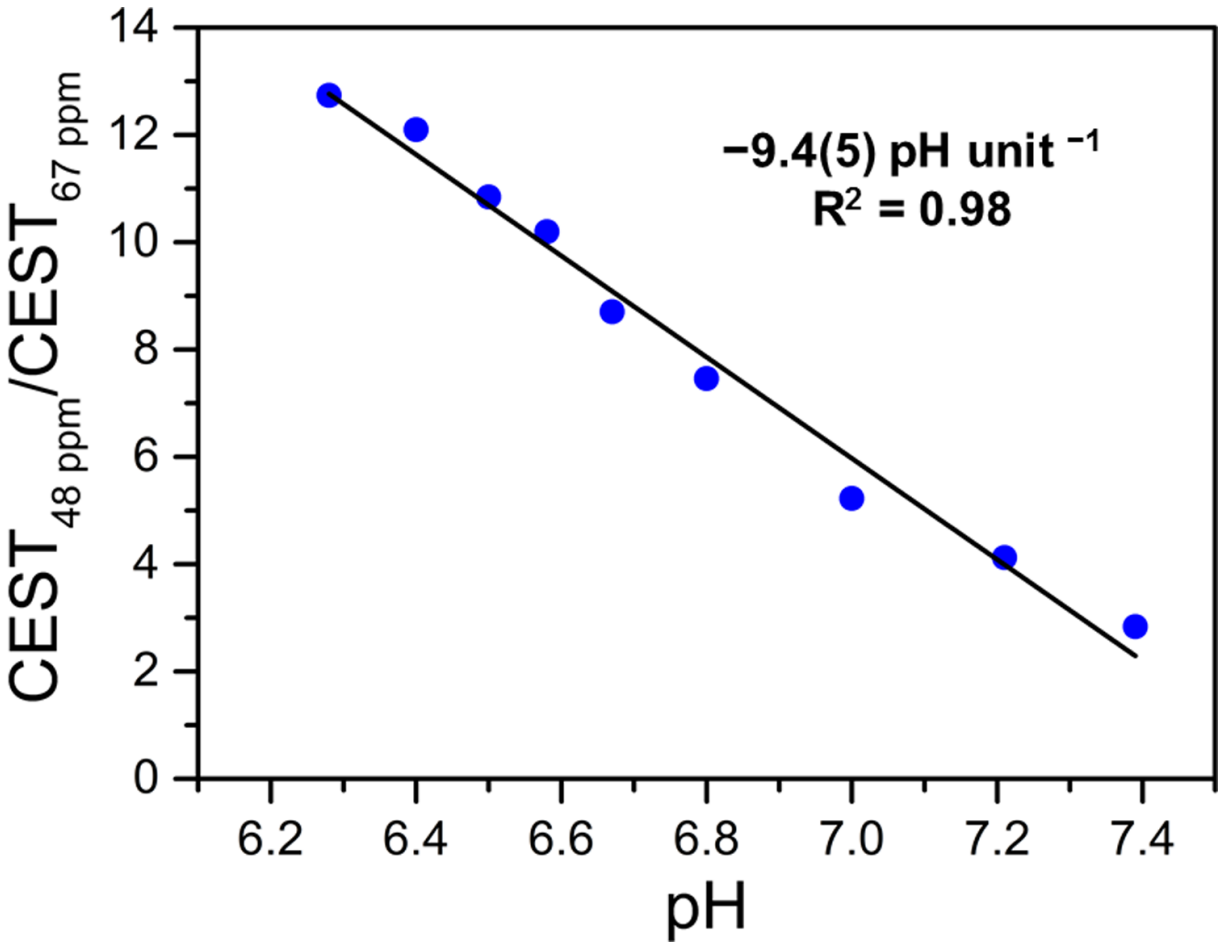

Figure 5.16 pH dependence of the ratio of CEST intensities from application of 2 s presaturation at 48 and 67 ppm using B_1 = 22 μT for 5 mM of **3** in aqueous solutions containing 50 mM HEPES and 100 mM NaCl, collected at 37 °C and 11.7 T. Blue circles represent experimental data and the solid black line denotes a linear fit to the data with the following equation: $CEST_{48\ ppm}/CEST_{67\ ppm} = -9.4(5) \times pH + 72(3)$; $R^2 = 0.98$.

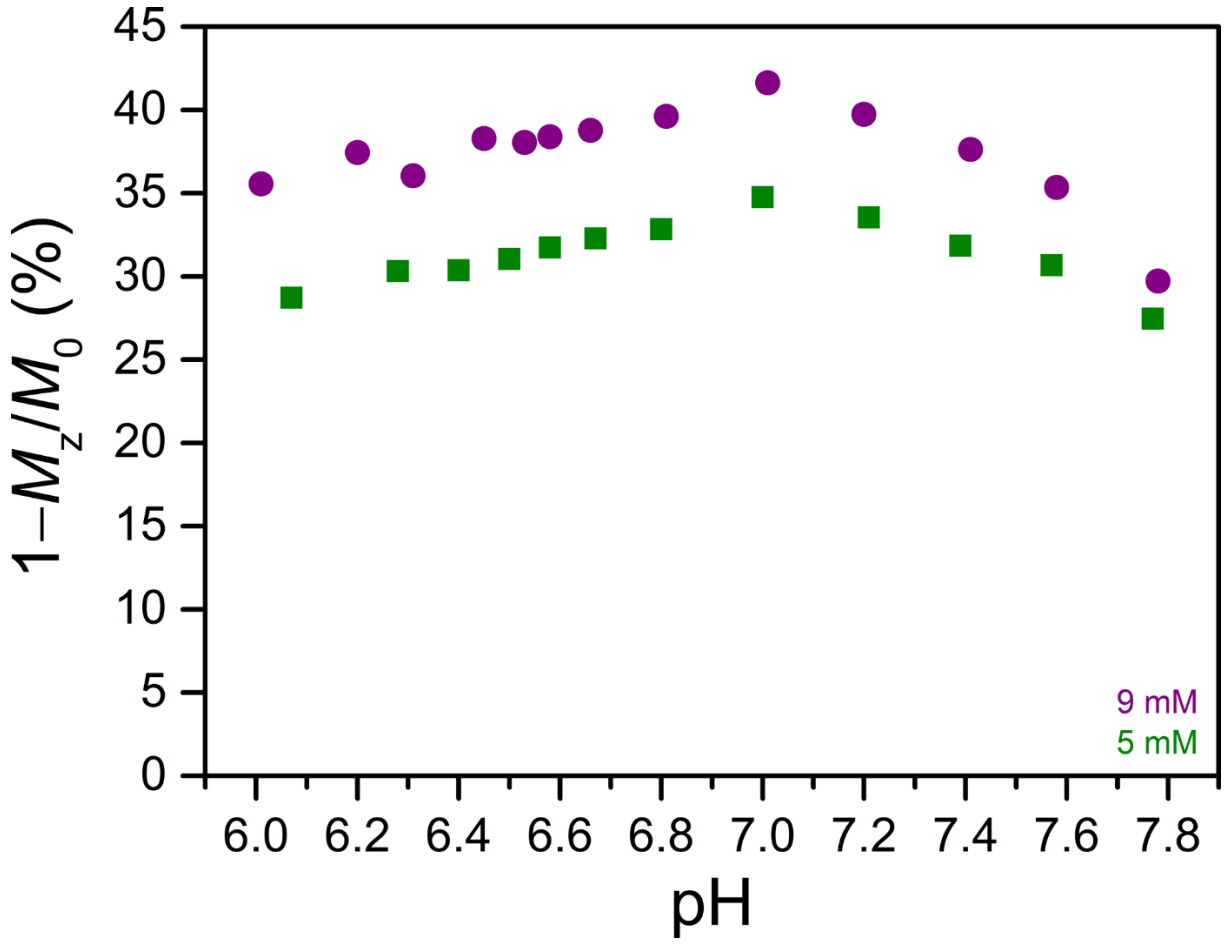

Figure 5.17 Comparison of the pH dependence of the CEST intensity from application of 2 s presaturation at 48 ppm using $B_1 = 22$ μT for various concentrations of **3** (see legend) in aqueous solutions containing 50 mM HEPES and 100 mM NaCl, collected at 37 °C and 11.7 T.

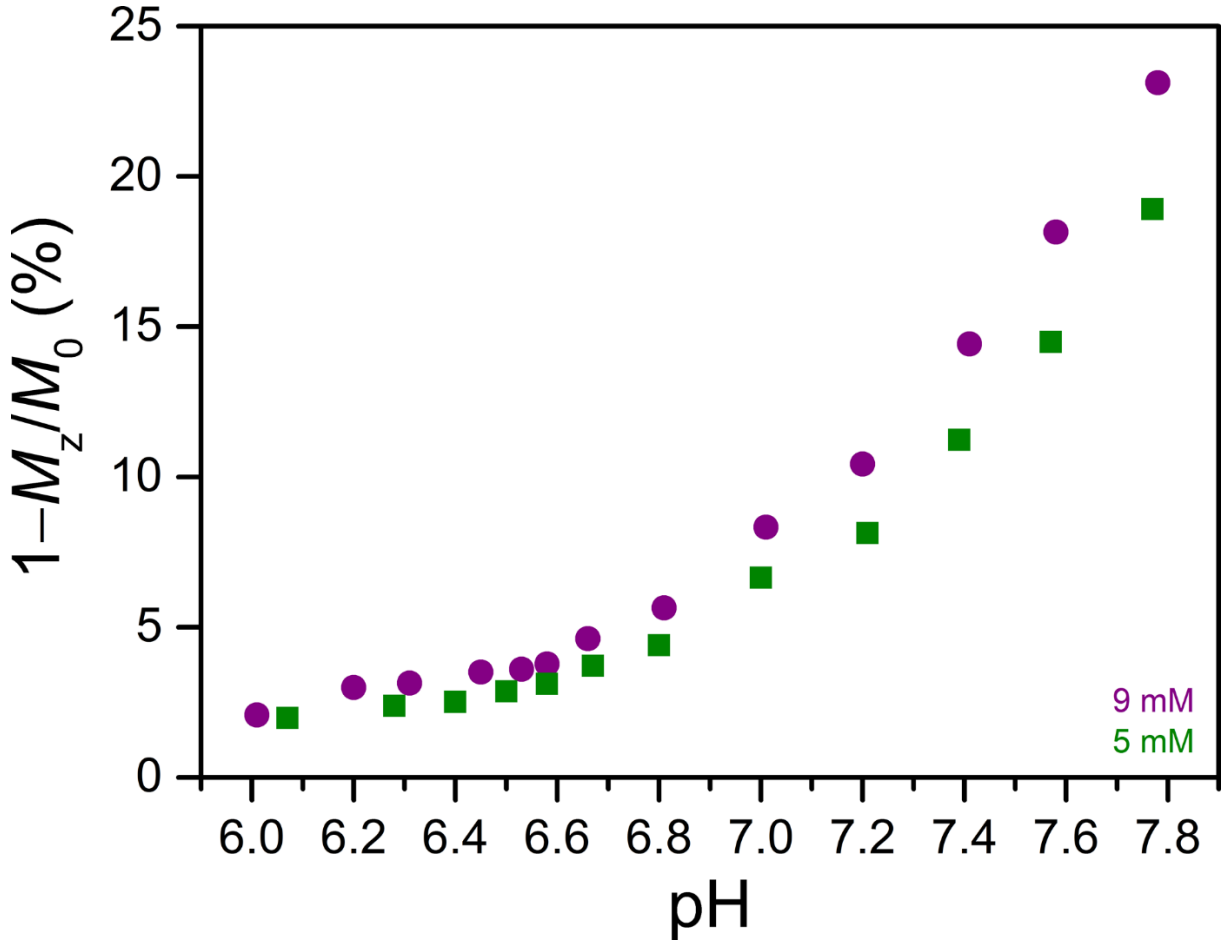

Figure 5.18 Comparison of the pH dependence of the CEST intensity from application of 2 s presaturation at 67 ppm using $B_1 = 22$ μT for various concentrations of **3** (see legend) in aqueous solutions containing 50 mM HEPES and 100 mM NaCl, collected at 37 °C and 11.7 T.

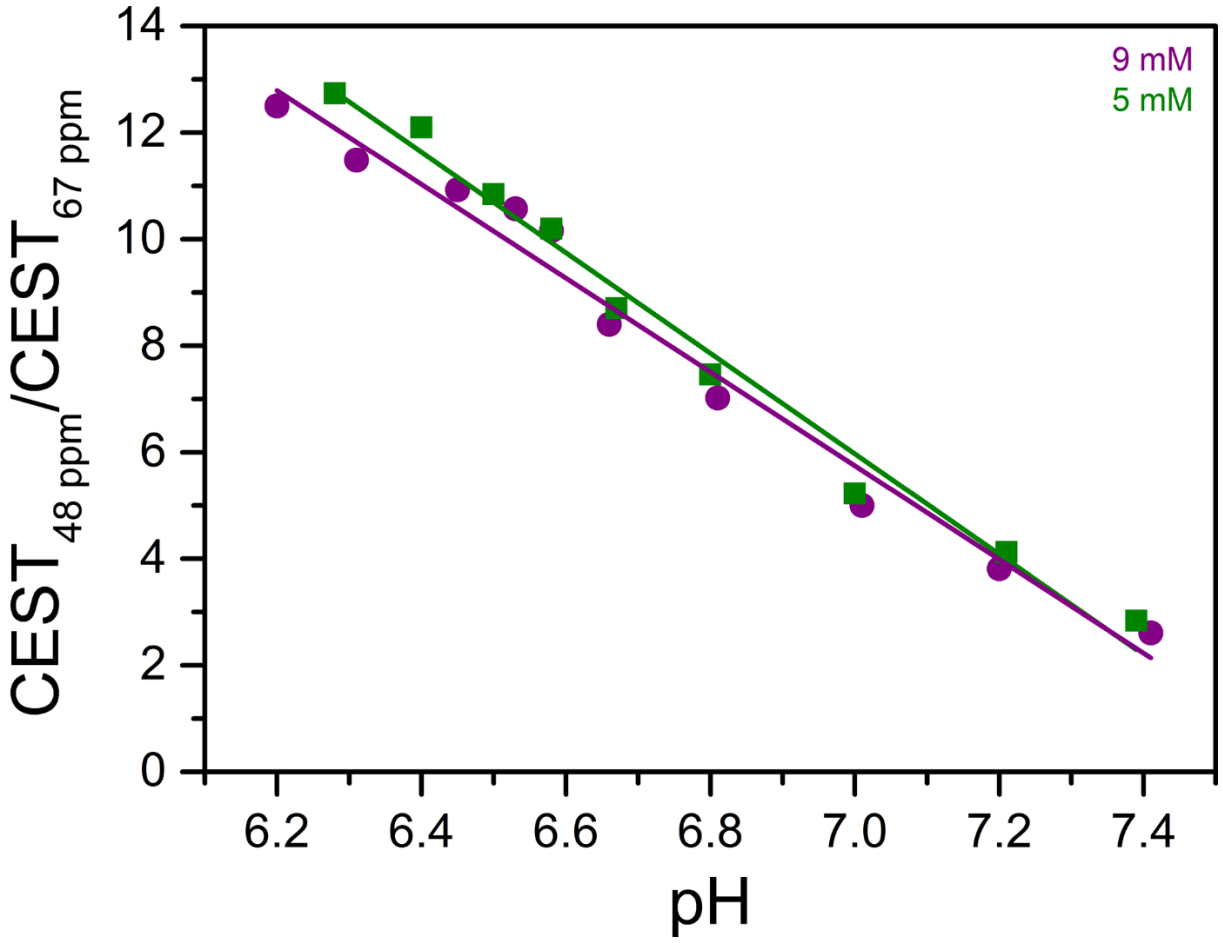

Figure 5.19 Comparison of the pH calibration curves obtained by taking the ratios of the CEST intensities from application of 2 s presaturation at 48 and 67 ppm using B_1 = 22 μT for various concentrations of **3** (see legend) in aqueous solutions containing 50 mM HEPES and 100 mM NaCl, collected at 37 °C and 11.7 T. Symbols represent experimental data and solid lines denote linear fits to the data with the following equations: (9 mM) $CEST_{48\ ppm}/CEST_{67\ ppm} = -8.8(5) \times pH + 67(4)$, $R^2 = 0.98$; (5 mM) $CEST_{48\ ppm}/CEST_{67\ ppm} = -9.4(5) \times pH + 72(3)$, $R^2 = 0.98$.

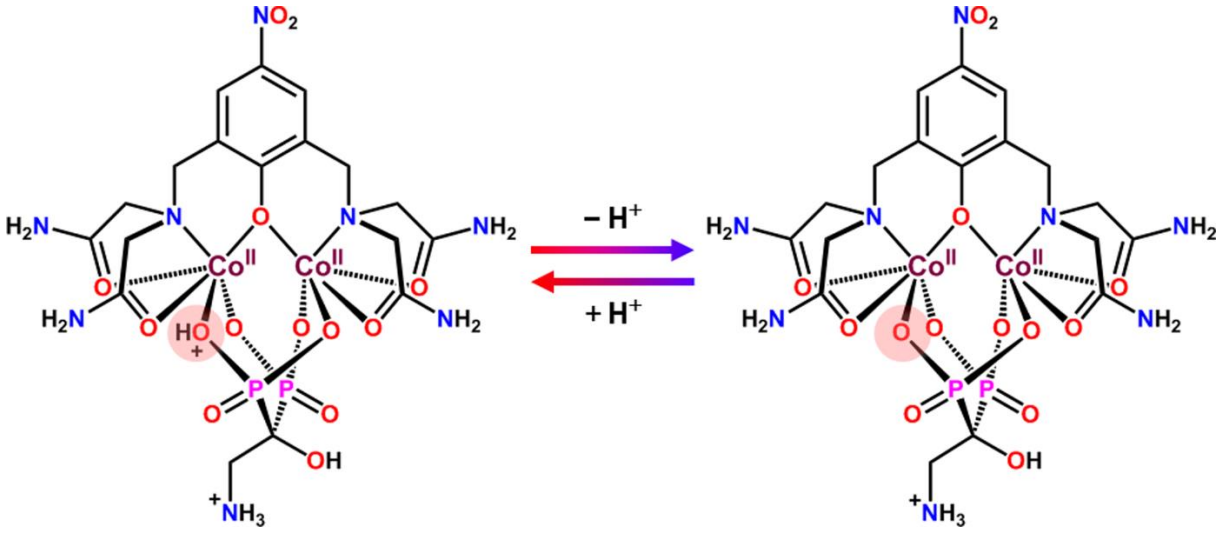

Figure 5.20 Scheme highlighting the ionization process taking place on the ancillary bisphosphonate ligand for the dicobalt complex in **3**, in the pH range 1.50–7.80.

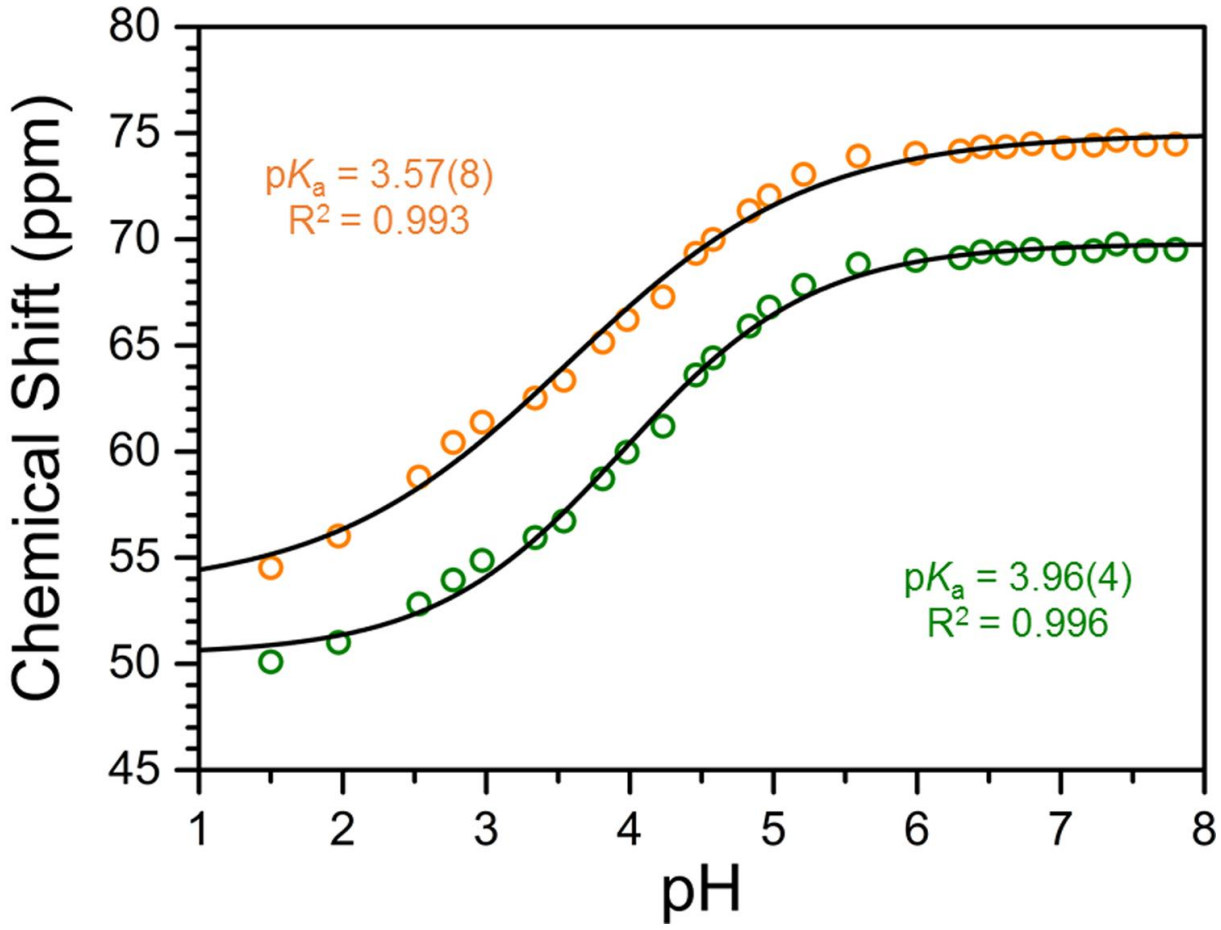

Figure 5.21 pH dependences of the ^{1}H NMR chemical shifts (reported as frequency offsets) of the two inequivalent methylene proton resonances from the ancillary bisphosphonate ligand for **3** in aqueous solutions containing 50 mM HEPES and 100 mM NaCl, collected at 37 °C and 11.7 T. Circles represent experimental data and solid lines correspond to sigmoidal fits to the data (see Equation 5.1). Fits to the data give pK_a = 3.57(8) (R^2 = 0.993) and 3.96(4) (R^2 = 0.996) for the two methylene proton resonances, respectively. The ionization process taking place on the ancillary bisphosphonate is highlighted with the schematics of the complex in Figure 5.20.

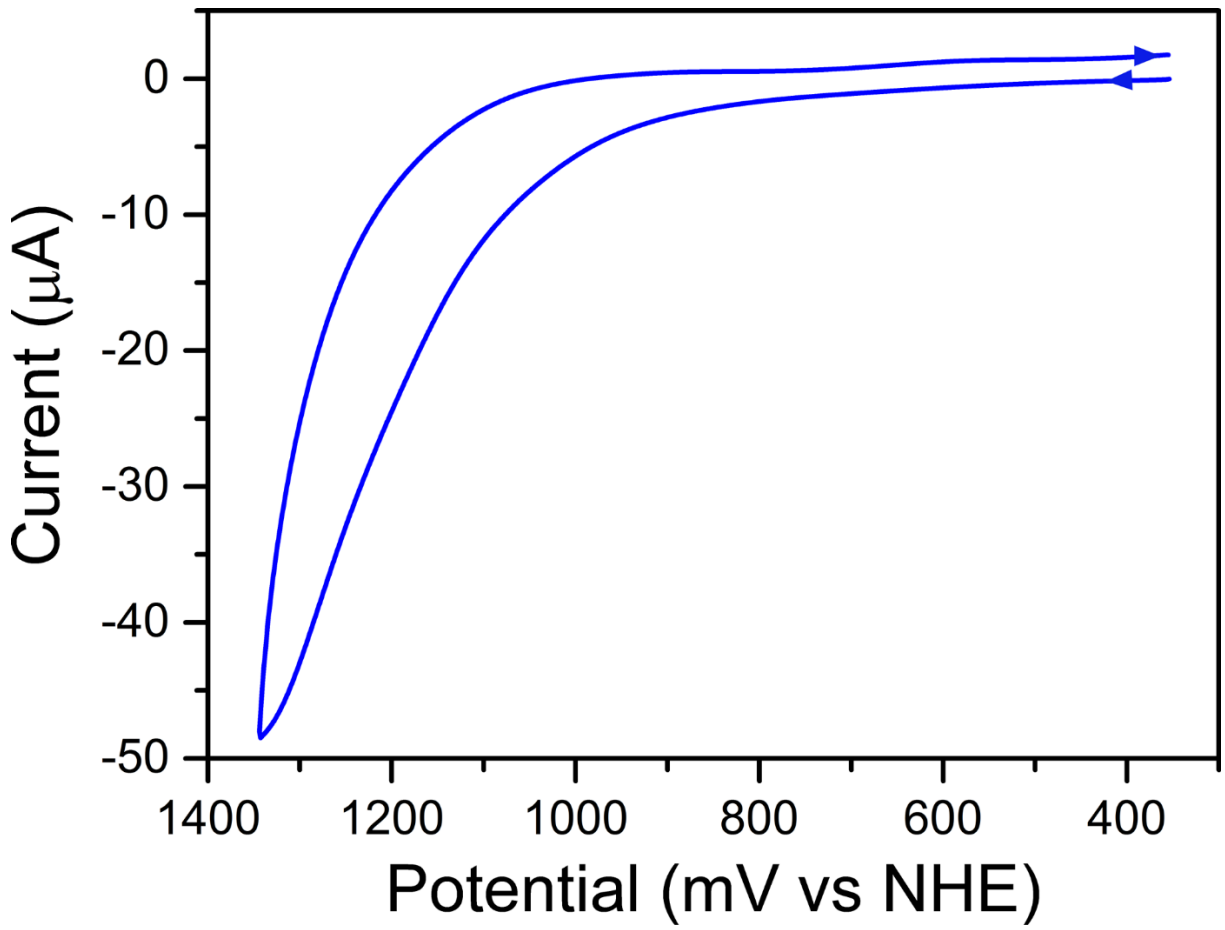

Figure 5.22 Cyclic voltammogram for 2 mM of **3** in an aqueous solution containing 50 mM HEPES and 100 mM NaCl buffered to pH 7.4. Measurements were carried out at ambient temperature using a glassy carbon electrode as a working electrode and 20 mV s^{-1} scan rate. The blue arrows denote the scan direction.

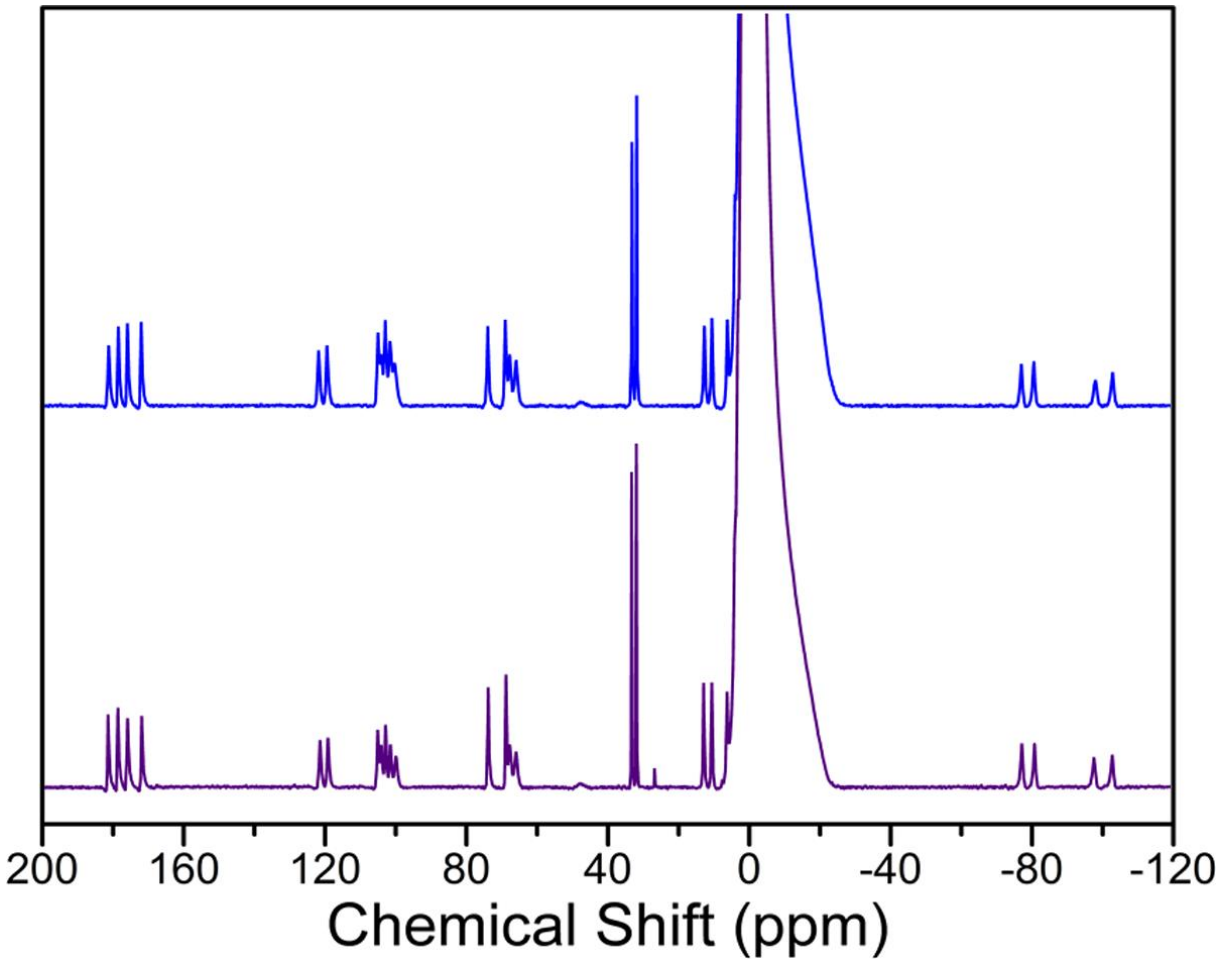

Figure 5.23 Stacked ^{1}H NMR spectra of 9 mM of **3** in an aqueous solution containing 50 mM HEPES and 100 mM NaCl buffered to pH 7.4 without (blue) and with (purple) the presence of 9 mM of each NaH_2PO_4, Na_3ADP ($(ADP)^{3-}$ = adenosine 5′-diphosphate), and Na_2H_2ATP ($(ATP)^{4-}$ = adenosine 5′-triphosphate), collected at 37 °C and 14.1 T. Note that compound **3** was incubated with the solution of the phosphate ions at 25 °C for 24 h prior to the NMR experiment.

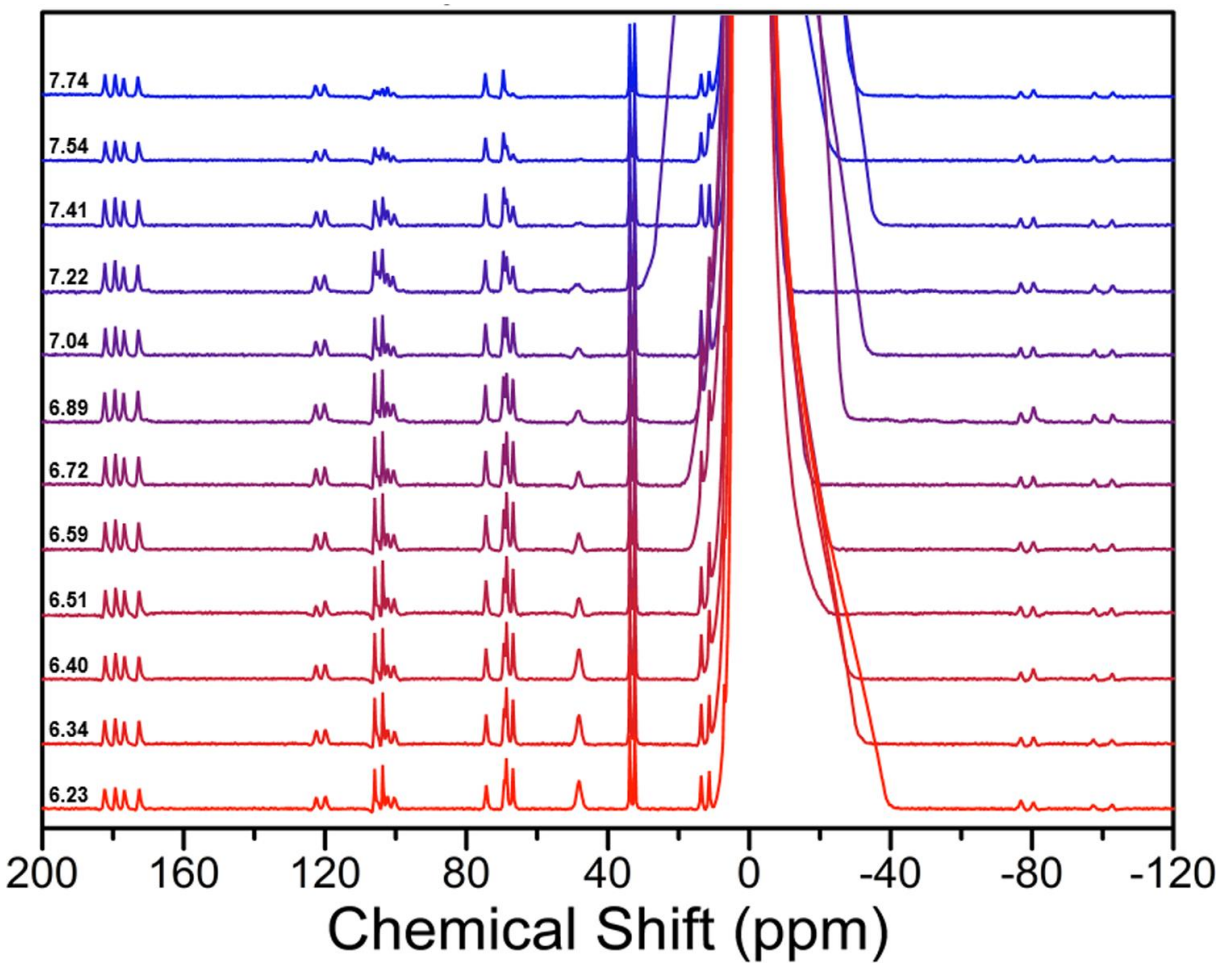

Figure 5.24 Variable-pH ^{1}H NMR spectra of 8 mM of **3** in FBS at various pH values, collected at 37 °C and 14.1 T. Black numbers on the left denote the pH of the NMR sample solutions measured with a pH electrode.

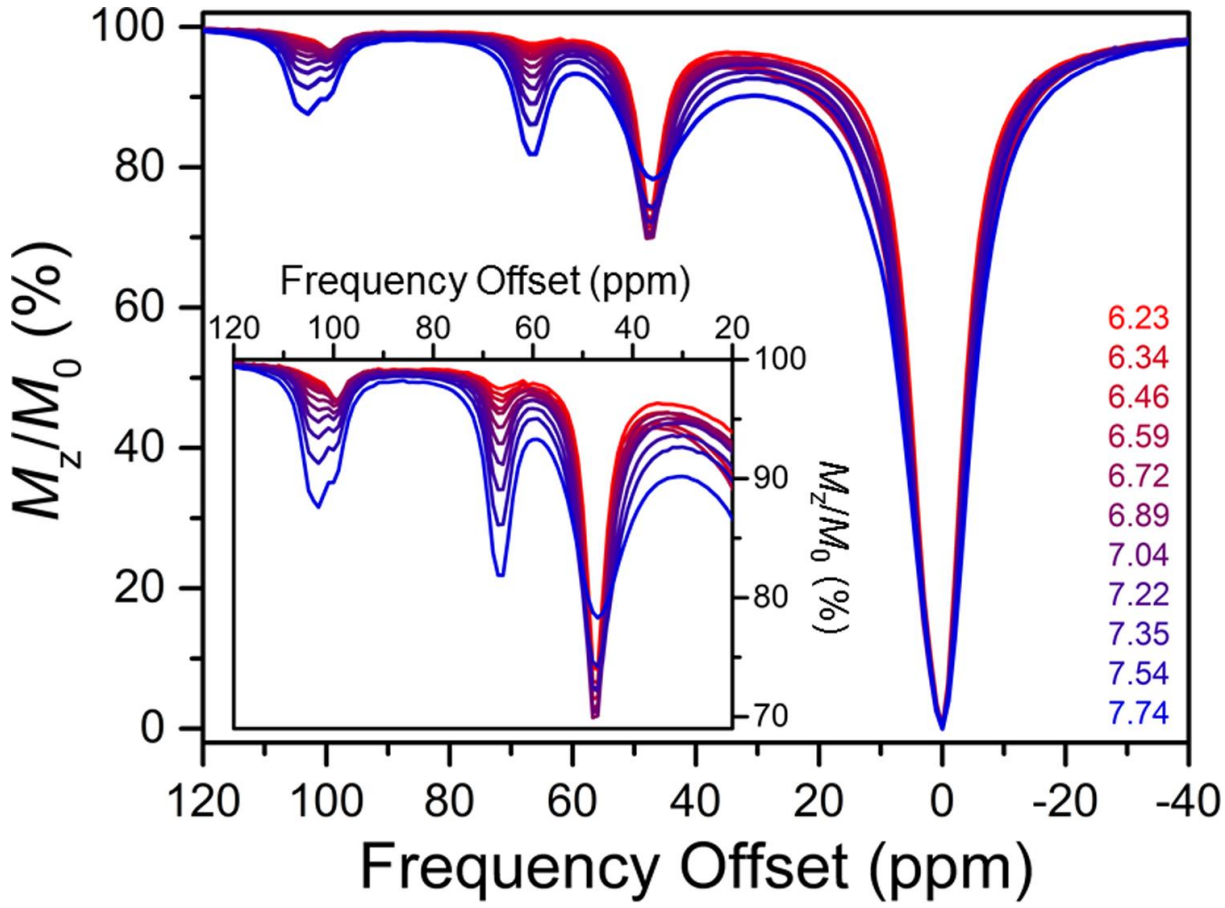

Figure 5.25 Variable-pH CEST spectra collected at 11.7 T and 37 °C using 2 s presaturation pulse and B_1 = 22 μT for 8 mM of **3** in FBS at pH 6.23–7.74 (red to blue). Colored numbers in the legend denote the pH of the solutions measured with a pH electrode and the corresponding color for each sample. Inset: Expanded view of the CEST peaks of interest.

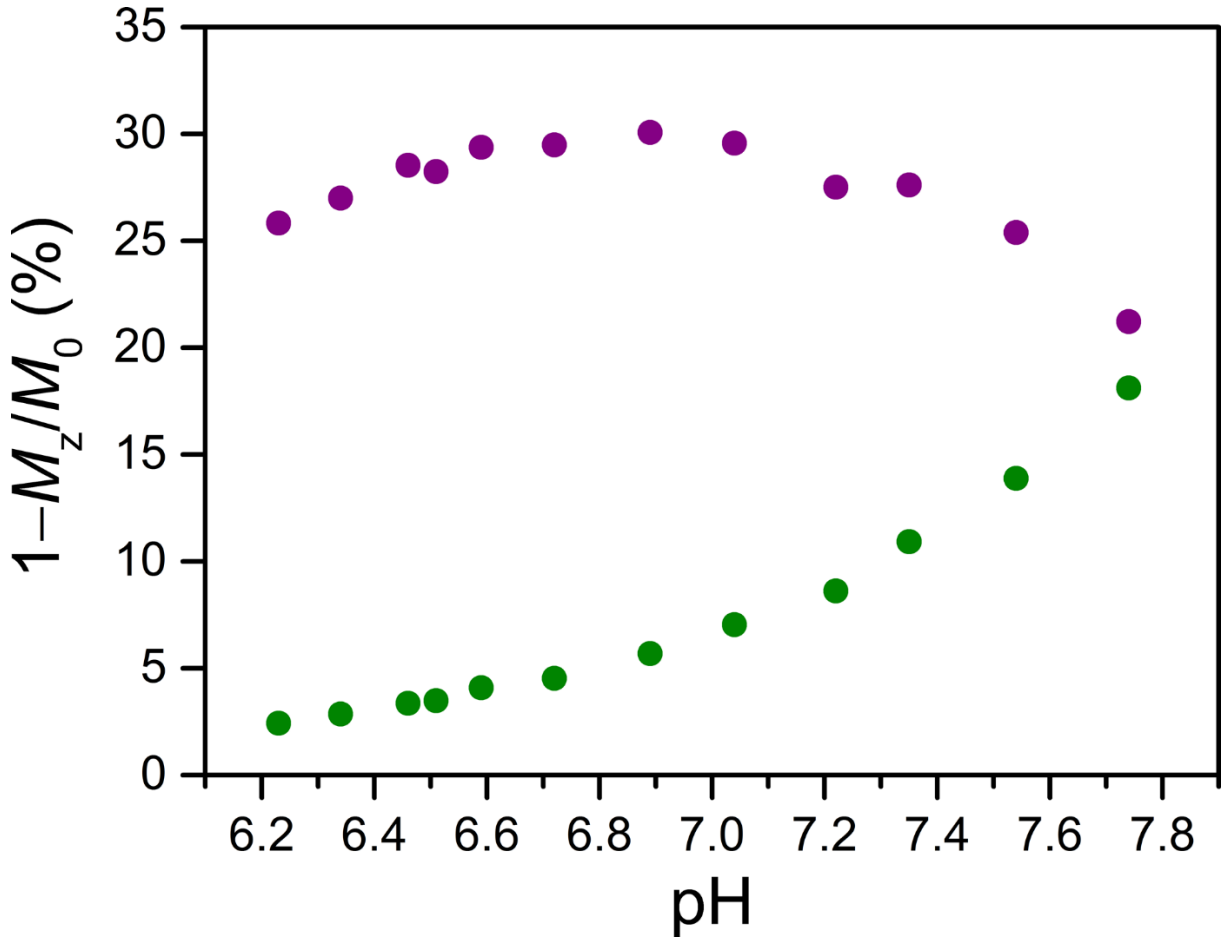

Figure 5.26 pH dependences of the CEST intensities from application of 2 s presaturation at 48 ppm (purple) and 67 ppm (green) using B_1 = 22 μT for 8 mM of **3** in FBS, collected at 37 °C and 11.7 T.

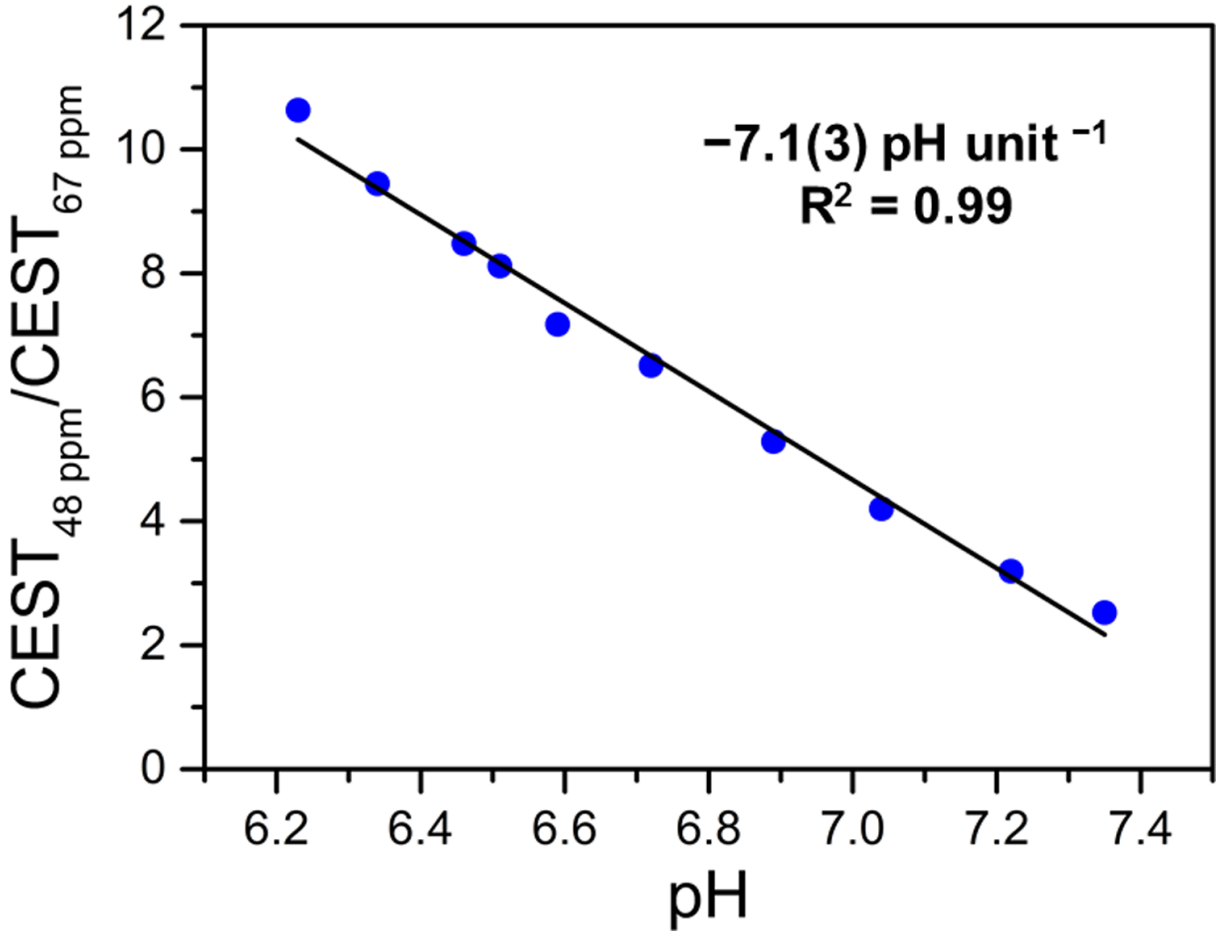

Figure 5.27 pH dependence of the ratio of CEST intensities from application of 2 s presaturation at 48 and 67 ppm using B_1 = 22 μT for 8 mM of **3** in FBS, collected at 37 °C and 11.7 T. Blue circles represent experimental data and the solid black line denotes a linear fit to the data with the following equation: $CEST_{48\ ppm}/CEST_{67\ ppm} = -7.1(3) \times pH + 55(2)$; $R^2 = 0.99$.

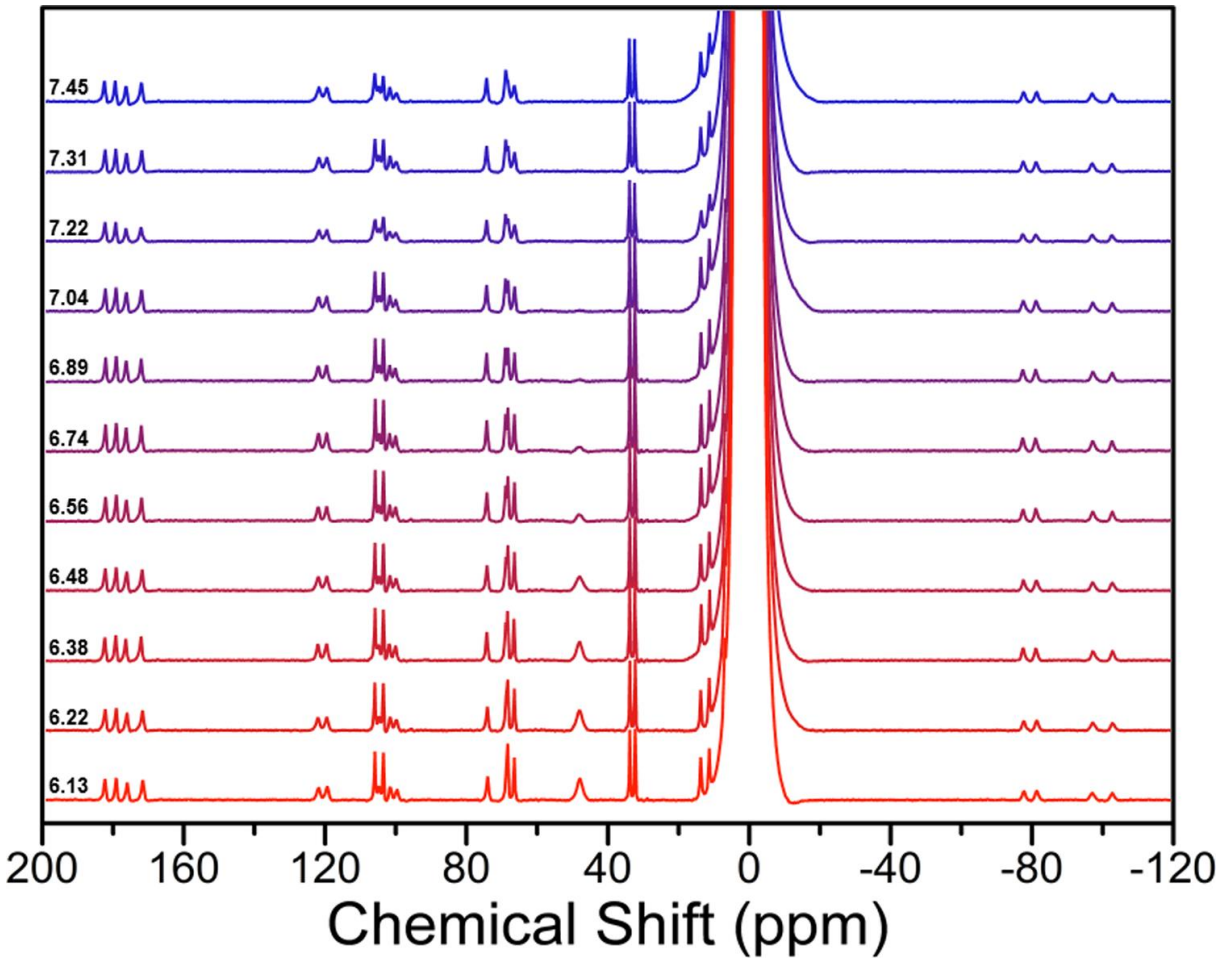

Figure 5.28 Variable-pH ^{1}H NMR spectra of 8 mM of **3** in 17% (w/v) gelatin gels at various pH values, collected at 37 °C and 14.1 T. Black numbers on the left denote the pH of the NMR samples measured with a pH electrode.

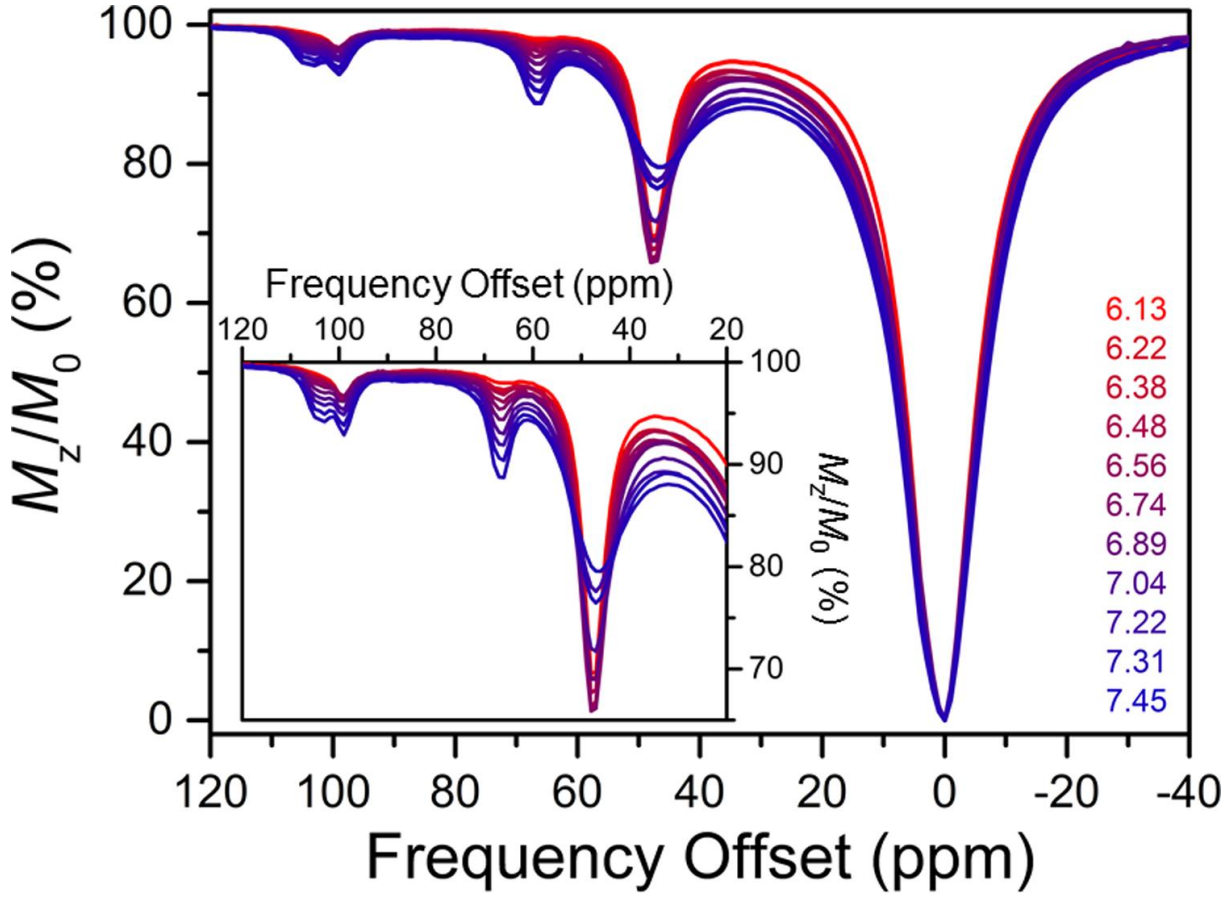

Figure 5.29 Variable-pH CEST spectra collected at 11.7 T and 37 °C using 2 s presaturation pulse and B_1 = 22 μT for 8 mM of **3** in 17% (w/v) gelatin gels at pH 6.13–7.45 (red to dark purple). Colored numbers in the legend denote the pH of the samples measured with a pH electrode and the corresponding color for each sample. Inset: Expanded view of the CEST peaks of interest.

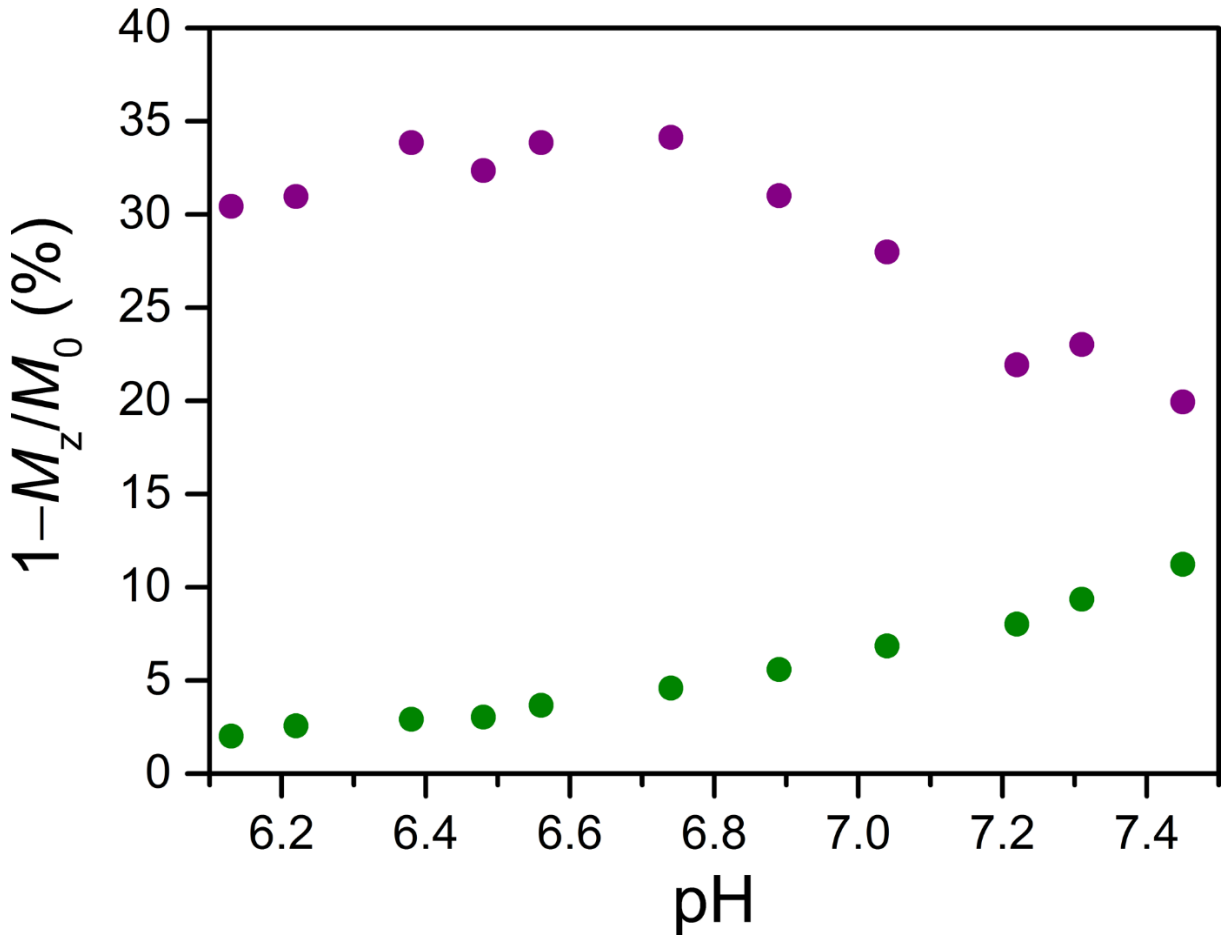

Figure 5.30 pH dependences of the CEST intensities from application of 2 s presaturation at 48 ppm (purple) and 67 ppm (green) using B_1 = 22 μT for 8 mM of **3** in 17% (w/v) gelatin gels, collected at 37 °C and 11.7 T.

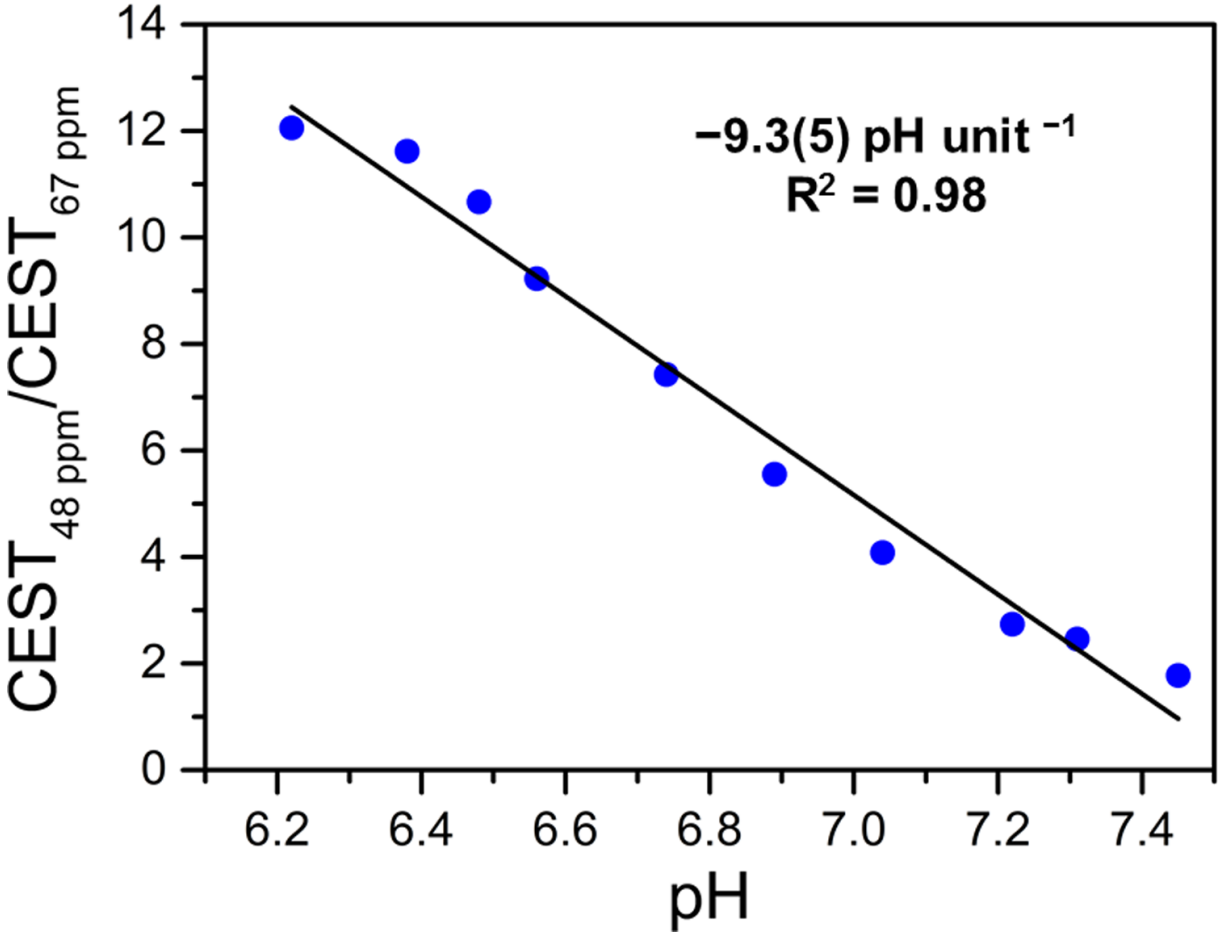

Figure 5.31 pH dependence of the ratio of CEST intensities from application of 2 s presaturation at 48 and 67 ppm using B_1 = 22 μT for 8 mM of **3** in 17% (w/v) gelatin gels, collected at 37 °C and 11.7 T. Blue circles represent experimental data and the solid black line denotes a linear fit to the data with the following equation: $CEST_{48\ ppm}/CEST_{67\ ppm} = -9.3(5) \times pH + 71(4)$; $R^2 = 0.98$.

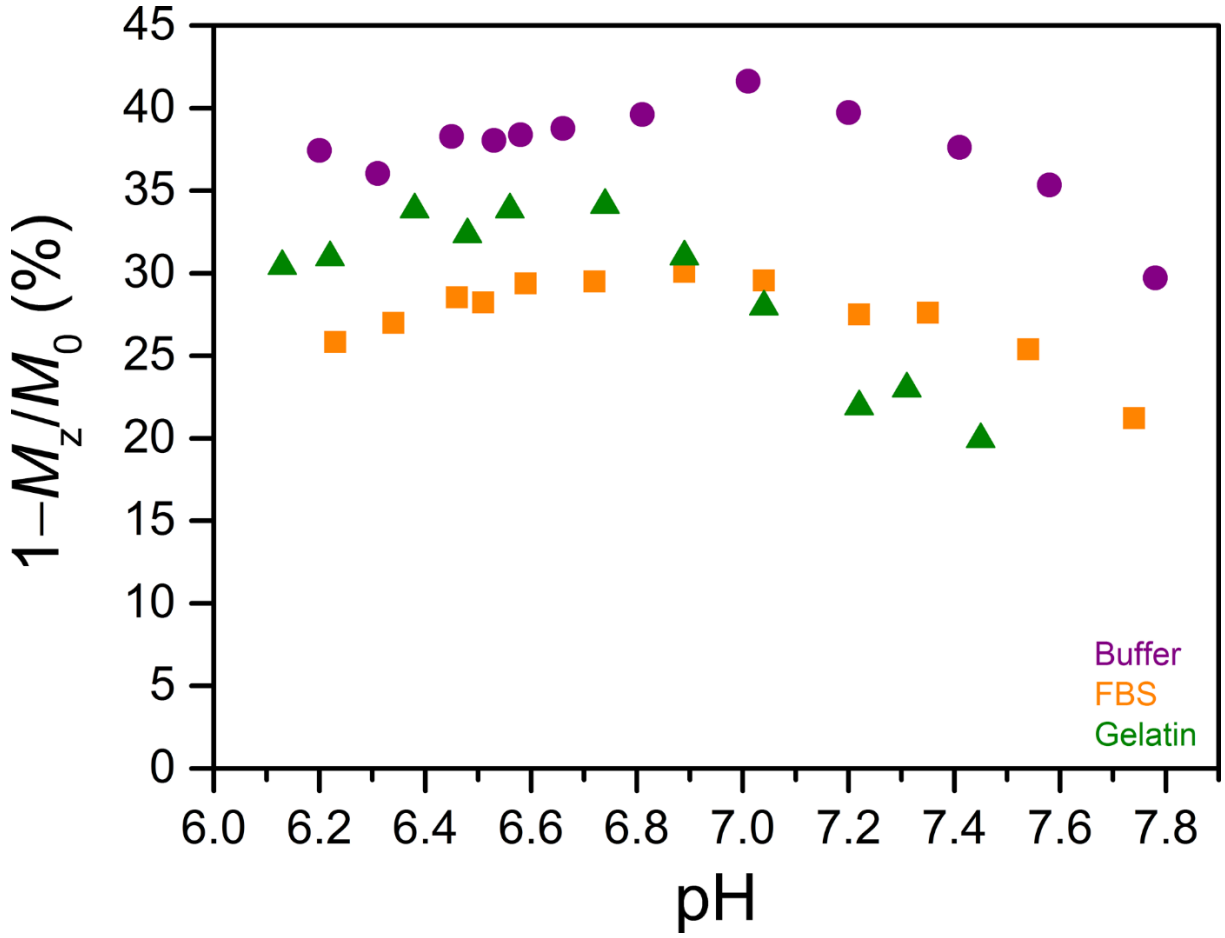

Figure 5.32 Comparison of the pH dependence of the CEST intensity from application of 2 s presaturation at 48 ppm using B_1 = 22 μT for **3** in aqueous buffer solutions containing 50 mM HEPES and 100 mM NaCl (purple; 9 mM), in FBS (orange; 8 mM), and in 17% (w/v) gelatin gels (green; 8 mM), collected at 37 °C and 11.7 T.

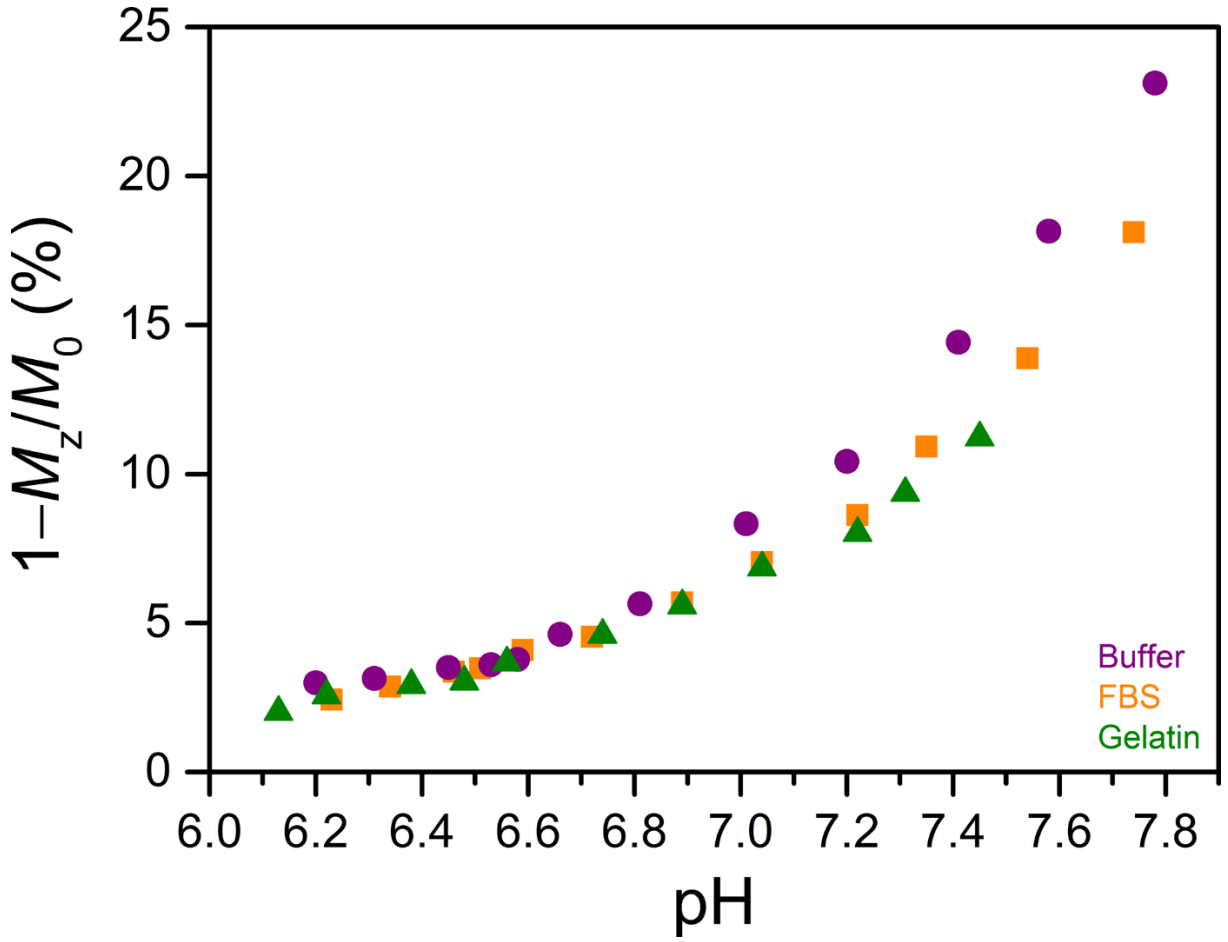

Figure 5.33 Comparison of the pH dependence of the CEST intensity from application of 2 s presaturation at 67 ppm using B_1 = 22 μT for **3** in aqueous buffer solutions containing 50 mM HEPES and 100 mM NaCl (purple; 9 mM), in FBS (orange; 8 mM), and in 17% (w/v) gelatin gels (green; 8 mM), collected at 37 °C and 11.7 T.

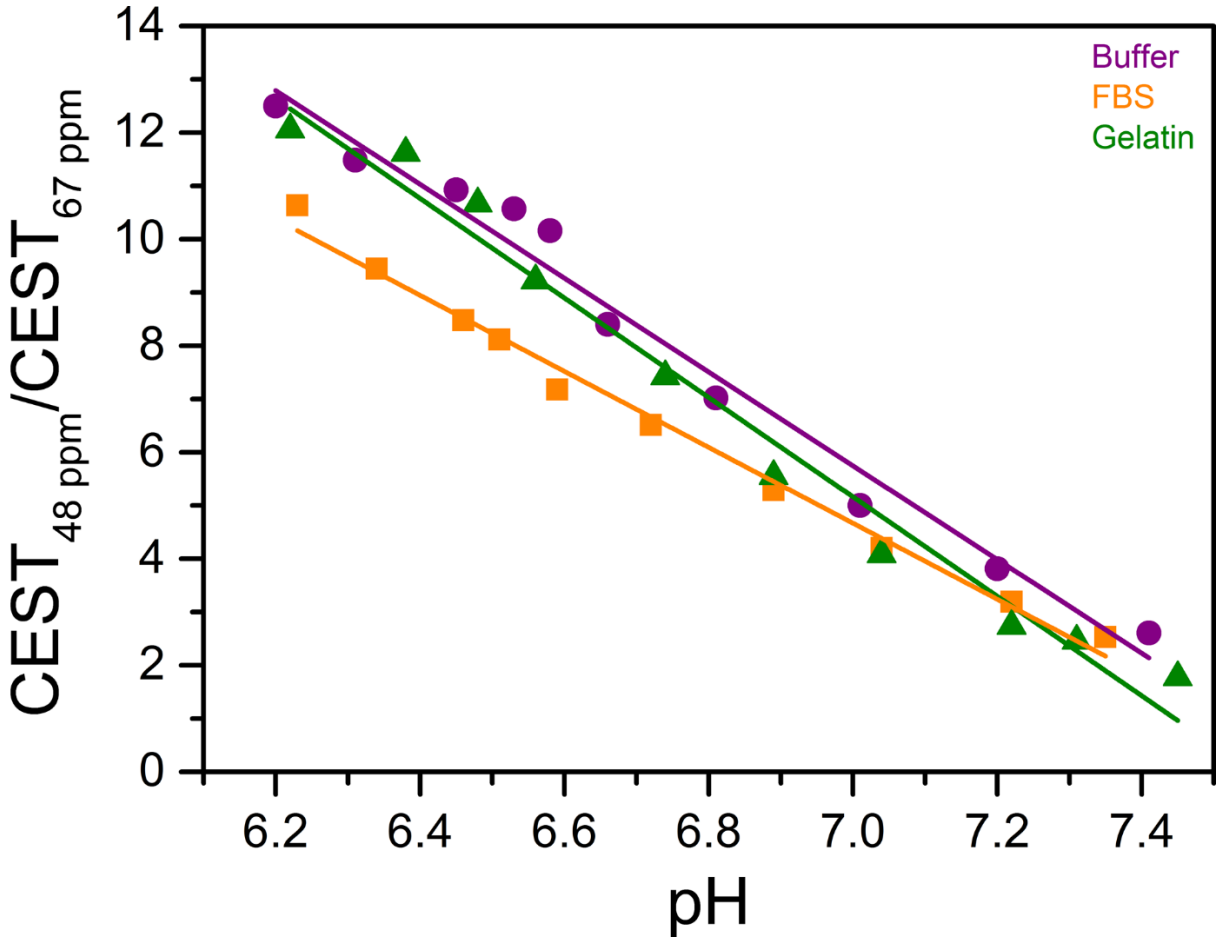

Figure 5.34 Comparison of the pH calibration curves obtained by taking the ratios of the CEST intensities from application of 2 s presaturation at 48 and 67 ppm using B_1 = 22 μT for **3** in aqueous buffer solutions containing 50 mM HEPES and 100 mM NaCl (purple), in FBS (orange), and in 17% (w/v) gelatin gels (green), collected at 37 °C and 11.7 T. See Section 5.3.6 and Figures 5.27 and 5.31 for the equations of the linear fits to the data.

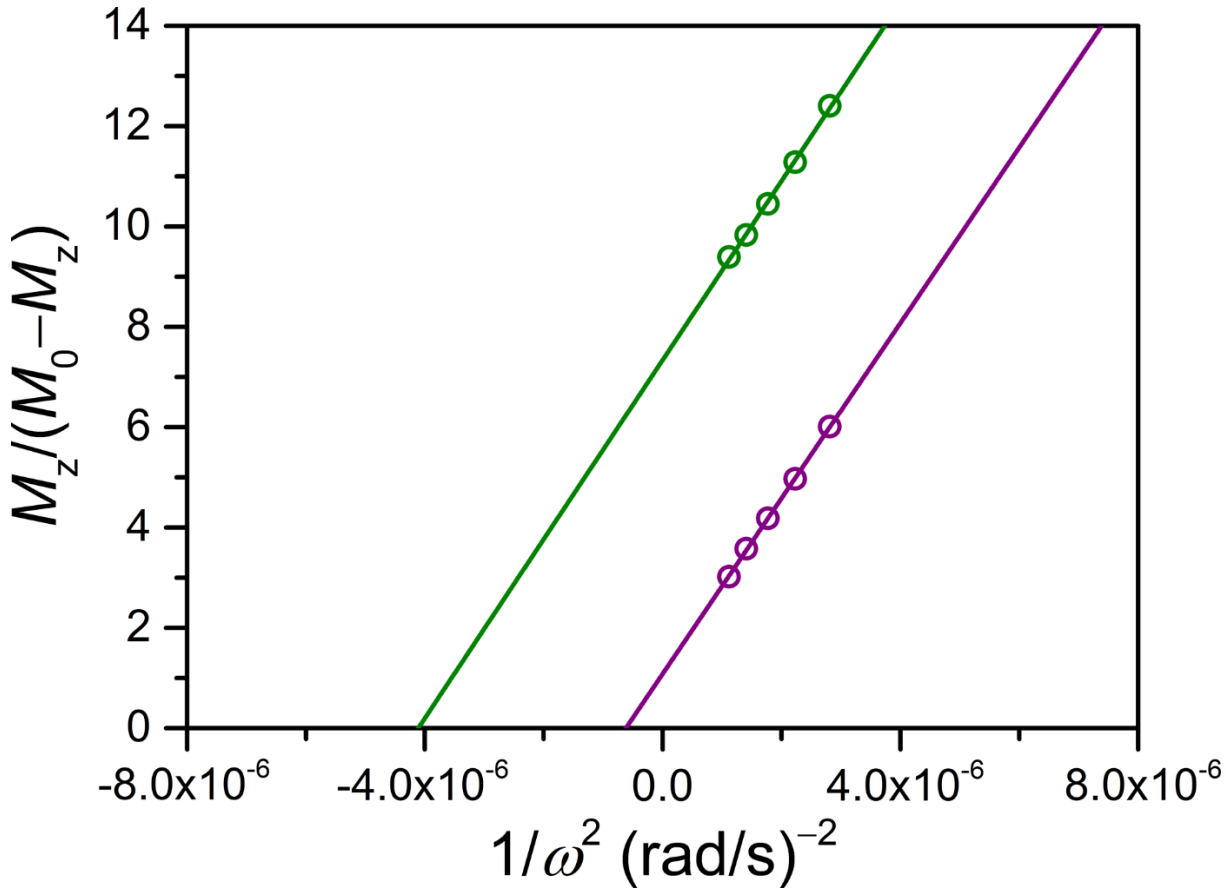

Figure 5.35 Omega plots of the CEST effects from application of 6 s presaturation at 48 ppm (purple) and 67 ppm (green) using B_1 = 14–22 μT for 8 mM of **3** in FBS at pH 7.46, collected at 37 °C and 11.7 T. Circles represent experimental data and lines represent linear fits to the data.

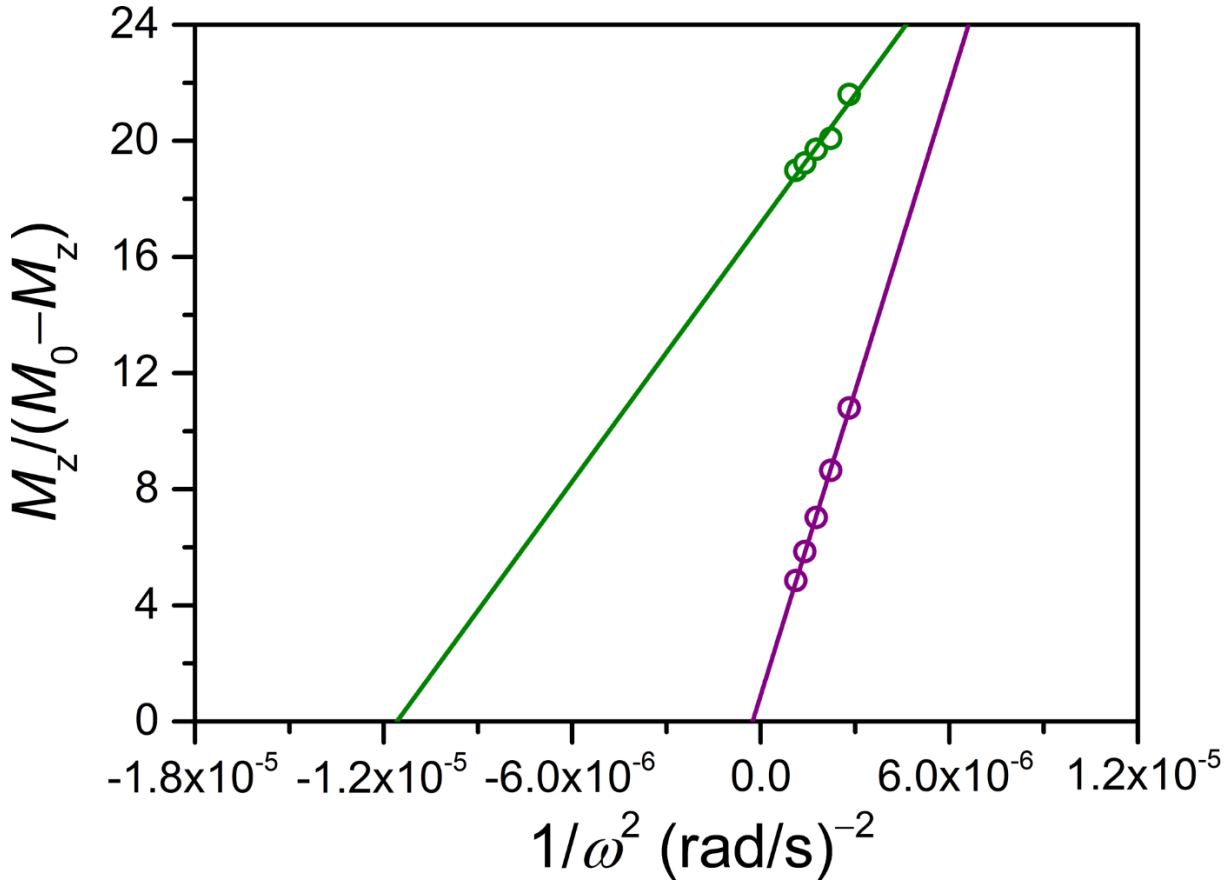

Figure 5.36 Omega plots of the CEST effects from application of 6 s presaturation at 48 ppm (purple) and 67 ppm (green) using B_1 = 14–22 μT for 8 mM of **3** in a 17% (w/v) gelatin gel at pH 7.22, collected at 37 °C and 11.7 T. Circles represent experimental data and lines represent linear fits to the data.

5.5.3 Supplementary Tables

Table 5.1 Summary of the average solution dc magnetic susceptibility data for **3**, collected at 37 °C and 11.7 T using the Evans method[20] (see Equation 5.2) for aqueous solutions with 50 mM HEPES and 100 mM NaCl buffered to various pH values (see Figure 5.7).

Average values	3
$\chi_M T$ ($cm^3\,K\,mol^{-1}$)	5.96(6)
$\chi_M T$ per Co^{II} ($cm^3\,K\,mol^{-1}$)	2.98(3)
μ_{eff} per Co^{II} (μ_B)[a]	4.88(7)
g per Co^{II} [b]	2.52(2)

[a] The relationship between μ_{eff} and $\chi_M T$ is as follows: $\mu_{eff} = (8\chi_M T)^{1/2}\mu_B$. [b] The relationship between $\chi_M T$ and g is as follows: $\chi_M T = (g^2 S(S+1))/8$. Note, here $S = {}^3/_2$.

Table 5.2 Comparison of proton exchange rate constants (k_{ex}) for **3** in an aqueous solution containing 50 mM HEPES and 100 mM NaCl buffered to pH 7.41 and in FBS at pH 7.46, obtained from Omega plots at 37 °C and 11.7 T.

	48 ppm	**67 ppm**
pH 7.41 buffer	$1.26(4) \times 10^3\ s^{-1}$	$4.4(2) \times 10^2\ s^{-1}$
pH 7.46 FBS	$1.27(3) \times 10^3\ s^{-1}$	$4.9(1) \times 10^2\ s^{-1}$

Table 5.3 Comparison of proton exchange rate constants (k_{ex}) for **3** in an aqueous solution containing 50 mM HEPES and 100 mM NaCl buffered to pH 7.20 and in a 17% (w/v) gelatin gel at pH 7.22, obtained from Omega plots at 37 °C and 11.7 T.

	48 ppm	**67 ppm**
pH 7.20 buffer	$9.9(2) \times 10^2\ s^{-1}$	$4.2(1) \times 10^2\ s^{-1}$
pH 7.22 gelatin	$2.0(2) \times 10^3\ s^{-1}$	$2.9(3) \times 10^2\ s^{-1}$

Table 5.4 Comparison of T_1 relaxation times of H_2O at 37 °C and 11.7 T in an aqueous solution containing 50 mM HEPES and 100 mM NaCl buffered to pH 7.35 and in FBS at pH 7.50.

	$\boldsymbol{T_1}$
pH 7.35 buffer	4.2(1) s
pH 7.50 FBS	3.5(1) s

Chapter 6: Selective Binding and Quantitation of Calcium with a Cobalt-Based Magnetic Resonance Probe

Reprinted with permission from:

Du, K.; Thorarinsdottir, A. E.; Harris, T. D. *Journal of the American Chemical Society* **2019**, *141*, 7163–7172.

This work was performed in collaboration with the co-authors listed above.

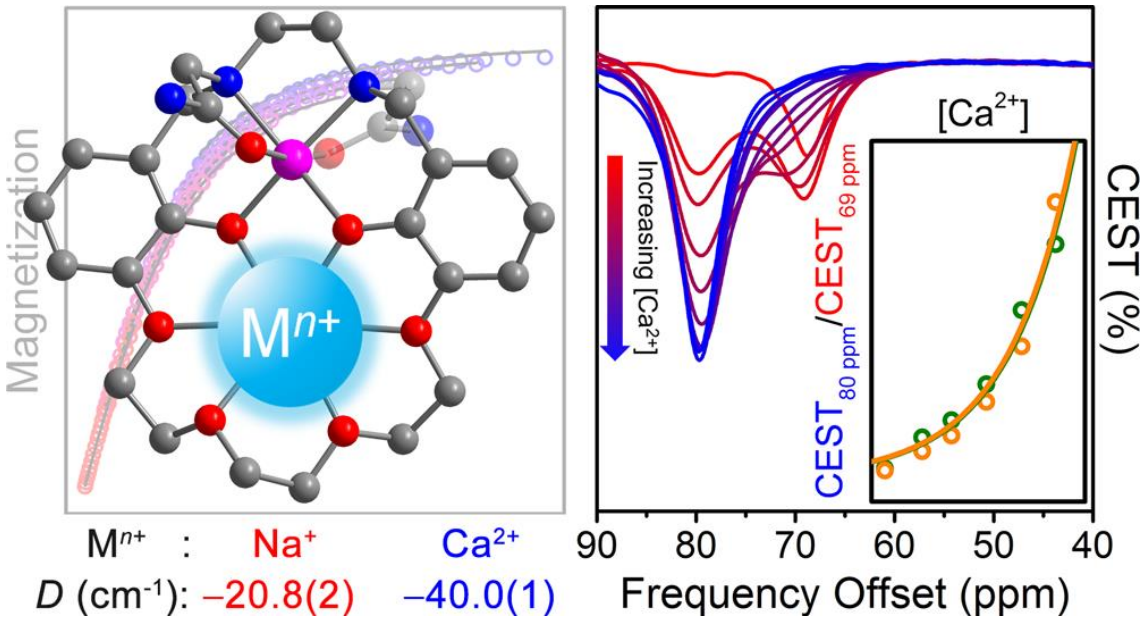

6.1 Introduction

The concentration of Ca^{2+} ions in blood serum is a vital biomarker for bone-related diseases, such as cancer,[1] hyperparathyroidism,[2] and Paget's disease.[3] These diseases are associated with the dissolution of bone tissue, which releases Ca^{2+} into the blood stream and results in hypercalcemia, a medical condition where the total Ca^{2+} concentration in serum exceeds 2.6 mM.[4] In current clinical settings, the presence and extent of hypercalcemia is evaluated by blood tests. This form of analysis provides only an estimate of the total Ca^{2+} concentration in serum, with no information on the spatial distribution or local concentration of Ca^{2+} near the bone lesion. As such, while blood tests can conveniently confirm the presence of hypercalcemia, they do not enable an assessment of the underlying source and cause of high Ca^{2+} concentrations.[5] For these reasons, realization of an imaging technique able to quantitate the local Ca^{2+} concentration near bone tissue would be highly useful in the early detection of bone-related diseases and in pathological studies.

Magnetic resonance imaging (MRI) is a non-invasive technique that is particularly well suited for measuring the concentration of Ca^{2+} near bone tissue owing to its unlimited depth penetration of tissue and its ability to provide spatiotemporal images.[6] Toward this end, several Gd^{III}-based probes have been developed to detect Ca^{2+} ions by virtue of relaxivity changes upon binding Ca^{2+}.[7] Here, extensive synthetic modifications have been employed to impart selective binding of Ca^{2+} in the presence of other cations.[7] Nevertheless, the utility of these probes is limited by heterogeneous biodistribution of Ca^{2+} and/or the probes themselves. It is therefore critical to develop MRI probes capable of selectively binding and quantitating Ca^{2+} through a concentration-independent method.

Lanthanide-[8] and transition metal-based[9] paramagnetic chemical exchange saturation transfer (PARACEST) probes, which deliver magnetization to bulk H_2O through chemical exchange of protons, have been reported to detect a number of biomarkers, such as redox environment,[10] pH,[9e,11] temperature,[12] and Zn^{2+} ions.[13] The exchangeable proton resonances, commonly from coordinating H_2O, carboxamides, and nitrogen heterocycles, are paramagnetically shifted, thus minimizing interference from labile protons in biological systems. Furthermore, the large chemical shifts allow for faster proton exchange, hence more pronounced contrast can be realized. The frequency-specific contrast afforded by PARACEST probes enables simultaneous detection of more than one CEST peak. As a result, the intensity ratio of two distinct CEST peaks that exhibit different responses can provide an effective and concentration-independent measure of biomarkers.[8b,9e,10c,11a,b,d–f,h,j,k]

An ideal Ca^{2+}-responsive PARACEST probe should feature a recognition moiety that is moderately selective for Ca^{2+},[8e] yet can reversibly bind other cations of concentrations that are relatively constant in serum, in order to enable a ratiometric measurement. One such cation is Na^+, which exhibits a relatively constant concentration of ca. 140 mM in serum.[14] In addition, the frequencies of CEST peaks for Ca^{2+}- and Na^+-bound complexes should be well separated to avoid interference, analogously to the attributes of a ^{19}F probe.[15] Along these lines, alkali and alkaline earth cations have been shown to significantly influence the magnetic anisotropy of a nearby paramagnetic metal ion, by causing distortions in the local coordination environment.[16] Because the proton hyperfine shift is highly sensitive to changes in metal coordination environment and magnetic anisotropy,[17] the CEST peak frequency can be indicative of the identity of the bound cation. As such, we set out to design a probe that features (1) a cation binding moiety with proper

affinities toward Ca^{2+} and Na^{+} to allow for an equilibrium between the Ca^{2+}- and Na^{+}-bound probes under physiological conditions, (2) a paramagnetic center with magnetic properties and coordination environment that is highly sensitive toward the identities of cations within its vicinity, and (3) a functional group capable of producing CEST effects.

A high-magnetic anisotropy Co^{II} complex that features coordinating carboxamide ligands and a proximate crown ether satisfies all of these criteria. Encouragingly, complexes of a Schiff base-18-crown-6 dinucleating ligand have recently been employed to modulate the electronic structure of Co^{II} via cation complexation.[18] Herein, we present a Co^{II}-based PARACEST probe that can reversibly bind Ca^{2+} and Na^{+} under physiological conditions. The ratio of CEST signal intensities from the resulting Ca^{2+}- and Na^{+}-bound probes enables, for the first time, the concentration-independent quantitation of Ca^{2+} concentration by an MR-based method.

6.2 Experimental Section

General Considerations. Unless otherwise specified, chemicals and solvents were purchased from commercial vendors and used without further purification. Deuterated solvents were purchased from Cambridge Isotope Laboratories. When necessary for moisture sensitive experiments, glassware was flame dried or stored in an oven at 150 °C for at least 4 h, followed by cooling in a desiccator. Air- and water-free manipulations were carried out in a Vacuum Atmosphere Nexus II glovebox or using standard Schlenk techniques under a dry dinitrogen atmosphere. Air-free experiments involving the use of water were carried out in an MBraun LABstar glovebox under a humid dinitrogen atmosphere. Acetonitrile (MeCN), diethyl ether (Et_2O), and methanol (MeOH) were dried using a commercial solvent purification system from Pure Process Technology. MeCN was stored over 4 Å molecular sieves prior to use. Water was

obtained from a purification system from EMD Millipore. Experimental details on the syntheses of organic ligand precursors are provided in Section 6.5.1.

Synthesis of 2,2'-(1^2,8^2-dihydroxy-9,12,15,18-tetraoxa-3,6-diaza-1,8(1,3)-dibenzenacyclooctadecaphane-3,6-diyl)diacetamide (H_2L, see Figure 6.1). Under a dry dinitrogen atmosphere, 13,16,19,22-tetraoxa-3,6-diazatricyclo[21.3.1.1^{8,12}]octacosa-1(27),8,10,12(28),23,25-hexaene-27,28-diol (0.20 g, 0.48 mmol) and *N*,*N*-diisopropylethylamine (0.12 g, 0.96 mmol) were dissolved in MeCN (20 mL) to give a brown solution. The solution was heated at reflux and 2-bromoacetamide (0.13 g, 0.96 mmol) was added dropwise to the boiling solution with vigorous stirring. After stirring at reflux for 12 h, basic alumina (2 g) was added and the mixture was evaporated to dryness under reduced pressure. The resulting powder was dry-loaded on a basic alumina column, which was packed using CH_2Cl_2 eluent. After loading, the column was first eluted with 2% (v/v) MeOH/CH_2Cl_2 until no compound was detected by thin-layer chromatography (TLC), as visualized by I_2 vapor, to remove an impurity (R_f = 0.6 in 5% (v/v) MeOH/CH_2Cl_2). The column was then eluted with 5% (v/v) MeOH/CH_2Cl_2 to obtain the desired product (R_f = 0.3 in 5% (v/v) MeOH/CH_2Cl_2). The combined fractions were evaporated to dryness under reduced pressure to give the product as an off-white solid (25 mg, 10%). ^{1}H NMR (MeOH-d_4): δ 6.88 (t, 2H), 6.72 (m, 4H), 4.14 (m, 4H), 3.88 (m, 4H), 3.77 (s, 4H), 3.65 (s, 4H), 3.03 (s, 4H), 2.72 (s, 4H).

Synthesis of LCo·3.1H_2O (**1**, see Figure 6.1). Under a dinitrogen atmosphere, H_2L (25 mg, 0.047 mmol) was dissolved in MeOH (5 mL). To this colorless solution, a solution of $Co(CH_3COO)_2{\cdot}4H_2O$ (12 mg, 0.048 mmol) in MeOH (5 mL) was added. The resulting light magenta solution was heated at reflux under a dinitrogen atmosphere for 12 h. The solution was

evaporated to dryness and the residue was dissolved in MeOH (2 mL). The pink solution was added to Et_2O (15 mL) with vigorous stirring, to induce the formation of a pink precipitate. The pink solid was collected by filtration, washed with Et_2O (5 mL), and dried in vacuo for 20 h to give **1** (25 mg, 82%). Anal. Calcd. for $C_{26}H_{40.2}CoN_4O_{11.1}$: C, 48.4; H, 6.28; N, 8.68%. Found: C, 48.2; H, 5.62; N, 9.14%. UV-Vis absorption spectrum (H_2O, 25 °C): 517 nm (ε = 59.5 M^{-1} cm^{-1}), 526 nm (ε = 57.7 M^{-1} cm^{-1}). FT-IR (ATR, cm^{-1}): 3341 (s, broad); 2916 (m); 2872 (m); 1662 (s); 1589 (s); 1562 (s); 1456 (s); 1304 (m); 1229 (s); 1110 (s); 1070 (s); 987 (m); 955 (m); 932 (m); 894 (m); 840 (m); 737 (s); 587 (w); 439 (w); 407 (w). Solution magnetic moment (D_2O, 37 °C): $\chi_M T$ = 2.4(3) cm^3 K mol^{-1}. Slow diffusion of acetone into a pink solution of **1** in H_2O over two weeks yielded single crystals of $LCo \cdot 0.50C_3H_6O \cdot 9.05H_2O$ (**1′**) suitable for X-ray structural analysis.

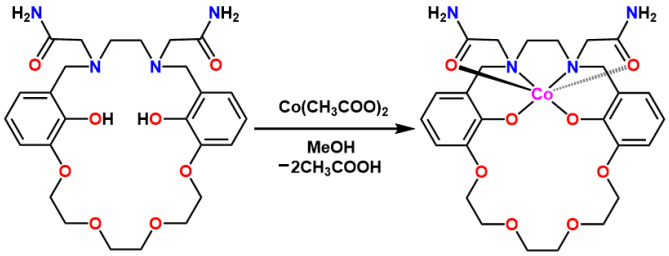

Figure 6.1 Synthesis and molecular structure of LCo.

*Synthesis of $LCoNa(NO_3) \cdot 1.7H_2O$ (**2**).* To a stirring pink solution of **1** (30 mg, 0.046 mmol) in MeOH (5 mL), a solution of $NaNO_3$ (4.3 mg, 0.051 mmol) in MeOH (0.5 mL) was added. The resulting pink solution was stirred for 5 min at ambient temperature and then filtered through diatomaceous earth. Slow diffusion of Et_2O into the pink solution over three days resulted in pink crystalline solid, which was collected by filtration and dried in vacuo for 20 h to afford **2** (34 mg, 95%). Anal. Calcd. for $C_{26}H_{37.4}CoN_5NaO_{12.7}$: C, 44.3; H, 5.35; N, 9.93%. Found: C, 44.3; H, 5.16; N, 10.1%. FT-IR (ATR, cm^{-1}): 3356 (s, broad); 2921 (m); 2873 (m); 1666 (s); 1591 (m); 1564 (m); 1476 (s); 1458 (s); 1302 (m); 1270 (m); 1231 (s); 1107 (s); 1086 (s); 987 (m); 956 (m); 930 (m); 896 (m); 840 (m); 741 (s); 409 (m). Slow diffusion of acetone into a pink solution of **2** in H_2O

over two weeks yielded single crystals of $[LCoNa(H_2O)](NO_3)_{0.5}(OH)_{0.5}\cdot 5.8H_2O$ (**2′**) suitable for X-ray structural analysis.

Synthesis of $LCoCa(NO_3)_2\cdot 0.25Et_2O\cdot 0.50H_2O$ (**3**). To a stirring pink solution of **1** (30 mg, 0.046 mmol) in MeOH (5 mL), a solution of $Ca(NO_3)_2\cdot 4H_2O$ (12 mg, 0.051 mmol) in H_2O (0.5 mL) was added. The resulting pink solution was stirred for 5 min at ambient temperature and then filtered through diatomaceous earth. Slow diffusion of Et_2O into the pink solution over four days resulted in pink crystalline solid, which was collected by filtration and dried in vacuo for 20 h to afford **3** (30 mg, 83%). Anal. Calcd. for $C_{27}H_{37.5}CaCoN_6O_{14.75}$: C, 41.5; H, 4.84; N, 10.8%. Found: C, 41.5; H, 5.03; N, 10.9%. FT-IR (ATR, cm^{-1}): 3341 (s, broad); 2922 (m); 2874 (m); 1662 (s); 1600 (m); 1566 (m); 1475 (s); 1325 (s); 1303 (m); 1233 (s); 1105 (s); 1086 (s); 1071 (s); 1022 (m); 983 (m); 958 (m); 942 (m); 843 (m); 828 (m); 738 (s); 444 (w); 431 (m). Slow diffusion of Et_2O into a pink solution of **3** in MeOH over two weeks yielded single crystals of $[LCoCa(NO_3)(MeOH)](NO_3)\cdot MeOH$ (**3′**) suitable for X-ray structural analysis.

X-ray Structure Determination. Single crystals of **1′**, **2′**, and **3′** were directly coated with Paratone-N oil and mounted on a MicroMounts rod. The crystallographic data were collected at 100 K on a Bruker APEX II diffractometer equipped with a MoKα sealed tube source. Raw data were integrated and corrected for Lorentz and polarization effects using Bruker APEX2 v. 2009.1.[19] The program SADABS was used to apply absorption correction.[20] Space group assignments were determined by examining systematic absences, E-statistics, and successive refinement of the structure. Structures were solved by SHELXT[21a,b] using direct methods and refined by SHELXL[21a,b] within the OLEX2 interface.[20c] All hydrogen atoms were placed at calculated positions using suitable riding models and refined using isotropic displacement

parameters derived from their parent atoms. Thermal parameters for all non-hydrogen atoms were refined anisotropically. The solvent mask procedure as implemented in OLEX2 was applied to the structures of **1′** and **2′** to account for severely disordered solvent molecules that could not be properly modeled. Void volumes of 9484.8 and 11161.8 $Å^3$ with a total of 4060.8 and 3043.0 electrons, respectively, were found per unit cell in the crystal structures of **1′**and **2′**, respectively. These were ascribed to 8.5 and 6.3 H_2O molecules per LCo unit in the structures of **1′** and **2′**, respectively. In the structure of **2′**, the occupancies of Na^+ and NO_3^- ions within each asymmetric unit were found to be 1.0 and 0.5, respectively. As such, 0.5 OH^- ion per LCo unit is likely present for charge balancing. Crystallographic data for **1′**, **2′**, and **3′** at 100 K and the details of data collection are listed in Table 6.3.

Solid-State Magnetic Measurements. Magnetic measurements of **1**, **2**, and **3** were performed on polycrystalline samples dispensed in eicosane. Samples were loaded in quartz tubes under a dinitrogen atmosphere, attached to a sealable hose adapter, and flame sealed under vacuum on a Schlenk manifold. All data were collected using a Quantum Design MPMS-XL SQUID magnetometer. The reduced magnetization data were collected between 1.8 and 10 K at applied dc fields ranging from 0 to +7 T. The program PHI[22] was employed to simulate and fit the reduced magnetization data using the following spin Hamiltonian:

$$\hat{H} = D\hat{S}_z^2 + g\mu_B \boldsymbol{S}\cdot\boldsymbol{H} \qquad (6.1)$$

In this Hamiltonian, D is the axial zero-field splitting parameter, $\hat{S}_z$ is the z component of the spin angular momentum operator, g is the electron spin g-factor, μ_B is the Bohr magneton, $\boldsymbol{S}$ is the spin angular momentum, and $\boldsymbol{H}$ is the applied magnetic field. Isotropic g values of 2.30(1), 2.28(1), and 2.33(1) were used for fitting the data for **1**, **2**, and **3**, respectively, to extract the D values (see

Table 6.1 and Figure 6.2).

Solution Magnetic Measurements. The solution magnetic moment of **1** was determined at 37 °C using the Evans method[23] by collecting ^{1}H NMR spectra on an Agilent DD2 500 MHz (11.7 T) system. Samples contained 5 mM of **1** in a mixture of 0.5% (w/w) of dimethyl sulfoxide (DMSO) in D_2O and were prepared under dinitrogen atmosphere to ensure no degradation due to oxidation by air. A capillary containing the same solvent mixture but without **1** was inserted into each NMR sample tube as a reference. Diamagnetic corrections were carried out based on the empirical formula of **1** using Pascal's constants.[24] The paramagnetic molar susceptibility χ_M^{para} ($cm^3\,mol^{-1}$) was calculated using the following equation:[23]

$$\chi_M^{para} = (3\Delta\nu M_w)/(4\pi\nu_0 m) - \chi_M^{dia} \qquad (6.2)$$

In this equation, $\Delta\nu$ is the frequency difference (Hz) between the DMSO resonance in the sample and reference solutions, M_w is the molecular mass of the paramagnetic compound (g mol^{-1}), ν_0 is the operating frequency of the NMR spectrometer (Hz), m is the concentration of the paramagnetic compound (g cm^{-3}), and χ_M^{dia} is the diamagnetic contribution to the molar susceptibility (cm^3 mol^{-1}). The reported value of $\chi_M T$ is an average from three independent measurements.

^{1}H NMR Spectroscopy. ^{1}H NMR spectra of H_2L and ligand precursors were collected at 25 °C on an automated Agilent DD MR 400 MHz (9.4 T), an Agilent DD2 500 MHz (11.7 T), or on a Varian Inova 500 MHz (11.7 T) spectrometers. All ^{1}H NMR spectra of cobalt complexes were recorded at 37 °C. Data for dissociation constant (K_d) measurements in D_2O were collected on a Bruker Avance III HD Nanobay 400 MHz (9.4 T) system (for Na^+ and K^+) or on a Bruker Neo

600 MHz (14.1 T) system equipped with a QCI-F cryoprobe (for Mg^{2+} and Ca^{2+}), and data for K_d measurements in 50 mM 4-(2-hydroxyethyl)-1-piperazineethanesulfonic acid (HEPES) buffer solutions at pH 7.3–7.5 were collected on an Agilent DD2 500 MHz (11.7 T) system. ^{1}H NMR spectra of samples of **1** in D_2O and in 50 mM HEPES buffer solutions at pH 7.4 were collected on a Bruker Avance III HD Nanobay 400 MHz (9.4 T) system and on an Agilent DD2 500 MHz (11.7 T) system, respectively. For the HEPES buffer solution samples, D_2O was placed in an inner capillary within each NMR sample tube to lock the sample. Samples were prepared and stored under dinitrogen atmosphere to ensure no degradation due to oxidation by air. Note that the pH of the buffer solutions was adjusted to the desired values using aqueous HCl and $(Me_4N)OH$ solutions to avoid introduction of inorganic cations. Chemical shift values (δ) are reported in ppm and referenced to residual signals from the deuterated solvents (7.26 ppm for $CDCl_3$, 3.31 ppm for MeOH-d_4, and 2.50 ppm for DMSO-d_6). For measurements of complexes in D_2O or H_2O, the chemical shift of the solvent signal was set to 0 ppm to simplify comparison between ^{1}H NMR and CEST spectra (see Figures 6.6 and 6.7).

CEST Experiments. All CEST experiments were performed at 37 °C on an Agilent DD2 500 MHz (11.7 T) or a Varian Inova 500 MHz (11.7 T) systems. Samples for measurements contained 2.5–11 mM of **1** in 50 mM HEPES buffer solutions at pH 7.4, in the absence and presence of inorganic cations. All samples were prepared and stored under dinitrogen atmosphere to ensure no degradation due to oxidation by air. Z-spectra (CEST spectra) were obtained according to the following protocol. ^{1}H NMR spectra were acquired from –100 to 100 ppm frequency offset (chemical shift with respect to the bulk H_2O signal) with a step increase of 1 ppm using a presaturation pulse applied for 3 s at a power level (B_1) of 21–22 μT. The B_1 values were calculated

based on the calibrated 90° pulse on a linear amplifier. D_2O was placed in an inner capillary within each NMR sample tube to lock the sample. The obtained ^{1}H NMR spectra were plotted as normalized integrations of the H_2O signal against frequency offset to produce a Z-spectrum. Direct saturation of the H_2O signal was set to 0 ppm. CEST peak intensities from 20 to 40 ppm were fitted using a linear model to construct baselines, based on which the relevant CEST intensities were corrected. Exchange rate constants were calculated based on a reported method.[25] In particular, ^{1}H NMR spectra were acquired at various presaturation power levels ranging from 7.4 to 21 μT applied for 6 s at 37 °C.

Determination of Dissociation Constants (K_d) by ^{1}H NMR Titration Experiments. ^{1}H NMR titration experiments were performed following modified literature procedures.[26] In order to obtain accurate chemical shift and peak integration values, samples were prepared in D_2O under dinitrogen atmosphere. Reported values of K_d for each cation-bound complex are averages from two independent experiments. For $[LCoM]^{+/2+}$ ($M^{+/2+}$ = Na^+, Mg^{2+}, K^+), values of K_d were estimated by monitoring changes in ^{1}H NMR chemical shift for two different resonances (see Table 6.4) and averages from these data sets are reported in Table 6.2. To estimate K_d for the interaction between LCo and Na^+ and Mg^{2+} ions, samples containing 2.5 or 1.0 mM of **1** were mixed with various amounts of $NaNO_3$ or $Mg(NO_3)_2$ to give final concentrations of Na^+ and Mg^{2+} ranging from 0 to 18.7 mM and 0 to 56.7 mM, respectively. The interconversion rate between $\{LCo + M^{+/2+}\}$ and $[LCoM]^{+/2+}$ ($M^{+/2+}$ = Na^+, Mg^{2+}) was fast compared to the ^{1}H NMR acquisition time scale (ca. 10^{-3} s), as evidenced by the presence of a single set of NMR resonances for the whole series of spectra for both ions. The changes in chemical shift ($\Delta\delta$) for the peaks at ca. 202 and 123 ppm were monitored for each added ion (see Figures 6.3, left, and 6.8–6.10) and fitted

using the program Dynafit[27] to extract values of K_d (see Section 6.5.1, and Tables 6.2 and 6.4). Representative fits of these data are shown in Figures 6.11–6.14.

Because K_d for $[LCoK]^+$ was expected to be lower than that for $[LCoNa]^+$, 150 mM of Na^+ was introduced to compete with K^+ for binding to LCo, so an equilibrium could be established at a concentration of **1** high enough to be observed by ^1H NMR. Samples containing 2.5 mM of **1** and 150 mM of $NaNO_3$ in D_2O were mixed with various amounts of KNO_3 to give final concentrations of K^+ ranging from 0 to 18.6 mM. The interconversion rate between $\{[LCoNa]^+ + K^+\}$ and $\{[LCoK]^+ + Na^+\}$ was fast compared to the ^1H NMR acquisition time scale (ca. 10^{-3} s), as evidenced by the presence of a single set of NMR resonances for the series of spectra. The changes in chemical shift ($\Delta\delta$) for the peaks at ca. 212 and 133 ppm (see Figures 6.15 and 6.16) were fitted using Dynafit,[27] using a competition model (see Section 6.5.1), to afford values of K_d (see Figures 6.17 and 6.18, and Tables 6.2 and 6.4).

To determine K_d for $[LCoCa]^{2+}$, K^+ was used as a competing ion. Samples containing 1.0 mM of **1** and 30 mM of KNO_3 were mixed with various amounts of $Ca(NO_3)_2$ to give final concentrations of Ca^{2+} ranging from 0 to 3.65 mM. The increase in the intensity of the peak at 245 ppm with increasing concentration of Ca^{2+} and the concomitant decrease in signal intensity for the peak at 207 ppm indicated a slow interconversion rate between $\{[LCoK]^+ + Ca^{2+}\}$ and $\{[LCoCa]^{2+} + K^+\}$ compared to the ^1H NMR acquisition time scale (ca. 10^{-3} s). The integration values for the peaks at 207 and 245 ppm were normalized to represent the relative percentages of $[LCoK]^+$ and $[LCoCa]^{2+}$ in the samples (see Figure 6.19). The value of K_d for $[LCoCa]^{2+}$ was estimated using the following equation (see Table 6.2):

$$K_{d\ (LCoCa)} = K_{d\ (LCoK)} \times [Ca^{2+}]/[K^+] \qquad (6.3)$$

In this equation, $K_{d\ (LCoK)}$ is the average K_d value obtained for $[LCoK]^+$, and $[Ca^{2+}]$ and $[K^+]$ are the concentrations of free Ca^{2+} and K^+ ions when $[LCoK]^+ : [LCoCa]^{2+} = 1 : 1$.

To investigate the effects of pH on cation binding to LCo and compare to the data obtained in D_2O, ^1H NMR titration experiments were repeated for Na^+ in deoxygenated 50 mM HEPES buffer solutions at pH 7.3–7.5. Samples containing 5.0 mM of **1** and 50 mM of HEPES buffered at pH 7.3, 7.4, and 7.5, respectively, were mixed with various amounts of $NaNO_3$ to give final concentrations of Na^+ ranging from 0 to 18.2 mM. The change in chemical shift ($\Delta\delta$) for the peak at ca. 123 ppm was monitored and fitted using a non-competition model in Dynafit[27] (see Section 6.5.1) to obtain values of K_d as described above. These data are summarized in Figures 6.20–6.22 and Table 6.5.

Electrochemical Measurements. Cyclic voltammetry measurements were carried out in a standard one-compartment cell using CH Instruments 760c potentiostat under a humid dinitrogen atmosphere inside an MBraun LABstar glovebox at ambient temperature. The cell consisted of a glassy carbon electrode as a working electrode, a platinum wire as a counter electrode, and a saturated calomel electrode (SCE) as a reference electrode. The analyte solutions were prepared using 50 mM of HEPES buffered at pH 7.4 with either 100 mM of $(Me_4N)Cl$ or a mixture of inorganic cations at their physiological concentrations (150 mM of NaCl, 4 mM of KNO_3, 2 mM of $Ca(NO_3)_2$, and 0.2 mM of $Mg(NO_3)_2$) as an electrolyte. The voltammograms were converted and referenced to the normal hydrogen electrode (NHE), using a literature conversion factor.[28]

Other Physical Measurements. Infrared data were collected on a Bruker Alpha FTIR spectrometer equipped with an attenuated total reflectance accessory (ATR). Solution UV-Vis-NIR spectra were obtained using an Agilent Cary 5000 spectrophotometer. Elemental analyses of

1, **2**, and **3** were performed by Midwest Microlab Inc.

6.3 Results and Discussion

6.3.1 Syntheses and Structures

An S_N2 reaction between 2-bromoacetamide and a reduced salen precursor afforded the ligand H_2L (see Scheme 6.1). The design and synthesis of this ligand were inspired by transition metal Schiff base complexes featuring an appended crown ether pocket precedent in the literature.[16a,18,29] However, in contrast with the tetradentate Schiff base ligands in these compounds, H_2L features a crown ether moiety that is fused with a reduced salen-based hexadentate chelating ligand. The crown ether group is responsible for cation recognition, whereas the hexadentate chelating fragment features exchangeable carboxamide protons and accommodates an anisotropic metal center suitable for PARACEST. Co^{II} is an ideal metal ion for these purposes owing to high magnetic anisotropy and fast electronic relaxation time.[17] The crown ether moiety was expected to be well suited for selective and reversible binding of Ca^{2+} under physiological conditions as it mimics the organic molecule 18-crown-6, which is well known to bind cations with different affinities based on their size and charge.[30] Furthermore, structural changes in the crown ether pocket caused by cation binding were envisioned to influence the coordination geometry of the hexadentate chelate, and thus affect the magnetic anisotropy of the paramagnetic Co^{II} center. These changes in magnetic anisotropy of Co^{II} were anticipated to impact the hyperfine shifts of carboxamide protons from the pendent donors, providing CEST peaks with cation-dependent frequencies.

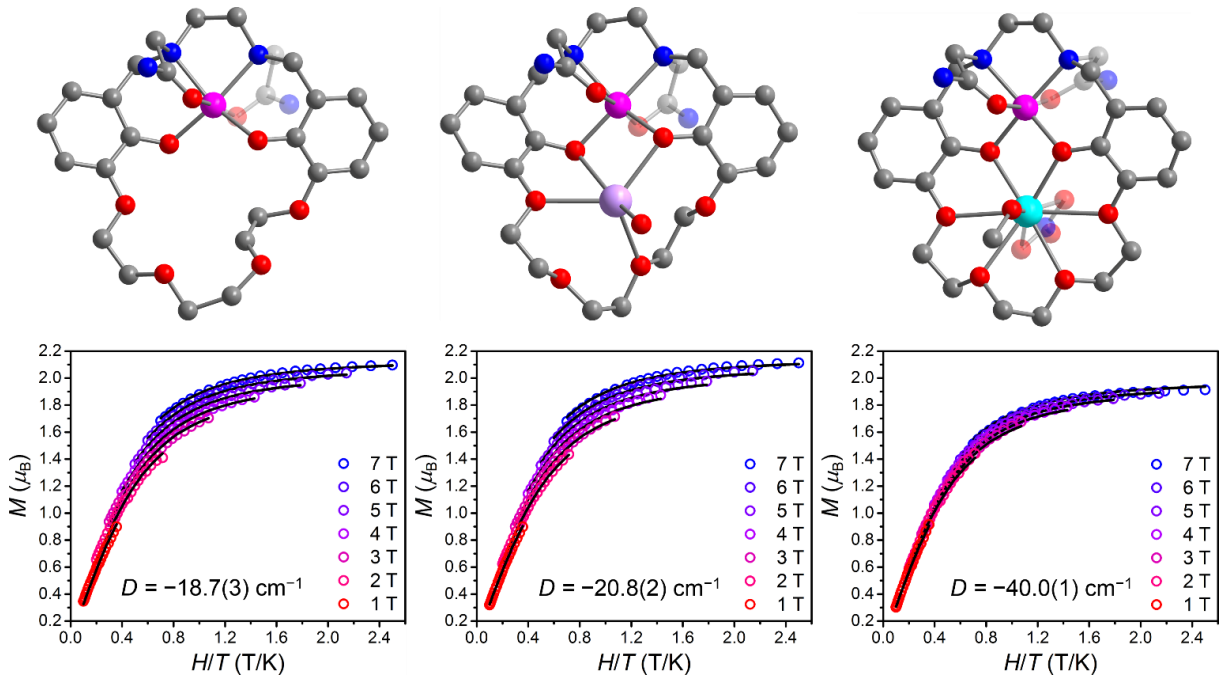

Figure 6.2 Top: Crystal structures of LCo (left), $[LCoNa(H_2O)]^+$ (center), and $[LCoCa(NO_3)(MeOH)]^+$ (right), as observed in **1′**, **2′**, and **3′**, respectively. Magenta, cyan, lilac, red, blue, and gray spheres represent Co, Ca, Na, O, N, and C atoms, respectively; H atoms are omitted for clarity. Bottom: Low-temperature magnetization data for **1** (left), **2** (center), and **3** (right), collected at selected dc fields (see legends). Colored circles and black solid lines represent experimental data and corresponding fits, respectively.

Reaction of H_2L with $Co(CH_3COO)_2\cdot 4H_2O$[16a,18,29] afforded the pink compound $LCo\cdot 3.1H_2O$ (**1**) in 82% yield (see Figure 6.1). Subsequent addition of stoichiometric amounts of $NaNO_3$ or $Ca(NO_3)_2\cdot 4H_2O$ yielded the compounds $LCoNa(NO_3)\cdot 1.7H_2O$ (**2**) or $LCoCa(NO_3)_2\cdot 0.25Et_2O\cdot 0.50H_2O$ (**3**), respectively. Slow diffusion of acetone into aqueous solutions of **1** or **2**, or Et_2O into a solution of **3** in MeOH, gave pink block-shaped crystals of $LCo\cdot 0.50C_3H_6O\cdot 9.05H_2O$ (**1′**), $[LCoNa(H_2O)](NO_3)_{0.5}(OH)_{0.5}\cdot 5.8H_2O$ (**2′**), and $[LCoCa(NO_3)(MeOH)](NO_3)\cdot MeOH$ (**3′**), respectively. Single-crystal X-ray diffraction analyses of **1′**–**3′** (see Table 6.3) revealed that the Co^{II} ion resides in a distorted octahedral environment in all three structures, with the N_2O_2 pocket of L^{2-} comprising the equatorial plane and the O atoms from the pendent carboxamide groups coordinating the axial sites (see Figure 6.2, top). In **2′**, a

Table 6.1 Selected mean interatomic distances and octahedral distortion parameter (Σ)[32] for **1′**–**3′**, and axial zero-field splitting parameter (*D*) for **1**–**3**.

	1′ / 1	**2′ / 2**	**3′ / 3**
$Co–O_{amide}$ (Å)	2.158(4)	2.15(3)	2.12(3)
$Co–O_{phenoxo}$ (Å)	2.00(2)	2.009(8)	1.978(1)
Co–N (Å)	2.22(3)	2.18(3)	2.141(5)
Σ (°)	97.8(5)	91.6(4)	66.3(2)
D (cm^{-1})	−18.7(3)	−20.8(2)	−40.0(1)

Na^+ ion is ligated by four of the six O atoms from the crown ether unit of L^{2-} and a H_2O molecule to give an irregular five-coordinate complex. In stark contrast, **3′** features a nine-coordinate Ca^{2+} ion that induces only a minimal distortion to the crown ether, where all six $Ca–O_{crown}$ distances are shorter than 2.74 Å. The remaining three coordination sites of Ca^{2+} are occupied by a MeOH molecule and an η^2-NO_3^- ion. Because Ca^{2+} and Na^+ have similar ionic radii,[31] the less distorted structure in **3′** than **2′** likely stems from greater electrostatic attraction between Ca^{2+} and the O atoms.

The conformational differences between the crown ether units in **1′**, **2′**, and **3′** caused significant structural differences at the Co^{II} center in the three compounds. This effect can be quantified through the octahedral distortion parameter (Σ), which is defined as the sum of the absolute deviations from 90° for all 12 *cis* L–Co–L angles.[32] Across the series, **1′** features the largest distortion from an octahedral geometry at Co^{II} with Σ = 97.8(5)°, followed by **2′** with Σ = 91.6(4)°, and **3′** with Σ = 66.3(2)° (see Table 6.1).

6.3.2 Solid-State Magnetic Properties

Given the significant differences in coordination geometry at Co^{II} across the three compounds, one would expect associated changes in magnetic anisotropy. To probe the influence of coordination geometry on magnetic anisotropy in these compounds, low-temperature magnetization data were collected for polycrystalline samples of **1**, **2**, and **3** at selected dc fields (see Figure 6.2, bottom). The non-superimposability of the resulting isofield curves for all

compounds, along with their saturation magnetization values below $M = 3\ \mu_B$ expected for an isotropic $S = {}^3/_2$ Co^{II} center, indicates the presence of significant zero-field splitting, which is a measure of magnetic anisotropy. This effect was quantified by fitting the data using Equation 6.1 (see Section 6.2),[22] giving axial zero-field splitting parameters of $D = -18.7(3)$, $-20.8(2)$, and $-40.0(1)$ cm^{-1} for **1**, **2**, and **3**, respectively. Here, the magnitude of D increases with decreasing distortion from octahedral geometry at Co^{II}, which is in line with a progression toward orbital degeneracy in moving from **1** to **2** to **3**.

6.3.3 Solution ^{1}H NMR Properties

To probe how changes in magnetic anisotropy of Co^{II} affect the NMR hyperfine shifts of ligand protons in **1**, **2**, and **3**, ^{1}H NMR spectra were collected at 37 °C for solutions containing 5 mM of **1** and 50 mM of HEPES buffered at pH 7.4, in the absence and presence of 15 mM of $NaNO_3$ or $Ca(NO_3)_2$. Note that excess amounts of Na^+ and Ca^{2+} were used to ensure complete cation binding, and no further spectral changes were observed beyond this concentration. Spectra for all three solutions display sharp peaks spanning from −23 to 245 ppm vs H_2O, consistent with high-spin Co^{II} in all compounds (see Figure 6.6). Carboxamide resonances were observed at 77, 69, and 80 ppm for **1**, $[LCoNa]^+$, and $[LCoCa]^{2+}$, respectively, as evidenced by their disappearance in the spectra recorded in D_2O (see Figure 6.7). The observation of a single carboxamide peak for all compounds suggests chemical equivalence of the two carboxamide groups in each molecule. Importantly, the difference in chemical shift of 11 ppm between the Ca^{2+}- and Na^+-bound compounds is more than two orders of magnitude greater than that of a diamagnetic analogue,[18] highlighting the high sensitivity of ^{1}H NMR hyperfine shift toward structural and magnetic differences at Co^{II}. Note that the carboxamide peak is not the most shifted resonance for any of the

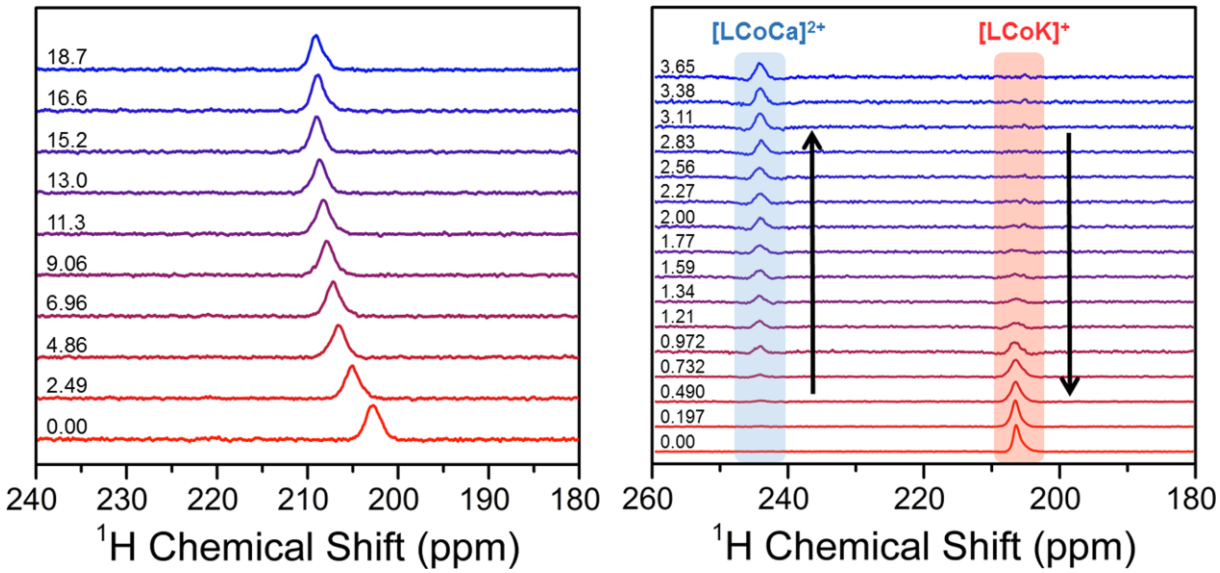

Figure 6.3 Left: Change in ^{1}H NMR chemical shift of a selected resonance for a 2.5 mM solution of **1** in D_2O upon incremental addition of $NaNO_3$. Right: Changes in ^{1}H NMR signal intensities of selected resonances for a D_2O solution containing 1.0 mM of **1** and 30 mM of KNO_3 upon incremental addition of $Ca(NO_3)_2$. The resonances at 207 and 245 ppm correspond to $[LCoK]^+$ and $[LCoCa]^{2+}$, respectively. Data were collected at 37 °C at 9.4 and 14.1 T for Na^+ and Ca^{2+}, respectively. Numbers next to spectra denote the concentrations of respective added cations (mM).

three compounds. The most shifted resonances for **1**, $[LCoNa]^+$, and $[LCoCa]^{2+}$ are located at 203, 210, and 245 ppm, respectively. The increase in maximum hyperfine shift in moving from **1** to $[LCoNa]^+$ to $[LCoCa]^{2+}$ is in good agreement with the increase in magnetic anisotropy across the series, as evident from solid-state magnetic measurements. The 35 ppm difference in maximum hyperfine shift between $[LCoCa]^{2+}$ and $[LCoNa]^+$ represents even higher cation sensitivity, suggesting that there is a large room for improving the sensitivity of cation-sensing MR probes.

6.3.4 Assessment of Cation Binding Affinities by ^{1}H NMR

While UV-Vis absorption spectroscopy is commonly used to determine dissociation constants, the UV-Vis spectra for aqueous solutions of **1**, $[LCoNa]^+$, and $[LCoCa]^{2+}$ reveal no significant differences (see Figure 6.23). However, because notable changes were observed between the ^{1}H NMR spectra for these compounds, and ^{1}H NMR has been employed in studying cation binding

Table 6.2 Summary of dissociation constants (K_d) for cation-bound complexes of **1** in D_2O at 37 °C.

	$[LCoNa]^+$	$[LCoMg]^{2+}$	$[LCoK]^+$	$[LCoCa]^{2+}$
K_d (mM)	4.8(3)[a]	23(2)[a]	0.3(2)[a]	0. 01(1)[b]

[a] Average value from monitoring ^1H NMR chemical shift changes upon cation addition for two different resonances. [b] Estimated by a method described in Section 6.2.

for other crown ether-based systems,[26] we decided to assess the binding affinities of **1** toward Na^+, Mg^{2+}, K^+, and Ca^{2+} through ^1H NMR titration experiments at 37 °C. Addition of Na^+ or Mg^{2+} to solutions of **1** in D_2O resulted in downfield shifting of ^1H NMR resonances. The resonances shifted non-linearly with increasing concentrations of Na^+ or Mg^{2+}, suggesting the presence of equilibrium (see Figures 6.3, left, and 6.8–6.10). The changes in chemical shift for the peaks at ca. 202 and 123 ppm were most pronounced and could be modeled[27] to provide average dissociation constants of K_d = 4.8(3) and 23(2) mM for $[LCoNa]^+$ and $[LCoMg]^{2+}$, respectively (see Figures 6.3, left, and 6.8–6.14, and Tables 6.2 and 6.4). Owing to the structural similarity between 18-crown-6 and the crown ether moiety of H_2L, **1** was expected to display higher affinity toward K^+ than toward the smaller ions Na^+ and Mg^{2+}.[18,29] As such, Na^+ was introduced to compete with K^+ for binding to LCo, so an equilibrium could be established at a concentration of **1** high enough to be observed by ^1H NMR. A similar non-linear shift of ^1H resonances was observed upon incremental addition of KNO_3 to a D_2O solution of **1** containing 150 mM of $NaNO_3$ as observed in the Na^+ and Mg^{2+} titration experiments, albeit less pronounced (see Figures 6.15 and 6.16). A fit to the data gave an average value of K_d = 0.3(2) mM for $[LCoK]^+$ (see Figures 6.17 and 6.18, and Tables 6.2 and 6.4).

For the NMR titrations of LCo with Na^+, Mg^{2+}, and K^+, only one set of ^1H resonances was observed in each case, indicating fast cation exchange rates compared to the ^1H NMR acquisition time scale (ca. 10^{-3} s). In contrast, when Ca^{2+} was added to a D_2O solution of **1** containing K^+ as a competing ion, two sets of ^1H resonances were observed (see Figure 6.3, right). This observation

suggests a slow cation exchange between $[LCoK]^+$ and $[LCoCa]^{2+}$ in aqueous solutions. Integrations of the peaks at 207 and 245 ppm, corresponding to $[LCoK]^+$ and $[LCoCa]^{2+}$, respectively, could be employed to derive the mole fraction of $[LCoCa]^{2+}$ as a function of $[Ca^{2+}]$ (see Figure 6.19). By using the previously determined K_d value for $[LCoK]^+$ and $[Ca^{2+}]$ at 50% $[LCoCa]^{2+}$ formation, a value of $K_d = 0.01(1)$ mM was estimated for $[LCoCa]^{2+}$ (see Equation 6.3). Average values of K_d for the different cation-bound complexes of **1** are summarized in Table 6.2. Cation affinity for **1** follows the order $Ca^{2+} > K^+ > Na^+ > Mg^{2+}$. The tightest binding of Ca^{2+} to **1** is likely a result of an optimal ionic radius in conjunction with a high positive charge. Most importantly, these K_d values suggest that **1** will near exclusively bind Ca^{2+} and Na^+ over Mg^{2+} and K^+ under physiological conditions owing to low affinities and/or low concentrations of the latter two ions. Furthermore, similar values of K_d = 1.8(9)–3.7(9) mM were obtained for $[LCoNa]^+$ in HEPES solutions buffered at pH 7.3–7.5 as observed in D_2O (see Figures 6.20–6.22 and Table 6.5), indicating that ion binding to **1** is minimally affected by pH in the physiological range.

6.3.5 CEST Properties

To investigate the potential of **1** as a cation-responsive PARACEST probe, CEST spectra were collected at 37 °C for solutions containing 5 mM of **1** and 50 mM of HEPES buffered at pH 7.4, in the absence and presence of 15 mM of Na^+ or Ca^{2+}. For

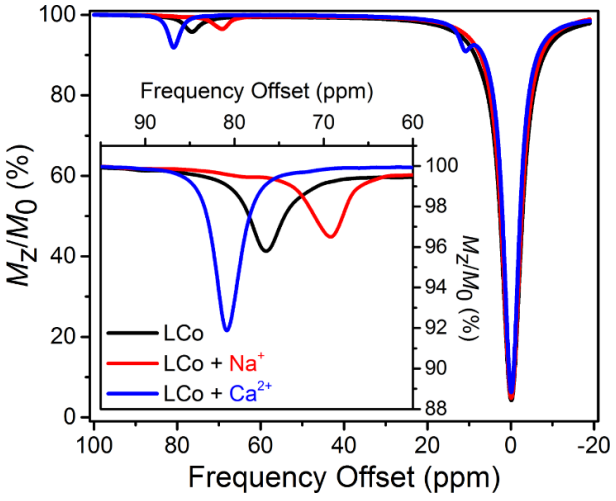

Figure 6.4 CEST spectra collected at 11.7 T and 37 °C using a 3 s presaturation pulse and B_1 = 21 μT for 5 mM aqueous solutions of **1** containing 50 mM of HEPES buffered at pH 7.4 (black), and with 15 mM of Na^+ (red) or Ca^{2+} (blue). Inset: Expanded view of relevant CEST peaks.

solutions of **1**, $[LCoNa]^+$, and $[LCoCa]^{2+}$, CEST peaks were observed at 77, 69, and 80 ppm, respectively, with 4.8, 3.9, and 8.5% H_2O signal reduction, respectively (see Figure 6.4). These CEST peak frequencies are consistent with the assignment of carboxamide resonances from the ^1H NMR spectra. Despite the low signal intensities, the frequency difference between the three CEST peaks highlights the effectiveness of LCo to distinguish between Na^+ and Ca^{2+} in solution. A second CEST peak was observed at 11 ppm in the spectrum for $[LCoCa]^{2+}$, likely stemming from a coordinating H_2O molecule. Exchange rates for the carboxamide protons were estimated by the Omega plot method at 37 °C and pH 7.4.[25] Rate constants of k_{ex} = 4.0(5) × 10^2, 3.0(6) × 10^2, and 2.4(2) × 10^2 s^{-1} were obtained for **1**, $[LCoNa]^+$, and $[LCoCa]^{2+}$, respectively, (see Figure 6.24). These values are in good agreement with those reported for other carboxamide-based PARACEST agents.[9,10c,11a,c,h–k] The stronger CEST effect observed for $[LCoCa]^{2+}$ compared to that for $[LCoNa]^+$, despite similar values of k_{ex} for the two complexes, could be due to the presence of a third pool of labile protons from the coordinating H_2O molecule in HEPES buffer solutions of $[LCoCa]^{2+}$. This hypothesis is supported by the observation of an additional peak at 11 ppm in the CEST spectrum for $[LCoCa]^{2+}$.

6.3.6 Quantitation of Ca^{2+} Concentration in Aqueous Solutions

To evaluate the ability of **1** to enable a ratiometric quantitation of the concentration of Ca^{2+} under physiological conditions, CEST spectra were collected at 37 °C for a solution containing 2.0 mM of **1**, 150 mM of NaCl, and 50 mM of HEPES buffered at pH 7.4, upon incremental addition of $Ca(NO_3)_2$. In the absence of Ca^{2+}, a single CEST peak at 69 ppm was observed, indicating complete formation of $[LCoNa]^+$. However, upon addition of Ca^{2+}, a new peak appeared at 80 ppm, corresponding to $[LCoCa]^{2+}$. The intensity of this peak increased monotonically until

reaching saturation at [Ca^{2+}] = 3.13 mM. Due to partial overlap with the peak at 80 ppm, the CEST peak intensity at 69 ppm first increased until [Ca^{2+}] = 1.00 mM, but then decreased substantially with increasing [Ca^{2+}], reaching a value of less than 1% at [Ca^{2+}] = 3.13 mM (see Figure 6.5, top). The appearance of the CEST peak at 80 ppm demonstrates that **1** selectively binds Ca^{2+} over Na^{+} under physiological conditions.[14] Importantly, the intensity of the $[LCoCa]^{2+}$ CEST peak at 80 ppm reached saturation at [Ca^{2+}] = 3.13 mM rather than 2.00 mM, indicating that cation selectivity is modest enough to allow for an equilibrium between $[LCoNa]^{+}$ and $[LCoCa]^{2+}$, thus enabling ratiometric quantitation of [Ca^{2+}]. These observations are consistent with the K_d values estimated for the two complexes.

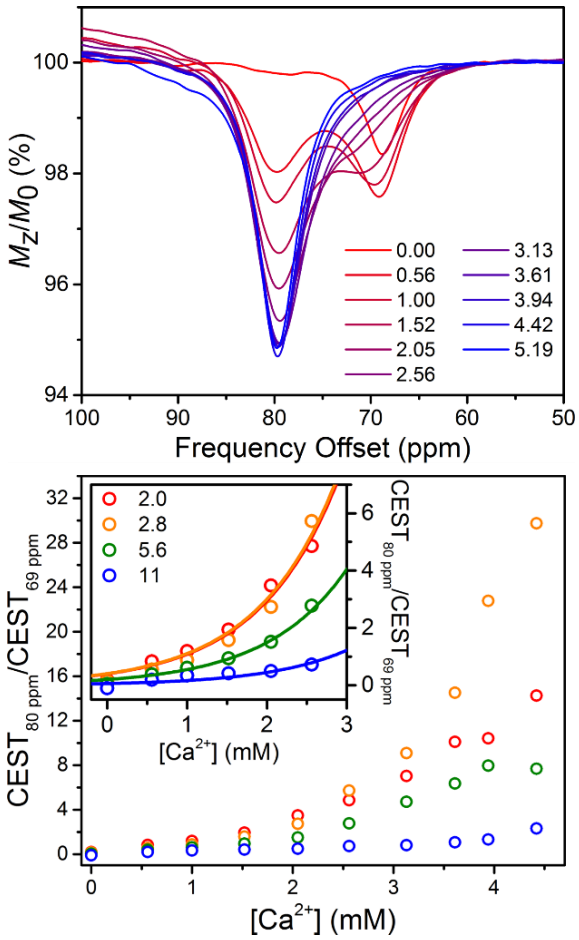

Figure 6.5 Top: CEST spectra collected at 11.7 T and 37 °C using a 3 s presaturation pulse and B_1 = 21 μT for 50 mM HEPES buffer solutions containing 2.0 mM of **1** and 150 mM of NaCl at pH 7.4 with increasing [Ca^{2+}]. The legend denotes [Ca^{2+}] (mM). Bottom: Ratio of CEST peak intensities from presaturation at 80 and 69 ppm vs [Ca^{2+}]. Inset: Expanded view of the relevant data. Circles and solid lines represent experimental data and fits, respectively. The legend denotes [**1**] (mM).

To assess the influence of probe concentration on the CEST properties of **1**, variable-[Ca^{2+}] CEST spectra were collected for various concentrations of **1** in analogy to the 2.0 mM sample (see Figures 6.25–6.27). The intensities of the CEST peaks at 80 and 69 ppm changed considerably as

the concentration of **1** was varied, demonstrating the shortcoming of detecting [Ca^{2+}] solely based on CEST peak intensities. However, the ratio of peak intensities at 80 and 69 ppm ($CEST_{80\ ppm}/CEST_{69\ ppm}$) was only minimally affected by the concentration of **1** (see Figure 6.5, bottom). Note that the CEST effect at 69 ppm cannot be accurately determined when [Ca^{2+}] > 3 mM owing to the low intensity (see Figure 6.5, top). As such, $CEST_{80\ ppm}/CEST_{69\ ppm}$ values for [Ca^{2+}] > 3 mM may contain significant error. The correlation between $CEST_{80\ ppm}/CEST_{69\ ppm}$ and [Ca^{2+}] for [Ca^{2+}] < 3 mM can be fitted using the following empirical exponential model:

$$CEST_{80\ ppm}/CEST_{69\ ppm} = \exp([Ca^{2+}] - x) \qquad (6.4)$$

Fits of the CEST data to Equation 6.4 afforded x = 0.92(4), 0.90(6), 1.6(1), and 2.8(2) for 2.0, 2.8, 5.6, and 11 mM of **1**, respectively. Therefore, when only data for [Ca^{2+}] < 3 mM are examined, the equations for 2.0 and 2.8 mM of **1** are statistically indistinguishable (see Figure 6.5, bottom, inset). However, the equations for 5.6 and 11 mM of **1** are significantly different, suggesting that [LCoNa]$^{+}$ and [LCoCa]$^{2+}$ are not in equilibrium at higher concentrations of **1** (≥ 5.6 mM), likely due to strong Ca^{2+} binding. These results establish the validity of using the CEST peak intensity ratio to quantitate [Ca^{2+}] independent of the concentration of **1** within a regime where the concentration of **1** is sufficiently low (< 3 mM) to allow for an equilibrium between [LCoNa]$^{+}$ and [LCoCa]$^{2+}$. Accordingly, to expand the range of concentration-independent quantitation of [Ca^{2+}] using PARACEST, the probe should exhibit weaker binding affinity toward Ca^{2+} and stronger CEST effects.

To further test the feasibility of **1** to quantitate [Ca^{2+}] in physiological environments, variable-[Ca^{2+}] CEST experiments were carried out at 37 °C for a pH 7.4 buffer solution containing 2.8 mM of **1**, 150 mM of Na^{+}, 4 mM of K^{+}, and 0.2 mM of Mg^{2+} to mimic their physiological

concentrations[14] (see Figure 6.28). Prior to addition of Ca^{2+}, a single CEST peak at 69 ppm was observed with 0.8% CEST effect, suggesting that LCo exclusively bound Na^{+}. Upon incremental addition of Ca^{2+}, the intensity of this peak first increased to 4% at $[Ca^{2+}]$ = 1.01 mM and then decreased monotonically with increasing $[Ca^{2+}]$, whereas a CEST signal at 80 ppm corresponding to $[LCoCa]^{2+}$ appeared and reached a maximum intensity of 6.5% at $[Ca^{2+}]$ = 3.40 mM. These spectral changes are analogous to those observed in the absence of K^{+} and Mg^{2+}. An equilibrium between $[LCoCa]^{2+}$ and $[LCoNa]^{+}$ was again established, as the CEST peak at 80 ppm reached a maximum intensity at $[Ca^{2+}] > 2.8$ mM. However, both CEST peaks were noticeably broader compared to those observed in the absence of K^{+} and Mg^{2+}. Specifically, the two peaks start to coalesce at $[Ca^{2+}] > 1$ mM, as evidenced by the downfield and upfield shifting of the CEST peaks at 69 and 80 ppm, respectively. Together, these observations suggest an accelerated cation exchange between $[LCoCa]^{2+}$ and $[LCoNa]^{+}$, likely stemming from the presence of K^{+} and Mg^{2+}.

The plot of $CEST_{80\ ppm}/CEST_{69\ ppm}$ vs $[Ca^{2+}]$, as depicted in Figure 6.29, reveals that $CEST_{80\ ppm}/CEST_{69\ ppm}$ increases with increasing $[Ca^{2+}]$, following a similar trend as the data shown in Figure 6.5, bottom. Fits of the data to Equation 6.4 using $[Ca^{2+}] < 2.5$ mM gave x = 1.56(8) (see Figure 6.30), which is significantly higher than the value of x = 0.90(6) obtained for the 2.8 mM sample of **1** in the absence of K^{+} and Mg^{2+}. This discrepancy can likely be attributed to the increased cation exchange rate between $[LCoCa]^{2+}$ and $[LCoNa]^{+}$ in the presence of K^{+} and Mg^{2+}. Note that the empirical exponential model provided in Equation 6.4 does not fit the $CEST_{80\ ppm}/CEST_{69\ ppm}$ vs $[Ca^{2+}]$ data for the physiological ion mixture very well. However, an alternative exponential model given in Equation 6.5 affords much better agreement, providing parameters of a = 0.38(6) and b = 0.73(7) (see Figure 6.31).

$$CEST_{80\ ppm}/CEST_{69\ ppm} = a \times \exp(b \times [Ca^{2+}]) \qquad (6.5)$$

Taken together, variable-$[Ca^{2+}]$ CEST experiments for solutions of **1** with different cations confirm that **1** selectively and reversibly binds Ca^{2+} and Na^{+} over the related cations K^{+} and Mg^{2+}, verifying the feasibility of ratiometric quantitation of $[Ca^{2+}]$ under physiological conditions.[14] While interference from binding other cations is insignificant, the rate of cation exchange was found to influence the CEST peak intensity ratio, highlighting the necessity of constructing a calibration curve under conditions that strongly resemble the targeted environment. As such, the effects of cation exchange rates on the CEST properties of different cation-bound probes should be strongly considered in the design of future cation-responsive CEST probes.

6.3.7 Stability Studies

Finally, we sought to investigate the stability of **1** in aqueous solutions. Cyclic voltammetry experiments were carried out for solutions of **1** with 50 mM of HEPES buffered at pH 7.4 in the absence and presence of a mixture of Na^{+}, K^{+}, Mg^{2+}, and Ca^{2+} ions at their physiological concentrations.[14] In the absence of the inorganic cations, **1** exhibits one pseudo-reversible redox process at 440 mV vs NHE that is assigned to the $Co^{II/III}$ potential (see Figure 6.32). Surprisingly, the pseudo-reversible $Co^{II/III}$ redox event was shifted cathodically to 374 mV vs NHE in the presence of the cation mixture (see Figure 6.33). The more reductive potential observed in the presence of the inorganic cations could be attributed to the different electrolytes in the sample solutions. Nevertheless, both potentials are more reductive than that for the reduction of O_2 to H_2O in a neutral solution,[28] suggesting that **1** is susceptible to oxidation in air. To further study the stability of **1** under aerobic conditions, a solution of **1** buffered at pH 7.4 was prepared under dinitrogen atmosphere and exposed to air while a UV-Vis absorption spectrum was recorded at

regular intervals (see Figure 6.34). Over a 24 h period, the intensities of the absorption bands centered at 247 and 296 nm gradually decreased, verifying the oxidation of Co^{2+} to Co^{3+} in the course of hours.

6.4 Conclusions

The foregoing results demonstrate the feasibility of quantitating Ca^{2+} concentration in a ratiometric manner through cation-dependent CEST effects. Importantly, the LCo probe features both a selective and a reversible binding of Ca^{2+} and Na^{+} in the presence of similar cations. The CEST peaks for the Ca^{2+}- and Na^{+}-bound probes are highly shifted and can be distinctively addressed, thanks to the sensitivity of ^{1}H NMR hyperfine shift and magnetic anisotropy to changes in the coordination environment at the paramagnetic Co^{II} center. Moreover, variable-[Ca^{2+}] CEST experiments confirmed the ability of LCo to quantitate [Ca^{2+}], independent of the probe concentration when an equilibrium between [$LCoCa^{2+}$] and [$LCoNa^{+}$] was achieved ([LCo] < 3 mM and [Ca^{2+}] < 3 mM).

The current proof-of-principle study represents a first step toward practical quantitation of [Ca^{2+}], and potentially other physiologically relevant cations, in a concentration-independent manner. While the weak CEST effects and air-sensitivity may preclude the practical use of the current LCo probe, we have established that the combination of magnetic anisotropy modulation and cation recognition by a crown ether moiety is a promising cation-sensing strategy. Future efforts will be directed toward tuning the transition metal and pendent CEST-active groups to optimize sensitivity, cation binding affinities, CEST peak intensities, and probe stability, as well as modifying the crown ether unit toward sensing cations of different sizes.

6.5 Supporting Information

6.5.1 Supplementary Experimental Details

Synthesis of 1,8-ditosyl-3,6-dioxaoctane.[33] Triethylene glycol (20 g, 0.13 mol) and *p*-toluenesulfonyl chloride (51 g, 0.27 mol) were dissolved in 150 mL of CH_2Cl_2. The resulting colorless solution was cooled to 0 °C by an ice/H_2O bath. To this solution, KOH (60 g, 1.1 mol) was added in small portions with vigorous stirring. After 12 h of stirring, cold H_2O (300 mL) was added and the CH_2Cl_2 layer was collected. The aqueous layer was then extracted with CH_2Cl_2 (3 × 150 mL). The combined CH_2Cl_2 solution was washed with H_2O (2 × 50 mL) and dried over $MgSO_4$. Evaporation of the solvent under reduced pressure afforded the title compound as a white solid (55 g, 92%). ^{1}H NMR ($CDCl_3$, 25 °C): δ 7.79 (d, 4H), 7.34 (d, 4H), 4.14 (t, 4H), 3.65 (t, 4H), 3.52 (s, 4H), 2.44 (s, 6H).

Synthesis of 3,3'-(3,6-dioxaoctane-1,8-diyldioxy)bis(2-hydroxybenzaldehyde).[16a] Under a dry dinitrogen atmosphere, 2,3-dihydroxybenzaldehyde (7.0 g, 0.051 mol) was dissolved in anhydrous dimethyl sulfoxide (DMSO) (30 mL). The resulting dark yellow solution was slowly transferred via cannula (ca. 1 drop per second) to a suspension of NaH (2.6 g, 0.11 mol) in anhydrous DMSO (30 mL), which was cooled to 0 °C by an ice/H_2O bath. After the addition was complete, the resulting dark brown mixture was stirred for 1 h at ambient temperature. Under a dry dinitrogen atmosphere, 1,8-ditosyl-3,6-dioxaoctane (11 g, 0.024 mol) was added, and the dark brown mixture was stirred for 20 h at ambient temperature. The resulting dark brown solution was added to H_2O (400 mL) and washed with $CHCl_3$ (2 × 200 mL). The pH of the aqueous layer was adjusted to 1 by addition of 6 M HCl solution in H_2O. The brown slurry was then extracted with $CHCl_3$ (3 × 100 mL). The combined organic layers were washed with 1 M HCl solution in H_2O (5 × 200 mL),

dried over $MgSO_4$, filtered, and evaporated to dryness under reduced pressure. The resulting brown oil was purified by column chromatography using silica gel. CH_2Cl_2 was passed through the column until no by-product was present in the eluent, as judged by thin-layer chromatography (TLC). Then 2% (v/v) MeOH in CH_2Cl_2 was used to elute the desired product (R_f = 0.35 in 2% (v/v) MeOH/CH_2Cl_2). Evaporation of the yellow solution under reduced pressure gave the title compound as a yellow solid (4.5 g, 48%). ^{1}H NMR ($CDCl_3$, 25 °C): δ 10.87 (s, 2H), 9.95 (s, 2H), 7.23 (d, 2H), 7.19 (d, 2H), 6.94 (t, 2H), 4.24 (t, 4H), 3.92 (t, 4H), 3.79 (s, 4H).

Synthesis of (13,16,19,22-tetraoxa-3,6-diazatricyclo[21.3.1.1^{8,12}]octacosa-1(27),2,6,8,10,12(28),23,25-octaene-27,28-diol)barium(2+) diperchlorate.[16a] $Ba(ClO_4)_2$ (1.7 g, 5.1 mmol) was dissolved in MeOH (80 mL) and the resulting solution was heated at reflux. To the colorless solution, a solution of 3,3'-(3,6-dioxaoctane-1,8-diyldioxy)bis(2-hydroxybenzaldehyde) (2.0 g, 5.1 mmol) in MeOH (20 mL) was added to give a yellow solution. After stirring at reflux for 15 min, a solution of ethylenediamine (0.31 g, 5.1 mmol) in MeOH (100 mL) was added dropwise to the yellow solution over the course of 4 h. The resulting yellow solution was heated at reflux for additional 2 h and then cooled to ambient temperature. The yellow solution was filtered, and the solvent was slowly evaporated in air to afford the desired product as a yellow crystalline solid. The solid was collected by filtration and dried with suction on the filter for 20 h (2.3 g, 59%). ^{1}H NMR (DMSO-d_6, 25 °C): δ 15.12 (s, 2H), 8.78 (d, 2H), 7.05 (d, 2H), 6.65 (t, 2H), 4.15 (d, 4H), 3.97 (s, 4H), 3.86 (d, 4H), 3.72 (s, 4H).

Synthesis of 13,16,19,22-tetraoxa-3,6-diazatricyclo[21.3.1.1^{8,12}]octacosa-1(27),2,6,8,10,12(28),23,25-octaene-27,28-diol.[16a] (13,16,19,22-Tetraoxa-3,6-diazatricyclo[21.3.1.1^{8,12}] octacosa-1(27),2,6,8,10,12(28),23,25-octaene-27,28-diol)barium(2+) diperchlorate (1.3 g, 1.7

mmol) was suspended in CH_2Cl_2 (50 mL). To the resulting white slurry, a solution of guanidinium sulfate (1.8 g, 17 mmol) in H_2O (50 mL) was added. The mixture was stirred vigorously for 1 h at ambient temperature. The CH_2Cl_2 layer was collected and dried over $MgSO_4$. Evaporation of the solvent under reduced pressure and subsequent drying in vacuo for 20 h afforded the title compound as a yellow solid (0.61 g, 89%). ^{1}H NMR (DMSO-d_6, 25 °C): δ 14.08 (s, 2H), 8.65 (s, 2H), 6.99 (m, 2H), 6.73 (t, 2H), 4.06 (m, 4H), 3.87 (s, 4H), 3.69 (m, 4H), 3.60 (s, 4H).

Synthesis of 13,16,19,22-tetraoxa-3,6-diazatricyclo[21.3.1.1^{8,12}]octacosa-1(27),8,10,12(28),23,25-hexaene-27,28-diol. 13,16,19,22-Tetraoxa-3,6-diazatricyclo[21.3.1.1^{8,12}]octacosa-1(27),2,6,8,10,12(28),23,25-octaene-27,28-diol (0.61 g, 1.5 mmol) was dissolved in CH_2Cl_2 (20 mL) and the resulting yellow solution was cooled to 0 °C by an ice/H_2O bath. MeOH (50 mL) was added to this stirring solution and subsequently tetramethylammonium borohydride (0.26 g, 3.0 mmol) was added as a solid in small portions. Small amount of bubbles formed during the addition and the solution became a pale slurry. The mixture was stirred in the ice/H_2O bath for 1 h and then warmed to ambient temperature and stirred for additional 20 min. The pH of the off-white mixture was adjusted to 1 by addition of 5 M HCl solution in H_2O. The mixture was then evaporated to dryness under reduced pressure to give a colorless oil. The oil was dissolved in H_2O (50 mL) and the pH of the solution was adjusted to 8 by addition of 1 M tetramethylammonium hydroxide solution in H_2O. The resulting slurry was extracted with CH_2Cl_2 (3 × 50 mL). The combined organic layers were dried over $MgSO_4$, filtered, and evaporated to dryness under reduced pressure. Further drying in vacuo for 20 h afforded the title compound as an off-white solid (0.44 g, 71%). ^{1}H NMR ($CDCl_3$, 25 °C): δ 6.70–6.72 (m, 2H), 6.66–6.67 (m, 4H), 4.10 (m, 4H), 3.87 (s, 4H), 3.85 (m, 4H), 3.74 (s, 4H), 2.90 (s, 4H).

Script for determining K_d from non-competitive ^1H NMR titrations.

```
[task]
 task = fit
 data = equilibrium

[mechanism]
 LCo + Cation <=> LCoCation : Kd dissoc

[constants] ; units: M
 Kd = [estimated Kd] ?

[concentrations] ; units: M
 LCo = “concentration of complex without cations”

[responses]
 LCoCation = “estimated response for LCoCation” ?
 LCo = 0

[data]
 variable “Cation” ; “Cation” is the concentration of added cation in the
 unit of M

 set LCo

[output]
 directory ./fit/kd

[set:LCo]

“data showing the concentration of cation in the first column and responses in the second column”

[end]
```

Script for determining K_d from competitive ^1H NMR titrations.

```
[task]
 task = fit
 data = equilibrium

[mechanism]
 LCo + Cation1 <=> LCoCation1 : Kd1 dissoc
 LCo + Cation2 <=> LCoCation2 : Kd2 dissoc

[constants] ; units: M
 Kd1 = [Kd for LCoCation1]
 Kd2 = [estimated Kd for LCoCation2] ?
```

```
[concentrations] ; units: M
 LCo = “concentration of complex without cations”
 Cation1 = “concentration of competing cation”

[responses]
 LCoCation2 = “estimated response for LCoCation2” ?
 LCoCation1 = 0
 LCo = 0

[data]
 variable “Cation2” ; “Cation2” is the concentration of Cation2 in the
 unit of M
 set LCo

[output]
 directory ./fit/kd

[set:LCo]

“data showing the concentration of cation in the first column and responses in the second column”

[end]
```

6.5.2 Supplementary Scheme

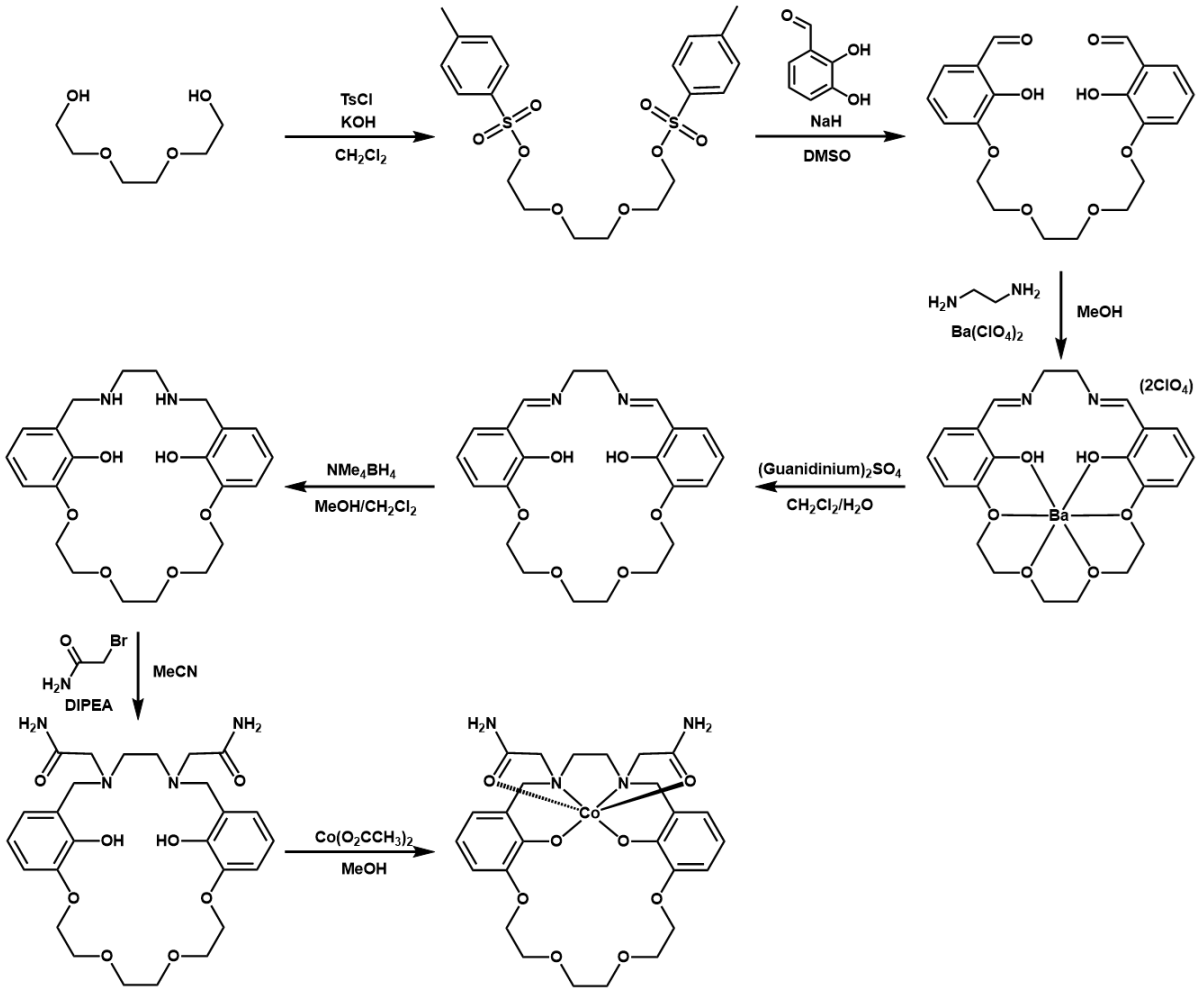

Scheme 6.1 Syntheses of H_2L and **1**.

6.5.3 Supplementary Figures

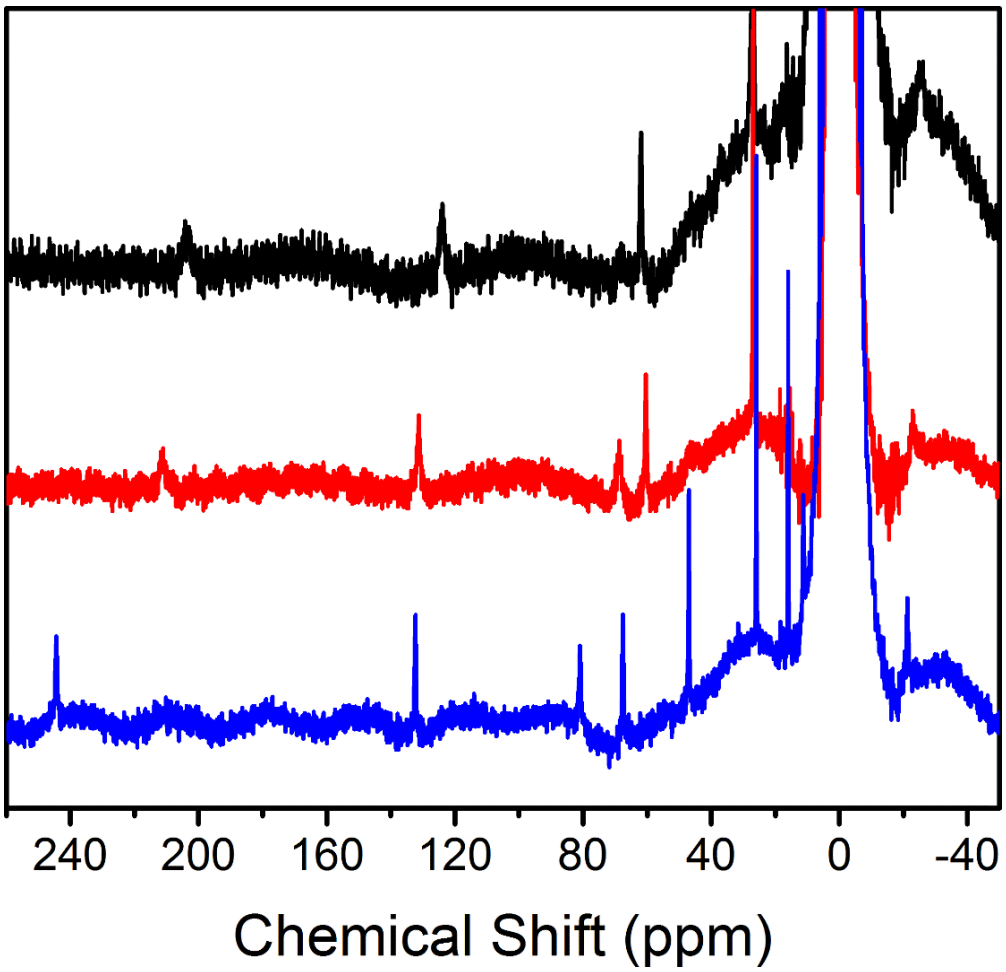

Figure 6.6 Stacked ^{1}H NMR spectra collected at 37 °C and 11.7 T for solutions containing 5 mM of **1** and 50 mM of HEPES buffered at pH 7.4 in the absence of inorganic cations (black), and in the presence of 15 mM of $NaNO_3$ (red) or 15 mM of $Ca(NO_3)_2$ (blue).

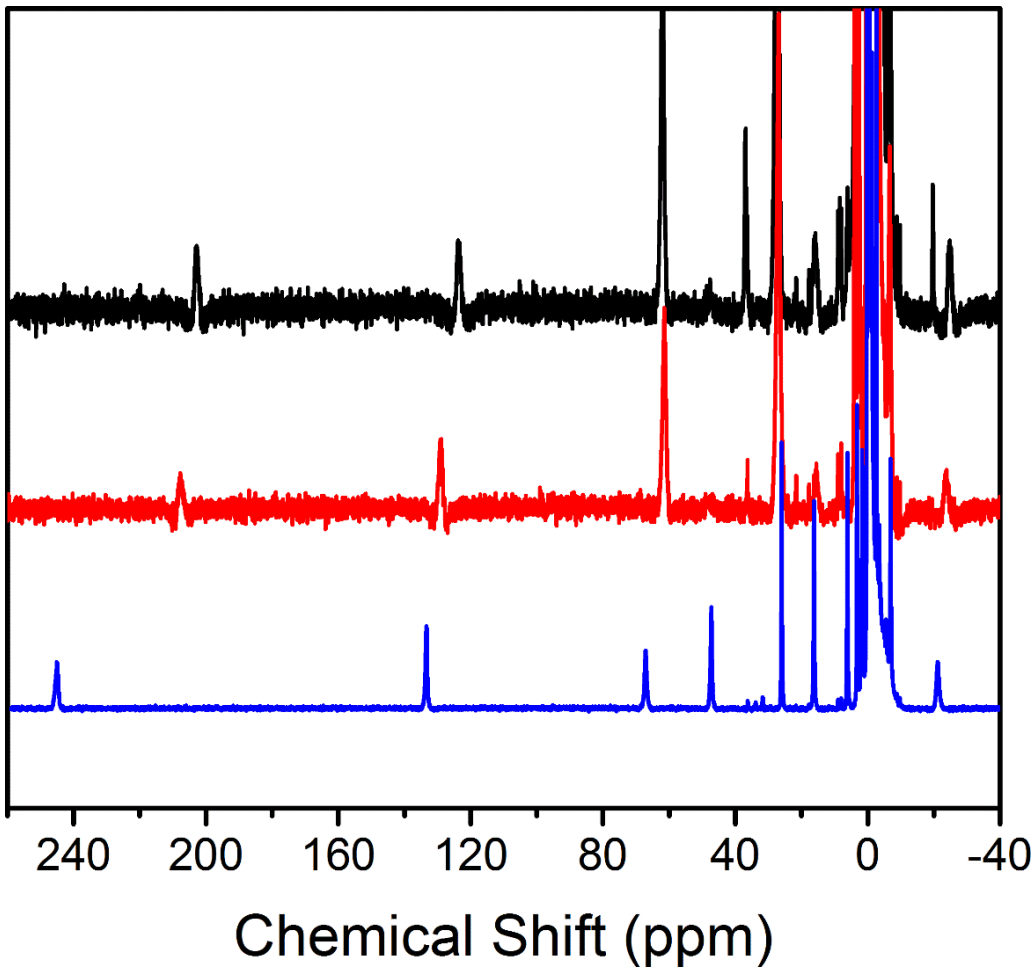

Figure 6.7 Stacked ^{1}H NMR spectra collected at 37 °C and 9.4 T for solutions containing 2.5 mM of **1** in D_2O in the absence of inorganic cations (black), and in the presence of 7.5 mM of $NaNO_3$ (red) or 7.5 mM of $Ca(NO_3)_2$ (blue).

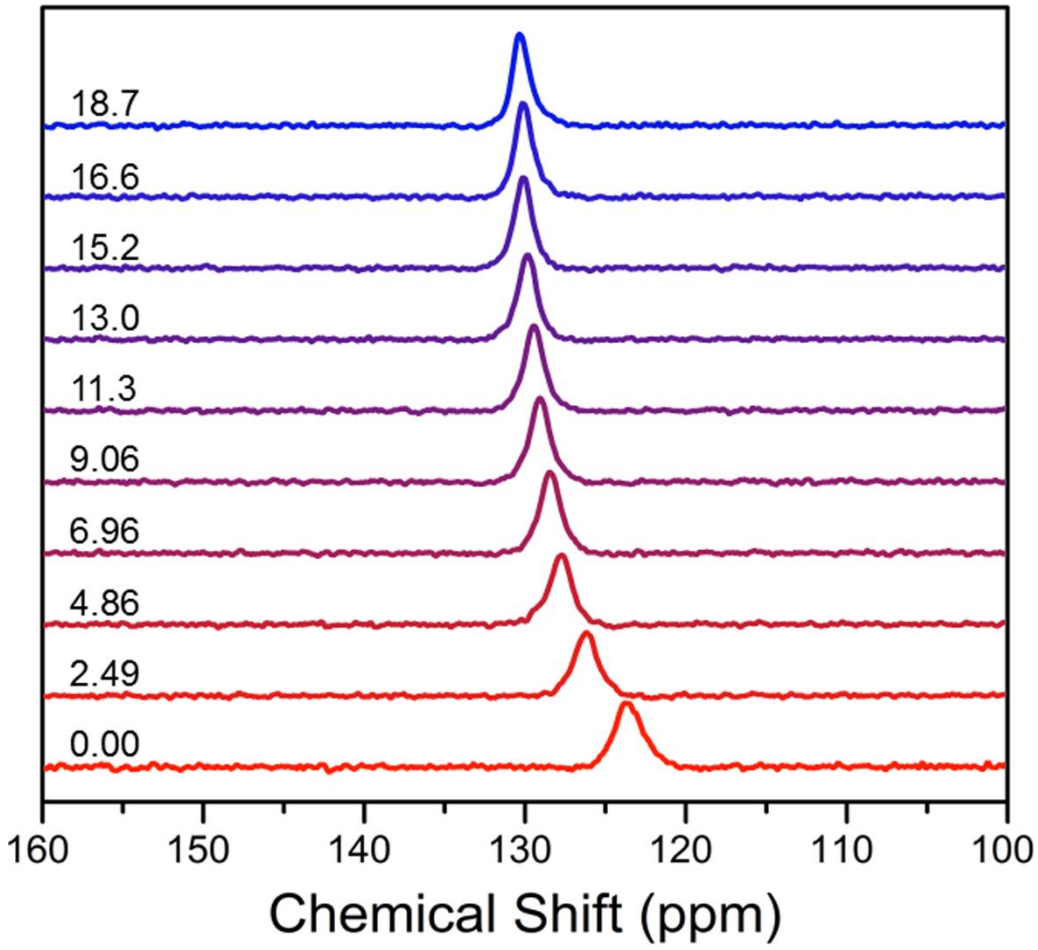

Figure 6.8 Stacked ^{1}H NMR spectra for a series of solutions containing 2.5 mM of **1** in D_2O with various concentrations of $NaNO_3$ ranging from 0 to 18.7 mM, collected at 37 °C and 9.4 T, highlighting the change in chemical shift for the resonance at ca. 123 ppm. The numbers next to spectra denote $[Na^+]$ (mM).

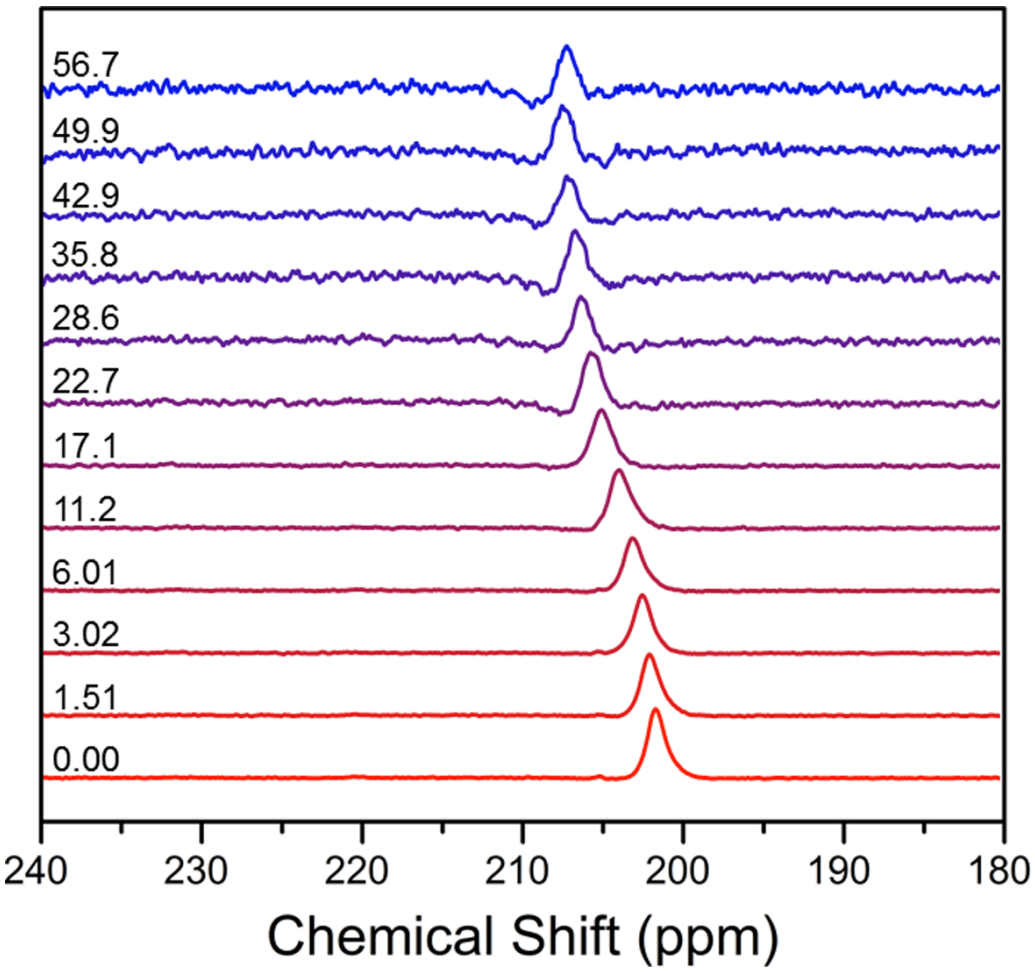

Figure 6.9 Stacked ^{1}H NMR spectra for a series of solutions containing 1.0 mM of **1** in D_2O with various concentrations of $Mg(NO_3)_2$ ranging from 0 to 56.7 mM, collected at 37 °C and 14.1 T, highlighting the change in chemical shift for the resonance at ca. 202 ppm. The numbers next to spectra denote [Mg^{2+}] (mM).

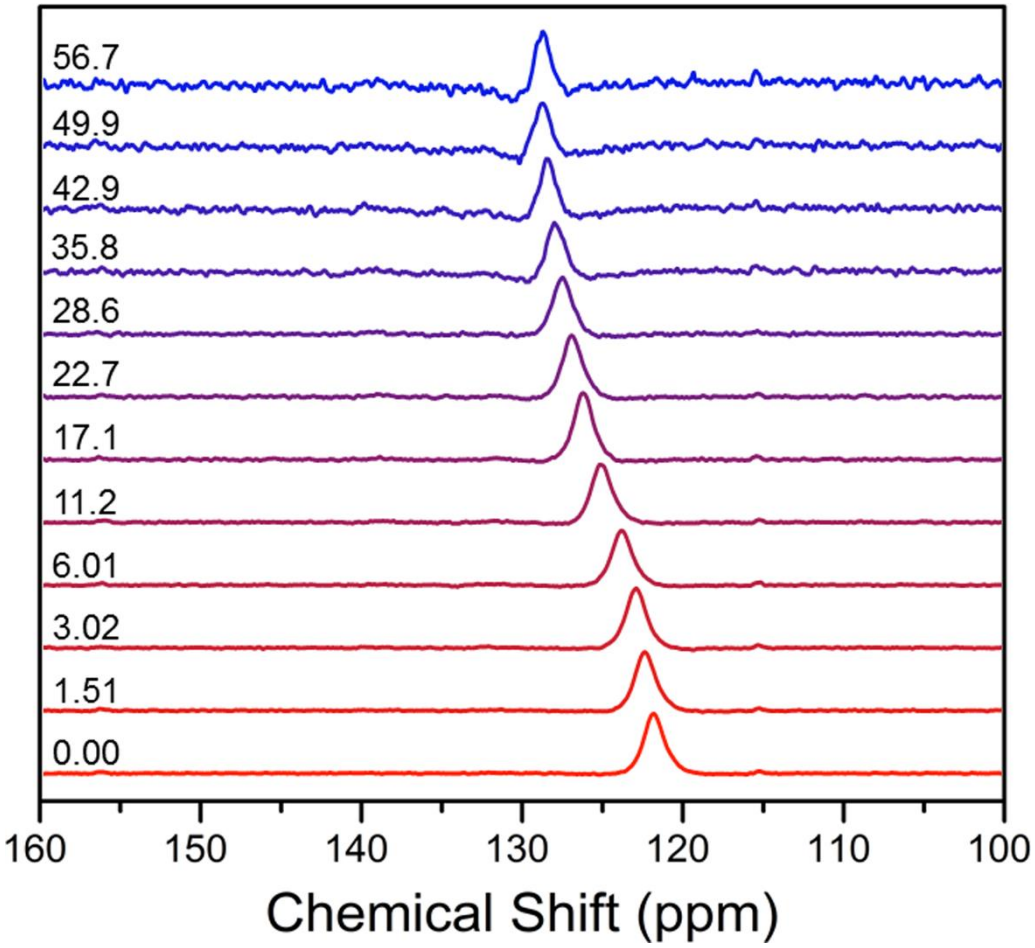

Figure 6.10 Stacked ^{1}H NMR spectra for a series of solutions containing 1.0 mM of **1** in D_2O with various concentrations of $Mg(NO_3)_2$ ranging from 0 to 56.7 mM, collected at 37 °C and 14.1 T, highlighting the change in chemical shift for the resonance at ca. 123 ppm. The numbers next to spectra denote $[Mg^{2+}]$ (mM).

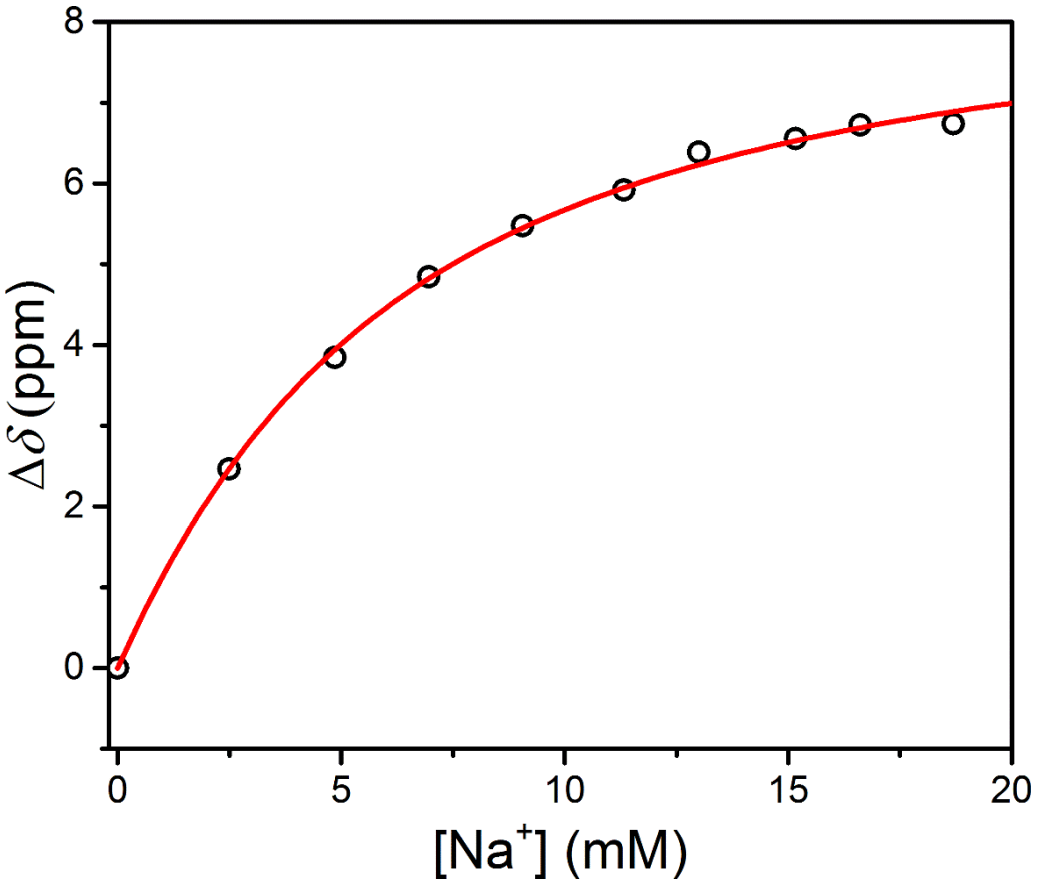

Figure 6.11 Change in ^{1}H NMR chemical shift ($\Delta\delta$) for the resonance at ca. 202 ppm vs [Na^+] for a series of solutions containing 2.5 mM of **1** in D_2O with various concentrations of $NaNO_3$ ranging from 0 to 18.7 mM, collected at 37 °C and 9.4 T (see Figure 6.3, left). Black circles represent experimental data and the red line represents a fit (see Section 6.2 for details).

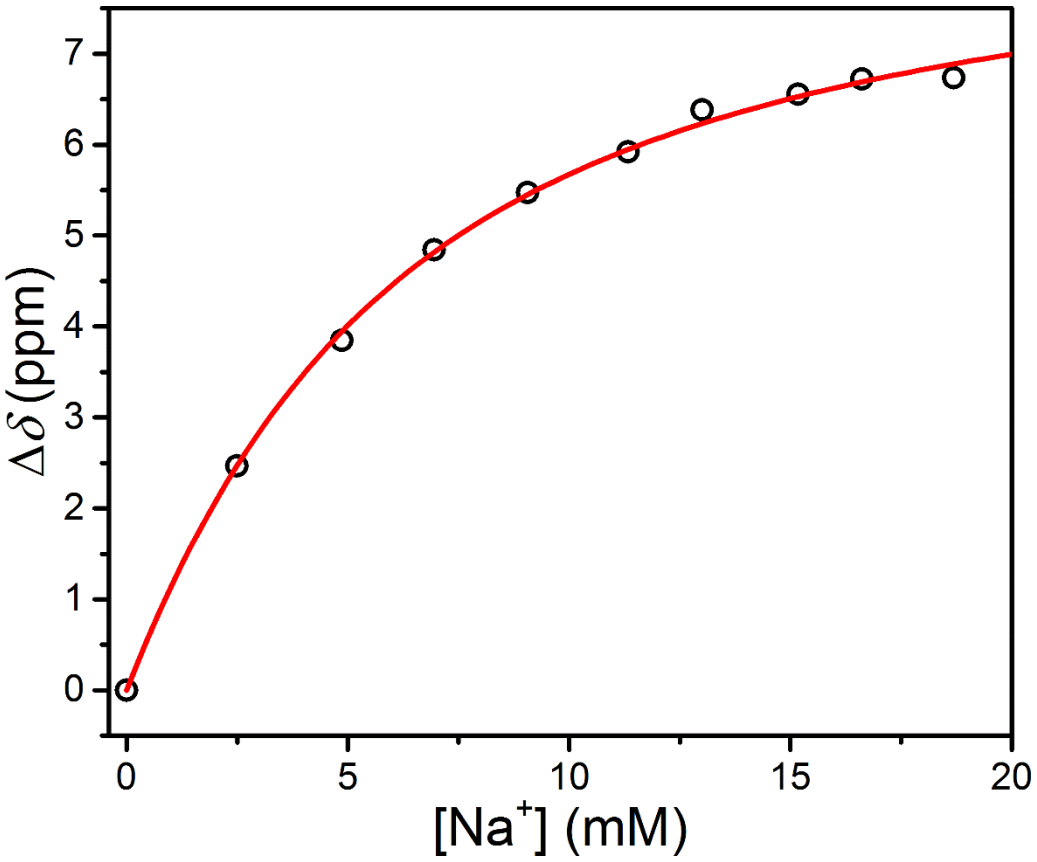

Figure 6.12 Change in ^{1}H NMR chemical shift ($\Delta\delta$) for the resonance at ca. 123 ppm vs [Na^+] for a series of solutions containing 2.5 mM of **1** in D_2O with various concentrations of $NaNO_3$ ranging from 0 to 18.7 mM, collected at 37 °C and 9.4 T (see Figure 6.8). Black circles represent experimental data and the red line represents a fit (see Section 6.2 for details).

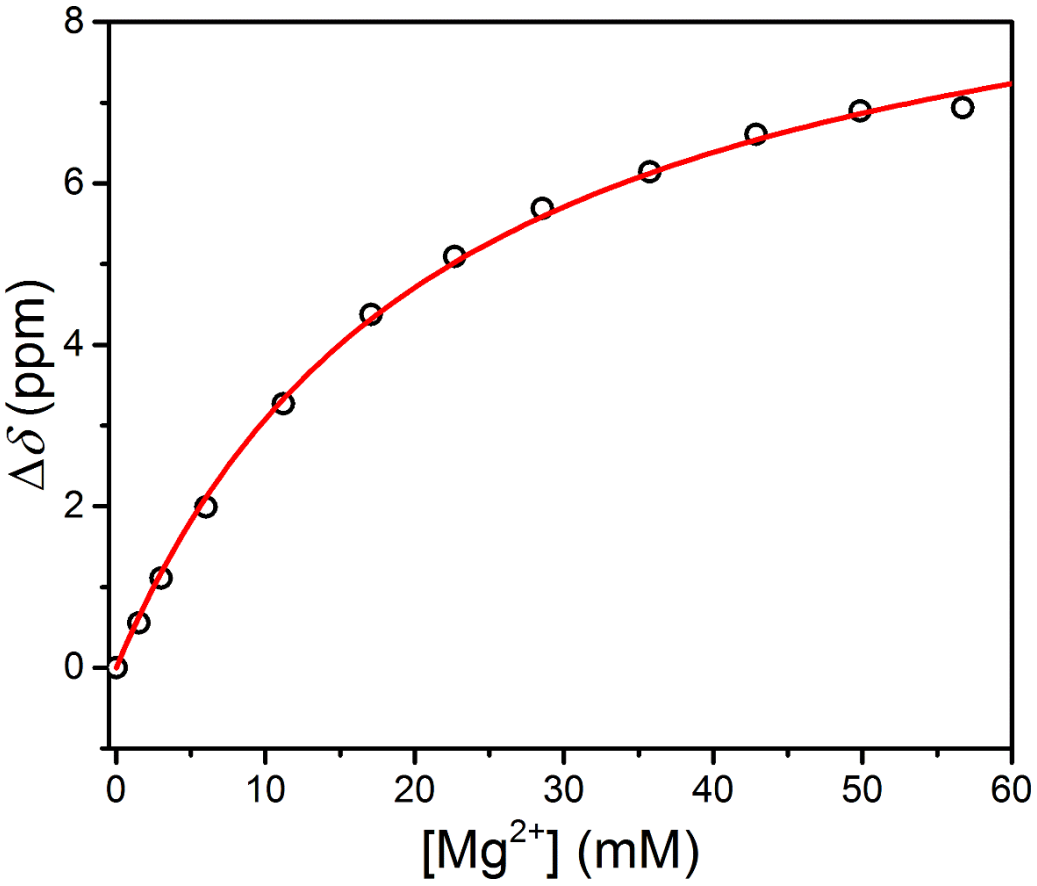

Figure 6.13 Change in ^{1}H NMR chemical shift ($\Delta\delta$) for the resonance at ca. 202 ppm vs [Mg^{2+}] for a series of solutions containing 1.0 mM of **1** in D_2O with various concentrations of $Mg(NO_3)_2$ ranging from 0 to 56.7 mM, collected at 37 °C and 14.1 T (see Figure 6.9). Black circles represent experimental data and the red line represents a fit (see Section 6.2 for details).

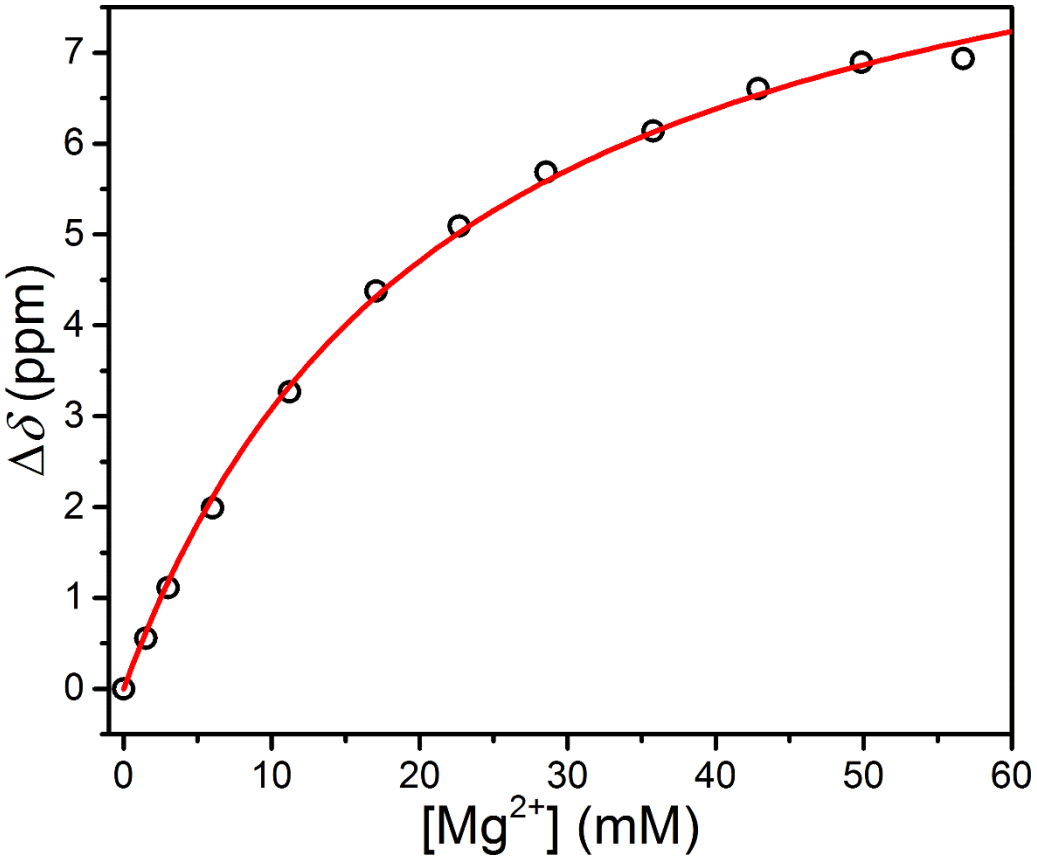

Figure 6.14 Change in ^{1}H NMR chemical shift ($\Delta\delta$) for the resonance at ca. 123 ppm vs [Mg^{2+}] for a series of solutions containing 1.0 mM of **1** in D_2O with various concentrations of $Mg(NO_3)_2$ ranging from 0 to 56.7 mM, collected at 37 °C and 14.1 T (see Figure 6.10). Black circles represent experimental data and the red line represents a fit (see Section 6.2 for details).

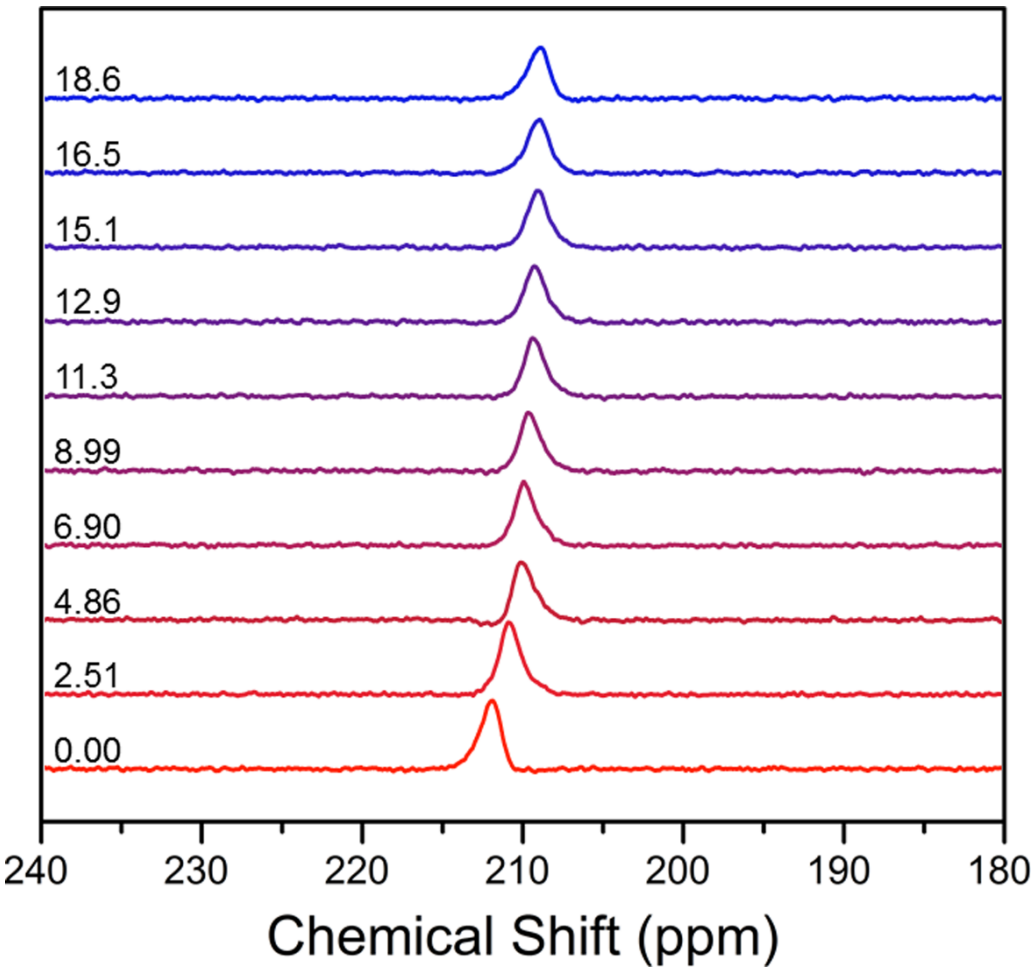

Figure 6.15 Stacked ^{1}H NMR spectra for a series of solutions containing 2.5 mM of **1** and 150 mM of $NaNO_3$ in D_2O with various concentrations of KNO_3 ranging from 0 to 18.6 mM, collected at 37 °C and 9.4 T, highlighting the change in chemical shift for the resonance at ca. 212 ppm. The numbers next to spectra denote $[K^+]$ (mM).

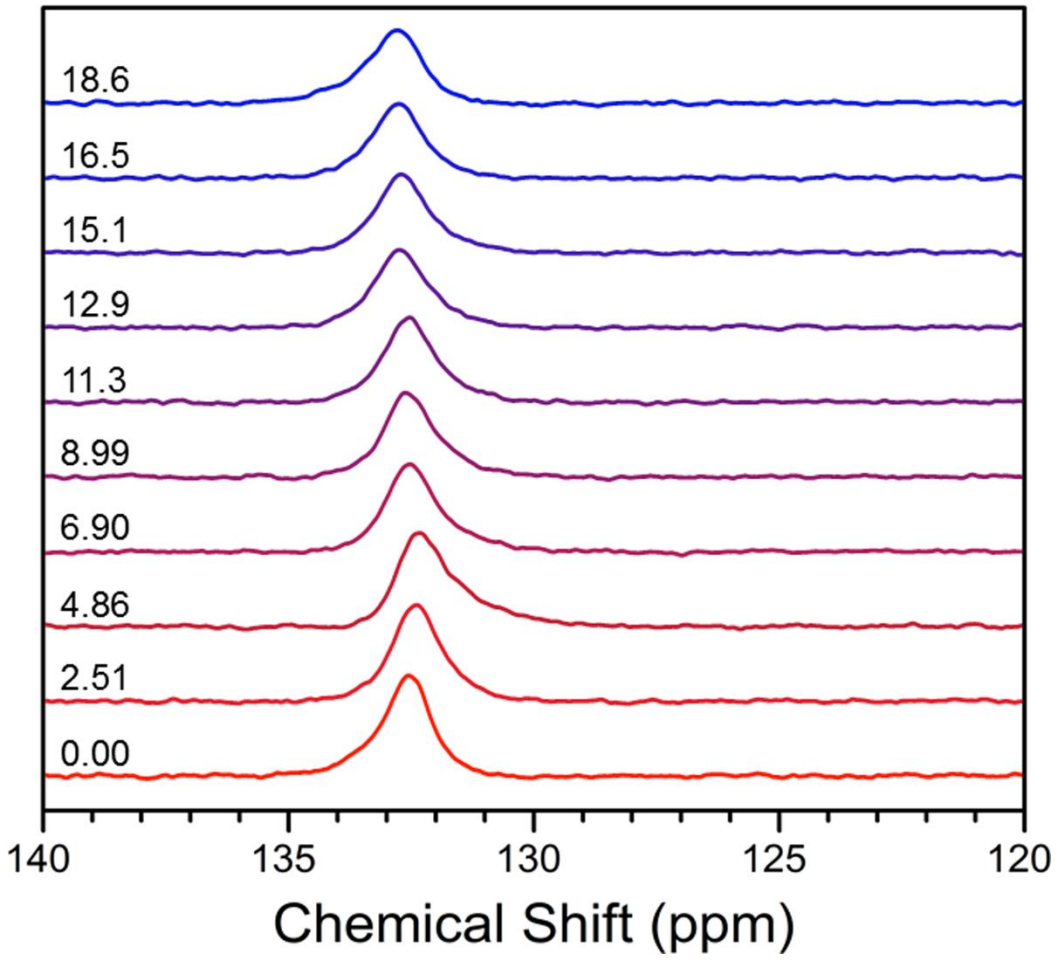

Figure 6.16 Stacked ^{1}H NMR spectra for a series of solutions containing 2.5 mM of **1** and 150 mM of $NaNO_3$ in D_2O with various concentrations of KNO_3 ranging from 0 to 18.6 mM, collected at 37 °C and 9.4 T, highlighting the change in chemical shift for the resonance at ca. 133 ppm. The numbers next to spectra denote [K^+] (mM).

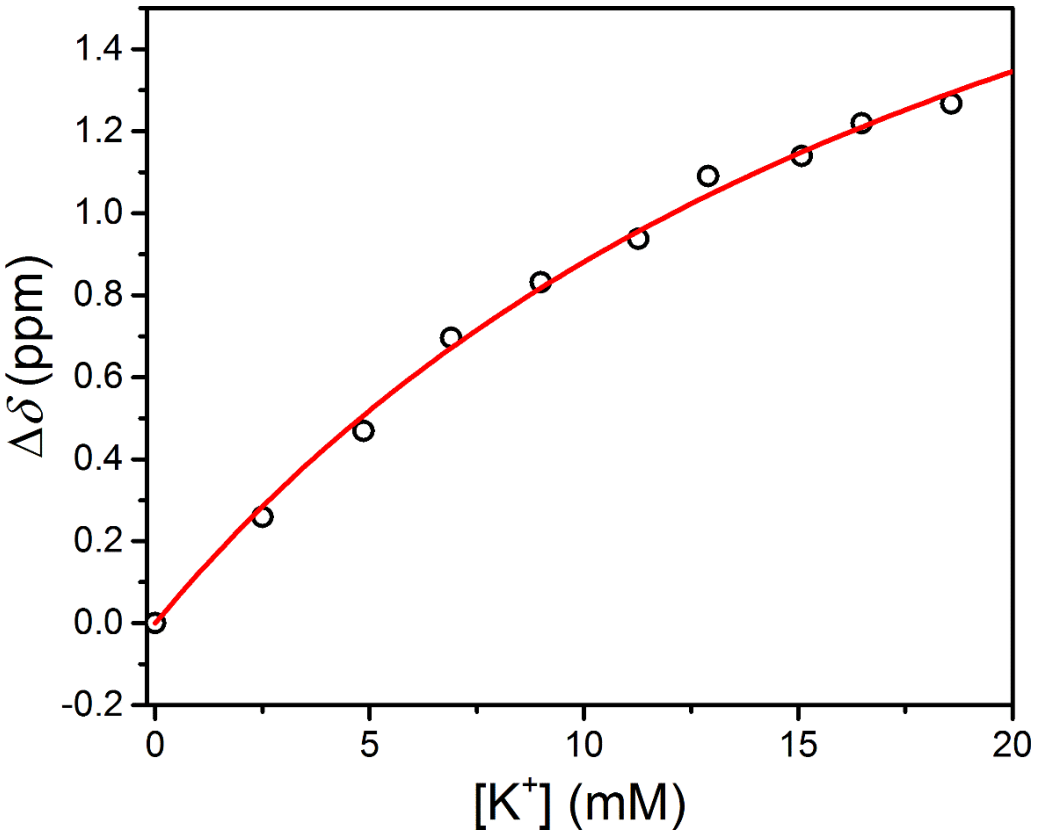

Figure 6.17 Change in ^{1}H NMR chemical shift ($\Delta\delta$) for the resonance at ca. 212 ppm vs [K^+] for a series of solutions containing 2.5 mM of **1** and 150 mM of $NaNO_3$ in D_2O with various concentrations of KNO_3 ranging from 0 to 18.6 mM, collected at 37 °C and 9.4 T (see Figure 6.15). Black circles represent experimental data and the red line represents a fit (see Section 6.2 for details).

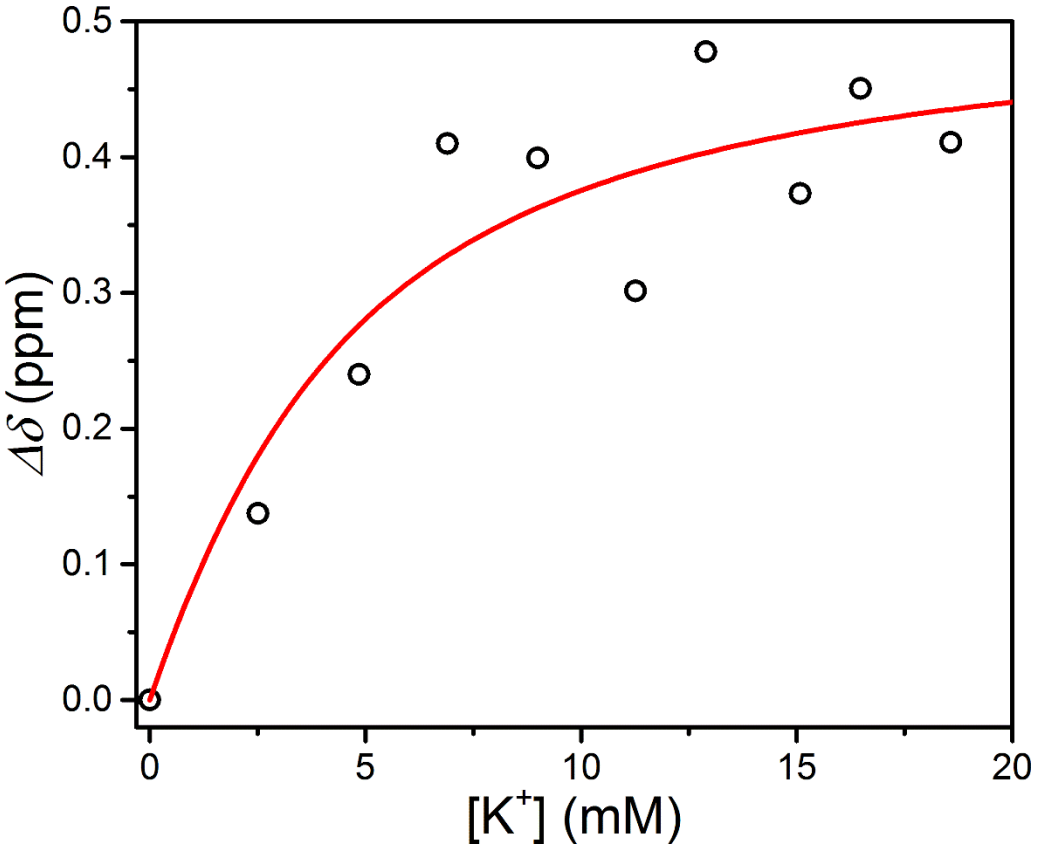

Figure 6.18 Change in ^{1}H NMR chemical shift ($\Delta\delta$) for the resonance at ca. 133 ppm vs [K^+] for a series of solutions containing 2.5 mM of **1** and 150 mM of $NaNO_3$ in D_2O with various concentrations of KNO_3 ranging from 0 to 18.6 mM, collected at 37 °C and 9.4 T (see Figure 6.16). Black circles represent experimental data and the red line represents a fit (see Section 6.2 for details).

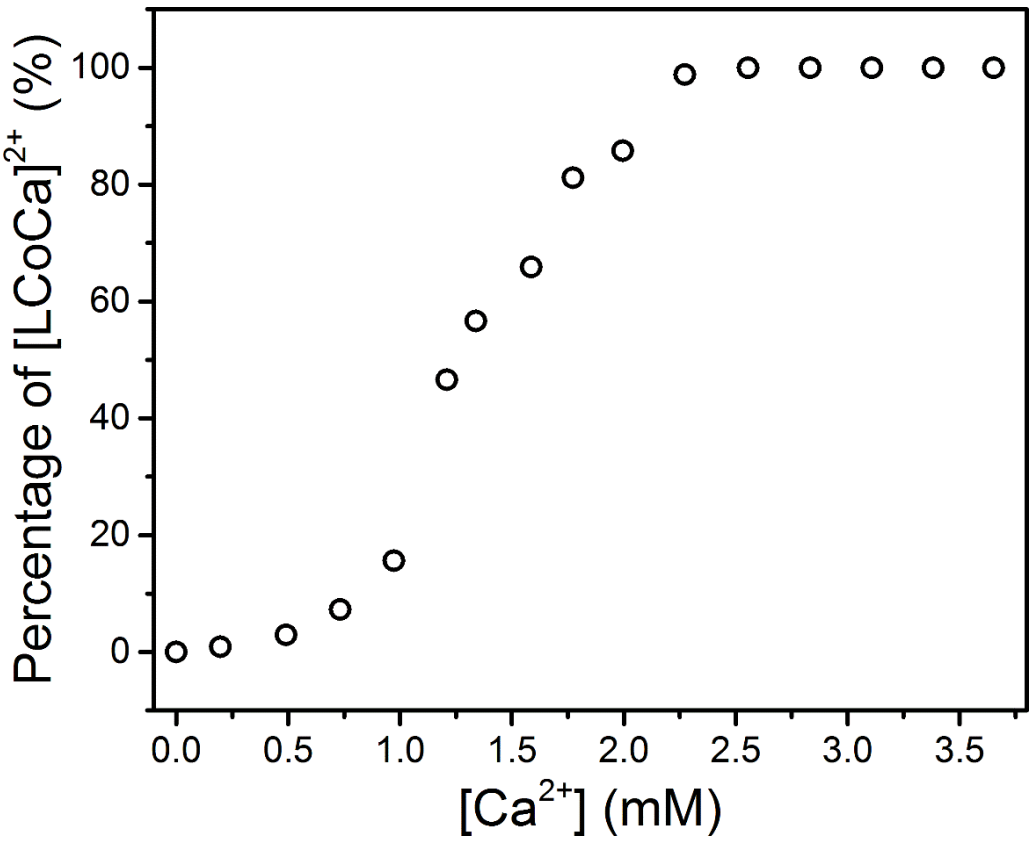

Figure 6.19 Change in mole fraction of $[LCoCa]^{2+}$ vs $[Ca^{2+}]$, as determined from the ratio of integration values of ^{1}H NMR peaks at 245 and 207 ppm ($I_{245\ ppm}/I_{207\ ppm}$) for a series of solutions containing 1.0 mM of **1** and 30 mM of KNO_3 in D_2O with various concentrations of $Ca(NO_3)_2$ ranging from 0 to 3.65 mM, collected at 37 °C and 14.1 T (see Figure 6.3, right).

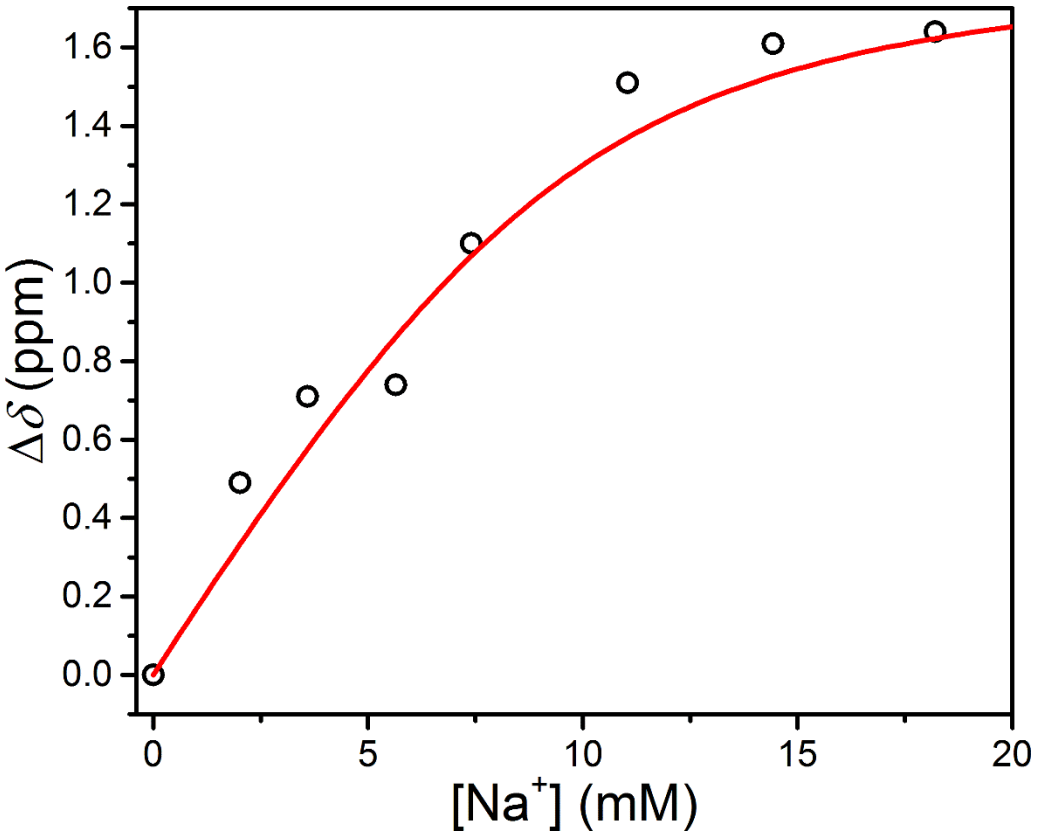

Figure 6.20 Change in ^{1}H NMR chemical shift ($\Delta\delta$) for the resonance at ca. 123 ppm vs [Na^+] for a series of solutions containing 5.0 mM of **1** and 50 mM of HEPES buffered at pH 7.3 with various concentrations of $NaNO_3$ ranging from 0 to 18.2 mM, collected at 37 °C and 11.7 T. Black circles represent experimental data and the red line represents a fit (see Section 6.2 for details).

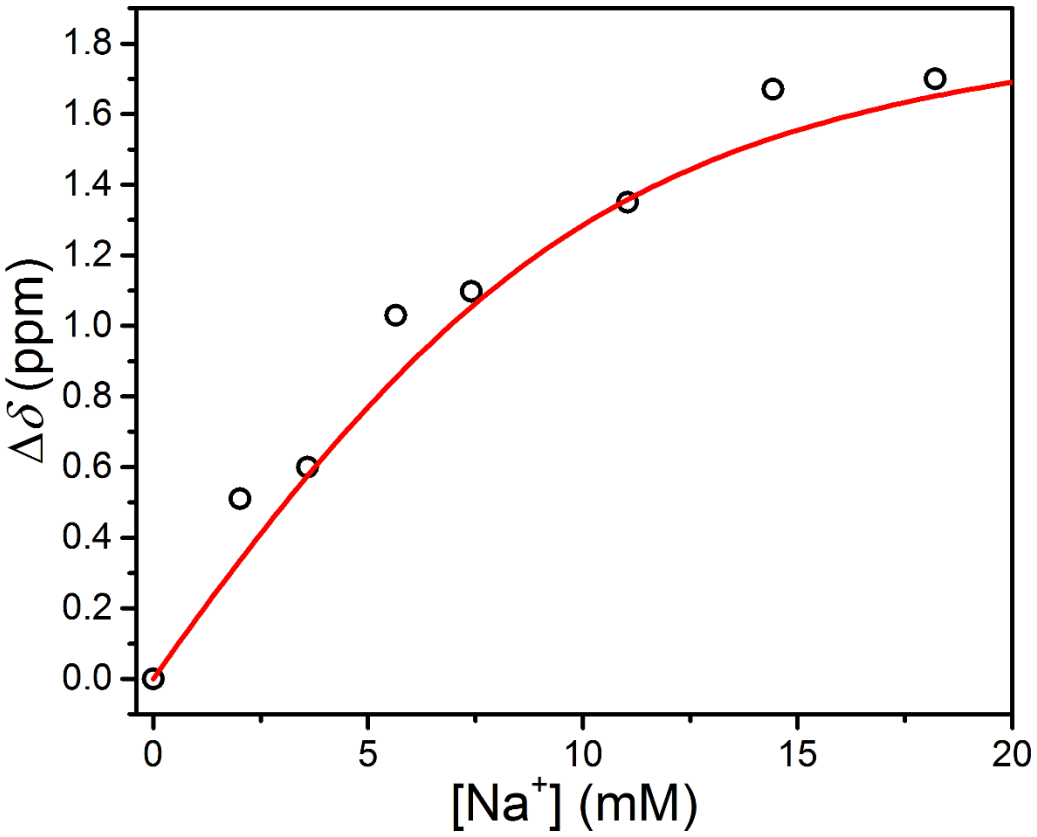

Figure 6.21 Change in ^{1}H NMR chemical shift ($\Delta\delta$) for the resonance at ca. 123 ppm vs [Na^+] for a series of solutions containing 5.0 mM of **1** and 50 mM of HEPES buffered at pH 7.4 with various concentrations of $NaNO_3$ ranging from 0 to 18.2 mM, collected at 37 °C and 11.7 T. Black circles represent experimental data and the red line represents a fit (see Section 6.2 for details).

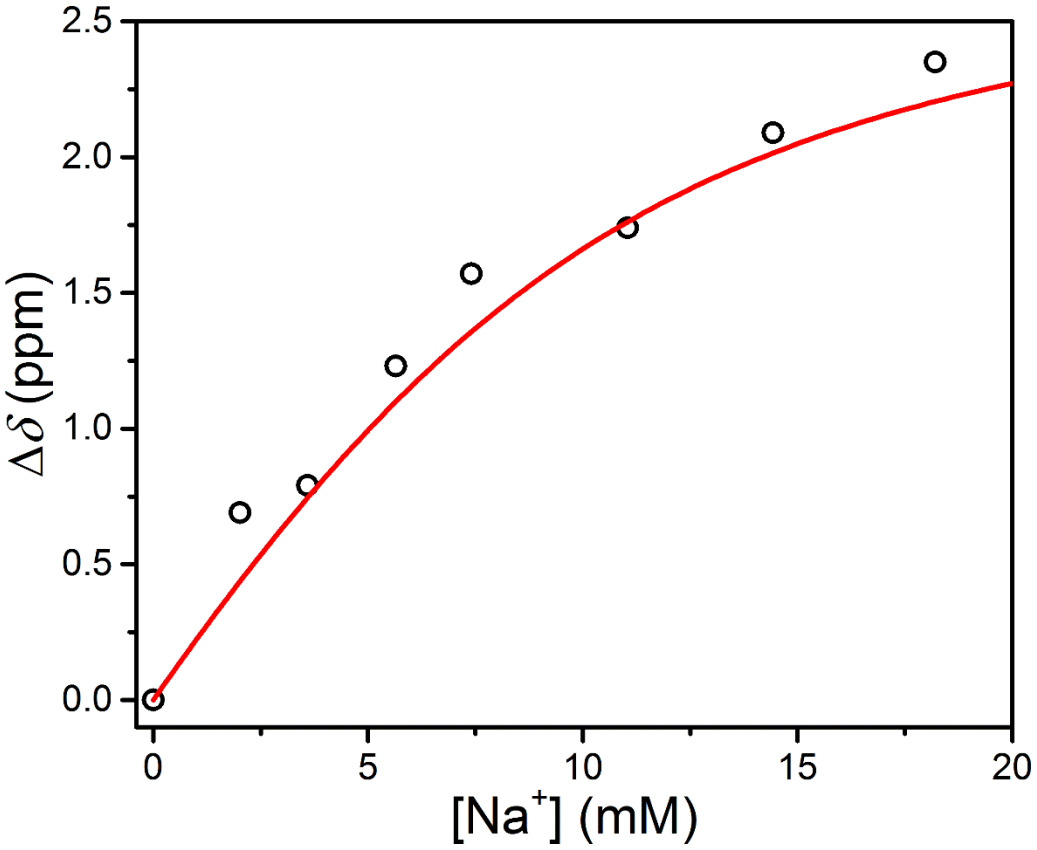

Figure 6.22 Change in ^{1}H NMR chemical shift ($\Delta\delta$) for the resonance at ca. 123 ppm vs [Na^+] for a series of solutions containing 5.0 mM of **1** and 50 mM of HEPES buffered at pH 7.5 with various concentrations of $NaNO_3$ ranging from 0 to 18.2 mM, collected at 37 °C and 11.7 T. Black circles represent experimental data and the red line represents a fit (see Section 6.2 for details).

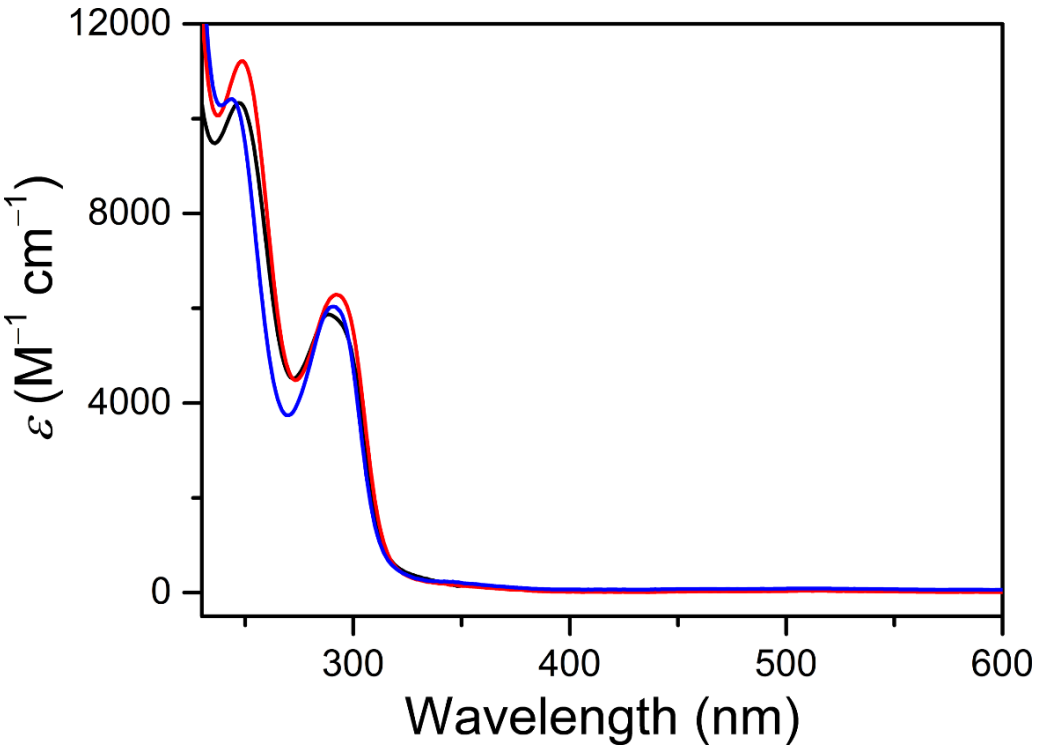

Figure 6.23 UV-Vis spectra collected at ambient temperature for **1** in 1 mM HEPES solutions buffered at pH 7.4 in the absence of inorganic cations (black), and in the presence of 3.0 equivalents of $NaNO_3$ (red) or 3.0 equivalents of $Ca(NO_3)_2$ (blue). Note that the sample solutions were prepared and measured under dinitrogen atmosphere.

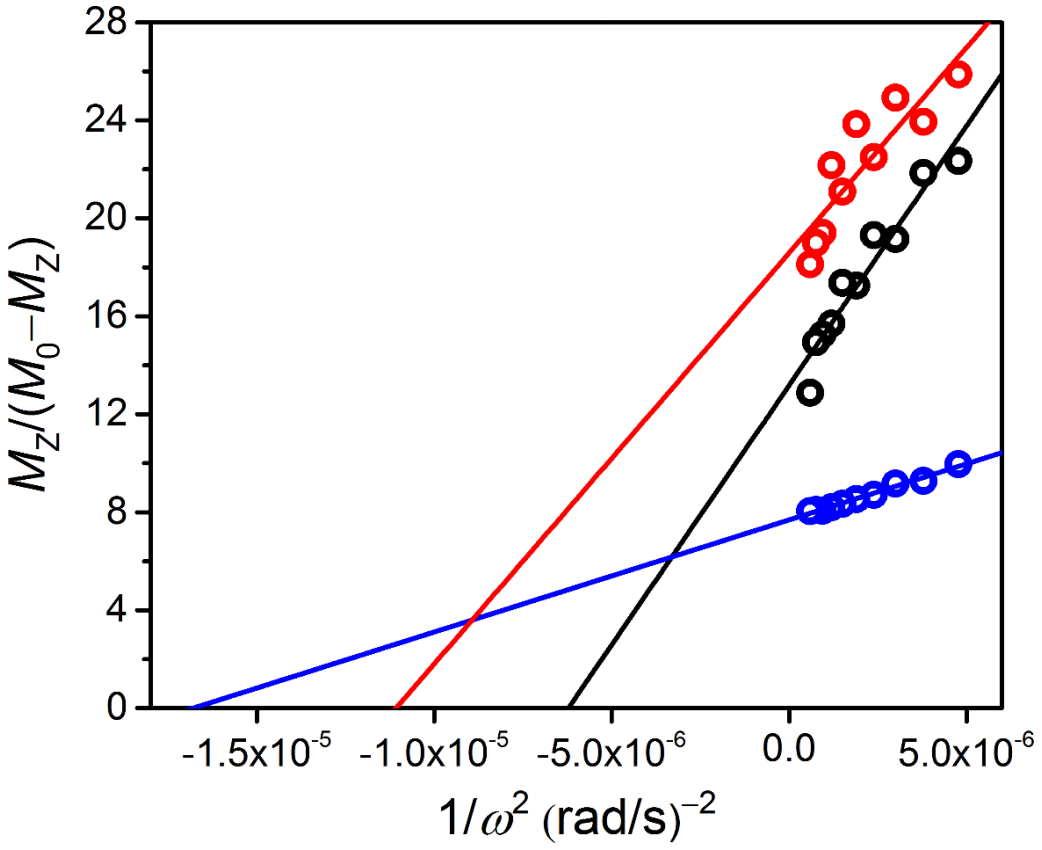

Figure 6.24 Omega plots of the CEST effects from application of 6 s presaturation pulses at 77, 69, and 80 ppm for samples containing 5 mM of **1** and 50 mM of HEPES buffered at pH 7.4 in the absence of inorganic cations (black), and in the presence of 15 mM of $NaNO_3$ (red) or 15 mM of $Ca(NO_3)_2$ (blue), respectively. The data were collected at 37 °C and 11.7 T using B_1 = 7.4–21 μT.

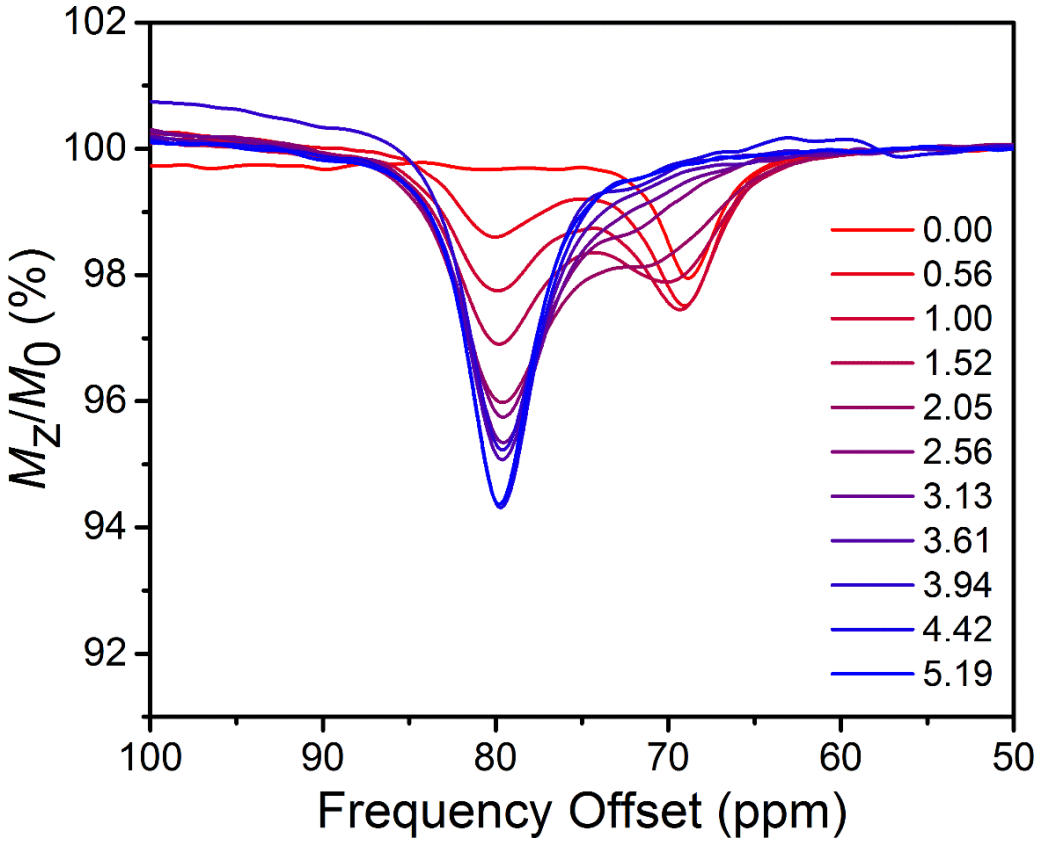

Figure 6.25 Stacked CEST spectra collected at 11.7 T and 37 °C using a 3 s presaturation pulse and B_1 = 21 μT for solutions containing 2.8 mM of **1**, 150 mM of NaCl, and 50 mM of HEPES buffered at pH 7.4 with various concentrations of $Ca(NO_3)_2$ ranging from 0 to 5.19 mM. The legend denotes $[Ca^{2+}]$ (mM).

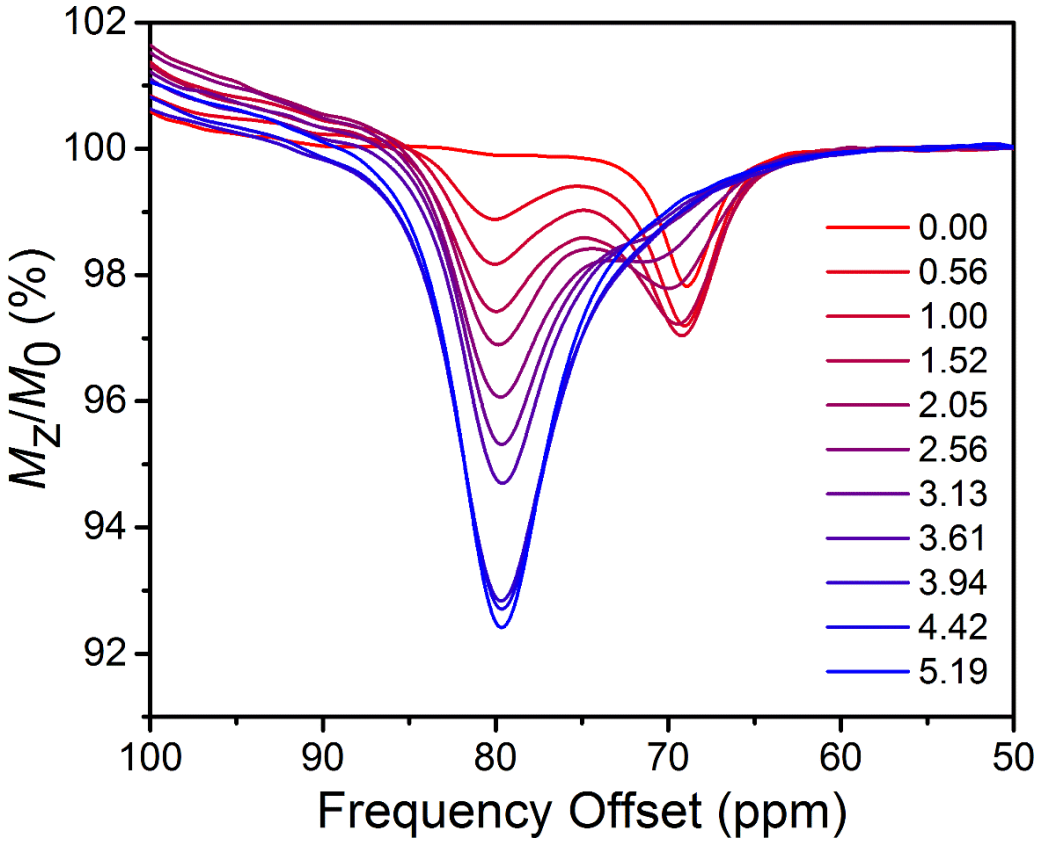

Figure 6.26 Stacked CEST spectra collected at 11.7 T and 37 °C using a 3 s presaturation pulse and B_1 = 21 μT for solutions containing 5.6 mM of **1**, 150 mM of NaCl, and 50 mM of HEPES buffered at pH 7.4 with various concentrations of $Ca(NO_3)_2$ ranging from 0 to 5.19 mM. The legend denotes $[Ca^{2+}]$ (mM).

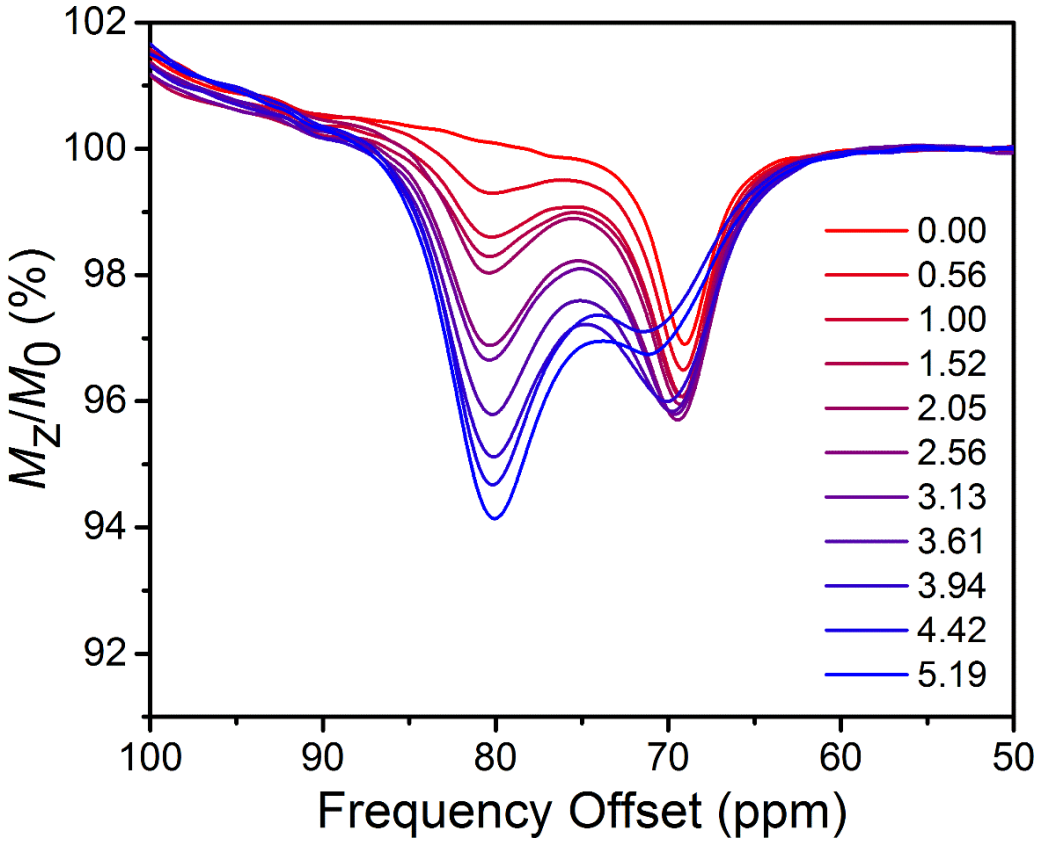

Figure 6.27 Stacked CEST spectra collected at 11.7 T and 37 °C using a 3 s presaturation pulse and B_1 = 21 μT for solutions containing 11 mM of **1**, 150 mM of NaCl and 50 mM of HEPES buffered at pH 7.4 with various concentrations of $Ca(NO_3)_2$ ranging from 0 to 5.19 mM. The legend denotes $[Ca^{2+}]$ (mM).

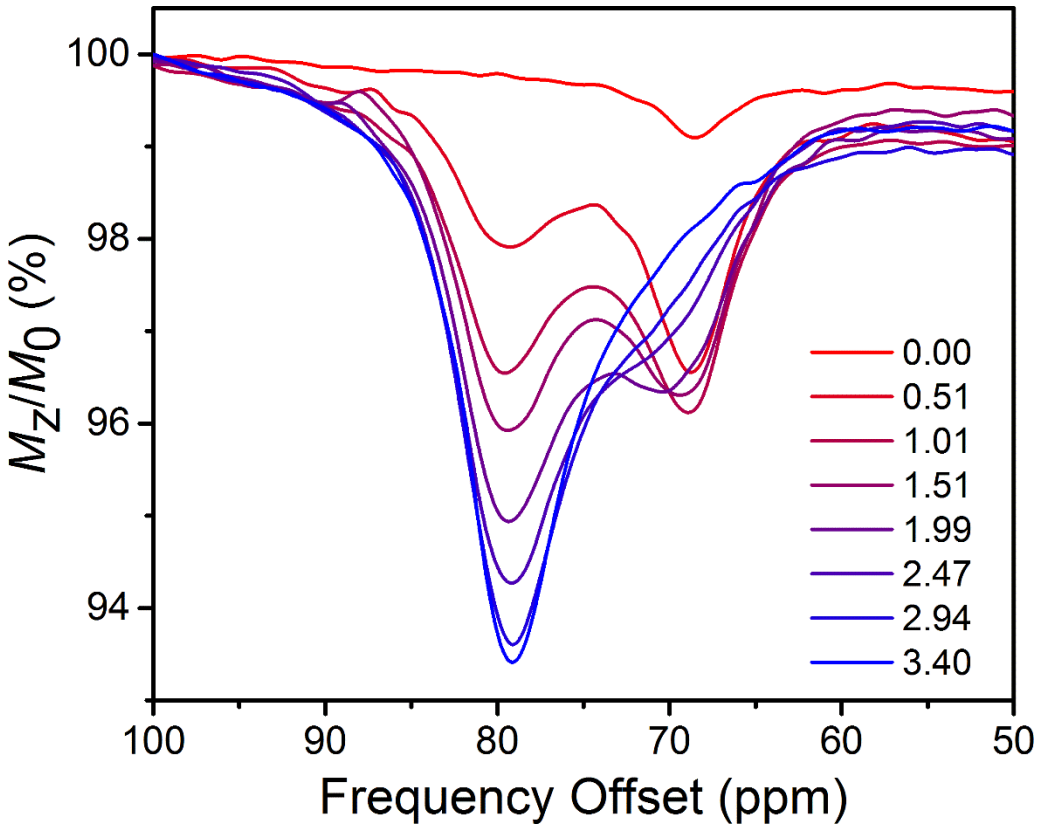

Figure 6.28 Stacked CEST spectra collected at 11.7 T and 37 °C using a 3 s presaturation pulse and B_1 = 22 μT for solutions containing 2.8 mM of **1**, 150 mM of NaCl, 4 mM of KNO_3, 0.2 mM of $Mg(NO_3)_2$, and 50 mM of HEPES buffered at pH 7.4 with various concentrations of $Ca(NO_3)_2$ ranging from 0 to 3.40 mM. The legend denotes [Ca^{2+}] (mM).

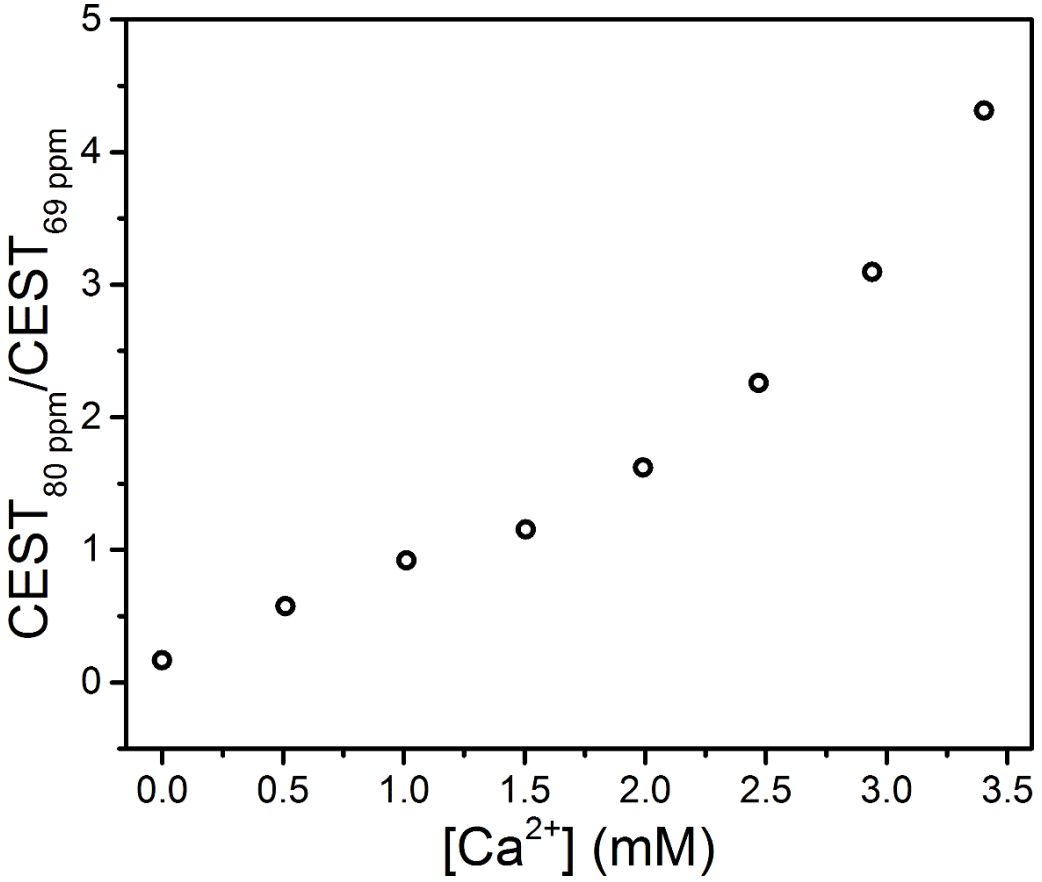

Figure 6.29 Ratio of CEST peak intensities at 80 and 69 ppm ($CEST_{80\ ppm}/CEST_{69\ ppm}$) vs [$Ca^{2+}$] for data collected at 11.7 T and 37 °C using a 3 s presaturation pulse and B_1 = 22 μT for solutions containing 2.8 mM of **1**, 150 mM of NaCl, 4 mM of KNO_3, 0.2 mM of $Mg(NO_3)_2$, and 50 mM of HEPES buffered at pH 7.4 with various concentrations of $Ca(NO_3)_2$ ranging from 0 to 3.40 mM (see Figure 6.28).

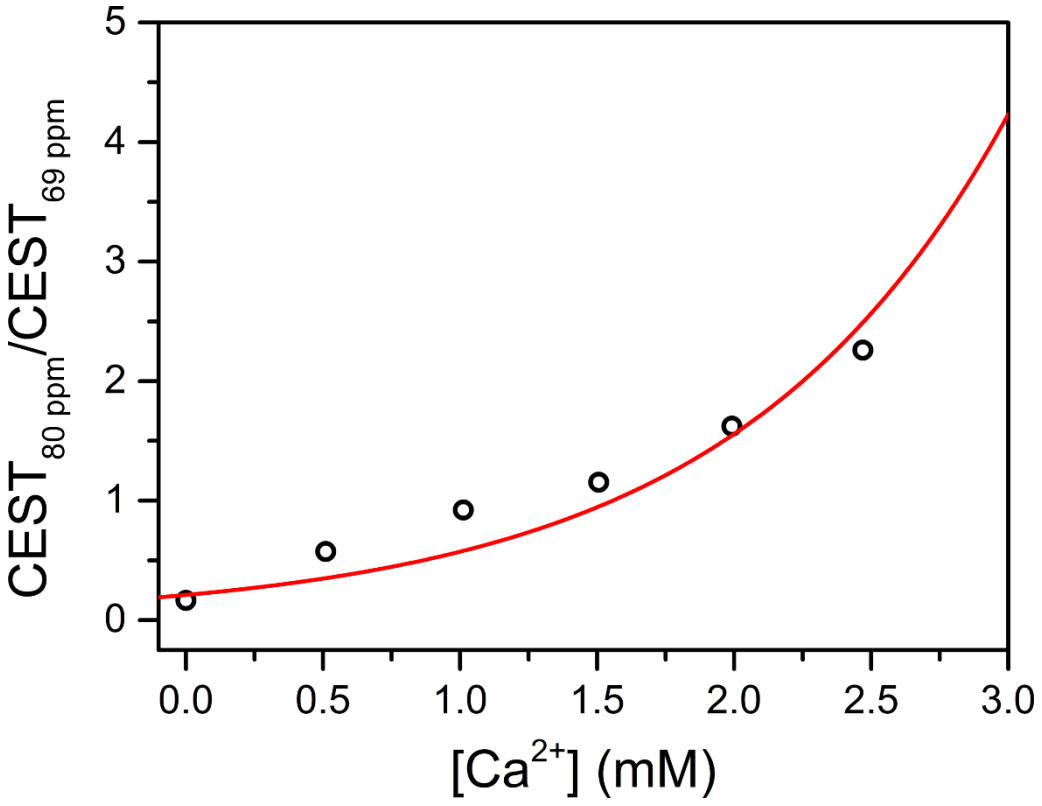

Figure 6.30 Expanded view of the ratio of CEST peak intensities at 80 and 69 ppm ($CEST_{80\ ppm}/CEST_{69\ ppm}$) vs [$Ca^{2+}$] for data shown in Figure 6.29 with [Ca^{2+}] ranging from 0 to 2.47 mM. Black circles represent experimental data and the red line represents a fit to the data using Equation 6.4.

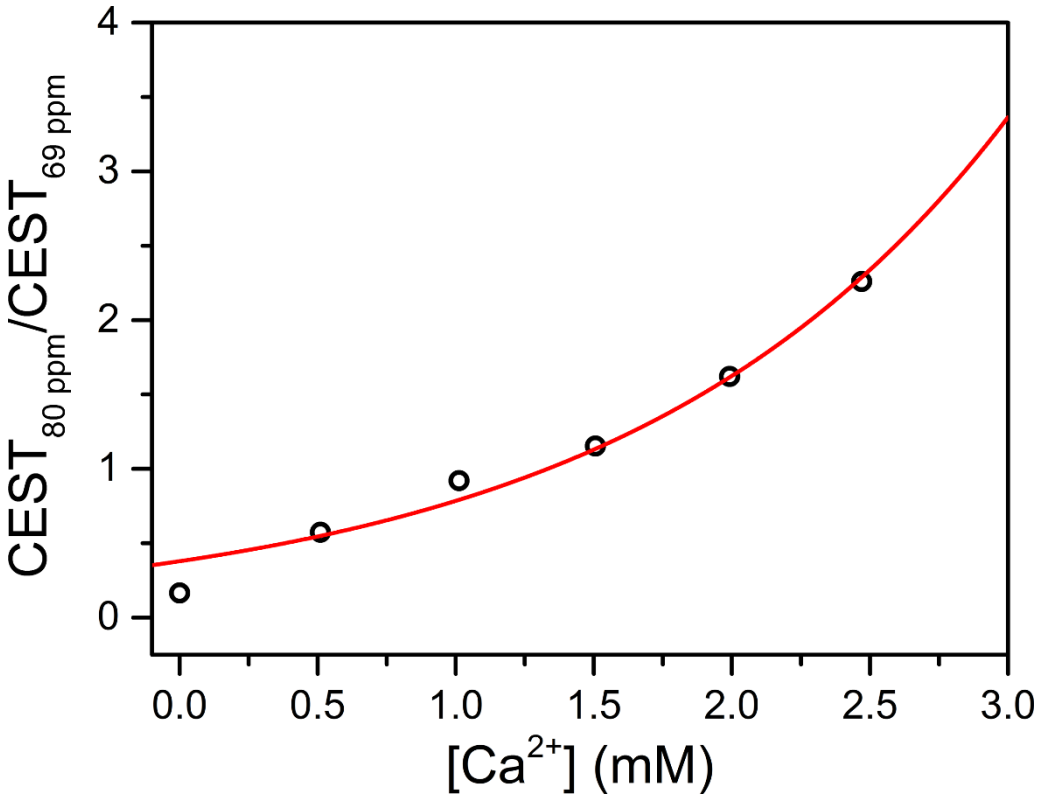

Figure 6.31 Expanded view of the ratio of CEST peak intensities at 80 and 69 ppm ($CEST_{80\ ppm}/CEST_{69\ ppm}$) vs [$Ca^{2+}$] for data shown in Figure 6.29 with [Ca^{2+}] ranging from 0 to 2.47 mM. Black circles represent experimental data and the red line represents a fit to the data using Equation 6.5.

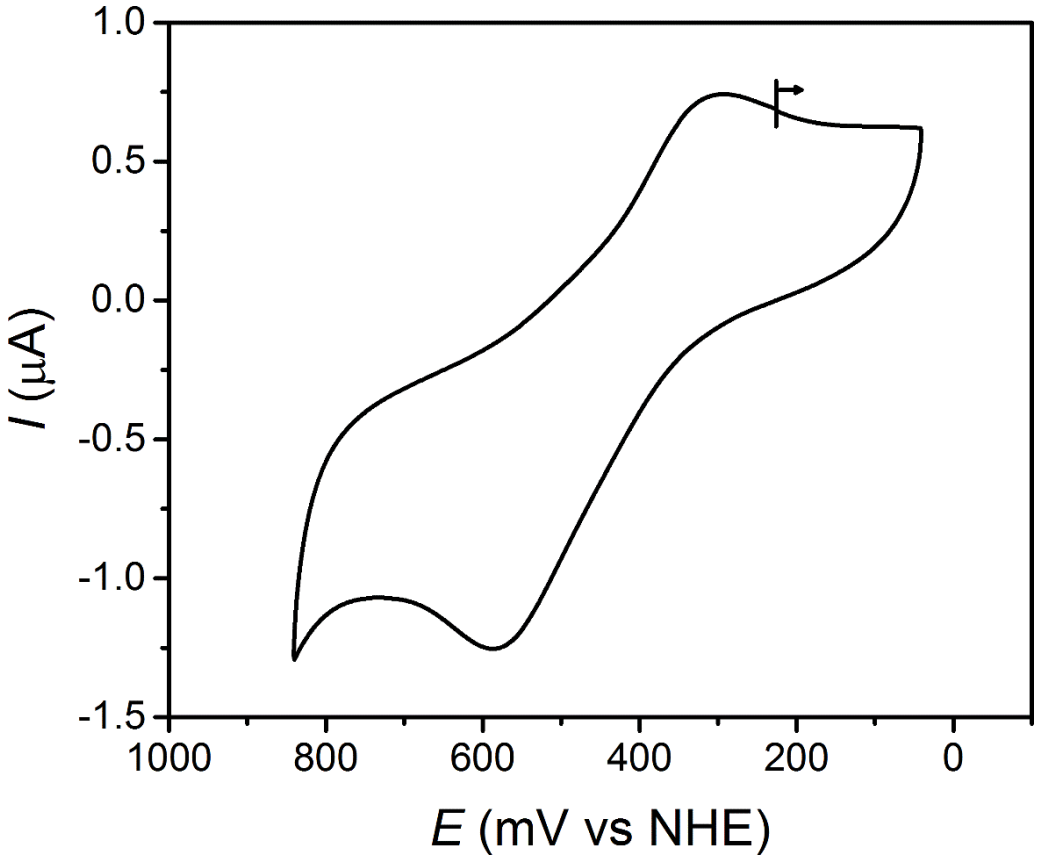

Figure 6.32 Cyclic voltammogram of **1** in an aqueous solution containing 100 mM of $(Me_4N)Cl$ and 50 mM of HEPES buffered at pH 7.4. Measurements were carried out using a scan rate of 100 mV s^{-1}. The black arrow denotes the scan direction.

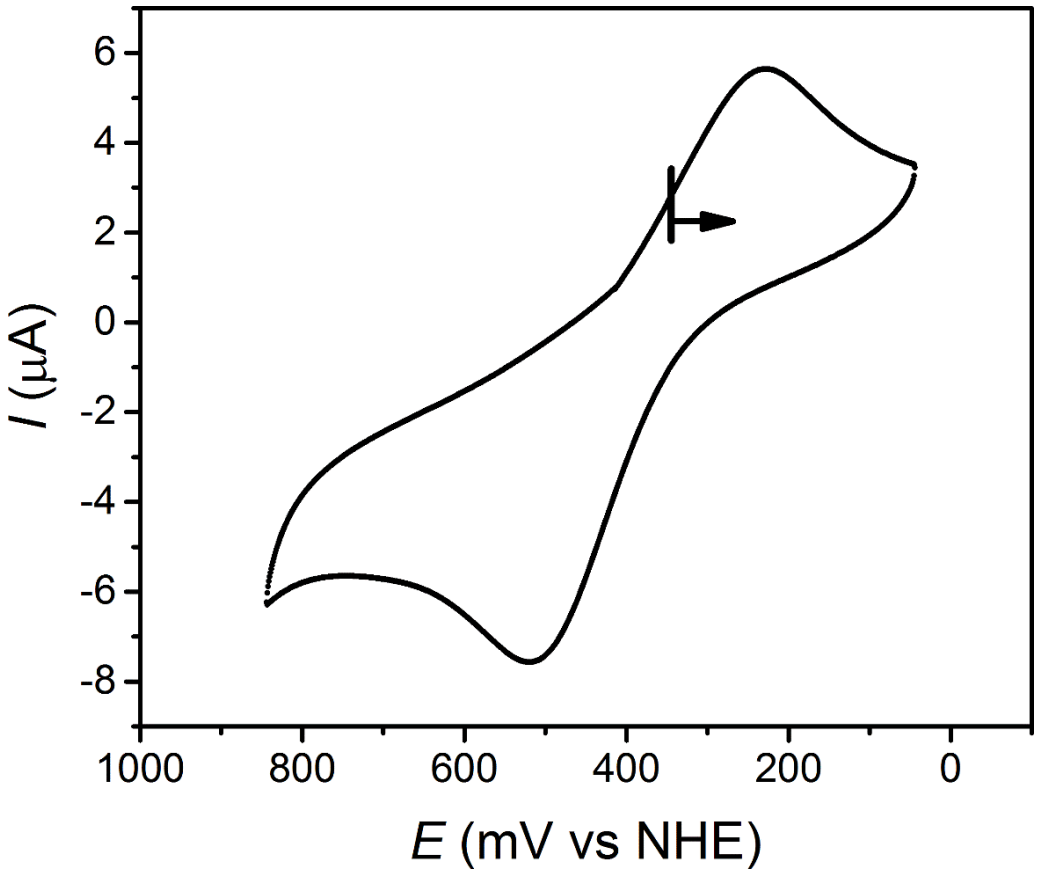

Figure 6.33 Cyclic voltammogram of **1** in an aqueous solution containing 150 mM of NaCl, 4 mM of KNO_3, 2 mM of $Ca(NO_3)_2$, 0.2 mM of $Mg(NO_3)_2$, and 50 mM of HEPES buffered at pH 7.4. Measurements were carried out using a scan rate of 100 mV s^{-1}. The black arrow denotes the scan direction.

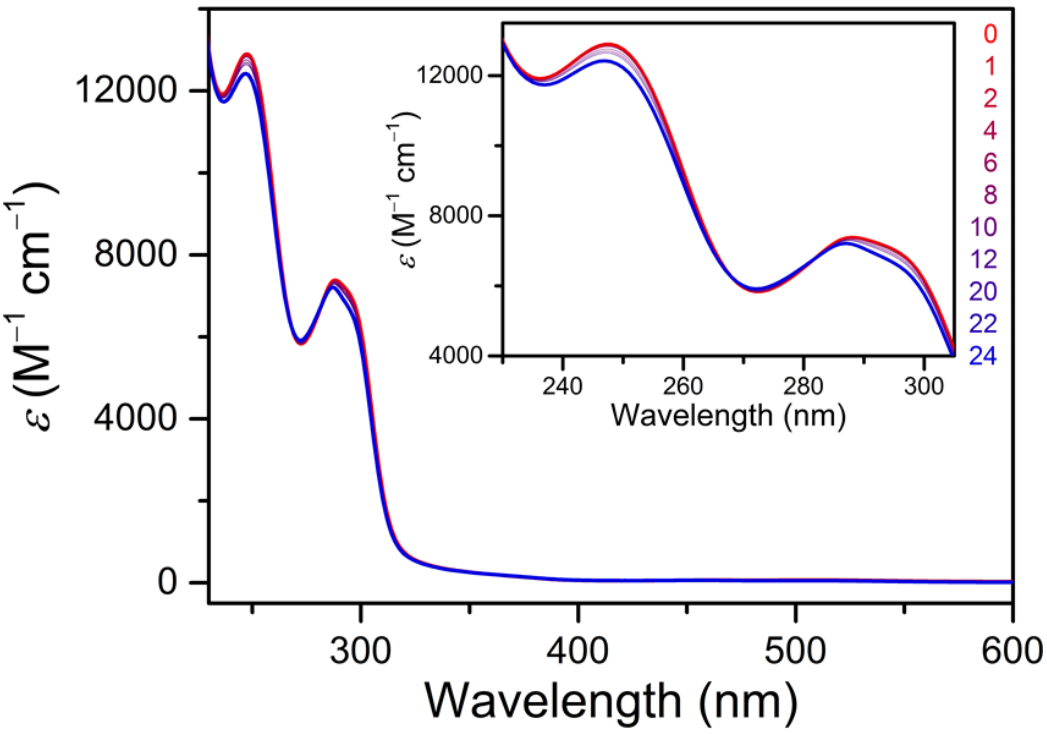

Figure 6.34 UV-Vis spectra collected at ambient temperature for **1** in an aqueous solution containing 1 mM of HEPES buffered at pH 7.4 after different hours of air exposure. Note that the sample solution was prepared and initially measured under dinitrogen atmosphere and then exposed to air. The legend denotes the time (in hours) that the sample solution had been exposed to air before data collection and the inset shows an expanded view of the relevant absorption peaks.

6.5.4 Supplementary Tables

Table 6.3 Crystallographic data for **1′–3′** at 100 K.

	1′	**2′**	**3′**
Empirical formula	$C_{55}H_{76.4}Co_2N_8O_{18.1}$	$C_{52}H_{72}Co_2N_9Na_2O_{21}$	$C_{29}H_{46}CaCoN_6O_{17}$
Formula weight, g mol^{-1}	1257.12	1323.02	849.73
Crystal system	Cubic	Cubic	Orthorhombic
Space group	*I*a–3	*I*a–3	*P*bca
Wavelength, Å	0.7103	0.71073	0.71073
Temperature, K	100	100	100
a, Å	35.066(7)	34.793(3)	10.7639(7)
b, Å	35.066(7)	34.793(3)	21.7165(14)
c, Å	35.066(7)	34.793(3)	31.819(2)
α, °	90	90	90
β, °	90	90	90
γ, °	90	90	90
V, Å^3	43118(27)	42117(11)	7437.9(8)
Z	24	24	8
ρ_{calcd}, g cm^{-3}	1.162	1.252	1.518
μ, mm^{-1}	0.526	0.556	0.681
Reflections coll./unique	7358/5013	7229/5967	11030/9688
R(int)	0.1111	0.1046	0.0990
R_1 $(I > 2\sigma(I))^a$	0.0805	0.1523	0.1350
wR_2 $(all)^b$	0.2755	0.4885	0.2880
GoF	1.064	2.320	1.204

^{a} $R_1 = \Sigma||F_0| - |F_C||/\Sigma|F_0|$, ^{b} $wR_2 = [\Sigma w(F_0^2 - F_C^2)^2/\Sigma w(F_0^2)^2]^{1/2}$.

Table 6.4 Summary of dissociation constants (K_d) estimated for $[LCoNa]^+$, $[LCoMg]^{2+}$, and $[LCoK]^+$ at 37 °C in D_2O by monitoring ^1H NMR chemical shift changes upon addition of Na^+, Mg^{2+}, or K^+ to solutions of LCo for different resonances. The data were collected at 9.4 T for $[LCoNa]^+$ and $[LCoK]^+$, and at 14.1 T for $[LCoMg]^{2+}$ (see Figures 6.3, left, and 6.8–6.18).

	$[LCoNa]^+$	**$[LCoMg]^{2+}$**	**$[LCoK]^+$**
$K_{d,\ 200–220\ ppm}$ (mM)	4.0(3)	22(3)	0.4(2)
$K_{d,\ 120–140\ ppm}$ (mM)	5.5(5)	24(2)	0.1(1)
$K_{d,\ average}$ (mM)	4.8(3)	23(2)	0.3(2)

Table 6.5 Summary of average dissociation constants (K_d) for $[LCoNa]^+$ at 37 °C in different aqueous solutions. The data were collected at 9.4 and 11.7 T for the D_2O and 50 mM HEPES buffer solutions, respectively.

	D_2O	**pH 7.3**	**pH 7.4**	**pH 7.5**
K_d (mM)	4.8(3)	3.7(9)	1.8(9)	2(1)

Chapter 7: Minimal Impact of Ligand Substitution on Magnetic Coupling in a Series of Semiquinoid Radical-Bridged Fe_2 Single-Molecule Magnets

Thorarinsdottir, A. E.; Harris, T. D. *In preparation.*

This work was performed in collaboration with the co-author listed above.

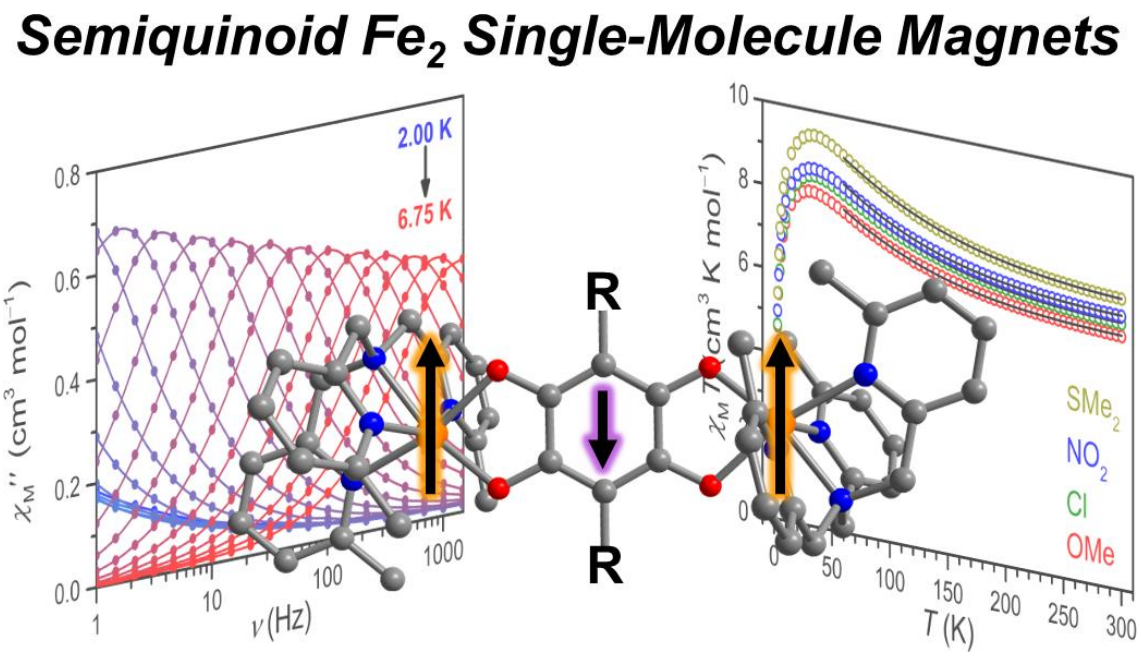

7.1 Introduction

Molecule-based magnetic materials, ranging from mono- and multinuclear metal complexes[1] to higher-dimensional frameworks,[2–9] have garnered tremendous interest over the past few decades as alternatives to conventional inorganic solid-state magnets. Specifically, the employment of molecular building blocks, typically paramagnetic metal ions and mono- or multiatom bridging ligands, enables the rational design of compounds with targeted structures and magnetic properties. Such synthetic bottom-up approach allows for the development of unique multifunctional materials, including those that exhibit coexisting magnetic order and electrical conductivity[6g,8d,9b,c,e,10–13] or luminescence properties.[14] Owing to their low density and high chemical tunability and processability, molecule-based magnetic materials may find use as lightweight permanent magnets, and in applications such as high-density information storage and processing, magnetic sensing, and gas separation.[8,15,16] However, despite significant recent advances, the operating temperatures of molecule-based magnets must be increased in order to realize these applications at practical temperatures.

In targeting molecule-based magnets with high operating temperatures, the strength of magnetic exchange interactions between spin centers is of critical importance. To illustrate, the strength of this interaction between paramagnetic centers is directly related to the isolation of the spin ground state of single-molecule magnets,[17] the thermal relaxation barrier of single-chain magnets,[18] and the magnetic ordering temperature of 2D and 3D permanent magnets.[19] As such, increasing the strength of magnetic exchange coupling between spin centers represents an attractive route toward increasing the operating temperatures of molecule-based magnets of all dimensions. Nevertheless, the vast majority of molecule-based magnets feature multiple

paramagnetic metal centers that interact through diamagnetic bridging ligands via a superexchange mechanism. While such superexchange interactions through short oxo and cyano ligands can be strong enough to afford room-temperature 3D magnets,[5c,d,6b] the coupling strength decreases dramatically as the number of atoms in the bridging ligand increases.[8b,c] Therefore, in order to achieve room-temperature molecule-based magnets featuring organic multiatom bridging ligands that provide much greater synthetic programmability and chemical tunability than oxo- and cyano-bridged analogues, stronger coupling between metal centers must be realized.

Two strategies to promote strong magnetic coupling have recently received increasing interest. The first approach centers on using mixed-valence compounds for which electron delocalization through a diamagnetic bridging ligand promotes a double-exchange interaction between metal centers, which can be significantly stronger than superexchange.[20] Alternatively, incorporation of an organic radical bridging ligand between paramagnetic metal ions can engender strong direct magnetic exchange coupling due to the direct overlap of the metal- and radical-based magnetic orbitals.[1u,21] In fact, the latter approach has been particularly successful, as exemplified by extensive studies on systems featuring nitroxide,[1u,2a,e,p,21a,b,e,22] organonitrile,[4,10,23] perchlorotriphenylmethyl,[24] triplet carbene[25], and pyrazine[26] radical ligands. Despite this progress, the low charges and monodentate binding mode of each of the coordinating functional group of these ligands limit the strength of metal–ligand interactions and prevent the assembly of compounds with well-defined structures.

Benzoquinoid ligands offer an ideal platform for the construction of radical-bridged molecule-based magnets with strong magnetic coupling, as these ligands (i) undergo facile redox chemistry to generate the semiquinoid radical (see Scheme 7.1), (ii) form strong metal–ligand bonds and

compounds with predictable structures thanks to their bis-bidentate binding mode and high negative charge, and (iii) display high functionalization capacity where a wide range of donor atoms and ring substituents can be introduced. Indeed, a number of dinuclear complexes,[27,28] a chain compound,[2w] and several extended frameworks[9,29] featuring semiquinoid radical bridging ligands have been shown to exhibit strong metal–radical interactions. In particular, the magnetic coupling between paramagnetic metal ions and semiquinoid radicals is exceptionally strong when nitrogen- or sulfur-based donors are employed in place of the more common oxygen-based donors owing to their more diffuse orbitals.[28] The strong magnetic coupling interactions in semiquinoid-bridged systems have led to fascinating discoveries in the field of molecular magnetism such as the single-molecule magnet that exhibits the strongest magnetic coupling yet observed,[28a] and a 2D electrically conductive permanent magnet that orders well above liquid nitrogen temperature.[9c]

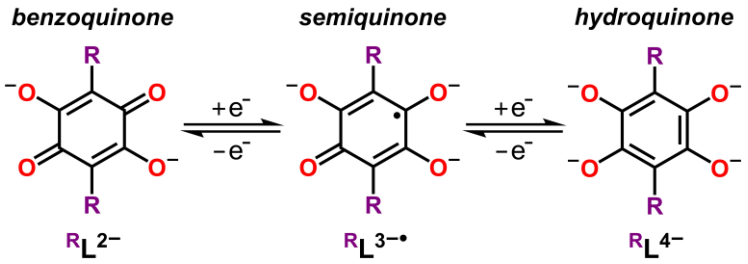

Scheme 7.1 Redox series of deprotonated benzoquinoid ligands with substituents R.

Despite the tremendous potential of quinoid-based ligands in furnishing magnetic materials with emerging properties and improved performances, studies that probe the effects of ring substituents on the magnetic coupling strength in semiquinoid-bridged systems are still lacking. Such analysis is essential to provide a clear understanding of the factors that govern the strength of magnetic interactions in radical-bridged quinoid-based materials and thus facilitate the rational design of new molecule-based magnets that function at high temperatures.

The observation of a linear correlation between the magnetic coupling strength and the electronegativity of the substituents on diamagnetic benzoquinoid bridging ligands for Cu^{II}_2 complexes[30] and 2D ferrimagnets,[12,31] where the least electronegative substituents gave rise to the strongest coupling, prompted us to investigate the role that ring substituents play in determining the magnetic properties of Fe^{II}_2 complexes bearing semiquinoid radical bridging ligands. Specifically, we sought to examine whether, and to what extent, the electron density on the semiquinoid ring can be tuned by introducing substituents of varying electronic nature to modulate the magnetic exchange interactions in these systems. Accordingly, we herein report a series of new benzoquinoid-bridged Fe^{II}_2 complexes $[(Me_3TPyA)_2Fe_2(^{R}L^{x-})]^{n+}$ ($x = 2$, $n = 2$: R = OMe, Cl, NO_2; $x = 0$, $n = 4$: R = SMe_2; Me_3TPyA = tris(6-methyl-2-pyridylmethyl)amine) and the radical semiquinoid-bridged congeners $[(Me_3TPyA)_2Fe_2(^{R}L^{x-}\bullet)]^{n+}$ ($x = 3$, $n = 1$: R = OMe, Cl, NO_2; $x = 1$, $n = 3$: R = SMe_2), and demonstrate that the effects of ligand substitution on the magnetic coupling strength are highly dependent on the redox state of the bridging ligand. To our knowledge, this series of semiquinoid-bridged complexes enables the first investigation of the influence of ligand substituents on magnetic interactions between paramagnetic metals and quinoid radicals.

7.2 Experimental Section

General Considerations. Unless otherwise specified, the manipulations described below were carried out under a dry dinitrogen atmosphere in a Vacuum Atmospheres Nexus II glovebox at ambient temperature. Syntheses of unreduced metal complexes were carried out in an MBraun LABstar glovebox, operated under a humid dinitrogen atmosphere. Synthesis of Me_3TPyA was performed using standard Schlenk line techniques. Glassware was oven-dried at 150 °C for at least 4 h and allowed to cool in an evacuated antechamber prior to use in the gloveboxes. Acetonitrile

(MeCN), dichloromethane (CH_2Cl_2), diethyl ether (Et_2O), *N*,*N*-diisopropylethylamine (DIPEA), methanol (MeOH), and tetrahydrofuran (THF) were dried using a commercial solvent purification system from Pure Process Technology and stored over 3 Å molecular sieves prior to use. H_2O was obtained from a purification system from EMD Millipore. Deuterated solvents were purchased from Cambridge Isotope Laboratories. All other reagents and solvents were purchased from commercial vendors and used without further purification. Experimental details on the syntheses of ligands and organic precursors are provided in the Section 7.5.1.

*Synthesis of [(Me$_3$TPyA)$_2$Fe$_2$(^{OMe}L)](BF$_4$)$_2$ (**1-OMe**).* A suspension of $Fe(BF_4)_2 \cdot 6H_2O$ (191 mg, 0.566 mmol) in MeCN (4 mL) was added dropwise to a stirring pale yellow solution of Me_3TPyA (188 mg, 0.566 mmol) in MeCN (5 mL) to give a dark yellow solution. In a separate vial, DIPEA (73.1 mg, 0.566 mmol) was added to a suspension of $H_2(^{OMe}L)$ (56.6 mg, 0.283 mmol) in MeCN (5 mL) to give a dark purple solution. This solution was added dropwise to the stirring dark yellow solution of $Fe(BF_4)_2 \cdot 6H_2O$ and Me_3TPyA to give a black solution. After stirring at 45 °C for 4.5 h, the reaction solution was filtered, and the filtrate was evaporated to dryness to give a dark green residue. The residue was washed with THF (8 × 20 mL) by stirring for 30–60 min for each wash and the resulting dark green solid was dried under reduced pressure for 1 h. Diffusion of Et_2O vapor into a concentrated solution of the dark green solid in MeCN (10 mL) afforded dark green crystalline needles that were washed with Et_2O (50 mL), dried under reduced pressure for 5 min, and washed with THF (8 × 10 mL) by stirring for 30 min for each wash. The resulting dark green solid was dried under reduced pressure for 1 h and recrystallized using diffusion of Et_2O vapor into a concentrated MeCN solution as previously described. The obtained dark green crystalline needles were washed with Et_2O (50 mL) and dried under reduced pressure for 24 h to

give **1-OMe** (106 mg, 33%). Anal. Calcd. for $C_{50}H_{54}B_2F_8Fe_2N_8O_6$: C, 52.30; H, 4.74; N, 9.76%. Found: C, 52.14; H, 4.59; N, 9.56%. UV-Vis-NIR absorption spectrum (MeCN, 298 K): 261 nm (ε = 29500 M^{-1} cm^{-1}), 348 nm (ε = 31300 M^{-1} cm^{-1}), 643 nm (ε = 1240 M^{-1} cm^{-1}). FT-IR (ATR, cm^{-1}): 3084 (w, broad), 3004 (w, broad), 2950 (w), 2925 (w), 2843 (w), 1604 (m), 1579 (w), 1523 (s), 1462 (w), 1445 (s), 1441 (s), 1375 (w), 1348 (s), 1280 (w), 1225 (w), 1192 (w), 1167 (m), 1095 (m), 1031 (s, broad), 963 (w), 935 (m), 902 (w), 887 (w), 780 (s), 760 (w), 718 (w), 688 (w), 640 (m), 558 (w), 521 (m). Slow diffusion of Et_2O vapor into a concentrated solution of **1-OMe** in MeCN afforded dark orange plate-shaped crystals of **1-OMe**·4.0MeCN suitable for single-crystal X-ray diffraction analysis.

*Synthesis of [(Me$_3$TPyA)$_2$Fe$_2$(^{Cl}L)](BF$_4$)$_2$·0.3H$_2$O (**1-Cl**).* A suspension of $Fe(BF_4)_2·6H_2O$ (185 mg, 0.548 mmol) in MeCN (4 mL) was added dropwise to a stirring pale yellow solution of Me_3TPyA (182 mg, 0.548 mmol) in MeCN (5 mL) to give a dark yellow solution. To this stirring solution, an orange suspension of 2,5-dihydroxy-3,6-dichloro-*p*-benzoquinone ($H_2(^{Cl}L)$; 57.3 mg, 0.274 mmol) in MeCN (5 mL) was added dropwise to give a black solution. After stirring at 45 °C for 4 h, the reaction solution was filtered, and the filtrate was evaporated to dryness to give a black residue. The residue was washed with THF (10 × 20 mL) by stirring for 30–60 min for each wash and the resulting dark gray solid was dried under reduced pressure for 1 h. Diffusion of Et_2O vapor into a concentrated solution of the dark gray solid in MeCN (10 mL) afforded dark green crystalline needles that were washed with Et_2O (50 mL), dried under reduced pressure for 5 min, and washed with THF (8 × 10 mL) by stirring for 30 min for each wash. The resulting dark green solid was dried under reduced pressure for 1 h and recrystallized using diffusion of Et_2O vapor into a concentrated MeCN solution as previously described. The obtained dark green crystalline needles

were washed with Et_2O (50 mL) and dried under reduced pressure for 24 h to give **1-Cl** (56.2 mg, 18%). Anal. Calcd. for $C_{48}H_{48.6}B_2Cl_2F_8Fe_2N_8O_{4.3}$: C, 49.59; H, 4.21; N, 9.64%. Found: C, 49.61; H, 4.34; N, 9.44%. UV-Vis-NIR absorption spectrum (MeCN, 298 K): 261 nm (ε = 28700 M^{-1} cm^{-1}), 350 nm (ε = 34700 M^{-1} cm^{-1}), 695 nm (ε = 1170 M^{-1} cm^{-1}). FT-IR (ATR, cm^{-1}): 3080 (w, broad), 2923 (w, broad), 2872 (w, broad), 1606 (m), 1577 (w), 1527 (s), 1451 (s), 1371 (m), 1355 (w), 1291 (w, broad), 1241 (w), 1225 (w), 1168 (m), 1093 (m), 1049 (s, broad), 1031 (s, broad), 1009 (s, broad), 968 (m), 916 (w), 885 (w), 852 (s), 782 (s), 758 (w), 747 (w), 718 (w), 605 (w), 578 (m), 521 (m). Slow diffusion of Et_2O vapor into a concentrated solution of **1-Cl** in MeCN afforded dark orange plate-shaped crystals of **1-Cl**·$0.7H_2O$ suitable for single-crystal X-ray diffraction analysis.

*Synthesis of [(Me$_3$TPyA)$_2$Fe$_2$(^{NO2}L)](BF$_4$)$_2$ (**1-NO$_2$**).* A suspension of $Fe(BF_4)_2·6H_2O$ (187 mg, 0.554 mmol) in MeCN (4 mL) was added dropwise to a stirring pale yellow solution of Me_3TPyA (185 mg, 0.556 mmol) in MeCN (5 mL) to give a dark yellow solution. To this stirring solution, an orange suspension of $Na_2(^{NO2}L)$ (76.0 mg, 0.278 mmol) in MeCN (5 mL) was added dropwise to give a dark green solution. After stirring at 45 °C for 4.5 h, the reaction solution was filtered, and the filtrate was evaporated to dryness to give a dark green residue. The residue was washed with THF (10 × 20 mL) by stirring for 30–60 min for each wash and the resulting dark green solid was dried under reduced pressure for 1 h. Diffusion of Et_2O vapor into a concentrated solution of the dark green solid in MeCN (10 mL) afforded dark purple crystalline blocks that were washed with Et_2O (50 mL), dried under reduced pressure for 5 min, washed with THF (2 × 10 mL), and further dried under reduced pressure for 1 h. The resulting dark green solid was recrystallized using diffusion of Et_2O vapor into a concentrated MeCN solution as previously described. The obtained

dark green crystalline blocks were washed with Et_2O (50 mL) and dried under reduced pressure for 24 h to give **1-NO₂** as dark green blocks (122 mg, 37%). Anal. Calcd. for $C_{48}H_{48}B_2F_8Fe_2N_{10}O_8$: C, 48.93; H, 4.11; N, 11.89%. Found: C, 48.79; H, 4.07; N, 11.89%. UV-Vis-NIR absorption spectrum (MeCN, 298 K): 262 nm (ε = 29700 M^{-1} cm^{-1}), 321 nm (ε = 29000 M^{-1} cm^{-1}), 735 nm (ε = 1510 M^{-1} cm^{-1}). FT-IR (ATR, cm^{-1}): 3090 (w, broad), 2919 (w, broad), 2855 (w, broad), 1637 (w), 1604 (m), 1571 (s, broad), 1495 (m), 1451 (s), 1390 (w), 1334 (m, broad), 1309 (m), 1239 (w), 1227 (w), 1165 (w), 1095 (m), 1048 (s, broad), 1031 (s, broad), 1009 (s, broad), 967 (m), 918 (m), 889 (m), 782 (s), 745 (m), 558 (w, broad), 521 (m). Slow diffusion of Et_2O vapor into a concentrated solution of **1-NO₂** in MeCN afforded dark orange plate-shaped crystals of **1-NO₂**·4.0MeCN suitable for single-crystal X-ray diffraction analysis.

*Synthesis of [(Me₃TPyA)₂Fe₂(^{SMe_2}L)](BF₄)₄ (**1-SMe₂**).* A suspension of $Fe(BF_4)_2{\cdot}6H_2O$ (182 mg, 0.539 mmol) in MeCN (4 mL) was added dropwise to a stirring pale yellow solution of Me_3TPyA (179 mg, 0.538 mmol) in MeCN (5 mL) to give a dark yellow solution. To this stirring solution, a yellow suspension of (^{SMe_2}L)·2.0AcOH (86.2 mg, 0.227 mmol) in MeCN (5 mL) was added dropwise to give a dark green solution. After stirring at 45 °C for 4 h, the reaction solution was filtered, and the filtrate was evaporated to dryness to give a dark green residue. The residue was washed with THF (10 × 20 mL) by stirring for 30–60 min for each wash and the resulting dark green solid was dried under reduced pressure for 1 h. Diffusion of Et_2O vapor into a concentrated solution of the dark green solid in MeCN (10 mL) afforded dark green crystalline needles that were washed with Et_2O (50 mL), dried under reduced pressure for 5 min, and washed with THF (8 × 10 mL) by stirring for 30 min for each wash. The resulting dark green solid was dried under reduced pressure for 1 h and recrystallized using diffusion of Et_2O vapor into a concentrated MeCN

solution as previously described. The obtained dark green crystalline material was washed with Et_2O (40 mL), dried under reduced pressure for 5 min, and the recrystallization step was repeated one more time to afford **1-SMe$_2$** as dark green blocks after drying under reduced pressure for 24 h (132 mg, 42%). Anal. Calcd. for $C_{52}H_{60}B_4F_{16}Fe_2N_8O_4S_2$: C, 45.12; H, 4.37; N, 8.10%. Found: C, 45.15; H, 4.29; N, 8.01%. UV-Vis-NIR absorption spectrum (MeCN, 298 K): 263 nm (ε = 37600 M^{-1} cm^{-1}), 298 nm (ε = 28600 M^{-1} cm^{-1}), 309 nm (ε = 25800 M^{-1} cm^{-1}), 383 nm (ε = 2450 M^{-1} cm^{-1}), 587 nm (ε = 290 M^{-1} cm^{-1}). FT-IR (ATR, cm^{-1}): 3088 (w), 3036 (w), 2942 (w), 1628 (w), 1606 (m), 1546 (s), 1470 (w), 1455 (m), 1418 (w), 1396 (w, broad), 1355 (w), 1311 (w, broad), 1299 (w, broad), 1248 (w), 1223 (w), 1169 (w), 1118 (m), 1046 (s, broad), 1029 (s, broad), 1011 (s, broad), 968 (m), 947 (w), 916 (w), 891 (w), 844 (w), 791 (m), 780 (m), 760 (w), 743 (w), 718 (w), 663 (w), 595 (w), 576 (w), 519 (m). Slow diffusion of Et_2O vapor into a concentrated solution of **1-SMe$_2$** in MeCN afforded dark orange plate-shaped crystals of **1-SMe$_2$**·4.0MeCN suitable for single-crystal X-ray diffraction analysis.

*Synthesis of [(Me$_3$TPyA)$_2$Fe$_2$(^{OMe}L)](BF$_4$) (**2-OMe**).* An orange solution of cobaltocene (3.9 mg, 0.021 mmol) in MeCN (3 mL) was added dropwise to a stirring dark green solution of **1-OMe** (23.7 mg, 0.0206 mmol) in MeCN (4 mL) to give a red-brown solution. After stirring at 25 °C for 1 h, the reaction solution was filtered. Diffusion of Et_2O vapor into the filtrate afforded a mixture of red-orange plates and polycrystalline red-brown solid that was washed with Et_2O (30 mL) and dried under reduced pressure for 1.5 h to give **2-OMe** (16.9 mg, 77%). Anal. Calcd. for $C_{50}H_{54}BF_4Fe_2N_8O_6$: C, 56.57; H, 5.13; N, 10.56%. Found: C, 56.58; H, 4.98; N, 10.57%. UV-Vis-NIR absorption spectrum (MeCN, 298 K): 261 nm (ε = 29500 M^{-1} cm^{-1}), 324 nm (ε = 12000 M^{-1} cm^{-1}), 478 nm (ε = 11100 M^{-1} cm^{-1}), 540 nm (ε = 3960 M^{-1} cm^{-1}). FT-IR (ATR, cm^{-1}): 3057 (w,

broad), 3006 (w, broad), 2966 (w), 2923 (w), 2892 (w, broad), 2814 (w), 1600 (m), 1575 (m), 1497 (w), 1441 (s, broad), 1415 (s, broad), 1348 (m), 1318 (m), 1270 (m), 1221 (w), 1194 (w), 1161 (m), 1106 (w), 1068 (m), 1050 (s, broad), 1005 (s), 972 (m), 935 (m), 912 (m), 885 (w, broad), 791 (m), 776 (s), 747 (w), 716 (w), 679 (w), 626 (w), 553 (w), 539 (w), 498 (m, broad). Slow diffusion of Et_2O vapor into a concentrated solution of **2-OMe** in MeCN afforded red-orange plate-shaped crystals of **2-OMe**·2.0MeCN suitable for single-crystal X-ray diffraction analysis.

*Synthesis of [(Me₃TPyA)₂Fe₂(ᶜˡL)](BF₄) (**2-Cl**).* An orange solution of cobaltocene (4.4 mg, 0.023 mmol) in MeCN (3 mL) was added dropwise to a stirring dark green solution of **1-Cl** (27.1 mg, 0.0233 mmol) in MeCN (4 mL) to give a red-brown solution. After stirring at 25 °C for 1 h, the reaction solution was filtered. Diffusion of Et_2O vapor into the filtrate afforded a mixture of red-orange plates and polycrystalline red-brown solid that was washed with Et_2O (30 mL) and dried under reduced pressure for 1.5 h to give **2-Cl** (13.9 mg, 57%). Anal. Calcd. for $C_{48}H_{48}BCl_2F_4Fe_2N_8O_4$: C, 53.86; H, 4.52; N, 10.47%. Found: C, 53.66; H, 4.78; N, 10.52%. UV-Vis-NIR absorption spectrum (MeCN, 298 K): 261 nm (ε = 29100 M^{-1} cm^{-1}), 334 nm (ε = 16700 M^{-1} cm^{-1}), 474 nm (ε = 10200 M^{-1} cm^{-1}), 540 nm (ε = 2900 M^{-1} cm^{-1}). FT-IR (ATR, cm^{-1}): 3086 (w), 3065 (w), 2915 (w, broad), 2847 (w, broad), 2731 (w), 1602 (m), 1575 (m), 1443 (s, broad), 1348 (m), 1295 (w), 1250 (m), 1221 (w), 1163 (m), 1118 (w), 1093 (m), 1054 (s), 1033 (s, broad), 1005 (s, broad), 974 (m), 949 (m), 914 (m), 887 (m), 832 (s), 780 (s), 758 (m), 746 (m), 570 (m), 518 (w). Slow diffusion of Et_2O vapor into a concentrated solution of **2-Cl** in MeCN afforded red-orange plate-shaped crystals of **2-Cl**·0.5Et_2O suitable for single-crystal X-ray diffraction analysis.

*Synthesis of [(Me₃TPyA)₂Fe₂(ᴺᴼ²L)](BF₄) (**2-NO₂**).* An orange solution of cobaltocene (10.0 mg, 0.0529 mmol) in MeCN (3 mL) was added dropwise to a stirring dark green solution of **1-**

NO$_2$ (62.0 mg, 0.0526 mmol) in MeCN (3 mL) to give a red-brown solution. After stirring at 25 °C for 1 h, the reaction solution was filtered. Diffusion of Et_2O vapor into the filtrate afforded red-orange plates that were washed with Et_2O (30 mL) and dried under reduced pressure for 30 min to give **2-NO$_2$** (44.1 mg, 77%). Anal. Calcd. for $C_{48}H_{48}BF_4Fe_2N_{10}O_8$: C, 52.82; H, 4.43; N, 12.83%. Found: C, 52.65; H, 4.52; N, 12.71%. UV-Vis-NIR absorption spectrum (MeCN, 298 K): 262 nm (ε = 29100 M^{-1} cm^{-1}), 313 nm (ε = 15600 M^{-1} cm^{-1}), 406 nm (ε = 13800 M^{-1} cm^{-1}), 525 nm (ε = 1930 M^{-1} cm^{-1}), 684 nm (ε = 710 M^{-1} cm^{-1}). FT-IR (ATR, cm^{-1}): 3071 (w, broad), 2960 (w), 2913 (w, broad), 2744 (w, broad), 1604 (m), 1577 (w), 1519 (s, broad), 1466 (s, broad), 1447 (s), 1388 (w), 1350 (m), 1295 (w), 1244 (m, broad), 1165 (m), 1108 (m), 1095 (m), 1050 (s, broad), 1007 (s), 968 (m), 916 (w), 900 (w), 887 (w), 784 (s), 772 (s), 745 (w), 719 (w), 659 (w), 546 (w, broad), 519 (w). Slow diffusion of Et_2O vapor into a concentrated solution of **2-NO$_2$** in MeCN afforded red-orange plate-shaped crystals of **2-NO$_2$** suitable for single-crystal X-ray diffraction analysis.

*Synthesis of [(Me$_3$TPyA)$_2$Fe$_2$(^{SMe_2}L)](BF$_4$)$_3$ (**2-SMe$_2$**).* An orange solution of cobaltocene (5.2 mg, 0.027 mmol) in MeCN (3 mL) was added dropwise to a stirring dark green solution of **1-SMe$_2$** (41.3 mg, 0.0298 mmol) in MeCN (3 mL) to give a green-brown solution. After stirring at 25 °C for 1 h, the reaction solution was filtered. Diffusion of Et_2O vapor into the filtrate afforded red-orange plates that were washed with Et_2O (30 mL) and dried under reduced pressure for 1 h to give **2-SMe$_2$** (31.0 mg, 88%). Anal. Calcd. for $C_{52}H_{60}B_3F_{12}Fe_2N_8O_4S_2$: C, 48.14; H, 4.66; N, 8.64%. Found: C, 48.05; H, 4.78; N, 8.51%. UV-Vis-NIR absorption spectrum (MeCN, 298 K): 263 nm (ε = 37700 M^{-1} cm^{-1}), 353 nm (ε = 16900 M^{-1} cm^{-1}), 369 nm (ε = 21000 M^{-1} cm^{-1}), 608 nm (ε = 1770 M^{-1} cm^{-1}). FT-IR (ATR, cm^{-1}): 3039 (w, broad), 2936 (w, broad), 2921 (w, broad), 1604 (m), 1577 (w), 1488 (s), 1466 (m, broad), 1453 (s, broad), 1344 (w, broad), 1324 (w), 1276

(m), 1196 (m), 1167 (w), 1047 (s, broad), 1029 (s, broad), 971 (m), 943 (m), 912 (m), 885 (w), 832 (w), 784 (s), 745 (w), 721 (w), 673 (w, broad), 576 (w), 558 (w), 519 (m). Slow diffusion of Et_2O vapor into a concentrated solution of **2-SMe$_2$** in MeCN afforded orange plate-shaped crystals of **2-SMe$_2$**·0.9MeCN·0.5Et_2O suitable for single-crystal X-ray diffraction analysis.

X-ray Structure Determination. Single crystals of **1-OMe**·4.0MeCN, **1-Cl**·0.7H_2O, **1-NO$_2$**·4.0MeCN, **1-SMe$_2$**·4.0MeCN, **2-OMe**·2.0MeCN, **2-Cl**·0.5Et_2O, **2-NO$_2$**, and **2-SMe$_2$**·0.9MeCN·0.5Et_2O suitable for X-ray analysis were directly coated with deoxygenated Paratone-N oil, mounted on a MicroMounts rod, and frozen under a stream of dinitrogen during data collection. The crystallographic data were collected at 100–106 K on Bruker Kappa APEX II diffractometers equipped with APEX II CCD detectors and a MoKα IμS microsource with MX Optics (**1-Cl**·0.7H_2O, **2-OMe**·2.0MeCN, **2-NO$_2$**, **2-SMe$_2$**·0.9MeCN·0.5Et_2O), or a MoKα sealed tube source with a Triumph monochromator (**1-NO$_2$**·4.0MeCN, **1-SMe$_2$**·4.0MeCN, **2-Cl**·0.5Et_2O), or a CuKα IμS microsource with MX Optics (**1-OMe**·4.0MeCN). Note that owing to temperature instability during the mounting of a crystal of **2-NO$_2$**, the data were collected at a slightly higher temperature than for the other compounds to ensure a stable temperature over the course of the data collection. Raw data were integrated and corrected for Lorentz and polarization effects with Bruker APEX2 version 2014.11–0.[32] Absorption corrections were applied using the program SADABS.[33] Space group assignments were determined by examining systematic absences, E-statistics, and successive refinement of the structures. Structures were solved using direct methods in SHELXT and refined by SHELXL[34] operated within the OLEX2 interface.[35] All hydrogen atoms were placed at calculated positions using suitable riding models and refined using isotropic displacement parameters derived from their parent atoms. Thermal parameters for all non-

hydrogen atoms were refined anisotropically.

In the crystal structures of **1-NO$_2$**·4.0MeCN and **2-SMe$_2$**·0.9MeCN·0.5Et$_2$O, one $(BF_4)^-$ anion per Fe_2 complex is disordered over two positions and the occupancies of these $(BF_4)^-$ ions were freely refined over the two positions. In the crystal structure of **2-OMe**·2.0MeCN, the $(BF_4)^-$ anion is positioned close to an inversion center. As such, it was modeled as two closely spaced ions, each with a fixed occupancy of 0.5. In the crystal structure of **2-SMe$_2$**·0.9MeCN·0.5Et$_2$O, MeCN and Et$_2$O solvent molecules were modeled with partial occupancies. Specifically, a MeCN molecule with an occupancy of 0.5 was positioned very close to a disordered Et$_2$O molecule with an occupancy of 0.5. The positional disorder of the Et$_2$O molecule was modeled by applying the SIMU restraint. In the crystal structure of **2-Cl**·0.5Et$_2$O, the solvent molecules are severely disordered and positioned close to an inversion center and, therefore, could not be modeled properly. As such, the solvent masking procedure as implemented in OLEX2 was used. A void volume of 134.9 Å^3 with 40.5 electrons was estimated per unit cell, which was ascribed to 0.5 Et$_2$O molecules per Fe_2 complex. Crystallographic data for all compounds and the details of data collection are listed in Tables 7.4–7.7.

Magnetic Measurements. Magnetic measurements for **1-R** and **2-R** (R = OMe, Cl, NO_2, SMe_2) were obtained for finely ground microcrystalline powders restrained in a frozen eicosane matrix. Samples were loaded into quartz tubes under a dry dinitrogen atmosphere, attached to a sealable hose adapter, frozen in liquid nitrogen, and flame-sealed under vacuum on a Schlenk manifold. All data were collected using a Quantum Design MPMS-XL SQUID magnetometer. Direct current (dc) magnetic susceptibility measurements were performed in the temperature range 2–300 K under an applied dc field of 1 T. Dc magnetization data were collected between 2 and 10 K under

applied dc fields of 1–7 T in 1 T increments. Alternating current (ac) magnetic susceptibility data were collected in the temperature range 2–8 K under zero applied dc field using a 4 Oe ac field oscillating at frequencies ranging from 1 to 1488 Hz. Ac susceptibility data for **2-R** (R = OMe, Cl, NO_2, SMe_2) were used to construct Cole–Cole plots, which were then fit using a generalized Debye model[36] for temperatures between 3.75 and 6.75 K, 2.00 and 6.50 K, 2.00 and 6.25 K, and 2.00 and 7.00 K for **2-OMe**, **2-Cl**, **2-NO_2**, and **2-SMe_2**, respectively, to estimate relaxation times (τ). Linear fits to the highest 7–9 temperature data points (gave $R^2 > 0.995$) in the Arrhenius plots for **2-R** (R = OMe, Cl, NO_2, SMe_2) afforded an effective spin-reversal barrier of U_{eff} ranging from 33(1) to 50(1) cm^{-1} and a pre-exponential factor of τ_0 in the range $3.3(6) \times 10^{-9} - 1.1(3) \times 10^{-7}$ s (see Figures 7.8, 7.91, 7.93, and 7.95, and Table 7.3). All magnetic susceptibility data were corrected for diamagnetic contributions from the eicosane matrix and the core diamagnetism of each sample, estimated from Pascal's constants.[37] For **1-R** (R = OMe, Cl, NO_2, SMe_2), significant amount of eicosane was located above the measuring window of the quartz tube. As a result, $\chi_M T$ vs T plots for these compounds showed a slight positive slope in the high-temperature regime. To correct for this mass error, the mass of eicosane was decreased until a constant value of $\chi_M T$ was achieved between 200 and 300 K. Note that this adjustment of the mass of eicosane was verified by opening the quartz tube and scraping out and weighing the eicosane that was located above the measuring window of the tube. Prior to full characterization, variable-field magnetization data were collected at 100 K. The excellent linearity of the M vs H curves (gave $R^2 = 1.00$), constructed from data collected under applied dc fields ranging from 0 to 3 T, confirmed the absence of ferromagnetic impurities in all samples. These data are plotted as magnetization in units of Bohr magneton (μ_B) per mol of Fe_2 complex against magnetic field in T (see Figures 7.50–7.57). Note

that corrections for the magnetic moment of the eicosane matrix were applied. The coherence of the collected magnetic data was checked across different measurements.

Fits and simulations of dc magnetic susceptibility and low-temperature magnetization data were performed with the program PHI[38] and the MagProp package within the program DAVE 2.5.[39] For **1-R** (R = OMe, Cl, NO_2, SMe_2), these data were fit to the Van Vleck equation according to the following spin Hamiltonian:[40]

$$\hat{H} = -2J(\hat{S}_{Fe1}\cdot\hat{S}_{Fe2}) + g\mu_B H(\hat{S}_{Fe1} + \hat{S}_{Fe2}) + D[\hat{S}_{Fe1,z}^2 + \hat{S}_{Fe2,z}^2 - 2S(S+1)/3] \qquad (7.1)$$

In this spin Hamiltonian, the first term is the exchange coupling term, the second term denotes the Zeeman interaction, and the last term denotes the axial zero-field interaction. The parameter J is the magnetic exchange coupling constant, $\hat{S}_{Fe1}$ and $\hat{S}_{Fe2}$ are the spin angular momentum operators for the two Fe^{II} centers, g is the isotropic electron spin g-factor ($g = g_{Fe1} = g_{Fe2}$), μ_B is the Bohr magneton, H is the applied magnetic field, D is the axial zero-field splitting parameter ($D = D_{Fe1} = D_{Fe2}$), $\hat{S}_{Fe1,z}$ and $\hat{S}_{Fe2,z}$ are the z components of the spin angular momentum operators for the two Fe^{II} centers, and S is the total spin quantum number.

To fit and simulate the low-temperature magnetization data for **2-R** (R = OMe, Cl, NO_2, SMe_2), an additional term corresponding to the radical bridging ligand was introduced into Equation 7.1 to afford the following spin Hamiltonian:[40]

$$\hat{H} = -2J[\hat{S}_{rad}\cdot(\hat{S}_{Fe1} + \hat{S}_{Fe2})] + g\mu_B H(\hat{S}_{Fe1} + \hat{S}_{Fe2} + \hat{S}_{rad}) + D[\hat{S}_{Fe1,z}^2 + \hat{S}_{Fe2,z}^2 - 2S(S+1)/3] \qquad (7.2)$$

In this Hamiltonian, $\hat{S}_{rad}$ corresponds to the spin angular momentum operator for the radical bridging ligand and the other terms are as defined for Equation 7.1. The dc magnetic susceptibility data for **2-R** (R = OMe, Cl, NO_2, SMe_2) were fit to the Van Vleck equation according to the spin Hamiltonian provided in Equation 7.3, where the axial zero-field interaction was neglected as only

the high-temperature data (60–300 K) were employed for fitting.

$$\hat{H} = -2J[\hat{S}_{rad}\cdot(\hat{S}_{Fe1} + \hat{S}_{Fe2})] + g\mu_B H(\hat{S}_{Fe1} + \hat{S}_{Fe2} + \hat{S}_{rad}) \qquad (7.3)$$

Note that we assume that the *g*-factor in Equations 7.1–7.3 is isotropic and $g = g_{Fe1} = g_{Fe2} = g_{rad}$. Furthermore, we assume that the axial zero-field splitting parameter *D* is identical for the two Fe^{II} centers in **1-R** and **2-R** (R = OMe, Cl, NO_2, SMe_2). These assumptions are validated by crystallographic analysis of these compounds as the two Fe^{II} sites within each Fe_2 complex are related through a crystallographic inversion center or a pseudo-inversion center (see below). Also note that introduction of a rhombic zero-field splitting parameter *E* to the spin Hamiltonians given in Equations 7.1 and 7.2 did not provide significant improvements to the fits and simulations of the magnetic data for **1-R** and **2-R** (R = OMe, Cl, NO_2, SMe_2). Specifically, the value of *E* was an order of magnitude smaller than the value of *D* for all compounds and thus the rhombic zero-field splitting term was omitted to avoid overparameterization.

To estimate the values of *J*, *g*, and *D* for **1-R** (R = OMe, Cl, NO_2, SMe_2), a simultaneous fit to the low-temperature magnetization data and the variable-temperature dc magnetic susceptibility data was performed in the program PHI.[38] Summary of the parameters obtained from these fits are provided in Table 7.3. Note that for **1-OMe** and **1-Cl** no reasonable fits were obtained when the low-temperature (<15 K) dc magnetic susceptibility data were included, presumably owing to intermolecular interactions that are not accounted for in the spin Hamiltonian in Equation 7.1, which can be significant at low temperatures. Furthermore, we noticed that the simultaneous fit to the low-temperature magnetization data and the variable-temperature dc magnetic susceptibility data for **1-SMe_2** overestimated the magnitude of *D*, as indicated by individual fits to the two data sets. As such, to get a better estimate of *D*, we fixed *g* and *J* to the values obtained from the

simultaneous fit to the data and allowed *D* to freely refine for the two datasets (see Table 7.8).

In contrast to the observations for **1-R**, simulations of the low-temperature magnetization data for **2-R** (R = OMe, Cl, NO_2, SMe_2) indicated that the data were not significantly affected by the magnitude of *J* (only the sign), as expected for the much stronger magnetic coupling in the radical-bridged complexes. Accordingly, simultaneous fits to the low-temperature magnetization data and the variable-temperature dc magnetic susceptibility data for **2-R** (R = OMe, Cl, NO_2, SMe_2) did not afford any reasonable results. Therefore, the values of *J* and *g* were estimated from fits to the high-temperature range of the dc magnetic susceptibility data using the spin Hamiltonian in Equation 7.3. Specifically, the temperature range 60–300 K was used for fitting because the data were found to be insensitive to *D* in that range. Low-temperature magnetization data were employed to estimate the values of *D* and *g*, using fixed values of *J*, as determined from the dc magnetic susceptibility data. We performed a survey of the sum of the squared residuals (χ^2) by varying *J* from 0 to −1000 cm^{-1} for each reduced Fe_2 complex to demonstrate the insensitivity of the low-temperature magnetization data to *J* for **2-R** (R = OMe, Cl, NO_2, SMe_2) and to justify the *J* values obtained from fits to the dc magnetic susceptibility data (see Tables 7.9–7.12). The errors in *D* values were estimated from the variations observed in these surveys for near constant values of χ^2 ($\Delta\chi^2 = \pm 0.0005$). The values of *g* obtained from fits to the low-temperature magnetization data agree well with those obtained from fits to the dc magnetic susceptibility data (see Section 7.3.4 and Table 7.3).

Note that the variable-temperature dc magnetic susceptibility data for **2-R** (R = OMe, Cl, NO_2, SMe_2) can be modeled fairly well using $J > 0$ ($J \sim 22$–25 cm^{-1}), however, those fits give unreasonably low values of *g* ($g < 1.98$) for high-spin Fe^{II} centers in pseudo-octahedral geometry,

along with large positive D values (D > 30 cm^{-1}), which are in disagreement with the low-temperature magnetization data. The observed frequency dependence of χ_M'' for **2-R** (R = OMe, Cl, NO_2, SMe_2) in the absence of an applied dc field further supports the negative values of D (see below). As such, we place trust in the fitting procedures detailed above, which indicate antiferromagnetic exchange interactions between the Fe^{II} centers and radical bridging ligand in **2-R** (R = OMe, Cl, NO_2, SMe_2).

NMR Spectroscopy. ^{1}H NMR spectra for ligands and organic precursors were collected at 298 K at 500 MHz frequency on an automated Bruker Avance III 500 MHz (11.7 T) system equipped with a DCH CryoProbe or on an automated Bruker Avance III 500 MHz (11.7 T) HD system equipped with a TXO Prodigy probe. $^{13}C\{^1H\}$ NMR spectra for the ligands were collected at 126 MHz frequency using an automated Bruker Avance III 500 MHz (11.7 T) system equipped with a DCH CryoProbe. ^{1}H NMR spectra for Fe_2 complexes **1-R** and **2-R** (R = OMe, Cl, NO_2, SMe_2) in MeCN-d_3 were collected at 295 K on a Bruker Avance III HD Nanobay 400 MHz (9.4 T) system (**1-R**, **2-NO$_2$**, **2-SMe$_2$**) or on a Bruker Neo 600 MHz (14.1 T) system equipped with a QCI-F cryoprobe (**2-OMe**, **2-Cl**). Samples for all Fe_2 complexes were prepared and stored under a dry dinitrogen atmosphere to ensure no degradation due to oxidation by air. All chemical shift values (δ) are reported in ppm and coupling constants (J) are reported in hertz (Hz). ^{1}H and $^{13}C\{^1H\}$ NMR spectra are referenced to residual proton and carbon signals, respectively, from the deuterated solvents (^{1}H: 7.26 ppm for $CDCl_3$, 4.79 ppm for D_2O, 2.50 ppm for DMSO-d_6, 1.94 ppm for MeCN-d_3; $^{13}C\{^1H\}$: 77.16 ppm for $CDCl_3$, 39.52 ppm for DMSO-d_6). The MestReNova 10.0 NMR data processing software was used to analyze and process all recorded NMR spectra.

Mössbauer Spectroscopy. Zero-field ^{57}Fe Mössbauer spectra were collected for **1-R** and **2-R**

(R = OMe, Cl, NO_2, SMe_2) with a constant acceleration spectrometer and a ^{57}Co/Rh source over a 4 mm s^{-1} window at 80 K. Prior to the measurements, the spectrometer was calibrated at 295 K with a 30 μm-thick α-Fe foil. The experimental errors in the isomer shift values (δ) estimated from calibration fitting were 0.002 mm s^{-1}, and those for quadrupole splitting values (ΔE_Q) and the widths of the right and left line of each doublet (Γ_R and Γ_L) were estimated to be 0.7% of their respective absolute values. Samples were prepared and stored under a dry dinitrogen atmosphere. A typical sample contained 17–52 mg of Fe_2 complex (1.6–4.9 mg of natural Fe/cm^2) and was prepared by adding polycrystalline material to a circular polyethylene holder of 1 cm^2 area and squeezing another holder with a slightly smaller diameter that had been covered with deoxygenated Paratone-N oil into the previous sample holder to completely encapsulate the solid sample. The sample was frozen in liquid nitrogen prior to handling in air. Collected spectra were analyzed using the WMOSS Mössbauer Spectral Analysis Software.[41] Isomer shifts (δ) are reported relative to the centroid of the Fe metal spectrum recorded at 295 K. All spectra were fit with Lorentzian doublets and statistical fitting errors were estimated from Monte Carlo simulations. Reported uncertainties in δ, ΔE_Q, Γ_R, and Γ_L are the square root of the sum of the squared experimental and statistical fitting errors.

UV-Vis-NIR Absorption Spectroscopy. Solution and solid-state UV-Vis-NIR spectra were collected at 298 K in the 200–1200 and 200–800 nm ranges, respectively, on an Agilent Cary 5000 UV-Vis-NIR spectrophotometer equipped with an integrating sphere for diffuse reflectance measurements. Solution spectra were collected for samples of ligands Me_3TPyA, $H_2(^{OMe}L)$, $H_2(^{Cl}L)$, $Na_2(^{NO2}L)$, and $(^{SMe2}L)\cdot 2.0AcOH$, and Fe_2 complexes **1-R** and **2-R** (R = OMe, Cl, NO_2, SMe_2) in MeCN. Samples for all Fe_2 complexes were prepared and stored under a dry dinitrogen

atmosphere to ensure no degradation due to oxidation by air. Diffuse reflectance spectra were collected on microcrystalline samples of **1-R** and **2-R** (R = OMe, Cl, NO_2, SMe_2). Samples for measurements were prepared by mixing microcrystalline samples of the compounds with dry $BaSO_4$ powder for a 3-fold dilution to give smooth, homogeneous powders. The data were treated with a background correction of $BaSO_4$ and the spectra are reported as normalized Kubelka-Munk transformation F(R) of the raw diffuse reflectance spectra, where F(R) for each compound was normalized with the strongest absorbance set to F(R) = 1.

Electrochemical Measurements. Cyclic voltammetry measurements were carried out in a standard one-compartment cell under a dry dinitrogen atmosphere at 298 K using CH Instruments 760c potentiostat. The cell consisted of a platinum electrode as a working electrode, a platinum wire as a counter electrode, and a silver wire as a pseudo-reference electrode. Ferrocene (Cp_2Fe) was added to the analyte solutions at the end of each measurement and used as an internal standard. Analytes were measured in MeCN solutions (ca. 1 mM) with 100 mM $(Bu_4N)(PF_6)$ supporting electrolyte at variable scan rates (25–1000 mV s^{-1}). Note that owing to the steric bulk of the $^{+}SMe_2$ substituent, the electron transfer kinetics for **1-SMe$_2$** are significantly slower than those for **1-OMe**, **1-Cl**, and **1-NO$_2$**. Therefore, greater reversibility for the $^{SMe2}L/^{SMe2}L^{-\bullet}$ redox couple was observed at slower scan rates. All potentials were converted and referenced to the $[Cp_2Fe]^{0/1+}$ redox couple.

Other Physical Measurements. Elemental analyses of all Fe_2 complexes were conducted by Midwest Microlab Inc. Infrared spectra were recorded for solid samples of ligands Me_3TPyA, $H_2(^{OMe}L)$, $H_2(^{Cl}L)$, $Na_2(^{NO2}L)$, and $(^{SMe2}L)\cdot 2.0AcOH$, and Fe_2 complexes **1-R** and **2-R** (R = OMe, Cl, NO_2, SMe_2) on Bruker Tensor 37 and Bruker Alpha II FTIR spectrometers equipped with

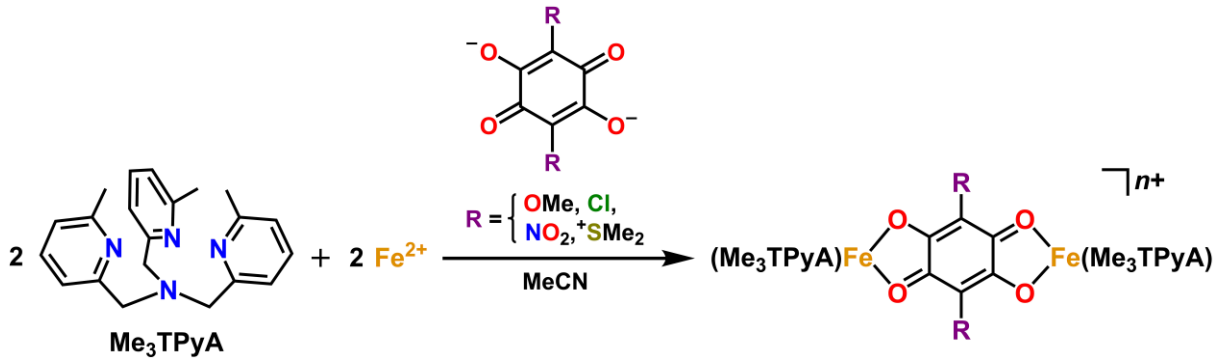

Figure 7.1 Synthesis of compounds $[(Me_3TPyA)_2Fe_2(^{R}L)]^{n+}$ (R = OMe, Cl, NO_2, SMe_2), as observed in **1-OMe** (*n* = 2), **1-Cl** (*n* = 2), **1-NO$_2$** (*n* = 2), and **1-SMe$_2$** (*n* = 4).

attenuated total reflectance (ATR) accessories. Samples for all Fe_2 complexes were prepared and measured under a dry dinitrogen atmosphere. The IR spectra for the Fe_2 complexes are provided in Figures 7.9–7.14. Inductively coupled plasma optical emission spectroscopy (ICP-OES) was used to quantify the concentration of Fe_2 complexes in solution samples. These measurements were performed on a Thermo iCAP 7600 dual view ICP-OES instrument equipped with a CETAC ASX520 240-position autosampler. Samples were dissolved in a 3% aqueous nitric acid solution and the emissions for Fe compared to standard solutions.

7.3 Results and Discussion

7.3.1 Syntheses, Structures, and Electrochemistry

With the goal of better understanding the effects of ligand substituents on electron delocalization and magnetic coupling in semiquinoid radical-bridged magnets, we employed dinuclear complexes as model systems owing to their structural simplicity and ease of magnetic characterization. Specifically, we targeted a series of isostructural Fe^{II}_2 complexes bridged by benzoquinoid ligands featuring an array of substituents with different electronic properties, ranging from electron-donating OMe groups to strongly electron-withdrawing $^{+}SMe_2$ groups.

Table 7.1 Selected mean interatomic distances (Å) and octahedral distortion parameter (Σ_{sum}) for **1-R**·solvent and **2-R**·solvent (R = OMe, Cl, NO_2, SMe_2).[a,b]

	1-OMe ·4.0MeCN	**2-OMe** ·2.0MeCN	**1-Cl** ·0.7H_2O	**2-Cl** ·0.5Et_2O	**1-NO_2** ·4.0MeCN	**2-NO_2**	**1-SMe_2** ·4.0MeCN	**2-SMe_2** ·0.9MeCN ·0.5Et_2O
Fe–N	**2.210(2)**	**2.2466(6)**	**2.195(3)**	**2.234(2)**	**2.1998(5)**	**2.2223(7)**	**2.196(2)**	**2.227(1)**
Fe–O1	2.003(3)	1.992(1)	2.051(5)	1.991(3)	2.0372(8)	2.010(2)	2.039(2)	2.038(2)
Fe–O2	2.203(3)	2.112(1)	2.187(3)	2.130(3)	2.1782(9)	2.143(1)	2.210(3)	2.140(2)
Fe–O	**2.103(3)**	**2.052(1)**	**2.119(3)**	**2.060(2)**	**2.1077(6)**	**2.076(1)**	**2.125(2)**	**2.084(1)**
O1–C1	1.294(5)	1.313(2)	1.269(6)	1.304(5)	1.258(2)	1.293(2)	1.254(4)	1.292(3)
O2–C2	1.245(5)	1.294(2)	1.238(8)	1.283(5)	1.240(2)	1.278(2)	1.240(3)	1.280(3)
O–C	**1.270(4)**	**1.304(2)**	**1.254(5)**	**1.293(4)**	**1.249(1)**	**1.285(2)**	**1.247(3)**	**1.286(2)**
C1–C2	1.516(6)	1.470(2)	1.532(9)	1.468(5)	1.532(2)	1.465(2)	1.526(4)	1.465(3)
C2–C3	1.429(6)	1.407(2)	1.409(7)	1.403(5)	1.411(2)	1.404(2)	1.404(4)	1.416(3)
C3–C1A	1.363(6)	1.389(2)	1.389(9)	1.395(6)	1.386(2)	1.396(2)	1.388(4)	1.408(3)
C–C	**1.436(4)**	**1.422(1)**	**1.443(5)**	**1.422(3)**	**1.443(1)**	**1.422(2)**	**1.439(3)**	**1.430(2)**
Fe···Fe[c]	7.996(3)	7.8652(9)	8.018(2)	7.823(2)	8.0219(8)	7.9330(9)	8.017(3)	7.9972(6)
Σ_{sum}[d]	106.3(5)	125.8(2)	110.2(7)	112.3(4)	109.8(2)	111.7(2)	111.2(3)	110.1(3)

[a] See Figure 7.2 for the atomic numbering scheme. [b] Average distances for specific types of bonds are shown in bold. [c] Intramolecular Fe···Fe distance. [d] Octahedral distortion parameter (Σ_{sum}) = sum of the absolute deviation from 90° for the 12 *cis* angle in $[FeN_4O_2]$.[46]

Reaction of $^{R}L^{x-}$ (x = 2: R = OMe, Cl, NO_2; x = 0: R = SMe_2) with two equivalents each of $Fe(BF_4)_2$·$6H_2O$ and Me_3TPyA in MeCN, followed by purification and subsequent crystallization, afforded the Fe_2 complexes $[(Me_3TPyA)_2Fe_2(^{OMe}L)](BF_4)_2$ (**1-OMe**), $[(Me_3TPyA)_2Fe_2(^{Cl}L)](BF_4)_2$·$0.3H_2O$ (**1-Cl**), $[(Me_3TPyA)_2Fe_2(^{NO2}L)](BF_4)_2$ (**1-NO_2**), and $[(Me_3TPyA)_2Fe_2(^{SMe2}L)](BF_4)_4$ (**1-SMe_2**) as dark green crystalline materials (see Figure 7.1). Slow diffusion of Et_2O vapor into concentrated MeCN solutions of **1-R** (R = OMe, Cl, NO_2, SMe_2) gave dark orange plate-shaped crystals of **1-OMe**·4.0MeCN, **1-Cl**·0.7H_2O, **1-NO_2**·4.0MeCN, and **1-SMe_2**·4.0MeCN suitable for single-crystal X-ray diffraction analysis. All compounds crystallized in the triclinic space group $P\bar{1}$, aside from **1-SMe_2**·4.0MeCN, which crystallized in the monoclinic space group $P2_1/c$ (see Tables 7.4–7.7). In general, the structures of $[(Me_3TPyA)_2Fe_2(^{R}L)]^{n+}$ (n =

2: R = OMe, Cl, NO_2; *n* = 4: R = SMe_2) consist of two crystallographically equivalent $[(Me_3TPyA)Fe]^{2+}$ moieties connected by a deprotonated $^{R}L^{x-}$ (*x* = 2: R = OMe, Cl, NO_2; *x* = 0: R = SMe_2) bridging ligand with a crystallographic site of inversion located at the center of the bridging ligand (see Figure 7.2). Each Fe^{II} center resides in a distorted octahedral coordination environment comprised of two *cis*-oriented O atoms from $^{R}L^{x-}$ (*x* = 2: R = OMe, Cl, NO_2; *x* = 0: R = SMe_2) and four N atoms from the Me_3TPyA capping ligand.

The mean Fe–N and Fe–O bond distances across the series fall in the ranges of 2.195(3)–2.210(2) Å and 2.103(3)–2.125(2) Å, respectively, consistent with reported distances for high-spin *S* = 2 Fe^{II} centers in similar coordination environments (see Table 7.1).[27d,42,43] Within the bridging ligand, the average C–O distance ranges from 1.247(3) to 1.270(4) Å across the series, which falls between the value expected for a single and a double bond.[44] Moreover, the mean C1–C2 bond distance of 1.516(6)–1.532(9) Å, typical for a single bond, is substantially longer than the average C2–C3 and C3–C1A bond distances, which range from 1.404(4) to 1.429(6) Å and 1.363(6) to 1.389(9) Å, respectively, across the series. These collective distances strongly suggest that the bridging ligand in **1-OMe**·4.0MeCN, **1-Cl**·0.7H_2O, **1-NO_2**·4.0MeCN, and **1-SMe_2**·4.0MeCN is best described as two localized 6-π-electron fragments connected by two C–C single bonds. The observation of two drastically different Fe–O bond distances, namely shorter Fe–O1 distances of 2.003(3)–2.051(5) Å and longer Fe–O2 distances of 2.1782(9)–2.210(3) Å further supports the formulation of the bridging ligand in these compounds as the diamagnetic benzoquinone $^{R}L^{x-}$ (*x* = 2: R = OMe, Cl, NO_2; *x* = 0: R = SMe_2). Finally, the Fe^{II}_2 complexes in **1-OMe**·4.0MeCN, **1-Cl**·0.7H_2O, **1-NO_2**·4.0MeCN, and **1-SMe_2**·4.0MeCN feature a mean intramolecular Fe···Fe distance ranging from 7.996(3) to 8.0219(8) Å, in accord with values reported for other

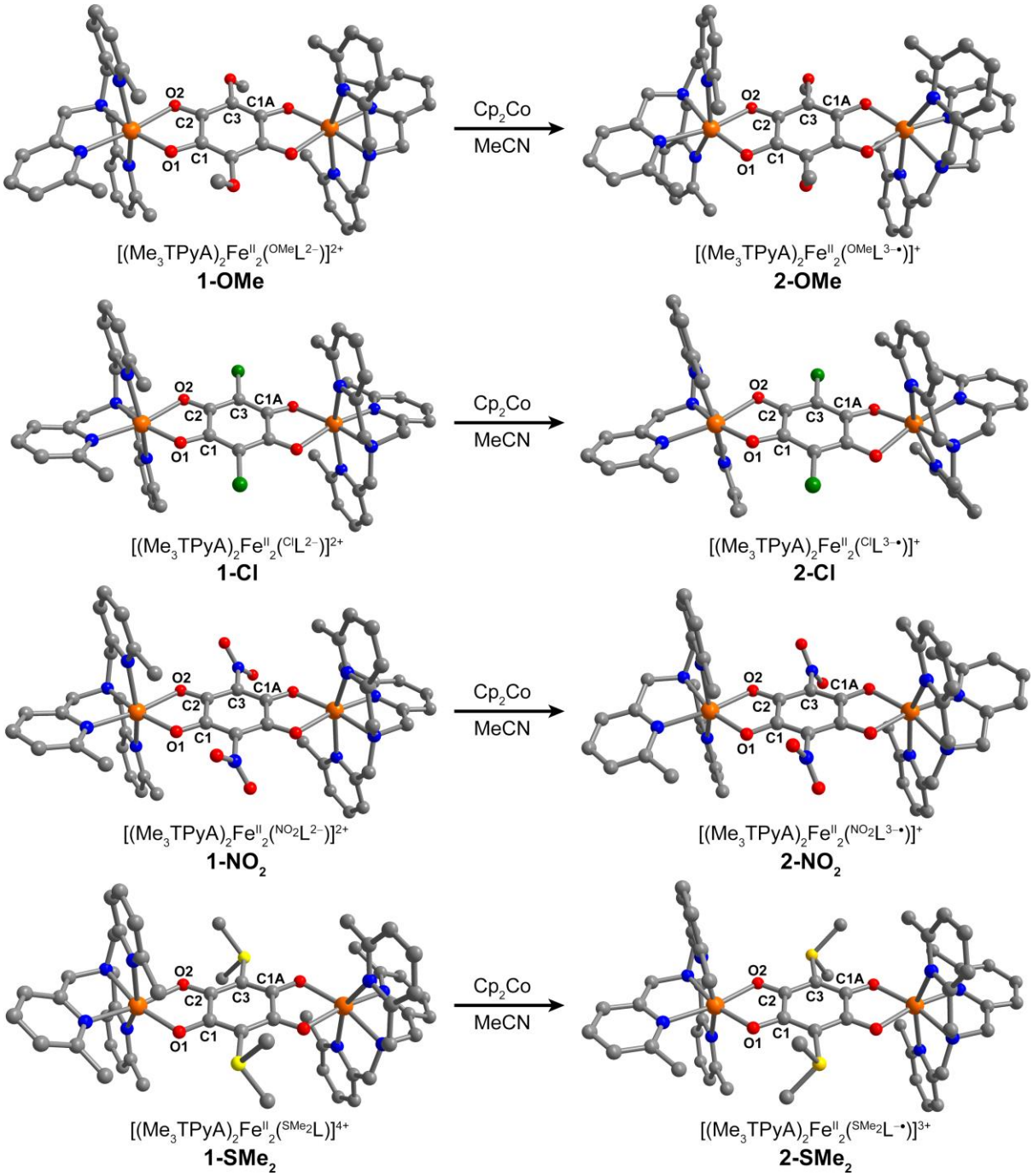

Figure 7.2 Crystal structures of the cationic complexes $[(Me_3TPyA)_2Fe_2(^RL)]^{4+/2+}$ (left) and $[(Me_3TPyA)_2Fe_2(^RL)]^{3+/1+}$ (right), as observed in **1-R**·solvent and **2-R**·solvent (R = OMe, Cl, NO_2, SMe_2), respectively. Orange, green, yellow, red, blue, and gray spheres represent Fe, Cl, S, O, N, and C atoms, respectively; H atoms are omitted for clarity.

benzoquinoid-bridged Fe^{II}_2 compounds.[27d,28a,43] Notably, the similar structural metrics for **1-OMe**

·4.0MeCN, **1-Cl**·0.7H_2O, **1-NO_2**·4.0MeCN, and **1-SMe_2**·4.0MeCN indicate that the solid-state structure of this family of Fe^{II}_2 complexes is minimally affected by the nature of the benzoquinoid substituents.

To probe the effects of benzoquinone substitution on the electronic structure of **1-R** (R = OMe, Cl, NO_2, SMe_2) and explore the feasibility of isolating the semiquinoid radical-bridged congeners, cyclic voltammetry experiments were carried out for MeCN solutions of these compounds at 298 K. The cyclic voltammograms of **1-R** (R = OMe, Cl, NO_2, SMe_2) are depicted in Figure 7.3. Each voltammogram exhibits two reversible processes at $E_{1/2}$ = +0.22 and −1.11 V, +0.33 and −0.86 V, +0.41 and −0.58 V, and +0.45 and −0.47 V vs $[Cp_2Fe]^{0/1+}$ for **1-OMe**, **1-Cl**, **1-NO_2**, and **1-SMe_2**, respectively. Based on precedent in other benzoquinoid-bridged Fe_2 complexes, we assign the wave at negative potential to the ligand-centered redox process $^{R}L^{x-/(x+1)-}$• (x = 2: R = OMe, Cl, NO_2; x = 0: R = SMe_2) and the wave at positive potential to the metal-based $Fe^{II}Fe^{II}/Fe^{II}Fe^{III}$ couple.[27d,28a,b,43] The variance of $E_{1/2}$ on substituent identity for both ligand- and

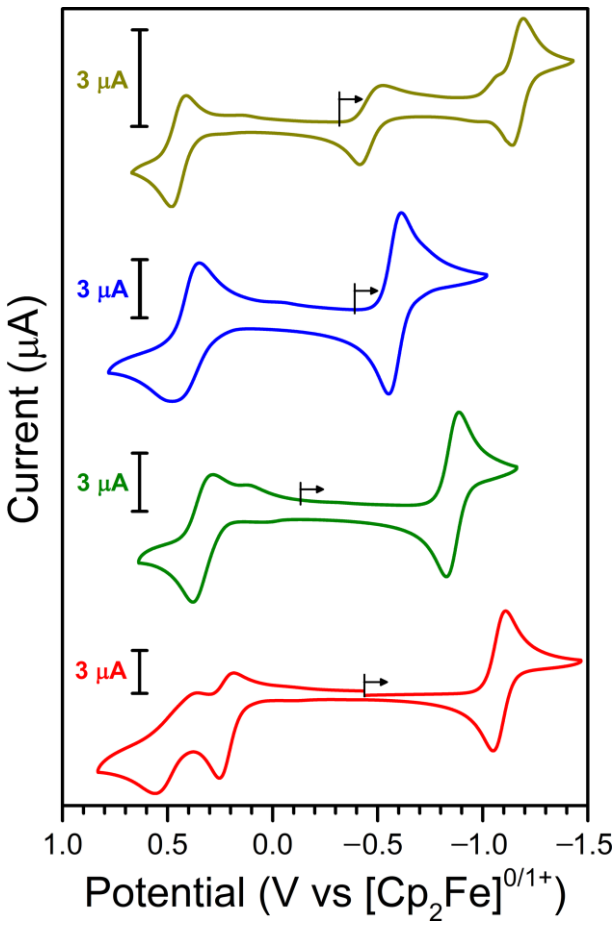

Figure 7.3 Cyclic voltammograms for solutions of **1-R** in MeCN containing 100 mM $(Bu_4N)(PF_6)$ supporting electrolyte, collected at 298 K; R = OMe (red), Cl (green), NO_2 (blue), SMe_2 (gold). Scan rate = 100 mV s^{-1} for R = OMe, Cl, and NO_2, and 25 mV s^{-1} for R = SMe_2. Black vertical lines and arrows denote the open circuit potential and scan direction, respectively. Each vertical scale bar represents a current of 3 μA.

metal-based processes correlates linearly with the Hammett substituent constant (σ_p), which quantifies the electronic properties of substituents by considering both inductive and resonance effects (see Figures 7.15 and 7.16).[45] In particular, $E_{1/2}$ for the $Fe^{II}Fe^{II}/Fe^{II}Fe^{III}$ couple shifts positively by 0.23 V when the benzoquinoid substituents are varied from electron-donating OMe groups to strongly electron-withdrawing $^{+}SMe_2$ groups, while the concurrent positive shift in the ligand-centered potential is 0.64 V. The more pronounced change in $E_{1/2}$ for $^{R}L^{x-/(x+1)-\bullet}$ (x = 2: R = OMe, Cl, NO_2; x = 0: R = SMe_2) is consistent with the substituents primarily affecting the energy levels of the benzoquinoid ligand, however, the clear variation in the metal-based potential indicates that the electronic properties of the substituents significantly modulate the metal–ligand interactions as well. The remaining oxidation event at +0.56 V vs $[Cp_2Fe]^{0/1+}$ for **1-OMe** is assigned to the metal-based $Fe^{II}Fe^{III}/Fe^{III}Fe^{III}$ oxidation, whereas the additional reversible redox event at $E_{1/2}$ = −1.17 V vs $[Cp_2Fe]^{0/1+}$ for **1-SMe$_2$** is assigned to the ligand-based $^{SMe_2}L^{-\bullet/2-}$ couple.

Together, the cyclic voltammetry measurements suggest that the radical-bridged Fe^{II}_2 complexes $[(Me_3TPyA)_2Fe_2(^{R}L^{x-\bullet})]^{n+}$ (x = 3, n = 1: R = OMe, Cl, NO_2; x = 1, n = 3: R = SMe_2) should be chemically accessible. Toward this end, dark green MeCN solutions of **1-R** (R = OMe, Cl, NO_2, SMe_2) were treated with stoichiometric amounts of the reductant cobaltocene (Cp_2Co) to give red-brown (R = OMe, Cl, NO_2) or green-brown (R = SMe_2) solutions. ^{1}H NMR analysis revealed the formation of new paramagnetic species (see Figures 7.17–7.30). Subsequent diffusion of Et_2O vapor into these solutions afforded red-orange (R = OMe, Cl, NO_2) or orange (R = SMe_2) plate-shaped crystals of the one-electron reduced compounds $[(Me_3TPyA)_2Fe_2(^{OMe}L)](BF_4)\cdot 2.0MeCN$ (**2-OMe**·2.0MeCN), $[(Me_3TPyA)_2Fe_2(^{Cl}L)](BF_4)\cdot 0.5Et_2O$ (**2-Cl**·0.5Et_2O), $[(Me_3TPyA)_2Fe_2(^{NO_2}L)](BF_4)$ (**2-NO$_2$**), and

$[(Me_3TPyA)_2Fe_2(^{SMe_2}L)](BF_4)_3{\cdot}0.9MeCN{\cdot}0.5Et_2O$ (**2-SMe$_2$**·0.9MeCN·0.5Et$_2$O). Subsequent drying of these crystals under reduced pressure gave the desolvated forms **2-R** (R = OMe, Cl, NO_2, SMe_2) in moderate yields of 57–88%.

The structures of the cationic complexes $[(Me_3TPyA)_2Fe_2(^{OMe}L)]^+$, $[(Me_3TPyA)_2Fe_2(^{NO_2}L)]^+$, and $[(Me_3TPyA)_2Fe_2(^{SMe_2}L)]^{3+}$ in **2-R**·solvent (R = OMe, NO_2, SMe_2) are very similar to those in **1-R**·solvent (R = OMe, Cl, NO_2, SMe_2), with the two Fe^{II} sites in each molecule related through a crystallographic inversion center, whereas the Fe^{II} centers in $[(Me_3TPyA)_2Fe_2(^{Cl}L)]^+$ are slightly inequivalent due to crystal packing of the $(BF_4)^-$ counterion. The near identical values of the octahedral distortion parameter (Σ_{sum})[46] for **1-R**·solvent and **2-R**·solvent (R = OMe, Cl, NO_2, SMe_2) illustrate that the coordination geometry at Fe^{II} is not significantly affected by the substituents and redox state of the bridging ligand.

In contrast, close comparison of the bond distances in the two series of compounds reveals several key differences. First, the mean C–C bond distance decreases slightly by 0.6–1.5%, from 1.436(4)–1.443(5) to 1.422(1)–1.430(2) Å, in moving from **1-R**·solvent to **2-R**·solvent (R = OMe, Cl, NO_2, SMe_2). Moreover, the mean C–O bond distance for **2-R**·solvent varies from 1.285(2) to 1.304(2) Å across the series, which represents a 2.7–3.1% increase, as compared to the values obtained for the unreduced analogues. These structural changes upon reduction reflect a net increase in C–C bond order and a net decrease in C–O bond order, in agreement with a ligand-centered reduction from $^{R}L^{x-}$ to $^{R}L^{(x+1)-\bullet}$ (x = 2: R = OMe, Cl, NO_2; x = 0: R = SMe_2), as has been observed for similar benzoquinoid-bridged metal complexes.[27d,28a,b] Furthermore, the mean Fe–O bond distance of 2.052(1)–2.084(1) Å in the **2-R**·solvent series is 1.5–2.8% shorter than the corresponding distances in **1-R**·solvent, and the mean intramolecular Fe···Fe distance decreases to

a similar degree in moving from **1-R**·solvent to **2-R**·solvent (R = OMe, Cl, NO_2, SMe_2). Together these observations highlight the stronger Fe–O interactions in the semiquinoid radical-bridged complexes $[(Me_3TPyA)_2Fe_2(^{R}L^{x-\bullet})]^{n+}$ (x = 3, n = 1: R = OMe, Cl, NO_2; x = 1, n = 3: R = SMe_2) than in the diamagnetic benzoquinoid-bridged analogues $[(Me_3TPyA)_2Fe_2(^{R}L^{x-})]^{n+}$ (x = 2, n = 2: R = OMe, Cl, NO_2; x = 0, n = 4: R = SMe_2) owing to the increase in negative charge. As a result of the stronger interactions between the Fe^{II} centers and the bridging ligand in **2-R**·solvent, the average Fe–N bond distance increases slightly by 1.0–1.8% in moving from **1-R**·solvent to **2-R**·solvent (R = OMe, Cl, NO_2, SMe_2).

7.3.2 Mössbauer Spectroscopy

To confirm the presence of a bridging ligand-centered reduction and further probe the effects

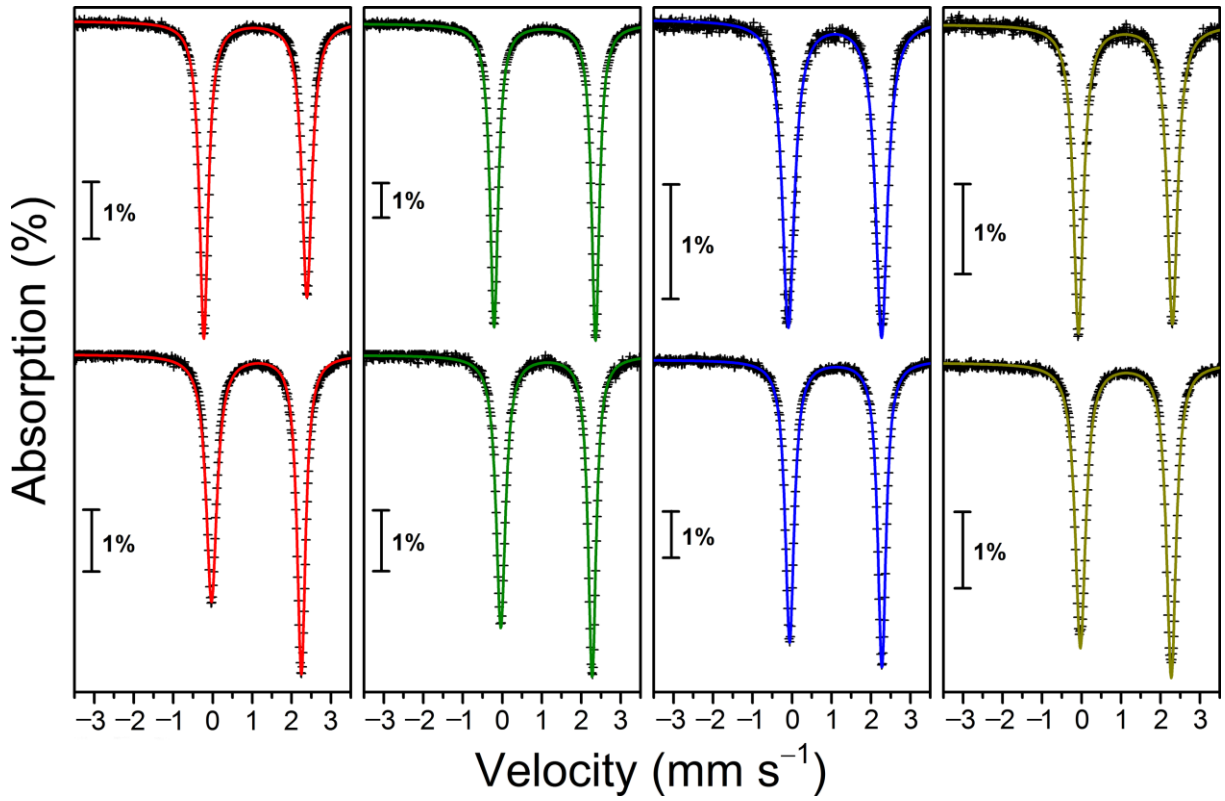

Figure 7.4 Zero-field ^{57}Fe Mössbauer spectra for polycrystalline samples of **1-R** (top) and **2-R** (bottom) at 80 K; R = OMe (red), Cl (green), NO_2 (blue), SMe_2 (gold). Black crosses represent experimental data and colored lines correspond to Lorentzian fits to the data. Each vertical scale bar represents an absorption of 1%.

Table 7.2 Summary of parameters obtained from fits to zero-field ^{57}Fe Mössbauer spectra for **1-R** and **2-R** (R = OMe, Cl, NO_2, SMe_2) at 80 K.[a]

	1-OMe	**2-OMe**	**1-Cl**	**2-Cl**	**1-NO_2**	**2-NO_2**	**1-SMe_2**	**2-SMe_2**
δ (mm s^{-1})	1.081(3)	1.108(3)	1.076(3)	1.118(3)	1.087(3)	1.108(3)	1.111(3)	1.121(3)
ΔE_Q (mm s^{-1})	2.61(2)	2.28(2)	2.57(2)	2.31(2)	2.36(2)	2.33(2)	2.38(2)	2.30(2)
Γ_L (mm s^{-1})[b]	0.263(3)	0.330(3)	0.249(2)	0.286(3)	0.371(4)	0.274(3)	0.302(4)	0.319(3)
Γ_R (mm s^{-1})[c]	0.306(3)	0.256(3)	0.240(2)	0.243(3)	0.362(4)	0.253(3)	0.315(4)	0.291(3)

[a] See Figure 7.4 for the experimental data and corresponding fits using Lorentzian doublets. The uncertainties in the parameter values were estimated from a combination of experimental and statistical fitting errors as described in Section 7.2. [b] Γ_L denotes the width of the left line of a quadrupole doublet. [c] Γ_R denotes the width of the right line of a quadrupole doublet.

of benzoquinoid substituents on the electronic structures of **1-R** and **2-R** (R = OMe, Cl, NO_2, SMe_2), zero-field ^{57}Fe Mössbauer spectra were collected for polycrystalline samples at 80 K. The Mössbauer spectra for **1-R** (R = OMe, Cl, NO_2, SMe_2) each exhibit a single sharp doublet (see Figure 7.4, top). Lorentzian fits to the data give an isomer shift of δ = 1.076(3)–1.111(3) mm s^{-1} and a quadrupole splitting of ΔE_Q = 2.36(2)–2.61(2) mm s^{-1} across the series (see Table 7.2). These parameters are consistent with high-spin Fe^{II} centers in pseudo-octahedral geometry and agree well with values reported for dinuclear complexes[28,43,47] and coordination polymers[48] featuring Fe^{II} ions in similar coordination environments.

The spectra for **2-R** (R = OMe, Cl, NO_2, SMe_2) display a similar quadrupole doublet (see Figure 7.4, bottom), with an isomer shift of δ = 1.108(3)–1.121(3) mm s^{-1} and a quadrupole splitting of ΔE_Q = 2.28(2)–2.33(2) mm s^{-1} for the series (see Table 7.2). The near identical isomer shifts in **1-R** and **2-R** (R = OMe, Cl, NO_2, SMe_2) confirm the one-electron reduction from **1-R** to **2-R** to be centered on the benzoquinoid bridging ligand. Notably, compounds **2-R** (R = OMe, Cl, NO_2, SMe_2) exhibit a smaller quadrupole splitting than their corresponding unreduced analogues **1-R**. This difference is especially pronounced for the OMe- and Cl-substituted derivatives (see Table 7.2) and likely stems from the change in ligand field at the Fe^{II} centers associated with the

reduction of the bridging ligand. The slight asymmetry of the quadrupole doublets for **1-OMe** and **2-R** (R = OMe, Cl, NO_2, SMe_2) may be attributed to several effects, including slow magnetic relaxation,[49] preferred orientation of crystallites,[49a,50] and lattice vibrational anisotropy.[49a,50] Complete understanding of the origin of this asymmetry requires detailed variable-temperature analysis that is beyond the scope of this work. Overall, Mössbauer spectroscopic analysis corroborates the assignment of the Fe_2 complexes in **1-R** and **2-R** as the benzoquinoid-bridged $[(Me_3TPyA)_2Fe_2(^{R}L^{x-})]^{n+}$ (x = 2, n = 2: R = OMe, Cl, NO_2; x = 0, n = 4: R = SMe_2) and the semiquinoid-bridged $[(Me_3TPyA)_2Fe_2(^{R}L^{x-\bullet})]^{n+}$ (x = 3, n = 1: R = OMe, Cl, NO_2; x = 1, n = 3: R = SMe_2), respectively, as evident from single-crystal X-ray diffraction analysis.

7.3.3 UV-Vis-NIR Spectroscopy

To gain further insight into the electronic structures of **1-R** and **2-R** (R = OMe, Cl, NO_2, SMe_2), UV-Vis-NIR absorption spectra were collected for MeCN solutions at 298 K. The spectra for all compounds show an intense absorption band centered at 261–263 nm (ε_{max} = 28700–37700 cm^{-1}), as depicted in Figure 7.5. Considering the identical feature in the spectrum for Me_3TPyA (see Figure 7.31) and the invariance of λ_{max} and ε_{max} on the redox state of the bridging ligand, we assign this

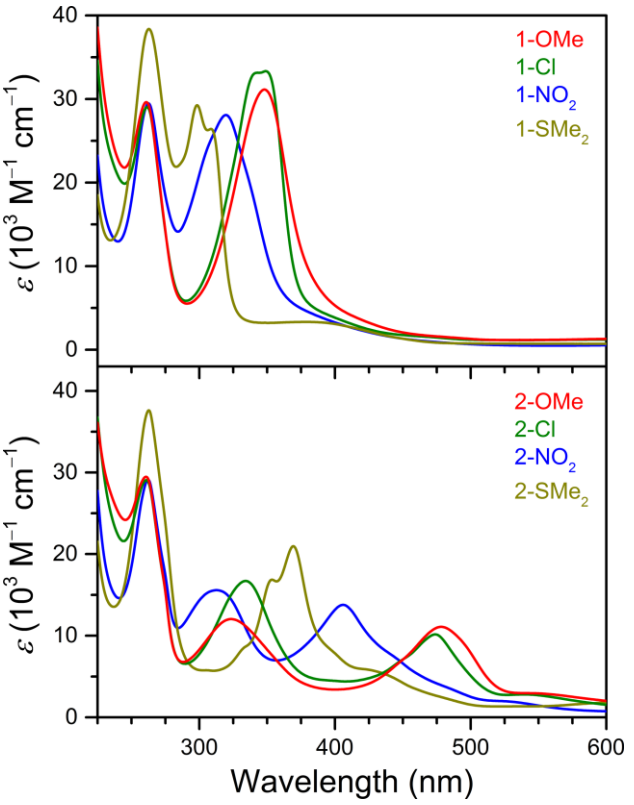

Figure 7.5 UV-Vis spectra for solutions of **1-R** (top) and **2-R** (bottom) in MeCN at 298 K.

absorption to a π–π* transition occurring within the Me_3TPyA capping ligand.[51] The spectra for **1-R** (R = OMe, Cl, NO_2, SMe_2) display an additional strong band in the near-UV region that exhibits a progressive red shift (λ_{max} = 298–350 nm; ε_{max} = 25800–34700 cm^{-1}) as the electron-donating ability of the benzoquinoid substituents increases (see Figure 7.5, top). Based on the similarity with the spectra for the free ligands (see Figures 7.32–7.35) and literature precedent for other complexes bearing quinoid-type ligands,[52] this band is ascribed to a π–π* transition within the bridging ligand. Notably, the spectra for **2-OMe**, **2-Cl**, and **2-NO_2** feature two broad benzoquinoid-centered π–π* bands[27e] at λ_{max} = 313–334 nm (ε_{max} = 12000–16700 cm^{-1}) and 406–478 nm (ε_{max} = 10200–13800 cm^{-1}) for the series, which are significantly weaker than those for the unreduced analogues (see Figure 7.5, bottom). In contrast, the spectrum for **2-SMe_2** exhibits a markedly different profile than those for **2-OMe**, **2-Cl**, and **2-NO_2**. Specifically, multiple overlapping benzoquinoid-centered π–π* bands are observed in the 300–500 nm range, with λ_{max} = 369 nm (ε_{max} = 21000 cm^{-1}). This discrepancy most likely arises from the different charges of the Fe^{II}_2 complexes in these compounds.

Close comparison of the Vis-NIR region of the spectra obtained for **1-R** and **2-R** (R = OMe, Cl, NO_2, SMe_2) reveals that compounds **1-R** generally feature stronger absorption in the NIR region than **2-R**, while additional bands are observed between 525 and 650 nm in the spectra for **2-R** (see Figures 7.36–7.41). We tentatively assign these new bands to charge transfer transitions based on the molar absorptivity values (ε_{max} = 1770–3960 cm^{-1}). Taken together, the spectral changes observed upon reduction of the benzoquinoid bridging ligand are in good agreement with the associated color change from dark green for **1-R** (R = OMe, Cl, NO_2, SMe_2) to red-brown (R = OMe, Cl, NO_2) or green-brown (R = SMe_2) for **2-R**. Furthermore, these studies demonstrate that

the solution electronic structures of **1-R** and **2-R** (R = OMe, Cl, NO_2, SMe_2) are significantly affected by the nature of the benzoquinoid substituents, although the establishment of a clear trend is complicated by broad features and differences in overall charges. Along these lines, the diffuse reflectance spectra collected for microcrystalline samples of **1-R** and **2-R** (R = OMe, Cl, NO_2, SMe_2) (see Figures 7.42–7.49) show similar features as the solution spectra, suggesting that the benzoquinoid substituents also plays an important role in determining the electronic properties of these compounds in the solid state.

7.3.4 Static Magnetic Properties

To probe and compare magnetic interactions in **1-R** and **2-R** (R = OMe, Cl, NO_2, SMe_2), variable-temperature dc magnetic susceptibility data were collected for microcrystalline samples under an applied field of 1 T. The resulting plots of $\chi_M T$ vs T for **1-R** (R = OMe, Cl, NO_2, SMe_2) are shown in Figure 7.6. At 300 K, the values of $\chi_M T$ are 6.90, 7.25, 7.32, and 7.47 cm^3 K mol^{-1} for **1-OMe**, **1-Cl**, **1-NO2**, and **1-SMe2**, respectively, corresponding to two magnetically non-interacting S = 2 Fe^{II} centers with g = 2.14, 2.20, 2.21, and 2.23, respectively. As the temperature is decreased, the data for **1-OMe** and **1-Cl** undergo a gradual then rapid increase, reaching maximum values of 9.29 and 9.82 cm^3 K mol^{-1} at 10 K, respectively. This increase in $\chi_M T$ with decreasing temperature

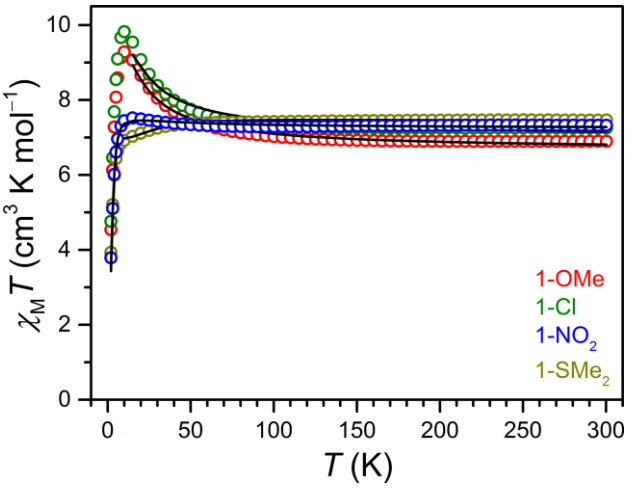

Figure 7.6 Variable-temperature dc magnetic susceptibility data for **1-R** (R = OMe, Cl, NO_2, SMe_2), collected under an applied field of 1 T. Colored circles represent experimental data and black lines correspond to fits to the data.

Table 7.3 Summary of parameters obtained from fits to magnetic data for **1-R** and **2-R** (R = OMe, Cl, NO_2, SMe_2).

	1-OMe	**1-Cl**	**1-NO_2**	**1-SMe_2**	**2-OMe**	**2-Cl**	**2-NO_2**	**2-SMe_2**
D (cm^{-1})	−4.8[a]	−8.0[a]	−7.0[a]	−15.2[b]	−16.9(2)[c]	−12.4(1)[c]	−20.7(3)[c]	−19.9(3)[c]
g	2.11[a]	2.16[a]	2.20[a]	2.22[a]	2.11[c]	2.14[c]	2.23[c]	2.36[c]
J (cm^{-1})	+1.2[a]	+1.2[a]	+0.3[a]	+0.3[a]	−57[d]	−60[d]	−58[d]	−65[d]
U_{eff} (cm^{-1})[e]	–	–	–	–	50(1)	41(1)	38(1)	33(1)
τ_0 (s)[e]	–	–	–	–	$3.3(6) \times 10^{-9}$	$1.0(2) \times 10^{-8}$	$1.8(3) \times 10^{-8}$	$1.1(3) \times 10^{-7}$

[a]These values were obtained from a simultaneous fit to low-temperature magnetization and dc magnetic susceptibility data as described in Section 7.2. [b]This value of D was obtained from an individual fit to low-temperature magnetization data using fixed values of g and J as described in Section 7.2 and Table 7.8. [c]These values were obtained from fitting low-temperature magnetization data as described in Section 7.2 . [d]These values of J were obtained from fitting dc magnetic susceptibility data in the temperature range 60–300 K using the spin Hamiltonian provided in Equation 7.3. [e]These values were obtained from ac magnetic susceptibility measurements collected under zero applied dc field.

is indicative of weak ferromagnetic coupling between the Fe^{II} centers via an indirect superexchange mechanism through the diamagnetic bridging ligand to give an $S = 4$ ground state. Below 10 K, $\chi_M T$ decreases sharply to minimum values of 4.54 and 4.76 cm^3 K mol^{-1} at 2.0 K for **1-OMe** and **1-Cl**, respectively, likely the result of Zeeman splitting, zero-field splitting, and potentially weak intermolecular interactions.

In contrast, the temperature dependence of $\chi_M T$ for **1-NO_2** and **1-SMe_2** is not as prominent as observed for **1-OMe** and **1-Cl**. Rather, the $\chi_M T$ data for **1-NO_2** show a gradual increase to a maximum value of $\chi_M T$ = 7.52 cm^3 K mol^{-1} at 15 K and then undergo a sharp decline to a minimum value of 3.79 cm^3 K mol^{-1} at 2.0 K. Similarly, the value of $\chi_M T$ for **1-SMe_2** is relatively constant above 60 K but then decreases gradually as the temperature is decreased from 60 K, and more sharply below 10 K, to a minimum value of 3.93 cm^3 K mol^{-1} at 2.0 K. The different profiles for **1-NO_2** and **1-SMe_2** than for **1-OMe** and **1-Cl** likely stems from weaker magnetic exchange interactions through diamagnetic benzoquinoid bridging ligands bearing electron-withdrawing substituents, as has been previously observed,[12,30,31] and/or larger zero-field splitting.

To assess the presence of magnetic anisotropy and confirm the spin ground states in **1-R** (R = OMe, Cl, NO_2, SMe_2), low-temperature magnetization data were collected at selected dc fields (see Figures 7.58–7.61). The saturation magnetization values of the resulting isofield curves fall in the range of M = 5.26–6.37 μ_B mol^{-1} across the series, in accord with the presence of an S = 4 ground state and significant magnetic anisotropy for all compounds.[20b]

To quantify the magnetic exchange interactions and magnetic anisotropy in **1-R** (R = OMe, Cl, NO_2, SMe_2), the variable-temperature dc magnetic susceptibility data and low-temperature magnetization data were simultaneously fit to the Van Vleck equation according to the spin Hamiltonian provided in Equation 7.1 (see Section 7.2) using the program PHI.[38] Fits to the data give an exchange constant of J = +1.2, +1.2, +0.3, and +0.3 cm^{-1} for **1-OMe**, **1-Cl**, **1-NO_2**, and **1-SMe_2**, respectively, along with values of the axial zero-field splitting parameter D ranging from −4.8 to −15.2 cm^{-1} and g = 2.11–2.22 across the series. These parameters are summarized in Table 7.3. Note that the values of g obtained from these fits are in excellent agreement with those estimated from the $\chi_M T$ values at 300 K. Furthermore, the magnitude and sign of J for **1-R** (R = OMe, Cl, NO_2, SMe_2) are consistent with other examples of benzoquinoid-bridged Fe^{II}_2 complexes.[20b,27d] Importantly, note, that the value of J is identical for **1-OMe** and **1-Cl**, and this value is four times larger than the value of J = +0.3 cm^{-1} obtained for both **1-NO_2** and **1-SMe_2**, demonstrating that strongly electron-withdrawing ligand substituents decrease the magnetic coupling strength through a diamagnetic benzoquinoid bridge. The lack of a linear correlation between J and the Hammett substituent constant σ_p for the **1-R** series may be attributed to the ability of halogens to donate a lone pair of electrons. Specifically, the electron-donating resonance effects may outweigh the electron-withdrawing inductive effects for the Cl substituent and thus

render the electronic properties of $^{Cl}L^{2-}$ similar to that of $^{OMe}L^{2-}$ when coordinated to metal ions. Indeed, the similar UV-Vis absorption spectra and Mössbauer parameters obtained for **1-OMe** and **1-Cl** support this hypothesis.

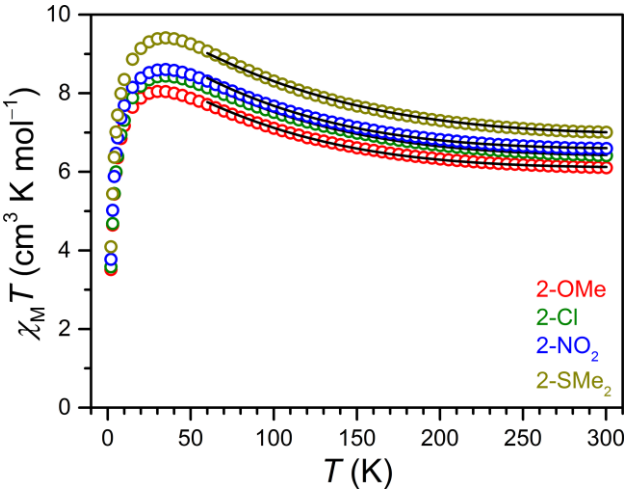

Figure 7.7 Variable-temperature dc magnetic susceptibility data for **2-R** (R = OMe, Cl, NO_2, SMe_2), collected under an applied field of 1 T. Colored circles represent experimental data and black lines correspond to fits to the data.

The plots of $\chi_M T$ vs T for **2-R** (R = OMe, Cl, NO_2, SMe_2) exhibit a markedly different profile than those for **1-R** (see Figure 7.7). The values of $\chi_M T$ at 300 K are 6.10, 6.41, 6.59, and 7.00 cm^3 K mol^{-1} for **2-OMe**, **2-Cl**, **2-NO$_2$**, and **2-SMe$_2$**, respectively. As the temperature is decreased to 150 K, $\chi_M T$ undergoes a gradual increase and then increases nearly linearly upon further decreasing the temperature to reach maximum values of 8.04, 8.44, 8.60, and 9.41 cm^3 K mol^{-1} at 30, 35, 35, and 35 K for **2-OMe**, **2-Cl**, **2-NO$_2$**, and **2-SMe$_2$**, respectively. This upturn in $\chi_M T$ with decreasing temperature suggests significant magnetic coupling between the two Fe^{II} centers and semiquinoid radical via direct exchange mechanism. To quantify this interaction and determine whether it is ferromagnetic or antiferromagnetic in nature, the data collected in the temperature range 60–300 K were fit to the Van Vleck equation according to the spin Hamiltonian provided in Equation 7.3 (see Section 7.2) to give exchange constants of J = −57, −60, −58, and −65 cm^{-1} for **2-OMe**, **2-Cl**, **2-NO$_2$**, and **2-SMe$_2$**, respectively (see Table 7.3), and g = 2.09, 2.14, 2.17, 2.23, respectively. Interestingly, the magnitude of J for **2-Cl** is over three times greater than that observed for an isostructural Fe^{II}_2 complex featuring a $^{Cl}L^{3-\bullet}$ radical bridging ligand and a

TPyA capping ligand.[27d] Moreover, that complex exhibits ferromagnetic metal–radical coupling, in contrast with the antiferromagnetic interactions observed for **2-R**. This different magnetic behavior may stem from the presence of a bulkier Me_3TPyA capping ligand in **2-R** rather than the unsubstituted TPyA ligand.

The rapid decline in $\chi_M T$ below 30 K can be attributed to Zeeman splitting, zero-field splitting, and possibly weak intermolecular interactions. Indeed, low-temperature magnetization data for **2-R** (R = OMe, Cl, NO_2, SMe_2) reveal the presence of substantial zero-field splitting, with fits to the data giving parameters of $D = -16.9(2)$, $-12.4(1)$, $-20.7(3)$, and $-19.9(3)$ cm^{-1} for **2-OMe**, **2-Cl**, **2-NO_2**, and **2-SMe_2**, respectively, and g = 2.11, 2.14, 2.23, 2.36, respectively (see Figures 7.62–7.65 and Table 7.3). Note that the values of g obtained from the low-temperature magnetization data agree well with those obtained from the variable-temperature dc-susceptibility data. Interestingly, for both the **1-R** and **2-R** series of compounds, the value of g follows the trend R = OMe < Cl < NO_2 < SMe_2. This increase in g across the series may stem from increasing electron-withdrawing ability of the bridging ligand substituents, however, other effects such as those arising from crystal packing cannot be ruled out.

The values of J for **2-R** (R = OMe, Cl, NO_2, SMe_2) are 48–217-fold greater than those observed for the **1-R** series (see Table 7.3), demonstrating the much stronger magnetic exchange between metal centers through a radical bridge, as has been previously observed for dinuclear benzoquinoid complexes.[27d,28a,b] However, the substituents on the semiquinoid ring do not significantly affect the magnitude of the metal–radical coupling for **2-R**. This is in contrast with the clearly distinct $\chi_M T$ vs T profiles and values of J for R = OMe, Cl and R = NO_2, SMe_2, observed for the **1-R** series. These results suggest that the effects of ligand substituents on magnetic coupling strength in

benzoquinoid-bridged compounds are highly dependent on the redox state of the bridging ligand. Accordingly, the contributions from substituent-based orbitals to the frontier orbitals of diamagnetic benzoquinoid ligands are significantly greater than such contributions to radical semiquinoid-based orbitals. This discrepancy may be attributed to the more favorable donation of electron density into the dianionic benzoquinoid ring than into the trianionic semiquinoid ring, owing to the greater negative charge and electron delocalization in the latter.

7.3.5 Dynamic Magnetic Properties

Finally, the presence of large negative values of *D* for **1-R** and **2-R** (R = OMe, Cl, NO_2, SMe_2) prompted us to probe single-molecule magnet behavior for these compounds. Accordingly, variable-frequency ac magnetic susceptibility data were collected under zero applied dc field in the temperature range 2.00–8.00 K. For **1-R** (R = OMe, Cl, NO_2, SMe_2), only onsets of peaks in the out-of-phase component (χ_M'') of the ac susceptibility are observed above 2.00 K and below 1488 Hz, indicating too fast magnetic relaxation (see Figures 7.66–7.73). In stark contrast, compounds **2-R** (R = OMe, Cl, NO_2, SMe_2), exhibit pronounced temperature- and frequency-dependent peaks in both the in-phase (χ_M') and out-of-phase component (χ_M'') of the ac susceptibility (see Figures 7.8, left, and 7.74–7.88), which demonstrates that the radical-bridged compounds are indeed

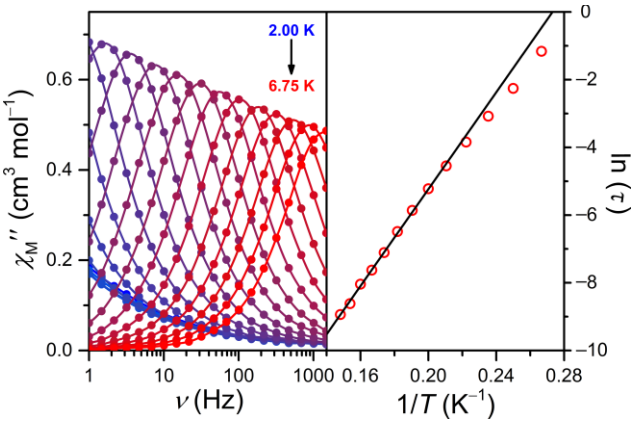

Figure 7.8 Left: Variable-frequency out-of-phase ac susceptibility data for **2-OMe**, collected under zero applied dc field in the temperature range 2.00–6.75 K. Right: Arrhenius plot of relaxation time. Circles denote experimental data. Colored lines are a guide to the eye and the black line corresponds to a linear fit to the data.

single-molecule magnets. These data were employed to construct Cole–Cole plots (see Figures 7.89, 7.90, 7.92, 7.94), which were fit using the generalized Debye model[36] to estimate relaxation times (τ). The corresponding Arrhenius plots of relaxation times exhibit linear regions at higher temperatures, between 4.75 and 6.75 K, 4.75 and 6.50 K, 4.25 and 6.25 K, and 5.50 and 7.00 K for **2-OMe**, **2-Cl**, **2-NO$_2$**, and **2-SMe$_2$**, respectively (see Figures 7.8, right, and 7.91, 7.93, and 7.95), indicating a thermally activated relaxation process for all compounds. Fits to the data in these temperature ranges afford a spin relaxation barrier of U_{eff} = 50(1), 41(1), 38(1), and 33(1) cm^{-1} for **2-OMe**, **2-Cl**, **2-NO$_2$**, and **2-SMe$_2$**, respectively, with a pre-exponential factor of τ_0 = 3.3(6) × 10^{-9}, 1.0(2) × 10^{-8}, 1.8(3) × 10^{-8}, and 1.1(3) × 10^{-7} s, respectively (see Table 7.3). These values are similar to those obtained for related semiquinoid-bridged Fe^{II}_2 complexes featuring exclusively nitrogen donors.[28a,b] Interestingly, **2-OMe** exhibits the largest relaxation barrier, albeit it displays the weakest metal–radical coupling. Moreover, the plot of U_{eff} vs the Hammett substituent constant σ_{p} for the **2-R** series reveals a good linear relationship (see Figure 7.96). A detailed understanding of this comparison is not immediately forthcoming, however, it suggests that while the ligand substituents do not act to significantly vary the energy levels of the spin ground and excited states directly in these compounds, they may affect the efficiency of competing relaxation processes.

At lower temperatures, the data begin to deviate from linearity and finally reach a plateau below 3.00, 2.75, and 4.00 K for **2-Cl**, **2-NO$_2$**, and **2-SMe$_2$**, respectively, suggesting the presence of additional fast relaxation processes, such as quantum tunneling and/or spin–spin relaxation, that shortcut the energy barrier. These additional relaxation processes are most prominent for **2-SMe$_2$**, as the temperature-dependent features in the plot of χ_{M}'' vs ν are observed at much higher

frequencies than those for **2-OMe**, **2-Cl**, and **2-NO2**. This discrepancy may arise from the different charges of the Fe^{II}_2 complexes in these compounds and/or the steric bulk of the $^{+}SMe_2$ groups.

7.4 Conclusions

The foregoing results demonstrate the modest effects of ligand substitution on the metal–radical exchange coupling in semiquinoid-bridged Fe^{II}_2 single-molecule magnets. Specifically, the radical-bridged complexes $[(Me_3TPyA)_2Fe_2(^{R}L^{x-\bullet})]^{n+}$ (x = 3, n = 1: R = OMe, Cl, NO_2; x = 1, n = 3: R = SMe_2) were synthesized and shown to exhibit single-molecule magnet behavior and similar exchange coupling constants of $J = -57$, -60, -58, and -65 cm^{-1} for R = OMe, Cl, NO_2, and SMe_2, respectively. In stark contrast, the analogous complexes featuring diamagnetic benzoquinoid bridging ligands showed 4-fold higher values of J for the compounds with R = OMe, Cl than for the derivatives with R = NO_2, SMe_2, demonstrating that the electronic effects of ligand substituents on the magnetic properties in benzoquinoid systems are highly dependent on the redox state of the bridging ligand. This first systematic investigation of the influence of ligand substituents on magnetic interactions in radical-bridged quinoid systems with paramagnetic metal centers provides important knowledge for the design of semiquinoid-based Fe^{II} magnets with targeted properties. Specifically, rather than selecting ligand derivatives based on the electronic properties of the ring substituents, factors such as steric effects, charge, and ability to participate in intermolecular interactions should be considered. Current work is geared toward performing computational analysis of these compounds, in an effort to better understand the magnetic properties of benzoquinoid-based systems and establish design principles for higher dimensional quinoid-based magnets that operate at high temperatures.

7.5 Supporting Information

7.5.1 Supplementary Experimental Details

Synthesis of tris(6-methyl-2-pyridylmethyl)amine (Me_3TPyA). This compound was synthesized following a modified literature procedure.[53] 6-Methyl-pyridine-2-carboxaldehyde (1.19 g, 9.82 mmol) was added to a stirred colorless solution of 2-aminomethylpyridine (0.600 g, 4.91 mmol) in CH_2Cl_2 (100 mL) at 25 °C. The resulting pale yellow solution was stirred at 25 °C for additional 10 min and sodium triacetoxyborohydride (2.08 g, 9.82 mmol) was subsequently added. The resulting white suspension was heated at reflux under a dinitrogen atmosphere for 6 h, then cooled to 25 °C and a saturated solution of sodium hydrogencarbonate in H_2O (50 mL) was added. The mixture was stirred for 20 min and then extracted with ethyl acetate (200 mL). The combined organic layer was dried over $MgSO_4$, filtered, and the solvent removed under reduced pressure. The light orange residue was extracted with pentane (2 × 100 mL) and filtered while hot. The solvent was removed under reduced pressure and the residue dried in vacuo for 12 h to give Me_3TPyA as a white solid (1.20 g, 70%). UV-Vis-NIR absorption spectrum (MeCN, 298 K): 266 nm (ε = 12700 M^{-1} cm^{-1}), 273 nm (shoulder; ε = 10300 M^{-1} cm^{-1}). FT-IR (ATR, cm^{-1}): 3071 (w), 2999 (w), 2959 (w), 2916 (w), 2877 (w), 2821 (m), 1593 (s), 1576 (s), 1463 (s), 1442 (m), 1362 (m), 1273 (m), 1233 (w), 1226 (w), 1161 (w), 1120 (m), 1035 (w), 1016 (w), 995 (w), 976 (w), 963 (w), 907 (w), 896 (w), 869 (w), 803 (s), 794 (s), 758 (s), 729 (w), 624 (m). ^{1}H NMR (500 MHz, $CDCl_3$, 298 K): δ 7.53 (t, J = 7.7 Hz, 3H), 7.44 (d, J = 7.7 Hz, 3H), 6.98 (d, J = 7.5 Hz, 3H), 3.85 (s, 6H), 2.51 (s, 9H). ^{13}C{^{1}H} NMR (126 MHz, $CDCl_3$, 298 K): δ 157.77, 136.97, 121.71, 119.82, 60.21, 24.48.

Synthesis of tetramethoxy-p-benzoquinone. This compound was synthesized following a

modified literature procedure.[54] Under an atmosphere of dinitrogen, a sodium methoxide solution was prepared by slowly adding sodium (0.930 g, 40.4 mmol) to MeOH (20 mL) cooled to −78 °C. After a complete reaction, the sodium methoxide solution was slowly added to a suspension of tetrachloro-*p*-benzoquinone (2.46 g, 10.0 mmol) in MeOH (5 mL). The resulting deep red reaction mixture was heated at 85 °C with stirring under a dinitrogen atmosphere for 6 h and then cooled to 25 °C. The resulting orange precipitate was collected by vacuum filtration, washed with deionized H_2O (50 mL), and dried with suction on the filter for 30 min. Further drying in vacuo for 16 h afforded the title compound as orange needles (1.42 g, 62%). ^{1}H NMR (500 MHz, $CDCl_3$, 298 K): δ 3.98 (s, 12H). $^{13}C\{^1H\}$ NMR (126 MHz, $CDCl_3$, 298 K): δ 180.47, 142.78, 61.38.

Synthesis of 2,5-dihydroxy-3,6-dimethoxy-p-benzoquinone ($H_2(^{OMe}L)$). This compound was synthesized following a modified literature procedure.[55] Tetramethoxy-*p*-benzoquinone (0.374 g, 1.64 mmol) was mixed with a 2 M solution of hydrochloric acid in H_2O (10 mL) and the resulting orange suspension was stirred at reflux under a dinitrogen atmosphere for 1 h. The reaction mixture was then cooled to 25 °C and the resulting purple solid was collected by vacuum filtration, washed with deionized H_2O (25 mL), and dried with suction on the filter for 1 h. The obtained solid was further dried in vacuo for 14 h to give $H_2(^{OMe}L)$ as a dark purple solid (0.225 g, 69%). UV-Vis-NIR absorption spectrum (MeCN, 298 K): 299 nm (ε = 14900 M^{-1} cm^{-1}), 491 nm (ε = 210 M^{-1} cm^{-1}). FT-IR (ATR, cm^{-1}): 3348 (m, broad), 3016 (w), 2966 (w), 2863 (w), 1643 (s), 1617 (s), 1531 (w), 1455 (m), 1444 (w), 1368 (w), 1264 (s), 1200 (m), 1069 (s), 1017 (s), 900 (w), 745 (m), 636 (s), 630 (s). ^{1}H NMR (500 MHz, DMSO-d_6, 298 K): δ 10.63 (s, 2H), 3.71 (s, 6H). $^{13}C\{^1H\}$ NMR (126 MHz, DMSO-d_6, 298 K): δ 135.27, 59.87.

Synthesis of 2,5-dihydroxy-3,6-dinitro-p-benzoquinone disodium salt ($Na_2(^{NO2}L)$). This

compound was synthesized following a modified literature procedure.[56] Sodium nitrite (5.02 g, 72.8 mmol) was dissolved in deionized H_2O (200 mL) to give a colorless solution. To this stirring solution, tetrachloro-*p*-benzoquinone (2.00 g, 8.13 mmol) was added in a single portion and the resulting orange suspension was heated at reflux for 2 h, during which an orange solution was formed. The solution was filtered while hot and slowly cooled to 25 °C. The solution was then cooled to 4 °C and left at that temperature for 12 h to afford orange crystalline needles. The orange needles were collected by vacuum filtration, washed with deionized H_2O (30 mL), and dried with suction on the filter for 20 min. Further drying in vacuo for 14 h afforded $Na_2(^{NO2}L)$ as orange crystalline needles (1.67 g, 75%). UV-Vis-NIR absorption spectrum (MeCN, 298 K): 299 nm, 315 nm (shoulder), 385 nm (shoulder). FT-IR (ATR, cm^{-1}): 3537 (m), 3435 (m), 1682 (w), 1620 (s), 1596 (s), 1541 (m), 1434 (m), 1288 (m), 1239 (s, broad), 1020 (m), 821 (w), 773 (m), 680 (s), 668 (s). $^{13}C\{^1H\}$ NMR (126 MHz, DMSO-d_6, 298 K): δ 168.61, 133.07.

Synthesis of 2,5-dihydroxy-3,6-dimethylsulfonium-p-benzoquinone diylide bis(acetic acid) ((^{SMe2}L)·2.0AcOH). This compound was synthesized following a modified literature procedure.[57] 2,5-Dihydroxy-*p*-benzoquinone (1.97 g, 14.1 mmol) was mixed with dimethylsulfoxide (DMSO; 24 mL) and acetic anhydride (12 mL). The resulting brown suspension was heated to 60 °C and left at that temperature for 1.5 h, during which a yellow precipitate was formed. The reaction mixture was then cooled to 25 °C, the yellow solid was collected by vacuum filtration, washed with DMSO (5 mL) and acetic acid (10 mL), and dried with suction on the filter for 1 h. Recrystallization from acetic acid (200 mL) and drying in vacuo for 12 h afforded (^{SMe2}L)·2.0AcOH as yellow crystalline needles (1.22 g, 23%). UV-Vis-NIR absorption spectrum (MeCN, 298 K): 284 nm, 303 nm (shoulder), 369 nm. FT-IR (ATR, cm^{-1}): 2831 (w, broad), 2564

(w), 2468 (w), 1764 (w), 1701 (s), 1656 (m, broad), 1611 (w), 1530 (s, broad), 1420 (m), 1390 (s), 1346 (m), 1316 (m), 1270 (s), 1241 (s), 1040 (m), 1021 (m), 1012 (m), 965 (m), 943 (m, broad), 929 (m), 880 (m), 837 (m), 677 (w), 611 (s). ^{1}H NMR (500 MHz, D_2O, 298 K): δ 2.99 (s, 12H), 2.00 (s, 6H). $^{13}C\{^{1}H\}$ NMR (126 MHz, D_2O, 298 K): δ 176.67, 176.11, 93.37, 24.43, 20.29.

7.5.2 Supplementary Scheme

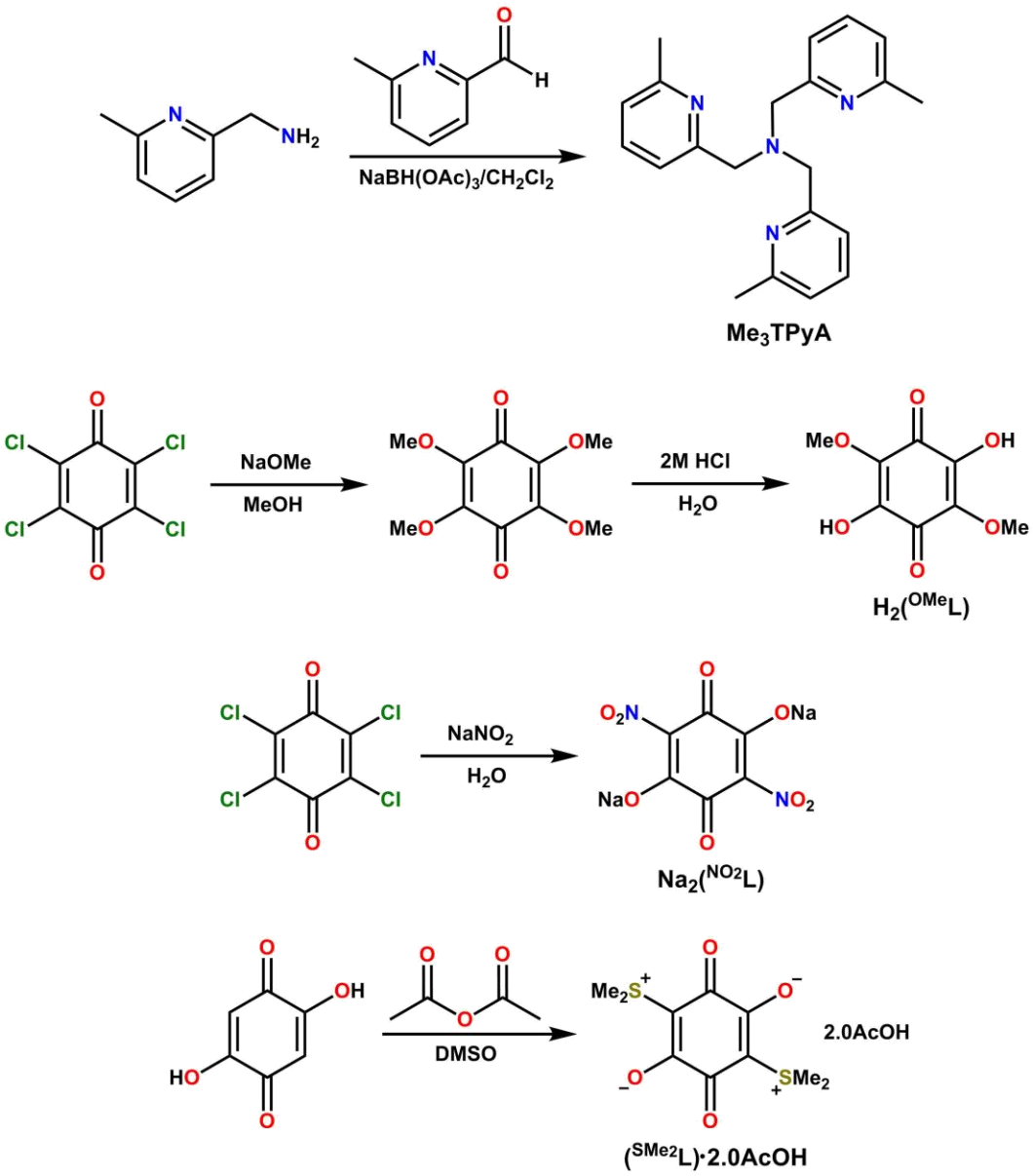

Scheme 7.2 Syntheses of ligands.

7.5.3 Supplementary Figures

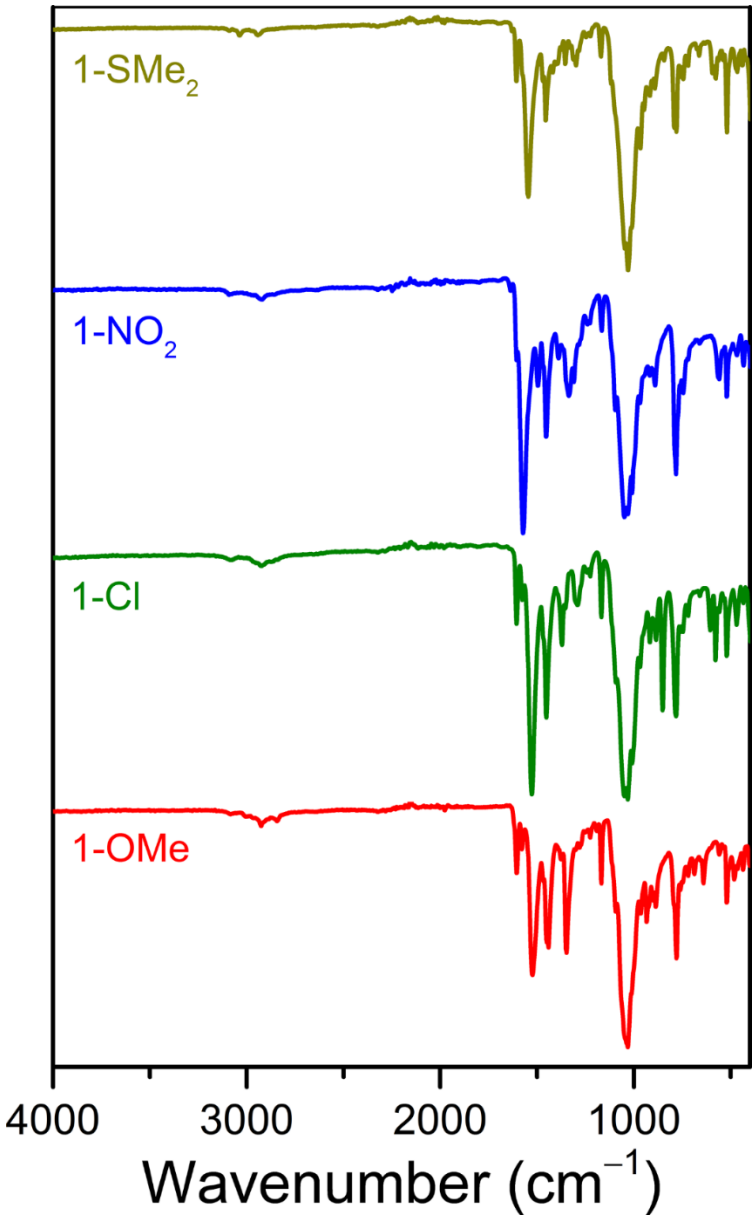

Figure 7.9 Stacked FT-IR spectra for solid samples of **1-R** at 298 K; R = OMe (red), Cl (green), NO_2 (blue), SMe_2 (gold).

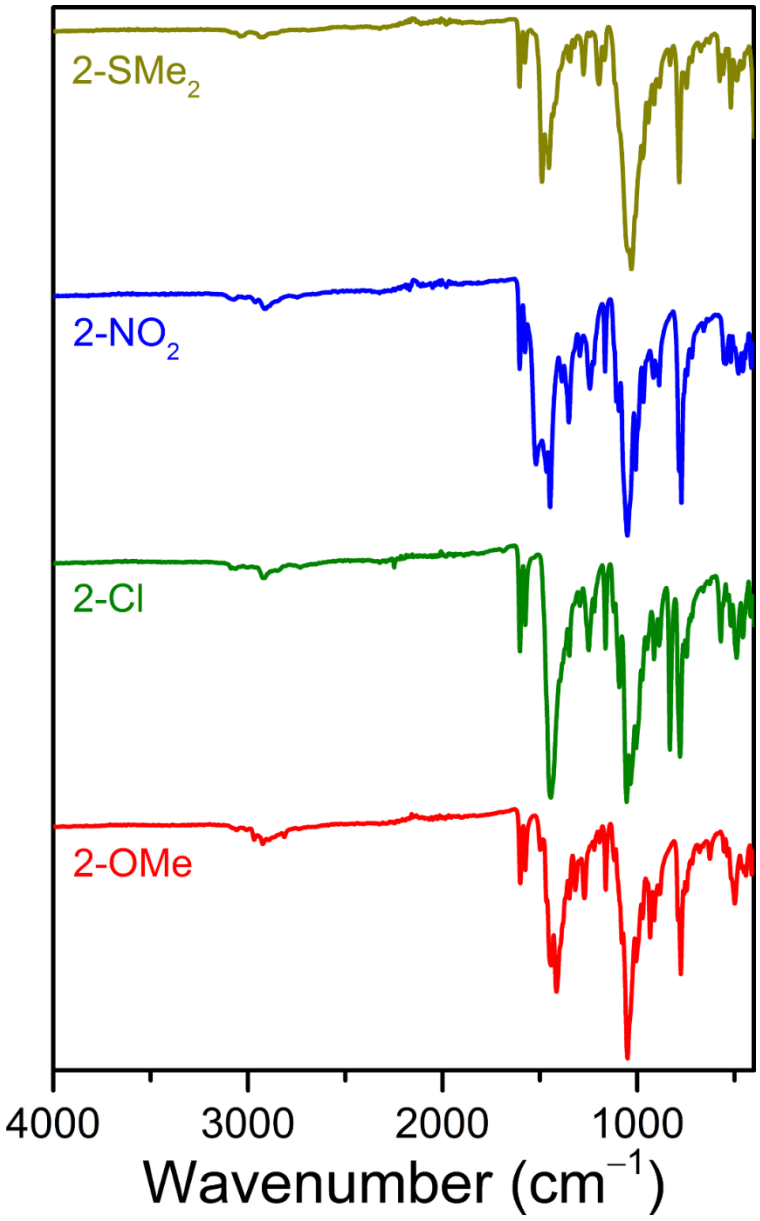

Figure 7.10 Stacked FT-IR spectra for solid samples of **2-R** at 298 K; R = OMe (red), Cl (green), NO_2 (blue), SMe_2 (gold).

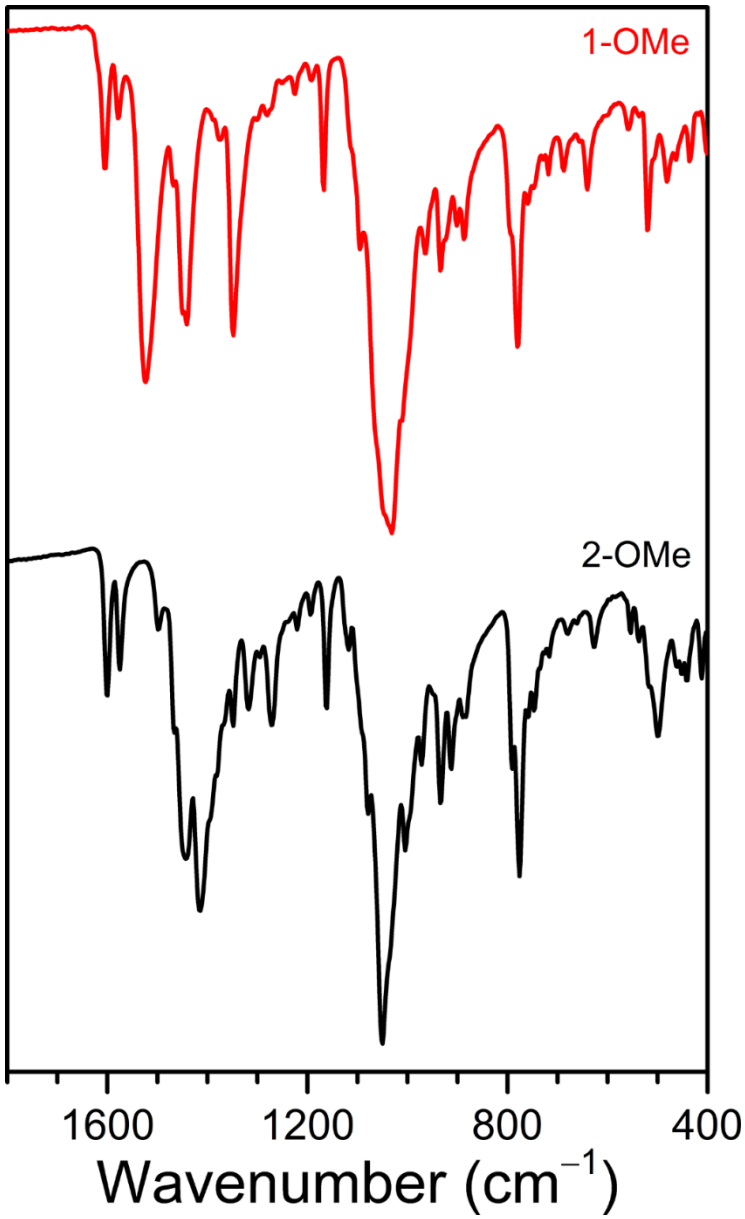

Figure 7.11 Stacked FT-IR spectra for solid samples of **1-OMe** (red) and **2-OMe** (black) at 298 K, highlighting the lower energy range 400–1800 cm^{-1}.

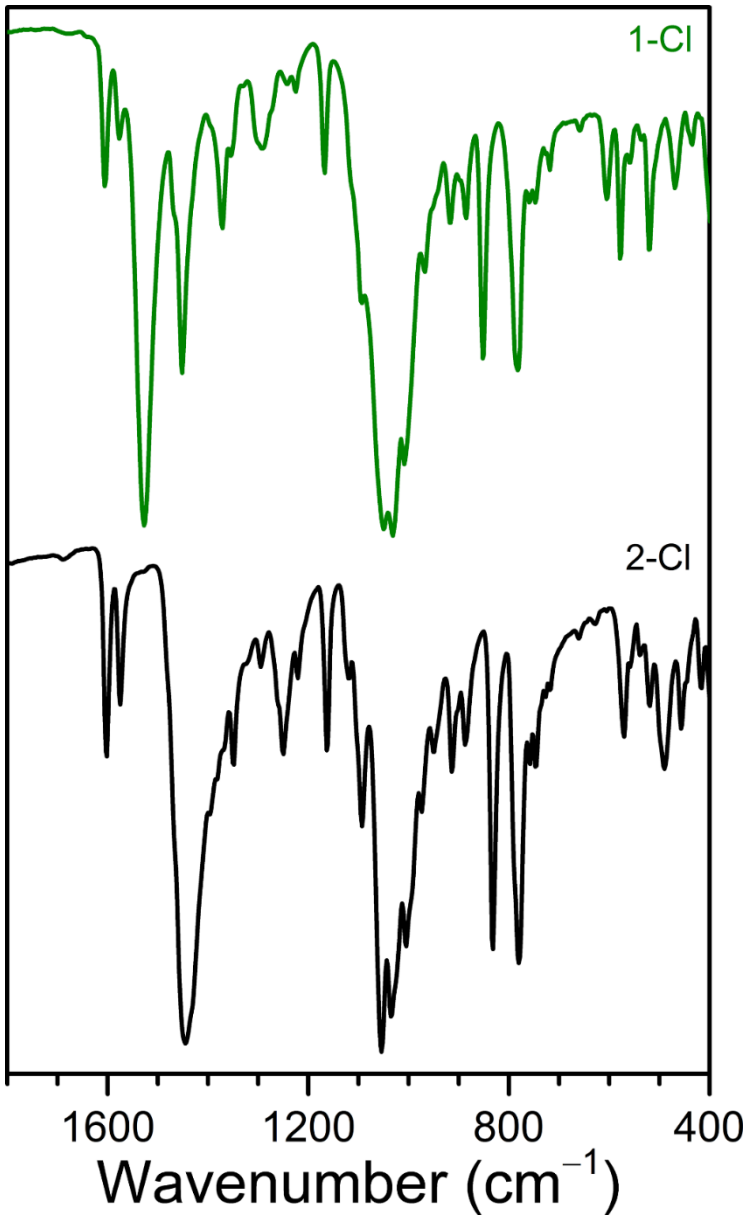

Figure 7.12 Stacked FT-IR spectra for solid samples of **1-Cl** (green) and **2-Cl** (black) at 298 K, highlighting the lower energy range 400–1800 cm^{-1}.

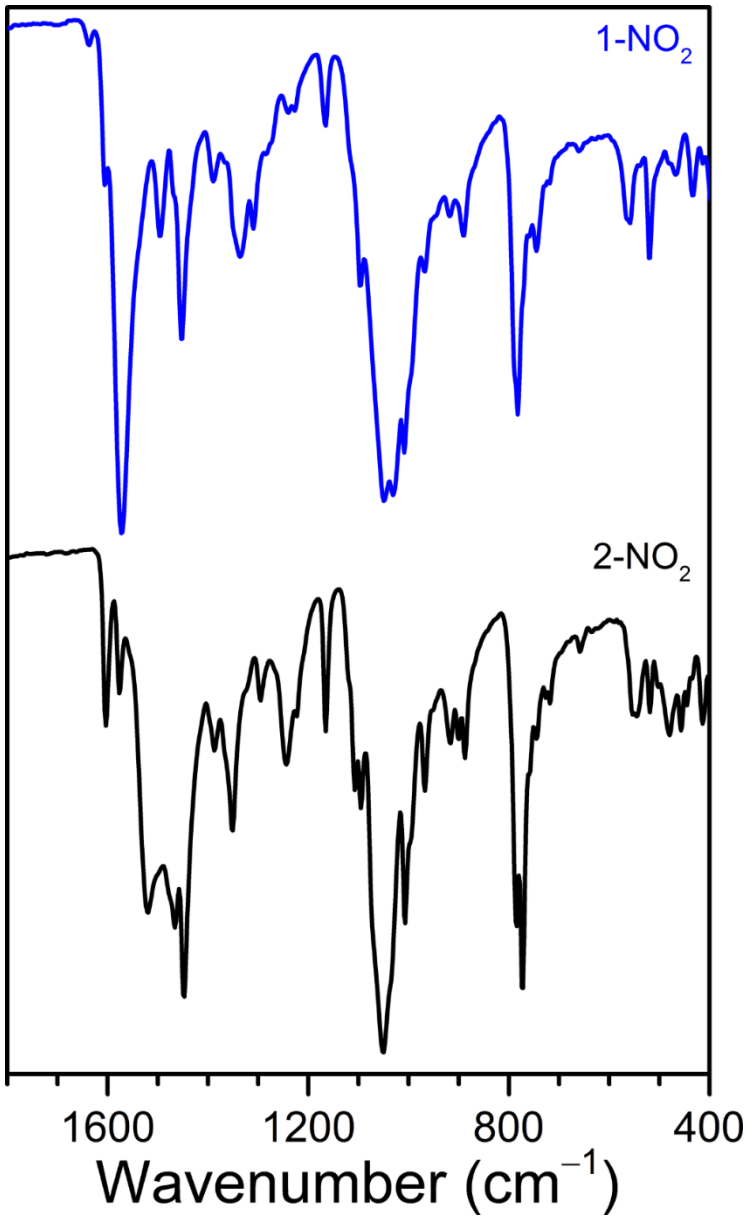

Figure 7.13 Stacked FT-IR spectra for solid samples of **1-NO$_2$** (blue) and **2-NO$_2$** (black) at 298 K, highlighting the lower energy range 400–1800 cm^{-1}.

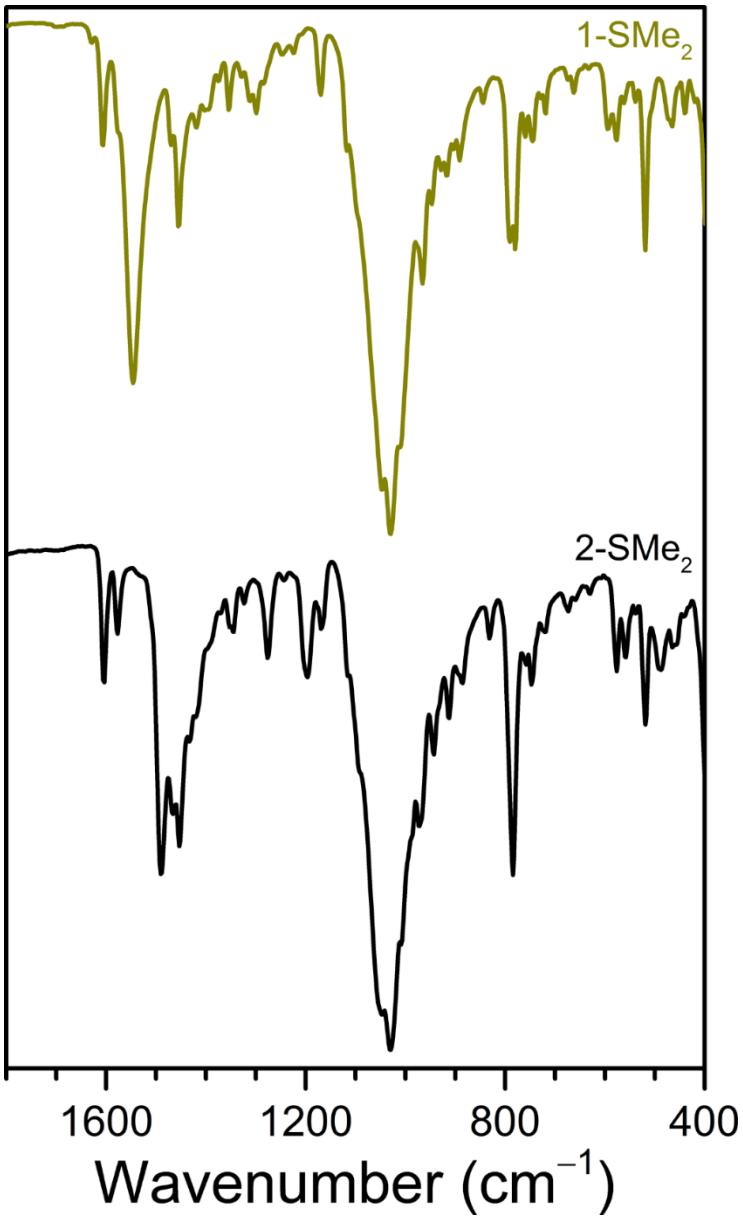

Figure 7.14 Stacked FT-IR spectra for solid samples of **1-SMe$_2$** (gold) and **2-SMe$_2$** (black) at 298 K, highlighting the lower energy range 400–1800 cm^{-1}.

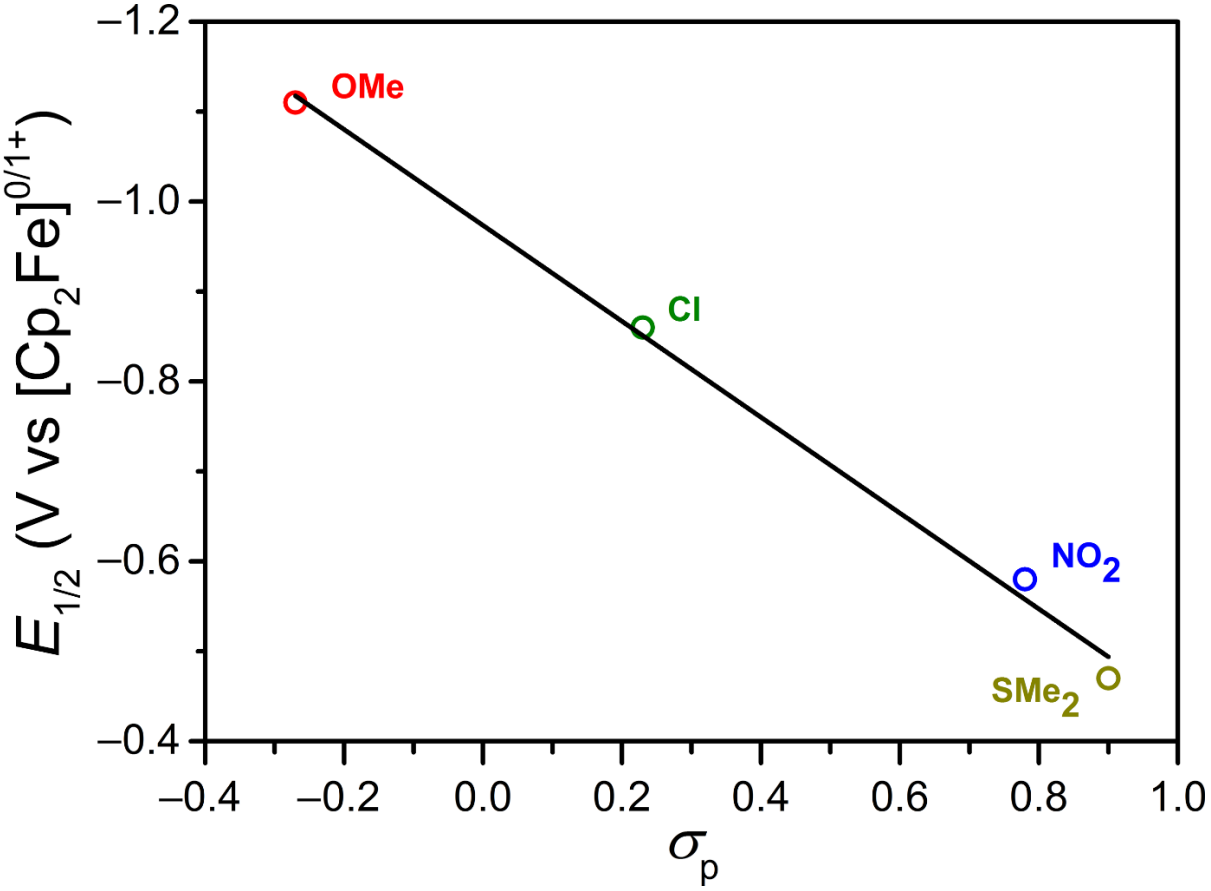

Figure 7.15 Plot of $E_{1/2}$ for the ligand-based redox process $^{R}L^{x-/(x+1)-}\bullet$ (x = 2: R = OMe, Cl, NO_2; x = 0: R = SMe_2) against the Hammett substituent constant σ_p for **1-R** (R = OMe, Cl, NO_2, SMe_2). The cyclic voltammograms, from which the values of $E_{1/2}$ are derived, were collected at 298 K for MeCN solutions of **1-R** (R = OMe, Cl, NO_2, SMe_2) with 100 mM (Bu_4N)(PF_6) as a supporting electrolyte, using a scan rate of 100 mV s^{-1} (R = OMe, Cl, NO_2) or 25 mV s^{-1} (R = SMe_2). The black line denotes a linear fit to the data, giving R^2 = 0.993.

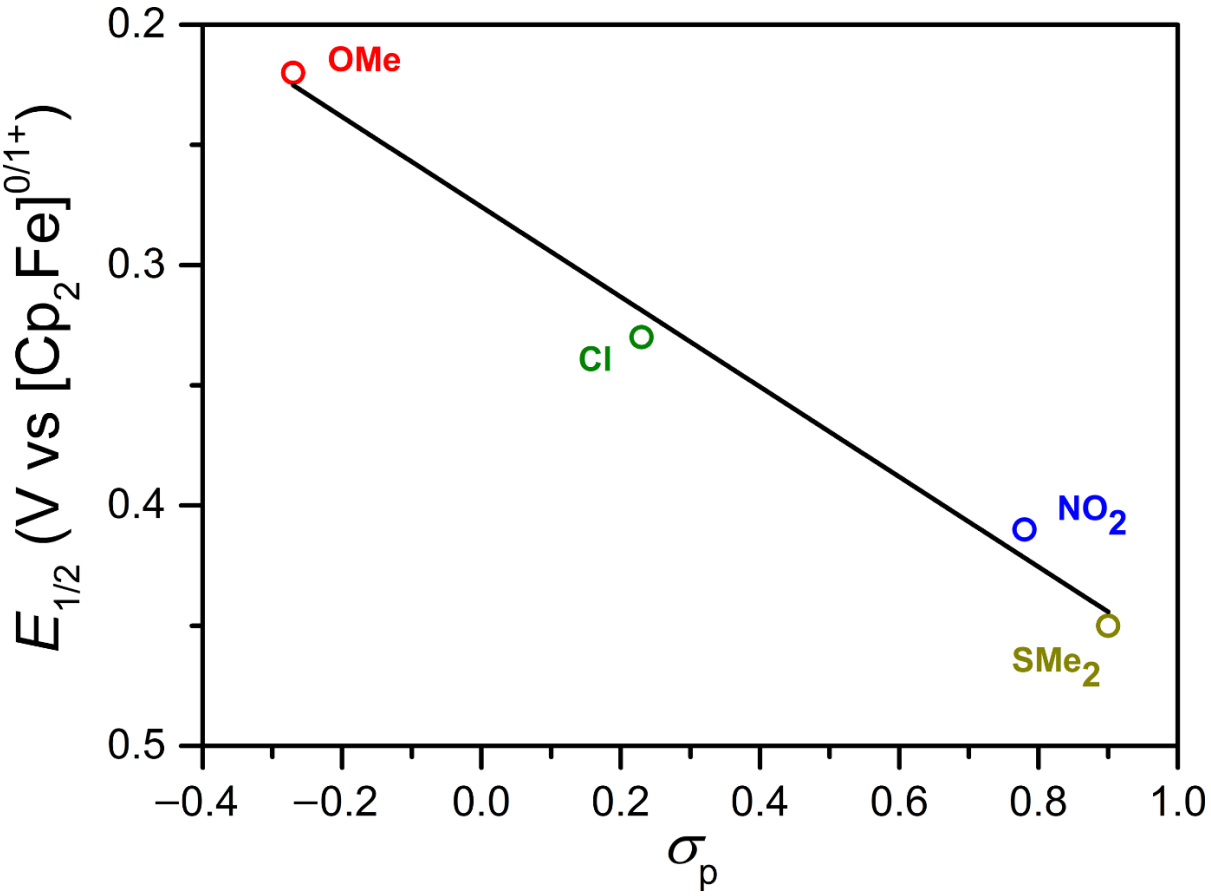

Figure 7.16 Plot of $E_{1/2}$ for the metal-based redox process $Fe^{II}Fe^{II}/Fe^{II}Fe^{III}$ against the Hammett substituent constant σ_p for **1-R** (R = OMe, Cl, NO_2, SMe_2). The cyclic voltammograms, from which the values of $E_{1/2}$ are derived, were collected at 298 K for MeCN solutions of **1-R** (R = OMe, Cl, NO_2, SMe_2) with 100 mM $(Bu_4N)(PF_6)$ as a supporting electrolyte, using a scan rate of 100 mV s^{-1} (R = OMe, Cl, NO_2) or 25 mV s^{-1} (R = SMe_2). The black line denotes a linear fit to the data, giving $R^2 = 0.984$.

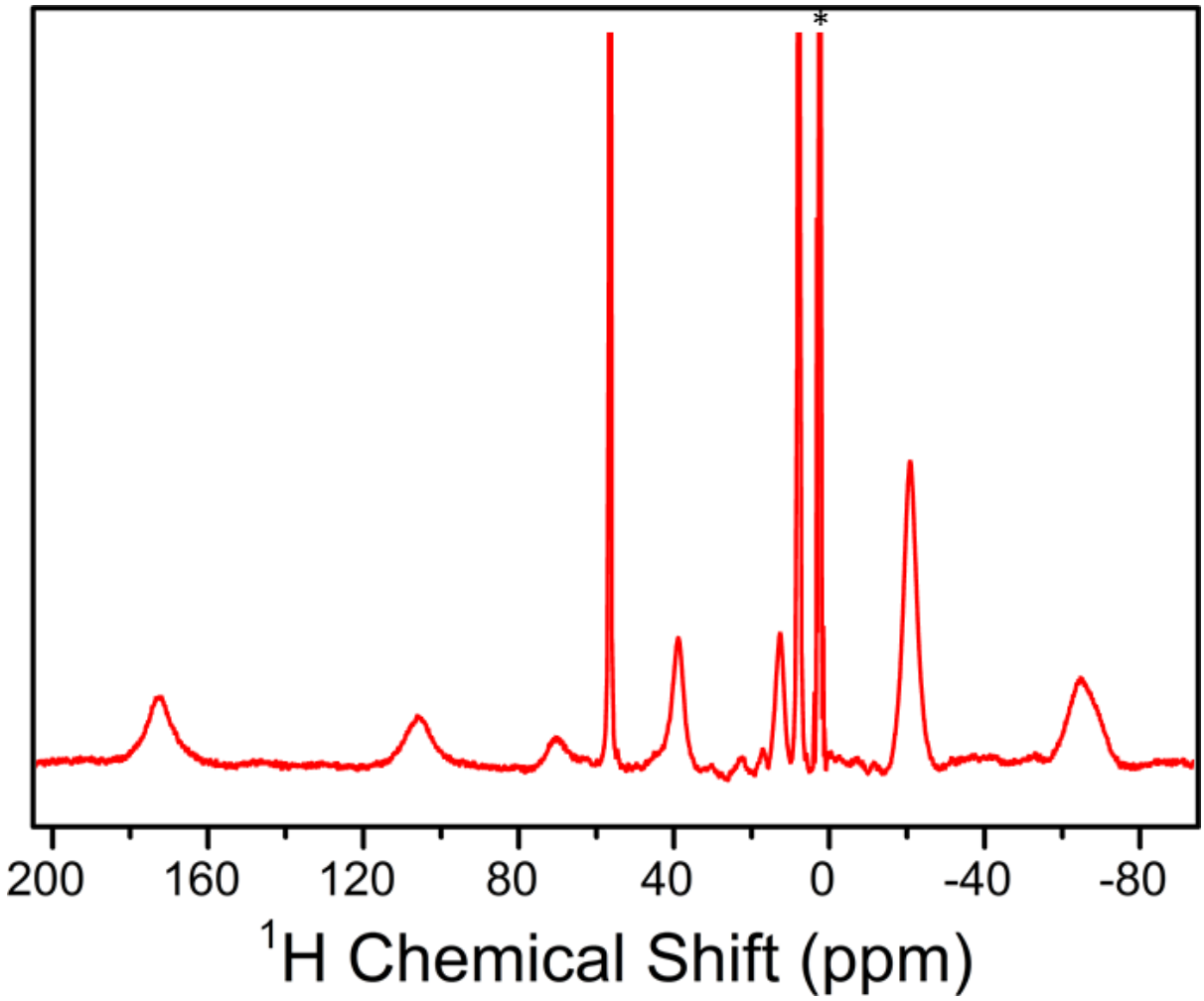

Figure 7.17 ^{1}H NMR spectrum for **1-OMe** in MeCN-d_3 at 295 K. The asterisk denotes the residual proton signal from the deuterated solvent at 1.94 ppm.

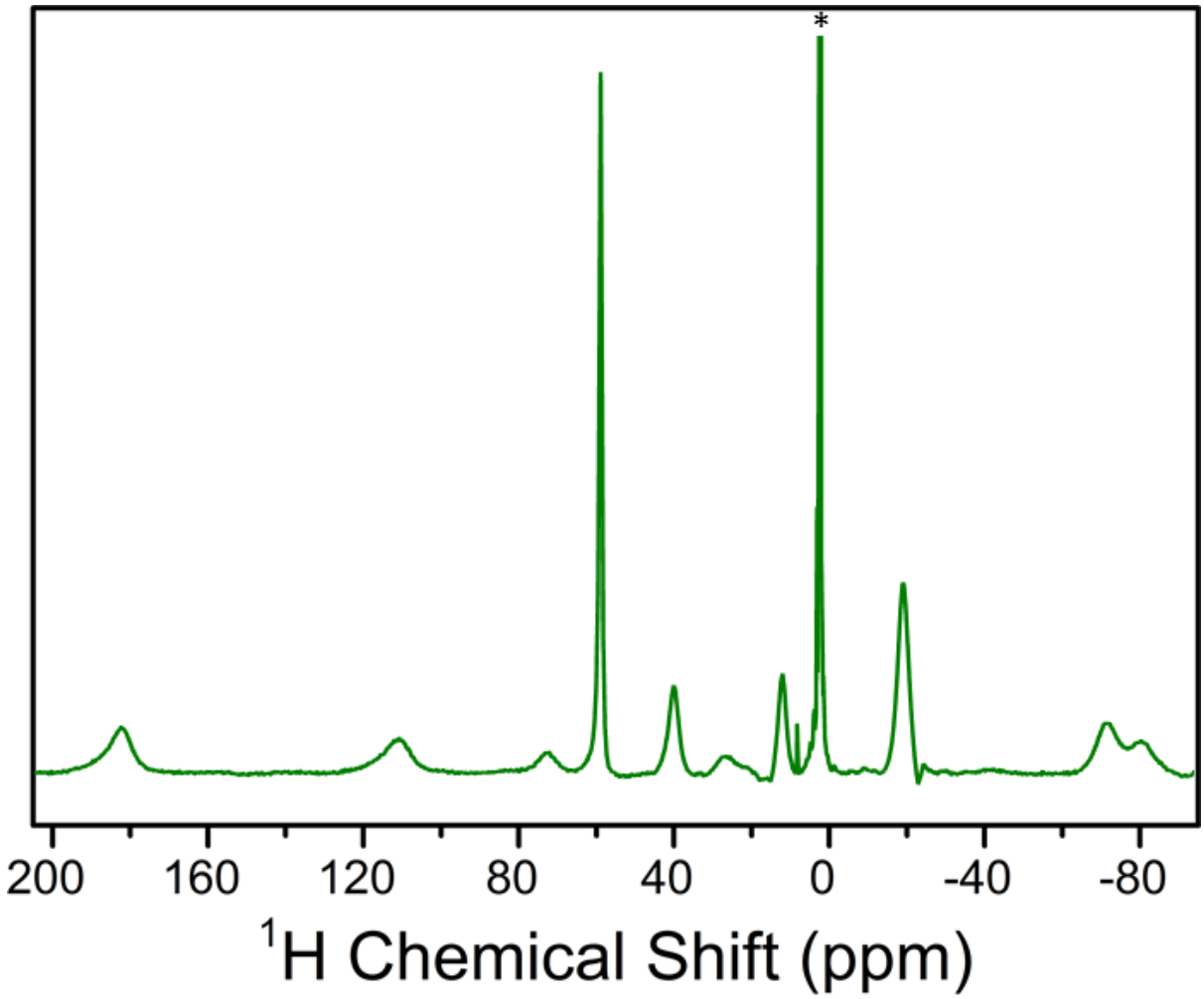

Figure 7.18 ^{1}H NMR spectrum for **1-Cl** in MeCN-d_3 at 295 K. The asterisk denotes the residual proton signal from the deuterated solvent at 1.94 ppm.

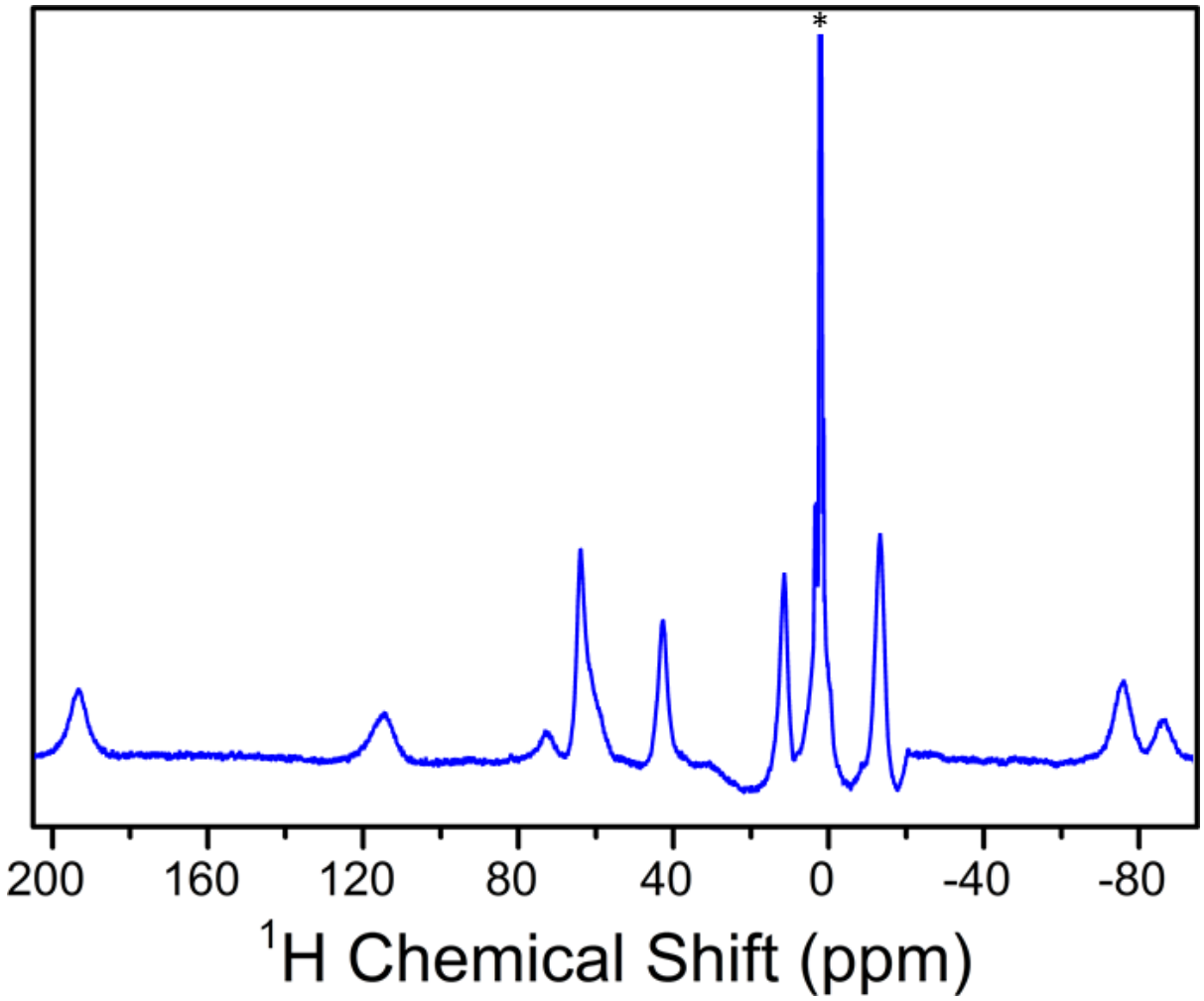

Figure 7.19 ^{1}H NMR spectrum for **1-NO$_2$** in MeCN-d_3 at 295 K. The asterisk denotes the residual proton signal from the deuterated solvent at 1.94 ppm.

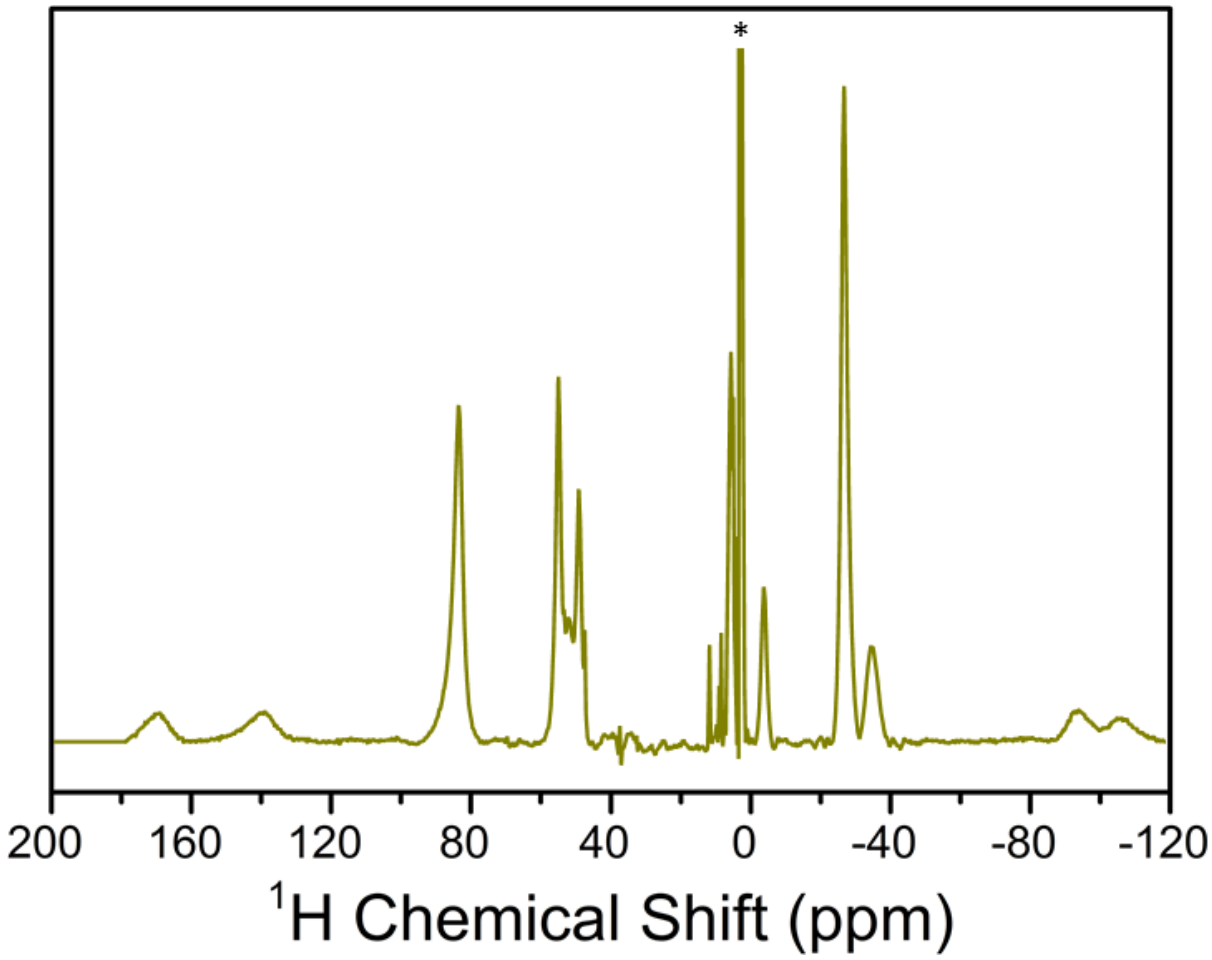

Figure 7.20 ^{1}H NMR spectrum for **1-SMe$_2$** in MeCN-d_3 at 295 K. The asterisk denotes the residual proton signal from the deuterated solvent at 1.94 ppm.

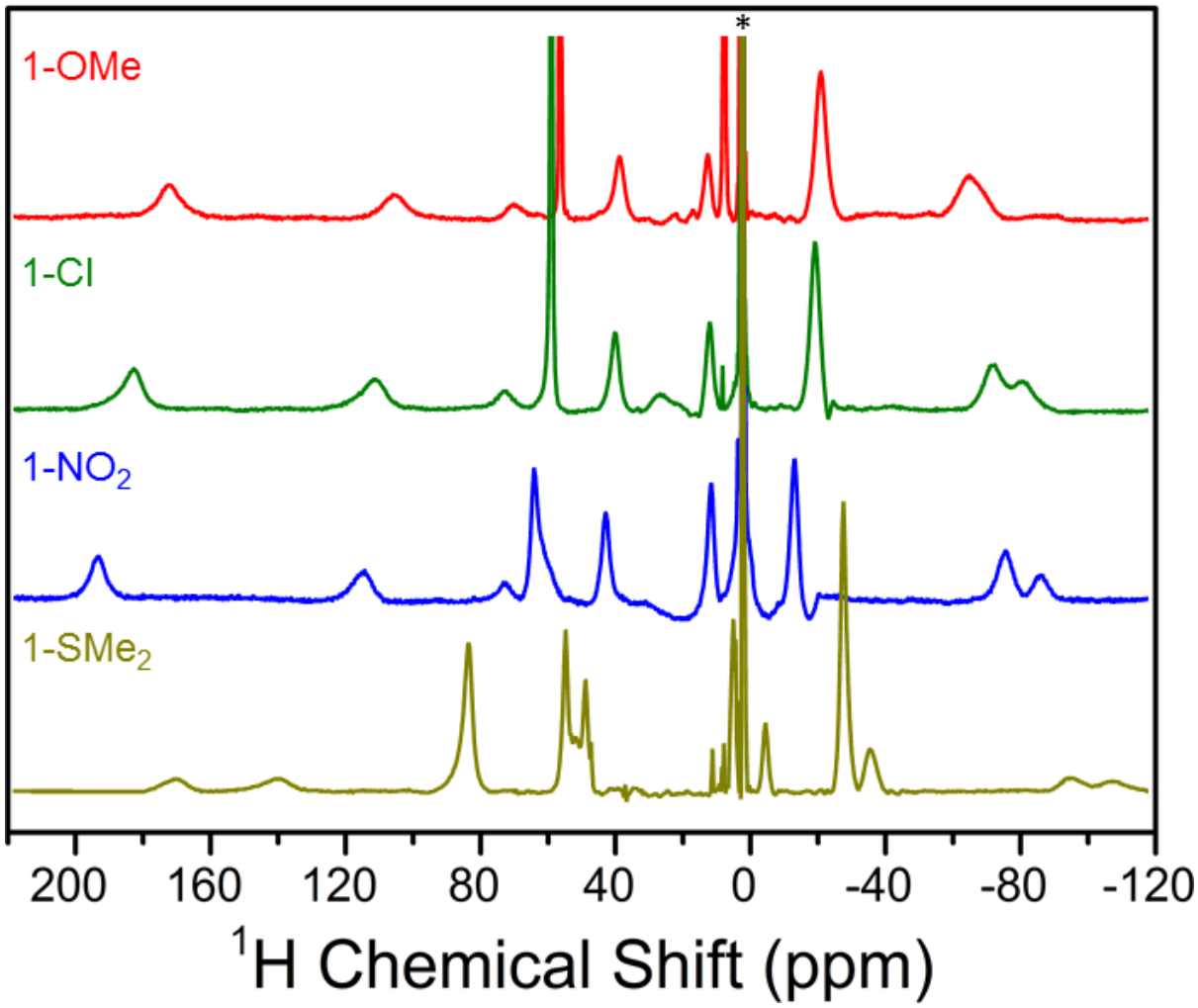

Figure 7.21 Stacked ^{1}H NMR spectra for **1-R** in MeCN-d_3 at 295 K; R = OMe (red), Cl (green), NO_2 (blue), SMe_2 (gold). The asterisk denotes the residual proton signal from the deuterated solvent at 1.94 ppm.

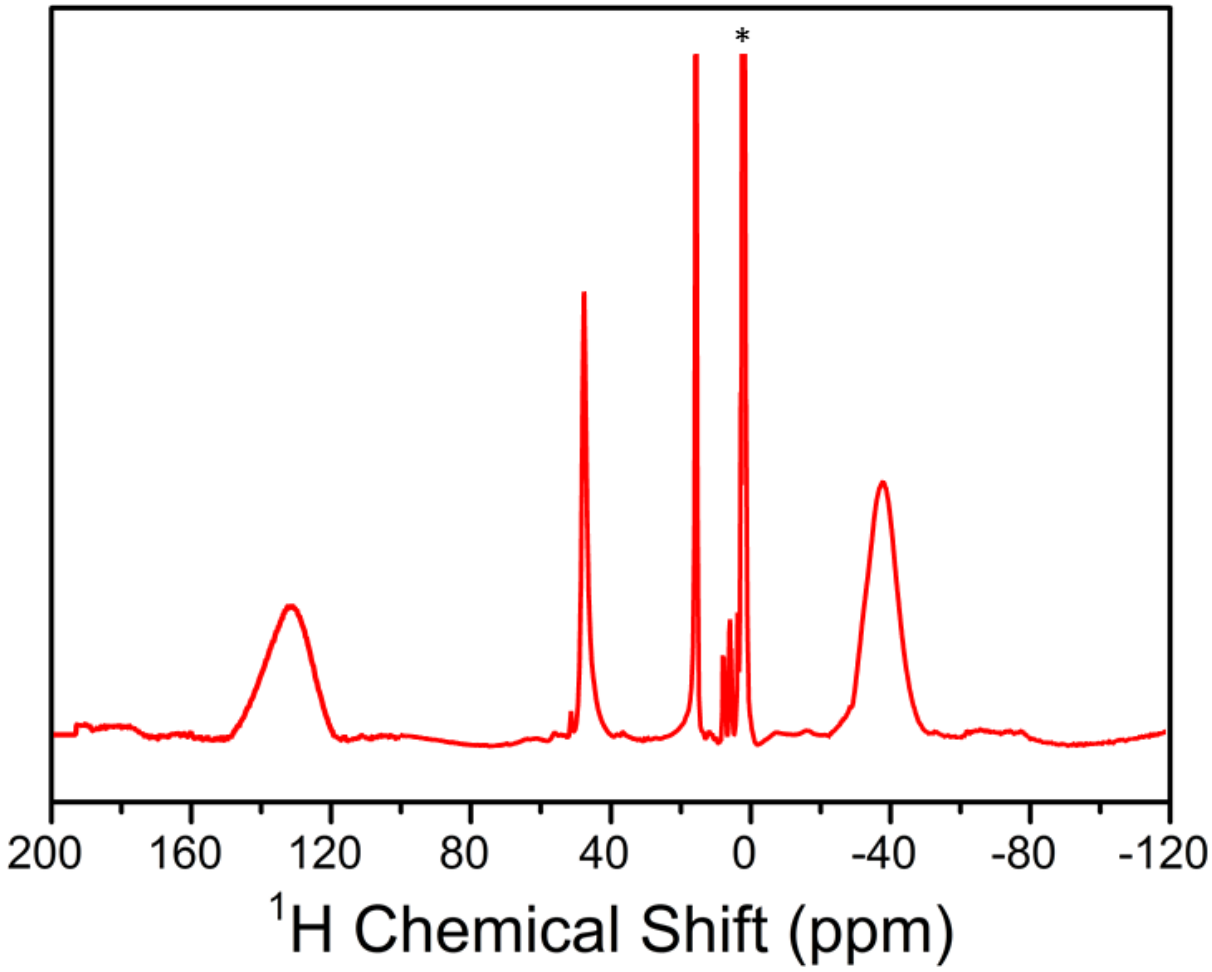

Figure 7.22 ^{1}H NMR spectrum for **2-OMe** in MeCN-d_3 at 295 K. The asterisk denotes the residual proton signal from the deuterated solvent at 1.94 ppm.

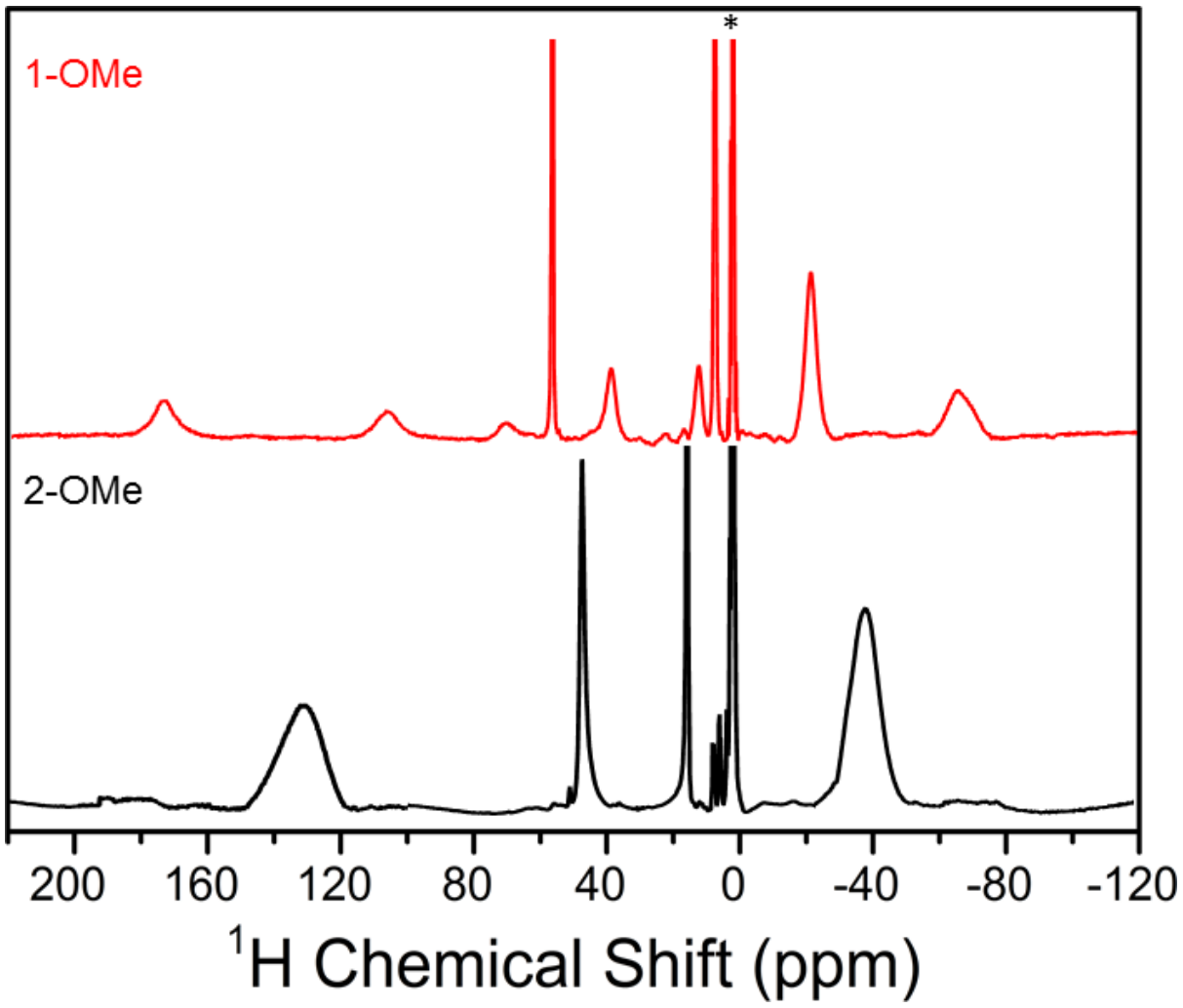

Figure 7.23 Stacked ^{1}H NMR spectra for **1-OMe** (red) and **2-OMe** (black) in MeCN-d_3 at 295 K. The asterisk denotes the residual proton signal from the deuterated solvent at 1.94 ppm.

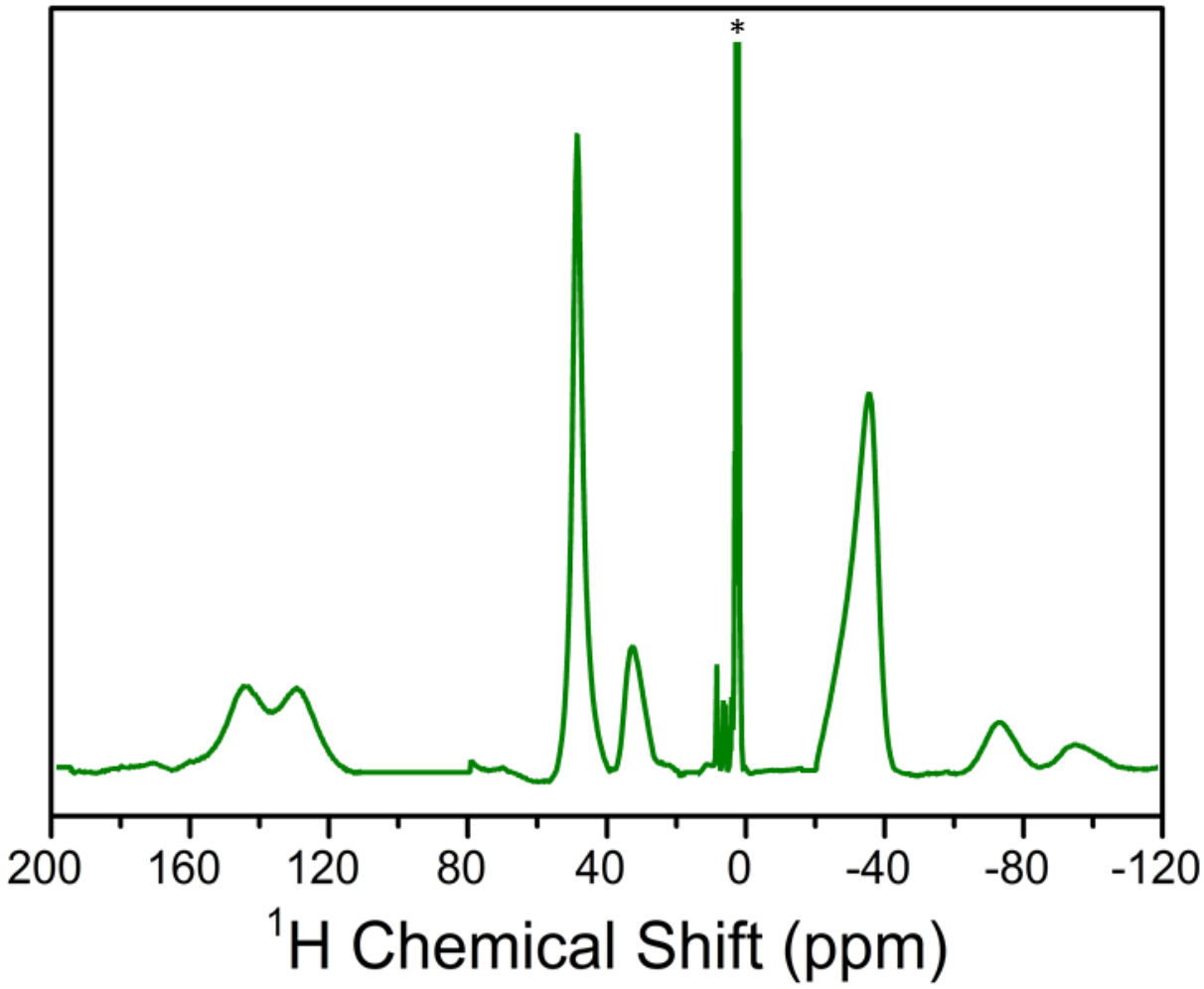

Figure 7.24 ^{1}H NMR spectrum for **2-Cl** in MeCN-d_3 at 295 K. The asterisk denotes the residual proton signal from the deuterated solvent at 1.94 ppm.

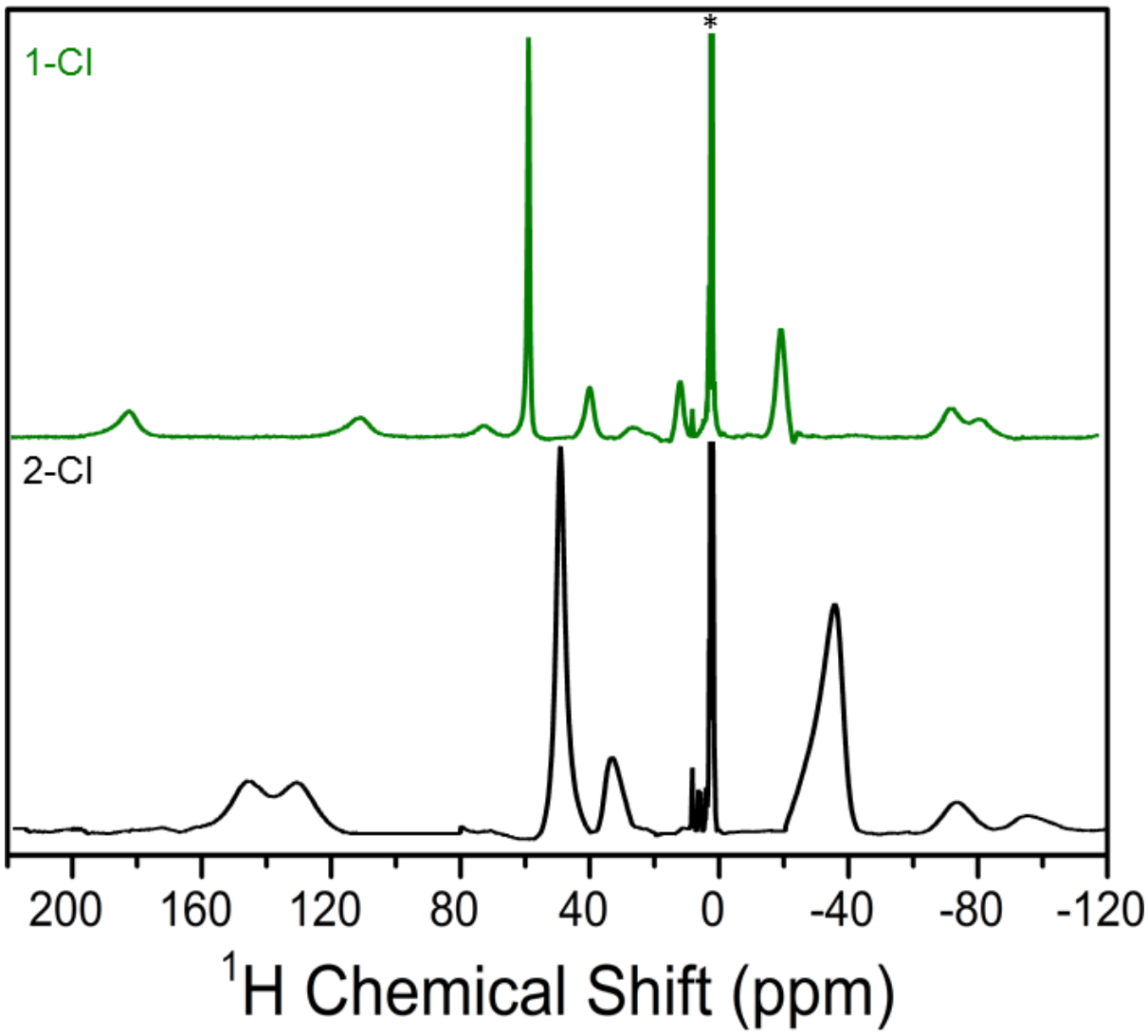

Figure 7.25 Stacked ^{1}H NMR spectra for **1-Cl** (green) and **2-Cl** (black) in MeCN-d_3 at 295 K. The asterisk denotes the residual proton signal from the deuterated solvent at 1.94 ppm.

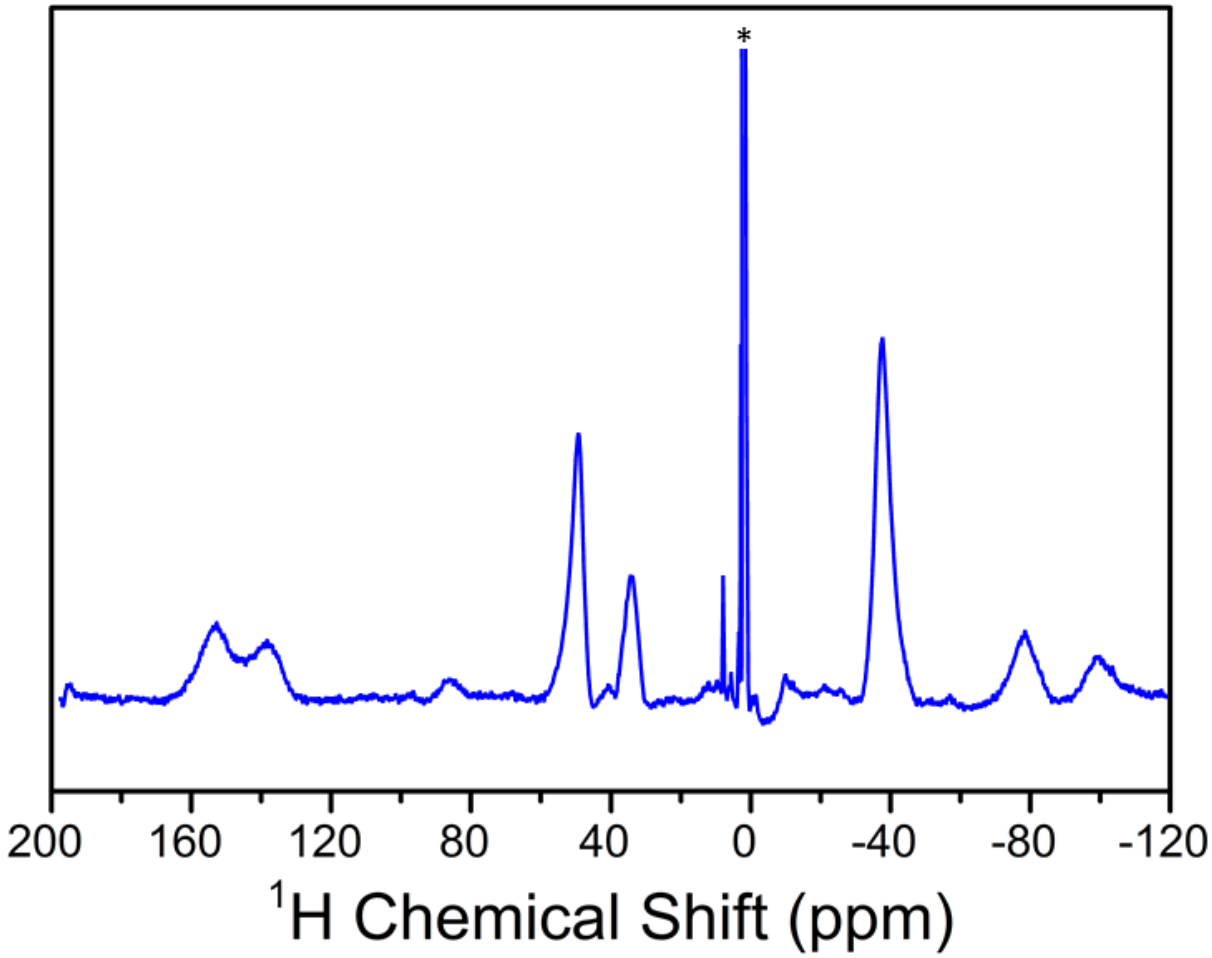

Figure 7.26 ^{1}H NMR spectrum for **2-NO$_2$** in MeCN-d_3 at 295 K. The asterisk denotes the residual proton signal from the deuterated solvent at 1.94 ppm.

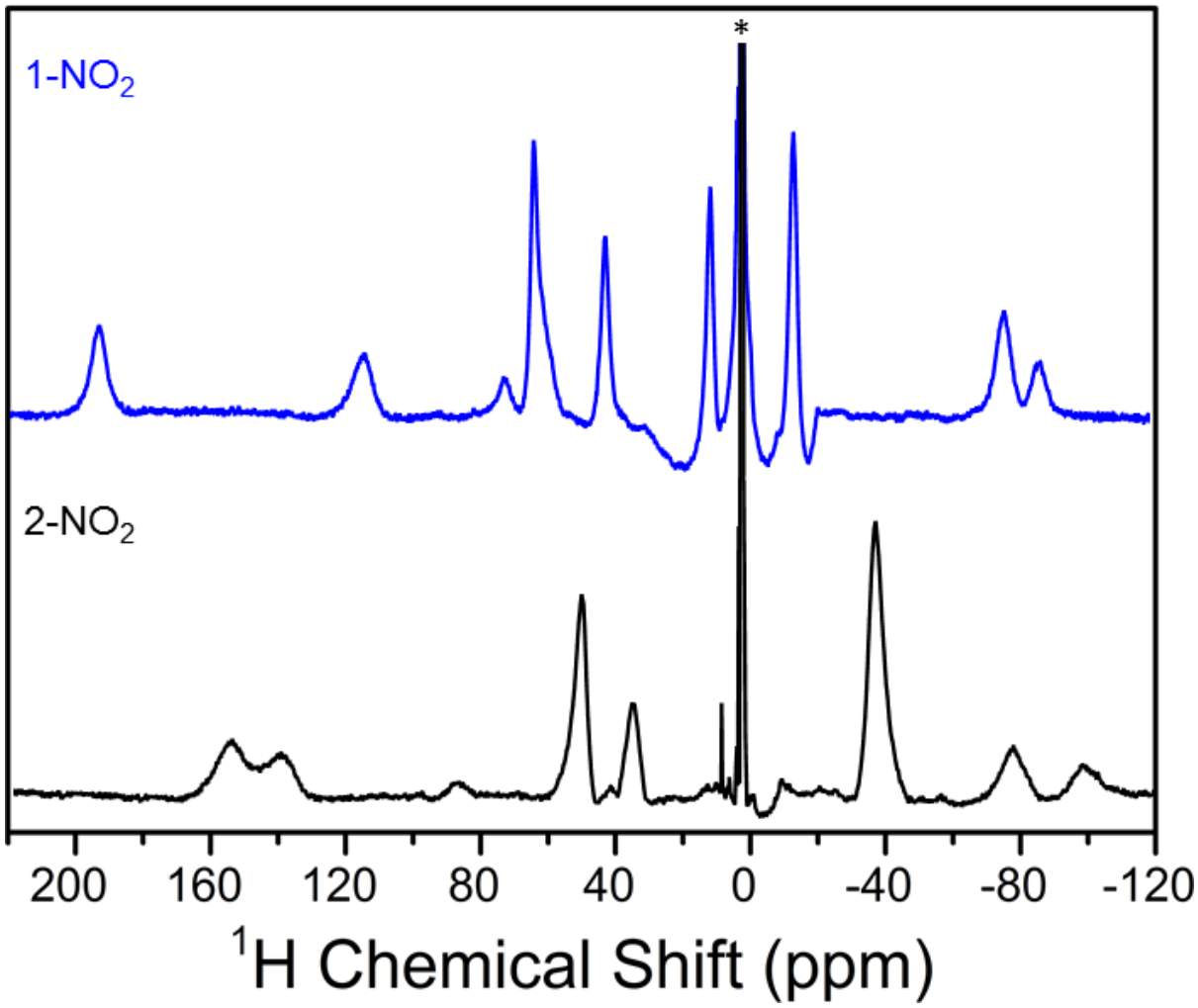

Figure 7.27 Stacked ^{1}H NMR spectra for **1-NO$_2$** (blue) and **2-NO$_2$** (black) in MeCN-d_3 at 295 K. The asterisk denotes the residual proton signal from the deuterated solvent at 1.94 ppm.

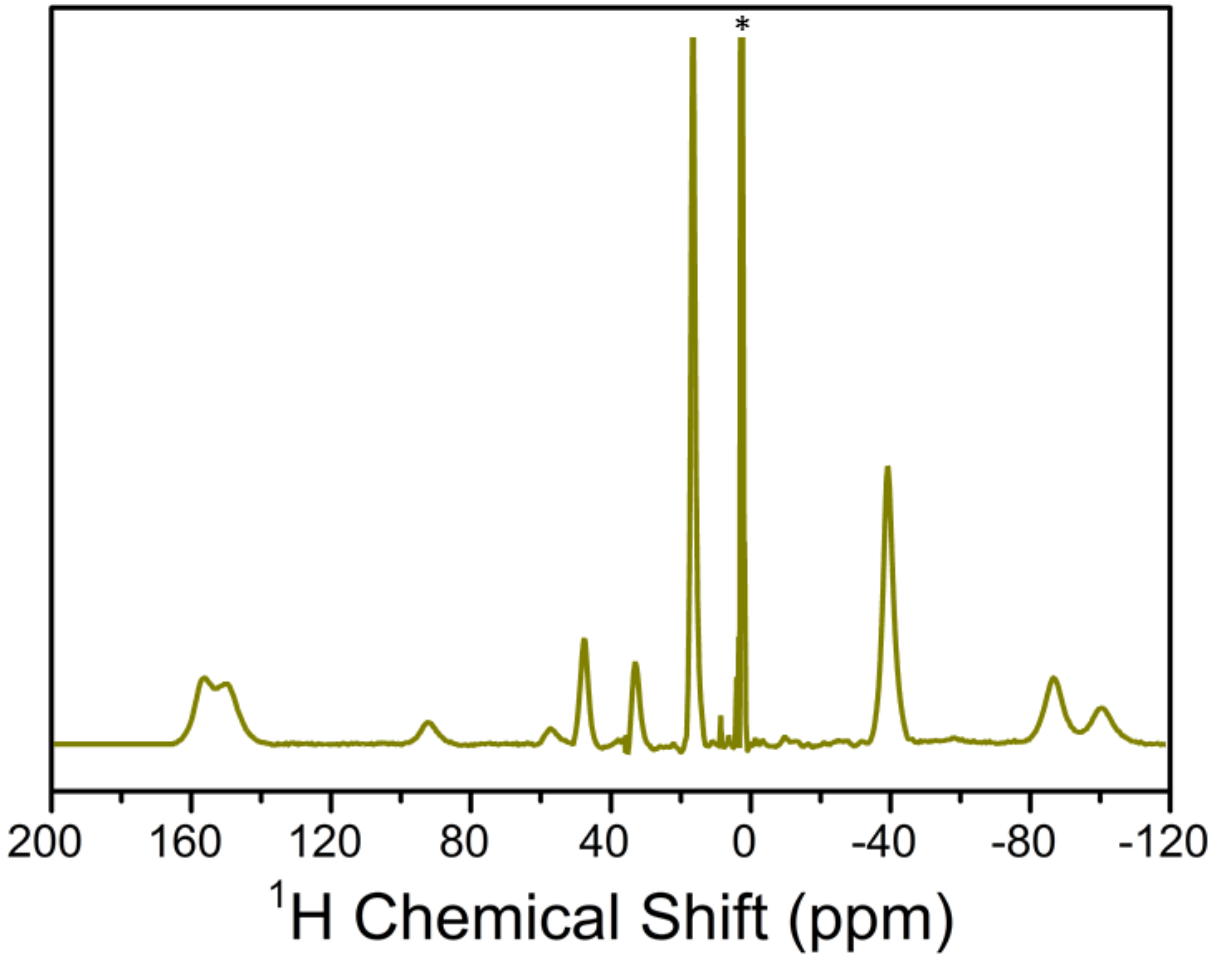

Figure 7.28 ^{1}H NMR spectrum for **2-SMe$_2$** in MeCN-d_3 at 295 K. The asterisk denotes the residual proton signal from the deuterated solvent at 1.94 ppm.

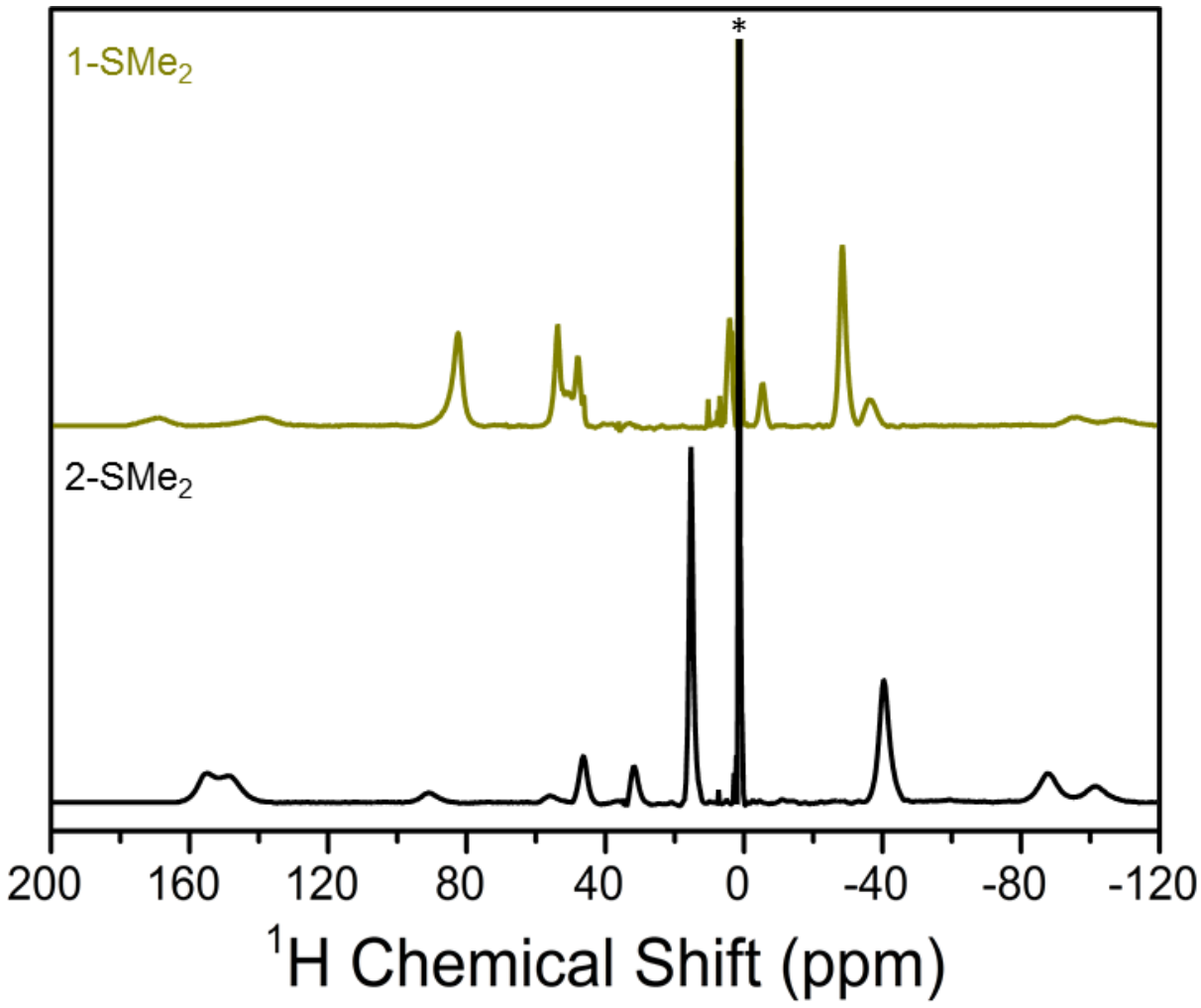

Figure 7.29 Stacked ^{1}H NMR spectra for **1-SMe$_2$** (gold) and **2-SMe$_2$** (black) in MeCN-d_3 at 295 K. The asterisk denotes the residual proton signal from the deuterated solvent at 1.94 ppm.

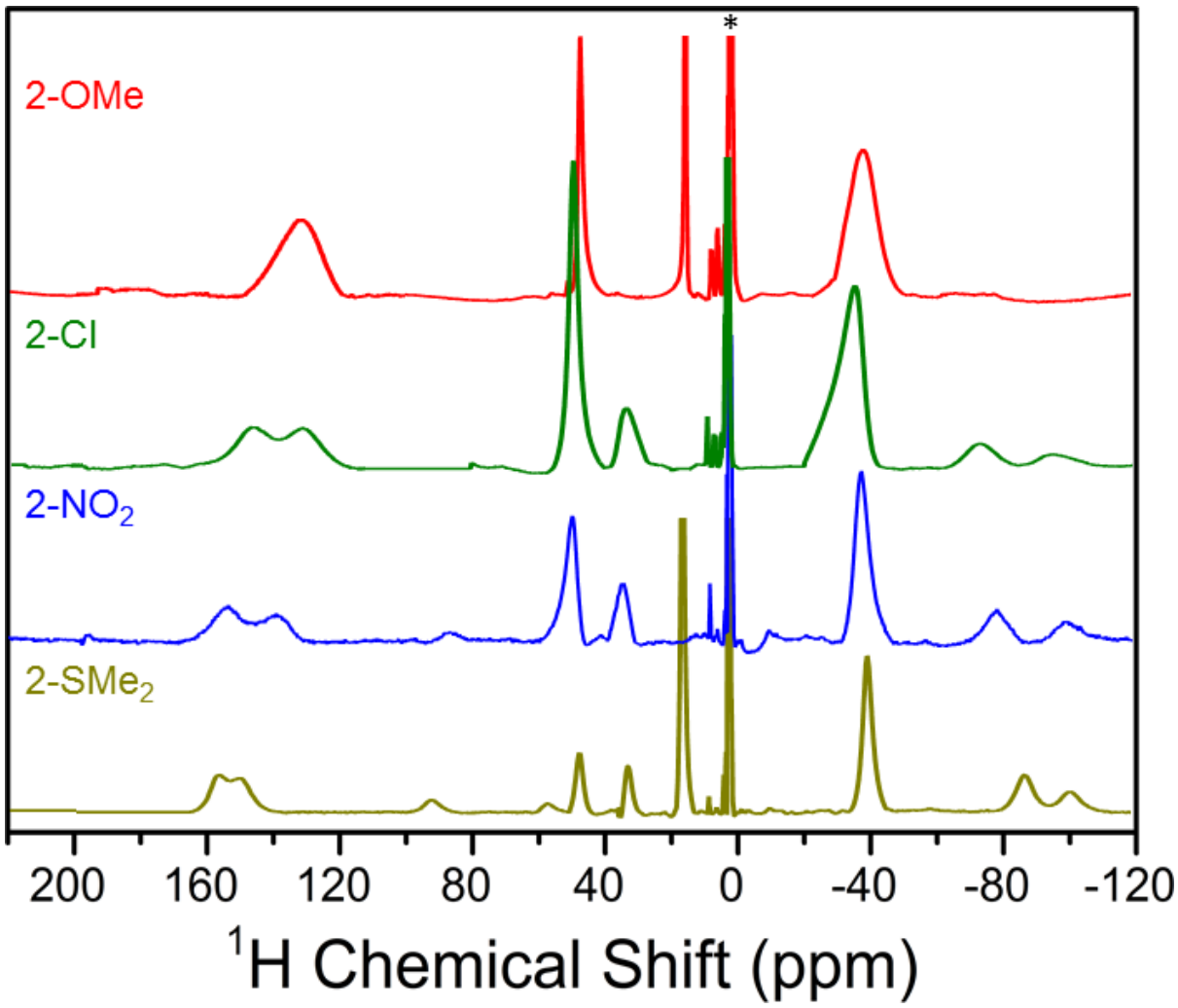

Figure 7.30 Stacked ^{1}H NMR spectra for **2-R** in MeCN-d_3 at 295 K; R = OMe (red), Cl (green), NO_2 (blue), SMe_2 (gold). The asterisk denotes the residual proton signal from the deuterated solvent at 1.94 ppm.

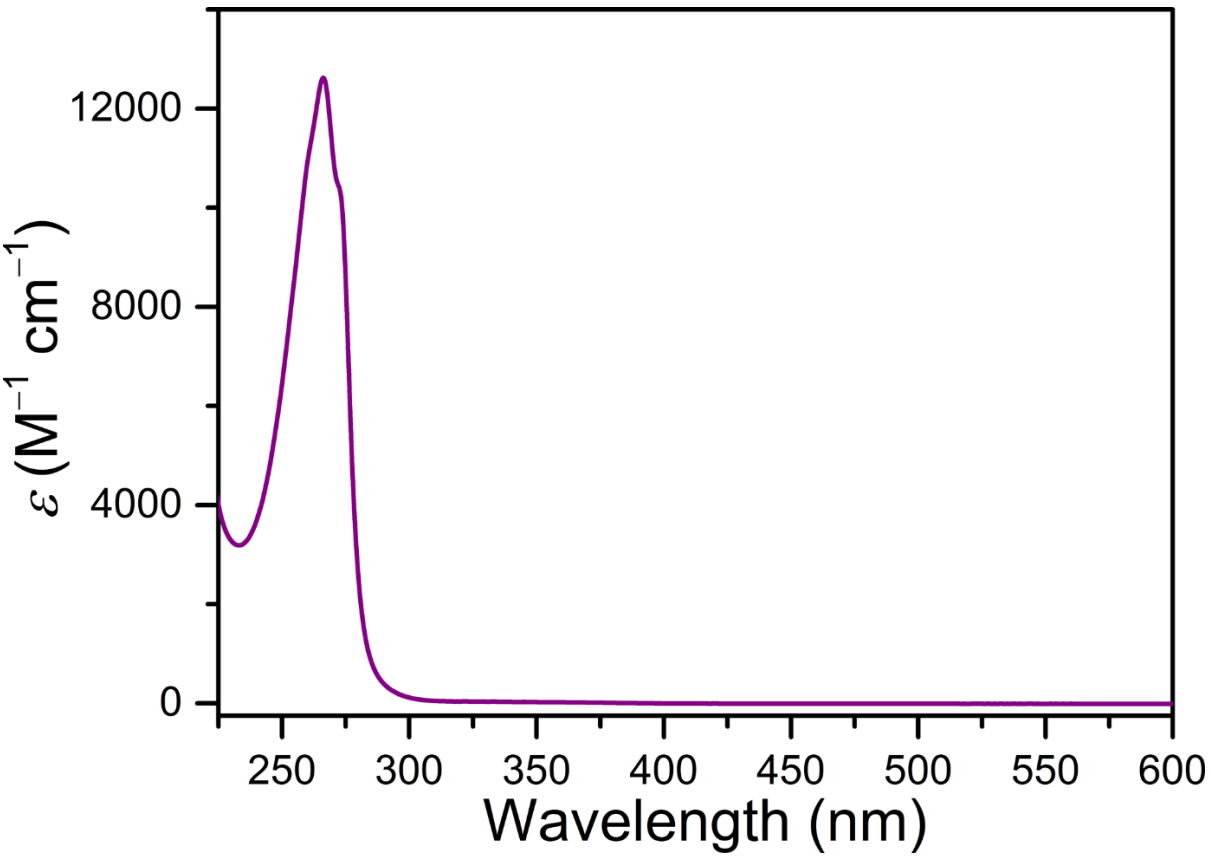

Figure 7.31 UV-Vis absorption spectrum for Me_3TPyA in MeCN at 298 K. Note that the molar absorptivity (ε) is plotted against wavelength.

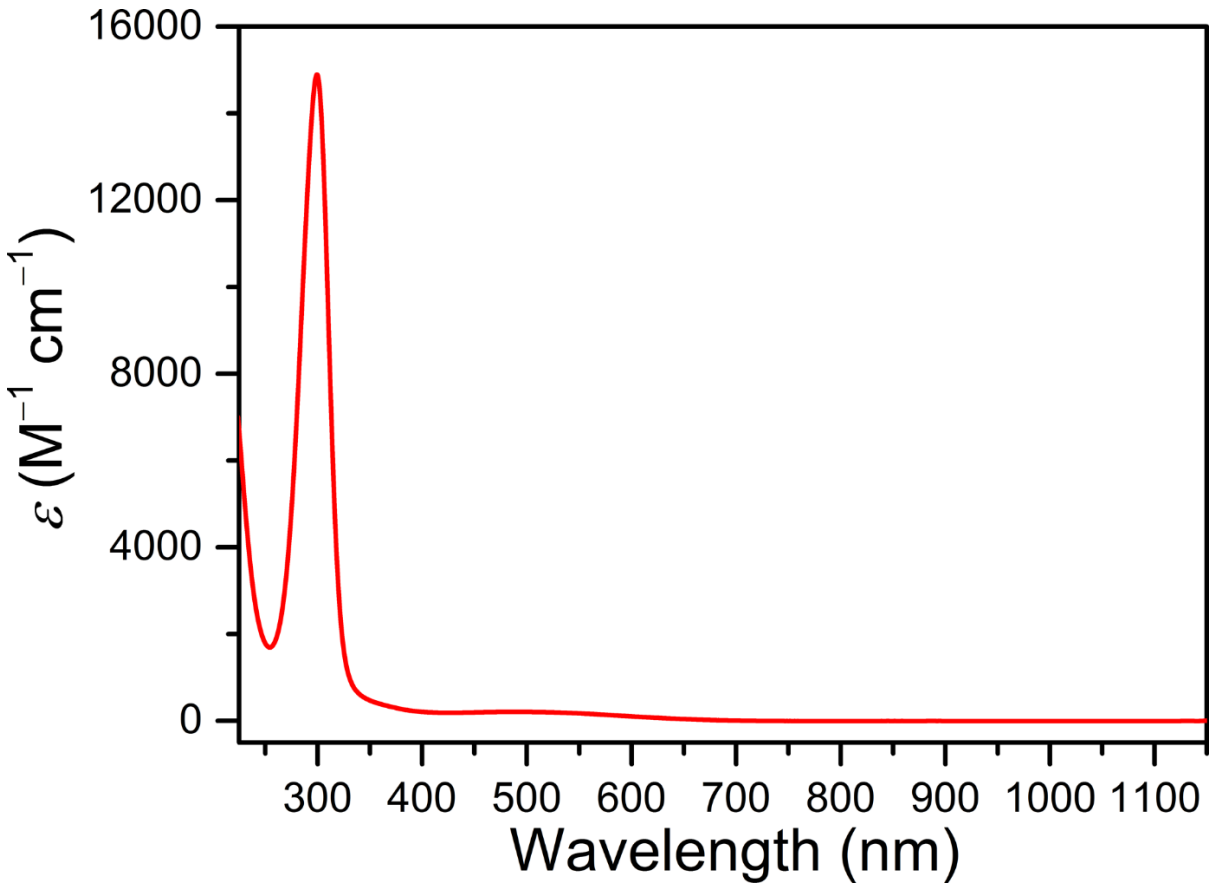

Figure 7.32 UV-Vis-NIR absorption spectrum for $H_2(^{OMe}L)$ in MeCN at 298 K. Note that the molar absorptivity (ε) is plotted against wavelength.

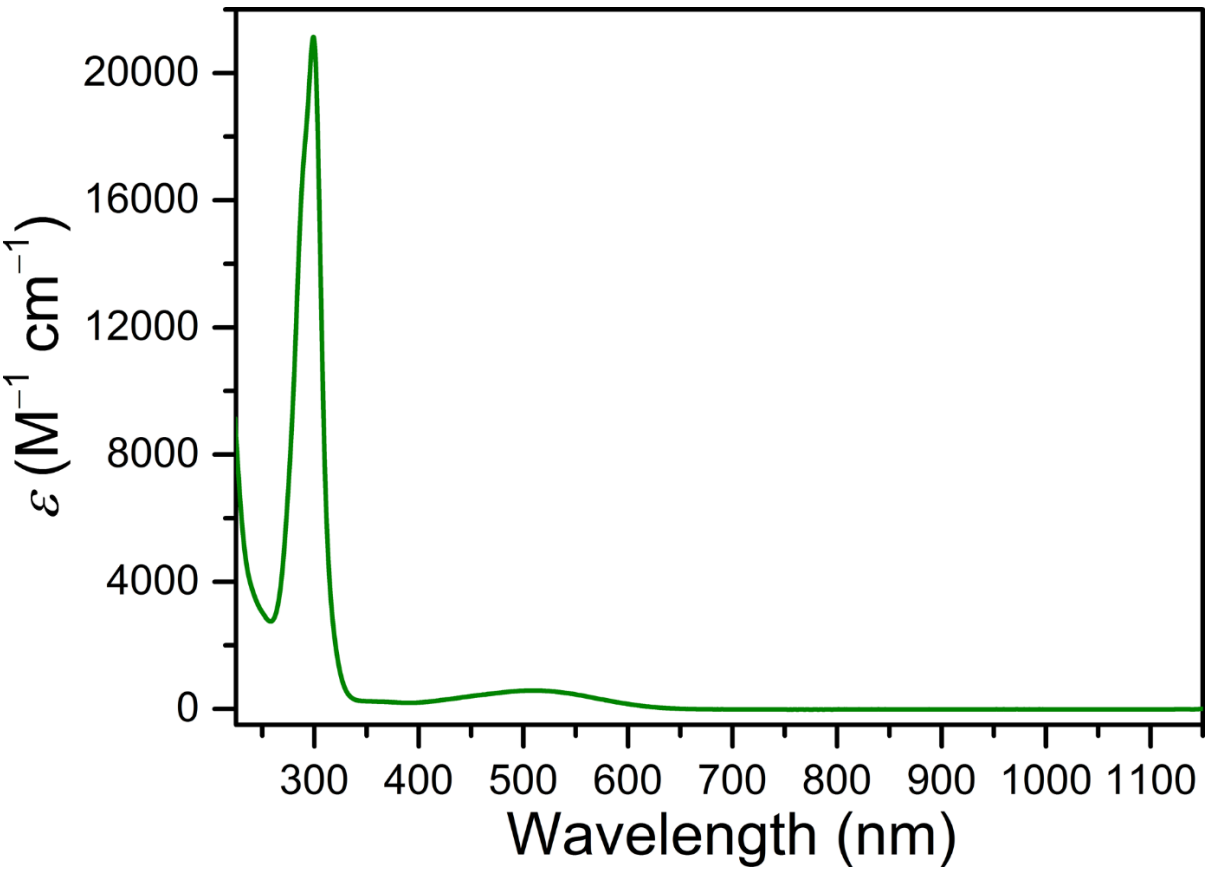

Figure 7.33 UV-Vis-NIR absorption spectrum for $H_2(^{Cl}L)$ in MeCN at 298 K. Note that the molar absorptivity (ε) is plotted against wavelength.

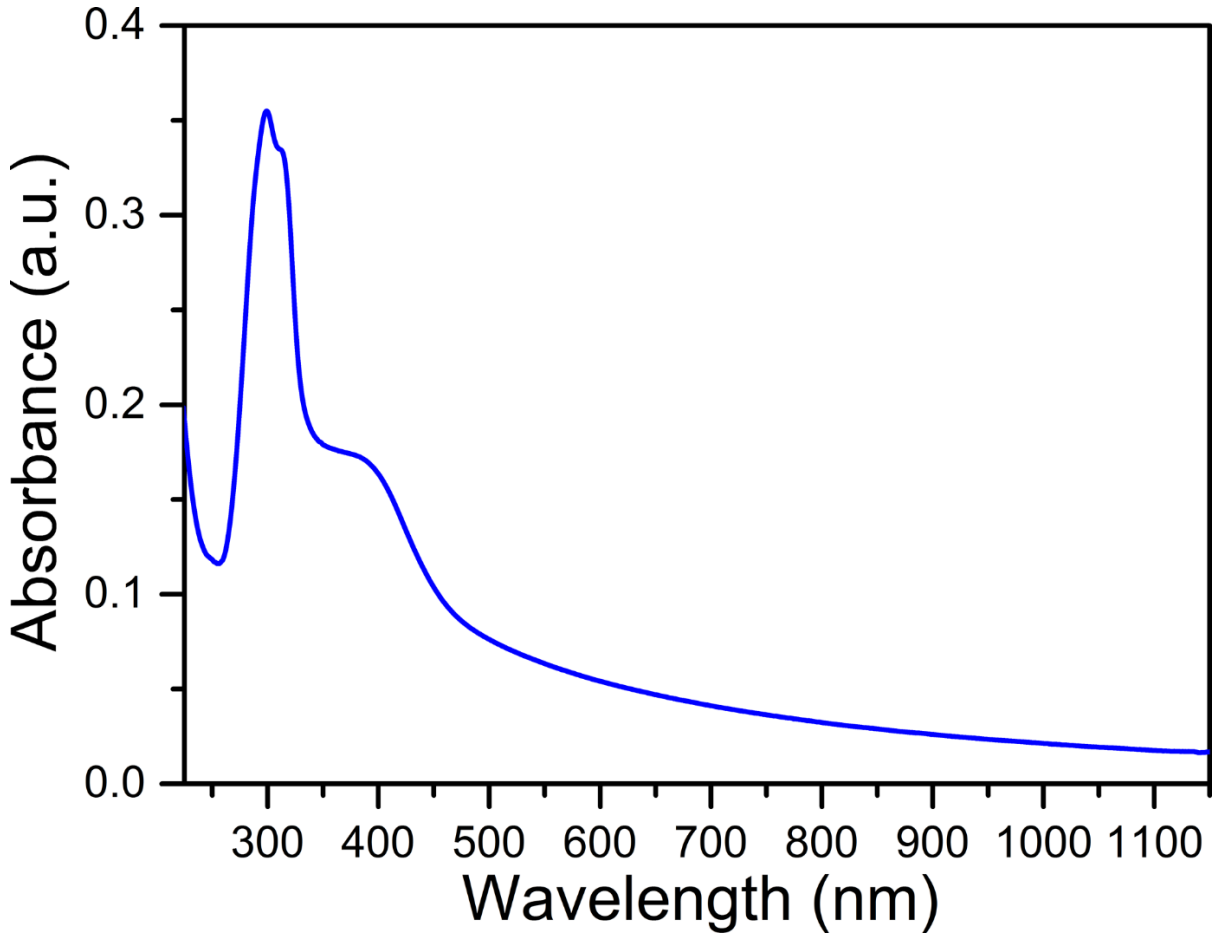

Figure 7.34 UV-Vis-NIR absorption spectrum for $Na_2(^{NO_2}L)$ in MeCN at 298 K.

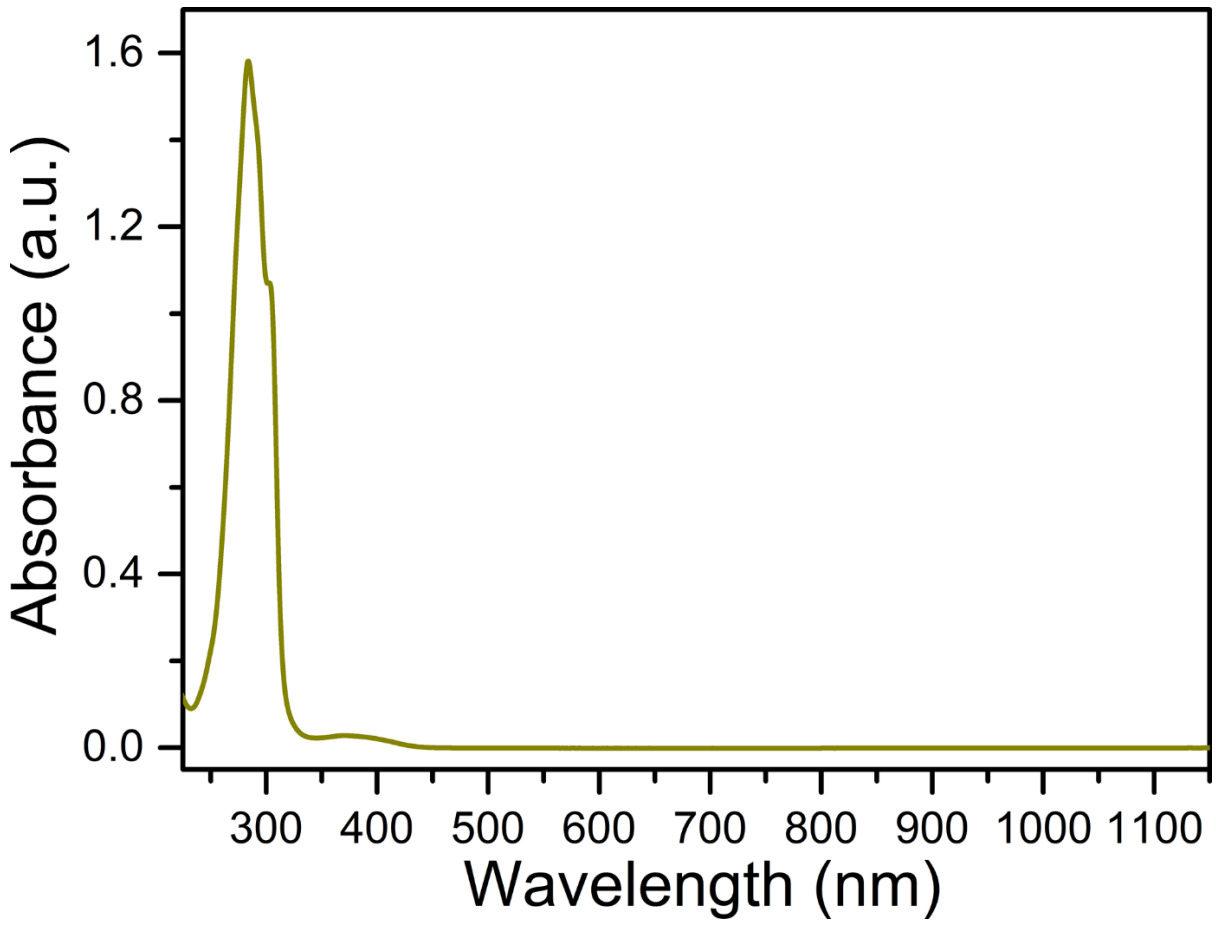

Figure 7.35 UV-Vis-NIR absorption spectrum for (^{SMe_2}L)·2.0AcOH in MeCN at 298 K.

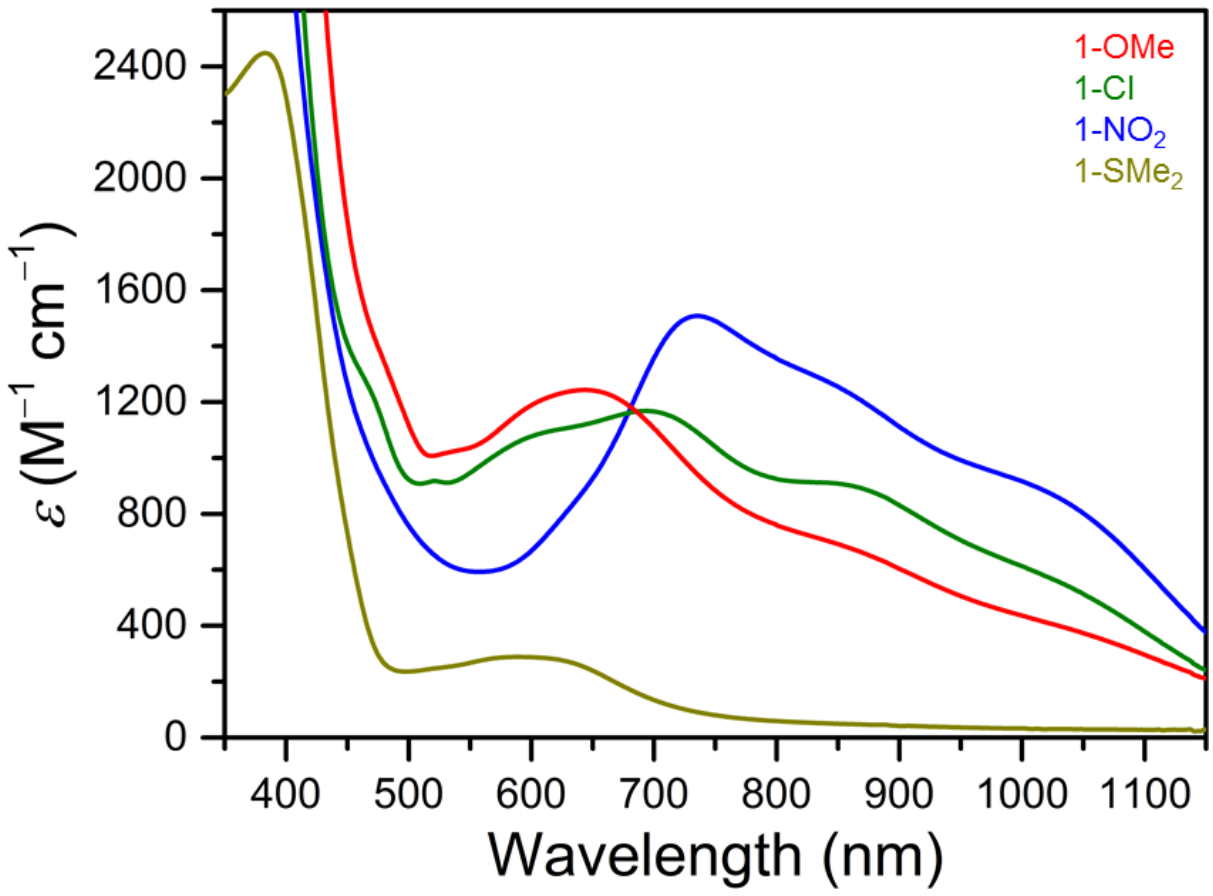

Figure 7.36 UV-Vis-NIR absorption spectra for **1-R** in MeCN at 298 K, highlighting the lower energy range 350–1150 nm; R = OMe (red), Cl (green), NO_2 (blue), SMe_2 (gold). Note that the molar absorptivity (ε) is plotted against wavelength.

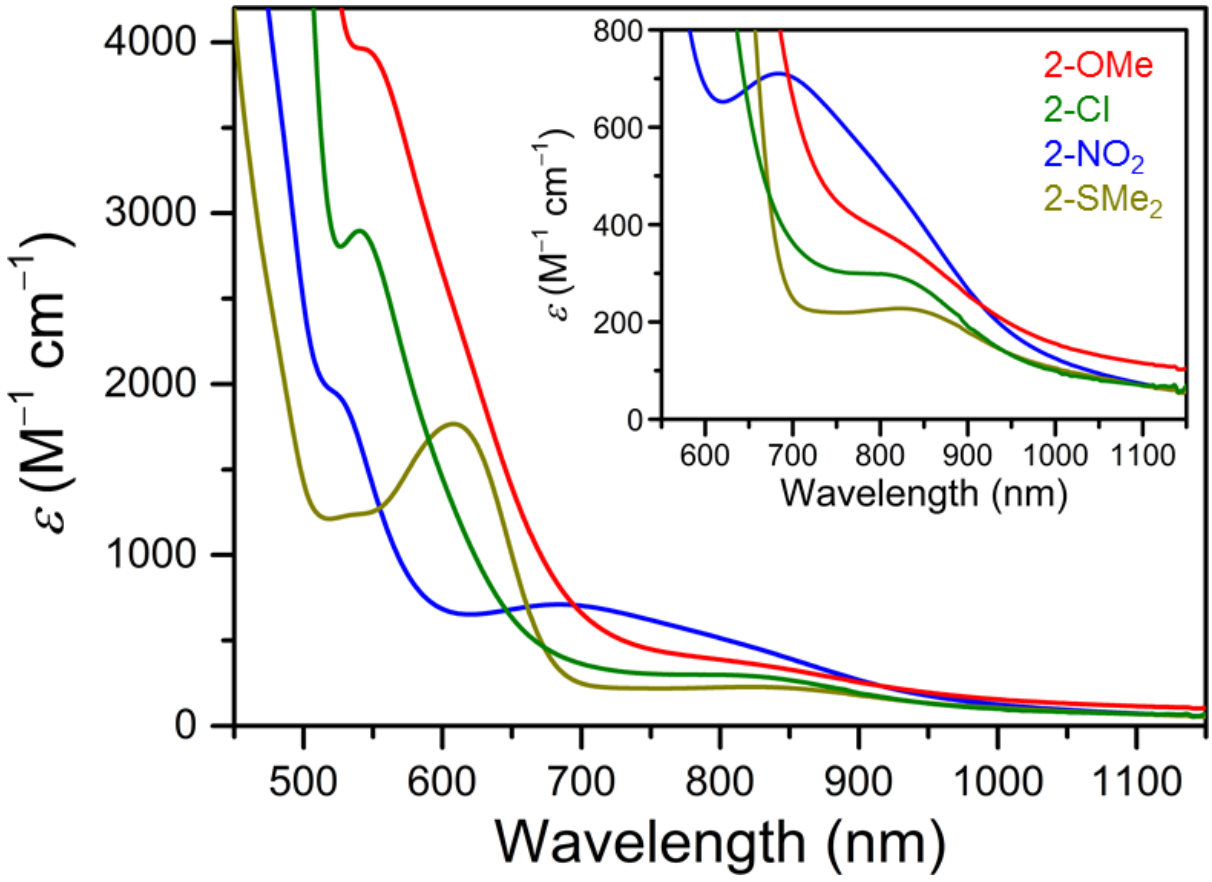

Figure 7.37 UV-Vis-NIR absorption spectra for **2-R** in MeCN at 298 K, highlighting the lower energy range 450–1150 nm; R = OMe (red), Cl (green), NO_2 (blue), SMe_2 (gold). Inset: Expanded view of the 550–1150 nm range. Note that the molar absorptivity (ε) is plotted against wavelength.

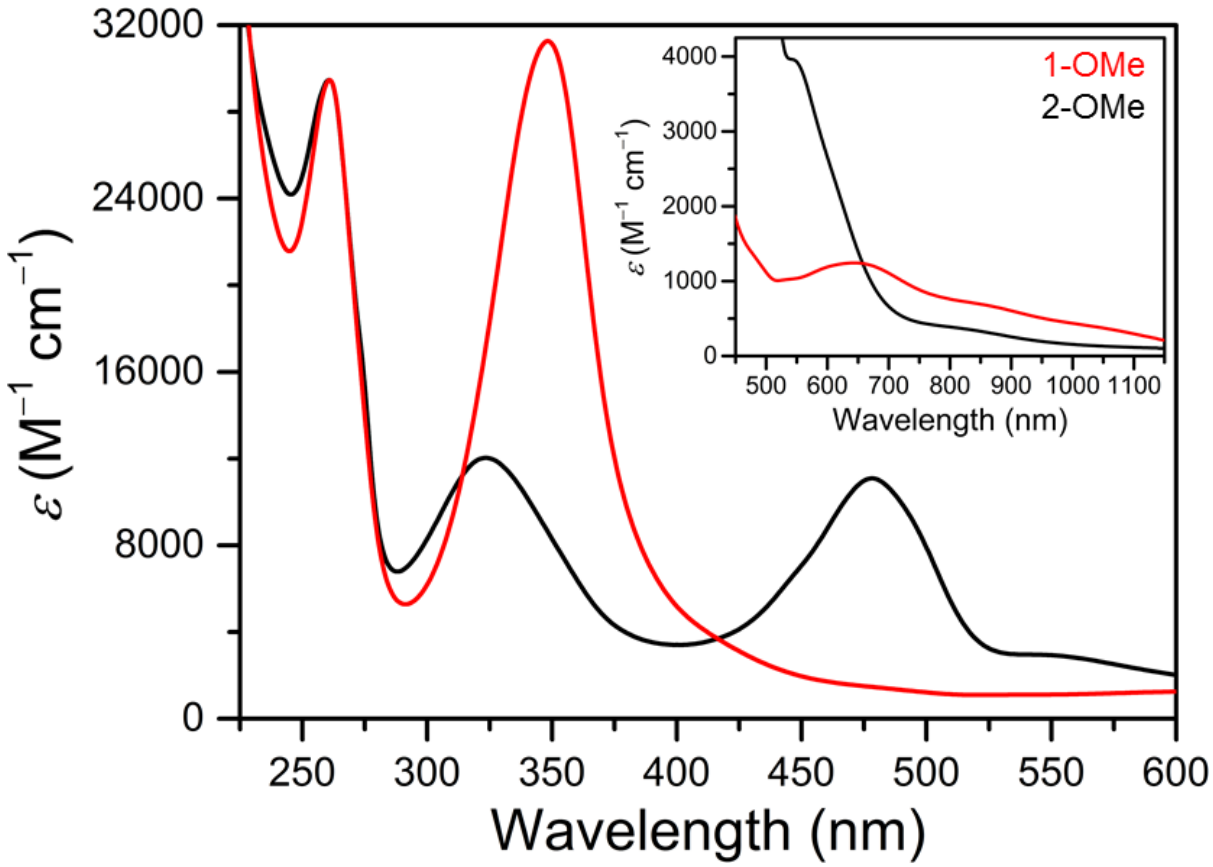

Figure 7.38 UV-Vis-NIR absorption spectra for **1-OMe** (red) and **2-OMe** (black) in MeCN at 298 K. Inset: Expanded view of the 450–1150 nm range. Note that the molar absorptivity (ε) is plotted against wavelength.

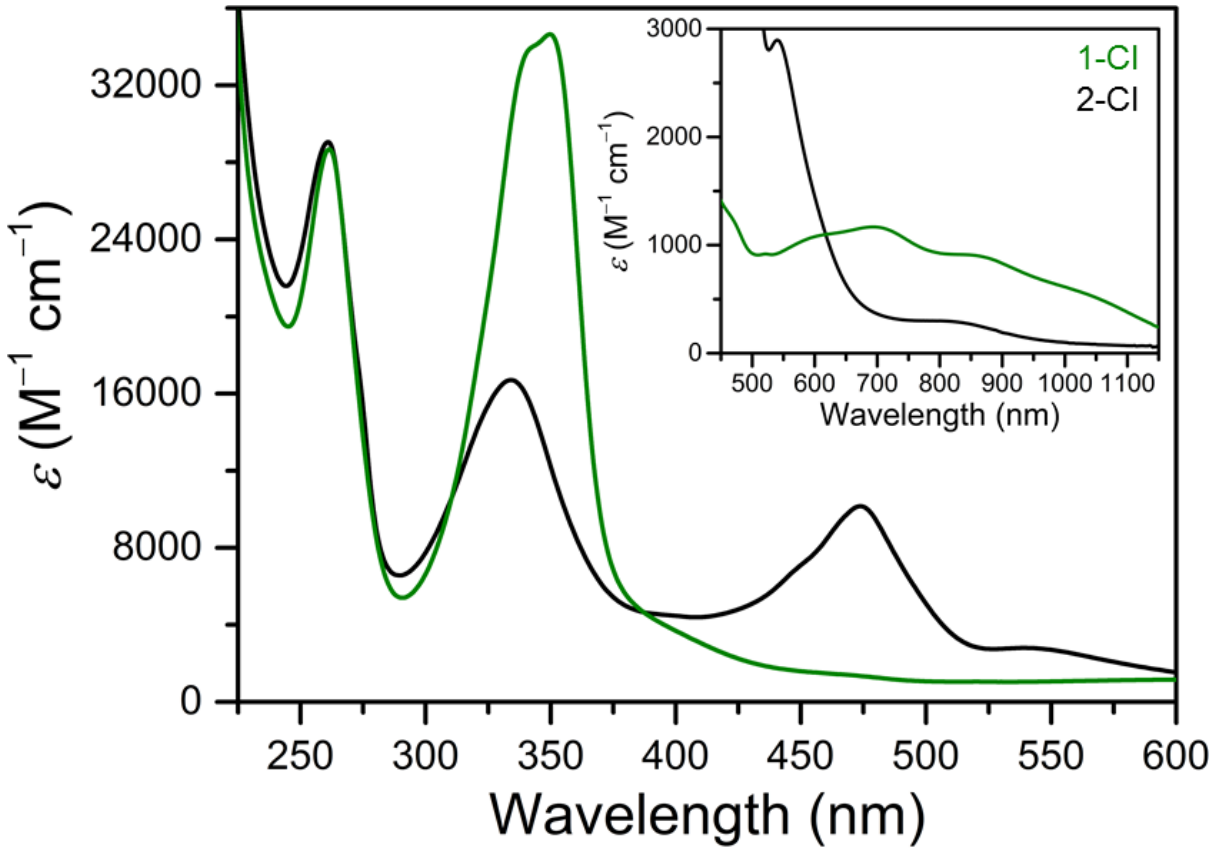

Figure 7.39 UV-Vis-NIR absorption spectra for **1-Cl** (green) and **2-Cl** (black) in MeCN at 298 K. Inset: Expanded view of the 450–1150 nm range. Note that the molar absorptivity (ε) is plotted against wavelength.

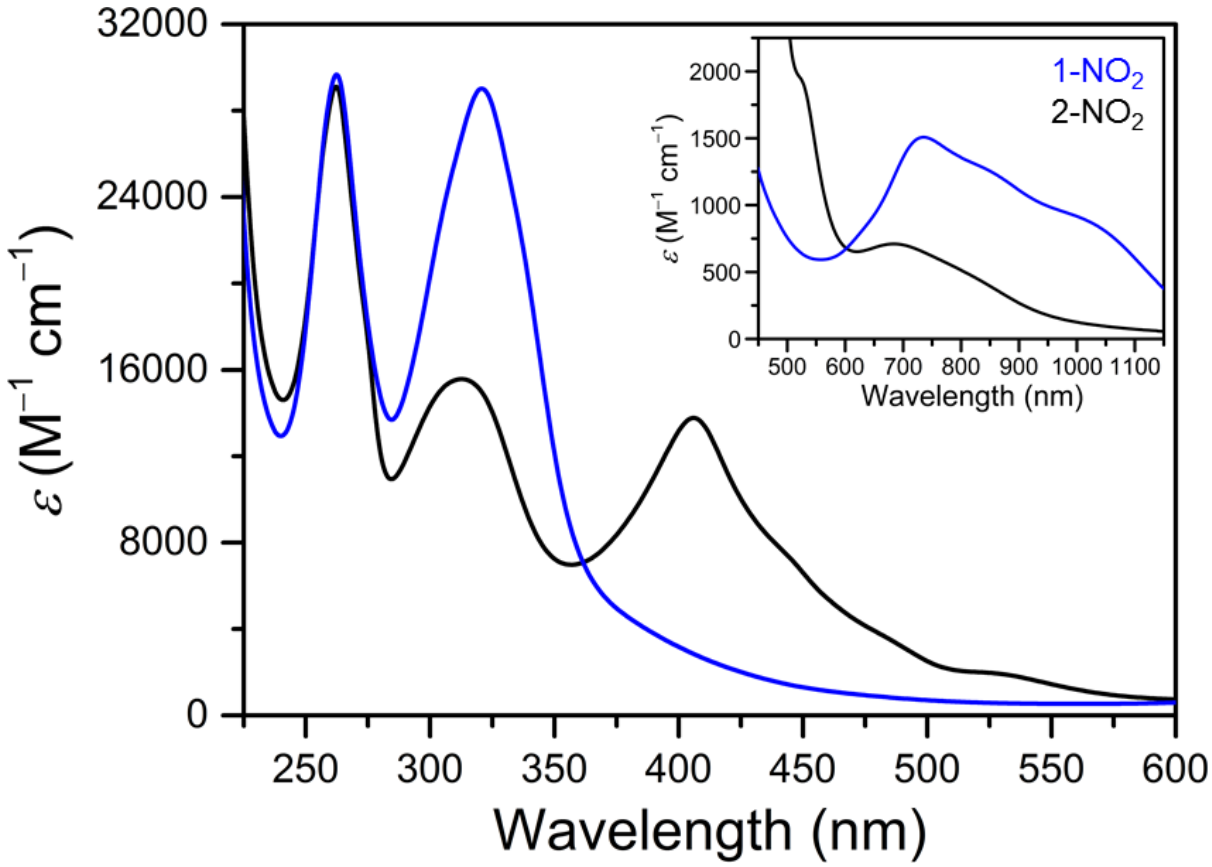

Figure 7.40 UV-Vis-NIR absorption spectra for **1-NO₂** (blue) and **2-NO₂** (black) in MeCN at 298 K. Inset: Expanded view of the 450–1150 nm range. Note that the molar absorptivity (ε) is plotted against wavelength.

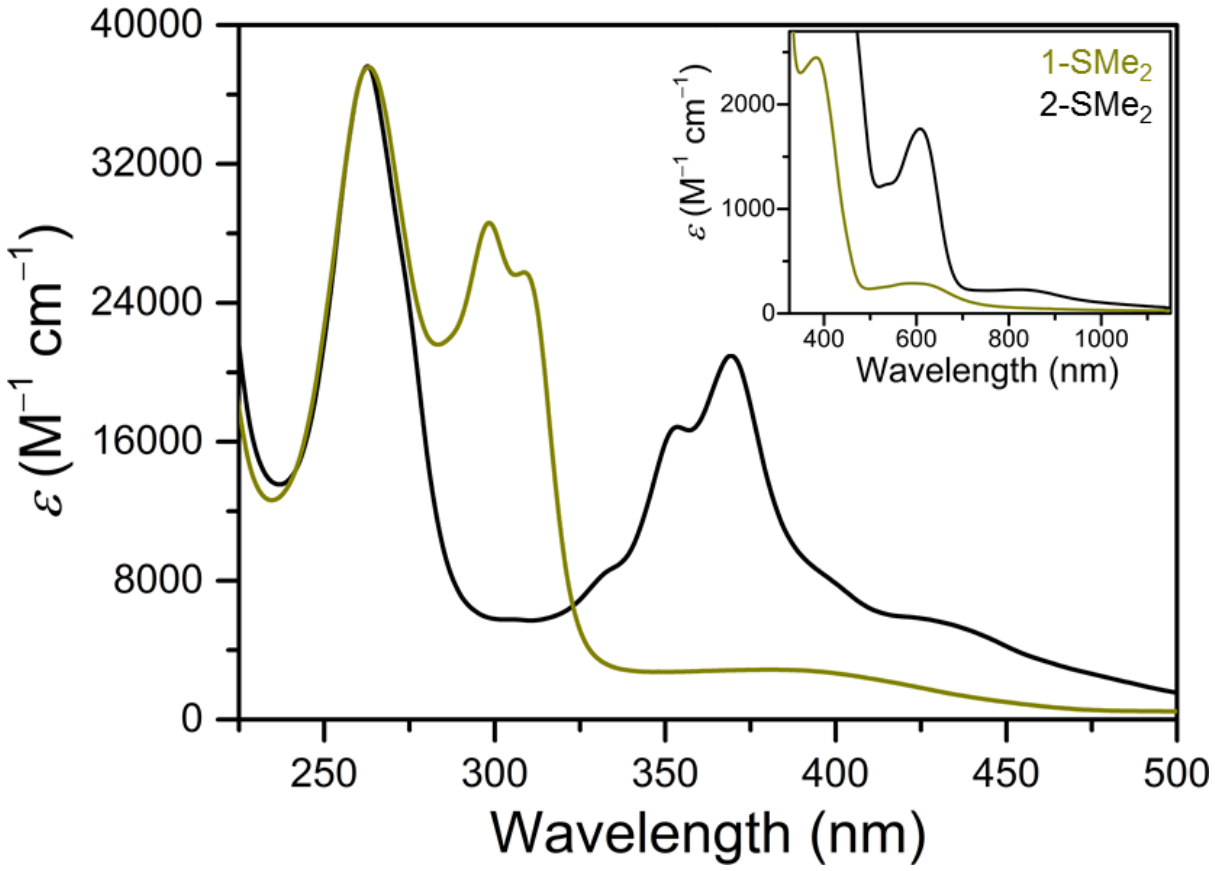

Figure 7.41 UV-Vis-NIR absorption spectra for **1-SMe$_2$** (gold) and **2-SMe$_2$** (black) in MeCN at 298 K. Inset: Expanded view of the 325–1150 nm range. Note that the molar absorptivity (ε) is plotted against wavelength.

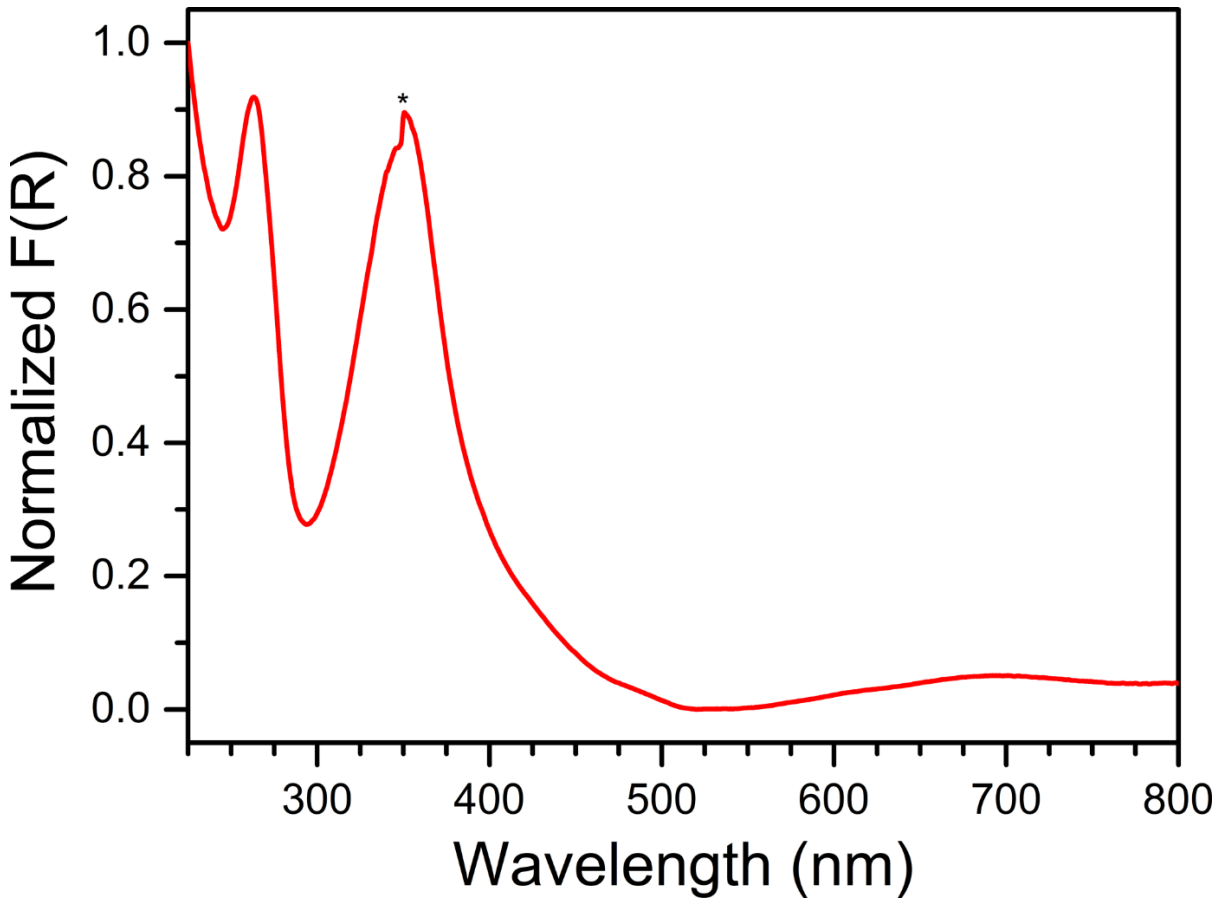

Figure 7.42 Diffuse reflectance UV-Vis spectrum for a microcrystalline sample of **1-OMe** diluted with $BaSO_4$ powder at 298 K. The spectrum is plotted as normalized Kubelka-Munk transformation F(R). The sharp feature at 350 nm denoted with an asterisk is an instrument-derived artifact arising from a detector change.

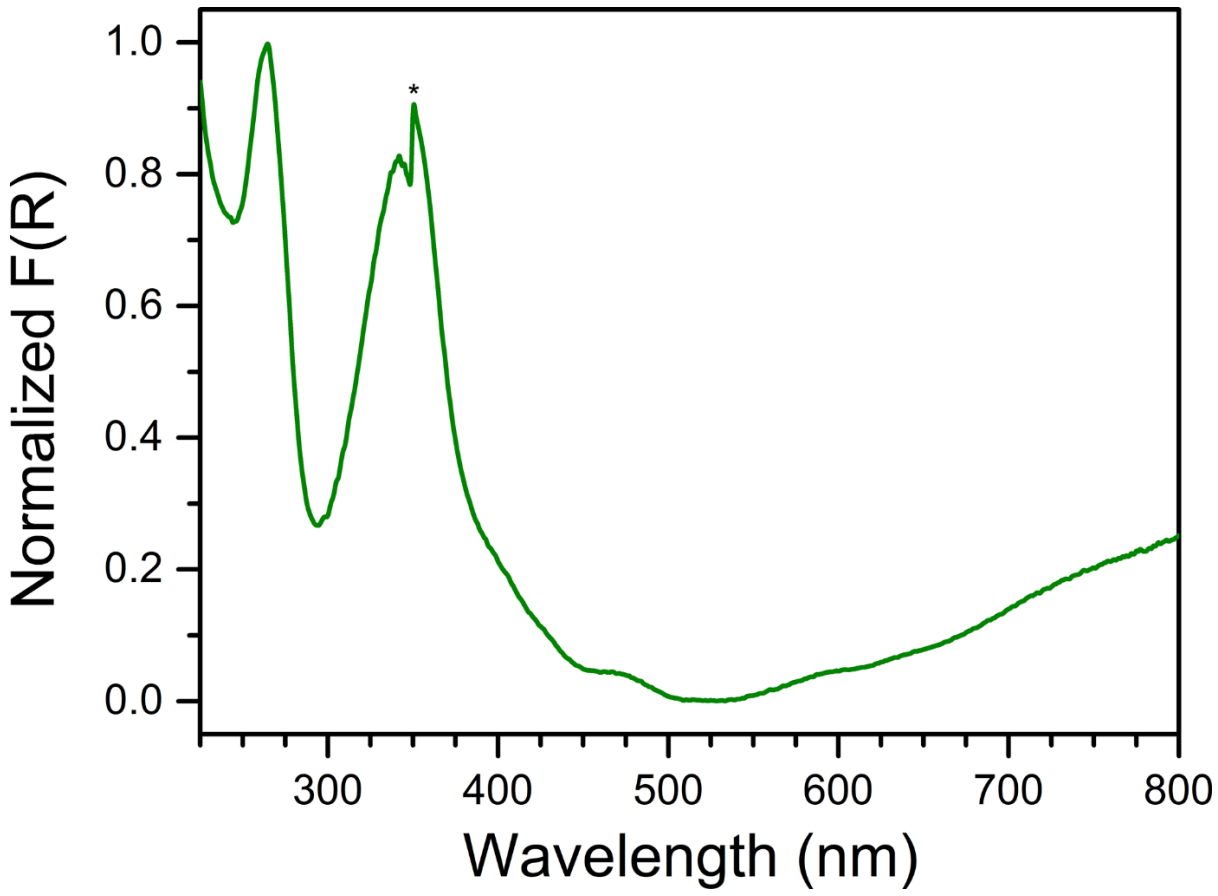

Figure 7.43 Diffuse reflectance UV-Vis spectrum for a microcrystalline sample of **1-Cl** diluted with $BaSO_4$ powder at 298 K. The spectrum is plotted as normalized Kubelka-Munk transformation F(R). The sharp feature at 350 nm denoted with an asterisk is an instrument-derived artifact arising from a detector change.

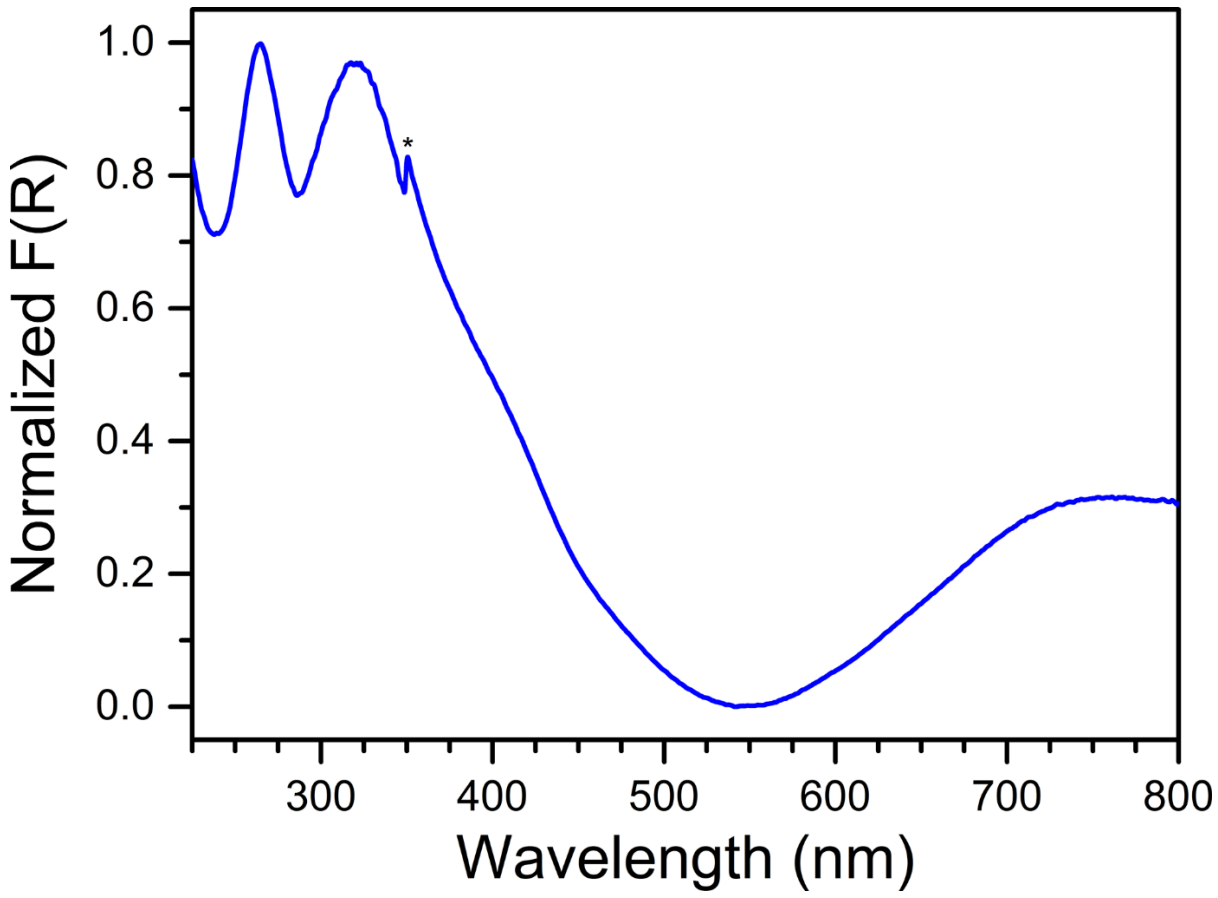

Figure 7.44 Diffuse reflectance UV-Vis spectrum for a microcrystalline sample of **1-NO_2** diluted with $BaSO_4$ powder at 298 K. The spectrum is plotted as normalized Kubelka-Munk transformation F(R). The sharp feature at 350 nm denoted with an asterisk is an instrument-derived artifact arising from a detector change.

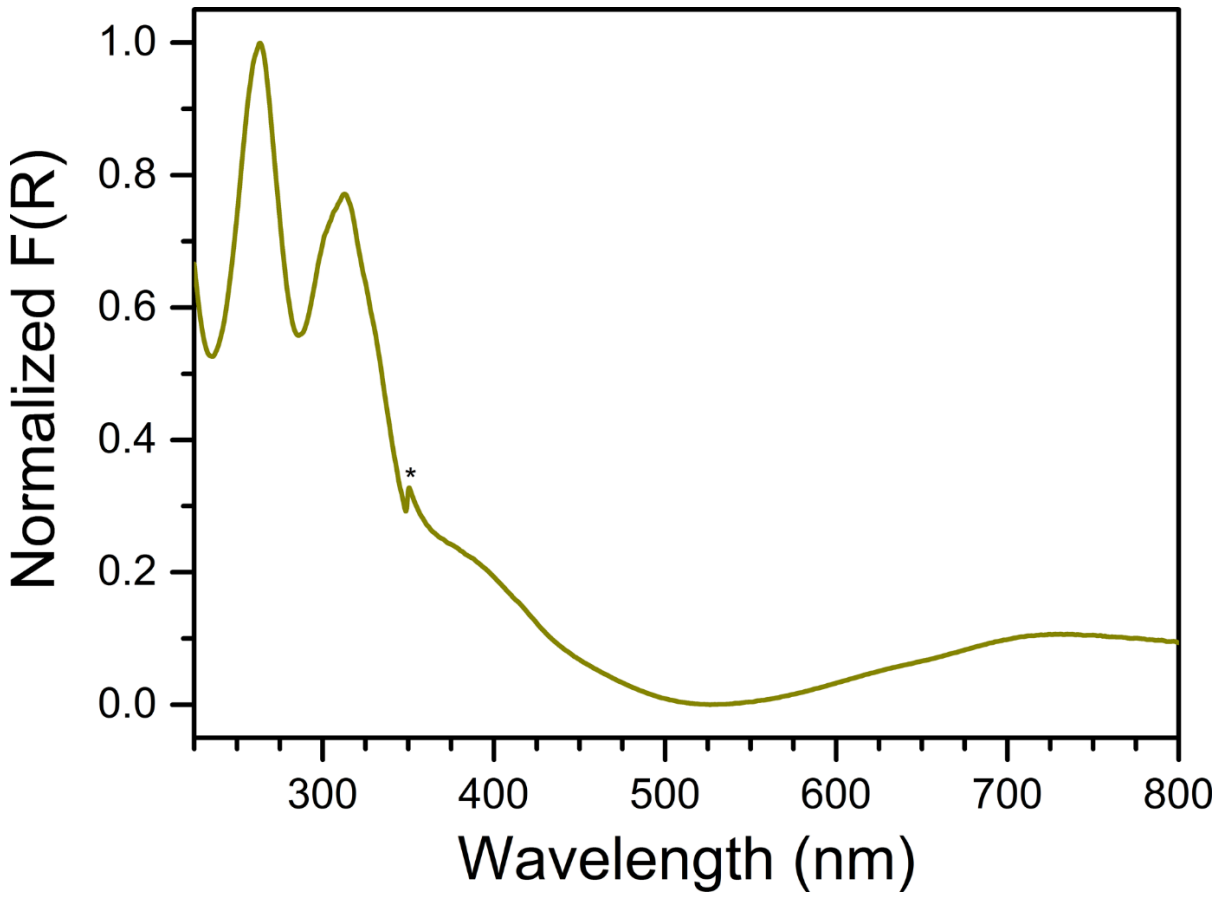

Figure 7.45 Diffuse reflectance UV-Vis spectrum for a microcrystalline sample of **1-SMe$_2$** diluted with $BaSO_4$ powder at 298 K. The spectrum is plotted as normalized Kubelka-Munk transformation F(R). The sharp feature at 350 nm denoted with an asterisk is an instrument-derived artifact arising from a detector change.

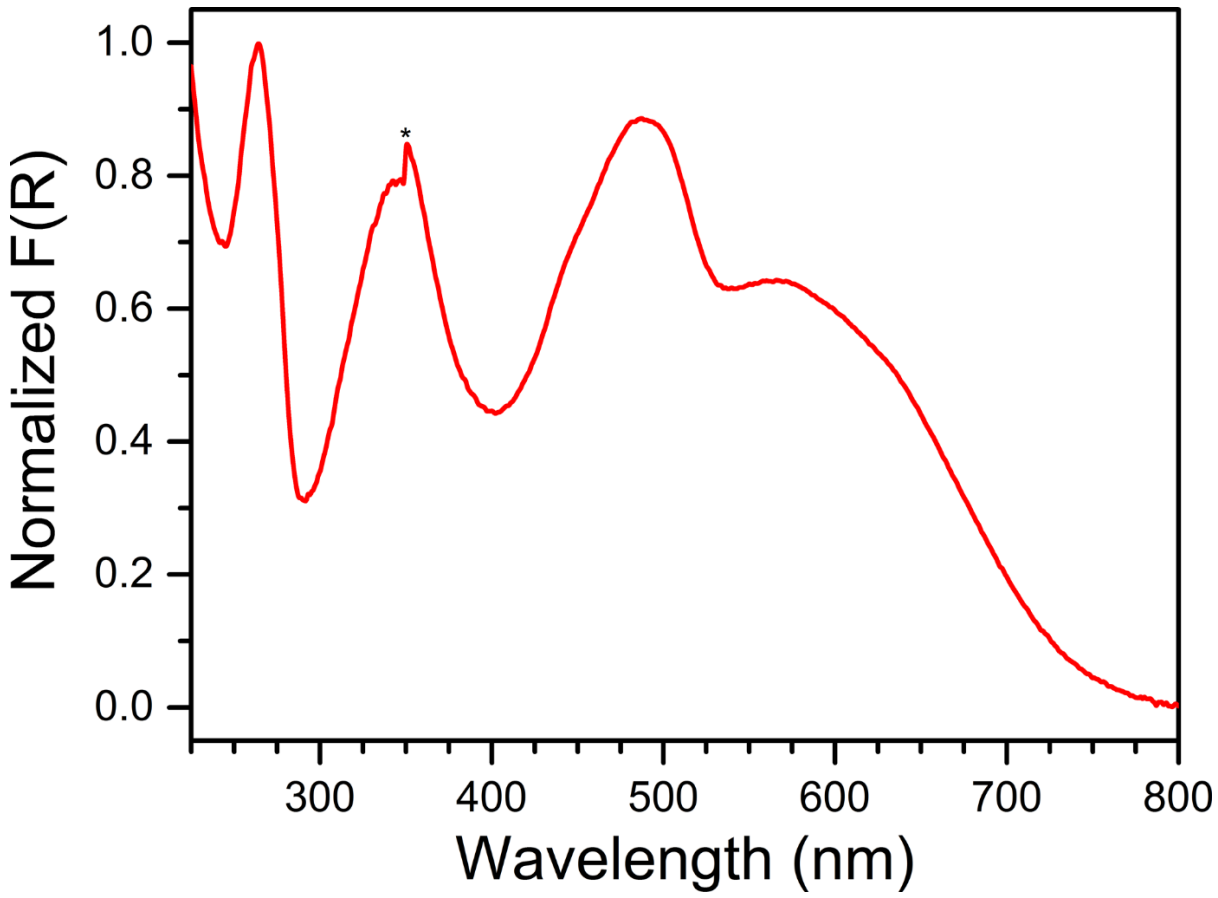

Figure 7.46 Diffuse reflectance UV-Vis spectrum for a microcrystalline sample of **2-OMe** diluted with $BaSO_4$ powder at 298 K. The spectrum is plotted as normalized Kubelka-Munk transformation F(R). The sharp feature at 350 nm denoted with an asterisk is an instrument-derived artifact arising from a detector change.

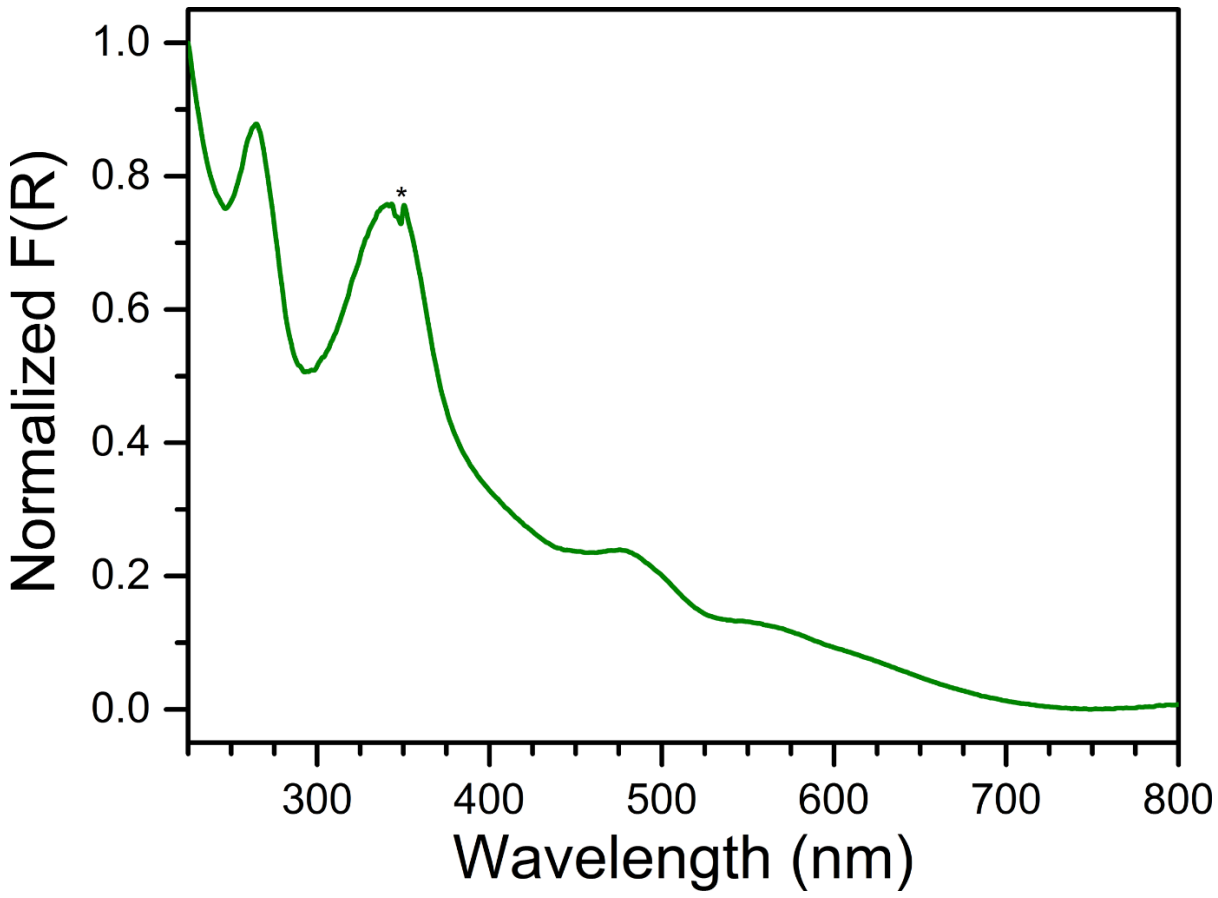

Figure 7.47 Diffuse reflectance UV-Vis spectrum for a microcrystalline sample of **2-Cl** diluted with $BaSO_4$ powder at 298 K. The spectrum is plotted as normalized Kubelka-Munk transformation F(R). The sharp feature at 350 nm denoted with an asterisk is an instrument-derived artifact arising from a detector change.

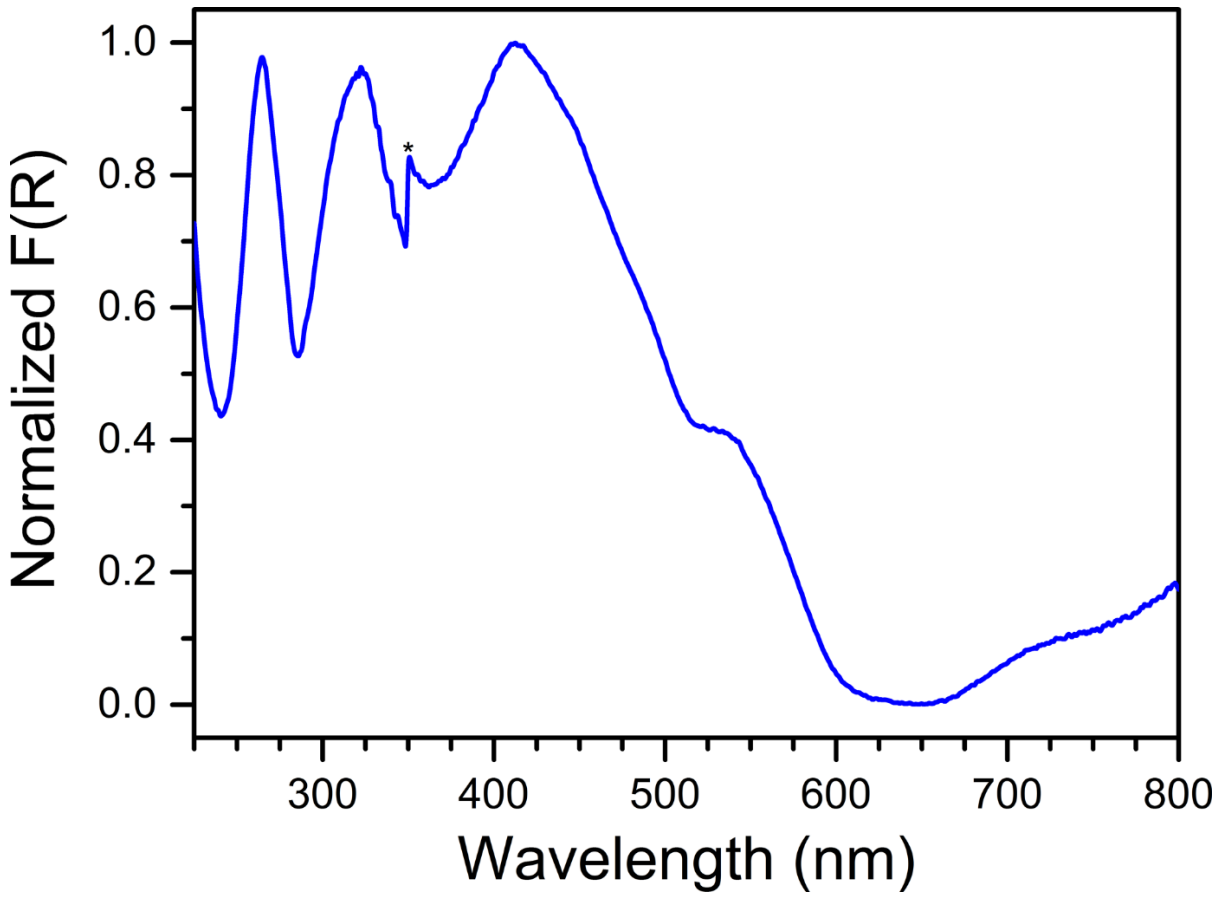

Figure 7.48 Diffuse reflectance UV-Vis spectrum for a microcrystalline sample of **2-NO_2** diluted with $BaSO_4$ powder at 298 K. The spectrum is plotted as normalized Kubelka-Munk transformation F(R). The sharp feature at 350 nm denoted with an asterisk is an instrument-derived artifact arising from a detector change.

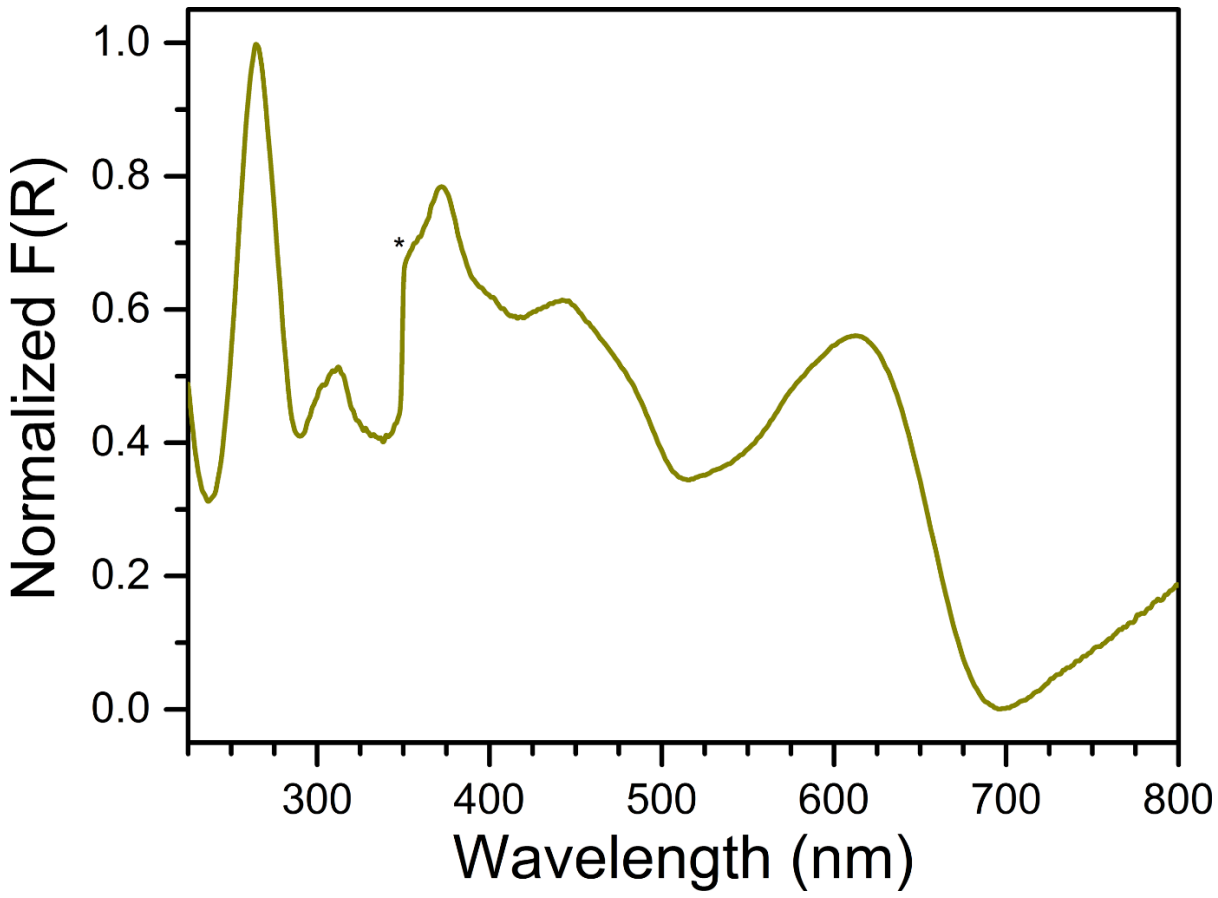

Figure 7.49 Diffuse reflectance UV-Vis spectrum for a microcrystalline sample of **2-SMe$_2$** diluted with $BaSO_4$ powder at 298 K. The spectrum is plotted as normalized Kubelka-Munk transformation F(R). The sharp feature at 350 nm denoted with an asterisk is an instrument-derived artifact arising from a detector change.

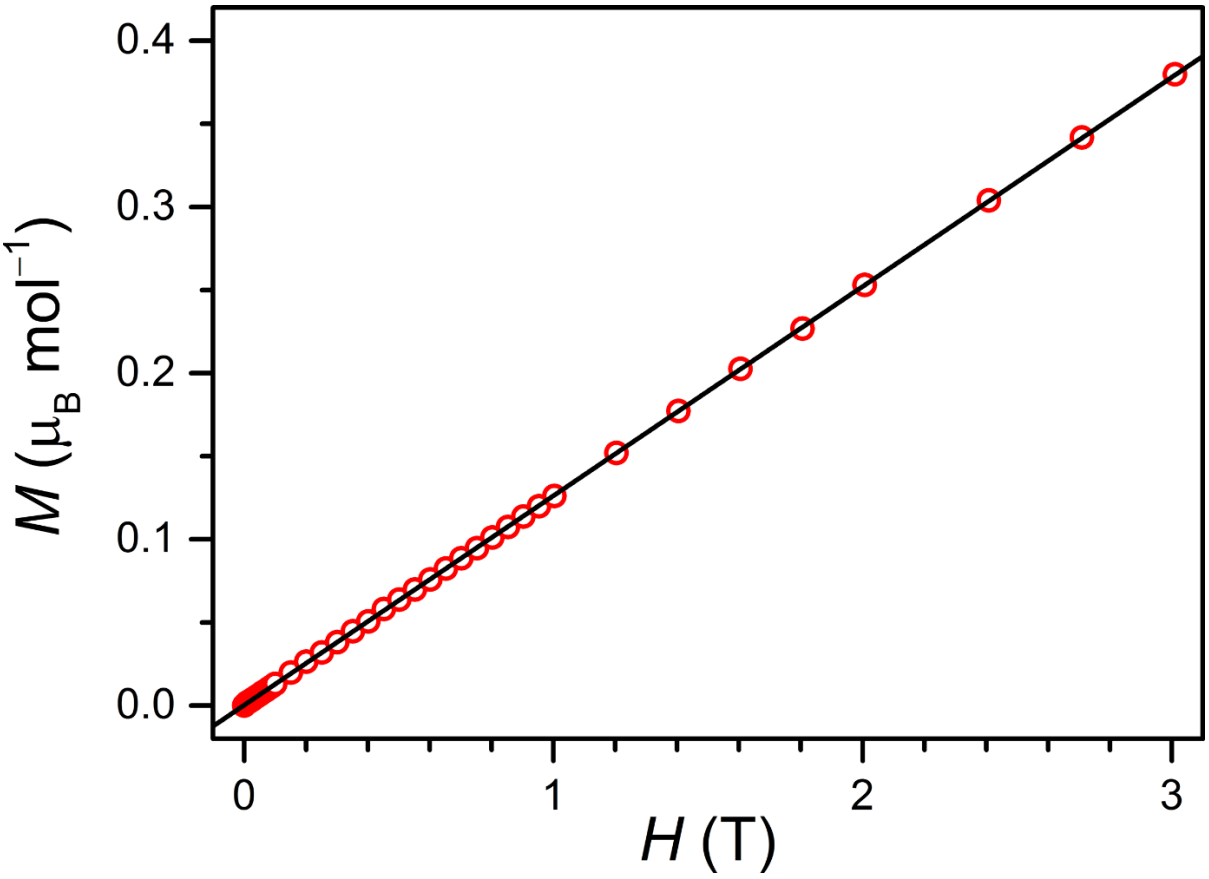

Figure 7.50 Variable-field magnetization of **1-OMe** collected at 100 K for a microcrystalline sample restrained in a frozen eicosane matrix. The red circles correspond to experimental data and the black line denotes a linear fit to the data. Note that the excellent linearity illustrates the absence of ferromagnetic impurities.

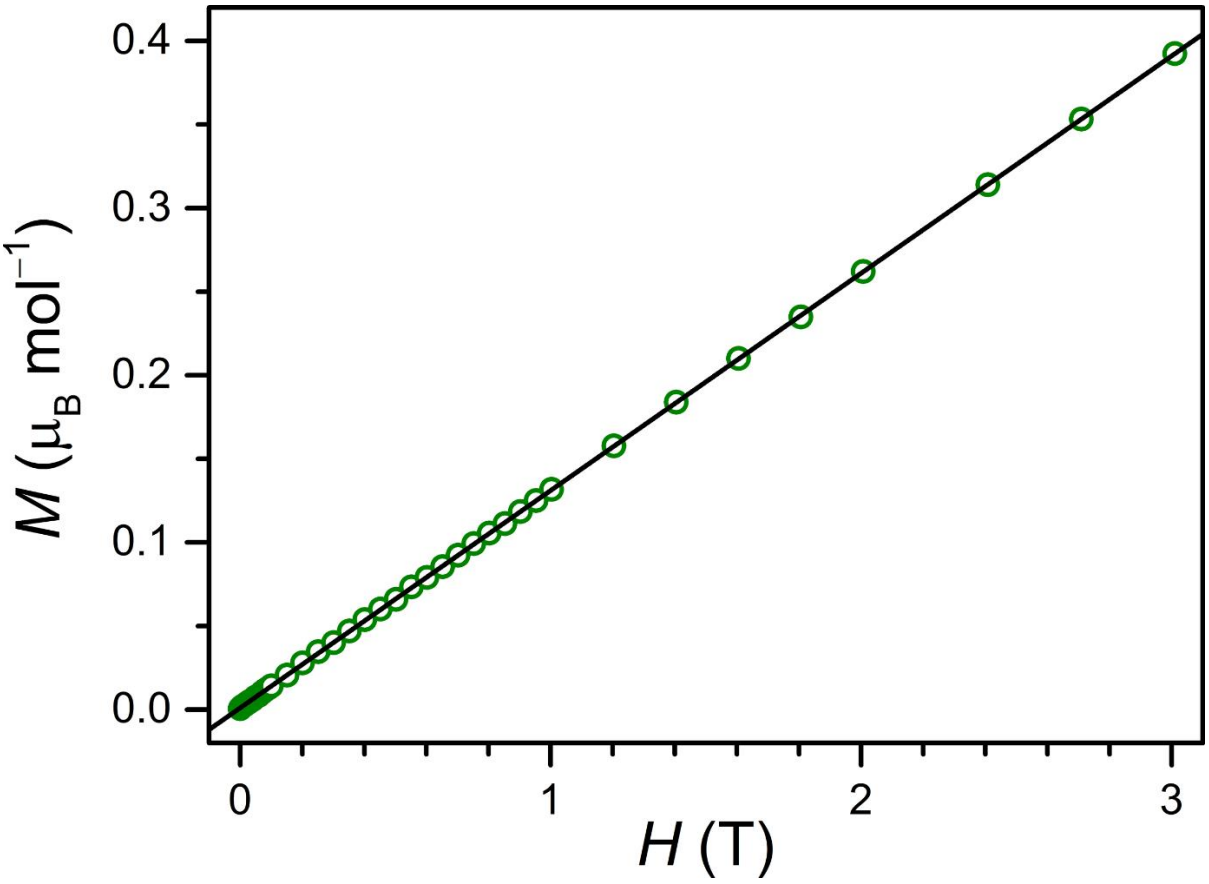

Figure 7.51 Variable-field magnetization of **1-Cl** collected at 100 K for a microcrystalline sample restrained in a frozen eicosane matrix. The green circles correspond to experimental data and the black line denotes a linear fit to the data. Note that the excellent linearity illustrates the absence of ferromagnetic impurities.

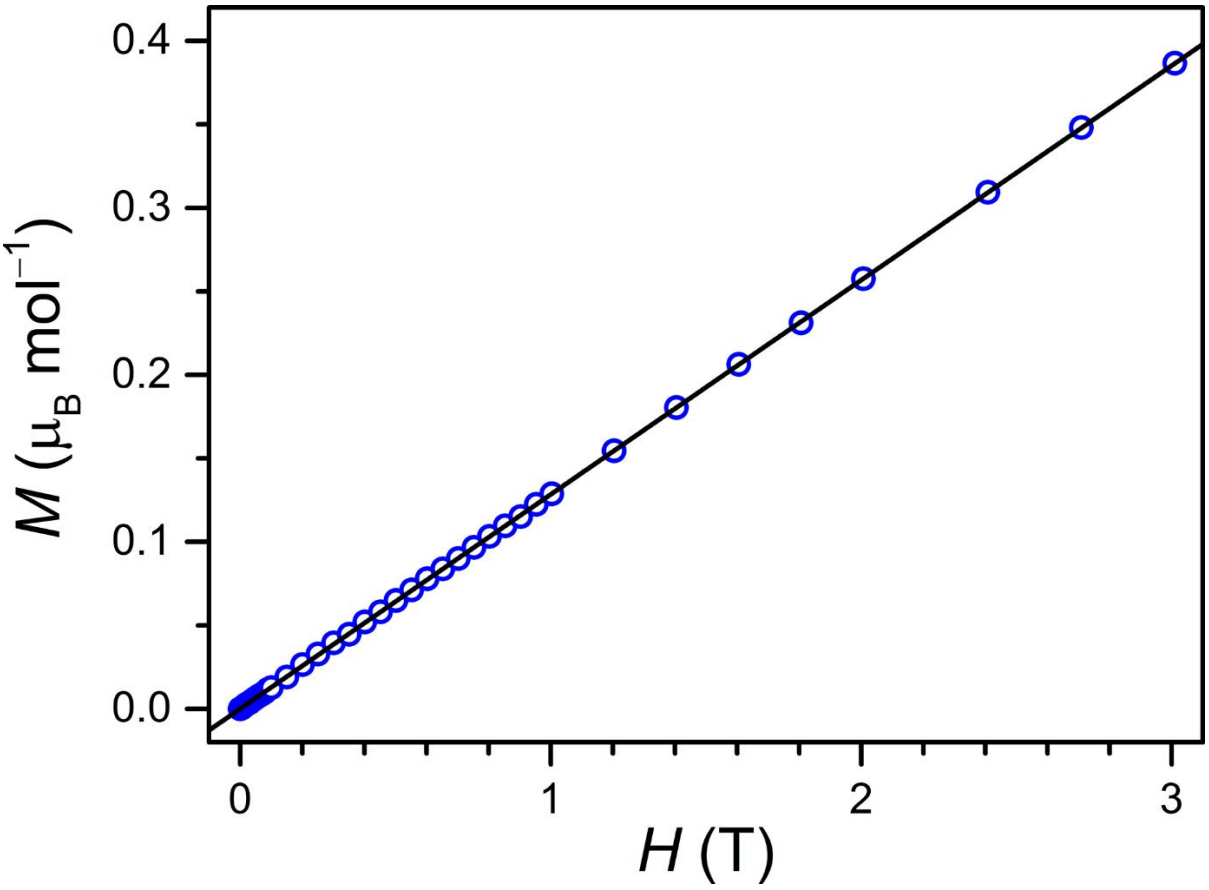

Figure 7.52 Variable-field magnetization of **1-NO_2** collected at 100 K for a microcrystalline sample restrained in a frozen eicosane matrix. The blue circles correspond to experimental data and the black line denotes a linear fit to the data. Note that the excellent linearity illustrates the absence of ferromagnetic impurities.

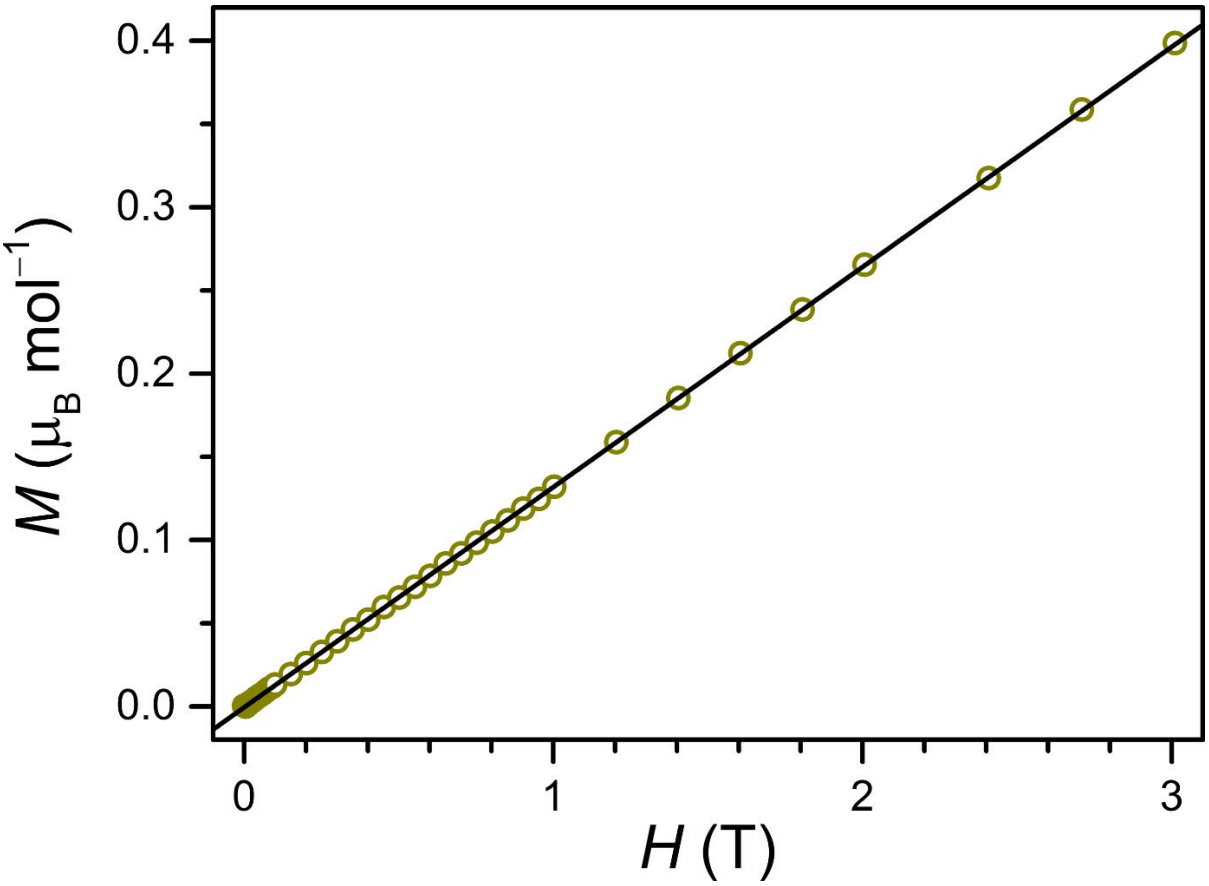

Figure 7.53 Variable-field magnetization of **1-SMe$_2$** collected at 100 K for a microcrystalline sample restrained in a frozen eicosane matrix. The gold circles correspond to experimental data and the black line denotes a linear fit to the data. Note that the excellent linearity illustrates the absence of ferromagnetic impurities.

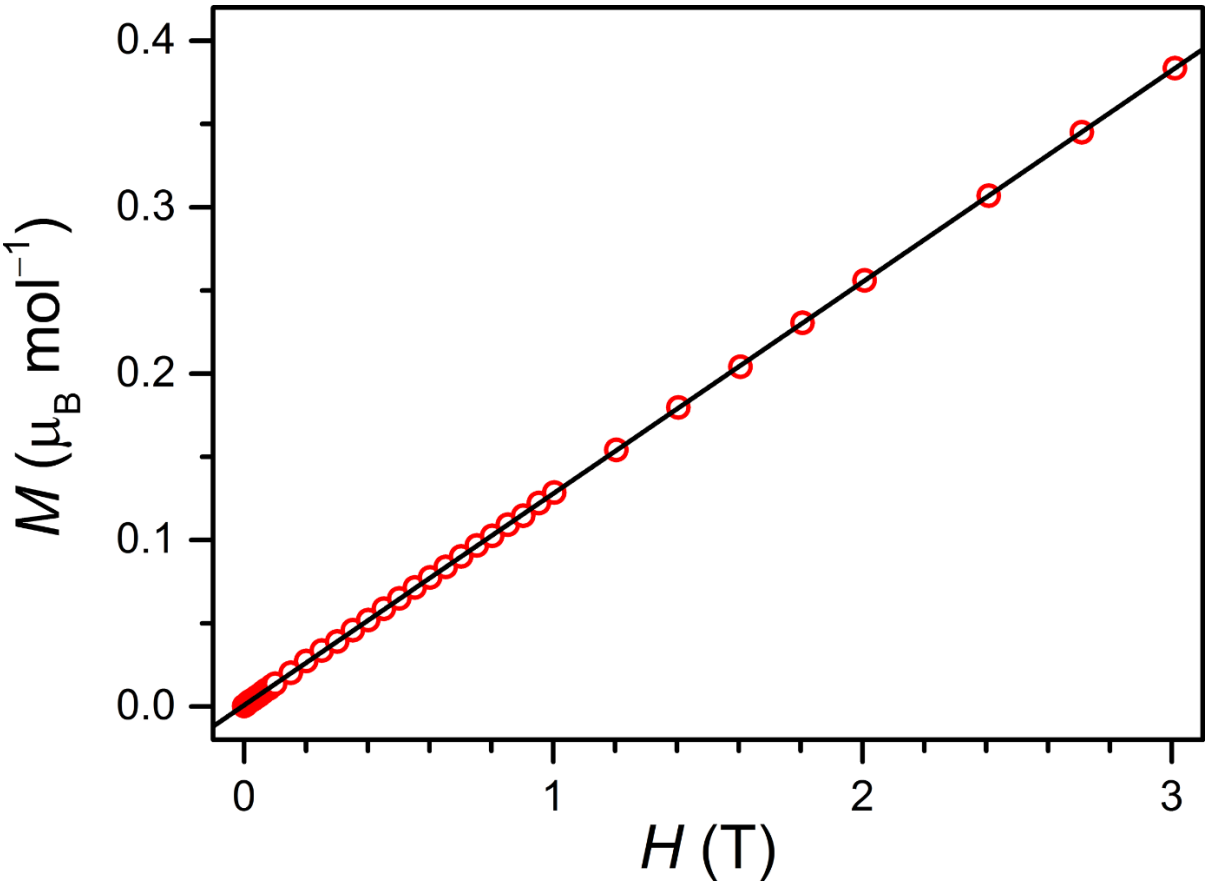

Figure 7.54 Variable-field magnetization of **2-OMe** collected at 100 K for a microcrystalline sample restrained in a frozen eicosane matrix. The red circles correspond to experimental data and the black line denotes a linear fit to the data. Note that the excellent linearity illustrates the absence of ferromagnetic impurities.

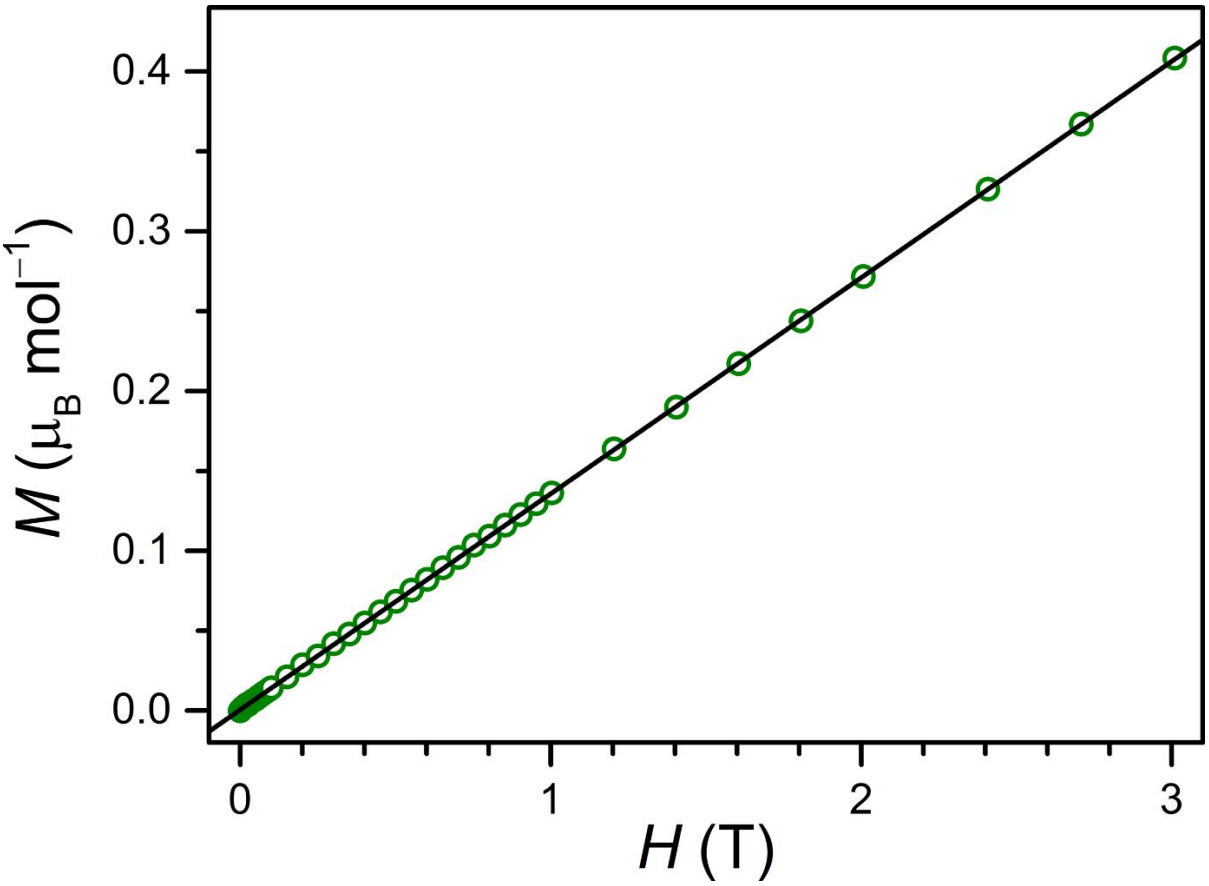

Figure 7.55 Variable-field magnetization of **2-Cl** collected at 100 K for a microcrystalline sample restrained in a frozen eicosane matrix. The green circles correspond to experimental data and the black line denotes a linear fit to the data. Note that the excellent linearity illustrates the absence of ferromagnetic impurities.

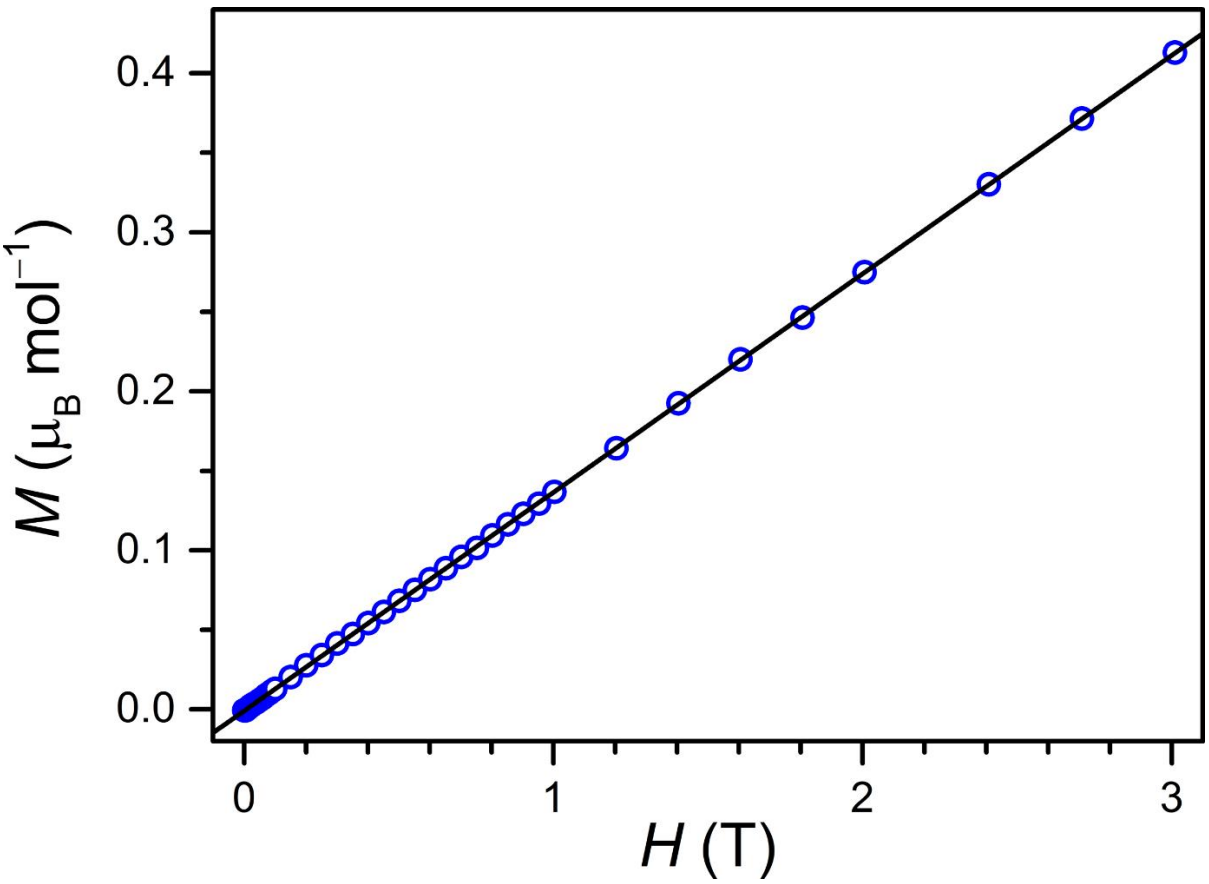

Figure 7.56 Variable-field magnetization of **2-NO_2** collected at 100 K for a microcrystalline sample restrained in a frozen eicosane matrix. The blue circles correspond to experimental data and the black line denotes a linear fit to the data. Note that the excellent linearity illustrates the absence of ferromagnetic impurities.

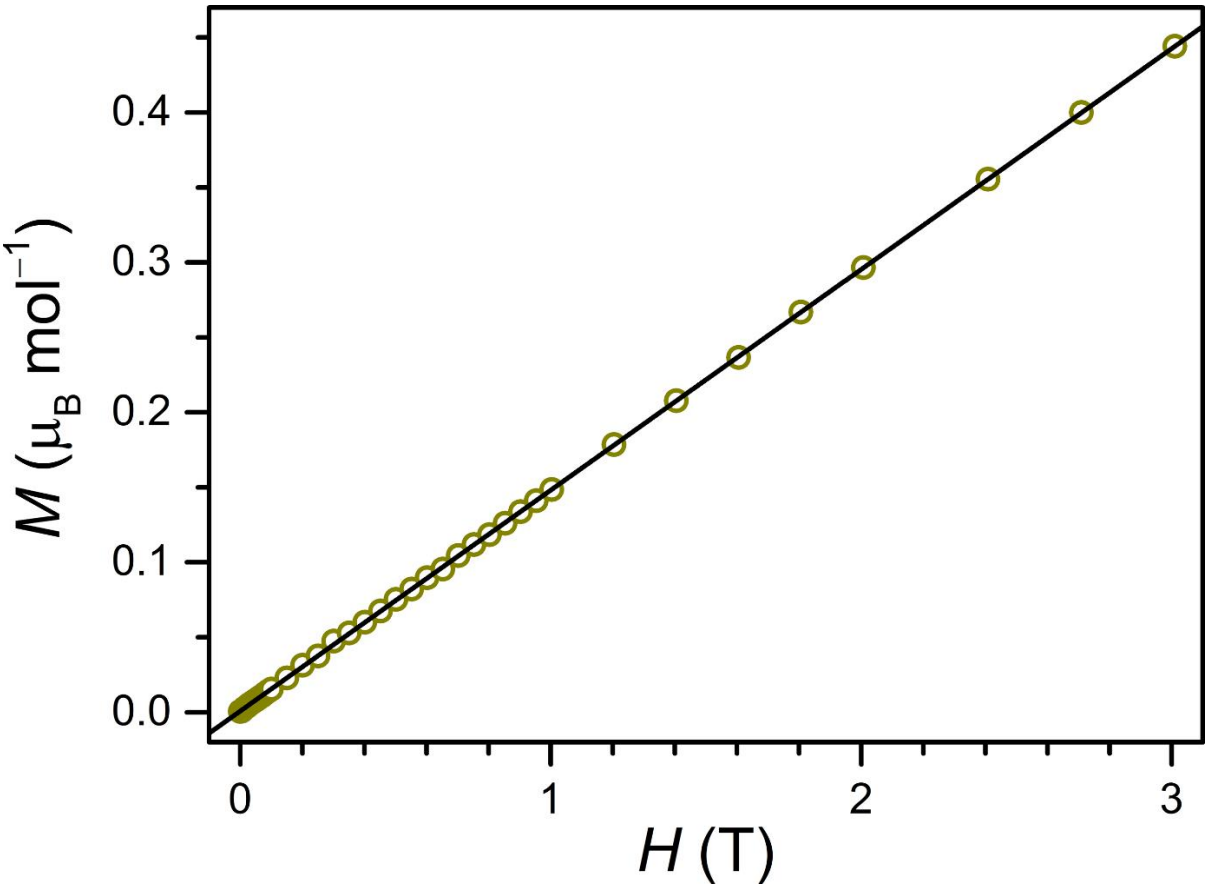

Figure 7.57 Variable-field magnetization of **2-SMe$_2$** collected at 100 K for a microcrystalline sample restrained in a frozen eicosane matrix. The gold circles correspond to experimental data and the black line denotes a linear fit to the data. Note that the excellent linearity illustrates the absence of ferromagnetic impurities.

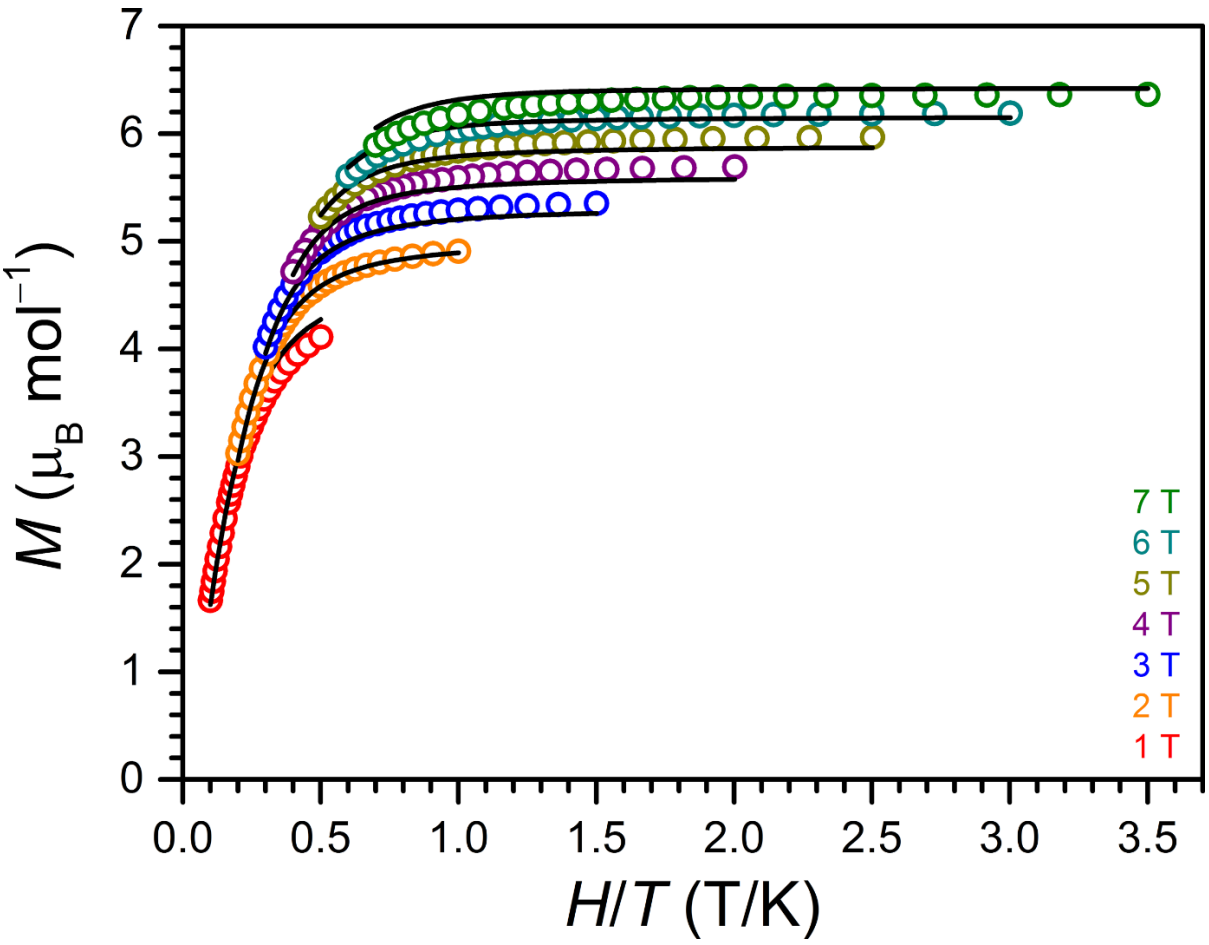

Figure 7.58 Low-temperature magnetization data for **1-OMe** collected at selected dc fields (see inset) for a microcrystalline sample restrained in a frozen eicosane matrix. The colored circles correspond to experimental data and the black lines denote fits to the data using the spin Hamiltonian given in Equation 7.1 and the procedure detailed in Section 7.2.

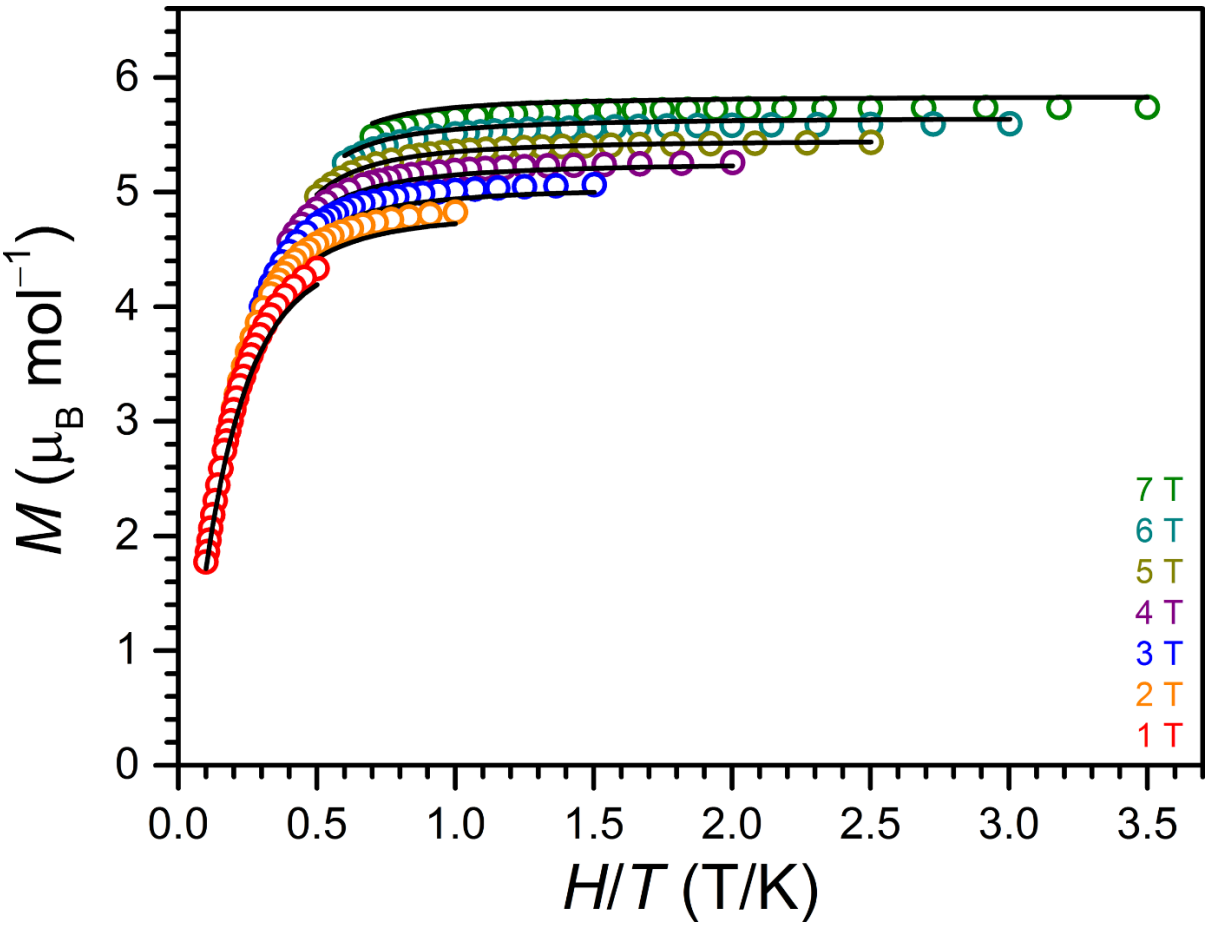

Figure 7.59 Low-temperature magnetization data for **1-Cl** collected at selected dc fields (see inset) for a microcrystalline sample restrained in a frozen eicosane matrix. The colored circles correspond to experimental data and the black lines denote fits to the data using the spin Hamiltonian given in Equation 7.1 and the procedure detailed in Section 7.2.

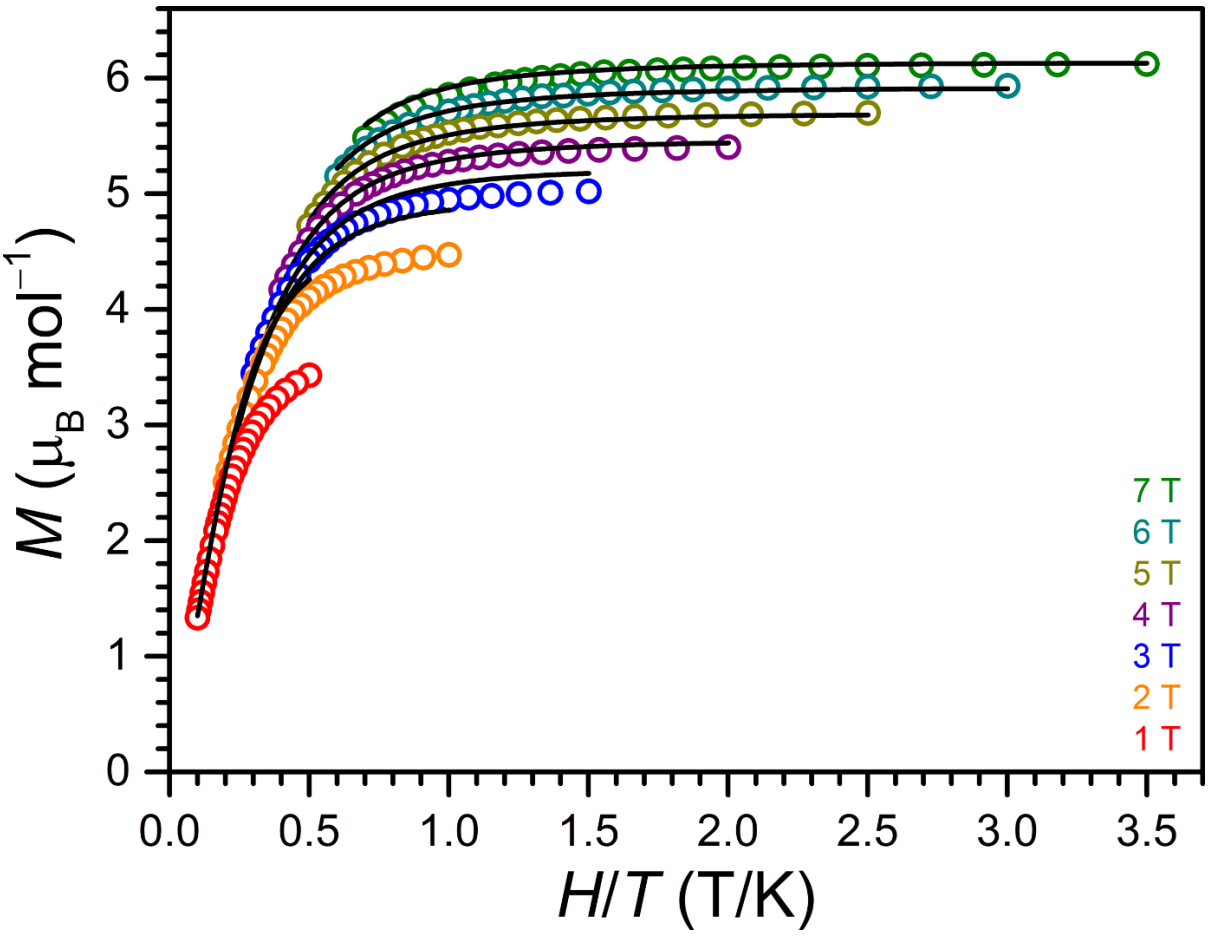

Figure 7.60 Low-temperature magnetization data for **1-NO$_2$** collected at selected dc fields (see inset) for a microcrystalline sample restrained in a frozen eicosane matrix. The colored circles correspond to experimental data and the black lines denote fits to the data using the spin Hamiltonian given in Equation 7.1 and the procedure detailed in Section 7.2.

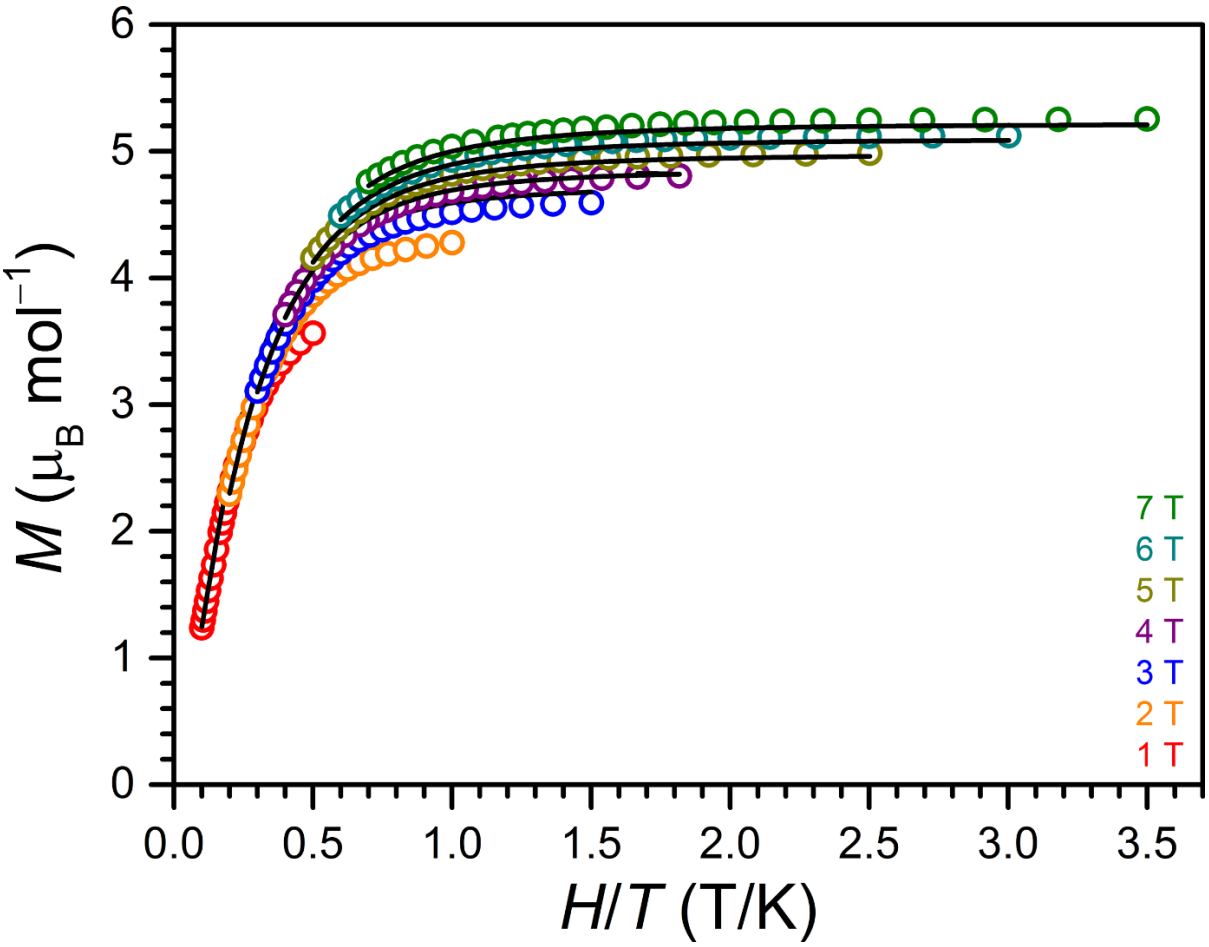

Figure 7.61 Low-temperature magnetization data for **1-SMe$_2$** collected at selected dc fields (see inset) for a microcrystalline sample restrained in a frozen eicosane matrix. The colored circles correspond to experimental data and the black lines denote fits to the data using the spin Hamiltonian given in Equation 7.1 and the procedure detailed in Section 7.2.

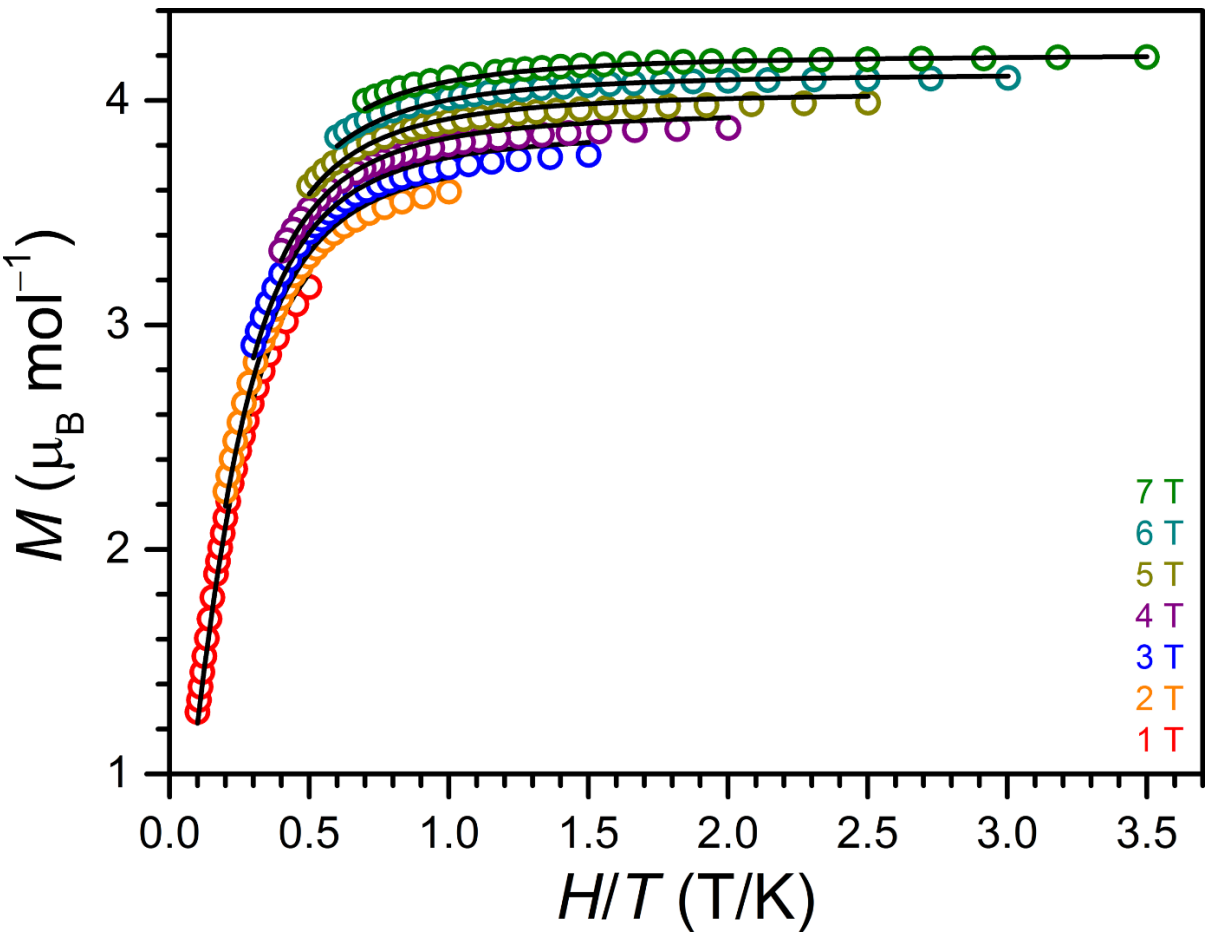

Figure 7.62 Low-temperature magnetization data for **2-OMe** collected at selected dc fields (see inset) for a microcrystalline sample restrained in a frozen eicosane matrix. The colored circles correspond to experimental data and the black lines denote fits to the data using the spin Hamiltonian given in Equation 7.2 and the procedure detailed in Section 7.2.

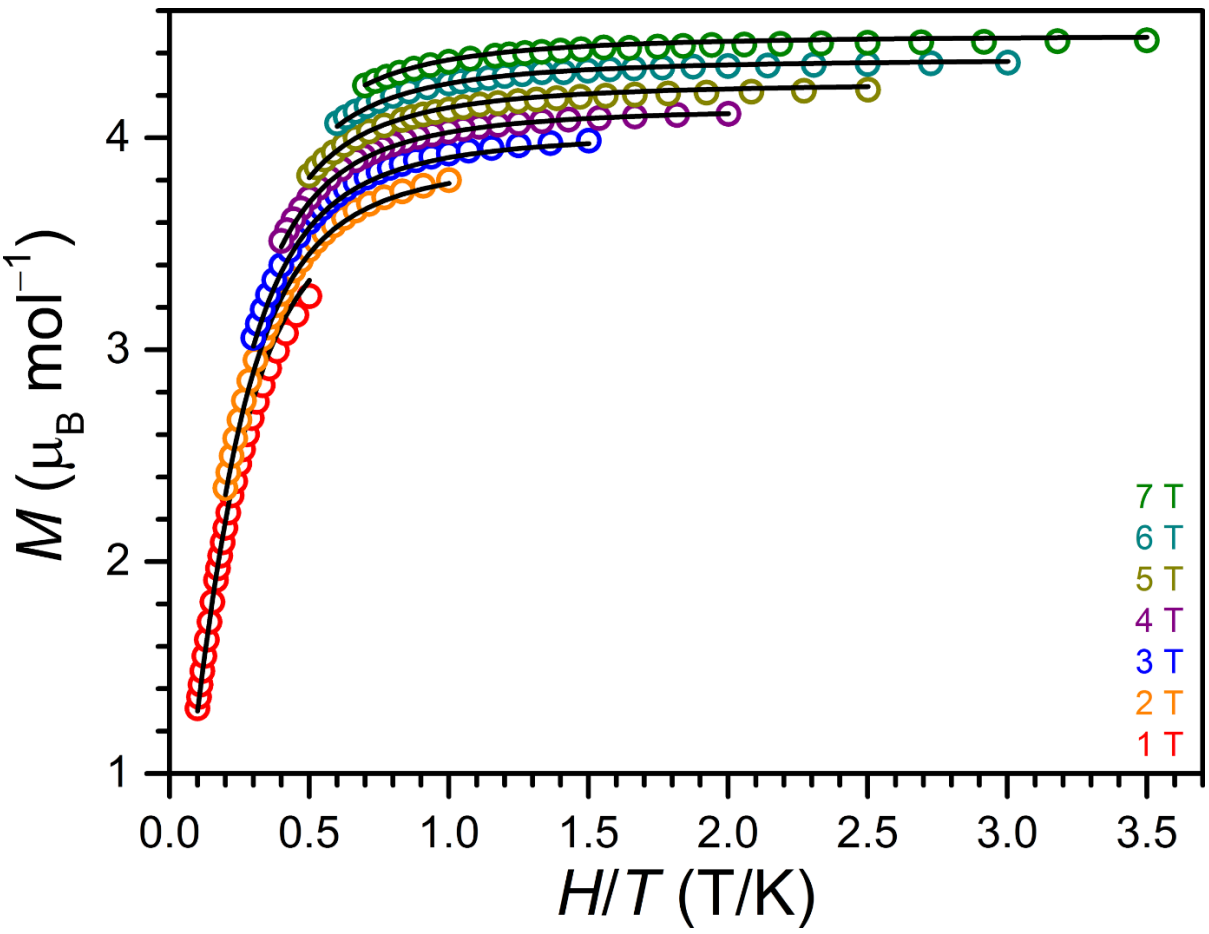

Figure 7.63 Low-temperature magnetization data for **2-Cl** collected at selected dc fields (see inset) for a microcrystalline sample restrained in a frozen eicosane matrix. The colored circles correspond to experimental data and the black lines denote fits to the data using the spin Hamiltonian given in Equation 7.2 and the procedure detailed in Section 7.2.

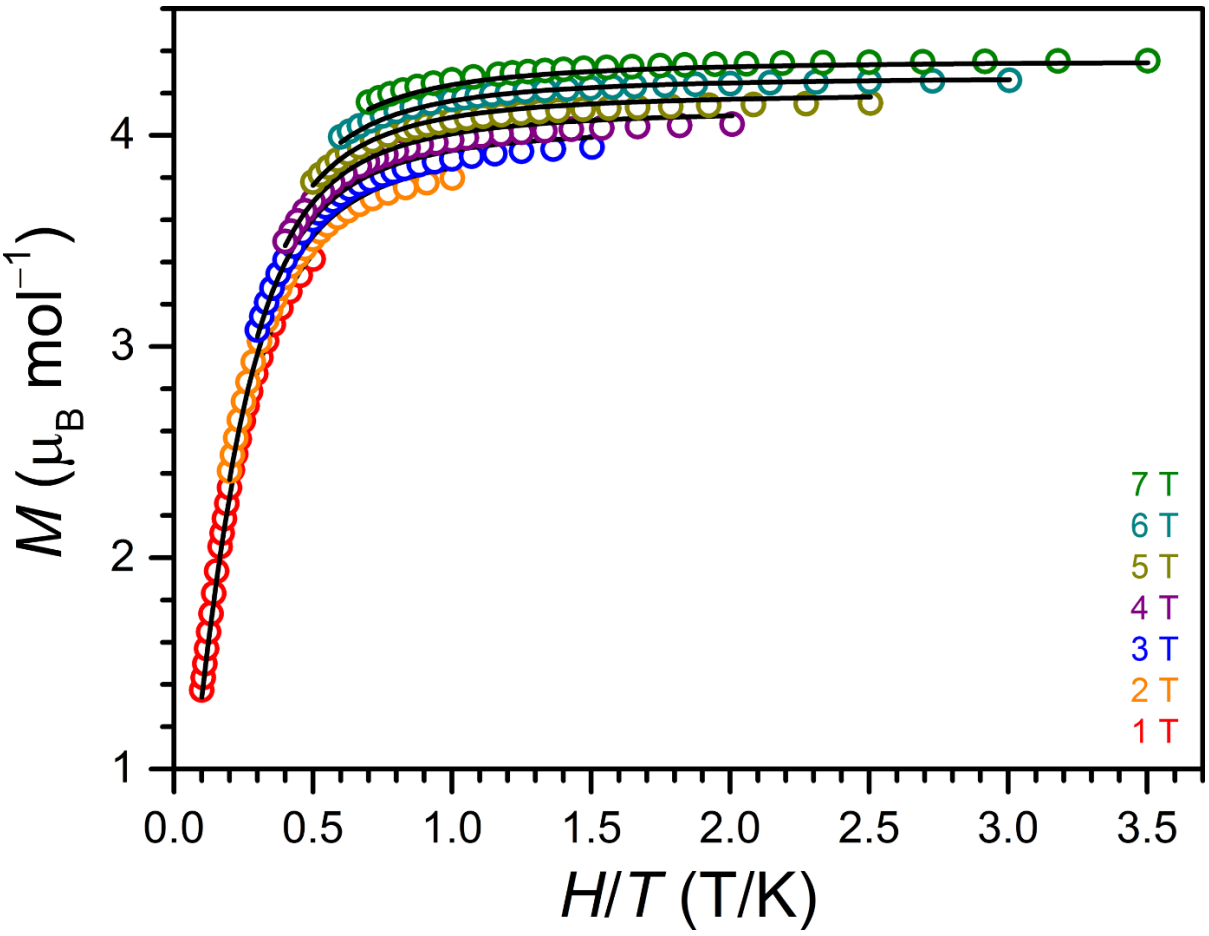

Figure 7.64 Low-temperature magnetization data for **2-NO₂** collected at selected dc fields (see inset) for a microcrystalline sample restrained in a frozen eicosane matrix. The colored circles correspond to experimental data and the black lines denote fits to the data using the spin Hamiltonian given in Equation 7.2 and the procedure detailed in Section 7.2.

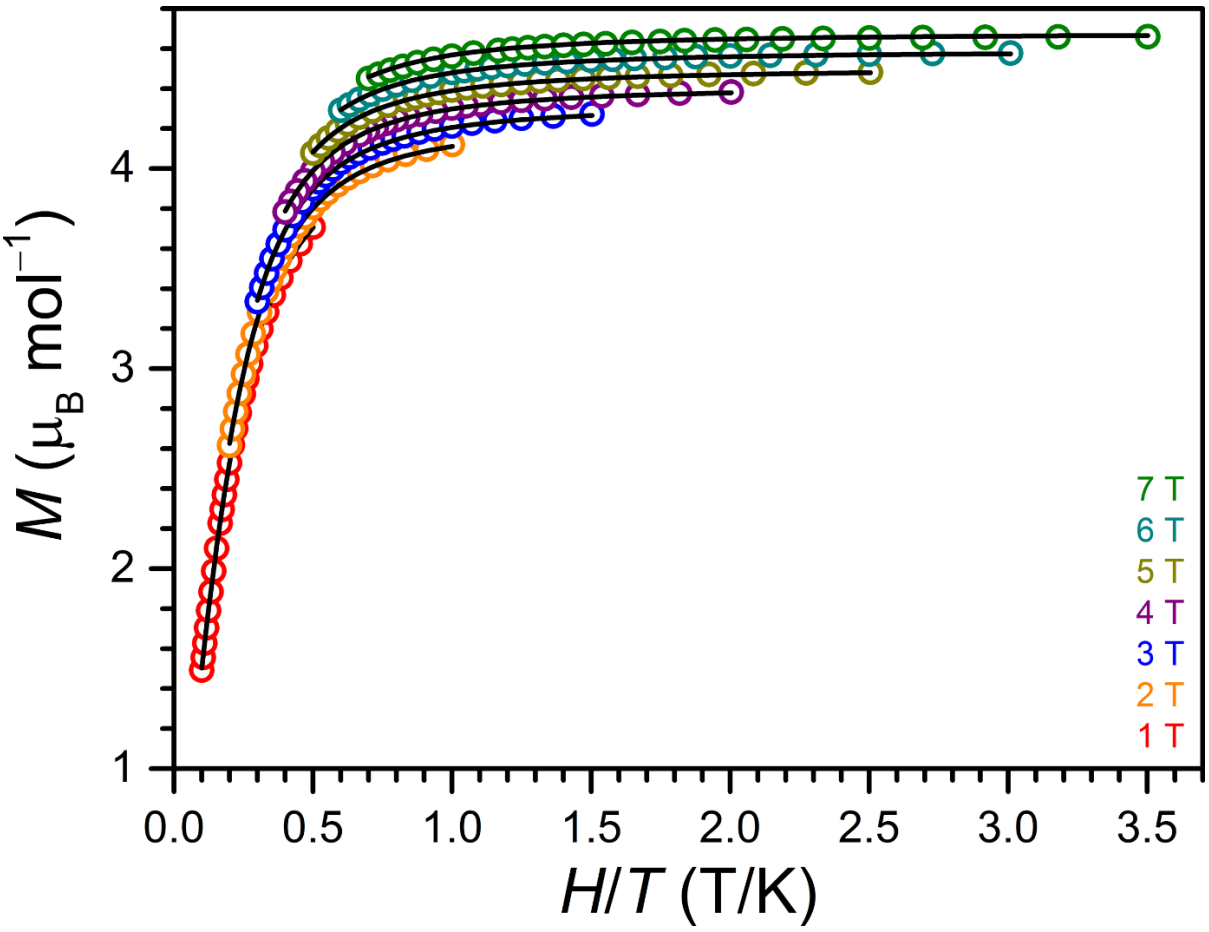

Figure 7.65 Low-temperature magnetization data for **2-SMe$_2$** collected at selected dc fields (see inset) for a microcrystalline sample restrained in a frozen eicosane matrix. The colored circles correspond to experimental data and the black lines denote fits to the data using the spin Hamiltonian given in Equation 7.2 and the procedure detailed in Section 7.2.

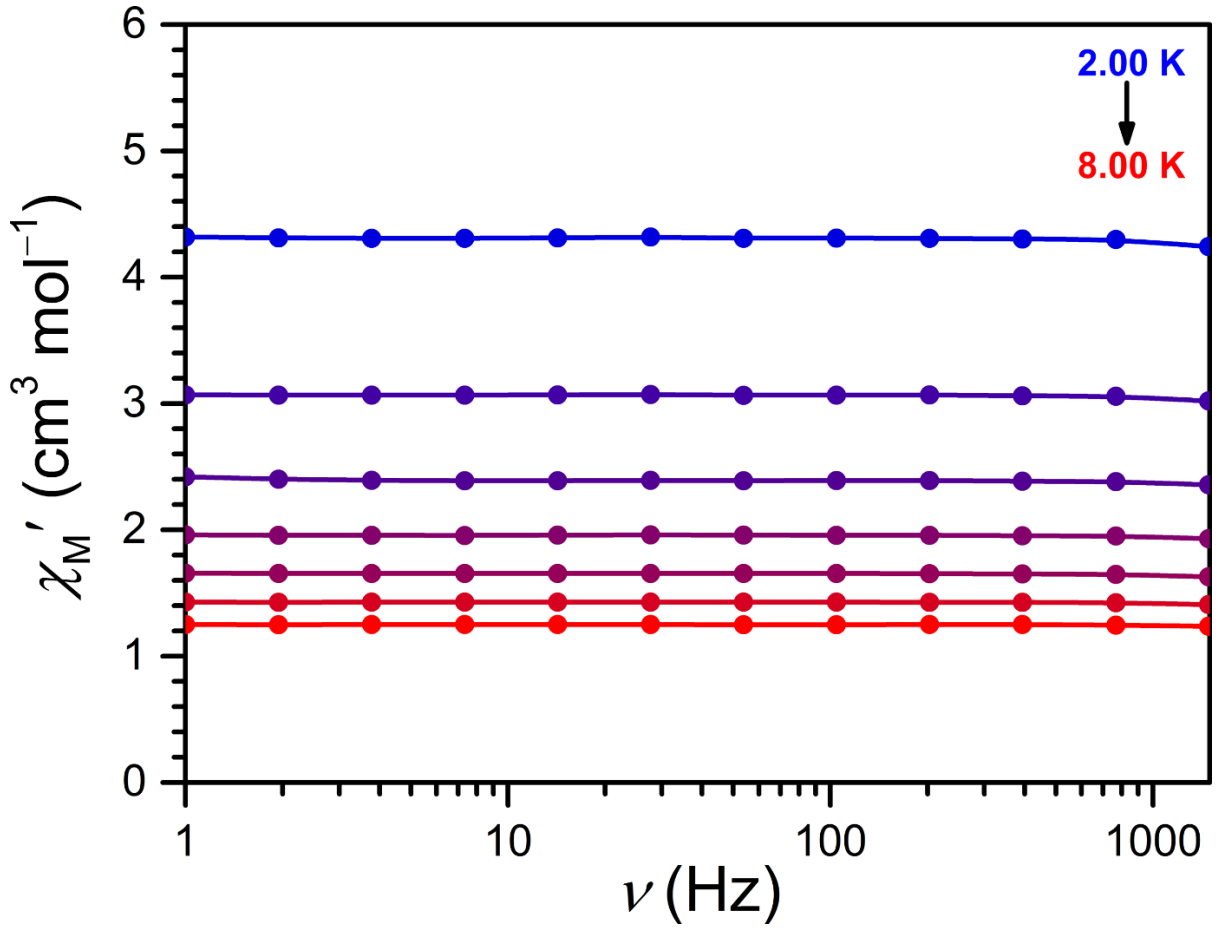

Figure 7.66 Plot of in-phase ac magnetic susceptibility (χ_M') against frequency for **1-OMe**. The data were collected from 2.00 to 8.00 K (blue to red) under zero applied dc field and an oscillating field of 4 Oe at frequencies ranging from 1 to 1488 Hz for a microcrystalline sample restrained in a frozen eicosane matrix. The colored circles correspond to experimental data and the colored lines are a guide to the eye.

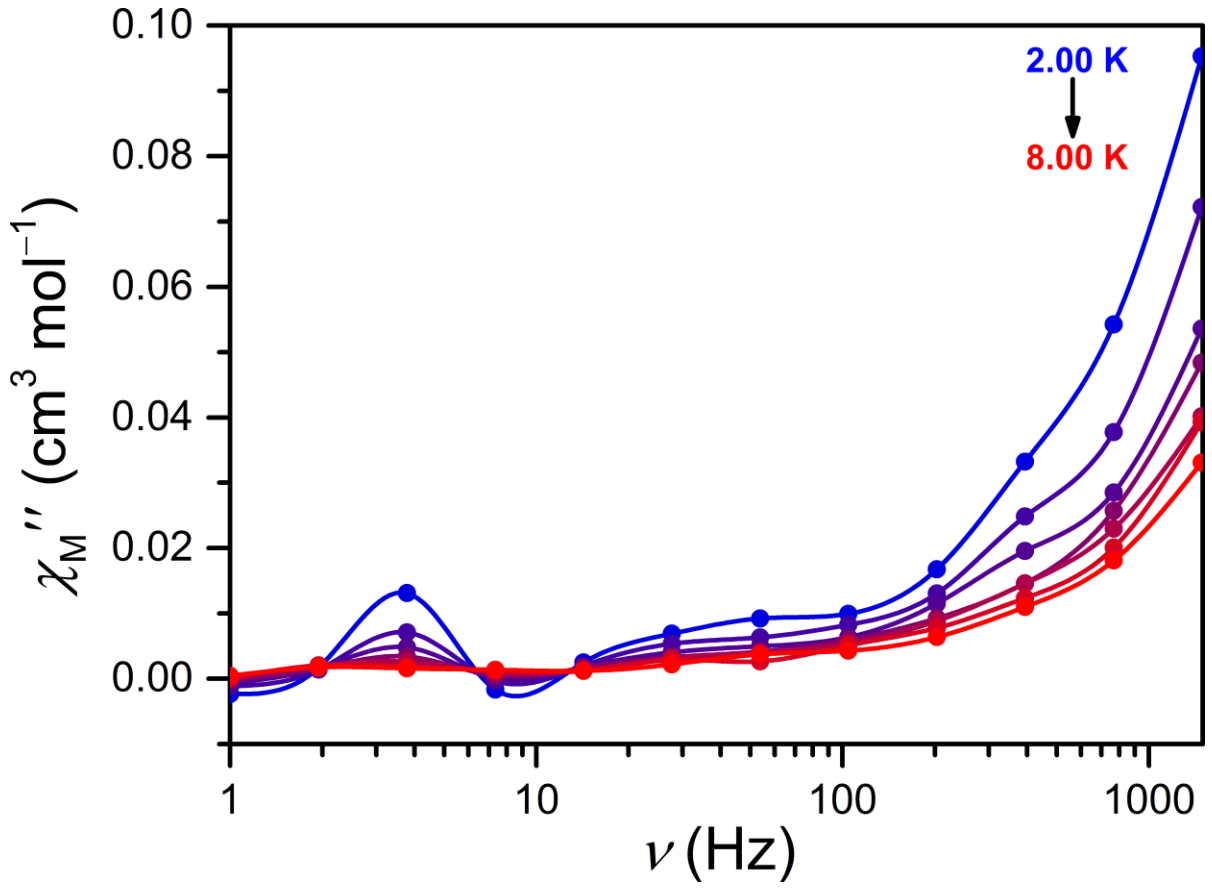

Figure 7.67 Plot of out-of-phase ac magnetic susceptibility (χ_M'') against frequency for **1-OMe**. The data were collected from 2.00 to 8.00 K (blue to red) under zero applied dc field and an oscillating field of 4 Oe at frequencies ranging from 1 to 1488 Hz for a microcrystalline sample restrained in a frozen eicosane matrix. The colored circles correspond to experimental data and the colored lines are a guide to the eye.

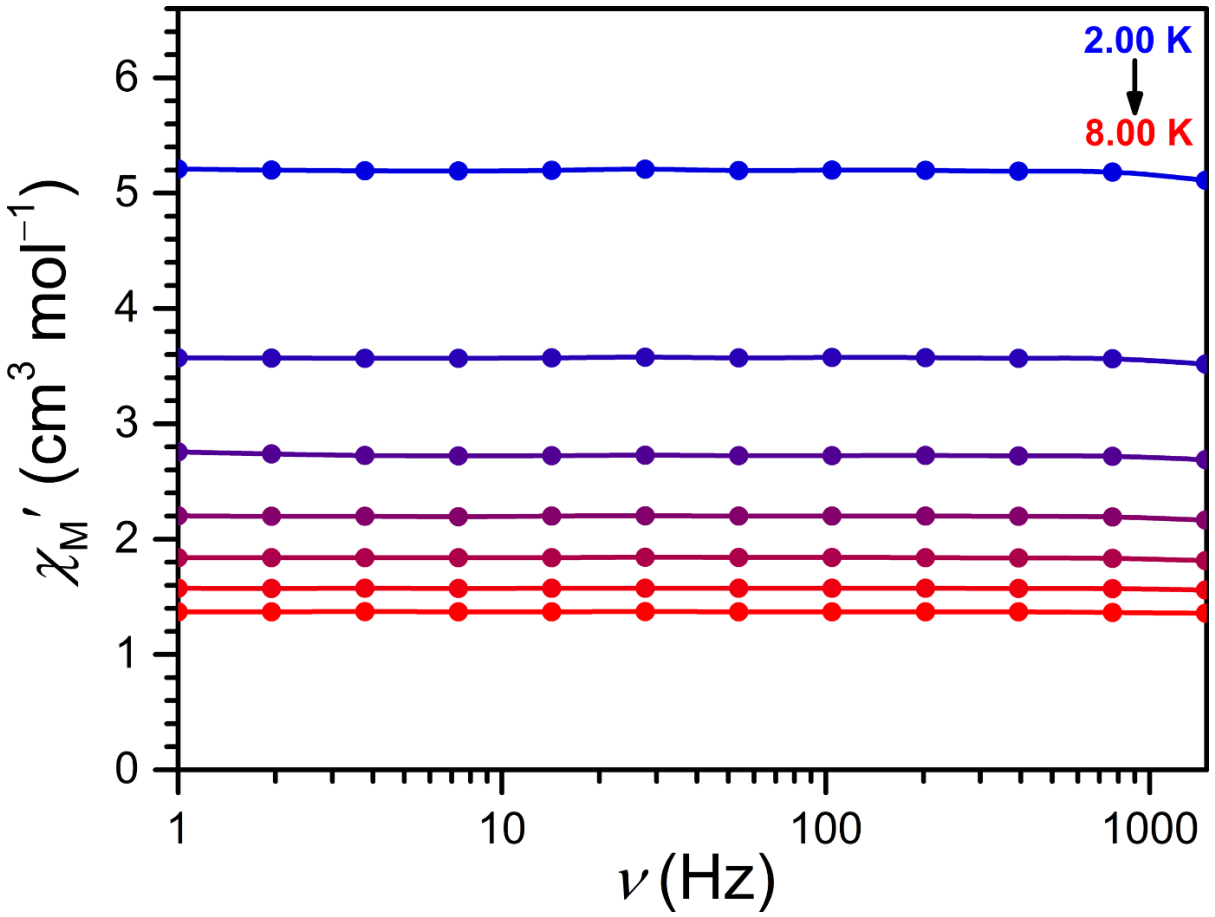

Figure 7.68 Plot of in-phase ac magnetic susceptibility (χ_M') against frequency for **1-Cl**. The data were collected from 2.00 to 8.00 K (blue to red) under zero applied dc field and an oscillating field of 4 Oe at frequencies ranging from 1 to 1488 Hz for a microcrystalline sample restrained in a frozen eicosane matrix. The colored circles correspond to experimental data and the colored lines are a guide to the eye.

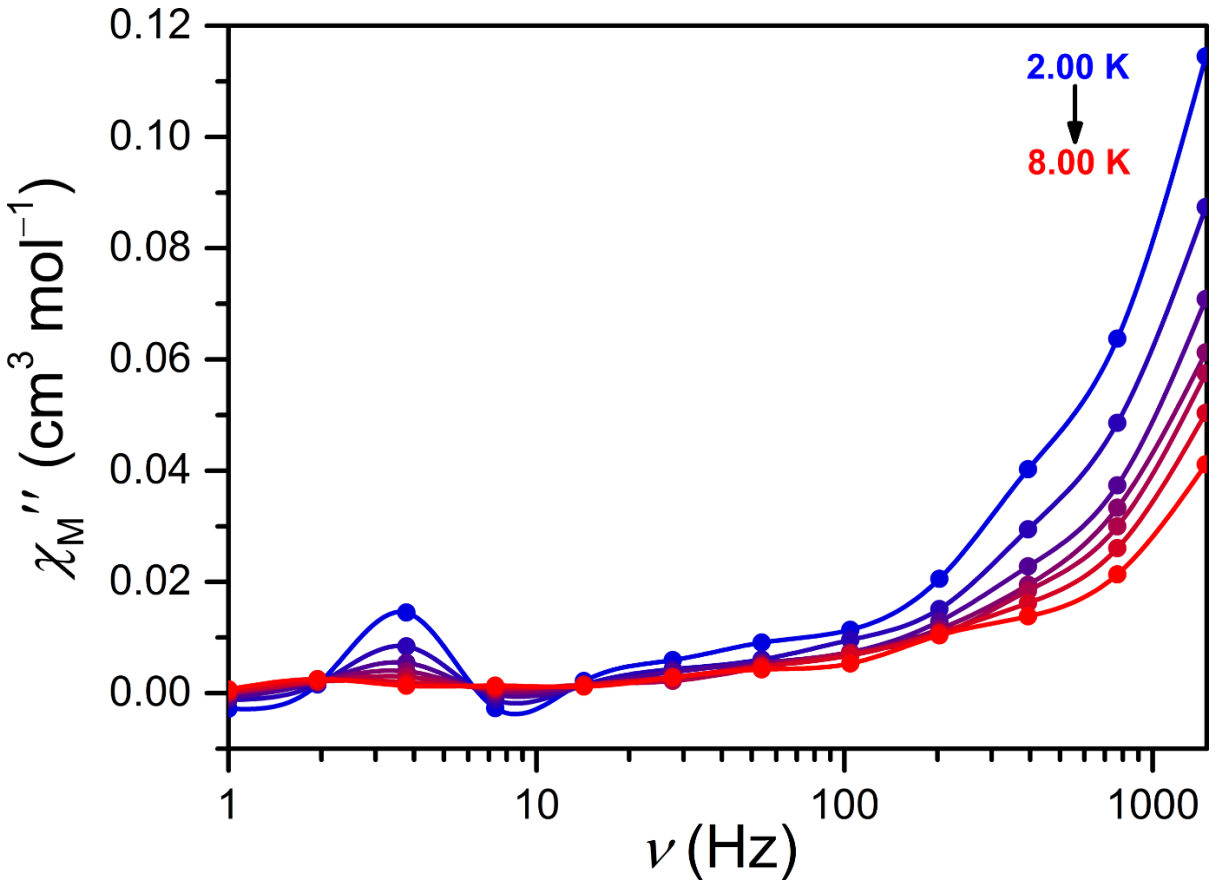

Figure 7.69 Plot of out-of-phase ac magnetic susceptibility (χ_M'') against frequency for **1-Cl**. The data were collected from 2.00 to 8.00 K (blue to red) under zero applied dc field and an oscillating field of 4 Oe at frequencies ranging from 1 to 1488 Hz for a microcrystalline sample restrained in a frozen eicosane matrix. The colored circles correspond to experimental data and the colored lines are a guide to the eye.

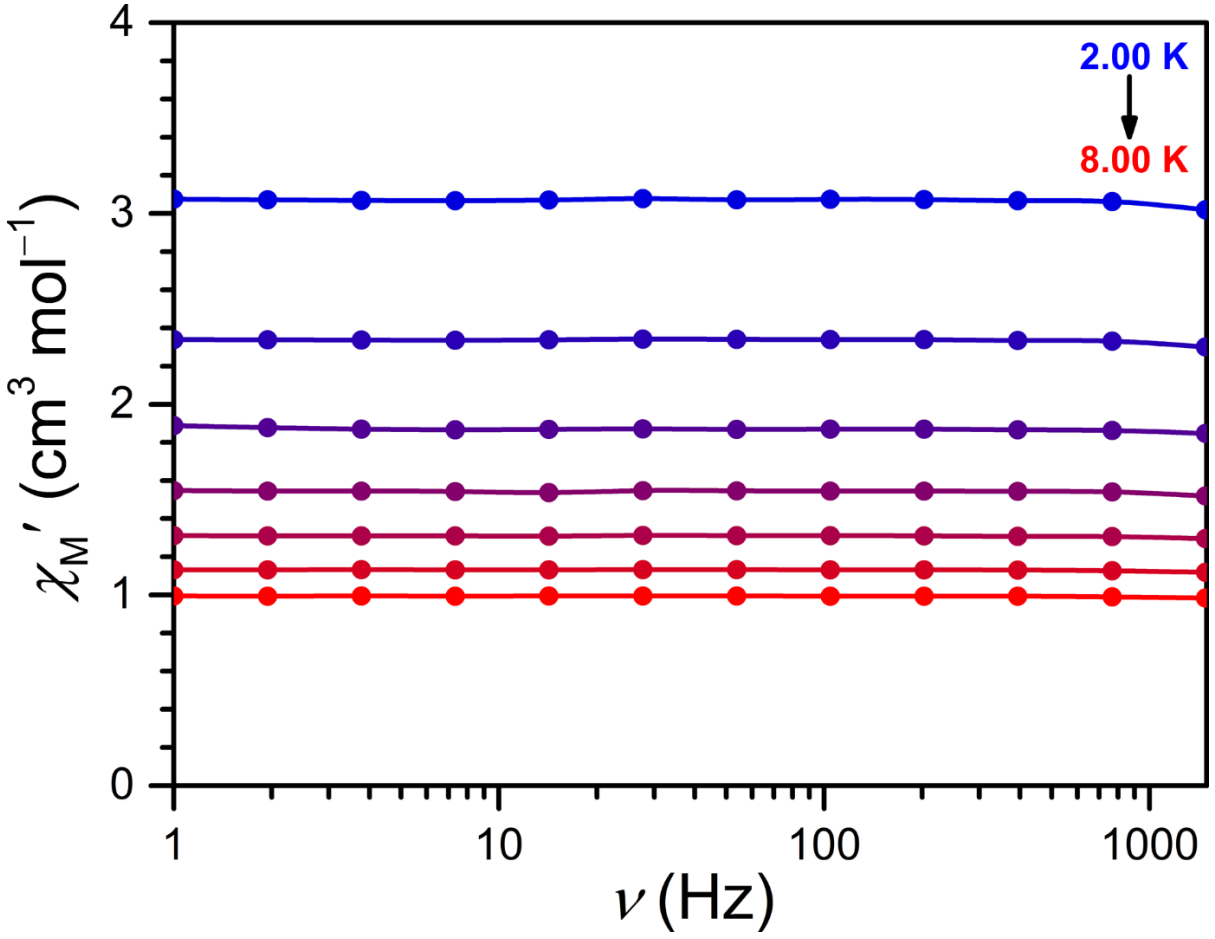

Figure 7.70 Plot of in-phase ac magnetic susceptibility (χ_M') against frequency for **1-NO$_2$**. The data were collected from 2.00 to 8.00 K (blue to red) under zero applied dc field and an oscillating field of 4 Oe at frequencies ranging from 1 to 1488 Hz for a microcrystalline sample restrained in a frozen eicosane matrix. The colored circles correspond to experimental data and the colored lines are a guide to the eye.

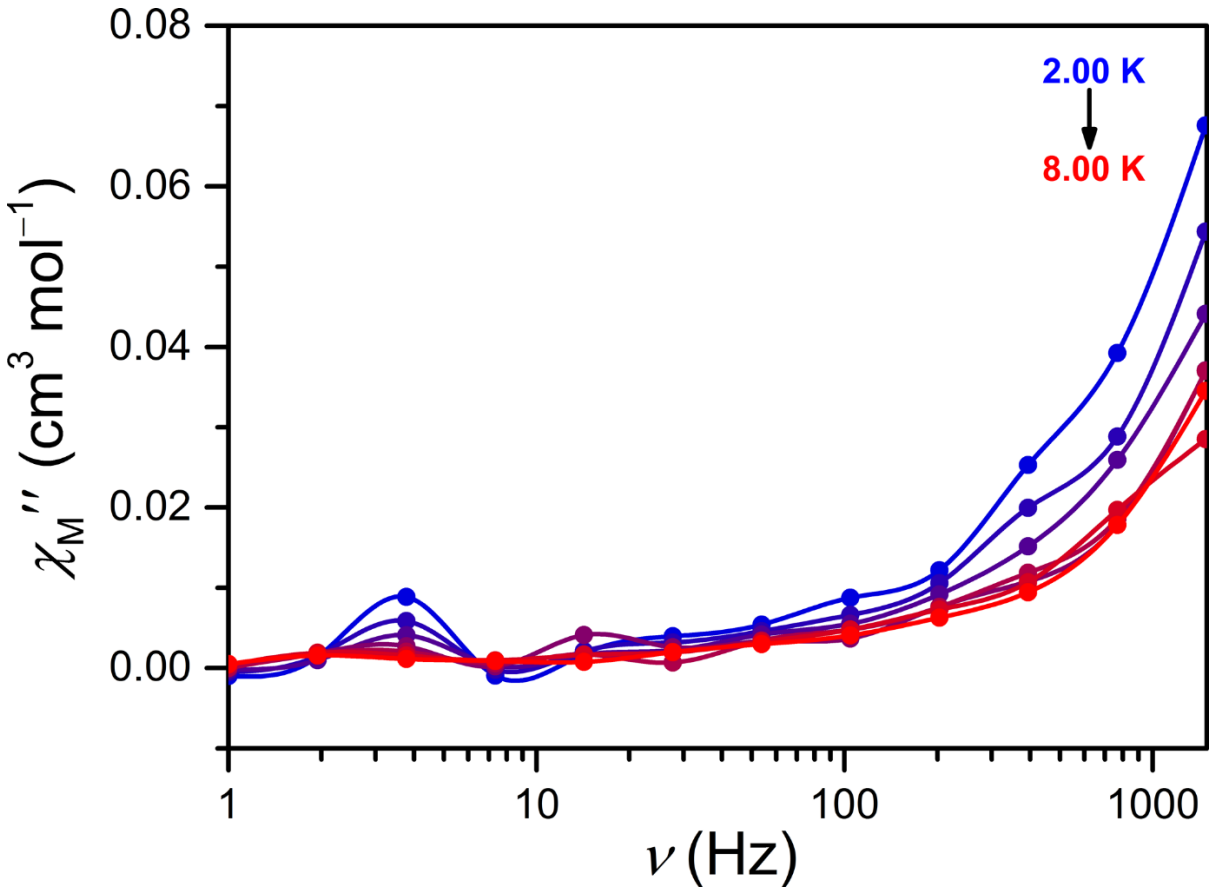

Figure 7.71 Plot of out-of-phase ac magnetic susceptibility (χ_M'') against frequency for **1-NO$_2$**. The data were collected from 2.00 to 8.00 K (blue to red) under zero applied dc field and an oscillating field of 4 Oe at frequencies ranging from 1 to 1488 Hz for a microcrystalline sample restrained in a frozen eicosane matrix. The colored circles correspond to experimental data and the colored lines are a guide to the eye.

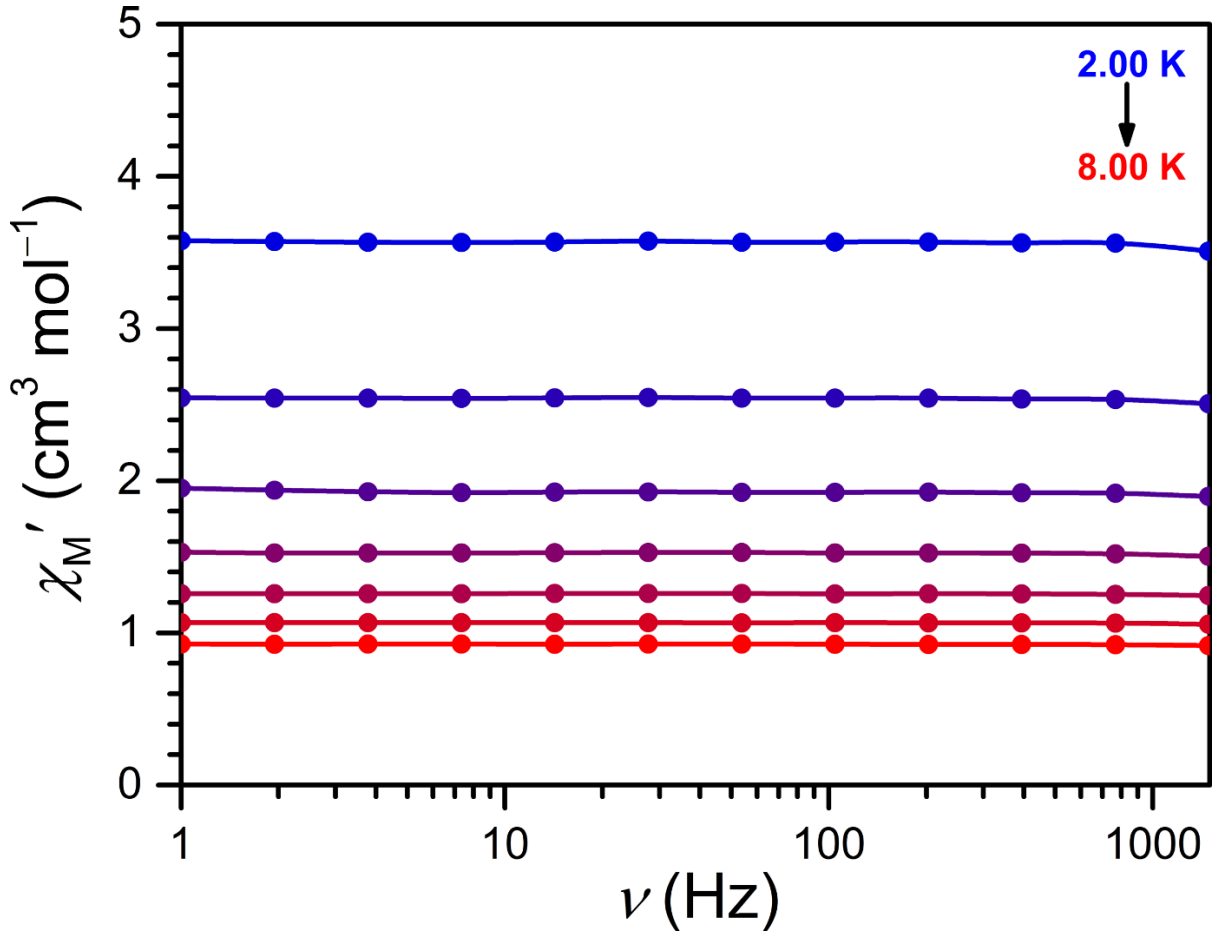

Figure 7.72 Plot of in-phase ac magnetic susceptibility (χ_M') against frequency for **1-SMe$_2$**. The data were collected from 2.00 to 8.00 K (blue to red) under zero applied dc field and an oscillating field of 4 Oe at frequencies ranging from 1 to 1488 Hz for a microcrystalline sample restrained in a frozen eicosane matrix. The colored circles correspond to experimental data and the colored lines are a guide to the eye.

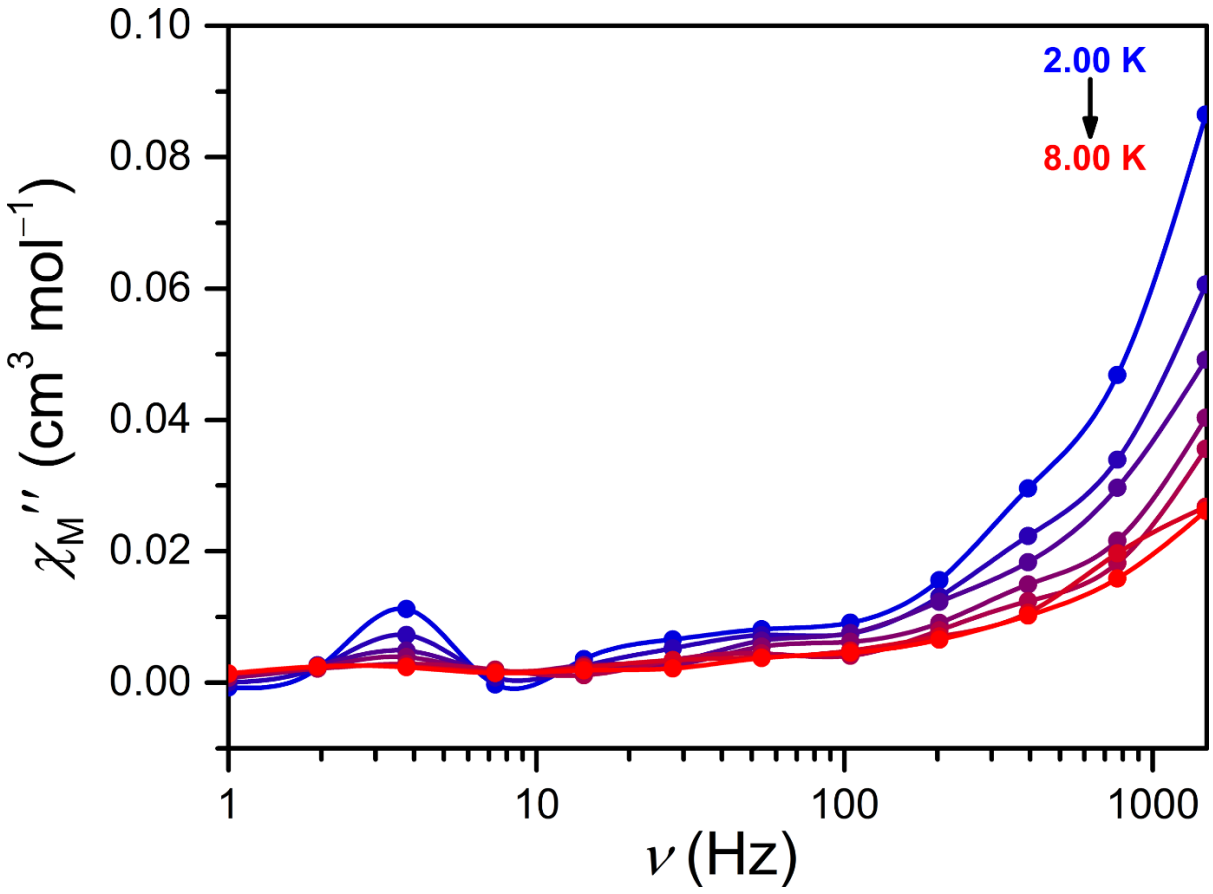

Figure 7.73 Plot of out-of-phase ac magnetic susceptibility (χ_M'') against frequency for **1-SMe$_2$**. The data were collected from 2.00 to 8.00 K (blue to red) under zero applied dc field and an oscillating field of 4 Oe at frequencies ranging from 1 to 1488 Hz for a microcrystalline sample restrained in a frozen eicosane matrix. The colored circles correspond to experimental data and the colored lines are a guide to the eye.

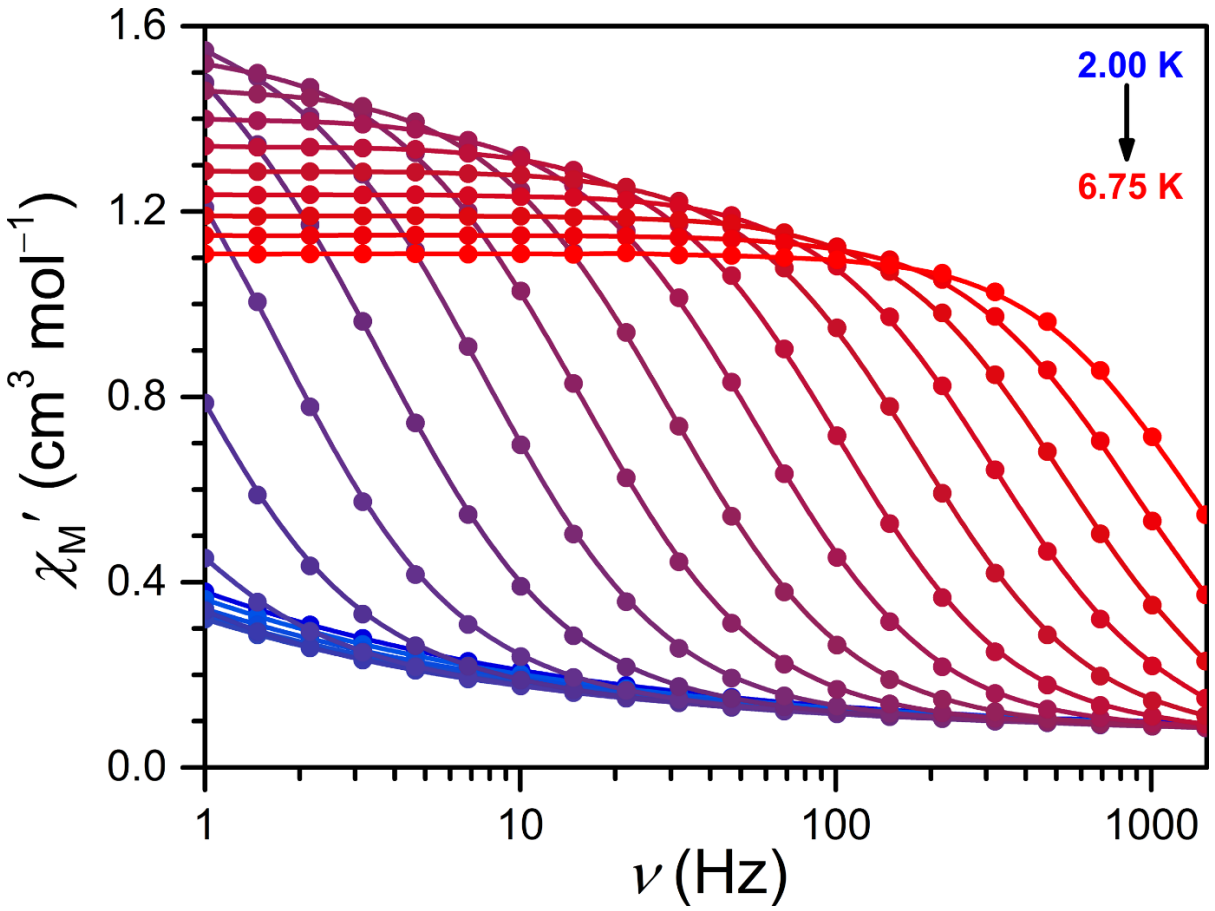

Figure 7.74 Plot of in-phase ac magnetic susceptibility (χ_M') against frequency for **2-OMe**. The data were collected from 2.00 to 6.75 K (blue to red) under zero applied dc field and an oscillating field of 4 Oe at frequencies ranging from 1 to 1488 Hz for a microcrystalline sample restrained in a frozen eicosane matrix. The colored circles correspond to experimental data and the colored lines are a guide to the eye.

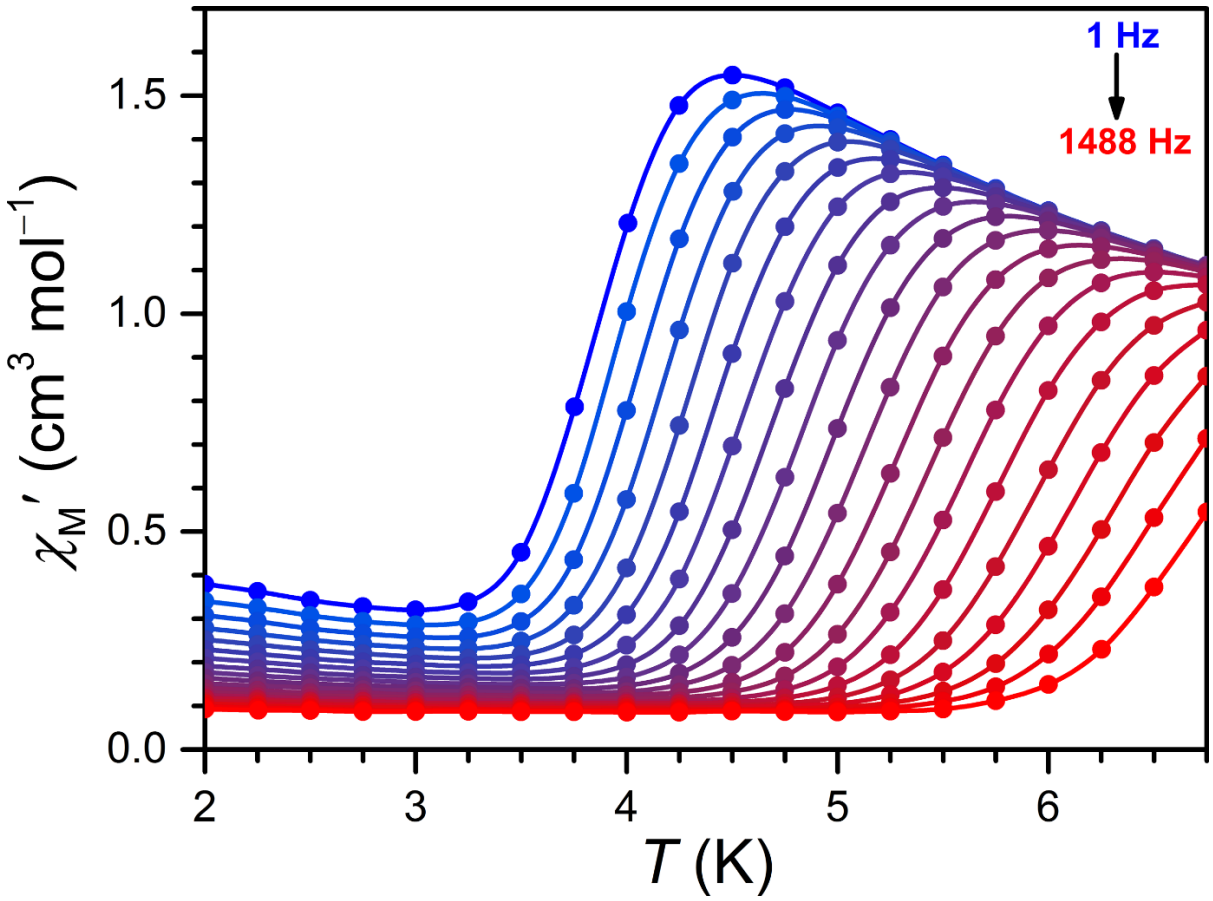

Figure 7.75 Plot of in-phase ac magnetic susceptibility (χ_M') against temperature for **2-OMe**. The data were collected from 2.00 to 6.75 K under zero applied dc field and an oscillating field of 4 Oe at frequencies ranging from 1 to 1488 Hz (blue to red) for a microcrystalline sample restrained in a frozen eicosane matrix. The colored circles correspond to experimental data and the colored lines are a guide to the eye.

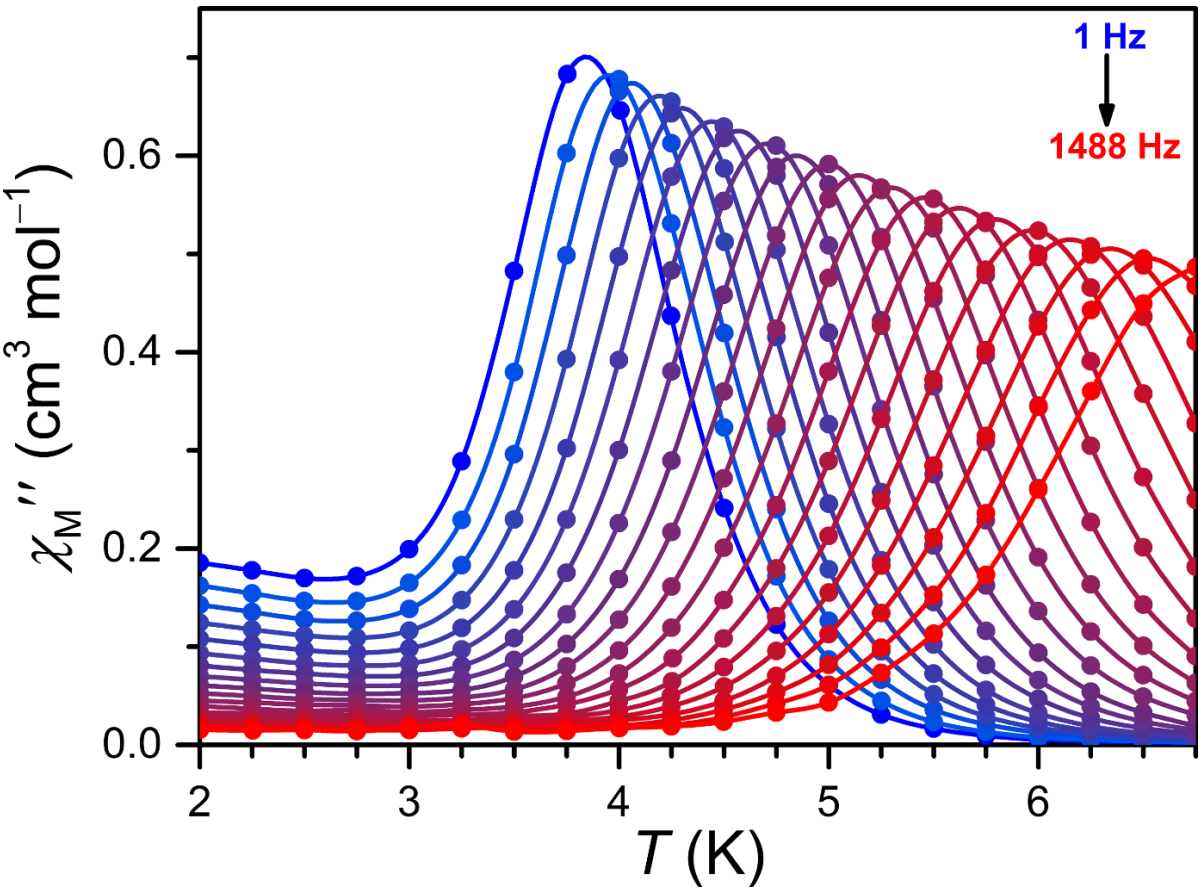

Figure 7.76 Plot of out-of-phase ac magnetic susceptibility (χ_M'') against temperature for **2-OMe**. The data were collected from 2.00 to 6.75 K under zero applied dc field and an oscillating field of 4 Oe at frequencies ranging from 1 to 1488 Hz (blue to red) for a microcrystalline sample restrained in a frozen eicosane matrix. The colored circles correspond to experimental data and the colored lines are a guide to the eye.

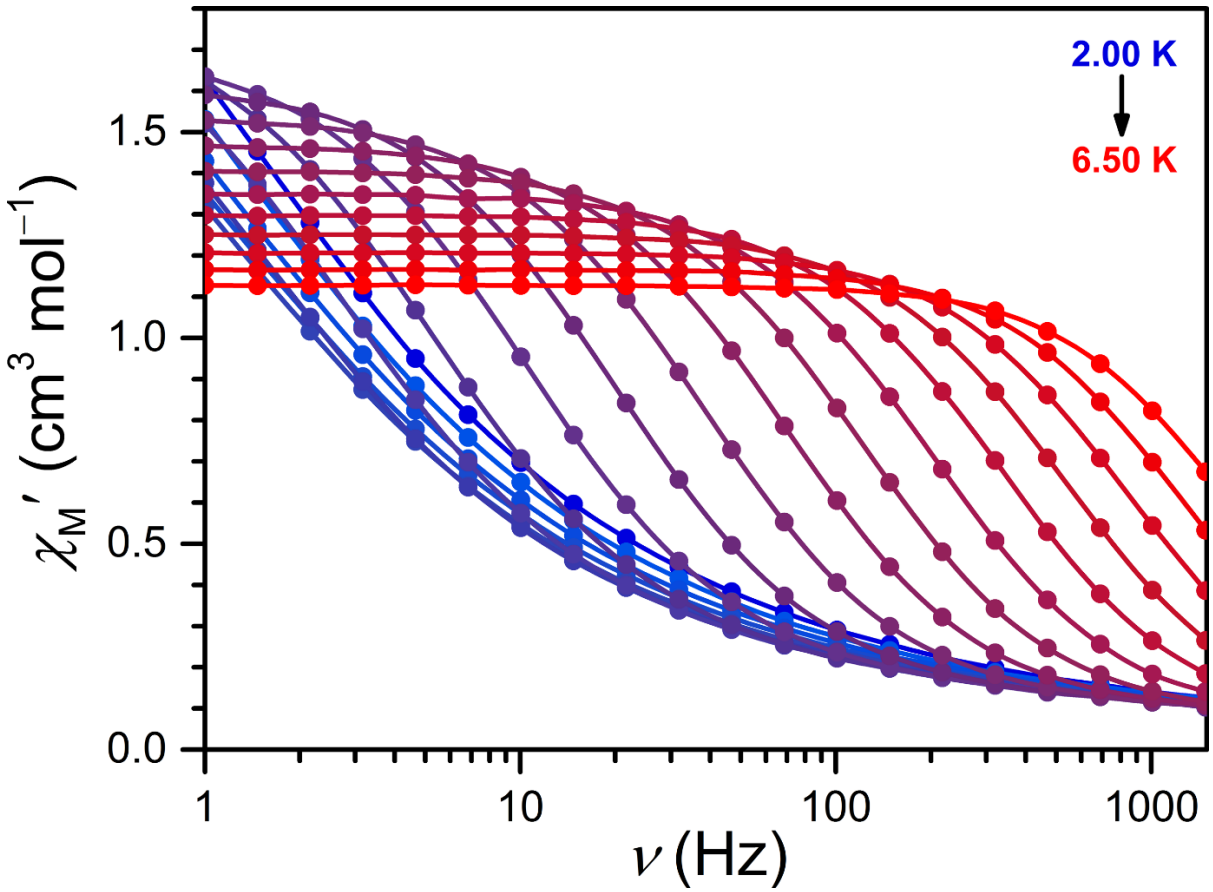

Figure 7.77 Plot of in-phase ac magnetic susceptibility (χ_M') against frequency for **2-Cl**. The data were collected from 2.00 to 6.50 K (blue to red) under zero applied dc field and an oscillating field of 4 Oe at frequencies ranging from 1 to 1488 Hz for a microcrystalline sample restrained in a frozen eicosane matrix. The colored circles correspond to experimental data and the colored lines are a guide to the eye.

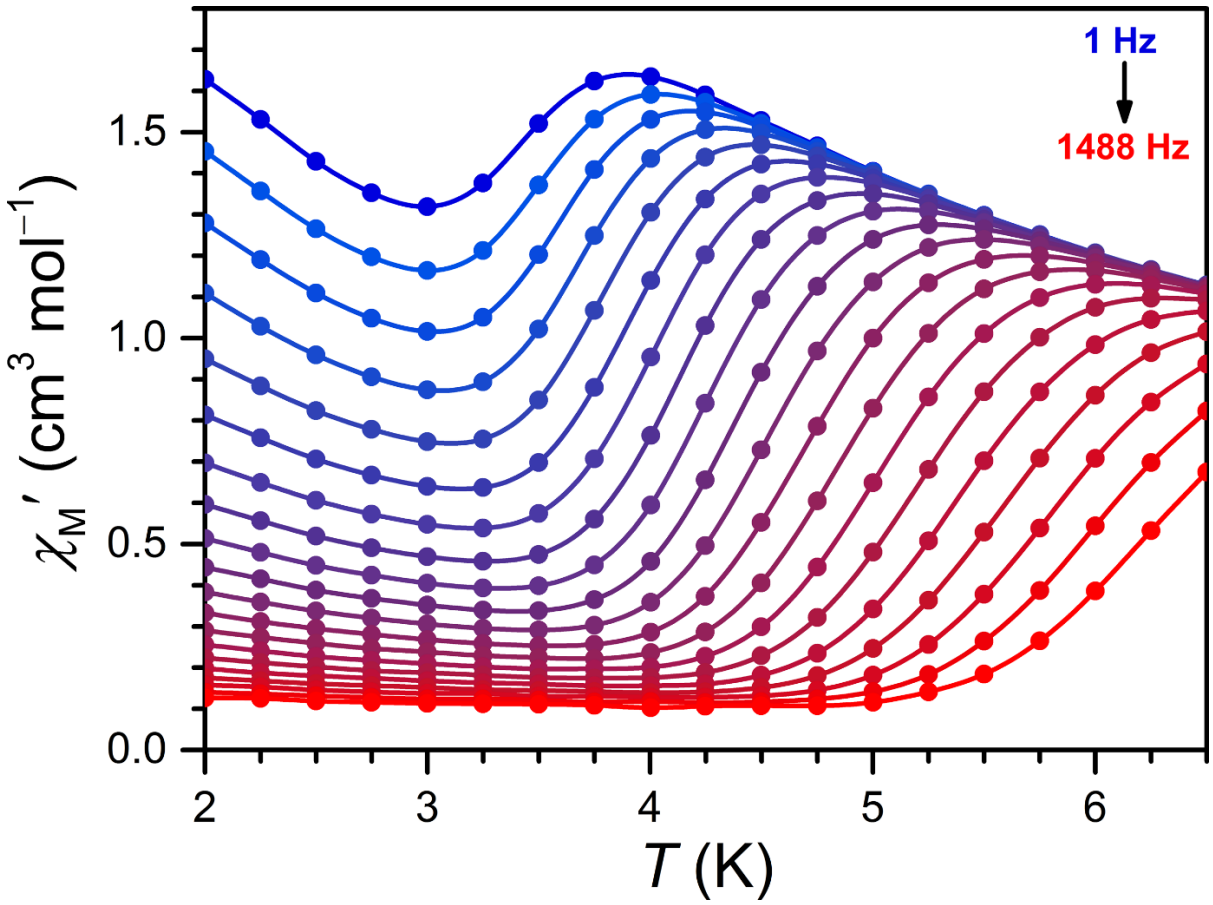

Figure 7.78 Plot of in-phase ac magnetic susceptibility (χ_M') against temperature for **2-Cl**. The data were collected from 2.00 to 6.50 K under zero applied dc field and an oscillating field of 4 Oe at frequencies ranging from 1 to 1488 Hz (blue to red) for a microcrystalline sample restrained in a frozen eicosane matrix. The colored circles correspond to experimental data and the colored lines are a guide to the eye.

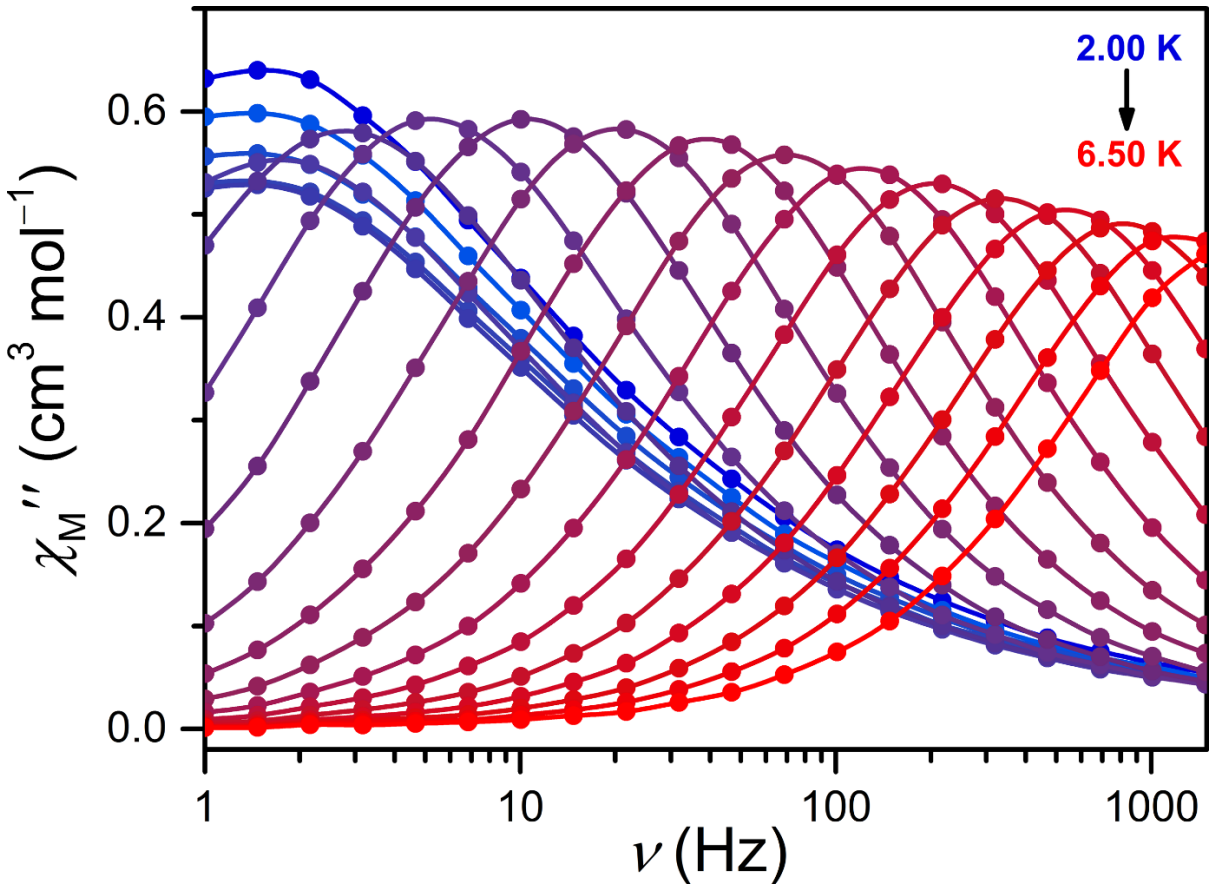

Figure 7.79 Plot of out-of-phase ac magnetic susceptibility (χ_M'') against frequency for **2-Cl**. The data were collected from 2.00 to 6.50 K (blue to red) under zero applied dc field and an oscillating field of 4 Oe at frequencies ranging from 1 to 1488 Hz for a microcrystalline sample restrained in a frozen eicosane matrix. The colored circles correspond to experimental data and the colored lines are a guide to the eye.

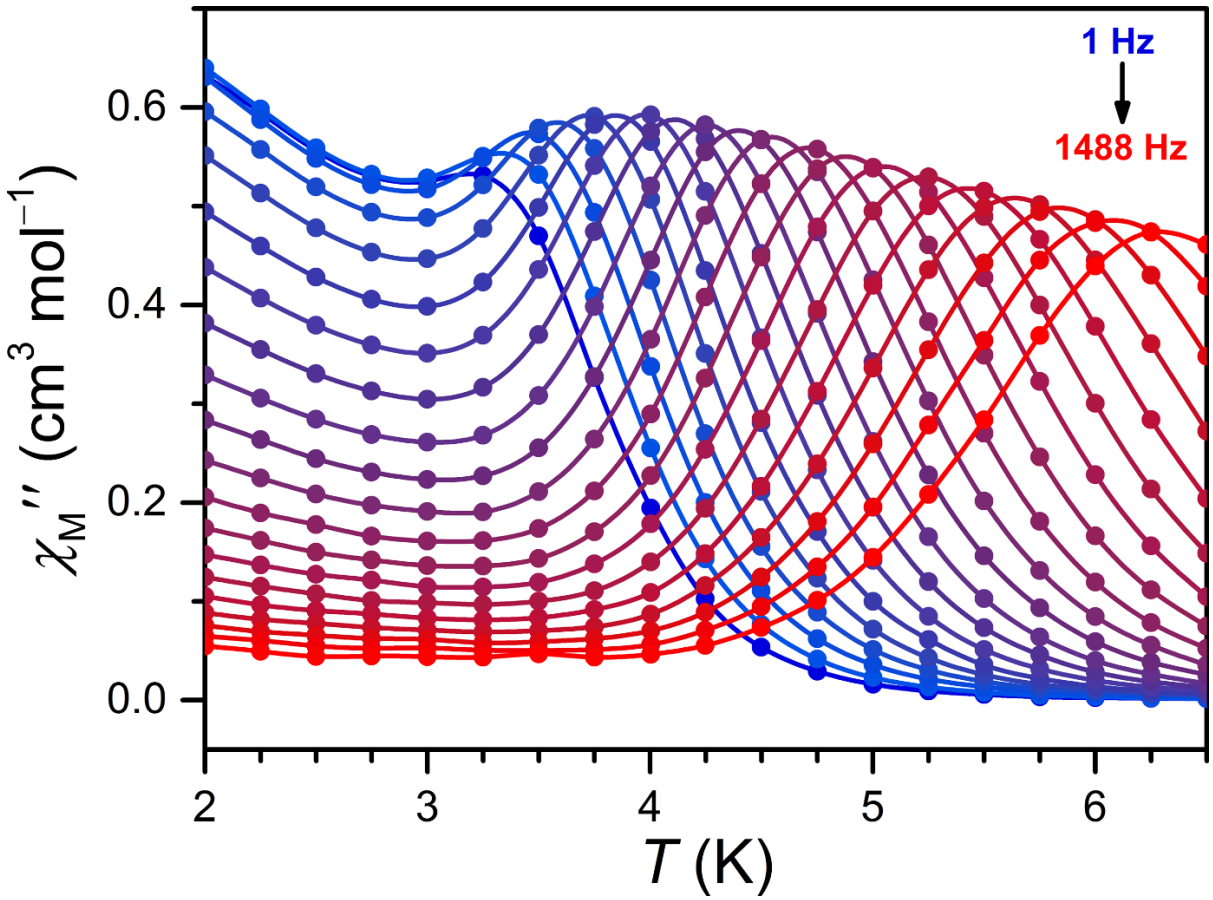

Figure 7.80 Plot of out-of-phase ac magnetic susceptibility (χ_M'') against temperature for **2-Cl**. The data were collected from 2.00 to 6.50 K under zero applied dc field and an oscillating field of 4 Oe at frequencies ranging from 1 to 1488 Hz (blue to red) for a microcrystalline sample restrained in a frozen eicosane matrix. The colored circles correspond to experimental data and the colored lines are a guide to the eye.

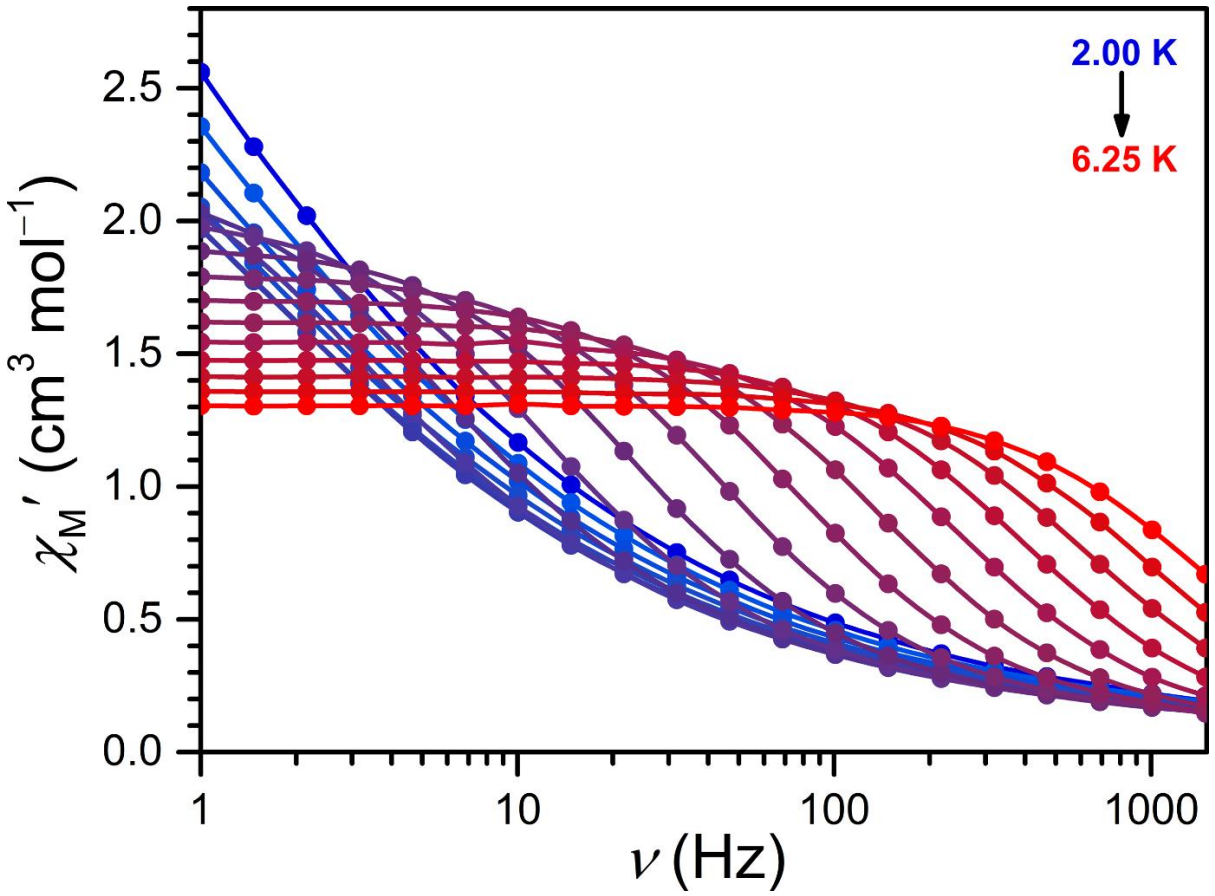

Figure 7.81 Plot of in-phase ac magnetic susceptibility (χ_M') against frequency for **2-NO$_2$**. The data were collected from 2.00 to 6.25 K (blue to red) under zero applied dc field and an oscillating field of 4 Oe at frequencies ranging from 1 to 1488 Hz for a microcrystalline sample restrained in a frozen eicosane matrix. The colored circles correspond to experimental data and the colored lines are a guide to the eye.

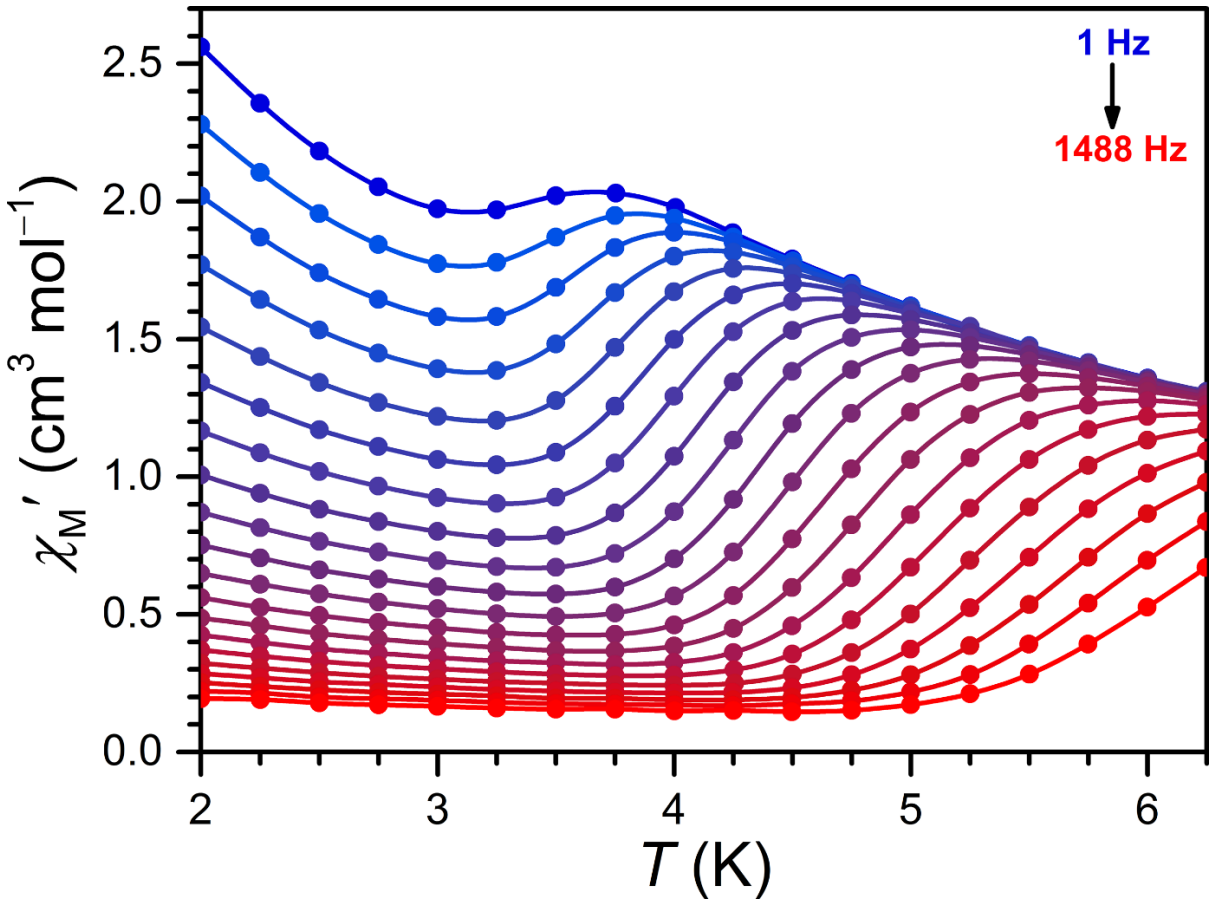

Figure 7.82 Plot of in-phase ac magnetic susceptibility (χ_M') against temperature for **2-NO₂**. The data were collected from 2.00 to 6.25 K under zero applied dc field and an oscillating field of 4 Oe at frequencies ranging from 1 to 1488 Hz (blue to red) for a microcrystalline sample restrained in a frozen eicosane matrix. The colored circles correspond to experimental data and the colored lines are a guide to the eye.

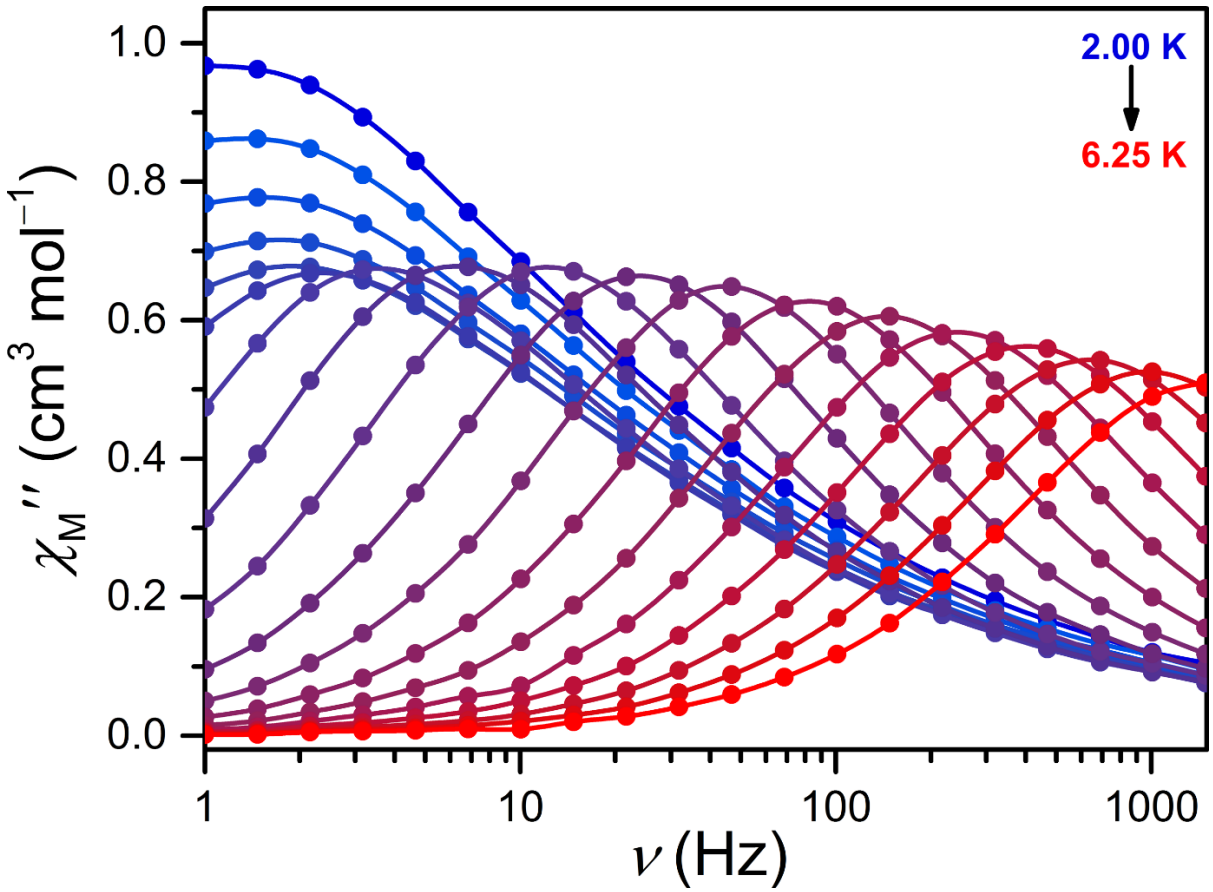

Figure 7.83 Plot of out-of-phase ac magnetic susceptibility (χ_M'') against frequency for **2-NO$_2$**. The data were collected from 2.00 to 6.25 K (blue to red) under zero applied dc field and an oscillating field of 4 Oe at frequencies ranging from 1 to 1488 Hz for a microcrystalline sample restrained in a frozen eicosane matrix. The colored circles correspond to experimental data and the colored lines are a guide to the eye.

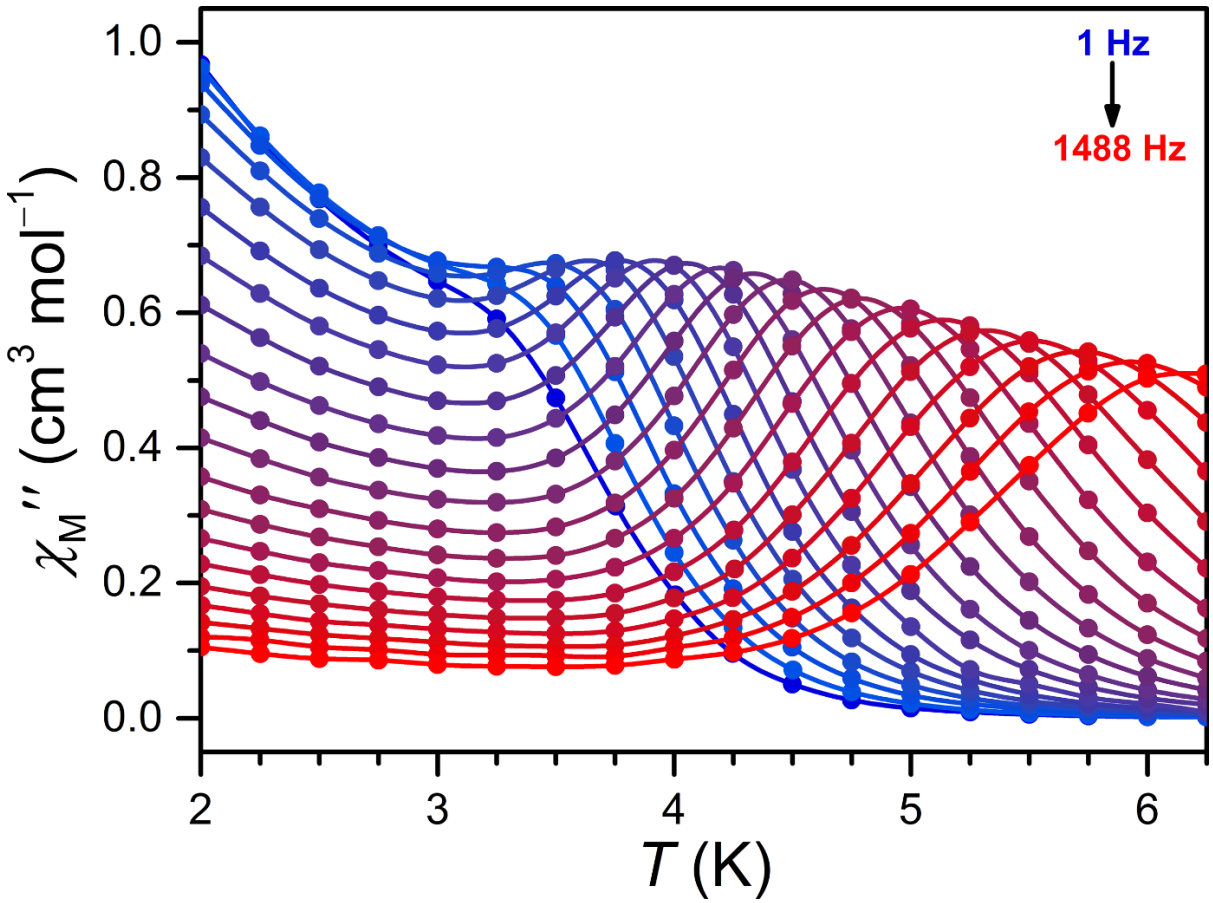

Figure 7.84 Plot of out-of-phase ac magnetic susceptibility (χ_M'') against temperature for **2-NO₂**. The data were collected from 2.00 to 6.25 K under zero applied dc field and an oscillating field of 4 Oe at frequencies ranging from 1 to 1488 Hz (blue to red) for a microcrystalline sample restrained in a frozen eicosane matrix. The colored circles correspond to experimental data and the colored lines are a guide to the eye.

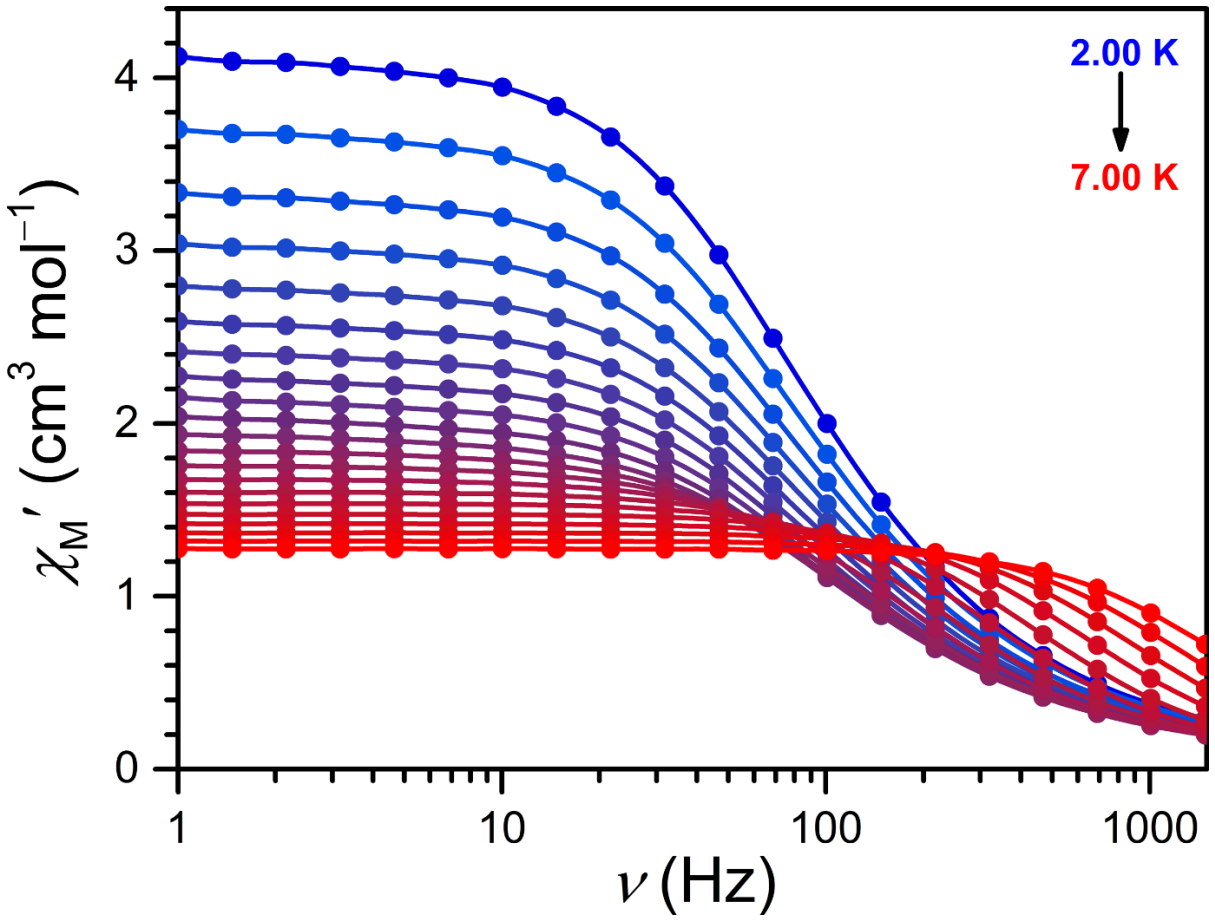

Figure 7.85 Plot of in-phase ac magnetic susceptibility (χ_M') against frequency for **2-SMe$_2$**. The data were collected from 2.00 to 7.00 K (blue to red) under zero applied dc field and an oscillating field of 4 Oe at frequencies ranging from 1 to 1488 Hz for a microcrystalline sample restrained in a frozen eicosane matrix. The colored circles correspond to experimental data and the colored lines are a guide to the eye.

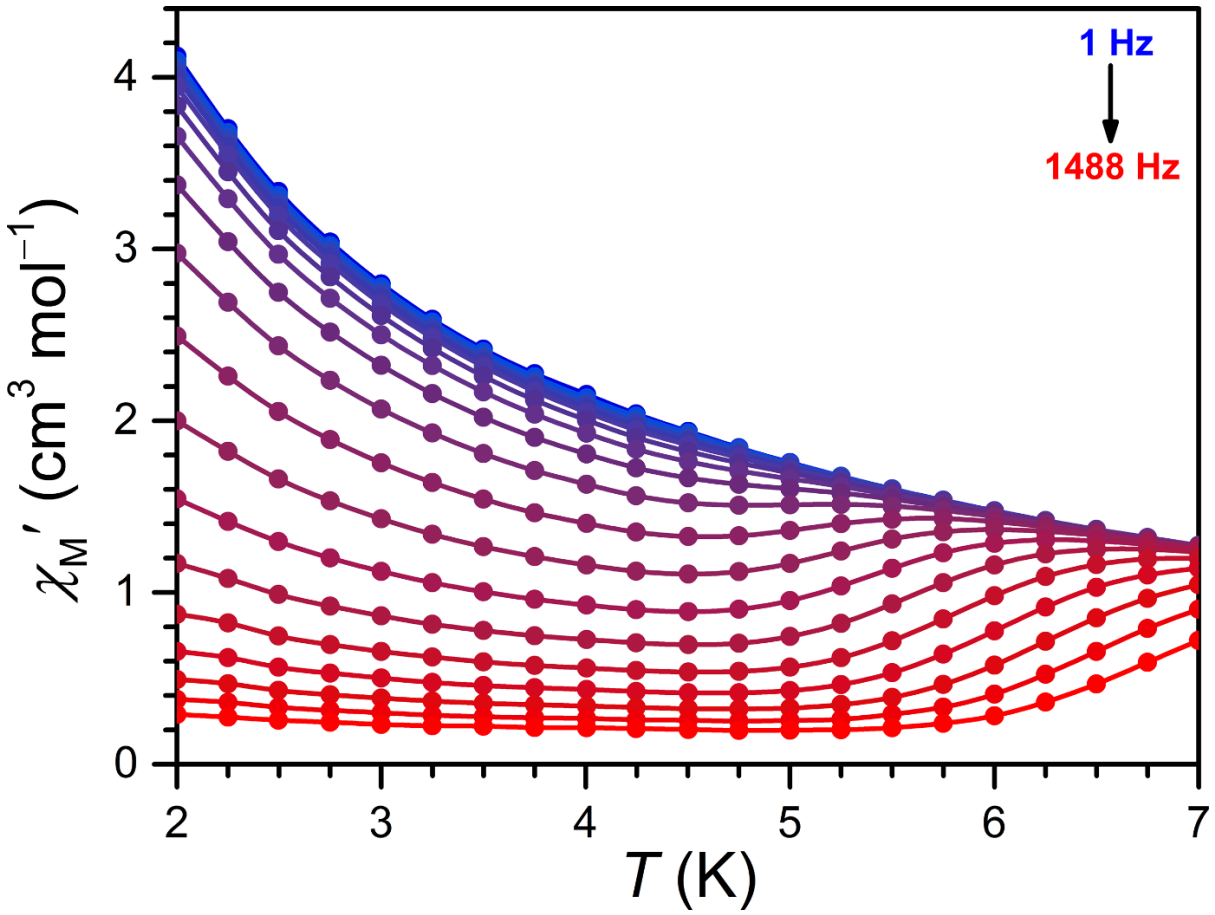

Figure 7.86 Plot of in-phase ac magnetic susceptibility (χ_M') against temperature for **2-SMe$_2$**. The data were collected from 2.00 to 7.00 K under zero applied dc field and an oscillating field of 4 Oe at frequencies ranging from 1 to 1488 Hz (blue to red) for a microcrystalline sample restrained in a frozen eicosane matrix. The colored circles correspond to experimental data and the colored lines are a guide to the eye.

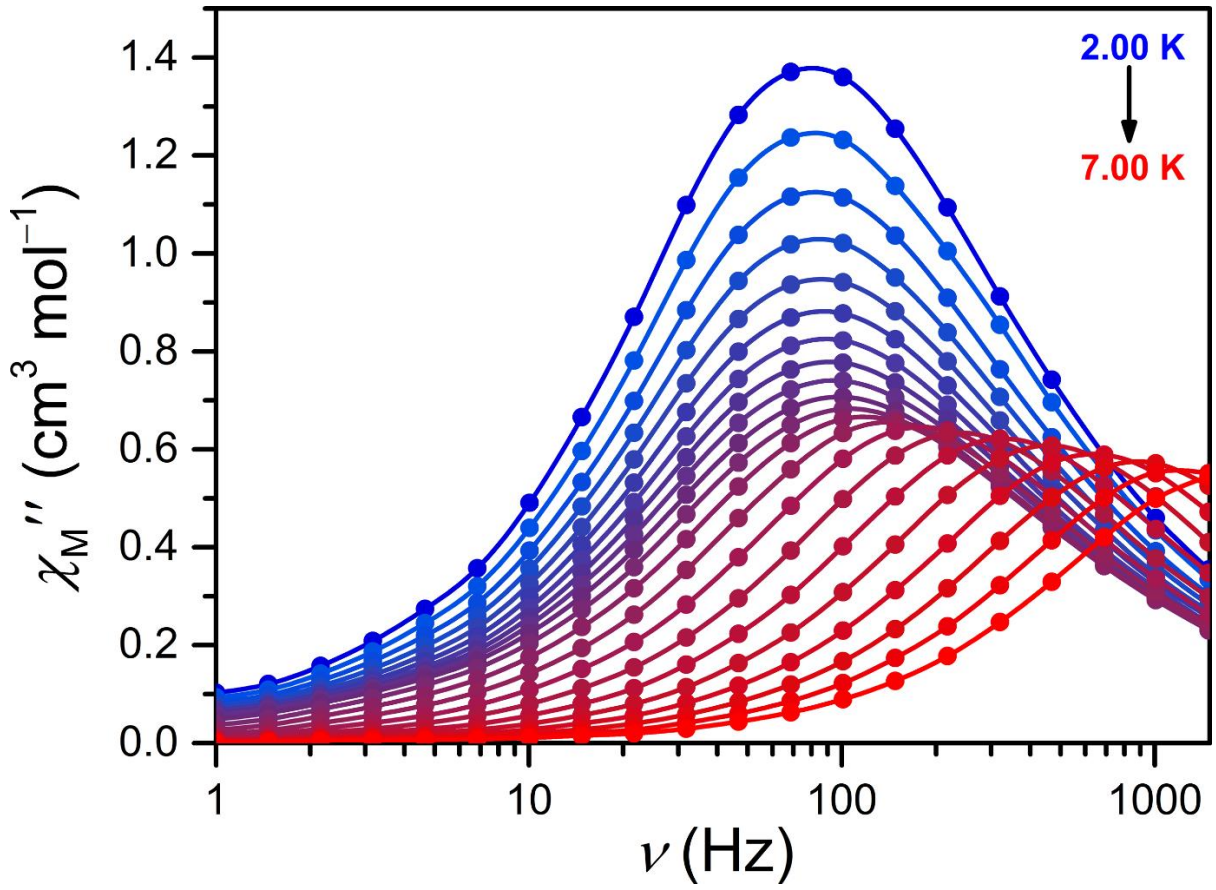

Figure 7.87 Plot of out-of-phase ac magnetic susceptibility (χ_M'') against frequency for **2-SMe$_2$**. The data were collected from 2.00 to 7.00 K (blue to red) under zero applied dc field and an oscillating field of 4 Oe at frequencies ranging from 1 to 1488 Hz for a microcrystalline sample restrained in a frozen eicosane matrix. The colored circles correspond to experimental data and the colored lines are a guide to the eye.

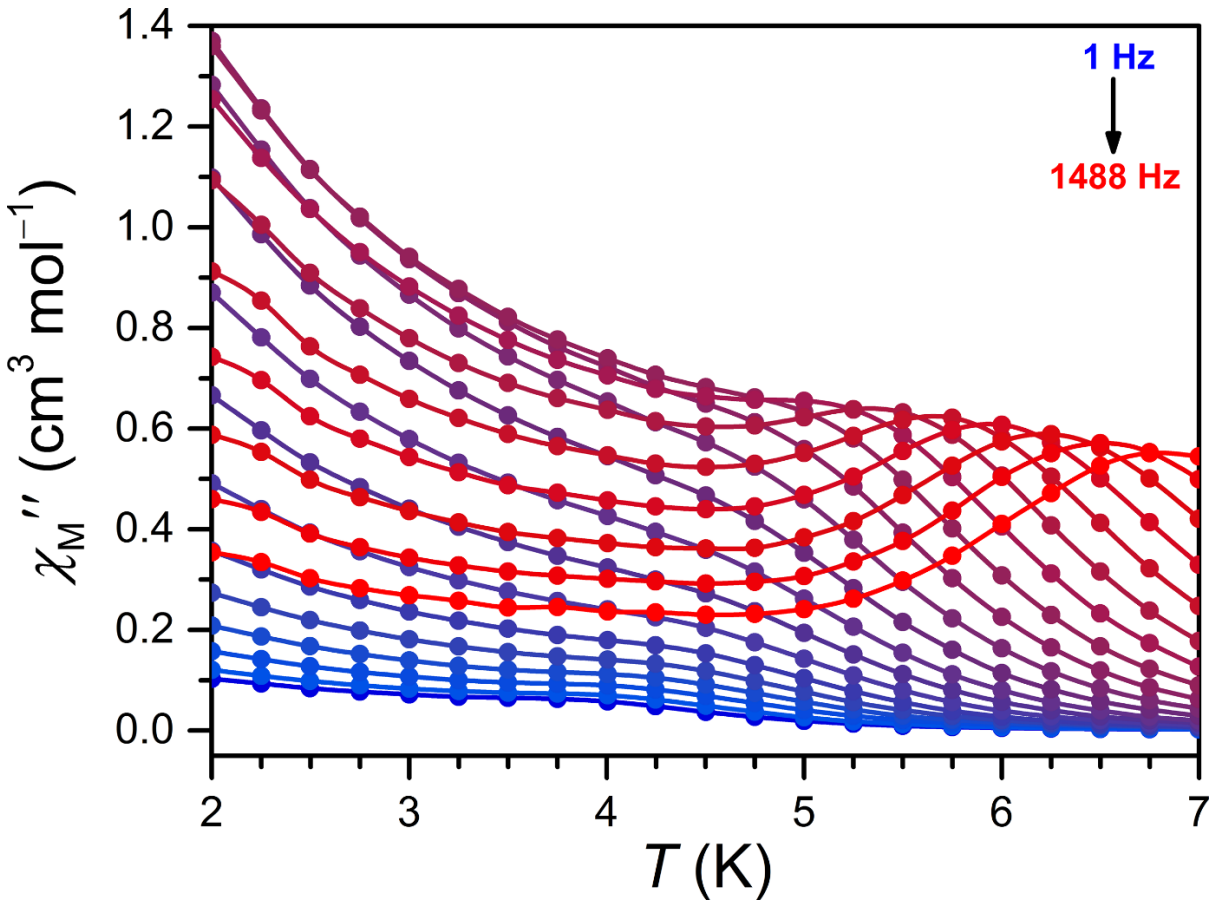

Figure 7.88 Plot of out-of-phase ac magnetic susceptibility (χ_M'') against temperature for **2-SMe$_2$**. The data were collected from 2.00 to 7.00 K under zero applied dc field and an oscillating field of 4 Oe at frequencies ranging from 1 to 1488 Hz (blue to red) for a microcrystalline sample restrained in a frozen eicosane matrix. The colored circles correspond to experimental data and the colored lines are a guide to the eye.

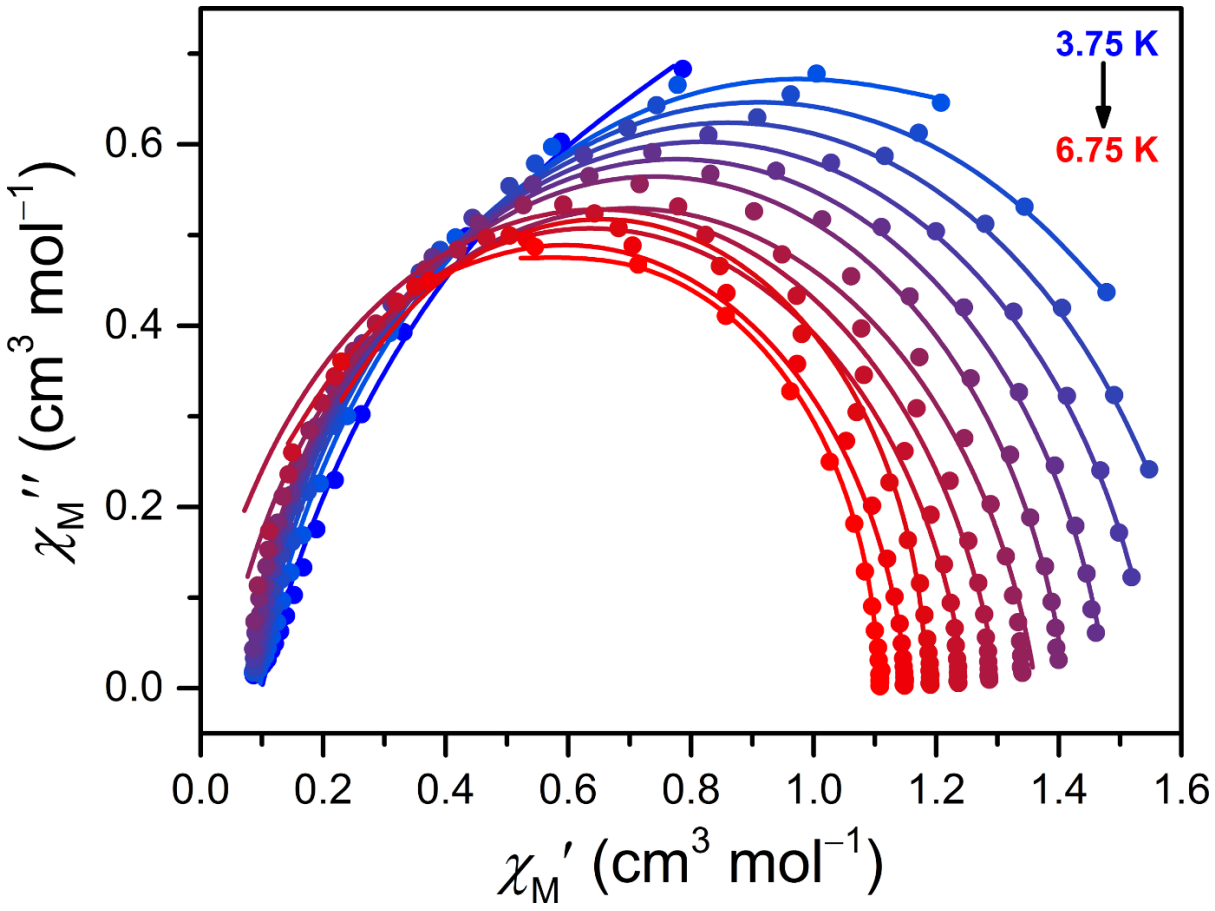

Figure 7.89 Cole–Cole plots for **2-OMe** generated from the in-phase (χ_M') and out-of-phase (χ_M'') ac magnetic susceptibility data collected from 3.75 to 6.75 K (blue to red) under zero applied dc field and an oscillating field of 4 Oe at frequencies ranging from 1 to 1488 Hz for a microcrystalline sample restrained in a frozen eicosane matrix. The colored circles correspond to experimental data and the colored lines denote fits to the data using the generalized Debye model.[36] The data were fit to obtain values of the relaxation time (τ) that were then used to construct the Arrhenius plot depicted in Figure 7.8, right. Values of α ranged from 0.22 at 3.75 K to 0 at 6.75 K, indicative of the distribution in relaxation processes at low temperature.

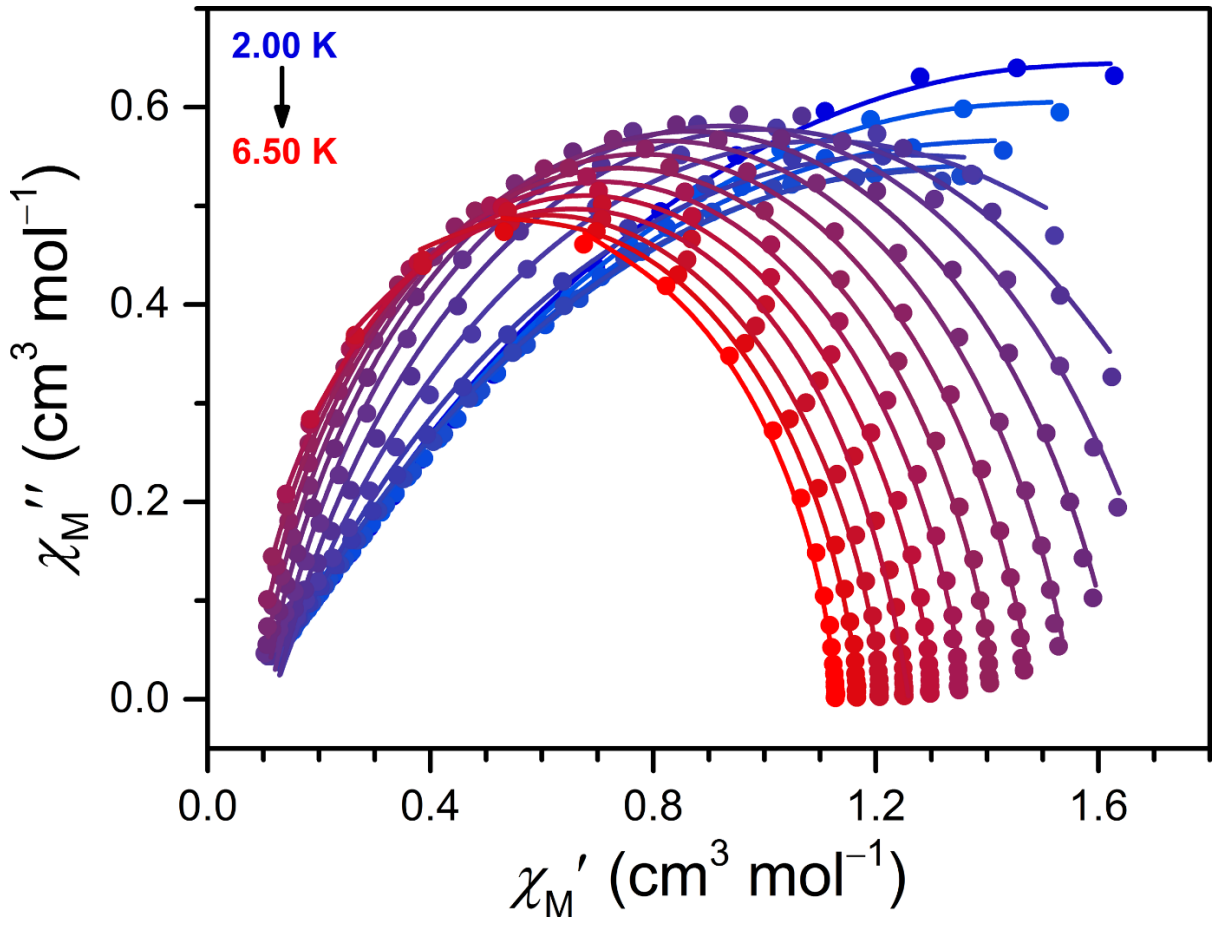

Figure 7.90 Cole–Cole plots for **2-Cl** generated from the in-phase (χ_M') and out-of-phase (χ_M'') ac magnetic susceptibility data collected from 2.00 to 6.50 K (blue to red) under zero applied dc field and an oscillating field of 4 Oe at frequencies ranging from 1 to 1488 Hz for a microcrystalline sample restrained in a frozen eicosane matrix. The colored circles correspond to experimental data and the colored lines denote fits to the data using the generalized Debye model.[36] The data were fit to obtain values of the relaxation time (τ) that were then used to construct the Arrhenius plot depicted in Figure 7.91. Values of α ranged from 0.48 at 2.00 K to 0.10 at 6.50 K, indicative of the distribution in relaxation processes at low temperature.

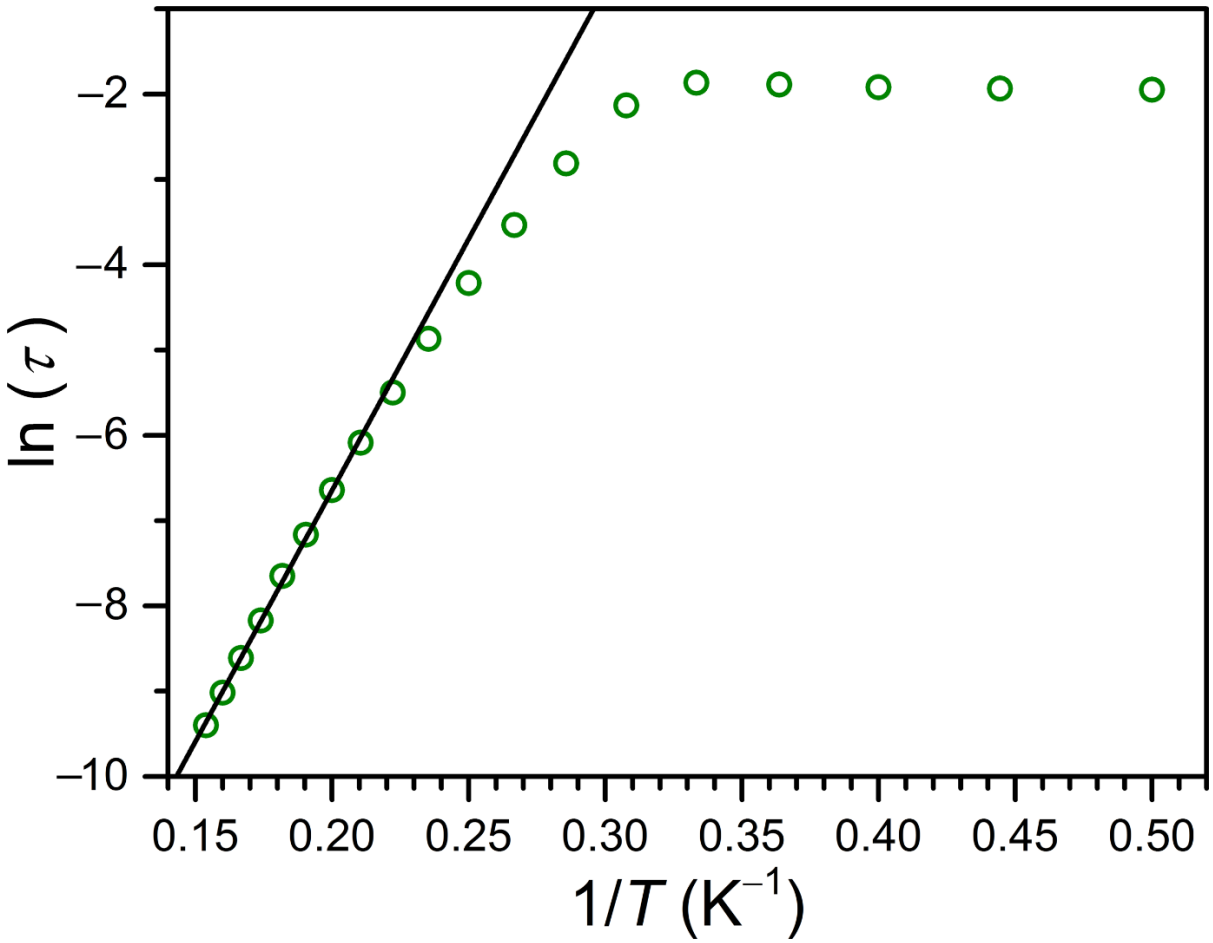

Figure 7.91 Arrhenius plot of relaxation time (τ) for **2-Cl**. The green circles correspond to values of τ obtained from fits to the Cole–Cole plots in Figure 7.90, which were constructed from data collected in the temperature range 2.00–6.50 K under zero applied dc field and an oscillating field of 4 Oe at frequencies ranging from 1 to 1488 Hz for a microcrystalline sample restrained in a frozen eicosane matrix. The black line corresponds to a linear fit to the data between 4.75 and 6.50 K, providing values of U_{eff} = 41(1) cm^{-1} and τ_0 = 1.0(2) × 10^{-8} s; R^2 = 0.999.

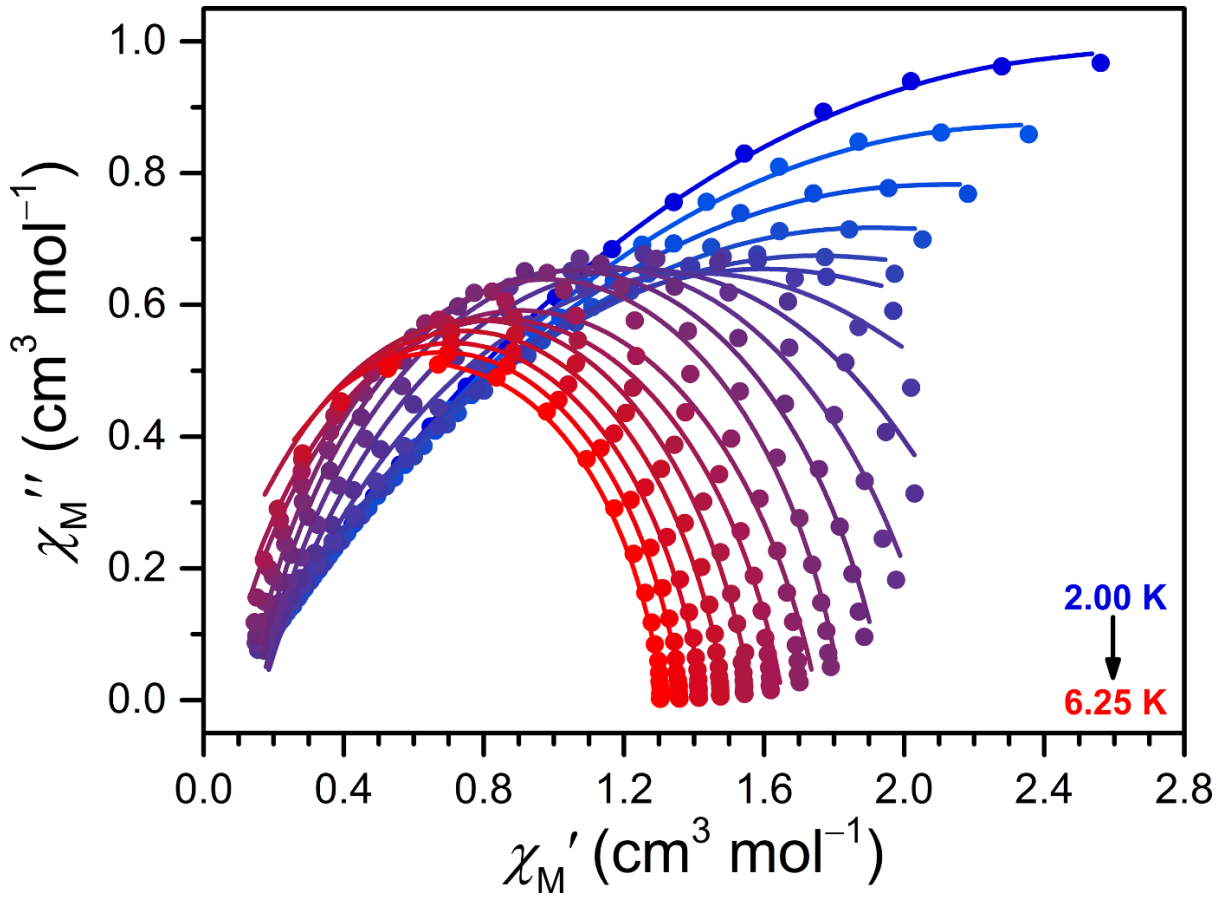

Figure 7.92 Cole–Cole plots for **2-NO$_2$** generated from the in-phase (χ_M') and out-of-phase (χ_M'') ac magnetic susceptibility data collected from 2.00 to 6.25 K (blue to red) under zero applied dc field and an oscillating field of 4 Oe at frequencies ranging from 1 to 1488 Hz for a microcrystalline sample restrained in a frozen eicosane matrix. The colored circles correspond to experimental data and the colored lines denote fits to the data using the generalized Debye model.[36] The data were fit to obtain values of the relaxation time (τ) that were then used to construct the Arrhenius plot depicted in Figure 7.93. Values of α ranged from 0.53 at 2.00 K to 0.14 at 6.25 K, indicative of the distribution in relaxation processes at low temperature.

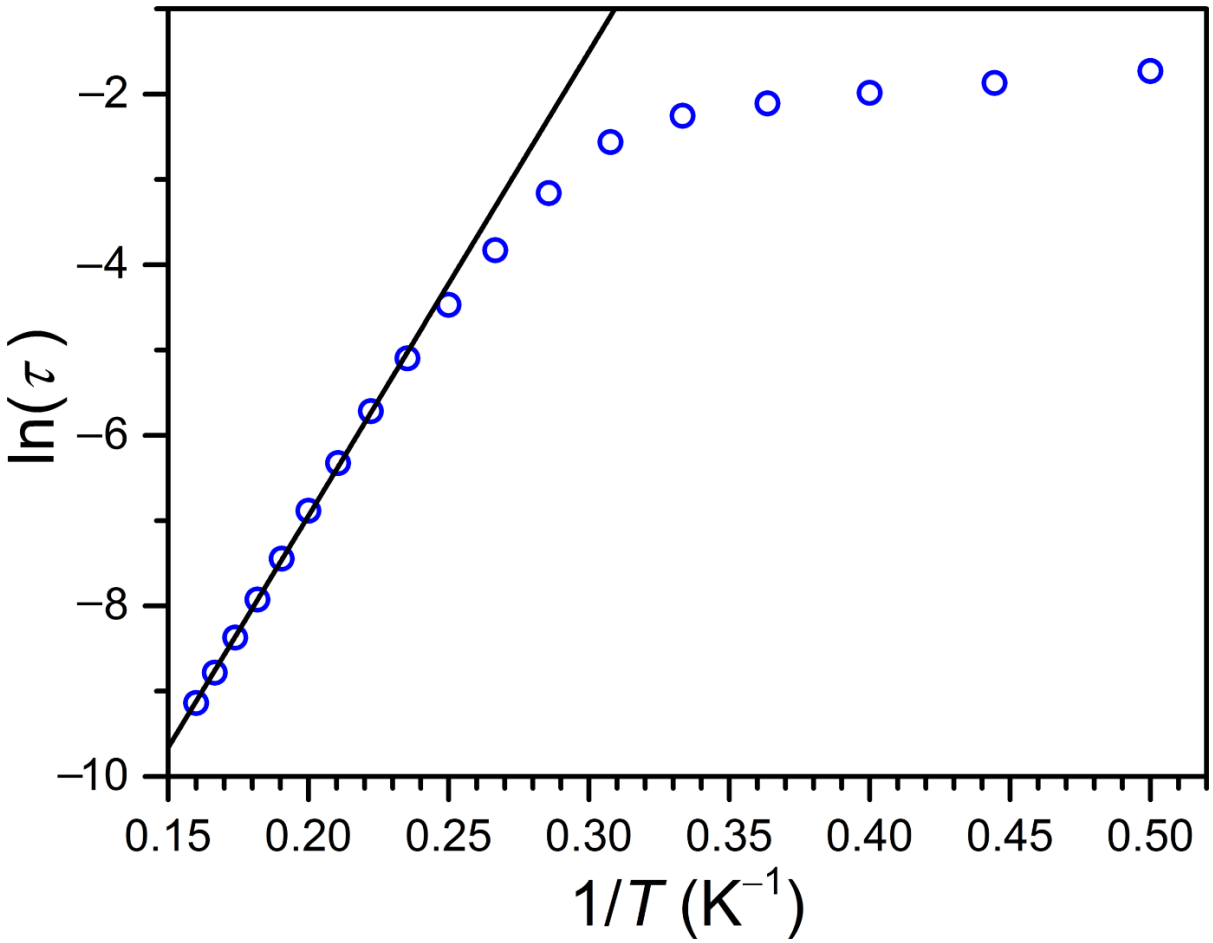

Figure 7.93 Arrhenius plot of relaxation time (τ) for **2-NO$_2$**. The blue circles correspond to values of τ obtained from fits to the Cole-Cole plots in Figure 7.92, which were constructed from data collected in the temperature range 2.00–6.25 K under zero applied dc field and an oscillating field of 4 Oe at frequencies ranging from 1 to 1488 Hz for a microcrystalline sample restrained in a frozen eicosane matrix. The black line corresponds to a linear fit to the data between 4.25 and 6.25 K, providing values of U_{eff} = 38(1) cm^{-1} and τ_0 = 1.8(3) × 10^{-8} s; R^2 = 0.999.

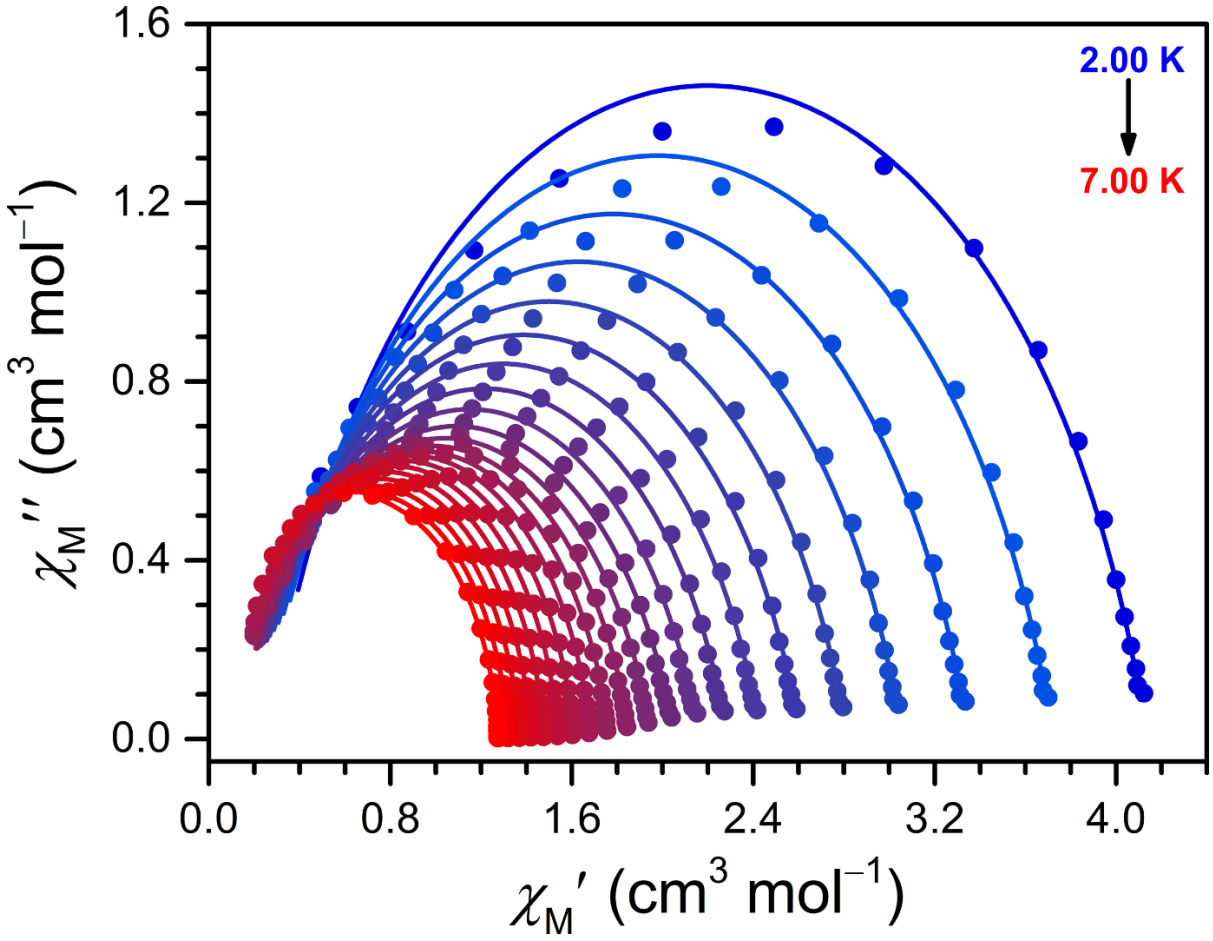

Figure 7.94 Cole–Cole plots for **2-SMe$_2$** generated from the in-phase (χ_M') and out-of-phase (χ_M'') ac magnetic susceptibility data collected from 2.00 to 7.00 K (blue to red) under zero applied dc field and an oscillating field of 4 Oe at frequencies ranging from 1 to 1488 Hz for a microcrystalline sample restrained in a frozen eicosane matrix. The colored circles correspond to experimental data and the colored lines denote fits to the data using the generalized Debye model.[36] The data were fit to obtain values of the relaxation time (τ) that were then used to construct the Arrhenius plot depicted in Figure 7.95. Values of α ranged from 0.19 at 4.25 K to 0.07 at 7.00 K, indicative of the distribution in relaxation processes in this temperature range. Note that the value of α (0.17–0.19) was near constant in the temperature range 2.00–4.25 K.

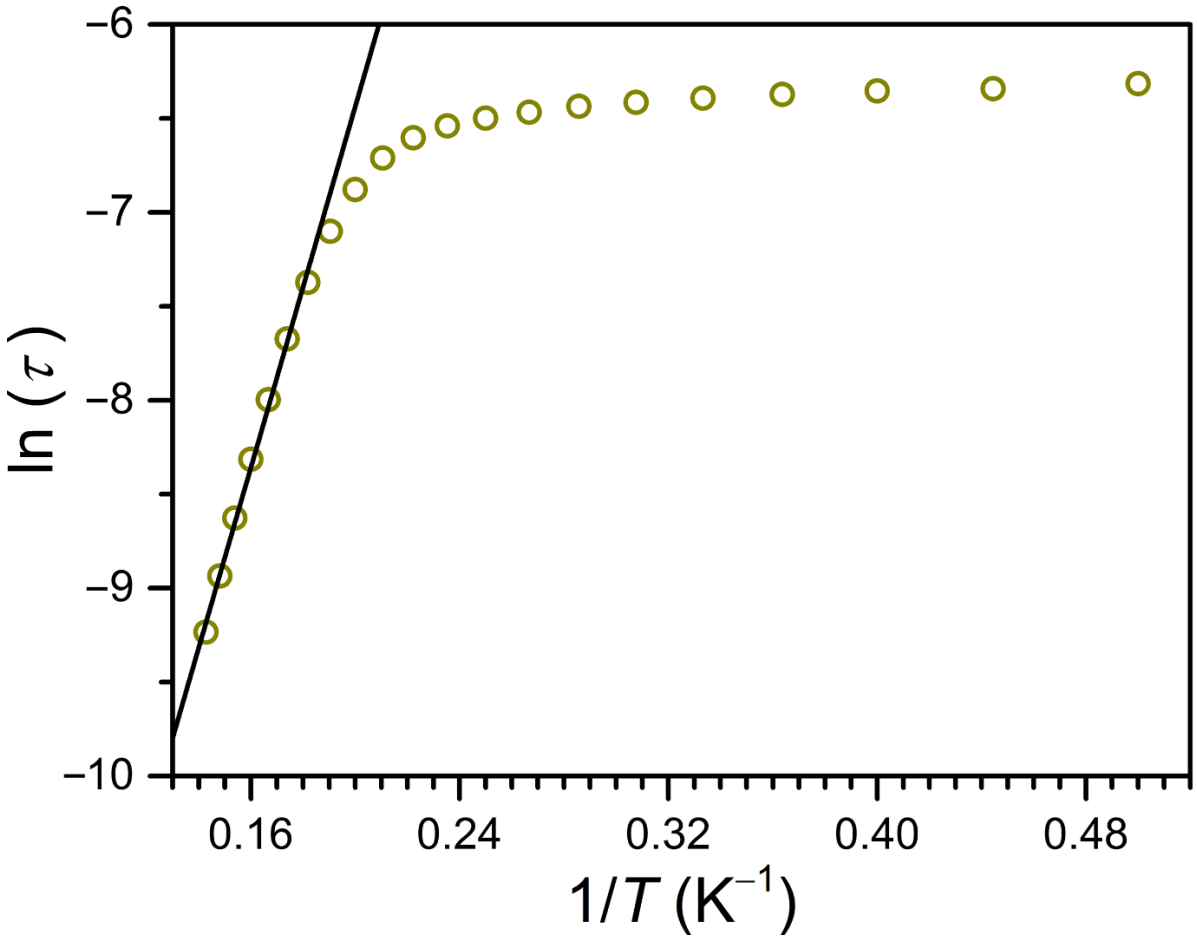

Figure 7.95 Arrhenius plot of relaxation time (τ) for **2-SMe$_2$**. The gold circles correspond to values of τ obtained from fits to the Cole–Cole plots in Figure 7.94, which were constructed from data collected in the temperature range 2.00–7.00 K under zero applied dc field and an oscillating field of 4 Oe at frequencies ranging from 1 to 1488 Hz for a microcrystalline sample restrained in a frozen eicosane matrix. The black line corresponds to a linear fit to the data between 5.50 and 7.00 K, providing values of U_{eff} = 33(1) cm^{-1} and τ_0 = 1.1(3) × 10^{-7} s; R^2 = 0.995.

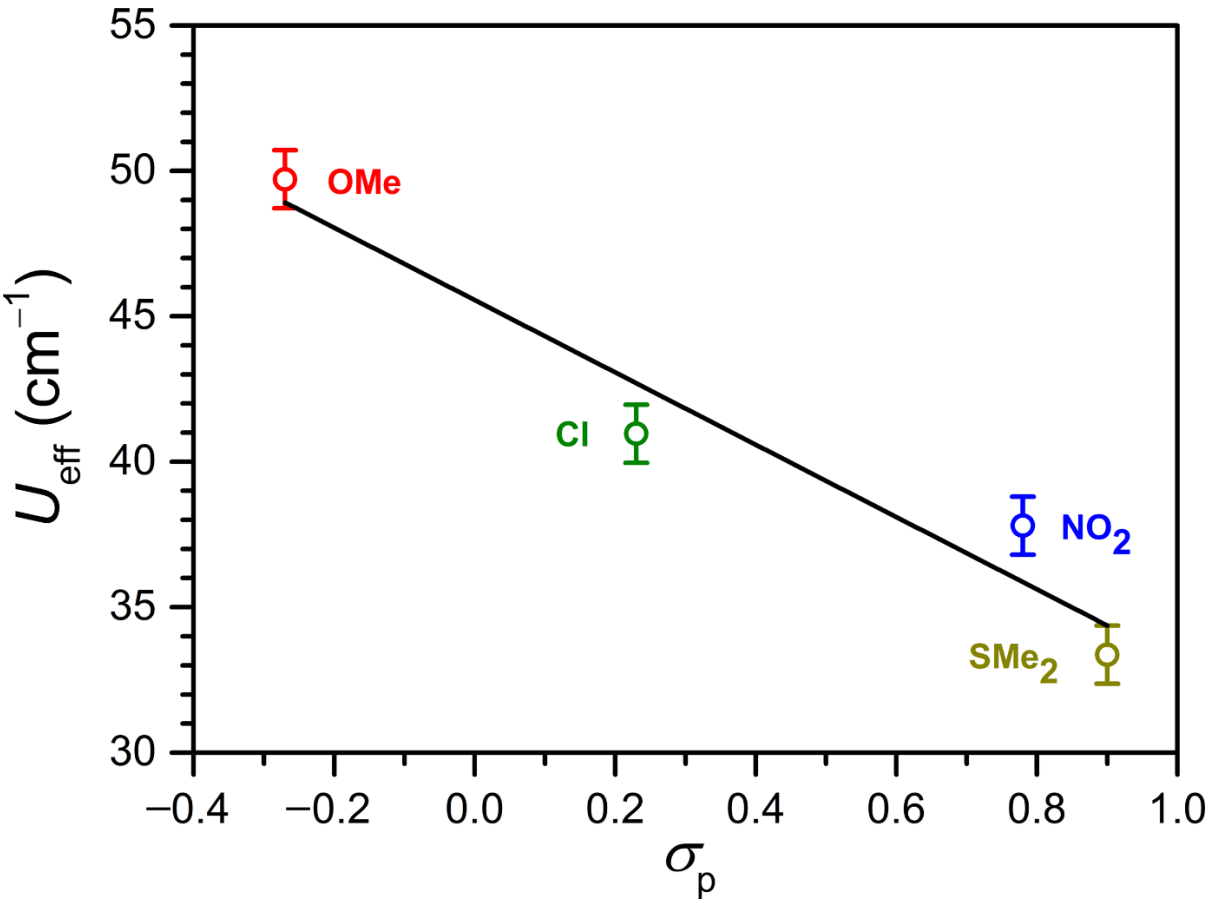

Figure 7.96 Plot of U_{eff} against the Hammett substituent constant σ_p for **2-R** (R = OMe, Cl, NO_2, SMe_2). The black line denotes a linear fit to the data, giving $R^2 = 0.912$.

7.5.4 Supplementary Tables

Table 7.4 Crystallographic data for **1-OMe**·4.0MeCN and **2-OMe**·2.0MeCN.

	1-OMe·4.0MeCN	**2-OMe**·2.0MeCN
Empirical formula	$C_{58}H_{66}B_2F_8Fe_2N_{12}O_6$	$C_{54}H_{60}BF_4Fe_2N_{10}O_6$
Formula weight, g mol^{-1}	1312.54	1143.63
Crystal system	Triclinic	Triclinic
Space group	$P\bar{1}$	$P\bar{1}$
Wavelength, Å	1.54178	0.71073
Temperature, K	100.01	100.04
a, Å	8.698(3)	9.249(2)
b, Å	12.199(4)	9.937(2)
c, Å	15.287(5)	15.874(2)
α, °	84.96(2)	88.085(6)
β, °	73.87(2)	81.585(7)
γ, °	79.59(2)	67.895(6)
V, Å^3	1531.3(8)	1336.7(3)
Z	1	1
ρ_{calcd}, g cm^{-3}	1.423	1.421
μ, mm^{-1}	4.521	0.617
Reflections coll./unique	7122/4030	62878/9053
R(int)	0.0630	0.0640
R_1 $(I > 2\sigma(I))^a$	0.0641	0.0373
wR_2 $(all)^b$	0.1830	0.0957
GoF	1.039	1.043

^{a} $R_1 = \Sigma||F_0| - |F_C||/\Sigma|F_0|$, ^{b} $wR_2 = [\Sigma w(F_0^2 - F_C^2)^2/\Sigma w(F_0^2)^2]^{1/2}$.

Table 7.5 Crystallographic data for **1-Cl**·0.7H_2O and **2-Cl**·0.5Et_2O.

	1-Cl·0.7H_2O	**2-Cl**·0.5Et_2O
Empirical formula	$C_{48}H_{50}B_2Cl_2F_8Fe_2N_8O_5$	$C_{50}H_{53}BCl_2F_4Fe_2N_8O_{4.5}$
Formula weight, g mol^{-1}	1175.18	1107.41
Crystal system	Triclinic	Triclinic
Space group	$P\bar{1}$	$P\bar{1}$
Wavelength, Å	0.71073	0.71073
Temperature, K	100.3	99.98
a, Å	9.383(2)	8.710(2)
b, Å	9.664(1)	16.120(4)
c, Å	15.326(2)	19.143(4)
α, °	98.675(8)	111.331(4)
β, °	91.366(9)	98.205(4)
γ, °	112.451(7)	102.357(4)
V, $Å^3$	1264.7(3)	2372.6(9)
Z	1	2
ρ_{calcd}, g cm^{-3}	1.543	1.498
μ, mm^{-1}	0.764	0.794
Reflections coll./unique	47922/6420	65713/9712
R(int)	0.1156	0.1041
R_1 $(I > 2\sigma(I))^a$	0.0918	0.0596
wR_2 $(all)^b$	0.2350	0.1719
GoF	1.086	1.019

[a] $R_1 = \Sigma||F_0| - |F_C||/\Sigma|F_0|$, [b] $wR_2 = [\Sigma w(F_0^2 - F_C^2)^2/\Sigma w(F_0^2)^2]^{1/2}$.

Table 7.6 Crystallographic data for **1-NO_2**·4.0MeCN and **2-NO_2**.

	1-NO_2·4.0MeCN	**2-NO_2**
Empirical formula	$C_{56}H_{60}B_2F_8Fe_2N_{14}O_8$	$C_{48}H_{48}BF_4Fe_2N_{10}O_8$
Formula weight, g mol^{-1}	1342.50	1091.47
Crystal system	Triclinic	Triclinic
Space group	$P\bar{1}$	$P\bar{1}$
Wavelength, Å	0.71073	0.71073
Temperature, K	100.08	105.51
a, Å	12.325(2)	8.8796(7)
b, Å	12.414(2)	8.8815(7)
c, Å	21.150(3)	16.548(2)
α, °	73.021(4)	102.937(4)
β, °	85.291(4)	102.908(5)
γ, °	88.876(4)	98.248(4)
V, $Å^3$	3084.5(8)	1213.8(2)
Z	2	1
ρ_{calcd}, g cm^{-3}	1.445	1.493
μ, mm^{-1}	0.559	0.678
Reflections coll./unique	155203/23750	55853/7477
R(int)	0.0311	0.0414
R_1 $(I > 2\sigma(I))^a$	0.0501	0.0350
wR_2 $(all)^b$	0.1443	0.0845
GoF	1.036	1.059

^{a} $R_1 = \Sigma||F_0| - |F_C||/\Sigma|F_0|$, ^{b} $wR_2 = [\Sigma w(F_0^2 - F_C^2)^2/\Sigma w(F_0^2)^2]^{1/2}$.

Table 7.7 Crystallographic data for **1-SMe**·4.0MeCN and **2-SMe$_2$**·0.9MeCN·0.5Et$_2$O.

	1-SMe·4.0MeCN	**2-SMe$_2$**·0.9MeCN·0.5Et$_2$O
Empirical formula	$C_{60}H_{72}B_4F_{16}Fe_2N_{14}O_4S_2$	$C_{55.8}H_{67.7}B_3F_{12}Fe_2N_{8.9}O_{4.5}S_2$
Formula weight, g mol^{-1}	1548.35	1371.33
Crystal system	Monoclinic	Triclinic
Space group	$P2_1/c$	$P\bar{1}$
Wavelength, Å	0.71073	0.71073
Temperature, K	100.31	99.99
a, Å	22.104(9)	8.9682(5)
b, Å	9.936(4)	15.1529(8)
c, Å	31.76(2)	24.184(2)
α, °	90	74.482(3)
β, °	98.796(8)	87.505(3)
γ, °	90	84.178(3)
V, Å^3	6894(5)	3149.8(3)
Z	4	2
ρ_{calcd}, g cm^{-3}	1.492	1.446
μ, mm^{-1}	0.580	0.615
Reflections coll./unique	232154/15272	129250/17928
R(int)	0.1224	0.0612
R_1 *(I >2σ(I))*[a]	0.0611	0.0602
wR_2 *(all)*[b]	0.1660	0.1808
GoF	1.026	1.033

[a] $R_1 = \Sigma||F_0| - |F_C||/\Sigma|F_0|$, [b] $wR_2 = [\Sigma w(F_0^2 - F_C^2)^2/\Sigma w(F_0^2)^2]^{1/2}$.

Table 7.8 Determination of the axial zero-field splitting parameter *D* for **1-SMe$_2$** from individual fits to the low-temperature magnetization data and variable-temperature dc magnetic susceptibility data. The values of *g* and *J* were fixed to those obtained from a simultaneous fit to the two data sets and the value of *D* was freely refined. Iterations were performed until no change in the squared residuals (χ^2) was observed. The MagProp package within DAVE 2.5[39] was employed for the individual fits to the magnetic data sets, using the spin Hamiltonian provided in Equation 7.1.

	Simultaneous fit	**Fit to low-temperature magnetization data**	**Fit to dc magnetic susceptibility data**
***J* (cm^{-1})**	+0.30	+0.30[a]	+0.30[a]
g	2.22	2.22[a]	2.22[a]
***D* (cm^{-1})**	−16.68	−15.22	−15.43

[a]These values were fixed to those obtained from a simultaneous fit to low-temperature magnetization and dc magnetic susceptibility data as described above and in Section 7.2.

Table 7.9 Determination of the axial zero-field splitting parameter *D* for **2-OMe** from fits to the low-temperature magnetization data. A survey of the sum of the squared residuals (χ^2) was performed by varying the value of *J* (fixed to the values noted below) from 0 to −1000 cm^{-1}, while the values of *D* and *g* (isotropic) were refined freely. Each refinement started from values of $D = -2$ cm^{-1} and $g = 2.1$ (estimated from variable-temperature dc magnetic susceptibility data). Iterations were performed until no change in χ^2 was observed. The MagProp package within DAVE 2.5[39] was employed for this survey, using the spin Hamiltonian provided in Equation 7.2.

J **(cm^{-1})**	***D*** **(cm^{-1})**	***g***	χ^2
0	−265200	2.0036	45.44
−5	−20.71	2.1290	0.6804
−10	−17.61	2.1106	0.1887
−20	−17.05	2.1092	0.1705
−30	−16.95	2.1092	0.1704
−40	−16.91	2.1092	0.1704
−50	−16.89	2.1091	0.1704
−60	−16.88	2.1091	0.1705
−80	−16.87	2.1091	0.1705
−100	−16.86	2.1091	0.1705
−150	−16.85	2.1091	0.1706
−200	−16.84	2.1091	0.1706
−300	−16.84	2.1091	0.1706
−400	−16.83	2.1091	0.1706
−500	−16.83	2.1091	0.1706
−600	−16.83	2.1091	0.1706
−800	−16.83	2.1091	0.1706
−1000	−16.83	2.1091	0.1706

Table 7.10 Determination of the axial zero-field splitting parameter *D* for **2-Cl** from fits to the low-temperature magnetization data. A survey of the sum of the squared residuals (χ^2) was performed by varying the value of *J* (fixed to the values noted below) from 0 to −1000 cm^{-1}, while the values of *D* and *g* (isotropic) were refined freely. Each refinement started from values of $D = -2$ cm^{-1} and $g = 2.1$ (estimated from variable-temperature dc magnetic susceptibility data). Iterations were performed until no change in χ^2 was observed. The MagProp package within DAVE 2.5[39] was employed for this survey, using the spin Hamiltonian provided in Equation 7.2.

J **(cm^{-1})**	***D*** **(cm^{-1})**	***g***	χ^2
0	−2055000	2.0874	40.45
−5	−14.29	2.1628	0.4987
−10	−12.74	2.1429	0.1212
−20	−12.48	2.1411	0.1082
−30	−12.43	2.1410	0.1078
−40	−12.40	2.1409	0.1077
−50	−12.39	2.1409	0.1077
−60	−12.39	2.1408	0.1076
−80	−12.38	2.1408	0.1076
−100	−12.37	2.1408	0.1075
−150	−12.36	2.1407	0.1074
−200	−12.36	2.1407	0.1074
−300	−12.35	2.1407	0.1073
−400	−12.35	2.1407	0.1073
−500	−12.35	2.1407	0.1073
−600	−12.35	2.1407	0.1073
−800	−12.35	2.1407	0.1073
−1000	−12.35	2.1407	0.1073

Table 7.11 Determination of the axial zero-field splitting parameter *D* for **2-NO$_2$** from fits to the low-temperature magnetization data. A survey of the sum of the squared residuals (χ^2) was performed by varying the value of *J* (fixed to the values noted below) from 0 to −1000 cm^{-1}, while the values of *D* and *g* (isotropic) were refined freely. Each refinement started from values of $D = -2$ cm^{-1} and $g = 2.2$ (estimated from variable-temperature dc magnetic susceptibility data). Iterations were performed until no change in χ^2 was observed. The MagProp package within DAVE 2.5[39] was employed for this survey, using the spin Hamiltonian provided in Equation 7.2.

J **(cm^{-1})**	***D*** **(cm^{-1})**	***g***	χ^2
0	−127300	2.0759	50.63
−5	−27.09	2.2461	0.5209
−10	−21.87	2.2269	0.1233
−20	−20.96	2.2257	0.1134
−30	−20.79	2.2256	0.1134
−40	−20.72	2.2256	0.1135
−50	−20.69	2.2256	0.1135
−60	−20.67	2.2256	0.1135
−80	−20.65	2.2256	0.1136
−100	−20.64	2.2256	0.1136
−150	−20.62	2.2256	0.1136
−200	−20.61	2.2256	0.1137
−300	−20.61	2.2256	0.1137
−400	−20.60	2.2256	0.1137
−500	−20.60	2.2255	0.1137
−600	−20.60	2.2255	0.1137
−800	−20.60	2.2255	0.1137
−1000	−20.59	2.2255	0.1137

Table 7.12 Determination of the axial zero-field splitting parameter *D* for **2-SMe$_2$** from fits to the low-temperature magnetization data. A survey of the sum of the squared residuals (χ^2) was performed by varying the value of *J* (fixed to the values noted below) from 0 to −1000 cm^{-1}, while the values of *D* and *g* (isotropic) were refined freely. Each refinement started from values of $D = -2$ cm^{-1} and $g = 2.2$ (estimated from variable-temperature dc magnetic susceptibility data). Iterations were performed until no change in χ^2 was observed. The MagProp package within DAVE 2.5[39] was employed for this survey, using the spin Hamiltonian provided in Equation 7.2.

J **(cm^{-1})**	***D*** **(cm^{-1})**	***g***	χ^2
0	−2207000	2.2003	51.47
−5	−25.75	2.3829	0.2143
−10	−20.94	2.3620	0.0050
−20	−20.13	2.3608	0.0062
−30	−19.97	2.3607	0.0062
−40	−19.91	2.3607	0.0062
−50	−19.88	2.3607	0.0062
−60	−19.87	2.3607	0.0062
−80	−19.84	2.3606	0.0062
−100	−19.83	2.3606	0.0062
−150	−19.82	2.3606	0.0062
−200	−19.81	2.3606	0.0062
−300	−19.80	2.3606	0.0062
−400	−19.80	2.3606	0.0062
−500	−19.80	2.3606	0.0062
−600	−19.80	2.3606	0.0061
−800	−19.79	2.3606	0.0061
−1000	−19.79	2.3606	0.0061

Chapter 8: Metal-Organic Framework Magnets

Thorarinsdottir, A. E.; Harris, T. D. *Submitted.*

This work was performed in collaboration with the co-author listed above.

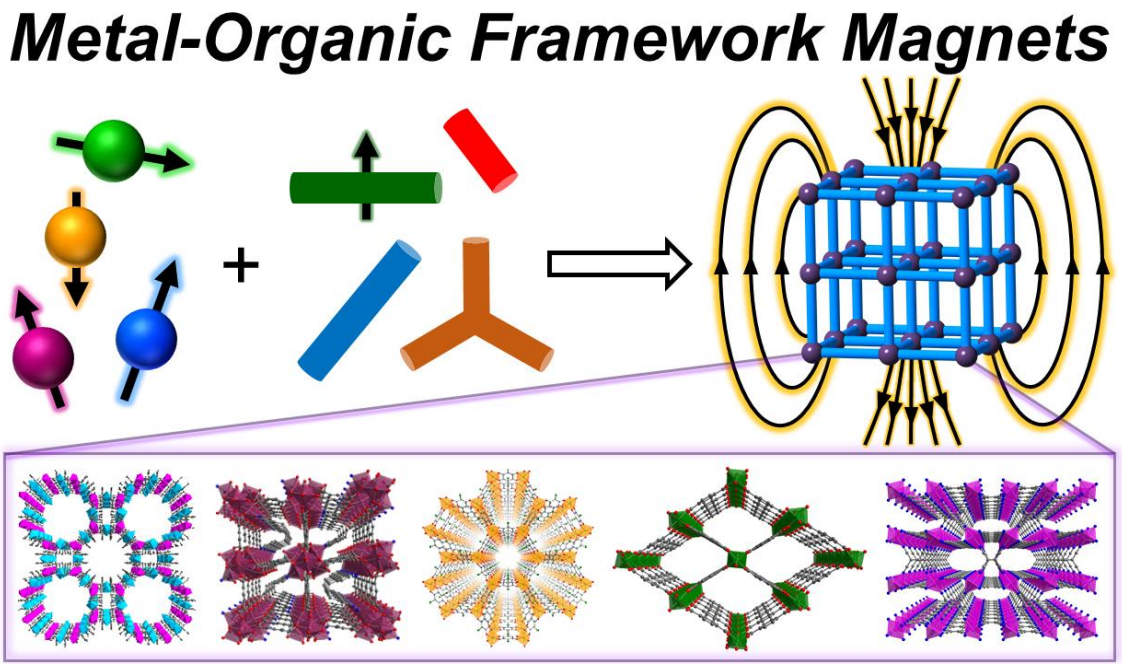

8.1 Introduction

Myriad technological gains of the 20th century were enabled by the discovery and optimization of permanent magnets – materials that can retain their magnetization in the absence of an applied magnetic field (H) below a certain critical ordering temperature (T_c).[1] For instance, nearly all portable electronic devices, household appliances, and information recording media rely on permanent magnet technology. In addition, permanent magnets are critical to the function of the motors that power electric cars and of the generators that convert renewable energy resources, such as wind and wave power, into electrical energy.[2–9] Accordingly, there is an increasing demand for generating new permanent magnets with various properties to meet the requirements of our fast growing society.

Conventional magnets comprise inorganic solids, typically rare earth- and transition metal-based intermetallic compounds or oxides,[9] where direct metal–metal bonding or short mono- or diatomic ligands allow for efficient long-range communication between spin centers.[1,4,10,11] While these materials have met tremendous success and exhibit high magnetic ordering temperatures and maximum energy density values ($(BH)_{max}$),[9] their all-inorganic compositions lead to dense materials with limited chemical programmability and tunability and a lack of processability. As such, the rational design of inorganic solid-state magnets with targeted structures and properties is exceedingly challenging.

In contrast, molecule-based magnets possess high synthetic programmability and tunability. In particular, this molecule-based approach has afforded single molecules, 1D chains, 2D layered materials, and 3D networks possessing unique magnetic behavior.[1,12–16] Moreover, some of these compounds have demonstrated fascinating multifunctional properties,[17,18] including coexistent

long-range magnetic order and electrical conductivity.[19–22] In addition, the low density of molecule-based magnets may enable their application as lightweight permanent magnets for electrical devices and energy technologies. Despite the many potential advantages of molecule-based magnets over traditional solid-state inorganic magnets, the vast majority of molecule-based magnets suffer from low operating temperatures, and thus an active focus of research in this area involves increasing the strength of magnetic exchange interactions between spin centers to realize the implementation of these and similar magnet materials in practical applications.

Toward developing molecule-based magnets that function at high temperatures, metal-organic frameworks (MOFs) represent an ideal, yet underexplored, chemical platform, owing to their unparalleled synthetic programmability and tunability, in conjunction with their extended and porous structures. Because long-range magnetic order necessitates strong interactions along two or more dimensions,[1,4,10,12,13,23] the organized arrangement of magnetic entities within MOFs can enable cooperative exchange interactions between spin centers through the organic linkers, thus engendering long-range magnetic order. Indeed, by leveraging the gains that coordination chemistry has provided to the fields of MOF synthesis and molecular magnetism over the past decades, in particular with regard to constructing metal coordination environments with high magnetic anisotropy, researchers can generate permanent magnets with specifically tailored structures and properties for targeted applications.

In addition, MOFs offer an opportunity for the simultaneous implementation of strong magnetic coupling and porosity, two properties that are generally inimical to one another. Specifically, while magnetic exchange interactions require short distances between spin centers, porosity is generally favored by employing extended organic linkers. Nevertheless, owing to the

extensive library of organic ligands capable of adopting versatile coordination modes, several design strategies have been demonstrated to successfully afford porous metal-organic magnets.[18] These strategies include the use of short linkers, typically with involving one-, two-, or three-atom[24] bridges, pre-formed metalloligands,[25] and radical organic linkers.[26,27] In addition to promoting potential applications such as magnetic gas separations[28–30] and sensing,[29,31–33] structural porosity offers a possible route to access unusual materials through post-synthetic chemical modification. For instance, post-synthetic redox chemistry can be employed to tune the electrical and optical properties,[34–37] and metal-[38–43] and linker-exchange[40–42,44,45] can provide kinetically metastable materials not accessible through direct synthesis.

8.1.1 Classes of Magnetic Order

In contrast to paramagnets, permanent magnets feature unpaired electrons with strong long-range interactions such that spontaneous order of the magnetic dipoles occurs at a sufficiently low temperature (T_c) where the spin–spin interactions outcompete thermal fluctuations. The relative alignment and magnitude of neighboring spin centers determines whether ferromagnetic, antiferromagnetic, or ferrimagnetic order is formed (see Figure 8.1).[1–4,10,12] To illustrate, parallel alignment of nearest-neighbor spins will lead to a ferromagnetic state, regardless of whether the spin centers are of the same or different magnitude. In this state, the spins are ferromagnetically coupled to one another (see Figure 8.1, top left). When neighboring spins adopt an antiparallel configuration, where the spins are antiferromagnetically coupled to one another, two possible ordered states may arise. If all spins are of the same magnitude, antiferromagnetic order with a non-magnetic $S = 0$ ground state is observed (see Figure 8.1, top right). In contrast, an uncompensated magnetic moment is obtained when the magnetic centers possess spins of unequal

magnitudes, giving rise to ferrimagnetic order (see Figure 8.1, bottom left). Accordingly, ferrimagnetism can be considered as a manifestation of antiferromagnetism, even though the magnetic behavior of ferrimagnets is closer to that of ferromagnets due to the presence of a permanent magnetic moment.

In addition to these three classes of magnetic order, tilting of the spins by a small angle about their axes leads to canted spin structures that show canted antiferromagnetic order (see Figure 8.1, bottom right). The presence of canted magnetic order is commonly encountered when the magnetic centers are crystallographically inequivalent and/or display large magnetic anisotropy. Note that this ordered state displays weak ferromagnetic-like behavior, as they result in a non-zero magnetic

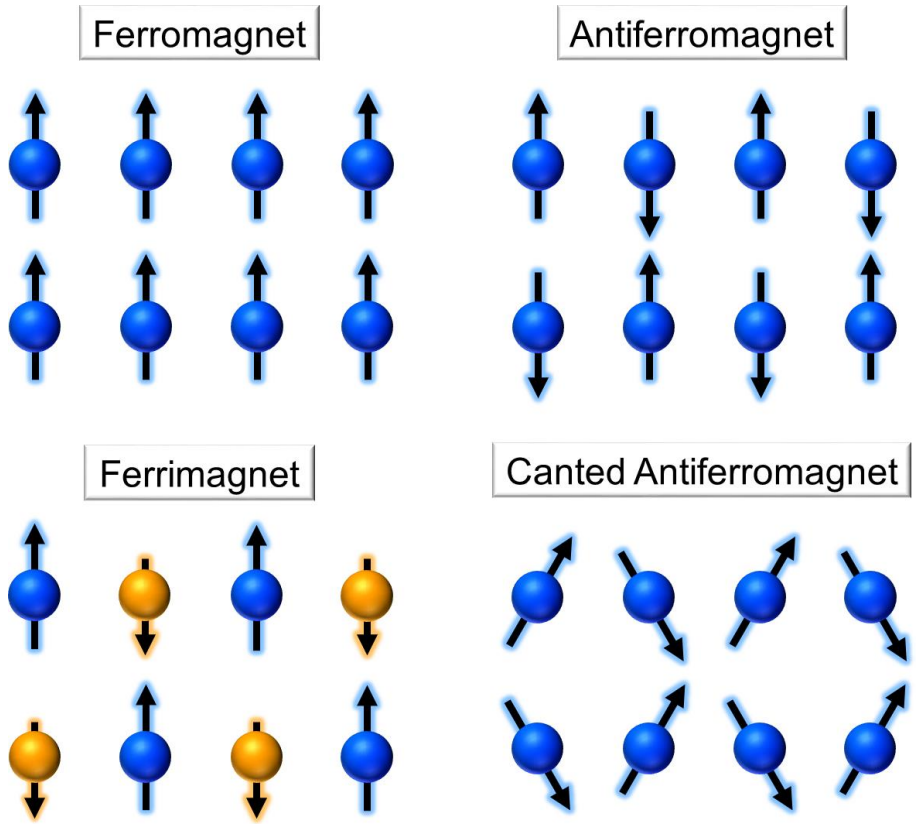

Figure 8.1 Scheme depicting spin interactions for different classes of magnets. Note that ferromagnets, ferrimagnets, and canted antiferromagnets all lead to permanent magnetism.

moment.

The magnetic ordered states summarized in Figure 8.1 are only present in materials below a specific critical ordering temperature (T_c), which is directly correlated to the strength of magnetic interactions between spin centers and the number of nearest-neighbor spins.[1,4,13,46] The magnetic ordering temperature is known as the Curie temperature (T_C) for ferromagnets and the Néel temperature (T_N) for antiferromagnets and ferrimagnets. Above the ordering temperature, paramagnetic behavior with non-interacting or weakly interacting spins is operative.[1–4,10,12,13,46] Overall, the magnetic properties of materials are determined by the relative orientations and magnitudes of their spin carriers, as well as the strength of the interactions between them.

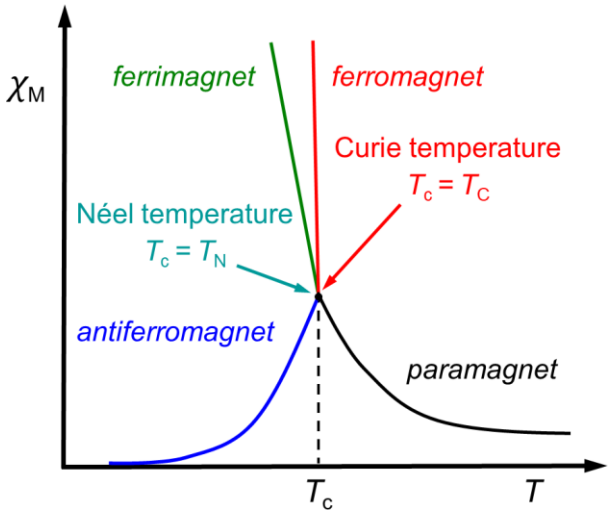

Figure 8.2 Plot of dc magnetic susceptibility (χ_M) vs temperature (T) for different magnetic behavior. Ferromagnets (red) show a characteristic sharp increase in χ_M below the Curie temperature (T_C), ferrimagnets (green) show a similar increase below the Néel temperature (T_N), albeit less pronounced, whereas antiferromagnets (blue) show a drastic decrease in χ_M below T_N.

8.1.2 Experimental Characterization of Magnetic Order

The occurrence of long-range magnetic order can be established by several experimental means, such as direct current (dc) and alternating current (ac) magnetic susceptibility (χ_M), magnetic hysteresis, neutron diffraction, muon spin rotation, and heat capacity measurements.[1–4,10,46] For instance, a magnetic phase transition is typically associated with a dramatic increase or decrease in dc magnetic susceptibility for ferromagnets/ferrimagnets and antiferromagnets,

respectively (see Figure 8.2). The observation of a minimum followed by a sharp upturn in a plot of $\chi_M T$ vs T is indicative of ferrimagnetic or canted antiferromagnetic order, as antiferromagnetic interactions dominate at high temperatures but non-zero spontaneous magnetization occurs below T_c.

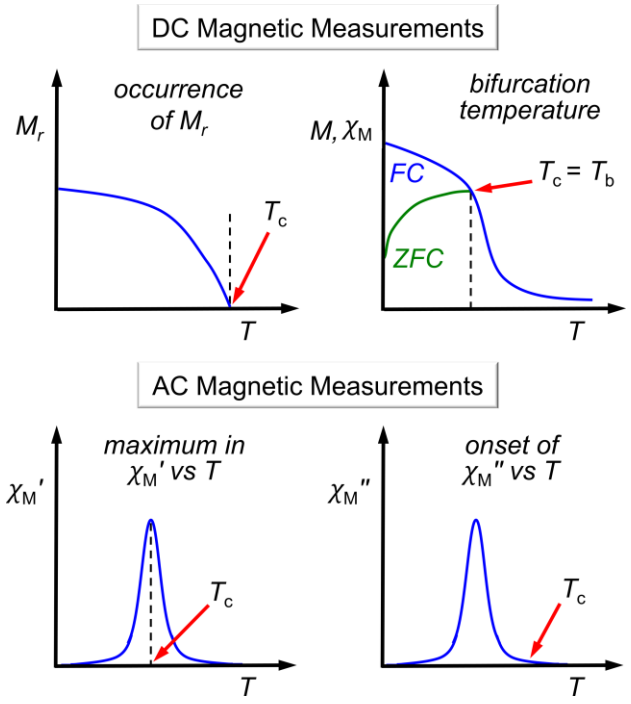

Figure 8.3 Magnetometry-based experimental methods employed to determine the magnetic ordering temperature (T_c) of a material. Top: Methods based on dc magnetic measurements: the occurrence of a remanent magnetization (left), and the bifurcation temperature (T_b) for zero-field-cooled (ZFC) and field-cooled (FC) dc magnetization or susceptibility (right). Bottom: Methods based on ac magnetic susceptibility measurements: maximum peak intensity in χ_M' vs T (left), and the onset of a peak in χ_M'' vs T.

Common methods for determining the magnetic ordering temperature from magnetic measurements[13,47] include (1) the occurrence of a remanent magnetization (M_r), (2) the bifurcation point of M vs H or χ_M vs H curves for data cooled in the absence and presence of a dc field, (3) the maximum of in-phase (χ_M') ac magnetic susceptibility, and (4) the onset of a peak in out-of-phase (χ_M'') ac magnetic susceptibility (see Figure 8.3). Note that an antiferromagnetic phase transition is not associated with energy dissipation and thus no χ_M'' signal is observed. In addition, canted antiferromagnets typically exhibit field-dependent magnetic properties and often show metamagnetic behavior, where a transition from an antiferromagnetic-like ground state to a ferromagnetic-like state is observed above a certain external critical magnetic field. This behavior, known as metamagnetism, is

characterized by a sigmoidal M vs H curve. Furthermore, some magnets show spin glass behavior,[48] which is often evident from broad and frequency-dependent peaks in χ_M' and/or χ_M''. Such glassiness can result from factors such as crystallographic disorder and topological spin frustration. Accordingly, it can be challenging to determine magnetic ordering temperatures from magnetic measurements, as the properties of permanent magnets can be highly complicated and dependent on the experimental conditions.

Several parameters in addition to the magnetic ordering temperature can be employed to characterize and compare the performance of permanent magnets. Specifically, permanent magnets – namely ferromagnets, ferrimagnets, and canted antiferromagnets – display hysteretic behavior, where a field of opposite direction is required to demagnetize the material after it has become magnetized.[1–4,10,13] The maximum width of the hysteresis loop is equal to twice the coercive field (H_c), also called coercivity, of the material (see Figure 8.4), and is defined as the field necessary to demagnetize the fully magnetized material. As such, the coercive field is a direct measure of the ability of magnets to withstand an external magnetic field without becoming demagnetized. Importantly, H_c is a kinetic parameter that

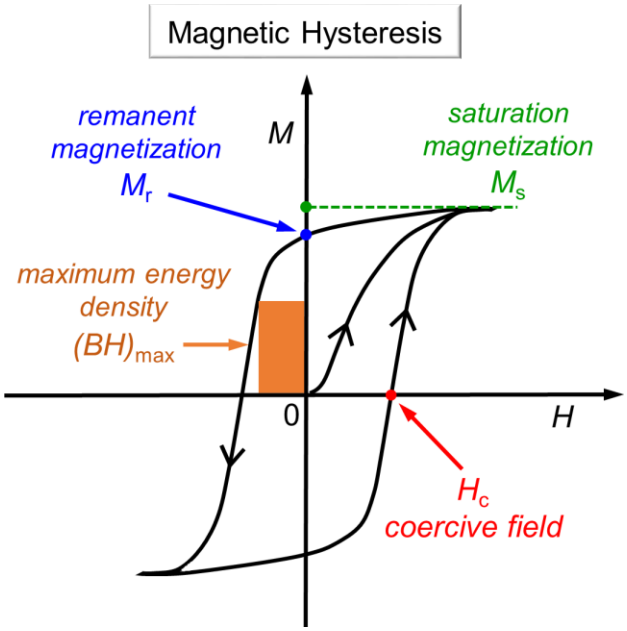

Figure 8.4 Illustration of a magnetic hysteresis curve observed for ferromagnets, ferrimagnets, and canted antiferromagnets, along with the following key parameters: saturation magnetization (M_s), remanent magnetization (M_r), coercive field (H_c), and maximum energy density ($(BH)_{max}$).

depends on the time scale over which a magnetization curve is measured, i.e. the sweep rate of the magnetic field. The magnetization remaining upon removal of the applied magntic field during the hysteresis measurement is known as the remanent magnetization (M_r) and can be significantly different from the saturation magnetization (M_s). In addition, the maximum energy density ($(BH)_{max}$)[9] may be extracted from a magnetic hysteresis loop, as illustrated in Figure 8.4. The parameters H_c, M_r, M_s, and $(BH)_{max}$ are all key variables that determine the practicality of magnets for specific applications. For example, hard magnets, which have $H_c > 100$ Oe and significant M_r, are required for data storage devices, whereas soft magnets, which have $H_c < 10$ Oe and $M_r \approx 0$ Oe, are better suited for magnetic shielding and electric motors.[13]

8.1.3 Scope and Structure of the Review

Within this review, we restrict the term "MOF magnet" to compounds that fall under the definition of a MOF and show magnetic order at a measurable temperature. Historically, multiple definitions of a MOF have been proposed based on different structural and functional characteristics.[49–51] Here, we adopt the IUPAC-approved definition, which states that a "MOF is a coordination network with organic ligands containing potential voids."[52] Although, according to this definition, crosslinked 1D chains can be considered MOFs, we limit our discussion to materials that are covalently linked to extend in at least two dimensions. While the presence of a metal is inherent to the term MOF, the nature of the organic components has led to some debate.[50,51] Molecules are typically considered organic if they feature C–C and/or C–H bonds. Furthermore, it is generally accepted that the organic ligands in MOFs should be multitopic, with two or more distinct functional groups available for metal binding, and form strong covalent bonds with metal ions or clusters.[49–52,54] Using these criteria, compounds based on cyanide, cyanamide,

and formate bridges do not fall within the definition of a MOF and thus will not be covered in depth in this review. However, those bridged by oxalate ($C_2O_4^{2-}$) and tetracyanoethylene ($C_2(CN)_4$) will be discussed, as they contain a C–C/C=C bond and multiple metal-binding groups. Since the precise establishment of structure–property relationships is critical to understanding the magnetic behavior of materials, we limit our discussion to structurally-characterized compounds. The structures should be derived from single-crystal X-ray diffraction (SCXRD) or from refinement of powder X-ray diffraction (PXRD) data. Furthermore, as the porosity of many frameworks is not well established, we include numerous compounds whose properties we view as are instructive to the reader within the context of this review, even though the presence of voids is not explicitly reported.

A large number of framework materials contain a mixture of small inorganic ligands, such as oxo, hydroxo, sulfato, chloro, azido, and thicyanoto, and organic multitopic linkers.[17,55] As such, differentiating between hybrid inorganic-organic coordination networks and MOFs can be challenging. For the purpose of this review, we restrict our discussion to compounds where the organic component contributes significantly to structural bonding and facilitates magnetic exchange interactions in at least two dimensions. Accordingly, neither 2D frameworks comprised of hydroxo-bridged chains nor 3D frameworks of hydroxo-bridged layers connected through organic linkers will be covered. The magnetic behavior of these 2D and 3D networks is dominated by intrachain and intralayer interactions, respectively, with minimal contributions from the organic components. The reader is referred to the following references for further discussions on 2D magnets with metal-hydroxide chains,[56–58] and on 3D magnets bearing hydroxide layers bridged by dicarboxylato,[59–68] oxalato,[69] and N-donor ligands.[70,71] These compounds exhibit magnetic

ordering temperatures up to T_c = 90 K.[69]

In this review, we survey the current state of metal-organic framework magnets. In Section 8.2, we briefly examine compounds that do not fall within the strict definition of a MOF, but have nonetheless led to important breakthroughs in the field of molecule-based magnetism and have contributed significantly to the development of MOF magnets. In Section 8.3, we provide an overview of 2D and 3D MOF magnets based on diamagnetic linkers, including phosphonates, oxalates, oxamates, carboxylates, and N-heterocycles, along with those featuring linkers bearing mixed N- and O-donors, and benzoquinoid-based ligands. In Section 8.4, we focus on surveying current examples of framework magnets based on organic radical linkers, including nitroxides, organonitriles, and semiquinoid derivatives. Note that this last class of compounds has provided the MOF magnets with the highest reported ordering temperature of T_c = 171 K.[72–74] Within all sections, we adopt the notation of the form I^mO^n to describe the inorganic and organic dimensionality of the structures where *m* and *n* represent the dimensionality of the inorganic and organic connectivity, respectively, as introduced by Cheetham and Rao *et al*.[55,75] Finally, Section 8.5 provides an outlook for the field and discusses some potential strategies toward increasing the ordering temperatures of MOF magnets above room temperature while retaining structural integrity and other functionality.

8.2 Toward Structurally-Characterized MOF Magnets

Many early efforts to synthesize molecule-based permanent magnets focused on extended structures featuring the organonitrile radical anions of tetracyanoethylene (TCNE) and 7,7,8,8-tetracyano-*p*-quinodimethane (TCNQ). These studies provided charge-transfer salts of formula $[Cp^*_2M^{III}]^+\bullet(TCNX)^{-\bullet}$ (M^{III} = Cr^{III}, Mn^{III}, Fe^{III}; X = E, Q; Cp^{*-} = pentamethylcyclopentadienyl

anion), possessing 1D chains of alternating donor and acceptor units held together by non-covalent interactions.[13,76–82] While $[Cp^*_2Fe^{III}]^{+\bullet}(TCNQ)^{-\bullet}$ displays metamagnetic behavior with an antiferromagnetic ground state,[76] moving to a smaller radical anion provided the first molecule-based ferro- and ferrimagnets $[Cp^*_2M^{III}]^{+\bullet}(TCNE)^{-\bullet}$ (M^{III} = Cr^{III}, Mn^{III}, Fe^{III}), with ordering temperatures of T_c = 3.65–8.8 K.[77–81] Remarkably, a similar synthesis using $V^0(C_6H_6)_2$ as a synthon led to the discovery of the first room-temperature molecule-based magnet, $V(TCNE)_x \cdot yCH_2Cl_2$ ($x \approx 2$; $y \approx 0.5$), with T_c > 350 K.[13,83–86] Unfortunately, the amorphous nature of this and related TCNE-[87–89] and TCNQ-[88,90–92] based magnets with high T_c has precluded structural characterization. Therefore, a structural rationale for such high ordering temperatures and coercive fields up to H_c = 6500 Oe in these systems remains elusive. Nevertheless, these pioneering studies demonstrated that molecule-based magnets that order above room temperature are achievable.

A number of structurally-characterized 1D chain compounds have been reported to exhibit long-range magnetic order.[11,93–123] This class includes metalloporphyrin-based magnets comprising linear chains of $[Mn^{III}(TPP)]^+$ (TPP^{2-} = *meso*-tetraphenylporphyrinato) or $[Mn^{III}(TXPP)]^+$ ($TXPP^{2-}$ = *meso*-tetrakis(4-halophenyl)porphyrinato; X = F, Cl, Br, I) cations and $TCNE^{-\bullet}$ or $QCl_4^{-\bullet}$ (QCl_4 = tetrachloro-1,4-benzoquinone) radical anions.[93–97] These materials behave as ferrimagnets or canted antiferromagnets with ordering temperatures in the range T_c = 3.5–28 K, owing to antiferromagnetic coupling between S = 2 Mn^{III} centers and S = ½ radical anions. However, complicated spin glass or metamagnetic behaviors are frequently observed at low temperature. Remarkably, one member of this family of compounds, $[Mn^{III}(TBrPP)]^+(TCNE)^{-\bullet}$ displays one of the largest coercive fields reported for a molecule-based material, affording a value of H_c = 2.7 T at 2.0 K.[97]

Chain compounds of transition metal[98–105] and lanthanide ions[106–112] bridged by nitronyl nitroxide and imino nitroxide radicals have also been shown to display bulk magnetic order. These chains exhibit strong antiferromagnetic metal–radical coupling, and the long-range order is driven by dipolar interactions between chains. Notably, chains featuring the highly anisotropic ions Co^{II}, Dy^{III}, and Tb^{III} can behave as single-chain magnets, thus providing examples of compounds with coexistent slow magnetic relaxation and long-range magnetic order.[105,109–112] The Co^{II}-based chain compound $Co^{II}(hfac)_2(BPNN)$ ($hfac^-$ = 1,1,1,5,5,5-hexafluoroacetylacetonate; BPNN = *p*-butoxyphenyl nitronyl nitroxide radical) is especially interesting, as it exhibits the highest magnetic ordering temperature of $T_c \approx 45$ K for this class of compounds, and displays a giant coercive field of $H_c = 5.2$ T at 6 K.[105] Indeed, this value of H_c exceeds the room-temperature values of commercial permanent magnets, such as $SmCo_5$ ($H_c = 4.4$ T) and $Nd_2Fe_{14}B$ ($H_c = 1.9$ T),[124] and renders $Co^{II}(hfac)_2(BPNN)$ the record holder of the largest coercive field known among permanent magnets.

In addition to these radical-bridged chains, diamagnetic oxamato,[113–116] oxalato,[117–121] and carboxylato[122,123] ligands have provided 1D chain compounds showing long-range magnetic order. Nevertheless, the majority of these compounds exhibit ordering temperatures below 10 K, likely stemming from weak interchain interactions. Indeed, only two structurally-characterized Co^{II} chain compounds order at a higher temperature. Specifically, the zigzag chains $Co^{II}(ox)(1,3\text{-pdiol})$[121] ($ox^{2-}$ = oxalate; 1,3-pdiol = 1,3-propanediol) and $K_2Co^{II}(ox)_2$[120] exhibit canted antiferromagnetic and antiferromagnetic order with $T_N = 10.6$ and 37 K, respectively. Note, however, that dehydration of bimetallic $Mn^{II}Cu^{II}$ and $Co^{II}Cu^{II}$ oxamate-based chains afford compounds with ordering temperatures of $T_c = 30$–38 K, but no structural data are available for

those compounds.[116,125]

In addition to 1D chains, 2D and 3D frameworks can also behave as single-chain magnets without magnetic order.[126] Compounds that show such behavior typically feature strong magnetic coupling through short bridging ligands along one direction and much weaker nearest-neighbor interactions along the other directions due to longer magnetic exchange pathways. One example of a 3D framework displaying this phenomenon is the compound $Co^{II}_2(H_{0.67}bdt)_3 \cdot 20H_2O$ (H_2bdt = 5,5′-(1,4-phenylene)bis(1*H*-tetrazole)), which is comprised of Co^{II}-tetrazolate chains linked through the phenyl tethers of the bdt^{2-} ligands in the other two directions.[127] Ac susceptibility and magnetic hysteresis measurements confirmed single-chain magnet behavior with a relaxation barrier of $\Delta_\tau = 30.2$ cm^{-1} and a pre-exponential factor of $\tau_0 = 5.1 \times 10^{-9}$ s, along with a coercive field of $H_c = 450$ Oe at 1.8 K. Other examples of compounds within this class of framework materials include 3D Co^{II}-based MOFs featuring 1D ferromagnetic chains of $[Co^{II}_3(OH)_2]^{4+}$ units with $\Delta_\tau = 11.0$ cm^{-1} ($\tau_0 = 2.03 \times 10^{-9}$ s),[128] or mixed carboxylato- and hydroxo-bridged Δ-chains with $\Delta_\tau = 74$ cm^{-1} ($\tau_0 = 2.80 \times 10^{-10}$ s).[129] Furthermore, a 2D framework comprised of carboxylato-bridged chains of Co^{II}_2 paddlewheel units exhibits energy barriers of $\Delta_{\tau1} = 56.2$ cm^{-1} ($\tau_0 = 5.19 \times 10^{-11}$ s) and $\Delta_{\tau2} = 34.9$ cm^{-1} ($\tau_0 = 5.59 \times 10^{-8}$ s) for two different temperature regimes.[130] A more unusual example of such single-chain magnet behavior within a framework is the 2D compound $(Pr_4N)_2[Fe_2(Cl_2An)_3] \cdot H_2O \cdot 2C_3H_6O$ (Cl_2An^{2-} = chloranilate) that consists of honeycomb layers and displays a thermally induced valence tautomerism between the iron centers and the chloranilate ligands with a transition temperature of $T_{1/2} = 236$–237 K. In both the low temperature phase $[Fe^{III}_2(Cl_2An^{2-})(Cl_2An^{3-\bullet})_2]^{2-}$ and the high temperature phase $[Fe^{II}Fe^{III}(Cl_2An^{2-})_2(Cl_2An^{3-\bullet})]^{2-}$, the structure can be described as a chain-knit network with two

ferrimagnetic or alternating para- and ferrimagnetic chains linked by diamagnetic Cl_2An^{2-} ligands, respectively. This compound exhibits an open hysteresis loop below 5 K with a coercive field of H_c = 629 Oe at 1.8 K and slow magnetic relaxation behavior with Δ_τ = 67.8 cm^{-1} ($\tau_0 = 6.0 \times 10^{-11}$ s).[131]

As noted above, frameworks bridged by small inorganic molecules or atoms, such as cyanide, cyanamide, tricyanomethanide, thiocyanide, azide, and halides, will not be covered in this review unless these ligands can be considered as coligands within otherwise organic ligand-bridged networks. Extensive research on Prussian blue analogues[132,133] over the last three decades has afforded a number of magnets with high ordering temperatures, reaching up to 376 K for $K V^{II}[Cr^{III}(CN)_6]\cdot 2H_2O$.[134] Other cyano-bridged solids, such as those based on octacyanometalates[135] and inorganic-organic networks,[136,137] along with those bridged by the polydentate cyanocarbons cyanamide[138–142] and tricyanomethanide,[143–145] have also been found to display long-range magnetic order. Some of these frameworks exhibit permanent microporosity, as has been recently reviewed.[146] Furthermore, 2D and 3D inorganic-organic compounds featuring thiocyanato-,[147–149] azido-,[147,150–160] and chloro-bridged[161,162] chains or layers commonly show permanent magnet-like behavior, where the highest ordering temperatures have been observed for the azido-linked networks.

The formate ion ($HCOO^-$) has long been employed as a linker to construct magnetic coordination solids, as its ability to act as a single- and three-atom connector facilitates strong exchange coupling between metal centers. As the smallest carboxylate, the formate ion may exhibit multiple different bridging modes, such as *syn–syn*, *anti–anti*, and *syn–anti* C–O–C, as well as monoatomic (see Figure 8.5). These different metal-binding modes can mediate ferro- or

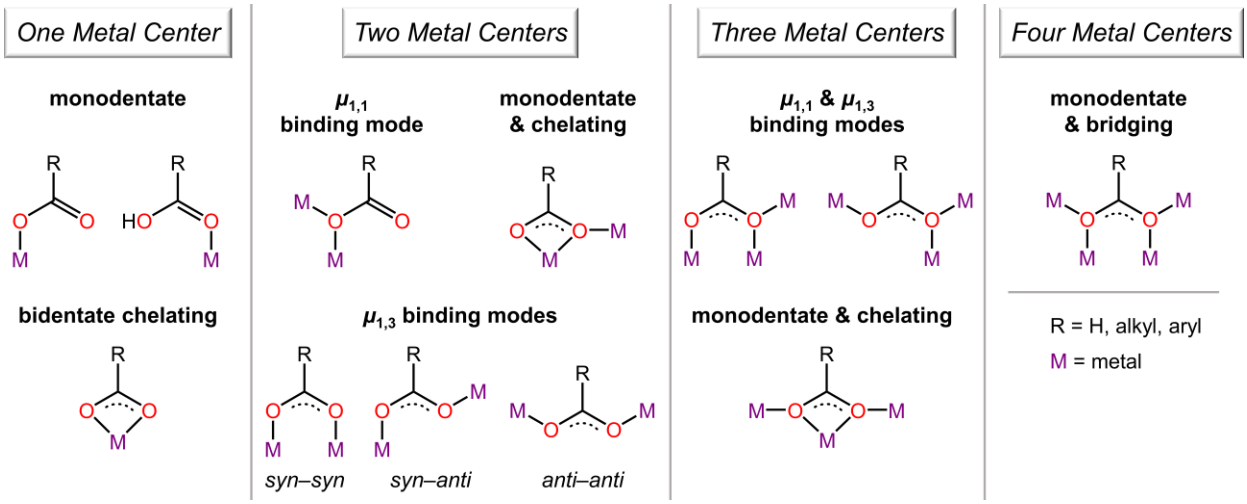

Figure 8.5 Summary of metal-binding modes for carboxylato ligands bearing one carboxylate group.

antiferromagnetic coupling between metal centers, depending on the type of bridging mode and identity of the metal ions. Based on the definition of a MOF we use here, coordination solids that are primarily bridged by formate fall outside the scope of this review, as the formato ligand cannot be considered as multitopic due to the presence of only a single carboxylate group. Nevertheless, owing to the important contribution of metal formate networks to the early development of the field of magnetic MOFs, we briefly survey below key examples within this series of compounds. We refer the reader to the following references for a more comprehensive account on magnetic metal-formate frameworks.[14,18,146]

Magnetic formate-based frameworks include 2D square lattice-type structures,[163–166] homoleptic mono-[167–209] and heterobimetallic[199] 3D frameworks, and 3D networks with 4,4′-bipyridine and related coligands.[210,211] Among these compounds, the monometallic Ni^{II} and mixed-valence $Fe^{II}Fe^{III}$ frameworks with $(Me_2NH_2)^+$ cations, $(Me_2NH_2)[Ni^{II}(HCOO)_3]$[184] and $(Me_2NH_2)[Fe^{II}Fe^{III}(HCOO)_6]$,[197,199,203] exhibit the highest magnetic ordering temperatures of T_c = 35.6 and 37 K, respectively. These 3D frameworks are isostructural, featuring distorted octahedral

metal centers linked by *anti–anti* O–C–O bridges that favor antiferromagnetic coupling between spin centers, and $(Me_2NH_2)^+$ cations are located in the cages of the networks. The Ni^{II} framework orders as a canted antiferromagnet, whereas the $Fe^{II}Fe^{III}$ network displays Néel N-type ferrimagnetism. Notably, these and other formate-based 3D frameworks show multiferroic behavior with coexistent and coupled magnetic and electric order,[190,198,202–205,209] which is a rare phenomenon among metal-based coordination networks bearing carbon-containing ligands.

8.3 MOF Magnets with Diamagnetic Bridging Ligands

8.3.1 Introduction

The majority of MOF magnets reported to date are comprised of paramagnetic metal centers bridged by diamagnetic ligands, where the magnetic interactions between metal centers occur via a superexchange coupling mechanism. The strength of this interaction, as quantified by the exchange coupling constant *J*, is directly correlated to the magnetic ordering temperature of 2D and 3D magnets.[23] As such, to realize magnets with high operating temperatures, the metal centers and linkers must be chosen with care to maximize the magnetic exchange interactions between spin centers. Because the coupling strength decreases drastically as the number of atoms in the bridge increases,[146] the use of short linkers providing one-, two-, or three-atom coupling pathways is favored.[24] However, most small ligands able to mediate strong exchange interactions between metal centers are inorganic in nature, such as oxo, hydroxo, azido, cyano, and thiocyanato ligands. Furthermore, short linkers often afford dense frameworks with no porosity. Therefore, a balance in linker length is critical to simultaneously impart strong magnetic interactions and structural voids in extended networks.

Carboxylate-based ligands are particularly well-suited toward this end,[212] as the carboxylate

group can link metal centers through both single-atom (M–O–M) and three-atom (M–O–C–O–M) bridges (see Figure 8.5). In addition, N-heterocycles, such as azolates and pyrimidines, are attractive linkers owing to their versatile bridging modes through short two- (M–N–N–M) or three-atom (M–N–C–N–M/M–N–N–N–M) linkages (see Figure 8.6). Notably, most MOF magnets are constructed from organic ligands featuring some degree of conjugation, as the presence of an extended π system enables an additional spin–spin coupling mechanism that may enhance the overall magnetic exchange interaction.

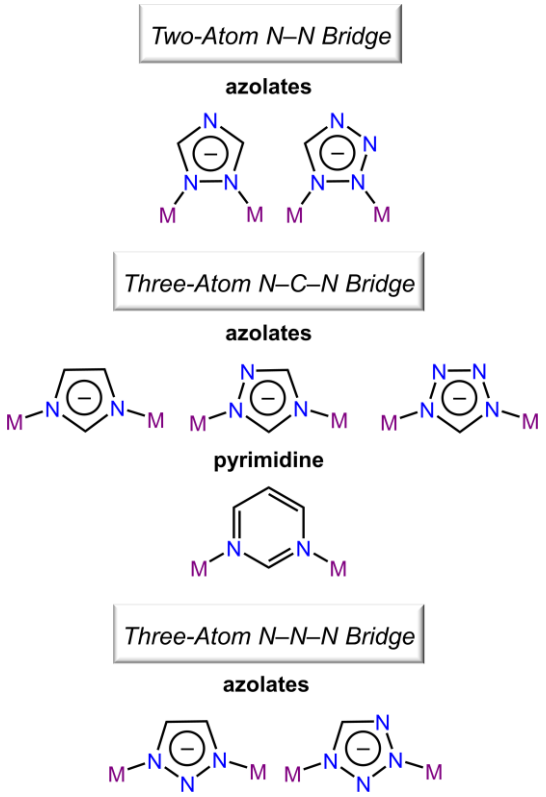

Figure 8.6 Examples of short bridging pathways between two metal centers provided by N-heterocyclic ligands. From top to bottom: two-atom N–N bridge, three-atom N–C–N bridge, and three-atom N–N–N bridge.

The use of organic linkers that provide three-atom bridges between metal centers is of particular interest, as based on symmetry considerations, this connectivity will in most cases allow the antisymmetric interaction known as the Dzyaloshinskii–Moriya interaction.[24,213,214] Specifically, this interaction is allowed when there is no inversion center between the two bridged metal centers, and it can lead to canted spin structures. As a result, canted antiferromagnetic behavior is often observed in three-atom-bridged systems.

MOF magnets bridged by diamagnetic linkers often feature mixed-ligand compositions. Such compounds may either be comprised of a multitopic organic ligand with small inorganic coligands, including oxo, hydroxo, aquo, sulfato, and azido ligands, or consist of two distinct multitopic

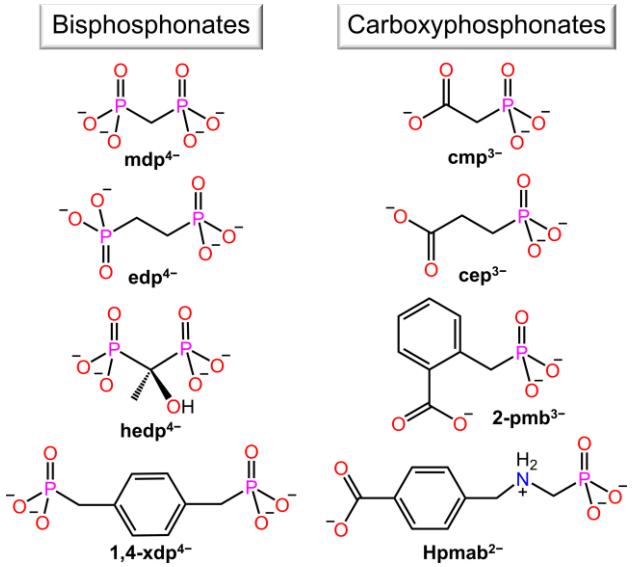

Figure 8.7 Multitopic phosphonato ligands discussed in this review.

organic ligands. For the latter case, the combination of carboxylates and N-heterocycles is most common, but the employment of two different carboxylato ligands is also well documented. A wide range of neutral and anionic multitopic organic linkers has been employed to construct magnets, as depicted in Figures 8.7–8.11. Many of these ligands are multifunctional in nature, as they contain two or more types of functional groups that can participate in metal binding. The following sections will survey structurally-characterized compounds that contain these ligands and that have been shown to exhibit long-range magnetic order. Framework magnets based on diamagnetic linkers are enumerated in Tables 8.1 and 8.2.

8.3.2 Phosphonate-Containing Compounds

Phosphonates are organophosphorus compounds containing direct C–P bonds, including $(C–PO_3)^{2–}$ and $C–PO(OR)_2$ moieties. Within this class, bisphosphonates and carboxylate-functionalized

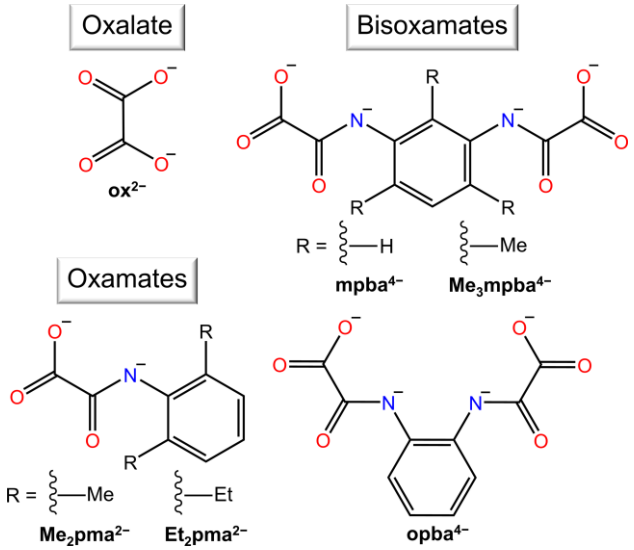

Figure 8.8 Oxamato ligands discussed in this review. The structure of the oxalato ligand is provided for comparison (top left).

phosphonates can be considered as multitopic organic ligands because they feature two metal-binding groups separated by an organic backbone (see Figure 8.7). Compared to carboxylates, the coordination chemistry of phosphonates is less predictable owing to a higher number of possible binding modes and protonation states. Furthermore, metal phosphonate compounds frequently form dense layered structures, rendering the formation of porous frameworks challenging.[215] Nevertheless, several open frameworks featuring bisphosphonato and carboxyphosphonato linkers have been shown to display long-range magnetic order at low temperature (see Tables 8.1 and 8.2).[216–222] Specifically, 2D and 3D Ni^{II} frameworks based on methylenediphosphonate (mdp^{4-}) order as ferromagnets with T_C = 3.1(1)–3.8(2) K.[216] In addition, 3D Cu^{II} frameworks with longer bisphosphonato linkers display long-range antiferromagnetic order with T_N = 4(1) K,[217] and a similar ordering temperature was observed for a compound featuring a hydroxo-substituted bisphosphonato ligand and a pyrazine coligand.[218]

Substituting bisphosphonato ligands for carboxyphosphonates has afforded compounds with similar low magnetic ordering temperatures. This class of compounds includes the Co^{II} frameworks $(H_2en)_{0.5}[Co^{II}(cmp)(H_2O)]\cdot H_2O$ (en = ethylenediamine; cmp^{3-} = carboxymethylphosphonate) and $Co^{II}(Hpmab)$ ($Hpmab^{2-}$ = 4-((phosphonatomethylammonio)methyl)benzoate), which order as canted antiferromagnets with T_N = 4.3 and 2.0 K, respectively.[219,220] However, using carboxylate-functionalized phosphonato ligands along with hydroxo coligands has been shown to provide dramatic improvements in magnetic properties.[221,222] In particular, the compound $Co^{II}_2(OH)$(2-pmb) (2-pmb^{3-} = 2-(phosphonomethyl)benzoate), displays long-range canted antiferromagnetic order with T_c = 31.0 K, which is an order of magnitude higher than the ordering temperatures for most phosphonate-

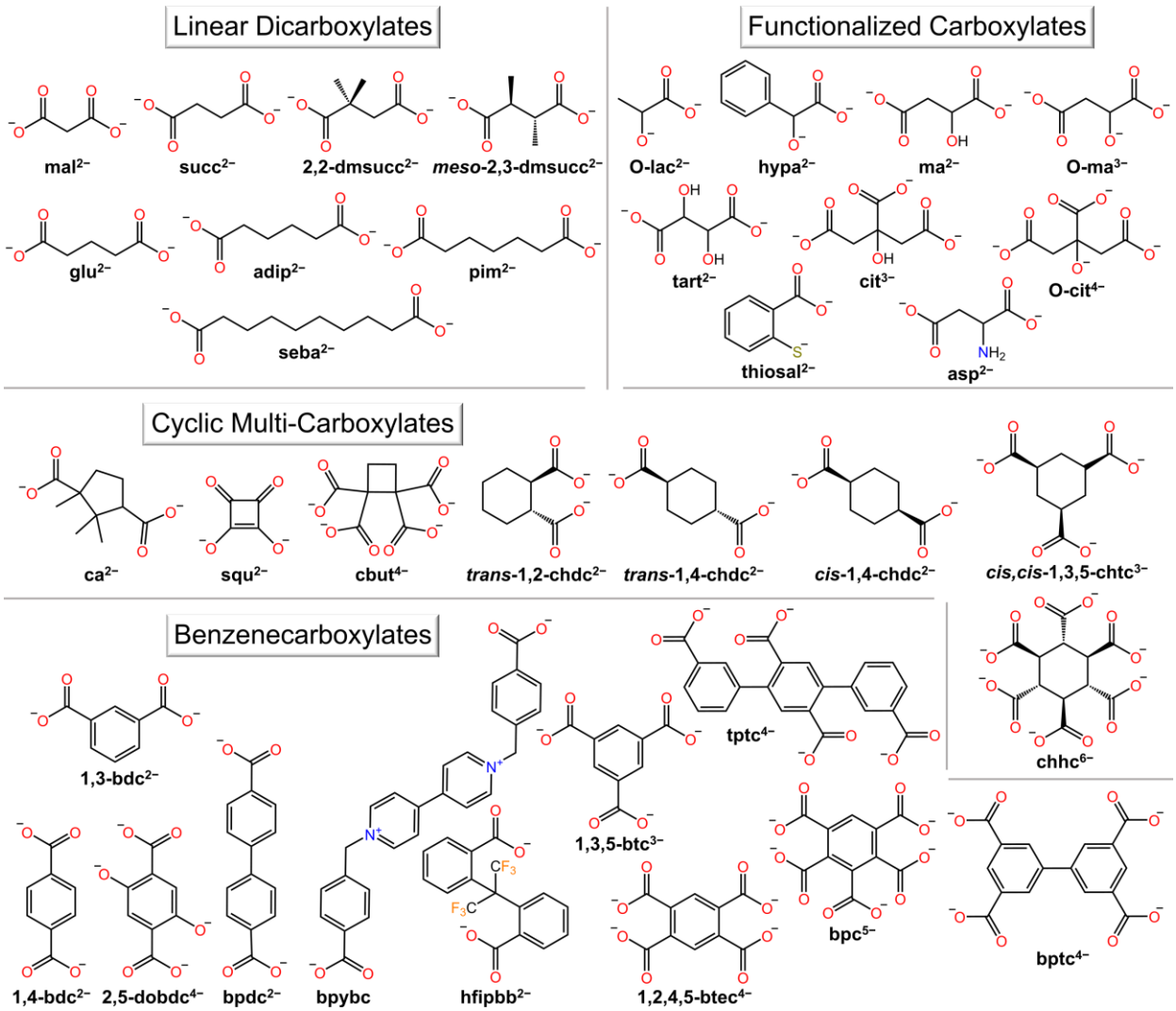

Figure 8.9 Multitopic carboxylato ligands discussed in this review.

containing magnets. This framework features a unique 2D layered structure made up of double chains of $Co^{II}_2(\mu_4\text{-}OH)O_3$ units connected by CPO_3^{2-} phosphonate groups. The aromatic backbone of the carboxyphosphonato ligand protrudes into the interlayer space, and the carboxylate groups provide a further support to the layered structure (see Figure 8.12, top and center). Note that the combination of edge- and face-sharing MO_6 octahedra and the presence of a central μ_4-OH group bridging two types of chains not previously been observed in a molecule-based material.

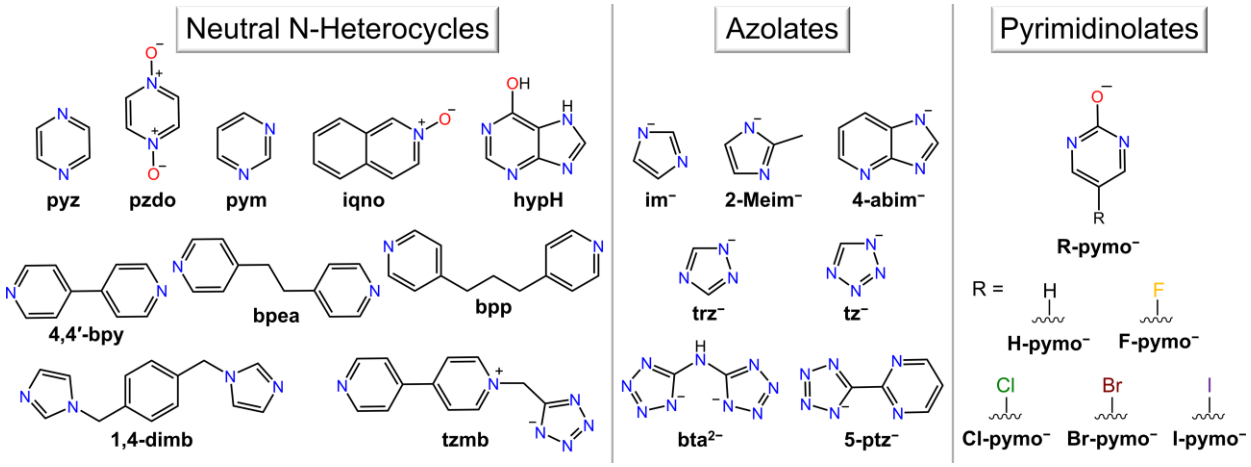

Figure 8.10 N-heterocyclic ligands discussed in this review.

Furthermore, the magnetic behavior of this compound is also unusual. In addition to the relatively high magnetic ordering temperature, hysteresis measurements carried out at 2 K established this compound as one of the hardest molecule-based magnet reported thus far, with a coercive field of H_c = 4.3 T (see Figure 8.12, bottom).[222]

8.3.3 Oxalate-Containing Compounds

8.3.3.1 Introduction

The oxalate ion ($C_2O_4^{2-}$) acts as a short multi-atom ligand (see Figure 8.8) that is commonly observed in 1D, 2D, and 3D magnetic materials owing to its ability to mediate both σ and π electronic pathways for magnetic superexchange through two connected O–C–O bridges. The presence of a C–C bond between the two carboxylate groups promotes the formation of an extended π system and facilitates a bis-bidentate ligand binding mode. The oxalato ligand has found enormous success in the rational design of molecule-based magnets, as a vast number of homo- and heterometallic 2D and 3D oxalate frameworks have shown permanent magnetism with ordering temperatures up to 70 K.[223] In this section, we discuss the synthetic strategies adopted to

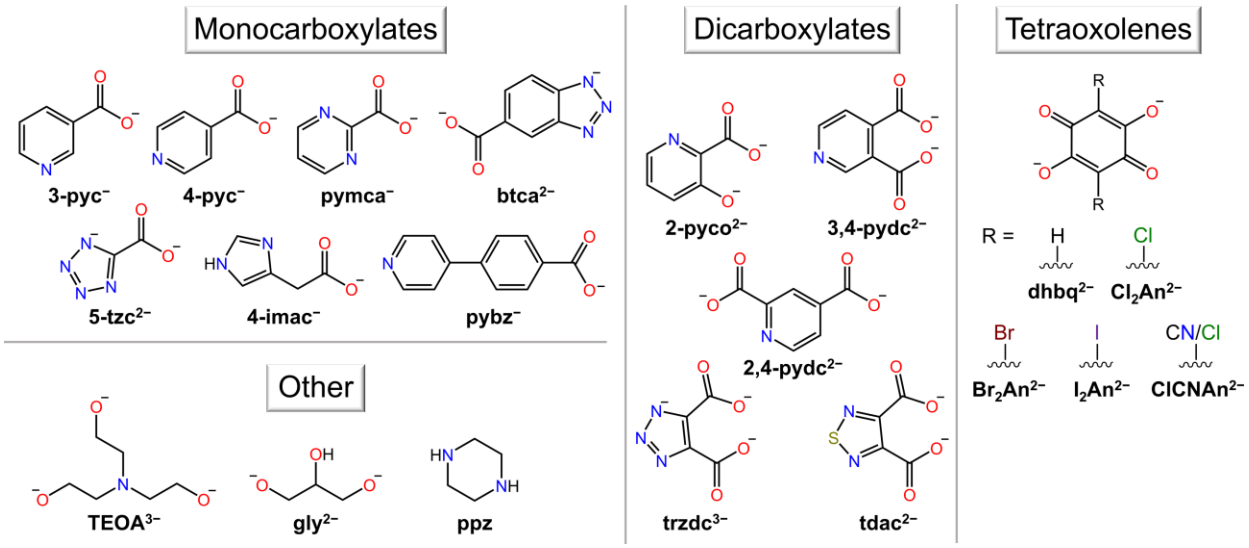

Figure 8.11 Ligands bearing both carboxylate groups and N-heterocycles discussed in this review. Other ligands discussed in this review, including tetraoxolene ligands, are also depicted.

afford oxalate-based magnets with different dimensionalities, structures, and magnetic properties. Specifically, we highlight the role of templating cations and the choice of metal centers in dictating the properties of these materials, and the different behaviors of homo- and heteroleptic frameworks. Finally, we conclude this section with a short discussion on the potential of these magnetic frameworks as multifunctional molecule-based materials. For a more comprehensive account on oxalate-based magnetic frameworks, the reader is referred to other review articles.[224,225]

8.3.3.2 2D Frameworks

A wide range of homoleptic mixed-valence metal oxalates of the general formula $(A)[M^{II}M^{III}(ox)_3]$ (M^{II} = Mn^{II}, Fe^{II}, Co^{II}, Ni^{II}, Cu^{II}; M^{III} = Cr^{III}, Fe^{III}, Ru^{III}; ox^{2-} = oxalate), where A^+ refers to a monovalent cation, have been reported[226–235] since the seminal contribution in 1990.[226] The structure of these frameworks features an anionic 2D honeycomb lattice consisting of alternating octahedral M^{II} and M^{III} ions that are each chelated by three bis-bidentate oxalato ligands. The formation of the honeycomb lattice requires adjacent metal centers to adopt opposite

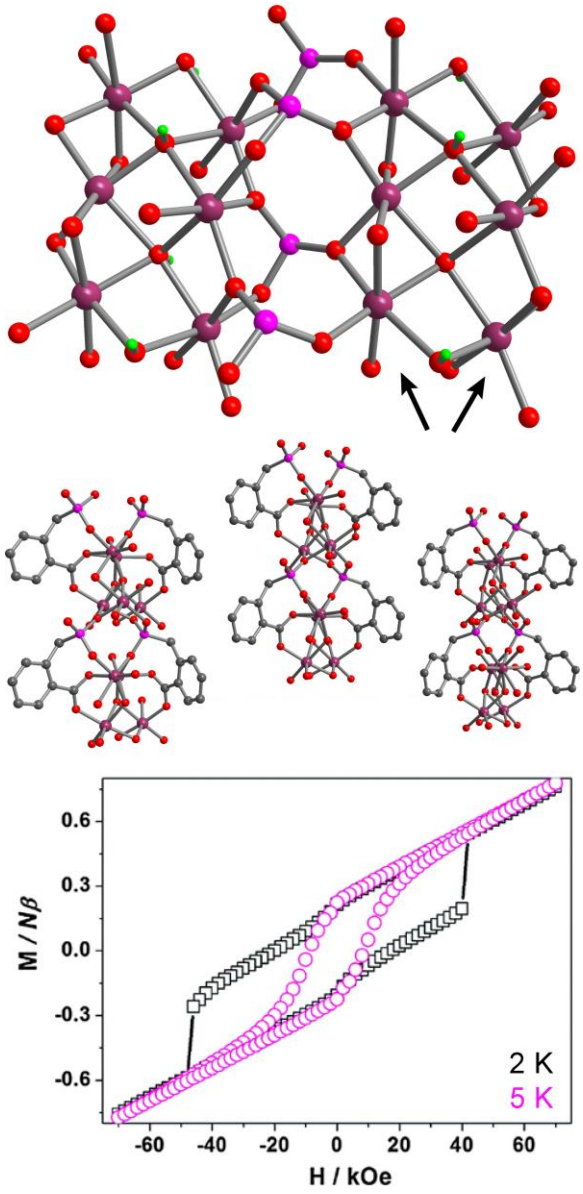

Figure 8.12 Top: Crystal structure of the inorganic layer in Co^{II}_2(OH)(2-pmb), highlighting the two distinct μ_4-OH-bridged chains (black arrows). Purple, magenta, red, gray, and light green spheres represent Co, P, O, C, and H atoms, respectively; terminal H atoms are omitted for clarity. Center: Crystal structure as viewed along the crystallographic *c* axis. Bottom: Variable-field dc magnetization data for Co^{II}_2(OH)(2-pmb), collected at selected temperatures. Reproduced from ref. 222 with permission from the Royal Society of Chemistry.

chirality (Δ or Λ) (see Figure 8.13), and the A^+ cations are typically interleaved between the anionic layers. The nature of magnetic exchange within the layers is dictated by the identity of the trivalent metal center. For instance, Cr^{III} and Ru^{III} promote ferromagnetic interactions, whereas Fe^{III} promotes antiferromagnetic interactions. Interactions between adjacent layers are generally minimal, and thus these compounds are best described as 2D magnets.

Investigations of the effects of different A^+ cations on the magnetic properties of homoleptic $Fe^{II}Fe^{III}$ 2D oxalate frameworks revealed that the nature of A^+ can play an important role in the magnetic behavior of these ferrimagnets.[227–229] While several quaternary ammonium frameworks exhibit similar ordering temperatures of T_c = 44–46 K, the value of T_c decreases to 34 and 36 K when Ph_4P^+ and Ph_4As^+ cations are used,

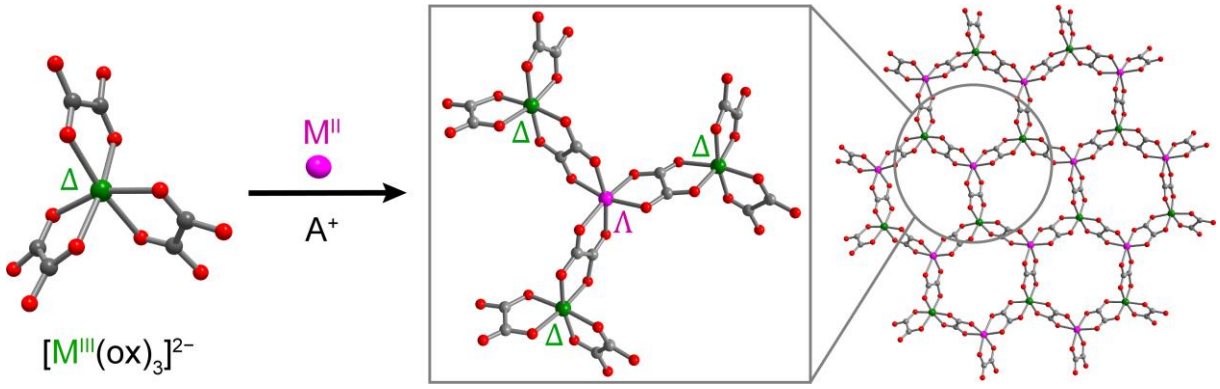

Figure 8.13 Synthesis of mixed-valence (A)[$M^{II}M^{III}(ox)_3$] 2D frameworks of honeycomb topology, illustrating the opposite chirality (Δ or Λ) of M^{II} and M^{III} metal centers. Green, magenta, red, and gray spheres represent M^{III}, M^{II}, O, and C atoms, respectively.

respectively (see Table 8.3). Furthermore, (Ph_4P)[$Fe^{II}Fe^{III}(ox)_3$] and (Ph_4As)[$Fe^{II}Fe^{III}(ox)_3$] display spin glass behavior below T_c, whereas the analogous frameworks incorporating other quaternary phosphonium or ammonium cations show anomalous negative magnetization below a compensation temperature (T_{comp}), defined as the temperature at which the net magnetization value is zero as it changes from a positive to a negative value (see Table 8.3). A compensation temperature should occur in the magnetization for a system with two spin lattices if the sublattice with smaller saturation magnetization initially orders more rapidly as the temperature is decreased than the lattice with the larger saturation magnetization. Accordingly, the observed Néel N-type ferrimagnetic order for these frameworks has been attributed to an initial steeper ordering of the Fe^{II} sublattice relative to the Fe^{III} lattice. This hypothesis was supported by analyzing the temperature dependence of the hyperfine fields experienced at the Fe^{II} and Fe^{III} nuclei through Mössbauer spectroscopy.[227–229]

Notably, the magnitude of the negative magnetization was later found to be influenced by the preparation conditions of these frameworks due to variable amounts of Fe^{II} vacancies.[230] However, only slight changes in ordering temperature (T_c = 44(1)–48(1) K) were observed when the alkyl

chain length of $(Ph_3RP)^+$ cations (R = Pr, Bu, Pe, Hx, Hp) was varied substantially, from three to seven carbons (see Table 8.3). These results are in agreement with only a modest expansion of the interlayer distance from 9.48 Å for R = Pr to 11.10 Å for R = Hp, which has been attributed to the nearly parallel arrangement of the alkyl chains with respect to the magnetic honeycomb layers.[230] Similar observations have been made for the series of isostructural $Mn^{II}Fe^{III}$ frameworks (see Table 8.4).[230] Overall, the ordering temperatures for the $Mn^{II}Fe^{III}$ honeycomb frameworks show a smaller variation by cation than the $Fe^{II}Fe^{III}$ analogues. Interestingly, the $Mn^{II}Fe^{III}$ compounds exhibit an uncompensated magnetic moment despite antiferromagnetic coupling between the high-spin Mn^{II} ($S = {}^5/_2$) and Fe^{III} ($S = {}^5/_2$) ions, which should give an $S = 0$ ground state. This behavior was originally attributed to spin canting,[229–232] but was later proposed to be caused by defects in the structure, namely Mn^{II} vacancies.[230]

The strong influence of the templating cation and solvent molecules in controlling the metal coordination environments in these systems, and the resulting magnetic properties, is exemplified in a series of heterobimetallic framework compounds of the general formula $[K(18\text{-crown-}6)]_3[M^{II}{}_3(H_2O)_4(M^{III}(ox)_3)_3]$ (M^{II} = Mn^{II}, Fe^{II}, Co^{II}, Ni^{II}, Cu^{II}; M^{III} = Cr^{III}, Fe^{III}).[236] These 2D frameworks are isostructural and display a honeycomb-like structure where

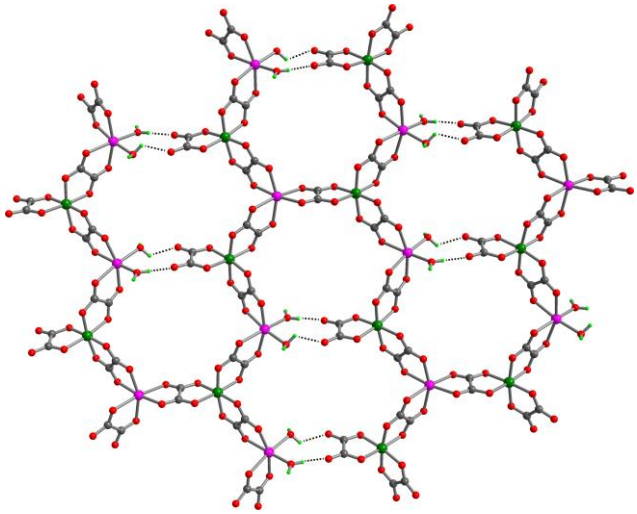

Figure 8.14 Crystal structure of the anionic 2D lattice for compounds $[K(18\text{-crown-}6)]_3[M^{II}{}_3(H_2O)_4(M^{III}(ox)_3)_3]$ (M^{II} = Mn^{II}, Fe^{II}, Co^{II}, Ni^{II}, Cu^{II}; M^{III} = Cr^{III}, Fe^{III}), as viewed along the crystallographic *c* axis. Hydrogen bonds between coordinated H_2O molecules and terminal oxalato ligands are highlighted with dashed lines. Green, magenta, red, gray, and light green spheres represent M^{III}, M^{II}, O, C, and H atoms, respectively.

two-thirds of the divalent metal ions are coordinated by two H_2O molecules that are hydrogen-bonded to terminal oxalato ligands (see Figure 8.14). The $[K(18\text{-crown-6})]^+$ cations are located in the hexagonal pores between layers and their large diameter promotes the fragmentation of the network. The $M^{II}Cr^{III}$ frameworks exhibit long-range ferromagnetic order with T_C = 3.2–8 K, whereas the $M^{II}Fe^{III}$ analogues behave as ferrimagnets (M^{II} = Fe^{II}, Co^{II}) or as a canted antiferromagnet (M^{II} = Mn^{II}) below T_c = 11.5–25.5 K (see Table 8.5). Notably, the ordering temperatures for this series of frameworks are considerably lower than those obtained for the analogous 2D networks of regular honeycomb topology,[227–232,237,238] highlighting that the superexchange through the longer M^{II}–O_{water}···O–C–O–M^{III} bridge in the fragmented compounds is significantly weaker than via the M^{II}–O–C–O–M^{III} linkage in conventional honeycomb frameworks.

The first example of a neutral oxalate-based layered magnet, the heterobimetallic $Co^{II}Cr^{III}$ compound $[Co^{II}(H_2O)_2]_3[Cr^{III}(ox)_3]_2\cdot 2$(18-crown-6), was reported in 2007.[239] The structure of this compound features layers of twelve-membered rings constituting six distorted octahedral Co^{II} ions and six $[Cr(ox)_3]^{3-}$ units, where two *trans*- or *cis*-oriented H_2O molecules complete the coordination sphere of Co^{II}. The crown ether moieties are located in the pores of the rings and provide further structural support through hydrogen bonding interactions (see Figure 8.15). Notably, the absence of interlamellar cations enables a short interlayer distance of 7.825(2) Å. This compound behaves as a ferromagnet with T_C = 7.4 K, in accord with other 2D $M^{II}Cr^{III}$ oxalate-based frameworks.[239] Magnetic hysteresis measurements at 2 K revealed a small coercive field of H_c = 160 Oe and a remanent magnetization of $M_r = 2.3\ \mu_B\ mol^{-1}$, indicative of a soft ferromagnet.[240]

The synthetic strategy of using a neutral crown ether guest molecule as a templating agent has been extended to other paramagnetic metal ions, providing an isostructural family of neutral 2D layered magnets of the general formula $[M^{II}(H_2O)_2]_3[M^{III}(ox)_3]_2\cdot 2$(18-crown-6) ($M^{II}$ = Mn^{II}, Fe^{II}, Co^{II}, Ni^{II}; M^{III} = Cr^{III}, Fe^{III}).[240] These frameworks exhibit ferro- (M^{III} = Cr^{III}) or ferrimagnetic (M^{III} = Fe^{III}) long-range order with T_c = 3.6–12.2 K (see Table 8.6). The use of a mixture of divalent metal ions in 1:1 ratio has also been explored. Among these compounds, the highest ordering temperature of T_c = 20.0 K was achieved for the $Fe^{II}Ni^{II}Fe^{III}$ framework, whereas the $Mn^{II}Co^{II}Fe^{III}$ framework provided the highest coercive field of H_c = 6300 Oe at 2 K (see Table 8.6). All other bi- and trimetallic compounds were classified as soft magnets. Interestingly, these and other crown ether-containing oxalate frameworks are soluble in H_2O but insoluble in organic solvents, which may allow for the growth of high-quality single crystals suitable for a suite of magnetic studies to provide a more detailed understanding of the associated magnetism.[240]

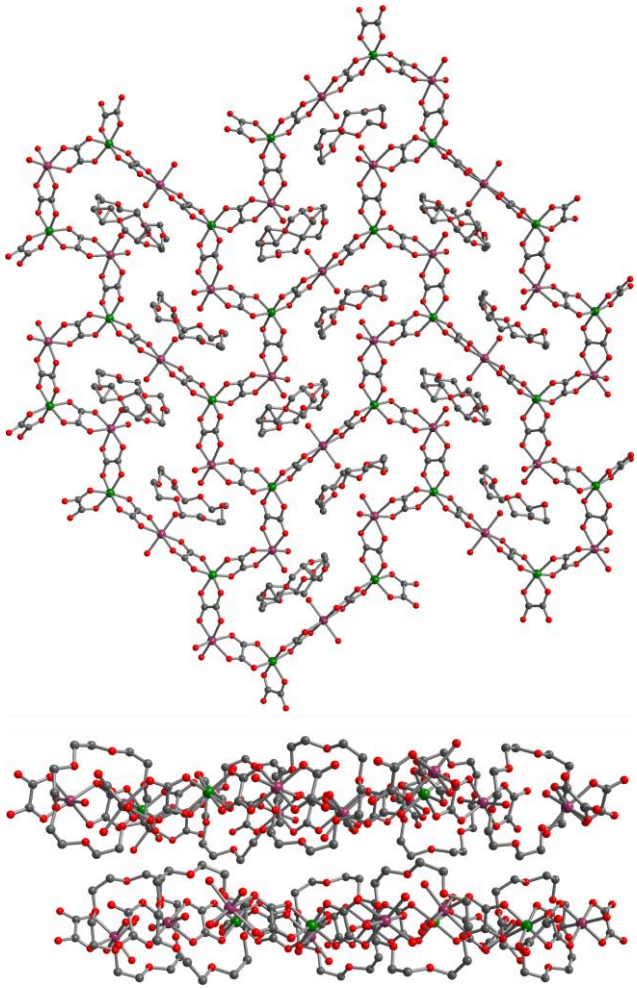

Figure 8.15 Crystal structure of $[Co^{II}(H_2O)_2]_3[Cr^{III}(ox)_3]_2\cdot 2$(18-crown-6), as viewed along the crystallographic *b* (top) and *a* axis (bottom). Purple, green, red, and gray spheres represent Co, Cr, O, and C atoms, respectively; H atoms are omitted for clarity.

Insertion of cations that may afford multifunctional magnetic materials owing to their unique magnetic and/or electrical properties has been investigated for 2D oxalate-based frameworks. For instance, employment of the paramagnetic decamethylferrocenium cation, $[Cp^*_2Fe^{III}]^+$ (Cp^{*-} = pentamethylcyclopentadienyl anion), afforded a series of mixed-valence frameworks of the general formula $[Cp^*_2Fe^{III}][M^{II}M^{III}(ox)_3]$ (M^{II} = Mn^{II}, Fe^{II}, Co^{II}, Ni^{II}, Cu^{II}; M^{III} = Cr^{III}, Fe^{III}, Ru^{III}).[233–235] These compounds feature the same regular honeycomb structure as the networks bearing quaternary ammonium, phosphonium, and arsenium counterions discussed above, with the organometallic cation residing in the interlayer space.[227–230] Despite the paramagnetic nature of $[Cp^*_2Fe^{III}]^+$, intercalation of this cation into the 2D honeycomb lattices does not significantly affect the magnetic properties of the resulting frameworks, as judged by the near identical values of T_c observed when $[Cp^*_2Fe^{III}]^+$ was replaced with the analogous diamagnetic decamethylmetallocenium cation $[Cp^*_2Co^{III}]^+$ (see Tables 8.7 and 8.8). Furthermore, the ordering temperatures for the decamethylmetallocenium frameworks are very similar to those bearing ammonium and phosphonium cations discussed above. These observations suggest that the interactions between the cationic and anionic layers are insignificant in these compounds and thus the two magnetic sublattices in $[Cp^*_2Fe^{III}][M^{II}M^{III}(ox)_3]$ behave essentially independently of each other.[233–235]

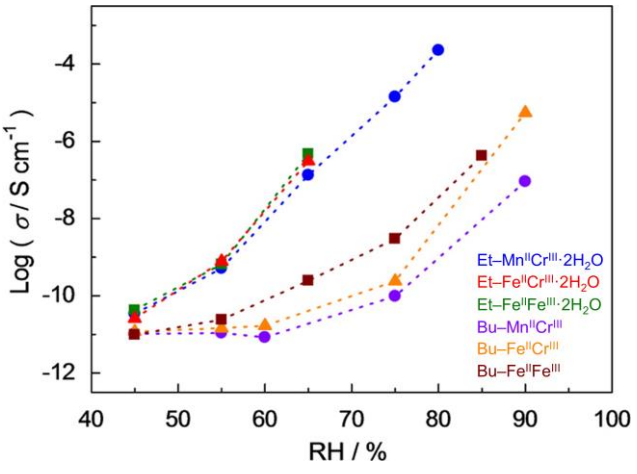

Figure 8.16 Proton conductivity vs relative humidity (RH) profiles at 25 °C for $(R_3(CH_2COOH)N)[M^{II}M^{III}(ox)_3]\cdot xH_2O$ (R = Et, Bu; M^{II} = Mn^{II}, Fe^{II}; M^{III} = Cr^{III}, Fe^{III}; x = 0, 2). Reprinted with permission from ref. 241. Copyright 2013 American Chemical Society.

Another example of the use of cation modulation to achieve multifunctional behavior is found in the series of proton-conductive oxalate frameworks $(R_3(CH_2COOH)N)[M^{II}M^{III}(ox)_3]\cdot xH_2O$ (R = Et, Bu; M^{II} = Mn^{II}, Fe^{II}; M^{III} = Cr^{III}, Fe^{III}; x = 0, 2).[241] These frameworks display the typical anionic 2D honeycomb structure as $(A)[M^{II}M^{III}(ox)_3]$, with $(R_3(CH_2COOH)N)^+$ ions interleaved in the interlayer space. The magnetic properties for these compounds are analogous to those observed for $(R_4N)[M^{II}M^{III}(ox)_3]$, with the $Mn^{II}Cr^{III}$ and $Fe^{II}Cr^{III}$ series of frameworks showing ferromagnetic order with T_C = 5.6–5.9 and 11.0–11.5 K, respectively, whereas the $Fe^{II}Fe^{III}$ species display magnetic behavior characteristic of Néel N-type ferrimagnetism with T_c = 42–44 K (see Table 8.9). The frameworks featuring $(Et_3(CH_2COOH)N)^+$ show high proton conduction, whereas those bearing $(Bu_3(CH_2COOH)N)^+$ display moderate proton conduction, as determined using alternating-current impedance measurements on pellet samples (see Figure 8.16). Notably, the conductivity values obtained for this series of frameworks at 45% relative humidity are an order of magnitude higher than those for $(Bu_4N)[Mn^{II}Cr^{III}(ox)_3]$. This discprepancy was attributed to the higher hydrophilicity of the polar $(R_3(CH_2COOH)N)^+$ (R = Et, Bu) ions compared to $(Bu_4N)^+$, where the carboxyl residue acts as a proton relay. The same rationale accounts for the higher conductivity observed for the $(Et_3(CH_2COOH)N)^+$ frameworks than the $(Bu_3(CH_2COOH)N)^+$ frameworks, which crystallize as dihydrates and anhydrates, respectively. Together, this series of proton-conductive oxalate frameworks provides rare examples of compounds that exhibit both ferromagnetism and proton conduction, along with the first report of coexistent Néel N-type ferrimagnetism and proton conduction. Accordingly, MOFs are attractive candidates for studying the interplay between proton conduction and magnetism, which may be of immediate interest for future technologies.

Along these lines, intercalation of the organic π-donor bis(ethylenedithio)tetrafulvalene (BEDT-TTF) into the bimetallic anionic oxalate network $[Mn^{II}Cr^{III}(ox)_3]^-$ provided the first example of coexistent ferromagnetism and metallic conductivity in a molecule-based compound.[21] Specificly, this compound behaves as a ferromagnet below T_C = 5.5 K and is metallic down to at least 0.3 K. However, the presence of electrically conducting organic layers between the oxalate layers did not afford enhanced magnetic performance, as the two sublattices are quasi-independent of one another. Building on this initial report, various tetrathiafulvalene derivatives, which form the basis of most known molecular electrical conductors and superconductors,[242] have been incorporated into 2D oxalate frameworks.[243–247] Structural analysis of these composite materials is challenging owing to the high crystallographic disorder of the oxalate-based layers, preventing the definitive assignment of atomic positions. Accordingly, accurate determination of the chemical formula, formal charges, and interactions between the conducting and magnetic layers is not immediately forthcoming. Although current attempts have not yet afforded compounds demonstrating synergy between the two phenomena, this may be an attractive strategy to furnish conductive magnetic materials.

Insertion of spin-crossover Fe^{III} complexes into homo- and heterobimetallic layered oxalate canted antiferromagnets and ferromagnets has also been reported.[244,248–253] The resulting compounds feature either a single or a double layer of the cationic spin-crossover complexes (see Figure 8.17). However, in either case, very little interplay between the two magnetic entities has been detected, likely due to the large difference in temperature at which spin-crossover and magnetic order occur. Specifically, while the spin-crossover takes place at high temperatures, in the range 100–350 K, the long-range magnetic order is only present below 8.1 K in these systems

(see Table 8.10). More recently, the coexistence of long-range ferromagnetic order and photoinduced spin-crossover, also known as light-induced excited spin state trapping (LIESST), has been demonstrated.[250,253] However, the photoinduced spin state change of the inserted Fe^{III} cations has a similar negligible influence on the magnetic behavior of the 2D oxalate framework. Nevertheless, since the LIESST effect is typically observed at lower temperatures than thermally-induced spin-crossover,[254] it may be a more promising route in realizing cooperativity between the two magnetic processes.

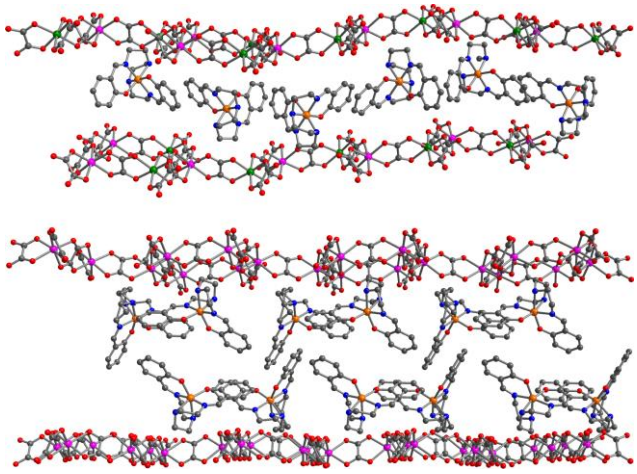

Figure 8.17 Crystal structures of $[Fe^{III}(sal_2\text{-trien})][Mn^{II}Cr^{III}(ox)_3]\cdot CH_2Br_2$, as viewed along the crystallographic *c* axis (top), and $[Fe^{III}(sal_2\text{-trien})]_2[Mn^{II}{}_2(ox)_3]\cdot 4H_2O\cdot DMF$, as viewed along the crystallographic *a* axis (bottom). Orange, magenta, green, red, blue, and gray spheres represent Fe, Mn, Cr, O, N, and C atoms, respectively; H atoms and solvent molecules are omitted for clarity. These compounds are representative examples of 2D oxalate frameworks with a single (top) or a double (bottom) layer of spin-crossover Fe^{III} complexes.

Several layered oxalate frameworks of other topologies have also been reported to show long-range magnetic order.[255–258] This set includes the homoleptic Fe^{II} compound $Fe^{II}(ox)(MeOH)$[258] and the first coordination networks featuring both bridging oxalato and 4,4′-bpy ligands, $M^{II}(ox)(4,4'\text{-bpy})$ (M^{II} = Fe^{II}, Co^{II}, Ni^{II}; ox^{2-} = oxalate; 4,4′-bpy = 4,4′-bipyridine).[255,256] These frameworks adopt a square-grid layered structure and exhibit long-range antiferromagnetic or canted antiferromagnetic order with T_N = 12–26 K.[255,256,258]

8.3.3.3 3D Frameworks

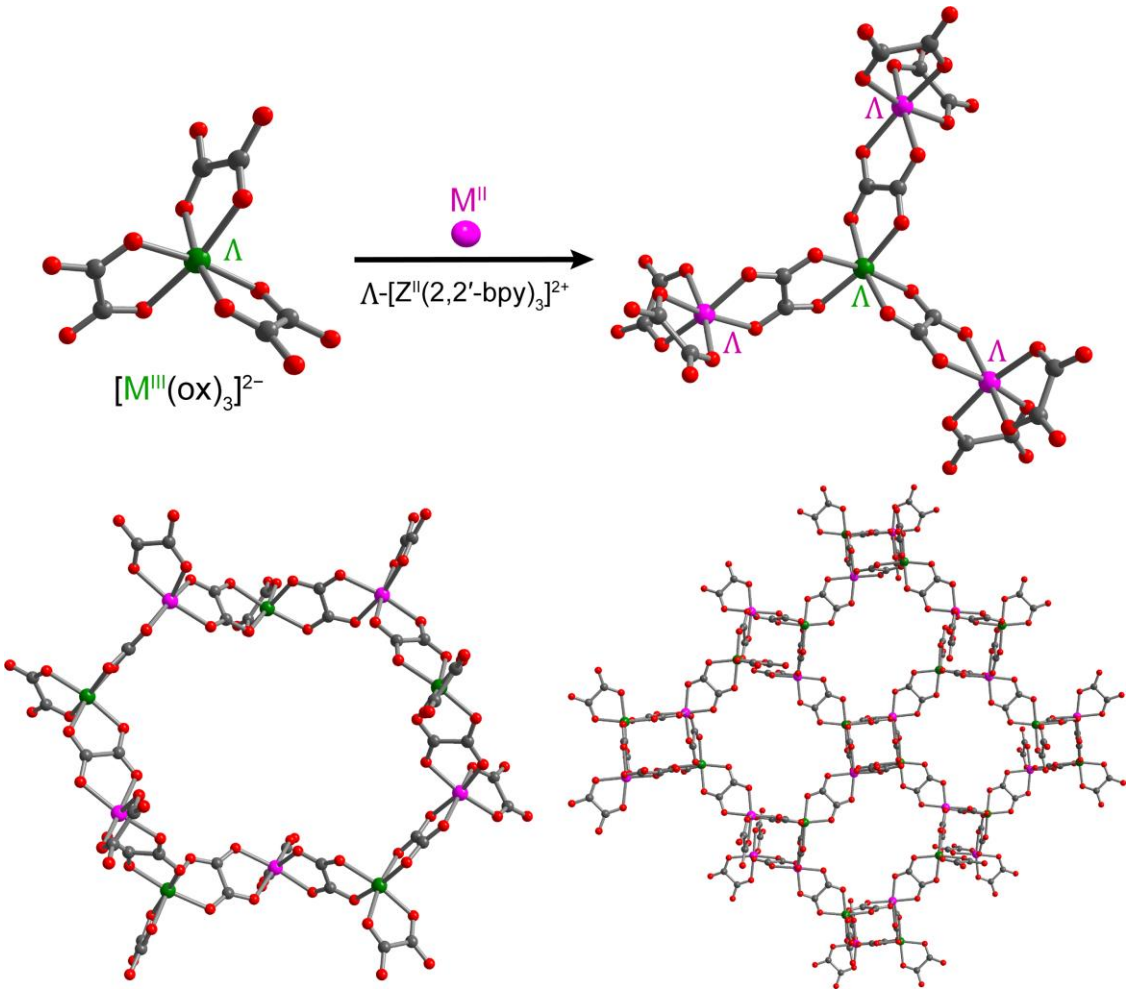

Figure 8.18 Top: Synthesis of mixed-valence $[Z^{II}(2,2'\text{-bpy})_3][M^{II}M^{III}(ox)_3](ClO_4)$ (Z^{II} = Fe^{II}, Co^{II}, Ni^{II}, Ru^{II}; M^{II} = Mn^{II}, Fe^{II}, Co^{II}, Ni^{II}, Cu^{II}; M^{III} = Cr^{III}, Fe^{III}) 3D frameworks of (10,3) net topology, illustrating the equivalent chirality of Z^{II}, M^{II}, and M^{III}. Bottom: Crystal structure of one ten-membered ring within the framework (left), and a view along the crystallographic *a* axis (right). Green, magenta, red, and gray spheres represent M^{III}, M^{II}, O, and C atoms, respectively. Counterions are omitted for clarity.

The formation of 3D oxalate-based framework magnets is favored when chiral metal complexes, such as $[Z^{II}(2,2'\text{-bpy})_3]^{2+}$ (Z^{II} = Fe^{II}, Co^{II}, Ni^{II}, Ru^{II}; 2,2′-bpy = 2,2′-bipyridine), are employed as templating agents. Here, chiral networks of the general formulas $[Z^{II}(2,2'\text{-bpy})_3][M^{II}_2(ox)_3]$ and $[Z^{II}(2,2'\text{-bpy})_3][M^{II}M^{III}(ox)_3](ClO_4)$ (Z^{II} = Fe^{II}, Co^{II}, Ni^{II}, Ru^{II}; M^{II} = Mn^{II}, Fe^{II}, Co^{II}, Ni^{II}, Cu^{II}; M^{III} = Cr^{III}, Fe^{III}) are generated for monovalent and mixed-valence oxalate species, respectively.[259–266] The 3D structure is comprised of trigonally distorted octahedral

M^{II}/M^{III} metal ions that are tris-chelated by bis-bidentate oxalato ligands and linked into three-connected ten-membered rings to give a network with (10,3) topology (see Figure 8.18). The cavities in the lattice are occupied by $[Z^{II}(2,2'\text{-bpy})_3]^{2+}$ cations and $(ClO_4)^-$ anions. When two types of metal centers are present in the oxalate-based lattice, they alternate in the framework. Notably, all the metal centers in these compounds possess the same configuration (Δ or Λ), as the chirality of the templating cationic entities determines the chirality of the anionic framework, with Δ–Δ and Λ–Λ interactions being favored. Indeed, the chiral or achiral character of the templating cation is commonly a dominant factor in determining whether a 2D or 3D oxalate system is formed.

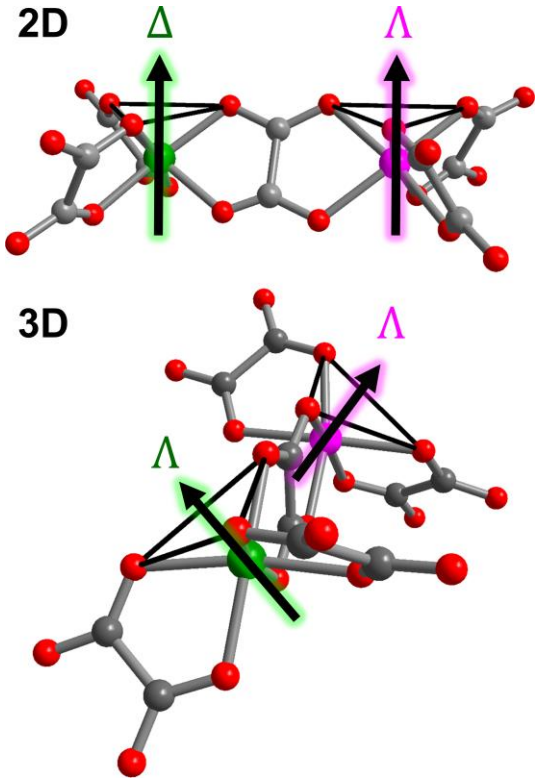

Figure 8.19 Schematic depiction of the orientation of the crystallographic C_3 axes for adjacent metal centers in chiral 2D (top) and 3D (bottom) metal oxalate frameworks. Green, magenta, red, and gray spheres represent M^{III}, M^{II}, O, and C atoms, respectively.

The magnetic ordering temperatures for the 3D series are generally somewhat lower than those for the 2D frameworks with the same combination of metal centers (see Tables 8.3–8.17). To illustrate, the 3D frameworks $[Fe^{II}(2,2'\text{-bpy})_3][M^{II}Cr^{III}(ox)_3](ClO_4)$ (M^{II} = Mn^{II}, Fe^{II}, Co^{II}) order as soft ferromagnets with T_C = 3.9–6.6 K (see Table 8.13),[259] whereas the 2D networks $[Cp^*_2Co^{III}][M^{II}Cr^{III}(ox)_3]$ (M^{II} = Mn^{II}, Fe^{II}, Co^{II}) exhibit ordering temperatures of T_C = 5.1–12.7 K (see Table 8.8).[234] The weaker exchange interactions between metal centers in the 3D frameworks,

despite higher dimensionality, has been attributed to the non-planarity of the structures. In particular, the non-planarity forces the C_3 axes of adjacent MO_6 octahedra to be perpendicular to each other rather than parallel, as in the 2D frameworks (see Figure 8.19). This different arrangement affects the overlap between metal- and ligand-based orbitals and thus the strength of magnetic exchange through the oxalate bridge.

The 3D oxalate frameworks are significantly more affected by the templating cation than are the 2D congeners, with a general trend of increasing ordering temperature with decreasing size of the cationic template. For instance, when the cation in $[Z^{II}(2,2'\text{-bpy})_3][M^{II}Fe^{III}(ox)_3](ClO_4)$ (Z^{II} = Fe^{II}, Ru^{II}; M^{II} = Mn^{II}, Fe^{II}) is varied from $[Fe^{II}(2,2'\text{-bpy})_3]^{2+}$ to $[Ru^{II}(2,2'\text{-bpy})_3]^{2+}$, the ordering temperature for the $Mn^{II}Fe^{III}$ derivatives decreases from T_c = 20.0 to 17.2 K. A similar decrease of ΔT_c = 1.2 K was observed for the $Fe^{II}Fe^{III}$ congeners.[260] However, this trend in T_c with the size of the templating cation seems only to be valid when comparing first-row and second-row transition metal complex cations, as illustrated through a family of ferromagnets with the formula $[Z^{II}(2,2'\text{-bpy})_3][M^{II}Fe^{III}(ox)_3](ClO_4)$ (Z^{II} = Fe^{II}, Co^{II}, Ni^{II}, Ru^{II}; M^{II} = Mn^{II}, Fe^{II}, Co^{II}, Ni^{II}).[259] Separate studies have revealed that varying the N-heterocyclic donors on the cationic template and solvent guest molecules can also be employed to modulate the magnetic properties for these systems.[261,262] For example, the ordering temperatures for the series $[Ir^{III}(ppy)_2(2,2'\text{-bpy})][M^{II}M^{III}(ox)_3]\cdot 0.5H_2O$ (ppy^- = 2-phenylpyridine anion; 2,2′-bpy = 2,2′-bipyridine; M^{II} = Mn^{II}, Fe^{II}, Co^{II}, Ni^{II}; M^{III} = Cr^{III}, Fe^{III}),[262] are up to three times higher than those for the $[Z^{II}(2,2'\text{-bpy})_3][M^{II}M^{III}(ox)_3](ClO_4)$ (Z^{II} = Fe^{II}, Ru^{II}) series (see Tables 8.13–8.15).[259] This significant increase in T_c in the presence of the larger Ir^{III} complexes has been hypothesized to be driven by shortening of the $M^{II}\cdots M^{III}$ bond distance and contraction of the unit cell when the lattice $(ClO_4)^-$ anions are replaced by smaller

H_2O molecules. Indeed, the values of T_c for $[Ir^{III}(ppy)_2(2,2'\text{-bpy})][M^{II}M^{III}(ox)_3]\cdot 0.5H_2O$ represent the highest ordering temperatures reported for 3D mixed-valence oxalate frameworks. Specifically, the $Mn^{II}Fe^{III}$ framework orders as a canted antiferromagnet with T_c = 31.0 K, the $Fe^{II}Fe^{III}$ analogue orders as a ferrimagnet with T_c = 28.0 K, and the $Ni^{II}Cr^{III}$ compound is a soft ferromagnet below T_C = 13.0 K.[262] The only monovalent 3D oxalate framework that orders at a higher temperature than these compounds is the Ni^{II}_2 framework $[Ru^{II}(2,2'\text{-bpy})_3][Ni^{II}_2(ox)_3]$, which is a canted antiferromagnet below T_c = 35 K.[263]

The 3D oxalate frameworks are attractive candidates for magneto-optical materials as they can be prepared in optically active forms.[261,263] Indeed, oxalate frameworks represent the first examples of 3D molecule-based magnets displaying optical activity.[261] Moreover, these ferromagnets were found to show measureable magnetic circular dichroism (MCD) below their ordering temperature.

The employment of the templating cation to impart additional physical properties to the oxalate framework has also been investigated. Introduction of a paramagnet cation, in this case nitronyl nitroxide radical cation, did not significantly affect the magnetic behavior of the oxalate network,[267] which is in line with previous studies for the 2D oxalate frameworks. Similarly, no cooperative magnetic properties have been observed when Fe^{II} and Fe^{III} spin-crossover complexes are used as templates in an attempt to furnish the formation of hybrid magnets. The modest change in the magnetic ordering temperature (T_C = 3.0–5.2 K) for the ferromagnetic $Mn^{II}Cr^{III}$ network in the presence of this set of cations likely stems from slight structural changes associated with the different sizes of the cationic complexes and the nature of the chelating ligands (see Table 8.16).[249,252,268–271]

In contrast, insertion of the single-molecule magnet $[Mn^{III}(salen)(H_2O)]_2^{2+}$ ($salen^{2-}$ = *N*,*N*′-ethylenebis(salicylidene-iminate)) into the ferromagnetic $Mn^{II}Cr^{III}$ lattice afforded the hybrid compound $[Mn^{III}(salen)(H_2O)]_2[Mn^{II}Cr^{III}(ox)_3]_2$ ·MeOH·2MeCN (see Figure 8.20, top), whose magnetic properties are not a simple sum of those for the two components, as illustrated by a comparison to control compounds.[272] Specifically, the two magnetic networks in this compound interact antiferromagnetically to give a ferrimagnetic phase that exhibits large magnetic hysteresis below 1 K, which contrasts with the behavior observed for the single-molecule magnet in a paramagnetic matrix and the ferromagnetic oxalate (see Figure 8.20, bottom). As such, this first example of the interplay between single-molecule magnetism and long-range magnetic order in an oxalate framework demonstrated that cooperative magnetic properties can be realized in these materials.

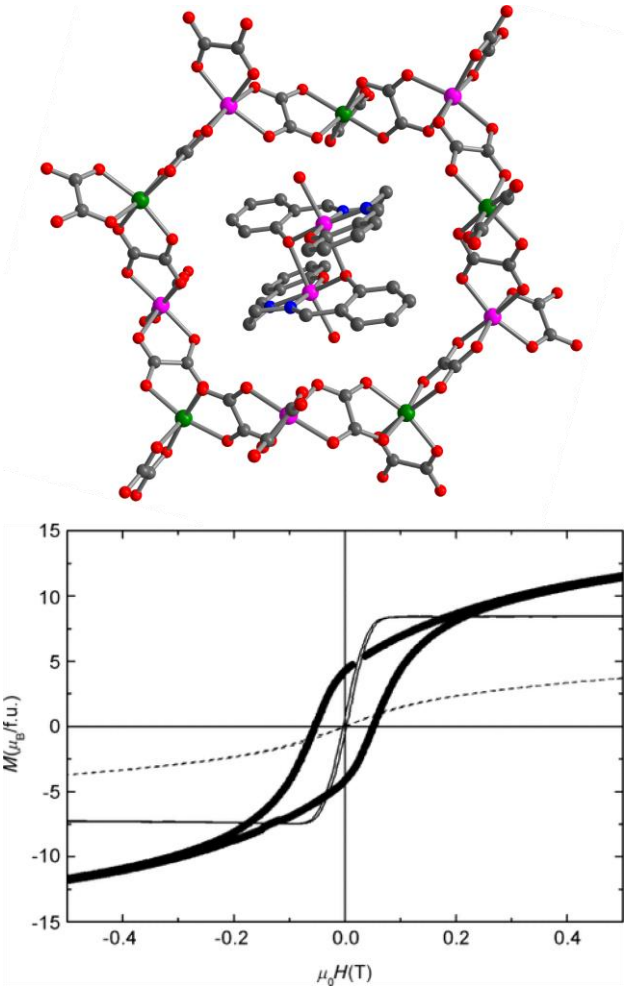

Figure 8.20 Top: Crystal structure of $[Mn^{III}(salen)(H_2O)]_2[Mn^{II}Cr^{III}(ox)_3]_2$·MeOH·2MeCN, as viewed along the crystallographic *a* axis. Magenta, green, red, blue, and gray spheres represent Mn, Cr, O, N, and C atoms, respectively; H atoms and solvent molecules are omitted for clarity. Bottom: Variable-field dc magnetization data for $[Mn^{III}(salen)(H_2O)]_2[Mn^{II}Cr^{III}(ox)_3]_2$·MeOH·2MeCN (solid dots), $[Mn^{III}(salen)(H_2O)]_2[Zn^{II}Cr^{III}(ox)_3]_2$·MeOH·2MeCN (dashed line), and $[In^{III}(sal_2\text{-trien})][Mn^{II}Cr^{III}(ox)_3]$·0.25$H_2O$·0.25MeOH·0.25MeCN (solid line), collected at 0.43 K with a field-sweep rate of 6 mT s^{-1}. Reproduced from ref. 272 with permission from Wiley-VCH Verlag GmbH & Co.

In addition to the homoleptic oxalate frameworks discussed above, several 3D frameworks featuring mixed oxalato and inorganic and/or organic linkers have demonstrated long-range magnetic order.[223,273–278] This includes compounds with oxo,[223,274,275] hydroxo,[223,273,276,277] piperazine,[276,277] and dicarboxylato[278] coligands (see Tables 8.2 and 8.17). Of these, a series of anionic Fe^{III} frameworks of formula $(A)_2[Fe^{III}_2O(ox)_2Cl_2]\cdot 2H_2O$ (A^+ = $(NH_4)^+$, $(MeNH_3)^+$, $(Me_2NH_2)^+$, $(EtNH_3)^+$, $(H_3O)^+$) provides the highest magnetic ordering temperatures.[223,274,275] These 3D frameworks are comprised of distorted octahedral Fe^{III} ions bridged by μ_2-O and oxalato ligands into a three-connected net of ten-membered rings with large channels that are occupied by cations and solvent molecules (see Figure 8.21). Remarkably, the ordering temperature for this family of canted antiferromagnets is drastically affected by the nature of the organic cation, despite near identical structural metrics, including the Fe^{III}–O–Fe^{III} superexchange angle. This angle only varies from

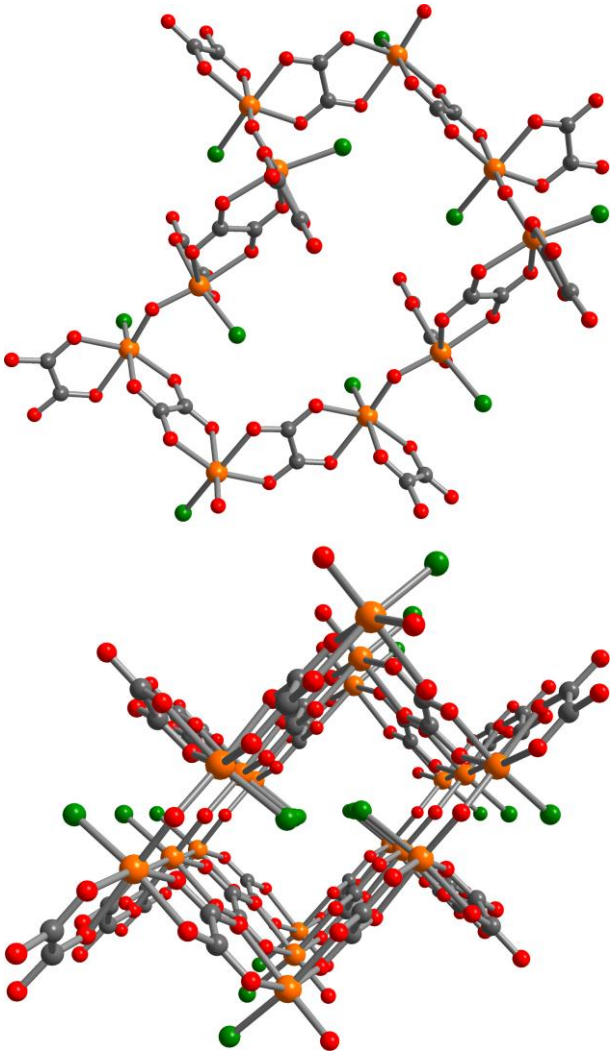

Figure 8.21 Crystal structure of $[Fe^{III}_2O(ox)_2Cl_2]^{2-}$, as observed in $(A)_2[Fe^{III}_2O(ox)_2Cl_2]\cdot 2H_2O$ (A^+ = $(NH_4)^+$, $(MeNH_3)^+$, $(Me_2NH_2)^+$, $(EtNH_3)^+$, $(H_3O)^+$). The top panel highlights the ten-membered ring with μ_2-O and oxalate bridges, while the bottom depicts a view along the crystallographic *c* axis. Orange, green, red, and gray spheres represent Fe, Cl, O, and C atoms, respectively.

135.9(4) to 137.1(2)° when the cation is changed from $(NH_4)^+$ to $(EtNH_3)^+$. Across the series, the ordering temperature increases from T_c = 40 K for the frameworks containing $(NH_4)^+$ and $(MeNH_3)^+$ to T_c = 52 and 56 K for the frameworks with $(Me_2NH_2)^+$ and $(EtNH_3)^+$ cations, respectively.[275] Moreover, the compound $(H_3O)(EtNH_3)[Fe^{III}_2O(ox)_2Cl_2]\cdot H_2O$ and its hydroxo-bridged congener $(EtNH_3)[Fe^{III}_2(OH)(ox)_2Cl_2]\cdot 2H_2O$ exhibit an even higher ordering temperature of T_c = 70 K (see Tables 8.2 and 8.17).[223] The reason for this modulation of T_c by the organic cations is not directly forthcoming, but it has been hypothesized to arise from their effects on the canting angle in these spin systems. Neutron diffraction experiments should provide deeper insight into the magnetic structures of these compounds. Note that the origin of spin canting in these frameworks is due to antisymmetric exchange,[24,213,214] owing to the isotropic nature of high-spin Fe^{III} ions.

Lastly, the transformation from $(EtNH_3)[Fe^{III}_2(OH)(ox)_2Cl_2]\cdot 2H_2O$ to $(H_3O)(EtNH_3)[Fe^{III}_2O(ox)_2Cl_2]\cdot H_2O$ is unique, as it involves intermolecular proton transfer in solid phase through a single-crystal-to-single-crystal process accompanied by a color change from yellow to deep red. Although the two compounds exhibit an identical magnetic ordering temperature, the oxo-bridged derivative is a significantly harder magnet, displaying a

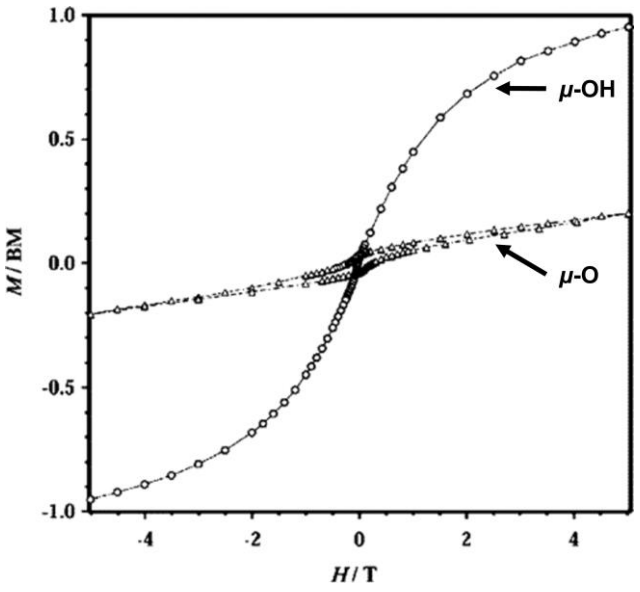

Figure 8.22 Variable-field dc magnetization data for $(EtNH_3)[Fe^{III}_2(OH)(ox)_2Cl_2]\cdot 2H_2O$ (circles) and $(H_3O)(EtNH_3)[Fe^{III}_2O(ox)_2Cl_2]\cdot H_2O$ (triangles), collected at 2.0 K. Reprinted with permission from ref. 223. Copyright 2005 American Chemical Society.

ten-fold higher coercive field of H_c = 2500 Oe at 2.0 K compared to the hydroxo-bridged framework (see Figure 8.22).[223]

Finally, note that a number of 3D inorganic-organic hybrid phosphate/phosphite oxalate materials, some of which fall within the definition of a MOF, display long-range antiferromagnetic order with T_N = 22–45 K.[279–284]

8.3.4 Oxamate-Containing Compounds

8.3.4.1 Introduction

A closely related family of building units that has been employed to construct porous frameworks with predictable structures and tunable magnetic properties are aromatic polyoxamato ligands (see Figure 8.8). One of the most prominent member of this series is the metallamacrocycle $[Cu^{II}_2(mpba)_2]^{4-}$ ($mpba^{4-}$ = *N*,*N*′-1,3-phenylenebis(oxamate)). This moiety features two S = ½ Cu^{II} centers that are ferromagnetically coupled through a double 1,3-phenylenediamidate cyclophane-type skeleton,[285] where the two aromatic rings are stacked in an eclipsed fashion to facilitate π–π interactions (see Figure 8.23).[286] When this dinuclear Cu^{II} complex is treated with divalent transition metal ions, such as Mn^{2+} or Co^{2+}, 2D or 3D frameworks are formed owing to coordination of the remaining two oxamate O atoms to the divalent metal centers. As such, the Cu^{II}_2 complex acts as a metalloligand toward divalent first-

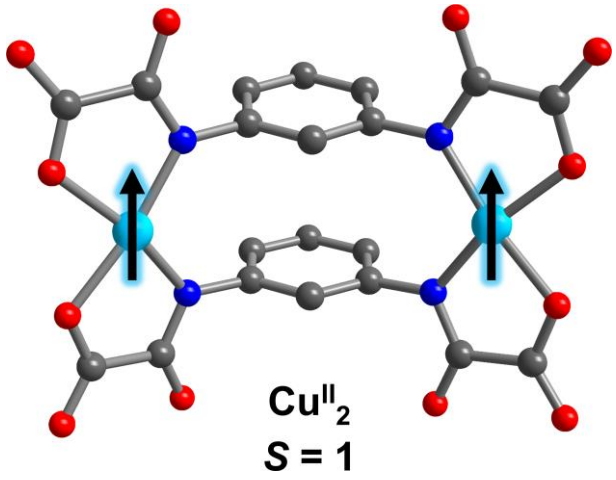

Figure 8.23 Crystal structure of $[Cu^{II}_2(mpba)_2]^{4-}$, highlighting the ferromagnetic coupling between two S = ½ Cu^{II} center to give an S = 1 metalloligand. Cyan, red, blue, and gray spheres represent Cu, O, N, and C atoms, respectively; H atoms are omitted for clarity.

row transition metal centers. Successful examples of this metalloligand approach to construct oxamate-based magnetic MOFs have recently been reviewed.[287]

8.3.4.2 2D Frameworks

The first framework featuring this building unit was the bimetallic compound $Co^{II}_2Cu^{II}_2(mpba)_2(H_2O)_6\cdot 6H_2O$.[288] Its structure is built up of chains of Co^{II} and Cu^{II} ions connected through bis-bidentate oxamate groups, which are further linked by cyclophane moieties to give a

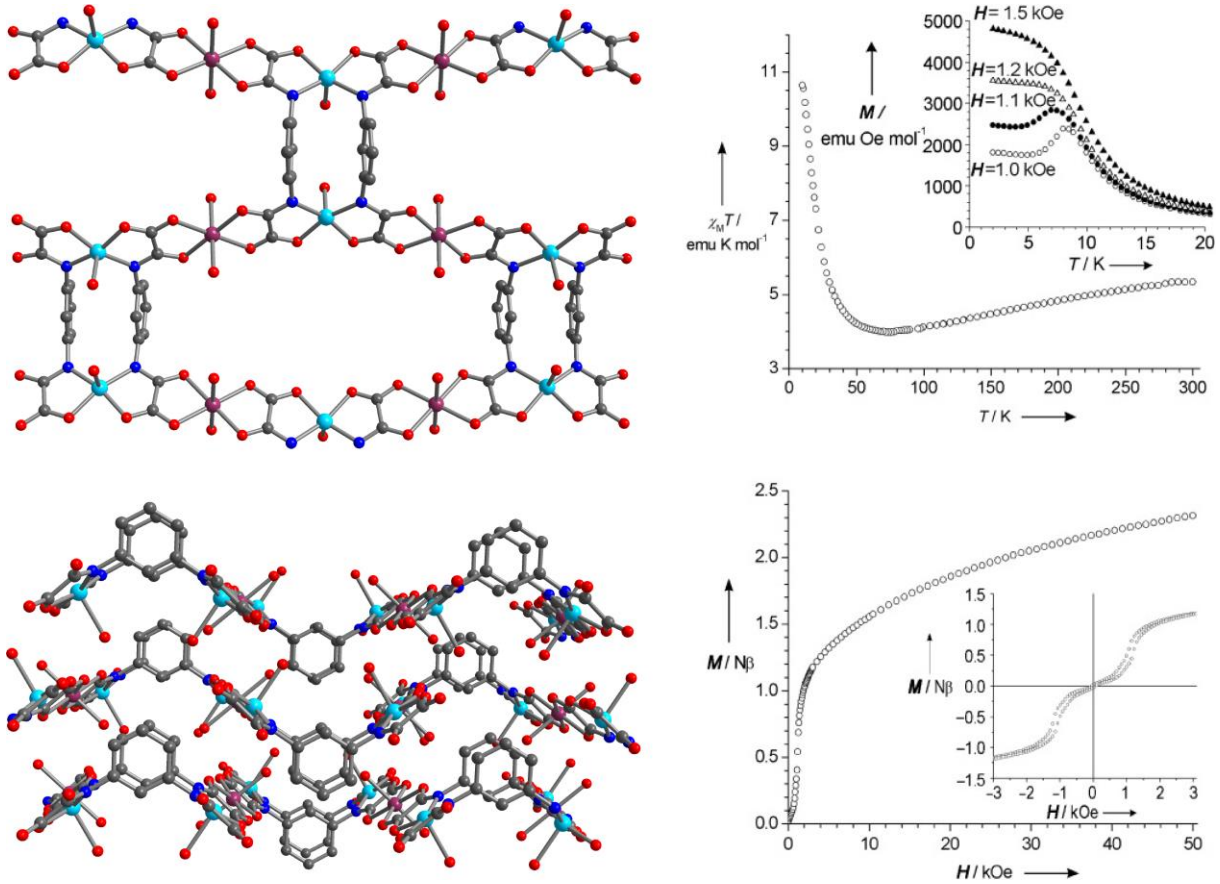

Figure 8.24 Left: Crystal structure of $Co^{II}_2Cu^{II}_2(mpba)_2(H_2O)_6\cdot 6H_2O$, as viewed along the crystallographic *b* (top) and *a* axis (bottom). Cyan, purple, red, blue, and gray spheres represent Cu, Co, O, N, and C atoms, respectively; H atoms and solvent molecules are omitted for clarity. Right: Variable-temperature dc magnetic susceptibility data for $Co^{II}_2Cu^{II}_2(mpba)_2(H_2O)_6\cdot 6H_2O$ (top), with variable-temperature dc magnetization data collected at selected fields shown in the inset. Variable-field dc magnetization data for $Co^{II}_2Cu^{II}_2(mpba)_2(H_2O)_6\cdot 6H_2O$ (bottom), collected at 2 K, with the low-field region shown in the inset. Reproduced from ref. 288 with permission from Wiley-VCH Verlag GmbH & Co.

corrugated 2D network of a brick wall-type topology. Each brick is formed by four Co^{II} ions in a distorted octahedral geometry and six square pyramidal Cu^{II} ions, where H_2O molecules complete the coordination spheres of the metal centers. The corrugated sheets stack in a zigzag fashion with H_2O solvent molecules occupying the space between the layers (see Figure 8.24, left). Strong antiferromagnetic interactions between Cu^{II} and Co^{II} ions within each layer, together with ferromagnetic interactions between adjacent Cu^{II} ions, afford overall ferrimagnetic layers. This compound orders as an antiferromagnet below 9.5 K. However, a magnetic field above 1200 Oe is sufficient to overcome the weak antiferromagnetic interlayer interactions to give a ferromagnetic-like state. This metamagnetic behavior is evident from the field dependence of the magnetization and a butterfly-shaped hysteresis loop, which was ascribed to reversal of the ferrimagnetic layers from an antiparallel to a parallel configuration (see Figure 8.24, right). Furthermore, ac magnetic susceptibility measurements revealed glassy magnetic behavior for this compound below the ordering temperature.

Interestingly, an analogous compound of formula $Mn^{II}_2Cu^{II}_2(Me_3mpba)_2(H_2O)_6\cdot 8H_2O$ (Me_3mpba^{4-} = 2,4,6-trimethyl-*N*,*N*′-1,3-phenylenebis(oxamate)) was shown to behave as a soft ferromagnet with T_C = 20.0 K.[289] No crystal structure is reported for this compound, but PXRD analysis indicates that it is isostructural to the $Co^{II}Cu^{II}$ brick wall layered framework described above. Here, the oxamato-bridged chains of Mn^{II} and Cu^{II} ions are linked into layers through a trimethyl-substituted 1,3-phenylenediamidate cyclophane spacer. The long-range ferromagnetic order was ascribed to ferromagnetic interactions between ferrimagnetic $Mn^{II}_2Cu^{II}_2$ layers, in contrast to the dominant antiferromagnetic interlayer interactions observed for the $Co^{II}Cu^{II}$ framework at low magnetic fields.

One example of a 2D oxamate magnet with an alternative topology is the compound $(MV)[Mn^{II}_2Cu^{II}_3(mpba)_3(H_2O)_3]\cdot 20H_2O$ (MV^{2+} = methylviologen dication).[290] It is built from tetrakis-bidentate square pyramidal Cu^{II}_2 anions, $[Cu^{II}_2(mpba)_2(H_2O)_2]^{4-}$, and tris-chelated octahedral Mn^{II} ions with alternating opposite chirality (Δ or Λ). These building blocks are connected into oxamato-bridged flat irregular hexagonal honeycomb layers. The layers are linked through two 1,3-phenylenediamidate spacers between the Cu^{II} ions to give a double layer architecture with hexagonal nanopores occupied by H_2O solvent molecules, whereas the MV^{2+} cations are located in the intralayer cavities. This framework exhibits long-range ferromagnetic order with T_C = 19.0 K owing to weak dipolar and/or through-bond ferromagnetic interactions between adjacent ferrimagnetic double layers, likely through hydrogen-bonded lattice H_2O molecules. Furthermore, this compound displays a reversible dehydration to an amorphous phase that shows shape-selective adsorption behavior and guest-induced luminescence.

8.3.4.3 3D Frameworks

This metalloligand design strategy has also afforded unique multifunctional oxamate-based bimetallic 3D MOFs.[287] For instance, the compound $[Na(H_2O)_4]_4[Mn^{II}_4(Cu^{II}_2(mpba)_2(H_2O)_4)_3]\cdot 56.5H_2O$ ($mpba^{4-}$ = *N*,*N*′-1,3-phenylenebis(oxamate)) features oxamato-bridged $Mn^{II}_4Cu^{II}_6$ layers interconnected through 1,3-phenylenediamidate spacers at the Cu^{II} centers to give a 3D structure with square and octagonal pores.[291] The large octagonal pores (21 × 30 $Å^2$) host solvated Na^+ ions and arrays of hydrogen-bonded H_2O molecules. This framework undergoes a reversible dehydration to an amorphous phase, in analogy to the 2D framework described above, with associated changes in magnetic behavior. The hydrated crystalline framework orders as a ferromagnet with T_C = 22.5 K, while the amorphous anhydrous

framework shows an onset of long-range ferromagnetic order below 2.3 K. The dramatic reduction in magnetic ordering temperature upon dehydration has been attributed to a change in the coordination environment at the Cu^{II} centers, from six- to four-coordinate Cu^{II}, leading to weaker intra- and interlayer interactions for the dehydrated framework. The isoreticular framework $[Na(H_2O)_{3.25}]_4[Mn^{II}_4(Cu^{II}_2(Me_3mpba)_2(H_2O)_{3.33})_3]\cdot 37H_2O$ (Me_3mpba^{4-} = 2,4,6-trimethyl-*N*,*N*′-1,3-phenylenebis(oxamate)), featuring a trimethyl-substituted 1,3-phenylenediamidate cyclophane linker, exhibits a similar structure and guest-dependent magnetic properties (see Figure 8.25).[292] The hydrated framework orders as a ferromagnet with T_C = 21.0 K, whereas the anhydrous derivative exhibits a dramatic solvent-dependent modulation of T_c. While the anhydrous framework itself is amorphous with T_c < 2.0 K, the MeOH adsorbate is crystalline and isostructural to the hydrated framework based on PXRD analysis, and orders as a ferromagnet below T_C = 6.5 K (see Figure 8.25, bottom). The coexistence of selective vapor (MeOH over MeCN and EtOH) and gas (CO_2 over CH_4) adsorption behavior, in conjunction with solvent-dependent changes in the magnetic ordering temperature for this framework makes it an attractive candidate for magnetic sensing of small guest molecules.

Furthermore, incorporation of the mononuclear Fe^{III} complex $[Fe^{III}(sal_2\text{-trien})]^+$ ($(sal_2\text{-trien})^{2-}$ = *N*,*N*′-disalicylidenetriethylenetetramine dianion) into the pores of the hydrated 3D framework in a single-crystal-to-single-crystal process afforded the hybrid material $[Fe^{III}(sal_2\text{-trien})]Na_3[Mn^{II}_4(Cu^{II}_2(Me_3mpba)_2)_3]\cdot 43H_2O$, which exhibits both long-range magnetic order and spin-crossover behavior.[293] Specifically, the Na^+ counterions are partially replaced by $[Fe^{III}(sal_2\text{-trien})]^+$ ions, which undergo a transition from an $S = {}^5/_2$ high-spin state to an S = ½ low-spin state upon decreasing the temperature from 400 to 100 K. Interestingly, no spin state change was

observed for the Fe^{III} precursor salt within this temperature range. Moreover, the magnetic ordering temperature for the framework was shown to increase from 14 to 19 K upon insertion of the spin-crossover complex, suggesting significant interactions between the two magnetic units. Note that the authors did not comment on the lower value of T_C obtained for the unmodified 3D framework relative to that initially reported (T_C = 14 K vs T_C = 21 K).[292,293] However, they pointed out that an aqueous suspension of the compound affords a value of T_C = 19 K. As such, it is possible that this discrepancy originates from the different sample preparation for magnetic measurements.

Along similar lines, the single-molecule magnet $[Mn^{III}(TPP)(H_2O)]^+$ (TPP^{2-} = *meso*-tetraphenylporphyrinato) was successfully incorporated into the

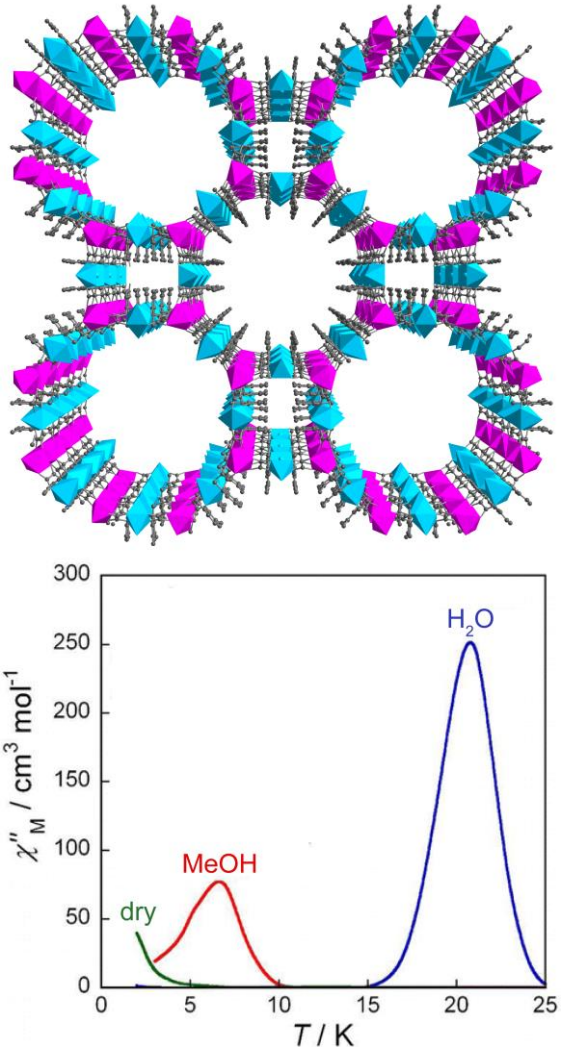

Figure 8.25 Top: Crystal structure of $[Mn^{II}_4(Cu^{II}_2(Me_3mpba)_2(H_2O)_{3.33})_3]^{4-}$, as observed in $[Na(H_2O)_{3.25}]_4[Mn^{II}_4(Cu^{II}_2(Me_3mpba)_2(H_2O)_{3.33})_3]\cdot 37H_2O$, as viewed along the crystallographic *c* axis, highlighting the square and octagonal pores. Cyan polyhedra represent $Cu^{II}N_2O_3$ and $Cu^{II}N_2O_4$ units, and magenta octahedra and gray spheres represent $Mn^{II}O_6$ units and C atoms, respectively; H atoms are omitted for clarity. Bottom: Variable-temperature out-of-phase (χ_M'') ac magnetic susceptibility data for $[Na(H_2O)_{3.25}]_4[Mn^{II}_4(Cu^{II}_2(Me_3mpba)_2(H_2O)_{3.33})_3]\cdot 37H_2O$ (blue), $[Na(H_2O)_{3.25}]_4[Mn^{II}_4(Cu^{II}_2(Me_3mpba)_2(H_2O)_{3.33})_3]\cdot 37MeOH$ (red), and $[Na(H_2O)_{3.25}]_4[Mn^{II}_4(Cu^{II}_2(Me_3mpba)_2(H_2O)_{3.33})_3]$ (green), collected under zero applied dc field at 1000 Hz frequency. Reprinted with permission from ref. 292. Copyright 2012 American Chemical Society.

pores of this 3D MOF magnet to afford a hybrid material with coexisting long-range magnetic order and slow magnetic relaxation.[294] Specifically, the magnetic lattice slowed down the quantum tunneling processes for the single-ion magnet such that slow magnetic relaxation was observed below 5 K in the absence of an applied dc field, in contrast to the behavior observed for $[Mn^{III}(TPP)(H_2O)](ClO_4)$. These two materials have enabled detailed studies of the interplay between magnetic host frameworks and magnetic molecular guests, adding to the extensive work in this area for oxalate-based frameworks.

The triple-stranded hexakis-bidentate complex $[M^{II}_2(mpba)_3]^{8-}$ (M^{II} = Ni^{II}, Co^{II}; $mpba^{4-}$ = *N*,*N*′-1,3-phenylenebis(oxamate)) represents another dinuclear metalloligand that can provide 3D frameworks. This building unit facilitates the formation of structures with honeycomb topology, however, it has thus far not afforded crystalline frameworks exhibiting long-range magnetic order.[295,296] Either amorphous compounds that display long-range ferromagnetic order, such as $Li_2[Mn^{II}_3Co^{II}_2(mpba)_3(H_2O)_6]\cdot 22H_2O$ (T_C = 6.5 K),[295] or crystalline materials that only show weak magnetic interactions have been reported. In contrast, dianionic mononuclear Cu^{II} complexes have been employed as bis-bidentate metalloligands toward solvated Mn^{2+} cations to afford crystalline oxamate frameworks that exhibit long-range magnetic order.[297]

Here, the dimensionality of oxamato-bridged heterobimetallic $Mn^{II}_2Cu^{II}_3$ frameworks can be controlled by varying the steric effects of alkyl substituents on *N*-phenyloxamato bridging ligands. To illustrate, the employment of Me_2pma^{2-} (*N*-2,6-dimethylphenyloxamate) as a bridging ligand afforded a 2D honeycomb framework of formula $(Bu_4N)_4[Mn^{II}_4Cu^{II}_6(Me_2pma)_{12}(DMSO)_2]\cdot 8DMSO\cdot 2H_2O$. However, replacing the Me groups on the oxamato ligand with slightly bulkier Et groups gave the compound

$(Bu_4N)_4[Mn^{II}_4Cu^{II}_6(Et_2pma)_{12}]\cdot DMSO\cdot 10H_2O$ (Et_2pma^{2-} = *N*-2,6-diethylphenyloxamate), which is a 3D decagonal network. Moderate antiferromagnetic intramolecular interactions between Cu^{II} and Mn^{II} ions were observed for both frameworks. However, while the 2D framework undergoes paramagnetic-to-ferromagnetic phase transition at T_C = 10 K, the 3D framework orders as a soft ferrimagnet at 20 K. The significantly different magnetic properties for the two frameworks are attributed to their different dimensionalities, as the coordination environments of the metal centers are very similar in these compounds.

8.3.5 Carboxylate-Containing Compounds

8.3.5.1 Introduction

After metal oxalates, carboxylate-based frameworks constitute the largest class of MOF magnets (see Tables 8.1 and 8.2). Some of these frameworks feature exclusively carboxylato ligands, while others have inorganic or organic coligands. Furthermore, the carboxylato linkers can be functionalized with OH, SH, and NH_2 groups that may participate in connecting metal-based nodes and thus affect the structures and properties of the materials. The highly versatile coordination modes of the carboxylate group are summarized in Figure 8.5. In addition to interacting with metal centers through ionic bonding, the carboxylate group can act as a monodentate and bidentate ligand toward a single metal ion, as well as link two or more metal centers through a number of bridging modes. Moreover, the presence of two or more carboxylate groups within the same molecule enables additional types of linkages between metal centers.

Owing to the myriad structures and versatile metal-binding modes of these ligands (see Figure 8.9), carboxylate-based frameworks exhibit a vast number of topologies and multiple types of magnetic exchange pathways. Specifically, the compounds discussed in this section display

structures with connectivities affording subnetworks of inorganic chains (I^1O^1, I^1O^2) and layers (I^2O^1), or exclusively inorganic (I^2O^0, I^3O^0) or organic networks (I^0O^2, I^0O^3), where carboxylato ligands are the primary organic moieties mediating magnetic exchange interactions. The magnitude and sign of magnetic exchange in these systems is highly affected by the type of bridge between metal centers, bridging angle, metal–metal distance, and the number of metal-based d electrons.[1] The strongest interactions are typically observed through monoatomic M–O–M bridges, followed by three-atom *syn–syn* and *anti–anti* M–O–C–O–M pathways.[298–304]

8.3.5.2 Malonate Compounds

Malonate, with a methylene group separating two carboxylate functionalities, is the shortest dicarboxylato ligand besides oxalate and has been employed to construct magnets with ordering temperatures falling in the range T_c = 2.6–24 K.[302,305,306] For instance, a series of isostructural 2D framework compounds of the formula $Na_2[M^{II}(mal)_2]\cdot 2H_2O$ (M^{II} = Mn^{II}, Fe^{II}, Co^{II}, Ni^{II}; mal^{2-} = malonate) order antiferromagnetically in different magnetic structures depending on the nature of the metal center.[305] These compounds are comprised of layers of slightly distorted $M^{II}O_6$ octahedra that are linked by *anti–anti* O–C–O carboxylate bridges, with Na^+ ions and H_2O molecules located in the interlayer space. The ordering temperature for this family of compounds ranges from T_N = 8 K for M^{II} = Mn^{II} to T_N = 24 K for the Ni^{II} congener, as confirmed by neutron diffraction studies. Furhermore, the Fe^{II} and Ni^{II} frameworks exhibit open magnetic hysteresis loops at 5 K with a remanent magnetization of M_r = 0.26 and 0.014 $\mu_B\,mol^{-1}$, respectively, owing to slight canting of the magnetic moments.

In addition to this family of 2D malonate frameworks, two 3D malonato-bridged Cu^{II} compounds, $Cu^{II}(mal)(DMF)$ and $Cu^{II}_2(mal)_2(pyz)\cdot 2H_2O$ (mal^{2-} = malonate; pyz = pyrazine),

exhibit long-range magnetic order, albeit with lower ordering temperatures of T_c = 2.6 and 3.2 K, respectively.[302,306] Ferromagnetic interactions through *syn–anti* O–C–O bridges are dominant for Cu^{II}(mal)(DMF),[302] whereas antiferromagnetic interactions through *syn–anti* carboxylate bridges and pyrazine ligands lead to an antiferromagnetic ground state for $Cu^{II}_2(mal)_2(pyz)\cdot 2H_2O$ in low magnetic fields.[306]

8.3.5.3 Succinate Compounds

Magnets featuring derivatives of the succinate molecule, which has an ethylene group separating the two carboxylate groups, are more common than those based on malonate. Many of these compounds feature both succinato and hydroxo ligands, such as the 2D frameworks $Co^{II}_3(OH)_2$(2,2-dmsucc)$_2$ (2,2-dmsucc^{2-} = 2,2-dimethylsuccinate), $Co^{II}_4(OH)_2(succ)_3(H_2O)_2\cdot 2H_2O$ (MIL-16), and $Ni^{II}_7(OH)_6(succ)_4(H_2O)_3\cdot 7H_2O$ (succ^{2-} = succinate) (MIL-73), and the 3D Co^{II}-based framework $Co^{II}_5(OH)_2(succ)_4$ (MIL-9).[307–310] Note, however, that these compounds do not strictly fall within this definition of a MOF, as the magnetic exchange interactions are governed by M^{II}–O–M^{II} superexchange paths in hydroxo-bridged chains or layers of $M^{II}O_x$ (M^{II} = Co^{II}, Ni^{II}; x = 4, 6) polyhedra, where the succinato ligands only contribute significantly to bonding in at most one dimension. Nevertheless, these networks order as ferrimagnets or antiferromagnets with ordering temperatures of T_c = 10–20 K.[307–310]

The homoleptic compound Mn^{II}(succ) (succ^{2-} = succinate) features a unique 3D structure and magnetic properties.[311,312] The structure consists of alternating layers containing chains of edge-sharing $Mn^{II}O_6$ octahedra and layers of corner-sharing $Mn^{II}O_6$ octahedra. The two types of layers are connected through succinate-based carboxylate groups with an interlayer separation of ca. 7.5 Å (see Figure 8.26). Interestingly, this framework features two magnetic structures. Specifically,

the chains of edge-sharing $Mn^{II}O_6$ octahedra order antiferromagnetically at 10 K, where $Mn^{II}O_6$ octahedra in individual chains are ferromagnetically coupled. At 6 K, the layers of corner-sharing $Mn^{II}O_6$ octahedra order antiferromagnetically, and the lower ordering temperature for these layers is consistent with their longer nearest-neighbor superexchange pathway (see Figure 8.26, bottom). Notably, the magnetic orders of the two distinct layers are essentially independent of each other. The two antiferromagnetic phases undergo further transitions under high applied dc fields, demonstrating the complex magnetic behavior of this succinate-based framework.

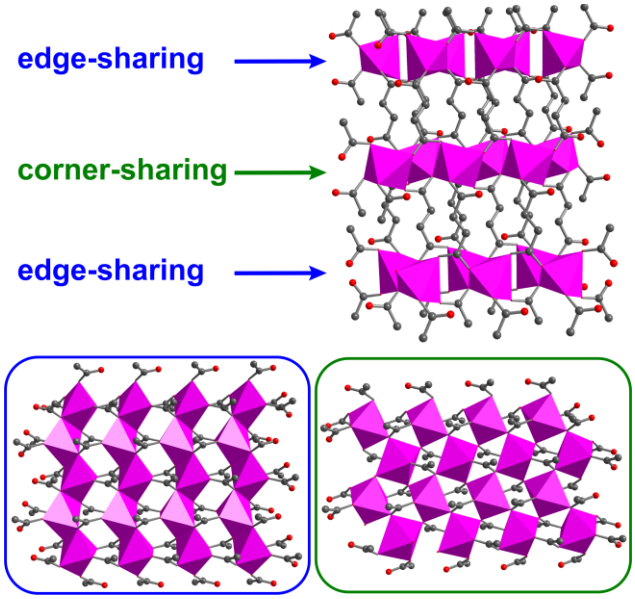

Figure 8.26 Crystal structure of Mn^{II}(succ), as viewed along the crystallographic *c* (top) and *a* axis (bottom), highlighting the alternating edge-sharing and corner-sharing layers of $Mn^{II}O_6$ octahedra in blue and green, respectively. Magenta octahedra represent $Mn^{II}O_6$ units, whereas red and gray spheres represent O and C atoms, respectively; H atoms are omitted for clarity.

While frameworks featuring the 2,2-dimethylsuccinato ligand favor 2D layered structures,[307,313] frameworks incorporating 2,3-dimethylsuccinate can either form 2D or 3D structures depending on the choice of isomer for the succinato ligand.[314] For instance, the chiral isomers (*D* and *L*) prefer an arrangement with the methyl and carboxylate groups *gauche* to the neighboring functional groups of the same type, favoring the formation of layered structures, whereas the *meso*-ligand prefers to adopt *trans* geometry, which reduces the steric hindrance and favors 3D structures (see Figure 8.27, top). Only frameworks containing the *meso*-ligand exhibit long-range magnetic order.[314] The 3D framework Mn^{II}(*meso*-2,3-dmsucc) (*meso*-2,3-dmsucc^{2-} =

meso-2,3-dimethylsuccinate) orders as a low-dimensional antiferromagnet with T_N = 50 K, as determined by the broad feature observed in a plot of χ_M vs *T*. Similar behavior was observed for 2D frameworks based on 2,2-dimethylsuccinate, albeit those compounds display much lower ordering temperatures.[307,313] The significantly higher value of T_N for Mn^{II}(*meso*-2,3-dmsucc) suggests that stronger magnetic exchange is achieved between edge-sharing $Mn^{II}O_6$ octahedra (see Figure 8.27, top and center) than corner-sharing octahedra. Furthermore, the degree of corrugation plays a critical role in determining the strength of magnetic interactions in these frameworks. For instance, the analogous hydrated compound Mn^{II}(*meso*-2,3-dmsucc)(H_2O)·H_2O exhibits a 3D structure with chains of edge- and corner-sharing $Mn^{II}O_6$ octahedra that are more corrugated than the edge-sharing chains in the structure for Mn^{II}(*meso*-2,3-dmsucc) (see Figure 8.27, bottom), and this compound orders as a 3D antiferromagnet with T_N = 7 K.[314] The higher magnetic dimensionality and lower ordering temperature for the hydrated framework suggests weaker intrachain but stronger interchain interactions compared to the anhydrous compound.

The isostructural Co^{II} congener of the anhydrous Mn^{II} framework further illustrates the weak interchain interactions in these succinate-based frameworks. This compound exhibits 3D antiferromagnetic order with T_N = 6 K in low magnetic fields, but undergoes a transition to a ferromagnetic-like state under applied fields above 1400 Oe.[314] Note that the ferromagnetic state arises from ferromagnetic nearest-neighbor interactions, consistent with the Goodenough-Kanamori rules for d^7 metal centers and a Co^{II}–O–Co^{II} superexchange angle of 86.00(7)°.[298,299] In contrast, the intrachain interactions are antiferromagnetic for the Mn^{II} frameworks.

One of the first reported transition metal frameworks with mixed linear dicarboxylato ligands is the compound $Co^{II}_6(OH)_2(succ)_4(adip)(H_2O)_4·5H_2O$ ($succ^{2-}$ = succinate; $adip^{2-}$ = adipate),

which features succinato, adipato, and hydroxo bridging ligands.[315] As the other hydroxo-containing succinate frameworks discussed in this section, this network represents a borderline case of a MOF. Hydroxo- and succinato-ligands provide intralayer connectivity, while the adipato ligands link adjacent layers together. This compound exhibits significant spin frustration, as assessed by a comparison between the Weiss constant (θ = −34.9 K for data above 40 K) and the magnetic ordering temperature (T_N = 2.2 K), affording a value of $f = |\theta|/T_N \approx 16$. In contrast, the 2D Mn^{II} framework $Mn^{II}_2(succ)(adip)(H_2O)_4 \cdot 2H_2O$ features no Mn^{II}–O–Mn^{II} connectivity.[315] Rather, the structure is comprised of distorted $Mn^{II}O_6$ octahedra that are arranged into dimers, which are connected via O–C–O carboxylate bridges from succinate ions in one direction and adipato ligands in a second direction. Despite the lack of an inorganic subnetwork, this

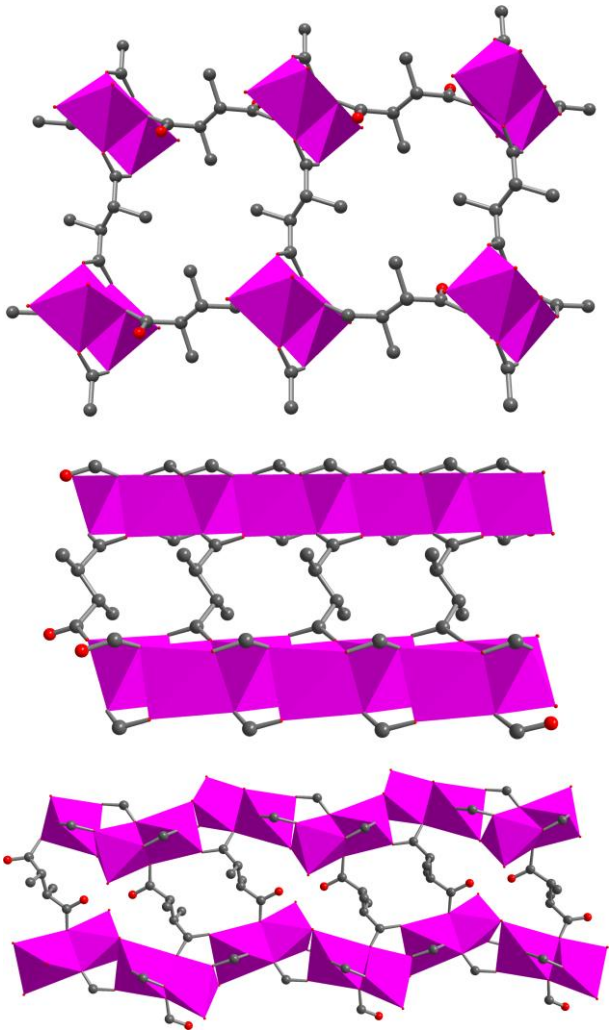

Figure 8.27 Crystal structure of Mn^{II}(*meso*-2,3-dmsucc), as viewed along the crystallographic *c* (top) and *b* axis (center), highlighting the *trans* geometry for the *meso*-2,3-dmsucc^{2-} ligand and the relatively flat edge-sharing layers, respectively. Bottom: Crystal structure of Mn^{II}(*meso*-2,3-dmsucc)$(H_2O)\cdot H_2O$, as viewed along the crystallographic *a* axis, highlighting the corrugated layers of edge- and corner-sharing $Mn^{II}O_6$ octahedra. Magenta octahedra represent $Mn^{II}O_6$ units, whereas red and gray spheres represent O and C atoms, respectively; H atoms and solvent molecules are omitted for clarity.

compound exhibits long-range antiferromagnetic order with a similar ordering temperature of T_N = 2.1 K. In sum, frameworks featuring a mixture of succinato and adipato bridging ligands possess significantly different architectures than those that only contain one of these ligands. Accordingly, the magnetic properties are drastically different for these families of compounds.

8.3.5.4 Glutarate Compounds

Two glutarate-bridged frameworks have been reported to exhibit permanent magnetic behavior.[316,317] The compound $Ni^{II}_{20}(glu)_{20}(H_2O)_8 \cdot 40H_2O$ (glu^{2-} = glutarate) (MIL-77) is a 3D inorganic framework built up from edge-sharing $Ni^{II}O_6$ octahedra bridged by glutarato and aquo ligands.[316] The $Ni^{II}O_6$ octahedra are connected into corrugated twenty-membered rings (see Figure 8.28, top) that intersect each other to generate crossing channels, which are occupied by the organic backbone of glutarato ligands along with H_2O lattice molecules. Upon heating, the lattice H_2O molecules can be reversibly removed without significant structural changes, affording a porous structure with a Brunauer–Emmett–Teller (BET) surface area of 346(10) $m^2\ g^{-1}$. This framework behaves as a ferromagnet below 4 K. Such ferromagnetic exchange interactions are in accord with edge-sharing $Ni^{II}O_6$ octahedra, and the low value of T_C for this compound was explained by the significant deviations of the Ni^{II}–O–Ni^{II} superexchange angles (97.1(4)–99.9(4)°) from the ideal 90° angle.[298,299]

The other glutarate-based framework magnet is $Co^{II}(glu)$ (glu^{2-} = glutarate). This 3D framework features exclusively three-atom *syn–anti* O–C–O carboxylate bridges between tetrahedral $Co^{II}O_4$ units.[317] The structure displays pseudo-2D square layers that are linked through the alkyl chains of glutarate (see Figure 8.28, bottom). One noticeable feature of the structure is that the glutarato ligands possess two different conformations, *gauche* and *anti* forms. This

framework displays long-range antiferromagnetic order with T_N = 14 K, where the dominant pathway for magnetic interactions is through the Co^{II}–O–C–O–Co^{II} linkages within the square-grid layers.

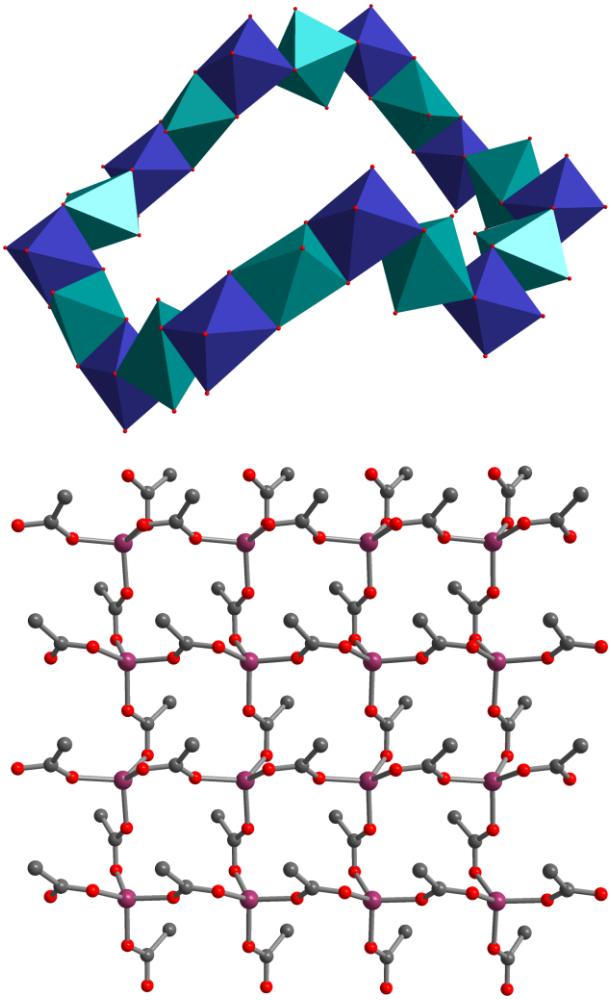

Figure 8.28 Top: Crystal structure of the corrugated twenty-membered ring in $Ni^{II}_{20}(glu)_{20}(H_2O)_8 \cdot 40H_2O$, comprised of two distinct $Ni^{II}O_6$ octahedra represented in indigo and teal. Bottom: Crystal structure of $Co^{II}(glu)$, as viewed along the crystallographic *c* axis, highlighting the square-grid layers with *syn–anti* O–C–O carboxylate bridges between $Co^{II}O_4$ tetrahedra. Purple, red, and gray spheres represent Co, O, and C atoms, respectively; H atoms and selected C atoms are omitted for clarity.

8.3.5.5 Adipate, Pimelate, and Sebacate-Compounds

Several frameworks featuring dicarboxylates with longer linear alkyl chains have been found to order magnetically below 20 K.[315,318–320] The compounds Co^{II}(adip) ($adip^{2-}$ = adipate)[315,318] and Co^{II}(pim) (pim^{2-} = pimelate)[319] (MIL-36) display analogous 3D structures as Co^{II}(glu) (glu^{2-} = glutarate), with layers of carboxylato-bridged $Co^{II}O_4$ tetrahedra that are linked through the alkyl chains of the carboxylato ligands along the third direction. The carboxylate groups on either end of the adipato ligand adopt a *syn* configuration, while those of the pimelato ligand possess an *anti* configuration. This is in contrast to the mixture of *anti* and *gauche* conformations found in the glutarate-based framework. The Co^{II}(adip) framework orders antiferromagnetically below 10 K,[318] whereas Co^{II}(pim) exhibits

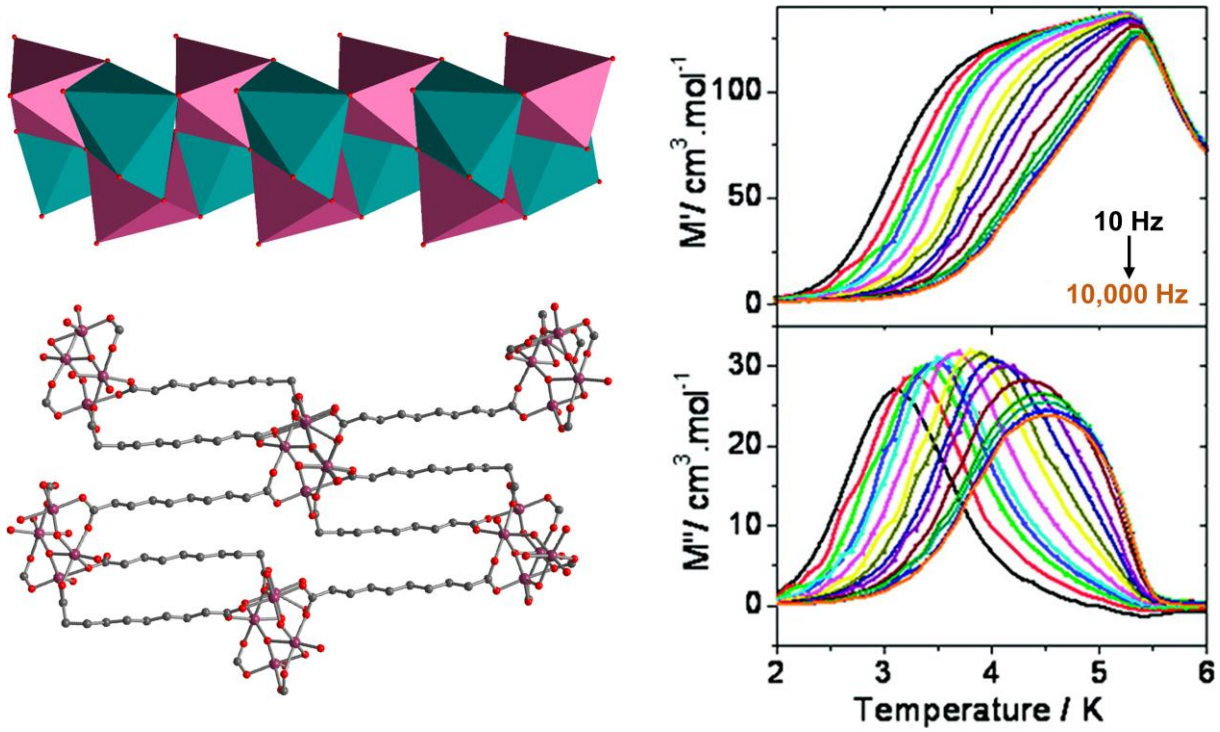

Figure 8.29 Left: Crystal structure of $Co^{II}_4(OH)_2(seba)_3$, as viewed along the crystallographic *c* (top) and *b* axis (bottom), highlighting the structure of the inorganic chains with $Co^{II}O_5$ and $Co^{II}O_6$ polyhedra represented in teal and purple (top), respectively, and the connectivity between chains (bottom). Purple, red, and gray spheres represent Co, O, and C atoms, respectively; H atoms are omitted for clarity. Right: Variable-temperature ac magnetization data for $Co^{II}_4(OH)_2(seba)_3$, collected under zero applied dc field at frequencies from 10 to 10,000 Hz (black to orange). Reprinted with permission from ref. 320. Copyright 2012 American Chemical Society.

canted antiferromagnet order with T_N = 20 K. Indeed, the latter compound displays an open magnetic hysteresis loop at 4.2 K, indicative of a weak ferromagnetism that is consistent with a canted spin structure.[319]

The 3D framework $Co^{II}_4(OH)_2(seba)_3$ ($seba^{2-}$ = sebacate) is comprised of inorganic chains that are linked by sebacato ligands through linear alkyl chains of ten carbon atoms.[320] The inorganic chains are made up of $Co^{II}O_x$ (x = 5, 6) polyhedra that are connected by carboxylato O atoms and μ_3-OH ligands (see Figure 8.29, top left). The magnetic properties for this framework are dominated by intrachain Co^{II}–O–Co^{II} superexchange interactions, as the intrachain $Co^{II}\cdots Co^{II}$

distances of 3.040–3.857 Å are much shorter than the interchain distances that range from 11.44 to 20.77 Å (see Figure 8.29, bottom left). Specifically, this compound exhibits both 3D long-range canted antiferromagnetic order and slow magnetic relaxation below 5.4 K. The canted antiferromagnetic order was postulated to be the result of uncompensated antiferromagnetic interactions within the Co^{II} chains, whereas the slow dynamic behavior under zero applied dc field was hypothesized to stem from domain-wall motion (see Figure 8.29, right). A fit of the Arrhenius plot of relaxation time for the frequency range 10–5000 Hz afforded a relaxation barrier of Δ_τ = 47(1) cm^{-1} and a pre-exponential factor of $\tau_0 = 1.4 \times 10^{-11}$ s, consistent with values reported for single-chain magnets.[126] As such, the unique magnetic properties for $Co^{II}_4(OH)_2(seba)_3$ arise from the combination of strong magnetic interactions within the 1D inorganic subnetwork and poor magnetic communication through the long sebacato ligands, highlighting that the length of the dicarboxylato bridging ligands plays an important role in determining magnetic behavior for this class of compounds.

8.3.5.6 Carboxylates with Additional Functional Groups

Several magnets have been reported that feature carboxylato ligands with additional functional groups, including NH_2, OH, and SH.[304,321–326] One such compound is Co^{II}_2(*L*-asp)$_2$(4,4′-bpy)·1.5H_2O (*L*-asp^{2-} = *L*-aspartate; 4,4′-bpy = 4,4′-bipyridine),[321] a 3D chiral framework comprised of corrugated square-grid layers of Co^{II} ions connected via O–C–O bridges of aspartato ligands. Each Co^{II} center resides in a distorted octahedral coordination environment, with the axial positions occupied by one aspartate N atom and one N atom from 4,4′-bipyridine, which link adjacent layers. The lattice H_2O molecules can be removed without altering the structure to create a porous network that exhibits a relatively high affinity toward H_2 molecules but is unable to adsorb

N_2. This discrepancy was ascribed to the small pores in the framework. The hydrated framework exhibits spontaneous weak magnetization below 14 K, which was ascribed to 3D long-range canted antiferromagnetic order. This interpretation was supported by a negative Weiss constant of $\theta = -7.68$ K (from data between 25 and 300 K), indicating overall antiferromagnetic interactions between Co^{II} centers. Furthermore, spin-canted weak ferromagnetism is frequently observed for non-centrosymmetric structures featuring aniosotropic Co^{II} ions.[210,327]

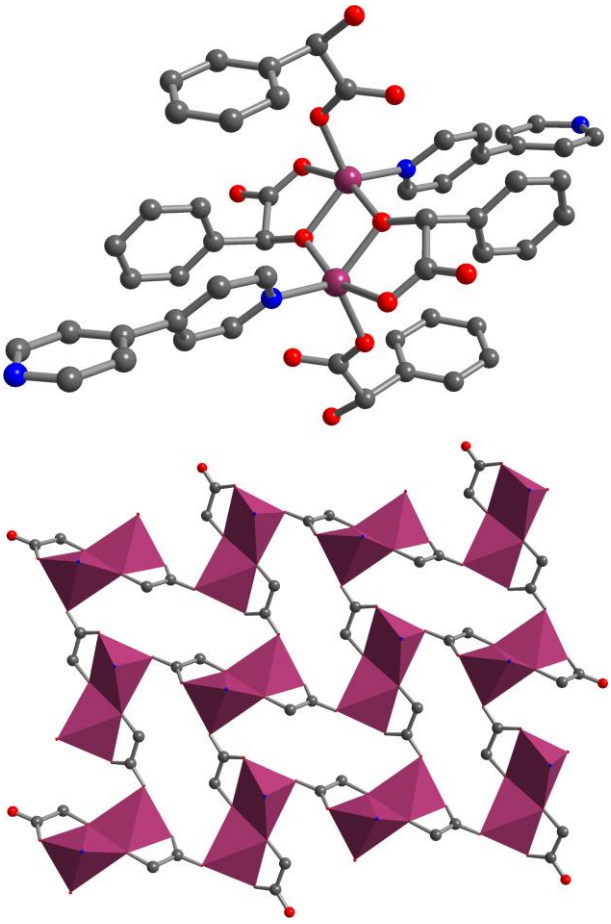

Figure 8.30 Crystal structure of $Co^{II}_2(hypa)_2(4,4'\text{-bpy})\cdot 1.5H_2O$, highlighting the dimeric Co^{II}_2 subunit (top) and the acetato-bridged layer viewed along the crystallographic *a* axis (bottom). Purple polyhedra represent $Co^{II}NO_4$ units. Purple, red, blue, and gray spheres represent Co, O, N, and C atoms, respectively; H atoms and solvent molecules are omitted for clarity.

Another framework that is comprised of carboxylato-bridged layers that are connected by 4,4′-bipyridine ligands is the compound $Co^{II}_2(hypa)_2(4,4'\text{-bpy})\cdot 1.5H_2O$ ($hypa^{2-}$ = 2-hydroxy-2-phenylacetate; 4,4′-bpy = 4,4′-bipyridine).[322] This 3D framework contains dimeric Co^{II} subunits, in which pentacoordinated Co^{II} ions are bridged by two alkoxy O atoms from distinct $hypa^{2-}$ ligands. The dimers are connected via *syn–anti* O–C–O carboxylate bridges into neutral layers (see Figure 8.30). This framework orders antiferromagnetically with T_N = 15.2 K. The dominant magnetic exchange pathway is

between Co^{II} ions in the dimers, and strong antiferromagnetic superexchange interactions are in accord with a Co^{II}–O^{II}–Co^{II} angle of 99.89(6)°.[298,299] Exchange interactions via the *syn–anti* O–C–O carboxylate bridges are also potentially antiferromagnetic; however, the long interlayer $Co^{II}\cdots Co^{II}$ distance of 11.191(1) Å suggests that magnetic interactions through 4,4′-bipyridine are extremely weak, thereby leading to overall 2D antiferromagnetic characteristics for this framework.

A few magnetic frameworks featuring the OH-functionalized malato ligand have been reported.[323] For instance, the compound Mn^{II}(*L*-ma)(H_2O) (*L*-ma^{2-} = *L*-malate) is a chiral 3D framework comprised of distorted $Mn^{II}O_6$ octahedra connected through O–C–O carboxylate bridges.[323] It exhibits long-range antiferromagnetic order with T_N = 3.5 K, and the curvature of *M* vs *H* data at 1.8 K suggests a spin-flop transition at high magnetic fields. Achiral frameworks with a similar 3D structure were obtained when a racemic mixture of malato ligands was used instead of the chiral *L*-malate dianion. Both the Co^{II} framework Co^{II}(*rac*-ma)(H_2O)·H_2O (*rac*-ma^{2-} = racemic mixture of *D* and *L* malate) and the isostructural Ni^{II} framework Ni^{II}(*rac*-ma)(H_2O)·H_2O exhibit ferromagnetic order with T_C = 1.63(1) and 2.7 K, respectively.[323] The occurrence of ferromagnetic interactions for the achiral frameworks is not directly obvious, but may result from slight changes in the angles between metal centers, which may affect the M^{II}–O–C–O–M^{II} exchange coupling. Note, however, that spin-canted antiferromagnetic interactions cannot be ruled out, and further experiments are needed to deduce the magnetic structure of these frameworks.

The tartrate-based frameworks M^{II}(*L*-tart) (M^{II} = Mn^{II}, Ni^{II}; *L*-$tart^{2-}$ = *L*-tartrate) constitute another series of chiral magnets.[324] These frameworks are built up from pseudo-tetragonal layers of distorted $M^{II}O_6$ octahedra bridged by *syn–anti* carboxylates. The layers are held together by the

backbone of the tartrato ligands to give overall 3D structures. Notably, the chirality of the tartrato ligand imposes all metal centers to adopt a Δ conformation. For the Mn^{II} framework, nearest-neighbor interactions within the layers are antiferromagnetic, but canting of the spins leads to a net magnetic moment. Accordingly, this compound behaves as a canted antiferromagnet below T_N = 3.3 K and exhibits a magnetic hysteresis loop with a coercive field of H_c = 450 Oe at 2 K. The Ni^{II} congener shows a more complicated magnetic behavior, exhibiting three distinct types of ordered states. In particular, it orders antiferromagnetically below T_N = 6 K in low magnetic fields, owing to antiferromagnetic coupling between ferromagnetic layers, and then undergoes a transition to a ferromagnetic-like state below 4.5 K under an applied field above 3000 Oe. This field-dependent magnetic behavior is typical for a metamagnet. In addition, an unusual second magnetic transition to a spin-canted antiferromagnetic phase occurs at lower applied fields.

In contrast to the malate- and tartrate-based frameworks discussed above, which contain dianionic carboxylato ligands with protonated hydroxyl groups, the framework Co^{II}_2(O-ma)(4-pyc)·$2H_2O$ (O-ma^{3-} = 2-oxidosuccinate; 4-pyc^- = 4-pyridinecarboxylate) features trianionic malato ligands with deprotonated hydroxyl groups.[304] This 3D framework consists of layers of distorted $Co^{II}NO_5$ octahedra and $Co^{II}O_5$ trigonal bipyramids connected by malato ligands through μ_2-alkoxy and μ_2-carboxylato O atoms (Co^{II}–O–Co^{II}) together with O–C–O carboxylate bridges. These layers are linked by 4-pyridinecarboxylato ligands to give saddle-like 1D channels (see Figure 8.31). Upon heating in vacuum at 200 °C, the lattice H_2O molecules can be removed without significant structural changes. Moreover, other guest molecules, including MeOH and $HCONH_2$, can be introduced into the framework via a single-crystal-to-single-crystal process to give isostructural compounds.

These frameworks display geometrical frustration due to multiple exchange pathways between adjacent metal centers (see Figure 8.31, top). Antiferromagnetic interactions, primarily arising from intralayer interactions, are dominant, as evidenced by negative Weiss constants (θ). Nevertheless, interlayer interactions cannot be neglected and the frameworks Co^{II}_2(O-ma)(4-pyc)·$2H_2O$, Co^{II}_2(O-ma)(4-pyc)·MeOH, and Co^{II}_2(O-ma)(4-pyc)·$HCONH_2$ order as canted antiferromagnets with T_N = 8, 3.6, and 3.6 K, respectively. Note, however, that only Co^{II}_2(O-ma)(4-pyc)·$2H_2O$ shows a clear evidence for a long-range magnetic order. Furthermore, while Co^{II}_2(O-ma)(4-pyc)·$2H_2O$ shows a weak spin glass behavior below the ordering temperature, Co^{II}_2(O-ma)(4-pyc)·MeOH and Co^{II}_2(O-ma)(4-pyc)·$HCONH_2$ exhibit metamagnetic behaviors. This discrepancy may be due to more pronounced spin frustration in the latter two compounds. Indeed, the degree of frustration in these systems, as quantified through the parameter $f = |\theta|/T_N$, increases as the guest is varied from H_2O to MeOH to $HCONH_2$, suggesting that different host–guest hydrogen bonding interactions affect geometrical frustration behavior, magnetic exchange, and spin canting in this family of magnetic

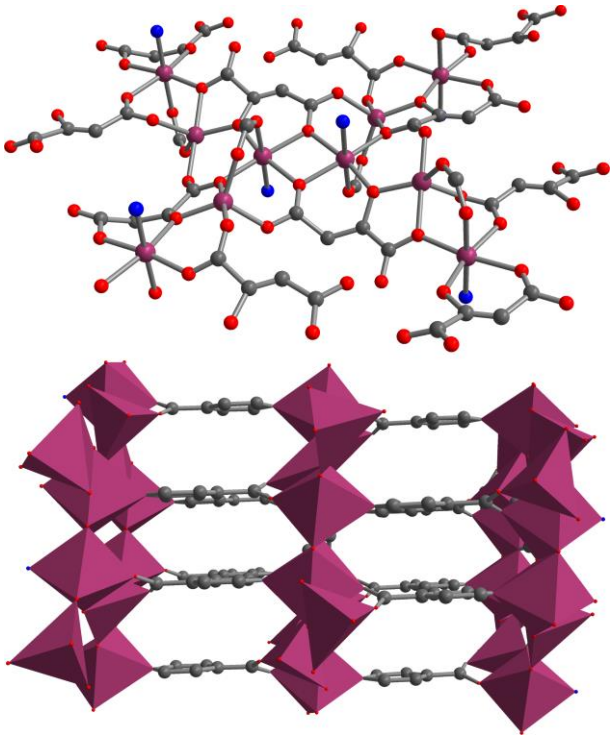

Figure 8.31 Crystal structure of Co^{II}_2(O-ma)(4-pyc)·$2H_2O$, showing the coordination environments of the Co^{II} centers (top) and the 3D connectivity along the crystallographic *b* axis (bottom). Purple polyhedra represent $Co^{II}O_5$ and $Co^{II}NO_5$ units. Purple, blue, red, and gray spheres represent Co, O, N, and C atoms, respectively; H atoms and solvent molecules are omitted for clarity.

MOFs.

An example of a framework that contains a mixture of carboxylato ligands with protonated and deprotonated hydroxyl groups is the citrate-based MOF $KCo^{II}_3(cit)(O\text{-}cit)(H_2O)_2\cdot 8H_2O$ (cit^{3-} = citrate; O-cit^{4-} = 2-oxidopropane-1,2,3-tricarboxylate).[325] This framework is built up from tetrahedral Co^{II} ions as trigonal nodes and tetranuclear Co^{II}_4 clusters as octahedral nodes to give a 3D network of (3,6)-connected anatase topology. The magnetic behavior of this framework is sensitive to applied magnetic field and is characteristic of a canted antiferromagnet with a canting angle of 28.9°. Ac susceptibility measurements revealed an onset of a frequency-dependent signal in the plot of χ_M'' vs T, but no peak was observed above 2 K, indicating a short-range order. Nevertheless, a magnet-type behavior was demonstrated by an open magnetic hysteresis loop at 2 K, with a coercive field of H_c = 20 Oe and a remanent magnetization of M_r = 92 Oe cm^3 mol^{-1}. Remarkably, the magnetic properties for this framework were largely retained after removal of the lattice H_2O molecules and the dehydrated framework was the first MOF to exhibit both microporosity and spin-canted antiferromagnetism.

8.3.5.7 Cyclic Multi-Carboxylate Compounds

Frameworks bearing cyclic multi-carboxylato ligands can also exhibit interesting magnetic properties. For instance, using camphoric acid as a bridging ligand in conjunction with 1,4-di-(1-imidazolylmethyl)benzene (1,4-dimb) afforded a series of chiral isostructural frameworks with the formula $M^{II}_2(D\text{-}ca)_2$(1,4-dimb) (M^{II} = Ni^{II} and/or Co^{II}; D-ca^{2-} = D-camphoric acid dianion) that behave as antiferromagnets or canted antiferromagnets with T_N = 8.0–19.5 K.[328] These frameworks feature dimeric paddlewheel building units that are connected into undulating (4,4) layers through carboxylato ligands, which are further linked by 1,4-di-(1-imidazolylmethyl)benzene molecules to

give non-interpenetrating 3D networks. The magnetic properties for the Ni^{II}_2 framework are most consistent with canted antiferromagnetic order below 19.5 K along with spin glass behavior, which was hypothesized to arise from metal ion disorder or defects in the crystal structure. The observed spin canting was attributed to high single-ion anisotropy and/or Dzyaloshinskii–Moriya antisymmetric exchange interaction that is symmetry-allowed due to the chirality of the structure.[213,214] Similar strong intradimer antiferromagnetic interactions are present in the Co^{II}_2 congener, however, this compound exhibits long-range antiferromagnetic order with T_N = 8 K and field-induced spin-flop behavior under an applied field above ca. 3 T. Furthermore, analogous mixed-metal frameworks demonstrated that the ordering temperature, coercive field, and remanent magnetization for this series of compounds can be tuned through metal ion modulation.[328]

The squarate dianion is another example of a cyclic dicarboxylate that can be employed to construct magnetic frameworks. The compound $Mn^{II}_2(OH)_2(squ)$ (squ^{2-} = squarate) consists of chains of hydroxo-bridged edge-sharing triangles of Mn^{II} ions in distorted octahedral geometry (see Figure 8.32, top). The chains are linked by squarate dianions into a 3D network.[329–331] This framework displays long-range antiferromagnetic order with T_N = 12.5 K, and its magnetic properties and structure have been deduced from neutron diffraction and muon spin relaxation studies.[329,330] The magnetic structure consists of two offset coparallel chains, with the spins aligned antiparallel along each chain. Systems comprised of approximately equilateral triangles are frequently subjected to spin frustration. However, no such frustration was observed for $Mn^{II}_2(OH)_2(squ)$. This surprising observation was attributed to the slight deviation from ideal equilateral symmetry, as evidenced by the variation in the Mn^{II}–O–Mn^{II} angles from 96.8(3) to 105.4(3)°.

In contrast, the 3D framework $Co^{II}_3(OH)_2(squ)_2 \cdot 3H_2O$ that consists of brucite-like ribbons formed from similar equilateral triangles (see Figure 8.32, bottom) displays complicated magnetic behavior attributed to geometrical frustration.[332–334] Notably, despite only small structural changes between the hydrated and anhydrous networks, drastic changes in magnetic properties were observed.[333,334] This discrepancy was speculated to be due to stronger antiferromagnetic interactions between the ferromagnetic ribbons in the hydrated compound, facilitated by hydrogen-bonded H_2O molecules.

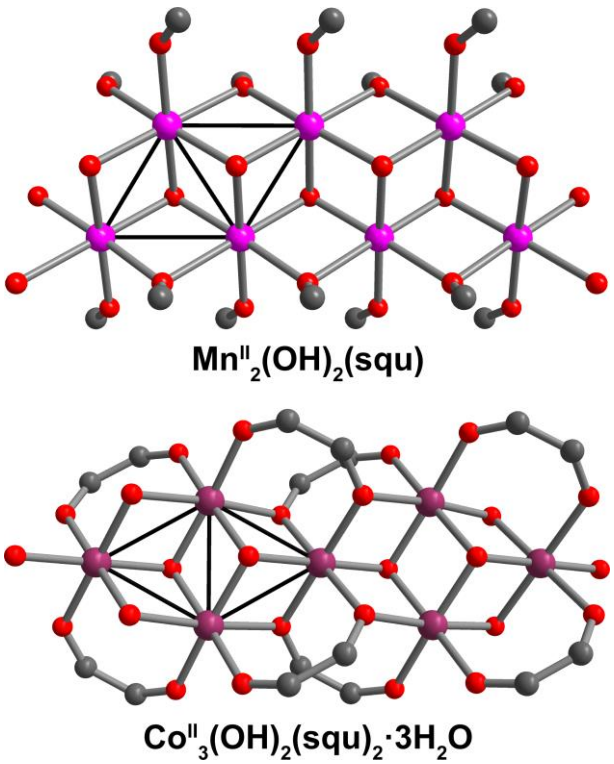

Figure 8.32 Crystal structures of $Mn^{II}_2(OH)_2(squ)$ (top) and $Co^{II}_3(OH)_2(squ)_2 \cdot 3H_2O$ (bottom), highlighting the hydroxo- and squarato-bridged chain motifs. The metal centers are arranged in an array of nearly equilateral triangles in both compounds, as illustrated with the black lines. Purple, magenta, red, and gray spheres represent Co, Mn, O, and C atoms, respectively; H atoms, the backbone of the squarato ligands, and solvent molecules are omitted for clarity.

One example of a squarate-based framework with magnetic properties that are not dominated by M–O–M superexchange interactions is the compound $Fe^{II}_3(OH)_3(squ)_{1.5}$, which features Fe^{II} ions that are bridged by squarate dianions adopting $\mu_{1,2}$ and $\mu_{1,3}$ binding modes in all three dimensions.[335] This framework orders as a canted antiferromagnet with T_N = 5.2 K, demonstrating that the squarate dianion can mediate strong magnetic interactions between metal centers even in the absence of M–O–M coupling pathways. Note, however, that the magnetic ordering temperatures for the frameworks

containing hydroxo-bridged chains are somewhat higher, in agreement with stronger interactions over shorter distances.

In addition to these dicarboxylato-bridged frameworks, one example of an analogous species with cyclobutanetetracarboxylato linkers has been reported.[336] The framework $Co^{II}_2(cbut)(H_2O)_3$ ($cbut^{4-}$ = 1,2,3,4-cyclobutanetetracarboxylate) contains chains of alternating doubly and triply bridged distorted octahedral Co^{II} ions through μ_2-carboxylato O atoms, *syn–syn* O–C–O carboxylate groups, and μ_2-H_2O molecules. These chains are linked into layers by a third type of $Co^{II}O_6$ octahedron via *syn–anti* and *anti–anti* O–C–O carboxylate bridges, and the layers are connected through the backbone of the organic ligand into a 3D structure (see Figure 8.33). The framework exhibits long-range antiferromagnetic order with T_N = 5.0 K. Furthermore, it displays metamagnetic behavior, as an application of a magnetic field greater than 1500 Oe is sufficient to overcome weak interlayer antiferromagnetic interactions and give a ferrimagnetic state. Analysis of the magnetic structure by neutron diffraction revealed that significant ferromagnetic interactions are present between Co^{II} ions within the chains, as expected for Co^{II}–O–Co^{II} exchange pathways with angles of 96.1–96.8° and *syn–syn* O–C–O carboxylate bridges.[1,298,299] The Co^{II} centers in the chains are antiferromagnetically coupled to the isolated Co^{II} ions, resulting in uncompensated ferrimagnetic layers. Weak antiferromagnetic interactions between the layers through the long cyclobutanetetracarboxylato ligands (ca. 7.0 Å) facilitate the long-range magnetic order.

8.3.5.8 Cyclohexanecarboxylate Compounds

Compounds with linkers based on a cyclohexane core comprise a related class of frameworks. These ligands exhibit greater chemical tunability and less steric strain than those bearing four- and

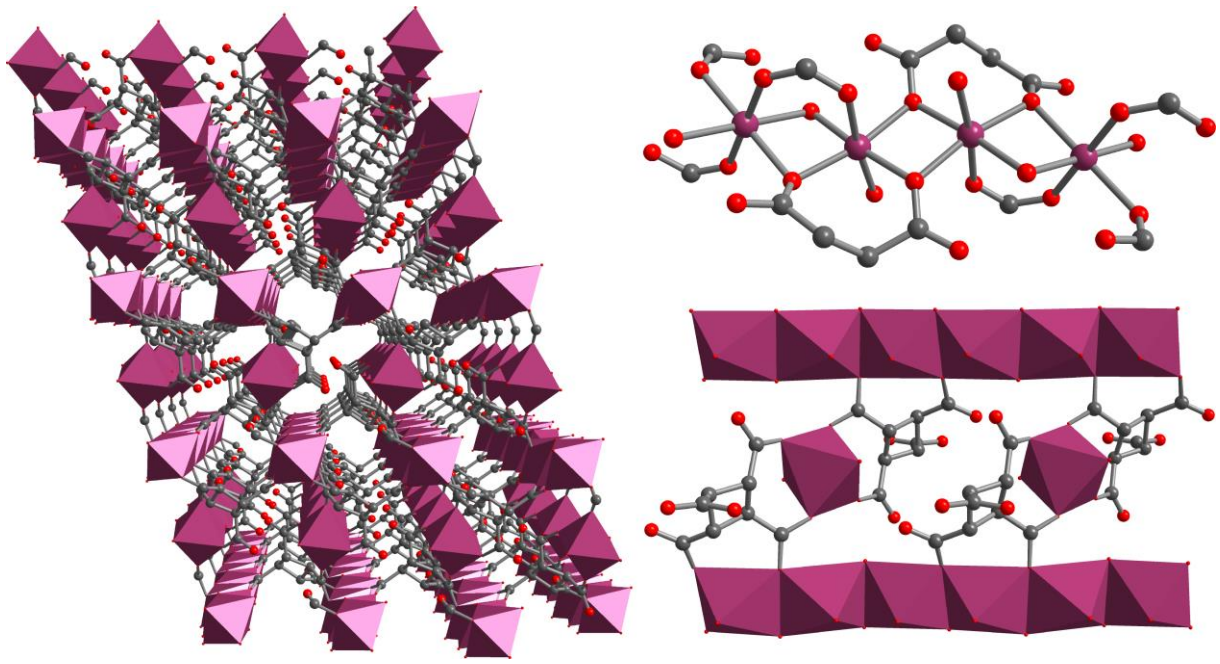

Figure 8.33 Crystal structure of $Co^{II}_2(cbut)(H_2O)_3$, as viewed along the crystallographic *b* axis (left), highlighting the structure of the chain motif (top right) and the connectivity of the chains into layers through distinct $Co^{II}O_6$ octahedra (bottom right). Purple octahedra represent $Co^{II}O_6$ units. Purple, red, and gray spheres represent Co, O, and C atoms, respectively; H atoms are omitted for clarity.

five-membered rings discussed above. Specifically, the cyclohexane core can adopt boat and chair conformations, with up to six carboxylate groups on its backbone able to coordinate metal centers in *cis* or *trans* configurations. For instance, *trans*-1,2-cyclohexanedicarboxylate (*trans*-1,2-chdc^{2-}) has been employed as a ligand to support triangular arrays of $[Co^{II}_3(\mu_3\text{-}OH)_2]^{4+}$ units featuring $Co^{II}O_4$ tetrahedra and $Co^{II}O_6$ octahedra and thus afford a Kagomé-like lattice.[337] The resulting compound $Co^{II}_3(OH)_2$(*trans*-1,2-chdc)$_2$ displays an inorganic-organic sandwich structure, with the cyclohexane rings decorating the 2D layers that are held together by weak van der Waals interactions. For the reasons outlined above for the hydroxo-succinato networks, this species represents a borderline example of a MOF. Nevertheless, it exhibits the coexistence of spin frustration ($f = |\theta/T_N| = 7.3$) and long-range spin-canted antiferromagnetic order with $T_N = 11$ K.

Distortion of the $[Co^{II}_3(\mu_3\text{-}OH)_2]^{4+}$ triangles, owing to different types of Co^{II} polyhedra and exchange pathways, was posited to weaken the spin frustration expected for an ideal Kagomé lattice system and thus lead to a canted spin structure. In addition, the occurrence of long-range order was attributed to dipolar interactions between the canted inorganic layers.

A framework of dramatically different topology was formed upon treating Ni^{II} ions with *cis*-1,4-cyclohexanedicarboxylate (*cis*-1,4-chdc^{2-}) in the presence of hydroxide ions. The resulting compound $Ni^{II}_3(OH)_2$(*cis*-1,4-chdc)$_2(H_2O)_4\cdot 2H_2O$ is made up of linear chains of pairs of edge-sharing distorted $Ni^{II}O_6$ octahedra that are connected through their apexes to distinct distorted $Ni^{II}O_6$ octahedra via μ_3-OH and carboxylate groups (see Figure 8.34, bottom).[338] The chains are further connected through *syn–syn* O–C–O bridges in a propeller blade fashion to give a 3D network with narrow channels (see Figure 8.34, top). This framework exhibits guest-dependent magnetic properties, as it can switch from a ferrimagnet with T_c = 2.1 K to a ferromagnet with T_C = 4.5 K upon partial desolvation. Powder X-ray diffraction analysis suggested subtle structural changes

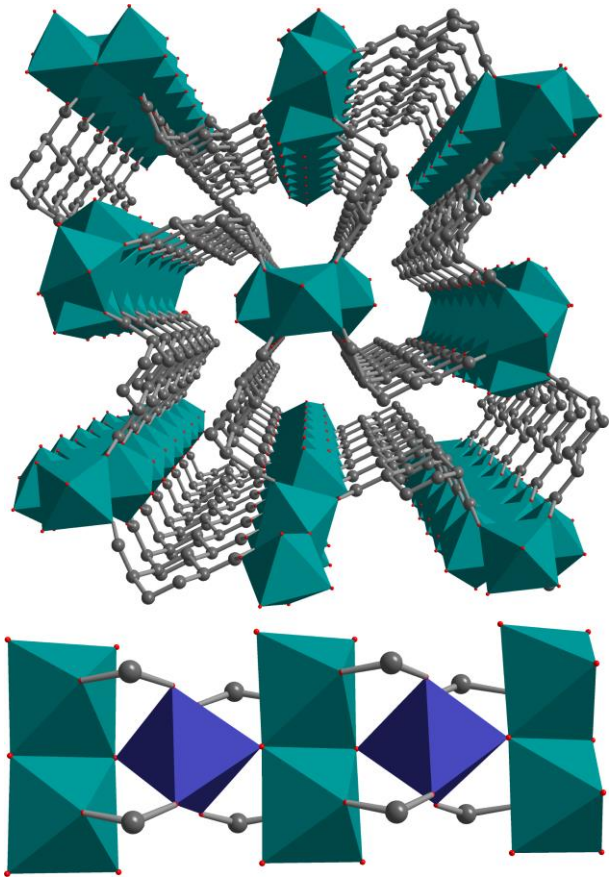

Figure 8.34 Crystal structure of $Ni^{II}_3(OH)_2$(*cis*-1,4-chdc)$_2(H_2O)_4\cdot 2H_2O$, as viewed along the crystallographic *a* axis (top), highlighting the structure of the linear chains (bottom) featuring two distinct $Ni^{II}O_6$ octahedra (teal and indigo). Red and gray spheres represent O and C atoms, respectively; H atoms and solvent molecules are omitted for clarity.

upon dehydration that are not fully reversible upon rehydration, although the magnetic properties are largely restored. The ferrimagnetic behavior of the hydrated framework was explained by ferromagnetic interactions between the edge-sharing Ni^{II} ions and weaker antiferromagnetic coupling between corner-sharing Ni^{II} centers, affording overall ferrimagnetic chains. At low temperatures, weak through-bond and/or dipolar interchain interactions were postulated to become important and afford a ferrimagnetic ordered state. Note that a framework of similar structure featuring *trans*-1,4-cyclohexanedicarboxylate (*trans*-1,4-chdc^{2-}) bridging ligands does not exhibit long-range magnetic order above 2 K. The difference in magnetic properties between the two frameworks was speculated to be due to larger cavities in the framework featuring the *trans* isomer of the ligand, resulting in weaker interchain interactions.[338]

Frameworks with related inorganic chain structures were formed when cyclohexane-based bridging ligands bearing three carboxylate groups are employed. In particular, the compound Co^{II}_3(*cis*,*cis*-1,3,5-chtc)$_2$(H_2O)$_4$·5H_2O (*cis*,*cis*-1,3,5-chtc^{3-} = *cis*,*cis*-1,3,5-cyclohexanetricarboxylate) features chains of similar trimeric structural units as the Ni^{II} framework described above, albeit the chains are arranged in a zigzag rather than linear fashion and bridged by μ_3-H_2O molecules instead of hydroxo groups.[339] The value of $\chi_M T$ for this 3D framework shows an abrupt increase below 4 K, in this case assigned to the onset of ferrimagnetic order. This behavior was attributed to antiferromagnetic interactions within the trimeric subunits, leading to an uncompensated magnetic moment within each chain.

The neutral 3D framework Co^{II}_3(chhc)(H_2O)$_6$ (chhc^{6-} = *trans*,*trans*,*trans*,*trans*,*trans*-1,2,3,4,5,6 cyclohexanehexacarboxylate) features a cyclohexanehexacarboxylato ligand with the carboxylate groups adopting a *trans* arrangement with one another.[340] The framework consists of

Co^{II} ions in an octahedral geometry that are connected by $\mu_{1,3}$-carboxylato ligands adopting a *syn–anti* bridging mode. From the viewpoint of magnetic superexchange pathways, the framework can be described as a quasi-regular 3D tetrahedral network. Magnetic studies revealed an antiferromagnetic order with T_N = 3.0 K, owing to antiferromagnetic interactions between the Co^{II} centers through the *syn–anti* carboxylate bridges. Moreover, field-dependent measurements indicated that the antiferromagnetic interactions are overcome by an external field above 1.5 T, characteristic of a metamagnetic behavior.

Finally, note that all the foregoing frameworks bearing cyclohexanecarboxylato ligands magnetically order below 12 K. These ordering temperatures are much lower than that of a porous layered Co^{II} hydroxide framework with *trans*-1,4-chdc^{2-} ligands linking the layers, which orders as a ferrimagnet with T_c = 60.5 K.[63] This comparison highlights that length, angle, type, and number of superexchange interactions all play a critical role in determining the magnetic coupling strength and thus the ordering temperature of framework materials.

8.3.5.9 Benzenecarboxylate Compounds

Benzenepolycarboxylate derivatives have been used extensively in the construction of frameworks for a vast array of applications.[341–343] These rigid organic linkers feature delocalized π electrons that can mediate relatively strong magnetic interactions despite the long distance, and have therefore been shown to promote magnetic order in a number of cases. Specifically, frameworks bearing linkers comprised of an aromatic core, such as benzene, biphenyl, and terphenyl, functionalized with two to five carboxylate groups have been shown to behave as ordered magnets (see Figure 8.9).[326,344–361] These frameworks are either homoleptic or feature additional coligands such as oxo, hydroxo, or pyridine derivatives.

The most common member of this family of ligands is 1,4-benzenedicarboxylate (1,4-bdc^{2-}). Three Mn^{II} frameworks of formulas Mn^{II}(1,4-bdc)(H_2O)$_2$,[344] Mn^{II}_2(1,4-bdc)$_2$(DMF)$_2$,[345] and Mn^{II}_3(1,4-bdc)$_3$(DEF)$_2$[345] exhibit antiferromagnetic order with T_N = 6.5, 4.2, and 4.3 K, respectively. The latter two compounds display considerable spin glass behavior, which can be attributed to strong intrachain coupling and very weak interchain interactions. This magnetic behavior can be well understood from considerations of their crystal structures. Namely, the structure of Mn^{II}_2(1,4-bdc)$_2$(DMF)$_2$ is comprised of $Mn^{II}_4O_{20}$ tetrameric building units that are linked into chains through O–C–O carboxylate bridges. These chains are then connected into a 3D network with 1D channels through the backbone of 1,4-benzenedicarboxylato ligands. The compound Mn^{II}_3(1,4-bdc)$_3$(DEF)$_2$ features a similar chain-like structure, except the chains consist of $Mn^{II}O_6$ octahedra that share both corners and edges.[345] Despite the Mn^{II}–O–Mn^{II} connectivity along the chains, which should strengthen the magnetic interactions, the magnetic ordering

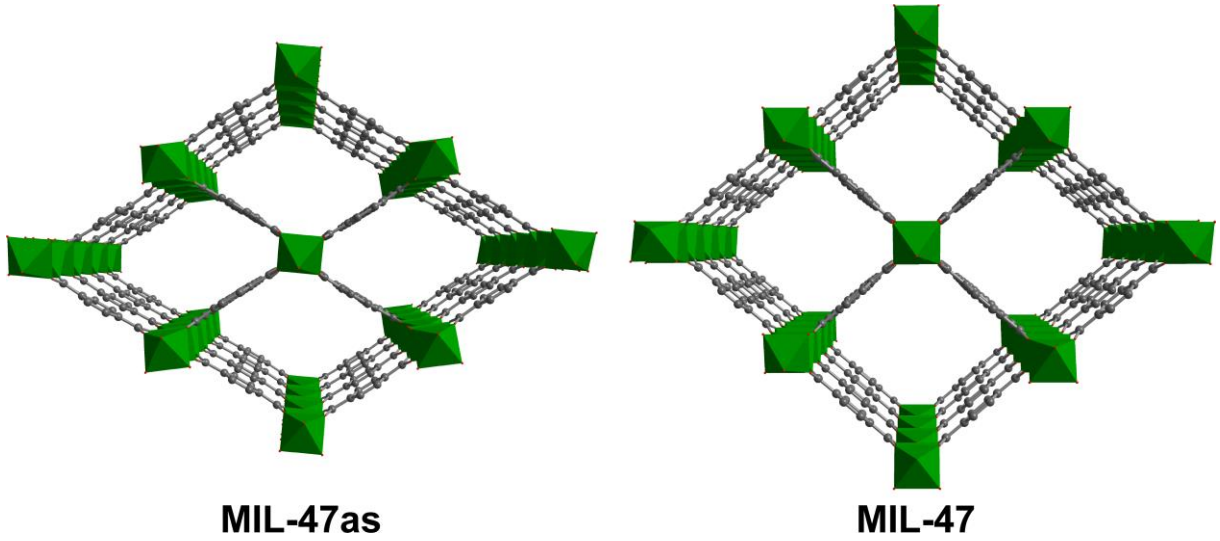

Figure 8.35 Crystal structures of V^{III}(OH)(1,4-bdc)·0.75(1.4-H_2bdc) (left; MIL-47as) and V^{IV}(O)(1,4-bdc) (right; MIL-47), as viewed along the crystallographic *b* axis, highlighting the rectangular 1D channels. Green octahedra represent VO_6 units. Red and gray spheres represent O and C atoms, respectively; H atoms and guest molecules are omitted for clarity.

temperature for this framework is nearly identical to that of $Mn^{II}_2(1,4\text{-bdc})_2(DMF)_2$. This observation strongly suggests that interchain interactions are responsible for the occurrence of long-range order in these compounds. To compare, the structure of $Mn^{II}(1,4\text{-bdc})(H_2O)_2$ is built up from layers of isolated $Mn^{II}O_6$ octahedra that are connected via O–C–O carboxylate bridges. The layers are further linked through the aromatic backbone of the dicarboxylato ligands.[344] Taken together, the low magnetic ordering temperatures for these frameworks illustrate the modest magnetic interactions mediated between Mn^{II} ions via 1,4-benzenedicarboxylato bridging ligands.

In contrast, 3D frameworks constructed from corner-sharing chains of $V^{III}O_6$ or $Cr^{III}O_6$ octahedra that are linked via O–C–O bridges through the backbone of 1,4-benzenedicarboxylato ligands display much higher ordering temperatures.[346–348] Specifically, the V^{III}-based framework $V^{III}(OH)(1,4\text{-bdc})\cdot 0.75(1.4\text{-}H_2bdc)$ (MIL-47as) features hydroxo-bridged $V^{III}O_6$ chains and orders as an antiferromagnet with T_N = 95(5) K (see Figure 8.35, left). Indeed, this compound exhibits the highest ordering temperature yet reported for a MOF with diamagnetic linkers. The large negative Weiss constant of $\theta = -186(4)$ K (for data between 180 and 300 K) suggests dominant antiferromagnetic interactions at high temperatures.[346] This is consistent with a V^{III}–O–V^{III} superexchange angle of 124.0(2)° that is far from 180°, which would favor strong ferromagnetic interactions according to the Goodenough–Kanamori rules.[298,299,362] As such, antiferromagnetic intra- and interchain interactions are anticipated. Notably, when this framework is heated to 300 °C, the terephthalic acid guest molecules are removed from the pores of the framework and oxidation of V^{III} to V^{IV} ions occurs, giving the compound $V^{IV}(O)(1,4\text{-bdc})$ (MIL-47). This framework exhibits very similar structure to MIL-47as, where the vertices in the 1D chains are oxo groups instead of hydroxo ligands (see Figure 8.35, right). Furthermore, the V–O–V

superexchange angle of 129.4° is slighty larger and the 1D channels have a more rectangular shape compared to those in MIL-47as (10.5 × 11.0 $Å^2$ for MIL-47 vs 7.9 × 12.0 $Å^2$ for MIL-47as) (see Figure 8.35). The activated framework displays permanent porosity with Brunauer–Emmett–Teller (BET) and Langmuir surface areas of 930(30) and 1320(2) $m^2\ g^{-1}$, respectively. Moreover, MIL-47 exhibits similar antiferromagnetism as MIL-47as, albeit with a lower ordering temperature of 75(5) K that was ascribed to weaker interactions between V^{IV} (d^1) ions than V^{III} (d^2) ions.[346]

The compound $Cr^{III}(OH)(1,4\text{-bdc})\cdot 0.75(1.4\text{-}H_2bdc)$ (MIL-53as) is isostructural to MIL-47as, with Cr^{III} ions replacing the V^{III} centers. This framework exhibits analogous antiferromagnetic behavior with T_N = 65 K. Removal of the terephthalic acid guest molecules is accomplished by heating at 300 °C to afford $Cr^{III}(OH)(1,4\text{-bdc})$ (MIL-53ht). This framework is highly hygroscopic and a compound of formula $Cr^{III}(OH)(1,4\text{-bdc})\cdot H_2O$ (MIL-53lt) is formed when MIL-53ht is left under ambient conditions.[347,348] All three compounds exhibit the same general 3D structure, but the pore sizes are considerably different, demonstrating the reversible breathing behavior of this framework. Notably, these Cr^{III}-based networks were the first 3D Cr^{III} dicarboxylate frameworks and the first microporous Cr^{III}-based solids (the Langmuir surface area for MIL-53ht is over 1500 $m^2\ g^{-1}$). The hydrated framework MIL-53lt shows canted antiferromagnetic behavior with T_N = 55 K. The different magnetic properties for MIL-53 and MIL-53lt was proposed to arise from the different Cr^{III}–O–Cr^{III} superexchange angles in the two structures (121.5° vs 124.8°).[348]

Compounds of formula $M^{II}_2(2,5\text{-dobdc})(H_2O)_2\cdot x$solvent ($M^{II}$ = Mg^{II}, Mn^{II}, Fe^{II}, Co^{II}, Ni^{II}, Zn^{II}; $2,5\text{-dobdc}^{4-}$ = 2,5-dioxido-1,4-benzenedicarboxylate) (MOF-74) represents a family of microporous frameworks that have been extensively studied owing to their excellent performance in gas separation applications.[363–367] These frameworks are composed of inorganic chains of edge-

sharing $M^{II}O_6$ octahedra that are connected through the backbone of 2,5-dioxido-1,4-benzenedicarboxylato ligands to give 3D networks of honeycomb topology with hexagonal 1D channels.[349,350,363–367] Both coordinating H_2O and non-coordinating solvent molecules can be reversibly removed, affording square-pyramidal metal centers with empty coordination sites, suitable for host–guest interactions. For MOF-74 frameworks featuring paramagnetic metal centers, such as Mn^{II}, Fe^{II}, Co^{II}, and Ni^{II}, ferromagnetic interactions are present within the chains, but weak antiferromagnetic interchain interactions result in non-magnetic ground states. Notably, the desolvated Fe^{II} framework Fe^{II}_2(2,5-dobdc) displays guest-dependent magnetic properties. For instance, adsorption of olefins favors antiparallel alignment of spins within the inorganic chains. However, the Fe^{II}-based frameworks do not show any indication of long-range magnetic order.[364–367]

In contrast, the compound Co^{II}_2(2,5-dobdc)$(H_2O)_2 \cdot 8H_2O$ (Co^{II}-MOF-74) exhibits antiferromagnetic order with T_N = 8 K. The relatively weak antiferromagnetic interactions between adjacent chains can be overcome upon application of a magnetic field above 2.0 T, resulting in a transition to a ferromagnetic-like ordered state.[349] Furthermore, while the Ni^{II} congener does not show long-range magnetic order above 2 K, the analoguos mixed-metal $Ni^{II}Fe^{III}$ frameworks display ferrimagnetic long-range order, together with permanent porosity. Specifically, controlled doping with high-spin Fe^{III} ions ($S = {}^5/_2$) introduces antiferromagnetic interactions into the metal-oxo chains, leading to coexisting antiferromagnetic and ferromagnetic intrachain coupling interactions. The ordering temperature for these frameworks can be modulated from 9.5 to 16.7 K upon varying the Fe^{III} doping level from ca. 20 to 2%. These compounds behave as relatively soft ferrimagnets with coercive fields smaller than 1000 Oe at 2 K.[350]

Frameworks comprised of dimeric tetracarboxylate paddlewheel motifs of the general formula $M^{II}_2(COO)_4$ have also been studied extensively.[368] In particular, frameworks featuring Cu^{II}_2 paddlewheel building blocks have been found to exhibit interesting magnetic properties.[351,352,369,370] For instance, the compound $Cu^{II}_2(1,3,\text{-bdc})_2(py)_2$ (1,3-bdc^{2-} = 1,3-benzenedicarboxylate) is comprised of bowl-shaped triangular secondary building units, where Cu^{II}_2 dimers are positioned at the lattice points and are connected by 1,3-benzenedicarboxylato ligands into a Kagomé-type 2D network with hexagonal channels (see Figure 8.36).[351] It is well known that strong antiferromagnetic coupling between Cu^{II} centers within the paddlewheel units results in overall diamagnetic $S = 0$ dimers.[300,371] As such, the observation of an open hysteresis loop at 5 K and apparent remanent magnetization at room temperature for the $Cu^{II}_2(1,3,\text{-bdc})_2(py)_2$ framework was surprising. Initially, the ferromagnetic-like behavior of this compound was attributed to a canted

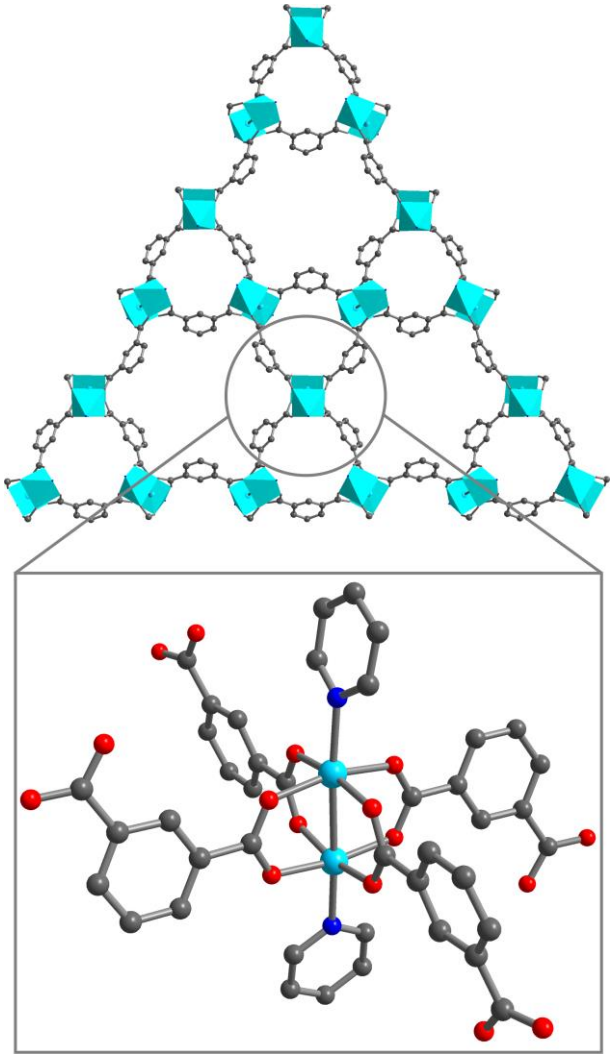

Figure 8.36 Crystal structure of $Cu^{II}_2(1,3,\text{-bdc})_2(py)_2$, as viewed along the crystallographic *c* axis, highlighting the Kagóme-type network (top) and the paddlewheel Cu^{II}_2 building unit (bottom). Cyan polyhedra represent $Cu^{II}_2N_2O_8$ units. Cyan, red, blue, and gray spheres represent Cu, O, N, and C atoms respectively; H atoms are omitted for clarity.

spin structure arising from the geometrically frustrated antiferromagnetic state.[351] However, this proposition was later questioned because a net spin is needed on each node to cause spin frustration, but the Cu^{II}_2 dimers do not possess a net spin.

More recently, theoretical calculations have indicated that the spontaneous magnetization in this and related $Cu^{II}_2(COO)_4$-based frameworks is caused by Cu^{II} vacancy point defects.[352] Specifically, the presence of Cu^{II} vacancies breaks the antiferromagnetic state in the Cu^{II}_2 dimers and creates quasi-localized spin states that interact ferromagnetically through itinerant π electrons in the conjugated aromatic ligands. Further analysis of the magnetic structure, for example through neutron diffraction, is needed to verify the origin of the ferromagnetic-like behavior of this Cu^{II} framework at low temperatures.

Similarly, more detailed magnetic measurements are required to establish the presence and nature of long-range magnetic order for the framework $Cu^{II}_3(1,3,5\text{-btc})_3(H_2O)_3$ ($1,3,5\text{-btc}^{3-}$ = 1,3,5-benzenetricarboxylate) (HKUST-1).[369,370] This compound is comprised of analogous $Cu^{II}_2(COO)_4$ paddlewheel building blocks as $Cu^{II}_2(1,3,\text{-bdc})_2(py)_2$, and preliminary magnetic studies suggested weak ferromagnetic interactions between the antiferromagnetically coupled Cu^{II}_2 dimers.[370] In contrast, a well-defined open magnetic hysteresis loop was observed at 5 K for the related compound $Cu^{II}_2(bptc)(H_2O)_3(DMF)_3$ ($bptc^{4-}$ = 3,3′,5,5′-biphenyltetracarboxylate) (MOF-505), indicative of a ferromagnetic-like ordered state. Fits of the high-temperature dc magnetic susceptibility data to the Curie–Weiss law provided an estimate of T_C = 11 K.[352] Whether the long-range order in MOF-505 originates from spin canting or ferromagnetic interactions between point defects is still not clear. Notably, the two biphenyl groups and two carboxylate groups of each tetracarboxylato bridging ligand are coplanar to one another, providing a highly

conjugated π system able to mediate significant magnetic communication between metal centers.[372]

Other examples of framework magnets featuring the 1,3,5-benzenetricarboxylato bridging ligand are the isostructural compounds $K[Co^{II}_3(1,3,5\text{-btc})(1,3,5\text{-Hbtc})_2]\cdot 5H_2O$ (MIL-45a) and $K[Co^{II}_{2.25}Fe^{II}_{0.75}(1,3,5\text{-btc})(1,3,5\text{-Hbtc})_2]\cdot 5H_2O$ (MIL-45b). These frameworks are comprised of undulating chains of edge- and corner-sharing $M^{II}O_6$ octahedra that are linked into 3D networks through the backbone of carboxylato ligands in different protonation states. Magnetic measurements revealed that both compounds behave as ferromagnets below T_C = 10 and 20 K for MIL-45a and MIL-45b, respectively, owing to ferromagnetic intra- and interchain interactions.[353]

Several frameworks containing the tetracarboxylato linker 1,2,4,5-benzenetetracarboxylate (1,2,4,5-btec^{4-}) have been found to exhibit long-range magnetic order.[354–359] For example. the homoleptic frameworks $M^{II}_2(1,2,4,5\text{-btec})$ (M^{II} = Mn^{II}, Fe^{II}, Co^{II}) are isostructural and consist of zigzag chains of edge-sharing $M^{II}O_6$ octahedra that are bridged into layers via O–C–O linkages, and the layers are further connected through the backbone of the aromatic ligand to give the 3D networks.[354,355] Both the Mn^{II} and Fe^{II} frameworks behave as antiferromagnets with T_N = 18 and 26 K, respectively. On the other hand, the Co^{II} framework exhibits a complicated magnetic behavior with three magnetic grounds states at low temperatures. Specifically, this compound exhibits long-range collinear antiferromagnetic order at 16 K, becomes a canted antiferromagnet at 12 K under low applied magnetic fields, and then undergoes a field-induced transition to a ferromagnetic state at higher fields (H > 1500 Oe). A proposed mechanism for the long-range antiferromagnetic order for this family of frameworks is the presence of antiferromagnetic interactions between ferromagnetic (Co^{II}) or antiferromagnetic (Mn^{II}, Fe^{II}) layers, as M^{II}–O–M^{II}

superexchange angles of ca. 104° can lead to either ferromagnetic or antiferromagnetic interactions.[298,299] However, the reason for the observed spin canting for the Co^{II} congener is still a mystery, as it can neither be explained by antisymmetric exchange[213,214] nor the difference in anisotropy of the magnetic centers because of the high crystal symmetry and only one crystallographically independent Co^{II} site in the structure. Accordingly, neutron diffraction studies are needed to provide a complete understanding of the magnetic phase diagram for Co^{II}_2(1,2,4,5-btec).

Related frameworks containing 1D inorganic subnetworks are the ferric carboxylate framework Fe^{III}(OH)(1,2,4,5-H_2btec)·0.88H_2O (MIL-82)[356] and the Co^{II}-based framework $Co^{II}_5(OH)_2$(1,2,4,5-btec)$_2$(bpp) (1,2,4,5-btec^{4-} = 1,2,4,5-benzenetetracarboxylate; bpp = 1,3-bis(4-pyridyl)propane).[357] The 3D structure of MIL-82 consists of chains of corner-sharing $Fe^{III}O_6$ octahedra that are connected via *trans*-2,5-carboxylate groups of the organic ligand, whereas the carboxyl functional groups in the 1 and 4 positions on the aromatic ring remain protonated and do not participate in covalent bonding within the framework.[356] However, despite the structure of MIL-82 is topologically related to those of MIL-47 (V^{III}) and MIL-53 (Cr^{III}) discussed above,[346–348] it does not undergo a reversible breathing effect during the dehydration/hydration process. This discrepancy is attributed to strong hydrogen bonds between the dangling carboxylic acid groups in MIL-82, which keep the structure intact up to 300 °C. Furthermore, MIL-82 undergoes long-range antiferromagnetic order at a much lower temperature of T_N = 5.5(1) K[356] than the related V^{III} and Cr^{III} frameworks. Since the Fe^{III}–O–Fe^{III} superexchange angle of 126.59(7)° is similar to those observed in MIL-47 and MIL-53, it is not obvious why the ordering temperature for MIL-82 is an order of magnitude lower than for the other two frameworks. One plausible explanation is that the

electronic communication through the partially protonated 1,2,4,5-H_2btec^{2-} bridging ligands is weaker than via 1,4-bdc^{2-} owing to the significant electron density present on the dangling carboxylic acid moieties.

The chain structure of $Co^{II}_5(OH)_2$(1,2,4,5-btec)$_2$(bpp) is significantly more complex, as it features both μ_3-OH and $\mu_{1,1}$-carboxylate bridges.[357] The Co^{II}–O backbone is comprised of edge-sharing octahedral trinuclear clusters that share corners with two distorted $Co^{II}O_5$ square pyramids.

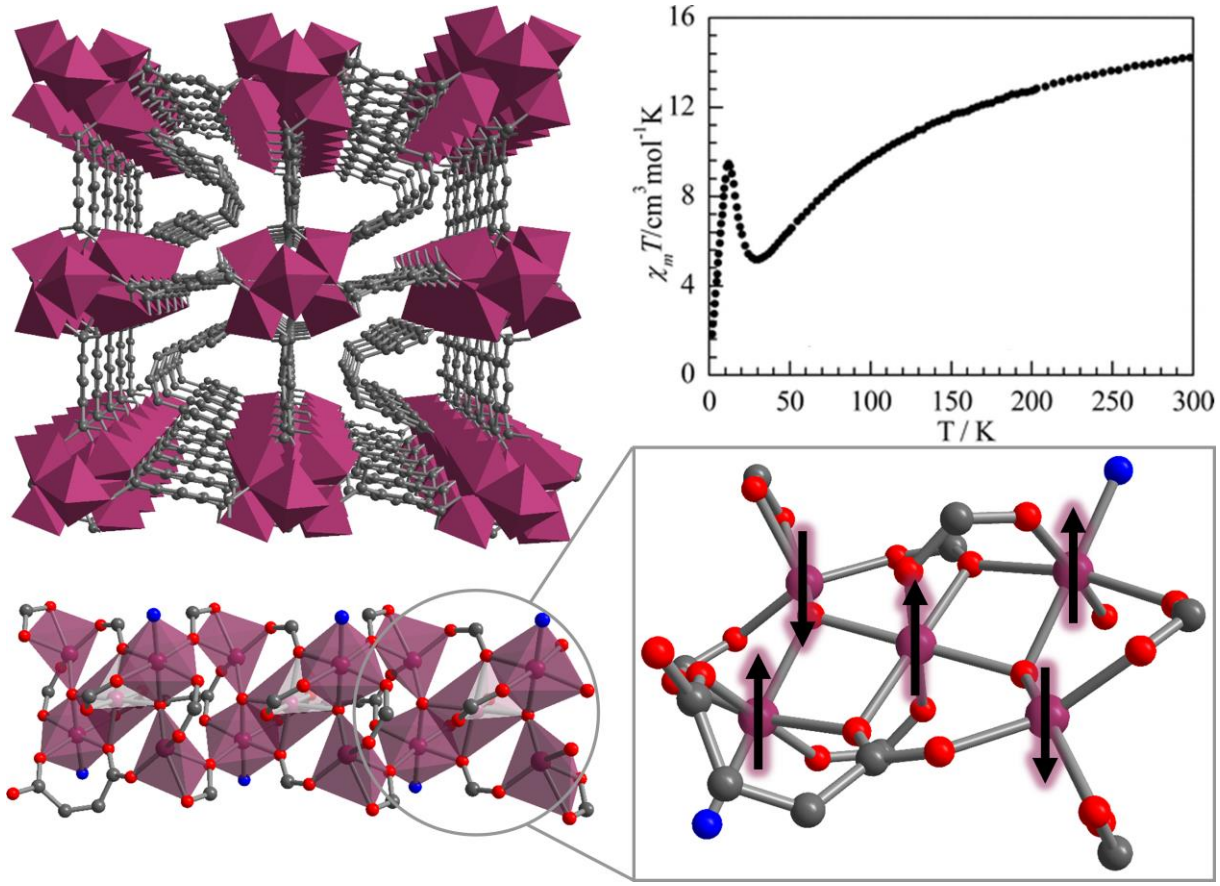

Figure 8.37 Left: Crystal structure of $Co^{II}_5(OH)_2$(1,2,4,5-btec)$_2$(bpp), as viewed along the crystallographic *a* axis (top), highlighting the metal-oxygen backbone (bottom). The expanded view in the bottom right illustrates the coordination environments of Co^{II} within the pentameric subunit and the associated spin topology. Purple polyhedra represent $Co^{II}O_5$, $Co^{II}NO_5$, and $Co^{II}O_6$ units. Purple, red, blue, and gray spheres represent Co, O, N, and C atoms, respectively; H atoms are omitted for clarity. Top right: Variable-temperature dc magnetic susceptibility data for $Co^{II}_5(OH)_2$(1,2,4,5-btec)$_2$(bpp), collected under an applied field of 5000 Oe. Reproduced from ref. 357 with permission from the Royal Society of Chemistry.

The chains are connected into a 3D network via 1,2,4,5-benzenetetracarboxylato ligands adopting two different coordination modes, and bowed 1,3-bis(4-pyridyl)propane ligands provide further structural support (see Figure 8.37, left). Owing to multiple types of nearest-neighbor magnetic exchange pathways between three crystallographically distinct Co^{II} centers in the chains, i.e. via hydroxo, $\mu_{1,1}$-carboxylate, and *syn–syn* $\mu_{1,3}$-carboxylate bridges, coexisting ferromagnetic and antiferromagnetic interactions are present, leading to overall ferrimagnetic-like behavior within the magnetic chains (see Figure 8.37, right). Upon application of magnetic fields below 3500 Oe, a transition to an antiferromagnetically ordered state was observed with T_N = 12.5 K. At higher fields, the weak antiferromagnetic interactions between the ferrimagnetic chains can be overcome to afford a ferrimagnetic-like ordered state.

In addition to the frameworks comprised of 1D inorganic subnetworks and 1,2,4,5-benzenetetracarboxylato bridging ligands, a few framework magnets without M–O–M linkages have been reported.[358,359] In particular, the 3D frameworks Ni^{II}_2(1,2,4,5-btec)$(H_2O)_4 \cdot 2H_2O$[358] and Cu^{II}_2(1,2,4,5-btec)$(hypH)_{0.5}(H_2O)_{0.5} \cdot 1.5H_2O$ (hypH = hypoxanthine)[359] exhibit long-range antiferromagnetic and ferromagnetic order with T_N = 3 K and T_C = 4.5 K, respectively. Notably, the latter compound represents the first MOF with nucleobase ligands that exhibits long-range magnetic order.[359]

One framework with benzenepentacarboxylato linkers has been shown to display long-range magnetic order.[360] Indeed, this Co^{II}-based compound of formula $Co^{II}_3(OH)(bpc)(H_2O)_3$ (bpc^{5-} = benzenepentacarboxylate) was one of the first coordination solids featuring this ligand. The 3D structure is comprised of distorted $Co^{II}O_6$ octahedra that are arranged into Co^{II}_6 secondary building units (see Figure 8.38, top), which are bridged by pairs of carboxylate groups into 1D tapes. These

1D motifs are further connected along the other two directions through the pentacarboxylato ligand. Notably, multiple exchange pathways are present within and between the Co^{II}_6 building units: μ_3-OH, μ_2-H_2O, $\mu_{1,1}$-carboxylate, and three types of $\mu_{1,3}$-carboxylate bridges (see Figure 8.38, top), resulting in a complicated magnetic structure. Magnetic measurements revealed long-range antiferromagnetic order below T_N = 3.8 K with some weak ferromagnetic-like contribution, attributed to either spin canting or competing antiferromagnetic and ferromagnetic interactions within the 1D tapes. Furthermore, a metamagnetic transition to a paramagnetic phase was observed at 1.9 K under an applied field greater than 4000 Oe.

Two Co^{II}-based framework compounds, $(Et_3NH)[Co^{II}_{1.5}(hfipbb)_2]$ and $Co^{II}_2(hfipbb)_2 \cdot PhMe$ ($hfipbb^{2-}$ = hexafluoroisopropylidenebis(benzoate)), contain the V-shaped dicarboxylato ligand hexafluoroisopropylidenebis(benzoate).[361] The structure of $(Et_3NH)[Co^{II}_{1.5}(hfipbb)_2]$ is built up from linear trimeric clusters of $Co^{II}O_5$–$Co^{II}O_6$–$Co^{II}O_5$ polyhedra that are

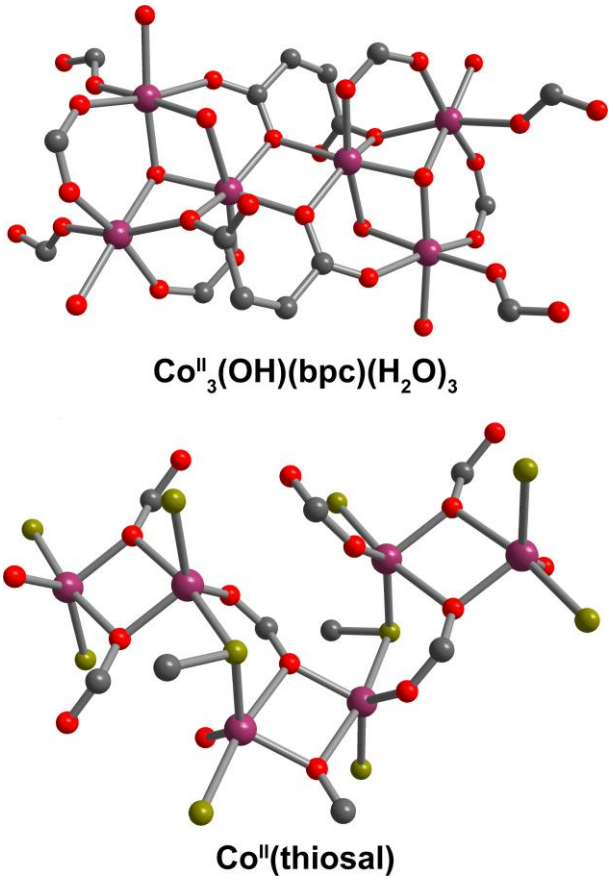

Figure 8.38 Crystal structures of $Co^{II}_3(OH)(bpc)(H_2O)_3$ (top) and $Co^{II}(thiosal)$ (bottom), highlighting the hexameric Co^{II}_6 building unit and the trigonal bipyramidal S_2O_3 coordination environment, respectively. Note that multiple magnetic exchange pathways are present in both compounds. Purple, gold, red, and gray spheres represent Co, S, O, and C atoms, respectively; H atoms and aromatic backbone of the ligands are omitted for clarity.

bridged by $hfipbb^{2-}$ into a 2D framework of square lattice topology with $(Et_3NH)^+$ counterions in the voids of the network. In contrast, the neutral compound $Co^{II}_2(hfipbb)_2 \cdot PhMe$ displays a 3D structure comprised of zigzag chains of edge-sharing $Co^{II}O_6$ octahedra that are connected in the other two dimensions through the backbone of the dicarboxylato ligands. Despite the drastically different structures of the two compounds, both exhibit long-range canted antiferromagnetic order with T_N = 7–8 K. The origin of the ordered magnetic states was attributed to weak antiferromagnetic interactions between ferromagnetic subunits – linear trimeric clusters for the 2D framework and zigzag chains for the 3D framework – where the ordered magnetic moments are slightly canted. For both compounds, the long-range magnetic order is destroyed upon application of a high enough magnetic field. In particular, the intercluster interactions in $(Et_3NH)[Co^{II}_{1.5}(hfipbb)_2]$ are very weak owing to the long distance between them (12.077–13.052 Å), and a magnetic field of 1000 Oe is sufficient to preclude magnetic order.

Finally, a framework that is bridged by a sulfur-containing carboxylato ligand and exhibits long-range magnetic order is the layered compound Co^{II}(thiosal) ($thiosal^{2-}$ = thiosalicylate).[326] This 2D framework features Co^{II} ions in a trigonal bipyramidal S_2O_3 coordination environment that are bridged by $thiosal^{2-}$ ligands (see Figure 8.38, bottom), with the phenyl groups protruding into the interlayer space. Four types of magnetic exchange pathways are present within the layers: Co^{II}–S–Co^{II}, Co^{II}–O–Co^{II}, and *syn–syn* and *syn–anti* Co^{II}–O–C–O–Co^{II} (see Figure 8.38, bottom). This framework exhibits strong antiferromagnetic coupling between Co^{II} ions at high temperatures, as indicated by a remarkably large negative value for the Weiss constant of θ = −585(3) K (from data above 100 K). Moreover, it displays long-range canted antiferromagnetic order with T_N = 9 K. Note that the observed weak ferromagnetic behavior was assigned to canted

antiferromagnetism rather than ferrimagnetism because of only one crystallographically unique Co^{II} center in the structure.

In summary, the majority of framework magnets containing carboxylato bridging ligands display magnetic ordering temperatures below 25 K. The current record holder for this class of compounds is the V^{III}-based framework MIL-47 with T_N = 95(5) K.[346] This compound features an inorganic chain structure, as detailed above. Accordingly, increasing the inorganic dimensionality does not necessarily afford frameworks with higher T_c. This may seem counterintuitive, as the strength of magnetic superexchange is typically greatest across short oxo or hydroxo bridges. However, frameworks of higher inorganic dimensionality (I^2O^0, I^2O^1, I^3O^0) often feature multiple types of superexchange pathways that may facilitate interactions of different signs and thus decrease the strength of the overall metal–metal interactions. Furthermore, these frameworks usually suffer from the lack of conjugated π systems that aid in establishing a long-range magnetic order.

8.3.6 Compounds Containing N-Heterocyclic Ligands

8.3.6.1 Introduction

Ligands based on N-heterocycles have been frequently employed in the construction of framework materials.[373] These aromatic N-donor ligands can be classified according to their charge into neutral or anionic linkers. Neutral donors include pyrazine, pyridine, pyrimidine, and imidazole derivatives, whereas imidazolate, triazolate, and tetrazolate are examples of anionic ligands (see Figure 8.10). In addition to linking magnetic oxo-, hydroxo-, phosphonato-, or carboxylato-bridged layers in magnetic materials,[70,71,218,321,322,328] N-heterocycles can also serve as primary ligands in the construction of framework magnets owing to the multiple relatively short

and efficient magnetic exchange pathways between metal centers possible through these π-conjugated ligands. For instance, azolate moieties may afford exchange pathways via two-atom N–N, three-atom N–C–N, and three-atom N–N–N bridges (see Figure 8.6). Due to the small size of these N-heterocycles, they are frequently connected by spacers of variable lengths to facilitate the formation of frameworks with higher porosity. Such assembly of two or more donor groups enables an additional control of ligand field strength and metal coordination geometry, and thus the magnetic properties of the resulting framework materials. In this section, we survey framework magnets constructed from one or two types of N-heterocyclic ligands (see Figure 8.10), where these ligands provide connectivity in at least two dimensions.

8.3.6.2 2D Frameworks

Following an extensive search for multi-atomic bridges to efficiently transmit magnetic interactions between paramagnetic metal centers, several 2D layered frameworks of Mn^{II}, Fe^{II}, and Co^{II} with N-heterocyclic linkers were found to display long-range magnetic order.[374–377] These frameworks consist of parallel square-grid layers of divalent transition metal ions that are bridged by bis-monodentate N-heterocycle-based ligands such as pyrazine (pyz), pyrazine-1,4-dioxide (pzdo), and pyrimidine (pym). Each metal center resides in a compressed octahedral geometry with two NCS^- ligands coordinating at the axial sites. Magnetic susceptibility measurements for the compound $Fe^{II}(pyz)_2(NCS)_2$ suggested the onset of antiferromagnetic order below ca. 9 K, and neutron powder diffraction enabled the observation of a 3D long-range order below T_N = 6.8 K. Nevertheless, even in the ordered phase, the magnetic behavior of this compound is primarily 2D in character owing to the very weak dipolar interactions between the magnetic pyrazine-bridged layers.[374,375] The analogous 2D frameworks $M^{II}(pzdo)_2(NCS)_2$ (M^{II} = Mn^{II}, Co^{II}) show similar

magnetic properties characteristic of antiferromagnets, with T_N = 8.4 and 11.2 K for M^{II} = Mn^{II} and Co^{II}, respectively.[376] The slightly higher ordering temperatures for these frameworks compared to the Fe^{II} framework with pyrazine bridging ligands may stem from the presence of weak hydrogen bonds between pyrazine-1,4-dioxide molecules in adjacent layers, which facilitates interlayer exchange interactions.

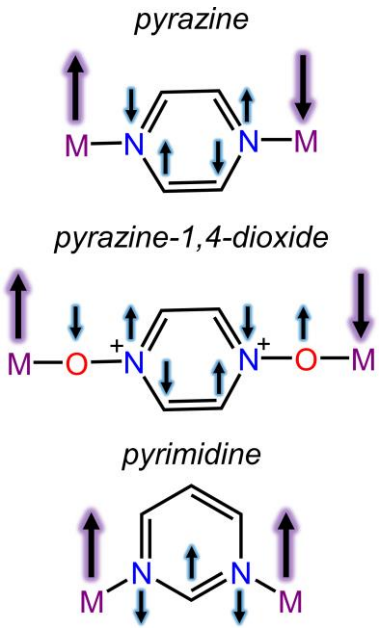

Figure 8.39 Representation of the spin polarization mechanism between two paramagnetic metal centers (M) through pyrazine (top), pyrazine-1,4-dioxide (center), and pyrimidine (bottom) linkers.

The antiferromagnetic behavior observed for the frameworks bridged by pyrazine derivatives can be explained by the topological symmetry of the conjugated π-electron network for these systems, also known as the spin polarization mechanism. The spin-polarization mechanism describes how an unpaired electron on one atom polarizes the electron cloud on adjacent atoms such that neighboring electrons adopt antiparallel arrangement.[377–380] Based on this exchange pathway alone, magnetic coupling between metal centers across the *para*-substituted N–C–C–N and O–N–C–C–N–O bridges in pyrazine and pyrazine-1,4-dioxide, respectively, should be antiferromagnetic (see Figure 8.39, top and center). In contrast, interactions through the *meta*-substituted N–C–N bridge in pyrimidine should be ferromagnetic (see Figure 8.39, bottom). Along these lines, the 2D Co^{II} framework $Co^{II}(pym)_2(NCS)_2$, which features the same layered structure as described above, exhibits ferromagnetic order below T_C = 8.2 K.[377] This compound behaves as a soft magnet, as evidenced from a magnetic hysteresis at 2.3 K with a small coercive field of H_c

= 120 Oe and a remanent magnetization of $M_r = 0.25\ \mu_B\ mol^{-1}$.

8.3.6.3 Pyrimidinolate 3D Frameworks

A number of frameworks based on deprotonated hydroxypyrimidine ligands, also known as pyrimidinolates, have been reported.[381–388] Specifically, 3D frameworks featuring 2-pyrimidinolate derivatives have been shown to display long-range magnetic order[385–388] and guest-dependent magnetic behavior.[385,386] Moreover, remote ligand substitution can be employed to tune the magnetic ordering temperature for these systems.[388] The compound $Co^{II}(F\text{-pymo})_2 \cdot 2.5H_2O$ (F-pymo$^-$ = 5-fluoro-2-pyrimidinolate) is comprised of distorted $Co^{II}N_4$ tetrahedra linked by *N*,*N*′-*exo*-bidentate 5-fluoro-2-pyrimidinolato ligands into a 3D framework with sodalite topology. The fluoro- and oxo-substituents alternatively protrude into the cavities of the framework and the remaining space is occupied by H_2O molecules (see Figure 8.40, left).[385] Upon heating at 92 °C, the lattice H_2O molecules can be reversibly removed without significant structural changes, however, further heating leads to an irreversible formation of a layered structure.

Antiferromagnetic nearest-neighbor interactions dominate in these compounds, and the hydrated 3D framework exhibits long-range antiferromagnetic order with $T_N = 29$ K. In contrast, the dehydrated layered phase shows hidden canted antiferromagnetic behavior below ca. 17 K. The variation in magnetic properties upon desolvation was attributed to changes in the coordination environment at Co^{II}, but the lack of structural data for the anhydrous layered phase precludes a detailed analysis. In addition to the modulation of the magnetic properties for this compound by thermal treatment, the anhydrous 3D framework exhibits selective adsorption of CO_2 over N_2, H_2, and CH_4,[385] indicating that this and related systems may be attractive targets for multifunctional magnetic materials.

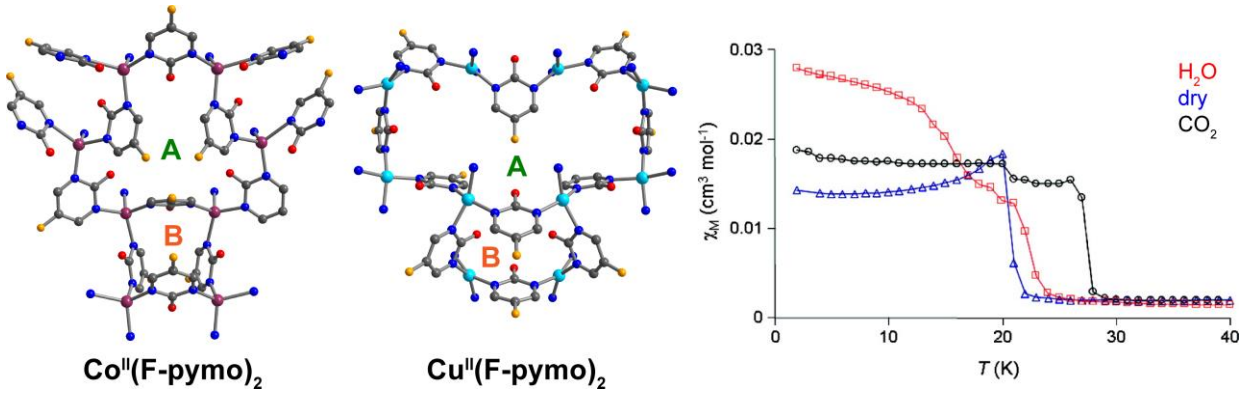

Figure 8.40 Crystal structures of $Co^{II}(F\text{-pymo})_2 \cdot 2.5H_2O$ (left) and $Cu^{II}(F\text{-pymo})_2 \cdot 1.25H_2O$ (center), highlighting the two types of structural motifs (A and B) in the frameworks. Cyan, purple, light orange, red, blue, and gray spheres represent Cu, Co, F, O, N, and C atoms, respectively; H atoms and solvent molecules are omitted for clarity. Right: Variable-temperature dc magnetic susceptibility data for $Cu^{II}(F\text{-pymo})_2 \cdot 1.25H_2O$ (red), activated $Cu^{II}(F\text{-pymo})_2$ (blue), and $Cu^{II}(F\text{-pymo})_2$ with CO_2 molecules in the pores (black), collected under an applied field of 100 Oe. Reprinted with permission from ref. 386. Copyright 2008 American Chemical Society.

A series of isostructural 3D frameworks with an acentric diamond-like topology are formed when the fluoro-substituted pyrimidinolato ligand is replaced by other 5-substituted halopyrimidinolates or the unsubstituted ligand. Specifically, the compounds of formula $Co^{II}(R\text{-pymo})_2$ (R = H, Cl, Br, I; R-pymo$^-$ = 2-pyrimidinolate or 5-halo-2-pyrimidinolate)[387,388] feature Co^{II} ions in similar tetrahedral coordination environment as the 3D frameworks with F-pymo$^-$ linkers discussed above. Nevertheless, the diamond-like frameworks exhibit weak ferromagnetism below the ordering temperatures of T_N = 19–22.5 K attributed to spin canting. The presence of a canted spin structure in these compounds was speculated to be a synergistic effect of the acentric crystal structure, structural distortions, and high magnetic anisotropy of Co^{II}. Notably, the magnetic ordering temperature is highest for $Co^{II}(Cl\text{-pymo})_2$ and decreases with decreasing electronegativity of the halo substituent. However, the derivative bearing the unsubstituted ligands (H-pymo$^-$) does not fit this trend, as it orders at T_N = 22 K. Furthermore, the coercive field obtained from magnetic hysteresis studies at 2 K follows the trend Br > Cl > I > H, whereas the remanent

magnetization follows the trend Br ≈ Cl > I > H. While the lack of a coherent trend for the magnetic behavior in this series of compounds precludes a definitive magnetostructural analysis,[388] this study nevertheless demonstrated that subtle changes in the steric and electronic properties of linkers can be employed to modulate the magnetic properties for framework materials.

By comparison, the hydrated Cu^{II} framework $Cu^{II}(F\text{-pymo})_2 \cdot 1.25H_2O$ (F-pymo$^-$ = 5-fluoro-2-pyrimidinolate) exhibits a 3D structure of gismondine topology with Cu^{II}_4 and Cu^{II}_8 structural motifs (see Figure 8.40, center) instead of the Co^{II}_4 and Co^{II}_6 rings found in $Co^{II}(F\text{-pymo})_2 \cdot xH_2O$ (x = 0, 2.5).[386] This framework also displays a reversible dehydration/hydration process while retaining the integrity of the structure. Magnetic measurements revealed antiferromagnetic coupling between square planar Cu^{II} centers through the N–C–N bridges of F-pymo$^-$. However, the non-centrosymmetry of the crystal structure allowed the presence of an antisymmetric effect, resulting in canting of the spins. As such, $Cu^{II}(F\text{-pymo})_2 \cdot 1.25H_2O$ displays long-range canted antiferromagnetic order with T_N = 24 K, in analogy to the majority of Co^{II} frameworks featuring 2-pyrimidinolato ligands. The magnetic properties for the dehydrated framework are very similar to those observed for the hydrated compound, but interestingly, incorporation of CO_2 molecules in the pores increases the ordering temperature from T_N = 22 to 29 K (see Figure 8.40, right). The uptake of CO_2 results in structural perturbation of the framework, as evidenced by PXRD analysis, which was presumed to lead to a less distorted square planar coordination environment around the Cu^{II} sites and thus provide greater overlap between the magnetic $d_{x^2-y^2}$ orbital of Cu^{II} and the orbitals of F-pymo$^-$.[386] Notably, this type of guest-modulated magnetic properties induced by gas molecules is exceedingly rare for framework materials.

In summary, the 3D frameworks discussed in this subsection illustrate that magnetic

interactions through the N–C–N linkage of 2-pyrimidinolato ligands are antiferromagnetic in nature, which is in contrast to the ferromagnetic interactions expected for pyrimidine-based ligands considering the spin-polarization mechanism depicted in Figure 8.39. Note, however, that the spin-polarization mechanism is based on π-exchange interactions only, but both σ- and π-orbitals of N-heterocycle-based ligands may be capable of mediating magnetic coupling between metal centers. As such, the presence of a negatively charged O atom midway in the exchange pathway may favor σ-type exchange interactions and thus lead to antiferromagnetic coupling between metal centers.

8.3.6.4 Imidazolate 3D Frameworks

Over the past several decades, a number of imidazolate-bridged dinuclear Cu^{II}_2 complexes and chain compounds have been shown to exhibit strong antiferromagnetic exchange coupling through the N–C–N linkage.[389–392] However, since the imidazolato ligand displays a similar *N,N′-exo*-bidentate binding mode toward metal centers as pyrimidine derivatives, one might expect favorable ferromagnetic interactions based on a π-type exchange pathway.[377–380] Indeed, heterobimetallic complexes and networks have demonstrated ferromagnetic exchange between metal centers through the imidazolate bridge.[393,394] As such, the electronic configuration and geometry of the metal ions, and the symmetry of the magnetic orbitals, all play an important role in determining the type of magnetic exchange through imidazolato ligands.[389–395]

Among of the first 3D imidazolate framework compounds reported to exhibit long-range magnetic order was $Fe^{II}_3(im)_6(imH)_2$ (im^- = imidazolate).[396] The structure of this framework is comprised of imidazolato-bridged chains of tetrahedral Fe^{II} ions that are crosslinked through octahedral Fe^{II} ions (see Figure 8.41, left). The compound behaves as a soft canted antiferromagnet below T_N = 17 K, and magnetic hysteresis measurements at 4.8 K show a coercive field of H_c =

200 Oe and a remanent magnetization of M_r = 2500 Oe cm^3 mol^{-1}. The strongest antiferromagnetic nearest-neighbor interactions are present between the tetrahedral Fe^{II} centers within the chains, and the canted spin structure is believed to originate from different relative orientations of the metal centers along the chains.

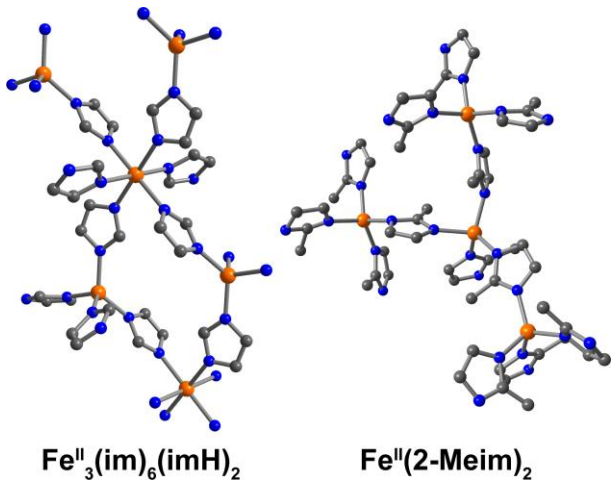

Figure 8.41 Crystal structures of $Fe^{II}_3(im)_6(imH)_2$ (left) and $Fe^{II}(2\text{-Meim})_2 \cdot 0.13(Cp_2Fe^{II})$ (right), highlighting the coordination environments of Fe^{II}. Orange, blue, and gray spheres represent Fe, N, and C atoms, respectively; H atoms and guest molecules are omitted for clarity.

Following this pioneering study, the effects of incorporating different substituents onto the imidazolate ring on the magnetic properties of this class of compounds were investigated.[397,398] Specifically, introduction of a methyl group onto the 2-position of the imidazolate ring afforded the compound $Fe^{II}(2\text{-Meim})_2 \cdot 0.13Cp_2Fe^{II}$ (2-Meim$^-$ = 2-methylimidazolate; Cp$^-$ = cyclopentadienyl anion).[397] This compound features exclusively tetrahedral Fe^{II} centers (see Figure 8.41, right) and exhibits long-range canted antiferromagnetic order with T_c = 27 K, which is currently the highest ordering temperature reported for a framework that is exclusively bridged by imidazolato ligands. Furthermore, this framework is a significantly harder magnet than $Fe^{II}_3(im)_6(imH)_2$, as evidenced by a 25-fold enhancement in the coercive field at 4.8 K, from H_c = 200 Oe for $Fe^{II}_3(im)_6(imH)_2$ to H_c = 5000 Oe for $Fe^{II}(2\text{-Meim})_2 \cdot 0.13Cp_2Fe^{II}$. In contrast, the use of a 4-azabenzimidazolato bridging ligand afforded a Fe^{II} framework with magnetic properties similar to those of the framework bearing the unsubstituted imidazolato linker.[398]

A series of homoleptic 3D imidazolate frameworks featuring tetrahedral Co^{II} centers has also been shown to exhibit long-range magnetic order at low temperatures.[399,400] In particular, various polymorphous frameworks of the general formula $Co^{II}(im)_2 \cdot x$solvent (im^- = imidazolate) have been synthesized under different solvothermal conditions to give desolvated and solvated 3D frameworks of different framework topologies. These compounds order as antiferromagnets or canted antiferromagnets with T_c = 10.6–16.8 K, highlighting that the magnetic properties for this family of compounds are significantly affected by the nature of the guest molecules in the pores as well as the topological arrangement of metal ions in the structures. To illustrate, replacing pyridine guest molecules with cyclohexanol molecules resulted in a change from an antiferromagnet with T_N = 13.1 K to a canted antiferromagnet with T_c = 15 K.[399] Furthermore, two frameworks of the same formula, $Co^{II}(im)_2 \cdot 0.5$DMA, display different zeolitic structures with magnetic ordering temperatures differing by 4.8 K.[400]

8.3.6.5 Tri- and Tetrazolate 3D Frameworks

In contrast to the pyrazine, pyrimidine, and imidazolate derivatives outlined above, triazolate- and tetrazolate-based ligands frequently link three or more metal centers through various bridging modes. As such, these ligands can furnish the formation of MOFs with unique structures and magnetic properties. Along these lines, several frameworks featuring triazolato and tetrazolato ligands have displayed long-range magnetic order.[401–405] Most of these compounds comprise Cu^{II} frameworks featuring inorganic coligands, such as OH^-,

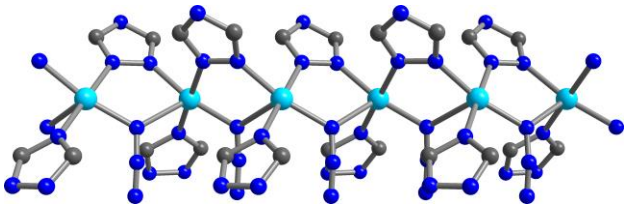

Figure 8.42 Crystal structure of $Cu^{II}(trz)(N_3)$, as viewed along the crystallographic *b* axis. Cyan, blue, and gray spheres represent Cu, N, and C atoms, respectively; H atoms are omitted for clarity.

Cl^-, N_3^-, SO_4^{2-}, and VO_3^-, resulting in the formation of various types of inorganic subunits.[401,403–405] Here, antiferromagnetic exchange interactions between Cu^{II} centers dominate, affording compounds with long-range antiferromagnetic,[401] ferrimagnetic,[404,405] or canted antiferromagnetic[403,405] order below ca. 20 K. Of these compounds, the first azido–metal–triazolate coordination polymer $Cu^{II}(trz)(N_3)$ (trz^- = 1,2,4-triazolate) exhibits the highest magnetic ordering temperature of ca. 20 K, based on the bifurcation temperature of zero-field-cooled and field-cooled dc magnetization curves.[403] The structure of this framework is comprised of chains of distorted square-pyramidal Cu^{II} ions bridged by $\mu_{1,2}$-trz^- and end-on azido ligands (see Figure 8.42). The chains are connected in the other two dimensions through the third N atom on the trz^- ligands to generate a 3D framework of (10,3)-*d* type topology. This compound exhibits field-dependent magnetic properties and a hysteresis loop at 2 K with a coercive field of $H_c \approx 200$ Oe and a remanent magnetization of $M_r = 0.0028\ \mu_B\ mol^{-1}$, indicating weak ferromagnetism. This behavior was attributed to the presence of a canted spin structure arising from tilting of the Cu^{II} spins in the chains. The main magnetic exchange coupling pathways in this framework are through the end-on azido (Cu^{II}–N–Cu^{II}) and $\mu_{1,2}$-trz^- (Cu^{II}–N–N–Cu^{II}) bridges within the chains. Note that magnetic coupling via end-on azido bridges is typically ferromagnetic, however, antiferromagnetic interactions can be favored when the Cu^{II}–N–Cu^{II} angle is larger than 104°,[406] as is observed here (117°).

8.3.7 Compounds Containing Mixed O- and N-Donor Ligands

8.3.7.1 Introduction

An alternative class of ligands to generate framework magnets are those based on N-heterocycles functionalized with carboxylate groups (see Figure 8.11). These multifunctional

ligands enable rich coordination chemistry and feature a conjugated π-system able to mediate strong magnetic exchange coupling via various types of two- to four-atom bridges. Moreover, this class of compounds shows high chemical tunability, as various combinations of the two components can be selected. Specifically, the geometry, denticity, and overall charge of the ligand can be readily modulated by changing the N-heterocycles and carboxylate moieties to construct materials for targeted applications. Accordingly, the employment of ligands featuring both N- and O-donors may provide advantages in the design of new multifunctional magnetic materials.

8.3.7.2 Pyridinecarboxylate Compounds

The use of pyridinecarboxylato ligands in the synthesis of framework magnets has received considerable attention. The first example of such was the 3D framework $Mn^{II}_3(3\text{-pyc})_4(N_3)_2(H_2O)_2$ (3-pyc^- = 3-pyridinecarboxylate) reported in 2001.[407] This compound is comprised of linear trinuclear Mn^{II}_3 subunits bridged by end-on azido and *syn–syn* carboxylato linkers, which are further connected into a 3D network through the aromatic backbone of 3-pyc^- ligands. This compound behaves as a soft ferrimagnet below T_c = 3.7 K under low applied magnetic fields, attributed to ferromagnetic exchange interactions between antiferromagnetically coupled Mn^{II}_3 clusters. Subsequent studies found that incorporation of a second carboxylate group onto the pyridyl backbone enabled the formation of frameworks with magnetic ordering temperatures up to T_c = 20.0 K.[408,409] Specifically, frameworks comprised of hydroxo-bridged Co^{II} chains have provided the highest ordering temperatures. For instance, the compound $Co^{II}_3(OH)_2(3,4\text{-pydc})_2(H_2O)_2$ ($3,4\text{-pydc}^{2-}$ = pyridine-3,4-dicarboxylate) features 1D chains of formula $[Co^{II}_3(OH)_2]^{4+}$, built up from edge-sharing $Co^{II}NO_5$ octahedra that share a corner with a $Co^{II}O_6$ octahedron. Antiferromagnetic interactions are favored within the trimeric building units, leading

to overall ferrimagnetic chains. The ferrimagnetic chains are coupled antiferromagnetically to give an ordered state below T_N = 20.0 K. Nevertheless, the interchain interactions are relatively weak and a spin-flop transition to a ferrimagnetic phase was observed under an external magnetic field above 7000 Oe. Accordingly, the compound displays an open hysteresis loop at 2 K with a coercive field of H_c = 2750 Oe.[408]

A recent study revealed that a similar enhancement in ordering temperature can be achieved by using a combination of carboxylate-functionalized N-heterocycles and hydroxo-substituted monocarboxylato ligands.[410] Namely, the compound Co^{II}_3(*rac*-O-lac)$_2$(pybz)$_2$·3DMF (*rac*-O-lac^{2-} = racemate 2-oxidopropanoate; pybz$^-$ = 4-(4-pyridyl)benzoate) represents the first lactato-bridged porous magnet.[410] Its structure is comprised of square tubular chains of alternating $Co^{II}NO_5$ and $Co^{II}O_4$ polyhedra connected by lactate dianions. The chains are then linked by pybz$^-$

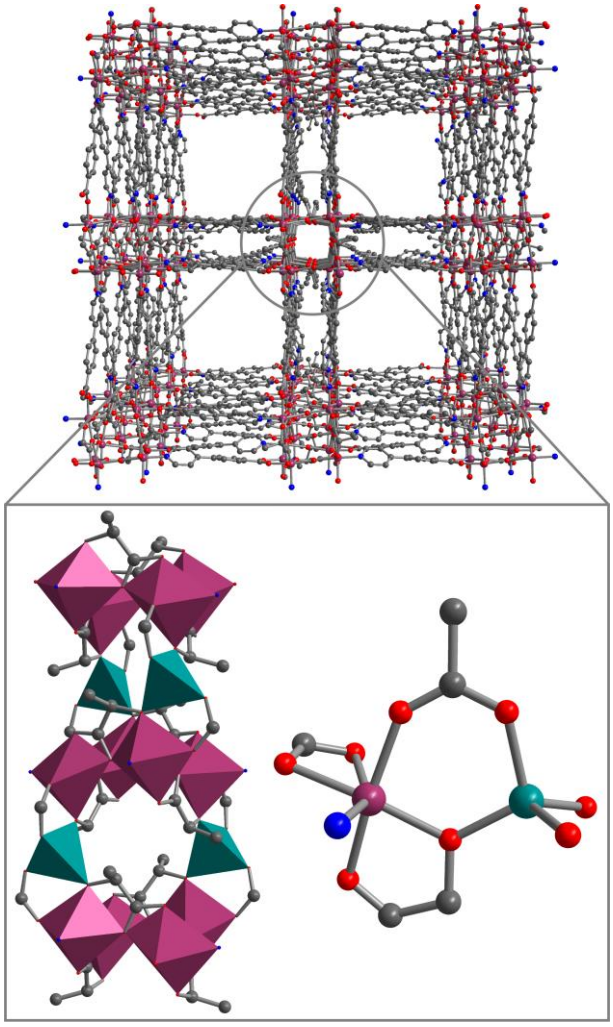

Figure 8.43 Crystal structure of Co^{II}_3(*rac*-O-lac)$_2$(pybz)$_2$·3DMF, as viewed along the crystallographic *c* axis (top). Purple, red, blue, and gray spheres represent Co, O, N, and C atoms, respectively; H atoms and solvent molecules are omitted for clarity. The expanded view highlights the square tubular chains of alternating $Co^{II}NO_5$ (purple) and $Co^{II}O_4$ (teal) polyhedra connected by lactate dianions and the two distinct coordination environments of Co^{II}.

ligands in the other two directions to generate a 3D framework with square channels (10.8 × 10.8 $Å^2$) (see Figure 8.43). Owing to the large separation between chains, the dominant magnetic exchange pathway is via Co^{II}–O–Co^{II} bridges in the lactato-bridged square chains. Notably, the solvent molecules can be removed from the pores of the framework and exchanged with selective guest molecules, such as MeOH, EtOH, PrOH, and benzene, without affecting structural integrity. Furthermore, the desolvated framework displays a Langmuir surface area of 1050 $m^2\ g^{-1}$ and adsorbs N_2, H_2, and CH_4 gas molecules. Remarkably, the magnetic properties for this framework can be significantly modulated by the nature of the guest molecules in the pores. While the solvated frameworks Co^{II}_3(*rac*-O-lac)$_2$(pybz)$_2$·*x*solvent (*x*solvent = 3DMF, 6MeOH, 4.5EtOH) exhibit long-range canted antiferromagnetic order with T_N = 17.5–18.7 K, the desolvated compound displays single-chain magnet behavior with a blocking temperature of T_B = 3 K. Upon exposing this framework to H_2O or I_2 molecules, structural changes and dramatic loss of crystallinity were observed due to H_2O coordination to Co^{II} and partial oxidation of Co^{II} to Co^{III}, respectively. The hydrated framework behaves as a ferrimagnet below T_c = 32 K, whereas the oxidized framework exhibits ferromagnetic order below T_C = 8 K. Note, however, that the latter two frameworks have not been crystallographically characterized. This compound represents the first example of a single material exhibiting four magnetic ground states. Switching between these states can be carried out through post-synthetic modification, which acts to modulate the magnitude and sign of interchain magnetic exchange interactions.

8.3.7.3 Pyrimidinecarboxylate Compounds

In contrast to pyridinecarboxylato ligands, pyrimidinecarboxylates can behave as bis-bidentate ligands and thus adopt a similar coordination mode as oxalato and oxamato ligands (see Figure

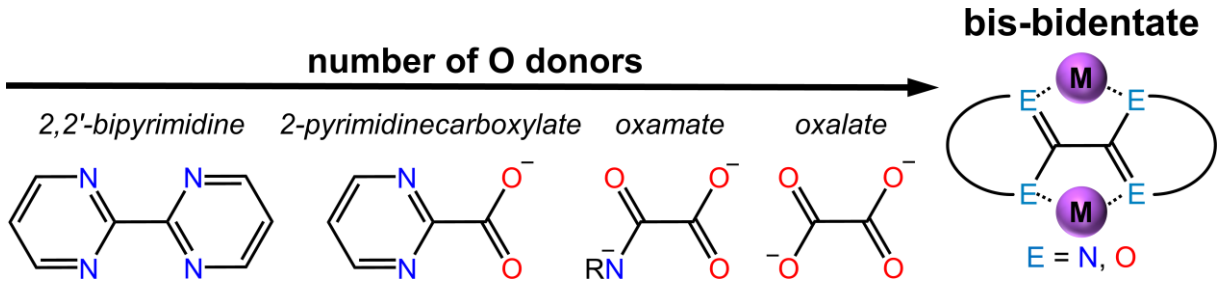

Figure 8.44 Comparison of bis-bidentate ligands with N_4, N_2O_2, NO_3, and O_4 donor sets.

8.44). As a result, these ligands can mediate relatively strong magnetic interactions between metal centers and furnish materials with synthetically predictable structures.

For instance, the two isostructural compounds $[M^{II}_2(pymca)_3](OH)\cdot H_2O$ (M^{II} = Fe^{II}, Co^{II}; $pymca^-$ = 2-pyrimidinecarboxylate) have been shown to exhibit long-range magnetic order.[411] These 2D frameworks consist of heterochiral cationic honeycomb layers that stack to generate hexagonal pores in which hydroxide counterions and H_2O solvent molecules reside (see Figure 8.45, top). Three types of exchange pathways between metal centers are present in the layers: N–C–N, *anti–anti* O–C–O, and *trans* N–C–C–O bridges (see Figure 8.45, bottom). These interactions collectively result in antiferromagnetic nearest-neighbor coupling within the layers. Owing to weak antiferromagnetic interactions between layers, the Fe^{II} framework orders as an antiferromagnet with T_N = 21 K, whereas the Co^{II} framework orders as a canted antiferromagnet with T_c = 10 K. The different magnetic behavior observed for these two isostructural compounds was proposed to arise from the higher anisotropy of octahedral Co^{II} ions compared to Fe^{II} centers. Specifically, the local anisotropy, in conjunction with the antisymmetric exchange interaction,[213,214] was posited to be the origin of spin canting in the Co^{II} framework.

8.3.7.4 Azole- and Azolatecarboxylate Compounds

In addition to the pyridine- and pyrimidinecarboxylate-based frameworks discussed above, one Fe^{II} framework and several Co^{II} frameworks featuring linkers made up of imidazole, triazole, tetrazole, and thiodiazole cores functionalized with one or two carboxylate groups have been shown to exhibit magnetic order at low temperatures.[412–416] The homoleptic compound $Fe^{II}(4\text{-imac})_2 \cdot 2MeOH$ (4-imac^- = 4-imidazoleacetate) was reported in 1991, and at that time it displayed the highest critical temperature (T_c = 15 K) for a molecule-based compound exhibiting canted antiferromagnetic order.[412] The structure of this compound is comprised of layers of distorted octahedral Fe^{II} ions linked by carboxylate groups, with MeOH solvent molecules located in the interlayer space that participate in hydrogen bonding interactions with the 2D framework. The presence of a canted spin structure was hypothesized to stem from the presence of two spin sublattices due to local distortion of the Fe^{II} centers. Accordingly, antiferromagnetic

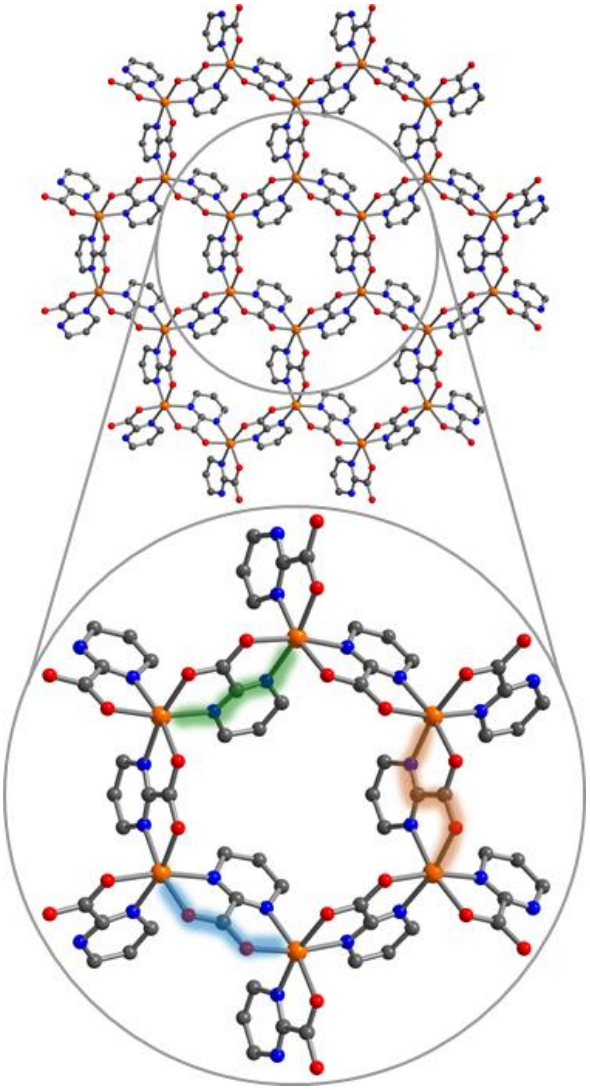

Figure 8.45 Crystal structure of $[Fe^{II}_2(pymca)_3](OH)\cdot H_2O$, as viewed along the crystallographic *c* axis. Orange, red, blue, and gray spheres represent Fe, O, N, and C atoms, respectively; H atoms and guest molecules are omitted for clarity. The expanded view highlights the three types of magnetic exchange pathways in the honeycomb layer: N–C–N (green), *anti–anti* O–C–O (light blue), and *trans* N–C–C–O (red orange).

nearest-neighbor interactions via the carboxylate bridges lead to an uncompensated magnetic moment within each layer, and magnetic interactions between layers, through the hydrogen-bonded network, were assumed to induce the formation of a long-range ordered state. Notably, this framework displays a hysteresis loop at 4.2 K with a large coercive field of H_c = 6200 Oe.

Of the Co-based frameworks within this series, the compound $Co^{II}_3(OH)_2(btca)_2 \cdot 3.7H_2O$ ($btca^{2-}$ = benzotriazolate-5-carboxylate) features similar hydroxo-bridged ferrimagnetic chains as the compound $Co^{II}_3(OH)_2(3,4\text{-}pydc)_2(H_2O)_2$ (see Figure 8.46, top and center), but it displays more complicated magnetic behavior. Namely, it orders as a ferrimagnet below T_c = 8 K and exhibits single-chain magnet behavior below the ordering temperature with a relaxation

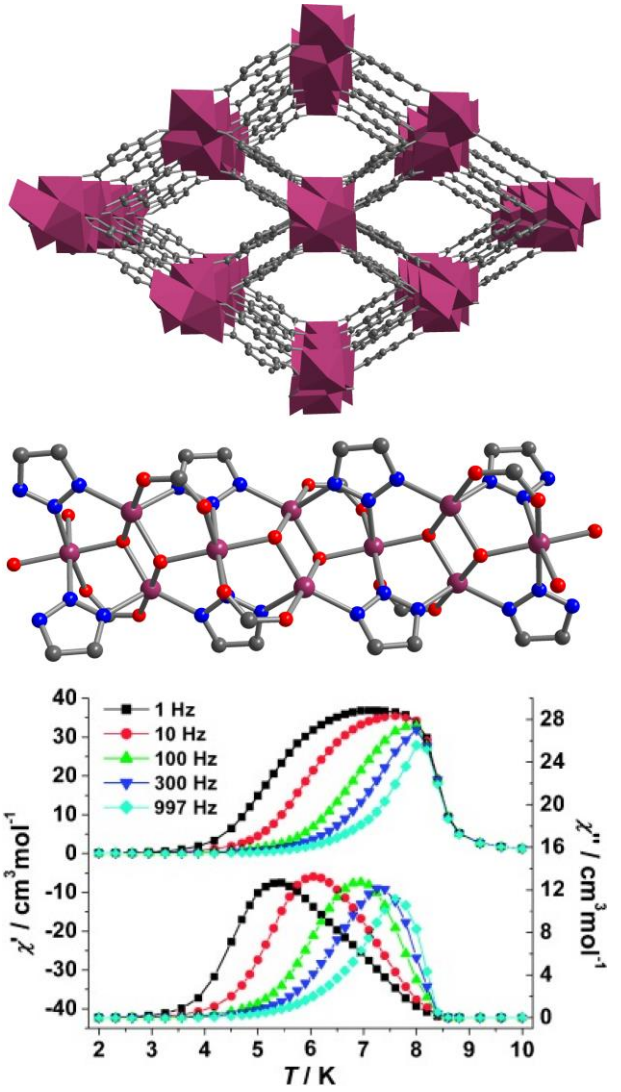

Figure 8.46 Crystal structure of $Co^{II}_3(OH)_2(btca)_2 \cdot 3.7H_2O$, as viewed along the crystallographic *c* (top) and *b* axis (center), highlighting the 1D channels and hydroxo-bridged chains, respectively. Purple polyhedra represent $Co^{II}N_2O_3$ and $Co^{II}N_2O_4$ units. Purple, red, blue, and gray spheres represent Co, O, N, and C atoms, respectively; H atoms and solvent molecules are omitted for clarity. Bottom: Variable-temperature ac magnetic susceptibility data for $Co^{II}_3(OH)_2(btca)_2 \cdot 3.7H_2O$, collected under zero applied dc field at various frequencies (see inset). Reproduced from ref. 413 with permission from Wiley-VCH Verlag GmbH & Co.

barrier of Δ_τ = 85(5) cm^{-1} and $\tau_0 = 2.6 \times 10^{-11}$ s (see Figure 8.46, bottom).[413] Interestingly, the desolvated framework retains the original structure and exhibits long-range canted antiferromagnetic order with T_N = 4.5 K and metamagnetic behavior. The change in magnetic properties observed upon desolvation was attributed to stronger antiferromagnetic interactions between the ferrimagnetic chains when the pores of the framework are empty rather than filled with H_2O molecules.[413] All other members within this series of frameworks feature 3D structures without inorganic subnetworks.[414–416] The magnetic properties for these compounds are characterized by spin-canted antiferromagnetism due to canting of the antiferromagnetically coupled magnetic moments of highly anisotropic octahedral Co^{II} ions. Accordingly, these frameworks exhibit long-range antiferromagnetic or canted antiferromagnetic order with T_N = 2.4–9 K,[414–416] with metamagnetic[415] and spin glassy behavior[414] also having been observed.

8.3.8 Compounds Containing Diamagnetic Benzoquinoid Ligands

8.3.8.1 Introduction

Encouraged by the success of oxalato linkers in furnishing magnets with predictable structures and relatively high ordering temperatures, researchers have also explored other types of bis-bidentate bridging ligands. Of particular interest are ligands that allow for greater chemical tunability than the oxalato ligand while retaining strong magnetic exchange coupling between metal centers. Such ligand modifications may be employed to tune the magnetic properties of the frameworks, as well as to introduce additional functionalities. Toward that end, 2,5-dihydroxy-1,4-benzoquinone and its derivatives are particularly attractive candidates (see Figure 8.47).[417] Specifically, these ligands can be readily accessed in three redox states (−2, −3•, −4), all of which allow for strong covalent interactions between the ligands and a wide range of metal centers to

afford compounds with well-defined structures.[418,419] In addition, despite the long distance between metal centers, the conjugated system can provide an effective pathway for magnetic exchange interactions. Both the substituents (R) on the aromatic ring and donor atoms (E = O, S, NR, PR, etc.) can be varied to investigate how electronic and steric effects of different atoms or groups affect the magnetic properties of the resulting frameworks. Together, this illustrates the high degree of chemical tunability for this family of ligands and their potential to provide magnetic materials with predictable structures and properties. In this section, we provide an overview of magnets featuring diamagnetic benzoquinoid linkers.

8.3.8.2 Benzoquinoid Compounds

Benzoquinoid ligands may furnish homo- and heterometallic 1D, 2D, and 3D coordination polymers of diverse structure types.[418–421] The topology of networks comprised of octahedral metal centers that are tris-chelated by bis-bidentate benzoquinoid ligands is dictated by the distribution of their absolute configurations, similar to what is observed for oxalate frameworks. Specifically, a 2D honeycomb lattice is formed when neighboring metal centers are of opposing chiralities (Δ or Λ), whereas a 3D network of (10,3)-*a* topology results when all the metal centers adopt the same absolute configuration. Owing to the bigger size of benzoquinoid ligands compared to oxalate, this type of 3D structure features two interpenetrated (10,3)-*a* nets of opposing chiralities, resulting in achiral compounds.[420,421] Note that the 3D (10,3)-*a* topology is rare for benzoquinoid-based coordination solids. Accordingly, all current examples of frameworks bridged by diamagnetic benzoquinoid derivatives that

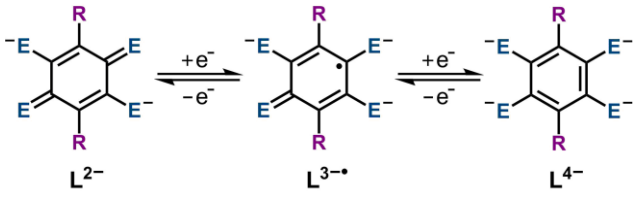

Figure 8.47 Redox series of deprotonated benzoquinoid ligands with donor atoms E and substituents R.

exhibit permanent magnetic behavior are 2D networks of honeycomb topology. Specifically, these compounds feature dianionic tetraoxolene-based ligands (E = O) and are synthesized following the metalloligand approach by reacting a pre-formed homoleptic tris-chelated octahedral metal complex of formula $[M^{III}(R_2An)_3]^{3-}$ (M^{III} = Cr^{III}, Fe^{III}; R = Cl, Br, I, H) with divalent transition metal ions, such as Mn^{2+}, Fe^{2+}, and Co^{2+}, in the presence of templating cations.[422–429]

The first structurally-characterized layered magnets of this type were three chiral compounds of formula $[(H_3O)(phz)_3][Mn^{II}M^{III}(R_2An)_3]\cdot$solvent (phz = phenazine; M^{III} = Cr^{III}, Fe^{III}; Cl_2An^{2-} = chloranilate; Br_2An^{2-} = bromanilate; solvent = H_2O, C_3H_6O) and the achiral compound $(Bu_4N)[Mn^{II}Cr^{III}(Cl_2An)_3]$ reported in 2013.[422] The honeycomb structure is comprised of anionic layers of $[Mn^{II}M^{III}(R_2An)_3]^-$ alternating with cationic layers formed by the chiral Δ-$[(H_3O)(phz)_3]^+$

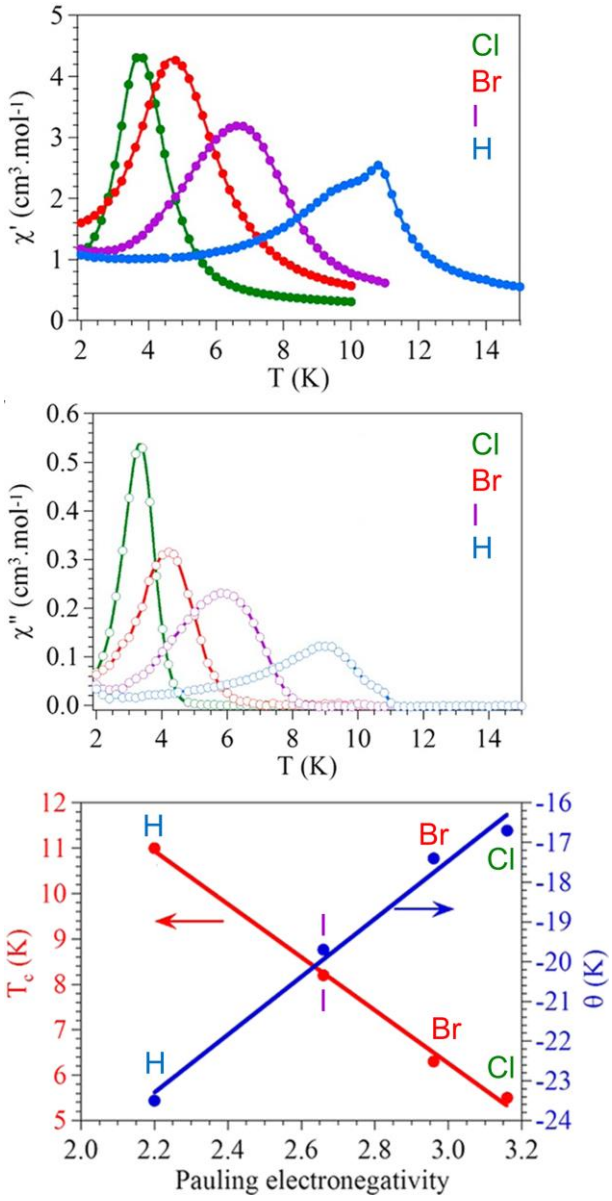

Figure 8.48 Variable-temperature ac magnetic susceptibility data for $(Bu_4N)[Mn^{II}Cr^{III}(R_2An)_3]$ (R = Cl, Br, I, H), collected under zero applied dc field at 1 Hz frequency (top and center). Bottom: Plot of magnetic ordering temperature (T_c; left scale, red) and Weiss temperature (θ; right scale, blue) vs Pauling electronegativity of the R substituents. Reprinted with permission from ref. 422. Copyright 2013 American Chemical Society.

or achiral $(Bu_4N)^+$ ions. The layers are eclipsed for the compounds with Δ-$[(H_3O)(phz)_3]^+$ cations, generating hexagonal channels, but display alternate packing when $(Bu_4N)^+$ counterions were employed. Note that the use of a chiral templating cation leads to a chiral structure owing to favorable Δ–Δ interactions, in analogy to what had previously been observed for similar metal oxalates.

Magnetic measurements on the $Mn^{II}Cr^{III}$ compounds revealed antiferromagnetic interactions between metals ions through the $(R_2An)^{2-}$ (R = Cl, Br) linkers to afford ferrimagnetic layers. Moreover, these compounds exhibit ferrimagnetic order with $T_c \approx 5$–6 K, as confirmed by ac susceptibility measurements. While the type of templating cation did not affect the ordering temperature of the anionic lattices, the value of T_c was found to be significantly affected by the nature of the substituent on the benzoquinoid ligand. Specifically, when the ligand substituent was varied from R = Cl to Br to I to H, the ordering temperature increased from T_c = 5.5 to 6.3 to 8.2 to 11.0 K for the series with $(Bu_4N)^+$ counterions (see Figure 8.48, top and center). This observed trend in T_c (Cl < Br < I < H) correlates linearly with the electronegativity of the ligand substituent (see Figure 8.48, bottom). Here, the higher electronegativity of the ligand substituent results in less electron density on the benzoquinoid ring, and thus weaker coupling and lower T_c. Indeed, the value of the Weiss temperature (θ) follows the same trend, with the strongest antiferromagnetic coupling observed for R = H (see Figure 8.48, bottom). As such, this study illustrates that the ligand substituent can be employed to tune the magnetic ordering temperature in these materials. Note however, that only the R = Cl derivative has been crystallographically characterized, as the poor crystallinity of the other members of this series has prevented full characterization. To compare, the $Mn^{II}Fe^{III}$ analogue displays similar antiferromagnetic intralayer interactions and a

long-range ordered state was observed below ca. 3.5 K owing to spin canting.[422]

Other strategies to tune the magnetism in this family of compounds include the employment of coligands and/or solvent guest molecules. For instance, the use of benzaldehyde as solvent in the preparation of these benzoquinoid frameworks afforded the compounds $(Bu_4N)[Mn^{II}Cr^{III}(R_2An)_3(PhCHO)]\cdot PhY$ (R = Cl, Br; Y = H, CHO), which feature heptacoordinated Mn^{II} ions.[428] These compounds display an analogous honeycomb structure as described above, with eclipsed layers, and exhibit ferrimagnetic order below T_c = 6.7–7.0 K. These ordering temperatures are slightly higher than those observed for $(Bu_4N)[Mn^{II}Cr^{III}(R_2An)_3]$ (R = Cl, Br), indicating that the presence of coligands and lattice solvent molecules can be employed to fine-tune the magnetic ordering temperature, attributed to slight structural changes that alter the strength of exchange interactions. More significant changes in T_c were observed upon incorporating other benzene derivatives (PhBr, PhCl, PhI, PhMe, PhCN, $PhNO_2$) into the hexagonal pores of the $(Bu_4N)[Mn^{II}Cr^{III}(Br_2An)_3]$ framework.[429] Specifically, these compounds afforded ordering temperatures ranging from T_c = 9.5 K for PhBr to T_c = 11.4 K for PhI, which are much higher values than that of T_c = 6.3 K obtained for the desolvated framework. The observed increase in T_c upon inclusion of the benzene derivatives was proposed to arise from host–guest interactions, namely π–π stacking interactions between the benzene rings of the solvates and benzoquinoid rings of the ligands, to give important structural and/or electronic changes. Unfortunately, full structural characterization for the desolvated framework is not yet available to test these hypotheses.

In line with earlier studies with bimetallic oxalates,[248–253] spin-crossover Fe^{III} cations have been incorporated into the pores of 2D benzoquinoid frameworks with the goal of achieving

multifunctional magnetic materials.[423,424] In contrast to the minimal impact of the inserted cations on T_c for the oxalate frameworks, a significant enhancement in the magnetic ordering temperature was observed upon introducing a range of cationic spin-crossover Fe^{III} complexes into the pores of anionic $[Mn^{II}Cr^{III}(R_2An)_3]^-$ (R = Cl, Br) lattices.[423,424] These compounds exhibit honeycomb structures and ferrimagnetic behavior, similar to the frameworks with $(Bu_4N)^+$ cations, albeit with a nearly two-fold increase in T_c, to values of ca. 10–11 K. Note, however, that the increase in T_c is likely not caused by magnetic interactions, as a near identical ordering temperature was obtained when a paramagnetic Fe^{III} complex was replaced by a diamagnetic Ga^{III} analogue.[424] Furthermore, the Fe^{III} complexes did not display spin-crossover behavior after inclusion into the benzoquinoid lattices, rather they remained exclusively in their low-spin or high-spin state,[423,424] presumably owing to the absence of intermolecular interactions that can facilitate cooperative spin-crossover. As such, these hybrid materials did not show coexistence of spin-crossover and long-range magnetic order, and the observed change in T_c likely stems from structural changes caused by introduction of larger cations into the frameworks.

Size effects of the templating cation on the magnetic properties of these materials have been further illustrated through a series of $Mn^{II}Cr^{III}$ frameworks with inserted alkylammonium cations of various sizes.[425] While the compounds $(Me_2NH_2)[Mn^{II}Cr^{III}(Br_2An)_3]\cdot 2H_2O$, $(Et_2NH_2)[Mn^{II}Cr^{III}(Br_2An)_3]$, and $(Et_3NH)[Mn^{II}Cr^{III}(Cl_2An)_3]$ feature the typical honeycomb layered structures with the ammonium cations occupying the cavities in the hexagonal channels (see Figure 8.49, left), the employment of the slightly larger $(Et^iPr_2NH)^+$ cation provided a different bilayer structure for the compound $(Et^iPr_2NH)[Mn^{II}Cr^{III}(Br_2An)_3]\cdot 0.5CHCl_3\cdot H_2O$. Here,

half of the cations resides in the pores and the other half is located in the interlayer space (see Figure 8.49, right). These structural changes have profound effects on the magnetic properties for these compounds. Specifically, the compounds possessing regular honeycomb structures display the typical long-range ferrimagnetic order below T_c = 7.9–8.9 K, whereas the bilayer compound with $(Et^iPr_2NH)^+$ cations exhibits weak antiferromagnetic interactions between the ferrimagnetic layers when it is measured in contact with the mother liquor. The solvated bilayer framework

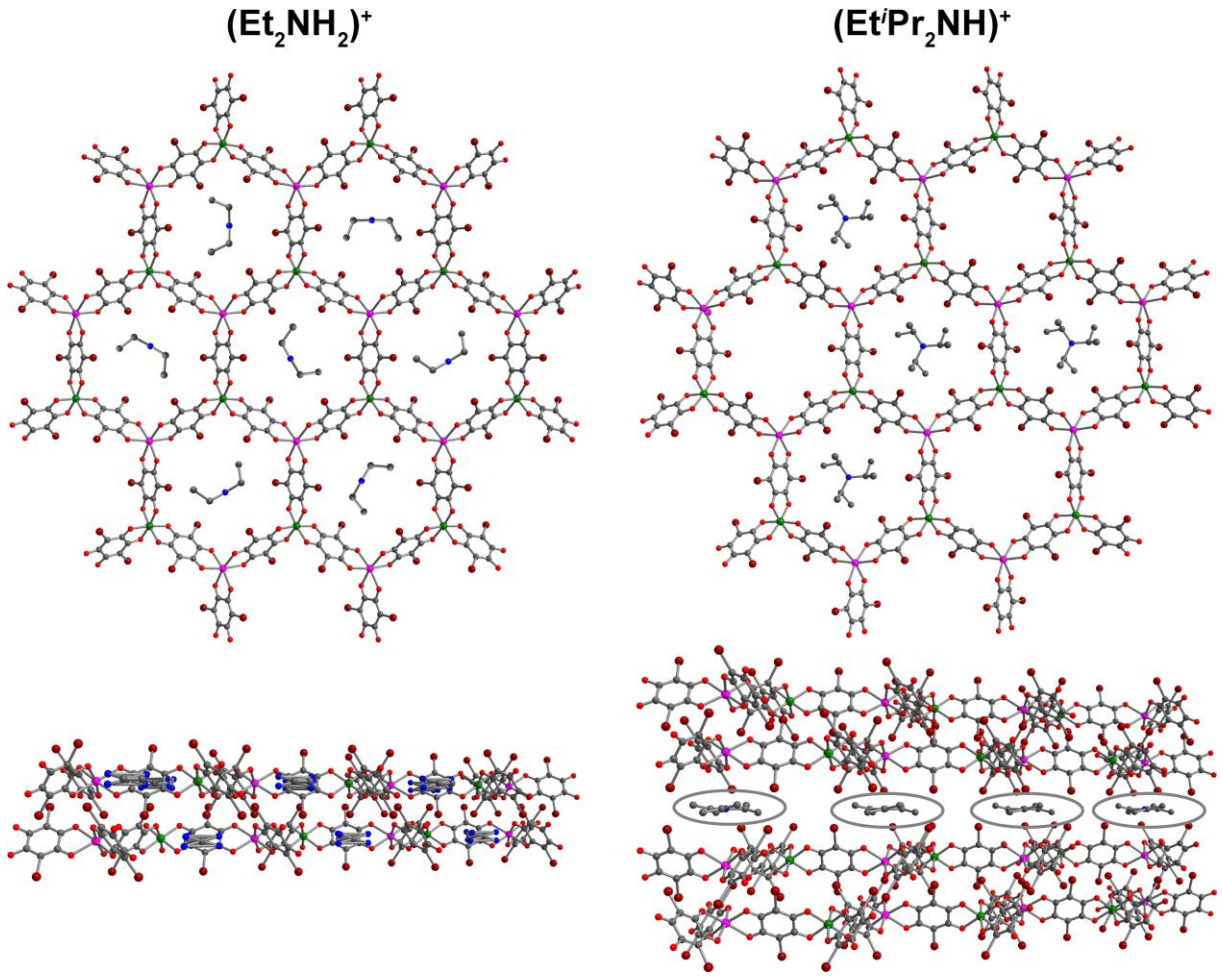

Figure 8.49 Crystal structures of $(Et_2NH_2)[Mn^{II}Cr^{III}(Br_2An)_3]$ (left) and $(Et^iPr_2NH)[Mn^{II}Cr^{III}(Br_2An)_3]\cdot 0.5CHCl_3\cdot H_2O$ (right), as viewed along the crystallographic *c* (top) and *b* axis (bottom), highlighting the different arrangement of alkylammonium cations in the two compounds. Dark red, magenta, green, red, blue, and gray spheres represent Br, Mn, Cr, O, N, and C atoms, respectively; H atoms and solvent molecules are omitted for clarity.

exhibits long-range antiferromagnetic order and metamagnetic behavior. Interestingly, the dried sample shows a ferrimagnetic-like order below T_c = 9.0 K, which is attributed to a collapse of the structure. Notably, the desolvation/solvation process is reversible, thereby demonstrating the reversible switching of magnetic properties for this compound. The origin of this guest-dependent behavior was speculated to arise from halogen–halogen interlayer interactions that are not present in the compounds with the smaller alkylammonium cations. Furthermore, these compounds show moderate proton conductivities, and thus belong to a rare class of multifunctional materials that show a coexistence of long-range magnetic order and proton conduction.

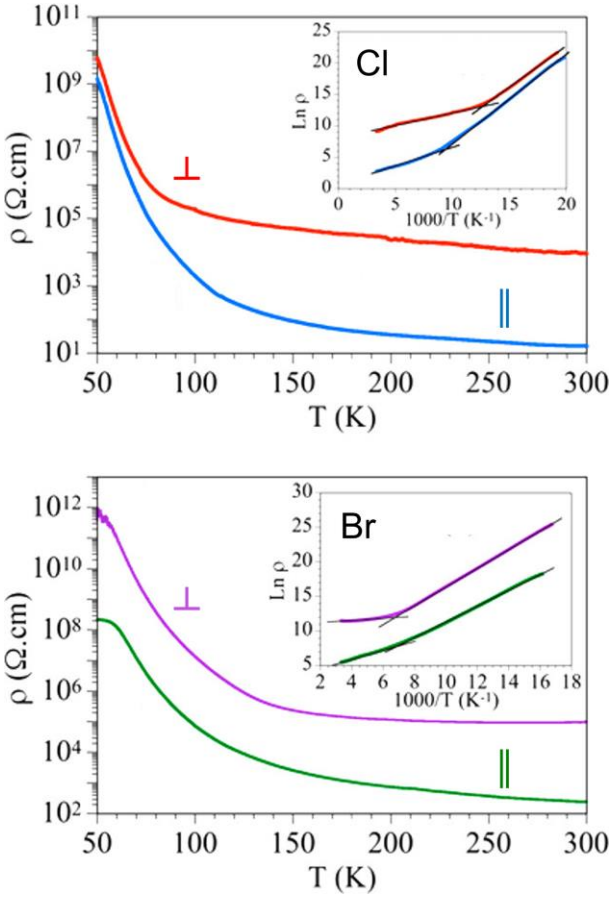

Figure 8.50 Variable-temperature electrical resistivity data for $[(H_3O)(H_2O)(phz)_3][Fe^{II}Fe^{III}(Cl_2An)_3]\cdot 12H_2O$ (top) and $[(H_3O)(H_2O)(phz)_3][Fe^{II}Fe^{III}(Br_2An)_3]\cdot 12H_2O$ (bottom), obtained along the hexagonal layers (∥) and perpendicular to the layers (⊥). Inset: Arrhenius plots of the data, with solid lines denoting linear fits to the Arrhenius law for the two semiconducting regimes. Reprinted with permission from ref. 426. Copyright 2017 American Chemical Society.

In addition to the heterobimetallic $Mn^{II}Cr^{III}$ and $Mn^{II}Fe^{III}$ 2D benzoquinoid frameworks, homometallic mixed-valence $Fe^{II}Fe^{III}$ frameworks have also been recently reported.[426,427] The compounds $[(H_3O)(H_2O)(phz)_3][Fe^{II}Fe^{III}(R_2An)_3]\cdot 12H_2O$ (phz = phenazine; Cl_2An^{2-} =

chloranilate; Br_2An^{2-} = bromanilate) show the honeycomb layered structure with eclipsed packing of layers.[426] Variable-temperature Q-band EPR spectra revealed that both frameworks are Robin–Day class II mixed-valence compounds, as the appearance of a signal at ca. 20–40 K attributed to the $S = {}^5/_2$ Fe^{III} center indicated that the delocalized electron becomes trapped at low temperatures. Indeed, magnetic susceptibility measurements are consistent with class II mixed valency, as the presence of distinct Fe^{II} and Fe^{III} sites at low temperature gives rise to ferrimagnetic long-range order.

Compared to the $Mn^{II}Cr^{III}$ frameworks with similar cations, the ordering temperatures for the $Fe^{II}Fe^{III}$ derivatives of T_c = 2.1–2.4 K are much lower.[422] Interestingly, the chloranilate-bridged compound (R = Cl) orders at a slightly higher temperature than the bromanilate-bridged (R = Br) congener, suggesting that the magnetic coupling strength increases as the electronegativity of R increases,[426] in contrast with the previous observation for the analogous $Mn^{II}Cr^{III}$ series with R = Cl, Br, I, H.[422] This different behavior may be explained by the double exchange mechanism present in the $Fe^{II}Fe^{III}$ series. Furthermore, the electron delocalization in these compounds provides high electrical conductivity in the plane parallel to the hexagonal layers, with room-temperature values of $\sigma_{\parallel}$ = 0.03 and 0.003 S cm^{-1} for R = Cl and Br, respectively (see Figure 8.50), confirming their semiconducting behaviors.[426] Similar behavior has been observed for the isostructural framework compound $(tag)[Fe^{II}Fe^{III}(ClCNAn)_3]\cdot 29H_2O$ (tag^+ = triaminoguanidinium; $ClCNAn^{2-}$ = chlorocyanoanilate), which features an asymmetric benzoquinoid ligand.[427] This compound has a slightly higher magnetic ordering temperature of T_c = 4 K and a slightly lower in-plane room-temperature conductivity of $\sigma_{\parallel}$ = 0.002 S cm^{-1}. Notably, the benzoquinoid-based $Fe^{II}Fe^{III}$ frameworks exhibit much higher electrical conductivity than analogous oxalate-bridged

compounds,[430] owing to their greater effectiveness in promoting electron delocalization through a small-polaron hopping mechanism.[427]

In summary, the 2D frameworks based on diamagnetic benzoquinoid linkers exhibit modest magnetic ordering temperatures (T_c = 5.5–11.4 K) that can be tuned by the choice metal centers, bridging ligand substituents, templating cations, and guest molecules. Furthermore, this family of materials represents rare examples of compounds that show both long-range magnetic order and electrical conductivity, making them attractive candidates for the creation of multifunctional magnetic materials.

8.4 MOF Magnets with Radical Bridging Ligands

8.4.1 Introduction

Magnetic exchange coupling between metal centers bridged by diamagnetic organic linkers, as discussed in previous sections, occur via an indirect, and often relatively weak, superexchange mechanism.[1,4,10] Moreover, the strength of these interactions is highly dependent on the relative orientation of the metal ions and decreases drastically when the distance between them increases.[1,4,10,14,146] As such, the realization of metal-organic materials with strong magnetic coupling and thus long-range magnetic order remains an important challenge. One strategy toward this end is to connect paramagnetic metal centers by organic radical linkers, as direct exchange coupling between the metals and radical spins can give rise to much stronger interactions. Here, the paramagnetic linker acts as a magnetic relay and its diffuse spin orbitals enable good overlap with metal-based magnetic orbitals, thereby facilitating effective magnetic communication over longer distances. Furthermore, the use of organic radical linkers offers facile redox chemistry that may allow for switchable magnetic properties and multifunctionality, such as coexistent long-

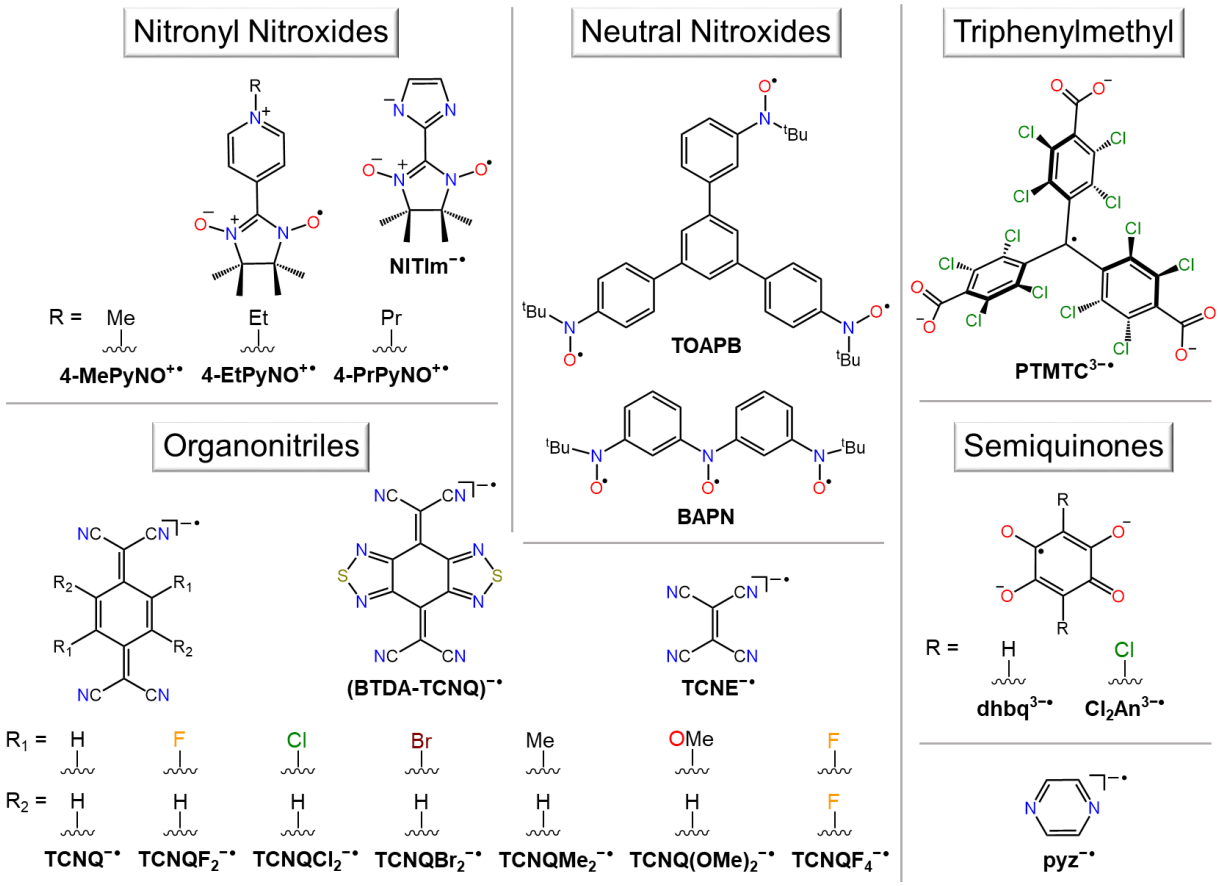

Figure 8.51 Organic radical linkers discussed in this review.

range magnetic order and electrical conductivity. This metal-radical approach[26,27] has been highly successful over the past two decades and has provided molecule-based magnets with unique magnetic properties and multifunctional behavior. In this section, we highlight remarkable benchmarks and recent advances in the field of radical-based framework magnets. A summary of the radical linkers discussed herein is provided in Figure 8.51. Note that compounds featuring paramagnetic radical cations that are not covalently bound to the magnetic framework will not be discussed here, but they are included in previous sections of this review. Framework magnets based on radical linkers are enumerated in Tables 8.18 and 8.19.

8.4.2 Nitroxide Radical-Bridged Compounds

Derivatives of nitronyl nitroxide represent a class of highly stable organic radicals that feature an unpaired electron delocalized over two coordinating O atoms (see Figure 8.51, top left). Accordingly, these radicals can behave as bis-monodentate ligands and are attractive spin carriers in magnetic materials. The main limitation of these ligands is the poor coordinating ability of the N–O group toward metal ions owing to its weak Lewis basicity. However, this problem can be circumvented by employing electron-withdrawing coligands, such as 1,1,1,5,5,5-hexafluoroacetylacetonate ($hfac^-$), which act to increase the Lewis acidity of the metal centers and thus facilitate the formation of compounds with strong metal–radical bonds. Nitronyl nitroxide radicals are most commonly encountered in 1D chain compounds,[98–112] but they have also been successfully incorporated into networks of higher dimensionalities.[431–435]

The first example of such a framework was the 3D oxamate-based compound $(4\text{-MePyNO})_2Mn^{II}_2(Cu^{II}(opba))_3(DMSO)_2\cdot 2H_2O$ ($4\text{-MePyNO}^{+\bullet}$ = 2-(4-*N*-methylpyridinium)-4,4,5,5-tetramethylimidazoline-1-oxyl-3-oxide radical; $opba^{4-}$ = 1,2-phenylenebis(oxamate)), which features a fully interlocked structure with three distinct spin carriers: $4\text{-MePyNO}^{+\bullet}$ ($S = ½$), Mn^{II} ($S = {}^5/_2$), and Cu^{II} ($S = ½$).[431,432] The structure consists of two nearly perpendicular hexagonal layers with Mn^{II} ions at the corners and Cu^{II} ions at the middle of the edges of each hexagon. Nitronyl nitroxide radical cations link two-thirds of the Cu^{II} centers to form linear chains, thereby connecting the two networks (see Figure 8.52). Variable-temperature dc susceptibility and magnetization data revealed characteristic ferrimagnetic behavior with the occurrence of a long-range order below $T_c = 22.5$ K, owing to strong antiferromagnetic coupling between Mn^{II} and Cu^{II} ions through the oxamate bridge. Moreover, the field dependence of the magnetization indicated that the radical cation interacts ferromagnetically with the Cu^{II} centers in the Cu^{II}-radical chain

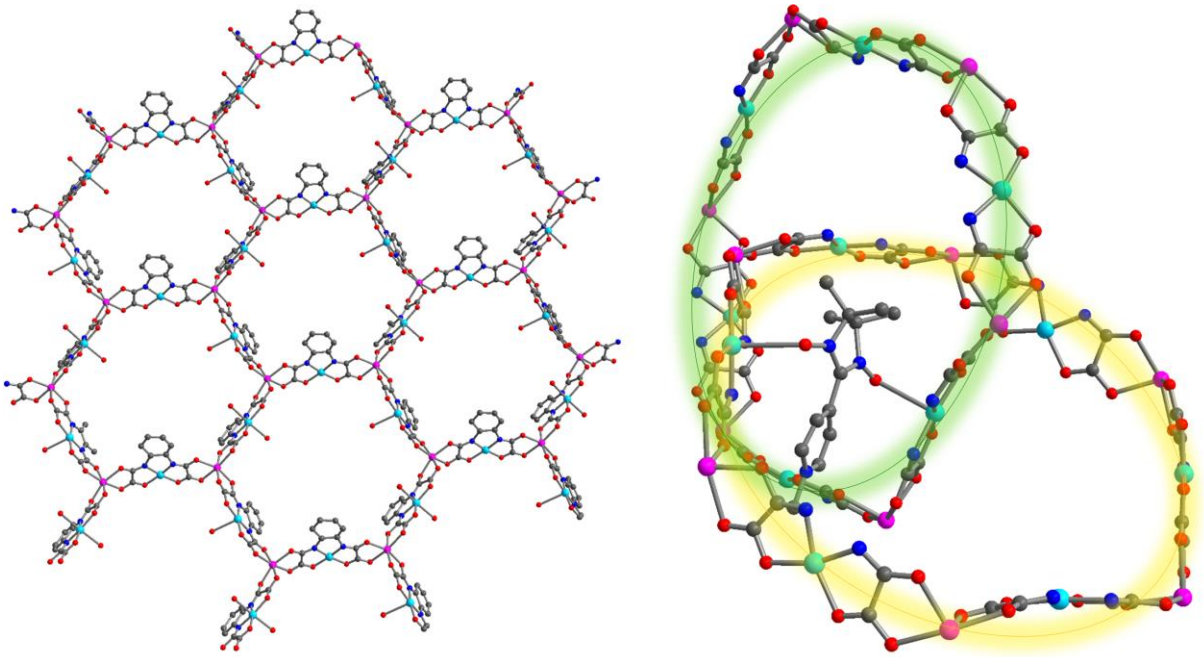

Figure 8.52 Crystal structure of (4-MePyNO)$_2$Mn$^{II}_2$(Cu^{II}(opba))$_3$(DMSO)$_2$·2H$_2$O, highlighting the honeycomb layer (left) and the interlocking motif of two nearly perpendicular hexagons (green and orange) formed by nitronyl nitroxide radical ligands bridging the Cu^{II} centers (right). Cyan, magenta, red, blue, and gray spheres represent Cu, Mn, O, N, and C atoms; H atoms and solvent molecules are omitted for clarity.

and antiferromagnetically with the Mn^{II} ions. Furthermore, this compound behaves as a soft magnet with a small coercive field (H_c < 10 Oe) at 4.2 K.

A similar interlocked structure and ferrimagnetic behavior (T_c = 22.8 K) was observed upon replacement of the methyl groups on the nitroxide radical cations with slightly larger ethyl groups.[433] However, upon exchanging the Mn^{II} ions for more anisotropic Co^{II} centers, the magnetic ordering temperature increased to T_c = 37 K with a drastic enhancement in the coercive field.[433,434] Specifically, the coercive field for the compound (4-EtPyNO)$_2$Co$^{II}_2$(Cu^{II}(opba))$_3$(DMSO)$_{0.5}$·DMSO·0.25H$_2$O (4-EtPyNO$^{+\bullet}$ = 2-(4-*N*-ethylpyridinium)-4,4,5,5-tetramethylimidazoline-1-oxyl-3-oxide radical), as obtained from magnetic hysteresis measurements at 6 K, was found to be highly dependent on the size of the

crystallites. While the largest crystals gave a value of H_c = 8500 Oe, a remarkable coercive field of H_c > 2.4 T was obtained for crystals that were ca. 50 times smaller.[433,434] The analogous (4-EtPyNO)$_2$Ni$^{II}_2$Cu$^{II}_3$ framework exhibits an ordering temperature (T_c = 28 K) and a coercive field (H_c = 500 Oe at 6 K) that fall in between the values for the (4-EtPyNO)$_2$Mn$^{II}_2$Cu$^{II}_3$ and (4-EtPyNO)$_2$Co$^{II}_2$Cu$^{II}_3$ congeners.[434]

A slightly larger increase in T_c was observed when nitronyl nitroxides with Pr substituents were employed.[435] In particular, the isostructural framework (PrPyNO)$_2$Mn$^{II}_2$(Cu^{II}(opba))$_3$·3.3DMSO·5H$_2$O (4-PrPyNO$^{+\bullet}$ = 2-(4-*N*-propylpyridinium)-4,4,5,5-tetramethylimidazoline-1-oxyl-3-oxide radical) features similar ferrimagnetic layers and ferromagnetic chains as the other members of this series of compounds and orders below T_c = 24.1 K. Interestingly, very low temperature magnetization data at 120 mK revealed a metamagnetic-like transition under a magnetic field of ca. 2.1 T, attributed to flipping of half of the radical spins in the Cu^{II}-radical chains.[435]

In addition to the oxamate-based frameworks, where the nitronyl nitroxide radicals act as coligands, two compounds featuring Mn^{II}(hfac)$_2$ complexes bridged by trinitroxide radicals have demonstrated permanent magnetism.[436,437] The employment of the three-fold symmetric ligand 1,3,5-tris(*p*-(*N*-*tert*-butyl-*N*-oxyamino)phenyl)benzene triradical (TOAPB) afforded a 2D layered structure of honeycomb topology. The resulting compound (TOAPB)$_2$(Mn^{II}(hfac)$_2$)$_3$·Hp exhibits long-range magnetic order with T_c = 3.4 K, which was speculated to arise from ferromagnetic coupling between ferrimagnetic layers.[436,437] However, moving to a linear trinitroxide radical that displays much stronger intramolecular nitroxide–nitroxide exchange coupling[438] provided a parallel cross-shaped 3D framework, (BAPN)$_2$(Mn^{II}(hfac)$_2$)$_3$ (BAPN = bis(3-*tert*-butyl-5-(*N*-oxy-

tert-butylamino)phenyl) nitroxide triradical), which orders at T_c = 46 K.[437] The magnetic data for this compound are consistent with antiferromagnetic interactions between Mn^{II} ions and nitroxide radicals, and ferromagnetic coupling between nitroxide radicals within each ligand, giving an overall $S = {}^9/_2$ ground state. Finally, note that despite the radical character of this compound it displays high chemical stability, as no degradation was observed after a year at room temperature in air.

Homoleptic Mn^{II} compounds featuring bis-chelating nitronyl-nitroxide ligands can also give rise to spontaneous magnetization.[439] Here, the metal coordination sphere is free of electron-withdrawing groups. One such compound of formula $[Mn^{II}_2(NITIm)_3](ClO_4)$ ($NITIm^{-\bullet}$ = 2-(2-imidazol-1-ide)-4,4,5,5-tetramethylimidazoline-1-oxyl-3-oxide radical) has been characterized by X-ray diffraction. The structure displays octahedral Mn^{II} centers that are tris-chelated by anionic bis-bidentate nitroxide ligands to give a *mer*-$Mn^{II}N_3O_3$ coordination sphere. These units are arranged into a 2D framework of honeycomb topology, with perchlorate counterions located in the interlayer space. This compound features ferrimagnetic layers, as confirmed by a saturation magnetization value of M_s = 6.7(1) μ_B mol^{-1} that is close to the theoretical value of 7 μ_B mol^{-1} expected for antiferromagnetic coupling between two $S = {}^5/_2$ Mn^{II} ions and three S = ½ radicals. Moreover, the framework exhibits magnetic order below T_c = 1.4 K and a hysteresis loop at 85 mK with a coercive field of H_c = 270 Oe and a remanent magnetization of M_r = 0.22 μ_B mol^{-1}.

8.4.3 Triphenylmethyl Radical-Bridged Compounds

Another stable multitopic organic radical linker suitable for the synthesis of framework materials is the polychlorinated triphenylmethyl tricarboxylate radical ($PTMTC^{3-\bullet}$) (see Figure 8.51, top right). This radical features a central carbon atom with high spin density that is sterically

shielded by the bulky chloro substituents, and the half-life of this species in solution at room temperature under aerobic conditions is estimated to be of the order of 100 years. Furthermore, it is thermally stable to temperatures up to 300 °C.[440] The trigonal symmetry of this polycarboxylato ligand facilitates the formation of 2D and 3D networks.

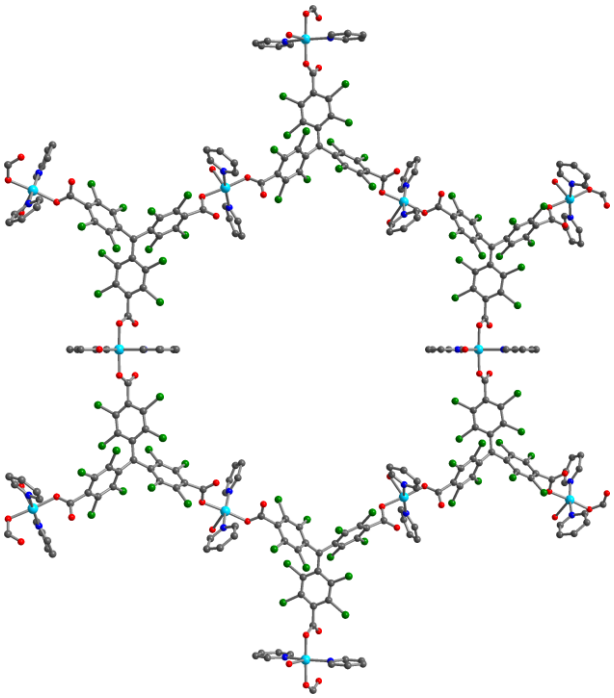

Figure 8.53 Crystal structure of $Cu^{II}_3(PTMTC)_2(py)_6(EtOH)_2(H_2O)\cdot 10EtOH\cdot 6H_2O$, as viewed along the crystallographic *c* axis. Cyan, green, red, blue, and gray spheres represent Cu, Cl, O, N, and C atoms, respectively; H atoms and solvent molecules are omitted for clarity.

The first example of a framework magnet incorporating this tricarboxylate-functionalized radical bridging ligand was the 2D framework compound $Cu^{II}_3(PTMTC)_2(py)_6(EtOH)_2(H_2O)\cdot 10EtOH\cdot 6H_2O$ (py = pyridine) (MOROF-1).[441] The structure of this compound features layers of honeycomb topology, with the central carbon on the $PTMTC^{3-\bullet}$ ligands occupying each vertex of the honeycomb. Each Cu^{II} center resides in a square pyramidal coordination environment made up of two monodentate carboxylate groups, two pyridine ligands, and one EtOH or H_2O molecule (see Figure 8.53). Eclipsed stacking of the layers generates 1D hexagonal channels with very large pores (31 × 28 $Å^2$).

Desolvation of this compound occurs rapidly at room temperature with dramatic contraction in crystal volume (25–35%) and complete loss of crystallinity. However, the original structure is mostly recovered upon soaking the material in EtOH or MeOH, as confirmed by PXRD analysis.

Notably, other organic solvents were unable to induce this quasi-reversible "shrinking–breathing" process. Variable-temperature dc magnetic susceptibility measurements on a crystalline sample in contact with EtOH revealed antiferromagnetic interactions between Cu^{II} and radical linkers to give an overall ferrimagnetic interaction, with a minimum value of $\chi_M T$ at 31 K followed by a rapid upturn. The large increase in the value of $\chi_M T$ at low temperature suggests the onset of a long-range magnetic order, which was confirmed by ac susceptibility measurements. In contrast, the desolvated compound behaves as a paramagnet.[441]

Treatment of the $PTMTC^{3-\bullet}$ radical ligand with Co^{II} ions afforded a framework with a different topology and distinct magnetic behavior.[442] Specifically, this compound of formula $Co^{II}_6(PTMTC)_4(py)_{17}(EtOH)(H_2O)_4$ (MOROF-3) exhibits an unusual (6,3)-helical 2D structure, and isothermal magnetization measurements at 1.8 K suggested coexisting ferro- and antiferromagnetic interactions between Co^{II} ions and $PTMTC^{3-\bullet}$ radicals. This behavior was attributed to the presence of mixed mono- and bidentate ligand binding modes in the structure and the asymmetry of the trigonal nodes. This compound did not reveal hysteretic behavior at 1.8 K; however, an onset of a signal in the out-of-phase ac susceptibility (χ_M'') under an external dc field of 500 Oe suggested that long-range magnetic order may occur at a lower temperature.

8.4.4 Organonitrile Radical-Bridged Compounds

8.4.4.1 TCNE Radical-Bridged Compounds

Building on the remarkable permanent magnetic behavior above room temperature observed for the amorphous compound $V(TCNE)_x \cdot yCH_2Cl_2$ ($x \approx 2$; $y \approx 0.5$),[83–86] a tremendous effort has been directed toward synthesizing and structurally-characterizing related materials featuring $TCNE^{-\bullet}$ radical ligands. Such in-depth structural analysis is critical to deduce the structure–

property relationships for this family of magnets and to enable the rational design of molecule-based magnets with high ordering temperatures for targeted applications.

The first structurally-characterized framework magnet featuring the $TCNE^{-\bullet}$ radical anion was the compound $[Fe^{II}(TCNE^{-\bullet})(MeCN)_2](Fe^{III}Cl_4)$ reported in 2006.[443] The structure, obtained from Rietveld refinement of synchroton PXRD data, is comprised of corrugated layers of Fe^{II} ions bridged by planar μ_4-$TCNE^{-\bullet}$ radical anions. The octahedral coordination sphere of the Fe^{II} centers is completed by two axial MeCN molecules and the interlayer space is occupied by $(Fe^{III}Cl_4)^-$ anions. This compound orders as an antiferromagnet below 90 K, and this order was attributed to antiferromagnetic coupling between ferrimagnetic $[Fe^{II}(TCNE^{-\bullet})(MeCN)_2]^+$ layers. However, this state is only metastable due to a strong structural magnetic anisotropy, and an irreversible transformation to a more stable ferrimagnetic state was observed upon application of a small magnetic field. Accordingly, this compound exhibits magnetic hysteresis at 50 K with a coercive field of H_c = 1730 Oe and a remanent magnetization of M_r = 7500 Oe cm^3 mol^{-1}.

More recently, the minimal impact of the counteranion on the 2D layered structure and magnetic properties for this type of compound was demonstrated.[444] In particular, replacing the $(Fe^{III}Cl_4)^-$ ions with larger $(Sb^{V}F_6)^-$ ions afforded the isostructural compounds $[M^{II}(TCNE^{-\bullet})(MeCN)_2](Sb^{V}F_6)\cdot x CH_2Cl_2 \cdot y MeCN$ (M^{II} = Mn^{II}, Fe^{II}) that display long-range magnetic order below 67 and 96 K for M^{II} = Mn^{II} and Fe^{II}, respectively. The Mn^{II} congener exhibits additional spin glass behavior, speculated to stem from the presence of a significant amount of an amorphous phase originating from partial loss of axially coordinated MeCN molecules.

Another important step toward better understanding the magnetic properties of $TCNE^{-\bullet}$ radical-based systems was the structural characterization of the compound

$Fe^{II}(TCNE)_2 \cdot 0.32CH_2Cl_2$.[445] Its structure possesses corrugated layers of octahedral Fe^{II} centers each bonded to four μ_4-$TCNE^{-\bullet}$ radical anions, and these layers are connected by diamagnetic μ_4-$[C_4(CN)_8]^{2-}$ ions to generate a 3D framework. Note that the diamagnetic ligands were formed in situ through the dimerization of $TCNE^{-\bullet}$ radical anions via C–C bond formation. Accordingly, the compound is best formulated as $Fe^{II}(TCNE^{-\bullet})[C_4(CN)_8]_{0.5} \cdot 0.32CH_2Cl_2$. The dominant spin interaction contributing to the ferrimagnetic behavior for this compound is the antiferromagnetic direct exchange coupling between Fe^{II} and $TCNE^{-\bullet}$ radical anions in the layers.[445] The realization of a mixture of paramagnetic and diamagnetic TCNE ligands in this compound clarified its high saturation magnetization value and the similar ordering temperature of ca. 100 K as observed for the previously characterized 2D layered frameworks discussed above.[87,88,445]

The isostructural Mn^{II} analogue of the mixed-TCNE ligand framework, $Mn^{II}(TCNE^{-\bullet})[C_4(CN)_8]_{0.5} \cdot 0.74CH_2Cl_2$, has also been reported.[72] Here, significant antiferromagnetic interactions between ferrimagnetic layers via the diamagnetic $[C_4(CN)_8]^{2-}$ ligands give rise to dominant antiferromagnetic behavior. This framework exhibits long-range antiferromagnetic order with T_N = 68 K, as determined by an insignificant χ_M'' signal and the coincidence of zero-field-cooled and field-cooled magnetization data.

The reaction of TCNE with $Mn^{II}I_2(THF)_3$ in CH_2Cl_2 afforded two compounds with drastically different structures depending on the reaction time. Interestingly, both compounds exhibit a magnetic ordering temperature of T_c = 171 K, which represents the current record among structurally-characterized MOF magnets.[72,73] A reaction time of two days gave the 3D framework $Mn^{II}(TCNE^{-\bullet})_{1.5}(I_3)_{0.5} \cdot 0.5THF$.[72] In contrast to the 3D frameworks discussed above, this

compound features exclusively $TCNE^{-\bullet}$ radical ligands. The structure comprises octahedral Mn^{II} ions bonded to six different μ_4-$TCNE^{-\bullet}$ ligands, four of which are involved in forming corrugated sheets and the other two bridge adjacent planes (see Figure 8.54, top). Notably, the angle between intra- and interlayer Mn^{II}–N bonds is ca. 90° and isolated linear chains of I_3^- ions are present for charge compensation. Variable-temperature dc susceptibility and magnetization measurements revealed characteristic ferrimagnetic behavior with a sharp upturn in $\chi_M T$ at ca. 185 K and a bifurcation temperature for the zero-field-cooled (ZFC) and field-cooled (FC) magnetization data of T_b = 171 K (see Figure 8.54, center and bottom). The presence of long-range magnetic order was further confirmed by ac susceptibility studies, and magnetic hysteresis was

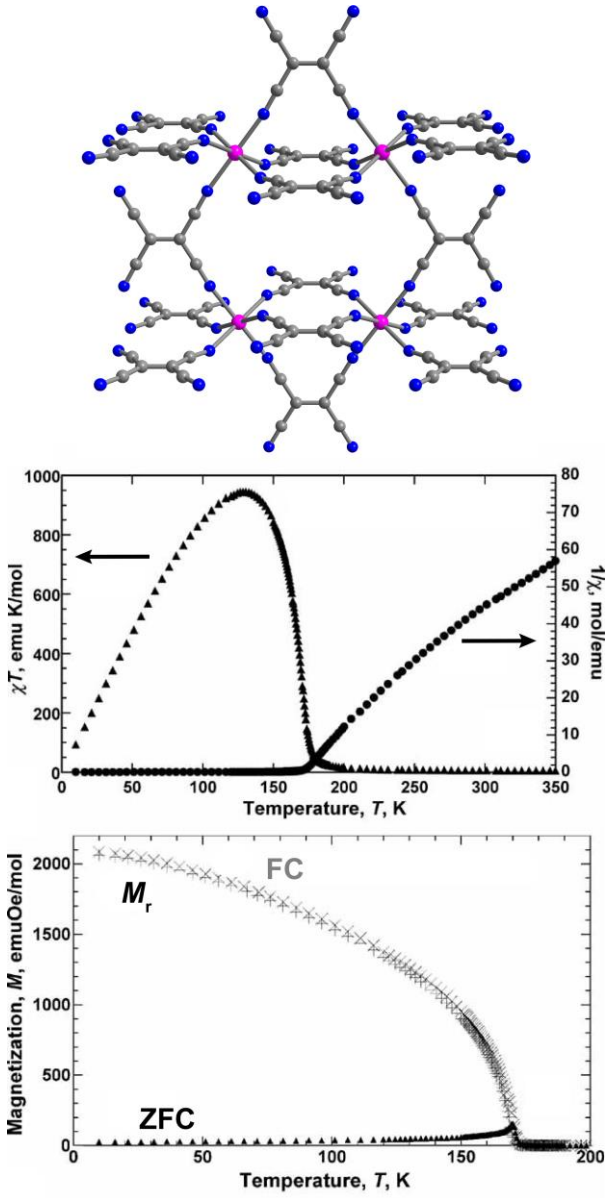

Figure 8.54 Top: Crystal structure of $Mn^{II}(TCNE^{-\bullet})_{1.5}(I_3)_{0.5}\cdot 0.5THF$. Magenta, blue, and gray spheres represent Mn, N, and C atoms, respectively; I_3^- ions and solvent molecules are omitted for clarity. Center: Variable-temperature dc magnetic susceptibility data for $Mn^{II}(TCNE^{-\bullet})_{1.5}(I_3)_{0.5}\cdot 0.5THF$, collected at 1000 Oe. Bottom: Zero-field-cooled (ZFC) and field-cooled (FC) magnetization data for $Mn^{II}(TCNE^{-\bullet})_{1.5}(I_3)_{0.5}\cdot 0.5THF$, collected at 5 Oe. Reproduced from ref. 72 with permission from Wiley-VCH Verlag GmbH & Co.

observed at 10 K with a coercive field of H_c = 600 Oe and a remanent magnetization of M_r = 8000 Oe cm^3 mol^{-1}. Overall, this magnetic behavior is indicative of a soft 3D ferrimagnet, which can be attributed to direct antiferromagnetic coupling between Mn^{II} and $TCNE^{-\bullet}$ radical ligands within and between layers. Interestingly, preliminary experiments revealed that the ordering temperature increases upon application of an external pressure, reaching a value of T_c = 273 K under 14.2 kbar pressure.[72]

The second compound, a 2D framework of the formula $Mn^{II}(TCNE^{-\bullet})I(H_2O)$, was obtained after allowing the reaction solution to stand for six months.[73] This species features a similar corrugated layered structure as $[M^{II}(TCNE^{-\bullet})(MeCN)_2]^+$ (M^{II} = Mn^{II}, Fe^{II}), albeit with two distinct environments for the μ_4-$TCNE^{-\bullet}$ ligands owing to different dihedral angles between the mean $Mn^{II}N_4$ and TCNE-C_6 planes (see Figure 8.55). Furthermore, the interlayer separation of 5.00 Å is significantly shorter than those in other structurally-characterized M^{II}-TCNE frameworks, which are all above 8.0 Å. The magnetic properties for this

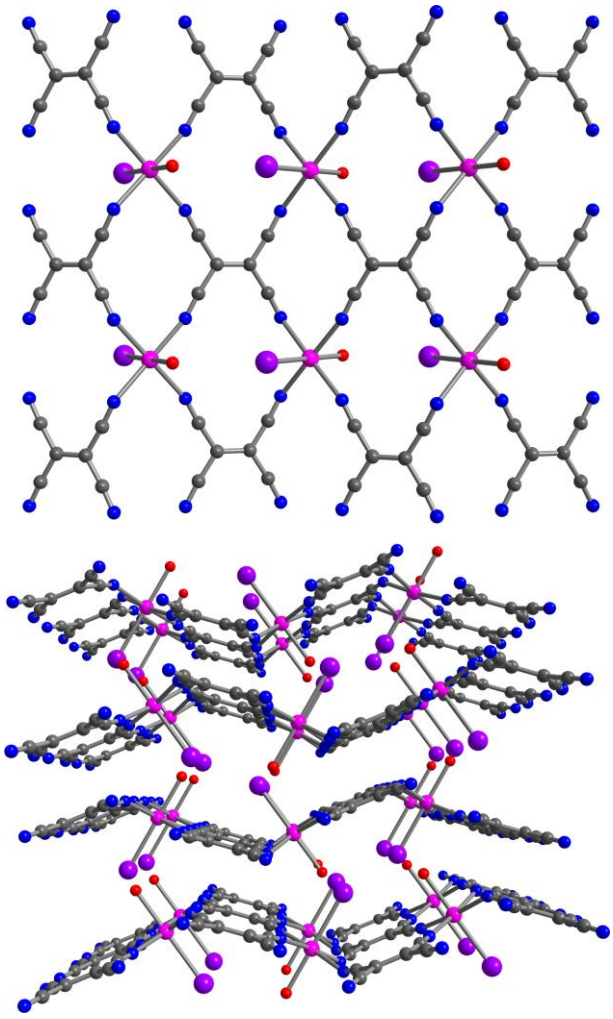

Figure 8.55 Crystal structure of $Mn^{II}(TCNE^{-\bullet})I(H_2O)$, as viewed along the crystallographic *b* (top) and *c* axis (bottom), highlighting the corrugated layered structure and two types of μ_4-$TCNE^{-\bullet}$ ligand environments. Violet, magenta, red, blue, and gray spheres represent I, Mn, O, N, and C atoms, respectively; H atoms are omitted for clarity.

compound are very similar to those observed for the 3D framework $Mn^{II}(TCNE^{-\bullet})_{1.5}(I_3)_{0.5}\cdot 0.5THF$. Specifically, the zero-field-cooled (ZFC) and field-cooled (FC) magnetization curves measured under an applied field of 5 Oe revealed a bifurcation temperature of T_b = 172 K and a remanent magnetization that was coincident with the field-cooled data. The latter provided an ordering temperature of T_c = 171 K, which was in agreement with ac susceptibility data. Furthermore, magnetic hysteresis at 10 K revealed a coercive field of H_c = 400 Oe and a remanent magnetization of M_r = 60 Oe cm^3 mol^{-1}.

The long-range order for $Mn^{II}(TCNE^{-\bullet})I(H_2O)$ was attributed to antiferromagnetic interactions between canted ferrimagnetic 2D layers. The lower saturation and remanent magnetization values compared to those obtained for $Mn^{II}(TCNE^{-\bullet})_{1.5}(I_3)_{0.5}\cdot 0.5THF$ provided support for this interpretation. Furthermore, the short inter- and intralayer distances, along with the high value of T_c suggest a 3D magnetic order for this compound, and thus non-negligible interlayer interactions. Finally, note that both $Mn^{II}(TCNE^{-\bullet})I(H_2O)$ and $Mn^{II}(TCNE^{-\bullet})_{1.5}(I_3)_{0.5}\cdot 0.5THF$ are soft magnets, which is expected given the nearly isotropic Mn^{II} centers in these compounds.

8.4.4.2 TCNQ Radical-Bridged Compounds

In addition to extensive studies on TCNE-based radical systems, compounds featuring the larger derivative 7,7,8,8-tetracyano-*p*-quinodimethane (TCNQ) have also been of immediate interest owing to the higher chemical tunability of this building unit. Specifically, the central aromatic ring can be functionalized with various substituents to tune both electronic and steric properties of the ligand (see Figure 8.51, bottom left). Linkers based on TCNQ derivatives have been of particular focus in the design of electrically conductive framework magnets. For that purpose, the employment of electron-rich dimeric Ru_2 paddlewheel building units and TCNQ-

based linkers has been highly successful, affording a number of frameworks that display permanent magnetic behavior.[446–452] Here, an electron transfer from the Ru^{II}_2 moieties to TCNQ-based ligands ($TCNQR_x$; R denotes the type of substituent on the aromatic ring and *x* denotes the number of substituents) can lead to a mixed-valence state of the form $[Ru_2^{4.5+}]$–$(TCNQR_x^{-\bullet})$–$[Ru_2^{4.5+}]$. Such electron transfer results in magnetic double-exchange interactions between $S = 1$ Ru^{II}_2 and $S = {}^3/_2$ $Ru^{II,III}_2$ units via the $TCNQR_x^{-\bullet}$ ($S = ½$) radical anion that may lead to long-range magnetic order.

The first example of a successful implementation of this strategy to generate a magnet was the 2D framework compound $(Ru_2(TFA)_4)_2(TCNQF_4)\cdot 3(p\text{-xylene})$ (TFA^- = trifluoroacetate; $TCNQF_4$ = 2,3,5,6-tetrafluoro-7,7,8,8-tetracyano-*p*-quinodimethane).[446,447] The structure of this compound displays $Ru_2(TFA)_4$ paddlewheel units with two cyano groups from distinct $TCNQF_4$ ligands coordinated to the axial sites of the Ru centers. The overall structure has a fishnet-like hexagonal topology (see Figure 8.56, top). The $Ru–O_{equatorial}$ bond distance is strongly influenced by the oxidation state of the Ru_2 paddlewheel core,

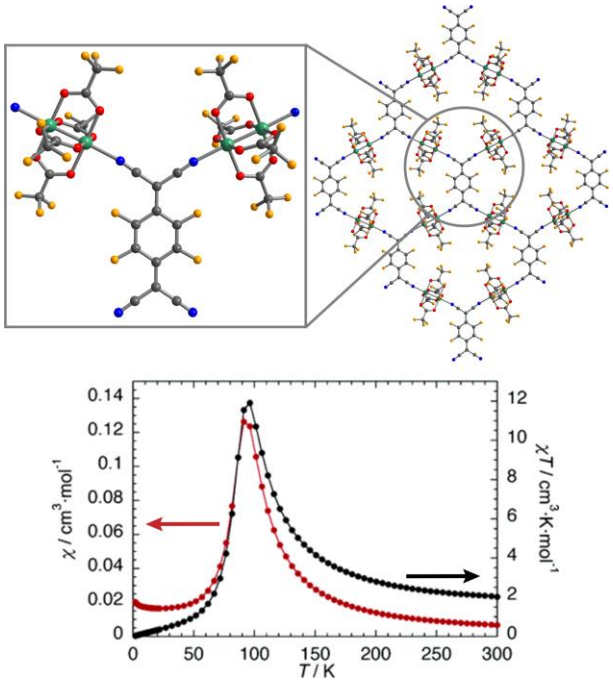

Figure 8.56 Top: Crystal structure of $(Ru_2(TFA)_4)_2(TCNQF_4)\cdot 3(p\text{-xylene})$, highlighting the paddlewheel unit (left) and the fishnet-like hexagonal topology (right). Green, light orange, red, blue, and gray spheres represent Ru, F, O, N, and C atoms, respectively; solvent molecules are omitted for clarity. Bottom: Variable-temperature dc magnetic susceptibility data for $(Ru_2(TFA)_4)_2(TCNQF_4)\cdot 3(p\text{-xylene})$, collected under an applied field of 1 T. Reprinted with permission from ref. 446. Copyright 2006 American Chemical Society.

indicative here of the partially oxidized state $Ru_2^{4.5+}$. Furthermore, analysis of the degree of charge transfer using the Kistenmacher relationship[453] for the $TCNQF_4$ ligand was consistent with one-electron transfer from two $Ru_2^{II}(TFA)_4$ units to one $TCNQF_4$ ligand, such that this compound is better formulated as $(Ru_2^{4.5+}(TFA)_4)(TCNQF_4^{-\bullet})(Ru_2^{4.5+}(TFA)_4)\cdot 3(p\text{-xylene})$. This compound exhibits long-range antiferromagnetic order below T_N = 95 K, as evidenced by a maximum value of $\chi_M T$ at 96 K (see Figure 8.56, bottom) and no χ_M'' signal. Additionally, a spin-flop transition to a paramagnetic phase was observed with a critical field of 4740 Oe at 1.82 K, and a large open butterfly-type hysteresis loop indicated an intermediate canted spin phase.

This metamagnetic-like behavior was posited to stem from antiferromagnetic interactions between strongly coupled magnetic layers and the strong magnetic anisotropy from the Ru_2 units. Notably, the room-temperature electrical conductivity for this compound is $\sigma = 4.6 \times 10^{-4}$ S cm^{-1}, which is 100 times greater than that observed for the analogue bearing Ru^{II}_2 and a diamagnetic TCNQ bridging ligand. Along these lines, the electron affinity of the $TCNQR_x$ acceptor plays a critical role in determining the efficiency of electron-transfer from the Ru_2^{II} core.[454,455] Indeed, the mixed-valence state was not accessed when the $TCNQF_4$ ligand was replaced by less electronegative TCNQ derivatives, including $TCNQH_4$, $TCNQBr_2$, $TCNQCl_2$, and $TCNQF_2$.[447] Accordingly, those compounds showed only paramagnetic behavior.

Interestingly, the mixed-valence state could also be accessed by employing Ru_2 paddlewheel units with 1,2-chlorobenzoate (1,2-$Clbz^-$) ligands in conjunction with $TCNQ(OMe)_2$ (2,5-dimethoxy-7,7,8,8-tetracyano-*p*-quinodimethane) bridging ligands.[448] The resulting compound $(Ru_2^{4.5+}(1,2\text{-}Clbz)_4)(TCNQ(OMe)_2^{-\bullet})(Ru_2^{4.5+}(1,2\text{-}Clbz)_4)\cdot CH_2Cl_2$ is isostructural to the 2D network described above and shows similar long-range antiferromagnetic order under low external

magnetic fields (H < 300 Oe) with T_N = 75 K, along with metamagnetic behavior. However, this compound undergoes a near reversible desolvation process without losing crystallinity, with associated changes in magnetic properties. Specifically, the desolvated framework behaves as a ferromagnet below $T_C \approx 56$ K, as evidenced by the growth of a χ_M'' signal during the desolvation process. The difference in magnetic behavior for the two compounds was attributed to slight structural changes caused by the order/disorder of 1,2-$Clbz^-$ ligands. In particular, the disorder of the phenyl groups in the desolvated framework was speculated to disturb the antiferromagnetic interlayer interactions that are responsible for the antiferromagnetic behavior of the solvated framework.[448] Note that the magnetic properties of TCNQ-based frameworks had previously been shown to be altered by a reversible desolvation/solvation process.[456] However, in that case, only the poorly crystalline desolvated compound displayed magnet-like behavior.

Another fascinating example of how drastic changes in magnetic behavior can be induced by desolvation/solvation treatments is the isostructural compound $(Ru_2(2,3,5\text{-}Clbz)_4)_2(TCNQMe_2)\cdot 4CH_2Cl_2$ (2,3,5-$Clbz^-$ = 2,3,5-trichlorobenzoate; $TCNQMe_2$ = 2,5-dimethyl-7,7,8,8-tetracyano-*p*-quinodimethane).[449] The solvated framework displays a charge-localized state that is formulated as $(Ru_2^{4+}(2,3,5\text{-}Clbz)_4)(TCNQMe_2^{-\bullet})(Ru_2^{5+}(2,3,5\text{-}Clbz)_4)\cdot 4CH_2Cl_2$ and orders below T_c = 101 K owing to ferromagnetic interactions between ferrimagnetic layers. In contrast, the desolvated framework displays a charge-disproportionate disordered state at ca. 100 K with a formula of $(Ru^{4/5+}{}_2(2,3,5\text{-}Clbz)_4)(TCNQMe_2^{-\bullet}/TCNQMe_2^{2-})(Ru_2^{5+}(2,3,5\text{-}Clbz)_4)$. This electronic state transfers to the nearly fully charge-transferred state of formula $(Ru_2^{5+}(2,3,5\text{-}Clbz)_4)(TCNQMe_2^{2-})(Ru_2^{5+}(2,3,5\text{-}Clbz)_4)$ at high temperatures. The desolvated framework also orders as a ferrimagnet, but with a drastically lower ordering temperature of T_c = 34 K that is in

accord with the presence of both $TCNQMe_2^{-\bullet}$ radical and diamagnetic dianionic bridging ligands. Notably, the desolvation/solvation process is mostly reversible, both with respect to structural and magnetic properties, demonstrating a switchable change in the magnetic ordering temperature of ca. 70 K, achieved by guest-induced electronic state and slight structural modulations. Although the electrical conductivity for these compounds has not been reported, this study highlights that a guest-induced modulation of electronic states may be an attractive route toward multifunctional magnetic MOFs and other porous materials.

A similar modification of the electronic states for these compounds was achieved by tuning the electron-donating ability of the TCNQ ligands.[450] Specifically, changing the position of fluorine atoms on the aromatic ring from *ortho* to *meta* to *para* afforded a series of three compounds of the general formula $(Ru_2(1,x\text{-}Fbz)_4)_2(TCNQ(OMe)_2)\cdot$solvent (1,*x*-$Fbz^-$ =1,*x*-difluorobenzoate; x = 2–4) that exhibit different charge-ordered states. While the framework bearing 1,2-Fbz^- ligands displays the mixed-valence state $(Ru_2^{4+}(1,2\text{-}Fbz)_4)(TCNQ(OMe)_2^{-\bullet})(Ru_2^{5+}(1,2\text{-}Fbz)_4)$, the analogue with 1,3-$Fbz^-$ ligands features exclusively Ru_2^{5+} paddlewheel units and diamagnetic $TCNQ(OMe)_2^{2-}$ linkers. On the other hand, the derivative bearing 1,4-Fbz^- ligands represents the intermediate charge-disproportionate ordered state with a mixture of Ru_2^{4+}, Ru_2^{5+}, $TCNQ(OMe)_2^{-\bullet}$, and $TCNQ(OMe)_2^{2-}$ moieties in the ratio 1:3:1:1, similar to the desolvated $(Ru_2(2,3,5\text{-}Clbz)_4)_2(TCNQMe_2)$ framework discussed above. The mixed-valence framework exhibits long-range ferrimagnetic order with T_c = 88 K, followed by antiferromagnetic order at T_N = 83 K, ascribed to antiferromagnetic coupling between ferrimagnetic layers. In contrast, the charge-disproportionate framework orders as a ferrimagnet at a much lower temperature of T_c = 27 K, owing to the alternating arrangement of strongly coupled

ferrimagnetic and weakly coupled paramagnetic domains via $TCNQ(OMe)_2^{-\bullet}$ and $TCNQ(OMe)_2^{2-}$ ligands, respectively. This change in T_c with charge state is in accord with the study discussed above. Note that this electronic state modulation can also be tuned by applied pressure.

Additional functional groups, such as 1,2,5-thiadiazole moieties, can be incorporated onto the TCNQ backbone to afford suitable bridging ligands for the synthesis of framework magnets. Two such 2D frameworks of fishnet-like topology feature localized mixed-valence $[Ru_2^{4+}]$–((BTDA-TCNQ)$^{-\bullet}$)–$[Ru_2^{5+}]$ (BTDA-TCNQ = bis(1,2,5-thiadiazolo)tetracyano-*p*-quinodimethane) states and exhibit ordering temperatures of T_c = 83–93 K, in accord with other members of this class of frameworks discussed above.[451] In addition, one 3D framework magnet featuring this ligand has been synthesized. This compound, $(Ru_2(1,3\text{-}Fbz)_4)_2(BTDA\text{-}TCNQ)\cdot 1.6(4\text{-}ClPhMe)\cdot 3.4CH_2Cl_2$, features similar Ru_2 paddlewheel units as the

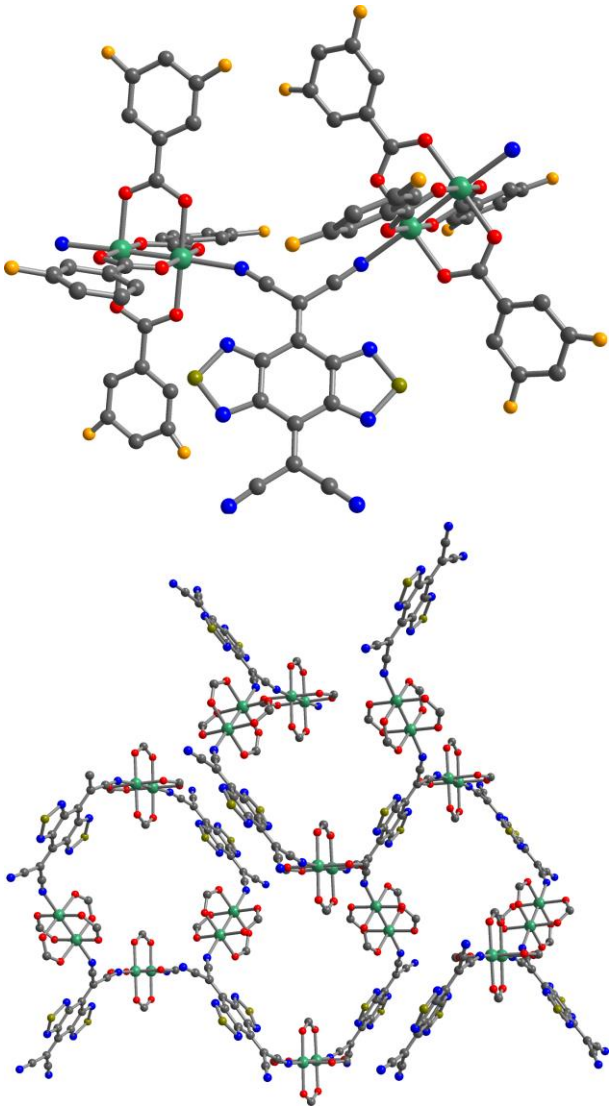

Figure 8.57 Crystal structure of $(Ru_2(1,3\text{-}Fbz)_4)_2(BTDA\text{-}TCNQ)\cdot 1.6(4\text{-}ClPhMe)\cdot 3.4CH_2Cl_2$, highlighting the paddlewheel unit (top) and the helical 3D network (bottom) viewed along the crystallographic *a* axis. Green, gold, light orange, red, blue, and gray spheres represent Ru, S, F, O, N, and C atoms, respectively; H atoms and solvent molecules are omitted for clarity.

2D frameworks, however, twisting of the μ_4-(BTDA-TCNQ) bridging ligands leads to the formation of helical chains that connect into a 3D network (see Figure 8.57).[452] Bond length analysis implies a charge-localized state with non-integer values, $(Ru_2^{(4+\delta)+}(1,3\text{-Fbz})_4)((BTDA\text{-}TCNQ)^{(1+\delta)-})(Ru_2^{5+}(1,3\text{-Fbz})_4)$ ($\delta \approx 0.1$–0.4). This compound exhibits long-range magnetic order with T_c = 107 K and coercive fields were detected up to 100 K, providing a value of H_c = 7250 Oe at 1.8 K.[452] Indeed, this is the highest magnetic ordering temperature reported for a TCNQ-based magnet. Note, however, that the value of T_c for this only example of a 3D TCNQ-based magnet is only 6 K higher than that for the best 2D analogue.[449] Both compounds feature the same charge-localized one-electron transfer state, as such a double-exchange mechanism is likely needed to provide much higher ordering temperatures for this family of magnets.

Finally, a homologous series of compounds of formula $M^{II}(TCNQ)_2$ (M^{II} = Mn^{II}, Fe^{II}, Co^{II}, Ni^{II}) has been reported to show spontaneous magnetization.[90] These compounds exhibit ordering temperatures of T_c = 7–44 K and behave as glassy magnets. However, owing to their poor structural characterization, these compounds will not be discussed further in this review.

8.4.5 Semiquinoid Radical-Bridged Compounds

As illustrated in the previous section, 2D framework magnets featuring diamagnetic tetraoxolene linkers exhibit high chemical tunability but modest magnetic ordering temperatures owing to the relatively weak superexchange coupling between metal centers through long diamagnetic linkers. As such, taking advantage of the facile redox chemistry of benzoquinoid ligands and building on the promise of the radical-bridged systems discussed above, recent efforts have focused on incorporating semiquinoid radical linkers into frameworks.

The compound $(Me_2NH_2)_2[Fe_2(Cl_2An)_3]\cdot 2H_2O\cdot 6DMF$ (Cl_2An^{2-} = chloranilate) represents the first example of a structurally-characterized extended solid with tetraoxolene radical linkers.[457] The structure of this compound features 2D honeycomb layers, with each Fe center ligated by three bis-bidentate chloranilate ligands. The layers are eclipsed, leading to the formation of 1D hexagonal channels, and the charge of the dianionic network is compensated by $(Me_2NH_2)^+$ ions situated in the pores within the layers. Bond distance analysis, in conjunction with Raman and Mössbauer spectroscopy, revealed delocalized ligand mixed-valency and the presence of exclusively high-spin Fe^{III} ions. As such, spontaneous electron transfer from the Fe^{II} starting material to Cl_2An^{2-} occurred during synthesis to provide a framework best formulated as $[Fe^{III}_2(Cl_2An^{8/3-})_3]^{2-}$. Variable-temperature magnetization studies showed a spontaneous magnetization to occur below 100 K (see Figure 8.58). The long-range order, which was posited to be of 2D ferrimagnetic nature, was confirmed by ac susceptibility measurements to provide an ordering temperature of T_c = 80 K. This compound behaves as a glassy magnet with a coercive field of H_c = 2630 Oe at 1.8 K. Furthermore, the framework remains intact upon desolvation and exhibits a very high Brunauer–Emmett–Teller (BET) surface area of 885(105) $m^2\ g^{-1}$. The desolvated

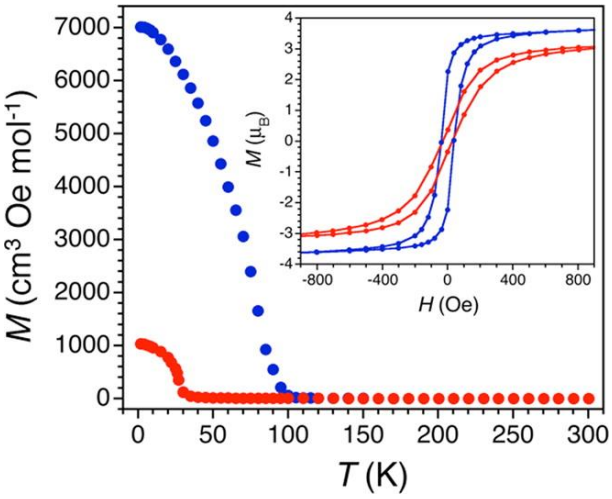

Figure 8.58 Variable-temperature field-cooled dc magnetization data for $(Me_2NH_2)_2[Fe_2(Cl_2An)_3]\cdot 2H_2O\cdot 6DMF$ (blue) and $(Me_2NH_2)_2[Fe_2(Cl_2An)_3]$ (red), collected under an applied field of 10 Oe. Inset: Variable-field dc magnetization data for $(Me_2NH_2)_2[Fe_2(Cl_2An)_3]\cdot 2H_2O\cdot 6DMF$ at 60 K (blue) and $(Me_2NH_2)_2[Fe_2(Cl_2An)_3]$ at 10 K (red). Reprinted with permission from ref. 457. Copyright 2015 American Chemical Society.

compound also displays ferrimagnetic behavior, albeit with a lower ordering temperature of T_c = 26 K, attributed to structural distortions of the framework. Accordingly, this framework magnet adds to the handful of metal-organic compounds that display reversible solvent-induced switching of magnetic ordering temperature. Furthermore, this compound exhibits high room-temperature electrical conductivity values of σ = 1.4(7) × 10^{-2} and 1.0(3) × 10^{-3} S cm^{-1} for the solvated and desolvated forms, respectively.[458] The coexistence of high-temperature magnetic order and high conductivity, as observed for these frameworks, is remarkable and nearly unprecedented in a metal-organic material (see Figure 8.59).

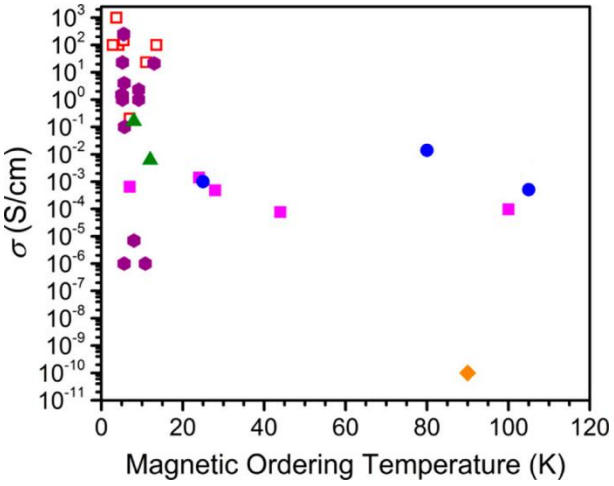

Figure 8.59 Plot comparing the magnetic ordering temperature and room-temperature electrical conductivity values for structurally-characterized metal-organic solids, highlighting the ability of 2D semiquinoid frameworks to exhibit high values of both properties. Blue circles = 2D semiquinoid frameworks; purple hexagons = metal-oxalate solids cocrystallized with conductive cations; magenta squares = TCNQ-bridged solids; green triangles = 3D iron-quinoid solids; orange diamonds = TCNE-bridged solids; hollow red squares = halogen-bonded salts. Reprinted with permission from ref. 458. Copyright 2017 American Chemical Society.

This compound can be reduced by one electron per formula unit with Cp_2Co^{II} (Cp^- = cyclopentadienyl anion) via post-synthetic single-crystal-to-single-crystal process to afford the compound $[Cp_2Co^{III}]_{1.43}(Me_2NH_2)_{1.57}[Fe^{III}_2(Cl_2An^{3-\bullet})_3]\cdot 4.9DMF$, which features exclusively $Cl_2An^{3-\bullet}$ radical bridging ligands. The 2D honeycomb structure remains intact and despite a net decrease in overall spin magnitude, the reduced compound exhibits long-range order with T_c = 105 K, which represents an increase of 25 K over that for the parent framework. This behavior was attributed to stronger intralayer coupling due to increased radical character and anionic charge of

the chloranilate ligands. This framework was also tentatively described as a 2D ferrimagnet. Notably, this compound exhibits an open magnetic hysteresis loop up to 100 K with coercive fields of H_c = 4520 and 9 Oe at 1.8 and 100 K, respectively. However, the room-temperature electrical conductivy for the reduced compound is $\sigma = 5.1(3) \times 10^{-4}$ S cm^{-1}, which is significantly less than that for the parent framework. The decrease in conductivity was hypothesized to arise from loss of ligand mixed-valency, as facile charge hopping is prevented when the hole is filled by an electron. Nevertheless, these combined values of T_c and σ are exceptionally high for metal-organic materials (see Figure 8.59), highlighting the tremendous potential for metal-semiquinoid frameworks as conductive magnets.

There is also a great interest in developing materials with simultaneously switchable magnetic and electrical properties, as they may enable dramatic improvements in spintronic technologies including data storage and processing.[459] Toward this end, the paramagnetic 2D Mn^{II} benzoquinoid framework compound $(Me_4N)_2[Mn^{II}_2(Cl_2An^{2-})_3]\cdot 3.2Et_2O$ was reduced by three electrons via post-synthetic single-crystal-to-single-crystal chemical reduction process, in analogy to the Fe^{III} framework discussed above, to afford the

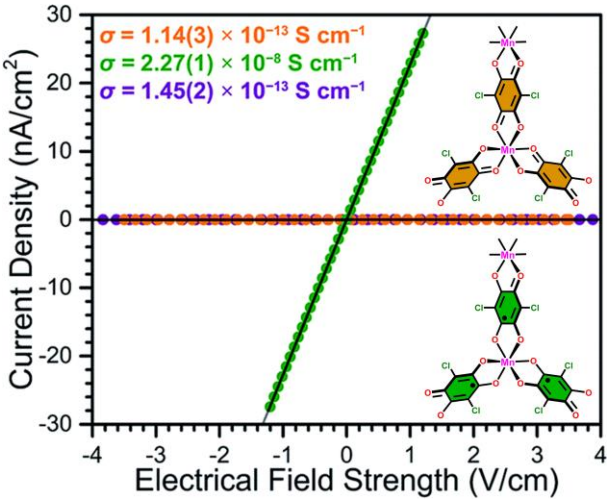

Figure 8.60 Plot of current density vs electrical field strength for $(Me_4N)_2[Mn^{II}_2(Cl_2An^{2-})_3]\cdot 3.2Et_2O$ (orange) and $Na_3(Me_4N)_2[Mn^{II}_2(Cl_2An^{3-\bullet})_3]\cdot 3.9THF$ (green), collected at 295 K, highlighting the much higher electrical conductivity for the latter compound. Inset: Schematic of the repeating units in these compounds with diamagnetic ligands in orange and radical ligands in green. The violet data points correspond to the re-oxidized compound, highlighting the reversibility of the redox-switching process. Reproduced from ref. 460 with permission from the Royal Society of Chemistry.

compound $Na_3(Me_4N)_2[Mn^{II}_2(Cl_2An^{3-\bullet})_3]\cdot 3.9THF$.[460] This reduced compound is a permanent magnet below T_c = 41 K (H_c = 300 Oe at 1.8 K) and exhibits a room-temperature conductivity value of $\sigma = 2.27(1) \times 10^{-8}$ S cm^{-1}, which is 200,000-fold higher than that for the parent compound (see Figure 8.60). Importantly, this redox chemistry is reversible (see Figure 8.60). While both the magnetic ordering temperature and electrical conductivity are modest, this framework provides an important proof-of-principle example that highlights the ability of MOFs to serve as a facile platform to achieve simultaneous redox-switching of permanent magnetic behavior and electrical conductivity.

In addition to these 2D metal-semiquinoid magnets, a structurally-characterized 3D framework of similar composition has demonstrated long-range magnetic order.[461] The compound $(Bu_4N)_2[Fe^{III}_2(dhbq^{3-\bullet})_2(dhbq^{2-})]$ ($dhbq^{2-}$ = 2,5-dioxidobenzoquinone) displays similar ligand mixed-valency as the 2D analogue above, with formally two $dhbq^{3-\bullet}$ radical ligands and one diamagnetic $dhbq^{2-}$ ligand per formula unit. The type of mixed-valency in this compound was established as Robin–

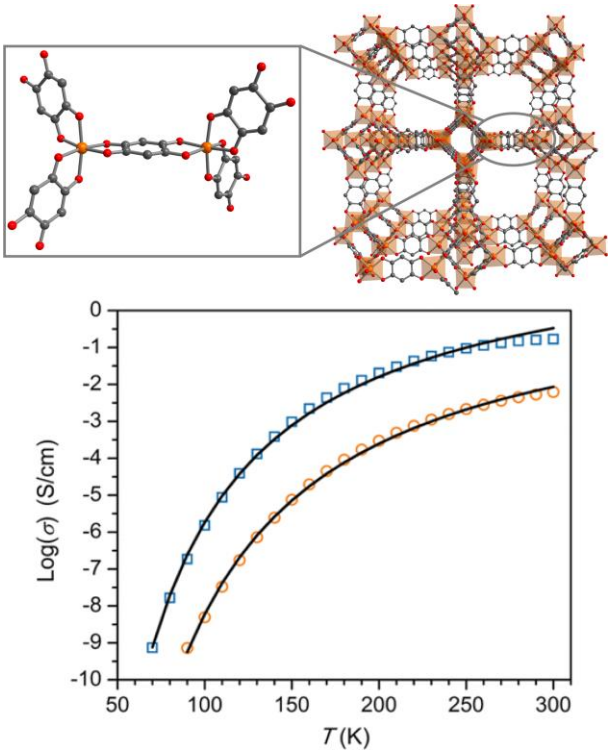

Figure 8.61 Top: Crystal structure of $(Bu_4N)_2[Fe^{III}_2(dhbq^{3-\bullet})_2(dhbq^{2-})]$, as viewed along the crystallographic *a* axis (right), highlighting the coordination environment of Fe^{III} (left). Orange, red, and gray spheres represent Fe, O, and C atoms, respectively; H atoms and $(Bu_4N)^+$ ions are omitted for clarity. Bottom: Variable-temperature electrical conductivity data for $(Bu_4N)_2[Fe^{III}_2(dhbq^{3-\bullet})_2(dhbq^{2-})]$ (blue squares) and $Na_{0.9}(Bu_4N)_{1.8}[Fe^{III}_2(dhbq^{3-\bullet})_{2.7}(dhbq^{2-})_{0.3}]$ (orange spheres). Black lines denote Arrhenius fits to the data. Reprinted with permission from ref. 461. Copyright 2015 American Chemical Society.

Day class II/III mixed-valency from the sharp absorption edge of the intervalence charge transfer band in the diffuse reflectance UV-Vis-NIR spectrum, representing the first observation of a class II/III mixed-valency in a MOF. The structure of this framework consists of two interpenetrated (10,3)-*a* nets of opposing chiralities, where the Fe^{III} ions are in an analogous octahedral coordination environment as in the 2D honeycomb structures (see Figure 8.61, top).[420,421] Variable-temperature dc magnetic susceptibility measurements, in conjunction with low-temperature magnetic hysteresis data, suggested competing ferromagnetic and antiferromagnetic interactions that prevented the occurrence of 3D order until antiferromagnetic metal−radical coupling prevailed at low temperature, giving rise to long-range ferrimagnetic order below T_c = 8 K.[461] In contrast to the low magnetic ordering temperature, this compound exhibits the highest room-temperature electrical conductivity value of $\sigma = 1.6(1) \times 10^{-1}$ S cm^{-1} reported for a 3D MOF (see Figure 8.61, bottom). The high conductivity was attributed to strong electronic correlation within this material owing to the mixed-valence state of the quinoid linkers.

Post-synthetic chemical reduction of this compound by 0.7 electrons per formula unit afforded the compound $Na_{0.9}(Bu_4N)_{1.8}[Fe^{III}_2(dhbq^{3-\bullet})_{2.7}(dhbq^{2-})_{0.3}]$, which exhibits a near identical 3D structure as the parent material based on PXRD analysis. This reduced compound exhibits a slightly higher magnetic ordering temperature of T_c = 12 K and a significantly lower room-temperature conductivity of $\sigma = 6.2(1) \times 10^{-3}$ S cm^{-1} compared to the parent framework (see Figure 8.61, bottom). These correlated changes in magnetic ordering temperature and electrical conductivity are in accord with those observed for the 2D analogue, consistent with the increased number of strong metal–radical interactions and fewer holes after reduction.

8.4.6 A Pyrazine Radical-Bridged Compound

Recently, the redox activity of the pyrazine ligand was exploited to generate an air-stable layered solid that exhibits both long-range magnetic order and high electronic conductivity.[462] Specifically, the charge-neutral compound $Cr^{III}Cl_2(pyz^{0.5-\bullet})_2$ (pyz = pyrazine) was accessed through a reaction between $Cr^{II}Cl_2$ and pyrazine at 200 °C. Its 2D structure is comprised of nearly square-grid layers of octahedral Cr^{III} ions bridged by pyrazine linkers, with the layers stacking in a staggered fashion. Crystallographic and spectroscopic analyses were consistent with a spontaneous one-electron reduction of the pyrazine moieties per formula unit occurring during synthesis, where the extra electron is delocalized over two ligands. Accordingly, this compound shows strong π–d conjugation and antiferromagnetic exchange coupling between Cr^{III} and the pyrazine radical ligands, giving rise to ferrimagnetic order below ca. 55 K. Furthermore, hysteretic behavior with a remanent magnetization was observed below the ordering temperature. The interlayer magnetic interactions are very weak, indicating a primarily 2D magnetic character for this compound. Moreover, $Cr^{III}Cl_2(pyz^{0.5-\bullet})_2$ exhibits a high room-temperature electrical conductivity of $\sigma = 3.2 \times 10^{-2}$ S cm^{-1}, which operates via 2D hopping-based transport mechanism. Notably, this conductivity value is on the same order of magnitude as that for the best 2D semiquinoid-bridged framework magnet.

To summarize this section, frameworks based on organic radical linkers often show unusually high magnetic ordering temperatures (see Tables 8.18 and 8.19), with many eclipsing liquid nitrogen temperature of 77 K, owing to the strong antiferromagnetic metal−radical exchange coupling. Furthermore, the redox activity of radical ligands, such as pyrazine and TCNQ- and semiquinoid-based ligands, has been exploited to furnish framework materials with exceptionally high electrical conductivity. The simultaneous high conductivity and magnetic ordering

temperature observed for these compounds is unprecedented among coordination solids. This behavior, along with the vast scope of chemical tunability possible for the radical bridging ligands, highlights the tremendous potential for this class of frameworks as magnetic conductors.

8.5 Conclusions and Outlook

The combination of the coordination chemistry toolbox and crystal engineering techniques has enabled the rational design of molecule-based framework magnets with exceptional properties. The foregoing discussion surveys the development of the field of metal-organic framework magnets, focusing on structurally-characterized compounds featuring a wide range of diamagnetic and radical linkers. The work highlighted above illustrates that the chemical versatility of organic ligands and their capability of mediating magnetic exchange between paramagnetic metal centers has furnished frameworks of numerous structure types exhibiting permanent magnetism and other novel magnetic and functional behavior.

Structural characterization of these compounds has been critical to elucidate the mechanism of long-range magnetic behavior, in particular the interplay between intra- and intersubunit exchange interactions. Such studies have provided important design principles for generating new framework magnets with high ordering temperatures. Specifically, the employment of π-conjugated organic linkers facilitates electronic and magnetic communication over much longer distances than their non-conjugated counterparts, and thus enables the formation of open framework structures with permanent magnetic behavior. Furthermore, compounds featuring one primary pathway of magnetic exchange typically exhibit higher values of T_c than those showing more complicated structures and multiple exchange pathways, as different interactions commonly act in opposing directions, and thus overall decrease the coupling strength between metal centers.

Along these lines, the incorporation of organic radical linkers has been particularly successful, affording the MOF magnets that display the highest ordering temperatures (T_c up to 171 K).[72,73] Despite the success and rapid advancement of these materials, their performance is still modest compared to those of inorganic solid-state magnets, which show permanent magnetic behavior above room temperature.

A few examples of amorphous room-temperature metal-organic magnets have already been realized,[13,83–86,89] suggesting that structural characterization of these types of compounds is within reach. Indeed, a layered mixed-valence phthalocyaninato $Fe^{II}Fe^{III}$ framework was recently reported to possess ferromagnetism and magnetic hysteresis up to 350 K.[463] This compound is polycrystalline, leading to superparamagnetic behavior with a large distribution of blocking temperatures. Accordingly, several strategies can be foreseen to design structurally well-defined MOF magnets that operate at high temperatures. One route that holds tremendous promise is the introduction of high-anisotropy metal ions, such as 4d/5d transition metal and lanthanide ions, into framework materials. Here, large spin-orbit coupling manifests in high magnetic anisotropy, which is an essential element in achieving hard permanent magnets. Since heavy transition metal centers typically adopt low-spin states, the combination of 3d and 4d/5d transition metal centers with high electronic spin and magnetic anisotropy, respectively, might be an attractive way to improve the performance of such magnets. Along these lines, combining first-row transition metals with Mo^{III} has enabled exceptionally strong magnetic coupling through cyanide in molecular complexes.[464,465] Furthermore, multimetallic transition metal-lanthanide frameworks are also of interest, as most high-performing inorganic solid-state magnets, such as $Nd_2Fe_{14}B$ and $SmCo_5$, feature both types of metal centers.

Another attractive approach toward increasing the ordering temperatures of framework magnets is to move from O- and N-based donors to S- and P-based ligands. The more radially diffuse orbitals of sulfur and phosphorous relative to oxygen and nitrogen should provide a route to stronger magnetic coupling between metal centers and organic linkers, as has been demonstrated in dinuclear semiquinoid-bridged Cr^{III} complexes.[466] Moreover, the use of sulfur-based ligands is particularly interesting owing to the high electrical conductivity of organosulfur compounds, such as tetrathiafulvalene and its derivatives,[242] rendering such frameworks promising candidates as conductive magnets. Notably, post-synthetic metal- and linker-exchange reactions, which have been the subject of substantial recent efforts,[38–45] may afford frameworks with irreversible metal–ligand coordination, as such materials are often not accessible through direct synthesis.

Finally, as illustrated with the examples in this review, emerging research has demonstrated that the magnetic and electronic properties of framework magnets can be modulated in a reversible manner through both chemical and physical processes, such as inclusion or removal of guest molecules and redox reactions. This multifunctional behavior highlights the prospect for these compounds in sensing applications and magnetic switching devices. Indeed, the high electrical conductivity of several radical-bridged framework magnets underscores the potential for these materials for spintronics applications.

8.6 Supporting Information

8.6.1 Supplementary Tables

Table 8.1 Magnetic data for 2D metal-organic framework magnets with diamagnetic bridging ligands.

Compound[a,b]	Magnetic order	T_c (K)	Other relevant structural and magnetic notes	Ref.
2D inorganic networks (I^2O^0)				
$Co^{II}(gly)$	CAFM	35.5	M–O–M connectivity	467,468
$Co^{II}_2(OH)(2\text{-pmb})$	CAFM	31.0	M–O–C–O–M/M–O–P–O–M/M–O–M connectivity; magnetic hysteresis at 2 K with H_c = 4.3 T and M_r = 0.22 μ_B mol^{-1}	222
$Co^{II}(thiosal)$	CAFM	9	M–S–M/M–O–M/M–O–C–O–M connectivity; magnetic hysteresis at 4.5 K with H_c = 45 Oe	326
$Ni^{II}_4(mdp)_2(H_2O)_3$ (VSB-2)	FM	3.1(1)	M–O–P–O–M/M–O–M connectivity	216
2D inorganic-organic networks (I^1O^1)				
$Mn^{II}_2Cu^{II}_2(Me_3mpba)_2(H_2O)_6\cdot 8H_2O$	FM	20.0	M–O–C–O–M/M–O–C–N–M connectivity; magnetic hysteresis at 2.0 K with H_c = 100 Oe	289
$(MV)[Mn^{II}_2Cu^{II}_3(mpba)_3(H_2O)_3]\cdot 20H_2O$	FM	19.0	M–O–C–O–M/M–O–C–N–M connectivity; reversible dehydration/hydration	290
$(Bu_4N)_4[Mn^{II}_4Cu^{II}_6(Me_2pma)_{12}(DMSO)_2]\cdot 8DMSO\cdot 2H_2O$	FM	10	M–O–C–O–M/M–O–C–N–M connectivity	297
$Co^{II}_2Cu^{II}_2(mpba)_2(H_2O)_6\cdot 6H_2O$	AFM	9.5	M–O–C–O–M/M–O–C–N–M connectivity; field-induced transition to a FM-like state below T_N when H > 1200 Oe; spin glass behavior below T_N	288
$Mn^{II}(2,2\text{-dmsucc})(H_2O)$	AFM	8	M–O–C–O–M/M–O–M connectivity	307
$Co^{II}(bpdc)(iqno)$	AFM	3.65	M–O–C–O–M/M–O–M connectivity; SCM behavior below T_N (Δ_τ = 20 cm^{-1}; $\tau_0 = 5.8 \times 10^{-9}$ s)	469
2D organic networks (I^0O^2)				
$(Ph_3HpP)[Fe^{II}Fe^{III}(ox)_3]$	FiM	48(1)	M–O–C–O–M connectivity	230
$(Ph_3PeP)[Mn^{II}Fe^{III}(ox)_3]$	FiM	33.2(2)	M–O–C–O–M connectivity	230
$Ni^{II}(ox)(4,4'\text{-bpy})$	AFM	26	M–O–C–O–M intrachain connectivity; field-induced transition to a FM-like state below T_N when H > 5.0 T	255,256
$[K(18\text{-crown-}6)]_3[Fe^{II}_3(H_2O)_4(Fe^{III}(ox)_3)_3]$	FiM	25.5	M–O–C–O–M connectivity	236
$Na_2[Ni^{II}(mal)_2]\cdot 2H_2O$	CAFM	24(1)	M–O–C–O–M connectivity; magnetic hysteresis at 5 K with M_r = 0.014 μ_B mol^{-1}	305
$Fe^{II}(ox)(MeOH)$	CAFM	23	M–O–C–O–M connectivity; magnetic hysteresis at 2 K with H_c = 250 Oe and M_r = 0.007 μ_B mol^{-1}	258
$[Fe^{II}_2(pymca)_3](OH)\cdot H_2O$	AFM	21	M–O–C–O–M/M–N–C–N–M connectivity	411
$[Fe^{II}(H_2O)_2]_{1.5}[Ni^{II}(H_2O)_2]_{1.5}[Fe^{III}(ox)_3]_2\cdot 2(18\text{-crown-}6)$	FiM	20.0	Magnetic hysteresis at 2 K with H_c = 160 Oe and M_r = 0.1 μ_B mol^{-1}	240
$[Fe^{II}(H_2O)_2]_{1.5}[Mn^{II}(H_2O)_2]_{1.5}[Fe^{III}(ox)_3]_2\cdot 2(18\text{-crown-}6)$	FiM	19.5	Magnetic hysteresis at 2 K with H_c < 100 Oe and M_r < 0.1 μ_B mol^{-1}	240

$[Cp^*_2Fe^{III}][Co^{II}Fe^{III}(ox)_3]$	FiM	19.5	M–O–C–O–M connectivity	233
$Na_2[Fe^{II}(mal)_2]\cdot 2H_2O$	CAFM	16(1)	M–O–C–O–M connectivity; magnetic hysteresis at 5 K with $M_r = 0.26\ \mu_B\ mol^{-1}$	305
$[K(18\text{-crown-6})]_3$ $[Co^{II}_3(H_2O)_4(Fe^{III}(ox)_3)_3]$	FiM	16	M–O–C–O–M connectivity; magnetic hysteresis at 2 K with $H_c = 1.53$ T and $M_r = 0.95\ \mu_B\ mol^{-1}$	236
$Fe^{II}(4\text{-imac})_2\cdot 2MeOH$	CAFM	15	M–O–C–O–M connectivity: magnetic hysteresis at 4.2 K with $H_c = 6200$ Oe and $M_r = 0.22\ \mu_B\ mol^{-1}$	412
$[Cp^*_2Fe^{III}][Ni^{II}Cr^{III}(ox)_3]$	FM	14.5	M–O–C–O–M connectivity; magnetic hysteresis at 5 K with $H_c = 250$ Oe	233
$[K(18\text{-crown-6})]_3$ $[Mn^{II}_3(H_2O)_4(Fe^{III}(ox)_3)_3]$	CAFM	14	M–O–C–O–M connectivity; magnetic hysteresis at 2 K with $H_c = 180$ Oe and $M_r = 1.14\ \mu_B\ mol^{-1}$	236
$[Cp^*_2Fe^{III}][Fe^{II}Ru^{III}(ox)_3]$	FM	13.8	M–O–C–O–M connectivity; magnetic hysteresis at 2 K with $H_c = 2210$ Oe and $M_r = 2.5\ \mu_B\ mol^{-1}$	217
$[Cp^*_2Fe^{III}][Fe^{II}Cr^{III}(ox)_3]$	FM	13.0	M–O–C–O–M connectivity; magnetic hysteresis at 2 K with $H_c = 1100$ Oe and $M_r = 3.60\ \mu_B\ mol^{-1}$	233,234
$Na_2[Co^{II}(mal)_2]\cdot 2H_2O$	AFM	13(1)	M–O–C–O–M connectivity	305
$Co^{II}(ox)(4,4'\text{-bpy})$	CAFM	13	M–O–C–O–M intrachain connectivity; field-induced transition to an AFM ordered state below T_N when $H > 1.0$ T	255,256
$[Fe^{II}(H_2O)_2]_3[Fe^{III}(ox)_3]_2$ $\cdot 2(18\text{-crown-6})$	FiM	12.2	M–O–C–O–M connectivity; magnetic hysteresis at 2 K with $H_c = 1100$ Oe and $M_r < 0.1\ \mu_B\ mol^{-1}$	240
$Fe^{II}(ox)(4,4'\text{-bpy})$	CAFM	12	M–O–C–O–M intrachain connectivity	255,256
$[Ga^{III}(acac_2\text{-trien})][Mn^{II}Cr^{III}(Br_2An)_3]$ $\cdot 2MeCN$	FiM	11.6	M–O–C–C–C–O–M connectivity	424
$[K(18\text{-crown-6})]_3$ $[Ni^{II}_3(H_2O)_4(Fe^{III}(ox)_3)_3]$	FiM	11.5	M–O–C–O–M connectivity; magnetic hysteresis at 2 K with $H_c = 230$ Oe and $M_r < 0.01\ \mu_B\ mol^{-1}$	236
$[Fe^{III}(acac_2\text{-trien})][Mn^{II}Cr^{III}(Br_2An)_3]$ $\cdot 2MeCN$	FiM	11.4	M–O–C–C–C–O–M connectivity	424
$Co^{II}(pzdo)_2(NCS)_2$	AFM	11.2	M–O–N–C–C–N–O–M connectivity	376
$Ba_2[Co^{II}_2(ox)_3Cl_2]\cdot 4H_2O$	AFM	11(1)	M–O–C–O–M connectivity	257
$[Fe^{III}(acac_2\text{-trien})][Mn^{II}Cr^{III}(Cl_2An)_3]$ $\cdot 2MeCN$	FiM	10.8	M–O–C–C–C–O–M connectivity	424
$[Fe^{III}(4\text{-OH-sal}_2\text{-trien})]$ $[Mn^{II}Cr^{III}(Cl_2An)_3]\cdot 23H_2O$	FiM	10.4	M–O–C–C–C–O–M connectivity; magnetic hysteresis at 2 K with $H_c = 870$ Oe	423
$[Fe^{III}(sal_2\text{-epe})]$ $[Mn^{II}Cr^{III}(Br_2An)_3]\cdot 6MeCN$	FiM	10.2	M–O–C–C–C–O–M connectivity; magnetic hysteresis at 2 K with $H_c = 100$ Oe	423
$[Co^{II}_2(pymca)_3](OH)\cdot H_2O$	CAFM	10	M–O–C–O–M/M–N–C–N–M connectivity; magnetic hysteresis at 2 K with $H_c = 580$ Oe and $M_r = 94$ Oe cm^3 mol^{-1}	411
$[Fe^{III}(sal_2\text{-trien})][Mn^{II}Cr^{III}(Cl_2An)_3]$ $\cdot 0.5CH_2Cl_2\cdot 0.5H_2O\cdot MeOH\cdot 5MeCN$	FiM	10	M–O–C–C–C–O–M connectivity; magnetic hysteresis at 2 K with $H_c = 350$ Oe	423,424

$[Fe^{III}(5\text{-Cl-sal}_2\text{-trien})][Mn^{II}Cr^{III}(Br_2An)_3]\cdot CH_2Cl_2\cdot 2MeOH\cdot 3.5MeCN\cdot 4H_2O$	FiM	9.8	M–O–C–C–C–O–M connectivity; magnetic hysteresis at 2 K with H_c = 660 Oe	423
$(Et^iPr_2NH)[Mn^{II}Cr^{III}(Br_2An)_3]\cdot 0.5CHCl_3\cdot H_2O$	AFM	9.6	M–O–C–C–C–O–M connectivity; reversible desolvation/solvation; guest-dependent modulation of T_c; field-induced transition to a CAFM state below T_N when H > 4900 Oe	425
$(Bu_4N)[Mn^{II}Cr^{III}(Br_2An)_3]\cdot 1.75PhBr$	FiM	9.5	M–O–C–C–C–O–M connectivity; guest-dependent modulation of T_c and H_c; magnetic hysteresis at 2 K with H_c = 330 Oe	429
$[Co^{II}(H_2O)_2]_{1.5}[Mn^{II}(H_2O)_2]_{1.5}[Fe^{III}(ox)_3]_2\cdot 2(18\text{-crown-6})$	FiM	9.4	Magnetic hysteresis at 2 K with H_c = 6300 Oe and M_r = 0.3 μ_B mol^{-1}	240
$[Cp^*_2Fe^{III}][Co^{II}Cr^{III}(ox)_3]$	FM	9.0	M–O–C–O–M connectivity; magnetic hysteresis at 2 K with H_c = 130 Oe and M_r = 1.20 μ_B mol^{-1}	233,234
$(Et_2NH_2)[Mn^{II}Cr^{III}(Br_2An)_3]$	FiM	8.9	M–O–C–C–C–O–M connectivity; magnetic hysteresis at 2 K with H_c = 1000 Oe	425
$Mn^{II}(pzdo)_2(NCS)_2$	AFM	8.4	M–O–N–C–C–N–O–M connectivity	376
$Co^{II}(pym)_2(NCS)_2$	FM	8.2	M–N–C–N–M connectivity; magnetic hysteresis at 2.3 K with H_c = 120 Oe and M_r = 0.25 μ_B mol^{-1}	377
$[Z^{III}(sal_2\text{-trien})]_2[Mn^{II}_2(ox)_3]\cdot$solvent	CAFM	8.1	M–O–C–O–M connectivity; magnetic hysteresis at 2 K with H_c = 48 Oe (Z = Fe^{III}) and 660 Oe (Z = In^{III})	248
$(Et_3NH)[Mn^{II}Cr^{III}(Cl_2An)_3]$	FiM	8.0	M–O–C–C–C–O–M connectivity; magnetic hysteresis at 2 K with H_c = 1500 Oe	425
$(Me_2NH_2)[Mn^{II}Cr^{III}(Br_2An)_3]\cdot 2H_2O$	FiM	7.9	M–O–C–C–C–O–M connectivity; magnetic hysteresis at 2 K with H_c = 900 Oe	425
$Na_2[Mn^{II}(mal)_2]\cdot 2H_2O$	AFM	8(1)	M–O–C–O–M connectivity	305
$(Et_3NH)[Co^{II}_{1.5}(hfipbb)_2]$	CAFM	8	Trimers of CoO_x (x = 5, 6); M–O–C–O–M/M–O–M connectivity	361
$[K(18\text{-crown-6})]_3[Fe^{II}_3(H_2O)_4(Cr^{III}(ox)_3)_3]$	FM	8	M–O–C–O–M connectivity; magnetic hysteresis at 2 K with H_c = 130 Oe and M_r = 2.32 μ_B mol^{-1}	236
$[Co^{II}(H_2O)_2]_3[Cr^{III}(ox)_3]_2\cdot 2(18\text{-crown-6})$	FM	7.4	M–O–C–O–M connectivity; magnetic hysteresis at 2 K with H_c = 160 Oe and M_r = 2.3 μ_B mol^{-1}	239,240
$[Cp^*_2Fe^{III}][Cu^{II}Cr^{III}(ox)_3]$	FM	7.0	M–O–C–O–M connectivity; magnetic hysteresis at 2 K with H_c = 180 Oe and M_r = 1.50 μ_B mol^{-1}	233,234
$(Bu_4N)[Mn^{II}Cr^{III}(Cl_2An)_3(PhCHO)]\cdot$PhY	FiM	6.8–7.0	M–O–C–C–C–O–M connectivity; guest-dependent modulation of T_c and H_c; magnetic hysteresis at 2 K with H_c = 76 (Y = H) and 50 Oe (Y = CHO)	428
$Fe^{II}(pyz)_2(NCS)_2$	AFM	6.8	M–N–C–C–N–M connectivity	374,375
$[Mn^{II}(H_2O)_2]_{1.5}[Ni^{II}(H_2O)_2]_{1.5}[Cr^{III}(ox)_3]_2\cdot 2(18\text{-crown-6})$	FM	6.8	Magnetic hysteresis at 2 K with H_c = 200 Oe and M_r = 2.4 μ_B mol^{-1}	240
$[Co^{II}(H_2O)_2]_{1.5}[Ni^{II}(H_2O)_2]_{1.5}[Cr^{III}(ox)_3]_2\cdot 2(18\text{-crown-6})$	FM	6.8	Magnetic hysteresis at 2 K with H_c = 200 Oe and M_r = 1.4 μ_B mol^{-1}	240
$(Bu_4N)[Mn^{II}Cr^{III}(Br_2An)_3(PhCHO)]\cdot$PhY	FiM	6.7	M–O–C–C–C–O–M connectivity; guest-dependent modulation of H_c; magnetic hysteresis at 2 K with H_c = 100 (Y = H) and 200 Oe (Y = CHO)	428
$(Pr_4N)[Mn^{II}Cr^{III}(ox)_3]$	FM	6.0	M–O–C–O–M connectivity	232

$[K(18\text{-crown-6})]_3[Co^{II}_3(H_2O)_4(Cr^{III}(ox)_3)_3]$	FM	6	M–O–C–O–M connectivity; magnetic hysteresis at 2 K with H_c = 170 Oe and M_r = 3.69 μ_B mol^{-1}	236
$[Mn^{II}(H_2O)_2(MeOH)_2][Mn^{II}(H_2O)(MeOH)]_2[Cr^{III}(ox)_3]_2\cdot$(18-crown-6)	FiM	5.5	M–O–C–O–M connectivity; thin magnetic hysteresis loop at 2 K	470
$(Bu_4N)[Mn^{II}Cr^{III}(Cl_2An)_3]$	FiM	5.5	M–O–C–C–C–O–M connectivity; magnetic hysteresis at 2 K with H_c = 118 Oe	422
$[Fe^{III}$(4-Br-sal$_2$-trien)$][Mn^{II}Cr^{III}(ox)_3]_{0.67}Cl_{0.33}\cdot$MeOH$\cdot$solvent	FM	5.2	M–O–C–O–M connectivity; magnetic hysteresis at 2 K with H_c = 70 Oe	251
$[(H_3O)_2(phz)_3][Mn^{II}_2(Cl_2An)_3]\cdot 2H_2O\cdot 2C_3H_6O$	AFM	5	M–O–C–C–C–O–M connectivity	471
$[K(18\text{-crown-6})]_3[Ni^{II}_3(H_2O)_4(Cr^{III}(ox)_3)_3]$	FM	4.5	M–O–C–O–M connectivity; magnetic hysteresis at 2 K with H_c = 790 Oe and M_r = 4.50 μ_B mol^{-1}	236
$(H_2en)_{0.5}[Co^{II}(cmp)(H_2O)]\cdot H_2O$	CAFM	4.3	M–O–C–O–M/M–O–P–O–M/M–O–P–C–O–M connectivity; spin glass behavior and field-induced transition to a FM-like state below T_N; magnetic hysteresis at 2 K with H_c = 71 Oe and M_r = 0.025 μ_B mol^{-1}	219
$(tag)[Fe^{II}Fe^{III}(ClCNAn)_3]\cdot 29H_2O$	FiM	4	M–O–C–C–C–O–M connectivity; spin glass behavior near T_c; magnetic hysteresis at 2 K with H_c = 60 Oe	427
$[Mn^{II}(H_2O)_2]_3[Cr^{III}(ox)_3]_2\cdot 2$(18-crown-6)	FM	3.6	M–O–C–O–M connectivity	240
$[K(18\text{-crown-6})]_3[Mn^{II}_3(H_2O)_4(Cr^{III}(ox)_3)_3]$	FM	3.5	M–O–C–O–M connectivity	236
$[(H_3O)(phz)_3][Mn^{II}Fe^{III}(Br_2An)_3]\cdot H_2O$	CAFM	~3.5	M–O–C–C–C–O–M connectivity	422
$[K(18\text{-crown-6})]_3[Cu^{II}_3(H_2O)_4(Cr^{III}(ox)_3)_3]$	FM	3.2	M–O–C–O–M connectivity	236
$[Cp^*_2Fe^{III}][Co^{II}Ru^{III}(ox)_3]$	FM	3.1	M–O–C–O–M connectivity	235
$Mn^{II}[Mn^{II}_3F(bta)_3(H_2O)_6]_2$	AFM	2.5	M–N–N–M/M–N–C–N–M connectivity; spin-frustrated system (f = 8.9)	402
$[(H_3O)(H_2O)(phz)_3][Fe^{II}Fe^{III}(Cl_2An)_3]\cdot 12H_2O$	FiM	2.4	M–O–C–C–C–O–M connectivity; magnetic hysteresis at 2 K with $H_c \approx$ 10 Oe	426
$[(H_3O)(H_2O)(phz)_3][Fe^{II}Fe^{III}(Br_2An)_3]\cdot 12H_2O$	FiM	2.1	M–O–C–C–C–O–M connectivity; magnetic hysteresis at 2 K with $H_c \approx$ 10 Oe.	426
$[Mn^{II}_2(succ)(adip)(H_2O)_4]\cdot 2H_2O$	AFM	2.1	M–O–C–O–M connectivity	315
$[(H_3O)(phz)_3][Mn^{II}Cr^{III}(Br_2An)_3]\cdot 2H_2O\cdot 2C_3H_6O$	FiM	—[c]	M–O–C–C–C–O–M connectivity; magnetic hysteresis at 2 K with H_c = 340 Oe	422
$[(H_3O)(phz)_3][Mn^{II}Cr^{III}(Cl_2An)_3(H_2O)]$	FiM	—[c]	M–O–C–C–C–O–M connectivity; magnetic hysteresis at 2 K with H_c = 194 Oe	422
Cu^{II}_2(1,3-bdc)$_2$(py)$_2$	CAFM	—[c]	M–O–C–O–M connectivity; open magnetic hysteresis loop at 5 K	351

[a] The bridging unit $(CPO_3)^{2-}$ is considered to be inorganic in nature, and therefore metal polyhedra bridged via three-atom O–P–O linkages are treated equivalently to those bridged by single-atom oxo bridges. [b] Only the metal oxalate frameworks with the highest ordering temperature for a given lattice type are included in this table. See Tables 8.3–8.11 for details on the variation in T_c with the cation. [c] The magnetic ordering temperature for this compound was not specified.

Table 8.2 Magnetic data for 3D metal-organic framework magnets with diamagnetic bridging ligands.

Compound[a,b]	Magnetic order	T_c (K)	Other relevant structural and magnetic notes	Ref.
3D inorganic networks (I^3O^0)				
$Ni^{II}_4(mdp)_2(H_2O)_2$ (VSB-3)	FM	3.8(1)	M–O–P–O–M/M–O–M connectivity	216
$Ni^{II}_4(mdp)_2$ (VSB-4)	FM	3.8(2)	M–O–P–O–M/M–O–M connectivity	216
$Ni^{II}_{20}(glu)_{20}(H_2O)_8 \cdot 40H_2O$ (MIL-77)	FM	4	M–O–C–O–M/M–O–M connectivity	316
3D inorganic-organic networks with inorganic layers (I^2O^1)				
$Mn^{II}(succ)$[c]	AFM	10/6	M–O–C–O–M/M–O–M connectivity; independent AFM phase transitions for two types of layers	311,312
Co^{II}_2(O-ma)(4-pyc)$\cdot 2H_2O$	CAFM	8	M–O–C–O–M/M–O–M intralayer connectivity Reversible dehydration/hydration; guest-dependent magnetic properties; spin glass behavior below T_N; magnetic hysteresis at 2 K with H_c = 93 Oe and M_r = 27 Oe cm^3 mol^{-1}	304
$Cu^{II}_4(hedp)_2(pyz)(H_2O)_4$	AFM	4.2	M–O–P–O–M connectivity within chains; field-induced transition to a FM-like state below T_N	218
$Cu^{II}_2(edp)(H_2O)_2$ (MIL-29)	AFM	4(1)	M–O–P–O–M/M–O–M intralayer connectivity	217
Cu^{II}_2(1,4-xdp)$(H_2O)_2$ (MIL-29)	AFM	4(1)	M–O–P–O–M/M–O–M intralayer connectivity	217
Co^{II}(Hpmab)	CAFM	2.0	M–O–P–O–M intralayer connectivity; magnetic hysteresis at 2 K with $M_r \approx 0.18$ μ_B mol^{-1}	220
3D inorganic-organic networks with inorganic chains (I^1O^2)				
V^{III}(OH)(1,4-bdc)$\cdot$0.75(1,4-H_2bdc) (MIL-47as)	AFM	95(5)	M–O–C–O–M/M–O–M connectivity	346
$V^{IV}O$(1,4-bdc) (MIL-47)	AFM	75(5)	M–O–C–O–M/M–O–M connectivity	346
Cr^{III}(OH)(1,4-bdc)$\cdot$0.75(1.4-H_2bdc) (MIL-53as)	AFM	65	M–O–C–O–M/M–O–M connectivity; reversible desolvation/solvation; guest-modulated magnetic properties	347,348
Mn^{II}(*meso*-2,3-dmsucc)	AFM	50	M–O–C–O–M/M–O–M connectivity	314
$Ba_4(ox)Cl_2[Fe^{II}(OH)(ox)]_4$	AFM	32	M–O–C–O–M/M–O–M connectivity	273
Fe^{II}_2(1,2,4,5-btec)	AFM	26	M–O–C–O–M/M–O–M connectivity	355
$(H_2(1,3\text{-dap}))[Fe^{III}_2(HPO_4)_2(ox)_{1.5}]_2$	AFM	25	M–O–C–O–M/M–O–P–O–M connectivity	282
$(H_2(1,3\text{-dahp}))[Fe^{III}_2(HPO_4)_2(ox)_{1.5}]_2$	AFM	25	M–O–C–O–M/M–O–P–O–M connectivity	282
$(H_2ppz)_{0.5}[Co^{II}_2(HPO_4)(ox)_{1.5}]$	AFM	25	M–O–C–O–M/M–O–P–O–M/M–O–M connectivity	281
$(H_2ppz)[Co^{II}_4(HPO_3)_2(ox)_3]$	AFM	22	M–O–C–O–M/M–O–P–O–M/M–O–M connectivity	284

$K[Co^{II}_{2.25}Fe^{II}_{0.75}$(1,3,5-btc)$(1,3,5\text{-Hbtc})_2]\cdot 5H_2O$ (MIL-45-CoFe)	FM	20	M–O–C–O–M/M–O–M connectivity	353
$Co^{II}_3(OH)_2$(3,4-pydc)$_2(H_2O)_2$	AFM	20.0	M–O–C–O–M/M–O–M connectivity; field-induced transition to a FiM state when H > 7000 Oe; magnetic hysteresis at 2 K with H_c = 2750 Oe	408
Co^{II}_3(*rac*-O-lac)$_2$(pybz)$_2\cdot$3DMF	CAFM	18.5	M–O–C–O–M/M–O–M intrachain connectivity; reversible desolvation/solvation; guest-dependent magnetic properties	410
Mn^{II}_2(1,2,4,5-btec)	AFM	18	M–O–C–O–M/M–O–M connectivity	355
Co^{II}_2(1,2,4,5-btec)	AFM	16	M–O–C–O–M/M–O–M connectivity; field-induced transition to a CAFM ordered state below T_N = 12 K when H is small and to a FM state when H > 1500 Oe	355
$Co^{II}_5(OH)_2$(1,2,4,5-btec)$_2$(bpp)	AFM	12.5	Pentameric subunits; M–O–C–O–M/M–O–M connectivity; field-induced transition to a FiM-like ordered state below T_N; magnetic hysteresis at 2 K with H_c = 880 Oe and M_r = 0.16 μ_B mol^{-1}	357
$Mn^{II}_2(OH)_2$(squ)	AFM	12.5	M–O–C–C–O–M/M–O–M connectivity	329,330, 331
$Fe^{II}_3(OH)_2(H_2O)_4$(Hcep)$_2$ (MIL-38)	AFM	10	M–O–P–O–M/M–O–M connectivity; field-induced transition to a FM-like state below T_N when H > 1.5 T	221
$K[Co^{II}_3$(1,3,5-btc)(1,3,5-Hbtc)$_2]$ $\cdot 5H_2O$ (MIL-45-Co)	FM	10	M–O–C–O–M/M–O–M connectivity	353
Cu^{II}_3(5-ptz)$_2(VO_3)_4$	FiM	10	M–N–C–N–M/M–N–N–N–M/M–O–V–O–M connectivity; magnetic hysteresis at 2 K with H_c < 20 Oe	404
Co^{II}_2(2,5-dobdc)$(H_2O)_2\cdot 8H_2O$	AFM	8	M–O–C–O–M/M–O–M connectivity; reversible dehydration/hydration; field-induced transition to a FM-like ordered state below T_N when H > 2.0 T	349
Co^{II}_2(Hhfipbb)(TEOA)	CAFM	8	M–O–C–O–M/M–O–M/M–N–C–C–O–M connectivity; magnetic hysteresis at 2 and 6.5 K with H_c = 950 and 45 Oe, respectively	361
$Co^{II}_3(OH)_2$(btca)$_2\cdot 3.7H_2O$	FiM	8	M–O–C–O–M/M–O–M/M–N–N–M/M–N–N–N–M connectivity; guest-dependent magnetic properties and SCM behavior; magnetic hysteresis at 2 K with H_c = 60 Oe and M_r = 1.16 μ_B mol^{-1}	413
$Co^{II}_3(OH)_2$(squ)$_2\cdot 3H_2O$	AFM	8	M–O–C–C–O–M/M–O–M connectivity; reversible dehydration/hydration; guest-dependent magnetic properties; transition to a CAFM state below 6 K	332,333, 334
$Cu^{II}_5(OH)_2$(tz)$_4$(SO$_4$)$_2$	FiM	7.0	Pentameric subunits; M–N–N–M/M–N–N–N–M/M–N–C–N–M/M–O–M/M–O–S–O–M connectivity; magnetic hysteresis at 2.0 K with H_c = 300 Oe and M_r = 0.4 μ_B mol^{-1}	405
Co^{II}_2(hfipbb)$_2\cdot$PhMe	CAFM	7	M–O–C–O–M/M–O–M connectivity	361
Mn^{II}(*meso*-2,3-dmsucc)$(H_2O)\cdot H_2O$	AFM	7	M–O–C–O–M/M–O–M connectivity	314
Co^{II}(*meso*-2,3-dmsucc)	AFM	6	M–O–C–O–M/M–O–M connectivity; field-induced transition to a FM-like state below T_N when H > 1400 Oe	314
$Co^{II}_3(OH)_2$(2,4-pydc)$_2\cdot 5H_2O$	CAFM	6	M–O–C–O–M/M–O–M connectivity; field-induced transition to a FM-like state below T_N when H > 5000 Oe; magnetic hysteresis at 2 K with H_c = 200 Oe and M_r = 80 Oe cm^3 mol^{-1}	409
Cu^{II}_3(trz)$_2(VO_3)_4$	AFM	6	M–N–N–M/M–N–C–N–M/M–O–M/M–O–V–O–M connectivity	401

$Fe^{III}(OH)(1,2,4,5\text{-}H_2btec)\cdot 0.88H_2O$ (MIL-82)	AFM	5.5(1)	M–O–C–O–M/M–O–M connectivity; field-induced transition to a FM-like state below T_N when $H >$ 5000 Oe	356
$Co^{II}_4(OH)_2(seba)_3$	CAFM	5.4	M–O–C–O–M/M–O–M intrachain connectivity; slow magnetic relaxation below T_N; magnetic hysteresis at 2 K with H_c = 50 Oe	320
$Co^{II}_2(cbut)(H_2O)_3$	AFM	5.0	M–O–C–O–M/M–O–M connectivity; field-induced transition to a FiM-like state below T_N when $H >$ 1500 Oe; magnetic hysteresis at 2 K with $H_c \approx 40$ Oe	336
$Mn^{II}_3(1,4\text{-}bdc)_3(DEF)_2$	AFM	4.3	M–O–C–O–M/M–O–M connectivity; spin glass behavior below T_N	345
$Co^{II}_3(tzmb)_2(N_3)_2(V_4O_{12})(H_2O)_3\cdot 5H_2O$	CAFM	3.6	M–N–N–M/M–N–N–N–M/M–N–C–N–M connectivity; open magnetic hysteresis loop at 2 K; SCM behavior with T_B = 3.9 K (Δ_τ = 31.2 cm^{-1}, $\tau_0 = 3.37 \times 10^{-8}$ s; Δ_τ = 84.1 cm^{-1}, $\tau_0 = 5.05 \times 10^{-18}$ s)	472
$Ni^{II}_3(OH)_2(cis\text{-}1,4\text{-}chdc)_2(H_2O)_4\cdot 2H_2O$	FiM	2.1	M–O–C–O–M/M–O–M connectivity; guest-modulated magnetic properties	338
$[Cu^{II}(HF_2)(pyz)_2](BF_4)$	AFM	1.54(1)	M–N–C–C–N–M intralayer connectivity	473
$Co^{II}_3(cis,cis\text{-}1,3,5\text{-}chtc)_2(H_2O)_4\cdot 5H_2O$	FiM	—[d]	M–O–C–O–M/M–O–M connectivity	339
$Co^{II}_3(OH)_2(2,4\text{-}pydc)_2\cdot 7H_2O$	AFM	—[d]	M–O–C–O–M/M–O–M connectivity	409
$Mn^{II}_3(OH)_2(tptc)(H_2O)_4$	AFM	—[d]	M–O–C–O–M/M–O–M connectivity	474
$Cu^{II}(trz)(N_3)$	CAFM	—[d]	M–N–M/M–N–N–M/M–N–C–N–M connectivity; magnetic hysteresis at 2 K with $H_c \approx 200$ Oe and $M_r = 0.0028\ \mu_B\ mol^{-1}$	373
3D organic networks (1^0O^3)				
$(H_3O)(EtNH_3)[Fe^{III}_2O(ox)_2Cl_2]\cdot H_2O$[e]	CAFM	70	M–O–C–O–M/M–O–M connectivity; magnetic hysteresis at 5 K with H_c = 2500 Oe and $M_r = 0.036\ \mu_B\ mol^{-1}$	223
$(EtNH_3)[Fe^{III}_2(OH)(ox)_2Cl_2]\cdot 2H_2O$[e]	CAFM	70	M–O–C–O–M/M–O–M connectivity; magnetic hysteresis at 5 K with H_c = 250 Oe and $M_r = 0.025\ \mu_B\ mol^{-1}$	223
$[Ru^{II}(2,2'\text{-}bpy)_3][Ni^{II}_2(ox)_3]$	CAFM	35	M–O–C–O–M connectivity; thin magnetic hysteresis loop at 2 K	263
$[Ir^{III}(ppy)_2(2,2'\text{-}bpy)][Mn^{II}Fe^{III}(ox)_3]\cdot 0.5H_2O$	CAFM	31.0	M–O–C–O–M connectivity; magnetic hysteresis at 2 K with H_c = 240 Oe	262
$Co^{II}(F\text{-}pymo)_2\cdot 2.5H_2O$	AFM	29	M–N–C–N–M connectivity; reversible dehydration/hydration; guest-dependent modulation of magnetic properties	385
$[Ir^{III}(ppy)_2(2,2'\text{-}bpy)][Fe^{II}Fe^{III}(ox)_3]\cdot 0.5H_2O$	FiM	28.0	M–O–C–O–M connectivity; magnetic hysteresis at 2 K with H_c = 300 Oe	262
$[Ru^{II}(2,2'\text{-}bpy)_3][Cu^{II}_{0.88}Ni^{II}_{1.12}(ox)_3]$	CAFM/FiM	28	M–O–C–O–M connectivity; thin magnetic hysteresis loop at 2 K	263
$[Ru^{II}(2,2'\text{-}bpy)_3][Cu^{II}_{0.3}Ni^{II}_{1.7}(ox)_3]$	CAFM/FiM	28	M–O–C–O–M connectivity; thin magnetic hysteresis loop at 2 K	263
$Fe^{II}(2\text{-}Meim)_2\cdot 0.13(Cp_2Fe^{II})$	CAFM	27	M–N–C–N–M connectivity; magnetic hysteresis at 4.8 K with H_c = 5000 Oe and M_r = 200 Oe $cm^3\ mol^{-1}$	397
$Co^{II}_7(OH)_8(ox)_3(ppz)_3$	AFM	26	Heptameric subunits; M–O–C–O–M/M–O–M connectivity; field-induced transition to a FM-like state below T_N	276

$Cu^{II}(F\text{-pymo})_2 \cdot 1.25H_2O$	CAFM	24	M–N–C–N–M connectivity; reversible dehydration/hydration; guest-dependent modulation of magnetic properties	386
$Co^{II}(Cl\text{-pymo})_2$	CAFM	22.5	M–N–C–N–M connectivity; magnetic hysteresis at 2 K with H_c = 1000 Oe and M_r = 0.0501 μ_B mol^{-1}	388
$Co^{II}(H\text{-pymo})_2$	CAFM	22	M–N–C–N–M connectivity; magnetic hysteresis at 4.8 K with H_c = 500 Oe and M_r = 0.0358 μ_B mol^{-1}	388
$[Na(H_2O)_4]_4[Mn^{II}_4(Cu^{II}_2(mpba)_2(H_2O)_4)_3] \cdot 56.5H_2O$	FM	22.5	M–O–C–O–M/M–O–C–N–M connectivity; reversible dehydration/hydration	291
$[Na(H_2O)_{3.25}]_4[Mn^{II}_4(Cu^{II}_2(Me_3mpba)_2(H_2O)_{3.33})_3] \cdot 37H_2O$	FM	21.0	M–O–C–O–M/M–O–C–N–M connectivity; reversible dehydration/hydration; guest-dependent modulation of T_c	292,293, 294
$Fe^{II}(4\text{-abim})_2$	CAFM	21	M–N–C–N–M connectivity; magnetic hysteresis at 4.8 K with H_c = 80 Oe and M_r = 2100 Oe cm^3 mol^{-1}	398
$Co^{II}(Br\text{-pymo})_2$	CAFM	20.5	M–N–C–N–M connectivity; magnetic hysteresis at 2 K with H_c = 2500 Oe and M_r = 0.0501 μ_B mol^{-1}	388
$(Bu_4N)_4[Mn^{II}_4Cu^{II}_6(Et_2pma)_{12}] \cdot DMSO \cdot 10H_2O$	FiM	20	M–O–C–O–M/M–O–C–N–M connectivity	297
Co^{II}(pim) (MIL-36)	CAFM	20	M–O–C–O–M connectivity; open magnetic hysteresis loop at 4.2 K	319
$Ni^{II}_2(D\text{-ca})_2$(1,4-dimb)	CAFM	19.5	Dimeric subunits; M–O–C–O–M/M–O–M connectivity; magnetic hysteresis at 1.8 K with H_c = 913 Oe and M_r = 1758 Oe cm^3 mol^{-1}; spin glass behavior below T_N	328
$Co^{II}(I\text{-pymo})_2$	CAFM	19	M–N–C–N–M connectivity; magnetic hysteresis at 2 K with H_c = 775 Oe and M_r = 0.0457 μ_B mol^{-1}	388
$Ni^{II}_7(OH)_8(ox)_3(ppz)_3$	AFM	17	Heptameric subunits; M–O–C–O–M/M–O–M connectivity	277
$Fe^{II}_3(im)_6(imH)_2$	CAFM	17	M–N–C–N–M connectivity; magnetic hysteresis at 4.8 K with H_c = 200 Oe and M_r = 2500 Oe cm^3 mol^{-1}	396
α-$Co^{II}(im)_2 \cdot 0.5DMA$	CAFM	16.8	M–N–C–N–M connectivity; open magnetic hysteresis loop at 1.8 K	370
$Co^{II}_2(hypa)_2(4,4'\text{-bpy}) \cdot 1.5H_2O$	AFM	15.2	Dimeric subunits; M–O–C–O–M/M–O–M intralayer connectivity	322
β-$Co^{II}(im)_2$	CAFM	15.5	M–N–C–N–M connectivity; magnetic hysteresis at 2 K with H_c = 7300 Oe and M_r = 0.07 μ_B mol^{-1}	399
$Ni^{II}Co^{II}(D\text{-ca})_2$(1,4-dimb)	CAFM	15	Dimeric subunits; M–O–C–O–M/M–O–M connectivity; spin glass behavior and field-induced spin-flop transition below T_N; magnetic hysteresis at 1.8 K with H_c = 205 Oe and M_r = 40 Oe cm^3 mol^{-1}	328
$Co^{II}(im)_2 \cdot 0.5CyOH$	CAFM	15	M–N–C–N–M connectivity; open magnetic hysteresis loop at 1.8 K	399
$Mn^{II}_2(bpybc)(ox)_2 \cdot 8H_2O$	AFM	14.7	M–O–C–O–M intralayer connectivity; guest-modulated magnetic properties; field-induced transition to a FM-like state below T_N when H > 3.4 T	278
$Co^{II}_2(L\text{-asp})_2(4,4'\text{-bpy}) \cdot 1.5H_2O$	CAFM	14.6	M–O–C–O–M intralayer connectivity; magnetic hysteresis at 1.8 K with H_c = 72 Oe	321
$Fe^{II}(im)_2(4,4'\text{-bpy})$	CAFM	14.5	M–N–C–N–M intralayer connectivity; magnetic hysteresis when H < 1.0 T; H_c = 8000 Oe at 2 K	475
Co^{II}(glu)	AFM	14	M–O–C–O–M connectivity	317

$Ni^{II}_{1.5}Co^{II}_{0.5}$(*D*-ca)$_2$(1,4-dimb)	CAFM	14	Dimeric subunits; M–O–C–O–M/M–O–M connectivity; magnetic hysteresis at 1.8 K with H_c = 67 Oe and M_r = 18 Oe cm^3 mol^{-1}; spin glass behavior below T_N	328
Co^{II}(im)$_2$·0.5py	AFM	13.1	M–N–C–N–M connectivity	399
[Fe^{II}(2,2′-bpy)$_3$][Mn^{II}_2(ox)$_3$]	AFM	13.0(5)	M–O–C–O–M connectivity	264,265
[Ir^{III}(ppy)$_2$(2,2′-bpy)][$Ni^{II}Cr^{III}$(ox)$_3$]·0.5H_2O	FM	13.0	M–O–C–O–M connectivity; magnetic hysteresis at 2 K with H_c = 30 Oe	262
$Ni^{II}_{1.33}Co^{II}_{0.67}$(*D*-ca)$_2$(1,4-dimb)	CAFM	13	Dimeric subunits; M–O–C–O–M/M–O–M connectivity; magnetic hysteresis at 1.8 K with H_c = 348 Oe and M_r = 284 Oe cm^3 mol^{-1}; spin glass behavior below T_N	328
Cu^{II}_3(tz)$_4Cl_2$·1.4MeOH	CAFM	12	Trimeric subunits; M–N–N–M/M–Cl–M and M–N–N–N–M/M–N–C–N–M intra- and interunit connectivity, respectively; magnetic hysteresis at 2.0 K with $H_c \approx$ 20 Oe and M_r = 0.01 μ_B mol^{-1}	405
β-Co^{II}(im)$_2$·0.5DMA	CAFM	12.0	M–N–C–N–M connectivity; hidden CAFM behavior below T_N; open magnetic hysteresis loop at 1.8 K	370
α-Co^{II}(im)$_2$	CAFM	11.5	M–N–C–N–M connectivity; magnetic hysteresis at 1.8 K with H_c = 1800 Oe and M_r = 0.016 μ_B mol^{-1}	399
Cu^{II}_2(bptc)(H_2O)$_3$(DMF)$_3$ (MOF-505)	CAFM	11	Dimeric subunits; M–O–C–O–M connectivity; open magnetic hysteresis loop at 5 K	252
Co^{II}(4-abim)$_2$	CAFM	11	M–N–C–N–M connectivity; magnetic hysteresis at 10 K with H_c = 400 Oe and M_r = 22 Oe cm^3 mol^{-1}	398
[Ru^{II}(2,2′-bpy)$_3$][$Cu^{II}_{1.28}Ni^{II}_{0.72}(ox)_3$]	CAFM/FiM	11	M–O–C–O–M connectivity; thin magnetic hysteresis loop at 2 K	263
Mn^{II}(ox)·0.25H_2O	CAFM	10.9	M–O–C–O–M/M–O–M connectivity; thin magnetic hysteresis loop at 2 K	476
Co^{II}_5(im)$_{10}$·2MeBuOH	CAFM	10.6	M–N–C–N–M connectivity; hidden CAFM behavior below T_N; open magnetic hysteresis loop at 5.0 K	399
$Ni^{II}_{0.67}Co^{II}_{1.33}$(*D*-ca)$_2$(1,4-dimb)	CAFM	10	Dimeric subunits; M–O–C–O–M/M–O–M connectivity; spin glass behavior and field-induced spin-flop transition below T_N; magnetic hysteresis at 1.8 K with H_c = 97 Oe and M_r = 26 Oe cm^3 mol^{-1}	328
Co^{II}(adip)	AFM	10	M–O–C–O–M connectivity	318
Co^{II}_2(5-tzc)$_2$(bpea)	AFM	9	M–N–N–M/M–N–N–N–M/M–N–C–N–M/M–O–C–O–M/M–O–C–C–N–M intralayer connectivity; field-induced transition to a CAFM state below T_N when H > 800 Oe; magnetic hysteresis at 2 K with H_c = 700 Oe and M_r = 0.13 μ_B mol^{-1}	415
[Co^{III}(2,2′-bpy)$_3$][Co^{II}_2(ox)$_3$](ClO_4)	CAFM	8	M–O–C–O–M connectivity; magnetic hysteresis at 2 K with H_c = 500 Oe and M_r = 50 Oe cm^3 mol^{-1}	266
Co^{II}_2(*D*-ca)$_2$(1,4-dimb)	AFM	8.0	Dimeric subunits; M–O–C–O–M/M–O–M connectivity; field-induced spin-flop transition below T_N	328
[Ru^{II}(2,2′-bpy)$_3$][$Cu^{II}_{1.8}Ni^{II}_{0.2}(ox)_3$]	CAFM/FiM	7	M–O–C–O–M connectivity; thin magnetic hysteresis loop at 2 K	263
[Fe^{II}(2,2′-bpy)$_3$][$Co^{II}Cr^{III}$(ox)$_3$](ClO_4)	FM	6.6	M–O–C–O–M connectivity; magnetic hysteresis at 2 K with H_c = 55 Oe	259
Mn^{II}(1,4-bdc)(H_2O)$_2$	AFM	6.5	M–O–C–O–M intralayer connectivity	68

Ni^{II}(*L*-tart)	AFM	6	M–O–C–O–M/M–O–C–C–O–M connectivity; transition to a CAFM ordered state below 4.5 K; field-induced transition to a FM ordered state below 4.5 K when H > 3000 Oe; magnetic hysteresis at 2 K with H_c = 600 Oe	324
$Co^{II}_2(tdac)_2(H_2O)_2$	CAFM	6	M–O–C–O–M/M–O–C–C–N–M/M–N–S–N–M connectivity; open magnetic hysteresis loop at 2 K	416
(4-MePyNO)[$Mn^{II}(H_2O)Cr^{III}(ox)_3$] ·2$H_2O$	AFM	6	M–O–C–O–M connectivity	267
[Ru^{II}(2,2′-bpy)$_2$(ppy)][$Mn^{II}Cr^{III}(ox)_3$]	FM	5.8	M–O–C–O–M connectivity; thin magnetic hysteresis loop at 2 K	261
$Fe^{II}_3(OH)_3(squ)_{1.5}$	CAFM	5.2	M–O–C–C–O–M/M–O–C–C–C–O–M connectivity; magnetic hysteresis at 1.8 K with H_c = 680 Oe and M_r = 0.35 μ_B mol^{-1}	335
[Fe^{II}(im$_2$-trien)][Mn^{II}(MeOH) $Cr^{III}(ox)_3]_2$·4MeOH·MeCN·H_2O	FM	5.2	M–O–C–O–M connectivity; magnetic hysteresis at 2 K with H_c = 20 Oe	271
[Ir^{III}(ppy)$_2$(2,2′-bpy)][$Fe^{II}Cr^{III}(ox)_3$] ·0.5H_2O	FM	5.0	M–O–C–O–M connectivity; magnetic hysteresis at 2 K with H_c = 40 Oe	262
[Ru^{II}(2,2′-bpy)$_3$][$Cu^{II}_2(ox)_3$]	CAFM	5	M–O–C–O–M connectivity; thin magnetic hysteresis loop at 2 K	263
KCo^{II}_3(cit)(O-cit)$(H_2O)_2$·8H_2O	CAFM	5	M–O–C–O–M intercluster connectivity; magnetic hysteresis at 2 K with H_c = 20 Oe and M_r = 92 Oe cm^3 mol^{-1}	325
Cu^{II}_2(1,2,4,5-btec)(hypH)$_{0.5}(H_2O)_{0.5}$ ·1.5H_2O	FM	4.5	M–O–C–O–M/M–O–C–C–N–M connectivity; magnetic hysteresis at 2 K with H_c = 20 Oe and M_r = 0.05 μ_B mol^{-1}	359
[Fe^{II}(tren(6-Mepy)$_3$)][$Mn^{II}Cr^{III}(ox)_3$] [$Mn^{II}(MeOH)_{0.58}(H_2O)_{0.42}Cr^{III}(ox)_3$] ·2MeOH·0.5MeCN·0.42$H_2O$	FM	4.3	M–O–C–O–M connectivity; magnetic hysteresis at 2 K with H_c = 20 Oe	271
Mn^{II}_2(1,4-bdc)$_2$(DMF)$_2$	AFM	4.2	Tetrameric subunits; M–O–C–O–M/M–O–M connectivity; spin glass behavior below T_N.	345
[Fe^{II}(tren-im$_3$)]$_2$[$Mn^{II}_{2.5}$(MeOH)$_3$ $Cr^{III}_3(ox)_9$]·4.75MeOH·4.25H_2O	FM	3.8	M–O–C–O–M connectivity	271
Co^{II}_3(OH)(bpc)$(H_2O)_3$	CAFM	3.8	Hexameric subunits; M–O–C–O–M/M–O–M connectivity	360
Mn^{II}_3(3-pyc)$_4(N_3)_2(H_2O)_2$	FiM	3.7	Trimeric subunits; M–N–M/M–O–C–O–M connectivity	407
Co^{II}_4(2-pyco)$_4$(4,4′-bpy)$_3(H_2O)_2$ ·2H_2O	CAFM	3.5	M–O–C–O–M/M–O–C–C–N–M intrachain connectivity; field-induced transition to a FM-like ordered state below T_N when H > 150 Oe	477
Mn^{II}(*L*-ma)(H_2O)	AFM	3.5	M–O–C–O–M/M–O–C–C–O–M connectivity	323
Mn^{II}(*L*-tart)	CAFM	3.3	M–O–C–O–M/M–O–C–C–O–M connectivity; magnetic hysteresis at 2 K with H_c = 450 Oe	324
Cu^{II}_2(mal)$_2$(pyz)·2H_2O	AFM	3.2	M–O–C–O–M/M–N–C–C–N–M connectivity; field-induced transition to a FM-like state below T_N	302,306
Co^{II}_3(chhc)$(H_2O)_6$	AFM	3.0	M–O–C–O–M connectivity	340
Ni^{II}_2(1,2,4,5-btec)$(H_2O)_4$·2H_2O	AFM	3	M–O–C–O–M intralayer connectivity; field-induced transition to a FM state below T_N	358
Ni^{II}(*rac*-ma)(H_2O)·H_2O	FM	2.7	M–O–C–O–M/M–O–C–C–O–M connectivity	323

Cu^{II}(mal)(DMF)	FM	2.6	M–O–C–O–M connectivity; magnetic hysteresis at 1.82 K with H_c = 28 Oe and M_r = 0.18 μ_B mol^{-1}	302
$(H_2NMe_2)[Co^{II}(trzdc)]\cdot 0.5H_2O$	CAFM	2.4	M–O–C–O–M/M–N–N–N–M/M–O–C–C–N–M; spin frustrated system ($f \approx 20$); spin glass behavior below T_N; open magnetic hysteresis loop at 1.8 K	414
$Mn^{II}_{0.79}Ni^{II}_{0.21}$(*L*-ma)($H_2O$)	FiM	2.3	M–O–C–O–M/M–O–C–C–O–M connectivity; magnetic hysteresis at 1.8 K with H_c = 70 Oe	323
$[Ru^{II}(2,2'\text{-bpy})_3][Cu^{II}Cr^{III}(ox)_3](ClO_4)$	FM	1.9	M–O–C–O–M connectivity; magnetic hysteresis at 2 K with H_c = 14 Oe	259
$Mn^{II}_{0.63}Co^{II}_{0.37}$(*L*-ma)($H_2O$)	FiM	~1.8	M–O–C–O–M/M–O–C–C–O–M connectivity	323
Co^{II}(*rac*-ma)(H_2O)·H_2O	FM	1.63(1)	M–O–C–O–M/M–O–C–C–O–M connectivity	323

[a] The bridging unit $(CPO_3)^{2-}$ is considered to be inorganic in nature, and therefore metal polyhedra bridged via three-atom O–P–O linkages are treated equivalently to those bridged by single-atom oxo bridges. [b] Only the metal oxalate frameworks with the highest ordering temperature for a given lattice type are included in this table. See Tables 8.12–8.17 for details on the variation in T_c with the cation. [c] This compound does not strictly fall into the I^2O^1 class, as it consists of alternating layers of I^1O^1 and I^2O^0 connectivity. [d] The magnetic ordering temperature for this compound is not specified. [e] This compound does not strictly fall into the I^0O^3 class, as it features mixed oxalato (M–O–C–O–M) and oxo/hydroxo (M–O–M) bridges in one direction.

Table 8.3 Magnetic data for 2D oxalate frameworks with honeycomb topology of formula $(A)[Fe^{II}Fe^{III}(ox)_3]$.

A^+	Magnetic order	T_c (K)	Other magnetic properties	Ref.
$(Pr_4N)^+$	FiM	44.5	Néel N-type FiM order with T_{comp} = 34 K	227–229
$(Bu_4N)^+$	FiM	45	Néel N-type FiM order with T_{comp} = 31.5 K; magnetic hysteresis at 40 K with H_c = 400 Oe	227–229
$(Bu_3BzN)^+$	FiM	44	Néel N-type FiM order	229
$(Pe_4N)^+$	FiM	46	Néel N-type FiM order with T_{comp} = 29.5 K	228, 229
PNP^+	FiM	43	Néel N-type FiM order with T_{comp} = 30.5 K	228, 229
$(Bu_4P)^+$	FiM	44.5	Néel N-type FiM order with T_{comp} = 33.5 K	228, 229
$(Ph_4P)^+$	FiM	34	Spin glass behavior below T_c; magnetic hysteresis at 20 K with H_c = 541 Oe	227–229
$(Ph_3PrP)^+$	FiM	42(1)	Néel N-type FiM order	230
$(Ph_3BuP)^+$	FiM	44(1)	Néel N-type FiM order	230
$(Ph_3PeP)^+$	FiM	44(1)	Néel N-type FiM order	230
$(Ph_3HxP)^+$	FiM	44(1)	Néel N-type FiM order	230
$(Ph_3HpP)^+$	FiM	48(1)	Néel N-type FiM order	230
$(Ph_4As)^+$	FiM	36	Spin glass behavior below T_c	228, 229

Table 8.4 Magnetic data for 2D oxalate frameworks with honeycomb topology of formula $(A)[Mn^{II}Fe^{III}(ox)_3]$.

A^+	Magnetic order[a]	T_c (K)	Ref.
$(Pr_4N)^+$	CAFM	28	229
$(Bu_4N)^+$	CAFM	28	229,232
$(Bu_3BzN)^+$	CAFM	26	229
$(Pe_4N)^+$	CAFM/FiM	27	229,231
PNP^+	CAFM	29	229
$(Bu_4P)^+$	CAFM	26	229
$(Ph_4P)^+$	CAFM	25	229
$(Ph_3PrP)^+$	FiM	32.5(2)	230
$(Ph_3BuP)^+$	FiM	30.0(2)	230
$(Ph_3PeP)^+$	FiM	33.2(2)	230
$(Ph_3HxP)^+$	FiM	33.0(2)	230
$(Ph_3HpP)^+$	FiM	32.9(2)	230
$(Ph_4As)^+$	CAFM	27	229

[a]The first studies reported CAFM order for these compounds, however, subsequent studies found that the uncompensated magnetic moment more likely originated from Mn^{II} vacancies, corresponding to FiM order. Here, we report the type of order that the authors speculated at the time of publication.

Table 8.5 Magnetic data for 2D oxalate frameworks with honeycomb-like topology of formula $[K(18\text{-crown-6})]_3[M^{II}{}_3(H_2O)_4(M^{III}(ox)_3)_3]$.

M^{II}	M^{III}	Magnetic order	T_c (K)	Other magnetic properties	Ref.
Mn	Cr	FM	3.5		236
Fe	Cr	FM	8	Magnetic hysteresis at 2 K with H_c = 130 Oe and M_r = 2.32 μ_B mol^{-1}	236
Co	Cr	FM	6	Magnetic hysteresis at 2 K with H_c = 170 Oe and M_r = 3.69 μ_B mol^{-1}	236
Ni	Cr	FM	4.5	Magnetic hysteresis at 2 K with H_c = 790 Oe and M_r = 4.50 μ_B mol^{-1}	236
Cu	Cr	FM	3.2		236
Mn	Fe	CAFM	14	Magnetic hysteresis at 2 K with H_c = 180 Oe and M_r = 1.14 μ_B mol^{-1}	236
Fe	Fe	FiM	25.5		236
Co	Fe	FiM	16	Magnetic hysteresis at 2 K with H_c = 1.53 T and M_r = 0.95 μ_B mol^{-1}	236
Ni	Fe	FiM	11.5	Magnetic hysteresis at 2 K with H_c = 230 Oe and M_r < 0.01 μ_B mol^{-1}	236

Table 8.6 Magnetic data for neutral 2D oxalate frameworks of formula $[M^{II}(H_2O)_2]_3[M^{III}(ox)_3]_2 \cdot 2(18\text{-crown-6})$.

M^{II}	M^{III}	Magnetic order	T_c (K)	Other magnetic properties	Ref.
Co	Cr	FM	7.4	Magnetic hysteresis at 2 K with H_c = 160 Oe and M_r = 2.3 μ_B mol^{-1}	239, 240
Mn	Cr	FM	3.6	Magnetic hysteresis at 2 K with H_c < 100 Oe and M_r < 0.1 μ_B mol^{-1}	240
Mn/Ni	Cr	FM	6.8	Magnetic hysteresis at 2 K with H_c = 200 Oe and M_r = 2.4 μ_B mol^{-1}	240
Co/Ni	Cr	FM	6.8	Magnetic hysteresis at 2 K with H_c = 200 Oe and M_r = 1.4 μ_B mol^{-1}	240
Mn/Fe	Fe	FiM	19.5	Magnetic hysteresis at 2 K with H_c < 100 Oe and M_r < 0.1 μ_B mol^{-1}	240
Mn/Co	Fe	FiM	9.4	Magnetic hysteresis at 2 K with H_c = 6300 Oe and M_r = 0.3 μ_B mol^{-1}	240
Fe	Fe	FiM	12.2	Magnetic hysteresis at 2 K with H_c = 1100 Oe and M_r < 0.1 μ_B mol^{-1}	240
Fe/Ni	Fe	FiM	20.0	Magnetic hysteresis at 2 K with H_c = 160 Oe and M_r = 0.1 μ_B mol^{-1}	240

Table 8.7 Magnetic data for 2D oxalate frameworks with honeycomb topology of formula $[Cp^*_2Fe^{III}][M^{II}M^{III}(ox)_3]$.

M^{II}	M^{III}	Magnetic order	T_c (K)	Other magnetic properties	Ref.
Mn	Cr	FM	5.3	Magnetic hysteresis at 2 K with H_c = 20 Oe and M_r = 0.15 μ_B mol^{-1}	233,234
Fe	Cr	FM	13.0	Magnetic hysteresis at 2 K with H_c = 1100 Oe and M_r = 3.60 μ_B mol^{-1}	233,234
Co	Cr	FM	9.0	Magnetic hysteresis at 2 K with H_c = 130 Oe and M_r = 1.20 μ_B mol^{-1}	233,234
Ni	Cr	FM	14.5	Magnetic hysteresis at 5 K with H_c = 250 Oe.	233
Cu	Cr	FM	7.0	Magnetic hysteresis at 2 K with H_c = 180 Oe and M_r = 1.50 μ_B mol^{-1}	233,234
Mn	Fe	CAFM	28.4	Magnetic hysteresis at 2 K with H_c = 120 Oe and M_r = 0.10 μ_B mol^{-1}	233,234
Fe	Fe	FiM	43.3	Magnetic hysteresis at 2 K with H_c = 370 Oe and M_r = 0.02 μ_B mol^{-1}	233,234
Co	Fe	FiM	19.5		233
Fe	Ru	FM	13.8	Magnetic hysteresis at 2 K with H_c = 2210 Oe and M_r = 2.5 μ_B mol^{-1}	235
Co	Ru	FM	3.1		235

Table 8.8 Magnetic data for 2D oxalate frameworks with honeycomb topology of formula $[Cp^*_2Co^{III}][M^{II}M^{III}(ox)_3]$.

M^{II}	M^{III}	Magnetic order	T_c (K)	Other magnetic properties	Ref.
Mn	Cr	FM	5.1	Magnetic hysteresis at 2 K with H_c = 40 Oe and M_r = 0.3 μ_B mol^{-1}	234
Fe	Cr	FM	12.7	Magnetic hysteresis at 2 K with H_c = 1940 Oe and M_r = 3.5 μ_B mol^{-1}	234
Co	Cr	FM	8.2	Magnetic hysteresis at 2 K with H_c = 250 Oe and M_r = 1.3 μ_B mol^{-1}	234
Cu	Cr	FM	6.7	Magnetic hysteresis at 2 K with H_c = 200 Oe and M_r = 1.7 μ_B mol^{-1}	234
Mn	Fe	CAFM	25.4	Magnetic hysteresis at 2 K with H_c = 150 Oe and M_r < 0.01 μ_B mol^{-1}	234
Fe	Fe	FiM	44.0	Magnetic hysteresis at 2 K with H_c = 100 Oe and M_r < 0.01 μ_B mol^{-1}	234
Fe	Ru	FM	12.8	Magnetic hysteresis at 2 K with H_c = 3200 Oe and M_r = 2.0 μ_B mol^{-1}	235
Co	Ru	FM	2.8		235

Table 8.9 Magnetic data for 2D oxalate frameworks with honeycomb topology of formula $(R_3(CH_2COOH)N)[M^{II}M^{III}(ox)_3]\cdot xH_2O$.

M^{II}	M^{III}	Magnetic order	T_c (K)	Other notes	Ref.
Mn	Cr	FM	5.9	R = Et, x = 2	241
Fe	Cr	FM	11.0	R = Et, x = 2	241
Fe	Fe	FiM	42–44	R = Et, x = 2; Néel N-type FiM order with $T_{comp} \approx$ 33 K	241
Mn	Cr	FM	5.6	R =Bu, x = 0	241
Fe	Cr	FM	11.5	R =Bu, x = 0	241
Fe	Fe	FiM	42–44	R =Bu, x = 0; Néel N-type FiM order with $T_{comp} \approx$ 33 K	241

Table 8.10 Magnetic data for 2D oxalate frameworks with intercalated spin-crossover Fe^{III} complexes or diamagnetic In^{III} analogues.

Compound	Magnetic order	T_c (K)	Other magnetic properties	Ref.
$[Fe(sal_2\text{-trien})]_2[Mn^{II}_2(ox)_3]\cdot 4H_2O\cdot DMF$	CAFM	8.1	Partial spin-crossover; magnetic hysteresis at 2 K with H_c = 48 Oe	248
$[In(sal_2\text{-trien})]_2[Mn^{II}_2(ox)_3]\cdot 3H_2O\cdot MeOH$	CAFM	8.1	Magnetic hysteresis at 2 K with H_c = 660 Oe	248
$[Fe(sal_2\text{-trien})][Mn^{II}Cr^{III}(ox)_3]\cdot CH_2Cl_2$	FM	5.4	Near complete spin-crossover with $T_{1/2}$ = 255 K; LIESST effect with T_{LIESST} = 41 K; magnetic hysteresis at 2 K with H_c = 20 Oe	249, 250
$[Fe(sal_2\text{-trien})][Mn^{II}Cr^{III}(ox)_3]\cdot CHCl_3$	FM	5.6	Near complete spin-crossover with $T_{1/2}$ = 180 K; LIESST effect with T_{LIESST} = 58 K; magnetic hysteresis at 2 K with H_c = 10 Oe	253
$[Fe(sal_2\text{-trien})][Mn^{II}Cr^{III}(ox)_3]\cdot CHBr_3$	FM	5.6	Partial spin-crossover with $T_{1/2}$ = 140 K; LIESST effect with T_{LIESST} = 62 K; magnetic hysteresis at 2 K with H_c = 30 Oe	253
$[Fe(sal_2\text{-trien})][Mn^{II}Cr^{III}(ox)_3]\cdot CH_2Br_2$	FM	5.6	Complete spin-crossover with $T_{1/2}$ = 230 K; LIESST effect with T_{LIESST} = 45 K; magnetic hysteresis at 2 K with H_c = 10 Oe	253
$[Fe(4\text{-Br-}sal_2\text{-trien})][Mn^{II}Cr^{III}(ox)_3]_{0.67}Cl_{0.33}\cdot MeOH\cdot solvent$	FM	5.2	Near complete spin-crossover; magnetic hysteresis at 2 K with H_c = 70 Oe	251
$[Fe(3\text{-Br-}sal_2\text{-trien})][Mn^{II}Cr^{III}(ox)_3]\cdot 2MeCN$	FM	5.4	High-spin Fe^{III}	251
$[Fe(3\text{-Cl-}sal_2\text{-trien})][Mn^{II}Cr^{III}(ox)_3]\cdot 2MeCN\cdot 2MeOH$	FM	5.0	Partial spin-crossover	251
$[Fe(3\text{-OMe-}sal_2\text{-trien})][Mn^{II}Cr^{III}(ox)_3]\cdot MeOH\cdot 1.5H_2O\cdot 0.5CH_2Cl_2$	FM	5.4	Partial spin-crossover	251
$[Fe(5\text{-}NO_2\text{-}sal_2\text{-trien})][Mn^{II}Cr^{III}(ox)_3]\cdot MeNO_2\cdot 0.5H_2O$	FM	5.6	Partial spin-crossover; magnetic hysteresis at 2 K with H_c = 5 Oe	252
$[Fe(pmha)_2][Mn^{II}Cr^{III}(ox)_3]$	FM	5.5	High-spin Fe^{III}	244

Table 8.11 Magnetic data for other 2D oxalate frameworks.

Compound	Magnetic order	T_c (K)	Other magnetic properties	Ref.
$(Pr_4N)[Mn^{II}Cr^{III}(ox)_3]$	FM	6		232
$(Ph_4P)[Mn^{II}Cr^{III}(ox)_3]$	FM	5.9		238
$(dams)[Mn^{II}Cr^{III}(ox)_3]$	FM	5.8		244
$[Mn^{II}(H_2O)_2(MeOH)_2][Mn^{II}(H_2O)(MeOH)]_2[Cr^{III}(ox)_3]_2 \cdot$(18-crown-6)	FiM	5.5	Thin magnetic hysteresis loop at 2 K	470

Table 8.12 Magnetic data for 3D chiral frameworks of formula $[(Z^{II+n})(2,2'\text{-bpy})_3][M^{II}_2(ox)_3](ClO_4)_n$ with homometallic anionic lattice.

Z^{II+n}	M^{II}	Magnetic order	T_c (K)	Other magnetic properties	Ref.
Fe^{II}	Mn	AFM	13.0(5)		264,265
Co^{III}	Co	CAFM	8	Magnetic hysteresis at 2 K with H_c = 500 Oe and M_r = 50 Oe cm^3 mol^{-1}	266
Fe^{II}	Co	CAFM	6	Magnetic hysteresis at 2 K with H_c = 300 Oe and M_r = 40 Oe cm^3 mol^{-1}	266
Ru^{II}	Cu	CAFM	5	Thin magnetic hysteresis loop at 2 K	263
Ru^{II}	Ni	CAFM	35	Thin magnetic hysteresis loop at 2 K	263

Table 8.13 Magnetic data for 3D chiral frameworks of formula $[Z^{I+n}][M^{II}Cr^{III}(ox)_3](ClO_4)_n$ with heterometallic anionic lattice.

Z^{I+n}	M^{II}	Magnetic order	T_c (K)	Other magnetic properties	Ref.
$[Ru(2,2'\text{-bpy})_3]^{2+}$	Mn	FM	4.2	Thin magnetic hysteresis loop at 2 K	261
$[Ru(2,2'\text{-bpy})_2(ppy)]^{+}$	Mn	FM	5.8	Thin magnetic hysteresis loop at 2 K	261
$[Ru(2,2'\text{-bpy})_3]^{2+}$	Fe	FM	2.5	Magnetic hysteresis at 2 K with H_c = 14 Oe	259
$[Ru(2,2'\text{-bpy})_3]^{2+}$	Co	FM	2.8	Magnetic hysteresis at 2 K with H_c = 8 Oe	259
$[Ru(2,2'\text{-bpy})_3]^{2+}$	Ni	FM	6.4	Magnetic hysteresis at 2 K with H_c = 22 Oe	259
$[Ru(2,2'\text{-bpy})_2(ppy)]^{+}$	Ni	FM	11.0	Thin magnetic hysteresis loop at 2 K	261
$[Ru(2,2'\text{-bpy})_3]^{2+}$	Cu	FM	1.9	Magnetic hysteresis at 2 K with H_c = 14 Oe	259
$[Fe(2,2'\text{-bpy})_3]^{2+}$	Mn	FM	3.9		259
$[Fe(2,2'\text{-bpy})_3]^{2+}$	Fe	FM	4.7	Magnetic hysteresis at 2 K with H_c = 80 Oe	259
$[Fe(2,2'\text{-bpy})_3]^{2+}$	Co	FM	6.6	Magnetic hysteresis at 2 K with H_c = 55 Oe	259
$[Ni(2,2'\text{-bpy})_3]^{2+}$	Mn	FM	2.3	Magnetic hysteresis at 2 K with H_c = 13 Oe	259
$[Ni(2,2'\text{-bpy})_3]^{2+}$	Fe	FM	4.0	Magnetic hysteresis at 2 K with H_c = 28 Oe	259
$[Co(2,2'\text{-bpy})_3]^{2+}$	Mn	FM	2.2	Magnetic hysteresis at 2 K with H_c = 13 Oe	259

Table 8.14 Magnetic data for 3D chiral frameworks of formula $[Z^{II}(2,2'\text{-bpy})_3][M^{II}Fe^{III}(ox)_3](ClO_4)$.

Z^{II}	M^{II}	Magnetic order	T_c (K)	Other magnetic properties	Ref.
Fe	Mn	CAFM	20.0	Magnetic hysteresis at 2 K with H_c = 250 Oe	260
Fe	Fe	FiM	9.1	Magnetic hysteresis at 2 K with H_c = 970 Oe	260
Ru	Mn	CAFM	17.2	Magnetic hysteresis at 2 K with H_c = 300 Oe	260
Ru	Fe	FiM	7.9	Magnetic hysteresis at 2 K with H_c = 860 Oe	260

Table 8.15 Magnetic data for 3D chiral frameworks of formula $[Ir^{III}(ppy)_2(2,2'\text{-bpy})][M^{II}M^{III}(ox)_3]\cdot 0.5H_2O$.

M^{II}	M^{III}	Magnetic order	T_c (K)	Other magnetic properties	Ref.
Mn	Cr	FM	5.1	Magnetic hysteresis at 2 K with H_c = 20 Oe	262
Fe	Cr	FM	5.0	Magnetic hysteresis at 2 K with H_c = 40 Oe	262
Co	Cr	FM	5.2	Magnetic hysteresis at 2 K with H_c = 50 Oe	262
Ni	Cr	FM	13.0	Magnetic hysteresis at 2 K with H_c = 30 Oe	262
Fe	Fe	FiM	28.0	Magnetic hysteresis at 2 K with H_c = 300 Oe	262
Mn	Fe	CAFM	31.0	Magnetic hysteresis at 2 K with H_c = 240 Oe	262

Table 8.16 Magnetic data for 3D oxalate frameworks with intercalated spin-crossover Fe^{II}/Fe^{III} complexes or diamagnetic In^{III} analogues.

Compound	Magnetic order	T_c (K)	Other magnetic properties	Ref.
$[Fe^{III}(sal_2\text{-trien})][Mn^{II}Cr^{III}(ox)_3]\cdot MeOH$	FM	5.2	Partial spin-crossover; magnetic hysteresis at 2 K with H_c = 30 Oe	249
$[In^{III}(sal_2\text{-trien})][Mn^{II}Cr^{III}(ox)_3]\cdot 0.25H_2O\cdot 0.25MeOH\cdot 0.25MeCN$	FM	5.2	Magnetic hysteresis at 2 K with H_c = 30 Oe	249
$[In^{III}(sal_2\text{-trien})][Mn^{II}Cr^{III}(ox)_3]\cdot MeNO_2\cdot 0.5H_2O$	FM	5.0	Magnetic hysteresis at 2 K with H_c = 30 Oe	249
$[Fe^{III}(5\text{-OMe-}sal_2\text{-trien})][Mn^{II}Cr^{III}(ox)_3]$	FM	5.1	Partial spin-crossover; magnetic hysteresis at 2 K with H_c = 60 Oe	252
$[Fe^{III}(5\text{-Cl-}sal_2\text{-trien})][Mn^{II}Cr^{III}(ox)_3]\cdot 0.5MeNO_2$	FM	4.8	Partial spin-crossover; magnetic hysteresis at 2 K with H_c = 30 Oe	268
$[In^{III}(5\text{-Cl-}sal_2\text{-trien})][Mn^{II}Cr^{III}(ox)_3]$	FM	5.0	Magnetic hysteresis at 2 K with H_c = 10 Oe	268
$[Fe^{III}(5\text{-Br-}sal_2\text{-trien})][Mn^{II}Cr^{III}(ox)_3]$	FM	4.8	Partial spin-crossover; magnetic hysteresis at 2 K with H_c = 30 Oe	268
$[Fe^{II}(bppy)_2][Mn^{II}Cr^{III}(ox)_3]_2\cdot bppy\cdot MeOH$	FM	3.0	Minimal spin-crossover	269
$[Fe^{II}(pyimH)_3][Mn^{II}Cr^{III}(ox)_3]_2\cdot solvent$	FM	4.5	Complete spin-crossover with $T_{1/2}$ = 350 K; LIESST effect below 60 K	270
$[Fe^{II}(im_2\text{-trien})][Mn^{II}(MeOH)Cr^{III}(ox)_3]_2\cdot 4MeOH\cdot MeCN\cdot H_2O$	FM	5.2	Partial spin-crossover; magnetic hysteresis at 2 K with H_c = 20 Oe	271
$[Fe^{II}(tren(6\text{-Mepy})_3)][Mn^{II}Cr^{III}(ox)_3][Mn^{II}(MeOH)_{0.58}(H_2O)_{0.42}Cr^{III}(ox)_3]\cdot 2MeOH\cdot 0.5MeCN\cdot 0.42H_2O$	FM	4.3	High-spin Fe^{II}; magnetic hysteresis at 2 K with H_c = 20 Oe	271
$[Fe^{III}(tren\text{-}im_3)]_2[Mn^{II}_{2.5}(MeOH)_3Cr^{III}_3(ox)_9]\cdot 4.75MeOH\cdot 4.25H_2O$	FM	3.8	Partial spin-crossover	271

Table 8.17 Magnetic data for 3D oxalate frameworks of formula $(A)_2[Fe^{III}_2O(ox)_2Cl_2]\cdot xH_2O$ (x = 1, 2, 4).

A^+	Magnetic order	T_c (K)	Other magnetic properties	Ref.
Li^+	CAFM	51	Magnetic hysteresis at 2 K with H_c = 1100 Oe and M_r = 0.030 μ_B mol^{-1}	478
Na^+	CAFM	26	Magnetic hysteresis at 2 K with H_c = 450 Oe and M_r = 0.012 μ_B mol^{-1}	478
K^+	CAFM	38	Magnetic hysteresis at 2 K with H_c = 1600 Oe and M_r = 0.016 μ_B mol^{-1}	478
$(NH_4)^+$	CAFM	40	Magnetic hysteresis at 5 K with H_c = 4000 Oe and M_r = 0.016 μ_B mol^{-1}	274
$(MeNH_3)^+$	CAFM	40	Magnetic hysteresis at 2 K with H_c = 400 Oe and M_r = 0.016 μ_B mol^{-1}	275
$(Me_2NH_2)^+$	CAFM	52	Magnetic hysteresis at 2 K with H_c = 350 Oe and M_r = 0.013 μ_B mol^{-1}	275
$(EtNH_3)^+$	CAFM	56	Magnetic hysteresis at 2 K with H_c = 85 Oe	275
$(H_3O)(EtNH_3)^+$	CAFM	70	Magnetic hysteresis at 5 K with H_c = 2500 Oe and M_r = 0.036 μ_B mol^{-1}	223

Table 8.18 Magnetic data for 2D metal-organic framework magnets with radical bridging ligands.[a]

Compound	Magnetic order	T_c (K)	Other relevant structural and magnetic notes	Ref.
$Mn^{II}(TCNE)I(H_2O)$	CAFM	171	Magnetic hysteresis at 10 K with H_c = 400 Oe and M_r = 60 Oe cm^3 mol^{-1}	73
$[Cp_2Co^{III}]_{1.43}(Me_2NH_2)_{1.57}$ $[Fe^{III}_2(Cl_2An)_3]\cdot 4.9DMF$	FiM	105	Open magnetic hysteresis loop up to 100 K with H_c = 9 Oe. At 1.8 K, H_c = 4520 Oe	458
$(Ru_2(2,3,5\text{-}Clbz)_4)_2(TCNQMe_2)$ $\cdot x CH_2Cl_2$	FiM	101 (x = 4) 34 (x = 0)	Guest-dependent modulation of T_c and H_c; magnetic hysteresis at 1.8 K with H_c = 1.16 T (x = 4) and H_c = 6700 Oe (x = 0)	449
$[Fe^{II}(TCNE)(MeCN)_2](SbF_6)$ $\cdot x CH_2Cl_2 \cdot y MeCN$[b]	FiM	96		444
$(Ru_2(TFA)_4)_2(TCNQF_4)\cdot 3(p\text{-xylene})$	AFM	95	Metamagnetic behavior; intermediate canted spin state with H_c > 0 up to 60 K	446,447
$(Ru_2(1,2\text{-}Fbz)_4)_2(BTDA\text{-}TCNQ)$ $\cdot 4CH_2Cl_2$	AFM	93	Phase transitions at T_c = 87 and 13 K corresponding to CAFM states; open magnetic hysteresis at 1.8 K	451
$[Fe^{II}(TCNE)(MeCN)_2](Fe^{III}Cl_4)$[b]	AFM	89.7(3)	Field-induced transition to a FiM ordered state; Magnetic hysteresis at 50 K with H_c = 1730 Oe and M_r = 7500 Oe cm^3 mol^{-1}	443
$(Ru_2(1,2\text{-}Fbz)_4)_2(TCNQ(OMe)_2)$ $\cdot 4CH_2Cl_2$	FiM/AFM	88/83	Field-induced transition to a FiM-like ordered state below T_N; open magnetic hysteresis loop up to a temperature close to T_N	450
$(Ru_2(1,4\text{-}Fbz)_4)_2(BTDA\text{-}TCNQ)\cdot 2(4\text{-}ClPhMe)\cdot 2CH_2Cl_2$	FM	83	Open magnetic hysteresis at 1.8 K	451
$(Me_2NH_2)_2[Fe^{III}_2(Cl_2An)_3]\cdot x H_2O$ $\cdot y$DMF	FiM	80 (x = 2, y = 6) 26 (x = y = 0)	Reversible desolvation/solvation; guest-dependent modulation of T_c and H_c; magnetic hysteresis at 1.8 K with H_c = 2630 Oe (x = 2, y = 6) and 4650 Oe (x = y = 0)	458
$(Ru_2(1,2\text{-}Clbz)_4)_2(TCNQ(OMe)_2)$ $\cdot x CH_2Cl_2$	AFM (x = 1) FM (x = 0)	75 (x = 1) 56 (x = 0)	Reversible desolvation/solvation; guest-dependent modulation of magnetic properties; field-induced transition to a CAFM state for x = 1; magnetic hysteresis at 1.8 K with H_c = 1.6 T	448
$[Mn^{II}(TCNE)(MeCN)_2](SbF_6)$ $\cdot x CH_2Cl_2 \cdot y MeCN$[b]	FiM	67	Spin glass behavior below T_c.	444
$Cr^{III}Cl_2(pyz)_2$	FiM	~55	Open magnetic hysteresis up to temperatures close to T_c	462
$Na_3(Me_4N)_2[Mn^{II}_2(Cl_2An)_3]$ $\cdot 3.9$THF	FiM	41	Open magnetic hysteresis loop up to 25 K with H_c = 12 Oe; at 1.8 K, H_c = 300 Oe	460
$(Ru_2(1,4\text{-}Fbz)_4)_2(TCNQ(OMe)_2)$ $\cdot 3CH_2Cl_2\cdot PhNO_2$	FiM	27	Mixture of radical and diamagnetic linkers; magnetic hysteresis at 1.8 K with $H_c \approx$ 8000 Oe and $M_r \approx$ 0.6 μ_B mol^{-1}	450
$(TOAPB)_2(Mn^{II}(hfac)_2)_3\cdot Hp$	FM	3.4	Magnetic hysteresis at 2 K with H_c = 3.8 Oe and M_r = 53.9 Oe cm^3 mol^{-1}	436
$Cu^{II}_3(PTMTC)_2(py)_6(EtOH)_2(H_2O)$ $\cdot 10EtOH\cdot 6H_2O$ (MOROF-1)	FiM/FM	2		441
$[Mn^{II}_2(NITIm)_3](ClO_4)$	FiM/FM	1.4	Magnetic hysteresis at 85 mK with H_c = 270 Oe and M_r = 0.22 μ_B mol^{-1}	439

[a] All compounds in this table are classified as I^0O^2. [b] The number of coordinated MeCN molecules per unit cell may vary slightly; see refs. 443 and 444 for details.

Table 8.19 Magnetic data for 3D metal-organic framework magnets with radical bridging ligands.[a]

Compound	Magnetic order	T_c (K)	Other relevant structural and magnetic notes	Ref.
$Mn^{II}(TCNE)_{1.5}(I_3)_{0.5}\cdot 0.5THF$	FiM	171	Magnetic hysteresis at 10 K with H_c = 600 Oe and M_r = 8000 Oe cm^3 mol^{-1}	72
$(Ru_2(1,3\text{-}Fbz)_4)_2(BTDA\text{-}TCNQ)\cdot 1.6(4\text{-}ClPhMe)\cdot 3.4CH_2Cl_2$	FM	107	Open magnetic hysteresis loop up to 100 K, with H_c = 7250 Oe at 1.8 K	452
$Fe^{II}(TCNE)[C_4(CN)_8]_{0.5}\cdot xCH_2Cl_2$	FiM	~100	Mixture of radical and diamagnetic linkers; metamagnetic behavior below T_c; magnetic hysteresis at 2 K with H_c = 2300 Oe (for x = 0.75)	87,88, 445
$Mn^{II}(TCNE)[C_4(CN)_8]_{0.5}\cdot 0.74CH_2Cl_2$	AFM	68		72
$(BAPN)_2(Mn^{II}(hfac)_2)_3$	FM	46		437
$(4\text{-}EtPyNO)_2Co^{II}_2(Cu^{II}(opba))_3(DMSO)_{0.5}\cdot DMSO\cdot 0.25H_2O$	FiM	37	Radical-bridged chains; magnetic hysteresis at 6 K with H_c > 2.4 T	433
$(4\text{-}EtPyNO)_2Ni^{II}_2(Cu^{II}(opba))_3\cdot 5DMSO\cdot 11H_2O$[b]	FiM	28	Radical-bridged chains; magnetic hysteresis at 6 K with H_c = 500 Oe	434
$(4\text{-}PrPyNO)_2Mn^{II}_2(Cu^{II}(opba))_3\cdot 3.3DMSO\cdot 5H_2O$[b]	FiM	24.1	Radical-bridged chains; metamagnetic-like transition at 120 mK when H > 2.1 T	435
$(4\text{-}EtPyNO)_2Mn^{II}_2(Cu^{II}(opba))_3(DMSO)_{0.5}\cdot 0.25H_2O$	FiM	22.8	Radical-bridged chains; magnetic hysteresis at 6 K with H_c < 10 Oe	433
$(4\text{-}MePyNO)_2Mn^{II}_2(Cu^{II}(opba))_3(DMSO)_2\cdot 2H_2O$	FiM	22.5	Radical-bridged chains; magnetic hysteresis at 4.2 K with H_c < 10 Oe	431
$Na_{0.9}(Bu_4N)_{1.8}[Fe^{III}_2(dhbq)_3]$	FiM	12	Magnetic hysteresis at 2 K with H_c = 350 Oe	461
$(Bu_4N)_2[Fe^{III}_2(dhbq)_3]$	FiM	8	Magnetic hysteresis at 2 K with H_c = 100 Oe	461

[a]All compounds in this table are classified as I^0O^3. [b]Some of the DMSO molecules may be coordinated to the Cu^{II} centers.

References

References for Chapter 1

(1) (a) Noodleman, L.; Han, W.-G. Structure, Redox, pK_a, Spin. A Golden Tetrad for Understanding Metalloenzyme Energetics and Reaction Pathways. *J. Biol. Inorg. Chem.* **2006**, *11*, 674–694. (b) Weiss, R.; Gold, A.; Terner, J. Cytochromes c′: Biological Models for the $S = {}^3/_2, {}^5/_2$ Spin-State Admixture? *Chem. Rev.* **2006**, *106*, 2550–2579. (c) Solomon, E. I.; Heppner, D. E.; Johnston, E. M.; Ginsbach, J. W.; Cirera, J.; Qayyum, M.; Kieber-Emmons, M. T.; Kjaergaard, C. H.; Hadt, R. G.; Tian, L. Copper Active Sites in Biology. *Chem. Rev.* **2014**, *114*, 3659–3853. (d) Poulos, T. L. Heme Enzyme Structure and Function. *Chem. Rev.* **2014**, *114*, 3919–3962. (e) dePolo, G. E.; Kaliakin, D. S.; Varganov, S. A. Spin-Forbidden Transitions Between Electronic States in the Active Site of Rubredoxin. *J. Phys. Chem. A* **2016**, *120*, 8691–8698. (f) Zanello, P. The Competition Between Chemistry and Biology in Assembling Iron–Sulfur Derivatives. Molecular Structures and Electrochemistry. Part V. {$[Fe_4S_4](S^{\gamma}_{cys})_4$}Proteins. *Coord. Chem. Rev.* **2017**, *335*, 172–227.

(2) (a) Heck, C. *Magnetic Materials and Their Applications*; Butterworth-Heinemann: Oxford, 1974. (b) Rocha, A. R.; García-Suárez, V. M.; Bailey, S. W.; Lambert, C. J.; Ferrer, J.; Sanvito, S. Towards Molecular Spintronics. *Nat. Mater.* **2005**, *4*, 335–339. (c) Bogani, L.; Wernsdorfer, W. Molecular Spintronics Using Single-Molecule Magnets. *Nat. Mater.* **2008**, *7*, 179–186. (d) Ardavan, A.; Blundell, S. J. Storing Quantum Information in Chemically Engineered Nanoscale Magnets. *J. Mater. Chem.* **2009**, *19*, 1754–1760. (e) *Spintronics for Next Generation Innovation Devices*; Sato, K., Saitoh, E., Eds.; John Wiley & Sons: New York, 2015. (f) Spaldin, N. A. *Magnetic Materials: Fundamentals and Applications*, 2nd ed.; Cambridge University Press: Cambridge, 2011. (g) Krishnan, K. M. *Fundamentals and Applications of Magnetic Materials*; Oxford University Press: Oxford, 2016. (h) Liu, H.; Zhang, C.; Malissa, H.; Groesbeck, M.; Kavand, M.; McLaughlin, R.; Jamali, S.; Hao, J.; Sun, D.; Davidson, R. A.; Wojcik, L.; Miller, J. S.; Boehme, C.; Vardeny, Z. V. Organic-Based Magnon Spintronics. *Nat. Mater.* **2018**, *17*, 308–312.

(3) (a) Chen, K.; Costas, M.; Que, L., Jr. Spin State Tuning of Non-Heme Iron-Catalyzed Hydrocarbon Oxidations: Participation of Fe^{III}–OOH and Fe^{V}=O Intermediates. *J. Chem. Soc., Dalton Trans.* **2002**, 672–679. (b) van der Vlugt, J. I. Cooperative Catalysis with First-Row Late Transition Metals. *Eur. J. Inorg. Chem.* **2012**, 363–375. (c) Crabtree, R. H. *The Organometallic Chemistry of the Transition Metals*, 6th ed.; John Wiley & Sons, Inc.: Hoboken, NJ, 2014. (d) Taylor, L. J.; Kays, D. L. Low-Coordinate First-Row Transition Metal Complexes in Catalysis and Small Molecule Activation. *Dalton Trans.* **2019**, *48*, 12365–12381.

(4) (a) Kahn, O. *Molecular Magnetism*; VCH: New York, 1993. (b) Benelli, C.; Gatteschi, D. *Introduction to Molecular Magnetism: From Transition Metals to Lanthanides*, 1st ed.;

Wiley-VCH: Weinheim, 2015. (c) *Magnetism: Molecules to Materials*; Miller, J. S., Drillon, M., Eds.; Wiley-VCH: Weinheim; Vol. 1–5.

(5) (a) Nielsen, M. A.; Chuang, I. L. *Quantum Computation and Quantum Information*, 10th Anniversary ed.; Cambridge University Press: Cambridge, 2000. (b) Childress, L.; Gurudev Dutt, M. V.; Taylor, J. M.; Zibrov, A. S.; Jelezko, F.; Wrachtrup, J.; Hemmer, P. R.; Lukin, M. D. Coherent Dynamics of Coupled Electron and Nuclear Spin Qubits in Diamond. *Science* **2006**, *314*, 281–285. (c) Koo, H. C.; Kwon, J. H.; Eom, J.; Chang, J.; Han, S. H.; Johnson, M. Control of Spin Precession in a Spin-Injected Field Effect Transistor. *Science* **2009**, *325*, 1515–1518. (d) Maurer, P. C.; Kucsko, G.; Latta, C.; Jiang, L.; Yao, N. Y.; Bennett, S. D.; Pastawski, F.; Hunger, D.; Chisholm, N.; Markham, M.; Twitchen, D. J.; Cirac, J. I.; Lukin, M. D. Room-Temperature Quantum Bit Memory Exceeding One Second. *Science* **2012**, *336*, 1283–1286. (e) Rugg, B. K.; Krzyaniak, M. D.; Phelan, B. T.; Ratner, M. A., Young, R. M.; Wasielewski, M. R. Photodriven Quantum Teleportation of an Electron Spin State in a Covalent Donor–Acceptor–Radical System. *Nat. Chem*. **2019**, *11*, 981–986.

(6) (a) Fedetov, I. V.; Doronina-Amitonova, L. V.; Voronin, A. A.; Levchenko, A. O.; Zibrov, S. A.; Siderov-Biryukov, D. A.; Fedotov, A. B.; Velichansky, V. L.; Zheltikov, A. M. Electron Spin Manipulation and Readout Through an Optical Fiber. *Sci. Rep*. **2014**, *4*, 5362. (b) Wu, Y.; Jelezko, F.; Plenio, M. B.; Weil, T. Diamond Quantum Devices in Biology. *Angew. Chem. Int. Ed*. **2016**, *55*, 6586–6598. (c) Bonato, C.; Blok, M. S.; Dinani, H. T.; Berry, D. W.; Markham, M. L.; Twitchen, D. J.; Hanson, R. Optimized Quantum Sensing with a Single Electron Spin Using Real-Time Adaptive Measurements. *Nat. Nanotechnol*. **2016**, *11*, 247–252.

(7) Selected references: (a) Troiani, F.; Affronte, M. Molecular Spins for Quantum Information Technologies. *Chem. Rev.* **2011**, *40*, 3119–3129. (b) Aromí, G.; Aguilà, D.; Gamez, P.; Luis, F.; Roubeau, O. Design of Magnetic Coordination Complexes for Quantum Computing. *Chem. Soc. Rev*. **2012**, *41*, 537–546. (c) Graham, M. J.; Zadrozny, J. M.; Shiddiq, M.; Anderson, J. S.; Fataftah, M. S.; Hill, S.; Freedman, D. E. Influence of Electronic Spin and Spin–Orbit Coupling on Decoherence in Mononuclear Transition Metal Complexes. *J. Am. Chem. Soc*. **2014**, *136*, 7623–7626. (d) Zadrozny, J. M.; Niklas, J.; Poluektov, O. G.; Freedman, D. E. Multiple Quantum Coherences from Hyperfine Transitions in a Vanadium(IV) Complex. *J. Am. Chem. Soc*. **2014**, *136*, 15841–15844. (e) Zadrozny, J. M.; Freedman, D. E. Qubit Control Limited by Spin–Lattice Relaxation in a Nuclear Spin-Free Iron(III) Complex. *Inorg. Chem*. **2015**, *54*, 12027–12031. (f) Zadrozny, J. M.; Niklas, J.; Poluektov, O. G.; Freedman, D. E. Millisecond Coherence Time in a Tunable Molecular Electronic Spin Qubit. *ACS Cent. Sci*. **2015**, *1*, 488–492. (g) Fataftah, M. S.; Zadrozny, J. M.; Coste, S. C.; Graham, M. J.; Rogers, D. M.; Freedman, D. E. Employing Forbidden Transitions as Qubits in a Nuclear Spin-Free Chromium Complex. *J. Am. Chem. Soc*. **2016**,

138, 1344–1348. (h) Zadrozny, J. M.; Graham, M. J.; Krzyaniak, M. D.; Wasielewski, M. R.; Freedman, D. E. Unexpected Suppression of Spin–Lattice Relaxation via High Magnetic Field in a High-Spin Iron(III) Complex. *Chem. Commun*. **2016**, *52*, 10175–10178. (i) Fataftah, M. S.; Coste, S. C.; Vlaisavljevich, B.; Zadrozny, J. M.; Freedman, D. E. Transformation of a Coordination Complex $[Co(C_3S_5)_2]^{2-}$ from a Molecular Magnet to a Potential Qubit. *Chem. Sci*. **2016**, *7*, 6160–6166. (j) Yu, C.-J.; Graham, M. J.; Zadrozny, J. M.; Niklas, J.; Krzyaniak, M. D.; Wasielewski, M. R.; Poluektov, O. G.; Freedman, D. E. Long Coherence Times in Nuclear Spin-Free Vanadyl Qubits. *J. Am. Chem. Soc*. **2016**, *138*, 14678–14685. (k) Graham, M. J.; Yu, C.-J.; Krzyaniak, M. D.; Wasielewski, M. R.; Freedman, D. E. Synthetic Approach to Determine the Effect of Nuclear Spin Distance on Electronic Spin Decoherence. *J. Am. Chem. Soc*. **2017**, *139*, 3196–3201. (l) Graham, M. J.; Zadrozny, J. M.; Fataftah, M. S.; Freedman, D. E. Forging Solid-State Qubit Design Principles in a Molecular Furnace. *Chem. Mater*. **2017**, *29*, 1885–1897. (m) Zadrozny, J. M.; Gallagher, A. T.; Harris, T. D.; Freedman, D. E. A Porous Array of Clock Qubits. *J. Am. Chem. Soc*. **2017**, *139*, 7089–7094. (n) Pearson, T. J.; Laorenza, D. W.; Krzyaniak, M. D.; Wasielewski, M. R.; Freedman, D. E. Octacyanometallate Qubit Candidates. *Dalton Trans*. **2018**, *47*, 11744–11748. (o) Yu, C.-J.; Krzyaniak, M. D.; Fataftah, M. S.; Wasielewski, M. R.; Freedman, D. E. A Concentrated Array of Copper Porphyrin Candidate Qubits. *Chem. Sci*. **2019**, *10*, 1702–1708. (p) Fataftah, M. S.; Krzyaniak, M. D.; Vlaisavljevich, B.; Wasielewski, M. R.; Zadrozny, J. M.; Freedman, D. E. Metal–Ligand Covalency Enables Room Temperature Molecular Qubit Candidates. *Chem. Sci*. **2019**, *10*, 6707–6714.

(8) Selected references: (a) *Spin-Crossover Materials: Properties and Applications*; Halcrow, M. A., Ed.; Wiley-VCH: Weinheim, 2013. (b) Xiang, H.; Cheng, J.; Ma, X.; Zhou, X.; Chruma, J. J. Near-Infrared Phosphorescence: Materials and Applications. *Chem. Soc. Rev*. **2013**, *42*, 6128–6185. (c) Jureschi, C.-M.; Linares, J.; Boulmaali, A.; Dahoo, P. R.; Rotaru, A.; Garcia, Y. Pressure and Temperature Sensors Using Two Spin Crossover Materials. *Sensors* **2016**, *16*, 187. (d) Sathish, V.; Ramdass, A.; Velayudham, M.; Lu, K.-L.; Thanasekaran, P.; Rajagopal, S. Development of Luminescent Sensors Based on Transition Metal Complexes for the Detection of Nitroexplosives. *Dalton Trans*. **2017**, *46*, 16738–16769. (e) Ramdass, A.; Sathish, V.; Babu, E.; Velayudham, M.; Thanasekaran, P.; Rajagopal, S. Recent Developments on Optical and Electrochemical Sensing of Copper(II) Ion Based on Transition Metal Complexes. *Coord. Chem. Rev*. **2017**, *343*, 278–307. (f) Shao, D.; Shi, L.; Yin, L.; Wang, B.-L.; Wang, Z.-Y.; Zhang, Y.-Q.; Wang, X.-Y. Reversible On–Off Switching of both Spin Crossover and Single-Molecule Magnet Behaviours via a Crystal-to-Crystal Transformation. *Chem. Sci*. **2018**, *9*, 7986–7991. (g) Enriquez, J. S.; Yu, M.; Bouley, B. S.; Xie, D.; Que, E. L. Copper(II) Complexes for Cysteine Detection Using ^{19}F Magnetic Resonance. *Dalton Trans*. **2018**, *47*, 15024–15030. (h) Yu, M.; Bouley, B. S.; Xie, D.; Enriquez, J. S.; Que, E. L. ^{19}F PARASHIFT Probes for Magnetic Resonance Detection of H_2O_2 and Peroxidase Activity. *J. Am. Chem. Soc*. **2018**, *140*, 10546–10552. (i) Benaicha, B.; Do, K. V.; Yangui, A.; Pittala, N.; Lusson, A.; Sy, M.; Bouchez, G.; Fourati,

H.; Gómez-García, C. J.; Triki, S.; Boukheddaden, K. Interplay Between Spin-Crossover and Luminescence in a Multifunctional Single Crystal Iron(II) Complex: Towards a New Generation of Molecular Sensors. *Chem. Sci*. **2019**, *10*, 6791–6798. (j) Pinto, S. M.; Tomé, V.; Calvete, M. J. F.; Castro, M. C. A.; Tóth, É.; Geraldes, C. F. G. C. Metal-Based Redox-Responsive MRI Contrast Agents. *Coord. Chem. Rev*. **2019**, *390*, 1–31. (k) Fikes, A. G.; Aggarwal, K.; Que, E. L. Glutathione-Mediated Activation of a Disulfide Containing Fe^{3+} Complex. Inorg. Chim. Acta **2019**, *490*, 139–143.

(9) (a) Gütlich, P.; Goodwin, H. A. Spin Crossover–An Overall Perspective. In *Spin Crossover in Transition Metal Compounds I. Topics in Current Chemistry*; Gütlich, P., Goodwin, H. A., Eds.; Springer: Berlin, 2004; Vol. 13, pp. 1–47. (b) Gaspar, A. B.; Seredyuk, M.; Gütlich, P. Spin Crossover in Iron(II) Complexes: Recent Advances. *J. Mol. Struct*. **2009**, *924–926*, 9–19. (c) Halcrow, M. A. Structure:Function Relationships in Molecular Spin-Crossover Complexes. *Chem. Soc. Rev*. **2011**, *40*, 4119–4142.

(10) Wei, R.-J.; Nakahara, R.; Cameron, J. M.; Newton, G. N.; Shiga, T.; Sagayama, H.; Kumai, R.; Murakami, Y.; Oshio, H. Solvent-Induced On/Off Switching of Intramolecular Electron Transfer in a Cyanide-Bridged Trigonal Bipyramidal Complex. *Dalton Trans*. **2016**, *45*, 17104–17107.

(11) Edelman, R. R. The History of MR Imaging as Seen Through the Pages of Radiology. *Radiology* **2014**, *274*, S181–S200.

(12) (a) Lauffer, R. B. Paramagnetic Metal Complexes as Water Proton Relaxation Agents for NMR Imaging: Theory and Design. *Chem. Rev*. **1987**, *87*, 901–927. (b) Caravan, P.; Ellison, J. J.; McMurry, T. J.; Lauffer, R. B. Gadolinium(III) Chelates as MRI Contrast Agents: Structure, Dynamics, and Applications. *Chem. Rev*. **1999**, *99*, 2293–2352. (c) Rieke, V.; Pauly, K. B. MR Thermometry. *J. Magn. Reson. Imaging* **2008**, *27*, 376–390.

(13) Werner, E. J.; Datta, A.; Jocher, C. J.; Raymond, K. N. High-Relaxivity MRI Contrast Agents: Where Coordination Chemistry Meets Medical Imaging. *Angew. Chem. Int. Ed*. **2008**, *47*, 8568–8580.

(14) Bertini, I.; Luchinat, C. *NMR of Paramagnetic Molecules in Biological Systems*; The Benjamin/Cummings Publishing Company, Inc.: Menlo Park, CA, 1986.

(15) (a) Kallinowski, F.; Schlenger, K. H.; Runkel, S.; Kloes, M.; Stohrer, M.; Okunieff, P.; Vaupel, P. Blood Flow, Metabolism, Cellular Microenvironment, and Growth Rate of Human Tumor Xenografts. *Cancer Res*. **1989**, *49*, 3759–3764. (b) Tannock, I. F.; Rotin, D. Acid pH in Tumors and Its Potential for Therapeutic Exploitation. *Cancer Res*. **1989**, *49*, 4373–4384. (c) Vaupel, P.; Kallinowski, F.; Okunieff, P. Blood Flow, Oxygen and Nutrient

Supply, and Metabolic Microenvironment of Human Tumors: A Review. *Cancer Res*. **1989**, *49*, 6449–6465. (d) Katsura, K.; Ekholm, A.; Asplund, B.; Siesjö, B. K. Extracellular pH in the Brain During Ischemia: Relationship to the Severity of Lactic Acidosis. *J. Cereb. Blood Flow Metab*. **1991**, *11*, 597–599. (e) Gillies, R. J.; Raghunand, N.; Karczmar, G. S.; Bhujwalla, Z. M. MRI of the Tumor Microenvironment. *J. Magn. Reson. Imaging* **2002**, *16*, 430–450. (f) Gatenby, R. A.; Gillies, R. J. Why Do Cancers Have High Aerobic Glycolysis? *Nat. Rev. Cancer* **2004**, *4*, 891–899. (g) Gillies, R. J.; Raghunand, N.; Garcia-Martin, M. L.; Gatenby, R. A. pH Imaging. A Review of pH Measurement Methods and Applications in Cancers. *IEEE Eng. Med. Biol. Mag*. **2004**, *23*, 57–64. (h) Hashim, A. I.; Zhang, X.; Wojtkowiak, J. W.; Martinez, G. V.; Gillies, R. J. Imaging pH and Metastasis. *NMR Biomed*. **2011**, *24*, 582–591. (i) Sun, P. Z.; Wang, E.; Cheung, J. S. Imaging Acute Ischemic Tissue Acidosis with pH-Sensitive Endogenous Amide Proton Transfer (APT) MRI–Correction of Tissue Relaxation and Concomitant RF Irradiation Effects Toward Mapping Quantitative Cerebral Tissue pH. *NeuroImage* **2012**, *60*, 1–6. (j) Kato, Y.; Ozawa, S.; Miyamoto, C.; Maehata, Y.; Suzuki, A.; Maeda, T.; Baba, Y. Acidic Extracellular Microenvironment and Cancer. *Cancer Cell Int*. **2013**, *13*, 89–96. (k) Rajamäki, K.; Nordström, T.; Nurmi, K.; Åkerman, K. E. O.; Kovanen, P. T.; Öörni, K.; Eklund, K. K. Extracellular Acidosis Is a Novel Danger Signal Alerting Innate Immunity via the NLRP3 Inflammasome. *J. Biol. Chem*. **2013**, *288*, 13410–13419. (l) Vieites-Prado, A.; Iglesias-Rey, R.; Fernández-Susavila, H.; da Silva-Candal, A.; Rodríguez-Castro, E.; Gröhn, O. H. J.; Wellman, S.; Sobrino, T.; Castillo, J.; Campos, F. Protective Effects and Magnetic Resonance Imaging Temperature Mapping of Systemic and Focal Hypothermia in Cerebral Ischemia. *Stroke* **2016**, *47*, 2386–2396.

(16) Selected references: (a) Dorazio, S. J.; Tsitovich, P. B.; Siters, K. E.; Spernyak, J. A.; Morrow, J. R. Iron(II) PARACEST MRI Contrast Agents. *J. Am. Chem. Soc*. **2011**, *133*, 14154–14156. (b) Dorazio, S. J.; Morrow, J. R. The Development of Iron(II) Complexes as ParaCEST MRI Contrast Agents. *Eur. J. Inorg. Chem*. **2012**, 2006–2014. (c) Dorazio, S. J.; Tsitovich, P. B.; Gardina, S. A.; Morrow, J. R. The Reactivity of Macrocyclic Fe(II) ParaCEST MRI Contrast Agents Towards Biologically Relevant Anions, Cations, Oxygen or Peroxide. *J. Inorg. Biochem*. **2012**, *117*, 212–219. (d) Tsitovich, P. B.; Morrow, J. R. Macrocyclic Ligands for Fe(II) ParaCEST and Chemical Shift MRI Contrast Agents. *Inorg. Chim. Acta* **2012**, *393*, 3–11. (e) Olatunde, A. O.; Dorazio, S. J.; Spernyak, J. A.; Morrow, J. R. The NiCEST Approach: Nickel(II) ParaCEST MRI Contrast Agents. *J. Am. Chem. Soc*. **2012**, *134*, 18503–18505. (f) Dorazio, S. J.; Morrow, J. R. Iron(II) Complexes Containing Octadentate Tetraazamacrocycles as ParaCEST Magnetic Resonance Imaging Contrast Agents. *Inorg. Chem*. **2012**, *51*, 7448–7450. (g) Tsitovich, P. B.; Spernyak, J. A.; Morrow, J. R. A Redox-Activated MRI Contrast Agent that Switches Between Paramagnetic and Diamagnetic States. *Angew. Chem. Int. Ed*. **2013**, *52*, 13997–14000. (h) Dorazio, S. J.; Olatunde, A. O.; Spernyak, J. A.; Morrow, J. R. CoCEST: Cobalt(II) Amide-Appended ParaCEST MRI Contrast Agents. *Chem. Commun*. **2013**, *49*, 10025–10027. (i) Dorazio, S.

J.; Olatunde, A. O.; Tsitovich, P. B.; Morrow, J. R. Comparison of Divalent Transition Metal Ion ParaCEST MRI Contrast Agents. *J. Biol. Inorg. Chem.* **2014**, *19*, 191–205. (j) Jeon, I.-R.; Park, J. G.; Haney, C. R.; Harris, T. D. Spin Crossover Iron(II) Complexes as PARACEST MRI Thermometers. *Chem. Sci*. **2014**, *5*, 2461–2465. (k) Olatunde, A. O.; Bond, C. J.; Dorazio, S. J.; Cox, J. M.; Benedict, J. B.; Daddario, M. D.; Spernyak, J. A.; Morrow, J. R. Six, Seven or Eight Coordinate Fe^{II}, Co^{II} or Ni^{II} Complexes of Amide-Appended Tetraazamacrocycles for ParaCEST Thermometry. *Chem. –Eur. J*. **2015**, *21*, 18290–18300. (l) Tsitovich, P. B.; Cox, J. M.; Benedict, J. B.; Morrow, J. R. Six-Coordinate Iron(II) and Cobalt(II) ParaSHIFT Agents for Measuring Temperature by Magnetic Resonance Spectroscopy. *Inorg. Chem*. **2016**, *55*, 700–716. (m) Tsitovich, P. B.; Cox, J. M.; Spernyak, J. A.; Morrow, J. R. Gear Up for a pH Shift: A Responsive Iron(II) 2-Amino-6-picolyl-Appended Macrocyclic ParaCEST Agent that Protonates at a Pendent Group. *Inorg. Chem*. **2016**, *55*, 12001–12010. (n) Du, K.; Harris, T. D. A Cu^{II}_2 Paramagnetic Chemical Exchange Saturation Transfer Contrast Agent Enabled by Magnetic Exchange Coupling. *J. Am. Chem. Soc*. **2016**, *138*, 7804–7807. (o) Du, K.; Waters, E. A.; Harris, T. D. Ratiometric Quantitation of Redox Status with a Molecular Fe_2 Magnetic Resonance Probe. *Chem. Sci*. **2017**, *8*, 4424–4430. (p) Burns, P. J.; Cox, J. M.; Morrow, J. R. Imidazole-Appended Macrocyclic Complexes of Fe(II), Co(II), and Ni(II) as ParaCEST Agents. *Inorg. Chem*. **2017**, *56*, 4545–4554.

(17) (a) Rhim, H.; Goldberg, S. N.; Dodd III, G. D.; Solbiati, L.; Lim, H. K.; Tonolini, M.; Cho, O. K. Essential Techniques for Successful Radiofrequency Thermal Ablation of Malignant Tumors. *RadioGraphics* **2001**, *21*, S17–S19. (b) Wust, P.; Hildebrandt, B.; Sreenivasa, G.; Rau, B.; Gellermann, J.; Riess, H.; Felix, R.; Schlag, P. M. Hyperthermia in Combined Treatment of Cancer. *Lancet Oncol*. **2002**, *3*, 487–497. (c) Weidensteiner, C.; Quesson, B.; Caire-Gana, B.; Kerioui, N.; Rullier, A.; Trillaud, H.; Moonen, C. T. W. Real-Time MR Temperature Mapping of Rabbit Liver In Vivo During Thermal Ablation. *Magn. Reson. Med*. **2003**, *50*, 322–330. (d) Wust, P.; Cho, C. H.; Hildebrandt, B.; Gellermann, J. Thermal Monitoring: Invasive, Minimal-Invasive and Non-Invasive Approaches. *Int. J. Hyperthermia* **2006**, *22*, 255–262. (e) Datta, N. R.; Ordóñez, S. G.; Gaipl, U. S.; Paulides, M. M.; Crezee, H.; Gellermann, J.; Marder, D.; Puric, E.; Bodis, S. Local Hyperthermia Combined with Radiotherapy and-/or Chemotherapy: Recent Advances and Promises for the Future. *Cancer Treat. Rev*. **2015**, *41*, 742–753.

(18) de Senneville, B. D.; Quesson, B.; Moonen, C. T. W. Magnetic Resonance Temperature Imaging. *Int. J. Hyperthermia* **2005**, *21*, 515–531.

(19) Selected references: (a) Zuo, C. S.; Bowers, J. L.; Metz, K. R.; Nosaka, T.; Sherry, A. D.; Clouse, M. E. $TmDOTP^{5-}$: A Substance for NMR Temperature Measurements In Vivo. *Magn. Reson. Med*. **1996**, *36*, 955–959. (b) Roth, K.; Bartholomae, G.; Bauer, H.; Frenzel, T.; Kossler, S.; Platzek, J.; Weinmann, H.-J. Pr[MOE-DO3A], a Praseodymium Complex of

a Tetraazacyclododecane: An In Vivo NMR Thermometer. *Angew. Chem. Int. Ed*. **1996**, *35*, 655–657. (c) Aime, S.; Botta, M.; Milone, L.; Terreno, E. Paramagnetic Complexes as Novel NMR pH Indicators. *Chem. Commun*. **1996**, 1265–1266. (d) Aime, S.; Botta, M.; Fasano, M.; Terreno, E.; Kinchesh, P.; Calabi, L.; Paleari, L. *Magn. Reson. Med*. **1996**, *35*, 648–651. (e) Frenzel, T.; Roth, K.; Koßler, S.; Radüchel, B.; Bauer, H.; Platzek, J.; Weinmann, H.-J. Noninvasive Temperature Measurement In Vivo Using a Temperature-Sensitive Lanthanide Complex and ^{1}H Magnetic Resonance Spectroscopy. *Magn. Reson. Med*. **1996**, *35*, 364–369. (f) Zuo, C. S.; Metz, K. R.; Sun, Y.; Sherry, A. D. NMR Temperature Measurements Using a Paramagnetic Lanthanide Complex. *J. Magn. Reson*. **1998**, *133*, 53–60. (g) Aime, S.; Botta, M.; Fasano, M.; Terreno, E. Lanthanide(III) Chelates for NMR Biomedical Applications. *Chem. Soc. Rev*. **1998**, *27*, 19–29. (h) Rohovec, J.; Lukeš, I.; Hermann, P. Lanthanide Complexes of a Cyclen Derivative with Phenylphoshinic Pendant Arms for Possible ^{1}H and ^{31}P MRI Temperature Sensitive Probes. *New J. Chem*. **1999**, *23*, 1129–1132. (i) Sun, Y.; Sugawara, M.; Mulkern, R. V.; Hynynen, K.; Mochizuki, S.; Albert, M.; Zuo, C. S. Simultaneous Measurements of Temperature and pH In Vivo Using NMR in Conjunction with TmDOTP^{5-}. *NMR Biomed*. **2000**, *13*, 460–466. (j) Zuo, C. S.; Mahmood, A.; Sherry, A. D. TmDOTA^{-}: A Sensitive Probe for MR Thermometry In Vivo. *J. Magn. Reson*. **2001**, *151*, 101–106. (k) Hekmatyar, S. K.; Hopewell, P.; Pakin, S. K.; Babsky, A.; Bansal, N. Noninvasive MR Thermometry Using Paramagnetic Lanthanide Complexes of 1,4,7,10-Tetraazacyclododecane-α,α′,α″,α‴-tetramethyl-1,4,7,10-tetraacetic Acid (DOTMA^{4-}). *Magn. Reson. Med*. **2005**, *53*, 294–303. (l) Hekmatyar, S. K.; Kerkhoff, R. M.; Pakin, S. K.; Hopewell, P.; Bansal, N. Noninvasive Thermometry Using Hyperfine-Shifted MR Signals from Paramagnetic Lanthanide Complexes. *Int. J. Hyperthermia* **2005**, *21*, 561–574. (m) Pakin, S. K.; Hekmatyar, S. K.; Hopewell, P.; Babsky, A.; Bansal, N. Non-Invasive Temperature Imaging with Thulium 1,4,7,10-Tetraazacyclododecane-1,4,7,10-tetramethyl-1,4,7,10-tetraacetic Acid (TmDOTMA^{-}). *NMR Biomed*. **2006**, *19*, 116–124. (n) Coman, D.; Trubel, H. K.; Rycyna, R. E.; Hyder, F. Brain Temperature and pH Measurements by ^{1}H Chemical Shift Imaging of a Thulium Agent. *NMR Biomed*. **2009**, *22*, 229–239. (o) James, J. R.; Gao, Y.; Miller, M. A.; Babsky, A.; Bansal, N. Absolute Temperature MR Imaging with Thulium 1,4,7,10-Tetraazacyclododecane-1,4,7,10-tetramethyl-1,4,7,10-tetraacetic Acid (TmDOTMA^{-}). *Magn. Reson. Med*. **2009**, *62*, 550–556. (p) Coman, D.; Trubel, H. K.; Hyder, F. Brain Temperature by Biosensor Imaging of Redundant Deviation in Shifts (BIRDS): Comparison Between TmDOTP^{5-} and TmDOTMA^{-}. *NMR Biomed*. **2010**, *23*, 277–285. (q) Milne, M.; Hudson, R. H. E. Contrast Agents Possessing High Temperature Sensitivity. *Chem. Commun*. **2011**, *47*, 9194–9196. (r) Coman, D.; de Graaf, R. A.; Rothman, D. L.; Hyder, F. In Vivo Three-Dimensional Molecular Imaging with Biosensor Imaging of Redundant Deviation in Shifts (BIRDS) at High Spatiotemporal Resolution. *NMR Biomed*. **2013**, *26*, 1589–1595.

(20) (a) Yu, J. X.; Kodibagkar, V. D.; Cui, W.; Mason, R. P. ^{19}F: A Versatile Reporter for Non-Invasive Physiology and Pharmacology Using Magnetic Resonance. *Curr. Med. Chem.*

2005, *12*, 819–848. (b) Chen, J.; Lanza, G. M.; Wickline, S. A. Quantitative Magnetic Resonance Fluorine Imaging: Today and Tomorrow. *WIREs Nanomed. Nanobiotechnol*. **2010**, *2*, 431–440. (c) Tirotta, I.; Dichiarante, V.; Pigliacelli, C.; Cavallo, G.; Terraneo, G.; Bombelli, F. B.; Metrangolo, P.; Resnati, G. ^{19}F Magnetic Resonance Imaging (MRI): From Design of Materials to Clinical Applications. *Chem. Rev*. **2015**, *115*, 1106–1129.

(21) Ward, K. M.; Aletras, A. H.; Balaban, R. S. A New Class of Contrast Agents for MRI Based on Proton Chemical Exchange Dependent Saturation Transfer (CEST). *J. Magn. Reson*. **2000**, *143*, 79–87.

(22) Selected references: (a) Zhang, S.; Winter, P.; Wu, K.; Sherry, A. D. A Novel Europium(III)-Based MRI Contrast Agent. *J. Am. Chem. Soc*. **2001**, *123*, 1517–1518. (b) Zhang, S.; Merritt, M.; Woessner, D. E.; Lenkinski, R. E.; Sherry, A. D. PARACEST Agents: Modulating MRI Contrast via Water Proton Exchange. *Acc. Chem. Res*. **2003**, *36*, 783–790. (c) Zhou, J.; van Zijl, P. C. M. Chemical Exchange Saturation Transfer Imaging and Spectroscopy. *Prog. Nucl. Magn. Reson. Spectrosc*. **2006**, *48*, 109–136. (d) Woods, M.; Woessner, D. E.; Sherry, A. D. Paramagnetic Lanthanide Complexes as PARACEST Agents for Medical Imaging. *Chem. Soc. Rev*. **2006**, *35*, 500–511. (e) Ali, M. M.; Liu, G.; Shah, T.; Flask, C. A.; Pagel, M. D. Using Two Chemical Exchange Saturation Transfer Magnetic Resonance Imaging Contrast Agents for Molecular Imaging Studies. *Acc. Chem. Res*. **2009**, *42*, 915–924. (f) Viswanathan, S.; Kovacs, Z.; Green, K. N.; Ratnakar, S. J.; Sherry, A. D. Alternatives to Gadolinium-Based Metal Chelates for Magnetic Resonance Imaging. *Chem. Rev*. **2010**, *110*, 2960–3018. (g) Terreno, E.; Castelli, D. D.; Viale, A.; Aime, S. Challenges for Molecular Magnetic Resonance Imaging. *Chem. Rev*. **2010**, *110*, 3019–3042. (h) Soesbe, T. C.; Wu, Y.; Sherry, A. D. Advantages of Paramagnetic CEST Complexes Having Slow-to-Intermediate Water Exchange Properties as Responsive MRI Agents. *NMR Biomed*. **2013**, *26*, 829–838.

(23) Selected references: (a) Wu, Y.; Soesbe, T. C.; Kiefer, G. E.; Zhao, P.; Sherry, A. D. A Responsive Europium(III) Chelate that Provides a Direct Readout of pH by MRI. *J. Am. Chem. Soc*. **2010**, *132*, 14002–14003. (b) Wang, X.; Wu, Y.; Soesbe, T. C.; Yu, J.; Zhao, P.; Kiefer, G. E.; Sherry, A. D. A pH-Responsive MRI Agent that Can Be Activated Beyond the Tissue Magnetization Transfer Window. *Angew. Chem. Int. Ed*. **2015**, *54*, 8662–8664. (c) Wu, Y.; Zhang, S.; Soesbe, T. C.; Yu, J.; Vinogradov, E.; Lenkinski, R. E.; Sherry, A. D. pH Imaging of Mouse Kidneys In Vivo Using a Frequency-Dependent ParaCEST Agent. *Magn. Reson. Med*. **2016**, *75*, 2432–2441.

(24) (a) Trokowski, R.; Ren, J.; Kálmán, F. K.; Sherry, A. D. Selective Sensing of Zinc Ions with a PARACEST Contrast Agent. *Angew. Chem. Int. Ed.* **2005**, *44*, 6920–6923. (b) Srivastava, K.; Ferrauto, G.; Harris, S. M.; Longo, D. L.; Botta, M.; Aime, S.; Pierre, V. C. Complete

On/Off Responsive ParaCEST MRI Contrast Agents for Copper and Zinc. *Dalton Trans.* **2018**, *47*, 11346–11357.

(25) (a) Aime, S.; Castelli, D. D.; Terreno, E. Novel pH-Reporter MRI Contrast Agents. *Angew. Chem. Int. Ed*. **2002**, *41*, 4334–4336. (b) Castelli, D. D.; Terreno, E.; Aime, S. Yb(III)-HPDO3A: A Dual pH- and Temperature-Responsive CEST Agent. *Angew. Chem. Int. Ed*. **2011**, *50*, 1798–1800. (c) Liu, G.; Li, Y.; Sheth, V. R.; Pagel, M. D. Imaging In Vivo Extracellular pH with a Single Paramagnetic Chemical Exchange Saturation Transfer Magnetic Resonance Imaging Contrast Agent. *Mol. Imaging* **2012**, *11*, 47–57. (d) Sheth, V. R.; Liu, G.; Li, Y.; Pagel, M. D. Improved pH Measurements with a Single PARACEST MRI Contrast Agent. *Contrast Media Mol. Imaging* **2012**, *7*, 26–34. (e) Sheth, V. R.; Li, Y.; Chen, L. Q.; Howison, C. M.; Flask, C. A.; Pagel, M. D. Measuring In Vivo Tumor pHe with CEST-FISP MRI. *Magn. Reson. Med*. **2012**, *67*, 760–768. (f) Castelli, D. D.; Ferrauto, G.; Cutrin, J. C.; Terreno, E.; Aime, S. In Vivo Maps of Extracellular pH in Murine Melanoma by CEST-MRI. *Magn. Reson. Med*. **2014**, *71*, 326–332. (g) Rancan, G.; Castelli, D. D.; Aime, S. MRI CEST at 1T with Large μ_{eff} Ln^{3+} Complexes Tm^{3+}-HPDO3A: An Efficient MRI pH Reporter. *Magn. Reson. Med*. **2016**, *75*, 329–336. (h) Krchová, T.; Gálisová, A.; Jirák, D.; Hermann, P.; Kotek, J. Ln(III)-Complexes of a DOTA Analogue with an Ethylenediamine Pendant Arm as pH-Responsive PARACEST Contrast Agents. *Dalton Trans*. **2016**, *45*, 3486–3496.

(26) McVicar, N.; Li, A. X.; Suchý, M.; Hudson, R. H. E.; Menon, R. S.; Bartha, R. Simultaneous In Vivo pH and Temperature Mapping Using a PARACEST-MRI Contrast Agent. *Magn. Reson. Med*. **2013**, *70*, 1016–1025.

(27) (a) Coleman, R. E. Metastatic Bone Disease: Clinical Features, Pathophysiology and Treatment Strategies. *Cancer Treat. Rev*. **2001**, *27*, 165–176. (b) Mundy, G. R. Metastasis to Bone: Causes, Consequences and Therapeutic Opportunities. *Nat. Rev. Cancer* **2002**, *2*, 584–593. (c) Kyle, R. A.; Rajkumar, S. V. Multiple Myeloma. *N. Engl. J. Med*. **2004**, *351*, 1860–1873. (d) Fraser, W. D. Hyperparathyroidism. *Lancet* **2009**, *374*, 145–158. (e) Ralston, S. H. Paget's Disease of Bone. *N. Engl. J. Med*. **2013**, *368*, 644–650. (f) Blaine, J.; Chonchol, M.; Levi, M. Renal Control of Calcium, Phosphate, and Magnesium Homeostasis. *Clin. J. Am. Soc. Nephrol*. **2015**, *10*, 1257–1272. (g) Tuck, S. P.; Layfield, R.; Walker, J.; Mekkayil, B.; Francis, R. Adult Paget's Disease of Bone: A Review. *Rheumatology* **2017**, *56*, 2050–2059.

(28) Gutfleisch, O.; Willard, M. A.; Brück, E.; Chen, C. H.; Sankar, S. G.; Liu, J. P. Magnetic Materials and Devices for the 21st Century: Stronger, Lighter, and More Energy Efficient. *Adv. Mater.* **2011**, *23*, 821–842.

(29) Selected references: (a) Cheetham, A. K.; Rao, C. N. R.; Feller, R. K. Structural Diversity and Chemical Trends in Hybrid Inorganic–Organic Framework Materials. *Chem. Commun*. **2006**, 4780–4795. (b) Miller, J. S. Magnetically Ordered Molecule-Based Assemblies. *Dalton Trans*. **2006**, 2742–2749. (c) Maspoch, D.; Ruiz-Molina, D.; Veciana, J. Old Materials with New Tricks: Multifunctional Open-Framework Materials. *Chem. Soc. Rev*. **2007**, *36*, 770–818. (d) Kurmoo, M. Magnetic Metal–Organic Frameworks. *Chem. Soc. Rev*. **2009**, *38*, 1353–1379. (e) Miller, J. S. Magnetically Ordered Molecule-Based Materials. *Chem. Soc. Rev*. **2011**, *40*, 3266–3296. (f) Demir, S.; Jeon, I.-R.; Long, J. R.; Harris, T. D. Radical Ligand-Containing Single-Molecule Magnets. *Coord. Chem. Rev*. **2015**, *289–290*, 149–176.

(30) Selected references: (a) Miyasaka, H.; Izawa, T.; Takahashi, N.; Yamashita, M.; Dunbar, K. R. Long-Range Ordered Magnet of a Charge-Transfer Ru_2^{4+}/TCNQ Two-Dimensional Network Compound. *J. Am. Chem. Soc*. **2006**, *128*, 11358–11359. (b) Motokawa, N.; Miyasaka, H.; Yamashita, M.; Dunbar, K. R. An Electron-Transfer Ferromagnet with T_c = 107 K Based on a Three-Dimensional $[Ru_2]_2$/TCNQ System. *Angew. Chem. Int. Ed*. **2008**, *47*, 7760–7763. (c) Motokawa, N.; Matsunaga, S.; Takaishi, S.; Miyasaka, H.; Yamashita, M.; Dunbar, K. R. Reversible Magnetism Between an Antiferromagnet and a Ferromagnet Related to Solvation/Desolvation in a Robust Layered $[Ru_2]_2$TCNQ Charge-Transfer System. *J. Am. Chem. Soc*. **2010**, *132*, 11943–11951. (d) Zhang, J.; Kosaka, W.; Sugimoto, K.; Miyasaka, H. Magnetic Sponge Behavior via Electronic State Modulations. *J. Am. Chem. Soc*. **2018**, *140*, 5644–5652.

(31) Selected references: (a) Pokhodnya, K. I.; Bonner, M.; Her, J.-H.; Stephens, P. W.; Miller, J. S. Magnetic Ordering (T_c = 90 K) Observed for Layered $[Fe^{II}(TCNE^{\bullet-})(NCMe)_2]^+[Fe^{III}Cl_4]^-$ (TCNE = Tetracyanoethylene). *J. Am. Chem. Soc*. **2006**, *128*, 15592–15593. (b) Her, J.-H.; Stephens, P. W.; Pokhodnya, K. I.; Bonner, M.; Miller, J. S. Cross-Linked Layered Structure of Magnetically Ordered $[Fe(TCNE)_2]\cdot zCH_2Cl_2$ Determined by Rietveld Refinement of Synchrotron Powder Diffraction Data. *Angew. Chem. Int. Ed*. **2007**, *46*, 1521–1524. (c) Stone, K. H.; Stephens, P. W.; McConnell, A. C.; Shurdha, E.; Pokhodnya, K. I.; Miller, J. S. $Mn^{II}(TCNE)_{3/2}(I_3)_{1/2}$—A 3D Network-Structured Organic-Based Magnet and Comparison to a 2D Analog. *Adv. Mater*. **2010**, *22*, 2514–2519. (d) Lapidus, S. H.; McConnell, A. C.; Stephens, P. W.; Miller, J. S. Structure and Magnetic Ordering of a 2-D $Mn^{II}(TCNE)I(OH_2)$ (TCNE = Tetracyanoethylene) Organic-Based Magnet (T_c = 171 K). *Chem. Commun*. **2011**, *47*, 7602–7604.

(32) Selected references: (a) Jeon, I.-R.; Negru, B.; Van Duyne, R. P.; Harris, T. D. A 2D Semiquinone Radical-Containing Microporous Magnet with Solvent-Induced Switching from T_c = 26 to 80 K. *J. Am. Chem. Soc*. **2015**, *137*, 15699–15702. (b) DeGayner, J. A.; Jeon, I.-R.; Sun, L.; Dincă, M.; Harris, T. D. 2D Conductive Iron-Quinoid Magnets Ordering up to T_c = 105 K via Heterogenous Redox Chemistry. *J. Am. Chem. Soc*. **2017**, *139*, 4175–4184.

(c) Darago, L. E.; Aubrey, M. L.; Yu, C. J.; Gonzalez, M. I.; Long, J. R. Electronic Conductivity, Ferrimagnetic Ordering, and Reductive Insertion Mediated by Organic Mixed-Valence in a Ferric Semiquinoid Metal−Organic Framework. *J. Am. Chem. Soc*. **2015**, *137*, 15703–15711.

(33) Selected references: (a) Miyasaka, H.; Motokawa, N.; Matsunaga, S.; Yamashita, M.; Sugimoto, K.; Mori, T.; Toyota, N.; Dunbar, K. R. Control of Charge Transfer in a Series of $Ru_2^{II,II}$/TCNQ Two-Dimensional Networks by Tuning the Electron Affinity of TCNQ Units: A Route to Synergistic Magnetic/Conducting Materials. *J. Am. Chem. Soc*. **2010**, *132*, 1532–1544. (b) Pedersen, K. S.; Perlepe, P.; Aubrey, M. L.; Woodruff, D. N.; Reyes-Lillo, S. E.; Reinholdt, A.; Voigt, L.; Li, Z.; Borup, K.; Rouzières, M.; Samohvalov, D.; Wilhelm, F.; Rogalev, A.; Neaton, J. B.; Long, J. R.; Clérac, R. Formation of the Layered Conductive Magnet $CrCl_2(pyrazine)_2$ Through Redox-Active Coordination Chemistry. *Nat. Chem*. **2018**, *10*, 1056–1061. (c) Liu, L.; DeGayner, J. A.; Sun, L.; Zee, D. Z.; Harris, T. D. Reversible Redox Switching of Magnetic Order and Electrical Conductivity in a 2D Manganese Benzoquinoid Framework. *Chem. Sci*. **2019**, *10*, 4652–4661. (d) Yang, C.; Dong, R.; Wang, M.; Petkov, P. S.; Zhang, Z.; Wang, M.; Han, P.; Ballabio, M.; Bräuninger, S. A.; Liao, Z.; Zhang, J.; Schwotzer, F.; Zschech, E.; Klauss, H.-H.; Cánovas, E.; Kaskel, S.; Bonn, M.; Zhou, S.; Heine, T.; Feng, X. A Semiconducting Layered Metal-Organic Framework Magnet. *Nat. Commun*. **2019**, *10*, 3260.

(34) Selected references: (a) Caneshi, A.; Gatteschi, D.; Sessoli, R. Alternating Current Susceptibility, High Field Magnetization, and Millimeter Band EPR Evidence for a Ground S = 10 State in $[Mn_{12}O_{12}(CH_3COO)_{16}(H_2O)_4]\cdot 2CH_3COOH\cdot 4H_2O$. *J. Am. Chem. Soc*. **1991**, *113*, 5873–5874. (b) Sessoli, R.; Gatteschi, D.; Caneshi, A.; Novak, M. A. Magnetic Bistability in a Metal-Ion Cluster. *Nature* **1993**, *365*, 141–143. (c) Sessoli, R.; Tsai, H.-L.; Schake, A. R.; Wang, S.; Vincent, J. B.; Folting, K.; Gatteschi, D.; Christou, G.; Hendrickson, D. N. High-Spin Molecules: $[Mn_{12}O_{12}(O_2CR)_{16}(H_2O)_4]$. *J. Am. Chem. Soc*. **1999**, *115*, 1804–1816. (d) Ishikawa, N.; Sugita, M.; Ishikawa, T.; Koshihara, S.-Y.; Kaizu, Y. Lanthanide Double-Decker Complexes Functioning as Magnets at the Single-Molecular Level. *J. Am. Chem. Soc*. **2003**, *125*, 8694–8695. (e) Tang, J.; Hewitt, I.; Madhu, N. T.; Chastanet, G.; Wernsdorfer, W.; Anson, C. E.; Benelli, C.; Sessoli, R.; Powell, A. K. Dysprosium Triangles Showing Single-Molecule Magnet Behavior of Thermally Excited Spin States. *Angew. Chem. Int. Ed*. **2006**, *45*, 1729–1733. (f) *Single-Molecule Magnets and Related Phenomena*; Winpenny, R. E. P., Ed.; Springer-Verlag: Berlin, 2006; Vol. 122, pp. 1–206. (g) Lin, P.-H.; Burchell, T. J.; Clérac, R.; Murugesu, M. Dinuclear Dysprosium(III) Single-Molecule Magnets with a Large Anisotropic Barrier. *Angew. Chem. Int. Ed*. **2008**, *47*, 8848–8851. (h) Bagai, R.; Christou, G. The *Drosophila* of Single-Molecule Magnetism: $[Mn_{12}O_{12}(O_2CR)_{16}(H_2O)_4]$. *Chem. Soc. Rev*. **2009**, *38*, 1011–1026. (i) Freedman, D. E.; Harman, W. H.; Harris, T. D.; Long, G. J.; Chang, C. J.; Long, J. R. Slow Magnetic Relaxation in a High-Spin Iron(II) Complex. *J. Am. Chem. Soc*. **2010**, *132*, 1224–1225. (j)

Rinehart, J. D.; Fang, M.; Evans, W. J.; Long, J. R. Strong Exchange and Magnetic Blocking in N_2^{3-}-Radical-Bridged Lanthanide Complexes. *Nat. Chem.* **2011**, *3*, 538–542. (k) Rinehart, J. D.; Fang, M.; Evans, W. J.; Long, J. R. A N_2^{3-} Radical-Bridged Terbium Complex Exhibiting Magnetic Hysteresis at 14 K. *J. Am. Chem. Soc*. **2011**, *133*, 14236–14239. (l) Mougel, V.; Chatelain, L.; Pécaut, J.; Caciuffo, R.; Colineau, E.; Griveau, J.-C.; Mazzanti, M. Uranium and Manganese Assembled in a Wheel-Shaped Nanoscale Single-Molecule Magnet with High Spin-Reversal Barrier. *Nat. Chem*. **2012**, *4*, 1011–1017. (m) Woodruff, D. N.; Winpenny, R. E. P.; Layfield, R. A. Lanthanide Single-Molecule Magnets. *Chem. Rev*. **2013**, *113*, 5110–5148. (n) Zhang, P.; Guo, Y.-N.; Tang, J. Recent Advances in Dysprosium-Based Single Molecule Magnets: Structural Overview and Synthetic Strategies. *Coord. Chem. Rev*. **2013**, *257*, 1728–1763. (o) Pedersen, K. S.; Bendix, J.; Clérac, R. Single-Molecule Magnet Engineering: Building-Block Approaches. *Chem. Commun.* **2014**, *50*, 4396–4415. (p) Meihaus, K. R.; Long, J. R. Actinide-Based Single-Molecule Magnets. *Dalton Trans*. **2015**, *44*, 2517–2528. (q) Craig, G. A.; Murrie, M. 3d Single-Ion Magnets. *Chem. Soc. Rev*. **2015**, *44*, 2135–2147. (r) Liu, J.; Chen, Y.-C.; Liu, J.-L.; Vieru, V.; Ungur, L.; Jia, J.-H.; Chibotaru, L. F.; Lan, Y.; Wernsdorfer, W.; Gao, S.; Chen, X.-M.; Tong, M.-L. A Stable Pentagonal Bipyramidal Dy(III) Single-Ion Magnet with a Record Magnetization Reversal Barrier over 1000 K. *J. Am. Chem. Soc*. **2016**, *138*, 5441–5450. (s) Ding, Y.-S.; Chilton, N. F.; Winpenny, R. E. P.; Zheng, Y.-Z. On Approaching the Limit of Molecular Magnetic Anisotropy: A Near-Perfect Pentagonal Bipyramidal Dysprosium(III) Single-Molecule Magnet. *Angew. Chem. Int. Ed*. **2016**, *55*, 16071–16074. (t) Guo, F.-S.; Day, B. M.; Chen, Y.-C.; Tong, M.-L.; Mansikkamäki, A.; Layfield, R. A. A Dysprosium Metallocene Single-Molecule Magnet Functioning at the Axial Limit. *Angew. Chem. Int. Ed*. **2017**, *56*, 11445–11449. (u) Demir, S.; Gonzalez, M. I.; Darago, L. E.; Evans, W. J.; Long, J. R. Giant Coercivity and High Magnetic Blocking Temperature for N_2^{3-} Radical-Bridged Dilanthanide Complexes Upon Ligand Dissociation. *Nat. Commun.* **2017**, *8*, 2144. (v) McClain, K. R.; Gould, C. A.; Chakarawet, K.; Teat, S. J.; Groshens, T. J.; Long, J. R.; Harvey, B. G. High-Temperature Magnetic Blocking and Magneto-Structural Correlations in a Series of Dysprosium(III) Metallocenium Single-Molecule Magnets. *Chem. Sci*. **2018**, *9*, 8492–8503.

(35) Selected references: (a) Caneschi, A.; Gatteschi, D.; Lalioti, N.; Sangregorio, C.; Sessoli, R.; Venturi, G.; Vindigni, A.; Rettori, A.; Pini, M. G.; Novak, M. A. Cobalt(II)-Nitronyl Nitroxide Chains as Molecular Magnetic Nanowires. *Angew. Chem. Int. Ed*. **2001**, *40*, 1760–1763. (b) Clérac, R.; Miyasaka, H.; Yamashita, M.; Coulon, C. Evidence for Single-Chain Magnet Behavior in a Mn^{III}–Ni^{II} Chain Designed with High Spin Magnetic Units: A Route to High Temperature Metastable Magnets. *J. Am. Chem. Soc*. **2002**, *124*, 12837–12844. (c) Bogani, L.; Sangregorio, C.; Sessoli, R.; Gatteschi, D. Molecular Engineering for Single-Chain-Magnet Behavior in a One-Dimensional Dysprosium–Nitronyl Nitroxide Compound. *Angew. Chem. Int. Ed*. **2005**, *44*, 5817–5821. (d) Bernot, K.; Bogani, L.; Caneschi, A.; Gatteschi, D.; Sessoli, R. A Family of Rare-Earth-Based Single Chain Magnets: Playing with

Anisotropy. *J. Am. Chem. Soc*. **2006**, *128*, 7947–7956. (e) Ishi, N.; Okamura, Y.; Chiba, S.; Nogami, T.; Ishida, T. Giant Coercivity in a One-Dimensional Cobalt-Radical Coordination Magnet. *J. Am. Chem. Soc*. **2008**, *130*, 24–25. (f) Miyasaka, H.; Julve, M.; Yamashita, M.; Clérac, R. Slow Dynamics of the Magnetization in One-Dimensional Coordination Polymers: Single-Chain Magnets. *Inorg. Chem.* **2009**, *48*, 3420–3437. (g) Zhang, W.-X.; Ishikawa, R.; Breedlove, B.; Yamashita, M. Single-Chain Magnets: Beyond the Glauber Model. *RSC Adv.* **2013**, *3*, 3772–3798. (h) Vaz, M. G. F.; Cassaro, R. A. A.; Akpinar, H.; Schlueter, J. A.; Lahti, P. M.; Novak, M. A. A Cobalt Pyrenylnitronylnitroxide Single-Chain Magnet with High Coercivity and Record Blocking Temperature. *Chem. –Eur. J*. **2014**, *20*, 5460–5467. (i) Cassaro, R. A. A.; Reis, S. G.; Araujo, T. S.; Lahti, P. M.; Novak, M. A.; Vaz, M. G. F. A Single-Chain Magnet with a Very High Blocking Temperature and a Strong Coercive Field. *Inorg. Chem*. **2015**, *54*, 9381–9383. (j) DeGayner, J. A.; Wang, K.; Harris, T. D. A Ferric Semiquinoid Single-Chain Magnet via Thermally-Switchable Metal–Ligand Electron Transfer. *J. Am. Chem. Soc*. **2018**, *57*, 12718–12726.

(36) Domb, C. Ising Model. In *Phase Transitions and Critical Phenomena*; Domb, C., Green, M. S., Eds.; Academic Press: London, 1974; Vol. 3, pp. 357–484.

(37) Dionne, G. F. *Magnetic Oxides*; Springer: New York, 2009.

(38) (a) Sagawa, M.; Fujimura, S.; Togawa, N.; Yamamoto, H.; Matsuura, Y. New Material for Permanent Magnets on a Base of Nd and Fe. *J. Appl. Phys*. **1984**, *55*, 2083–2087. (b) Herzer, G. Nanocrystalline Soft Magnetic Materials. *J. Magn. Magn. Mater*. **1992**, *112*, 258–262.

(39) Dechambenoit, P.; Long, J. R. Microporous Magnets. *Chem. Soc. Rev*. **2011**, *40*, 3249–3265.

(40) (a) Caneschi, A.; Gatteschi, D.; Sessoli, R.; Rey, P. Toward Molecular Magnets: The Metal–Radical Approach. *Acc. Chem. Res*. **1989**, *22*, 392–398. (b) Faust, T. B.; D′Alessandro, D. M. Radicals in Metal–Organic Frameworks. *RSC Adv*. **2014**, *4*, 17498–17512.

(41) Selected references: (a) Caneschi, A.; Gatteschi, D.; Laugier, J.; Rey, P. Ferromagnetic Alternating Spin Chains. *J. Am. Chem. Soc*. **1987**, *109*, 2191–2192. (b) Caneschi, A.; Gatteschi, D.; Renard, J. P.; Rey, P.; Sessoli, R. Magnetic Phase Transitions in Manganese(II) Pentafluorobenzoate Adducts with Nitronyl Nitroxides. *J. Am. Chem. Soc*. **1989**, *111*, 785–786. (c) Caneschi, A.; Ferraro, F.; Gatteschi, D.; Rey, P.; Sessoli, R. Structure and Magnetic Properties of a Chain Compound Formed by Copper(II) and a Tridentate Nitronyl Nitroxide Radical. *Inorg. Chem.* **1991**, *30*, 3162–3166. (d) Caneschi, A.; Gatteschi, D.; Rey, P.; Sessoli, R. Structure and Magnetic Ordering of a Ferrimagnetic Helix Formed by Manganese(II) and a Nitronyl Nitroxide Radical. *Inorg. Chem.* **1991**, *30*, 3936–3941. (e) Stumpf, H. O.; Ouahab, L.; Pei, Y.; Grandjean, D.; Kahn, O. A Molecular-Based Magnet with a Fully Interlocked Three-Dimensional Structure. *Science* **1993**, *261*, 447–449.

(f) Stumpf, H. O.; Ouahab, L.; Pei, Y.; Bergerat, P.; Kahn, O. Chemistry and Physics of a Molecular-Based Magnet Containing Three Spin Carriers, with a Fully Interlocked Structure. *J. Am. Chem. Soc*. **1994**, *116*, 3866–3874. (g) Inoue, K.; Iwamura, H. Ferro- and Ferrimagnetic Ordering in a Two-Dimensional Network Formed by Manganese(II) and 1,3,5-Tris[*p*-(*N*-*tert*-butyl-*N*-oxyamino)phenyl]benzene. *J. Am. Chem. Soc*. **1994**, *116*, 3173–3174. (h) Caneschi, A.; Gatteschi, D.; Le Lirzin, A. Crystal Structure and Magnetic Properties of a New Ferrimagnetic Chain Containing Manganese(II) and a Nitronyl-Nitroxide Radical. *J. Mater. Chem*. **1994**, *4*, 319–326. (i) Inoue, K.; Hayamizu, T.; Iwamura, H.; Hashizume, D.; Ohashi, Y. Assemblage and Alignment of the Spins of the Organic Trinitroxide Radical with a Quartet Ground State by Means of Complexation with Magnetic Metal Ions. A Molecule-Based Magnet with Three-Dimensional Structure and High T_C of 46 K. *J. Am. Chem. Soc*. **1996**, *118*, 1803–1804. (j) Fegy, K.; Luneau, D.; Ohm, T.; Paulsen, C.; Rey, P. Two-Dimensional Nitroxide-Based Molecular Magnetic Materials. *Angew. Chem. Int. Ed*. **1998**, *37*, 1270–1273. (k) Numata, Y.; Inoue, K.; Baranov, N.; Kurmoo, M.; Kikuchi, K. Field-Induced Ferrimagnetic State in a Molecule-Based Magnet Consisting of a Co^{II} Ion and a Chiral Triplet Bis(nitroxide) Radical. *J. Am. Chem. Soc*. **2007**, *129*, 9902–9909. (l) Vostrikova, K. E. High-Spin Molecules Based on Metal Complexes of Organic Free Radicals. *Coord. Chem. Rev*. **2008**, *252*, 1409–1419. (m) Meng, X.; Shi, W.; Cheng, P. Magnetism in One-Dimensional Metal–Nitronyl Nitroxide Radical System. *Coord. Chem. Rev*. **2019**, *378*, 134–150. (n) Liu, X.; Wang, Y.-X.; Han, Z.; Han, T.; Shi, W.; Cheng, P. Tuning the Magnetization Dynamics of Tb^{II}-Based Single-Chain Magnets Through Substitution on the Nitronyl Nitroxide Radical. *Dalton Trans*. **2019**, *48*, 8989–8994.

(42) Selected references: (a) Zhao, H.; Heintz, R. A.; Ouyang, X.; Dunbar, K. R. Spectroscopic, Thermal, and Magnetic Properties of Metal/TCNQ Network Polymers with Extensive Supramolecular Interactions Between Layers. *Chem. Mater*. **1999**, *11*, 736–746. (b) Clérac, R.; O'Kane, S.; Cowen, J.; Quyang, X.; Heintz, R.; Zhao, H.; Bazile, Jr., M. J.; Dunbar, K. R. Glassy Magnets Composed of Metals Coordinated to 7,7,8,8-Tetracyanoquinodimethane: $M(TCNQ)_2$ (M = Mn, Fe, Co, Ni). *Chem. Mater*. **2003**, *15*, 1840–1850. (c) Lopez, N.; Zhao, H.; Prosvirin, A. V.; Chouai, A.; Shatruk, M.; Dunbar, K. R. Conversion of a Porous Material Based on a Mn^{II}–$TCNQF_4$ Honeycomb Net to a Molecular Magnet upon Desolvation. *Chem. Commun*. **2007**, 4611–4613. (d) Motokawa, N.; Oyama, T.; Matsunaga, S.; Miyasaka, H.; Yamashita, M.; Dunbar, K. R. Charge-Transfer Two-Dimensional Layers Constructed from a 2:1 Assembly of Paddlewheel Diruthenium(II,II) Complexes and Bis[1,2,5]thiadizolotetracyanoquinodimethane: Bulk Magnetic Behavior as a Function of Inter-Layer Interactions. *Cryst. Eng. Commun*. **2009**, *11*, 2121–2130. (e) Olson, C.; Heth, C. L.; Lapidus, S. H.; Stephens, P. W.; Halder, G. J.; Pokhodnya, K. I. Spectroscopic Study of (Two-Dimensional) Molecule-Based Magnets: $[M^{II}(TCNE)(NCMe)_2][SbF_6]$ (M = Fe, Mn, Ni). *J. Chem. Phys*. **2011**, *135*, 024503. (f) McConnell, A. C.; Fishman, R. S.; Miller, J. S. Mean Field Analysis of the Exchange Coupling (*J*) for Two-and Three-Dimensional Structured Tetracyanoethenide ($TCNE^{\bullet-}$)-Based Magnets. *J. Phys. Chem. C* **2012**, *116*,

16154–16160. (g) Olson, C. S.; Gangopadhyay, S.; Hoang, K.; Alema, F.; Kilina, S.; Pokhodnya, K. Magnetic Exchange in Mn^{II}[TCNE] (TCNE = Tetracyanoethylene) Molecule-Based Magnets with Two- and Three-Dimensional Magnetic Networks. *J. Phys. Chem. C* **2015**, *119*, 25036–25046.

(43) (a) Maspoch, D.; Ruiz-Molina, D.; Wurst, K.; Domingo, N.; Cavallini, M.; Biscarini, F.; Tejada, J.; Rovira, C.; Veciana, J. A Nanoporous Molecular Magnet with Reversible Solvent-Induced Mechanical and Magnetic Properties. *Nat. Mater*. **2003**, *2*, 190–195. (b) Maspoch, D.; Domingo, N.; Ruiz-Molina, D.; Wurst, K.; Hernández, J.-M.; Vaughan, G.; Rovira, C.; Lloret, F.; Tejada, J.; Veciana, J. Coexistence of Ferro- and Antiferromagnetic Interactions in a Metal–Organic Radical-Based (6,3)-Helical Network with Large Channels. *Chem. Commun*. **2005**, 5035–5037.

(44) (a) Koga, N.; Ishimaru, Y.; Iwamura, H. Diazodi(4-pyridyl)methane and Diazophenyl-(4-pyridyl)methane as Photoresponsive Ligands for Metal–Carbene Hetero-Spin Systems. *Angew. Chem. Int. Ed*. **1996**, *35*, 755–757. (b) Yoshihara, D.; Karasawa, S.; Koga, N. Cyclic Single-Molecule Magnet in Heterospin System. *J. Am. Chem. Soc*. **2008**, *130*, 10460–10461. (c) Yoshihara, D.; Karasawa, S.; Koga, N. Heterospin Single-Molecule Magnets with Extra-Large Anisotropic Barrier. *Polyhedron* **2011**, *30*, 3211–3217.

(45) (a) Manriquez, J. M.; Yee, G. T.; McLean, R. S.; Epstein, A. J.; Miller, J. S. A Room-Temperature Molecular/Organic-Based Magnet. *Science* **1991**, *252*, 1415–1417. (b) Zhou, P.; Morin, B. G.; Miller, J. S.; Epstein, A. J. Magnetization and Static Scaling of the High-T_c Disordered Molecular-Based Magnet V(tetracyanoethylene)$_x$·y(CH_3CN) with $x \sim 1.5$ and $y \sim 2$. *Phys. Rev. B* **1993**, *48*, 1325–1328. (c) Du, G.; Joo, J.; Epstein, A. J.; Miller, J. S. Anomalous Charge Transport Phenomena in Molecular-Based Magnet V(TCNE)$_x$·y(solvent). *J. Appl. Phys*. **1993**, *73*, 6566–6568. (d) Zhou, P.; Long, S. M.; Miller, J. S.; Epstein, A. J. Static Magnetic Properties and Critical Behavior of V(TCNE)$_x$·y(C_4H_8O), a High T_c Molecular-Based Disordered Magnet. *Phys. Lett. A* **1993**, *181*, 71–79. (e) Pokhodnya, K. I.; Vickers, E. B.; Bonner, M.; Epstein, A. J.; Miller, J. S. Solid Solution $V_xFe_{1-x}[TCNE]_2$·zCH_2Cl_2 Room-Temperature Magnets. *Chem. Mater*. **2004**, *16*, 3218–3223.

(46) (a) Min, K. S.; Rheingold, A. L.; DiPasquale, A. G.; Miller, J. S. Characterization of the Chloranilate(•3−) π Radical as a Strong Spin-Coupling Bridging Ligand. *Inorg. Chem*. **2006**, *45*, 6135–6137. (b) Min, K. S.; DiPasquale, A. G.; Golen, J. A.; Rheingold, A. L.; Miller, J. S. Synthesis, Structure, and Magnetic Properties of Valence Ambiguous Dinuclear Antiferromagnetically Coupled Cobalt and Ferromagnetically Coupled Iron Complexes Containing the Chloranilate(2−) and the Significantly Stronger Coupling Chloranilate(•3−) Radical Trianion. *J. Am. Chem. Soc*. **2007**, *129*, 2360–2368. (c) Jeon, I.-R.; Park, J. G.; Xiao, D. J.; Harris, T. D. An Azophenine Radical-Bridged Fe_2 Single-Molecule Magnet with

Record Magnetic Exchange Coupling. *J. Am. Chem. Soc*. **2013**, *135*, 16845–16848. (d) DeGayner, J. A.; Jeon, I.-R.; Harris, T. D. A Series of Tetraazalene Radical-Bridged M_2 (M = Cr^{III}, Mn^{II}, Fe^{II}, Co^{II}) Complexes with Strong Magnetic Exchange Coupling. *Chem. Sci*. **2015**, *6*, 6639–6648. (e) Murase, R.; Abrahams, B. F.; D'Allessandro, D. M.; Davies, C. G.; Hudson, T. A.; Jameson, G. N. L.; Moubaraki, B.; Murray, K. S.; Robson, R.; Sutton, A. L. Mixed Valency in a 3D Semiconducting Iron–Fluoranilate Coordination Polymer. *Inorg. Chem*. **2017**, *56*, 9025–9035. (f) Hua, C.; DeGayner, J. A.; Harris, T. D. *Inorg. Chem*. **2019**, *58*, 7044–7053.

(47) (a) Kitagawa, S.; Kawata, S. Coordination Compounds of 1,4-Dihydroxybenzoquinone and Its Homologues. Structures and Properties. *Coord. Chem. Rev*. **2002**, *224*, 11–34. (b) Abrahams, B. F.; Coleiro, J.; Ha, K.; Hoskins, B. F.; Orchard, S. D.; Robson, R. Dihydroxybenzoquinone and Chloranilic Acid Derivatives of Rare Earth Metals. *J. Chem. Soc., Dalton Trans*. **2002**, 1586–1594. (c) Mercuri, M. L.; Congiu, F.; Concas, G.; Sahadevan, S. A. Recent Advances on Anilato-Based Molecular Materials with Magnetic and/or Conducting Properties. *Magnetochemistry* **2017**, *3*, 17.

(48) (a) Tinti, F.; Verdaguer, M.; Kahn, O.; Savariault, J.-M. Interaction Between Copper(II) Ions Separated by 7.6 Å. Crystal Structure and Magnetic Properties of (*μ*-Iodanilato)bis[(*N*,*N*,*N*′,*N*′-tetramethylethylenediamine)copper(II)] Diperchlorate. *Inorg. Chem*. **1987**, *26*, 2380–2384. (b) Schweinfurth, D.; Khusniyarov, M. M.; Bubrin, D.; Hohloch, S.; Su, C.-Y.; Sarkar, B. Tuning Spin–Spin Coupling in Quinonoid-Bridged Dicopper(II) complexes Through Rational Bridge Variation. *Inorg. Chem*. **2013**, *52*, 10332–10339. (c) Atzori, A.; Benmansour, S.; Espallargas, G. M.; Clemente-León, M.; Abhervé, A.; Gómez-Claramunt, P.; Coronado, E.; Artizzu, F.; Sessini, E.; Deplano, P.; Serpe, A.; Mercuri, M. L.; Gómez-García, C. J. A Family of Layered Chiral Porous Magnets Exhibiting Tunable Ordering Temperatures. *Inorg. Chem*. **2013**, *52*, 10031–10040.

References for Chapter 2

(1) Rieke, V.; Pauly, K. B. MR Thermometry. *J. Magn. Reson. Imaging* **2008**, *27*, 376–390.

(2) (a) Rhim, H.; Goldberg, S. N.; Dodd III, G. D.; Solbiati, L.; Lim, H. K.; Tonolini, M.; Cho, O. K. Essential Techniques for Successful Radiofrequency Thermal Ablation of Malignant Tumors. *RadioGraphics* **2001**, *21*, S17–S19. (b) Wust, P.; Hildebrandt, B.; Sreenivasa, G.; Rau, B.; Gellermann, J.; Riess, H.; Felix, R.; Schlag, P. M. Hyperthermia in Combined Treatment of Cancer. *Lancet Oncol*. **2002**, *3*, 487–497. (c) Weidensteiner, C.; Quesson, B.; Caire-Gana, B.; Kerioui, N.; Rullier, A.; Trillaud, H.; Moonen, C. T. W. Real-Time MR Temperature Mapping of Rabbit Liver In Vivo During Thermal Ablation. *Magn. Reson. Med*. **2003**, *50*, 322–330. (d) Wust, P.; Cho, C. H.; Hildebrandt, B.; Gellermann, J. Thermal Monitoring: Invasive, Minimal-Invasive and Non-Invasive Approaches. *Int. J. Hyperthermia* **2006**, *22*, 255–262. (e) Datta, N. R.; Ordóñez, S. G.; Gaipl, U. S.; Paulides, M. M.; Crezee, H.; Gellermann, J.; Marder, D.; Puric, E.; Bodis, S. Local Hyperthermia Combined with Radiotherapy and-/or Chemotherapy: Recent Advances and Promises for the Future. *Cancer Treat. Rev*. **2015**, *41*, 742–753.

(3) Lévy, S. Biophysical Basis and Cardiac Lesions Caused by Different Techniques of Cardiac Arrhythmia Ablation. *Arch. Mal. Coeur Vaiss*. **1995**, *88*, 1465–1469.

(4) Jayasundar, R.; Singh, V. P. In Vivo Temperature Measurements in Brain Tumors Using Proton MR Spectroscopy. *Neurol. India* **2002**, *50*, 436–439.

(5) Quesson, B.; de Zwart, J. A.; Moonen, C. T. W. Magnetic Resonance Temperature Imaging for Guidance of Thermotherapy. *J. Magn. Reson. Imaging* **2000**, *12*, 525–533.

(6) (a) Hindman, J. C. Proton Resonance Shift of Water in the Gas and Liquid States. *J. Chem. Phys.* **1966**, *44*, 4582–4592. (b) Ishihara, Y.; Calderon, A.; Watanabe, H.; Okamoto, K.; Suzuki, Y.; Kuroda, K.; Suzuki, Y. A Precise and Fast Temperature Mapping Using Water Proton Chemical Shift. *Magn. Reson. Med*. **1995**, *34*, 814–823. (c) Wlodarczyk, W.; Hentschel, M.; Wust, P.; Noeske, R.; Hosten, N.; Rinneberg, H.; Felix, R. *Phys. Med. Biol*. **1999**, *44*, 607–624.

(7) (a) Kuroda, K. Non-Invasive MR Thermography Using the Water Proton Chemical Shift. *Int. J. Hyperthermia* **2005**, *21*, 547–560. (b) Roujol, S.; Ries, M.; Quesson, B.; Moonen, C. T. W.; de Senneville, B. D. Real-Time MR-Thermometry and Dosimetry for Interventional Guidance on Abdominal Organs. *Magn. Reson. Med*. **2010**, *63*, 1080–1087. (c) Liu, G.; Qin, Q.; Chan, K. W. Y.; Li, Y.; Bulte, J. W. M.; McMahon, M. T.; van Zijl, P. C. M.; Gilad, A. A. Non-Invasive Temperature Mapping Using Temperature-Responsive Water Saturation Shift Referencing (T-WASSR) MRI. *NMR Biomed*. **2014**, *27*, 320–331. (d) Winter, L.;

Oberacker, E.; Paul, K.; Ji, Y.; Oezerdem, C.; Ghadjar, P.; Thieme, A.; Budach, V.; Wust, P.; Niendorf, T. Magnetic Resonance Thermometry: Methodology, Pitfalls and Practical Solutions. *Int. J. Hyperthermia* **2016**, *32*, 63–75.

(8) de Senneville, B. D.; Quesson, B.; Moonen, C. T. W. Magnetic Resonance Temperature Imaging. *Int. J. Hyperthermia* **2005**, *21*, 515–531.

(9) (a) Zuo, C. S.; Bowers, J. L.; Metz, K. R.; Nosaka, T.; Sherry, A. D.; Clouse, M. E. $TmDOTP^{5-}$: A Substance for NMR Temperature Measurements In Vivo. *Magn. Reson. Med*. **1996**, *36*, 955–959. (b) Roth, K.; Bartholomae, G.; Bauer, H.; Frenzel, T.; Kossler, S.; Platzek, J.; Weinmann, H.-J. Pr[MOE-DO3A], a Praseodymium Complex of a Tetraazacyclododecane: An In Vivo NMR Thermometer. *Angew. Chem. Int. Ed*. **1996**, *35*, 655–657. (c) Aime, S.; Botta, M.; Milone, L.; Terreno, E. Paramagnetic Complexes as Novel NMR pH Indicators. *Chem. Commun*. **1996**, 1265–1266. (d) Aime, S.; Botta, M.; Fasano, M.; Terreno, E.; Kinchesh, P.; Calabi, L.; Paleari, L. *Magn. Reson. Med*. **1996**, *35*, 648–651. (e) Frenzel, T.; Roth, K.; Koßler, S.; Radüchel, B.; Bauer, H.; Platzek, J.; Weinmann, H.-J. Noninvasive Temperature Measurement In Vivo Using a Temperature-Sensitive Lanthanide Complex and ^{1}H Magnetic Resonance Spectroscopy. *Magn. Reson. Med*. **1996**, *35*, 364–369. (f) Zuo, C. S.; Metz, K. R.; Sun, Y.; Sherry, A. D. NMR Temperature Measurements Using a Paramagnetic Lanthanide Complex. *J. Magn. Reson*. **1998**, *133*, 53–60. (g) Aime, S.; Botta, M.; Fasano, M.; Terreno, E. Lanthanide(III) Chelates for NMR Biomedical Applications. *Chem. Soc. Rev*. **1998**, *27*, 19–29. (h) Rohovec, J.; Lukeš, I.; Hermann, P. Lanthanide Complexes of a Cyclen Derivative with Phenylphoshinic Pendant Arms for Possible ^{1}H and ^{31}P MRI Temperature Sensitive Probes. *New J. Chem*. **1999**, *23*, 1129–1132. (i) Sun, Y.; Sugawara, M.; Mulkern, R. V.; Hynynen, K.; Mochizuki, S.; Albert, M.; Zuo, C. S. Simultaneous Measurements of Temperature and pH In Vivo Using NMR in Conjunction with $TmDOTP^{5-}$. *NMR Biomed*. **2000**, *13*, 460–466. (j) Zuo, C. S.; Mahmood, A.; Sherry, A. D. $TmDOTA^{-}$: A Sensitive Probe for MR Thermometry In Vivo. *J. Magn. Reson*. **2001**, *151*, 101–106. (k) Hekmatyar, S. K.; Hopewell, P.; Pakin, S. K.; Babsky, A.; Bansal, N. Noninvasive MR Thermometry Using Paramagnetic Lanthanide Complexes of 1,4,7,10-Tetraazacyclododecane-α,α′,α″,α‴-tetramethyl-1,4,7,10-tetraacetic Acid ($DOTMA^{4-}$). *Magn. Reson. Med*. **2005**, *53*, 294–303. (l) Hekmatyar, S. K.; Kerkhoff, R. M.; Pakin, S. K.; Hopewell, P.; Bansal, N. Noninvasive Thermometry Using Hyperfine-Shifted MR Signals from Paramagnetic Lanthanide Complexes. *Int. J. Hyperthermia* **2005**, *21*, 561–574. (m) Pakin, S. K.; Hekmatyar, S. K.; Hopewell, P.; Babsky, A.; Bansal, N. Non-Invasive Temperature Imaging with Thulium 1,4,7,10-Tetraazacyclododecane-1,4,7,10-tetramethyl-1,4,7,10-tetraacetic Acid ($TmDOTMA^{-}$). *NMR Biomed*. **2006**, *19*, 116–124. (n) Coman, D.; Trubel, H. K.; Rycyna, R. E.; Hyder, F. Brain Temperature and pH Measurements by ^{1}H Chemical Shift Imaging of a Thulium Agent. *NMR Biomed*. **2009**, *22*, 229–239. (o) James, J. R.; Gao, Y.; Miller, M. A.; Babsky, A.; Bansal, N. Absolute Temperature MR Imaging with Thulium 1,4,7,10-Tetraazacyclododecane-1,4,7,10-tetramethyl-1,4,7,10-tetraacetic

Acid (TmDOTMA^{-}). *Magn. Reson. Med*. **2009**, *62*, 550–556. (p) Coman, D.; Trubel, H. K.; Hyder, F. Brain Temperature by Biosensor Imaging of Redundant Deviation in Shifts (BIRDS): Comparison Between TmDOTP^{5-} and TmDOTMA^{-}. *NMR Biomed*. **2010**, *23*, 277–285. (q) Milne, M.; Hudson, R. H. E. Contrast Agents Possessing High Temperature Sensitivity. *Chem. Commun*. **2011**, *47*, 9194–9196. (r) Coman, D.; de Graaf, R. A.; Rothman, D. L.; Hyder, F. In Vivo Three-Dimensional Molecular Imaging with Biosensor Imaging of Redundant Deviation in Shifts (BIRDS) at High Spatiotemporal Resolution. *NMR Biomed*. **2013**, *26*, 1589–1595.

(10) Tsitovich, P. B.; Cox, J. M.; Benedict, J. B.; Morrow, J. R. Six-Coordinate Iron(II) and Cobalt(II) ParaSHIFT Agents for Measuring Temperature by Magnetic Resonance Spectroscopy. *Inorg. Chem*. **2016**, *55*, 700–716.

(11) (a) Palasz, A.; Czekaj, P. Toxicological and Cytophysiological Aspects of Lanthanides Action. *Acta Biochim. Pol*. **2000**, *47*, 1107–1114. (b) Rydahl, C.; Thomsen, H. S.; Marckmann, P. High Prevalence of Nephrogenic Systemic Fibrosis in Chronic Renal Failure Patients Exposed to Gadodiamide, a Gadolinium-Containing Magnetic Resonance Contrast Agent. *Invest. Radiol*. **2008**, *43*, 141–144. (c) Rim, K. T.; Koo, K. H.; Park, J. S. Toxicological Evaluations of Rare Earths and Their Health Impacts to Workers: A Literature Review. *Safety and Health at Work*, **2013**, *4*, 12–26.

(12) Bertini, I.; Luchinat, C. *NMR of Paramagnetic Molecules in Biological Systems*; The Benjamin/Cummings Publishing Company, Inc.: Menlo Park, 1986.

(13) (a) Gütlich, P.; Goodwin, H. A. Spin Crossover–An Overall Perspective. In *Spin Crossover in Transition Metal Compounds I. Topics in Current Chemistry*; Gütlich, P., Goodwin, H. A., Eds.; Springer: Berlin, 2004; Vol. 13, pp. 1–47. (b) Gaspar, A. B.; Seredyuk, M.; Gütlich, P. Spin Crossover in Iron(II) Complexes: Recent Advances. *J. Mol. Struct*. **2009**, *924–926*, 9–19. (c) Halcrow, M. A. Structure:Function Relationships in Molecular Spin-Crossover Complexes. *Chem. Soc. Rev*. **2011**, *40*, 4119–4142. (d) *Spin-Crossover Materials: Properties and Applications*; Halcrow, M. A., Ed.; Wiley-VCH: Weinheim, 2013.

(14) Muller, R. N.; Vander Elst, L.; Laurent, S. Spin Transition Molecular Materials: Intelligent Contrast Agents for Magnetic Resonance Imaging. *J. Am. Chem. Soc*. **2003**, *125*, 8405–8407.

(15) Jeon, I.-R.; Park, J. G.; Haney, C. R.; Harris, T. D. Spin Crossover Iron(II) Complexes as PARACEST MRI Thermometers. *Chem. Sci*. **2014**, *5*, 2461–2465.

(16) Dolbier, W. R. *Guide to Fluorine NMR for Organic Chemists*; John Wiley & Sons: Hoboken, 2009.

(17) (a) Yu, J. X.; Kodibagkar, V. D.; Cui, W.; Mason, R. P. ^{19}F: A Versatile Reporter for Non-Invasive Physiology and Pharmacology Using Magnetic Resonance. *Curr. Med. Chem.* **2005**, *12*, 819–848. (b) Chen, J.; Lanza, G. M.; Wickline, S. A. Quantitative Magnetic Resonance Fluorine Imaging: Today and Tomorrow. *WIREs Nanomed. Nanobiotechnol.* **2010**, *2*, 431–440. (c) Tirotta, I.; Dichiarante, V.; Pigliacelli, C.; Cavallo, G.; Terraneo, G.; Bombelli, F. B.; Metrangolo, P.; Resnati, G. ^{19}F Magnetic Resonance Imaging (MRI): From Design of Materials to Clinical Applications. *Chem. Rev.* **2015**, *115*, 1106–1129.

(18) (a) Smirnov, V. V.; Woller, E. K.; DiMagno, S. G. ^{19}F NMR and Structural Evidence for Spin-State Modulation of Six-Coordinate Cobalt(II) in a Weak Field Porphyrin Ligand. *Inorg. Chem.* **1998**, *37*, 4971–4978. (b) Yatsunyk, L.; Walker, F. A. 19F Isotropic Shifts in Paramagnetic Iron(III) Octaethyltetraphenylporphyrinate and Tetraphenylporphyrinate Complexes of a Variety of Electronic Ground States: Implications for the Electron Configuration of Chloroiron Tri-(pentafluorophenyl)correlate. *Inorg. Chim. Acta* **2002**, *337*, 266–274. (c) Song, B.; Yu, B. Fluorine-19 NMR Spectroscopic Studies of Phenyl-Fluorinated Iron Tetraarylporphyrin Complexes. *Bull. Korean Chem. Soc.* **2003**, *24*, 981–985.

(19) (a) Senanayake, P. K.; Kenwright, A. M.; Parker, D.; van der Hoorn, S. Responsive Fluorinated Lanthanide Probes for ^{19}F Magnetic Resonance Spectroscopy. *Chem. Commun.* **2007**, 2923–2925. (b) Kenwright, A. M.; Kuprov, I.; De Luca, E.; Parker, D.; Pandya, S. U.; Senanayake, P. K.; Smith, D. G. ^{19}F NMR Based pH Probes: Lanthanide(III) Complexes with pH-Sensitive Chemical Shifts. *Chem. Commun*. **2008**, 2514–2516. (c) Chalmers, K. H.; De Luca, E.; Hogg, N. H. M.; Kenwright, A. M.; Kuprov, I.; Parker, D.; Botta, M.; Wilson, J. I.; Blamire, A. M. *Chem. –Eur. J*. **2010**, *16*, 134–148. (d) Harvey, P.; Kuprov, I.; Parker, D. Lanthanide Complexes as Paramagnetic Probes for ^{19}F Magnetic Resonance. *Eur. J. Inorg. Chem*. **2012**, 2015–2022. (e) Harvey, P.; Blamire, A. M.; Wilson, J. I.; Finney, K.-L. N. A.; Funk, A. M.; Senanayake, P. K.; Parker, D. Moving the Goal Posts: Enhancing the Sensitivity of PARASHIFT Proton Magnetic Resonance Imaging and Spectroscopy. *Chem. Sci*. **2013**, *4*, 4251–4258.

(20) (a) Berkowitz, B. A.; Handa, J. T.; Wilson, C. A. Perfluorocarbon Temperature Measurements using ^{19}F NMR. *NMR Biomed.* **1992**, *5*, 65–68. (b) Webb, A. G.; Smith, N. B.; Ellis, D. S.; O'Brien, W. D., Jr. Non-Invasive In Vivo Temperature Mapping of Ultrasound Heating Using Fluorine-Based Magnetic Resonance Imaging Agents. *Proc.–IEEE Ultrason. Symp*. **1995**, *2*, 1609–1612.

(21) Schoenfeldt, N. J.; Korinda, A. W.; Notestein, J. M. A Heterogeneous, Selective Oxidation Catalyst Based on Mn Triazacyclononane Grafted Under Reaction Conditions. *Chem. Commun.* **2010**, *46*, 1640–1642.

(22) *SAINT*, version 8.34A; Bruker Analytical X-ray Systems, Inc.: Madison, WI, 2013.

(23) Sheldrick, G. M. *SADABS*, version 2.03; Bruker Analytical X-ray Systems, Inc.: Madison, WI, 2000.

(24) (a) Sheldrick, G. M. *SHELXTL*, version 6.12; Bruker Analytical X-ray Systems, Inc.: Madison, WI, 2000. (b) Sheldrick, G. M. *SHELXT* – Integrated Space-Group and Crystal-Structure Determination. *Acta Crystallogr., Sect. A: Found. Adv*. **2015**, *71*, 3–8.

(25) Dolomanov, O. V.; Bourhis, L. J.; Gildea, R. J.; Howard, J. A. K.; Puschmann, H. *OLEX2*: A Complete Structure Solution, Refinement and Analysis Program. *J. Appl. Crystallogr*. **2009**, *42*, 339–341.

(26) (a) Evans, D. F. The Determination of the Paramagnetic Susceptibility of Substances in Solution by Nuclear Magnetic Resonance. *J. Chem. Soc*. **1959**, 2003−2005. (b) Schubert, E. M. Utilizing the Evans Method with a Superconducting NMR Spectrometer in the Undergraduate Laboratory. *J. Chem. Educ*. **1992**, 69, 62.

(27) Bain, G. A.; Berry, J. F. Diamagnetic Corrections and Pascal's Constants. *J. Chem. Educ*. **2008**, *85*, 532−536.

(28) Weber, B.; Walker, F. A. Solution NMR Studies of Iron(II) Spin-Crossover Complexes. *Inorg. Chem.* **2007**, *46*, 6794−6803.

(29) (a) Stavila, V.; Allali, M.; Canaple, L.; Stortz, Y.; Franc, C.; Maurin, P.; Beuf, O.; Dufay, O.; Samarut, J.; Janier, M.; Hasserodt, J. Significant Relaxivity Gap Between a Low-Spin and a High-Spin Iron(II) Complex of Structural Similarity: An Attractive Off–On System for the Potential Design of Responsive MRI Probes. *New J. Chem*. **2008**, *32*, 428–435. (b) Dorazio, S. J.; Tsitovich, P. B.; Siters, K. E.; Spernyak, J. A.; Morrow, J. R. Iron(II) PARACEST MRI Contrast Agents. *J. Am. Chem. Soc.* **2011**, *133*, 14154–14156. (c) Hasserodt, J. Magnetogenic Probes that Respond to Chemical Stimuli in an Off–On Mode. *New J. Chem*. **2012**, *36*, 1707–1712. (d) Tsitovich, P. B.; Morrow, J. R. Macrocyclic Ligands for Fe(II) ParaCEST and Chemical Shift MRI Contrast Agents. *Inorg. Chim. Acta* **2012**, *393*, 3–11. (e) Dorazio, S. J.; Tsitovich, P. B.; Gardina, S. A.; Morrow, J. R. The Reactivity of Macrocyclic Fe(II) ParaCEST MRI Contrast Agents Towards Biologically Relevant Anions, Cations, Oxygen or Peroxide. *J. Inorg. Biochem*. **2012**, *117*, 212–219. (f) Touti, F.; Maurin, P.; Hasserodt, J. Magnetogenesis under Physiological Conditions with Probes that Report on (Bio-)Chemical Stimuli. *Angew. Chem. Int. Ed*. **2013**, *52*, 4654–4658. (g) Tsitovich, P. B.; Spernyak, J. A.; Morrow, J. R. A Redox-Activated MRI Contrast Agent that Switches Between Paramagnetic and Diamagnetic States. *Angew. Chem. Int. Ed*. **2013**, *52*, 13997–14000. (h) Dorazio, S. J.; Olatunde, A. O.; Tsitovich, P. B.; Morrow, J. R. Comparison of

Divalent Transition Metal Ion ParaCEST MRI Contrast Agents. *J. Biol. Inorg. Chem*. **2014**, *19*, 191–205. (i) Gondrand, C.; Touti, F.; Godart, E.; Berezhanskyy, Y.; Jeanneau, E.; Maurin, P.; Hasserodt, J. Spring-Loaded Iron(II) Complexes as Magnetogenic Probes Reporting on a Chemical Analyte in Water. *Eur. J. Inorg. Chem*. **2015**, 1376–1382. (j) Wang, J.; Gondrand, C.; Touti, F.; Hasserodt, J. A Pair of Highly Biotolerated Diamagnetic and Paramagnetic Iron(II) Complexes Displaying Electroneutrality. *Dalton Trans*. **2015**, *44*, 15391–15395.

(30) Prat, I.; Company, A.; Corona, T.; Parella, T.; Ribas, X.; Costas, M. Assessing the Impact of Electronic and Steric Tuning of the Ligand in the Spin State and Catalytic Oxidation Ability of the Fe^{II}(Pytacn) Family of Complexes. *Inorg. Chem*. **2013**, *52*, 9229–9244.

(31) (a) Diebold, A.; Hagen, K. S. Iron(II) Polyamine Chemistry: Variation of Spin State and Coordination Number in Solid State and Solution with Iron(II) Tris(2-pyridylmethyl)amine Complexes. *Inorg. Chem*. **1998**, *37*, 215–223. (b) Chen, K.; Que, L., Jr. Stereospecific Alkane Hydroxylation by Non-Heme Iron Catalysts: Mechanistic Evidence for an Fe^{V}=O Active Species. *J. Am. Chem. Soc*. **2001**, *123*, 6327–6337. (c) Goldsmith, C. R.; Jonas, R. T.; Cole, A. P.; Stack, T. D. P. A Spectrochemical Walk: Single-Site Perturbation within a Series of Six-Coordinate Ferrous Complexes. *Inorg. Chem*. **2002**, *41*, 4642–4652. (d) Rudd, D. J.; Goldsmith, C. R.; Cole, A. P.; Stack, T. D. P.; Hodgson, K. O.; Hedman, B. X-ray Absorption Spectroscopic Investigation of the Spin-Transition Character in a Series of Single-Site Perturbed Iron(II) Complexes. *Inorg. Chem*. **2005**, *44*, 1221–1229.

(32) Britovsek, G. J. P.; England, J.; White, A. J. P. Non-Heme Iron(II) Complexes Containing Tripodal Tetradentate Nitrogen Ligands and Their Application in Alkane Oxidation Catalysis. *Inorg. Chem*. **2005**, *44*, 8125–8134.

(33) (a) Schlager, O.; Wieghardt, K.; Grondey, H.; Rufinska, A.; Nuber, B. The Hexadentate Ligand 1,4,7-Tris(o-aminobenzyl)-1,4,7-triazacyclononane and Its Complexes with Zinc(II), cadmium(II), and Mercury(II) in Solution and in the Solid State. *Inorg. Chem*. **1995**, *34*, 6440–6448. (b) Fry, F. H.; Fallon, G. D.; Spiccia, L. Zinc(II) Complexes of Xylyl Bridged Bis(1,4,7-triazacyclononane) Derivatives. *Inorg. Chim. Acta* **2003**, *346*, 57–66. (c) Fry, F. H.; Jensen, P.; Kepert, C. M.; Spiccia, L. Macrocyclic Copper(II) and Zinc(II) Complexes Incorporating Phosphate Esters. *Inorg. Chem*. **2003**, *42*, 5637–5644.

(34) Drew, M. G. B.; Harding, C. J.; McKee, V.; Morgan, G. G.; Nelson, J. Geometric Control of Manganese Redox States. *J. Chem. Soc., Chem. Commun*. **1995**, 1035–1038.

(35) (a) Shannon, R. D. Revised Effective Ionic Radii and Systematic Studies of Interatomic Distances in Halides and Chalcogenides. *Acta Crystallogr., Sect. A: Cryst. Phys., Diffr., Theor. Gen. Crystallogr*. **1976**, *32*, 751–767. (b) Yang, Q.; Cheng, X.; Gao, C.; Wang, B.;

Wang, Z.; Gao, S. Structural Distortion Controlled Spin-Crossover Behavior. *Cryst. Growth Des*. **2015**, *15*, 2565–2567. (c) Takahashi, K.; Kawamukai, K.; Okai, M.; Mochida, T.; Sakurai, T.; Ohta, H.; Yamamoto, T.; Einaga, Y.; Shiota, Y.; Yoshizawa, K. A New Family of Anionic Fe^{III} Spin Crossover Complexes Featuring a Weak-Field N_2O_4 Coordination Octahedron. *Chem. –Eur. J*. **2016**, *22*, 1253–1257.

(36) (a) Bernal, I.; Jensen, I. M.; Jensen, K. B.; McKenzie, C. J.; Toftlund, H.; Tuchagues, J.-P. Iron(II) Complexes of Polydentate Aminopyridyl Ligands and an Exchangeable Sixth Ligand; Reactions with Peroxides. Crystal Structure of $[FeL^1(H_2O)][PF_6]_2 \cdot H_2O$ [L^1=*N*,*N*′-bis-(6-methyl-2-pyridylmethyl)-*N*,*N*′-bis(2-pyridylmethyl)ethane-1,2-diamine]. *J. Chem. Soc., Dalton Trans*. **1995**, 3667–3675. (b) Balland, V.; Banse, F.; Anxolabéhère-Mallart, E.; Nierlich, M.; Girerd, J.-J. Iron Complexes Containing the Ligand *N*,*N*′-Bis(6-methyl-2-pyridylmethyl)-*N*,*N*′-bis(2-pyridylmethyl)ethane-1,2-diamine: Structural, Spectroscopic, and Electrochemical Studies, Reactivity with Hydrogen Peroxide and the Formation of a Low-Spin Fe−OOH Complex. *Eur. J. Inorg. Chem*. **2003**, 2529–2535. (c) England, J.; Britovsek, G. J. P.; Rabadia, N.; White, A. J. P. Ligand Topology Variations and the Importance of Ligand Field Strength in Non-Heme Iron Catalyzed Oxidations of Alkanes. *Inorg. Chem*. **2007**, *46*, 3752–3767.

(37) Linert, W.; Konecny, M.; Renz, F. Spin-State Equilibria in Non-Aqueous Solution and Quantum-Mechanical Investigations of Iron(II) and Nickel(II) Complexes with 4-Substituted 2,6-Bis(benzimidazol-2-yl)pyridines. *J. Chem. Soc., Dalton Trans*. **1994**, 1523–1531.

(38) Ni, Z.; McDaniel, A. M.; Shores, M. P. Ambient Temperature Anion-Dependent Spin State Switching Observed in "Mostly Low Spin" Heteroleptic Iron(II) Diimine Complexes. *Chem. Sci*. **2010**, *1*, 615–621.

(39) Strauß, B.; Gutmann, V.; Linert, W. Investigations on the Spin-Crossover Complex $[Fe(bzimpy)_2](ClO_4)_2$ and Its Mn^{2+}, Co^{2+}, Ni^{2+} and Zn^{2+} Analogues. *Monatsh. Chem*. **1993**, *124*, 391–399.

(40) (a) Brinen, J. S.; Koren, J. G.; Olmstead, H. D.; Hirt, R. C. Charge-Transfer Absorption and Luminescence Spectra of Alkyl Halide Salts of Pyridine. *J. Phys. Chem*. **1965**, *69*, 3791–3794. (b) Dubroca, C. Temperature Effect Upon the UV Absorption Spectra of Aniline Derivatives. *Chem. Phys. Lett*. **1972**, *15*, 207–210. (c) Chang, H. R.; McCusker, J. K.; Toftlund, H.; Wilson, S. R.; Trautwein, A. X.; Winkler, H.; Hendrickson, D. N. [Tetrakis(2-pyridylmethyl)ethylenediamine]iron(II) Perchlorate, the First Rapidly Interconverting Ferrous Spin-Crossover Complex. *J. Am. Chem. Soc*. **1990**, *112*, 6814–6827. (d) Mialane, P.; Nivorojkine, A.; Pratviel, G.; Azéma, L.; Slany, M.; Godde, F.; Simaan, A.; Banse, F.;

Kargar-Grisel, T.; Bouchoux, G.; Sainton, J.; Horner, O.; Guilhem, J.; Tchertanova, L.; Meunier, B.; Girerd, J.-J. *Inorg. Chem*. **1999**, *38*, 1085–1092.

(41) Johnson, C. J.; Morgan, G. G.; Albrecht, M. Predictable Adjustment of Spin Crossover Temperature in Solutions of Iron(III) Complexes Functionalized with Alkyl-Urea Tails. *J. Mater. Chem. C* **2015**, *3*, 7883–7889.

(42) (a) Gutmann, V.; Wychera, E. Coordination Reactions in Non Aqueous Solutions – The Role of the Donor Strength. *Inorg. Nucl. Chem. Lett*. **1966**, *2*, 257–260. (b) Turner, J. W.; Schultz, F. A. Solution Characterization of the Iron(II) Bis(1,4,7-Triazacyclononane) Spin-Equilibrium Reaction. *Inorg. Chem*. **2001**, *40*, 5296–5298. (c) Kershaw Cook, L. J.; Mohammed, R.; Sherborne, G.; Roberts, T. D.; Alvarez, S.; Halcrow, M. A. Spin State Behavior of Iron(II)/dipyrazolylpyridine Complexes. New Insights from Crystallographic and Solution Measurements. *Coord. Chem. Rev*. **2015**, *289–290*, 2–12.

(43) Equation 2.2 provided in Section 2.2 was used to simulate the data, see ref. 28 for further details.

(44) Toftlund, H.; McGarvey, J. J. Iron(II) Spin Crossover Systems with Multidentate Ligands. *Top. Curr. Chem*. **2004**, *233*, 151–166.

(45) The temperature coefficient of the chemical shift (CT) is defined as the slope of a linear fit to the data of a chemical shift vs temperature (δ vs T) plot.

(46) Valyaev, D. A.; Clair, S.; Patrone, L.; Abel, M.; Porte, L.; Chuzel, O.; Parrain, J.-L. Grafting a Homogeneous Transition Metal Catalyst onto a Silicon AFM Probe: A Promising Strategy for Chemically Constructive Nanolithography. *Chem. Sci.* **2013**, *4*, 2815–2821.

(47) Krishnaiah, M.; Jin, C. H.; Sheen, Y. Y.; Kim, D.-K. Synthesis and Biological Evaluation of 5-(Fluoro-substituted-6-methylpyridin-2-yl)-4-([1,2,4]triazolo[1,5-*a*]pyridin-6-yl)imidazoles as Inhibitors of Transforming Growth Factor-β Type I Receptor Kinase. *Bioorg. Med. Chem. Lett.* **2015**, *25*, 5228–5231.

References for Chapter 3

(1) (a) Kallinowski, F.; Schlenger, K. H.; Runkel, S.; Kloes, M.; Stohrer, M.; Okunieff, P.; Vaupel, P. Blood Flow, Metabolism, Cellular Microenvironment, and Growth Rate of Human Tumor Xenografts. *Cancer Res*. **1989**, *49*, 3759–3764. (b) Tannock, I. F.; Rotin, D. Acid pH in Tumors and Its Potential for Therapeutic Exploitation. *Cancer Res*. **1989**, *49*, 4373–4384. (c) Vaupel, P.; Kallinowski, F.; Okunieff, P. Blood Flow, Oxygen and Nutrient Supply, and Metabolic Microenvironment of Human Tumors: A Review. *Cancer Res*. **1989**, *49*, 6449–6465. (d) Gillies, R. J.; Raghunand, N.; Karczmar, G. S.; Bhujwalla, Z. M. MRI of the Tumor Microenvironment. *J. Magn. Reson. Imaging* **2002**, *16*, 430–450. (e) Gatenby, R. A.; Gillies, R. J. Why Do Cancers Have High Aerobic Glycolysis? *Nat. Rev. Cancer* **2004**, *4*, 891–899. (f) Gillies, R. J.; Raghunand, N.; Garcia-Martin, M. L.; Gatenby, R. A. pH Imaging. A Review of pH Measurement Methods and Applications in Cancers. *IEEE Eng. Med. Biol. Mag*. **2004**, *23*, 57–64. (g) Hashim, A. I.; Zhang, X.; Wojtkowiak, J. W.; Martinez, G. V.; Gillies, R. J. Imaging pH and Metastasis. *NMR Biomed*. **2011**, *24*, 582–591. (h) Kato, Y.; Ozawa, S.; Miyamoto, C.; Maehata, Y.; Suzuki, A.; Maeda, T.; Baba, Y. Acidic Extracellular Microenvironment and Cancer. *Cancer Cell Int*. **2013**, *13*, 89–96.

(2) (a) Katsura, K.; Ekholm, A.; Asplund, B.; Siesjö, B. K. Extracellular pH in the Brain During Ischemia: Relationship to the Severity of Lactic Acidosis. *J. Cereb. Blood Flow Metab*. **1991**, *11*, 597–599. (b) Sun, P. Z.; Wang, E.; Cheung, J. S. Imaging Acute Ischemic Tissue Acidosis with pH-Sensitive Endogenous Amide Proton Transfer (APT) MRI–Correction of Tissue Relaxation and Concomitant RF Irradiation Effects Toward Mapping Quantitative Cerebral Tissue pH. *NeuroImage* **2012**, *60*, 1–6. (c) Rajamäki, K.; Nordström, T.; Nurmi, K.; Åkerman, K. E. O.; Kovanen, P. T.; Öörni, K.; Eklund, K. K. Extracellular Acidosis Is a Novel Danger Signal Alerting Innate Immunity via the NLRP3 Inflammasome. *J. Biol. Chem*. **2013**, *288*, 13410–13419.

(3) (a) Wike-Hooley, J. L.; Haveman, J.; Reinhold, H. S. The Relevance of Tumour pH to the Treatment of Malignant Disease. *Radiother. Oncol*. **1984**, *2*, 343–366. (b) Gerweck, L. E.; Seetharaman, K. Cellular pH Gradient in Tumor Versus Normal Tissue: Potential Exploitation for the Treatment of Cancer. *Cancer Res*. **1996**, *56*, 1194–1198. (c) Wojtkowiak, J. W.; Verduzco, D.; Schramm, K. J.; Gillies, R. J. Drug Resistance and Cellular Adaption to Tumor Acidic pH Microenvironment. *Mol. Pharm*. **2011**, *8*, 2032–2038. (d) Pilon-Thomas, S.; Kodumudi, K. N.; El-Kenawi, A. E.; Russell, S.; Weber, A. M.; Luddy, K.; Damaghi, M.; Wojtkowiak, J. W.; Mulé, J. J.; Ibrahim-Hashim, A.; Gillies, R. J. Neutralization of Tumor Acidity Improves Antitumor Responses to Immunotherapy. *Cancer Res*. **2016**, *76*, 1381–1390.

(4) (a) Lauffer, R. B. Paramagnetic Metal Complexes as Water Proton Relaxation Agents for NMR Imaging: Theory and Design. *Chem. Rev*. **1987**, *87*, 901–927. (b) Caravan, P.; Ellison,

J. J.; McMurry, T. J.; Lauffer, R. B. Gadolinium(III) Chelates as MRI Contrast Agents: Structure, Dynamics, and Applications. *Chem. Rev*. **1999**, *99*, 2293–2352. (c) Rieke, V.; Pauly, K. B. MR Thermometry. *J. Magn. Reson. Imaging* **2008**, *27*, 376–390.

(5) Ward, K. M.; Aletras, A. H.; Balaban, R. S. A New Class of Contrast Agents for MRI Based on Proton Chemical Exchange Dependent Saturation Transfer (CEST). *J. Magn. Reson*. **2000**, *143*, 79–87.

(6) Selected references: (a) Zhang, S.; Winter, P.; Wu, K.; Sherry, A. D. A Novel Europium(III)-Based MRI Contrast Agent. *J. Am. Chem. Soc*. **2001**, *123*, 1517–1518. (b) Zhang, S.; Merritt, M.; Woessner, D. E.; Lenkinski, R. E.; Sherry, A. D. PARACEST Agents: Modulating MRI Contrast via Water Proton Exchange. *Acc. Chem. Res*. **2003**, *36*, 783–790. (c) Zhou, J.; van Zijl, P. C. M. Chemical Exchange Saturation Transfer Imaging and Spectroscopy. *Prog. Nucl. Magn. Reson. Spectrosc*. **2006**, *48*, 109–136. (d) Woods, M.; Woessner, D. E.; Sherry, A. D. Paramagnetic Lanthanide Complexes as PARACEST Agents for Medical Imaging. *Chem. Soc. Rev*. **2006**, *35*, 500–511. (e) Ali, M. M.; Liu, G.; Shah, T.; Flask, C. A.; Pagel, M. D. Using Two Chemical Exchange Saturation Transfer Magnetic Resonance Imaging Contrast Agents for Molecular Imaging Studies. *Acc. Chem. Res*. **2009**, *42*, 915–924. (f) Viswanathan, S.; Kovacs, Z.; Green, K. N.; Ratnakar, S. J.; Sherry, A. D. Alternatives to Gadolinium-Based Metal Chelates for Magnetic Resonance Imaging. *Chem. Rev*. **2010**, *110*, 2960–3018. (g) Terreno, E.; Castelli, D. D.; Viale, A.; Aime, S. Challenges for Molecular Magnetic Resonance Imaging. *Chem. Rev*. **2010**, *110*, 3019–3042. (h) Soesbe, T. C.; Wu, Y.; Sherry, A. D. Advantages of Paramagnetic CEST Complexes Having Slow-to-Intermediate Water Exchange Properties as Responsive MRI Agents. *NMR Biomed*. **2013**, *26*, 829–838.

(7) (a) Wu, Y.; Soesbe, T. C.; Kiefer, G. E.; Zhao, P.; Sherry, A. D. A Responsive Europium(III) Chelate that Provides a Direct Readout of pH by MRI. *J. Am. Chem. Soc*. **2010**, *132*, 14002–14003. (b) Wang, X.; Wu, Y.; Soesbe, T. C.; Yu, J.; Zhao, P.; Kiefer, G. E.; Sherry, A. D. A pH-Responsive MRI Agent that Can Be Activated Beyond the Tissue Magnetization Transfer Window. *Angew. Chem. Int. Ed*. **2015**, *54*, 8662–8664. (c) Wu, Y.; Zhang, S.; Soesbe, T. C.; Yu, J.; Vinogradov, E.; Lenkinski, R. E.; Sherry, A. D. pH Imaging of Mouse Kidneys In Vivo Using a Frequency-Dependent ParaCEST Agent. *Magn. Reson. Med*. **2016**, *75*, 2432–2441. (d) Tsitovich, P. B.; Cox, J. M.; Spernyak, J. A.; Morrow, J. R. Gear Up for a pH Shift: A Responsive Iron(II) 2-Amino-6-picolyl-Appended Macrocyclic ParaCEST Agent that Protonates at a Pendent Group. *Inorg. Chem*. **2016**, *55*, 12001–12010.

(8) McVicar, N.; Li, A. X.; Suchý, M.; Hudson, R. H. E.; Menon, R. S.; Bartha, R. Simultaneous In Vivo pH and Temperature Mapping Using a PARACEST-MRI Contrast Agent. *Magn. Reson. Med*. **2013**, *70*, 1016–1025.

(9) (a) Aime, S.; Castelli, D. D.; Terreno, E. Novel pH-Reporter MRI Contrast Agents. *Angew. Chem. Int. Ed*. **2002**, *41*, 4334–4336. (b) Castelli, D. D.; Terreno, E.; Aime, S. Yb(III)-HPDO3A: A Dual pH- and Temperature-Responsive CEST Agent. *Angew. Chem. Int. Ed*. **2011**, *50*, 1798–1800. (c) Liu, G.; Li, Y.; Sheth, V. R.; Pagel, M. D. Imaging In Vivo Extracellular pH with a Single Paramagnetic Chemical Exchange Saturation Transfer Magnetic Resonance Imaging Contrast Agent. *Mol. Imaging* **2012**, *11*, 47–57. (d) Sheth, V. R.; Liu, G.; Li, Y.; Pagel, M. D. Improved pH Measurements with a Single PARACEST MRI Contrast Agent. *Contrast Media Mol. Imaging* **2012**, *7*, 26–34. (e) Sheth, V. R.; Li, Y.; Chen, L. Q.; Howison, C. M.; Flask, C. A.; Pagel, M. D. Measuring In Vivo Tumor pHe with CEST-FISP MRI. *Magn. Reson. Med*. **2012**, *67*, 760–768. (f) Dorazio, S. J.; Olatunde, A. O.; Spernyak, J. A.; Morrow, J. R. CoCEST: Cobalt(II) Amide-Appended ParaCEST MRI Contrast Agents. *Chem. Commun*. **2013**, *49*, 10025–10027. (g) Castelli, D. D.; Ferrauto, G.; Cutrin, J. C.; Terreno, E.; Aime, S. In Vivo Maps of Extracellular pH in Murine Melanoma by CEST-MRI. *Magn. Reson. Med*. **2014**, *71*, 326–332. (h) Rancan, G.; Castelli, D. D.; Aime, S. MRI CEST at 1T with Large μ_{eff} Ln^{3+} Complexes Tm^{3+}-HPDO3A: An Efficient MRI pH Reporter. *Magn. Reson. Med*. **2016**, *75*, 329–336. (i) Krchová, T.; Gálisová, A.; Jirák, D.; Hermann, P.; Kotek, J. Ln(III)-Complexes of a DOTA Analogue with an Ethylenediamine Pendant Arm as pH-Responsive PARACEST Contrast Agents. *Dalton Trans*. **2016**, *45*, 3486–3496.

(10) (a) Wolff, S. D.; Balaban, R. S. Magnetization Transfer Contrast (MTC) and Tissue Water Proton Relaxation In Vivo. *Magn. Reson. Med*. **1989**, *10*, 135–144. (b) Zaiss, M.; Bachert, P. Chemical Exchange Saturation Transfer (CEST) and MR Z-Spectroscopy In Vivo: A Review of Theoretical Approaches and Methods. *Phys. Med. Biol*. **2013**, *58*, R221–R269.

(11) Selected references: (a) Dorazio, S. J.; Tsitovich, P. B.; Siters, K. E.; Spernyak, J. A.; Morrow, J. R. Iron(II) PARACEST MRI Contrast Agents. *J. Am. Chem. Soc*. **2011**, *133*, 14154–14156. (b) Dorazio, S. J.; Morrow, J. R. The Development of Iron(II) Complexes as ParaCEST MRI Contrast Agents. *Eur. J. Inorg. Chem*. **2012**, 2006–2014. (c) Dorazio, S. J.; Tsitovich, P. B.; Gardina, S. A.; Morrow, J. R. The Reactivity of Macrocyclic Fe(II) ParaCEST MRI Contrast Agents Towards Biologically Relevant Anions, Cations, Oxygen or Peroxide. *J. Inorg. Biochem*. **2012**, *117*, 212–219. (d) Tsitovich, P. B.; Morrow, J. R. Macrocyclic Ligands for Fe(II) ParaCEST and Chemical Shift MRI Contrast Agents. *Inorg. Chim. Acta* **2012**, *393*, 3–11. (e) Olatunde, A. O.; Dorazio, S. J.; Spernyak, J. A.; Morrow, J. R. The NiCEST Approach: Nickel(II) ParaCEST MRI Contrast Agents. *J. Am. Chem. Soc*. **2012**, *134*, 18503–18505. (f) Dorazio, S. J.; Morrow, J. R. Iron(II) Complexes Containing Octadentate Tetraazamacrocycles as ParaCEST Magnetic Resonance Imaging Contrast Agents. *Inorg. Chem*. **2012**, *51*, 7448–7450. (g) Tsitovich, P. B.; Spernyak, J. A.; Morrow, J. R. A Redox-Activated MRI Contrast Agent that Switches Between Paramagnetic and Diamagnetic States. *Angew. Chem. Int. Ed*. **2013**, *52*, 13997–14000. (h) Dorazio, S. J.; Olatunde, A. O.; Tsitovich, P. B.; Morrow, J. R. Comparison of Divalent Transition Metal

Ion ParaCEST MRI Contrast Agents. *J. Biol. Inorg. Chem*. **2014**, *19*, 191–205. (i) Jeon, I.-R.; Park, J. G.; Haney, C. R.; Harris, T. D. Spin Crossover Iron(II) Complexes as PARACEST MRI Thermometers. *Chem. Sci*. **2014**, *5*, 2461–2465. (j) Olatunde, A. O.; Bond, C. J.; Dorazio, S. J.; Cox, J. M.; Benedict, J. B.; Daddario, M. D.; Spernyak, J. A.; Morrow, J. R. Six, Seven or Eight Coordinate Fe^{II}, Co^{II} or Ni^{II} Complexes of Amide-Appended Tetraazamacrocycles for ParaCEST Thermometry. *Chem. –Eur. J*. **2015**, *21*, 18290–18300. (k) Tsitovich, P. B.; Cox, J. M.; Benedict, J. B.; Morrow, J. R. Six-Coordinate Iron(II) and Cobalt(II) ParaSHIFT Agents for Measuring Temperature by Magnetic Resonance Spectroscopy. *Inorg. Chem*. **2016**, *55*, 700–716. (l) Du, K.; Harris, T. D. A Cu^{II}_2 Paramagnetic Chemical Exchange Saturation Transfer Contrast Agent Enabled by Magnetic Exchange Coupling. *J. Am. Chem. Soc*. **2016**, *138*, 7804–7807. (m) Du, K.; Waters, E. A.; Harris, T. D. Ratiometric Quantitation of Redox Status with a Molecular Fe_2 Magnetic Resonance Probe. *Chem. Sci*. **2017**, *8*, 4424–4430. (n) Burns, P. J.; Cox, J. M.; Morrow, J. R. Imidazole-Appended Macrocyclic Complexes of Fe(II), Co(II), and Ni(II) as ParaCEST Agents. *Inorg. Chem*. **2017**, *56*, 4545–4554.

(12) (a) James, T. L. *Nuclear Magnetic Resonance in Biochemistry: Principles and Applications*; Academic Press: New York, 1975. (b) Bertini, I.; Luchinat, C. *NMR of Paramagnetic Molecules in Biological Systems*; The Benjamin/Cummings Publishing Company, Inc.: Menlo Park, 1986. (c) Bertini, I.; Luchinat, C. Hyperfine Shift and Relaxation in the Presence of Chemical Exchange. *Coord. Chem. Rev*. **1996**, *150*, 111–130. (d) Bertini, I.; Luchinat, C.; Parigi, G. *Solution NMR of Paramagnetic Molecules: Applications to Metallobiomolecules and Models*; Elsevier Science B.V.: Amsterdam, 2001.

(13) *APEX2*, version 2014.11-0; Bruker Analytical X-ray Systems, Inc.: Madison, WI, 2014.

(14) Sheldrick, G. M. *SADABS*, version 2.03; Bruker Analytical X-ray Systems, Inc.: Madison, WI, 2000.

(15) (a) Sheldrick, G. M. *SHELXTL*, version 6.12; Bruker Analytical X-ray Systems, Inc.: Madison, WI, 2000. (b) Sheldrick, G. M. *SHELXT* – Integrated Space-Group and Crystal-Structure Determination. *Acta Crystallogr., Sect. A: Found. Adv*. **2015**, *71*, 3–8.

(16) Dolomanov, O. V.; Bourhis, L. J.; Gildea, R. J.; Howard, J. A. K.; Puschmann, H. *OLEX2*: A Complete Structure Solution, Refinement and Analysis Program. *J. Appl. Crystallogr*. **2009**, *42*, 339–341.

(17) *OriginPro*, version 9.0; OriginLab, Corp.: Northampton, MA, 2003.

(18) Dixon, W. T.; Ren, J.; Lubag, A. J. M.; Ratnakar, S. J.; Vinogradov, E.; Hancu, I.; Lenkinski, R. E.; Sherry, A. D. A Concentration-Independent Method to Measure Exchange Rates in PARACEST Agents. *Magn. Reson. Med*. **2010**, *63*, 625–632.

(19) (a) Chen, L. Q.; Howison, C. M.; Jeffery, J. J.; Robey, I. F.; Kuo, P. H.; Pagel, M. D. Evaluations of Extracellular pH Within In Vivo Tumors Using AcidoCEST MRI. *Magn. Reson. Med*. **2014**, *72*, 1408–1417. (b) Moon, B. F.; Jones, K. M.; Chen, L. Q.; Liu, P.; Randtke, E. A.; Howison, C. M.; Pagel, M. D. A Comparison of Iopromide and Iopamidol, Two AcidoCEST MRI Contrast Media that Measure Tumor Extracellular pH. *Contrast Media Mol. Imaging* **2015**, *10*, 446–455.

(20) Aime, S.; Barge, A.; Castelli, D. D.; Fedeli, F.; Mortillaro, A.; Nielsen, F. U.; Terreno, E. Paramagnetic Lanthanide(III) Complexes as pH-Sensitive Chemical Exchange Saturation Transfer (CEST) Contrast Agents for MRI Applications. *Magn. Reson. Med*. **2002**, *47*, 639–648.

(21) (a) Evans, D. F. The Determination of the Paramagnetic Susceptibility of Substances in Solution by Nuclear Magnetic Resonance. *J. Chem. Soc*. **1959**, 2003−2005. (b) Schubert, E. M. Utilizing the Evans Method with a Superconducting NMR Spectrometer in the Undergraduate Laboratory. *J. Chem. Educ*. **1992**, 69, 62.

(22) Bain, G. A.; Berry, J. F. Diamagnetic Corrections and Pascal's Constants. *J. Chem. Educ*. **2008**, *85*, 532−536.

(23) Sawyer, D. T.; Sobkowiak, A.; Roberts, J. L., Jr. *Electrochemistry for Chemists, 2nd ed*.; John Wiley & Sons: New York, 1995.

(24) Selected references: (a) Sakiyama, H.; Ito, R.; Kumagai, H.; Inoue, K.; Sakamoto, M.; Nishida, Y.; Yamasaki, M. Dinuclear Cobalt(II) Complexes of an Acyclic Phenol-Based Dinucleating Ligand with Four Methoxyethyl Chelating Arms − First Magnetic Analyses in an Axially Distorted Octahedral Field. *Eur. J. Inorg. Chem*. **2001**, 2027–2032. (b) Hossain, M. J.; Yamasaki, M.; Mikuriya, M.; Kuribayashi, A.; Sakiyama, H. Synthesis, Structure, and Magnetic Properties of Dinuclear Cobalt(II) Complexes with a New Phenol-Based Dinucleating Ligand with Four Hydroxyethyl Chelating Arms. *Inorg. Chem*. **2002**, *41*, 4058–4062. (c) Tian, J.-L.; Gu, W.; Yan, S.-P.; Liao, D.-Z.; Jiang, Z.-H. Synthesis, Structures and Magnetic Properties of Two Binuclear Cobalt(II) Complexes Bridged by Bis(p-nitrophenyl) Phosphate or Diphenylphosphinate Ion. *Z. Anorg. Allg. Chem*. **2008**, *634*, 1775–1779. (d) Daumann, L. J.; Comba, P.; Larrabee, J. A.; Schenk, G.; Stranger, R.; Cavigliasso, G.; Gahan, L. R. Synthesis, Magnetic Properties, and Phosphoesterase Activity of Dinuclear Cobalt(II) Complexes. *Inorg. Chem*. **2013**, *52*, 2029–2043.

(25) (a) Johansson, F. B.; Bond, A. D.; Nielsen, U. G.; Moubaraki, B.; Murray, K. S.; Berry, K. J.; Larrabee, J. A.; McKenzie, C. J. Dicobalt II−II, II−III, and III−III Complexes as Spectroscopic Models for Dicobalt Enzyme Active Sites. *Inorg. Chem*. **2008**, *47*, 5079–5092. (b) Seidler-Egdal, R. K.; Johansson, F. B.; Veltzé, S.; Skou, E. M.; Bond, A. D.; McKenzie, C. J. Tunability of the $M^{II}M^{III}/M^{II}{}_2$ and $M^{III}{}_2/M^{II}M^{III}$ (M = Mn, Co) Couples in Bis-μ-*O*,*O′*-carboxylato-μ-OR Bridged Complexes. *Dalton Trans*. **2011**, *40*, 3336–3345.

(26) (a) Wayland, B. B.; Drago, R. S.; Henneike, H. F. Amide Contact Shift Studies and the Assignment of the Methyl Peaks in N,N-Dimethylamides. *J. Am. Chem. Soc*. **1966**, *88*, 2455–2458. (b) Stewart, W. E.; Siddall, T. H. Nuclear Magnetic Resonance Studies of Amides. *Chem. Rev*. **1970**, *70*, 517–551. (c) Ming, L.-J.; Lauffer, R. B.; Que, L., Jr. Proton Nuclear Magnetic Resonance Studies of Iron(II/III)–Amide Complexes. Spectroscopic Models for Non-Heme Iron Proteins. *Inorg. Chem*. **1990**, *29*, 3060–3064.

(27) Huang, C.-H.; Morrow, J. R. Cerium(III), Europium(III), and Ytterbium(III) Complexes with Alcohol Donor Groups as Chemical Exchange Saturation Transfer Agents for MRI. *Inorg. Chem*. **2009**, *48*, 7237–7243.

(28) (a) Woods, M.; Woessner, D. E.; Zhao, P.; Pasha, A.; Yang, M.-Y.; Huang, C.-H.; Vasalitiy, O.; Morrow, J. R.; Sherry, A. D. Europium(III) Macrocyclic Complexes with Alcohol Pendant Groups as Chemical Exchange Saturation Transfer Agents. *J. Am. Chem. Soc*. **2006**, *128*, 10155–10162. (b) Huang, C.-H.; Morrow, J. R. A PARACEST Agent Responsive to Inner- And Outer-Sphere Phosphate Ester Interactions for MRI Applications. *J. Am. Chem. Soc*. **2009**, *131*, 4206–4207. (c) Huang, C.-H.; Hammell, J.; Ratnakar, S. J.; Sherry, A. D.; Morrow, J. R. Activation of a PARACEST Agent for MRI Through Selective Outersphere Interactions with Phosphate Diesters. *Inorg. Chem*. **2010**, *49*, 5963–5970. (d) Hammell, J.; Buttarazzi, L.; Huang, C.-H.; Morrow, J. R. Eu(III) Complexes as Anion-Responsive Luminescent Sensors and Paramagnetic Chemical Exchange Saturation Transfer Agents. *Inorg. Chem*. **2011**, *50*, 4857–4867. (e) Ferrauto, G.; Castelli, D. D.; Terreno, E.; Aime, S. In Vivo MRI Visualization of Different Cell Population Labeled with PARACEST Agents. *Magn. Reson. Med*. **2013**, *69*, 1703–1711.

(29) Note that the common logarithm with base 10 was used throughout this study. For brevity, the notation "log" is employed in the pH calibration equations rather than the precise notation "$\log_{10}$."

(30) (a) Ward, K. M.; Balaban, R. S. Determination of pH Using Water Protons and Chemical Exchange Dependent Saturation Transfer (CEST). *Magn. Reson. Med*. **2000**, *44*, 799–802. (b) Terreno, E.; Castelli, D. D.; Cravotto, G.; Milone, L.; Aime, S. Ln(III)-DOTAMGly Complexes: A Versatile Series to Assess the Determinants of the Efficacy of Paramagnetic

Chemical Exchange Saturation Transfer Agents for Magnetic Resonance Imaging Applications. *Invest. Radiol*. **2004**, *39*, 235–243.

(31) Wood, P. M. The Potential Diagram for Oxygen at pH 7. *Biochem. J*. **1988**, *253*, 287–289.

(32) (a) Raymond, G. G.; Born, J. L. An Updated pKa Listing of Medicinal Compounds. *Drug Intell. Clin. Pharm*. **1986**, *20*, 683–686. (b) Vepsäläinen, J. J. Bisphosphonate Prodrugs. *Curr. Med. Chem*. **2002**, *9*, 1201–1208. (c) Alanne, A.-L.; Hyvönen, H.; Lahtinen, M.; Ylisirniö, M.; Turhanen, P.; Kolehmainen, E.; Peräniemi, S.; Vepsäläinen, J. J. Systematic Study of the Physicochemical Properties of a Homologous Series of Aminobisphosphonates. *Molecules* **2012**, *17*, 10928–10945.

(33) (a) Hu, J.; Zhao, J.; Hou, H.; Fan, Y. Syntheses, Structures and Fluorescence Studies of Two New Cadmium(II) Pyridyl-diphosphonates. *Inorg. Chem. Commun*. **2008**, *11*, 1110–1112. (b) Guo, Z.-F.; Li, B.; Guo, J.-Z.; Yang, P.; Shi, L.-F.; Liu, L. Syntheses, Structures, Thermal Stabilities and Magnetic Properties of Two-Layered Metal Diphosphonates. *Transition Met. Chem*. **2014**, *39*, 353–360.

(34) (a) de Mendoza, J.; Nieto, P. M.; Prados, P.; Sánchez, C. A Stepwise Synthesis of Functionalized Calix[4]arenes and a Calix[6]arene with Alternate Electron-Withdrawing Substituents. *Tetrahedron* **1990**, *46*, 671–682. (b) Mameri, S.; Ako, A. M.; Yesil, F.; Hibert, M.; Lan, Y.; Anson, C. E.; Powell, A. K. Coordination Cluster Analogues of the High-Spin [Mn_{19}] System with Functionalized 2,6-Bis(hydroxymethyl)phenol Ligands. *Eur. J. Inorg. Chem*. **2014**, 4326–4334.

(35) Dau, P. V.; Zhang, Z.; Dau, P. D.; Gibson, J. K.; Rao, L. Thermodynamic Study of the Complexation Between Nd^{3+} and Functionalized Diacetamide Ligands in Solution. *Dalton Trans*. **2016**, *45*, 11968–11975.

(36) McKenna, C. E.; Khawli, L. A.; Ahmad, W.-Y.; Pham, P.; Bongartz, J.-P. Synthesis of α-Halogenated Methanediphosphonates. *Phosphorus, Sulfur, Silicon Relat. Elem*. **1988**, *37*, 1–12.

References for Chapter 4

(1) (a) Tannock, I. F.; Rotin, D. Acid pH in Tumors and Its Potential for Therapeutic Exploitation. *Cancer Res*. **1989**, *49*, 4373–4384. (b) Vaupel, P.; Kallinowski, F.; Okunieff, P. Blood Flow, Oxygen and Nutrient Supply, and Metabolic Microenvironment of Human Tumors: A Review. *Cancer Res*. **1989**, *49*, 6449–6456. (c) Gillies, R. J.; Raghunand, N.; Karczmar, G. S.; Bhujwalla, Z. M. MRI of the Tumor Microenvironment. *J. Magn. Reson. Imaging* **2002**, *16*, 430–450. (d) Gatenby, R. A.; Gillies, R. J. Why do Cancers Have High Aerobic Glycolysis? *Nat. Rev. Cancer* **2004**, *4*, 891–899. (e) Gillies, R. J.; Raghunand, N.; Garcia-Martin, M. L.; Gatenby, R. A. pH Imaging: A Review of pH Measurement Methods and Applications in Cancers. *IEEE Eng. Med. Biol. Mag*. **2004**, *23*, 57–64. (f) Hashim, A. I.; Zhang, X.; Wojtkowiak, J. W.; Martinez, G. V.; Gillies, R. J. Imaging pH and Metastasis. *NMR Biomed*. **2011**, *24*, 582–591. (g) Kato, Y.; Ozawa, S.; Miyamoto, C.; Maehata, Y.; Suzuki, A.; Maeda, T.; Baba, Y. Acidic Extracellular Microenvironment and Cancer. *Cancer Cell Int*. **2013**, *13*, 89–96.

(2) (a) Katsura, K.; Ekholm, A.; Asplund, B.; Siesjö, B. K. Extracellular pH in the Brain During Ischemia: Relationship to the Severity of Lactic Acidosis. *J. Cereb. Blood Flow Metab*. **1991**, *11*, 597–599. (b) Sun, P. Z.; Wang, E.; Cheung, J. S. Imaging Acute Ischemic Tissue Acidosis with pH-Sensitive Endogenous Amide Proton Transfer (APT) MRI–Correction of Tissue Relaxation and Concomitant RF Irradiation Effects Toward Mapping Quantitative Cerebral Tissue pH. *NeuroImage* **2012**, *60*, 1–6. (c) Rajamäki, K.; Nordström, T.; Nurmi, K.; Åkerman, K. E. O.; Kovanen, P. T.; Öörni, K.; Eklund, K. K. Extracellular Acidosis Is a Novel Danger Signal Alerting Innate Immunity via the NLRP3 Inflammasome. *J. Biol. Chem*. **2013**, *288*, 13410–13419.

(3) (a) Lauffer, R. B. Paramagnetic Metal Complexes as Water Proton Relaxation Agents for NMR Imaging: Theory and Design. *Chem. Rev*. **1987**, *87*, 901–927. (b) Caravan, P.; Ellison, J. J.; McMurry, T. J.; Lauffer, R. B. Gadolinium(III) Chelates as MRI Contrast Agents: Structure, Dynamics, and Applications. *Chem. Rev*. **1999**, *99*, 2293–2352. (c) Rieke, V.; Pauly, K. B. MR Thermometry. *J. Magn. Reson. Imaging* **2008**, *27*, 376–390.

(4) (a) Wike-Hooley, J. L.; Haveman, J.; Reinhold, H. S. The Relevance of Tumour pH to the Treatment of Malignant Disease. *Radiother. Oncol*. **1984**, *2*, 343–366. (b) Gerweck, L. E.; Seetharaman, K. Cellular pH Gradient in Tumor Versus Normal Tissue: Potential Exploitation for the Treatment of Cancer. *Cancer Res*. **1996**, *56*, 1194–1198. (c) Wojtkowiak, J. W.; Verduzco, D.; Schramm, K. J.; Gillies, R. J. Drug Resistance and Cellular Adaptation to Tumor Acidic pH Microenvironment. *Mol. Pharm*. **2011**, *8*, 2032–2038. (d) Pilon-Thomas, S.; Kodumudi, K. N.; El-Kenawi, A. E.; Russell, S.; Weber, A. M.; Luddy, K.; Damaghi, M.; Wojtkowiak, J. W.; Mulé, J. J.; Ibrahim-Hashim, A.; Gillies, R. J.

Neutralization of Tumor Acidity Improves Antitumor Responses to Immunotherapy. *Cancer Res*. **2016**, *76*, 1381–1390.

(5) Selected references: (a) Zhang, S.; Winter, P.; Wu, K.; Sherry, A. D. A Novel Europium(III)-Based MRI Contrast Agent. *J. Am. Chem. Soc*. **2001**, *123*, 1517–1518. (b) Zhang, S.; Merritt, M.; Woessner, D. E.; Lenkinski, R. E.; Sherry, A. D. PARACEST Agents: Modulating MRI Contrast via Water Proton Exchange. *Acc. Chem. Res*. **2003**, *36*, 783–790. (c) Zhou, J.; van Zijl, P. C. M. Chemical Exchange Saturation Transfer Imaging and Spectroscopy. *Prog. Nucl. Magn. Reson. Spectrosc*. **2006**, *48*, 109–136. (d) Woods, M.; Woessner, D. E.; Sherry, A. D. Paramagnetic Lanthanide Complexes as PARACEST Agents for Medical Imaging. *Chem. Soc. Rev*. **2006**, *35*, 500–511. (e) Ali, M. M.; Liu, G.; Shah, T.; Flask, C. A.; Pagel, M. D. Using Two Chemical Exchange Saturation Transfer Magnetic Resonance Imaging Contrast Agents for Molecular Imaging Studies. *Acc. Chem. Res*. **2009**, *42*, 915–924. (f) Viswanathan, S.; Kovacs, Z.; Green, K. N.; Ratnakar, S. J.; Sherry, A. D. Alternatives to Gadolinium-Based Metal Chelates for Magnetic Resonance Imaging. *Chem. Rev*. **2010**, *110*, 2960–3018. (g) Soesbe, T. C.; Wu, Y.; Sherry, A. D. Advantages of Paramagnetic CEST Complexes Having Slow-to-Intermediate Water Exchange Properties as Responsive MRI Agents. *NMR Biomed*. **2013**, *26*, 829–838.

(6) Srivastava, K.; Ferrauto, G.; Young, V. G., Jr.; Aime, S.; Pierre, V. C. Eight-Coordinate, Stable Fe(II) Complex as a Dual ^{19}F and CEST Contrast Agent for Ratiometric pH Imaging. *Inorg. Chem*. **2017**, *56*, 12206–12213.

(7) (a) Jeon, I.-R.; Park, J. G.; Haney, C. R.; Harris, T. D. Spin Crossover Iron(II) Complexes as PARACEST MRI Thermometers. *Chem. Sci*. **2014**, *5*, 2461–2465. (b) Du, K.; Harris, T. D. A Cu^{II}_2 Paramagnetic Chemical Exchange Saturation Transfer Contrast Agent Enabled by Magnetic Exchange Coupling. *J. Am. Chem. Soc*. **2016**, *138*, 7804–7807. (c) Du, K.; Waters, E. A.; Harris, T. D. Ratiometric Quantitation of Redox Status with a Molecular Fe_2 Magnetic Resonance Probe. *Chem. Sci*. **2017**, *8*, 4424–4430. (d) Thorarinsdottir, A. E.; Du, K.; Collins, J. H. P.; Harris, T. D. Ratiometric pH Imaging with a Co^{II}_2 MRI Probe via CEST Effects of Opposing pH Dependences. *J. Am. Chem. Soc*. **2017**, *139*, 15836–15847.

(8) (a) Dorazio, S. J.; Tsitovich, P. B.; Siters, K. E.; Spernyak, J. A.; Morrow, J. R. Iron(II) PARACEST MRI Contrast Agents. *J. Am. Chem. Soc*. **2011**, *133*, 14154–14156. (b) Tsitovich, P. B.; Morrow, J. R. Macrocyclic Ligands for Fe(II) ParaCEST and Chemical Shift MRI Contrast Agents. *Inorg. Chim. Acta* **2012**, *393*, 3–11. (c) Olatunde, A. O.; Dorazio, S. J.; Spernyak, J. A.; Morrow, J. R. The NiCEST Approach: Nickel(II) ParaCEST MRI Contrast Agents. *J. Am. Chem. Soc*. **2012**, *134*, 18503–18505. (d) Dorazio, S. J.; Morrow, J. R. Iron(II) Complexes Containing Octadentate Tetraazamacrocycles as ParaCEST Magnetic Resonance Imaging Contrast Agents. *Inorg. Chem*. **2012**, *51*, 7448–7450. (e) Dorazio, S. J.; Olatunde, A. O.; Spernyak, J. A.; Morrow, J. R. CoCEST: Cobalt(II) Amide-Appended

ParaCEST MRI Contrast Agents. *Chem. Commun*. **2013**, *49*, 10025–10027. (f) Tsitovich, P. B.; Spernyak, J. A.; Morrow, J. R. A Redox-Activated MRI Contrast Agent that Switches Between Paramagnetic and Diamagnetic States. *Angew. Chem. Int. Ed*. **2013**, *52*, 13997–14000. (g) Olatunde, A. O.; Cox, J. M.; Daddario, M. D.; Spernyak, J. A.; Benedict, J. B.; Morrow, J. R. Seven-Coordinate Co^{II}, Fe^{II} and Six-Coordinate Ni^{II} Amide-Appended Macrocyclic Complexes as ParaCEST Agents in Biological Media. *Inorg. Chem*. **2014**, *53*, 8311–8321. (h) Dorazio, S. J.; Olatunde, A. O.; Tsitovich, P. B.; Morrow, J. R. Comparison of Divalent Transition Metal Ion ParaCEST MRI Contrast Agents. *J. Biol. Inorg. Chem*. **2014**, *19*, 191–205. (i) Olatunde, A. O.; Bond, C. J.; Dorazio, S. J.; Cox, J. M.; Benedict, J. B.; Daddario, M. D.; Spernyak, J. A.; Morrow, J. R. Six, Seven or Eight Coordinate Fe^{II}, Co^{II} or Ni^{II} Complexes of Amide-Appended Tetraazamacrocycles for ParaCEST Thermometry. *Chem. –Eur. J*. **2015**, *21*, 18290–18300. (j) Tsitovich, P. B.; Cox, J. M.; Spernyak, J. A.; Morrow, J. R. Gear Up for a pH Shift: A Responsive Iron(II) 2-Amino-6-picolyl-Appended Macrocyclic ParaCEST Agent that Protonates at a Pendent Group. *Inorg. Chem*. **2016**, *55*, 12001–12010. (k) Burns, P. J.; Cox, J. M.; Morrow, J. R. Imidazole-Appended Macrocyclic Complexes of Fe(II), Co(II), and Ni(II) as ParaCEST Agents. *Inorg. Chem*. **2017**, *56*, 4545–4554. (l) Abozeid, S. M.; Snyder, E. M.; Tittiris, T. Y.; Steuerwald, C. M.; Nazarenko, A. Y.; Morrow, J. R. Inner-Sphere and Outer-Sphere Water Interactions in Co(II) ParaCEST Agents. *Inorg. Chem*. **2018**, *57*, 2085–2095.

(9) (a) James, T. L. *Nuclear Magnetic Resonance in Biochemistry: Principles and Applications*; Academic Press: New York, 1975. (b) Bertini, I.; Luchinat, C. *NMR of Paramagnetic Molecules in Biological Systems*; The Benjamin/Cummings Publishing Company, Inc.: Menlo Park, 1986. (c) Bertini, I.; Luchinat, C.; Parigi, G. *Solution NMR of Paramagnetic Molecules: Applications to Metallobiomolecules and Models*; Elsevier Science B.V.: Amsterdam, 2001.

(10) Ward, K. M.; Aletras, A. H.; Balaban, R. S. A New Class of Contrast Agents for MRI Based on Proton Chemical Exchange Dependent Saturation Transfer (CEST). *J. Magn. Reson*. **2000**, *143*, 79–87.

(11) Charisiadis, P.; Kontogianni, V. G.; Tsiafoulis, C. G.; Tzakos, A. G.; Siskos, M.; Gerothanassis, I. P. ^{1}H-NMR as a Structural and Analytical Tool of Intra- and Intermolecular Hydrogen Bonds of Phenol-Containing Natural Products and Model Compounds. *Molecules* **2014**, *19*, 13643–13682.

(12) (a) Wolff, S. D.; Balaban, R. S. Magnetization Transfer Contrast (MTC) and Tissue Water Proton Relaxation In Vivo. *Magn. Reson. Med*. **1989**, *10*, 135–144. (b) Zaiss, M.; Bachert, P. Chemical Exchange Saturation Transfer (CEST) and MR Z-Spectroscopy In Vivo: A Review of Theoretical Approaches and Methods. *Phys. Med. Biol*. **2013**, *58*, R221–R269.

(13) (a) Aime, S.; Castelli, D. D.; Terreno, E. Novel pH-Reporter MRI Contrast Agents. *Angew. Chem. Int. Ed*. **2002**, *41*, 4334–4336. (b) Castelli, D. D.; Terreno, E.; Aime, S. Yb^{III}-HPDO3A: A Dual pH- and Temperature-Responsive CEST Agent. *Angew. Chem. Int. Ed*. **2011**, *50*, 1798–1800. (c) Liu, G.; Li, Y.; Sheth, V. R.; Pagel, M. D. Imaging In Vivo Extracellular pH with a Single Paramagnetic Chemical Exchange Saturation Transfer Magnetic Resonance Imaging Contrast Agent. *Mol. Imaging* **2012**, *11*, 47–57. (d) Sheth, V. R.; Liu, G.; Li, Y.; Pagel, M. D. Improved pH Measurements with a Single PARACEST MRI Contrast Agent. *Contrast Media Mol. Imaging* **2012**, *7*, 26–34. (e) Sheth, V. R.; Li, Y.; Chen, L. Q.; Howison, C. M.; Flask, C. A.; Pagel, M. D. Measuring In Vivo Tumor pHe with CEST-FISP MRI. *Magn. Reson. Med*. **2012**, *67*, 760–768. (f) Castelli, D. D.; Ferrauto, G.; Cutrin, J. C.; Terreno, E.; Aime, S. In Vivo Maps of Extracellular pH in Murine Melanoma by CEST–MRI. *Magn. Reson. Med*. **2014**, *71*, 326–332. (g) Rancan, G.; Castelli, D. D.; Aime, S. MRI CEST at 1T with Large μ_{eff} Ln^{3+} Complexes Tm^{3+}-HPDO3A: An Efficient MRI pH Reporter. *Magn. Reson. Med*. **2016**, *75*, 329–336. (h) Krchová, T.; Gálisová, A.; Jirák, D.; Hermann, P.; Kotek, J. Ln(III)-Complexes of a DOTA Analogue with an Ethylenediamine Pendant Arm as pH-Responsive PARACEST Contrast Agents. *Dalton Trans*. **2016**, *45*, 3486–3496.

(14) *APEX2*, version 2014.11–0; Bruker Analytical X-ray Systems, Inc.: Madison, WI, 2014.

(15) Sheldrick, G. M. *SADABS*, version 2.03; Bruker Analytical X-ray Systems, Inc.: Madison, WI, 2000.

(16) (a) Sheldrick, G. M. *SHELXTL*, version 6.12; Bruker Analytical X-ray Systems, Inc.: Madison, WI, 2000. (b) Sheldrick, G. M. *SHELXT* – Integrated Space-Group and Crystal-Structure Determination. *Acta Crystallogr., Sect. A: Found. Adv*. **2015**, *71*, 3–8.

(17) Dolomanov, O. V.; Bourhis, L. J.; Gildea, R. J.; Howard, J. A. K.; Puschmann, H. *OLEX2*: A Complete Structure Solution, Refinement and Analysis Program. *J. Appl. Crystallogr*. **2009**, *42*, 339–341.

(18) *OriginPro*, version 9.0; OriginLab, Corp.: Northampton, MA, 2003.

(19) Dixon, W. T.; Ren, J.; Lubag, A. J. M.; Ratnakar, J.; Vinogradov, E.; Hancu, I.; Lenkinski, R. E.; Sherry, A. D. A Concentration-Independent Method to Measure Exchange Rates in PARACEST Agents. *Magn. Reson. Med*. **2010**, *63*, 625–632.

(20) (a) Evans, D. F. The Determination of the Paramagnetic Susceptibility of Substances in Solution by Nuclear Magnetic Resonance. *J. Chem. Soc*. **1959**, 2003–2005. (b) Schubert, E.

M. Utilizing the Evans Method with a Superconducting NMR Spectrometer in the Undergraduate Laboratory. *J. Chem. Educ*. **1992**, *69*, 62.

(21) Bain, G. A.; Berry, J. F. Diamagnetic Corrections and Pascal's Constants. *J. Chem. Educ*. **2008**, *85*, 532–536.

(22) Sawyer, D. T.; Sobkowiak, A.; Roberts, J. L., Jr. Electrochemistry for Chemists, 2nd ed.; John Wiley & Sons: New York, 1995.

(23) Aime, S.; Barge, A.; Castelli, D. D.; Fedeli, F.; Mortillaro, A.; Nielsen, F. U.; Terreno, E. Paramagnetic Lanthanide(III) Complexes as pH-Sensitive Chemical Exchange Saturation Transfer (CEST) Contrast Agents for MRI Applications. *Magn. Reson. Med*. **2002**, *47*, 639–648.

(24) Daumann, L. J.; Comba, P.; Larrabee, J. A.; Schenk, G.; Stranger, R.; Cavigliasso, G.; Gahan, L. R. Synthesis, Magnetic Properties, and Phosphoesterase Activity of Dinuclear Cobalt(II) Complexes. *Inorg. Chem*. **2013**, *52*, 2029–2043.

(25) Selected references: (a) Sakiyama, H.; Ito, R.; Kumagai, H.; Inoue, K.; Sakamoto, M.; Nishida, Y.; Yamasaki, M. Dinuclear Cobalt(II) Complexes of an Acyclic Phenol-Based Dinucleating Ligand with Four Methoxyethyl Chelating Arms – First Magnetic Analyses in an Axially Distorted Octahedral Field. *Eur. J. Inorg. Chem*. **2001**, 2027–2032. (b) Hossain, M. J.; Yamasaki, M.; Mikuriya, M.; Kuribayashi, A.; Sakiyama, H. Synthesis, Structure, and Magnetic Properties of Dinuclear Cobalt(II) Complexes with a New Phenol-Based Dinucleating Ligand with Four Hydroxyethyl Chelating Arms. *Inorg. Chem*. **2002**, *41*, 4058–4062. (c) Tian, J.-L.; Gu, W.; Yan, S.-P.; Liao, D.-Z.; Jiang, Z.-H. Synthesis, Structures and Magnetic Properties of Two Binuclear Cobalt(II) Complexes Bridged by Bis(*p*-nitrophenyl) Phosphate or Diphenylphosphinate Ion. *Z. Anorg. Allg. Chem*. **2008**, *634*, 1775–1779.

(26) Johansson, F. B.; Bond, A. D.; Nielsen, U. G.; Moubaraki, B.; Murray, K. S.; Berry, K. J.; Larrabee, J. A.; McKenzie, C. J. Dicobalt II–II, II–III, and III–III Complexes as Spectroscopic Models for Dicobalt Enzyme Active Sites. *Inorg. Chem*. **2008**, *47*, 5079–5092.

(27) Seidler-Egdal, R. K.; Johansson, F. B.; Veltzé, S.; Skou, E. M.; Bond, A. D.; McKenzie, C. J. Tunability of the $M^{II}M^{III}/M^{II}_2$ and $M^{III}_2/M^{II}M^{III}$ (M = Mn, Co) Couples in Bis-μ-*O*,*O′*-carboxylato-μ-OR Bridged Complexes. *Dalton Trans*. **2011**, *40*, 3336–3345.

(28) Nazeeruddin, M. K.; Zakeeruddin, S. M.; Kalyanasundaram, K. Enhanced Intensities of the Ligand-to-Metal Charge-Transfer Transitions in Ru(III) and Os(III) Complexes of Substituted Bipyridines. *J. Phys. Chem.* **1993**, *97*, 9607–9612.

(29) (a) Wayland, B. B.; Drago, R. S.; Henneike, H. F. Amide Contact Shift Studies and the Assignment of the Methyl Peaks in N,N-Dimethylamides. *J. Am. Chem. Soc.* **1966**, *88*, 2455–2458. (b) Stewart, W. E.; Siddall, T. H. Nuclear Magnetic Resonance Studies of Amides. *Chem. Rev.* **1970**, *70*, 517–551. (c) Ming, L.-J.; Lauffer, R. B.; Que, Jr., L. Proton Nuclear Magnetic Resonance Studies of Iron(II/III)–Amide Complexes. Spectroscopic Models for Non-Heme Iron Proteins. *Inorg. Chem.* **1990**, *29*, 3060–3064.

(30) (a) Raymond, G. G.; Born, J. L. An Updated pKa Listing of Medicinal Compounds. *Drug Intell. Clin. Pharm.* **1986**, 20, 683–686. (b) Vepsäläinen, J. J. Bisphosphonate Prodrugs. *Curr. Med. Chem.* **2002**, *9*, 1201–1208. (c) Alanne, A.-L.; Hyvönen, H.; Lahtinen, M.; Ylisirniö, M.; Turhanen, P.; Kolehmainen, E.; Peräniemi, S.; Vepsäläinen, J. J. Systematic Study of the Physicochemical Properties of a Homologous Series of Aminobisphosphonates. *Molecules* **2012**, *17*, 10928–10945.

(31) (a) Hu, J.; Zhao, J.; Hou, H.; Fan, Y. Syntheses, Structures and Fluorescence Studies of Two New Cadmium(II) Pyridyl-Diphosphonates. *Inorg. Chem. Commun.* **2008**, *11*, 1110–1112. (b) Guo, Z.-F.; Li, B.; Guo, J.-Z.; Yang, P.; Shi, L.-F.; Liu, L. Syntheses, Structures, Thermal Stabilities and Magnetic Properties of Two-Layered Metal Diphosphonates. *Transition Met. Chem.* **2014**, *39*, 353–360.

(32) Huang, C.-H.; Morrow, J. R. Cerium(III), Europium(III), and Ytterbium(III) Complexes with Alcohol Donor Groups as Chemical Exchange Saturation Transfer Agents for MRI. *Inorg. Chem.* **2009**, *48*, 7237–7243.

(33) Note that the common logarithm with base 10 was used throughout this study. For brevity, the notation "log" is employed in the pH calibration equations and in the insets of Figure 4.6 rather than the precise notation "$\log_{10}$."

(34) Wood, P. M. The Potential Diagram For Oxygen at pH 7. *Biochem. J.* **1988**, *253*, 287–289.

(35) (a) de Mendoza, J.; Nieto, P. M.; Prados, P.; Sánchez, C. A Stepwise Synthesis of Functionalized Calix[4]arenes and a Calix[6]arene with Alternate Electron-Withdrawing Substituents. *Tetrahedron* **1990**, *46*, 671–682. (b) Mameri, S.; Ako, A. M.; Yesil, F.; Hibert, M.; Lan, Y.; Anson, C. E.; Powell, A. K. Coordination Cluster Analogues of the High-Spin [Mn_{19}] System with Functionalized 2,6-Bis(hydroxymethyl)phenol Ligands. *Eur. J. Inorg. Chem.* **2014**, 4326–4334.

(36) Trost, B. M.; Yeh, V. S. C.; Ito, H.; Bremeyer, N. Effect of Ligand Structure on the Zinc-Catalyzed Henry Reaction. Asymmetric Syntheses of (−)-Denopamine and (−)-Arbutamine. *Org. Lett*. **2002**, *4*, 2621–2623.

(37) Yu, M.; Xie, D.; Phan, K. P.; Enriquez, J. S.; Luci, J. J.; Que, E. L. A Co^{II} Complex for ^{19}F MRI-Based Detection of Reactive Oxygen Species. *Chem. Commun*. **2016**, *52*, 13885–13888.

(38) Dau, P. V.; Zhang, Z.; Dau, P. D.; Gibson, J. K.; Rao, L. Thermodynamic Study of the Complexation Between Nd^{3+} and Functionalized Diacetamide Ligands in Solution. *Dalton Trans*. **2016**, *45*, 11968–11975.

References for Chapter 5

(1) (a) Hingorani, D. V.; Bernstein, A. S.; Pagel, M. D. A Review of Responsive MRI Contrast Agents: 2005–2014. *Contrast Media Mol. Imaging* **2015**, *10*, 245–265. (b) Angelovski, G. What We Can Really Do with Bioresponsive MRI Contrast Agents. *Angew. Chem. Int. Ed*. **2016**, *55*, 7038–7046. (c) Sinharay, S.; Pagel, M. D. Advances in Magnetic Resonance Imaging Contrast Agents for Biomarker Detection. *Annu. Rev. Anal. Chem*. **2016**, *9*, 95–115.

(2) (a) Caravan, P.; Ellison, J. J.; McMurry, T. J.; Lauffer, R. B. Gadolinium(III) Chelates as MRI Contrast Agents: Structure, Dynamics, and Applications. *Chem. Rev*. **1999**, *99*, 2293–2352. (b) Rieke, V.; Pauly, K. B. MR Thermometry. *J. Magn. Reson. Imaging* **2008**, *27*, 376–390.

(3) Weissleder, R.; Ross, B. D.; Rehemtulla, A.; Gambhir, S. S. *Molecular Imaging: Principles and Practice*; People's Medical Publishing House: Shelton, 2010.

(4) (a) Zhang, S.; Malloy, C. R.; Sherry, A. D. MRI Thermometry Based on PARACEST Agents. *J. Am. Chem. Soc*. **2005**, *127*, 17572–17573. (b) Settecase, F.; Sussman, M. S.; Roberts, T. P. L. A New Temperature-Sensitive Contrast Mechanism for MRI: Curie Temperature Transition-Based Imaging. *Contrast Media Mol. Imaging* **2007**, *2*, 50–54. (c) Jeon, I.-R.; Park, J. G.; Haney, C. R.; Harris, T. D. Spin Crossover Iron(II) Complexes as PARACEST MRI Thermometers. *Chem. Sci*. **2014**, *5*, 2461–2465. (d) Tsitovich, P. B.; Cox, J. M.; Benedict, J. B.; Morrow, J. R. Six-Coordinate Iron(II) and Cobalt(II) ParaSHIFT Agents for Measuring Temperature by Magnetic Resonance Spectroscopy. *Inorg. Chem*. **2016**, *55*, 700–716. (e) Thorarinsdottir, A. E.; Gaudette, A. I.; Harris, T. D. Spin-Crossover and High-Spin Iron(II) Complexes as Chemical Shift ^{19}F Magnetic Resonance Thermometers. *Chem. Sci*. **2017**, *8*, 2448–2456.

(5) (a) Aime, S.; Castelli, D. D.; Terreno, E. Novel pH-Reporter MRI Contrast Agents. *Angew. Chem. Int. Ed*. **2002**, *41*, 4334–4336. (b) Wu, Y.; Soesbe, T. C.; Kiefer, G. E.; Zhao, P.; Sherry, A. D. A Responsive Europium(III) Chelate that Provides a Direct Readout of pH by MRI. *J. Am. Chem. Soc*. **2010**, *132*, 14002–14003. (c) Huang, Y.; Coman, D.; Herman, P.; Rao, J. U.; Maritim, S.; Hyder, F. Towards Longitudinal Mapping of Extracellular pH in Gliomas. *NMR Biomed*. **2016**, *29*, 1364–1372. (d) Finney, K.-L. N. A.; Harnden, A. C.; Rogers, N. J.; Senanayake, P. K.; Blamire, A. M.; O'Hogain, D.; Parker, D. Simultaneous Triple Imaging with Two PARASHIFT Probes: Encoding Anatomical, pH and Temperature Information Using Magnetic Resonance Shift Imaging. *Chem. –Eur. J*. **2017**, *23*, 7976–7989. (e) Gaudette, A. I.; Thorarinsdottir, A. E.; Harris, T. D. pH-Dependent Spin State Population and ^{19}F NMR Chemical Shift via Remote Ligand Protonation in an Iron(II) Complex. *Chem. Commun*. **2017**, *53*, 12962–12965. (f) Thorarinsdottir, A. E.; Du, K.; Collins, J. H. P.; Harris, T. D. Ratiometric pH Imaging with a Co^{II}_2 MRI Probe via CEST

Effects of Opposing pH Dependences. *J. Am. Chem. Soc*. **2017**, *139*, 15836–15847. (g) Thorarinsdottir, A. E.; Tatro, S. M.; Harris, T. D. Electronic Effects of Ligand Substitution in a Family of Co^{II}_2 PARACEST pH Probes. *Inorg. Chem*. **2018**, *57*, 11252–11263.

(6) (a) Ratnakar, S. J.; Viswanathan, S.; Kovacs, Z.; Jindal, A. K.; Green, K. N.; Sherry, A. D. Europium(III) DOTA-tetraamide Complexes as Redox-Active MRI Sensors. *J. Am. Chem. Soc*. **2012**, *134*, 5798–5800. (b) Loving, G. S.; Mukherjee, S.; Caravan, P. Redox-Activated Manganese-Based MR Contrast Agent. *J. Am. Chem. Soc*. **2013**, *135*, 4620–4623. (c) Tsitovich, P. B.; Spernyak, J. A.; Morrow, J. R. A Redox-Activated MRI Contrast Agent that Switches Between Paramagnetic and Diamagnetic States. *Angew. Chem. Int. Ed*. **2013**, *52*, 13997–14000. (d) Du, K.; Waters, E. A.; Harris, T. D. Ratiometric Quantitation of Redox Status with a Molecular Fe_2 Magnetic Resonance Probe. *Chem. Sci*. **2017**, *8*, 4424–4430.

(7) (a) Moats, R. A.; Fraser, S. E.; Meade, T. J. A "Smart" Magnetic Resonance Imaging Agent that Reports on Specific Enzymatic Activity. *Angew. Chem. Int. Ed*. **1997**, *36*, 726–728. (b) Mizukami, S.; Takikawa, R.; Sugihara, F.; Hori, Y.; Tochio, H.; Wälchli, M.; Shirakawa, M.; Kikuchi, K. Paramagnetic Relaxation-Based ^{19}F MRI Probe To Detect Protease Activity. *J. Am. Chem. Soc*. **2008**, *130*, 794–795. (c) Chauvin, T.; Durand, P.; Bernier, M.; Meudal, H.; Doan, B.-T.; Noury, F.; Badet, B.; Beloeil, J.-C.; Tóth, É. Detection of Enzymatic Activity by PARACEST MRI: A General Approach to Target a Large Variety of Enzymes. *Angew. Chem. Int. Ed*. **2008**, *47*, 4370–4372.

(8) (a) Que, E. L.; Chang, C. J. A Smart Magnetic Resonance Contrast Agent for Selective Copper Sensing. *J. Am. Chem. Soc*. **2006**, *128*, 15942–15943. (b) Major, J. L.; Parigi, G.; Luchinat, C.; Meade, T. J. The Synthesis and In Vitro Testing of a Zinc-Activated MRI Contrast Agent. *Proc. Natl. Acad. Sci. U. S. A*. **2007**, *104*, 13881–13886. (c) Bar-Shir, A.; Gilad, A. A.; Chan, K. W. Y.; Liu, G.; van Zijl, P. C. M.; Bulte, J. W. M.; McMahon, M. T. Metal Ion Sensing Using Ion Chemical Exchange Saturation Transfer ^{19}F Magnetic Resonance Imaging. *J. Am. Chem. Soc*. **2013**, *135*, 12164–12167.

(9) (a) Aime, S.; Castelli, D. D.; Fedeli, F.; Terreno, E. A Paramagnetic MRI-CEST Agent Responsive to Lactate Concentration. *J. Am. Chem. Soc*. **2002**, *124*, 9364–9365. (b) Shapiro, M. G.; Westmeyer, G. G.; Romero, P. A.; Szablowski, J. O.; Küster, B.; Shah, A.; Otey, C. R.; Langer, R.; Arnold, F. H.; Jasanoff, A. Directed Evolution of a Magnetic Resonance Imaging Contrast Agent for Noninvasive Imaging of Dopamine. *Nat. Biotechnol*. **2010**, *28*, 264–270.

(10) (a) Tannock, I. F.; Rotin, D. Acid pH in Tumors and Its Potential for Therapeutic Exploitation. *Cancer Res*. **1989**, *49*, 4373–4384. (b) Kato, Y.; Ozawa, S.; Miyamoto, C.; Maehata, Y.; Suzuki, A.; Maeda, T.; Baba, Y. Acidic Extracellular Microenvironment and Cancer. *Cancer Cell Int*. **2013**, *13*, 89–96. (c) Rajamäki, K.; Nordström, T.; Nurmi, K.;

Åkerman, K. E. O.; Kovanen, P. T.; Öörni, K.; Eklund, K. K. Extracellular Acidosis Is a Novel Danger Signal Alerting Innate Immunity via the NLRP3 Inflammasome. *J. Biol. Chem*. **2013**, *288*, 13410–13419.

(11) (a) James, T. L. *Nuclear Magnetic Resonance in Biochemistry: Principles and Applications*; Academic Press: New York, 1975. (b) Bertini, I.; Luchinat, C. *NMR of Paramagnetic Molecules in Biological Systems*; The Benjamin/Cummings Publishing Company, Inc.: Menlo Park, 1986.

(12) Ward, K. M.; Aletras, A. H.; Balaban, R. S. A New Class of Contrast Agents for MRI Based on Proton Chemical Exchange Dependent Saturation Transfer (CEST). *J. Magn. Reson*. **2000**, *143*, 79–87.

(13) (a) Dorazio, S. J.; Tsitovich, P. B.; Siters, K. E.; Spernyak, J. A.; Morrow, J. R. Iron(II) PARACEST MRI Contrast Agents. *J. Am. Chem. Soc*. **2011**, *133*, 14154–14156. (b) Dorazio, S. J.; Olatunde, A. O.; Spernyak, J. A.; Morrow, J. R. CoCEST: Cobalt(II) Amide-Appended ParaCEST MRI Contrast Agents. *Chem. Commun*. **2013**, *49*, 10025–10027.

(14) (a) Wolff, S. D.; Balaban, R. S. Magnetization Transfer Contrast (MTC) and Tissue Water Proton Relaxation In Vivo. *Magn. Reson. Med*. **1989**, *10*, 135–144. (b) Zaiss, M.; Bachert, P. Chemical Exchange Saturation Transfer (CEST) and MR Z-Spectroscopy In Vivo: A Review of Theoretical Approaches and Methods. *Phys. Med. Biol*. **2013**, *58*, R221–R269.

(15) *OriginPro*, version 9.0; OriginLab, Corp.: Northampton, MA, 2003.

(16) Dixon, W. T.; Ren, J.; Lubag, A. J. M.; Ratnakar, J.; Vinogradov, E.; Hancu, I.; Lenkinski, R. E.; Sherry, A. D. A Concentration-Independent Method to Measure Exchange Rates in PARACEST Agents. *Magn. Reson. Med*. **2010**, *63*, 625–632.

(17) (a) Evans, D. F. The Determination of the Paramagnetic Susceptibility of Substances in Solution by Nuclear Magnetic Resonance. *J. Chem. Soc*. **1959**, 2003−2005. (b) Schubert, E. M. Utilizing the Evans Method with a Superconducting NMR Spectrometer in the Undergraduate Laboratory. *J. Chem. Educ*. **1992**, *69*, 62.

(18) Bain, G. A.; Berry, J. F. Diamagnetic Corrections and Pascal's Constants. *J. Chem. Educ*. **2008**, *85*, 532−536.

(19) Sawyer, D. T.; Sobkowiak, A.; Roberts, J. L., Jr. *Electrochemistry for Chemists, 2nd ed*.; John Wiley & Sons: New York, 1995.

(20) (a) Liu, G.; Li, Y.; Pagel, M. D. Design and Characterization of a New Irreversible Responsive PARACEST MRI Contrast Agent that Detects Nitric Oxide. *Magn. Reson. Med.* **2007**, *58*, 1249–1256. (b) Liu, G.; Li, Y.; Sheth, V. R.; Pagel, M. D. Imaging In Vivo Extracellular pH with a Single Paramagnetic Chemical Exchange Saturation Transfer Magnetic Resonance Imaging Contrast Agent. *Mol. Imaging* **2012**, *11*, 47–57. (c) Sheth, V. R.; Liu, G.; Li, Y.; Pagel, M. D. Improved pH Measurements with a Single PARACEST MRI Contrast Agent. *Contrast Media Mol. Imaging* **2012**, *7*, 26–34. (d) Sheth, V. R.; Li, Y.; Chen, L. Q.; Howison, C. M.; Flask, C. A.; Pagel, M. D. Measuring In Vivo Tumor pHe with CEST-FISP MRI. *Magn. Reson. Med*. **2012**, *67*, 760–768.

(21) (a) Johansson, F. B.; Bond, A. D.; Nielsen, U. G.; Moubaraki, B.; Murray, K. S.; Berry, K. J.; Larrabee, J. A.; McKenzie, C. J. Dicobalt II−II, II−III, and III−III Complexes as Spectroscopic Models for Dicobalt Enzyme Active Sites. *Inorg. Chem*. **2008**, *47*, 5079–5092. (b) Tian, J.-L.; Gu, W.; Yan, S.-P.; Liao, D.-Z.; Jiang, Z.-H. Synthesis, Structures and Magnetic Properties of Two Binuclear Cobalt(II) Complexes Bridged by Bis(p-nitrophenyl) Phosphate or Diphenylphosphinate Ion. *Z. Anorg. Allg. Chem*. **2008**, *634*, 1775–1779.

(22) (a) Margiotta, N.; Ostuni, R.; Gandin, V.; Marzano, C.; Piccinonna, S.; Natile, G. Synthesis, Characterization, and Cytotoxicity of Dinuclear Platinum-Bisphosphonate Complexes to Be Used as Prodrugs in the Local Treatment of Bone Tumours. *Dalton Trans*. **2009**, 10904–10913. (b) Demoro, B.; Caruso, F.; Rossi, M.; Benítez, D.; González, M.; Cerecetto, H.; Galizzi, M.; Malayil, L.; Docampo, R.; Faccio, R.; Mombrú, Á. W.; Gambino, D.; Otero, L. Bisphosphonate Metal Complexes as Selective Inhibitors of Trypanosoma Cruzi Farnesyl Diphosphate Synthase. *Dalton Trans*. **2012**, *41*, 6468–6476.

(23) (a) Sakiyama, H.; Ito, R.; Kumagai, H.; Inoue, K.; Sakamoto, M.; Nishida, Y.; Yamasaki, M. Dinuclear Cobalt(II) Complexes of an Acyclic Phenol-Based Dinucleating Ligand with Four Methoxyethyl Chelating Arms − First Magnetic Analyses in an Axially Distorted Octahedral Field. *Eur. J. Inorg. Chem*. **2001**, 2027–2032. (b) Hossain, M. J.; Yamasaki, M.; Mikuriya, M.; Kuribayashi, A.; Sakiyama, H. Synthesis, Structure, and Magnetic Properties of Dinuclear Cobalt(II) Complexes with a New Phenol-Based Dinucleating Ligand with Four Hydroxyethyl Chelating Arms. *Inorg. Chem*. **2002**, *41*, 4058–4062.

(24) Longo, D. L.; Sun, P. Z.; Consolino, L.; Michelotti, F. C.; Uggeri, F.; Aime, S. A General MRI-CEST Ratiometric Approach for pH Imaging: Demonstration of In Vivo pH Mapping with Iobitridol. *J. Am. Chem. Soc*. **2014**, *136*, 14333–14336.

(25) Wood, P. M. The Potential Diagram for Oxygen at pH 7. *Biochem. J*. **1988**, *253*, 287–289.

(26) Egorov, M.; Aoun, S.; Padrines, M.; Redini, F.; Heymann, D.; Lebreton, J.; Mathé-Allainmat, M. A One-Pot Synthesis of 1-Hydroxy-1,1-bis(phosphonic acid)s Starting from the Corresponding Carboxylic Acids. *Eur. J. Org. Chem*. **2011**, 7148–7154.

References for Chapter 6

(1) (a) Coleman, R. E. Metastatic Bone Disease: Clinical Features, Pathophysiology and Treatment Strategies. *Cancer Treat. Rev.* **2001**, *27*, 165–176. (b) Mundy, G. R. Metastasis to Bone: Causes, Consequences and Therapeutic Opportunities. *Nat. Rev. Cancer* **2002**, *2*, 584–593. (c) Kyle, R. A.; Rajkumar, S. V. Multiple Myeloma. *N. Engl. J. Med.* **2004**, *351*, 1860–1873.

(2) (a) Fraser, W. D. Hyperparathyroidism. *Lancet* **2009**, *374*, 145–158. (b) Blaine, J.; Chonchol, M.; Levi, M. Renal Control of Calcium, Phosphate, and Magnesium Homeostasis. *Clin. J. Am. Soc. Nephrol.* **2015**, *10*, 1257–1272.

(3) (a) Ralston, S. H. Paget's Disease of Bone. *N. Engl. J. Med.* **2013**, *368*, 644–650. (b) Tuck, S. P.; Layfield, R.; Walker, J.; Mekkayil, B.; Francis, R. Adult Paget's Disease of Bone: A Review. *Rheumatology* **2017**, *56*, 2050–2059.

(4) Minisola, S.; Pepe, J.; Piemonte, S.; Cipriani, C. The Diagnosis and Management of Hypercalcaemia. *BMJ* **2015**, *350*, h2723.

(5) Ziegler, R. Hypercalcemic Crisis. *J. Am. Soc. Nephrol.* **2001**, *12*, S3–S9.

(6) (a) Lauffer, R. B. Paramagnetic Metal Complexes as Water Proton Relaxation Agents for NMR Imaging: Theory and Design. *Chem. Rev.* **1987**, *87*, 901–927. (b) Caravan, P.; Ellison, J. J.; McMurry, T. J.; Lauffer, R. B. Gadolinium(III) Chelates as MRI Contrast Agents: Structure, Dynamics, and Applications. *Chem. Rev.* **1999**, *99*, 2293–2352. (c) Caravan, P. Strategies for Increasing the Sensitivity of Gadolinium Based MRI Contrast Agents. *Chem. Soc. Rev.* **2006**, *35*, 512–523.

(7) (a) Li, W.; Fraser, S. E.; Meade, T. J. A Calcium-Sensitive Magnetic Resonance Imaging Contrast Agent. *J. Am. Chem. Soc.* **1999**, *121*, 1413–1414. (b) Li, W.; Parigi, G.; Fragai, M.; Luchinat, C.; Meade, T. J. Mechanistic Studies of a Calcium-Dependent MRI Contrast Agent. *Inorg. Chem.* **2002**, *41*, 4018–4024. (c) Atanasijevic, T.; Shusteff, M.; Fam, P.; Jasanoff, A. Calcium-Sensitive MRI Contrast Agents Based on Superparamagnetic Iron Oxide Nanoparticles and Calmodulin. *Proc. Natl. Acad. Sci. U. S. A.* **2006**, *103*, 14707–14712. (d) Mishra, A.; Fousková, P.; Angelovski, G.; Balogh, E.; Mishra, A. K.; Logothetis, N. K.; Tóth, É. Facile Synthesis and Relaxation Properties of Novel Bispolyazamacrocyclic Gd^{3+} Complexes: An Attempt towards Calcium-Sensitive MRI Contrast Agents. *Inorg. Chem.* **2008**, *47*, 1370–1381. (e) Dhingra, K.; Maier, M. E.; Beyerlein, M.; Angelovski, G.; Logothetis, N. K. Synthesis and Characterization of a Smart Contrast Agent Sensitive to Calcium. *Chem. Commun.* **2008**, *0*, 3444–3446. (f) Angelovski, G.; Fousková, P.; Mamedov, I.; Canals, S.; Tóth, É.; Logothetis, N. K. Smart Magnetic Resonance Imaging Agents that Sense Extracellular Calcium Fluctuations. *ChemBioChem* **2008**, *9*, 1729–1734. (g) Que, E.

L.; Chang, C. J. Responsive Magnetic Resonance Imaging Contrast Agents as Chemical Sensors for Metals in Biology and Medicine. *Chem. Soc. Rev.* **2010**, *39*, 51–60. (h) Mamedov, I.; Canals, S.; Henig, J.; Beyerlein, M.; Murayama, Y.; Mayer, H. A.; Logothetis, N. K.; Angelovski, G. In Vivo Characterization of a Smart MRI Agent That Displays an Inverse Response to Calcium Concentration. *ACS Chem. Neurosci.* **2010**, *1*, 819–828. (i) Heffern, M. C.; Matosziuk, L. M.; Meade, T. J. Lanthanide Probes for Bioresponsive Imaging. *Chem. Rev.* **2014**, *114*, 4496–4539. (j) Kadjane, P.; Platas-Iglesias, C.; Boehm-Sturm, P.; Truffault, V.; Hagberg, G. E.; Hoehn, M.; Logothetis, N. K.; Angelovski, G. Dual-Frequency Calcium-Responsive MRI Agents. *Chem. –Eur. J.* **2014**, *20*, 7351–7362. (k) MacRenaris, K. W.; Ma, Z.; Krueger, R. L.; Carney, C. E.; Meade, T. J. Cell-Permeable Esterase-Activated Ca(II)-Sensitive MRI Contrast Agent. *Bioconjugate Chem.* **2016**, *27*, 465–473.

(8) Selected references: (a) Zhang, S.; Michaudet, L.; Burgess, S.; Sherry, A. D. The Amide Protons of an Ytterbium(III) Dota Tetraamide Complex Act as Efficient Antennae for Transfer of Magnetization to Bulk Water. *Angew. Chem. Int. Ed.* **2002**, *41*, 1919–1921. (b) Aime, S.; Delli Castelli, D.; Terreno, E. Novel pH-Reporter MRI Contrast Agents. *Angew. Chem. Int. Ed.* **2002**, *41*, 4334–4336. (c) Terreno, E.; Delli Castelli, D.; Cravotto, G.; Milone, L.; Aime, S. Ln(III)-DOTAMGly Complexes: A Versatile Series to Access the Determinants of the Efficacy of Paramagnetic Chemical Exchange Saturation Transfer Agents for Magnetic Resonance Imaging Applications. *Invest. Radiol*. **2004**, *39*, 235–243. (d) Woods, M.; Woessner, D. E.; Zhao, P.; Pasha, A.; Yang, M.-Y.; Huang, C.-H.; Vasalitiy, O.; Morrow, J. R.; Sherry, A. D. Europium(III) Macrocyclic Complexes with Alcohol Pendant Groups as Chemical Exchange Saturation Transfer Agents. *J. Am. Chem. Soc.* **2006**, *128*, 10155–10162. (e) Angelovski, G.; Chauvin, T.; Pohmann, R.; Logothetis, N. K.; Tóth, É. Calcium-Responsive Paramagnetic CEST Agents. *Bioorg. Med. Chem.* **2011**, *19*, 1097–1105.

(9) Selected references: (a) Dorazio, S. J.; Tsitovich, P. B.; Siters, K. E.; Spernyak, J. A.; Morrow, J. R. Iron(II) PARACEST MRI Contrast Agents. *J. Am. Chem. Soc.* **2011**, *133*, 14154–14156. (b) Tsitovich, P. B.; Morrow, J. R. Macrocyclic Ligands for Fe(II) ParaCEST and Chemical Shift MRI Contrast Agents. *Inorg. Chim. Acta* **2012**, *393*, 3–11. (c) Olatunde, A. O.; Dorazio, S. J.; Spernyak, J. A.; Morrow, J. R. The NiCEST Approach: Nickel(II) ParaCEST MRI Contrast Agents. *J. Am. Chem. Soc.* **2012**, *134*, 18503–18505. (d) Dorazio, S. J.; Morrow, J. R. Iron(II) Complexes Containing Octadentate Tetraazamacrocycles as ParaCEST Magnetic Resonance Imaging Contrast Agents. *Inorg. Chem.* **2012**, *51*, 7448–7450. (e) Dorazio, S. J.; Olatunde, A. O.; Spernyak, J. A.; Morrow, J. R. CoCEST: Cobalt(II) Amide-Appended ParaCEST MRI Contrast Agents. *Chem. Commun.* **2013**, *49*, 10025–10027. (f) Du, K.; Harris, T. D. A Cu^{II}_2 Paramagnetic Chemical Exchange Saturation

Transfer Contrast Agent Enabled by Magnetic Exchange Coupling. *J. Am. Chem. Soc.* **2016**, *138*, 7804–7807.

(10) (a) Tsitovich, P. B.; Spernyak, J. A.; Morrow, J. R. A Redox-Activated MRI Contrast Agent That Switches Between Paramagnetic and Diamagnetic States. *Angew. Chem. Int. Ed.* **2013**, *52*, 13997–14000. (b) Tsitovich, P. B.; Burns, P. J.; McKay, A. M.; Morrow, J. R. Redox-Activated MRI Contrast Agents Based on Lanthanide and Transition Metal Ions. *J. Inorg. Biochem.* **2014**, *133*, 143–154. (c) Du, K.; Waters, E. A.; Harris, T. D. Ratiometric Quantitation of Redox Status with a Molecular Fe_2 Magnetic Resonance Probe. *Chem. Sci.* **2017**, *8*, 4424–4430.

(11) (a) Liu, G.; Li, Y.; Sheth, V. R.; Pagel, M. D. Imaging in Vivo Extracellular pH with a Single Paramagnetic Chemical Exchange Saturation Transfer Magnetic Resonance Imaging Contrast Agent. *Mol. Imaging* **2012**, *11*, 47–57. (b) Sheth, V. R.; Li, Y.; Chen, L. Q.; Howison, C. M.; Flask, C. A.; Pagel, M. D. Measuring in Vivo Tumor pHe with CEST-FISP MRI. *Magn. Reson. Med.* **2012**, *67*, 760–768. (c) McVicar, N.; Li, A. X.; Suchý, M.; Hudson, R. H. E.; Menon, R. S.; Bartha, R. Simultaneous in Vivo pH and Temperature Mapping Using a PARACEST-MRI Contrast Agent. *Magn. Reson. Med.* **2013**, *70*, 1016–1025. (d) Delli Castelli, D.; Ferrauto, G.; Cutrin, J. C.; Terreno, E.; Aime, S. In Vivo Maps of Extracellular pH in Murine Melanoma by CEST-MRI. *Magn. Reson. Med.* **2014**, *71*, 326–332. (e) Rancan, G.; Delli Castelli, D.; Aime, S. MRI CEST at 1T with Large μ_{eff} Ln^{3+} Complexes Tm^{3+}-HPDO3A: An Efficient MRI pH Reporter. *Magn. Reson. Med.* **2016**, *75*, 329–336. (f) Wu, Y.; Zhang, S.; Soesbe, T. C.; Yu, J.; Vinogradov, E.; Lenkinski, R. E.; Sherry, A. D. pH Imaging of Mouse Kidneys in Vivo Using a Frequency-Dependent ParaCEST Agent. *Magn. Reson. Med.* **2016**, *75*, 2432–2441. (g) Tsitovich, P. B.; Cox, J. M.; Spernyak, J. A.; Morrow, J. R. Gear Up for a pH Shift: A Responsive Iron(II) 2-Amino-6-Picolyl-Appended Macrocyclic ParaCEST Agent That Protonates at a Pendent Group. *Inorg. Chem.* **2016**, *55*, 12001–12010. (h) Thorarinsdottir, A. E.; Du, K.; Collins, J. H. P.; Harris, T. D. Ratiometric pH Imaging with a Co^{II}_2 MRI Probe via CEST Effects of Opposing pH Dependences. *J. Am. Chem. Soc.* **2017**, *139*, 15836–15847. (i) Srivastava, K.; Ferrauto, G.; Young, V. G.; Aime, S.; Pierre, V. C. Eight-Coordinate, Stable Fe(II) Complex as a Dual ^{19}F and CEST Contrast Agent for Ratiometric pH Imaging. *Inorg. Chem.* **2017**, *56*, 12206–12213. (j) Thorarinsdottir, A. E.; Tatro, S. M.; Harris, T. D. Electronic Effects of Ligand Substitution in a Family of Co^{II}_2 PARACEST pH Probes. *Inorg. Chem.* **2018**, *57*, 11252–11263. (k) Thorarinsdottir, A. E.; Harris, T. D. Dramatic Enhancement in pH Sensitivity and Signal Intensity Through Ligand Modification of a Dicobalt PARACEST Probe. *Chem. Commun.* **2019**, *55*, 794–797.

(12) (a) Zhang, S.; Malloy, C. R.; Sherry, A. D. MRI Thermometry Based on PARACEST Agents. *J. Am. Chem. Soc.* **2005**, *127*, 17572–17573. (b) Li, A. X.; Wojciechowski, F.; Suchý, M.; Jones, C. K.; Hudson, R. H. E.; Menon, R. S.; Bartha, R. A Sensitive PARACEST

Contrast Agent for Temperature MRI: Eu^{3+}-DOTAM-Glycine(Gly)-Phenylalanine(Phe). *Magn. Reson. Med.* **2008**, *59*, 374–381. (c) Delli Castelli, D.; Terreno, E.; Aime, S. Yb(III)-HPDO3A: A Dual pH- and Temperature-Responsive CEST Agent. *Angew. Chem. Int. Ed.* **2011**, *50*, 1798–1800. (d) Jeon, I.-R.; Park, J. G.; Haney, C. R.; Harris, T. D. Spin Crossover Iron(II) Complexes as PARACEST MRI Thermometers. *Chem. Sci*. **2014**, *5*, 2461–2465.

(13) (a) Trokowski, R.; Ren, J.; Kálmán, F. K.; Sherry, A. D. Selective Sensing of Zinc Ions with a PARACEST Contrast Agent. *Angew. Chem. Int. Ed.* **2005**, *44*, 6920–6923. (b) Srivastava, K.; Ferrauto, G.; Harris, S. M.; Longo, D. L.; Botta, M.; Aime, S.; Pierre, V. C. Complete On/Off Responsive ParaCEST MRI Contrast Agents for Copper and Zinc. *Dalton Trans.* **2018**, *47*, 11346–11357.

(14) (a) Wan, Q. J.; Kubáň, P.; Tanyanyiwa, J.; Rainelli, A.; Hauser, P. C. Determination of Major Inorganic Ions in Blood Serum and Urine by Capillary Electrophoresis with Contactless Conductivity Detection. *Anal. Chim. Acta* **2004**, *525*, 11–16. (b) Le, T.; Bhushan, V.; Sochat, M.; Kallianos, K.; Chavda, Y.; Zureick, A. H.; Kalani, M. *First Aid for the USMLE Step 1: 2018 a Student-to-Student Guide*, 28th ed.; McGraw-Hill Education: New York, 2017.

(15) Bar-Shir, A.; Gilad, A. A.; Chan, K. W. Y.; Liu, G.; van Zijl, P. C. M.; Bulte, J. W. M.; McMahon, M. T. Metal Ion Sensing Using Ion Chemical Exchange Saturation Transfer ^{19}F Magnetic Resonance Imaging. *J. Am. Chem. Soc.* **2013**, *135*, 12164–12167.

(16) (a) van Staveren, C. J.; van Eerden, J.; van Veggel, F. C. J. M.; Harkema, S.; Reinhoudt, D. N. Cocomplexation of Neutral Guests and Electrophilic Metal Cations in Synthetic Macrocyclic Hosts. *J. Am. Chem. Soc.* **1988**, *110*, 4994–5008. (b) Caneschi, A.; Sorace, L.; Casellato, U.; Tomasin, P.; Vigato, P. A. d- or f-Mononuclear and Related Heterodinuclear Complexes with [1+1] Asymmetric Compartmental Macrocycles. *Eur. J. Inorg. Chem.* **2004**, 3887–3900. (c) Pierre, V. C.; Harris, S. M.; Pailloux, S. L. Comparing Strategies in the Design of Responsive Contrast Agents for Magnetic Resonance Imaging: A Case Study with Copper and Zinc. *Acc. Chem. Res.* **2018**, *51*, 342–351.

(17) (a) Bertini, I.; Luchinat, C. *NMR of Paramagnetic Molecules in Biological Systems*; The Benjamin/Cummings Publishing Company, Inc.: Menlo Park, 1986. (b) Bertini, I.; Luchinat, C. The Hyperfine Shift. *Coord. Chem. Rev.* **1996**, *150*, 29–75. (c) Bertini, I.; Luchinat, C. Relaxation. *Coord. Chem. Rev.* **1996**, *150*, 77–110. (d) Bertini, I.; Luchinat, C.; Parigi, G. *Solution NMR of Paramagnetic Molecules: Applications to Metallobiomolecules and Models*; Elsevier Science B.V.: Amsterdam, 2001.

(18) Reath, A. H.; Ziller, J. W.; Tsay, C.; Ryan, A. J.; Yang, J. Y. Redox Potential and Electronic Structure Effects of Proximal Nonredox Active Cations in Cobalt Schiff Base Complexes. *Inorg. Chem*. **2017**, *56*, 3713–3718.

(19) *APEX2*, version. 2009.1; Bruker Analytical X-ray Systems, Inc.: Madison, WI, 2009.

(20) Sheldrick, G. M. *SADABS*, version 2.03; Bruker Analytical X-ray Systems, Inc.: Madison, WI, 2000.

(21) (a) Sheldrick, G. M. *SHELXTL*, version 6.12; Bruker Analytical X-ray Systems, Inc.: Madison, WI, 2000. (b) Sheldrick, G. M. SHELXT–Integrated Space-Group and Crystal-Structure Determination. *Acta Crystallogr., Sect. A: Found. Adv.* **2015**, *71*, 3–8. (c) Dolomanov, O. V.; Bourhis, L. J.; Gildea, R. J.; Howard, J. A. K.; Puschmann, H. OLEX2: A Complete Structure Solution, Refinement and Analysis Program. *J. Appl. Crystallogr.* **2009**, *42*, 339–341.

(22) Chilton, N. F.; Anderson, R. P.; Turner, L. D.; Soncini, A.; Murray, K. S. PHI: A Powerful New Program for the Analysis of Anisotropic Monomeric and Exchange-Coupled Polynuclear d- and f-Block Complexes. *J. Comput. Chem.* **2013**, *34*, 1164–1175.

(23) (a) Evans, D. F. The Determination of the Paramagnetic Susceptibility of Substances in Solution by Nuclear Magnetic Resonance. *J. Chem. Soc.* **1959**, *0*, 2003–2005. (b) Schubert, E. M. Utilizing the Evans Method with a Superconducting NMR Spectrometer in the Undergraduate Laboratory. *J. Chem. Educ.* **1992**, *69*, 62.

(24) Bain, G. A.; Berry, J. F. Diamagnetic Corrections and Pascal's Constants. *J. Chem. Educ.* **2008**, *85*, 532–536.

(25) Dixon, W. T.; Ren, J.; Lubag, A. J. M.; Ratnakar, J.; Vinogradov, E.; Hancu, I.; Lenkinski, R. E.; Sherry, A. D. A Concentration-Independent Method to Measure Exchange Rates in PARACEST Agents. *Magn. Reson. Med.* **2010**, *63*, 625–632.

(26) (a) Hirose, K. A Practical Guide for the Determination of Binding Constants. *J. Incl. Phenom. Macrocycl. Chem.* **2001**, *39*, 193–209. (b) Ellis, A. L.; Mason, J. C.; Lee, H.-W.; Strekowski, L.; Patonay, G.; Choi, H.; Yang, J. J. Design, Synthesis, and Characterization of a Calcium-Sensitive Near Infrared Dye. *Talanta* **2002**, *56*, 1099–1107. (c) Reuter, K.; Buchner, M. R.; Thiele, G.; von Hänisch, C. Stable Alkali-Metal Complexes of Hybrid Disila-Crown Ethers. *Inorg. Chem.* **2016**, *55*, 4441–4447. (d) Pauric, A. D.; Jin, S.; Fuller, T. J.; Balogh, M. P.; Halalay, I. C.; Goward, G. R. NMR Determination of the Relative

Binding Affinity of Crown Ethers for Manganese Cations in Aprotic Nonaqueous Lithium Electrolyte Solutions. *J. Phys. Chem. C* **2016**, *120*, 3677–3683.

(27) Kuzmič, P. Program DYNAFIT for the Analysis of Enzyme Kinetic Data: Application to HIV Proteinase. *Anal. Biochem.* **1996**, *237*, 260–273.

(28) (a) Wood, P. M. The Potential Diagram for Oxygen at pH 7. *Biochem. J.* **1988**, *253*, 287−289. (b) Sawyer, D. T.; Sobkowiak, A.; Roberts, J. L. *Electrochemistry for Chemists*, 2nd ed.; John Wiley & Sons: New York, 1995.

(29) Chantarojsiri, T.; Ziller, J. W.; Yang, J. Y. Incorporation of Redox-Inactive Cations Promotes Iron Catalyzed Aerobic C–H Oxidation at Mild Potentials. *Chem. Sci.* **2018**, *9*, 2567–2574.

(30) Izatt, R. M.; Pawlak, K.; Bradshaw, J. S.; Bruening, R. L. Thermodynamic and Kinetic Data for Macrocycle Interactions with Cations and Anions. *Chem. Rev.* **1991**, *91*, 1721–2085.

(31) (a) Shannon, R. D. Revised Effective Ionic Radii and Systematic Studies of Interatomic Distances in Halides and Chalcogenides. *Acta Crystallogr., Sect. A* **1976**, *32*, 751–767. (b) Lang, P. F.; Smith, B. C. Ionic Radii for Group 1 and Group 2 Halide, Hydride, Fluoride, Oxide, Sulfide, Selenide and Telluride Crystals. *Dalton Trans.* **2010**, *39*, 7786–7791.

(32) Drew, M. G. B.; Harding, C. J.; McKee, V.; Morgan, G. G.; Nelson, J. Geometric Control of Manganese Redox State. *J. Chem. Soc., Chem. Commun.* **1995**, *0*, 1035–1038.

(33) Bonger, K. M.; van den Berg, R. J. B. H. N.; Heitman, L. H.; IJzerman, A. P.; Oosterom, J.; Timmers, C. M.; Overkleeft, H. S.; van der Marel, G. A. Synthesis and Evaluation of Homo-Bivalent GnRHR Ligands. *Bioorg. Med. Chem.* **2007**, *15*, 4841–4856.

References for Chapter 7

(1) (a) Caneschi, A.; Gatteschi, D.; Sessoli, R; Barra, A. L.; Brunel, L. C.; Guillot, M. Alternating Current Susceptibility, High Field Magnetization, and Millimeter Band EPR Evidence for a Ground S = 10 State in $[Mn_{12}O_{12}(CH_3COO)_{16}(H_2O)_4]\cdot 2CH_3COOH\cdot 4H_2O$. *J. Am. Chem. Soc*. **1991**, *113*, 5873–5874. (b) Sessoli, R.; Gatteschi, D.; Caneschi, A.; Novak, M. A. Magnetic Bistability in a Metal-Ion Cluster. *Nature* **1993**, *365*, 141–143. (c) Sessoli, R.; Tsai, H.-L.; Schake, A. R.; Wang, S.; Vincent, J. B.; Folting, K.; Gatteschi, D.; Christou, G.; Hendrickson, D. N. High-Spin Molecules: $[Mn_{12}O_{12}(O_2CR)_{16}(H_2O)_4]$. *J. Am. Chem. Soc*. **1993**, *115*, 1804–1816. (d) Ishikawa, N.; Sugita, M.; Ishikawa, T.; Koshihara, S.-Y.; Kaizu, Y. Lanthanide Double-Decker Complexes Functioning as Magnets at the Single-Molecular Level. *J. Am. Chem. Soc*. **2003**, *125*, 8694–8695. (e) Berlinguette, C. P.; Vaughn, D.; Cañada-Vilalta, C.; Galán-Mascarós, J. R.; Dunbar, K. R. A Trigonal-Bipyramidal Cyanide Cluster with Single-Molecule-Magnet Behavior: Synthesis, Structure, and Magnetic Properties of $\{[Mn^{II}(tmphen)_2]_3[Mn^{III}(CN)_6]_2\}$. *Angew. Chem. Int. Ed*. **2003**, *42*, 1523–1526. (f) Tang, J.; Hewitt, I.; Madhu, N. T.; Chastanet, G.; Wernsdorfer, W.; Anson, C. E.; Benelli, C.; Sessoli, R.; Powell, A. K. Dysprosium Triangles Showing Single-Molecule Magnet Behavior of Thermally Excited Spin States. *Angew. Chem. Int. Ed*. **2006**, *45*, 1729–1733. (g) Gatteschi, D.; Sessoli, R.; Villain, J. *Molecular Nanomagnets*; Oxford University Press: Oxford, 2006. (h) *Single-Molecule Magnets and Related Phenomena. Structure and Bonding*; Winpenny, R. E. P., Ed.; Springer-Verlag: Berlin, 2006; Vol. 122, pp. 1–206. (i) Lin, P.-H.; Burchell, T. J.; Clérac, R.; Murugesu, M. Dinuclear Dysprosium(III) Single-Molecule Magnets with a Large Anisotropic Barrier. *Angew. Chem. Int. Ed*. **2008**, *47*, 8848–8851. (j) Bagai, R.; Christou, G. The *Drosophila* of Single-Molecule Magnetism: $[Mn_{12}O_{12}(O_2CR)_{16}(H_2O)_4]$. *Chem. Soc. Rev*. **2009**, *38*, 1011–1026. (k) Freedman, D. E.; Harman, W. H.; Harris, T. D.; Long, G. J.; Chang, C. J.; Long, J. R. Slow Magnetic Relaxation in a High-Spin Iron(II) Complex. *J. Am. Chem. Soc*. **2010**, *132*, 1224–1225. (l) Rinehart, J. D.; Fang, M.; Evans, W. J.; Long, J. R. Strong Exchange and Magnetic Blocking in N_2^{3-}-Radical-Bridged Lanthanide Complexes. *Nat. Chem*. **2011**, *3*, 538–542. (m) Rinehart, J. D.; Fang, M.; Evans, W. J.; Long, J. R. A N_2^{3-} Radical-Bridged Terbium Complex Exhibiting Magnetic Hysteresis at 14 K. *J. Am. Chem. Soc*. **2011**, *133*, 14236–14239. (n) Mougel, V.; Chatelain, L.; Pécaut, J.; Caciuffo, R.; Colineau, E.; Griveau, J.-C.; Mazzanti, M. Uranium and Manganese Assembled in a Wheel-Shaped Nanoscale Single-Molecule Magnet with High Spin-Reversal Barrier. *Nat. Chem*. **2012**, *4*, 1011–1017. (o) Ganivet, C. R.; Ballesteros, B.; de la Torre, G.; Clemente-Juan, J. M.; Coronado, E.; Torres, T. Influence of Peripheral Substitution on the Magnetic Behavior of Single-Ion Magnets Based on Homo- and Heteroleptic Tb^{III} Bis(phthalocyaninate). *Chem. –Eur. J*. **2013**, *19*, 1457–1465. (p) Woodruff, D. N.; Winpenny, R. E. P.; Layfield, R. A. Lanthanide Single-Molecule Magnets. *Chem. Rev*. **2013**, *113*, 5110–5148. (q) Zhang, P.; Guo, Y.-N.; Tang, J. Recent Advances in Dysprosium-Based Single Molecule Magnets: Structural Overview and Synthetic Strategies. *Coord. Chem. Rev*. **2013**, *257*, 1728–1763. (r) Pedersen, K. S.; Bendix,

J.; Clérac, R. Single-Molecule Magnet Engineering: Building-Block Approaches. *Chem. Commun.* **2014**, *50*, 4396–4415. (s) Meihaus, K. R.; Long, J. R. Actinide-Based Single-Molecule Magnets. *Dalton Trans*. **2015**, *44*, 2517–2528. (t) Craig, G. A.; Murrie, M. 3d Single-Ion Magnets. *Chem. Soc. Rev*. **2015**, *44*, 2135–2147. (u) Demir, S.; Jeon, I.-R.; Long, J. R.; Harris, T. D. Radical Ligand-Containing Single-Molecule Magnets. *Coord. Chem. Rev*. **2015**, *289–290*, 149–176. (v) Chen, Y.-C.; Liu, J.-L.; Ungur, L.; Liu, J.; Li, Q.-W.; Wang, L.-F.; Ni, Z.-P.; Chibotaru, L. F.; Chen, X.-M.; Tong, M.-L. Symmetry-Supported Magnetic Blocking at 20 K in Pentagonal Bipyramidal Dy(III) Single-Ion Magnets. *J. Am. Chem. Soc*. **2016**, *138*, 2829–2837. (w) Liu, J.; Chen, Y.-C.; Liu, J.-L.; Vieru, V.; Ungur, L.; Jia, J.-H.; Chibotaru, L. F.; Lan, Y.; Wernsdorfer, W.; Gao, S.; Chen, X.-M.; Tong, M.-L. A Stable Pentagonal Bipyramidal Dy(III) Single-Ion Magnet with a Record Magnetization Reversal Barrier over 1000 K. *J. Am. Chem. Soc*. **2016**, *138*, 5441–5450. (x) Ding, Y.-S.; Chilton, N. F.; Winpenny, R. E. P.; Zheng, Y.-Z. On Approaching the Limit of Molecular Magnetic Anisotropy: A Near-Perfect Pentagonal Bipyramidal Dysprosium(III) Single-Molecule Magnet. *Angew. Chem. Int. Ed*. **2016**, *55*, 16071–16074. (y) Guo, F.-S.; Day, B. M.; Chen, Y.-C.; Tong, M.-L.; Mansikkamäki, A.; Layfield, R. A. A Dysprosium Metallocene Single-Molecule Magnet Functioning at the Axial Limit. *Angew. Chem. Int. Ed*. **2017**, *56*, 11445–11449. (z) Demir, S.; Gonzalez, M. I.; Darago, L. E.; Evans, W. J.; Long, J. R. Giant Coercivity and High Magnetic Blocking Temperature for N_2^{3-} Radical-Bridged Dilanthanide Complexes Upon Ligand Dissociation. *Nat. Commun.* **2017**, *8*, 2144. (α) McClain, K. R.; Gould, C. A.; Chakarawet, K.; Teat, S. J.; Groshens, T. J.; Long, J. R.; Harvey, B. G. High-Temperature Magnetic Blocking and Magneto-Structural Correlations in a Series of Dysprosium(III) Metallocenium Single-Molecule Magnets. *Chem. Sci*. **2018**, *9*, 8492–8503.

(2) (a) Caneschi, A.; Gatteschi, D.; Lalioti, N.; Sangregorio, C.; Sessoli, R.; Venturi, G.; Vindigni, A.; Rettori, A.; Pini, M. G.; Novak, M. A. Cobalt(II)-Nitronyl Nitroxide Chains as Molecular Magnetic Nanowires. *Angew. Chem. Int. Ed*. **2001**, *40*, 1760–1763. (b) Clérac, R.; Miyasaka, H.; Yamashita, M.; Coulon, C. Evidence for Single-Chain Magnet Behavior in a Mn^{III}–Ni^{II} Chain Designed with High Spin Magnetic Units: A Route to High Temperature Metastable Magnets. *J. Am. Chem. Soc*. **2002**, *124*, 12837–12844. (c) Lescouëzec, R.; Vaissermann, J.; Ruiz-Pérez, C.; Lloret, F.; Carrasco, R.; Julve, M.; Verdaguer, M.; Dromzee, Y.; Gatteschi, D.; Wernsdorfer, W. Cyanide-Bridged Iron(III)–cobalt(II) Double Zigzag Ferromagnetic Chains: Two New Molecular Magnetic Nanowires. *Angew. Chem. Int. Ed*. **2003**, *42*, 1483–1486. (d) Ferbinteanu, M.; Miyasaka, H.; Wernsdorfer, W.; Nakata, K.; Sugiura, K.-I.; Yamashita, M.; Coulon, C.; Clérac, R. Single-Chain Magnet $(NEt_4)[Mn_2(5\text{-MeOsalen})_2Fe(CN)_6]$ Made of Mn^{III}–Fe^{III}– Mn^{III} Trinuclear Single-Molecule Magnet with an $S_T = {}^9/_2$ Spin Ground State. *J. Am. Chem. Soc*. **2005**, *127*, 3090–3099. (e) Bogani, L.; Sangregorio, C.; Sessoli, R.; Gatteschi, D. Molecular Engineering for Single-Chain-Magnet Behavior in a One-Dimensional Dysprosium–Nitronyl Nitroxide Compound. *Angew. Chem. Int. Ed*. **2005**, *44*, 5817–5821. (f) Bernot, K.;

Bogani, L.; Caneschi, A.; Gatteschi, D.; Sessoli, R. A Family of Rare-Earth-Based Single Chain Magnets: Playing with Anisotropy. *J. Am. Chem. Soc*. **2006**, *128*, 7947–7956. (g) Xu, H.-B.; Wang, B.-W.; Pan, F.; Wang, Z.-M.; Gao, S. Stringing Oxo-Centered Trinuclear $[Mn^{III}_3O]$ Units into Single-Chain Magnets with Formate or Azide Linkers. *Angew. Chem. Int. Ed*. **2007**, *46*, 7388–7392. (h) Ishii, N.; Okamura, Y.; Chiba, S.; Nogami, T.; Ishida, T. Giant Coercivity in a One-Dimensional Cobalt-Radical Coordination Magnet. *J. Am. Chem. Soc*. **2008**, *130*, 24–25. (i) Miyasaka, H.; Julve, M.; Yamashita, M.; Clérac, R. Slow Dynamics of the Magnetization in One-Dimensional Coordination Polymers: Single-Chain Magnets. *Inorg. Chem*. **2009**, *48*, 3420–3437. (j) Visinescu, D.; Madalan, A. M.; Andruh, M.; Duhayon, C.; Sutter, J.-P.; Ungur, L.; Van den Heuvel, W.; Chibotaru, L. F. First Heterotrimetallic {3d-4d-4f} Single Chain Magnet, Constructed from Anisotropic High-Spin Heterometallic Nodes and Paramagnetic Spacers. *Chem. –Eur. J*. **2009**, *15*, 11808–11814. (k) Harris, T. D.; Bennett, M. V.; Clérac, R.; Long, J. R. $[ReCl_4(CN)_2]^{2-}$: A High Magnetic Anisotropy Building Unit Giving Rise to the Single-Chain Magnets $(DMF)_4MReCl_4(CN)_2$ (M = Mn, Fe, Co, Ni). *J. Am. Chem. Soc*. **2010**, *132*, 3980–3988. (l) Sun, H.-L.; Wang, Z.-M.; Gao, S. Strategies Towards Single-Chain Magnets. *Coord. Chem. Rev*. **2010**, *254*, 1081–1100. (m) Feng, X.; Harris, T. D.; Long, J. R. Influence of Structure on Exchange Strength and Relaxation Barrier in a Series of $Fe^{II}Re^{IV}(CN)_2$ Single-Chain Magnets. *Chem. Sci*. **2011**, *2*, 1688–1694. (n) Hoshino, N.; Iijima, F.; Newton, G. N.; Yoshida, N.; Shiga, T.; Nojiri, H.; Nakao, A.; Kumai, R.; Murakami, Y.; Oshio, H. Three-Way Switching in a Cyanide-Bridged [CoFe] Chain. *Nat. Chem*. **2012**, *4*, 921–926. (o) Zhang, W.-X.; Ishikawa, R.; Breedlove, B.; Yamashita, M. Single-Chain Magnets: Beyond the Glauber Model. *RSC Adv*. **2013**, *3*, 3772–3798. (p) Vaz, M. G. F.; Cassaro, R. A. A.; Akpinar, H.; Schlueter, J. A.; Lahti, P. M.; Novak, M. A. A Cobalt Pyrenylnitronylnitroxide Single-Chain Magnet with High Coercivity and Record Blocking Temperature. *Chem. –Eur. J*. **2014**, *20*, 5460–5467. (q) Mougel, V.; Chatelain, L.; Hermle, J.; Caciuffo, R.; Colineau, E.; Tuna, F.; Magnani, N.; de Geyer, A.; Pécaut, J.; Mazzanti, M. A Uranium-Based UO_2^+–Mn^{2+} Single-Chain Magnet Assembled Through Cation–Cation Interactions. *Angew. Chem. Int. Ed*. **2014**, *53*, 819–823. (r) Chatelain, L.; Tuna, F.; Pécaut, J.; Mazzanti, M. A Zig-Zag Uranyl(V)–Mn(II) Single Chain Magnet with a High Relaxation Barrier. *Chem. Commun*. **2015**, *51*, 11309–11312. (s) Cassaro, R. A. A.; Reis, S. G.; Araujo, T. S.; Lahti, P. M.; Novak, M. A.; Vaz, M. G. F. A Single-Chain Magnet with a Very High Blocking Temperature and a Strong Coercive Field. *Inorg. Chem*. **2015**, *54*, 9381–9383. (t) Wei, R.-M.; Cao, F.; Li, J.; Yang, L.; Han, Y.; Zhang, X.-L.; Zhang, Z.; Wang, X.-Y.; Song, Y. Single-Chain Magnets Based on Octacyanotungstate with the Highest Energy Barriers for Cyanide Compounds. *Sci. Rep*. **2016**, *6*, 24372. (u) Jiang, W.; Jiao, C.; Meng, Y.; Zhao, L.; Liu, Q.; Liu, T. Switching Single Chain Magnet Behavior via Photoinduced Bidirectional Metal-to-Metal Charge Transfer. *Chem. Sci*. **2018**, *9*, 617–622. (v) Drahoš, B.; Herchel, R.; Trávníček, Z. Single-Chain Magnet Based on 1D Polymeric Azido-Bridged Seven-Coordinate Fe(II) Complex with a Pyridine-Based Macrocyclic Ligand. *Inorg. Chem*. **2018**, *57*, 12718–12726. (w) DeGayner, J. A.; Wang, K.; Harris, T. D. A Ferric Semiquinoid Single-Chain Magnet

via Thermally-Switchable Metal–Ligand Electron Transfer. *J. Am. Chem. Soc*. **2018**, *140*, 6550–6553.

(3) (a) Kahn, O.; Pei, Y.; Verdaguer, M.; Renard, J. P.; Sletten, J. Magnetic Ordering of $Mn^{II}Cu^{II}$ Bimetallic Chains: Design of a Molecular-Based Ferromagnet. *J. Am. Chem. Soc*. **1988**, *110*, 782–789. (b) Pereira, C. L. M.; Pedroso, E. F.; Doriguetto, A. C.; Ellena, J. A.; Boubekeur, K.; Filali, Y.; Journaux, Y.; Novak, M. A.; Stumpf, H. O. Design of 1D and 2D Molecule-Based Magnets with the Ligand 4,5-Dimethyl-1,2-phenylenebis(oxamato). *Dalton Trans*. **2011**, *40*, 746–754.

(4) (a) Miller, J. S.; Calabrese, J. C.; Epstein, A. J.; Bigelow, R. W.; Zhang, J. H.; Reiff, W. M. Ferromagnetic Properties of One-Dimensional Decamethylferrocenium Tetracyanoethylenide (1 : 1): $[Fe(\eta^5\text{-}C_5Me_5)_2]^{\bullet+}[TCNE]^{\bullet-}$. *J. Chem. Soc., Chem. Commun*. **1986**, 1026–1028. (b) Manriquez, J. M.; Yee, G. T.; McLean, R. S.; Epstein, A. J.; Miller, J. S. A Room-Temperature Molecular/Organic-Based Magnet. *Science* **1991**, *252*, 1415–1417. (c) Pokhodnya, K. I.; Bonner, M.; Her, J.-H.; Stephens, P. W.; Miller, J. S. Magnetic Ordering (T_c = 90 K) Observed for Layered $[Fe^{II}(TCNE^{\bullet-})(NCMe)_2]^+[Fe^{III}Cl_4]^-$ (TCNE = Tetracyanoethylene). *J. Am. Chem. Soc*. **2006**, *128*, 15592–15593. (d) Miller, J. S. Magnetically Ordered Molecule-Based Assemblies. *Dalton Trans*. **2006**, 2742–2749. (e) Stone, K. H.; Stephens, P. W.; McConnell, A. C.; Shurdha, E.; Pokhodnya, K. I.; Miller J. S. $Mn^{II}(TCNE)_{3/2}(I_3)_{1/2}$–A 3D Network-Structured Organic-Based Magnet and Comparison to a 2D Analog. *Adv. Mater*. **2010**, *22*, 2514–2519. (f) Lapidus, S. H.; McConnell, A. C.; Stephens, P. W.; Miller, J. S. Structure and Magnetic Ordering of a 2-D $Mn^{II}(TCNE)I(OH_2)$ (TCNE = Tetracyanoethylene) Organic-Based Magnet (T_c = 171 K). *Chem. Commun*. **2011**, *47*, 7602–7604. (g) Zhang, J.; Kosaka, W.; Sugimoto, K.; Miyasaka, H. Magnetic Sponge Behavior via Electronic State Modulations. *J. Am. Chem. Soc*. **2018**, *140*, 5644–5652.

(5) (a) Mallah, T.; Thiébaut, S.; Verdaguer, M.; Veillet, P. High-T_c Molecular-Based Magnets: Ferrimagnetic Mixed-Valence Chromium(III)-Chromium(II) Cyanides with T_c at 240 and 190 Kelvin. *Science* **1993**, *262*, 1554–1557. (b) Entley, W. R.; Girolami, G. S. High-Temperature Molecular Magnets Based on Cyanovanadate Building Blocks: Spontaneous Magnetization at 230 K. *Science* **1995**, *268*, 397–400. (c) Ferlay, S.; Mallah, T.; Ouahès, R.; Veillet, P.; Verdaguer, M. A Room-Temperature Organometallic Magnet Based on Prussian Blue. *Nature* **1995**, *378*, 701–703. (d) Dujardin, E.; Ferlay, S.; Phan, X.; Desplanches, C.; Cartier dit Moulin, C.; Sainctavit, P.; Baudelet, F.; Dartyge, E.; Veillet, P.; Verdaguer, M. Synthesis and Magnetization of New Room-Temperature Molecule-Based Magnets: Effect of Stoichiometry on Local Magnetic Structure by X-ray Magnetic Circular Dichroism. *J. Am. Chem. Soc*. **1998**, *120*, 11347–11352.

(6) (a) Larionova, J.; Clérac, R.; Sanchiz, J.; Kahn, O.; Golhen, S.; Ouahab, L. Ferromagnetic Ordering, Anisotropy, and Spin Reorientation for the Cyano-Bridged Bimetallic Compound

$Mn_2(H_2O)_5Mo(CN)_7 \cdot 4H_2O$ (α Phase). *J. Am. Chem. Soc*. **1998**, *120*, 13088–13095. (b) Holmes, S. M.; Girolami, G. S. Sol–Gel Synthesis of $KV^{II}[Cr^{III}(CN)_6] \cdot 2H_2O$: A Crystalline Molecule-Based Magnet with a Magnetic Ordering Temperature above 100 °C. *J. Am. Chem. Soc*. **1999**, *121*, 5593–5594. (c) Verdaguer, M.; Girolami, G. S. Magnetic Prussian Blue Analogs. In *Magnetism: Molecules to Materials V*; Miller, J. S., Drillon, M., Eds.; Wiley-VCH: Weinheim, 2005, pp. 283–346. (d) Tomono, K.; Tsunobuchi, Y.; Nakabayashi, K.; Ohkoshi, S.-I. Vanadium(II) Heptacyanomolybdate(III)-Based Magnet Exhibiting a High Curie Temperature of 110 K. *Inorg. Chem*. **2010**, *49*, 1298–1300. (e) Her, J.-H.; Stephens, P. W.; Kareis, C. M.; Moore, J. G.; Min, K. S.; Park, J.-W.; Bali, G.; Kennon, B. S.; Miller, J. S. Anomalous Non-Prussian Blue Structures and Magnetic Ordering of $K_2Mn^{II}[Mn^{II}(CN)_6]$ and $Rb_2Mn^{II}[Mn^{II}(CN)_6]$. *Inorg. Chem*. **2010**, *49*, 1524–1534. (f) Ohkoshi, S.-I.; Imoto, K.; Tsunobuchi, Y.; Takano, S.; Tokoro, H. Light-Induced Spin-Crossover Magnet. *Nat. Chem*. **2011**, *3*, 564–569. (g) Tokoro, H.; Ohkoshi, S.-I. Novel Magnetic Functionalities of Prussian Blue Analogs. *Dalton Trans*. **2011**, *40*, 6825–6833.

(7) (a) Beauvais, L. G.; Long, J. R. $Co_3[Co(CN)_5]_2$: A Microporous Magnet with an Ordering Temperature of 38 K. *J. Am. Chem. Soc*. **2002**, *124*, 12096–12097. (b) Milon, J.; Daniel, M.-C.; Kaiba, A.; Guionneau, P.; Brandès, S.; Sutter, J.-P. Nanoporous Magnets of Chiral and Racemic $[\{Mn(HL)\}_2Mn\{Mo(CN)_7\}_2]$ with Switchable Ordering Temperatures (T_C = 85 K ↔ 106 K) Driven by H_2O Sorption (L = *N*,*N*-Dimethylalaninol). *J. Am. Chem. Soc*. **2007**, *129*, 13872–13878. (c) Kaye, S. S.; Choi, H. J.; Long, J. R. Generation and O_2 Adsorption Studies of the Microporous Magnets $CsNi[Cr(CN)_6]$ (T_C = 75 K) and $Cr_3[Cr(CN)_6]_2 \cdot 6H_2O$ (T_N = 219 K). *J. Am. Chem. Soc*. **2008**, *130*, 16921–16925.

(8) (a) Maspoch, D.; Ruiz-Molina, D.; Veciana, J. Magnetic Nanoporous Coordination Polymers. *J. Mater. Chem*. **2004**, *14*, 2713–2723. (b) Kurmoo, M. Magnetic Metal–Organic Frameworks. *Chem. Soc. Rev*. **2009**, *38*, 1353–1379. (c) Dechambenoit, P.; Long, J. R. Microporous Magnets. *Chem. Soc. Rev*. **2011**, *40*, 3249–3265. (d) Clemente-León, M.; Coronado, E.; Martí-Gastaldo, C.; Romero, F. M. Multifunctionality in Hybrid Magnetic Materials Based on Bimetallic Oxalate Complexes. *Chem. Soc. Rev*. **2011**, *40*, 473–497. (e) Coronado, E.; Espallargas, G. M. Dynamic Magnetic MOFs. *Chem. Soc. Rev*. **2013**, *42*, 1525–1539. (f) Espallargas, G. M.; Coronado, E. Magnetic Functionalities in MOFs: From the Framework to the Pore. *Chem. Soc. Rev*. **2018**, *47*, 533–557.

(9) (a) Jeon, I.-R.; Negru, B.; Van Duyne, R. P.; Harris, T. D. A 2D Semiquinone Radical-Containing Microporous Magnet with Solvent-Induced Switching from T_c = 26 to 80 K. *J. Am. Chem. Soc*. **2015**, *137*, 15699–15702. (b) Darago, L. E.; Aubrey, M. L.; Yu, C. J.; Gonzalez, M. I.; Long, J. R. Electronic Conductivity, Ferrimagnetic Ordering, and Reductive Insertion Mediated by Organic Mixed-Valence in a Ferric Semiquinoid Metal–Organic Framework. *J. Am. Chem. Soc*. **2015**, *137*, 15703–15711. (c) DeGayner, J. A.; Jeon, I.-R.; Sun, L.; Dincă, M.; Harris, T. D. 2D Conductive Iron-Quinoid Magnets Ordering up to T_c =

105 K via Heterogenous Redox Chemistry. *J. Am. Chem. Soc*. **2017**, *139*, 4175–4184. (d) Chen, J.; Sekine, Y.; Komatsumaru, Y.; Hayami, S.; Miyasaka, H. Thermally Induced Valence Tautomeric Transition in a Two-Dimensional Fe-Tetraoxolene Honeycomb Network. *Angew. Chem. Int. Ed*. **2018**, *57*, 12043–12047. (e) Liu, L.; DeGayner, J. A.; Sun, L.; Zee, D. Z.; Harris, T. D. Reversible Redox Switching of Magnetic Order and Electrical Conductivity in a 2D Manganese Benzoquinoid Framework. *Chem. Sci.* **2019**, *10*, 4652–4661.

(10) (a) Du, G.; Joo, J.; Epstein, A. J.; Miller, J. S. Anomalous Charge Transport Phenomena in Molecular-Based Magnet V(TCNE)$_x$·y(solvent). *J. Appl. Phys*. **1993**, *73*, 6566–6568. (b) Miyasaka, H.; Izawa, T.; Takahashi, N.; Yamashita, M.; Dunbar, K. R. Long-Range Ordered Magnet of a Charge-Transfer Ru_2^{4+}/TCNQ Two-Dimensional Network Compound. *J. Am. Chem. Soc*. **2006**, *128*, 11358–11359. (c) Motokawa, N.; Miyasaka, H.; Yamashita, M.; Dunbar, K. R. An Electron-Transfer Ferromagnet with T_c = 107 K Based on a Three-Dimensional $[Ru_2]_2$/TCNQ System. *Angew. Chem. Int. Ed*. **2008**, *47*, 7760–7763. (d) Miyasaka, H.; Motokawa, N.; Matsunaga, S.; Yamashita, M.; Sugimoto, K.; Mori, T.; Toyota, N.; Dunbar, K. R. Control of Charge Transfer in a Series of $Ru_2^{II,II}$/TCNQ Two-Dimensional Networks by Tuning the Electron Affinity of TCNQ Units: A Route to Synergistic Magnetic/Conducting Materials. *J. Am. Chem. Soc*. **2010**, *132*, 1532–1544. (e) Pokhodnya, K.; Bonner, M.; Prigodin, V.; Epstein, A. J.; Miller, J. S. Carrier Transport in the V[TCNE]$_x$ (TCNE = Tetracyanoethylene; x ~ 2) Organic-Based Magnet. *J. Phys.: Condens. Matter* **2013**, *25*, 196001.

(11) (a) Coronado, E.; Galán-Mascarós, J. R.; Gómez-García, C. J.; Laukhin, V. Coexistence of Ferromagnetism and Metallic Conductivity in a Molecule-Based Layered Compound. *Nature* **2000**, *408*, 447–449. (b) Alberola, A.; Coronado, E.; Galán-Mascarós, J. R.; Giménez-Saiz, C.; Gómez-García, C. J. A Molecular Metal Ferromagnet from the Organic Donor Bis(ethylenedithio)tetraselenafulvalene and Bimetallic Oxalate Complexes. *J. Am. Chem. Soc*. **2003**, *125*, 10774–10775. (c) Coronado, E.; Galán-Mascarós, J. R. Hybrid Molecular Conductors. *J. Mater. Chem*. **2005**, *15*, 66–74. (d) Fujiwara, E.; Yamamoto, K.; Shimamura, M.; Zhou, B.; Kobayashi, A.; Takahashi, K.; Okano, Y.; Cui, H.; Kobayashi, H. (^{n}Bu$_4$N)[Ni(dmstfdt)$_2$]: A Planar Nickel Coordination Complex with an Extended-TTF Ligand Exhibiting Metallic Conduction, Metal–Insulator Transition, and Weak Ferromagnetism. *Chem. Mater*. **2007**, *19*, 553–558. (e) Galán-Mascarós, J. R.; Coronado, E.; Goddard, P. A.; Singleton, J.; Coldea, A. I.; Wallis, J. D.; Coles, S. J.; Alberola, A. A Chiral Ferromagnetic Molecular Metal. *J. Am. Chem. Soc*. **2010**, *132*, 9271–9273.

(12) (a) Benmansour, S.; Abhervé, A.; Gómez-Claramunt, P.; Vallés-García, C.; Gómez-García, C. J. Nanosheets of Two-Dimensional Magnetic and Conducting Fe(II)/Fe(III) Mixed-Valence Metal–Organic Frameworks. *ACS Appl. Mater. Interfaces* **2017**, *9*, 26210–26218. (b) Yang, C.; Dong, R.; Wang, M.; Petkov, P. S.; Zhang, Z.; Wang, M.; Han, P.; Ballabio,

M.; Bräuninger, S. A.; Liao, Z.; Zhang, J.; Schwotzer, F.; Zschech, E.; Klauss, H.-H.; Cánovas, E.; Kaskel, S.; Bonn, M.; Zhou, S.; Heine, T.; Feng, X. A Semiconducting Layered Metal-Organic Framework Magnet. *Nat. Commun.* **2019**, *10*, 3260.

(13) Sekine, Y.; Kosaka, W.; Taniguchi, K.; Miyasaka, H. Conductive Molecular Magnets. In *Molecular Magnetic Materials: Concepts and Applications*; Sieklucka, B., Pinkowicz, D., Eds.; Wiley-VCH: Weinheim, 2017, pp. 369–404.

(14) (a) Rueff, J.-M.; Nierengarten, J.-F.; Gilliot, P.; Demessence, A.; Cregut, O.; Drillon, M.; Rabu, P. Influence of Magnetic Ordering on the Luminescence in a Layered Organic–Inorganic OPV–Ni(II) Compound. *Chem. Mater.* **2004**, *16*, 2933–2937. (b) Chelebaeva, E.; Larionova, J.; Guari, Y.; Ferreira, R. A. S.; Carlos, L. D.; Almeida Paz, F. A.; Trifonov, A.; Guérin, C. Luminescent and Magnetic Cyano-Bridged Coordination Polymers Containing 4d–4f Ions: Toward Multifunctional Materials. *Inorg. Chem.* **2009**, *48*, 5983–5995. (c) Ferrando-Soria, J.; Khajavi, H.; Serra-Crespo, P.; Gascon, J.; Kapteijn, F.; Julve, M.; Lloret, F.; Pasán, J.; Ruiz-Pérez, C.; Journaux, Y.; Pardo, E. Highly Selective Chemical Sensing in a Luminescent Nanoporous Magnet. *Adv. Mater.* **2012**, *24*, 5625–5629. (d) Chelebaeva, E.; Long, J.; Larionova, J.; Ferreira, R. A. S.; Carlos, L. D.; Almeida Paz, F. A.; Gomes, J. B. R.; Trifonov, A.; Guérin, C.; Guari, Y. Bifunctional Mixed-Lanthanide Cyano-Bridged Coordination Polymers $Ln_{0.5}Ln'_{0.5}(H_2O)_5[W(CN)_8]$ (Ln/Ln′ = Eu^{3+}/Tb^{3+}, Eu^{3+}/Gd^{3+}, Tb^{3+}/Sm^{3+}). *Inorg. Chem.* **2012**, *51*, 9005–9016. (e) Chorazy, S.; Nakabayashi, K.; Ohkoshi, S.-I.; Sieklucka, B. Green to Red Luminescence Switchable by Excitation Light in Cyanido-Bridged Tb^{III}–W^{V} Ferromagnet. *Chem. Mater.* **2014**, *26*, 4072–4075. (f) Perfetti, M.; Pointillart, F.; Cador, O.; Sorace, L.; Ouahab, L. Luminescent Molecular Magnets. In *Molecular Magnetic Materials: Concepts and Applications*; Sieklucka, B., Pinkowicz, D., Eds.; Wiley-VCH: Weinheim, 2017, pp. 345–368. (g) Benmansour, S.; Cerezo-Navarrete, C.; Canet-Ferrer, J.; Muñoz-Matutano, G.; Martínez-Pastor, J.; Gómez-García, C. J. A Fluorescent Layered Oxalato-Based Canted Antiferromagnet. *Dalton Trans.* **2018**, *47*, 11909–11916.

(15) (a) Rocha, A. R.; García-Suárez, V. M.; Bailey, S. W.; Lambert, C. J.; Ferrer, J.; Sanvito, S. Towards Molecular Spintronics. *Nat. Mater.* **2005**, *4*, 335–339. (b) Bogani, L.; Wernsdorfer, W. Molecular Spintronics Using Single-Molecule Magnets. *Nat. Mater.* **2008**, *7*, 179–186. (c) Ardavan, A.; Blundell, S. J. Storing Quantum Information in Chemically Engineered Nanoscale Magnets. *J. Mater. Chem.* **2009**, *19*, 1754–1760. (d) Liu, H.; Zhang, C.; Malissa, H.; Groesbeck, M.; Kavand, M.; McLaughlin, R.; Jamali, S.; Hao, J.; Sun, D.; Davidson, R. A.; Wojcik, L.; Miller, J. S.; Boehme, C.; Vardeny, Z. V. Organic-Based Magnon Spintronics. *Nat. Mater.* **2018**, *17*, 308–312.

(16) (a) Gwak, J.; Ayral, A.; Rouessac, V.; Cot, L.; Grenier, J.-C.; Choy, J.-H. Synthesis and Characterization of Porous Ferrimagnetic Membranes. *Micropor. Mesopor. Mater.* **2003**, *63*,

177–184. (b) Madaeni, S. S.; Enayati, E.; Vatanpour, V. Separation of Nitrogen and Oxygen Gases by Polymeric Membrane Embedded with Magnetic Nano-Particle. *Polym. Adv. Technol*. **2011**, *22*, 2556–2563. (c) Ferrando-Soria, J.; Serra-Crespo, P.; de Lange, M.; Gascon, J.; Kapteijn, F.; Julve, M.; Cano, J.; Lloret, F.; Pasán, J.; Ruiz-Pérez, C.; Journaux, Y.; Pardo, E. Selective Gas and Vapor Sorption and Magnetic Sensing by an Isoreticular Mixed-Metal–Organic Framework. *J. Am. Chem. Soc*. **2012**, *134*, 15301–15304.

(17) Kahn, O. *Molecular Magnetism*; VCH: New York, 1993.

(18) (a) Coulon, C.; Miyasaka, H.; Clérac, R. Single-Chain Magnets: Theoretical Approach and Experimental Systems. In *Single-Molecule Magnets and Related Phenomena. Structure and Bonding*; Winpenny, R. E. P., Ed.; Springer-Verlag: Berlin, 2006; Vol. 122, pp. 163–206. (b) Gatteschi, D.; Vindigni, A. Single-Chain Magnets. In *Molecular Magnets: Physics and Applications*; Bartolomé, J., Luis, F., Fernández, J. F., Eds.; Springer-Verlag: Berlin, 2014; Vol. 1, pp. 191–220. (c) Coulon, C.; Pianet, V.; Urdampilleta, M.; Clérac, R. Single-Chain Magnets and Related Systems. In *Molecular Nanomagnets and Related Phenomena. Structure and Bonding*; Song, G., Ed.; Springer-Verlag: Berlin, 2014; Vol. 164, pp. 143–184.

(19) Domb, C. Ising Model. In *Phase Transitions and Critical Phenomena*; Domb, C., Green, M. S., Eds.; Academic Press: London, 1974; Vol. 3, pp. 357–484.

(20) (a) Bechlars, B.; D′Alessandro, D. M.; Jenkins, D. M.; Iavarone, A. T.; Glover, S. D.; Kubiak, C. P.; Long, J. R. High-Spin Ground States via Electron Delocalization in Mixed-Valence Imidazolate-Bridged Divanadium Complexes. *Nat. Chem*. **2010**, *2*, 362–368. (b) Gaudette, A. I.; Jeon, I.-R.; Anderson, J. S.; Grandjean, F.; Long, G. J.; Harris, T. D. Electron Hopping Through Double-Exchange Coupling in a Mixed-Valence Diiminobenzoquinone-Bridged Fe_2 Complex. *J. Am. Chem. Soc*. **2015**, *137*, 12617–12626.

(21) (a) Caneschi, A.; Gatteschi, D.; Sessoli, R.; Rey, P. Toward Molecular Magnets: The Metal–Radical Approach. *Acc. Chem. Res*. **1989**, *22*, 392–398. (b) Vostrikova, K. E. High-Spin Molecules Based on Metal Complexes of Organic Free Radicals. *Coord. Chem. Rev*. **2008**, *252*, 1409–1419. (c) *Stable Radicals: Fundamentals and Applied Aspects of Odd Electron Compounds*; Hicks, R. G., Ed.; John Wiley & Sons, Inc.: Chichester, 2010. (d) Lemaire, M. T. Progress and Design Challenges for High-Spin Molecules. *Pure Appl. Chem*. **2011**, *83*, 141–149. (e) Iwamura, H. What Role Has Organic Chemistry Played in the Development of Molecule-Based Magnets? *Polyhedron* **2013**, *66*, 3–14.

(22) Selected references: (a) Caneschi, A.; Gatteschi, D.; Laugier, J.; Rey, P. Ferromagnetic Alternating Spin Chains. *J. Am. Chem. Soc*. **1987**, *109*, 2191–2192. (b) Caneschi, A.; Gatteschi, D.; Renard, J. P.; Rey, P.; Sessoli, R. Magnetic Phase Transitions in

Manganese(II) Pentafluorobenzoate Adducts with Nitronyl Nitroxides. *J. Am. Chem. Soc*. **1989**, *111*, 785–786. (c) Caneschi, A.; Ferraro, F.; Gatteschi, D.; Rey, P.; Sessoli, R. Structure and Magnetic Properties of a Chain Compound Formed by Copper(II) and a Tridentate Nitronyl Nitroxide Radical. *Inorg. Chem.* **1991**, *30*, 3162–3166. (d) Caneschi, A.; Gatteschi, D.; Rey, P.; Sessoli, R. Structure and Magnetic Ordering of a Ferrimagnetic Helix Formed by Manganese(II) and a Nitronyl Nitroxide Radical. *Inorg. Chem.* **1991**, *30*, 3936–3941. (e) Stumpf, H. O.; Ouahab, L.; Pei, Y.; Grandjean, D.; Kahn, O. A Molecular-Based Magnet with a Fully Interlocked Three-Dimensional Structure. *Science* **1993**, *261*, 447–449. (f) Inoue, K.; Iwamura, H. Ferro- and Ferrimagnetic Ordering in a Two-Dimensional Network Formed by Manganese(II) and 1,3,5-Tris[*p*-(*N*-*tert*-butyl-*N*-oxyamino)phenyl]benzene. *J. Am. Chem. Soc*. **1994**, *116*, 3173–3174. (g) Caneschi, A.; Gatteschi, D.; Le Lirzin, A. Crystal Structure and Magnetic Properties of a New Ferrimagnetic Chain Containing Manganese(II) and a Nitronyl-Nitroxide Radical. *J. Mater. Chem*. **1994**, *4*, 319–326. (h) Inoue, K.; Hayamizu, T.; Iwamura, H.; Hashizume, D.; Ohashi, Y. Assemblage and Alignment of the Spins of the Organic Trinitroxide Radical with a Quartet Ground State by Means of Complexation with Magnetic Metal Ions. A Molecule-Based Magnet with Three-Dimensional Structure and High T_C of 46 K. *J. Am. Chem. Soc*. **1996**, *118*, 1803–1804. (i) Fegy, K.; Luneau, D.; Ohm, T.; Paulsen, C.; Rey, P. Two-Dimensional Nitroxide-Based Molecular Magnetic Materials. *Angew. Chem. Int. Ed*. **1998**, *37*, 1270–1273. (j) Numata, Y.; Inoue, K.; Baranov, N.; Kurmoo, M.; Kikuchi, K. Field-Induced Ferrimagnetic State in a Molecule-Based Magnet Consisting of a Co^{II} Ion and a Chiral Triplet Bis(nitroxide) Radical. *J. Am. Chem. Soc*. **2007**, *129*, 9902–9909. (k) Meng, X.; Shi, W.; Cheng, P. Magnetism in One-Dimensional Metal–Nitronyl Nitroxide Radical System. *Coord. Chem. Rev*. **2019**, *378*, 134–150. (l) Liu, X.; Wang, Y.-X.; Han, Z.; Han, T.; Shi, W.; Cheng, P. Tuning the Magnetization Dynamics of Tb^{II}-Based Single-Chain Magnets Through Substitution on the Nitronyl Nitroxide Radical. *Dalton Trans*. **2019**, *48*, 8989–8994.

(23) Selected references: (a) Zhao, H.; Heintz, R. A.; Ouyang, X.; Dunbar, K. R.; Campana, C. F.; Rogers, R. D. Spectroscopic, Thermal, and Magnetic Properties of Metal/TCNQ Network Polymers with Extensive Supramolecular Interactions Between Layers. *Chem. Mater*. **1999**, *11*, 736–746. (b) Clérac, R.; O'Kane, S.; Cowen, J.; Quyang, X.; Heintz, R.; Zhao, H.; Bazile, Jr., M. J.; Dunbar, K. R. Glassy Magnets Composed of Metals Coordinated to 7,7,8,8-Tetracyanoquinodimethane: $M(TCNQ)_2$ (M = Mn, Fe, Co, Ni). *Chem. Mater*. **2003**, *15*, 1840–1850. (c) Motokawa, N.; Matsunaga, S.; Takaishi, S.; Miyasaka, H.; Yamashita, M.; Dunbar, K. R. Reversible Magnetism Between an Antiferromagnet and a Ferromagnet Related to Solvation/Desolvation in a Robust Layered $[Ru_2]_2TCNQ$ Charge-Transfer System. *J. Am. Chem. Soc*. **2010**, *132*, 11943–11951. (d) McConnell, A. C.; Fishman, R. S.; Miller, J. S. Mean Field Analysis of the Exchange Coupling (*J*) for Two-and Three-Dimensional Structured Tetracyanoethenide ($TCNE^{\bullet-}$)-Based Magnets. *J. Phys. Chem. C* **2012**, *116*, 16154–16160. (e) Olson, C. S.; Gangopadhyay, S.; Hoang, K.; Alema, F.; Kilina,

S.; Pokhodnya, K. Magnetic Exchange in Mn^{II}[TCNE] (TCNE = Tetracyanoethylene) Molecule-Based Magnets with Two- and Three-Dimensional Magnetic Networks. *J. Phys. Chem. C* **2015**, *119*, 25036–25046.

(24) (a) Maspoch, D.; Ruiz-Molina, D.; Wurst, K.; Domingo, N.; Cavallini, M.; Biscarini, F.; Tejada, J.; Rovira, C.; Veciana, J. A Nanoporous Molecular Magnet with Reversible Solvent-Induced Mechanical and Magnetic Properties. *Nat. Mater*. **2003**, *2*, 190–195. (b) Maspoch, D.; Domingo, N.; Ruiz-Molina, D.; Wurst, K.; Hernández, J.-M.; Vaughan, G.; Rovira, C.; Lloret, F.; Tejada, J.; Veciana, J. Coexistence of Ferro- and Antiferromagnetic Interactions in a Metal–Organic Radical-Based (6,3)-Helical Network with Large Channels. *Chem. Commun*. **2005**, 5035–5037.

(25) (a) Koga, N.; Ishimaru, Y.; Iwamura, H. Diazodi(4-pyridyl)methane and Diazophenyl-(4-pyridyl)methane as Photoresponsive Ligands for Metal–Carbene Hetero-Spin Systems. *Angew. Chem. Int. Ed*. **1996**, *35*, 755–757. (b) Yoshihara, D.; Karasawa, S.; Koga, N. Cyclic Single-Molecule Magnet in Heterospin System. *J. Am. Chem. Soc*. **2008**, *130*, 10460–10461. (c) Yoshihara, D.; Karasawa, S.; Koga, N. Heterospin Single-Molecule Magnets with Extra-Large Anisotropic Barrier. *Polyhedron* **2011**, *30*, 3211–3217.

(26) Pedersen, K. S.; Perlepe, P.; Aubrey, M. L.; Woodruff, D. N.; Reyes-Lillo, S. E.; Reinholdt, A.; Voigt, L.; Li, Z.; Borup, K.; Rouzières, M.; Samohvalov, D.; Wilhelm, F.; Rogalev, A.; Neaton, J. B.; Long, J. R.; Clérac, R. Formation of the Layered Conductive Magnet $CrCl_2(pyrazine)_2$ Through Redox-Active Coordination Chemistry. *Nat. Chem*. **2018**, *10*, 1056–1061.

(27) (a) Johnston, R. F.; Holwerda, R. A. Ethanol Oxidation by Chromium(III) Complexes of Chloranilic Acid. Spectroscopic, Electrochemical, Magnetic, and Chromatographic Studies of Chloraniliate Semiquinone-Bridged Polynuclear Chromium Ions. *Inorg. Chem*. **1985**, *24*, 153–159. (b) Dei, A.; Gatteschi, D.; Pardi, L.; Russo, U. Tetraoxolene Radical Stabilization by the Interaction with Transition-Metal Ions. *Inorg. Chem*. **1991**, *30*, 2589–2594. (c) Min, K. S.; Rheingold, A. L.; DiPasquale, A. G.; Miller, J. S. Characterization of the Chloranilate(•3−) π Radical as a Strong Spin-Coupling Bridging Ligand. *Inorg. Chem*. **2006**, *45*, 6135–6137. (d) Min, K. S.; DiPasquale, A. G.; Golen, J. A.; Rheingold, A. L.; Miller, J. S. Synthesis, Structure, and Magnetic Properties of Valence Ambiguous Dinuclear Antiferromagnetically Coupled Cobalt and Ferromagnetically Coupled Iron Complexes Containing the Chloranilate(2−) and the Significantly Stronger Coupling Chloranilate(•3−) Radical Trianion. *J. Am. Chem. Soc*. **2007**, *129*, 2360–2368. (e) Guo, D.; McCusker, J. K. Spin Exchange Effects on the Physicochemical Properties of Tetraoxolene-Bridged Bimetallic Complexes. *Inorg. Chem*. **2007**, *46*, 3257–3274. (f) Miller, J. S.; Min, K. S. Oxidation Leading to Reduction: Redox-Induced Electron Transfer (RIET). *Angew. Chem. Int. Ed*. **2009**, *48*, 262–272. (g) Baum, A. E.; Lindeman, S. V.; Fiedler, A. T. Preparation of

a Semiquinonate-Bridged Diiron(II) Complex and Elucidation of Its Geometric and Electronic Structures. *Chem. Commun*. **2013**, *49*, 6531–6533.

(28) (a) Jeon, I.-R.; Park, J. G.; Xiao, D. J.; Harris, T. D. An Azophenine Radical-Bridged Fe_2 Single-Molecule Magnet with Record Magnetic Exchange Coupling. *J. Am. Chem. Soc*. **2013**, *135*, 16845–16848. (b) DeGayner, J. A.; Jeon, I.-R.; Harris, T. D. A Series of Tetraazalene Radical-Bridged M_2 (M = Cr^{III}, Mn^{II}, Fe^{II}, Co^{II}) Complexes with Strong Magnetic Exchange Coupling. *Chem. Sci*. **2015**, *6*, 6639–6648. (c) Hua, C.; DeGayner, J. A.; Harris, T. D. Thiosemiquinoid Radical-Bridged Cr^{III}_2 Complexes with Strong Magnetic Exchange Coupling. *Inorg. Chem*. **2019**, *58*, 7044–7053.

(29) Murase, R.; Abrahams, B. F.; D'Alessandro, D. M.; Davies, C. G.; Hudson, T. A.; Jameson, G. N. L.; Moubaraki, B.; Murray, K. S.; Robson, R.; Sutton, A. L. Mixed Valency in a 3D Semiconducting Iron–Fluoranilate Coordination Polymer. *Inorg. Chem*. **2017**, *56*, 9025–9035.

(30) (a) Tinti, F.; Verdaguer, M.; Kahn, O.; Savariault, J.-M. Interaction Between Copper(II) Ions Separated by 7.6 Å. Crystal Structure and Magnetic Properties of (μ-Iodanilato)bis[(*N*,*N*,*N*′,*N*′-tetramethylethylenediamine)copper(II)] Diperchlorate. *Inorg. Chem*. **1987**, *26*, 2380–2384. (b) Schweinfurth, D.; Khusniyarov, M. M.; Bubrin, D.; Hohloch, S.; Su, C.-Y.; Sarkar, B. Tuning Spin–Spin Coupling in Quinonoid-Bridged Dicopper(II) Complexes Through Rational Bridge Variation. *Inorg. Chem*. **2013**, *52*, 10332–10339.

(31) Atzori, M.; Benmansour, S.; Espallargas, G. M.; Clemente-León, M.; Abhervé, A.; Gómez-Claramunt, P.; Coronado, E.; Artizzu, F.; Sessini, E.; Deplano, P.; Serpe, A.; Mercuri, M. L.; Gómez-García, C. J. A Family of Layered Chiral Porous Magnets Exhibiting Tunable Ordering Temperatures. *Inorg. Chem*. **2013**, *52*, 10031–10040.

(32) *APEX2*, version 2014.11–0; Bruker Analytical X-ray Systems, Inc.: Madison, WI, 2014.

(33) Sheldrick, G. M. *SADABS*, version 2.03; Bruker Analytical X-ray Systems, Inc.: Madison, WI, 2000.

(34) (a) Sheldrick, G. M. *SHELXTL*, version 6.12; Bruker Analytical X-ray Systems, Inc.: Madison, WI, 2000. (b) Sheldrick, G. M. *SHELXT* – Integrated Space-Group and Crystal-Structure Determination. *Acta Crystallogr., Sect. A: Found. Adv*. **2015**, *71*, 3–8.

(35) Dolomanov, O. V.; Bourhis, L. J.; Gildea, R. J.; Howard, J. A. K.; Puschmann, H. *OLEX2*: A Complete Structure Solution, Refinement and Analysis Program. *J. Appl. Crystallogr*. **2009**, *42*, 339–341.

(36) (a) Cole, K. S.; Cole, R. H. Dispersion and Absorption in Dielectrics I. Alternating Current Characteristics. *J. Chem. Phys.* **1941**, *9*, 341–351. (b) Böttcher, C. J. F. *Theory of Electric Polarisation*; Elsevier: Amsterdam, 1952. (c) Aubin, S. M. J.; Sun, Z.; Pardi, L.; Krzystek, J.; Folting, K.; Brunel, L.-C.; Rheingold, A. L.; Christou, G.; Hendrickson, D. N. Reduced Anionic Mn_{12} Molecules with Half-Integer Ground States as Single-Molecule Magnets. *Inorg. Chem*. **1999**, *38*, 5329–5340.

(37) Bain, G. A.; Berry, J. F. Diamagnetic Corrections and Pascal's Constants. *J. Chem. Educ*. **2008**, *85*, 532–536.

(38) Chilton, N. F.; Anderson, R. P.; Turner, L. D.; Soncini, A.; Murray, K. S. PHI: A Powerful New Program for the Analysis of Anisotropic Monomeric and Exchange-Coupled Polynuclear *d*- and *f*-Block Complexes. *J. Comput. Chem.* **2013**, *34*, 1164−1175.

(39) (a) Tregenna-Piggott, P. L. W. *MagProp (part of the NIST DAVE software suite)*, version 2.5; http://www.ncnr.nist.gov/dave, 2008. (b) Azuah, R. T.; Kneller, L. R.; Qiu, Y.; Tregenna-Piggott, P. L. W.; Brown, C. M.; Copley, J. R. D.; Dimeo, R. M. DAVE: A Comprehensive Software Suite for the Reduction, Visualization, and Analysis of Low Energy Neutron Spectroscopic Data. *J. Res. Natl. Inst. Stand. Technol*. **2009**, *114*, 341–358.

(40) Boča, R. *Theoretical Foundations of Molecular Magnetism*; Elsevier: Amsterdam, 1999.

(41) Prisecaru, I. *WMOSS4 Mössbauer Spectral Analysis Software*, version WMOSS4F; www.wmoss.org, 2009–2016.

(42) Baum, A. E.; Park, H.; Wang, D.; Lindeman, S. V.; Fiedler, A. T. Structural, Spectroscopic, and Electrochemical Properties of Nonheme Fe(II)–Hydroquinonate Complexes: Synthetic Models of Hydroquinone Dioxygenases. *Dalton Trans.* **2012**, *41*, 12244–12253.

(43) Park, J. G.; Jeon, I.-R.; Harris, T. D. Electronic Effects of Ligand Substitution on Spin Crossover in a Series of Diiminoquinonoid-Bridged Fe^{II}_2 Complexes. *Inorg. Chem*. **2015**, *54*, 359–369.

(44) Feilchenfeld, H. A Relation Between the Lengths of Single, Double and Triple Bonds. *J. Phys. Chem*. **1959**, *63*, 1346.

(45) Hansch, C.; Leo, A.; Taft, R. W. A Survey of Hammett Substituent Constants and Resonance and Field Parameters. *Chem. Rev*. **1991**, *91*, 165–195.

(46) Drew, M. G. B.; Harding, C. J.; McKee, V.; Morgan, G. G.; Nelson, J. Geometric Control of Manganese Redox State. *J. Chem. Soc., Chem. Commun*. **1995**, 1035−1038.

(47) Li, F.; Chakrabarti, M.; Dong, Y.; Kauffmann, K.; Bominaar, E. L.; Münck, E.; Que, Jr., L. Structural, EPR, and Mössbauer Characterization of (μ-Alkoxo)(μ-Carboxylato)Diiron(II,III) Model Complexes for the Active Sites of Mixed-Valent Diiron Enzymes. *Inorg. Chem*. **2012**, *51*, 2917–2929.

(48) (a) Kawata, S.; Kitagawa, S.; Kumagai, H.; Ishiyama, T.; Honda, K.; Tobita, H.; Adachi, K.; Katada, M. Novel Intercalation Host System Based on Transition Metal (Fe^{2+}, Co^{2+}, Mn^{2+})–Chloranilate Coordination Polymers. Single Crystal Structures and Properties. *Chem. Mater*. **1998**, *10*, 3902–3912. (b) Nagayoshi, K.; Kabir, M. K.; Tobita, H.; Honda, K.; Kawahara, M.; Katada, M.; Adachi, K.; Nishikawa, H.; Ikemoto, I.; Kumagai, H.; Hosokoshi, Y.; Inoue, K.; Kitagawa, S.; Kawata, S. Design of Novel Inorganic–Organic Hybrid Materials Based on Iron-Chloranilate Mononuclear Complexes: Characteristics of Hydrogen-Bond-Supported Layers Toward the Intercalation of Guests. *J. Am. Chem. Soc*. **2003**, *125*, 221–232.

(49) (a) Kessel, S. L.; Hendrickson, D. N. Magnetic Exchange Interactions in Binuclear Transition-Metal Complexes. 16. Binuclear Ferric Complexes From the Reaction of Fe^{II}(salen) with *p*-Quinones. *Inorg. Chem*. **1978**, *17*, 2630–2636. (b) Zall, C. M.; Zherebetskyy, D.; Dzubak, A. L.; Bill, E.; Gagliardi, L.; Lu, C. C. A Combined Spectroscopic and Computational Study of a High-Spin S = 7/2 Diiron Complex with a Short Iron–Iron Bond. *Inorg. Chem*. **2012**, *51*, 728–736. (c) Zadrozny, J. M.; Xiao, D. J.; Long, J. R.; Atanasov, M.; Neese, F.; Grandjean, F.; Long, G. J. Mössbauer Spectroscopy as a Probe of Magnetization Dynamics in the Linear Iron(I) and Iron(II) Complexes $[Fe(C(SiMe_3)_3)_2]^{1-/0}$. *Inorg. Chem*. **2013**, *52*, 13123–13131.

(50) Pfannes, H.-D.; Gonser, U. Goldanskii-Karyagin Effect Versus Preferred Orientations (Texture). *Appl. Phys*. **1973**, *1*, 93–102.

(51) Weisser, F.; Stevens, H.; Klein, J.; van der Meer, M.; Hohloch, S.; Sarkar, B. Tailoring Ru^{II} Pyridine/Triazole Oxygenation Catalysts and Using Photoreactivity to Probe Their Electronic Properties. *Chem. –Eur. J*. **2015**, *21*, 8926–8938.

(52) (a) Mulyana, Y.; Alley, K. G.; Davies, K. M.; Abrahams, B. F.; Moubaraki, B.; Murray, K. S.; Boskovic, C. Dinuclear Cobalt(II) and Cobalt(III) Complexes of Bis-Bidentate Napthoquinone Ligands. *Dalton Trans*. **2014**, *43*, 2499–2511. (b) Atzori, M.; Artizzu, F.;

Marchiò, L.; Loche, D.; Caneschi, A.; Serpe, A.; Deplano, P.; Avarvari, N.; Mercuri, M. L. Switching-On Luminescence in Anilate-Based Molecular Materials. *Dalton Trans*. **2015**, *44*, 15786–15802.

(53) Beni, A.; Dei, A.; Laschi, S.; Rizzitano, M.; Sorace, L. Tuning the Charge Distribution and Photoswitchable Properties of Cobalt–Dioxolene Complexes by Using Molecular Techniques. *Chem. –Eur. J.* **2008**, *14*, 1804–1813.

(54) Barrès, A.-L.; Geng, J.; Bonnard, G.; Renault, S.; Gottis, S.; Mentré, O.; Frayret, C.; Dolhem, F.; Poizot, P. High-Potential Reversible Li Deintercalation in a Substituted Tetrahydroxy-*p*-benzoquinone Dilithium Salt: An Experimental and Theoretical Study. *Chem. –Eur. J.* **2012**, *18*, 8800–8812.

(55) Verter, H. S.; Rogers, J. Preparation of 2,5-Bis(alkylamino)-3,6-dimethoxy-*p*-benzoquinones. *J. Org. Chem.* **1966**, *31*, 987–988.

(56) Huang, Y.; Gao, H.; Twamley, B.; Shreeve, J. M. Highly Dense Nitranilates-Containing Nitrogen-Rich Cations. *Chem. –Eur. J.* **2009**, *15*, 917–923.

(57) (a) Beaumont, P. C.; Edwards, R. L. Constituents of the Higher Fungi. Part X. The Chromenols and Chromanols of Bovinone and a Synthesis of Hydroxy(methylthio)-quinones. *J. Chem. Soc. C* **1971**, 1000–1004. (b) Rosenau, T.; Mereiter, K.; Jäger, C.; Schmid, P.; Kosma, P. Sulfonium Yilides Derived from 2-Hydroxy-benzoquinones: Crystal and Molecular Structure and Their One-Step Conversion into Mannich Bases by Amine *N*-Oxides. *Tetrahedron* **2004**, *60*, 5719–5723.

References for Chapter 8

(1) Kahn, O. *Molecular Magnetism*. VCH: New York, 1993.

(2) Heck, C. *Magnetic Materials and Their Applications*. Butterworth-Heinemann: Oxford, 1974.

(3) Krishnan, K. M. *Fundamentals and Applications of Magnetic Materials*. Oxford University Press: Oxford, 2016.

(4) Spaldin, N. A. *Magnetic Materials: Fundamentals and Applications,* 2nd ed. Cambridge University Press: Cambridge, 2011.

(5) Rocha, A. R.; García-Suárez, V. M.; Bailey, S. W.; Lambert, C. J.; Ferrer, J.; Sanvito, S. Towards Molecular Spintronics. *Nat. Mater*. **2005**, *4*, 335–339.

(6) Bogani, L.; Wernsdorfer, W. Molecular Spintronics Using Single-Molecule Magnets. *Nat. Mater*. **2008**, *7*, 179–186.

(7) Ardavan, A.; Blundell, S. J. Storing Quantum Information in Chemically Engineered Nanoscale Magnets. *J. Mater. Chem*. **2009**, *19*, 1754–1760.

(8) Liu, H.; Zhang, C.; Malissa, H.; Groesbeck, M.; Kavand, M.; McLaughlin, R.; Jamali, S.; Hao, J.; Sun, D.; Davidson, R. A.; Wojcik, L.; Miller, J. S.; Boehme, C.; Vardeny, Z. V. Organic-Based Magnon Spintronics. *Nat. Mater*. **2018**, *17*, 308–312.

(9) Gutfleisch, O.; Willard, M. A.; Brück, E.; Chen, C. H.; Sankar, S. G.; Liu, J. P. Magnetic Materials and Devices for the 21st Century: Stronger, Lighter, and More Energy Efficient. *Adv. Mater*. **2011**, *23*, 821–842.

(10) Orchard, A. F. *Magnetochemistry*. Oxford University Press: Oxford, 2003.

(11) Miller, J. S. Magnetically Ordered Molecule-Based Assemblies. *Dalton Trans*. **2006**, 2742–2749.

(12) *Magnetism: Molecules to Materials*; Miller, J. S., Drillon, M., Eds.; Wiley-VCH: Weinheim; Vol. 1–5.

(13) Miller, J. S. Magnetically Ordered Molecule-Based Materials. *Chem. Soc. Rev*. **2011**, *40*, 3266–3296.

(14) Kurmoo, M. Magnetic Metal–Organic Frameworks. *Chem. Soc. Rev*. **2009**, *38*, 1353–1379.

(15) Demir, S.; Jeon, I.-R.; Long, J. R.; Harris, T. D. Radical Ligand-Containing Single-Molecule Magnets. *Coord. Chem. Rev*. **2015**, *289–290*, 149–176.

(16) Benelli, C.; Gatteschi, D. *Introduction to Molecular Magnetism: From Transition Metals to Lanthanides*, 1st ed. Wiley-VCH: Weinheim, 2015.

(17) Maspoch, D.; Ruiz-Molina, D.; Veciana, J. Old Materials with New Tricks: Multifunctional Open-Framework Materials. *Chem. Soc. Rev*. **2007**, *36*, 770–818.

(18) Espallargas, G. M.; Coronado, E. Magnetic Functionalities in MOFs: From the Framework to the Pore. *Chem. Soc. Rev*. **2018**, *47*, 533–557.

(19) Tokoro, H.; Ohkoshi, S.-I. Novel Magnetic Functionalities of Prussian Blue Analogs. *Dalton Trans*. **2011**, *40*, 6825–6833.

(20) Clemente-León, M.; Coronado, E.; Martí-Gastaldo, C.; Romero, F. M. Multifunctionality in Hybrid Magnetic Materials Based on Bimetallic Oxalate Complexes. *Chem. Soc. Rev*. **2011**, *40*, 473–497.

(21) Coronado, E.; Galán-Mascarós, J. R.; Gómez-García, C. J.; Laukhin, V. Coexistence of Ferromagnetism and Metallic Conductivity in a Molecule-Based Layered Compound. *Nature* **2000**, *408*, 447–449.

(22) Sekine, Y.; Kosaka, W.; Taniguchi, K.; Miyasaka, H. Conductive Molecular Magnets. In *Molecular Magnetic Materials: Concepts and Applications*; Sieklucka, B., Pinkowicz, D., Eds.; Wiley-VCH: Weinheim, 2017, pp. 369–404.

(23) Domb, C. Ising Model. In *Phase Transitions and Critical Phenomena*; Domb, C., Green, M. S., Eds.; Academic Press: London, 1974; Vol. 3, pp. 357–484.

(24) Wang, X.-Y.; Wang, Z.-M.; Gao, S. Constructing Magnetic Molecular Solids by Employing Three-Atom Ligands as Bridges. *Chem. Commun*. **2008**, 281–294.

(25) Pardo, E.; Ruiz-García, R.; Cano, J.; Ottenwaelder, X.; Lescouëzec, R.; Journaux, Y.; Lloret, F.; Julve, M. Ligand Design for Multidimensional Magnetic Materials: A Metallosupramolecular Perspective. *Dalton Trans*. **2008**, 2780–2805.

(26) Caneschi, A.; Gatteschi, D.; Sessoli, R.; Rey, P. Toward Molecular Magnets: The Metal–Radical Approach. *Acc. Chem. Res*. **1989**, *22*, 392–398.

(27) Faust, T. B.; D′Alessandro, D. M. Radicals in Metal–Organic Frameworks. *RSC Adv*. **2014**, *4*, 17498–17512.

(28) Li, J.-R.; Kuppler, R. J.; Zhou, H.-C. Selective Gas Adsorption and Separation in Metal–Organic Frameworks. *Chem. Soc. Rev*. **2009**, *38*, 1477–1504.

(29) Li, B.; Wen, H.-M.; Cui, Y.; Zhou, W.; Qian, G.; Chen, B. Emerging Multifunctional Metal–Organic Framework Materials. *Adv. Mater*. **2016**, *28*, 8819–8860.

(30) Li, J.-R.; Sculley, J.; Zhou, H.-C. Metal–Organic Frameworks for Separations. *Chem. Rev*. **2012**, *112*, 869–932.

(31) Hu, Z.; Deibert, B. J.; Li, J. Luminescent Metal–Organic Frameworks for Chemical Sensing and Explosive Detection. *Chem. Soc. Rev*. **2014**, *43*, 5815–5840.

(32) Fang, X.; Zong, B.; Mao, S. Metal–Organic Framework-Based Sensors for Environmental Contaminant Sensing. *Nano-Micro Lett*. **2018**, *10*, 64.

(33) Kreno, L. E.; Leong, K.; Farha, O. K.; Allendorf, M.; Van Duyne, R. P.; Hupp, J. T. Metal–Organic Framework Materials as Chemical Sensors. *Chem. Rev*. **2012**, *112*, 1105–1125.

(34) Kobayashi, Y.; Jacobs, B.; Allendorf, M. D.; Long, J. R. Conductivity, Doping, and Redox Chemistry of a Microporous Dithiolene-Based Metal−Organic Framework. *Chem. Mater*. **2010**, *22*, 4120–4122.

(35) Talin, A. A.; Centrone, A.; Ford, A. C.; Foster, M. E.; Stavila, V.; Haney, P.; Kinney, R. A.; Szalai, V.; Gabaly, F. E.; Yoon, H. P.; Léonard, F.; Allendorf, M. D. Tunable Electrical Conductivity in Metal-Organic Framework Thin-Film Devices. *Science* **2014**, *343*, 66–69.

(36) Tulchinsky, Y.; Hendon, C. H.; Lomachenko, K. A.; Borfecchia, E.; Melot, B. C.; Hudson, M. R.; Tarver, J. D.; Korzyński, M. D.; Stubbs, A. W.; Kagan, J. J.; Lamberti, C.; Brown, C. M.; Dincă, M. Reversible Capture and Release of Cl_2 and Br_2 with a Redox-Active Metal–Organic Framework. *J. Am. Chem. Soc*. **2017**, *139*, 5992–5997.

(37) Nidamanuri, N.; Saha, S. Metal-Organic Frameworks with Tunable Electrical and Optical Properties. In *Monographs in Supramolecular Chemistry*; Banerjee, R., Ed.; The Royal Society of Chemistry: Cambridge, 2017; Vol. 22, pp. 217–246.

(38) Brozek, C. K.; Dincă, M. Cation Exchange at the Secondary Building Units of Metal–Organic Frameworks. *Chem. Soc. Rev*. **2014**, *43*, 5456–5467.

(39) Evans, J. D.; Sumby, C. J.; Doonan, C. J. Post-Synthetic Metalation of Metal–Organic Frameworks. *Chem. Soc. Rev*. **2014**, *43*, 5933–5951.

(40) Deria, P.; Mondloch, J. E.; Karagiaridi, O.; Bury, W.; Hupp, J. T.; Farha, O. K. Beyond Post-Synthesis Modification: Evolution of Metal–Organic Frameworks via Building Block Replacement. *Chem. Soc. Rev*. **2014**, *43*, 5896–5912.

(41) Cohen, S. M. The Postsynthetic Renaissance in Porous Solids. *J. Am. Chem. Soc*. **2017**, *139*, 2855–2863.

(42) Bosch, M.; Yuan, S.; Rutledge, W.; Zhou, H.-C. Stepwise Synthesis of Metal-Organic Frameworks. *Acc. Chem. Res*. **2017**, *50*, 857–865.

(43) Liu, L.; Li, L.; DeGayner, J. A.; Winegar, P. H.; Fang, Y.; Harris, T. D. Harnessing Structural Dynamics in a 2D Manganese−Benzoquinoid Framework to Dramatically Accelerate Metal Transport in Diffusion Limited Metal Exchange Reactions. *J. Am. Chem. Soc*. **2018**, *140*, 11444–11453.

(44) Kim, M.; Cahill, J. F.; Su, Y.; Prather, K. A.; Cohen, S. M. Postsynthetic Ligand Exchange as a Route to Functionalization of 'Inert' Metal–Organic Frameworks. *Chem. Sci*. **2012**, *3*, 126–130.

(45) Liu, C.; Luo, T.-Y.; Feura, E. S.; Zhang, C.; Rosi, N. L. Orthogonal Ternary Functionalization of a Mesoporous Metal–Organic Framework via Sequential Postsynthetic Ligand Exchange. *J. Am. Chem. Soc*. **2015,** *137*, 10508–10511.

(46) Miller, J. S.; Epstein, A. J. Organic and Organometallic Molecular Magnetic Materials—Designer Magnets. *Angew. Chem. Int. Ed. Engl*. **1994**, *33*, 385–415.

(47) Balanda, M. AC Suceptibility Studies of Phase Transitions and Magnetic Relaxation: Conventional, Molecular and Low-Dimensional Magnets. *Acta Phys. Pol. A* **2013**, *124*, 964–976.

(48) Mydosh, J. A. *Spin Glasses: An Experimental Introduction*. Taylor & Francis: Washington, D. C., 1993.

(49) O′Keeffe, M. Design of MOFs and Intellectual Content in Reticular Chemistry: A Personal View. *Chem. Soc. Rev*. **2009**, *38*, 1215–1217.

(50) Batten, S. R.; Champness, N. R.; Chen, X.-M.; Garcia-Martinez, J.; Kitagawa, S.; Öhrström, L.; O′Keeffe, M.; Suh, M. P.; Reedijk, J. Coordination Polymers, Metal–Organic Frameworks and the Need for Terminology Guidelines. *Cryst. Eng. Commun*. **2012**, *14*, 3001–3004.

(51) Seth, S.; Matzger, A. J. Metal−Organic Frameworks: Examples, Counterexamples, and an Actionable Definition. *Cryst. Growth Des*. **2017**, *17*, 4043–4048.

(52) Batten, S. R.; Champness, N. R.; Chen, X.-M.; Garcia-Martinez, J.; Kitagawa, S.; Öhrström, L.; O′Keeffe, M.; Suh, M. P.; Reedijk, J. Terminology of Metal–Organic Frameworks and Coordination Polymers (IUPAC Recommendations 2013). *Pure Appl. Chem*. **2013**, *85*, 1715–1724.

(53) Rowsell, J. L. C.; Yaghi, O. M. Metal–Organic Frameworks: A New Class of Porous Materials. *Micropor. Mesopor. Mater*. **2004**, *73*, 3–14.

(54) Tranchemontagne, D. J.; Mendoza-Cortés, J. L.; O′Keeffe, M.; Yaghi, O. M. Secondary Building Units, Nets and Bonding in the Chemistry of Metal–Organic Frameworks. *Chem. Soc. Rev*. **2009**, *38*, 1257–1283.

(55) Rao, C. N. R.; Cheetham, A. K.; Thirumurugan, A. Hybrid Inorganic–Organic Materials: A New Family in Condensed Matter Physics. *J. Phys.: Condens. Matter* **2008**, *20*, 083202.

(56) Humphrey, S. M.; Wood, P. T. Multiple Areas of Magnetic Bistability in the Topological Ferrimagnet $[Co_3(NC_5H_3(CO_2)_2\text{-}2,5)_2(\mu_3\text{-}OH)_2(OH_2)_2]$. *J. Am. Chem. Soc*. **2004**, *126*, 13236–13237.

(57) Zhuang, W.; Sun, H.; Xu, H.; Wang, Z.; Gao, S.; Jin, L. Reversible De-/Resolvation and Accompanied Magnetism Modulation in a Framework of Topologically Ferrimagnetic $[Co_3(\mu_3\text{-}OH)_2]_n$ Chains Linked by a V-Shaped Ligand 4,4′-Dicarboxybiphenyl Sulfone. *Chem. Commun*. **2010**, *46*, 4339–4341.

(58) Hu, S.; Yun, L.; Zheng, Y.-Z.; Lan, Y.-H.; Powell, A. K.; Tong, M.-L. Ferrimagnetic $[Co^{II}_3(\mu_3\text{-}OH)_2(RCO_2)_4]$ Chains Embedded in a Laminar Hybrid Material Exhibiting Single-Chain Magnet Behaviour. *Dalton Trans*. **2009**, 1897–1900.

(59) Kurmoo, M. Ferrimagnetism in Dicarboxylate-Bridged Cobalt Hydroxide Layers. *J. Mater. Chem*. **1999**, *9*, 2595–2598.

(60) Kurmoo, M. Ferrimagnetic and Metamagnetic Layered Cobalt(II)-Hydroxides: First Observation of a Coercive Field Greater than 5 T. *Phil. Trans. R. Soc. Lond. A* **1999**, *357*, 3041–3061.

(61) Lovett, B. W.; Blundell, S. J.; Kumagai, H.; Kurmoo, M. Cobalt(II)-Hydroxide Terephthalate - A Metamagnet with a Large Coercive Field. *Synth. Met*. **2001**, *121*, 1814–1815.

(62) Kurmoo, M.; Kumagai, H.; Green, M. A.; Lovett, B. W.; Blundell, S. J.; Ardavan, A.; Singleton, J. Two Modifications of Layered Cobaltous Terephthalate: Crystal Structures and Magnetic Properties. *J. Solid State Chem*. **2001**, *159*, 343–351.

(63) Kurmoo, M.; Kumagai, H.; Hughes, S. M.; Kepert, C. J. Reversible Guest Exchange and Ferrimagnetism (T_C = 60.5 K) in a Porous Cobalt(II)−Hydroxide Layer Structure Pillared with *trans*-1,4-Cyclohexanedicarboxylate. *Inorg. Chem*. **2003**, *42*, 6709–6722.

(64) Feyerherm, R.; Loose, A.; Rabu, P.; Drillon, M. Neutron Diffraction Studies of Canted Antiferromagnetic Ordering in Co^{II} Hydroxide Terephtalate. *Solid State Sci*. **2003**, *5*, 321–326.

(65) Barthelet, K.; Adil, K.; Millange, F.; Serre, C.; Riou, D.; Férey, G. Synthesis, Structure Determination and Magnetic Behaviour of the First Porous Hybrid Oxyfluorinated Vanado(III)carboxylate: MIL-71 or $V^{III}_2(OH)_2F_2\{O_2C\text{-}C_6H_4\text{-}CO_2\}\cdot H_2O$. *J. Mater. Chem*. **2003**, *13*, 2208–2212.

(66) Mesbah, A.; Carton, A.; Aranda, L.; Mazet, T.; Porcher, F.; François, M. *Ab-Initio* Crystal Structure of Hydroxy Adipate of Nickel and Hydroxy Subarate of Nickel and Cobalt from Synchrotron Powder Diffraction and Magnetic Properties. *J. Solid State Chem*. **2008**, *181*, 3229–3235.

(67) Mesbah, A.; Sibille, R.; Mazet, T.; Malaman, B.; Lebègue, S.; François, M. Magnetism in the $(Co_{1-x}Fe_x)_2(OH)_2(C_8H_4O_4)$ Solid Solutions: A Combined Neutron Diffraction and Magnetic Measurements Study. *J. Mater. Chem*. **2010**, *20*, 9386–9391.

(68) Sibille, R.; Mesbah, A.; Mazet, T.; Malaman, B.; Capelli, S.; François, M. Magnetic Measurements and Neutron Diffraction Study of the Layered Hybrid Compounds $Mn(C_8H_4O_4)(H_2O)_2$ and $Mn_2(OH)_2(C_8H_4O_4)$. *J. Solid State Chem*. **2012**, *186*, 134–141.

(69) Price, D. J.; Lionti, F.; Ballou, R.; Wood, P. T.; Powell, A. K. Large Metal Clusters and Lattices with Analogues to Biology. *Phil. Trans. R. Soc. Lond. A* **1999**, *357*, 3099–3118.

(70) Rujiwatra, A.; Kepert, C. J.; Rosseinsky, M. J. The Organo-Pillared Porous Magnetic Framework $Co_4(SO_4)(OH)_6(H_2NC_2H_4NH_2)_{0.5}\cdot 3H_2O$. *Chem. Commun*. **1999**, 2307–2308.

(71) Rujiwatra, A.; Kepert, C. J.; Claridge, J. B.; Rosseinsky, M. J.; Kumagai, H.; Kurmoo, M. Layered Cobalt Hydroxysulfates with Both Rigid and Flexible Organic Pillars: Synthesis, Structure, Porosity, and Cooperative Magnetism. *J. Am. Chem. Soc*. **2001**, *123*, 10584–10594.

(72) Stone, K. H.; Stephens, P. W.; McConnell, A. C.; Shurdha, E.; Pokhodnya, K. I.; Miller, J. S. $Mn^{II}(TCNE)_{3/2}(I_3)_{1/2}$—A 3D Network-Structured Organic-Based Magnet and Comparison to a 2D Analog. *Adv. Mater*. **2010**, *22*, 2514–2519.

(73) Lapidus, S. H.; McConnell, A. C.; Stephens, P. W.; Miller, J. S. Structure and Magnetic Ordering of a 2-D $Mn^{II}(TCNE)I(OH_2)$ (TCNE = Tetracyanoethylene) Organic-Based Magnet (T_c = 171 K). *Chem. Commun*. **2011**, *47*, 7602–7604.

(74) Olson, C. S.; Gangopadhyay, S.; Hoang, K.; Alema, F.; Kilina, S.; Pokhodnya, K. I. Magnetic Exchange in Mn^{II}[TCNE] (TCNE = Tetracyanoethylene) Molecule-Based Magnets with Two- and Three-Dimensional Magnetic Networks. *J. Phys. Chem. C* **2015**, *119*, 25036–25046.

(75) Cheetham, A. K.; Rao, C. N. R.; Feller, R. K. Structural Diversity and Chemical Trends in Hybrid Inorganic–Organic Framework Materials. *Chem. Commun*. **2006**, 4780–4795.

(76) Candela, G. A.; Swartzendruber, L. J.; Miller, J. S.; Rice, M. J. Metamagnetic Properties of One-Dimensional Decamethylferrocenium 7,7,8,8-Tetracyano-*p*-quinodimethanide (1:1): $[Fe(\eta^5\text{-}C_5Me_5)_2]^{+\bullet}(TCNQ)^{-\bullet}$. *J. Am. Chem. Soc*. **1979**, *101*, 2755–2756.

(77) Miller, J. S.; Calabrese, J. C.; Epstein, A. J.; Bigelow, R. W.; Zhang, J. H.; Reiff, W. M. Ferromagnetic Properties of One-dimensional Decamethylferrocenium Tetracyanoethylenide (1 : 1): $[Fe(\eta^5\text{-}C_5Me_5)_2]^{+\bullet}[TCNE]^{-\bullet}$. *J. Chem. Soc., Chem. Commun*. **1986**, 1026–1028.

(78) Miller, J. S.; Calabrese, J. C.; Rommelmann, H.; Chittipeddi, S. R.; Zhang, J. H.; Reiff, W. M.; Epstein, A. J. Ferromagnetic Behavior of $[Fe(C_5Me_5)_2]^{+\bullet}[TCNE]^{-\bullet}$. Structural and Magnetic Characterization of Decamethylferrocenium Tetracyanoethenide,

$[Fe(C_5Me_5)_2]^{\bullet+}[TCNE]^{\bullet+}\cdot MeCN$, and Decamethylferrocenium Pentacyanopropenide, $[Fe(C_5Me_5)_2]^{\bullet+}[C_3(CN)_5]^{-}$. *J. Am. Chem. Soc.* **1987**, *109*, 769–781.

(79) Chittipeddi, S.; Cromack, K. R.; Miller, J. S.; Epstein, A. J. Ferromagnetism in Molecular Decamethylferrocenium Tetracyanoethenide (DMeFc TCNE). *Phys. Rev. Lett*. **1987**, *58*, 2695–2698.

(80) Miller, J. S.; O′Hare, D. M.; Chakraborty, A.; Epstein, A. J. Ferromagnetically Coupled Linear Electron-Transfer Complexes. Structural and Magnetic Characterization of $[Cr(\eta^6\text{-}C_6Me_xH_{6-x})_2][TCNE]$ (x = 0, 3, 6) and S = 0 $[TCNE]_2^{2-}$. *J. Am. Chem. Soc.* **1989**, *111*, 7853–7860.

(81) Yee, G. T.; Manriquez, J. M.; Dixon, D. A.; McLean, R. S.; Groski, D. M.; Flippen, R. B.; Narayan, K. S.; Epstein, A. J.; Miller, J. S. Decamethylmanganocenium Tetracyanoethenide, $[Mn(C_5Me_5)_2]^{\bullet\bullet+}[TCNE]^{\bullet-}$–A Molecular Ferromagnet with an 8.8 K T_c. *Adv. Mater*. **1991**, *3*, 309–311.

(82) Miller, J. S.; Epstein, A. J. Molecule-Based Magnets—An Overview. *MRS Bull*. **2000**, 21–30.

(83) Manriquez, J. M.; Yee, G. T.; McLean, R. S.; Epstein, A. J.; Miller, J. S. A Room-Temperature Molecular/Organic-Based Magnet. *Science* **1991**, *252*, 1415–1417.

(84) Zhou, P.; Morin, B. G.; Miller, J. S.; Epstein, A. J. Magnetization and Static Scaling of the High-T_c Disordered Molecular-Based Magnet V(tetracyanoethylene)$_x\cdot y(CH_3CN)$ with x ~ 1.5 and y ~ 2. *Phys. Rev. B* **1993**, *48*, 1325–1328.

(85) Du, G.; Joo, J.; Epstein, A. J.; Miller, J. S. Anomalous Charge Transport Phenomena in Molecular-Based Magnet V(TCNE)$_x\cdot y$(solvent). *J. Appl. Phys*. **1993**, *73*, 6566–6568.

(86) Zhou, P.; Long, S. M.; Miller, J. S.; Epstein, A. J. Static Magnetic Properties and Critical Behavior of V(TCNE)$_x\cdot y(C_4H_8O)$, a High T_c Molecular-Based Disordered Magnet. *Phys. Lett. A* **1993**, *181*, 71–79.

(87) Zhang, J.; Ensling, J.; Ksenofontov, V.; Gütlich, P.; Epstein, A. J.; Miller, J. S. $[M^{II}(tcne)_2]\cdot xCH_2Cl_2$ (M = Mn, Fe, Co, Ni) Molecule-Based Magnets with T_c Values Above 100 K and Coercive Fields up to 6500 Oe. *Angew. Chem. Int. Ed*. **1998**, *37*, 657–660.

(88) Pokhodnya, K. I.; Petersen, N.; Miller, J. S. Iron Pentacarbonyl as a Precursor for Molecule-Based Magnets: Formation of Fe[TCNE]$_2$ (T_c = 100 K) and Fe[TCNQ]$_2$ (T_c = 35 K) Magnets. *Inorg. Chem*. **2002**, *41*, 1996–1997.

(89) Pokhodnya, K. I.; Vickers, E. B.; Bonner, M.; Epstein, A. J.; Miller, J. S. Solid Solution $V_xFe_{1-x}[TCNE]_2 \cdot zCH_2Cl_2$ Room-Temperature Magnets. *Chem. Mater*. **2004**, *16*, 3218–3223.

(90) Clérac, R.; O′Kane, S.; Cowen, J.; Ouyang, X.; Heintz, R.; Zhao, H.; Bazile, M. J.; Dunbar, K. R. Glassy Magnets Composed of Metals Coordinated to 7,7,8,8-Tetracyanoquinodimethane: M(TCNQ)$_2$ (M = Mn, Fe, Co, Ni). *Chem. Mater*. **2003**, *15*, 1840–1850.

(91) Vickers, E. B.; Selby, T. D.; Thorum, M. S.; Taliaferro, M. L.; Miller, J. S. Vanadium 7,7,8,8-Tetracyano-*p*-quinodimethane (V[TCNQ]$_2$)-Based Magnets. *Inorg. Chem*. **2004**, *43*, 6414–6420.

(92) Vickers, E. B.; Giles, I. D.; Miller, J. S. M[TCNQ]$_y$-Based Magnets (M = Mn, Fe, Co, Ni; TCNQ = 7,7,8,8-Tetracyano-*p*-quinodimethane). *Chem. Mater*. **2005**, *17*, 1667–1672.

(93) Miller, J. S.; Calabrese, J. C.; McLean, R. S.; Epstein, A. J. *meso*-(Tetraphenylporphinato)manganese(III)-tetracyanoethenide, $[Mn^{III}TPP]^{\cdot+}[TCNE]^{\bullet-}$. A New Structure-Type Linear-Chain Magnet with a T_c of 18 K. *Adv. Mater*. **1992**, *4*, 498–501.

(94) Brinckerhoff, W. B.; Morin, B. G.; Brandon, E. J.; Miller, J. S.; Epstein, A. J. Magnetization and Dynamics of Reentrant Ferrimagnetic Spin-Glass $[MnTPP]^{\cdot+}[TCNE]^{\bullet-} \cdot 2PhMe$. *J. Appl. Phys*. **1996**, *79*, 6147–6149.

(95) Brandon, E. J.; Rogers, R. D.; Burkhart, B. M.; Miller, J. S. The Structure and Ferrimagnetic Behavior of *meso*-Tetraphenylporphinatomanganese(III) Tetrachloro-1,4-Benzoquinonide, $[Mn^{III}TPP]^{+}[QCl_4]^{\bullet-} \cdot PhMe$: Evidence of a Quinoidal Structure for $[QCl_4]^{\bullet-}$. *Chem. –Eur. J*. **1998**, *4*, 1938–1943.

(96) Rittenberg, D. K.; Miller, J. S. Observation of Magnetic Ordering as High as 28 K for *meso*-Tetrakis(4-halophenyl)porphinatomanganese(III) Tetracyanoethenide, [MnTXPP][TCNE] (X = F, Br, I). *Inorg. Chem*. **1999**, *38*, 4838–4848.

(97) Rittenberg, D. K.; Sugiura, K.; Sakata, Y.; Mikami, S.; Epstein, A. J.; Miller, J. S. Large Coercivity and High Remanent Magnetization Organic-Based Magnets. *Adv. Mater*. **2000**, *12*, 126–130.

(98) Caneschi, A.; Gatteschi, D.; Ray, P.; Sessoli, R. Structure and Magnetic Properties of Ferrimagnetic Chains Formed by Manganese(II) and Nitronyl Nitroxides. *Inorg. Chem*. **1988**, *27*, 1756–1761.

(99) Caneschi, A.; Gatteschi, D.; Renard, J. P.; Rey, P.; Sessoli, R. Ferromagnetic Phase Transitions of Two One-Dimensional Ferrimagnets Formed by Manganese(II) and Nitronyl Nitroxides Cis Octahedrally Coordinated. *Inorg. Chem*. **1989**, *28*, 3314–3319.

(100) Caneschi, A.; Gatteschi, D.; Renard, J. P.; Rey, P.; Sessoli, R. Magnetic Coupling in Zero- and One-Dimensional Magnetic Systems Formed by Nickel(II) and Nitronyl Nitroxides. Magnetic Phase Transition of a Ferrimagnetic Chain. *Inorg. Chem*. **1989**, *28*, 2940–2944.

(101) Caneschi, A.; Gatteschi, D.; Rey, P.; Sessoli, R. Structure and Magnetic Ordering of a Ferrimagnetic Helix Formed by Manganese(II) and a Nitronyl Nitroxide Radical. *Inorg. Chem*. **1991**, *30*, 3936–3941.

(102) Caneschi, A.; Gatteschi, D.; Le Lirzin, A. Crystal Structure and Magnetic Properties of a New Ferrimagnetic Chain Containing Manganese(II) and a Nitronyl-Nitroxide Radical. *J. Mater. Chem*. **1994**, *4*, 319–326.

(103) Ise, T.; Ishida, T.; Hashizume, D.; Iwasaki, F.; Nogami, T. Ferro- and Ferrimagnetic Chains of hin-Bridged Copper(II) and Manganese(II) and hnn-Bridged Manganese(II) Complexes (hin = 4,4,5,5-Tetramethylimidazolin-1-oxyl; hnn = 4,4,5,5-Tetramethylimidazolin-1-oxyl 3-Oxide). *Inorg. Chem*. **2003**, *42*, 6106–6113.

(104) Numata, Y.; Inoue, K.; Baranov, N.; Kurmoo, M.; Kikuchi, K. Field-Induced Ferrimagnetic State in a Molecule-Based Magnet Consisting of a Co^{II} Ion and a Chiral Triplet Bis(nitroxide) Radical. *J. Am. Chem. Soc*. **2007**, *129*, 9902–9909.

(105) Ishi, N.; Okamura, Y.; Chiba, S.; Nogami, T.; Ishida, T. Giant Coercivity in a One-Dimensional Cobalt-Radical Coordination Magnet. *J. Am. Chem. Soc*. **2008**, *130*, 24–25.

(106) Benelli, C.; Caneschi, A.; Gatteschi, D.; Sessoli, R. Magnetic Ordering in a Molecular Material Containing Dysprosium(III) and a Nitronyl Nitroxide. *Adv. Mater*. **1992**, *4*, 504–505.

(107) Benelli, C.; Caneschi, A.; Gatteschi, D.; Sessoli, R. Magnetic Properties and Phase Transitions in Molecular Based Materials Containing Rare Earth Ions and Organic Radicals. *J. Appl. Phys*. **1993**, *73*, 5333–5337.

(108) Benelli, C.; Caneschi, A.; Gatteschi, D.; Sessoli, R. Magnetic Interactions and Magnetic Ordering in Rare Earth Metal Nitronyl Nitroxide Chains. *Inorg. Chem*. **1993**, *32*, 4797–4801.

(109) Liu, R.; Ma, Y.; Yang, P.; Song, X.; Xu, G.; Tang, J.; Li, L.; Liao, D.; Yan, S. Dynamic Magnetic Behavior and Magnetic Ordering in One-Dimensional Tb-Nitronyl Nitroxide Radical Chain. *Dalton Trans*. **2010**, *39*, 3321–3325.

(110) Liu, R.; Zhang, C.; Mei, X.; Hu, P.; Tian, H.; Li, L.; Liao, D.; Sutter, J.-P. Slow Magnetic Relaxation and Antiferromagnetic Ordering in a One Dimensional Nitronyl Nitroxide–Tb(III) Chain. *New J. Chem*. **2012**, *36*, 2088–2093.

(111) Tian, H.; Wang, X.; Mei, X.; Liu, R.; Zhu, M.; Zhang, C.; Ma, Y.; Li, L.; Liao, D. Magnetic Relaxation in Tb^{III} Magnetic Chains with Nitronyl Nitroxide Radical Bridges That Undergo 3D Antiferromagnetic Ordering. *Eur. J. Inorg. Chem*. **2013**, 1320–1325.

(112) Hu, P.; Wang, X.; Ma, Y.; Wang, Q.; Li, L.; Liao, D. A New Family of Ln–Radical Chains (Ln = Nd, Sm, Gd, Tb and Dy): Synthesis, Structure, and Magnetic Properties. *Dalton Trans*. **2014**, *43*, 2234–2243.

(113) Pei, Y.; Verdaguer, M.; Kahn, O; Sletten, J.; Renard, J.-P. Ferromagnetic Transition in a Bimetallic Molecular System. *J. Am. Chem. Soc*. **1986**, *108*, 7428–7430.

(114) Stumpf, H. O.; Pei, Y.; Ouahab, L.; Le Berre, F.; Codjovi, E.; Kahn, O. Crystal Structure and Metamagnetic Behavior of the Ferrimagnetic Chain Compound $MnCu(opba)(H_2O)_2\cdot$DMSO (opba = *o*-Phenylenebis(oxamato) and DMSO = Dimethyl Sulfoxide). *Inorg. Chem*. **1993**, *32*, 5687–5691.

(115) Baron, V.; Gillon, B.; Sletten, J.; Mathonière, C.; Codjovi, E.; Kahn, O. Interchain Interactions and Three-Dimensional Magnetic Ordering in Mn(II)Cu(II) Chain Compounds; Crystal Structure and Metamagnetic Properties of $MnCu(pbaOH)(H_2O)_3\cdot 2H_2O$, with pbaOH = 2-Hydroxo-1,3-propylenebis(oxamato). *Inorg. Chim. Acta* **1995**, *235*, 69–76.

(116) Turner, S.; Kahn, O.; Rabardel, L. Crossover Between Three-Dimensional Antiferromagnetic and Ferromagnetic States in Co(II)Cu(II) Ferrimagnetic Chain Compounds. A New Molecular-Based Magnet with T_c = 38 K and a Coercive Field of 5.66 × 10^3 Oe. *J. Am. Chem. Soc*. **1996**, *118*, 6428–6432.

(117) Śledzińska, I.; Murasik, A.; Fischer, P. The Magnetic Structure of α-$CoC_2O_4\cdot 2D_2O$ Investigated by Means of Neutron Diffraction. *J. Phys. C: Solid State Phys*. **1988**, *21*, 5273–5285.

(118) Lukin, J. A.; Simizu, S.; VanderVen, N. S.; Friedberg, S. A. Low-Dimensional Magnetic Behavior of α-$CoC_2O_4 \cdot 2H_2O$. *J. Magn. Magn. Mater*. **1995**, *140–144*, 1669–1670.

(119) Castillo, O.; Luque, A.; Román, P.; Lloret, F.; Julve, M. Syntheses, Crystal Structures, and Magnetic Properties of One-Dimensional Oxalato-Bridged Co(II), Ni(II), and Cu(II) Complexes with *n*-Aminopyridine (*n* = 2–4) as Terminal Ligand. *Inorg. Chem*. **2001**, *40*, 5526–5535.

(120) Hursthouse, M. B.; Light, M. E.; Price, D. J. One-Dimensional Magnetism in Anhydrous Iron and Cobalt Ternary Oxalates with Rare Trigonal-Prismatic Metal Coordination Environment. *Angew. Chem. Int. Ed*. **2004**, *43*, 472–475.

(121) Duan, Z.; Zhang, Y.; Zhang, B.; Zhu, D. $Co(C_2O_4)(HO(CH_2)_3OH)$: An Antiferromagnetic Neutral Zigzag Chain Compound Showing Long-Range Ordering of Spin Canting. *Inorg. Chem*. **2008**, *47*, 9152–9154.

(122) Gavrilenko, K. S.; Cador, O.; Bernot, K.; Rosa, P.; Sessoli, R.; Golhen, S.; Pavlishchuk, V. V.; Ouahab, L. Delicate Crystal Structure Changes Govern the Magnetic Properties of 1D Coordination Polymers Based on 3d Metal Carboxylates. *Chem. –Eur. J*. **2008**, *14*, 2034–2043.

(123) Oka, Y.; Inoue, K.; Kumagai, H.; Kurmoo, M. Long-Range Magnetic Ordering at 5.5 K for Cobalt(II)−Hydroxide Diamond Chains Isolated by 17 Å with α-Phenylcinnamate. *Inorg. Chem*. **2013**, *52*, 2142–2149.

(124) Fidler, J.; Schrefl, T.; Hoefinger, S.; Hajduga, M. Recent Developments in Hard Magnetic Bulk Materials. *J. Phys.: Condens. Matter* **2004**, *16*, S455–S470.

(125) Nakatani, K.; Bergerat, P.; Codjovi, E.; Mathonière, C.; Pei, Y.; Kahn, O. Optimization of a Molecular-Based Magnet $MnCu(pbaOH)(H_2O)_2$ (pbaOH = 2-Hydroxy- l,3-propanediylbis(oxamato)) with T_c = 30 K. *Inorg. Chem*. **1991**, *30*, 3978–3980.

(126) Wang, M.; Gou, X.; Shi, W.; Cheng, P. Single-Chain Magnets Assembled in Cobalt(II) Metal–Organic Frameworks. *Chem. Commun*. **2019**, *55*, 11000–11012.

(127) Ouellette, W.; Prosvirin, A. V.; Whitenack, K.; Dunbar, K. R.; Zubieta, J. A Thermally and Hydrolytically Stable Microporous Framework Exhibiting Single-Chain Magnetism: Structure and Properties of $[Co_2(H_{0.67}bdt)_3] \cdot 20H_2O$. *Angew. Chem. Int. Ed*. **2009**, *48*, 2140–2143.

(128) Wu, Y.; Cheng, S.; Liu, J.; Yang, G.; Wang, Y.-Y. New Porous Co(II)-Based Metal-Organic Framework Including 1D Ferromagnetic Chains with Highly Selective Gas Adsorption and Slow Magnetic Relaxation. *J. Solid State Chem*. **2019**, *276*, 226–231.

(129) Cheng, X.-N.; Zhang, W.-X.; Zheng, Y.-Z.; Chen, X.-M. The Slow Magnetic Relaxation Observed in a Mixed Carboxylate/Hydroxide-Bridged Compound $[Co_2Na(4\text{-cpa})_2(\mu_3\text{-}OH)(H_2O)]_\infty$ Featuring Magnetic Δ-Chains. *Chem. Commun*. **2006**, 3603–3605.

(130) Zheng, Y.-Z.; Tong, M.-L.; Zhang, W.-X.; Chen, X.-M. Assembling Magnetic Nanowires into Networks: A Layered Co^{II} Carboxylate Coordination Polymer Exhibiting Single-Chain-Magnet Behavior. *Angew. Chem. Int. Ed*. **2006**, *45*, 6310–6314.

(131) Chen, J.; Sekine, Y.; Komatsumaru, Y.; Hayami, S.; Miyasaka, H. Thermally Induced Valence Tautomeric Transition in a Two-Dimensional Fe-Tetraoxolene Honeycomb Network. *Angew. Chem. Int. Ed*. **2018**, *57*, 12043–12047.

(132) Verdaguer, M.; Bleuzen, A.; Marvaud, V.; Vaissermann, J.; Seuleiman, M.; Desplanches, C.; Scuiller, A.; Train, C.; Garde, R.; Gelly, G.; Lomenech, C.; Rosenman, I.; Veillet, P.; Cartier, C.; Villain, F. Molecules to Build Solids: High T_C Molecule-Based Magnets by Design and Recent Revival of Cyano Complexes Chemistry. *Coord. Chem. Rev*. **1999**, *190–192*, 1023–1047.

(133) Garde, R.; Villain, F.; Verdaguer, M. Molecule-Based Room-Temperature Magnets: Catalytic Role of V(III) in the Synthesis of Vanadium–Chromium Prussian Blue Analogues. *J. Am. Chem. Soc*. **2002**, *124*, 10531–10538.

(134) Holmes, S. M.; Girolami, G. S. Sol–Gel Synthesis of $KV^{II}[Cr^{III}(CN)_6]\cdot 2H_2O$: A Crystalline Molecule-Based Magnet with a Magnetic Ordering Temperature above 100 °C. *J. Am. Chem. Soc*. **1999**, *121*, 5593–5594.

(135) Sieklucka, B.; Podgajny, R.; Pinkowicz, D.; Nowicka, B.; Korzeniak, T.; Balanda, M.; Wasiutyński, T.; Pelka, R.; Makarewicz, M.; Czapla, M.; Rams, M.; Gawei, B.; Lasocha, W. Towards High T_c Octacyanometalate-Based Networks. *Cryst. Eng. Commun*. **2009**, *11*, 2032–2039.

(136) Podgajny, R.; Pinkowicz, D.; Korzeniak, T.; Nitek, W.; Rams, M.; Sieklucka, B. High T_c Ferrimagnetic Organic–Inorganic Hybrid Materials with Mn^{II}–L–Mn^{II} and Mn^{II}–NC–Nb^{IV} Linkages (L = Pyrazine, Pyrazine-*N*,*N′*-dioxide, Bipyrimidine). *Inorg. Chem*. **2007**, *46*, 10416–10425.

(137) Toma, L. M.; Ruiz-Pérez, C.; Pasán, J.; Wernsdorfer, W.; Lloret, F.; Julve, M. Molecular Engineering to Control the Magnetic Interaction Between Single-Chain Magnets Assembled in a Two-Dimensional Network. *J. Am. Chem. Soc*. **2012**, *134*, 15265–15268.

(138) Manson, J. L.; Incarvito, C. D.; Rheingold, A. L.; Miller, J. S. Structure and Magnetic Properties of $Mn^{II}[N(CN)_2]_2$(pyrazine). An Antiferromagnet with an Interpenetrating 3-D Network Structure. *J. Chem. Soc., Dalton Trans*. **1998**, 3705–3706.

(139) Kmety, C. R.; Manson, J. L.; Huang, Q.; Lynn, J. W.; Erwin, R. W.; Miller, J. S.; Epstein, A. J. Collinear Ferromagnetism and Spin Orientation in the Molecule-Based Magnets $M[N(CN)_2]_2$ (*M* = Co, Ni). *Phys. Rev. B* **1999**, *60*, 60–63.

(140) Kmety, C. R.; Huang, Q.; Lynn, J. W.; Erwin, R. W.; Manson, J. L.; McCall, S.; Crow, J. E.; Stevenson, K. L.; Miller, J. S.; Epstein, A. J. Noncollinear Antiferromagnetic Structure of the Molecule-Based Magnet $Mn[N(CN)_2]_2$. *Phys. Rev. B* **2000**, *62*, 5576–5588.

(141) Kusaka, T.; Ishida, T.; Hashizume, D.; Iwasaki, F.; Nogami, T. Low-Temperature Magnets $M[N(CN)_2]_2$.(pyrimidine) (M = Fe and Co) with a 3-D Network. *Chem. Lett*. **2000**, *29*, 1146–1147.

(142) Yeung, W.-F.; Gao, S.; Wong, W.-T.; Lau, T.-C. Antiferromagnetic Ordering in a Novel Five-Connected 3D Polymer $\{Cu_2(2,5\text{-}Me_2pyz)[N(CN)_2]_4\}_n$ (2,5-Me_2pyz = 2,5-Dimethylpyrazine). *New J. Chem*. **2002**, *26*, 523–525.

(143) Manson, J. L.; Ressouche, E.; Miller, J. S. Spin Frustration in $M^{II}[C(CN)_3]_2$ (M = V, Cr). A Magnetism and Neutron Diffraction Study. *Inorg. Chem*. **2000**, *39*, 1135–1141.

(144) Feyerherm, R.; Loose, A.; Manson, J. L. Unusual Magnetic-Field Dependence of Partially Frustrated Triangular Ordering in Manganese Tricyanomethanide. *J. Phys.: Condens. Matter* **2003**, *15*, 663–673.

(145) Feyerherm, R.; Loose, A.; Landsgesell, S.; Manson, J. L. Magnetic Ordering in Iron Tricyanomethanide. *Inorg. Chem*. **2004**, *43*, 6633–6639.

(146) Dechambenoit, P.; Long, J. R. Microporous Magnets. *Chem. Soc. Rev*. **2011**, *40*, 3249–3265.

(147) Wang, X.-Y.; Li, B.-L.; Zhu, X.; Gao, S. Extended Networks of Co^{2+} and Mn^{2+} Bridged by NCS^-/N_3^- Anions and Flexible Long Spacers: Syntheses, Structures, and Magnetic Properties. *Eur. J. Inorg. Chem*. **2005**, 3277–3286.

(148) Wriedt, M.; Sellmer, S.; Näther, C. Coordination Polymer Changing Its Magnetic Properties and Colour by Thermal Decomposition: Synthesis, Structure and Properties of New Thiocyanato Iron(II) Coordination Polymers Based on 4,4′-Bipyridine as Ligand. *Dalton Trans*. **2009**, 7975–7984.

(149) Wöhlert, S.; Boeckmann, J.; Wriedt, M.; Näther, C. Coexistence of Metamagnetism and Slow Relaxation of the Magnetization in a Cobalt Thiocyanate 2D Coordination Network. *Angew. Chem. Int. Ed*. **2011**, *50*, 6920–6923.

(150) Cortés, R.; Lezama, L.; Pizarro, J. L.; Arriortua, M. I.; Rojo, T. Alternating Ferro- and Antiferromagnetic Interactions in Honeycomb-Like Layers of an Azidomanganese(II) Compound. *Angew. Chem. Int. Ed. Engl*. **1996**, *35*, 1810–1812.

(151) Cortés, R.; Urtiaga, M. K.; Lezama, L.; Pizarro, J. L.; Arriortua, M. I.; Rojo, T. Influence of Pseudohalide Ions on the Molecular Structure and Magnetic Properties of the Manganese(II)-Bipyrimidine-Pseudohalide System. *Inorg. Chem*. **1997**, *36*, 5016–5021.

(152) Manson, J. L.; Arif, A. M.; Miller, J. S. $Mn^{II}(N_3)_2$(pyrazine). A 2-D Layered Structure Consisting of Ferromagnetically Coupled 1-D $\{Mn(\mu\text{-}1,1\text{-}N_3)_2\}_n$ Chains. *Chem. Commun*. **1999**, 1479–1480.

(153) Hao, X.; Wei, Y.; Zhang, S. Crystal Structure and Metamagnetic Property of a 2-D Layered Complex, $[Fe^{II}(N_3)_2(pyz)]_n$ (pyz = Pyrazine). *Chem. Commun*. **2000**, 2271–2272.

(154) Han, S.; Manson, J. L.; Kim, J.; Miller, J. S. Weak Ferromagnetism in a Three-Dimensional Manganese(II) Azido Complex, $[Mn(4,4'\text{-bipy})(N_3)_2]_n$ (bipy = Bipyridine). *Inorg. Chem*. **2000**, *39*, 4182–4185.

(155) Ma, B.-Q.; Sun, H.-L.; Gao, S.; Su, G. A Novel Azido and Pyrazine-Dioxide Bridged Three-Dimensional Manganese(II) Network with Antiferromagnetic Ordering (T_N = 62 K) and a Spin Flop State. *Chem. Mater*. **2001**, *13*, 1946–1948.

(156) Fu, A.; Huang, X.; Li, J.; Yuen, T.; Lin, C. L. Controlled Synthesis and Magnetic Properties of 2D and 3D Iron Azide Networks $^{2}_{\infty}[Fe(N_3)_2(4,4'\text{-bpy})]$ and $^{3}_{\infty}[Fe(N_3)_2(4,4'\text{-bpy})]$. *Chem. –Eur. J*. **2002**, *8*, 2239–2247.

(157) Escuer, A.; Vicente, R.; Mautner, F. A.; Goher, M. A. S.; Abu-Youssef, M. A. M. $[M(N_3)_2(L)]_n$: Building 3-D M^{II}-Azido Networks with New Topologies. *Chem. Commun*. **2002**, 64–65.

(158) Gao, E.-Q.; Wang, Z.-M.; Yan, C.-H. From Manganese(II)-Azido Layers to a Novel Three-Dimensional Molecular Magnet: Spin Canting and Metamagnetism. *Chem. Commun*. **2003**, 1748–1749.

(159) Wang, X.-Y.; Wang, L.; Wang, Z.-M.; Gao, S. Solvent-Tuned Azido-Bridged Co^{2+} Layers: Square, Honeycomb, and *Kagomé*. *J. Am. Chem. Soc*. **2006**, *128*, 674–675.

(160) Sun, W.-W.; Tian, C.-Y.; Jing, X.-H.; Wang, Y.-Q.; Gao, E.-Q. Solvent-Modulated Metamagnetism in a Nickel(II) Coordination Polymer with Mixed Azide and Carboxylate Bridges. *Chem. Commun*. **2009**, 4741–4743.

(161) Lawandy, M. A.; Huang, X.; Wang, R.-J.; Li, J.; Lu, J. Y.; Yuen, T.; Lin, C. L. Two-Dimensional Coordination Polymers with One-Dimensional Magnetic Chains: Hydrothermal Synthesis, Crystal Structure, and Magnetic and Thermal Properties of $^{2}_{\infty}[MCl_2(4,4'\text{-bipyridine})]$ (M = Fe, Co, Ni, Co/Ni). *Inorg. Chem*. **1999**, *38*, 5410–5414.

(162) Duan, Z.; Zhang, Y.; Zhang, B.; Zhu, D. Crystal-to-Crystal Transformation from Antiferromagnetic Chains into a Ferromagnetic Diamondoid Framework. *J. Am. Chem. Soc*. **2009**, *131*, 6934–6935.

(163) Yamagata, K.; Saito, Y.; Abe, T.; Hashimoto, M. Preparation and Characterization of $M(HCOO)_2 \cdot 2(NH_2)_2CO$: M = Fe, Co, Ni/Mg, Zn, Cd. *J. Phys. Soc. Jpn*. **1989**, *58*, 3865–3866.

(164) Ridwan. Extensive Structural Investigations of $M(HCOO)_2 \cdot 2(NH_2)_2CO$ (M = Mg, Mn, Zn, Co and Cd) in View of Two-Dimensional Magnetic Interactions. *Jpn. J. Appl. Phys*. **1992**, *31*, 3559–3563.

(165) Yamagata, K.; Abe, T.; Higuchi, Y.; Deguchi, H.; Takeda, K.; Kaneko, K.; Nojiri, H.; Motokawa, M. Thermal and Magnetic Properties of $M(HCOO)_2 \cdot 2$urea: M = Mn, Fe, Co, Ni. *J. Magn. Magn. Mater*. **1992**, *104–107*, 803–804.

(166) Rettig, S. J.; Thompson, R. C.; Trotter, J.; Xia, S. Crystal Structure and Magnetic Properties of Polybis(formamide)bis(μ-formato)cobalt(II): An Extended Two-Dimensional Square Lattice Material Which Exhibits Spontaneous Magnetization Below 9 K. *Inorg. Chem*. **1999**, *38*, 1360–1363.

(167) Kobayashi, H.; Haseda, T. The Magnetic Properties of Cupric Formate Tetrahydrate at Low Temperatures. *J. Phys. Soc. Jpn*. **1963**, *18*, 541–550.

(168) Flippen, R. B.; Friedberg, S. A. Low-Temperature Magnetic Susceptibilities of Some Hydrated Formates of Cu^{++} and Mn^{++}. *J. Chem. Phys*. **1963**, *38*, 2652–2657.

(169) Abe, H.; Morigaki, H.; Matsuura, M.; Torii, K.; Yamagata, K. Magnetic Properties of Manganese Formate Dihydrate. *J. Phys. Soc. Jpn*. **1964**, *19*, 775–776.

(170) Abe, H.; Torii, K. Susceptibility of Manganese Formate Dihydrate. *J. Phys. Soc. Jpn*. **1965**, *20*, 183–184.

(171) Hoy, G. R.; Barros, S. D. S.; Barros, F. D. S.; Friedberg, S. A. Inequivalent Magnetic Ions in Dihydrated Formates of Fe^{++} and Ni^{++}. *J. Appl. Phys*. **1965**, *36*, 936–937.

(172) Yamagata, K. Weak Ferromagnetism of $Mn(HCOO)_2 \cdot 2H_2O$. *J. Phys. Soc. Jpn*. **1967**, *22*, 582–589.

(173) Pierce, R. D.; Friedberg, S. A. Heat Capacity of $Mn(HCOO)_2 \cdot 2H_2O$ Between 1.4 and 20°K. *Phys. Rev*. **1968**, *165*, 680–687.

(174) Skalyo, J., Jr.; Shirane, G.; Friedberg, S. A. Two-Dimensional Antiferromagnetism in $Mn(HCOO)_2 \cdot 2H_2O$. *Phys. Rev*. **1969**, *188*, 1037–1041.

(175) Pierce, R. D.; Friedberg, S. A. Heat Capacities of $Fe(HCOO)_2 \cdot 2H_2O$ and $Ni(HCOO)_2 \cdot 2H_2O$ Between 1.4 and 20 °K. *Phys. Rev. B* **1971**, *3*, 934–942.

(176) Takeda, K.; Kawasaki, K. Magnetism and Phase Transition in Two-Dimensional Lattices; $M(HCOO)_2 \cdot 2H_2O$ (M; Mn, Fe, Ni, Co). *J. Phys. Soc. Jpn*. **1971**, *31*, 1026–1036.

(177) Yamakawa, H.; Matsuura, M. Ordering of $Co(HCOO)_2 \cdot 2H_2O$ Studied by Proton NMR — Magnetic Sandwich System of Antiferromagnetic Planes with Paramagnetic Ions—. *J. Phys. Soc. Jpn*. **1976**, *41*, 798–803.

(178) Burger, N.; Fuess, H. Crystal Structure and Magnetic Properties of Copper Format Anhydrate [α-$Cu(HCOO)_2$]. *Solid State Commun*. **1980**, *34*, 699–703.

(179) Sapiña, F.; Burgos, M.; Escrivá, E.; Folgado, J.-V.; Marcos, D.; Beltrán, A.; Beltrán, D. Ferromagnetism in the α and β Polymorphs of Anhydrous Copper(II) Formate: Two Molecular-Based Ferromagnets with Ordering Temperatures of 8.2 and 30.4 K. *Inorg. Chem*. **1993**, *32*, 4337–4344.

(180) Radhakrishna, P.; Gillon, B.; Chevrier, G. Superexchange in Manganese Formate Dihydrate, Studied by Polarized-Neutron Diffraction. *J. Phys.: Condens. Matter* **1993**, *5*, 6447–6460.

(181) Cornia, A.; Caneschi, A.; Dapporto, P.; Fabretti, A. C.; Gatteschi, D.; Malavasi, W.; Sangregorio, C.; Sessoli, R. Manganese(III) Formate: A Three-Dimensional Framework That Traps Carbon Dioxide Molecules. *Angew. Chem. Int. Ed.* **1999**, *38*, 1780–1782.

(182) Kageyama, H.; Khomskii, D. I.; Levitin, R. Z.; Vasil'ev, A. N. Weak Ferrimagnetism, Compensation Point, and Magnetization Reversal in $Ni(HCOO_2)\cdot 2H_2O$. *Phys. Rev. B* **2003**, *67*, 224422.

(183) Viertelhaus, M.; Henke, H.; Anson, C. E.; Powell, A. K. Solvothermal Synthesis and Structure of Anhydrous Manganese(II) Formate, and Its Topotactic Dehydration from Manganese(II) Formate Dihydrate. *Eur. J. Inorg. Chem*. **2003**, 2283–2289.

(184) Wang, X.-Y.; Gan, L.; Zhang, S.-W.; Gao, S. Perovskite-Like Metal Formates with Weak Ferromagnetism and as Precursors to Amorphous Materials. *Inorg. Chem*. **2003**, *43*, 4615–4625.

(185) Wang, Z.; Zhang, B.; Otsuka, T.; Inoue, K.; Kobayashi, H.; Kurmoo, M. Anionic NaCl-Type Frameworks of $[Mn^{II}(HCOO)_3^-]$, Templated by Alkylammonium, Exhibit Weak Ferromagnetism. *Dalton Trans*. **2004**, 2209–2216.

(186) Wang, Z.; Zhang, B.; Fujiwara, H.; Kobayashi, H.; Kurmoo, M. $Mn_3(HCOO)_6$: A 3D Porous Magnet of Diamond Framework with Nodes of Mn-Centered $MnMn_4$ Tetrahedron and Guest-Modulated Ordering Temperature. *Chem. Commun*. **2004**, 416–417.

(187) Wang, Z.; Zhang, B.; Kurmoo, M.; Green, M. A.; Fujiwara, H.; Otsuka, T.; Kobayashi, H. Synthesis and Characterization of a Porous Magnetic Diamond Framework, $Co_3(HCOO)_6$, and Its N_2 Sorption Characteristic. *Inorg. Chem*. **2005**, *44*, 1230–1237.

(188) Viertelhaus, M.; Adler, P.; Clérac, R.; Anson, C. E.; Powell, A. K. Iron(II) Formate $[Fe(O_2CH)_2]\cdot 1/3HCO_2H$: A Mesoporous Magnet – Solvothermal Syntheses and Crystal Structures of the Isomorphous Framework Metal(II) Formates $[M(O_2CH)_2]\cdot n$(Solvent) (M = Fe, Co, Ni, Zn, Mg). *Eur. J. Inorg. Chem*. **2005**, 692–703.

(189) Stride, J. A.; Kurmoo, M.; Wang, Z. Investigations of Guest-Modulated Ordering Temperatures in Open-Framework 3D Porous Magnets. *Physica B* **2006**, *385–386*, 465–467.

(190) Cui, H.; Wang, Z.; Takahashi, K.; Okano, Y.; Kobayashi, H.; Kobayashi, A. Ferroelectric Porous Molecular Crystal, $[Mn_3(HCOO)_6](C_2H_5OH)$, Exhibiting Ferrimagnetic Transition. *J. Am. Chem. Soc*. **2006**, *128*, 15074–15075.

(191) Wang, Z.; Zhang, B.; Inoue, K.; Fujiwara, H.; Otsuka, T.; Kobayashi, H.; Kurmoo, M. Occurrence of a Rare $4^9 \cdot 6^6$ Structural Topology, Chirality, and Weak Ferromagnetism in the $[NH_4][M^{II}(HCOO)_3]$ (M = Mn, Co, Ni) Frameworks. *Inorg. Chem*. **2007**, *46*, 437–445.

(192) Wang, Z.; Zhang, X.; Batten, S. R.; Kurmoo, M.; Gao, S. $[CH_3NH_2(CH_2)_2NH_2CH_3][M_2(HCOO)_6]$ (M = Mn^{II} and Co^{II}): Weak Ferromagnetic Metal Formate Frameworks of Unique Binodal 6-Connected $(4^{12} \cdot 6^3)(4^9 \cdot 6^6)$ Topology, Templated by a Diammonium Cation. *Inorg. Chem*. **2007**, *46*, 8439–8441.

(193) Wang, Z.; Zhang, Y.; Liu, T.; Kurmoo, M.; Gao, S. $[Fe_3(HCOO)_6]$: A Permanent Porous Diamond Framework Displaying H_2/N_2 Adsorption, Guest Inclusion, and Guest-Dependent Magnetism. *Adv. Funct. Mater*. **2007**, *17*, 1523–1536.

(194) Zhang, B.; Wang, Z.; Kurmoo, M.; Gao, S.; Inoue, K.; Kobayashi, H. Guest-Induced Chirality in the Ferrimagnetic Nanoporous Diamond Framework $Mn_3(HCOO)_6$. *Adv. Funct. Mater*. **2007**, *17*, 577–584.

(195) Wang, Z.; Zhang, B.; Zhang, Y.; Kurmoo, M.; Liu, T.; Gao, S.; Kobayashi, H. A Family of Porous Magnets, $[M_3(HCOO)_6]$ (M = Mn, Fe, Co and Ni). *Polyhedron* **2007**, *26*, 2207–2215.

(196) Hu, K.-L.; Kurmoo, M.; Wang, Z.; Gao, S. Metal–Organic Perovskites: Synthesis, Structures, and Magnetic Properties of $[C(NH_2)_3][M^{II}(HCOO)_3]$ (M = Mn, Fe, Co, Ni, Cu, and Zn; $C(NH_2)_3$ = Guanidinium). *Chem. –Eur. J*. **2009**, *15*, 12050–12064.

(197) Hagen, K. S.; Naik, S. G.; Huynh, B. H.; Masello, A.; Christou, G. Intensely Colored Mixed-Valence Iron(II) Iron(III) Formate Analogue of Prussian Blue Exhibits Néel N-Type Ferrimagnetism. *J. Am. Chem. Soc*. **2009**, *131*, 7516–7517.

(198) Jain, P.; Ramachandran, V.; Clark, R. J.; Zhou, H. D.; Toby, B. H.; Dalal, N. S.; Kroto, H. W.; Cheetham, A. K. Multiferroic Behavior Associated with an Order–Disorder Hydrogen Bonding Transition in Metal–Organic Frameworks (MOFs) with the Perovskite ABX_3 Architecture. *J. Am. Chem. Soc*. **2009**, *131*, 13625–13627.

(199) Zhao, J.-P.; Hu, B.-W.; Lloret, F.; Tao, J.; Yang, Q.; Zhang, X.-F.; Bu, X.-H. Magnetic Behavior Control in Niccolite Structural Metal Formate Frameworks

$[NH_2(CH_3)_2][Fe^{III}M^{II}(HCOO)_6]$ (M = Fe, Mn, and Co) by Varying the Divalent Metal Ions. *Inorg. Chem*. **2010**, *49*, 10390–10399.

(200) Wang, Z.; Hu, K.; Gao, S.; Kobayashi, H. Formate-Based Magnetic Metal–Organic Frameworks Templated by Protonated Amines. *Adv. Mater*. **2010**, *22*, 1526–1533.

(201) Duan, Z.; Wang, Z.; Gao, S. Irreversible Transformation of Chiral to Achiral Polymorph of $K[Co(HCOO)_3]$: Synthesis, Structures, and Magnetic Properties. *Dalton Trans*. **2011**, *40*, 4465–4473.

(202) Xu, G.-C.; Zhang, W.; Ma, X.-M.; Chen, Y.-H.; Zhang, L.; Cai, H.-L.; Wang, Z.-M.; Xiong, R.-G.; Gao, S. Coexistence of Magnetic and Electric Orderings in the Metal–Formate Frameworks of $[NH_4][M(HCOO)_3]$. *J. Am. Chem. Soc*. **2011**, *133*, 14948–14951.

(203) Cañadillas-Delgado, L.; Fabelo, O.; Rodríguez-Velamazán, J. A.; Lemée-Cailleau, M.-H.; Mason, S. A.; Pardo, E.; Lloret, F.; Zhao, J.-P.; Bu, X.-H.; Simonet, V.; Colin, C. V.; Rodrígúez-Carvajal, J. The Role of Order−Disorder Transitions in the Quest for Molecular Multiferroics: Structural and Magnetic Neutron Studies of a Mixed Valence Iron(II)−Iron(III) Formate Framework. *J. Am. Chem. Soc*. **2012**, *134*, 19772–19781.

(204) Di Sante, D.; Stroppa, A.; Jain, P.; Picozzi, S. Tuning the Ferroelectric Polarization in a Multiferroic Metal−Organic Framework. *J. Am. Chem. Soc*. **2013**, *135*, 18126–18130.

(205) Tian, Y.; Stroppa, A.; Chai, Y.; Yan, L.; Wang, S.; Barone, P.; Picozzi, S.; Sun, Y. Cross Coupling Between Electric and Magnetic Orders in a Multiferroic Metal-Organic Framework. *Sci. Rep*. **2014**, *4*, 6062.

(206) Tian, Y.; Wang, W.; Chai, Y.; Cong, J.; Shen, S.; Yan, L.; Wang, S.; Han, X.; Sun, Y. Quantum Tunneling of Magnetization in a Metal-Organic Framework. *Phys. Rev. Lett*. **2014**, *112*, 017202.

(207) Saines, P. J.; Paddison, J. A. M.; Thygesen, P. M. M.; Tucker, M. G. Searching Beyond Gd for Magnetocaloric Frameworks: Magnetic Properties and Interactions of the $Ln(HCO_2)_3$ Series. *Mater. Horiz*. **2015**, *2*, 528–535.

(208) Harcombe, D. R.; Welch, P. G.; Manuel, P.; Saines, P. J.; Goodwin, A. L. One-Dimensional Magnetic Order in the Metal-Organic Framework $Tb(HCOO)_3$. *Phys. Rev. B* **2016**, *94*, 174429.

(209) Gómez-Aguirre, L. C.; Pato-Doldán, B.; Mira, J.; Castro-García, S.; Señarís-Rodríguez, M. A.; Sánchez-Andújar, M.; Singleton, J.; Zapf, V. S. Magnetic Ordering-Induced Multiferroic

Behavior in $[CH_3NH_3][Co(HCOO)_3]$ Metal−Organic Framework. *J. Am. Chem. Soc*. **2016**, *138*, 1122–1125.

(210) Wang, X.-Y.; Wei, H.-Y.; Wang, Z.-M.; Chen, Z.-D.; Gao, S. Formates–The Analogue of Azide: Structural and Magnetic Properties of $M(HCOO)_2(4,4'\text{-bpy})\cdot nH_2O$ (M = Mn, Co, Ni; n = 0, 5). *Inorg. Chem*. **2005**, *44*, 572–583.

(211) Wang, X.-Y.; Wang, Z.-M.; Gao, S. A Pillared Layer MOF with Anion-Tunable Magnetic Properties and Photochemical [2 + 2] Cycloaddition. *Chem. Commun*. **2007**, 1127–1129.

(212) Tiana, D.; Hendon, C. H.; Walsh, A. Ligand Design for Long-Range Magnetic Order in Metal–Organic Frameworks. *Chem. Commun*. **2014**, *50*, 13990–13993.

(213) Dzyaloshinsky, I. A Thermodynamic Theory of "Weak" Ferromagnetism of Antiferromagnetics. *J. Phys. Chem. Solids* **1958**, *4*, 241–255.

(214) Moriya, T. Anisotropic Superexchange Interaction and Weak Ferromagnetism. *Phys. Rev*. **1960**, *120*, 91–98.

(215) Shimizu, G. K. H.; Vaidhyanathan, R.; Taylor, J. M. Phosphonate and Sulfonate Metal Organic Frameworks. *Chem. Soc. Rev*. **2009**, *38*, 1430–1449.

(216) Gao, Q.; Guillou, N.; Noguès, M.; Cheetham, A. K.; Férey, G. Structure and Magnetism of VSB-2, -3, and -4 or $Ni_4(O_3P\text{-}(CH_2)\text{-}PO_3)_2\cdot(H_2O)_n$ (n = 3, 2, 0), the First Ferromagnetic Nickel(II) Diphosphonates: Increase of Dimensionality and Multiple Coordination Changes During a Quasi Topotactic Dehydration. *Chem. Mater*. **1999**, *11*, 2937–2947.

(217) Riou, D.; Belier, F.; Serre, C.; Noguès, M.; Vichard, D.; Férey, G. Hybrid Open-Frameworks: Hydrothermal Synthesis, Structure Determinations and Magnetic Properties of MIL-29, Two Copper Diphosphonates $(Cu^{II}(H_2O))_2\{O_3P–X–PO_3\}$ with X = C_2H_4, $CH_2–C_6H_4–CH_2$. *Int. J. Inorg. Mater*. **2000**, *2*, 29–33.

(218) Yin, P.; Zheng, L.-M.; Gao, S.; Xin, X.-Q. $Cu_4\{CH_3C(OH)(PO_3)_2\}_2(C_4H_4N_2)(H_2O)_4$: A Novel, Three-Dimensional Copper Diphosphonate with Metamagnetism. *Chem. Commun*. **2001**, 2346–2347.

(219) Zhang, Y.-Y.; Zeng, M.-H.; Qi, Y.; Sang, S.-Y.; Liu, Z.-M. Honeycomb-Like Layered Cobalt(II) Phosphonate with $[O_2CCH(OH)PO_3]^{3-}$ as Ligand: Hydrothermal Synthesis, Crystal Structure, and Magnetic Properties. *Inorg. Chem. Commun*. **2007**, *10*, 33–36.

(220) Zhou, T.-H.; He, Z.-Z.; Xu, X.; Qian, X.-Y.; Mao, J.-G. Ligand Geometry Directed Polar Cobalt(II) Phosphonate Displaying Weak Ferromagnetism. *Cryst. Growth Des*. **2013**, *13*, 838–843.

(221) Riou-Cavellec, M.; Sanselme, M.; Noguès, M.; Grenèche, J.-M.; Férey, G. Synthesis, Structure and Metamagnetic Behaviour of a Three-Dimensional Fe(II) Carboxyethylphosphonate: $[Fe_3(OH)_2(H_2O)_4(O_3P–(CH_2)_2–CO_2H)_2]$ or MIL-38. *Solid State Sci*. **2002**, *4*, 619–625.

(222) Yang, X.-J.; Bao, S.-S.; Ren, M.; Hoshino, N.; Akutagawa, T.; Zheng, L.-M. Polar Metal Phosphonate Containing Unusual μ_4-OH Bridged Double Chains Showing Canted Antiferromagnetism with Large Coercivity. *Chem. Commun*. **2014**, *50*, 3979–3981.

(223) Armentano, D.; De Munno, G.; Mastropietro, T. F.; Julve, M.; Lloret, F. Intermolecular Proton Transfer in Solid Phase: A Rare Example of Crystal-to-Crystal Transformation from Hydroxo- to Oxo-Bridged Iron(III) Molecule-Based Magnet. *J. Am. Chem. Soc*. **2005**, *127*, 10778–10779.

(224) Day, P. Co-Ordination Complexes as Organic–Inorganic Layer Magnets. *J. Chem. Soc., Dalton Trans*. **1997**, 701–705.

(225) Coronado, E.; Clemente-León, M.; Galán-Mascarós, J. R.; Giménez-Saiz, C.; Gómez-García, C. J.; Martínez-Ferrero, E. Design of Molecular Materials Combining Magnetic, Electrical and Optical Properties. *J. Chem. Soc., Dalton Trans*. **2000**, 3955–3961.

(226) Zhong, Z. J.; Matsumoto, N.; Ōkawa, H.; Kida, S. Ferromagnetic Hetero-Metal Assemblies, $\{NBu_4[CuCr(ox)_3]\}_x$ and $\{[\{Cu(bpy)\}_2Cr(ox)_3]NO_3\}_x$. *Chem. Lett*. **1990**, 87–90.

(227) Mathonière, C.; Carling, S. G.; Yusheng, D.; Day, P. Molecular-Based Mixed Valency Ferrimagnets $(XR_4)Fe^{II}Fe^{III}(C_2O_4)_3$ (X = N, P; R = *n*-Propyl, *n*-Butyl, Phenyl): Anomalous Negative Magnetization in the Tetra-*n*-butylammonium Derivative. *J. Chem. Soc., Chem. Commun*. **1994**, 1551–1552.

(228) Nuttall, C. J.; Day, P. Magnetization of the Layer Compounds $AFe^{II}Fe^{III}(C_2O_4)_3$ (A = Organic Cation), in Low and High Magnetic Fields: Manifestation of Néel N and Q Type Ferrimagnetism in a Molecular Lattice. *Chem. Mater*. **1998**, *10*, 3050–3057.

(229) Mathonière, C.; Nuttall, C. J.; Carling, S. G.; Day, P. Ferrimagnetic Mixed-Valency and Mixed-Metal Tris(oxalato)iron(III) Compounds: Synthesis, Structure, and Magnetism. *Inorg. Chem*. **1996**, *35*, 1201–1206.

(230) Watts, I. D.; Carling, S. G.; Day. P. Synthesis, Structure and Magnetic Properties of Organic-Intercalated Bimetallic Molecular-Based Ferrimagnets (n-C_nH_{2n+1})$PPh_3M^{II}Fe^{III}(C_2O_4)_3$, ($M^{II}$ = Mn, Fe; n = 3–7). *J. Chem. Soc., Dalton Trans*. **2002**, 1429–1434.

(231) Carling, S. G.; Mathonière, C.; Day, P.; Malik, K. M. A.; Coles, S. J.; Hursthouse, M. B. Crystal Structure and Magnetic Properties of the Layer Ferrimagnet N(n-$C_5H_{11})_4Mn^{II}Fe^{III}(C_2O_4)_3$. *J. Chem. Soc., Dalton Trans*. **1996**, 1839–1843.

(232) Pellaux, R.; Schmalle, H. W.; Huber, R.; Fischer, P.; Hauss, T.; Ouladdiaf, B.; Decurtins, S. Molecular-Based Magnetism in Bimetallic Two-Dimensional Oxalate-Bridged Networks. An X-Ray and Neutron Diffraction Study. *Inorg. Chem*. **1997**, *36*, 2301–2308.

(233) Clemente-León, M.; Coronado, E.; Galán-Mascarós, J.-R.; Gómez-García, C. J. Intercalation of Decamethylferrocenium Cations in Bimetallic Oxalate-Bridged Two-Dimensional Magnets. *Chem. Commun*. **1997**, 1727–1728.

(234) Coronado, E.; Galán-Mascarós, J.-R.; Gómez-García, C.-J.; Ensling, J.; Gütlich, P. Hybrid Molecular Magnets Obtained by Insertion of Decamethylmetallocenium Cations into Layered, Bimetallic Oxalate Complexes: $[Z^{III}Cp^*_2][M^{II}M^{III}(ox)_3]$ (Z^{III} = Co, Fe; M^{III} = Cr, Fe; M^{II} = Mn, Fe, Co, Cu, Zn; ox = Oxalate; Cp* = Pentamethylcyclopentadienyl). *Chem. – Eur. J*. **2000**, *6*, 552–563.

(235) Coronado, E.; Galán-Mascarós, J. R.; Gómez-García, C. J.; Martínez-Agudo, J. M.; Martínez-Ferrero, E.; Waerenborgh, J. C.; Almeida, M. Layered Molecule-Based Magnets Formed by Decamethylmetallocenium Cations and Two-Dimensional Bimetallic Complexes $[M^{II}Ru^{III}(ox)_3]^-$ (M^{II} = Mn, Fe, Co, Cu and Zn; ox = Oxalate). *J. Solid State Chem*. **2001**, *159*, 391–402.

(236) Coronado, E.; Galán-Mascarós, J. R.; Martí-Gastaldo, C.; Waerenborgh, J. C.; Gaczyński, P. Oxalate-Based Soluble 2D Magnets: The Series [K(18-crown-6)]$_3[M^{II}_3(H_2O)_4\{M^{III}(ox)_3\}_3]$ (M^{III} = Cr, Fe; M^{II} = Mn, Fe, Ni, Co, Cu; ox = $C_2O_4^{2-}$; 18-crown-6 = $C_{12}H_{24}O_6$). *Inorg. Chem*. **2008**, *47*, 6829–6839.

(237) Tamaki, H.; Zhong, Z. J.; Matsumoto, N.; Kida, S.; Koikawa, M.; Achiwa, N.; Hashimoto, Y.; Ōkawa, H. Design of Metal-Complex Magnets. Syntheses and Magnetic Properties of Mixed-Metal Assemblies $\{NBu_4[MCr(ox)_3]\}_x$ (NBu_4^+ = Tetra(n-butyl)ammonium Ion; ox^{2-} = Oxalate Ion; M = Mn^{2+}, Fe^{2+}, Co^{2+}, Ni^{2+}, Cu^{2+}, Zn^{2+}). *J. Am. Chem. Soc*. **1992**, *114*, 6974–6979.

(238) Decurtins, S.; Schmalle, H. W.; Oswald, H. R.; Linden, A.; Ensling, J.; Gütlich, P.; Hauser, A. A Polymeric Two-Dimensional Mixed-Metal Network. Crystal Structure and Magnetic Properties of $\{[P(Ph)_4][MnCr(ox)_3]\}_n$. *Inorg. Chim. Acta* **1994**, *216*, 65–73.

(239) Coronado, E.; Galán-Mascarós, J. R.; Martí-Gastaldo, C. A "Cation-Less" Oxalate-Based Ferromagnet Formed by Neutral Bimetallic Layers: $\{[Co(H_2O)_2]_3[Cr(ox)_3]_2(18\text{-crown-}6)_2\}_\infty$ (ox = Oxalate Dianion; 18-crown-6 = $C_{12}H_{24}O_6$). *Inorg. Chem.* **2007**, *46*, 8108–8110.

(240) Coronado, E.; Martí-Gastaldo, C.; Galán-Mascarós, J. R.; Cavallini, M. Polymetallic Oxalate-Based 2D Magnets: Soluble Molecular Precursors for the Nanostructuration of Magnetic Oxides. *J. Am. Chem. Soc.* **2010**, *132*, 5456–5468.

(241) Ōkawa, H.; Sadakiyo, M.; Yamada, T.; Maesato, M.; Ohba, M.; Kitagawa, H. Proton-Conductive Magnetic Metal−Organic Frameworks, $\{NR_3(CH_2COOH)\}[M_a^{II}M_b^{III}(ox)_3]$: Effect of Carboxyl Residue upon Proton Conduction. *J. Am. Chem. Soc.* **2013**, *135*, 2256–2262.

(242) Williams, J. M.; Schultz, A. J.; Geiser, U.; Carlson, K. D.; Kini, A. M.; Wang, H. H.; Kwok, W.-K.; Whangbo, M.-H.; Schirber, J. E. Organic Superconductors–New Benchmarks. *Science* **1991**, *252*, 1501–1508.

(243) Alberola, A.; Coronado, E.; Galán-Mascarós, J. R.; Giménez-Saiz, C.; Gómez-García, C. J. A Molecular Metal Ferromagnet from the Organic Donor Bis(ethylenedithio)tetraselenafulvalene and Bimetallic Oxalate Complexes. *J. Am. Chem. Soc.* **2003**, *125*, 10774–10775.

(244) Coronado, E.; Galán-Mascarós, J. R.; Gómez-García, C. J. Hybrid Molecular Magnets Incorporating Organic Donors and Other Electroactive Molecules. *Synth. Met.* **1999**, *102*, 1459–1460.

(245) Coronado, E.; Galán-Mascarós, J. R. Hybrid Molecular Conductors. *J. Mater. Chem.* **2005**, *15*, 66–74.

(246) Alberola, A.; Coronado, E.; Galán-Mascarós, J. R.; Giménez-Saiz, C.; Gómez-García, C. J.; Martínez-Ferrero, E.; Murcia-Martínez, A. Multifunctionality in Hybrid Molecular Materials: Design of Ferromagnetic Molecular Metals. *Synth. Met.* **2003**, *135–136*, 687–689.

(247) Coronado, E.; Galán-Mascarós, J. R.; Gómez-García, C. J.; Martínez-Ferrero, E.; van Smaalen, S. Incommensurate Nature of the Multilayered Molecular Ferromagnetic Metals

Based on Bis(ethylenedithio)tetrathiafulvalene and Bimetallic Oxalate Complexes. *Inorg. Chem.* **2004**, *43*, 4808–4810.

(248) Clemente-León, M.; Coronado, E.; Giménez-López, M. C.; Soriano-Portillo, A.; Waerenborgh, J. C.; Delgado, F. S.; Ruiz-Pérez, C. Insertion of a Spin Crossover Fe^{III} Complex into an Oxalate-Based Layered Material: Coexistence of Spin Canting and Spin Crossover in a Hybrid Magnet. *Inorg. Chem.* **2008**, *47*, 9111–9120.

(249) Clemente-León, M.; Coronado, E.; López-Jordà, M.; Espallargas, G. M.; Soriano-Portillo, A.; Waerenborgh, J. C. Multifunctional Magnetic Materials Obtained by Insertion of a Spin-Crossover Fe^{III} Complex into Bimetallic Oxalate-Based Ferromagnets. *Chem. –Eur. J.* **2010**, *16*, 2207–2219.

(250) Clemente-León, M.; Coronado, E.; López-Jordà, M.; Desplanches, C.; Asthana, S.; Wang, H.; Létard, J.-F. A Hybrid Magnet with Coexistence of Ferromagnetism and Photoinduced Fe(III) Spin-Crossover. *Chem. Sci*. **2011**, *2*, 1121–1127.

(251) Clemente-León, M.; Coronado, E.; López-Jordà, M. 2D Bimetallic Oxalate-Based Ferromagnets with Inserted $[Fe(4\text{-}Br\text{-}sal_2\text{-}trien)]^+$ and $[Fe(3\text{-}R\text{-}sal_2\text{-}trien)]^+$ (R = Br, Cl and CH_3O) Fe^{III} Spin-Crossover Complexes. *Eur. J. Inorg. Chem*. **2013**, 753–762.

(252) Clemente-León, M.; Coronado, E.; López-Jordà, M. 2D and 3D Bimetallic Oxalate-Based Ferromagnets Prepared by Insertion of Different Fe^{III} Spin Crossover Complexes. *Dalton Trans*. **2010**, *39*, 4903–4910.

(253) Clemente-León, M.; Coronado, E.; López-Jordà, M.; Waerenborgh, J. C.; Desplanches, C.; Wang, H.; Létard, J.-F.; Hauser, A.; Tissot, A. Stimuli Responsive Hybrid Magnets: Tuning the Photoinduced Spin-Crossover in Fe(III) Complexes Inserted into Layered Magnets. *J. Am. Chem. Soc*. **2013**, *135*, 8655–8667.

(254) Hauser, A. Light-Induced Spin Crossover and the High-Spin→Low-Spin Relaxation. *Top. Curr. Chem*. **2004**, *234*, 155–198.

(255) Lu, J. Y.; Lawandy, M. A.; Li, J.; Yuen, T.; Lin, C. L. A New Type of Two-Dimensional Metal Coordination Systems: Hydrothermal Synthesis and Properties of the First Oxalate-bpy Mixed-Ligand Framework $^{2}_{\infty}[M(ox)(bpy)]$ (M = Fe(II), Co(II), Ni(II), Zn(II); ox = $C_2O_4^{2-}$; bpy = 4,4′-Bipyridine). *Inorg. Chem*. **1999**, *38*, 2695–2704.

(256) Yuen, T.; Lin, C. L.; Mihalisin, T. W.; Lawandy, M. A.; Li, J. Magnetic Ordering in M(ox)(bpy) System (M = Fe, Co, Ni; ox = $C_2O_4^{2-}$; bpy = 4,4′-Bipyridine). *J. Appl. Phys*. **2000**, *87*, 6001–6003.

(257) Price, D. J.; Powell, A. K.; Wood, P. T. A New Series of Layered Transition Metal Oxalates: Hydrothermal Synthesis, Structural and Magnetic Studies. *Dalton Trans*. **2003**, 2478–2482.

(258) Zhang, B.; Zhang, Y.; Zhang, J.; Li, J.; Zhu, D. A Neutral Molecular-Based Layered Magnet $[Fe(C_2O_4)(CH_3OH)]_n$ Exhibiting Magnetic Ordering at $T_N \approx 23$ K. *Dalton Trans*. **2008**, 5037–5040.

(259) Coronado, E.; Galán-Mascarós, J. R.; Gómez-García, C. J.; Martínez-Agudo; J. M. Molecule-Based Magnets Formed by Bimetallic Three-Dimensional Oxalate Networks and Chiral Tris(bipyridyl) Complex Cations. The Series $[Z^{II}(bpy)_3][ClO_4][M^{II}Cr^{III}(ox)_3]$ (Z^{II} = Ru, Fe, Co, and Ni; M^{II} = Mn, Fe, Co, Ni, Cu, and Zn; ox = Oxalate Dianion). *Inorg. Chem*. **2001**, *40*, 113–120.

(260) Coronado, E.; Galán-Mascarós, J. R.; Gómez-García, C. J.; Martínez-Ferrero, E.; Almeida, M.; Waerenborgh, J. C. Oxalate-Based 3D Chiral Magnets: The Series $[Z^{II}(bpy)_3][ClO_4][M^{II}Fe^{III}(ox)_3]$ (Z^{II} = Fe, Ru; M^{II} = Mn, Fe; bpy = 2,2′-Bipyridine; ox = Oxalate Dianion). *Eur. J. Inorg. Chem*. **2005**, 2064–2070.

(261) Andrés, R.; Brissard, M.; Gruselle, M.; Train, C.; Vaissermann, J.; Malézieux, B.; Jamet, J.-P.; Verdaguer, M. Rational Design of Three-Dimensional (3D) Optically Active Molecule-Based Magnets: Synthesis, Structure, Optical and Magnetic Properties of $\{[Ru(bpy)_3]^{2+}$, ClO_4^-, $[Mn^{II}Cr^{III}(ox)_3]^-\}_n$ and $\{[Ru(bpy)_2ppy]^+$, $[M^{II}Cr^{III}(ox)_3]^-\}_n$, with M^{II} = Mn^{II}, Ni^{II}. X-Ray Structure of $\{[\Delta Ru(bpy)_3]^{2+}$, ClO_4^-, $[\Delta Mn^{II}\Delta Cr^{III}(ox)_3]^-\}_n$ and $\{[\Lambda Ru(bpy)_2ppy]^+$, $[\Lambda Mn^{II}\Lambda Cr^{III}(ox)_3]^-\}_n$. *Inorg. Chem*. **2001**, *40*, 4633–4640.

(262) Clemente-León, M.; Coronado, E.; Gómez-García, C. J.; Soriano-Portillo, A. Increasing the Ordering Temperatures in Oxalate-Based 3D Chiral Magnets: the Series $[Ir(ppy)_2(bpy)][M^{II}M^{III}(ox)_3]\cdot 0.5H_2O$ ($M^{II}M^{III}$ = MnCr, FeCr, CoCr, NiCr, ZnCr, MnFe, FeFe); bpy = 2,2′-Bipyridine; ppy = 2-Phenylpyridine; ox = Oxalate Dianion). *Inorg. Chem*. **2006**, *45*, 5653–5660.

(263) Pointillart, F.; Train, C.; Gruselle, M.; Villain, F.; Schmalle, H. W.; Talbot, D.; Gredin, P.; Decurtins, S.; Verdaguer, M. Chiral Templating Activity of Tris(bipyridine)ruthenium(II) Cation in the Design of Three-Dimensional (3D) Optically Active Oxalate-Bridged $\{[Ru(bpy)_3][Cu_{2x}Ni_{2(1-x)}(C_2O_4)_3]\}_n$ ($0 \le x \le 1$; bpy = 2,2′-Bipyridine): Structural, Optical, and Magnetic Studies. *Chem. Mater*. **2004**, *16*, 832–841.

(264) Decurtins, S.; Schmalle, H. W.; Schneuwly, P.; Ensling, J.; Gütlich, P. A Concept for the Synthesis of 3-Dimensional Homo- and Bimetallic Oxalate-Bridged Networks $[M_2(ox)_3]_n$. Structural, Mössbauer, and Magnetic Studies in the Field of Molecular-Based Magnets. *J. Am. Chem. Soc.* **1994**, *116*, 9521–9528.

(265) Decurtins, S.; Schmalle, H. W.; Pellaux, R.; Huber, R.; Fischer, P.; Ouladdiaf, B. Three-Dimensional Helical Supramolecules–Elucidation of Magnetic Ordering for an Antiferromagnetic Phase. *Adv. Mater*. **1996**, *8*, 647–651.

(266) Hernández-Molina, M.; Lloret, F.; Ruiz-Pérez, C.; Julve, M. Weak Ferromagnetism in Chiral 3-Dimensional Oxalato-Bridged Cobalt(II) Compounds. Crystal Structure of $[Co(bpy)_3][Co_2(ox)_3]ClO_4$. *Inorg. Chem.* **1998**, *37*, 4131–4135.

(267) Ballester, G.; Coronado, E.; Giménez-Saiz, C.; Romero, F. M.; Nitroxide Radicals as Templating Agents in the Synthesis of Magnets Based on Three-Dimensional Oxalato-Bridged Heterodimetallic Networks. *Angew. Chem. Int. Ed.* **2001**, *40*, 792–795.

(268) Clemente-León, M.; Coronado, E.; López-Jordà, M.; Waerenborgh, J. C. Multifunctional Magnetic Materials Obtained by Insertion of Spin-Crossover Fe^{III} Complexes into Chiral 3D Bimetallic Oxalate-Based Ferromagnets. *Inorg. Chem.* **2011**, *50*, 9122–9130.

(269) Coronado, E.; Galán-Mascarós, J. R.; Giménez-López, M. C.; Almeida, M.; Waerenborgh, J. C. Spin Crossover Fe^{II} Complexes as Templates for Bimetallic Oxalate-Based 3D Magnets. *Polyhedron* **2007**, *26*, 1838–1844.

(270) López-Jordà, M.; Giménez-Marqués, M.; Desplanches, C.; Espallargas, G. M.; Clemente-León, M.; Coronado, E. Insertion of a $[Fe^{II}(pyimH)_3]^{2+}$ [pyimH = 2-(1*H*-Imidazol-2-yl)pyridine] Spin-Crossover Complex Inside a Ferromagnetic Lattice Based on a Chiral 3D Bimetallic Oxalate Network. *Eur. J. Inorg. Chem.* **2016**, 2187–2192.

(271) Ben Djamâa, A.; Clemente-León, M.; Coronado, E.; López-Jordà, M. Insertion of Fe^{II} Complexes with Schiff Base Ligands Derived from Imidazole or Pyridine into 3D Bimetallic Oxalate-Based Ferromagnets. *Polyhedron* **2013**, *64*, 142–150.

(272) Clemente-León, M.; Coronado, E.; Gómez-García, C. J.; López-Jordà, M.; Camón, A.; Repollés, A.; Luis, F. Insertion of a Single-Molecule Magnet Inside a Ferromagnetic Lattice Based on a 3D Bimetallic Oxalate Network: Towards Molecular Analogues of Permanent Magnets. *Chem. –Eur. J.* **2014**, *20*, 1669–1676.

(273) Price, D. J.; Tripp, S.; Powell, A. K.; Wood, P. T. Hydrothermal Synthesis, X-Ray Structure and Complex Magnetic Behaviour of $Ba_4(C_2O_4)Cl_2[\{Fe(C_2O_4)(OH)\}_4]$. *Chem. –Eur. J.* **2001**, *7*, 200–208.

(274) Armentano, D.; De Munno, G.; Lloret, F.; Palii, A. V.; Julve, M. Novel Chiral Three-Dimensional Iron(III) Compound Exhibiting Magnetic Ordering at T_c = 40 K. *Inorg. Chem.* **2002**, *41*, 2007–2013.

(275) Armentano, D.; De Munno, G.; Mastropietro, T. F.; Proserpio, D. M.; Julve, M.; Lloret, F. The Cation as a Tool to Get Spin-Canted Three-Dimensional Iron(III) Networks. *Inorg. Chem.* **2004**, *43*, 5177–5179.

(276) Chiang, R.-K.; Huang, C.-C.; Wur, C.-S. Hydrothermal Synthesis and Structural Characterization of a Coordination Polymer Containing Heptanuclear $Co_7(\mu_3\text{-}OH)_8$ Clusters. *Inorg. Chem.* **2001**, *40*, 3237–3239.

(277) Keene, T. D.; Hursthouse, M. B.; Price, D. J. Ferromagnetic Coupling in a Heptanuclear Nickel Cluster with a Vertex-Shared Dicubane Structure. *New J. Chem.* **2004**, *28*, 558–561.

(278) Yao, Q.-X.; Pan, L.; Jin, X.-H.; Li, J.; Ju, Z.-F.; Zhang, J. Bipyridinium Array-Type Porous Polymer Displaying Hydrogen Storage, Charge-Transfer-Type Guest Inclusion, and Tunable Magnetic Properties. *Chem. –Eur. J.* **2009**, *15*, 11890–11897.

(279) Choudhury, A.; Natarajan, S.; Rao, C. N. R. A Hybrid Open-Framework Iron Phosphate–Oxalate with a Large Unidimensional Channel, Showing Reversible Hydration. *Chem. Mater.* **1999**, *11*, 2316–2318.

(280) Choudhury, A.; Natarajan, S. A Hybrid Open-Framework Structure: Synthesis and Structure of an Iron Phosphate Oxalate, $[C_{10}N_4H_{28}][Fe_2(HPO_4)_3(C_2O_4)]_2$. *J. Mater. Chem.* **1999**, *9*, 3113–3117.

(281) Choudhury, A.; Natarajan, S. Inorganic Hybrid Open-Framework Structures: Synthesis and Structure of a Cobalt Phosphate-Oxalate, $[C_4N_2H_{12}]_{0.5}[Co_2(HPO_4)(C_2O_4)_{1.5}]$. *Solid State Sci.* **2000**, *2*, 365–372.

(282) Choudhury, A.; Natarajan, S.; Rao, C. N. R. Hybrid Open-Framework Iron Phosphate – Oxalates Demonstrating a Dual Role of the Oxalate Unit. *Chem. –Eur. J.* **2000**, *6*, 1168–1175.

(283) Jiang, Y.-C.; Wang, S.-L.; Lii, K.-H.; Nguyen, N.; Ducouret, A. Synthesis, Crystal Structure, Magnetic Susceptibility, and Mössbauer Spectroscopy of a Mixed-Valence Organic–

Inorganic Hybrid Compound: $(H_3DETA)[Fe_3(C_2O_4)_2(HPO_4)_2(PO_4)]$ (DETA = Diethylenetriamine). *Chem. Mater*. **2003**, *15*, 1633–1638.

(284) Mandal, S.; Natarajan, S. Inorganic–Organic Hybrid Structure: Synthesis, Structure and Magnetic Properties of a Cobalt Phosphite–Oxalate, $[C_4N_2H_{12}][Co_4(HPO_3)_2(C_2O_4)_3]$. *J. Solid State Chem*. **2005**, *178*, 2376–2382.

(285) Cano, J.; Ruiz, E.; Alemany, P.; Lloret, F.; Alvarez, S. Theoretical Study of the Exchange Coupling in Copper(II) Binuclear Compounds with Oxamidate and Related Polyatomic Bridging Ligands. *J. Chem. Soc., Dalton Trans*. **1999**, 1669–1676.

(286) Fernández, I.; Ruiz, R.; Faus, J.; Julve, M.; Lloret, F.; Cano, J.; Ottenwaelder, X.; Journaux, Y.; Muñoz, M. C. Ferromagnetic Coupling Through Spin Polarization in a Dinuclear Copper(II) Metallacyclophane. *Angew. Chem. Int. Ed*. **2001**, *40*, 3039–3042.

(287) Grancha, T.; Ferrando-Soria, J.; Castellano, M.; Julve, M.; Pasán, J.; Armentano, D.; Pardo, E. Oxamato-Based Coordination Polymers: Recent Advances in Multifunctional Magnetic Materials. *Chem, Commun*. **2014**, *50*, 7569–7585.

(288) Pereira, C. L. M.; Pedroso, E. F.; Stumpf, H. O.; Novak, M. A.; Ricard, L.; Ruiz-García, R.; Rivière, E.; Journaux, Y. A $Cu^{II}Co^{II}$ Metallacyclophane-Based Metamagnet with a Corrugated Brick-Wall Sheet Architecture. *Angew. Chem. Int. Ed*. **2004**, *43*, 956–958.

(289) Ferrando-Soria, J.; Pasán, J.; Ruiz-Pérez, C.; Journaux, Y.; Julve, M.; Lloret, F.; Cano, J.; Pardo, E. Spin Control in Oxamato-Based Manganese(II)–Copper(II) Coordination Polymers with Brick-Wall Layer Architectures. *Inorg. Chem*. **2011**, *50*, 8694–8696.

(290) Ferrando-Soria, J.; Khajavi, H.; Serra-Crespo, P.; Gascon, J.; Kapteijn, F.; Julve, M.; Lloret, F.; Pasán, J.; Ruiz-Pérez, C.; Journaux, Y.; Pardo, E. Highly Selective Chemical Sensing in a Luminescent Nanoporous Magnet. *Adv. Mater*. **2012**, *24*, 5625–5629.

(291) Ferrando-Soria, J.; Ruiz-García, R.; Cano, J.; Stiriba, S.-E.; Vallejo, J.; Castro, I.; Julve, M.; Lloret, F.; Amorós, P.; Pasán, J.; Ruiz-Pérez, C.; Journaux, Y.; Pardo, E. Reversible Solvatomagnetic Switching in a Spongelike Manganese(II)–Copper(II) 3D Open Framework with a Pillared Square/Octagonal Layer Architecture. *Chem. –Eur. J*. **2012**, *18*, 1608–1617.

(292) Ferrando-Soria, J.; Serra-Crespo, P.; de Lange, M.; Gascon, J.; Kapteijn, F.; Julve, M.; Cano, J.; Lloret, F.; Pasán, J.; Ruiz-Pérez, C.; Journaux, Y.; Pardo, E. Selective Gas and Vapor

Sorption and Magnetic Sensing by an Isoreticular Mixed-Metal–Organic Framework. *J. Am. Chem. Soc*. **2012**, *134*, 15301–15304.

(293) Abhervé, A.; Grancha, T.; Ferrando-Soria, J.; Clemente-León, M.; Coronado, E.; Waerenborgh, J. C.; Lloret, F.; Pardo, E. Spin-Crossover Complex Encapsulation Within a Magnetic Metal–Organic Framework. *Chem. Commun*. **2016**, *52*, 7360–7363.

(294) Mon, M.; Pascual-Álvarez, A.; Grancha, T.; Cano, J.; Ferrando-Soria, J.; Lloret, F.; Gascon, J.; Pasán, J.; Armentano, D.; Pardo, E. Solid-State Molecular Nanomagnet Inclusion into a Magnetic Metal–Organic Framework: Interplay of the Magnetic Properties. *Chem. –Eur. J*. **2016**, *22*, 539–545.

(295) Pardo, E.; Cangussu, D.; Dul, M.-C.; Lescouëzec, R.; Herson, P.; Journaux, Y.; Pedroso, E. F.; Pereira, C. L. M.; Muñoz, M. C.; Ruiz-García, R.; Cano, J.; Amorós, P.; Julve, M.; Lloret, F. A Metallacryptand-Based Manganese(II)–Cobalt(II) Ferrimagnet with a Three-Dimensional Honeycomb Open-Framework Architecture. *Angew. Chem. Int. Ed*. **2008**, *47*, 4211–4216.

(296) Cangussu, D.; Pardo, E.; Dul, M.-C.; Lescouëzec, R.; Herson, P.; Journaux, Y.; Pedroso, E. F.; Pereira, C. L. M.; Stumpf, H. O.; Muñoz, M. C.; Ruiz-García, R.; Cano, J.; Julve, M.; Lloret, F. Rational Design of a New Class of Heterobimetallic Molecule-Based Magnets: Synthesis, Crystal Structures, and Magnetic Properties of Oxamato-Bridged M'_3M_2 (M' = Li^{I} and Mn^{II}; M = Ni^{II} and Co^{II}) Open-Frameworks with a Three-Dimensional Honeycomb Architecture. *Inorg. Chim. Acta* **2008**, *361*, 3394–3402.

(297) Ferrando-Soria, J.; Grancha, T.; Julve, M.; Cano, J.; Lloret, F.; Journaux, Y.; Pasán, J.; Ruiz-Pérez, C.; Pardo, E. Ligand Effects on the Dimensionality of Oxamato-Bridged Mixed-Metal Open-Framework Magnets. *Chem. Commun*. **2012**, *48*, 3539–3541.

(298) Goodenough, J. B. *Magnetism and the Chemical Bond*. Wiley: New York, 1963.

(299) Kanamori, J. Superexchange Interaction and Symmetry Properties of Electron Orbitals. *J. Phys. Chem. Solids* **1959**, *10*, 87–98.

(300) Rakitin, Y. V.; Kalinnikov, V. T. Mechanism of Exchange Interactions in Some Transition Metal Carboxylates, Sulfates, and Chlorides. *Theoret. Chim. Acta* **1977**, *45*, 167–176.

(301) Kumagai, H.; Kepert, C. J.; Kurmoo, M. Construction of Hydrogen-Bonded and Coordination-Bonded Networks of Cobalt(II) with Pyromellitate: Synthesis, Structures, and Magnetic Properties. *Inorg. Chem*. **2002**, *41*, 3410–3422.

(302) Liu, T.-F.; Sun, H.-L.; Gao, S.; Zhang, S.-W.; Lau, T.-C. Ferromagnetic Ordering and Metamagnetism in Malonate Bridged 3D Diamond-like and Honeycomb-like Networks: $[Cu(mal)(DMF)]_n$ and $\{[Cu(mal)(0.5pyz)]\cdot H_2O\}n$ (mal = Malonate Dianion, DMF = *N*,*N*-Dimethylformamide, pyz = Pyrazine). *Inorg. Chem*. **2003**, *42*, 4792–4794.

(303) Maji, T. K.; Sain, S.; Mostafa, G.; Lu, T.-H.; Ribas, J.; Monfort, M.; Chaudhuri, N. R. Magneto−Structural Correlations in 2D and 3D Extended Structures of Manganese(II)−Malonate Systems. *Inorg. Chem*. **2003**, *42*, 709–716.

(304) Zeng, M.-H.; Feng, X.-L.; Zhang, W.-X.; Chen, X.-M. A Robust Microporous 3D Cobalt(II) Coordination Polymer with New Magnetically Frustrated 2D Lattices: Single-Crystal Transformation and Guest Modulation of Cooperative Magnetic Properties. *Dalton Trans*. **2006**, 5294–5303.

(305) Rousse, G.; Radtke, G.; Klein, Y.; Ahouari, H. Long-Range Antiferromagnetic Order in Malonate-Based Compounds $Na_2M(H_2C_3O_4)_2\cdot 2H_2O$ (M = Mn, Fe, Co, Ni). *Dalton Trans*. **2016**, *45*, 2536–2548.

(306) Zhang, X.; Lu, C.; Zhang, Q.; Lu, S.; Yang, W.; Liu, J.; Zhuang, H. Synthesis, Structure and Characterization of Two New Complexes $[Cu_2(C_3H_2O_4)_2(C_4H_4N_2)]\cdot 2H_2O$ and $[Zn_2(OH_2)_2(C_3H_2O_4)_2(C_4H_4N_2)]$. *Eur. J. Inorg. Chem*. **2003**, 1181–1185.

(307) Saines, P. J.; Tan, J.-C.; Yeung, H. H.-M.; Barton, P. T.; Cheetham, A. K. Layered Inorganic–Organic Frameworks Based on the 2,2-Dimethylsuccinate Ligand: Structural Diversity and Its Effect on Nanosheet Exfoliation and Magnetic Properties. *Dalton Trans*. **2012**, *41*, 8585–8593.

(308) Guillou, N.; Livage, C.; van Beek, W.; Noguès, M.; Férey, G. A Layered Nickel Succinate with Unprecedented Hexanickel Units: Structure Elucidation from Powder-Diffraction Data, and Magnetic and Sorption Properties. *Angew. Chem. Int. Ed*. **2003**, *42*, 643–647.

(309) Livage, C.; Egger, C.; Noguès, M.; Férey, G. Hybrid Open Frameworks (MIL-*n*). Part 5 Synthesis and Crystal Structure of MIL-9: A New Three-Dimensional Ferrimagnetic Cobalt(II) Carboxylate with a Two-Dimensional Array of Edge-Sharing Co Octahedra with 12-Membered Rings. *J. Mater. Chem*. **1998**, *8*, 2743–2747.

(310) Livage, C.; Egger, C.; Férey, G. Hybrid Open Networks (MIL 16): Synthesis, Crystal Structure, and Ferrimagnetism of $Co_4(OH)_2(H_2O)_2(C_4H_4O_4)_3\cdot 2H_2O$, a New Layered Cobalt(II) Carboxylate with 14-Membered Ring Channels. *Chem. Mater*. **1999**, *11*, 1546–1550.

(311) Saines, P. J.; Melot, B. C.; Seshadri, R.; Cheetham, A. K. Synthesis, Structure and Magnetic Phase Transitions of the Manganese Succinate Hybrid Framework, $Mn(C_4H_4O_4)$. *Chem. – Eur. J*. **2010**, *16*, 7579–7585.

(312) Saines, P. J.; Hester, J. R.; Cheetham, A. K. Neutron Diffraction Study of the Magnetic Structures of Manganese Succinate $Mn(C_4H_4O_4)$: A Complex Inorganic-Organic Framework. *Phys. Rev. B* **2010**, *82*, 144435.

(313) Tan, J.-C.; Saines, P. J.; Bithell, E. G.; Cheetham, A. K. Hybrid Nanosheets of an Inorganic–Organic Framework Material: Facile Synthesis, Structure, and Elastic Properties. *ACS Nano* **2012**, *6*, 615–621.

(314) Saines, P. J.; Steinmann, M.; Tan, J.-C.; Yeung, H. H.-M.; Li, W.; Barton, P. T.; Cheetham, A. K. Isomer-Directed Structural Diversity and Its Effect on the Nanosheet Exfoliation and Magnetic Properties of 2,3-Dimethylsuccinate Hybrid Frameworks. *Inorg. Chem*. **2012**, *51*, 11198–11209.

(315) Saines, P. J.; Barton, P. T.; Jain, P.; Cheetham, A. K. Structures and Magnetic Properties of Mn and Co Inorganic–Organic Frameworks with Mixed Linear Dicarboxylate Ligands. *Cryst. Eng. Commun*. **2012**, *14*, 2711–2720.

(316) Guillou, N.; Livage, C.; Drillon, M.; Férey, G. The Chirality, Porosity, and Ferromagnetism of a 3D Nickel Glutarate with Intersecting 20-Membered Ring Channels. *Angew. Chem. Int. Ed*. **2003**, *42*, 5314–5317.

(317) Lee, E.; Kim, Y.; Jung, D.-Y. A Coordination Polymer of Cobalt(II)–Glutarate: Two-Dimensional Interlocking Structure by Dicarboxylate Ligands with Two Different Conformations. *Inorg. Chem*. **2002**, *41*, 501–506.

(318) Saines, P. J.; Barton, P. T.; Jura, M.; Knight, K. S.; Cheetham, A. K. Cobalt Adipate, $Co(C_6H_8O_4)$: Antiferromagnetic Structure, Unusual Thermal Expansion and Magnetoelastic Coupling. *Mater. Horiz*. **2014**, *1*, 332–337.

(319) Livage, C.; Egger, C.; Noguès, M.; Férey, G. Synthesis, Structural and Magnetic Characterisation of MIL 36, $Co(C_7H_{10}O_4)$, a Three-Dimensional Coordination Polymer. *C. R. Acad. Sci., Ser. IIc: Chim*. **2001**, *4*, 221–226.

(320) Sibille, R.; Mazet, T.; Malaman, B.; Gaudisson, T.; François, M. $Co_4(OH)_2(C_{10}H_{16}O_4)_3$ Metal−Organic Framework: Slow Magnetic Relaxation in the Ordered Phase of Magnetic Chains. *Inorg. Chem*. **2012**, *51*, 2885–2892.

(321) Zhu, P.; Gu, W.; Cheng, F.-Y.; Liu, X.; Chen, J.; Yan, S.-P.; Liao, D.-Z. Design of Two 3D Homochiral Co(II) Metal–Organic Open Frameworks by Layered-Pillar Strategy: Structure and Properties. *Cryst. Eng. Commun*. **2008**, *10*, 963–967.

(322) Zeng, M.-H.; Gao, S.; Chen, X.-M. A Novel 3D Coordination Polymer Containing Pentacoordinate Cobalt(II) Dimers with Antiferromagnetic Ordering. *Inorg. Chem. Commun*. **2004**, *7*, 864–867.

(323) Beghidja, A.; Rabu, P.; Rogez, G.; Welter, R. Synthesis, Structure and Magnetic Properties of Chiral and Nonchiral Transition-Metal Malates. *Chem. –Eur. J*. **2006**, *12*, 7627–7638.

(324) Coronado, E.; Galán-Mascarós, J. R.; Gómez-García, C. J.; Murcia-Martínez, A. Chiral Molecular Magnets: Synthesis, Structure, and Magnetic Behavior of the Series [M(L-tart)] (M = Mn^{II}, Fe^{II}, Co^{II}, Ni^{II}; L-tart = (2*R*,3*R*)-(+)-Tartrate). *Chem. –Eur. J*. **2006**, *12*, 3484–3492.

(325) Xiang, S.; Wu, X.; Zhang, J.; Fu, R.; Hu, S.; Zhang, X. A 3D Canted Antiferromagnetic Porous Metal–Organic Framework with Anatase Topology Through Assembly of an Analogue of Polyoxometalate. *J. Am. Chem. Soc*. **2005**, *127*, 16352–16353.

(326) Cave, D.; Gascon, J.-M.; Bond, A. D.; Teat, S. J.; Wood, P. T. Layered Metal Organosulfides: Hydrothermal Synthesis, Structure and Magnetic Behavior of the Spin-Canted Magnet Co(1,2-$(O_2C)(S)C_6H_4$). *Chem. Commun.* **2002**, 1050−1051.

(327) Wang, X.-T.; Wang, Z.-M.; Gao, S. Honeycomb Layer of Cobalt(II) Azide Hydrazine Showing Weak Ferromagnetism. *Inorg. Chem*. **2007**, *46*, 10452–10454.

(328) Zeng, M.-H.; Wang, B.; Wang, X.-Y.; Zhang, W.-X.; Chen, X.-M.; Gao, S. Chiral Magnetic Metal-Organic Frameworks of Dimetal Subunits: Magnetism Tuning by Mixed-Metal Compositions of the Solid Solutions. *Inorg. Chem.* **2006**, *45*, 7069–7076.

(329) Yufit, D. S.; Price, D. J.; Howard, J. A. K.; Gutschke, S. O. H.; Powell, A. K.; Wood, P. T. New Type of Metal Squarates. Magnetic and Multi-Temperature X-Ray Study of Di-hydroxy(μ_6-squarato)manganese. *Chem. Commun*. **1999**, 1561–1562.

(330) Mole, R. A.; Stride, J. A.; Wills, A. S.; Wood, P. T. Static and Dynamic Properties of $Mn_2(OH)_2(C_4O_4)$. *Physica B* **2006**, *385–386*, 435–437.

(331) Mole, R. A.; Cottrell, S. P.; Stride, J. A.; Wood, P. T. Muon Spin Relaxation Study of Manganese Hydroxy Squarate. *Inorg. Chim. Acta* **2008**, *361*, 3718–3722.

(332) Gutschke, S. O. H.; Molinier, M.; Powell, A. K.; Wood, P. T. Hydrothermal Synthesis of Microporous Transition Metal Squarates: Preparation and Structure of $[Co_3(\mu_3\text{-}OH)_2(C_4O_4)_2]\cdot 3H_2O$. *Angew. Chem. Int. Ed. Engl.* **1997**, *36*, 991–992.

(333) Kurmoo, M.; Kumagai, H.; Chapman, K. W.; Kepert, C. J. Reversible Ferromagnetic–Antiferromagnetic Transformation upon Dehydration–Hydration of the Nanoporous Coordination Framework, $[Co_3(OH)_2(C_4O_4)_2]\cdot 3H_2O$. *Chem. Commun*. **2005**, 3012–3014.

(334) Mole, R. A.; Stride, J. A.; Henry, P. F.; Hoelzel, M.; Senyshyn, A.; Alberola, A.; Gómez-García, C. J.; Raithby, P. R.; Wood, P. T. Two Stage Magnetic Ordering and Spin Idle Behavior of the Coordination Polymer $Co_3(OH)_2(C_4O_4)_2\cdot 3H_2O$ Determined Using Neutron Diffraction. *Inorg. Chem*. **2011**, *50*, 2246–2251.

(335) Goswami, S.; Adhikary, A.; Jema, H. S.; Biswas, S.; Konar, S. A 3D Iron(II)-Based MOF with Squashed Cuboctahedral Nanoscopic Cages Showing Spin-Canted Long-Range Antiferromagnetic Ordering. *Inorg. Chem*. **2013**, *52*, 12064–12069.

(336) Díaz-Gallifa, P.; Fabelo, O.; Pasán, J.; Cañadillas-Delgado, L.; Rodríguez-Carvajal, J.; Lloret, F.; Julve, M.; Ruiz-Pérez, C. Synthesis, Crystal Structure, and Magnetic Characterization of the Three-Dimensional Compound $[Co_2(cbut)(H_2O)_3]_n$ (H_4cbut = 1,2,3,4-Cyclobutanetetracarboxylic Acid). *Inorg. Chem*. **2014**, *53*, 5674–5683.

(337) Zheng, Y.-Z.; Tong, M.-L.; Zhang, W.-X.; Chen, X.-M. Coexistence of Spin Frustration and Long-Range Magnetic Ordering in a Triangular $Co^{II}_3(\mu_3\text{-}OH)$-Based Two-Dimensional Compound. *Chem. Commun*. **2006**, 165–167.

(338) Kurmoo, M.; Kumagai, H.; Akita-Tanaka, M.; Inoue, K.; Takagi, S. Metal−Organic Frameworks from Homometallic Chains of Nickel(II) and 1,4-Cyclohexanedicarboxylate Connectors: Ferrimagnet−Ferromagnet Transformation. *Inorg. Chem*. **2006**, *45*, 1627–1637.

(339) Kumagai, H.; Akita-Tanaka, M.; Inoue, K.; Kurmoo, M. Hydrothermal Synthesis and Characterization of a New 3D-Network Containing the Versatile *cis*,*cis*-Cyclohexane-1,3,5-tricarboxylate. *J. Mater. Chem*. **2001**, *11*, 2146–2151.

(340) Wang, J.; Zheng, L.-L.; Li, C.-J.; Zheng, Y.-Z.; Tong, M.-L. Coexistence of Planar and Chair-Shaped Cyclic Water Hexamers in a Unique Cyclohexanehexacarboxylate-Bridged Metal–Organic Framework. *Cryst. Growth Des*. **2006**, *6*, 357–359.

(341) Britt, D.; Tranchemontagne, D.; Yaghi, O. M. Metal-Organic Frameworks with High Capacity and Selectivity for Harmful Gases. *Proc. Natl. Acad. Sci. U. S. A.* **2008**, *105*, 11623–11627.

(342) Kirchon, A.; Feng, L.; Drake, H. F.; Joseph, E. A.; Zhou, H.-C. From Fundamentals to Applications: A Toolbox for Robust and Multifunctional MOF Materials. *Chem. Soc. Rev.* **2018**, *47*, 8611–8638.

(343) Abednatanzi, S.; Derakhshandeh, P. G.; Depauw, H.; Coudert, F.-X.; Vrielinck, H.; Van Der Voort, P.; Leus, K. Mixed-Metal Metal-Organic Frameworks. *Chem. Soc. Rev.* **2019**, *48*, 2535–2565.

(344) Sibille, R.; Mesbah, A.; Mazet, T.; Malaman, B.; Capelli, S.; François, M. Magnetic Measurements and Neutron Diffraction Study of the Layered Hybrid Compounds $Mn(C_8H_4O_4)(H_2O)_2$ and $Mn_2(OH)_2(C_8H_4O_4)$. *J. Solid State Chem.* **2012**, *186*, 134–141.

(345) Asha, K. S.; Ranjith, K. M.; Yogi, A.; Nath, R.; Mandal, S. Magnetic Properties of Manganese Based One-Dimensional Spin Chains. *Dalton Trans.* **2015**, *44*, 19812–19819.

(346) Barthelet, K.; Marrot, J.; Riou, D.; Férey, G. A Breathing Hybrid Organic–Inorganic Solid with Very Large Pores and High Magnetic Characteristics. *Angew. Chem. Int. Ed.* **2002**, *41*, 281–284.

(347) Millange, F.; Serre, C.; Férey, G. Synthesis, Structure Determination and Properties of MIL-53as and MIL-53ht: The First Cr^{III} Hybrid Inorganic–Organic Microporous Solids: $Cr^{III}(OH)\cdot\{O_2C–C_6H_4–CO_2\}\cdot\{HO_2C–C_6H_4–CO_2H\}_x$. *Chem Commun.* **2002**, 822–823.

(348) Serre, C.; Millange, F.; Thouvenot, C.; Noguès, M.; Marsolier, G.; Louër, D.; Férey, G. Very Large Breathing Effect in the First Nanoporous Chromium(III)-Based Solids: MIL-53 or $Cr^{III}(OH)\cdot\{O_2C–C_6H_4–CO_2\}\cdot\{HO_2C–C_6H_4–CO_2H\}_x\cdot H_2O_y$. *J. Am. Chem. Soc.* **2002**, *124*, 13519–13526.

(349) Dietzel, P. D. C.; Morita, Y.; Blom, R.; Fjellvåg, H. An In Situ High-Temperature Single-Crystal Investigation of a Dehydrated Metal–Organic Framework Compound and Field-Induced Magnetization of One-Dimensional Metal–Oxygen Chains. *Angew. Chem. Int. Ed.* **2005**, *44*, 6354–6358.

(350) Rubio-Giménez, V.; Waerenborgh, J. C.; Clemente-Juan, J. M.; Martí-Gastaldo, C. Spontaneous Magnetization in Heterometallic NiFe-MOF-74 Microporous Magnets by Controlled Iron Doping. *Chem. Mater.* **2017**, *29*, 6181–6185.

(351) Moulton, B.; Lu, J.; Hajndl, R.; Hariharan, S.; Zaworotko, M. J. Crystal Engineering of a Nanoscale Kagomé Lattice. *Angew. Chem. Int. Ed*. **2002**, *41*, 2821–2824.

(352) Shen, L.; Yang, S.-W.; Xiang, S.; Liu, T.; Zhao, B.; Ng, M.-F.; Göettlicher, J.; Yi, J.; Li, S.; Wang, L.; Ding, J.; Chen, B.; Wei, S.-H.; Feng, Y. P. Origin of Long-Range Ferromagnetic Ordering in Metal−Organic Frameworks with Antiferromagnetic Dimeric-Cu(II) Building Units. *J. Am. Chem. Soc*. **2012**, *134*, 17286−17290.

(353) Riou-Cavellec, M.; Albinet, C.; Livage, C.; Guillou, N.; Noguès, M.; Grenèche, J. M.; Férey, G. Ferromagnetism of the Hybrid Open Framework $K[M_3(BTC)_3]\cdot 5H_2O$ (M = Fe, Co) or MIL-45. *Solid State Sci*. **2002**, *4*, 267−270.

(354) Kumagai, H.; Kepert, C. J.; Kurmoo, M. Construction of Hydrogen-Bonded and Coordination-Bonded Networks of Cobalt(II) with Pyromellitate: Synthesis, Structures, and Magnetic Properties. *Inorg. Chem*. **2002**, *41*, 3410−3422.

(355) Kumagai, H.; Chapman, K. W.; Kepert, C. J.; Kurmoo, M. Binary Metal(II)–Pyromellitate Coordination Polymers, M_2(pm) (M = Co, Fe, Mn): Synthesis, Structures and Magnetic Properties. *Polyhedron* **2003**, *22*, 1921−1927.

(356) Sanselme, M.; Grenèche, J.-M.; Riou-Cavellec, M.; Férey, G. The First Ferric Carboxylate with a Three-Dimensional Hydrid Open-Framework (MIL-82): Its Synthesis, Structure, Magnetic Behavior and Study of Its Dehydration by Mössbauer Spectroscopy. *Solid State Sci*. **2004**, *6*, 853−858.

(357) Jia, H.-P.; Li, W.; Ju, Z.-F.; Zhang, J. $[Co_5(\mu_3\text{-}OH)_2(btec)_2(bpp)]_n$: A Three-Dimensional Homometallic Molecular Metamagnet Built from the Mixed Hydroxide/Carboxylate-Bridged Ferrimagnetic-Like Chains. *Dalton Trans*. **2007**, 3699−3704.

(358) Nakakuma, M.; Yamamoto, J.; Takagi, S.; Mito, M.; Deguchi, H.; Yoshihiro, M.; Kyritsakas, N.; Kurmoo, M. Crystal Structure and Magnetic Properties of Hydrated and Dehydrated Nickel(II)-Pyromellitate. *J. Magn. Magn. Mater*. **2007**, *310*, 1435−1437.

(359) Yang, E.-C.; Liu, Z.-Y.; Liu, Z.-Y.; Zhao, L.-N.; Zhao, X.-J. Long-Range Ferromagnetic Ordering in a 3D Cu^{II}-Tetracarboxylate Framework Assisted by an Unprecedented Bidentate μ_2-O1,N4 Hypoxanthine Nucleobase. *Dalton Trans*. **2010**, 8868−8871.

(360) Wang, X.-Y.; Sevov, S. C. Synthesis, Structures, and Magnetic Properties of Metal-Coordination Polymers with Benzenepentacarboxylate Linkers. *Inorg. Chem*. **2008**, *47*, 1037−1043.

(361) Bernini, M. C.; de Paz, J. R.; Snejko, N.; Sáez-Puche, R.; Gutierrez-Puebla, E.; Monge, M. Á. Unusual Magnetic Behaviors and Electronic Configurations Driven by Diverse Co(II) or Mn(II) MOF Architectures. *Inorg. Chem*. **2014**, *53*, 12885−12895.

(362) Weihe, H.; Güdel, H. U. Quantitative Interpretation of the Goodenough–Kanamori Rules: A Critical Analysis. *Inorg. Chem*. **1997**, *36*, 3632–3639.

(363) Bloch, E. D.; Murray, L. J.; Queen, W. L.; Chavan, S.; Maximoff, S. N.; Bigi, J. P.; Krishna, R.; Peterson, V. K.; Grandjean, F.; Long, G. J.; Smit, B.; Bordiga, S.; Brown, C. M.; Long, J. R. Selective Binding of O_2 over N_2 in a Redox–Active Metal–Organic Framework with Open Iron(II) Coordination Sites. *J. Am. Chem. Soc*. **2011**, *133*, 14814–14822.

(364) Bloch, E. D.; Queen, W. L.; Krishna, R.; Zadrozny, J. M.; Brown, C. M.; Long, J. R. Hydrocarbon Separations in a Metal-Organic Framework with Open Iron(II) Coordination Sites. *Science* **2012**, *335*, 1606–1610.

(365) Park, J.; Kim, H.; Jung, Y. Origin of Selective Guest-Induced Magnetism Transition in Fe/MOF-74. *J. Phys. Chem.* Lett. **2013**, *4*, 2530–2534.

(366) Kim, H.; Park, J.; Jung, Y. The Binding Nature of Light Hydrocarbons on Fe/MOF-74 for Gas Separation. *Phys. Chem. Chem. Phys*. **2013**, *15*, 19644–19650.

(367) Han, S.; Kim, H.; Kim, J.; Jung, Y. Modulating the Magnetic Behavior of Fe(II)–MOF-74 by the High Electron Affinity of the Guest Molecule. *Phys. Chem. Chem. Phys*. **2015**, *17*, 16977–16982.

(368) Köberl, M.; Cokoja, M.; Herrmann, W. A.; Kühn, F. E. From Molecules to Materials: Molecular Paddle-Wheel Synthons of Macromolecules, Cage Compounds and Metal–Organic Frameworks. *Dalton Trans*. **2011**, *40*, 6834–6859.

(369) Chui, S. S.-Y.; Lo, S. M.-F.; Charmant, J. P. H.; Orpen, A. G.; Williams, I. D. A Chemically Functionalizable Nanoporous Material $[Cu_3(TMA)_2(H_2O)_3]_n$. *Science* **1999**, *283*, 1148−1150.

(370) Zhang, X. X.; Chui, S. S.-Y.; Williams, I. D. Cooperative Magnetic Behavior in the Coordination Polymers $[Cu_3(TMA)_2L_3]$ (L = H_2O, Pyridine). *J. Appl. Phys*. **2000**, *87*, 6007−6009.

(371) Pöppl, A.; Kunz, S.; Himsl, D.; Hartmann, M. CW and Pulsed ESR Spectroscopy of Cupric Ions in the Metal–Organic Framework Compound $Cu_3(BTC)_2$. *J. Phys. Chem. C* **2008**, *112*, 2678–2684.

(372) Chen, B.; Ockwig, N. W.; Millward, A. R.; Contreras, D. S.; Yaghi, O. M. High H_2 Adsorption in a Microporous Metal–Organic Framework with Open Metal Sites. *Angew. Chem. Int. Ed*. **2005**, *44*, 4745−4749.

(373) Desai, A. V.; Sharma, S.; Let, S.; Ghosh, S. K. N-Donor Linker Based Metal-Organic Frameworks (MOFs): Advancement and Prospects as Functional Materials. *Coord. Chem. Rev*. **2019**, *395*, 146–192.

(374) Real, J. A.; De Munno, G.; Muñoz, M. C.; Julve, M. Crystal Structure and Magnetic Properties of $[Fe(pyz)_2(NCS)_2]_n$ (pyz = Pyrazine), a 2D Sheetlike Polymer. *Inorg. Chem*. **1991**, *30*, 2701–2704.

(375) Bordallo, H. N.; Chapon, L.; Manson, J. L.; Hernández-Velasco, J.; Ravot, D.; Reiff, W. M.; Argyriou, D. N. S = ½ Ising Behavior in the Two-Dimensional Molecular Magnet $Fe(NCS)_2$(pyrazine)$_2$. *Phys. Rev. B* **2004**, *69*, 224405.

(376) Sun, H.-L.; Ma, B.-Q.; Gao, S.; Su, G. Pyrazine Dioxide Bridged Two-Dimensional Antiferromagnets $[M(NCS)_2(pzdo)_2]$ (M = Mn, Co; pzdo = Pyrazine Dioxide). *Chem. Commun*. **2001**, 2586–2587.

(377) Lloret, F.; De Munno, G.; Julve, M.; Cano, J.; Ruiz, R.; Caneschi, A. Spin Polarization and Ferromagnetism in Two-Dimensional Sheetlike Cobalt(II) Polymers: $[Co(L)_2(NCS)_2]$ (L = Pyrimidine or Pyrazine). *Angew. Chem. Int. Ed*. **1998**, *37*, 135–138.

(378) McConnell, H. M. Ferromagnetism in Solid Free Radicals. *J. Chem. Phys*. **1963**, *39*, 1910.

(379) Mataga, N. Possible “Ferromagnetic States” of Some Hypothetical Hydrocarbons. *Theor. Chim. Acta* **1968**, *10*, 372–376.

(380) Oshio, H.; Ichida, H. Control of Intramolecular Magnetic Interaction by the Spin Polarization of d_π Spin to p_π Orbital of an Organic Bridging Ligand. *J. Phys. Chem*. **1995**, *99*, 3294–3302.

(381) Barea, E.; Navarro, J. A. R.; Salas, J. M.; Masciocchi, N.; Galli, S.; Sironi, A. Coordination Frameworks Containing the Pyrimidin-4-olate Ligand. Synthesis, Thermal, Magnetic, and *ab Initio* XRPD Structural Characterization of Nickel and Zinc Derivatives. *Inorg. Chem*. **2004**, *43*, 473–481.

(382) Barea, E.; Quirós, M.; Navarro, J. A. R.; Salas, J. M. Heteroleptic Pyrimidine-2-olate and 4,4′-Bipyridine Copper(II) Layered Metal–Organic Frameworks with Swelling Properties. *Dalton Trans*. **2005**, 1743–1746.

(383) Llabrés i Xamena, F. X.; Casanova, O.; Galiasso Tailleur, R.; Garcia, H.; Corma, A. Metal Organic Frameworks (MOFs) as Catalysts: A Combination of Cu^{2+} and Co^{2+} MOFs as an Efficient Catalyst for Tetralin Oxidation. *J. Catal*. **2008**, *255*, 220–227.

(384) Schuster, S.; Klemm, E.; Bauer, M. The Role of Pd^{2+}/Pd^{0} in Hydrogenation by $[Pd(2\text{-pymo})_2]_n$: An X-Ray Absorption and IR Spectroscopic Study. *Chem. –Eur. J*. **2012**, *18*, 15831–15837.

(385) Galli, S.; Masciocchi, N.; Tagliabue, G.; Sironi, A.; Navarro, J. A. R.; Salas, J. M.; Mendez-Liñan, L.; Domingo, M.; Perez-Mendoza, M.; Barea, E. Polymorphic Coordination Networks Responsive to CO_2, Moisture, and Thermal Stimuli: Porous Cobalt(II) and Zinc(II) Fluoropyrimidinolates. *Chem. –Eur. J*. **2008**, *14*, 9890–9901.

(386) Navarro, J. A. R.; Barea, E.; Rodríguez-Diéguez, A.; Salas, J. M.; Ania, C. O.; Parra, J. B.; Masciocchi, N.; Galli, S.; Sironi, A. Guest-Induced Modification of a Magnetically Active Ultramicroporous, Gismondine-like, Copper(II) Coordination Network. *J. Am. Chem. Soc*. **2008**, *130*, 3978–3984.

(387) Masciocchi, N.; Galli, S.; Sironi, A.; Barea, E.; Navarro, J. A. R.; Salas, J. M.; Tabares, L. C. Rich Structural and Magnetic Chemistry of Cobalt(II) Pyrimidin-2-olate and Pyrimidin-4-olate Complexes. Synthesis, X-Ray Powder Diffraction Studies, and Thermal Behavior. *Chem. Mater*. **2003**, *15*, 2153–2160.

(388) Masciocchi, N.; Galli, S.; Sironi, A.; Cariati, E.; Galindo, M. A.; Barea, E.; Romero, M. A.; Salas, J. M.; Navarro, J. A. R.; Santoyo-González, F. Tuning the Structural and Magnetic Properties of Thermally Robust Coordination Polymers. *Inorg. Chem*. **2006**, *45*, 7612–7620.

(389) Kolks, G.; Lippard, S. J.; Waszczak, J. V.; Lilienthal, H. R. Magnetic Exchange in Imidazolate-Bridged Copper(II) Complexes. *J. Am. Chem. Soc*. **1982**, *104*, 717–725.

(390) Coughlin, P. K.; Lippard, S. J. Magnetic, ESR, Electrochemical, and Potentiometric Titration Studies of the Imidazolate-Bridged Dicopper(II) Ion in a Binucleating Macrocycle. *Inorg. Chem*. **1984**, *23*, 1446–1451.

(391) Bencini, A.; Benelli, C.; Gatteschi, D.; Zanchini, C. Magnetic Coupling in a Linear-Chain Copper(II)–Imidazolate Compound. Mechanism of the Exchange Interaction Through Bridging Imidazolate Ligands. *Inorg. Chem.* **1986**, *25*, 398–400.

(392) Coronado, E.; Giménez-Marqués, M.; Espallargas, G. M.; Brammer, L. Tuning the Magneto-Structural Properties of Non-Porous Coordination Polymers by HCl Chemisorption. *Nat. Commun.* **2012**, *3*, 828.

(393) Koch, C. A.; Reed, C. A.; Brewer, G. A.; Rath, N. P.; Scheidt, W. R.; Gupta, G.; Lang, G. Ferromagnetic Coupling via Imidazolate in an Iron(III)–Porphyrin–Dicopper(II) System. *J. Am. Chem. Soc.* **1989**, *111*, 7645–7648.

(394) Lambert, F.; Renault, J.-P.; Policar, C.; Morgenstern-Badarau, I.; Cesario, M. A Polymeric, Layered Bimetallic Mn(II)Fe(III) Imidazolate Network; Crystal Structure and Magnetic Properties. *Chem. Commun.* **2000**, 35–36.

(395) Costes, J.-P.; Laurent, J.-P. New Route to Bimetallic Imidazolate-Bridged Complexes V. Spin Delocalization in Pyridine Adducts of Mononuclear and Dinuclear Nickel(II) Complexes: A ^{1}H NMR Study. *Inorg. Chim. Acta* **1990**, *177*, 277–282.

(396) Rettig, S. J.; Storr, A.; Summers, D. A.; Thompson, R. C.; Trotter, J. Transition Metal Azolates from Metallocenes. 2. Synthesis, X-Ray Structure, and Magnetic Properties of a Three-Dimensional Polymetallic Iron(II) Imidazolate Complex, a Low-Temperature Weak Ferromagnet. *J. Am. Chem. Soc.* **1997**, *119*, 8675–8680.

(397) Rettig, S. J.; Storr, A.; Summers, D. A.; Thompson, R. C.; Trotter, J. Iron(II) 2-Methylimidazolate and Copper(II) 1,2,4-Triazolate Complexes: Systems Exhibiting Long-Range Ferromagnetic Ordering at Low Temperatures. *Can. J. Chem.* **1999**, *77*, 425–433.

(398) Rettig, S. J.; Sánchez, V.; Storr, A.; Thompson, R. C.; Trotter, J. Polybis(4-azabenzimidazolato)-Iron(II) and -Cobalt(II). 3-D Single Diamond-Like Framework Materials which Exhibit Spin Canting and Ferromagnetic Ordering at Low Temperatures. *J. Chem. Soc., Dalton Trans.* **2000**, 3931–3937.

(399) Tian, Y.-Q.; Cai, C.-X.; Ren, X.-M.; Duan, C.-Y.; Xu, Y.; Gao, S.; You, X.-Z. The Silica-Like Extended Polymorphism of Cobalt(II) Imidazolate Three-Dimensional Frameworks: X-Ray Single-Crystal Structures and Magnetic Properties. *Chem. –Eur. J.* **2003**, *9*, 5673–5685.

(400) Tian, Y.-Q.; Chen, Z.-X.; Weng, L.-H.; Guo, H.-B.; Gao, S.; Zhao, D. Y. Two Polymorphs of Cobalt(II) Imidazolate Polymers Synthesized Solvothermally by Using One Organic Template *N*,*N*-Dimethylacetamide. *Inorg. Chem.* **2004**, *43*, 4631–4635.

(401) Hagrman, P. J.; Bridges, C.; Greedan, J. E.; Zubieta, J. A Three-Dimensional Organic–Inorganic Composite Material Constructed from Copper–Triazolate Networks Linked Through Vanadium Oxide Chains: [{$Cu_3(trz)_2$}V_4O_{12}]. *J. Chem. Soc., Dalton Trans*. **1999**, 2901–2903.

(402) Gao, E.-Q.; Liu, N.; Cheng, A.-L.; Gao, S. Novel Frustrated Magnetic Lattice Based on Triangular [$Mn_3(\mu_3$-F)] Clusters with Tetrazole Ligands. *Chem. Commun*. **2007**, 2470–2472.

(403) Li, J.-R.; Yu, Q.; Sañudo, E. C.; Tao, Y.; Bu, X.-H. An Azido–Cu^{II}–Triazolate Complex with utp-Type Topological Network, Showing Spin-Canted Antiferromagnetism. *Chem. Commun*. **2007**, 2602–2604.

(404) Li, J.-R.; Yu, Q.; Sañudo, E. C.; Tao, Y.; Song, W.-C.; Bu, X.-H. Three-Dimensional Homospin Inorganic–Organic Ferrimagnet Constructed from $(VO_3^-)_n$ Chains Linking {[5-(Pyrimidin-2-yl)tetrazolato-$(Cu^{II})_{1.5}]^{2+}\}_n$ Layers. *Chem. Mater*. **2008**, *20*, 1218–1220.

(405) Hou, Z.-J.; Liu, Z.-Y.; Liu, N.; Yang, E.-C.; Zhao, X.-J. Four Tetrazolate-Based 3D Frameworks with Diverse Subunits Directed by Inorganic Anions and Azido Coligand: Hydro/Solvothermal Syntheses, Crystal Structures, and Magnetic Properties. *Dalton Trans*. **2015**, *44*, 2223–2233.

(406) Ruiz, E.; Cano, J.; Alvarez, S.; Alemany, P. Magnetic Coupling in End-On Azido-Bridged Transition Metal Complexes: A Density Functional Study. *J. Am. Chem. Soc*. **1998**, *120*, 11122–11129.

(407) Chen, H.-J.; Mao, Z.-W.; Gao, S.; Chen, X.-M. Ferrimagnetic-Like Ordering in a Unique Three-Dimensional Coordination Polymer Featuring Mixed Azide/Carboxylate-Bridged Trinuclear Manganese(II) Clusters as Subunits. *Chem. Commun*. **2001**, 2320–2321.

(408) Tong, M.-L.; Kitagawa, S.; Chang, H.-C.; Ohba, M. Temperature-Controlled Hydrothermal Synthesis of a 2D Ferromagnetic Coordination Bilayered Polymer and a Novel 3D Network with Inorganic $Co_3(OH)_2$ Ferrimagnetic Chains. *Chem. Commun*. **2004**, 418–419.

(409) Huang, Y.-G.; Yuan, D.-Q.; Pan, L.; Jiang, F.-L.; Wu, M.-Y.; Zhang, X.-D.; Wei, W.; Gao, Q.; Lee, J. Y.; Li, J.; Hong, M.-C. A 3D Porous Cobalt–Organic Framework Exhibiting Spin-

Canted Antiferromagnetism and Field-Induced Spin-Flop Transition. *Inorg. Chem*. **2007**, *46*, 9609–9615.

(410) Zeng, M.-H.; Yin, Z.; Tan, Y.-X.; Zhang, W.-X.; He, Y.-P.; Kurmoo, M. Nanoporous Cobalt(II) MOF Exhibiting Four Magnetic Ground States and Changes in Gas Sorption upon Post-Synthetic Modification. *J. Am. Chem. Soc*. **2014**, *136*, 4680–4688.

(411) Rodríguez-Diéguez, A.; Cano, J.; Kivekäs, R.; Debdoubi, A.; Colacio, E. Self-Assembled Cationic Heterochiral Honeycomb-Layered Metal Complexes with the In Situ Generated Pyrimidine-2-carboxylato Bisdidentate Ligand. Hydrothermal Synthesis, Crystal Structures, Magnetic Properties, and Theoretical Study of $[M_2(\mu\text{-pymca})_3]OH\cdot H_2O$ ($M = Fe^{II}$, Co^{II}). *Inorg. Chem*. **2007**, *46*, 2503–2510.

(412) Martinez-Lorente, M.-A.; Tuchagues, J.-P.; Pétrouléas, V.; Savariault, J.-M.; Poinsot, R.; Drillon, M. $[Fe(4\text{-imidazoleacetate})_2]\cdot 2CH_3OH$: A 2D Antiferromagnetic Iron(II) System Exhibiting 3D Long-Range Ordering with a Net Magnetic Moment at 15 K. *Inorg. Chem*. **1991**, *30*, 3587–3589.

(413) Zhang, X.-M.; Hao, Z.-M.; Zhang, W.-X.; Chen, X.-M. Dehydration-Induced Conversion from a Single-Chain Magnet into a Metamagnet in a Homometallic Nanoporous Metal–Organic Framework. *Angew. Chem. Int. Ed*. **2007**, *46*, 3456–3459.

(414) Zhang, W.-X.; Xue, W.; Lin, J.-B.; Zheng, Y.-Z.; Chen, X.-M. 3D Geometrically Frustrated Magnets Assembled by Transition Metal Ion and 1,2,3-Triazole-4,5-dicarboxylate as Triangular Nodes. *Cryst. Eng. Commun*. **2008**, *10*, 1770–1776.

(415) Jia, Q.-X.; Wang, Y.-Q.; Yue, Q.; Wang, Q.-L.; Gao, E.-Q. Isomorphous Co^{II} and Mn^{II} Materials of Tetrazolate-5-carboxylate with an Unprecedented Self-Penetrating Net and Distinct Magnetic Behaviours. *Chem. Commun*. **2008**, 4894–4896.

(416) Li, J.-R.; Yu, Q.; Tao, Y.; Bu, X.-H.; Ribas, J.; Batten, S. R. Magnetic Canting or not? Two Isomorphous 3D Co^{II} and Ni^{II} Coordination Polymers with the Rare Non-Interpenetrated (10,3)-d Topological Network, Showing Spin-Canted Antiferromagnetism only in the Co^{II} System. *Chem. Commun*. **2007**, 2290–2292.

(417) Mercuri, M. L.; Congiu, F.; Concas, G.; Sahadevan, S. A. Recent Advances on Anilato-Based Molecular Materials with Magnetic and/or Conducting Properties. *Magnetochemistry* **2017**, *3*, 17.

(418) Kitagawa, S.; Kawata, S. Coordination Compounds of 1,4-Dihydroxybenzoquinone and Its Homologues. Structures and Properties. *Coord. Chem. Rev*. **2002**, *224*, 11–34.

(419) Abrahams, B. F.; Coleiro, J.; Ha, K.; Hoskins, B. F.; Orchard, S. D.; Robson, R. Dihydroxybenzoquinone and Chloranilic Acid Derivatives of Rare Earth Metals. *J. Chem. Soc., Dalton Trans*. **2002**, 1586–1594.

(420) Abrahams, B. F.; Hudson, T. A.; McCormick, L. J.; Robson, R. Coordination Polymers of 2,5-Dihydroxybenzoquinone and Chloranilic Acid with the (10,3)-*a* Topology. *Cryst. Growth Des*. **2011**, 2717–2720.

(421) Benmansour, S.; Vallés-García, C.; Gómez-Claramunt, P.; Espallargas, G. M.; Gómez-García, C. J. 2D and 3D Anilato-Based Heterometallic M(I)M(III) Lattices: The Missing Link. *Inorg. Chem*. **2015**, *54*, 5410–5418.

(422) Atzori, M.; Benmansour, S.; Espallargas, G. M.; Clemente-León, M.; Abhervé, A.; Gómez-Claramunt, P.; Coronado, E.; Artizzu, F.; Sessini, E.; Deplano, P.; Serpe, A.; Mercuri, M. L.; Gómez-García, C. J. A Family of Layered Chiral Porous Magnets Exhibiting Tunable Ordering Temperatures. *Inorg. Chem*. **2013**, *52*, 10031–10040.

(423) Abhervé, A.; Clemente-León, M.; Coronado, E.; Gómez-García, C. J.; Verneret, M. One-Dimensional and Two-Dimensional Anilate-Based Magnets with Inserted Spin-Crossover Complexes. *Inorg. Chem*. **2014**, *53*, 12014–12026.

(424) Abhervé, A.; Mañas-Valero, S.; Clemente-León, M.; Coronado, E. Graphene Related Magnetic Materials: Micromechanical Exfoliation of 2D Layered Magnets Based on Bimetallic Anilate Complexes with Inserted $[Fe^{III}(acac_2\text{-trien})]^+$ and $[Fe^{III}(sal_2\text{-trien})]^+$ Molecules. *Chem. Sci*. **2015**, *6*, 4665–4673.

(425) Palacios-Corella, M.; Fernández-Espejo, A.; Bazaga-García, M.; Losilla, E. R.; Cabeza, A.; Clemente-León, M.; Coronado, E. Influence of Proton Conducting Cations on the Structure and Properties of 2D Anilate-Based Magnets. *Inorg. Chem*. **2017**, *56*, 13865–13877.

(426) Benmansour, S.; Abhervé, A.; Gómez-Claramunt, P.; Vallés-García, C.; Gómez-García, C. J. Nanosheets of Two-Dimensional Magnetic and Conducting Fe(II)/Fe(III) Mixed-Valence Metal−Organic Frameworks. *ACS Appl. Mater. Interfaces* **2017**, *9*, 26210–26218.

(427) Sahadevan, S. A.; Abhervé, A.; Monni, N.; de Pipaón, C. S.; Galán-Mascarós, J. R.; Waerenborgh, J. C.; Vieira, B. J. C.; Auban-Senzier, P.; Pillet, S.; Bendeif, E.-E.; Alemany, P.; Canadell, E.; Mercuri, M. L.; Avarvari, N. Conducting Anilate-Based Mixed-Valence

Fe(II)Fe(III) Coordination Polymer: Small-Polaron Hopping Model for Oxalate-Type Fe(II)Fe(III) 2D Networks. *J. Am. Chem. Soc*. **2018**, *140*, 12611–12621.

(428) Martínez-Hernández, C.; Benmansour, S.; Gómez-García, C. J. Modulation of the Ordering Temperature in Anilato-Based Magnets. *Polyhedron* **2019**, *170*, 122–131.

(429) Martínez-Hernández, C.; Gómez-Claramunt, P.; Benmansour, S.; Gómez-García, C. J. Pre- and Post-Synthetic Modulation of the Ordering Temperatures in a Family of Anilato-Based Magnets. *Dalton Trans*. **2019**, *48*, 13212–13223.

(430) Bhattacharjee, A.; Bhakat, D.; Roy, M.; Kusz, J. Electrical Conduction Property of Molecular Magnetic Material—$\{N(n\text{-}C_4H_9)_4[Fe(II)Fe(III)(C_2O_4)_3]\}_\infty$: Before and After Thermal Degradation. *Physica B* **2010**, *405*, 1546–1550.

(431) Stumpf, H. O.; Ouahab, L.; Pei, Y., Grandjean, D.; Kahn, O. A Molecular-Based Magnet with a Fully Interlocked Three-Dimensional Structure. *Science* **1993**, *261*, 447–449.

(432) Stumpf, H. O.; Ouahab, L.; Pei, Y.; Bergerat, P.; Kahn, O. Chemistry and Physics of a Molecular-Based Magnet Containing Three Spin Carriers, with a Fully Interlocked Structure. *J. Am. Chem. Soc*. **1994**, *116*, 3866–3874.

(433) Vaz, M. G. F.; Pinheiro, L. M. M.; Stumpf, H. O.; Alcântara, A. F. C.; Golhen, S.; Ouahab, L.; Cador, O.; Mathonière, C.; Kahn, O. Soft and Hard Molecule-Based Magnets of Formula $[(Etrad)_2M_2\{Cu(opba)\}_3]\cdot S$ [$Etrad^+$ = Radical Cation, M^{II} = Mn^{II} or Co^{II}, opba = *Ortho*-phenylenebis(oxamato), S = Solvent Molecules], with a Fully Interlocked Structure. *Chem. –Eur. J*. **1999**, *5*, 1486–1495.

(434) Cador, O.; Vaz, M. G. F.; Stumpf, H. O.; Mathonière, C.; Kahn, O. Molecule-Based Magnets with a Fully Interlocked Three-Dimensional Structure. *Synth. Met*. **2001**, *122*, 559–567.

(435) Novak, M. A.; Vaz, M. G. F.; Speziali, N. L.; Costa, W. V.; Stumpf, H. O. Magnetic Properties of an Interlocked Molecular Magnet. *Polyhedron* **2003**, *22*, 2391–2394.

(436) Inoue, K.; Iwamura, H. Ferro- and Ferrimagnetic Ordering in a Two-Dimensional Network Formed by Manganese(Il) and l,3,5-Tris[*p*-(*N*-*tert*-butyl-*N*-oxyamino)phenyl]benzene. *J. Am. Chem. Soc*. **1994**, *116*, 3173–3174.

(437) Inoue, K.; Hayamizu, T.; Iwamura, H.; Hashizume, D.; Ohashi, Y. Assemblage and Alignment of the Spins of the Organic Trinitroxide Radical with a Quartet Ground State by

Means of Complexation with Magnetic Metal Ions. A Molecule-Based Magnet with Three-Dimensional Structure and High T_C of 46 K. *J. Am. Chem. Soc*. **1996**, *118*, 1803–1804.

(438) Ishida, T.; Iwamura, H. Bis[3-*tert*-butyl-5-(*N*-oxy-*tert*-butylamino)phenyl] Nitroxide in a Quartet Ground State: A Prototype for Persistent High-Spin Poly[(oxyimino)-1,3-phenylenes]. *J. Am. Chem. Soc*. **1991**, *113*, 4238–4241.

(439) Fegy, K.; Luneau, D.; Ohm, T.; Paulsen, C.; Rey, P. Two-Dimensional Nitroxide-Based Molecular Magnetic Materials. *Angew. Chem. Int. Ed*. **1998**, *37*, 1270–1273.

(440) Ballester, M. Inert Free Radicals (IFR): A Unique Trivalent Carbon Species. *Acc. Chem. Res*. **1985**, *18*, 380–387.

(441) Maspoch, D.; Ruiz-Molina, D.; Wurst, K.; Domingo, N.; Cavallini, M.; Biscarini, F.; Tejada, J.; Rovira, C.; Veciana, J. A Nanoporous Molecular Magnet with Reversible Solvent-Induced Mechanical and Magnetic Properties. *Nat. Mater*. **2003**, *2*, 190–195.

(442) Maspoch, D.; Domingo, N.; Ruiz-Molina, D.; Wurst, K.; Hernández, J.-M.; Vaughan, G.; Rovira, C.; Lloret, F.; Tejada, J.; Veciana, J. Coexistence of Ferro- and Antiferromagnetic Interactions in a Metal–Organic Radical-Based (6,3)-Helical Network with Large Channels. *Chem. Commun*. **2005**, 5035–5037.

(443) Pokhodnya, K. I.; Bonner, M.; Her, J.-H.; Stephens, P. W.; Miller, J. S. Magnetic Ordering (T_c = 90 K) Observed for Layered $[Fe^{II}(TCNE^{\bullet-})(NCMe)_2]^+[Fe^{III}Cl_4]^-$ (TCNE = Tetracyanoethylene). *J. Am. Chem. Soc*. **2006**, *128*, 15592–15593.

(444) Olson, C.; Heth, C. L.; Lapidus, S. H.; Stephens, P. W.; Halder, G. J.; Pokhodnya, K. I. Spectroscopic Study of (Two-Dimensional) Molecule-Based Magnets: $[M^{II}(TCNE)(NCMe)_2][SbF_6]$ (M = Fe, Mn, Ni). *J. Chem. Phys*. **2011**, *135*, 024503.

(445) Her, J.-H.; Stephens, P. W.; Pokhodnya, K. I.; Bonner, M.; Miller, J. S. Cross-Linked Layered Structure of Magnetically Ordered $[Fe(TCNE)_2]\cdot zCH_2Cl_2$ Determined by Rietveld Refinement of Synchrotron Powder Diffraction Data. *Angew. Chem. Int. Ed*. **2007**, *46*, 1521–1524.

(446) Miyasaka, H.; Izawa, T.; Takahashi, N.; Yamashita, M.; Dunbar, K. R. Long-Range Ordered Magnet of a Charge-Transfer Ru_2^{4+}/TCNQ Two-Dimensional Network Compound. *J. Am. Chem. Soc*. **2006**, *128*, 11358–11359.

(447) Miyasaka, H.; Motokawa, N.; Matsunaga, S.; Yamashita, M.; Sugimoto, K.; Mori, T.; Toyota, N.; Dunbar, K. R. Control of Charge Transfer in a Series of $Ru_2^{II,II}$/TCNQ Two-

Dimensional Networks by Tuning the Electron Affinity of TCNQ Units: A Route to Synergistic Magnetic/Conducting Materials. *J. Am. Chem. Soc*. **2010**, *132*, 1532–1544.

(448) Motokawa, N.; Matsunaga, S.; Takaishi, S.; Miyasaka, H.; Yamashita, M.; Dunbar, K. R. Reversible Magnetism Between an Antiferromagnet and a Ferromagnet Related to Solvation/Desolvation in a Robust Layered $[Ru_2]_2$TCNQ Charge-Transfer System. *J. Am. Chem. Soc*. **2010**, *132*, 11943–11951.

(449) Zhang, J.; Kosaka, W.; Sugimoto, K.; Miyasaka, H. Magnetic Sponge Behavior via Electronic State Modulations. *J. Am. Chem. Soc*. **2018**, *140*, 5644–5652.

(450) Fukunaga, H.; Yoshino, T.; Sagayama, H.; Yamaura, J.; Arima, T.; Kosaka, W.; Miyasaka, H. A Charge-Disproportionate Ordered State with δ = 0.75 in a Chemically Sensitive Donor/Acceptor $D^{\delta+}{}_2A^{2\delta-}$ Layered Framework. *Chem. Commun*. **2015**, *51*, 7795–7798.

(451) Motokawa, N.; Oyama, T.; Matsunaga, S.; Miyasaka, H.; Yamashita, M.; Dunbar, K. R. Charge-Transfer Two-Dimensional Layers Constructed from a 2:1 Assembly of Paddlewheel Diruthenium(II,II) Complexes and Bis[1,2,5]thiadizolotetracyanoquinodimethane: Bulk Magnetic Behavior as a Function of Inter-Layer Interactions. *Cryst. Eng. Commun*. **2009**, *11*, 2121–2130.

(452) Motokawa, N.; Miyasaka, H.; Yamashita, M.; Dunbar, K. R. An Electron-Transfer Ferromagnet with T_c = 107 K Based on a Three-Dimensional $[Ru_2]_2$/TCNQ System. *Angew. Chem. Int. Ed*. **2008**, *47*, 7760–7763.

(453) Kistenmacher, T. J.; Emge, T. J.; Bloch, A. N.; Cowan, D. O. Structure of the Red, Semiconducting Form of 4,4′,5,5′-Tetramethyl-$\Delta^{2,2'}$-bi-1,3-diselenole-7,7,8,8-tetracyano-*p*-quinodimethane, TMTSF-TCNQ. *Acta Crystallogr., Sect. B* **1982**, *38*, 1193–1199.

(454) Nakabayashi, K.; Nishio, M.; Kubo, K.; Kosaka, W.; Miyasaka, H. An Ionicity Diagram for the Family of $[\{Ru_2(CF_3CO_2)_4\}_2(TCNQR_x)]$ ($TCNQR_x$ = R-Substituted 7,7,8,8-Tetracyano-*p*-quinodimethane). *Dalton Trans*. **2012**, *41*, 6072–6074.

(455) Miyasaka, H. Control of Charge Transfer in Donor/Acceptor Metal–Organic Frameworks. *Acc. Chem. Res*. **2013**, *46*, 248–257.

(456) Lopez, N.; Zhao, H.; Prosvirin, A. V.; Chouai, A.; Shatruk, M.; Dunbar, K. R. Conversion of a Porous Material Based on a Mn^{II}–$TCNQF_4$ Honeycomb Net to a Molecular Magnet upon Desolvation. *Chem. Commun*. **2007**, 4611–4613.

(457) Jeon, I.-R.; Negru, B.; Van Duyne, R. P.; Harris, T. D. A 2D Semiquinone Radical-Containing Microporous Magnet with Solvent-Induced Switching from T_c = 26 to 80 K. *J. Am. Chem. Soc.* **2015**, *137*, 15699–15702.

(458) DeGayner, J. A.; Jeon, I.-R.; Sun, L.; Dincă, M.; Harris, T. D. 2D Conductive Iron-Quinoid Magnets Ordering up to T_c = 105 K via Heterogenous Redox Chemistry. *J. Am. Chem. Soc.* **2017**, *139*, 4175–4184.

(459) *Spintronics for Next Generation Innovation Devices*; Sato, K., Saitoh, E., Eds.; John Wiley & Sons: New York, 2015.

(460) Liu, L.; DeGayner, J. A.; Sun, L.; Zee, D. Z.; Harris, T. D. Reversible Redox Switching of Magnetic Order and Electrical Conductivity in a 2D Manganese Benzoquinoid Framework. *Chem. Sci*. **2019**, *10*, 4652–4661.

(461) Darago, L. E.; Aubrey, M. L.; Yu, C. J.; Gonzalez, M. I.; Long, J. R. Electronic Conductivity, Ferrimagnetic Ordering, and Reductive Insertion Mediated by Organic Mixed-Valence in a Ferric Semiquinoid Metal−Organic Framework. *J. Am. Chem. Soc*. **2015**, *137*, 15703–15711.

(462) Pedersen, K. S.; Perlepe, P.; Aubrey, M. L.; Woodruff, D. N.; Reyes-Lillo, S. E.; Reinholdt, A.; Voigt, L.; Li, Z.; Borup, K.; Rouzières, M.; Samohvalov, D.; Wilhelm, F.; Rogalev, A.; Neaton, J. B.; Long, J. R.; Clérac, R. Formation of the Layered Conductive Magnet $CrCl_2(pyrazine)_2$ Through Redox-Active Coordination Chemistry. *Nat. Chem*. **2018**, *10*, 1056–1061.

(463) Yang, C.; Dong, R.; Wang, M.; Petkov, P. S.; Zhang, Z.; Wang, M.; Han, P.; Ballabio, M.; Bräuninger, S. A.; Liao, Z.; Zhang, J.; Schwotzer, F.; Zschech, E.; Klauss, H.-H.; Cánovas, E.; Kaskel, S.; Bonn, M.; Zhou, S.; Heine, T.; Feng, X. A Semiconducting Layered Metal-Organic Framework Magnet. *Nat. Commun*. **2019**, *10*, 3260.

(464) Pinkowicz, D.; Southerland, H.; Wang, X.-Y.; Dunbar, K. R. Record Antiferromagnetic Coupling for a 3d/4d Cyanide-Bridged Compound. *J. Am. Chem. Soc*. **2014**, *136*, 9922–9924.

(465) Valdez-Moreira, J. A.; Thorarinsdottir, A. E.; DeGayner, J. A.; Lutz, S. A.; Chen, C.-H.; Losovyj, Y.; Pink, M.; Harris, T. D.; Smith, J. M. Strong π-Backbonding Enables Record Magnetic Exchange Coupling Through Cyanide. *J. Am. Chem. Soc*. **2019**, *141*, 17092–17097.

(466) Hua, C.; DeGayner, J. A.; Harris, T. D. Thiosemiquinoid Radical-Bridged Cr^{III}_2 Complexes with Strong Magnetic Exchange Coupling. *Inorg. Chem*. **2019**, *58*, 7044–7053.

(467) Eckberg, R. P.; Hatfield, W. E.; Losee, D. B. Unusual Magnetic Properties of Polymeric Cobalt(II) Monoglycerolate, a Compound Containing Alkoxo-Bridged Cobalt(II) Ions. *Inorg. Chem*. **1974**, *13*, 740–742.

(468) Pratt, F. L.; Baker, P. J.; Blundell, S. J.; Lancaster, T.; Green, M. A.; Kurmoo, M. Chiral-Like Critical Behavior in the Antiferromagnet Cobalt Glycerolate. *Phys. Rev. Lett*. **2007**, *99*, 017202.

(469) Kawamura, A.; Filatov, A. S.; Anderson, J. S.; Jeon, I.-R. Slow Magnetic Relaxation of Co(II) Single Chains Embedded Within Metal–Organic Superstructures. *Inorg. Chem*. **2019**, *58*, 3764–3773.

(470) Coronado, E.; Galán-Mascarós, J. R.; Martí-Gastaldo, C. A Neutral 2D Oxalate-Based Soluble Magnet Assembled by Hydrogenbonding Interactions. *Inorg. Chim. Acta* **2008**, *361*, 4017–4023.

(471) Shilov, G. V.; Nikitina, Z. K.; Ovanesyan, N. S.; Aldoshin, S. M.; Makhaev, V. D. Phenazineoxonium Chloranilatomanganate and Chloranilatoferrate: Synthesis, Structure, Magnetic Properties, and Mössbauer Spectra. *Russ. Chem. Bull. Int. Ed*. **2011**, *60*, 1209–1219.

(472) Li, R.; Xiao, Y.; Wang, S.-H.; Jiang, X.-M.; Tang, Y.-Y.; Xu, J.-G.; Yan, Y.; Zheng, F.-K.; Guo, G.-C. A 3D Metal–Organic Framework Built from Vanadate Clusters and Diamond Chains Showing Weak Ferromagnetic Single-Chain-Magnet Like Behavior. *J. Mater. Chem. C* **2017**, *5*, 513–517.

(473) Manson, J. L.; Conner, M. M.; Schlueter, J. A.; Lancaster, T.; Blundell, S. J.; Brooks, M. L.; Pratt, F. L.; Papageorgiou, T.; Bianchi, A. D.; Wosnitza, J.; Whangbo, M.-H. $[Cu(HF_2)(pyz)_2]BF_4$ (pyz = Pyrazine): Long-Range Magnetic Ordering in a Pseudo-Cubic Coordination Polymer Comprised of Bridging HF_2^- and Pyrazine Ligands. *Chem. Commun*. **2006**, 4894–4896.

(474) Wu, Y.-L.; Guo, F.-S.; Yang, G.-P.; Wang, L.; Jin, J.-C.; Zhou, X.; Zhang, W.-Y.; Wang, Y.-Y. Two Isostructural Metal−Organic Frameworks Directed by the Different Center Metal Ions, Exhibiting the Ferrimagnetic Behavior and Slow Magnetic Relaxation. *Inorg. Chem*. **2016**, *55*, 6592–6596.

(475) López-Cabrelles, J.; Giménez-Marqués, M.; Espallargas, G. M.; Coronado, E. Solvent-Free Synthesis of a Pillared Three-Dimensional Coordination Polymer with Magnetic Ordering. *Inorg. Chem*. **2015**, *54*, 10490–40496.

(476) Zhang, B.; Zhang, Y.; Zhang, J.; Hao, X.; Zhu, D. $Mn(C_2O_4)(H_2O)_{0.25}$: An Antiferromagnetic Oxalato-Based Cage Compound. *Dalton Trans*. **2011**, *40*, 5430–5432.

(477) Zeng, M.-H.; Zhang, W.-X.; Sun, X.-Z.; Chen, X.-M. Spin Canting and Metamagnetism in a 3D Homometallic Molecular Material Constructed by Interpenetration of Two Kinds of Cobalt(II)-Coordination-Polymer Sheets. *Angew. Chem. Int. Ed*. **2005**, *44*, 3079–3082.

(478) Armentano, D.; Mastropietro, T. F.; De Munno, G.; Rossi, P.; Lloret, F.; Julve, M. New Extended Magnetic Systems Based on Oxalate and Iron(III) Ions. *Inorg. Chem*. **2008**, *47*, 3772–3786.